ISSN: 2620-2832

SERBIATRIB '19

Vol. 1, No. 1 (2019)

Proceedings on Engineering Sciences

16th International Conference on Tribology

15 – 17 May 2019, Kragujevac, Serbia

SERBIATRIB '19

SERBIATRIB '19

SERBIATRIB '19

ISSN: 2620-2832

Proceedings on
Engineering Sciences

Serbian Tribology Society

University of Kragujevac
Faculty of Engineering

Proceedings on Engineering Sciences

16th International Conference on Tribology

15 – 17 May 2019, Kragujevac, Serbia

SERBIATRIB ‘19

EDITOR: Slobodan Mitrović

SERBIATRIB ‘19

Proceedings on Engineering Sciences
16th International Conference on Tribology – SERBIATRIB '19

Vol. 1, No. 1 (2019)

ISSN: 2620-2832

Editor:	**Slobodan Mitrović** Faculty of Engineering, University of Kragujevac
Editorial Assistant:	**Dragan Džunić** Faculty of Engineering, University of Kragujevac
Technical editor:	**Marko Pantić** Faculty of Engineering, University of Kragujevac
Publisher:	**Faculty of Engineering, University of Kragujevac** Sestre Janjić 6, 34000 Kragujevac, Serbia
Editorial Address:	Faculty of Engineering, University of Kragujevac, Sestre Janjić 6, 34000 Kragujevac, Serbia
Frequency:	2 issues per year
Printed by:	**Inter Print** Jurija Gagarina 12, 34000 Kragujevac, Serbia
Circulation:	150 copies

The publication of this Proceedings was financially supported by the Ministry of Education, Science and Technological Development of the Republic of Serbia.

Supported by

Ministry of Education, Science and Technological Development of the Republic of Serbia

Conference Founder

Branko Ivković	Serbian Tribology Society

International Scientific Committee

Miroslav Babić, President	University of Kragujevac (Serbia)
Aleksandar Marinković	University of Belgrade (Serbia)
Aleksandar Vencl	University of Belgrade (Serbia)
Andrei Tudor	University Politehnica of Bucharest (Romania)
Bharat Bhushan	The Ohio State University (USA)
Branko Škorić	University of Novi Sad (Serbia)
Cristiano Fragassa	University of Bologna (Italy)
Dušan Stamenković	University of Niš (Serbia)
Đorde Vukelić	University of Novi Sad (Serbia)
Emilia Assenova	Society of Bulgarian Tribologists (Bulgaria)
Fatima Živić	University of Kragujevac (Serbia)
Friedrich Franek	AC^{2}T research GmbH, Wiener Neustadt (Austria)
Gordana Globočki Lakić	University of Banja Luka (Bosnia and Herzegovina)
Hakan Kaleli	Yildiz Technical University (Turkey)
Igor Budak	University of Novi Sad (Serbia)
J. Paulo Davim	University of Aveiro (Portugal)
Konstantinos-Dionysios Bouzakis	Aristotle University of Thessaloniki (Greece) Turkish-German University (TAU) (Turkey)
Lorena Deleanu	University Dunarea de Jos of Galati (Romania)
Mara Kandeva	Technical University of Sofia (Bulgaria)
Mehmet Baki Karamis	Erciyes University (Turkey)
Michel Fillon	University of Poitiers (France)
Niculae Napoleon Antonescu	Petroleum-Gas University of Ploiesti (Romania)
Nikolai Myshkin	National Academy of Sciences of Belarus (Belarus)
Nikolaos M. Vaxevanidis	School of Pedagogical and Technological Education (Greece)
Pantelis G. Nikolakopoulos	University of Patras (Greece)
Razvan George Ripeanu	Petroleum-Gas University of Ploiesti (Romania)
Sergey V. Fedorov	Kaliningrad State Technical University (Russian Federation)
Sergei Yu. Tarasov	Institute of Strength Physics and Materials Sciences (Russian Federation)
Slobodan Mitrović	University of Kragujevac (Serbia)

Organising Committee

Slobodan Mitrović, President	University of Kragujevac (Serbia)
Dragan Džunić, Conference Secretary	University of Kragujevac (Serbia)
Marko Pantić, Technical Coordinator	University of Kragujevac (Serbia)
Fatima Zivić	University of Kragujevac (Serbia)
Suzana Petrović Savić	University of Kragujevac (Serbia)

Preface

The International Conference on Tribology – SERBIATRIB, is traditionally organized by the Serbian Tribology Society every two years, since 1989. The previous conferences were held in Kragujevac (1989, 1991, 1993, 1999, 2005, 2007, 2011 and 2013, 2017), Herceg Novi (1995), Kopaonik (1997), Belgrade (2001, 2003, 2009 and 2015). This year the 16th International Conference on Tribology – SERBIATRIB '19 also takes place on May 15-17, 2019 in Kragujevac.

This Conference is organized by the University of Kragujevac, Faculty of Engineering and the Serbian Tribology Society (STS). Organizing Scientific Conferences, STS plays a significant role in helping engineers and researchers to introduce in the fundamentals of tribology and to present their experience, solutions and research results.

The scope of the 16th International Conference on Tribology – SERBIATRIB '19 embraces the state of art and future trends in tribology research and application. The following two aspects of tribology practice require special attention. Firstly, the requirement for higher productivity of machinery means that machines must operate under higher loads and at higher speeds and temperatures, and that is why finding the right solutions for tribological processes is extremely important. Secondly, the good tribology knowledge can greatly contribute to the saving of material and energy.

The Conference program generally includes the following topics: fundamentals of friction and wear; tribological properties of solid materials; surface engineering and coating tribology; lubricants and lubrication; tribotesting and tribosystem monitoring; tribology in machine elements; tribology in manufacturing processes; tribology in transportation engineering; design and calculation of tribocontacts; sealing tribology; biotribology; nano and microtribology and other topics related to tribology.

All together 93 papers of authors from 30 countries (Algeria, Austria, Belgium, Bosnia and Herzegovina, Brazil, Bulgaria, Croatia, Czech Republic, Egypt, France, Germany, Greece, Hungary, India, Iraq, Italy, Lithuania, Malaysia, México, Montenegro, Nigeria, Republic of Srpska, Tajikistan, Romania, Russia, Serbia, Slovakia, Slovenia, Turkey, UK, USA) are published in the Proceedings.

All papers are classified into nine chapters:

- Plenary lectures (4)
- Tribological Properties of Solid Materials (17)
- Surface Engineering and Coating Tribology (14)
- Tribology of Machine Elements and Systems (16)
- Tribology of Manufacturing Processes (14)
- Lubricants and Lubrication (11)
- Tribometry (11)
- Biotribology (6)

It was a great pleasure for us to organize this Conference and we hope that the Conference, bringing together specialists, research scientists and industrial technologists, and Proceedings will stimulate new ideas and concepts, promoting further advances in the field of tribology. The Editor would like to thank the Scientific and the Organizing Committee and all those who have helped in making the Conference better.

The Conference is financially supported by the Ministry of Education, Science and Technological Development, Republic of Serbia, Rtec Instruments, Trokut Test, MC Labor, Labena, UTS Scientific Instruments and Lotrič Metrology.

We wish to all participants a pleasant stay in Kragujevac and we are looking forward to seeing you all together at the 17th International Conference on Tribology – SERBIATRIB '21.

Kragujevac, May 2019

Editor
Slobodan Mitrović

Contents

Plenary Lectures

Tribological Properties of Solid Materials

Surface Engineering and Coating Tribology

Tribology of Machine Elements and Systems

Lubricants and Lubrication

Tribometry

Biotribology

Plenary Lectures

Serbian Tribology Society

SERBIATRIB '19

16th International Conference on Tribology

Faculty of Engineering
University of Kragujevac

Kragujevac, Serbia, 15 – 17 May 2019

EXPERIMENTAL STUDY OF MOS_2 COATED GEARS TESTED IN VACUUM AFTER EXPOSURE TO HUMIDITY

Iqbal SHAREEF[1,*], Timothy KRANTZ[2], Zachary CAMERON[2], Tysen MULDER[2]
[1]Bradley University, Peoria, IL, USA
[2] NASA Glenn Research Center, Cleveland, OH, USA
*Corresponding author: shareef@bradley.edu

Abstract: *Space Industry commonly uses molybdenum disulphide (MoS_2) as a solid lubricant film on gears in a variety of mechanisms. These mechanisms are often exposed to humid air during fabrication, integration into higher-level assemblies, and storage. It is generally accepted that operating MoS_2 films in humid environments has a detrimental effect on the film's lifetime compared to operation in vacuum. However, the effect of exposure of such films to humid air with subsequent operation in vacuum is not well understood. In this study, a sputtered MoS_2 dry film lubricant coating was applied to steel gears, which were then tested in a vacuum environment. Half of the spur gears coated with MoS_2 were exposed to approximately 58 percent relative humidity for up to 77 days before testing. The other half set of gears were not exposed to humid air before testing. All gears were tested in a vacuum gear test rig. Gear tooth forces and the radial displacement of the gears were recorded during testing. These data together with photos, videos, Scanning Electron Microscope (SEM) inspections of worn gears, and Energy-Dispersive X-ray (EDX) spectra were analysed. For purposes of this study, the coating durability was defined as the time until the start of the coating degradation as was evident from increase of friction. Assessment of the results obtained from all experiments indicate that gears exposed to humid air prior to operation in vacuum showed nearly 36 percent reduction in coating durability, on average. SEM and EDX analyses of wear debris indicate mainly MoS_2 was present with minor traces of other elements. The worn surfaces of gears show significant content of MoS_2 still remaining in the gear teeth's contact area.*

Keywords: *Molybdenum Disulfide, Solid Lubricant, Thin Film, Surface Coating, Spur Gears, Rolling Contact, Mild Wear, Debris Formation.*

1. INTRODUCTION

The purpose of this work was to study the effect of humid air exposure on the durability of a molybdenum disulfide (MoS_2) dry film lubricant coating on spur gears operated in vacuum. Certain extreme space environments preclude the use of wet lubrication. For such situations, MoS_2-based coatings are often used for a wide variety of space mechanisms. Such coatings are typically exposed to humid air environments during integration, ground operations, and storage prior to launch. It is well known that if a mechanism with a MoS_2 sputtered coating is operated in humid air instead of vacuum its durability is reduced. However, the practical implications of exposing MoS_2 coatings to humidity for extended periods of time, and then subsequently operating them in vacuum, are not fully understood.

Lince, Loewenthal, and Clark provide a recent, and thorough, discussion of previous studies regarding MoS_2 aging and oxidation. They comment that life test data for sputter-deposited MoS_2 coatings that were held in long-term storage are uncommon [1]. They also completed and reported a study on the degradation of three nanocomposite MoS_2 coatings after storage in humid air. The tests used to evaluate coating endurance were pin-on-disk tests, and storage times were up to 2.3 years. They found that exposure to humid air could degrade the endurance of the coatings by up to 55 percent. The severity of degradation depended on both the duration of exposure and the composition of the coating.

A dedicated study of such effects has not been conducted for MoS_2 coatings on gear teeth. The purpose of this study was to investigate the influence of exposure to humid air on the subsequent durability of a sputtered MoS_2 coating on spur gears. While previous work by others studied nanocomposite MoS_2 coatings [1], the focus of this work was a pure MoS_2 coating.

2. EXPERIMENTAL METHODOLOGY

2.1 MoS_2 Coated Test gears

Readily available stock gears with the appropriate center distances to fit in the test stand were selected and customized for this study. The customizations of the stock gear design were the bore diameters and the face widths. The pinions and gears were 3mm module spur gears with standard tooth proportions. The pinions had 26 teeth and a 13 mm face width. The gears had 48 teeth and a 10 mm face width. The study used six pairs of pinions and gears made from S45C steel (equivalent to AISI 1045). The teeth were induction hardened to surface hardness of 50-60 HRC, and then finished ground.

All twelve test pinions and gears were coated with sputtered MoS_2. Because of the sputtering chamber capacity, two coating runs were required. Witness coupons were in the chamber during sputtering. The thickness of the coating on the witness coupons was reported by the vendor to be 37,000 angstroms for the first run and 30,000 angstroms for the second run. After coating, the test gears were sealed in bags using a dry inert cover gas. Pinions and gears to be tested as unexposed remained in the sealed bags until they were to be installed in the test rig. The time from the opening of the bag, until the gears were in a vacuum condition in the test rig, was minimized to all practical extent.

Prior to sputtering, the tooth surface roughness was measured along the involute profile direction of a randomly selected pinion tooth using a stylus profilometer. An untested coated pinion tooth that had been exposed to humidity was also inspected. The surface roughness data were filtered using an ISO standard Gaussian filter with 0.8 mm cutoff and 300:1 bandwidth. The resulting calculated roughness average value of 0.42 micrometer Ra was the same for both of the profilometer traces. The peak-to-valley range of the filtered roughness data was approximately the same as the measured coating thickness. The roughness topography features were the same prior to and after sputtering as shown in Fig. 1.

One half of the available mating tooth surface pairs were exposed to humid air prior to testing. The exposure was done in a closed chamber with the gears placed on a perforated plate. Beneath the plate was a saturated solution of water and sodium bromide. The saturated salt solution provided a relative humidity of approximately 58 percent, this value being near to the upper limit 60 percent relative humidity of certain storage conditions for the mechanisms of interest.

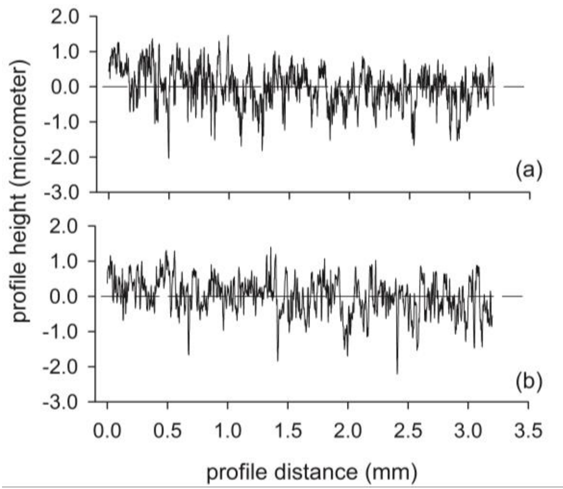

Figure 1. Surface roughness profiles along the involute direction of pinion teeth: (a) Prior to sputtering, (b) After sputtering, and exposure to humid air.

2.2 Gear Test Rig

To accomplish gear testing, a vacuum test rig, previously used for roller testing [2-4], was adapted for gear testing. To adapt the rig, the spacing from the input to the output shaft was increased from 36 mm to 112 mm. Otherwise, the rig setup was the same as had been used for roller testing.

The vacuum gear rig is depicted as a schematic in Figure 2. The pinion is driven by a variable speed electric motor. A magnetic-particle brake attached to the output shaft imposes torque on the gear. The position of the pinion is controlled by a pressurized air cylinder, which moves the drive motor plate about a pivot point. Increasing the air cylinder's height swings the pinion, in an arc motion, into mesh with the gear. The pressure to the cylinder, and thereby shaft center distance, is adjusted by a hand-operated valve. A linear variable displacement transducer (LVDT) measures the position of the drive motor plate relative to the bedplate the output of which was used to establish the proper operating center distance. The rig turntable, when rotated, provides controlled misalignment of shafts for roller experiments. For gear testing, the turntable was adjusted to provide for an aligned shaft condition. A turbomolecular pump, assisted by a scroll pump, provides vacuum in the test chamber. Ferrofluid seals maintain the vacuum at the shaft-chamber interfaces. The typical condition in the test chamber is a pressure of $3x10^{-7}$ Torr. The most prevalent remaining constituent in the chamber during testing is water vapor as was determined using a residual gas analyzer.

The torque on the output shaft is measured by a strain-gage type torque meter with a capacity of 22 N-m (200 in-lb). Calibration was done in place using deadweights acting on a torque arm attached at the test gear position and reacted by the output shaft to ground.

The force created by the meshing gear teeth can be described as three orthogonal forces. Each of these force components influences a sensor described with the aid of Figure 2.

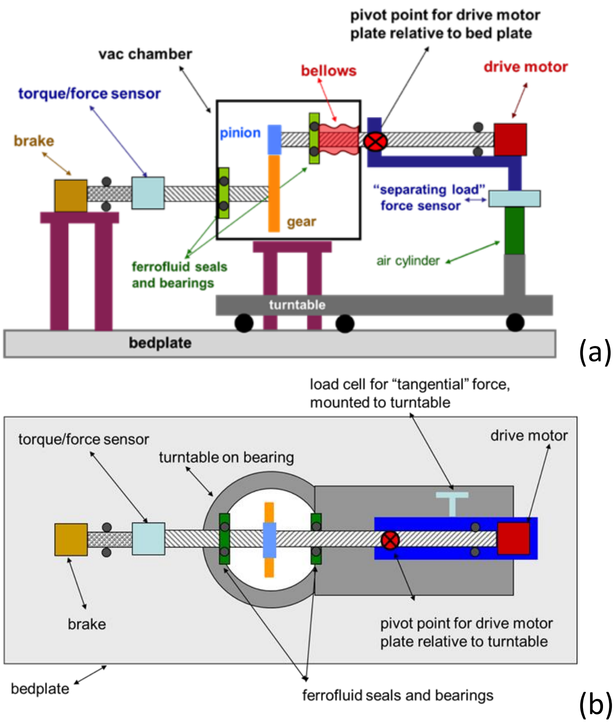

Figure 2. Schematic representation of vacuum gear rig: (a) Side view, (b) Overhead view.

The tooth force component directed tangent to the pitch circle is termed the tangential force. The torque on the gear is a product of the tangential force and the operating pitch radius. The gear tooth tangential force attempts to rotate the drive motor plate about a pivot axis, but the table is constrained to the turntable through a load sensor termed as the "tangential" force sensor in Figure 2. The separating force is the tooth force directed along the line joining the gear centers, which acts through a pivot axis and attempts to tilt the drive motor table. This motion is resisted by the air cylinder through a sensor termed the "separating load" force sensor. Because the drive motor plate is not balanced about the pivot point, the force measured on this "separating load" force sensor is a combination of the gear separating force action and the unbalanced overhung weight of the motor and plate. The third component of gear tooth force acts along the axial direction of the gear shaft, the gearing thrust force. The force is measured using a strain-gage type force sensor that is integrated with the torque meter. Although spur gears theoretically create zero thrust forces, in practice a thrust force is created because of inevitable manufacturing tolerances and small mounting misalignments. The magnitude of the resulting thrust force depends in part on the friction between the mating gear teeth. The action of spur gears creating a thrust force is analogous to the friction-dependent thrust forces created by misaligned rollers [2].

Shaft speeds and total number of shaft revolutions were measured using encoders on each shaft. The encoder pulses were counted and recorded via a digital pulse counter. The encoders provide 6,000 pulses for each shaft revolution.

The LVDT measures the tilting position of the drive motor plate. The tilting of the plate changes the pinion-to-gear center distance, and so the LVDT output thereby measures the operating center distance of the gears. As the gears operate, the operating center distance changes slightly because of the gearing action. As the tooth contact position on the pinion moves from the dedendum, through the pitch point, and then to the addendum region, the friction force changes direction. This changing friction force causes slight changes in the instantaneous center distance, because of elastic deflections, and thereby the friction condition affects the output of the LVDT.

The gear teeth surface conditions were photographed at regular intervals during testing through a viewport. The images were captured using a 12-megapixel digital single-lens reflex camera with a 150 mm micro lens.

2.3 Experimental Procedure

The experimental approach was to conduct an equal number of tests using unexposed and exposed surfaces. The test matrix is shown in Table 1. The pinions and gears were assigned randomly as six test pairings per Table 1. With the ability to test front (side “A”) and back (side ”B”) faces of each tooth, 12 tests were possible. Test article pairings 1 through 4 were assigned to have side “A” tested with zero exposure to humid air, except for some minimal exposure time in air during installation of the MoS_2 coated gears into the test rig. For purposes of this study, such minimal exposure is considered as zero exposure for all analysis purposes. For test article pairings one through four, once sides “A” of the teeth were tested, the pair was placed into the humidity exposure chamber to begin the exposure time for the tooth sides “B”. For gear pair five, there was zero exposure to humidity before sides “A” of the teeth was tested. Then the vacuum test rig was opened for minimum amount of time needed to remove the gears from the mounting shafts and immediately reinstall the gears for testing of teeth sides “B” as also unexposed. For test article pair six, the pinion and gear were placed into the humidity exposure chamber at the beginning of the test program to obtain a long exposure time while testing the other gears. Both sides “A” and “B” of pair 6 were tested after an exposure time of 77 days. The exposure times for other test were less than 77 days as was dictated by the testing pace and sequence.

As the test sequence progressed, it was decided that photo documentation of the conditions of the teeth prior to testing might prove insightful. Beginning with the fifth test in the testing order sequence (test MoS_2 4-A, per Table 1), the first step of the testing sequence was to document the visual condition of each gear with digital photographs. Next, the gear pair was mounted onto the test rig shafts, and then the chamber vacuum condition was established over several hours (typically overnight). The chamber pressure was $7x10^{-7}$ Torr or less at the beginning of each test. Figure 3 shows a pair of the MoS_2 coated test gears out of sealed bags just prior to test, and in the test chamber just prior to closing the vacuum chamber door for testing.

Testing was done at a constant motor speed, and brake torque. The test speed was 80 rpm for the pinion and consequently 43.3 rpm for the gear. The speed was selected as the maximum speed that did not induce any significant rig dynamic loading or vibrations as had been determined by previous testing of similar test gears. The torque was 6.8 Nm for the gear as applied by the brake and measured by torque sensor. The power transmitted was 31 watts. The torque was selected to provide tooth load intensity (force per unit face width) similar to the tooth load intensity for the mechanisms of interest. Testing for endurance of the coatings typically required durations longer than a working day, and unattended testing was not desirable. The testing was paused overnight, as needed, with the test chamber vacuum maintained by continuous operation of the turbo-pump. Testing would then be resumed the following day.

The test progression was monitored by visual inspection of the tooth surfaces through a viewport, aided at times by a strobe light to "freeze" the rotating motion of the gears. The visual condition was also recorded by digital photographs illuminated by a short duration flash through a second viewport that provided a view of the gear teeth, but not of pinion teeth. In addition, a video camera was used to continuously record the contacting region of the gear and pinion at all times except during the visual examination with a strobe light.

Table 1. Test matrix, naming conventions, and test sequence.

Test Name	Test Article Pairing	Pinion Serial Number	Gear Serial Number	Tooth Side Loaded	Exposed	Total Exposure Time (days)	Testing Order Sequence
MOS_2 1-A	1	P4	G1	A	No	-	1
MOS_2 1-B				B	Yes	10	3
MOS_2 2-A	2	P6	G6	A	No	-	2
MOS_2 2-B				B	Yes	28	6
MOS_2 3-A	3	P2	G2	A	No	-	4
MOS_2 3-B				B	Yes	17	9
MOS_2 4-A	4	P1	G3	A	No	-	5
MOS_2 4-B				B	Yes	17	10
MOS_2 5-A	5	P3	G5	A	No	-	7
MOS_2 5-B				B	No	-	8
MOS_2 6-A	6	P5	G4	A	Yes	77	11
MOS_2 6-B				B	Yes	77	12


(a)

(b)

Figure 3. Test gears: (a) Just prior to testing, (b) Installed in rig just prior to closing test chamber.

The test progression was monitored by displays of the sensor data plotted as functions of pinion revolutions. Previous developmental tests revealed that as wear severity and friction of the MoS_2 coating increased, sensor outputs became more erratic even though their mean value remains nearly same. For example, when friction of the gear teeth increases, the range of the instantaneous separation force increases even though the mean value over time may still be the same. This phenomenon is the result of the tooth friction force reversing direction as the tooth contact passes through the pitch point. Thereby, the friction force first adds to, and then subtracts from, the magnitude of the separating force during the tooth mesh cycle. With higher tooth friction the excursions from the mean value becomes larger. These observations and experience in health monitoring of geared machines led to the definition and use of “condition indicators” as a means to monitor the overall capability of the MoS_2 films to provide low friction.

Condition indicators were defined as follows. Data records were collected for 1 second at 1 kHz sampling rate. For each second of data recorded, the standard deviation was calculated as the “condition indicator”, stored, and plotted as a function of accumulated pinion revolutions. Such condition indicators proved to be reliable indicators of a change in the MoS_2 coating’s performance. Figure 4(a) provides a trend plot from test MoS_2 1-B of the condition indicator for the LVDT sensor that measures gear center distance changes. Marked on the plot is the indication where the MoS_2 began to become compromised. Also marked are three regions: Region I being the break-in and smooth running regime, Region II where the MoS_2 first showed indication of being compromised, and Region III being a significant friction regime. An example of raw recorded data, from which a “condition indicator” was calculated, is shown in Figure 4(b) for the thrust force sensor during operation in Region III. In plot of 4(b) there was relatively high tooth friction during the last 400 samples of this particular data record causing a varying thrust force.

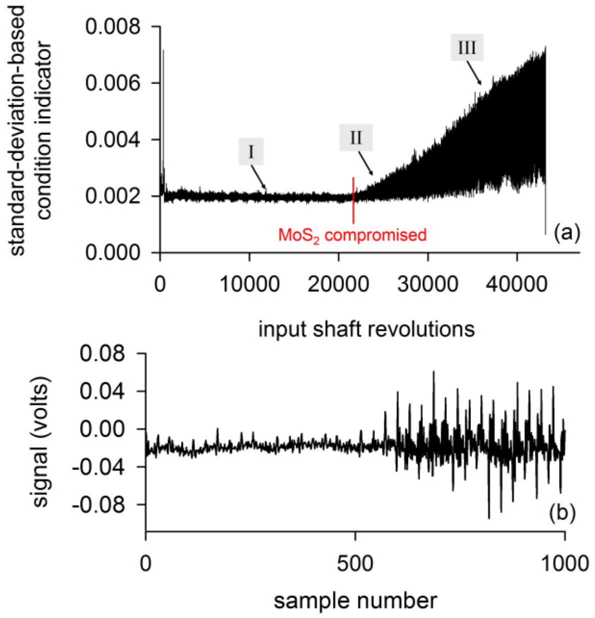

Figure 4. Typical trend and features of a condition indicator of MoS_2 film function: (a) Trend of condition indicator for the center distance (LVDT sensor) for test 1-B, (b) Typical data record for calculation of standard-deviation-based condition indicator.

Film durability was determined using the condition indicator trend plots. The film durability was defined as the number of pinion revolutions until the film compromise started, as indicated on Figure 4. The film compromise was defined as the very beginning of progressive degradation of the film’s performance. A mechanism may continue to perform its intended function for some time after such film degradation begins. For this study defining the durability as the beginning of performance degradation provided a useful comparison of the film durability with and without exposure to humid air.

3. RESULTS

The results of quantitative measures of film durability will be discussed first. As described in the previous section, “condition indicators” were calculated from sensor data. A condition indicator value was calculated every second for each force and displacement sensor monitored. Figure 4(a) is an example of condition indicator data trend plot from the test 1-B. The number of pinion revolutions corresponding to the start of film compromise, as marked on Figure 4, was determined for each test by visual inspection of such trend plots. The film's durability measure was determined from three sensors: the gear center distance, the gear thrust force, and the gear tangent force sensors. For each test, film durability was calculated as the average of the cycles till compromised indicator from each of the three sensors. The results are shown in Table 2.

Table 2. Test Results of Film Durability.

		Film Durability (pinion revolutions)			
Test Name	Exposure (days)	Center Distance	Thrust Force	Tangent Force	Average Value *
MOS2 1-A	0	52,000	52,000	56,000	53,333
MOS2 2-A	0	59,000	61,000	65,000	61,667
MOS2 3-A	0	207,000	184,000	180,000	190,333
MOS2 4-A	0	86,000	69,000	94,000	83,000
MOS2 5-A	0	125,000	125,000	136,000	128,667
MOS2 5-B	0	83,000	80,000	89,000	84,000
MOS2 1-B	10	21,000	20,000	22,000	21,000
MOS2 2-B	28	69,000	55,000	74,000	66,000
MOS2 3-B	17	59,000	65,000	66,000	63,333
MOS2 4-B	17	81,000	78,000	95,000	84,667
MOS2 6-A	77	84,000	76,000	88,000	82,667
MOS2 6-B	77	70,000	71,000	74,000	71,667

* average value is the average of the 3 colums to the left

unexposed group	average = 100,200	median = 83,500
exposed group	average = 64,900	median = 68,800
percent reduction	35%	18%

As can be seen from Table 2, on average the film durability was shorter for gears exposed to humid air compared to gears with zero exposure. The film durability for gears with zero exposure ranged from 53,300 to 190,300 pinion revolutions with an average value of 100,200 and a median value of 83,500 revolutions. The film durability for gears exposed to humid air ranged from 21,000 to 84,700 pinion revolutions with an average value of 64,900 and a median value of 68,800 revolutions. Using the unexposed-gear film durability as a baseline, the exposure reduced the film durability by 35 percent based on average values or 18 percent based on median values. These reductions in film durability are similar in magnitude compared to the 55 to 20 percent range of reductions reported by Lince, Loewenthal, and Clark [1].

The film durability values, from the "Average Value" column of Table 2, are plotted as a function of the duration of exposure to humid air in Figure 5. The plot shows that while as a group the durability was longest for zero days of exposure, there is no clear trend of rate of reduction with exposure time. The range of scatter of the film durability for six tests at zero time of exposure is greater than the difference between average durability of exposed and unexposed gears.

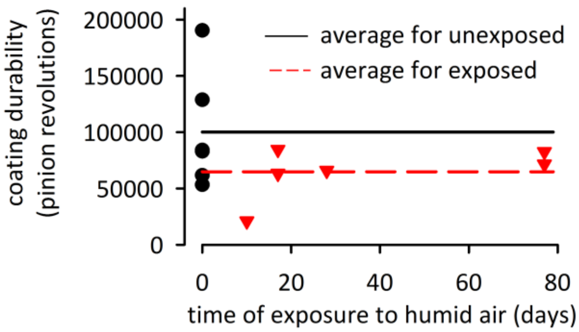

Figure 5. Film durability as function of time of exposure to humid air.

The wear of the MoS_2 films was also evaluated with high-resolution optical microphotographs, profilometry scans of the tooth faces, and SEM inspections. During initial running of each gear pair, it was observed that it required very few tooth meshing cycles for the MoS_2 coating's appearance to change. The tooth surface's appearance became glossier and more reflective after only a few revolutions. However, subsequent further visual changes to the tooth surfaces occurred at a very slow and steady rate. Figure 6 illustrates typical results of how the gear surface's visual appearance changed during a test. The first image from left to right shows the teeth prior to any running. The second image was taken after only 1 percent of the total test duration. The other two images of Figure 6 show the teeth after 50 percent and 99 percent of the test duration. These images indicate little change in gear tooth appearance in comparison to the change depicted in the initial 1 percent of the test.

Wear, and running in of pinion teeth were assessed using a stylus profilometer. The teeth were inspected moving the stylus with a 2- m radius conisphere tip across the face width. Because the mating gear tooth face width was slightly less than that of the pinion, there were regions of the pinion tooth near each edge that did not experience contact with the gear.

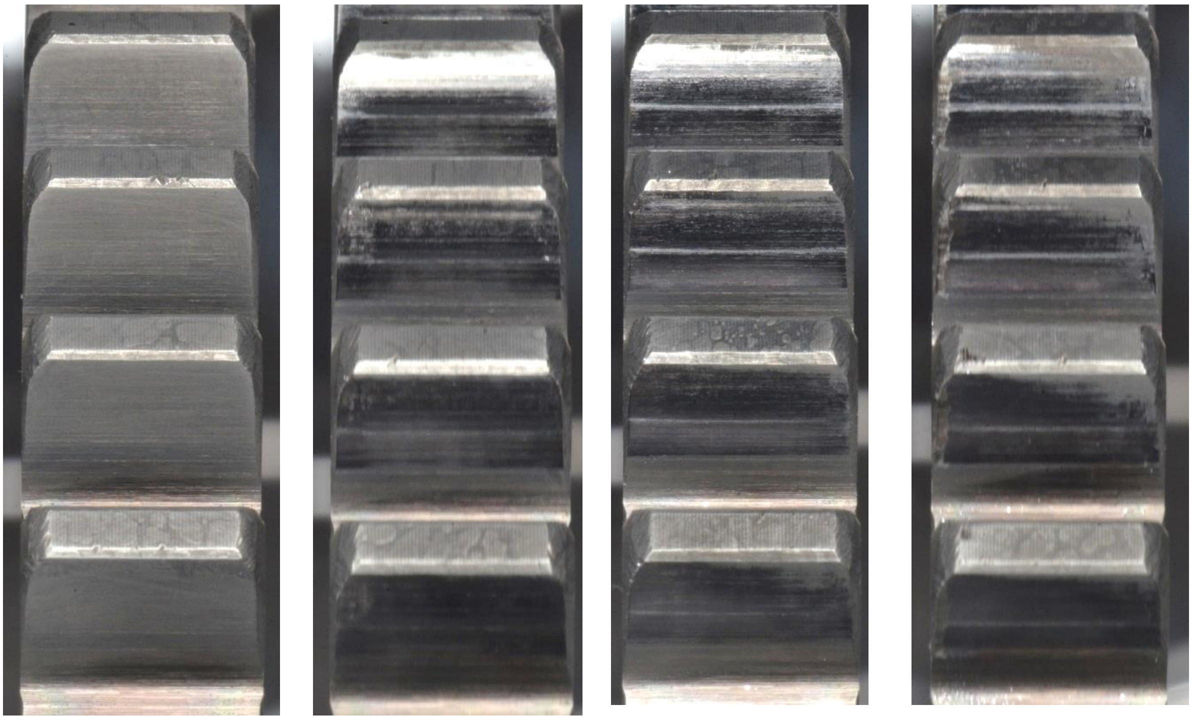

Figure 6. Gear teeth surface appearance for different durations of testing.

The data were processed to remove a least-squares linear form, using only the small regions from each edge of the trace that did not experience contact to accomplish the form removal. Traces of teeth prior to test were collected and processed in the same manner. Typical results of the inspections are provided in Figure 7. The data plots of Figures 7(a) and 7(b) is for teeth prior to test. The surfaces show some waviness and some peak and valley features, with peak to valley distances on order of 3 micrometers. The data plots of Figures 7(c) and 7(d) are for tested teeth, and there is an overall wear depth of about 2 micrometers, of which there are some worn regions that are very smooth.

After 77 days of exposure to humid air, small areas of reddish-brown coloration were noted on some teeth of gear set 6. Figure 8 is an example of the noted red-brownish colored spots seen on gear teeth testing in Test 6-A before testing. Close study of digital photographs of the pinions and gears recorded prior to testing revealed that similar spots appeared as early as 17 days after exposure to humidity. However, not all teeth exposed to humidity had colored spots that could be detected. For the pinion and gear pair exposed for 77 days, there were more red-brownish spots on the gear than there were on the pinion.

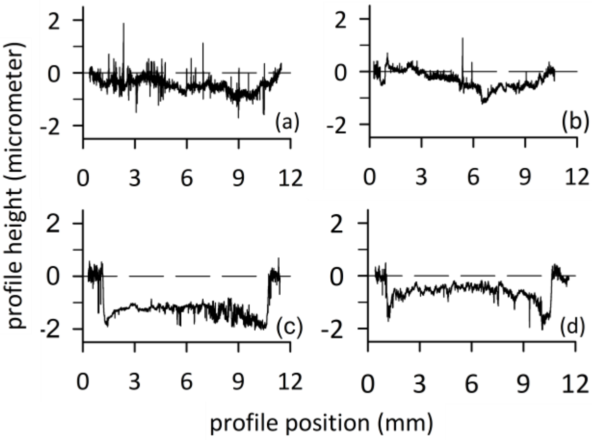

Figure 7. Profilometer inspections of pinion teeth with traces along the face width direction: (a) & (b) Prior to test, and (c) & (d) After test.

Teeth with noticeable spots were inspected using a scanning electron microscope (SEM). SEM images were taken at six increasing levels of magnification, and are provided in Figure 9. The image orientation has the gear tooth face width direction in the vertical direction. The vertical lines are topography resulting from grinding of the teeth. This region inspected by SEM revealed that the colored areas included raised material above the surrounding surface.

The highest magnification image reveals details suggesting a "growth" pushing aside and/or through the film.

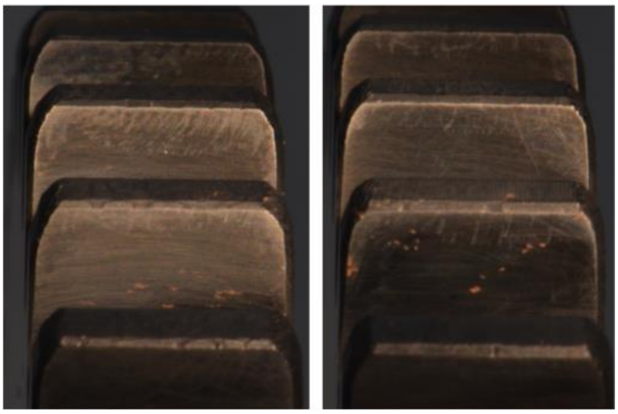

Figure 8. Red-brown coloration noted after 77 days exposure to humid air from Test 6-A Gears.

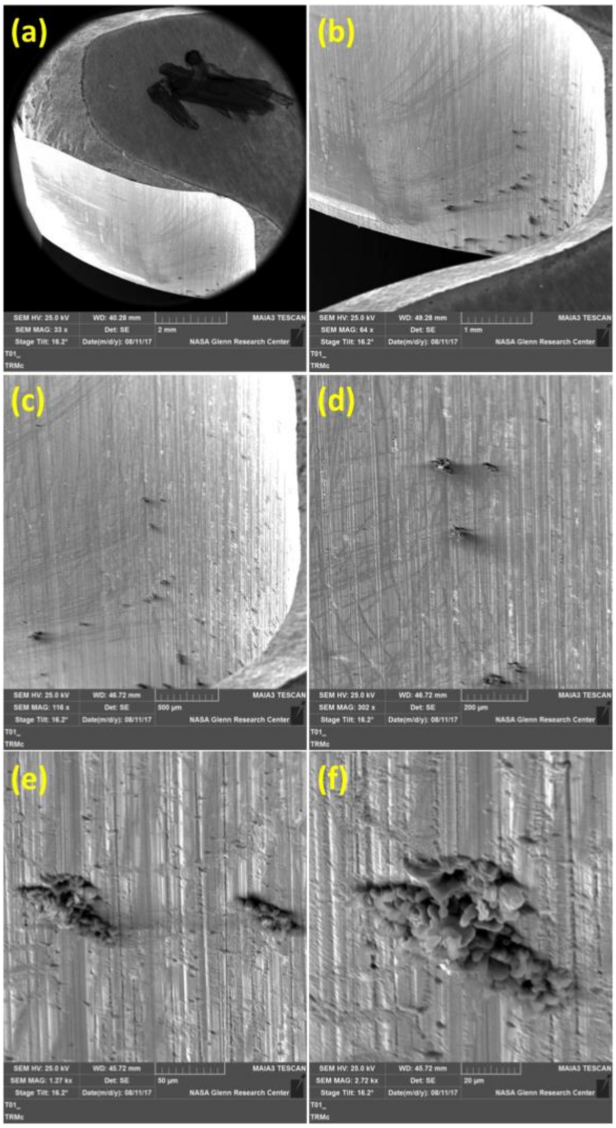

Figure 9. SEM Photos of a region having red-brown coloration at six increasing levels of magnification from Test 6-A pinion. The vertical direction is the tooth's face width direction.

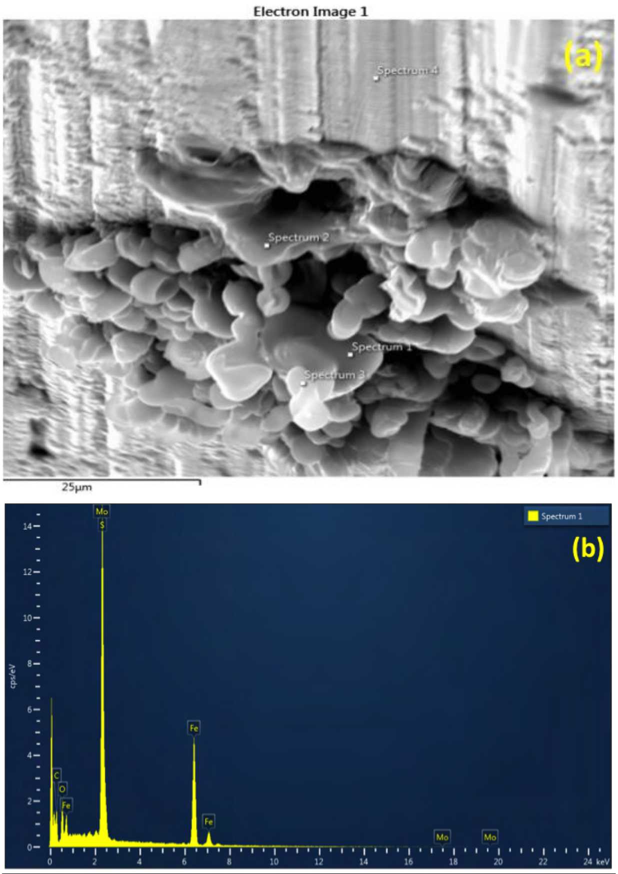

Spectrum Label	Spectrum 1	Spectrum 2	Spectrum 3	Spectrum 4
C	36.83	35	36.07	32.53
O	24.63	24.82	25.84	22.7
Si		0.3		
S	10.09	10.39	9.98	10.58
Mn			0.17	0.24
Fe	14.27	13.86	12.31	16.53
Ni		0.28	0.28	
Mo	14.19	15.35	15.34	17.41
Total	100	100	100	100

Statistics	C	O	Si	S	Mn	Fe	Ni	Mo
Max	36.83	25.84	0.3	10.58	0.24	16.53	0.28	17.41
Min	32.53	22.7	0.3	9.98	0.17	12.31	0.28	14.19
Average	35.11	24.5		10.26		14.24		15.57
Std. D	1.87	1.31		0.28		1.74		1.34

Figure 10. SEM inspection using energy-dispersive spectroscopy: (a) Regions inspected, per markings, (b) Spectrum #1 of 4 taken from region 1, typical of all four inspections.

Figure 10(a) provides another SEM image of a similar structure as that of Figure 9(f), from a slightly different viewpoint. During this inspection, energy-dispersive spectroscopy (EDX) was done at the four locations as marked by rectangular regions on Fig. 10(a). The resulting spectrum of Fig. 10(b) is typical of all four inspections. The most prominent peak of the spectrum is associated with Mo (molybdenum), and S (Sulphur). The second prominent peak is associated with Fe (iron). It is speculated that iron oxidation was occurring at the MoS_2 film-substrate interface and progressed to eventually become evident at the surface.

Study of profilometry data of teeth, prior to test, revealed an inspection with an interesting topography that suggests a fortuitous tracing over a region such as revealed in the SEM images of Figures 9(b) and 10(a). The profilometry data of this inspection, plotted using three different aspect ratios, are provided in Figure 11. The inspection was of pinion P5, in the face width direction, tooth side "B" that later was subjected to test MoS_2 6-B per Table 1. Figure 11(a) reveals a localized valley feature of about 1.5-micrometer depth but having a prominent peak feature rising above, out of the valley, by about 6 micrometer. Figure 11(b) plotted using an aspect ratio of 20:1 shows some details of the shape of the feature, while Figure 11(c) illustrates the shape with true aspect ratio. The breadth of this feature is about 1.5 micrometer.

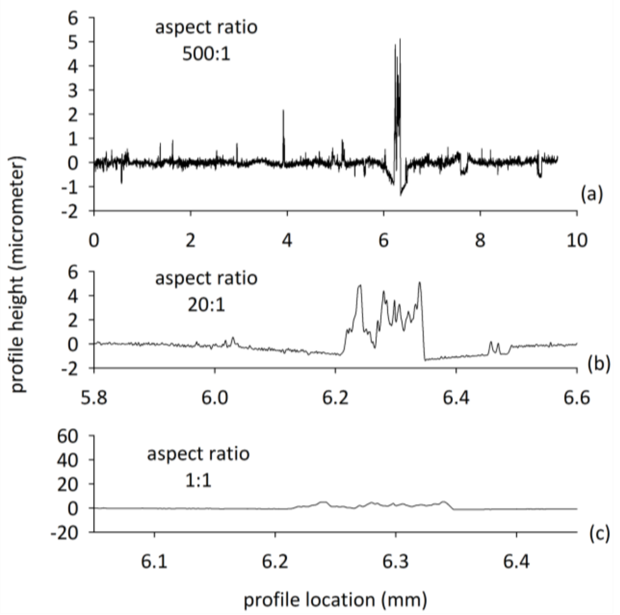

Figure 11. Profilometer inspection of a tooth after exposure to humidity for 77 days, prior to test. The same data are plotted using three aspect ratios: 500:1, 20:1, and 1:1.

SEM inspection of a pinion gear tooth, after test 2-A, which was conducted without exposure per Table 1, revealed a wide variety of features on the worn tooth surface. An inspection summary is provided in Figure 12. Figure 12(a) is an optical microscope photo of the Tooth #1 of the pinion used in Test 2-A, which shows the location of the SEM photomicrographs taken. Figures 12 (b-f) shows a series of SEM photomicrographs of increasing magnification. Figures 12(a) can be used to locate the features of Figures 12(b-c) showing highly smoothed MoS_2. As the magnification increases in Figure 12(d) slight blistering can be seen around highly smoothed MoS_2, and with further increase in magnification in Figure 12(e) a region of loss of film thickness is seen, thereby revealing the underlying grinding-line striation topography.

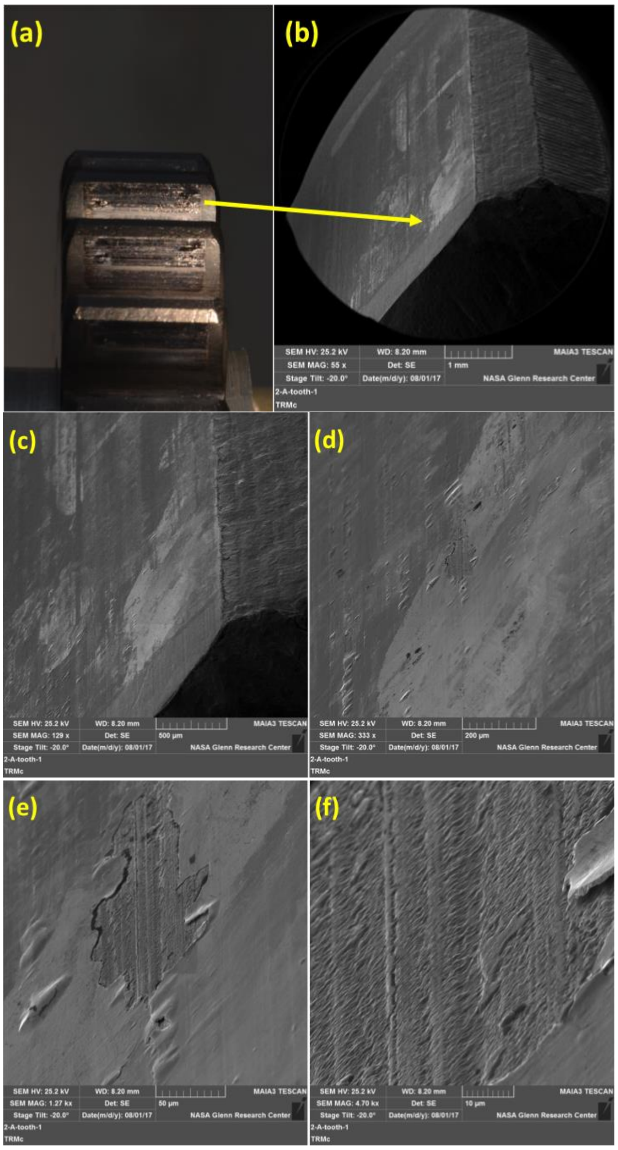

Figure 12. Optical and SEM inspection summary of a pinion tooth #1 after test 2A with no exposure to humidity prior to testing: (a) Optical image showing location of SEM inspection, (b) & (c) SEM image of smooth regions of MoS_2 near tooth tip, (d) SEM image of blistering and delamination of the film, (e) & (f) Close up of delaminated region.

The elongated blister features are aligned with the direction of rolling and sliding. Although the "delaminated" region of Fig. 12(e) might suggest exposure of the steel substrate, the higher magnified image of 12(f) has appearance of material flowing in the direction of rolling and sliding.

To investigate the underlying material, an EDX examination of the surface near the center of this region was done at Spectrum location 17 shown in Figure 13(a), and the corresponding Spectrum is shown in Figure 13(b). The result of EDX examination in Figure 13(b) shows spectrum associated with Molybdenum (Mo), Sulfur (S), and Iron (Fe), thus showing that the region did not experience a complete loss of all MoS_2 through this region. To compare the region below the MoS_2 coating with respect to the MoS_2 coating itself, another EDX examination was done at Spectrum location 18 shown in Figure 13(a), and the corresponding Spectrum is shown in Figure 13(c). A careful examination of the Spectrum 17 and 18 indicate no statistical difference between the underlying region below MoS_2 coating, and the amount of Molybdenum and Sulfur in MoS_2 coating itself.

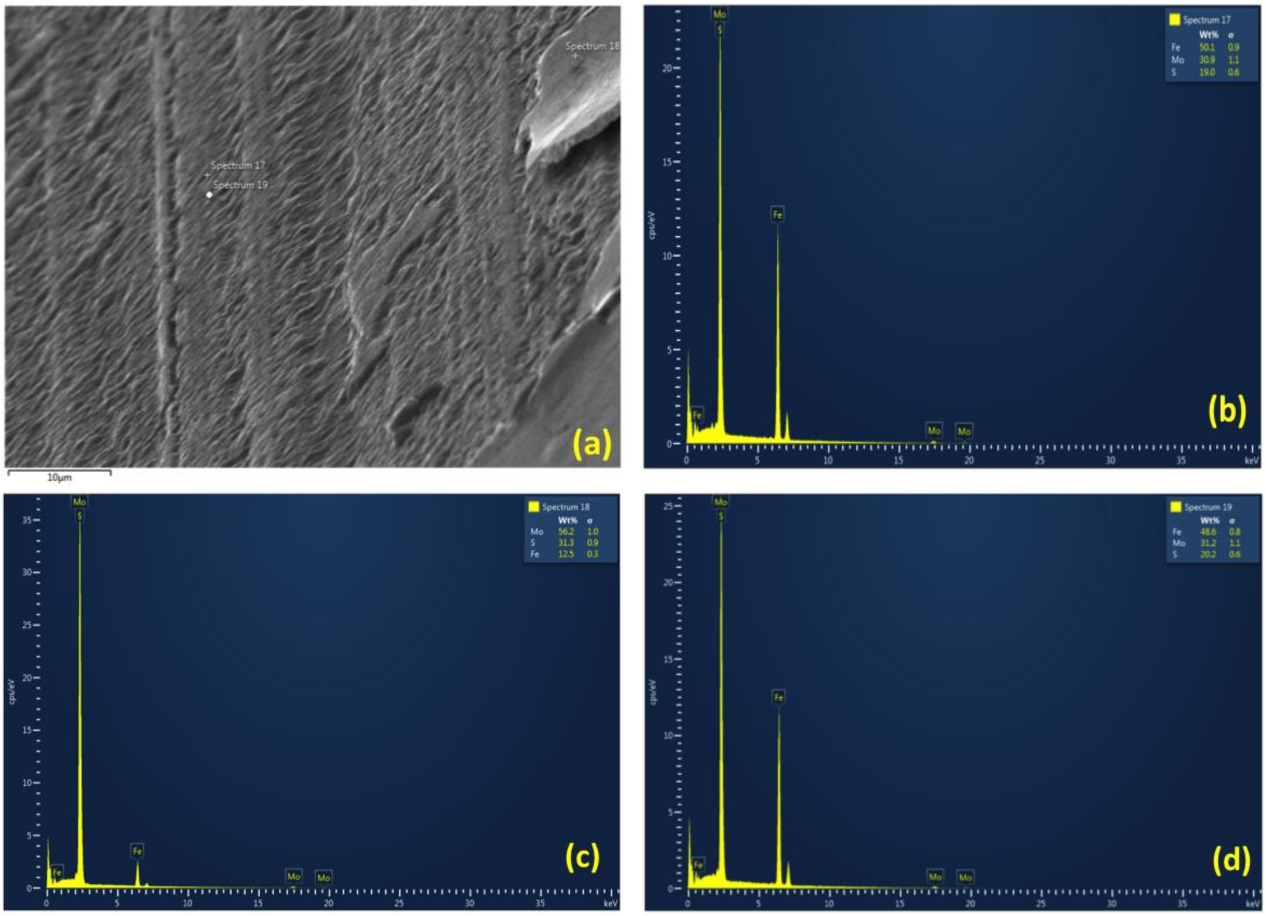

Spectrum Label	Spectrum 17 (b)		Spectrum 18 (c)		Spectrum 19 (d)	
	Wt %	Std. D	Wt %	Std. D	Wt %	Std. D
Fe	50.1	0.9	56.2	1	48.6	0.8
Mo	30.9	1.1	31.3	0.9	31.2	1.1
S	19	0.6	12.5	0.3	20.2	0.6

Figure 13. EDX examination of the underlying surface below MoS_2 layer: (a) three locations where Spectrum was taken, (b) & (d) spectrums taken from the center of the image, and (c) taken near the right edge.

To double-check the results of the EDX examination of Spectrum 17, another EDX examination was done next to Spectrum 17 location. The location of this EDX probe is shown in Figure 13(a), and the corresponding Spectrum 19 is shown in Figure 13(c) together with a table of Mo, S, Fe weight percentages for all three Spectrums. Comparing the two Spectrums 17 and 19 in the underlying region below MoS_2 coating with the Spectrum 18 of MoS_2 coating itself, it is clear that the underlying region still has significant amount of MoS_2 even after the delamination of the coating layers from the surface.

4. SUMMARY

The purpose of this work was to study the effect of exposure to humid air on the durability of a molybdenum disulfide (MoS_2) dry film lubricant applied to test spur gears, and subsequently tested in a vacuum environment. MoS_2 was applied by sputtering onto gears made from induction hardened and ground S45C steel. Twelve gear tests were completed in a vacuum gear rig at constant speed and torque. For this study, film durability was defined as the initiation of compromise of the MoS_2's ability to provide low friction. Test durations were long enough to initiate this compromise. One-half of the gears tested had zero exposure time to humid air prior to testing. The other half set of the gears were exposed to air of 58 percent relative humidity for exposure durations up to 77 days prior to testing.

On average the film durability time was shorter for gears exposed to humid air compared to gears with zero exposure. The film durability for gears with zero exposure ranged from 190,300 to 53,300 pinion revolutions with an average value of 100,200 and a median value of 83,500 revolutions. The film durability for gears exposed to humid air ranged from 84,700 to 21,000 pinion revolutions with an average value of 64,900 and a median value of 68,800 revolutions. Using the unexposed-gear film durability as a baseline, the exposure reduced the film durability by 35 percent based on average values or 18 percent based on median values. These reductions in film durability are similar in magnitude to the 55 percent to 20 percent range of reductions reported by Lince, Loewenthal, and Clark [1].

The gear teeth had a very glossy appearance after very few revolutions of the gears. After this initial running in, further change in the appearance of the teeth was a slow, and steady process. Profilometry revealed that the wear depth at test completion was on the order of the specified MoS_2 film thickness.

Red-brown coloration was noted on some of the teeth that had been exposed to humid air. The colored regions appeared as soon as 17 days after exposure to humid air. SEM inspections showed that at least some of these colored areas included material raised above the surrounding MoS_2 film.

ACKNOWLEDGEMENT

The NASA Engineering Safety Center (NESC) supported this research. The NASA GRC Summer Faculty Fellowship Program supported Dr. Iqbal Shareef.

REFERENCES

[1] J. Lince, S. Loewenthal, C. Clark, “Degradation of Sputter-Deposited Nanocomposite MoS_2 Coatings for NIRCam during Storage in Air”, Proceedings of the 43rd Aerospace Mechanisms Symposium, (May, 2016) pp. 221-234, NASA/CP-2016-219090.

[2] T. Krantz, C. DellaCorte, M. Dube, "Experimental Investigation of Forces Produced by Misaligned Steel Rollers." Proceedings of the 40th Aerospace Mechanisms Symposium, NASA/CP-2010-216272.

[3] T. Krantz, I. Shareef, "Wear of Steel and Ti6Al4V Rollers in Vacuum." Proceedings of the 41st Aerospace Mechanisms Symposium, NASA/CP-2012-21763.

[4] C. Dellacorte, T. Krantz, M. Dube, “ISS Solar Array Rotary Joint (SARJ) Bearing Failure and Recovery: Technical and Project Management Lessons Learned”, NASA/TP-2011-217116.

Serbian Tribology Society

SERBIATRIB '19

16th International Conference on Tribology

Faculty of Engineering University of Kragujevac

Kragujevac, Serbia, 15 – 17 May 2019

TRIBOLOGICAL BEHAVIOR OF COARSE RAPESEED OIL ADDITIVATED WITH NANOPARTICLES OF ZINC OXIDE

Traian Florian IONESCU[1], Dionis GUGLEA[1], Constantin GEORGESCU[1], Petrica ALEXANDRU[1], Lorena DELEANU[1,*]

[1]"Dunărea de Jos" University of Galati, Faculty of Faculty of Engineering, Galati, Romania

*Corresponding author: lorena.deleanu@ugal.ro

Abstract: *This paper presents the influence of ZnO as additive in refined rapeseed oil in a mass concentration of 1%wt on the tribological parameters. Tests are done on a four-ball machine from the laboratory LubriTest, at "Dunarea de Jos" University of Galati. The test parameters were load: 100 N, 200 N and 300 N and the rotational speed 1000 rpm, 1400 rpm and 1800 rpm, corresponding to the following sliding speeds, 0.38 m/s, 0.53 m/s and 0.69 m/s, respectively. Particles of ZnO have 14 5 nm. The rapeseed oil was supplied by Expur SA Bucharest. For the tested ranges of the parameters, the additivation of rapeseed oil with ZnO does not improve the friction coefficient, but the wear rate of WSD seems to be less sensitive for the more severe regimes when the vegetal oil is additivated. The additivation of rapeseed oil with ZnO is still efficient for the tested ranges of load and speed as compared to the neat rapeseed oil, but there is visible that friction coefficient and analysed wear parameter are less influenced by the regime for the concentration of 1% ZnO in rapeseed oil.*

Keywords: *rapeseed oil, additive, ZnO, four ball test, friction coefficient, wear rate*

1. INTRODUCTION

The rapeseed oil is in the focus of the researchers for replacing lubricants that are not friendly with the environment.

Metal oxides as additives in lubricants improve especially the wear parameters, protecting the initial texture of the contacting surfaces. Based on experimental results on four ball tribotester, Asrul [1] concluded that the higher concentrate of CuO (3%), the better the tribological behavior.

In a recent review, Shahnazar [2] mentioned ZnO as having good characteristic for improving the tribological behavior of a lubricant due to large surface area, high surface energy, good adsorption on metallic surfaces, good diffusion, easy sintering and a low melting point [3]. Due to the low solubility of ZnO in oil, their dispersion in the base oil or even in water-based fluids could be a challenge [4].

In 2011, Qian et al. [5] prepared ZnO (average size 125 nm) by a homogeneous precipitation method using lauryl sodium sulphate as the surfactant and studied the oil solubility, anti-corrosion, and tribological properties of ZnO used as an additive, but they did not mentioned the base oil. Taking into account the solubility, the addition of 1.0%, 2.0%, 3.0%, and 4.0% mass concentration of ZnO improve the tribological behavior of this type of lubricant (friction reduction and anti-wear properties).

Using the ball-on-disk tests, Gara and Zou [6] investigated the friction and wear properties of ZnO and Al_2O_3 in waterbased nanofluids. The combination of these nanoparticles reduces friction for smooth surfaces, but nanoparticles acted as abrasive wear particles.

Tang and Li [22] considered the nanoparticles a class of additives that have particular mechanisms of reducing friction and wear: rolling effect as in a third-body friction, protective spacers against directly rubbing the solid bodies, mending process if the particle size is smaller than texture parameters and polishing due to their mild abrasive process till the surfaces accommodate.

In a very recent review, Uflyand [7] mentioned the following metal oxides used as additives: TiO_2, CuO, Fe_3O_4, ZnO, Co_3O_4 and Al_2O_3, and results are also reported in [8], [9], [10], [11], [12], [16], [18], [28], [30]. Their mechanisms during lubrication are similar to those of metal nanoparticles, and the authors including the formation of tribo-film or adsorption film, the rolling effect, and the sintering or repair effect. The friction reduction can be due to the effect of viscosity at lower temperature and the rolling effect at higher temperature. The wear reducing mechanism is associated with the deposition of nanoparticles into the texture of the friction surfaces.

The use of ZnO and CuO nanoparticles as lubricant additives [19], [27], [15], [13] in vegetal oils (soybean, rapeseed oil and sunflower) are biodegradable and have better tribological behavior in boundary lubrication.

Song [24] tested monodispersed spherical zinc aluminate spinel ($ZnAl_2O_4$) nanoparticles, modified by oleic acid in cyclohexanol solution. The dispersion ability of nanoparticles in lubricant oil was good for tested concentrations (0.05, 0.1, 0.5, and 1 wt.%). The tribological properties of the $ZnAl_2O_4$ nanoparticles as an additive in lubricant oil were evaluated with four-ball test and thrust-ring test. For comparison, ZnO and Al_2O_3 nanoparticles as additive in lubricant oil were also tested. The $ZnAl_2O_4$ nanoparticles exhibit better tribology properties in terms of anti-wear and anti-friction than ZnO or Al_2O_3 nanoparticles, separately. The lubricating effect of $ZnAl_2O_4$ nanoparticles can be explained by their rolling effect and sintering process. When the $ZnAl_2O_4$ nanoparticles concentration is 0.1 wt%, there was obtained an optimal effect on reducing both friction and wear.

Magnetic Fe_3O_4 nanoparticles with an average diameter of 11.7 nm were dispersed in alpha-olefin hydrocarbon synthetic lubricating oil with a concentration of 0 to 10 wt% [21], [20]. This resulted in a reduction in COF and the diameter of the wear scar by 45% and 30%, respectively, at the optimal concentration value (4 wt%). The rolling mechanism is responsible for reducing COF and the nanoparticles act as spacers between the asperities and reduce the diameter of the wear scar.

Chan et al. [25] underlined that nano particles as CuO, TiO_2 and ZnO are non-toxic anti-wear additives for lubricants. With their sizes ranging from 2 to several hundreds nanometers, these are able to fill in asperity valleys, creating a thin, smooth and solid lamellar film on contacting surface. The authors of this paper revealed by SEM investigation that there is not a continuous film, but a disperse powder that prevents the two solid bodies to directly contact each other. If the particle size is smaller than the surface roughness, the wear volume decreases with the decrease of additive size. When particle size is larger than the surface texture, grooves are produced due to abrasion. The problem is that small nanoparticles agglomerate and, thus, the particle size in contact becomes a variable during sliding. If particles become larger, they could not be dragged into contact and their beneficial effect is very much reduced. And if they enter into contact they could produce oscillations of friction coefficient and severe wear when they left the contact to be between the solid bodies with wear traces already produced.

A parameter affecting frictional and wear behavior is the concentration of the additive.

The excessive additive particles in the asperities valleys could either give insignificant improvement in tribological performance, or produce abrasive wear (ploughing effects). The latter may be due to the interference of the additive particles causing poor adsorption of base stock at the contact area resulting in inadequate lubrication, as observed in the case of nanoparticles in polar oils such as ester-based oils and vegetal oils.

Bhaumik [27] noticed an increasing trend in viscosity with the increase in concentration of ZnO nanoparticles. The coefficient of friction in case of castor oil samples is found to be less than the commercially available mineral oil, but the coefficient of friction did not decrease further after a certain concentration of ZnO (0.1 wt% ZnO is the optimum in this case). The wear rate is found to be the lowest and it increased with the increase in concentration of ZnO. The formation of tribo-film due to the adsorption of castor oil and the diffusion of zinc oxide in the surface grooves prevented the metal to metal interaction, thus decreasing the coefficient of friction and controlling the surface roughness, but higher percentage of zinc oxide led to deteriorations of the surfaces.

Hernandez Battez et al. [26] studied the anti-wear behaviour of nanoparticle CuO, with a block-on-ring tester, under a load of 165 N, sliding speed of 2 m/s and a total distance of 3,066 m. All formulated lubricants with nanoparticle exhibited reductions in friction and wear compared to the base oil; the lubricants with 0.5% of ZnO and 0.5% ZrO_2 had improved characteristics for wear but the friction coefficient increased.

Sepyani et al. [29] investigated the effect of ZnO nanoparticles on rheological behavior of SAE 50 oil, at different temperatures. Viscosity at different shear rates revealed a Newtonian behavior of the formulated lubricants, having the maximum increase in viscosity of 12% for more concentrated samples, at low temperature.

The aim of this study is to assess the influence of ZnO in coarse rapeseed oil on the tribological characteristics. The authors analysed the friction coefficient and the wear rate of wear scar diameter, but also recorded the temperature in the oil cup, during the tests.

2. THE LUBRICANT AND THE TESTING METHODOLOGY

The additive was supplied by PlasmaChem [32] and has the following characteristics (Fig. 1): average particle size ca. 14 nm, specific surface area: 30±5 m^2/g, purity: >99% and this study presents the results for the neat rapeseed oil (Table 1) and the same vegetal oil additivated with 1% ZnO.

Table 1. Typical composition in fatty acids of the rapeseed oil (from Expur Bucharest).

Fat acid	Symbol	Composition, %wt
Myristic acid	C14:0	0.06
Palmitic acid	C16:0	4.60
Palmitoleic acid	C16:1	0.21
Heptadecanoic acid	C17:0	0.07
Heptadecenoic acid	C17:1	0.18
Stearic acid	C18:0	1.49
Oleic acid	C18:1	60.85
Linoleic acid	C18:2	19.90
Linolenic acid	C18:3	7.64
Arachidic acid	C20:0	0.49
Eicosenoic acid	C20:1	1.14
others		3.37

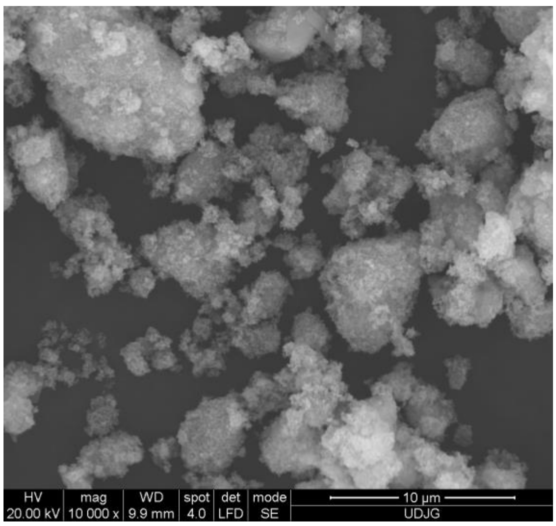

Figure 1. A SEM image of nanoparticles of ZnO

The formulated lubricant was obtained in small amounts of 200 g, each. The steps followed in this laboratory technology were similar to those presented by Cristea [17]:

- mechanical mixing of the additive and an equal mass of dispersing agent (guaiacol, supplied by Fluka Chemica, with the chemical formula $C_6H_4(OH)OCH_3$ (2-methoxyphenol)), for 20 minutes;
- gradually adding rapeseed oil, mixing with a magnetic homogenizer for 1 hour;
- ultrasonication + cooling of formulated lubricant in step of 10 minutes; the fluid is heating to about 70 °C during sonication; the cooling time was 1 hour; this technological step is repeated 5 times to have a total time of 60 minutes. The parameters of ultrasonic regime are power 100 W, frequency 20 kHz ± 500 Hz, continuous mode.

The test balls are lime polished, made of chrome alloyed steel balls, having 12.7±0.0005 mm in diameter, with 64-66 HRC hardness, as delivered by SKF. The oil volume required for each test was 8 ml ±1 ml. The test method for investigating the lubricating capacity was that from SR EN ISO 20623:2018 [32].

The test parameters for each test were:

- loading force on the machine spindle - 100 N, 200 N and 300 N (± 5%);
- sliding speeds of 0.38 m/s, 0.53 m/s and 0.69 m/s, corresponding to the spindle speeds of the four-ball machine of 1000 rpm, 1400 rpm and 1800 rpm (± 6 rpm), respectively;
- test time - 60 minutes (± 1%).

3. RESULTS

3.1. Friction coefficient

The authors agree with the conclusion of Shahnazar [2] that ZnO nano particles could decrease the wear of direct contact areas by being depositing onto the sliding surfaces, but SEM images do not prove that ZnO forms a lubricating layer on rubbing surfaces as many researches have believed (Fig. 2).

Figure 3 presents the average value of COF as obtained from two tests, for both tested lubricants. It is obvious that the neat oil has lower values, especially for heavy regimes, but the additivated oil has this parameter less sensitive to sliding speed for F=300 N. This is recommended for machines that frequently change their working regime.

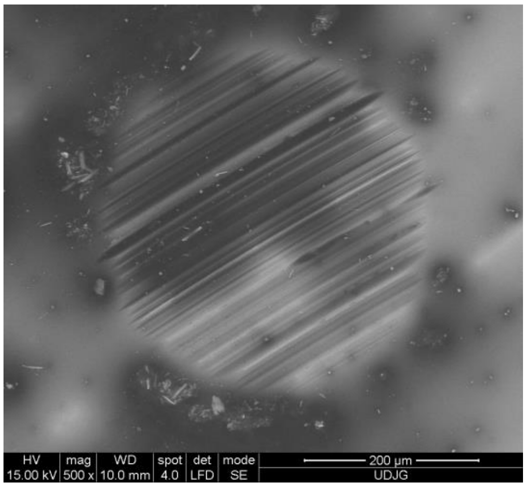

a) F=100 N, v=0.38 m/s

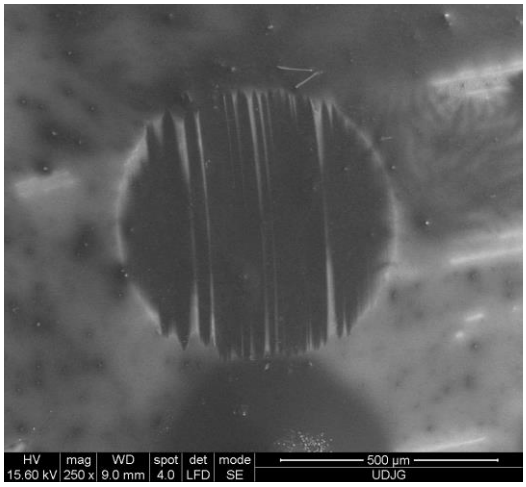

b) F=300 N, v=0.69 m/s

Figure 2. SEM images of the wear scars without pulling out the lubricants, at the end of the test

3.2. Wear rate of the wear scar diameter

Measurement of wear trace diameters was performed with the optical microscope, in accordance with the procedure given in SR EN ISO 20623:2018 [31]. Three wear marks were obtained for each test, these being located on the three fixed balls. Two diameters, the first diameter measured along the sliding direction, the second diameter measured perpendicular to the first, were measured for each wear trace.

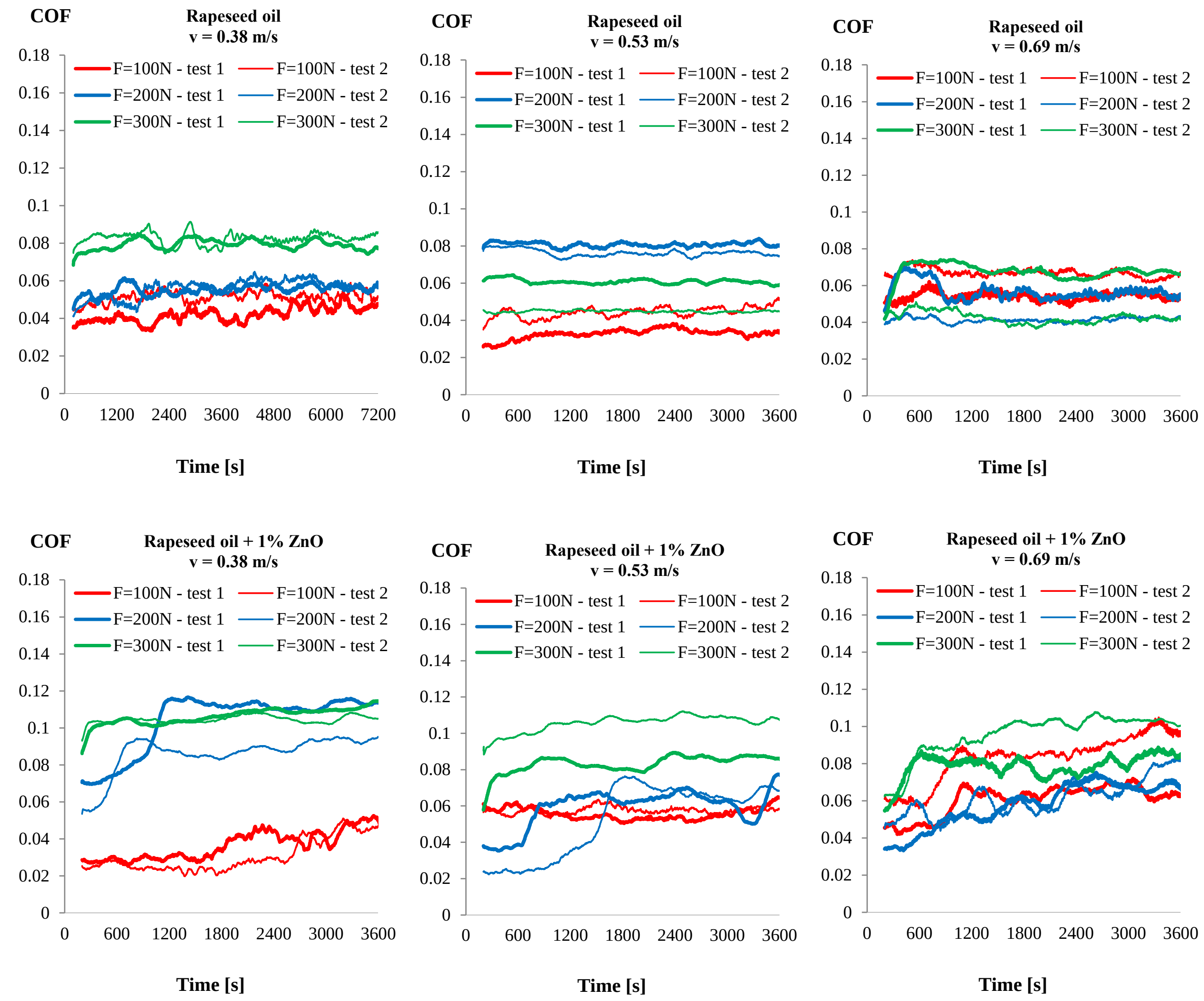

Figure 3. COF evolution in time

(2 sample per second and a moving average on 200 consecutive values)

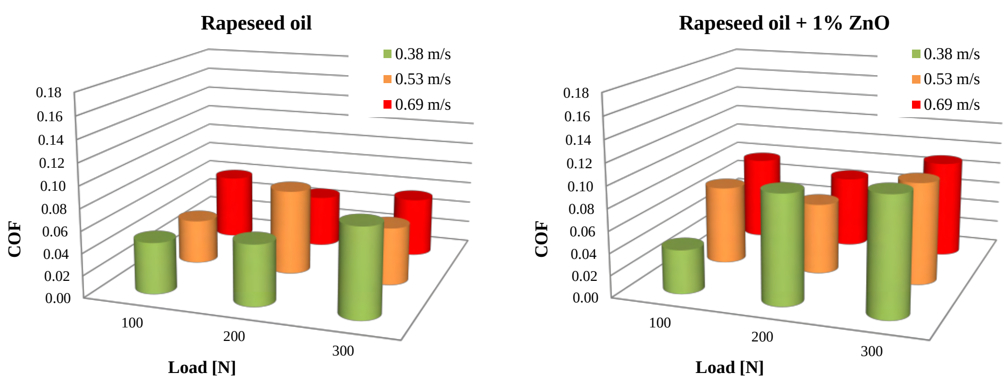

Figure 4. Average of COF for two values (two tests done under the same parameters)

With three traces of wear, six diameters were obtained and their mean value was calculated. This value represents the diameter of the wear scar, reported for each of the tests performed. The same method of obtaining the wear diameter is also given in specialized reports [31].

Figure 5 shows images of the wear scars as obtained with the help of an optical microscope. One may notice that the contact surfaces as resulted after testing with the additivated oil is less damaged.

The graphs of the wear scar diameters (WSD) as a function of speed could not reflect in a relevant way the influence of testing regimes, because all tests has 1 h (with different sliding distances for each speed), and, thus, the authors studied the influence of additive concentration with the help of wear rate of the scar diameter, noted by w(WSD). The w(WSD) is calculated with the help of the following relationship:

$$\mathrm{w(WSD)} = \frac{WSD}{F\ L}\ mm/(N\ mm)\ . \qquad (1)$$

where WSD is the average value of six measurements of the wear scar diameter, two on each fixed ball (one along the sliding direction and the other perpendicular to it), F is the load applied on the main shaft of the tribotester (carrying the rotating ball) and L is the sliding distance. The product F×L is the mechanical work done by the tribotester. Thus, the wear rate of WSD reflects the dimensional modification of WSD for the unit of mechanical work.

Figure 6 presents the wear rate of WSD and the values are lower for heavy regimes (F=200...300 N) for all sliding speeds. Only when tested at lowest speed (v=0.38 m/s) this parameter is close for both tested lubricants.

3.3. Temperature in the oil bath

The evolution of oil bath temperature during a test of 1 h is given in Figure 8.

The difference among final registration of temperature (at the end of the test) is small for low regimes (v=0.38...0.53 m/s) and its value is kept in the range 43...55°C, but for the highest speed (v=0.69 m/s), the temperature values are spread on a larger interval.

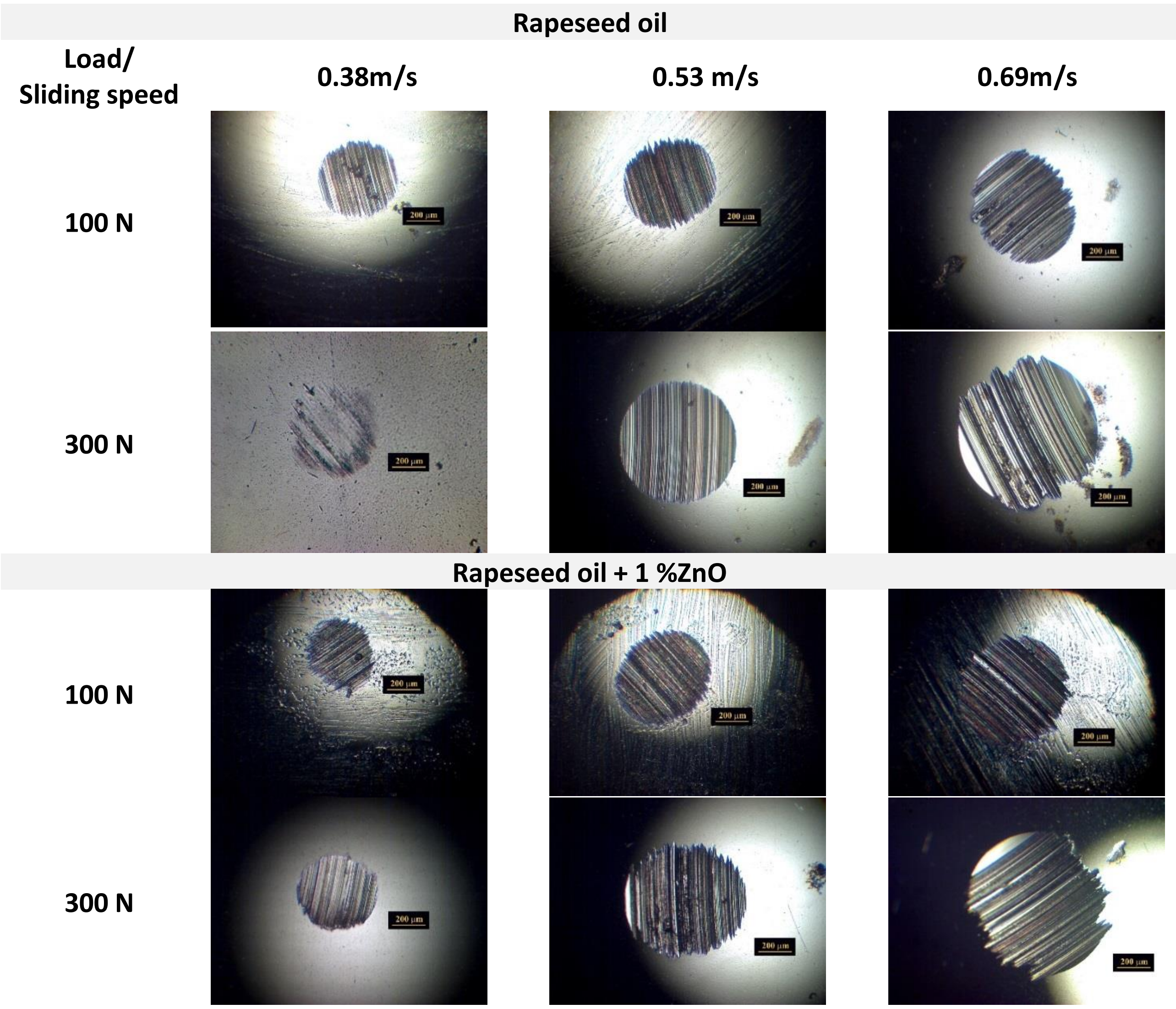

Figure 5 Typical wear scars for different regimes

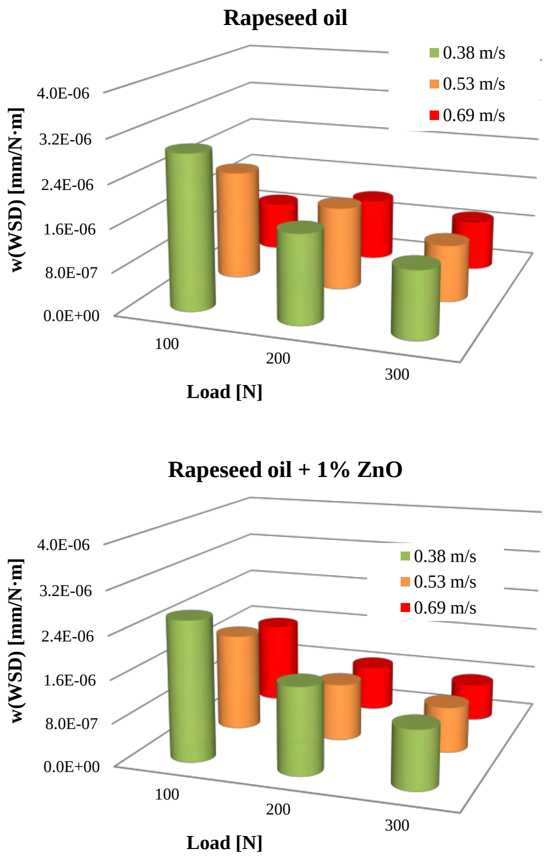

Figure 6. Wear rate of the wear scar diameter for the two tested lubricants, for different regimes

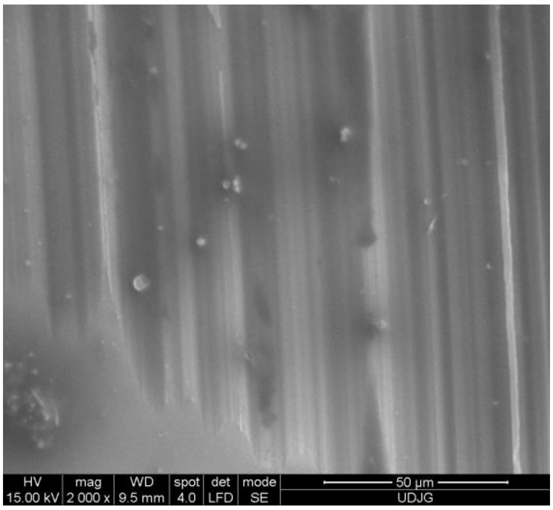

Figure 7. A detail of the wear scar without cleaning the lubricant

For the most severe regime the final recorded temperature for the rapeseed oil is about 70°C. The rapeseed oil additivated with ZnO has these temperatures higher, in the range of 50...60°C for v=0.38...0.53 m/s and for the highest speed the interval is larger (60...77°C). The supplementary heat generation could be explained by the friction of intermediate particles of Zn, rolling or being dragged in contact.

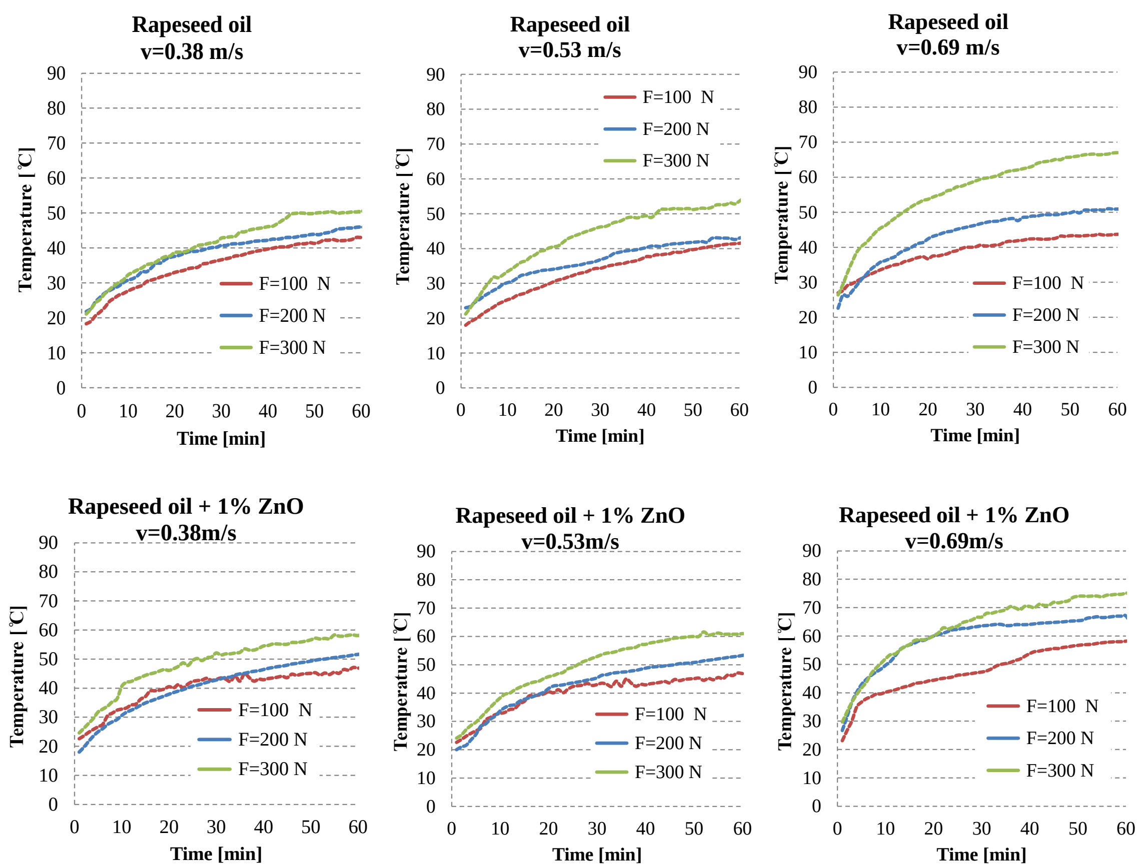

Figure 8. Temperature evolution

4. CONCLUSIONS

At least for the tested ranges of the parameters (v=0.38...0.69 m/s and F=100...300 N), the additivation of rapeseed oil with nanoparticles of ZnO does not improve the friction coefficient. But this additive was efficient for wear reduction, the authors pointed this out by comparing the values of the wear rate of wear scar diameter.

ACKNOWLEDGEMENT

This paper was supported by Doctoral School for Mechanical and Industrial Engineering of "Dunarea de Jos" University of Galati.

REFERENCES

[1] T.M. Asrul, N.W.M. Zulkifli, H. H. Masjuki, M.A. Kalam: Tribological properties and lubricant mechanism of nanoparticle in engine oil, Procedia Engineering, Vol. 68, pp. 320–325, 2013.

[2] S. Shahnazar, S. Bagheri, S. B. Abd Hamid: Enhancing lubricant properties by nanoparticle additives, International Journal of Hydrogen Energy, Vol. 41, pp. 3153-3170, 2016.

[3] J.W. Soares, J.E. Whitten, D.W. Oblas, D.M. Steeves: Novel photoluminescence properties of surface-modified nanocrystalline zinc oxide: toward a reactive scaffold, Langmuir, Vol. 24, No. 2, pp. 371-374, 2007.

[4] E. Tang, G. Cheng, X. Ma, X. Pang, Q. Zhao: Surface modification of zinc oxide nanoparticle by PMAA and its dispersion in aqueous system, Applied Surface Science, Vol. 252, No. 14, pp. 5227-5232, 2006.

[5] J. Qian, Y. Zhang, L. Wang, J. Xing: China Petroleum Processing and Petrochemical Technology, Vol. 13, No. 3, pp. 69-73, 2011.

[6] L. Gara, Q. Zou: Friction and wear characteristics of waterbased ZnO and Al_2O_3 nanofluids. Tribology Transactions, Vol. 55, No.3, pp. 345-350, 2012.

[7] I. E. Uflyand, V. A. Zhinzhilo, V. E. Burlakova: Metal-containing nanomaterials as lubricant additives: State-of-the-art and future development, Friction, Vol. 7, No. 2, pp. 93–116, 2019.

[8] I.E. Uflyand, V.A. Zhinzhilo, L.S. Lapshina, A.A. Novikova, V.E. Burlakova, G.I. Dzhardimalieva: Conjugated thermolysis of metal chelate monomers based on cobalt acrylate complexes with polypyridyl ligands and tribological performance of nanomaterials obtained, Chemistry Select, Vol. 3, pp. 8998–9007, 2018.

[9] S.S. Sanukrishna, S. Vishnu, T.S. Krishnakumar, M.J. Prakash: Effect of oxide nanoparticles on the thermal, rheological and tribological behaviours of refrigerant compressor oil: An experimental investigation, International Journal of Refrigeration, Vol. 90, pp. 32–45 2018.

[10] G.C. Cristea, D. Cazamir, D. Dima, C. Georgescu, L. Deleanu: Influence of TiO_2 as nano additive in rapeseed oil, ACME 2018, The 8th International Conference on Advanced Concepts in Mechanical Engineering, June 07-08, Iasi, IOP Conference Series: Materials Science and Engineering, 444, Machine Design. Tribology, 022011

[11] S. Ingole, A. Charanpahari, A. Kakade, S. Umare, D.V. Bhatt, J. Menghani: Tribological behavior of nano TiO_2 as an additive in base oil, Wear, Vol. 301, pp. 776–785, 2013.

[12] P. Zulhanafi, S. Syahrullail, M.M. Faridzuan: Tribological performance of palm kernel oil added with nanoparticlecopper oxide using fourball tribotester, Jurnal Teknologi, Vol. 79, pp. 53–59, 2017.

[13] M.F. Trajano, E.I.F. Moura, K.S.B. Ribeiro, S.M. Alves: Study of oxide nanoparticles as additives for vegetable lubricants, Materials Research, Vol. 17, pp. 1124–1128, 2014.

[14] S. Bhaumik, R. Maggirwar, S. Datta, S.D. Pathak: Analyses of anti-wear and extreme pressure properties of castor oil with zinc oxide nano friction modifiers, Applied Surface Science, Vol. 449, pp. 277-286, 2018.

[15] F.A. Essa, Q. Zhang, X. Huang, A.M.M. Ibrahim, M.K.A. Ali, M.A.A. Abdelkareem, A. Elagouz: Improved friction and wear of M50 steel composites incorporated with ZnO as a solid lubricant with different concentrations under different load, Journal of Materials Engineering Performance, Vol. 26, pp. 4855-4866, 2017.

[16] V.P. Suresh Kumar, N. Manikandan, C. Subakaran, Y.G. Sterbin Jeso: An experimental effect of ZnO nanoparticles in SAE 20W50 oil, International Research Journal of Engineering Technology (IRJET), Vol. 5, pp. 1069–1073, 2018.

[17] G.C. Cristea: *Tribological characterization of soybean oil additivated with nano materials based on carbon (black carbon, graphite and graphene*, PhD thesis: “Dunarea de Jos” University of Galati, Romania, 2017.
[18] X. Ran, X. Yu, Q. Zou: Effect of particle concentration on tribological properties of ZnO nanofluids, Tribology Transactions, Vol. 60, pp. 154-158, 2017.
[19] S. Arumugam, G. Sriram: Synthesis and characterization of rapeseed oil bio-lubricant dispersed with nano copper oxide: its effect on wear and frictional behavior of piston ring–cylinder liner combination, Proceedings of the Institution of Mechanical Engineers, Part J: Journal of Engineering Tribology, Vol. 228, p. 1308, 2014.
[20] G. Zhou, Y. Zhu, X. Wang, M. Xia, Y. Zhang, H. Ding: Sliding tribological properties of 0.45% carbon steel lubricated with Fe3O4 magnetic nanoparticle additives in base oil, Wear, Vol. 301, pp. 753–757, 2013.
[21] K. Trivedi, K. Parekh, R.V. Upadhyay: Nanolubricant: magnetic nanoparticle based, Material Research Express, Vol. 4, 114003, 2017.
[22] Z. Tang, S. Li S: A review of recent developments of friction modifiers for liquid lubricants (2007–present) Current Opinion in Solid State and Materials Science, Vol. 18, pp 119–139, 2014.
[23] E. Tang, G. Cheng, X. Ma, X. Pang, Q. Zhao: Surface modification of zinc oxide nanoparticle by PMAA and its dispersion in aqueous system, Applied Surface Science, Vol. 252, No. 14, pp. 5227-5232, 2006.
[24] X. Song, S. Zheng, J. Zhang, W. Li, Q. Chen, B. Cao: Synthesis of monodispersed $ZnAl_2O_4$ nanoparticles and their tribology properties as lubricant additives, Material Research Bulletin, Vol. 47 No. 12, pp. 4305-4310, 2012.
[25] C.H. Chan, S.W. Tang, K. Noor, Mohd, W.H. Lim, S.K. Yeong, Z. Idris: Tribological behavior of biolubricant base stocks and additives, Renewable and Sustainable Energy Reviews, Vol. 93, pp. 145-157, 2018.
[26] A. Hernandez Battez, R. Gonzalez, J.L. Viesca, J.E. Fernandez, J.M. Dıaz Fernandez, A. Machado, R. Chou, J. Riba: CuO, ZrO_2 and ZnO nanoparticles as antiwear additive in oil lubricants, Wear, Vol. 265, pp. 422-428, 2008.
[27] S. Bhaumik, R. Maggirwar, S. Datta, S.D. Pathak: Analyses of anti-wear and extreme pressure properties of castor oil with zinc oxide nano friction modifiers, Applied Surface Science, Vol. 449, pp. 277–286, 2018.
[28] M.V. Thottackkad, P.K. Rajendrakumar, N.K. Prabhakaran: Experimental studies on the tribological behaviour of engine oil (SAE15W40) with the addition of CuO nanoparticles, Industrial Lubrication and Tribology, Vol. 66, pp. 289-297, 2014.
[29] K. Sepyani, M. Afrand, M.H. Esfe: An experimental evaluation of the effect on ZnO nanoparticles on the rheological behavior of engine oil, Journal of Molecular Liquids, Vol. 236, pp. 198-204, 2017.
[30] P. Yang, X. Zhao, Y. Liu, X. Lai: Preparation and tribological properties of dual-coated CuO nanoparticles as water based lubricant additives, Journal of Nanoscience and Nanotechnology, Vol. 16, p. 9683, 2016.
[31] SR EN ISO 20623 Petroleum and related products. Determination of the extreme-pressure and anti-wear properties of lubricants. Four-ball method (European conditions), 2018.
[32] Nanomaterials and related products, 2016, PlasmaChem, available at: http://www.plasmachem.com/download/PlasmaChem-General_Catalogue_Nanomaterials.pdf, accessed 20.02.2016.

Serbian Tribology Society

SERBIATRIB '19

16th International Conference on Tribology

Faculty of Engineering University of Kragujevac

Kragujevac, Serbia, 15 – 17 May 2019

THE EFFECTS OF DIFFERENT NANOPARTICLES IN PALM OIL OLEIN AS SOLID ADDITIVES

Mohamad Ali AHMAD[1,*], Izatul Hamimi ABDUL RAZAK[1,2], Nadia Nurul Nabihah AHMAD FUAD[1], Khairul Syazwani SHAHRUDIN[1]

[1]Faculty of Mechanical Engineering, Universiti Teknologi MARA, 40450 Shah Alam Selangor, Malaysia

[2]Mechanical & Manufacturing Section, Universiti Kuala Lumpur Malaysia France Institute, 43650 Bandar Baru Bangi, Selangor, Malaysia

*Corresponding author: mohama9383@uitm.edu.my, mohamad9383@salam.uitm.edu.my

Abstract: *Palm oil olein and palm oil ester is well-known potential candidate in plant-based oil to replace the conventional mineral oil. Harvested all year round, the advantages and benefits initiate the palm oil to be used in varieties of application. In this paper, palm oil olein was tested on its capability as a lubricant to replace the mineral oil. To enrich the performance of this oil, different types of nanoparticles additives were added. Previous studies proved that by adding small size of additives into lubricating oil can lessen the friction and improve anti-wear properties. The adjustment of the lubricating oil with nanoparticle additives will reduce the friction between two contact surfaces and produce less heat. In his study, three type material of solid additives namely nanoclay and carbon nanotubes were used. Four ball tester following ASTM D4072-94 was conducted to determine the optimum concentration of each additives and its tribological properties under boundary lubrication (metal to metal contact). Result obtained shows that the addition of 0.04 wt% of carbon nanotubes recorded the lowest coefficient of friction with a 10.8% improvement compared to the pure palm oil. The additive also contributed to better wear scar diameters and possessed good anti-wear properties for palm oil. This thus shows the significant potential of carbon nanotubes as the wear preventive additive for palm oil olein. It is also discovered that 0.04 wt% of nanoclays additive is the optimum concentration of the mixture with coefficient of friction reduced 22.16% compared to mineral oil.*

Keywords: *fourball tester, nanoclay, carbon nanotubes, graphene, extreme pressure, wear profile, scar diameter.*

1. INTRODUCTION

The depletion of conventional lubricant sources and the need to reduce environmental emissions have urged researchers to innovate and investigate alternatives green or renewable lubricant. In this regard, palm oil from agricultural feedstocks is a suitable substitute for petroleum lubricants because vegetable – based lubricants present biodegradability, and easy disposal. However, the resistance to extreme pressure, anti-wear characteristics, insufficiencies on low thermal and oxidation stability of this palm oil lubricant are questionable when evaluated against those of commercial petroleum oils [1, 2]. The prospect of solving the problems (extreme pressure and anti-wear characteristic) improved with the advent of nanotribology, while the insufficiencies on low thermal and oxidation stability have been improved via the inducement of chemical changes.

The palm oil is a well-known potential candidate in plant-based oil to replace the conventional mineral oil. Harvested all year round, the advantages and benefits initiate the palm oil to be used in varieties of application. Nowadays the utilization of palm oil as feedstock for bio-lubricants has been recognized in many studies [3, 4]. This is due to issues related to the depletion of world crude oil reserve, increasing crude oil prices and conservation of oil, which brought interest in the bio-based materials. Therefore, efforts have been placed with emphasis to develop a renewable, biodegradable, and environmentally friendly industrial fluids, or lubricant.

Lubricant plays a significant role in a tribology system to enhance the reliability and service life of friction units. Not only expected to perform as anti-friction media, it also should be able to facilitate smooth operations, reduce wear and heat loss from moving contact surfaces, prevent rust and reduces oxidation as well as act as seal against dirt, dust and water [5, 6].

Increasing demands for lubricant in present and future consumptions are in line with current technological growth. This promotes the development of alternatives for current industrial lubricants, particularly mineral and crude oils. In recent time, there are high growing interests in the alternative bio-lubricants derived from vegetable based. Numerous development and research have been carried out to explore the potential of vegetable oils to perform effectively as petroleum-based lubricants in ranges of applications including in automotive, metal working, machineries and others. The addition of several types of additives may also improve the friction reduction and anti-wear properties of the oils [3, 4].

The use of nanoparticles in vegetable lubricant as oil additives have extensively being studied in this past few years with main purpose to improve the oil properties. Metal-based, metal oxide, metal composite, boron-based and carbon-based nanoparticles are the five major groups of nanoparticles that usually added to lubricant [7]. The addition of few types of nanoparticles such as cuprum oxide (CuO), Molybdenum disulfide (MoS_2), Titanium Oxide (TiO_2), Zink Oxide (ZnO), graphite, graphene, and other metallic nanoparticles into the vegetable oils have proven the good contribution to wear and friction reductions [8–11]. This is due to the fine size of the nanoparticles which normally less than 100 nm allows it been easily deposited on the friction surfaces and forms a protective deposit film. Thottackkad *et. al.* [12] found that an optimum concentration of nanoparticles may improve the coefficient of friction and the specific wear rate. The study was carried out on the tribological properties of coconut oil with addition of CuO nanoparticles as additive. The authors also studied the optimum concentration of the additive. Kiu et al. [7] on his study was added graphene nanoparticles as additives to palm oil and found a significant improvement in the reduction of friction coefficient and wear scar diameter.

In the present study, the carbon nanotube (CNT) and nanoclays optimum weight percentage (wt%) were utilized as an additive in palm oil bio-based lubricant and the tribological properties were investigated. The different wt% concentration amount of the carbon nanotubes was tested and the ability in friction and wear characteristic was analysed.

2. METHODOLOGY

2.1 Sample preparation

The properties of palm oil olein and commercial mineral oil (20W-40) which were used in this study were listed in Table 1. Mineral oil (20W-40) was selected as reference during this testing. Single-walled carbon nanotube (>70% TGA) and nanoclays (size <20 nm) as oil additive was mixed with palm oil as base oil and shaken by using an ultrasonic vibrator to ensure homogeneous dispersion of mixture without agglomeration. Seven samples from each of additives were prepared for the testing specimens, which are palm olein oil mixed with carbon nanotube particle and palm olein oil mixed with nanoclays at 0.02 %, 0.03 %, 0.04 % 0.05 %, 0.06 %, 0.07 % and 0.08 % of weight percentages. Both carbon nanotubes and nanoclays were supplied by Sigma Aldrich Ltd.

Table 1. Palm oil olein and properties

Properties	Value
Palm Oil Olein	
Density (g/ml)	0.9081
Kinematic viscosity at 40˚C (mm^2/s)	43.85
Kinematic viscosity at 100˚C (mm^2/s)	8.72
Viscosity Index	182
Total acid number (mm KoH/g)	6.35
Mineral oil (20W-40)	
Density (g/ml)	0.883
Kinematic viscosity at 40˚C (mm^2/s)	134.1
Kinematic viscosity at 100˚C (mm^2/s)	14.7
Viscosity index	109

2.2 Four ball testing

A four-ball friction and wear tester produced by Koehler Instrument Company, Inc., were used to study the tribological properties of carbon nanotubes and nanoclays in palm olein oil as additive. The purpose of the four-ball wear test in this study is to test the wear preventive (WP) properties of a lubricant. In the WP test, the lubricant's coefficient of friction and the wear scar diameter when sliding actions between the balls with certain load can be measured.

The series of tests were conducted in accordance with ASTM D4172 (WP) [13] by four ball friction and wear tester equipment, with different concentration amount of carbon nanotubes additive. A new set of four steel balls (AISI 52100) was used for each set of tests with 14.7 mm ball mean diameter and hardness range between 61 to 63 HRC. These balls were thoroughly cleaned with n-Heptane and dried prior the test set up. The three stationary balls then been clamped into the ball pot and the forth ball was held in a rotating spindle. A sample volume of approximately 10 ml lubricant was poured into the ball pot assembly for each test. Figure 1 illustrates the four-ball assembly installed in the wear tester equipment. After the completion of the test, wear scar on the con-tact surfaces of balls was then observed under a digital optical microscope. The summary of test parameters for the WP test was listed in Table 2.

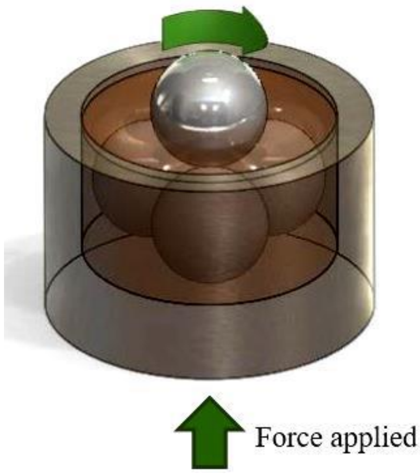

Figure 1. Four ball assembly

Table 2. Four ball tester parameters according to ASTM standard

Parameter	D4172
Load (kgf)	40±2
Duration (min)	60±1
Rotating speed (rpm)	1200±60
Temperature (°C)	75±2

3. RESULTS & DISCUSSION

3.1 Coefficient of friction

Carbon nanotubes (CNT) and nanoclays in the range of 0.02-0.08 wt% concentrations were added in commercial palm olein oil and the friction and wear properties were analysed. The average friction coefficient of the palm olein oil added with the different concentrations of CNT and nanoclays were depicted in Figure 3 and Figure 4. It shows the variation of coefficient of friction of the palm olein oil with seven concentrations of CNT additive. The coefficient of friction value reduced to from 0.073 to 0.067 and keeps reducing with the addition of 0.04 wt% of CNT.

In the case of nanoclay, the lowest coefficient of friction recorded was at wt% of 0.04 with the value of 0.081.

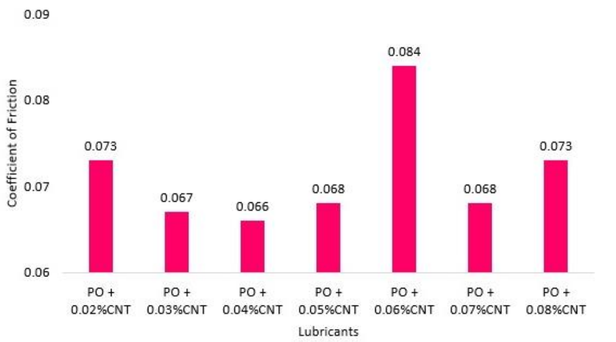

Figure 3. Average coefficient of friction with different wt% of carbon nanotubes

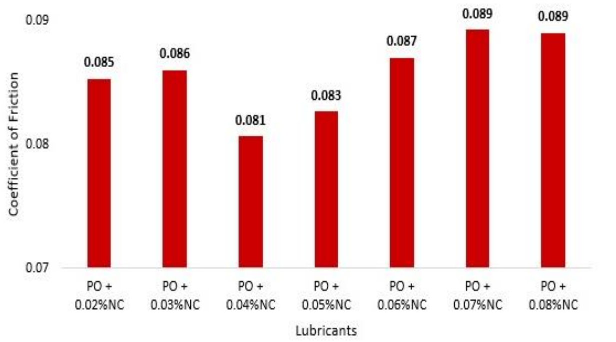

Figure 4. Average coefficient of friction with different wt% of nanoclay

The friction of friction obtained from minimum wt% of CNT and nanoclay was compared with the coefficient of friction obtained from commercial mineral oil and pure palm olein oil as show in Figure 5. The coefficient of friction value of 0.04 wt% of CNT, recorded the lowest coefficient of friction among the other samples with a 10.8% improvement compared to the pure palm olein oil. In this condition, the nanoparticles provided a thin lubrication film on the surfaces and minimize friction at the sliding interfaces.

The similar finding was also obtained by Kiu et al. [14] whose demonstrated the reduction in friction coefficient and wear when carbon nanotubes was added in the studied on vegetable oil. in addition, according to Cornelio *et al.* [15], the positive effect on lubricant properties by the addition of CNT is might be due to the high elastic modulus of the CNT which reducing the metallic contact between surfaces and leads to reduction of adhesive wear and friction coefficient. The authors added that, if higher contact pressure is applied, the carbon nanotubes can deform and forms a lamellar solid on the contact surfaces.

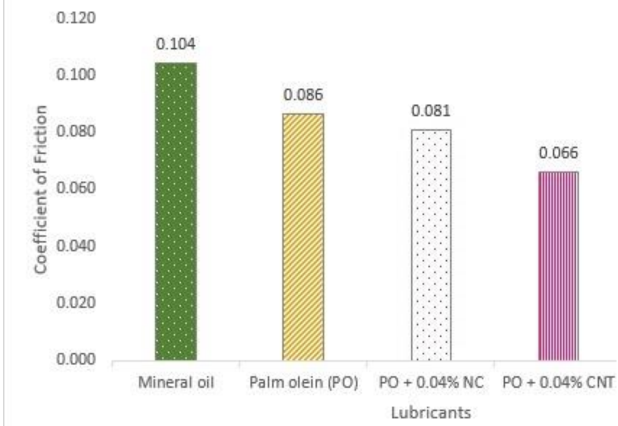

Figure 5. Comparison coefficient of friction between minimum concentration of mixed palm olein with additive with mineral oil and pure palm olein

Nanoclay able to reduced the 6% and 22% of coefficient of frictions compared to pure palm olein oil and mineral oil. Capability of nanoclay as crystalline materials to layer themselve would be possilitity of this reduction [16].

3.2 Wear scar diameter

Ball surface investigation by optical microscopy shows the different wear surface and scar diameter when the carbon nanotubes and nanoclays additive was included in palm oil. Figure 6 tabulated the average wear scar diameter for the palm oil with various concentration of CNT, nanoclays additive, pure palm olein oil and commercial mineral oil. Wear scar diameter is damaged on the balls contact surfaces due to the material removal during sliding contact.

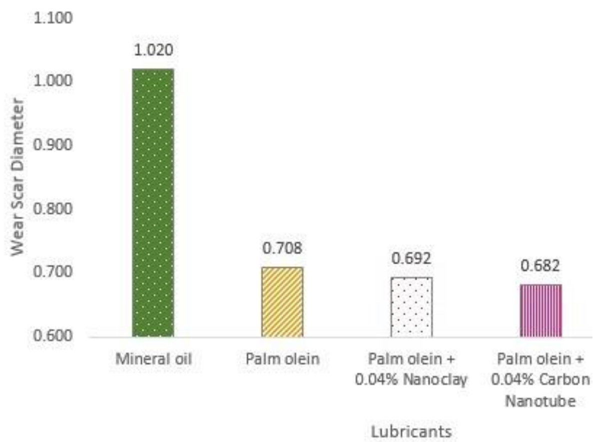

Figure 6. Wear scar diameter (WSD) between optimum concentration of mixed palm olein with additive, pure palm olein and mineral oil

The significance improvement in wear scar diameter was found for palm oil with 0.04 wt% of CNT, at 0.682 mm which is about 5.1% reduction compared to palm oil without additive. This shows that the CNT possess a good anti-wear behaviour with minimal concentration. Although the optimum concentration of the CNT additive (0.04 wt%) showing higher wear scar diameter, yet it still better as compared to the pure palm oil with about 2.4% improvement.

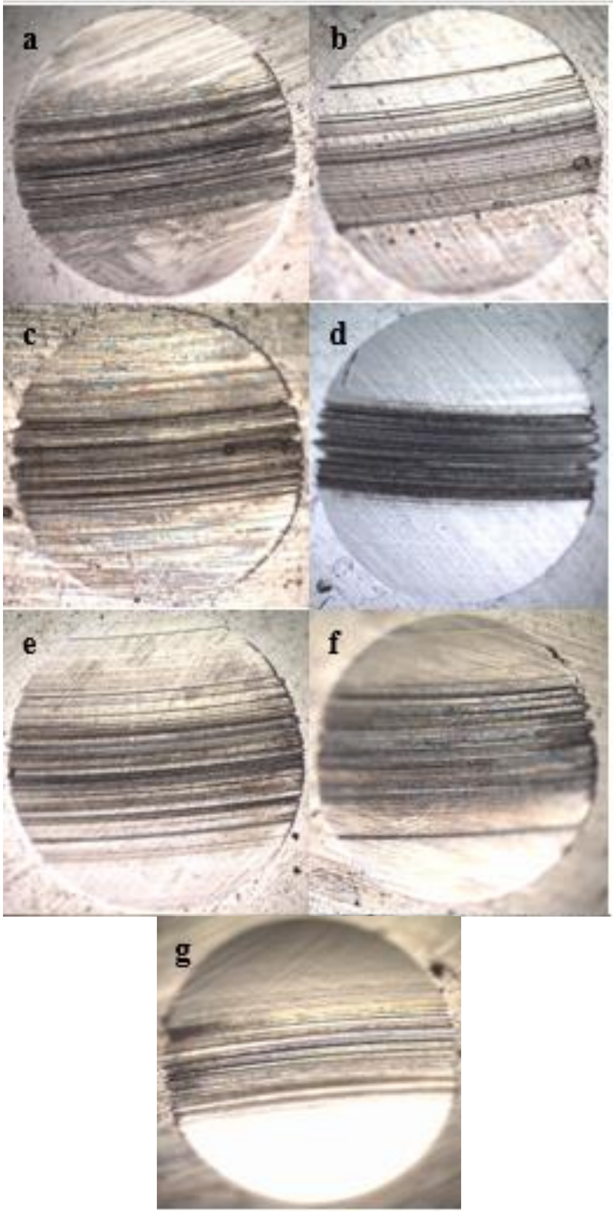

Figure 7. Optical micrograph of wear scars for palm oils with CNT concentration (magnification 200X): (a) 0.02 wt%, (b) 0.03 wt%, (c) 0.04 wt%, (d) 0.05 wt%, (e) 0.06 wt%, (f) 0.07 wt% and (g) 0.08 wt%

The optical micrograph images of the ball specimen wear scars are illustrated in Fig. 7. Observing the wear scar produced with palm oils with the solid additives, the presence of CNT particles can be seen on the scratch groove surfaces. The scattered CNT particles was observed in Fig. 5(c) for the palm oil with 0.04 wt% CNT, and a smoother scar edges was produced. The particles might contribute to less friction between the contact surfaces and producing lower coefficient of friction and wear scar size. This was supported by Gulzar et al. [3] who claimed that the precipitation of nanoparti-cles on the contact surface contributing to the smooth surface.

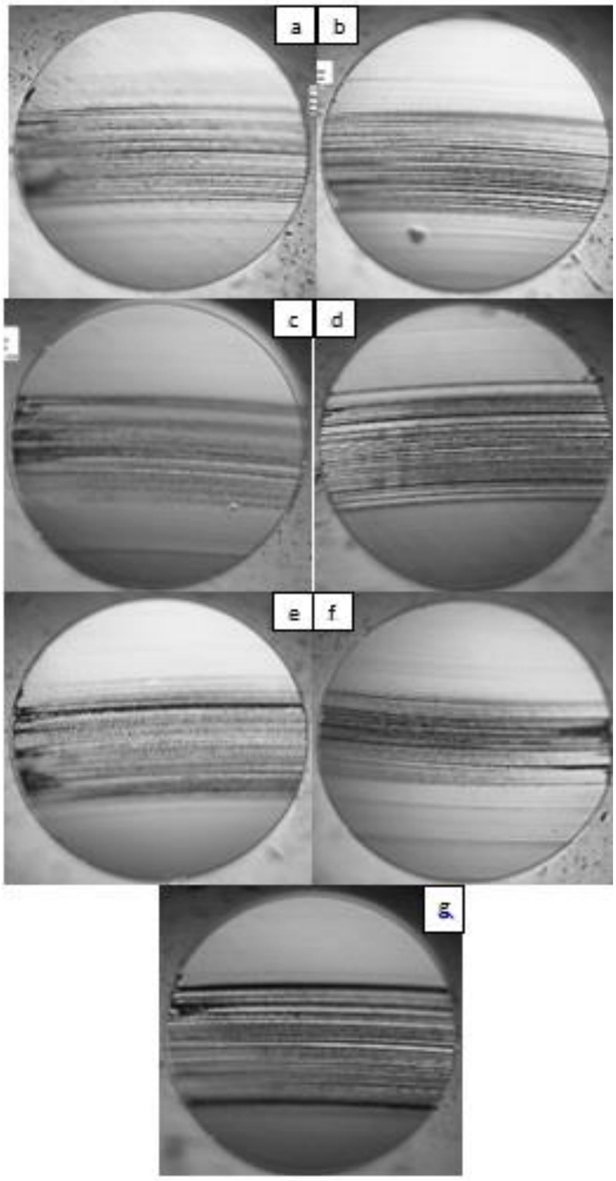

Figure 14. Optical micrograph of wear scars for palm oils with CNT concentration (magnification 200X): (a) 0.02 wt%, (b) 0.03 wt%, (c) 0.04 wt%, (d) 0.05 wt%, (e) 0.06 wt%, (f) 0.07 wt% and (g) 0.08 wt%

For the case of nanoclays, specimen wear scars are illustrated in Figure 8. As we can see, scratch on the surface is lesser compared to CNT. Nanoclays capability to stacked and layer themselve becomes benefits on surface protection compared to CNT.

4. CONCLUSION

This study focused to replace the conventional mineral oil to friendlier environment lubricant which was plant-based lubricant. The tribological testing were performed to prove that additional additives did improved and gave benefits to the palm olein lubricant. The improvement performance was compared with mineral oil which is the conventional lubricants that been used in the industry.

i. Nanoclays improve 22.12% for coefficient of friction while for wear scar diameter reduced by 32.16%.
ii. Carbon nanotube improved 36.54% for coefficient of friction while for wear scar diameter reduced by 33.14%.

In conclusion, addition of additives into the palm olein did gave improvement to the lubricant. It shows massive potential as an alternative to replace the current industrial mineral oil as lubricant.

ACKNOWLEDGEMENT

The authors would like to express gratitude to Institute of Research Management & Innovation (IRMI) of Universiti Teknologi MARA for the Research University Grant, LESTARI (087/2017), Faculty of Mechanical Engineering UiTM, and Ministry of Higher Education, Malaysia for their support.

REFERENCES

[1] T.M. Panchal, A. Patel, D.D. Chauhan, M. Thomas, J.V. Patel: A methodological review on bio-lubricants from vegetable oil based resources, Renewable and Sustainable Energy Reviews, Vol. 70, pp. 65–70, 2017.

[2] R.E. Gapinski, I.E. Joseph, B.D. Layzell: A vegetable oil-based tractor lubricant, SAE Tech Paper, 941785, pp. 1–9, 1994.

[3] M. Gulzar, H.H. Masjuki, M. Varman, M.A. Kalam, R.A. Mufti, N.W.M. Zulkifli, R. Yunus, R. Zahid: Improving the AW/EP abil-ity of chemically modified palm oil by adding CuO and MoS nano – particles, Tribology International, Vol. 88, pp. 271–279, 2015.

[4] E.K. Heikal, M.S. Elmelawy, S.A. Khalil, N.M. Elbasuny: Manufacturing of environment friendly biolubricants from vegetable oils, Egyptian Journal of Petroleum, Vol. 26, No. 1, pp. 53–59, 2017.

[5] H.M. Mobarak, E. Niza Mohamad, H.H. Masjuki, M.A. Kalam, K.A.H. Al Mahmud, M. Habibullah, A.M. Ashraful: The prospects of biolubricants as alternatives in automotive applications, Renewable and Sustainable Energy Reviews, Vol. 33, pp. 34–43, 2014.

[6] S.Z. Erhan, B.K. Sharma, J.M. Perez: Oxidation and low temperature stability of vegetable oil-based lubricants, Industrial Crops and Products, Vol. 24, pp.292-299, 2006.

[7] S.S.K. Kiu, S. Yusup, C.V. Soon, T. Arpin, S. Samion, R.N.M. Kamil: Tribological investigation of graphene as lubricant additive in vegetable oil, Journal of Physical Science, Vol. 28, pp. 257–267, 2017.

[8] N.W.M. Zulkifli, S.S.N. Azman, M.A. Kalam, H.H. Masjuki, R. Yunus, M. Gulzar: Lubricity of bio-based lubricant derived from different chemically modified fatty acid methyl ester, Tribology In-ternational, Vol. 93, pp. 555–562, 2016.

[9] A.G. Zen, G.W. Rashmi: Tribological Evaluation of Nano Graphene Platelets as an Additive to Biolubricant Base Fluid, EURECA, pp. 10–11, 2013.

[10] N.W.M. Zulkifli, M.A. Kalam, H.H. Masjuki, R. Yunus: Experimental analysis of tribological properties of biolubricant with nanoparticle additive, Procedia Eng, Vol. 68, pp. 152–157, 2013.

[11] Y. Su, L. Gong, D. Chen: An Investigation on Tribologi-cal Properties and Lubrication Mechanism of Graphite Nanoparti-cles as Vegetable Based Oil Additive, J. Nanomater, pp. 1–7, 2015.

[12] M.V. Thottackkad, R.K. Perikinalil, P.N. Kumarapillai: Experimental evaluation on the tribological properties of coconut oil by the addition of CuO nanoparticles, International Journal of Pre-cision Engineering and Manufacturing, Vol. 13, No. 1, pp. 111–116, 2012.

[13] ASTM4172-94 *Standard test method for wear preventive character-istics of lubricating fluid (four-ball method),* 2009.

[14] S.S.K. Kiu, S. Yusup, V.S. Chok, A. Taufiq, R.N.M. Kamil, S. Syahrullail, B.L.F. Chin: Comparison on tribological properties of vegetable oil upon addition of carbon-based nanoparticles, IOP Conference Series: Materials Science and Engineering, Vol. 206, No. 1, 2017.

[15] J.A.C. Cornelio, P.A. Cuervo, L.M. Hoyos-palacio, J. Lara-romero, A. Toro: Tribological properties of carbon nanotubes as lub-ricant additive in oil and water for a wheel – rail system, Journal of Materials Research and Technology, Vol. 5, No. 1, pp. 68–76, 2016.

[16] M. S.Nazir, M. H. M. Kassim, L. Mohapatra, M. A. Gilani, M. R. Raza, K. Majeed: Characteristic properties of nanoclays and characterization of nanoparticulates and nanocomposites, In R.M. Nasir, E.A. Rahim (Eds.) *Nanoclay reinforced polymer composites,* Springer, Singapore, pp. 35-55, 2017.

Serbian Tribology Society

SERBIATRIB '19

16th International Conference on Tribology

Faculty of Engineering University of Kragujevac

Kragujevac, Serbia, 15 – 17 May 2019

DEVELOPMENT OF A MULTIFUNCTIONAL TRIBOMETER: DESIGN CONCEPT

Gencaga PURCEK*, Harun YANAR
Department of Mechanical Engineering, Karadeniz Technical University, Trabzon, Turkey
* Corresponding author: purcek@ktu.edu.tr

Abstract: *Tribometer is a testing device which is used to measure tribological properties of materials or systems like friction force, wear rate and related phenomenon developed between surfaces in a relative motion. Until it was first invented by Leonardo da Vinci – the first tribologist, many types of tribometers have been developed. Since tribological problems are present in almost any field of engineering, various tribometers are in use to simulate all kinds of situations encountered in the real applications. In recent years, modular or multi-functional tribometers have been developed and transferred to the tests applications. In this study, a new tribological test platform is presented concerning its design, modular concept, operative system and loading options. This multi-functional tribometer was designed to conduct various tribological tests in the same test platform by chancing the modules. Developed tribometer can work together with the modules of "pin-on-disc", "linear reciprocating", "block-on-ring", "high temperature", "tribo-corrosion", "lubrication" and "piston ring on cylinder liner". The test platform was also designed to be flexible, and new simulators or modules can be adapted added if they are needed. On the other hand, the system has four main motion types of rotary, reciprocating, block on ring and angular rotary. The innovative design aspects are suitable to allow for a variety of probes, sample surfaces, and testing conditions. A user friendly software was also developed to evaluate, control and digitalize the data coming from the sensors and other electronic parts during testing.*

Keywords: *Tribometer, tribotester, multi-functional tribometer, modular tribometer, tribology, friction, wear, lubrication.*

1. INTRODUCTION

Tribology is the science and technology that investigates the interaction of surfaces in relative motion in the form of friction, wear, lubrication and other design aspects of materials science. These concepts of tribology have several practical implications in our everyday lives. For example, the friction between our feet and the ground allows us to walk and drive each day. Tribology, on the other hand, is an experiment-oriented branch of a complex, interdisciplinary science, in which testing plays a major role in the solution and/or understanding of technical problems [1]. Tribological problems are often complex, and their understanding and solution rely on experimental data obtained from laboratory tests. Various standard or non-standart test methods have been developed and used for this purpose. The results obtained from these tests are sensitive to the choice of test method and test conditions.

A tribometer (or tribotester) is a generic name given to a machine or device used to perform tests and simulations of wear, friction and lubrication [2]. In this regard, the first tribometer was invented by Leonrado da Vinci

– the first tribologist [3,4]. His first concepts are shown in Fig. 1.

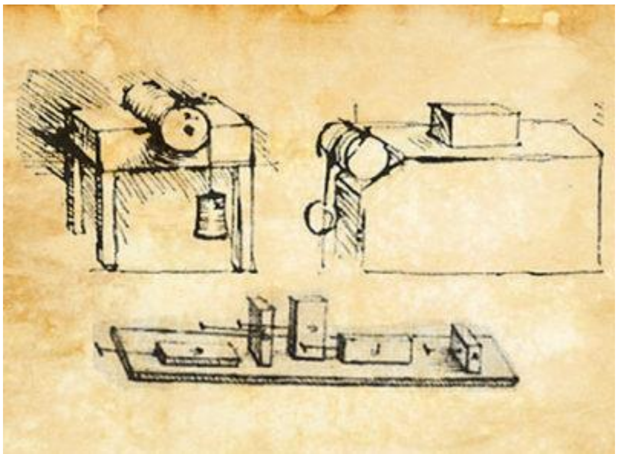

Figure 1. First tribometer concepts invented by Leonardo da Vinci who is known as the first tribologist.

In the tribometers, for generating the displacement, two basic movements are used: an oscillating linear (or reciprocating) movement (e.g., in the sledge configuration) or a rotating movement (e.g., in the pin-on-disk configuration). The advantage of the linear movement is to have the same relative displacement for each point of the contact area. The disadvantage is the restricted velocity which can be achieved. A rotating movement allows much higher relative velocities and is mostly used if a constant velocity is desired [5,6], On the other hand, new movements have been applied to the tribometers like angular reciprocating by using new driving system like servo- or stepper-motors. By using such motions types, more simulations become possible in tribological applications.

There are various tribological testing instruments in the market. Most of them have single or limited functional test capability. But in recent years, modular or multifunctional tribometers have been developed and transferred to the market. As looking at the tribometers developed so far, each has its original concept design regarding the application areas. Some of them have been developed devoid of multi-functionality, although some have limited multi-functionality. So it seems to be very beneficial to develop tribological test platform where more modules can work separately on that platform. Also, new driving and loading systems are required to adapt to such new multi-functional tribometers. Recently, some tribology-oriented companies have focussed on this issue and developed such tribometers. But each tribometer has its secret design concept and/or patent productions.

Therefore, this work presents the design, development and production of a new flexible tribological test platform (multi-functional tribometer) by which various modules can be worked. For this purpose, a special software was also developed to handle and process large amounts of high throughput tribological data.

2. MULTIFUNCTIONAL TRIBOMETER

2.1. Design concept and system overview

Before designing a new apparatus, one must identify its particular purposes. This determines the functional requirements of the apparatus, and it will differ for each machine part, type of machinery, and system. For the multifunctional tribometer developed, the following main features or parameters were selected initially:

- ✓ Standard loads up to 100 N. But it can be upgraded or low-graded by selecting high- or low-capacity load-cells.
- ✓ Speed control of the rotating disk
- ✓ Disc rotational speeds up to 3000 rpm
- ✓ A new user friendly software to set up experiments, handle, store and analyse the data with real time display of measurement data
- ✓ Continuous wear depth measurement option between
- ✓ Variable test path radius
- ✓ Variable stroke and frequency in reciprocating module
- ✓ Automatic stop when the coefficient of friction reaches a threshold value or when a specified number of turns is reached
- ✓ Measuring the test temperature continuously near or inside the abrading samples
- ✓ Measuring the environment temperature and relative humidity continuously

- ✓ Capturing the coefficient of friction between the sliding parts or samples.
- ✓ Test temperature options from room temperature up to 1000 C with a sophisticated high temperature module.
- ✓ Tribo-corrosion tests option in variety of corrosive liquid with well-designed trbo-corrosion module.
- ✓ Test option for conforming surfaces with a specifically designed block-on-ring module.
- ✓ A specified test option for piston-ring configurations with piston ring and cylinder liner test module.
- ✓ A test option for lubricated system with lubrication or liquid module.
- ✓ Test options with dead weights or spring-assisted mechanically loading
- ✓ Measuring the applied normal loads by a sensor.

Figure 2 shows a general 3-D view of the developed tribometer platform with the main modules, which is constructed based on the design rules described above. The instrument can be roughly divided into three sections: An upper loading and measuring section, a middle test platform section and a lower controlling and driving section. The upper loading and measuring section has the critical parts of the tribometer. Because the loading is required to change the loading force which influences the friction force. This part has two important components: First one is the arm having a load-cell for measuring the friction force and a sensitive distance sensor for measuring the wear depth consciously during the tests. The second one is preferable loading system which can be operated with dead weights and also spring-assisted weights. This may give the users to choose one of them according to their budget and system requirements. Furthermore, this system was especially designed to be able to adapt a closed-loop loading control with servo-driving system. The middle section provides a platform for modular exchange where all developed modules can easily be fixed and changed. This section includes driving shaft, a sled system on which the upper portion was built. Also the mechanical loading system was also fixed on this section. The lower section has the control and driving components as well as sensor's amplifiers.

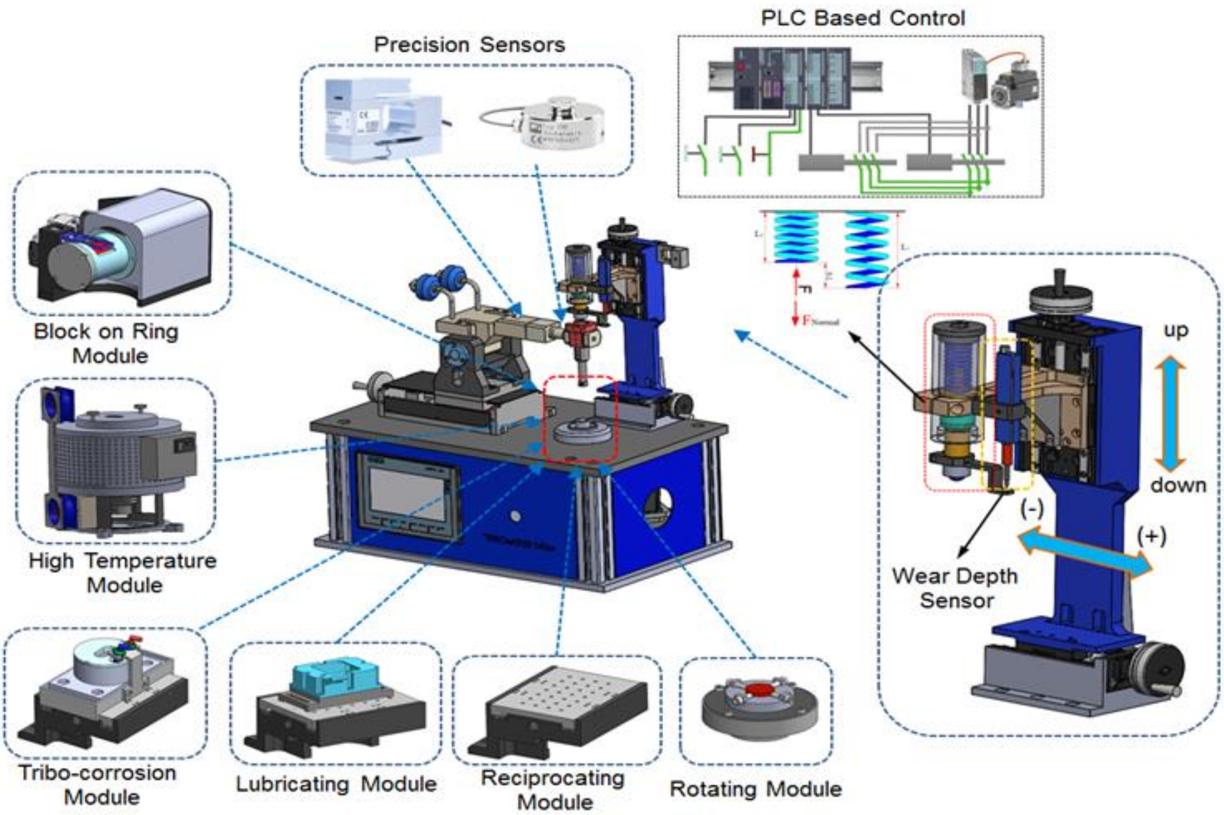

Figure 2. A general 3-D views of multifunctional tribometer with the main moudules.

2.2. Modules developed for Multi-Functional Tribometer

There are three main motion mode in developed tribometer: rotary, reciprocating and angular rotary. All functional modules were developed to be able to work with these motions modes. The main modules developed are summarized below:

Pin-on-disc module (Rotary Module)

This module was designed to be able to conduct the rotary tests according to ASTM G-99. A general 3D view of that module is shown in Fig. 4. In this module, various specimen holders were designed to be able to fixed the specimens from simple to the complex shapes. A rod connected to the loading arm was especially designed on which pin and ball type of samples can easily be fixed. The normal load is applied via this rod.

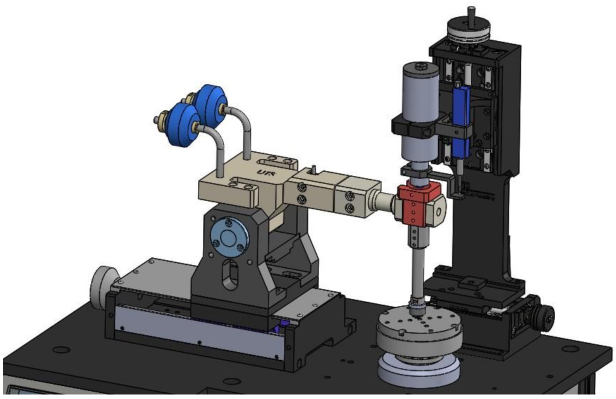

Figure 4. A general 3D view of the pin-on-disc (rotary) module.

Linear reciprocating module

This module was designed to be able to conduct the reciprocating tests according to ASTM G-133 [7]. A general 3D view of this module is shown in Fig. 5. In this module, a special disk and plate holder are used. Plate holder is mounted on guide pillars trough guide bushes with ball-bearing, which assure precise movement. In this system, the rotational motion is changed to a linear forward and backward motion (reciprocating) by a special mechanism. Thus, there is no need to use one more driving system and only one driving unit is used for both rotary and reciprocating motion modes. The stroke of the test can easily be fixed by a screw, and frequency is fixed by adjusting speed of the driving unit. The length of reciprocating moving depends on diameter of the disk. A special sample holders were placed onto the upper plate by which it is possible to fix the test samples by various shapes.

High Temperature module

High temperature test module was developed to analyse of friction and wear properties of the materials. especially for the development and quality control of some systems/tools like cutting tools, combustion engines and steam turbines, jet engines and power plants.

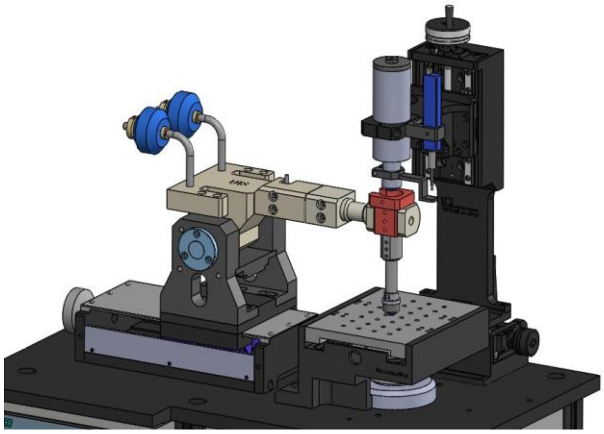

Figure 5. A general 3D view of linear reciprocating module.

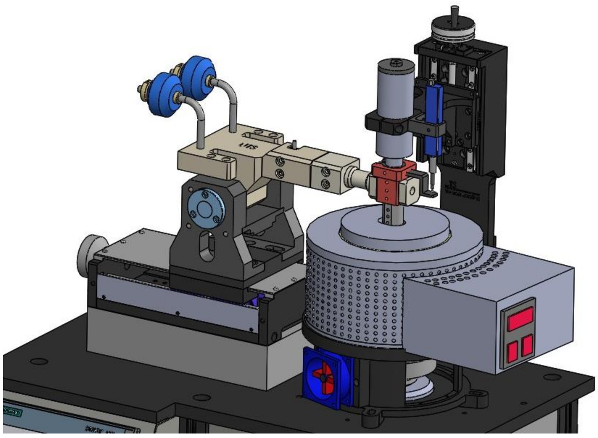

Figure 6. A general 3D view of high temperature module developed for the multi-functional tribometer.

This module warms up the sample homogeneously with a well-designed furnace/oven, and it accurately controls the sample temperature up to 1000 °C to simulate materials' in-service condition. The rotating parts inside the oven was manufactured by super alloys or high temperature stainless steels to be able to guarantee the minimum distortion during testing. Temperature set-point, set as a gradual increase or decrease in temperature, or even cycled through a series of steps can be programmed and controlled by PID controller. The oven of this system ensures that both disc and counter specimens are at the same temperature. The oven is fixed on a lover platform which includes cooling fans and design-assisted cooling parts. The model was designed concerning the minimum heat spreading out of the oven. A general 3D view of this module is shown in Fig. 6.

Block-on-ring module

The block-on-ring module is typically used to evaluate friction and wear of materials and lubricants where a ring/bearing/shaft is rotated under axial load according mainly to the ASTM G77 [8]. This allows to test the bearings, rings, shafts, seals, lubricant, grease etc. Thus this setup is a highly used one in the oil industry. The system has its own measuring and driving units except for normal loading. The loading is applied by main tribometer. The system allows both dry and lubricated tests. A special lubrication cap was designed to be able to evaluate the effect of lubrication in-between tribological systems.

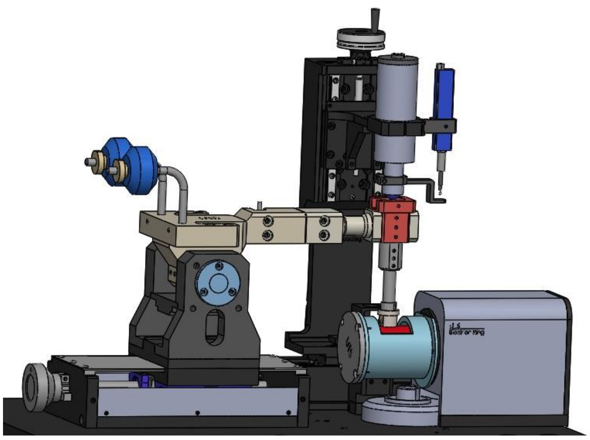

Figure 7. A general 3D view of block-on-ring module developed for the multi-functional tribometer.

The tests can be easily configured by defining the temperature (up to 200 C), test load (up to 100 N) and rotation speed (up to 3000 rpm). The rotating shaft is supported from both ends to prevent bending under high loads. With this developed module, several customized tests can also be performed including testing real components. A general 3D view of this module is shown in Fig. 7.

Tribocorrosion module

Tribo-corrosion module is characterized the materials/systems working under the combined effects of mechanical wear and corrosion. It is indispensable for evaluation of systems like pipes, pumps, fuel cells, batteries, biomedical and marine products and any material exposed to wear in a corrosive environment.

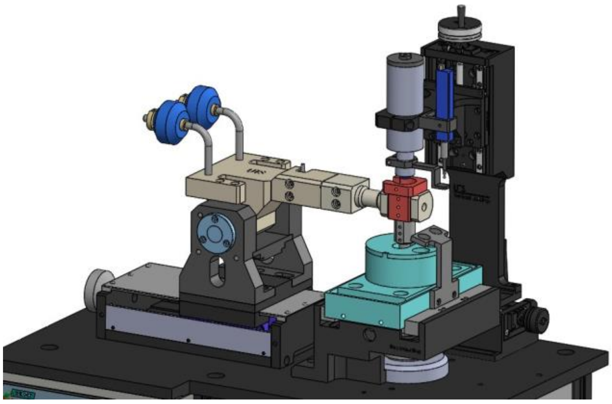

Figure 8. A general 3D view of tribocorrosion module developed for for the multi-functional tribometer.

This module was designed to be able to conduct the friction and wear tests into various corrosive environments (such as salt water, body fluid, acidic solutions, etc) on both rotative and reciprocating modules. The module designed for reciprocating motion mode can make the electro-tribocorrosion tests by the addition of potansiyostat. The module is made of corrosion-resistant material. For the removal of the heat generated during tribo-corrosion tests, a constant temperature bath with a water circulation system can be adapted. A general 3D view of this module is shown in Fig. 8.

Lubrication module

It is well known that for many industrial applications, friction and wear behavior of materials or systems working in liquid or oily environments and their characterization are extremely important. This module can work with both rotary and reciprocating main motion modes. This can also be used for different liquid environments with special corrosion cell design. An optional oil/liquid heating system is also developed.

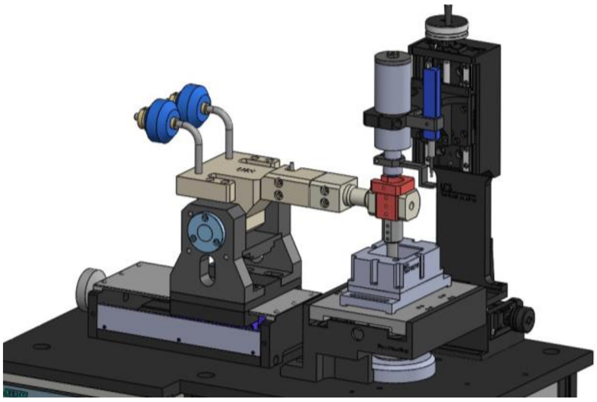

Figure 9. A general view of lubrication module and/or liquid container developed for the multi-functional tribometer.

This module was developed for two different options. In the first option, a cell was developed by wich test samples are immersed into the liquid or oil bath. In the other option, a drop-in lubrication was simulated . With this option, a flow rate regulated oil can be sent to the sample container as dropping after fixing by a sensetive valf. A genral 3D view of lubrication module is shown in Fig. 9.

Piston Ring and Cylinder Liner Test module

A significant portion of the friction loss in the power cylinder system stems from the contact between the piston skirt and the cylinder liner. The interaction between the piston skirt, lubricant, and cylinder interfaces is quite complex due to the constant changes in force, temperature, and speed in a real life engine. Optimizing each factor is key to obtaining optimal engine performance. The friction coefficient and wear rate will be observed to better understand how the interfaces behave in real-life applications. For evaluate the friction-lubrication and wear of such system, a special module was developed. This module works mainly with the reciprocating motion mode both in oily and oil-free environments. The module can make tests in different frequency and strokes. In addition, the module was designed to be heated in both dry and oily environments up to 200 °C with a precision heating system. A design has been made with the cylinder on the table and the segment on the upper arm.

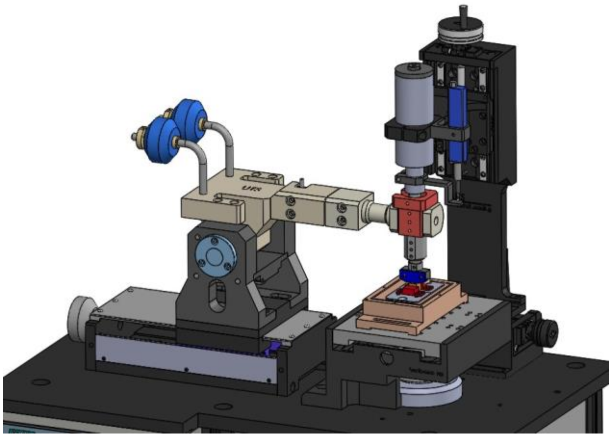

Figure 10. A general view of piston ring and cylinder liner test module.

A special ring catch is attached to the upper arm to be able to simulate the actual conditions. It is also possible to perform tribological characterization of the lubricants used with this module. A general 3D view of this module is shown in Fig. 10.

Environment chamber option

A chamber was also designed to create a gaseous environment in the test area in which non-corrosive gases like Argon, Nitrogen or controlled humidity air can be created.

2.3. Software and control of the tribometer

A special software was developed for this multifunctional tribometer. The control and software diagram is shown in Fig. 11. This software has four parts: Machine control, data acquisition, analysis and display. Test plan and sample related information is entered in the machine control module before starting of a test. Software controls the test parameters like speed, cycle, test duration, sling distance. Various outputs like friction force, coefficient of friction, wear depth and temperature are acquired. Acquired data can be presented in several ways. Graphs of individual test can be printed.

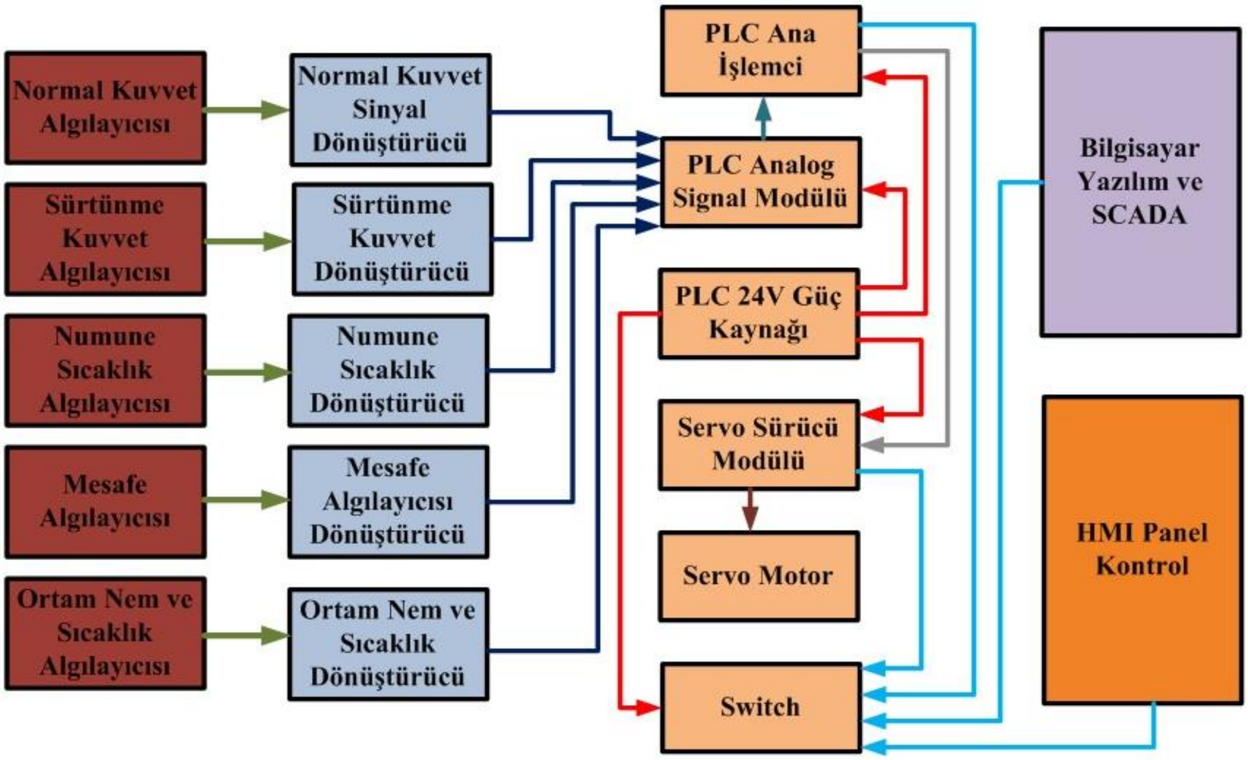

Figure 11. Software and control diagram of developed tribometer.

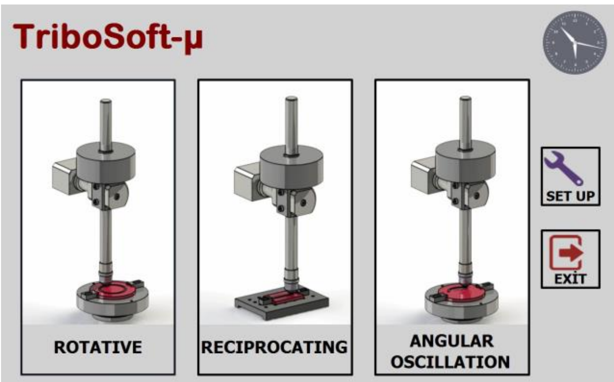

(a)

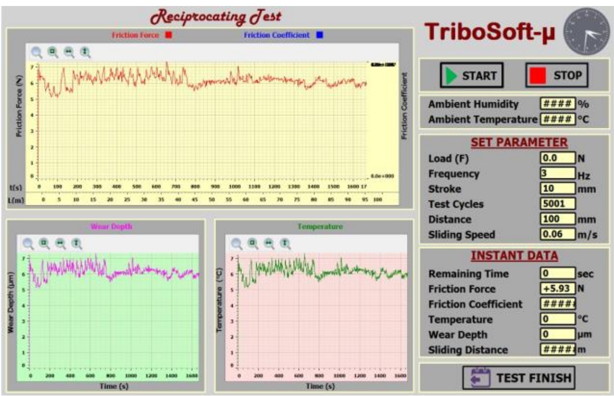

(b)

Fig. 12. A general view of the test screen of the software: (a) Initial screen where the proper drive mode is chosen and (b) main test screen where all set and measuring parameters can be screened as both numerical and graphical.

The system calculates the coefficient of friction values based on the measured values of the normal and frictional forces and displays them on a graph in real time. Acquired data can be exported to other software in Excel format. Some representative views of interfaces are shown in Fig. 12.

3. CONCLUSIONS

In this study, a new multifunctional tribological test platform was designed and built. Developed tribometer can work together with the modules of “pin-on-disc”, “linear reciprocating”, “block-on-ring”, “high temperature”, “tribo-corrosion”, “lubrication” and “piston ring on cylinder liner”. On the other hand, the system has four main motion types of rotary, reciprocating, block on ring and angular rotary. The innovative design aspects are suitable to allow for a variety of probes, sample surfaces, and testing conditions. A user friendly software was also developed to evaluate, control and digitalize the data coming from the sensors and other electronic parts during testing.

ACKNOWLEDGEMENT

This study was supported by the Scientific and Technological Research Council of Turkey (TUBITAK) under Grant No: 117M510.

REFERENCES

[1] E. Zdravecká, M. Ondáč, J. Tkáčová, The wear tribometer and digitalization of tribological tests data, Journal of Achievement in Materials and Manufacturing Engineering, Vol. 61, No. 2, pp. 321-326, 2013.

[2] H. Kaleli, New Universal Tribometer as Pin or Ball-on-Disc and Reciprocating Pin-on-Plate Types , Tribology in Industry, Vol. 38, No. 2, pp. 235-240, 2016.

[3] B. Bhushan, “Chapter 12: Friction and Wear Screening Test Methods.” Springer Handbook of Nanotechnology, Berlin, 2006.

[4] Tribometers, available at: http://www.tribonet.org /tribometer/, accessed: 10.04.2019.

[5] V. Kalihari, S.J. Timpe, L McCarty, M. Ninke, and J. Whitehead: An automated high throughput tribometer for adhesion, wear, and friction measurements, Review of Scientific Instruments, Vol. 84, pp. 1-9, 2013.

[6] M.S. Alsoufi, D.G. Chetwynd, Design and Preliminary Evaluation of a New Feedback-controlled Micro-tribometer, Proceedings of the 10th euspen International Conference – Delft , 2010.

[7] N. Marjanovic, B. Tadic, B. Ivkovic, S. Mitrovic: Design of Modern Concept Tribometer with Circular and Reciprocating Movement, Tribology in industry, Vol. 28, No. 3&4, 2006.

[8] ASTM G77-98 Standard Test Method for Ranking Resistance of Materials to Sliding Wear Using Block-on-Ring Wear Test, 1998.

Tribological Properties of Solid Materials

16th International Conference on Tribology – SERBIATRIB '19

15 – 17 May 2019, Kragujevac, Serbia

Serbian Tribology Society

SERBIATRIB '19

16th International Conference on Tribology

Faculty of Engineering University of Kragujevac

Kragujevac, Serbia, 15 – 17 May 2019

OPTIMIZATION OF LOAD AND HBN CONTENT FOR IMPROVING TRIBOLOGICAL PERFORMANCE OF A SI_3N_4-HBN CERAMIC COMPOSITE USING TAGUCHI-GREY RELATIONAL ANALYSIS

Sachin GHALME[1,*], Yogesh BHALERAO[2], Michael MORGAN[3]

[1*] Dept. of Mechanical Engg., Sandip Institute of Tech. & Research Centre, Nashik (MS), India.

[2]Dept. of Mechanical Engg., MIT Academy of Engg., Alandi, Pune (MS), India.

[3]Faculty of Engg. & Tech., Liverpool John Moores University, UK.

*Corresponding author: sachinghalme@hotmail.com

Abstract: *Silicon nitride (Si_3N_4) is common in various industrial applications and proven its applicability with its high fracture toughness, strength and wear properties. The material has a proven capability in the biomedical field in the context of orthopedic applications. This paper reports the experimental and Taguchi based grey relational analysis for the tribological behavior of Si_3N_4-hBN ceramic composite sliding against steel (ASTM 316L) in the dry condition. The wear tests were conducted with 0, 4, 8, 12, and 16 % volume of hBN in Si_3N_4 at loading conditions in the range 5N < Load < 25N, with 5N increments using Pin-on-Disc (PoD) tribometer. A weighted grey relational grade is calculated for minimization of volumetric wear rate and coefficient of friction with aim of improving tribological performance of Si_3N_4-hBN ceramic composite applicable for various industrial and biomedical applications. Load and % volume of hBN addition are two factors considered for optimization. Analysis of variance (ANOVA) presented % vol of hBN is significant factor followed by load. In the Si_3N_4-hBN / steel contact pair, the main phenomenon of wear observed was an adhesive type of wear at both low load and at high load.*

Keywords: *Silicon Nitride (Si_3N_4), hexagonal Boron Nitride (hBN), Steel, Taguchi-Grey Relational Analysis, Wear, Coefficient of Friction (CoF).*

1. INTRODUCTION

In 1859, Deville and Wohler developed synthetic Si_3N_4 and in 1950's commercial interest in Si_3N_4 increased with a better understanding of its properties. Properties of Si_3N_4 have made it a highly suitable material for the biomedical field along with various industrial applications and extreme operating conditions, in particular those demanding high strength, low density, and low wear rate [1]. Treatment for the hip, knee, shoulder, and other articulated parts in the body has been revolutionized with the development of biomaterials. Important characteristics of biomaterials are that they are inert within the body environment and sufficiently mechanically stable to sustain loads consistent with those of the human body. The most common materials used for hip/knee joint replacement are metal (M), Plastic (P), and ceramic (C). The plastic is generally used for cup applications only while other metal and ceramic materials are used for both cup and socket applications. The most common material combinations available in the market are Metal-on-Metal (MoM), Metal-on-Plastic (MoP), Ceramic-on-Plastic (CoP), Ceramic-on-Ceramic (CoC), and Ceramic-on –Metal (CoM). In the MoM category, titanium alloys and stainless steel are frequently used in total hip replacement (THR). Metal-on-UHMWPE has become preferable to the MoM system, because of the adverse reaction of metal ions release during wear in MoM pair [2, 3]. Si_3N_4 is biocompatible and along with its superior mechanical properties presented itself as an alternative material in the field of orthopedic surgery [4]. Si_3N_4 is suitable in the field of biomedical for developing hip and knee joints and spine disc surgery bearings [5, 6].

Tribological studies of articulating surfaces have focused on friction and wear performance during articulation. The study of articulating surfaces present in the human body or in animals, such as an artificial joint, is referred to as bio-tribology. Bio-tribology is very important in order to understand the performance or lifespan of an artificial joint. Wear in an artificial joint remains a critical issue limiting the lifespan of artificial joints. Although Si_3N_4 is suitable for joint replacement applications the wear performance of Si_3N_4 is still an issue of debate. One of the common opinions on the wear performance of Si_3N_4 is that the absence of material oxidation helps it to minimize friction in the presence of water lubricants [7]. The Amedica Corporation, USA have developed various prototype total hip bearings using sintered Si_3N_4, and in testing have confirmed the improved strength and fracture toughness over medical grade oxide ceramic alumina (Al_2O_3) [8] and a number of research works have already proved the enhanced wear performance of Si_3N_4 in the presence of water lubrication. The wear performance of Si_3N_4 will be more favorable in the human synovial fluid, as it is an excellent lubricant irrespective of bearing material [9, 10]. One of the unique properties of Si_3N_4 is its ability to be formulated into a porous substrate and hard glassy bearing surface, capable of providing direct bone in-growth. The tribological study of ceramic has shown that the wear mechanism in ceramic depends upon the contact conditions. Wear in the Si_3N_4 occurs through surface fracture with a load exceeding the threshold value and further wear occurs due to surface oxidation [11].

The wear performance of Si_3N_4 against steel in the dry lubricant condition is still unclear. Akdogan and Stolarski [12] evaluated the wear performance of Si_3N_4 sliding against steel; they found that main types of wear are abrasive and adhesive wear of the surface. Olofsson *et al.* [13] evaluated the wear performance of a Si_3N_4 and CoCr disc against a Si_3N_4 and Al_2O_3 ball in the presence of a Phosphate Buffered Saline (PBS) and a bovine serum using PoD tribometer. In the case of Si_3N_4 sliding against Si_3N_4, it was shown the formation of a tribofilm on Si_3N_4 controlled friction and wear in both PBS and bovine serum comparable to other pairs.

Hexagonal boron nitride (hBN) is a bio-compatible, solid situ lubricating material [14-16]. Some researchers proposed the addition of hBN in ceramic materials to improve their wear performance. Incorporation of hBN in silicon nitride leads to the generation of hydrated layers of an oxides (H_3NO_3 and BN $(H_2O)_x$) during sliding thereby minimizing the wear coefficient. Li *et al*. [17] investigated the effect of the hBN addition on the friction and wear performance of B4C-hBN ceramics in dry friction conditions. With 20% of hBN content in the Si_3N_4-hBN ceramic composites, the CoF reached a minimum value of 0.179. Carrapichano *et al.* [18] conducted the sliding wear test on a pin-on-disc tribometer for the Si_3N_4-BN composite in a self-mated pair, with 10, 18 and 25% vol. of BN in Si_3N_4. They concluded that the addition of Boron up to 10% improved the tribological properties of Si_3N_4 and further addition affected the mechanical properties of Si_3N_4. Wei *et al.* [19] analyzed the tribological behavior of Si_3N_4-hBN (with 0%, 2%, 4%, 6%, 8%, and 10% of hBN) sliding against pure Si_3N_4. The analysis of the experimental results presented a decrease in CoF with an increase in the hBN content.

Along with the addition of lubricants, various factors including speed and load have a significant effect on the tribological performance of silicon nitride. In an earlier study, it has been demonstrated that wear loss of Si_3N_4-hBN ceramic composite sliding against steel is a function of the interaction between load and % volume of hBN addition [20]. Chen [21] evaluated the tribological performance of Si_3N_4-based ceramic materials for various loading conditions. At low loading the wear mechanism was abrasive, with an increase in load; the adhesive wear mechanism was prominent. Wei Chen *et al.* [22] evaluated the effect of sliding speed on the tribological performance of Si_3N_4-hBN sliding against steel. The analysis of results revealed that with an increase in speed the degree of abrasive wear decreased leading to a decrease in the coefficient of friction. In another work, Wei Chen [23] evaluated the effect of load on the tribological performance of a Si_3N_4-hBN ceramic sliding against ASS and 45 steel. It was reported that the SN10/ASS sliding pair presented the minimum value of wear rate and CoF. But, with the increasing load for the same pair, the CoF increased with a combined abrasive and adhesive mechanism.

In this study, we evaluated the tribological performance of Si_3N_4-hBN ceramic composite sliding against ASTM 316L medical grade steel without lubricant. Volumetric wear rate and coefficient of friction (CoF) were evaluated for analysis of tribological performance. Taguchi based grey relational analysis applied with aim of optimization of load and hBN content for simultaneous minimization of wear rate and CoF

2. SPECIMEN PREPARATION AND TEST METHOD

Giving consideration to earlier research works the parameters for our tribological study were selected to be: % volume of hBN in silicon nitride at 0%, 4%, 8%, 12%, and 16% level (SN0 –SN16). Table 1 shows the factors and corresponding levels selected for the tribological study of a Si_3N_4-hBN ceramic composite in a dry environment.

The pin samples were prepared with a 99 % pure powder of Si_3N_4 and hBN of 1-µm size mixed in five different proportions with the aid of ball mill. The mixed powder with an additive of polyvinyl alcohol was sintered by uniaxial

Table 1. Control parameters and its level values

Control para.	**Levels**				
	1	**2**	**3**	**4**	**5**
% Vol. of hBN	0 (SN0)	4 (SN4)	8 (SN8)	12 (SN12)	16 (SN16)
Load (N)	5	10	15	20	25

Table 2. Properties of sintered sample*

Properties	**Samples**				
	SN0	**SN4**	**SN8**	**SN12**	**SN16**
Density (gm/cc)	2.04	1.96	1.96	1.93	1.84
Vickers Hardness (MPa)	7484.51	2775.88	2318.17	1741.07	907.96

*Testing at Central Glass and Ceramic Research Institute, Kolkata (India).

Table 3. Typical properties of steel disc

Desig.	**Density (gm/cc)**	**Mod. of elasti. in tension (GPa)**	**Mean coeff. of thermal expansion from 293 to 873 ◦K (10^{-6}/K)**	**Thermal conductivity at 373 ◦K (W/m K)**	**Avg. surface roughness Ra (µm)**
ASTM 316L	7.95	186.4	18.5	16	0.242

hot-pressing in an inert atmosphere at 30 MPa, 1600 °C and 60 min dwell time in the form of a pin of the dimension 10 mm diameter and 15 mm length.

Tables 2 and 3 show corresponding properties of Si_3N_4-hBN ceramic composite and steel disc.

The wear experiments were performed on a Ducom TRLE-PMH400 pin-on-disc tribometer having a maximum normal load capacity of 200 N. Tests were performed according to ASTMF732 standards [24]. During tests the composite was used as the pin specimen loaded through a vertical specimen holder against a flat steel disc as the counterface rotating at a speed of 200 rpm for a 20-min duration.

Wear rate and coefficient of friction recorded online during wear test. Wear measurement- wear volume loss or volumetric wear rate was calculated per meter of sliding distance using the following equation:

$$Vol.Wear\ Rate\ \left(mm^3/m\right) = \frac{Wear\ loss \times 10^{-3} \times CS\ Area\ of\ pin}{Sliding\ distance} \quad (1)$$

Where, wear loss is in microns, CS area in mm^2, and sliding distance in m.

3. METHODOLOGY

3.1 Design of Experiment-Taguchi Method

Design of experiment –Taguchi method is a statistical technique, helps to study a number of parameters simultaneously and economical way. Taguchi method helps to plan experimental layout using Orthogonal Array (OA) to study the effect of control parameter through a minimal number of experiments [25]. Orthogonal Array used to plan experiment for two control parameters such as load and % vol. of hBN addition in silicon nitride. Each control parameter varied through five levels as shown in Table 1. Based on two control parameters and five levels L25 orthogonal array selected with 25 numbers of experiments. To evaluate the process parameters, Taguchi method uses signal-to-noise (S/N) ratio as an objective function for the desired output. S/N ratio is a measure of robustness helps to identify control factors that reduce variability in a product or process by minimizing the effects of uncontrollable factors. S/N ratio is characterized into three categories: Nominal the best (NB), Lower the better (LB) and Higher the better (HB). Regardless of desired output, the maximum value of S/N ratio is corresponds optimized control parameters for desired output. Taguchi method can't optimize multi-objective optimization problems. To overcome this, Taguchi method is integrated with Grey relational analysis (GRA) to optimize multi-objective problems.

3.2 Grey Relational Analysis

In 1982, Deng proposed Grey system theory to uncertainties in system models and analyze the relation between systems. Grey relational analysis helps to convert multi-response problem into single response problem by calculating grey relational grade (GRG). The various steps followed in the grey relational analysis are as follow:

1. Normalization of data in the range of 0 or 1.

The collected raw experimental data is normalized into 0 or 1, using two criteria wise lower is better (LB) and higher is better (HB). A LB criterion is used to normalize data when the objective is to minimize. Equation 2 is used for LB criteria. A HB criterion is used to normalize data when the objective is to maximize. Equation 3 is used for HB criteria

$$x_i(k) = \frac{\max y_i(k) - y_i(k)}{\max y_i(k) - \min y_i(k)} \quad (2)$$

$$x_i(k) = \frac{y_i(k) - \min y_i(k)}{\max y_i(k) - \min y_i(k)} \quad (3)$$

Where, $x_i(k)$ is the value after the grey relational generation, $\min y_i(k)$ is the smallest value of $y_i(k)$ for the k^{th} response, and $\max y_i(k)$ is the largest value of $y_i(k)$ for the k^{th} response. i = 1, 2, 3… the number of experiments and k =1, 2, 3… the number of responses.

2. Calculation of Grey Relational Coefficient (GRC)

GRC is calculated to determine the relation between ideal and actual normalized experimental data. GRC (ξ) is calculated using equation 4.

$$\xi_i(k) = \frac{\Delta_{min} + \psi\Delta_{max}}{\Delta_{oi}(k) + \psi\Delta_{max}} \qquad (4)$$

Where $\Delta_{oi}(k) = \|x_0(k) - x_i(k)\|$ = difference of the absolute value of $x_0(k)$ and $x_i(k)$; ψ is the distinguishing coefficient; $0 < \psi < 1$, Δ_{min} is the smallest value of $\Delta_{oi}(k)$ and Δ_{max} is the largest value of $\Delta_{oi}(k)$.

3. Calculation of Grey Relational Grade (GRG)

The analysis of multiple outputs characteristic is based on grey relational grade. The GRG (γ) is an average sum of GRC and calculated using equation 5. Its value lies between 0 and 1.

$$\gamma_o = \frac{1}{n}\sum_{k=1}^{n} \xi_i(k) \qquad (5)$$

Where, n is a number of process responses.

4. RESULTS AND DISCUSSION

The output characteristic wise, the coefficient of friction recorded online and volumetric wear rate calculated using equation 1. The collected experimental data is further processed following steps 1 to 3 for calculation of GRG. To improve the tribological performance of Si3N4-hBN ceramic composite, both CoF and volumetric wear rate needs to be minimized. The experimental data is normalized with LB criterion using equation 2. After calculating GRC, the weighted GRG is calculated with 70% weightage to volumetric wear rate and 30% weightage to CoF.

$$Weighted\ GRG = \frac{1}{2}(0.7\,\xi_i\,VWR + 0.3\,\xi_i\,CoF) \qquad (6)$$

Table 4, shows experimental data processed into a weighted grey relational grade.

Figure 1 shows the column map for a grey relational grade of Si_3N_4-hBN ceramic composite sliding against steel under dry conditions. From Table 4 and Figure 1 it is clear that the maximum value of GRG- 0.467 observed at 5N load and 12% volume of hBN in silicon nitride. The experiment number 3 corresponding to 5N load and 12% volume of hBN presents optimal condition for minimum volumetric wear rate and coefficient of friction simultaneously.

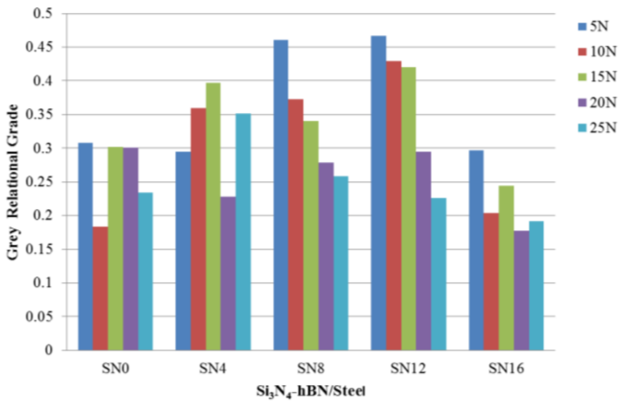

Figure 1. Column Map for GRG of Si_3N_4-hBN/Steel Pairs under Different Loads

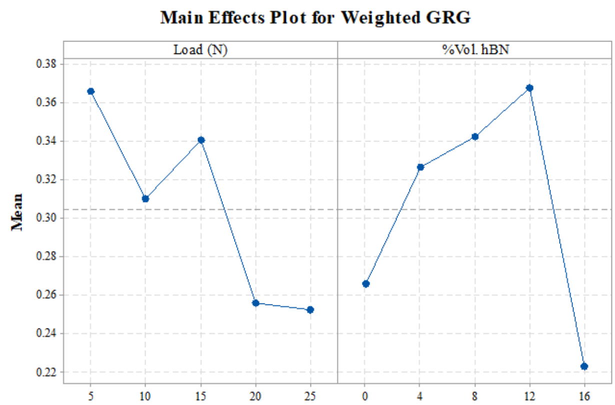

Figure 2. Main Effect Plot for Weighted GRG

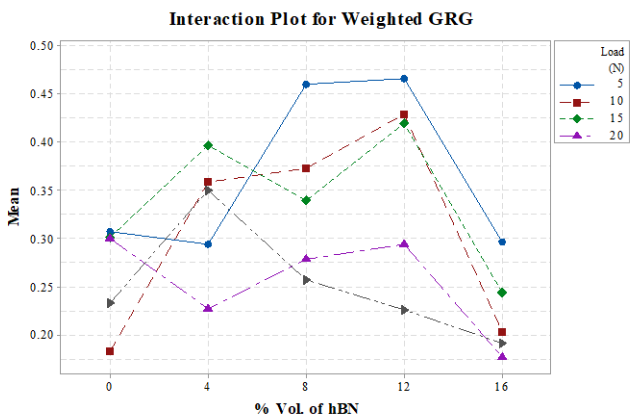

Figure 3. Interaction Plot for Weighted GRG

The main effect plot and interaction plot of load and % vol. of hBN on weighted grey relational grade is presented in Figure 2 and 3.

Table 4. Data Processing of Each Performance Characteristic (Grey Relational Analysis)

Expt. No.	Control Parameter		Performance Characteristic		GRC (ξ)		GRG (γ)	Rank
	Load (N)	% Vol. hBN	Vol. Wear Rate (mm^3/m)	CoF	Vol. Wear Rate (mm^3/m)	CoF		
1	5	4	0.6671	0.01	0.415	1	0.295	15
2	5	8	0.0653	0.014	0.898	0.978	0.461	2
3	5	12	0.0381	0.03	0.948	0.899	0.467	1
4	5	16	0.4209	0.074	0.533	0.737	0.297	13
5	5	0	0.4983	0.028	0.49	0.909	0.308	10
6	10	4	0.2215	0.06	0.69	0.782	0.359	7
7	10	8	0.1481	0.096	0.775	0.677	0.373	6
8	10	12	0.0656	0.065	0.898	0.766	0.429	3
9	10	16	0.8591	0.17	0.355	0.53	0.204	22
10	10	0	1.5294	0.097	0.235	0.674	0.183	24
11	15	4	0.0621	0.164	0.903	0.539	0.397	5
12	15	8	0.1869	0.146	0.727	0.569	0.34	9
13	15	12	0.0126	0.217	1	0.465	0.42	4
14	15	16	0.4835	0.216	0.498	0.466	0.244	19
15	15	0	0.2615	0.194	0.652	0.495	0.302	11
16	20	4	0.5499	0.243	0.464	0.436	0.228	21
17	20	8	0.3556	0.179	0.576	0.516	0.279	16
18	20	12	0.2116	0.369	0.701	0.334	0.295	14
19	20	16	0.9441	0.276	0.333	0.404	0.177	25
20	20	0	0.2061	0.335	0.706	0.356	0.301	12
21	25	4	0.1153	0.252	0.819	0.427	0.351	8
22	25	8	0.5195	0.129	0.479	0.602	0.258	17
23	25	12	0.4759	0.37	0.502	0.333	0.226	18
24	25	16	0.7868	0.278	0.376	0.402	0.192	23
25	25	0	0.4672	0.3085	0.506	0.376	0.234	20

From main effect plot, it is clear that 5N load and 12% volume of hBN has the maximum value of weighted GRG, presenting optimum parameter level for load and hBN addition. Interaction plot presents strong interaction of load and hBN addition on weighted GRG or on tribological performance of silicon nitride.

4.1 Analysis of Variance (ANOVA)

The analysis of variance (ANOVA) is implemented to evaluate the significant factor affecting the tribological performance of silicon nitride. The ANOVA is performed for GRG considering load and % volume of hBN as two factors. The ANOVA is carried out at 99% of confidence level [25]. Table 5 shows ANOVA for the weighted grey relational grade.

Table 5. ANOVA for Weighted Grey Relational Grade

Source	DF	Adj. SS	Adj. MS	F-Value	P-Value
Load (N)	4	0.05075	0.012687	3.63	0.028
% Vol. hBN	4	0.07014	0.017534	5.01	0.008
Error	16	0.05599	0.003500		
Total	24	0.17688			

The last column of Table 5 showing P-value indicating the significance of control parameters on the tribological performance of silicon nitride. % volume of hBN has P-value 0.008 is less than alpha value 0.05, indicating it is a more significant parameter affecting the tribological performance of silicon nitride.

5. CONCLUSION

In this study, an attempt has been made for simultaneous minimization of wear rate along with the coefficient of friction in SN-hBN/steel sliding pair under dry lubricating conditions so as improve its overall tribological performance. Load and addition of hBN are two factors were selected for optimization in order to improve tribological performance of Si_3N_4–hBN ceramic composite. Summarizing the experimental results, the following conclusions can be drawn:

1. Among all SN-hBN/steel sliding pairs, the best tribological performance was observed with the SN12/ steel pair under a load of 5N condition. This is the optimal condition of load and % volume of hBN for minimization of wear rate and coefficient of friction in Si_3N_4-hBN ceramic composite sliding against steel.
2. There may be a formation of a film or hydrated layers on the surface of the pin at 5N in the SN12 pin, due to the incorporation of hBN. The tribo-chemical reaction leads to the formation of layers on the pin surface protecting the pin surface from wear.
3. Under the all loading condition, the 12% volume of hBN was a reasonable amount for the formation of a protecting film on the surface. The protecting film could not be formed for SN0/steel, SN4/steel, and SN8/steel pairs under the same loading condition and this may be because of low hBN content. A high value of wear rate was observed in the SN16 /steel pair because of its poor physical and mechanical properties.
4. Based on ANOVA results, the most effective parameter is the addition of hBN in silicon nitride improving its tribological performance.

REFERENCES

[1] J.F. Dill: Hybrid bearing technology for advanced turbomachinery: rolling contact fatigue testing, Journal of Engineering for Gas Turbines and Power, Vol. 118, No. 1, pp. 173-178, 1996.

[2] H. McKellop, F.W. Shen, B. Lu, P. Cambell, R. Salovey: Development of an extremely wear-resistant ultra-high molecular weight polyethylene for total hip replacement, Journal of Orthopaedic Research, Vol. 17, No. 2, pp. 157–167, 1999.

[3] O.K. Muratoglu, C.R. Bragdon, D.O. O'Connor, M. Jasty, W.H. Harris, R. Gul,F. McGarry: Unified wear model for highly crosslinked ultra-high molecular weight polyethylenes (UHMWPE), Biomaterials, Vol. 20, No. 16, pp. 1463–1470, 1999.

[4] B. Cappi, S. Neuss, J. Salber, R. Telle, R. Knüchel, H. Fischer: Cytocompatibility of high strength non-oxide ceramics, Journal of biomedical materials research, Vol. 93, No.1, pp. 67−76, 2010.

[5] B.S. Bal, A. Khandkar, R. Lakshminarayanan, I. Clarke, A.A. Hoffman, M.N. Rahaman: Testing of silicon nitride ceramic bearings for total hip arthroplasty, Journal of biomedical materials research Part B: Applied Biomaterials, Vol. 87, No. 2, pp. 447–454, 2008.

[6] A. Neumann, C. Unkel, C. Werry, C.U. Herborn, H.R. Maier, B.C. Ragoss, K. Jahnke: Prototype of a silicon nitride ceramic-based miniplate osteofixation system for the midface, Otolaryngology—Head and Neck Surgery, Vol. 134, No. 6, pp. 923–930, 2006.

[7] M. Mazzocchi, A. Bellosi: On the possibility of silicon nitride as a ceramic for structural orthopaedic implants. Part I: Processing, microstructure, mechanical properties, cytotoxicity, Journal of Materials Science: Materials in Medicine, Vol. 19, No. 8, pp. 2881-2887, 2008.

[8] B.S. Bal, A. Khandkar, R. Lakshminarayanan, I. Clarke, A.A. Hoffman, M.N. Rahaman: Fabrication and Testing of Silicon Nitride Bearings in Total Hip Arthroplasty, Journal of Arthroplasty, Vol. 24, No. 1, pp. 110-116, 2009.

[9] M.E. Blewis, G.E. Nugent-Derfus, T.A. Schmidt, B.L. Schumacher, R.L. Sah: A model of synovial fluid lubricant

composition in normal and injured joints, European Cells & Materials, Vol. 13, pp. 26-39, 2007.
[10] D. Mazzucco, M. Spector: The John Charnley Award Paper. The role of joint fluid in the tribology of total joint arthroplasty, Clinical Orthopaedics & Related Research, Vol. 429, pp. 17-32, 2004.
[11] S. Jahanmir: Wear transitions and tribochemical reactions in ceramics. Proceedings of the Institution of Mechanical Engineers, Part J: Journal of Engineering Tribology, Vol. 216, No. 6, pp. 371-385, 2002.
[12] G. Akdogan, T.A. Stolarski: Wear in metal/silicon nitride sliding pairs, Ceramic International, Vol. 29, pp. 435–446, 2003.
[13] J. Olofsson, T.M. Grehk, T. Berlind, C. Persson, S. Jacobson, H. Engqvist: Evaluation of silicon nitride as a wear resistant and resorbable alternative for total joint replacement, Biomatter, Vol. 2, No. 2, pp. 1-9, 2012.
[14] A. Gangopadhyay, S. Jahanmir, M.B. Peterson: Self-lubricating ceramic matrix composites, in S. Jahanmir (Ed.): *Friction and Wear of Ceramic*, Marcel Dekker, New York, pp. 163-197, 1997.
[15] T. Saito, Y. Imada, F. Honda: Chemical influence on wear of Si_3N_4 and hBN in water, Wear, Vol. 236, No. 1-2, pp. 153-158, 1999.
[16] U.S. Faiz, S. Glavatskih, O.N. Antzutkin: Boron in Tribology: from borates to ionic liquids, Tribology Letters, Vol. 51, No. 3, pp. 281-301, 2013.
[17] X. Li, Y. Gao, W. Pan, Z. Zhong, L. Song, W. Chen, Q. Yang: Effect of hBN content on the friction and wear characteristics of B4C–hBN ceramic composites under dry sliding condition, Ceramic International, Vol. 41, pp. 3918–3926, 2015.
[18] J.M. Carrapichano, J.R. Gomes, R.F. Silva : Tribological behaviour of Si_3N_4-BN ceramic material for dry sliding applications, Wear, Vol. 253, No. 9-10, pp. 1070-1076, 2002.
[19] D.Q. Wei, Q.C. Meng, D.C. Jia: Mechanical and tribological properties of hot-pressed hBN/Si_3N_4 ceramic composites, Ceramic International, Vol. 32, pp. 549–554, 2006.
[20] S. Ghalme, A. Mankar, Y. Bhalerao: Integrated Taguchi- Simulated Annealing (SA) Approach for Analyzing Wear Behaviour of Silicon Nitride, Journal of Applied Research and Technology, Vol. 15, pp. 624-632, 2018.
[21] X.J. Chen: *Study on Preparation and Properties of Si_3N_4 based Ceramics*, Master Dissertation of Central South University, China, 2012.
[22] W. Chen, Y. Gao , L. Chen, H. Li: Influence of Sliding Speed on the Tribological Characteristics of Si_3N_4-hBN Ceramic Materials, Tribology Transactions, Vol. 56, No. 6, pp. 1035-1045, 2013.
[23] W. Chen, D. Zhang, X. Ai : Effect of load on the friction and wear characteristics of Si_3N_4-hBN ceramic composites sliding against steels, Ceramic International, Vol. 43, No. 5, pp. 4379-4389, 2016.
[24] ASTM F732-00 *Standard Test Method for Wear Testing of Polymeric Materials Used in Total Joint Prostheses*, 2011.
[25] R.K. Roy: *Design of Experiments using the Taguchi Approach: 16 Steps to Product and Process Improvement*, John Wiley & Sons, USA, 2001.

Serbian Tribology Society

SERBIATRIB '19

16th International Conference on Tribology

Faculty of Engineering University of Kragujevac

Kragujevac, Serbia, 15 – 17 May 2019

TRIBOLOGICAL CHARACTERISTICS OF EXPERIMENTAL HARD ALLOY GRADES WITH MODIFIED COBALT BINDER UNDER CONDITIONS OF DRY FRICTION ON TITANIUM-ALUMINUM ALLOY VT-3

Aleksey N. BESKOPYLNY[1], Evgeny V. FOMINOV[1]*, Constantine G. SHUCHEV[1], Anatoly A. RYZHKIN[1]

[1]Don State Technical University, Rostov-na-Donu, Russian Federation

*Corresponding author: fominoff83@mail.ru

Abstract: *The paper is dedicated to investigations of tribological characteristics of experimental tool hard alloy (HA) grades based on tungsten carbide with modified cobalt binder under conditions of dry friction on disks made of titanium-aluminum alloy VT-3, as well as measures of their surface micro-hardness. All measured parameters were compared with similar characteristics of standard HA grade VK8, on the basis of which these experimental grades were developed. The research found that the surface micro-hardness of all experimental HA grades as pins were higher than that for the basic grade VK8; the highest value was fixed for the HA grade with symbol mark 2.22 (composition of the binder - 5.65% Co +1.8% Mo +0.6% Ti). The highest wear resistance was obtained for 2.23 (5.1%Co+2.7%Mo+0.61%Ti) and 2.21 (5.4%Co+1.43%Fe+0.82% Cu), the lowest – for grade 2.22. The analysis of friction processes peculiarities allows to explain the high wear resistance of grades 2.21 and 2.23 by features of surface structures ("the third body") formation during friction. Friction process for these HA grades include the periods of "the third body" intensive growth to the considerable thickness values, as well as the periods of its abrasion; due to this phenomena resulting wear rates for these two grades proved to be significantly lower than for the base grade VK8. The "third body" generated during friction protects surfaces from wear, at the same time it has its own significant shear resistance and increases actual contact area, due to this phenomena the friction forces for grades 2.21 and 2.23 are somewhat higher than for basic grade VK8. The grade 2.22 is characterized by the highest average friction force and its r.m.s. deviation value, which result in the greatest wear rates for both the HA pins and rotating disks. So according to the results of testing the best results among the investigated experimental HA grades were obtained for grade 2.23: the lowest average friction coefficient and the lowest track surface roughness on rotating disks, as well as the highest wear resistance values.*

Keywords: *tool materials, hard alloys, friction, wear resistance, surface micro-hardness, "the third body" formation.*

1. INTRODUCTION

Among the modern trends in improving performance and cutting properties of hard alloys (HA) used as inserts to equip the cutting tools (CT) the direction associated with improving carbide phase composition and the search for new materials for binding phases can be selected [1],[2],[3],[4].

The studies of thermodynamic processes in the friction zone based on entropy balance equations obtained analytical dependence indicating that wear rates are lower for HA grades with large values of the thermal entropy *S* [1],[5]. It has been established experimentally that HA grades with high values of *S* have smaller values of absolute or relative thermo electrical moving force (thermo-EMF), which leads to a decrease in the magnitude of thermo currents in the cutting (or friction) zone and reduce the oxidative wear rates [1],[6]. Thus, when designing new HA grades preference should be given to structures characterized by highest values of the thermal entropy and minimal values of the thermo-EMF.

In accordance with the above mentioned principles at the «Metal-cutting machines and tools» department of Don State Technical University experimental HA grades based on standard alloy VK8 were developed [7]. The compositions of these new grades of HA consist of WC carbide phase and modified binders of three types: Co-Mo, Co-Fe-Cu and Co-Mo-Ti. The values of relative thermo-EMF of these binders towards carbide phase are lower, and their entropy values are higher than for the base alloy VK8, obtaining their increased electrochemical stability. As a result of the tests, it was established that the best wear resistance when cutting stainless steel [1] and high resistance to gas corrosion [7] have alloys which chemical composition and properties are listed in table 1, 2.

Table 1. Composition of experimental hard alloys grades [1]

Grade	Chemical composition
2.21	5,4%Co+1,43%Fe+0,82%Cu+92,45WC
2.22	5,65%Co+1,8%Mo+0,6%Ti+91,95%WC
2.23	5,1% Co+2,7%Mo+0,61%Ti+91,59%WC
VK8 (basic)	7,5-8%Co; <0,3% Fe; 92,0%WC

Wear resistance of the material depends on its physical-mechanical properties including the modulus of elasticity and hardness [9],[10]. Rubbing bodies come into contact with each other on the picks of surface asperities; therefore the wear resistance of the material under conditions of friction without lubricant will primarily be determined by hardness of its surface sub contact layer on micro level. Micro hardness of the surface layer of material measured using the dynamic method of scratching is the best suited for simulation of friction conditions and is widely used for wear resistance evaluation of materials and coatings [11],[12],[13]. This parameter permits to evaluate the ability of the material to resist surface micro relief changes in dynamic interaction with picks on the surface of the second body or with solid wear particles having abrasive action. In places of metal contact of two rubbing bodies adhesive joints (or junctions) are formed, then, in addition to the destruction of surface layers as a result of plastic and elastic-plastic contact additional wear processes due to formation/destruction of adhesive joints will occur [10],[14],[15].

Table 2. Physical-mechanical properties of experimental hard alloys grades [1]

Grade	Entropy, J/mol·^{o}K	Absolute thermo e.m.f. ε, mV	Density, kg/m^3
2.21	35,18	3,75	1476
2.22	35,26	3,32	1421
2.23	35,16	4,5	1410
VK8 (basic)	35,00	9,8	1460

The processes of formation of adhesive junctions and of their destruction should be separated according to their influence on the total wear rate. For example, for some combinations of rubbing materials the process of adhesive joints formation can be quite intense, but the junctions may have comparatively low shear resistance, hence friction force will not significantly increase [10]. During machining processes CT material and material of work-piece may have high propensity to adhesive joints formation [15], [16]. In these cases wear mechanism is specifically based on the incorporation of the machined material over two well-localized areas of the cutting tool: at the edge, giving rise to the Built-Up Edge (BUE); and at the rake face, giving rise to a Built-Up Layer (BUL). Both types of material incorporation may modify the initial cutting geometry, affecting the surface quality of the machined parts [17],[18],[19]. At the same time, a thin and stable BUE can protect the tool from wear by reducing the friction between the cutting tool and work piece and by its shielding effect [20].

Among materials processed using tools with cemented carbide inserts titanium-aluminum alloys can be selected, which due to their heat resistance, corrosion resistance and excellent physical and mechanical properties are widely used in various areas of engineering, including aerospace and medical equipment production [21],[22]. The alloy VT-3 refers to high-strength (α+β)-martensitic alloys of the Ti-Al-Mo-Cr-Fe-Si type and is widely used for various components in the aircraft industry. According to modern requirements to ecology and economy of production, machining work pieces made of VT-3 alloy occurs mainly under conditions of Minimum Quantity Lubrication (MQL) [23] or without lubricant at all. Taking into account above mentioned, the studies of peculiarities of the interaction between the new experimental HA grades and titanium-aluminum alloy under conditions of dry friction will be an important task.

The aim of this work is to study the tribological properties of the new experimental HA grades under conditions of dry friction on titanium-aluminum alloy VT-3, as well as the measurement of their surface micro-hardness as one of the most important factors determining wear resistance of the tool materials. All measured parameters will be compared with similar characteristics of standard HA grade VK8, on the basis of which these experimental grades were developed. This work is a part of complex researches of physical-mechanical, tribological and cutting properties of the new experimental HA grades with modified cobalt binder.

2. EXPERIMENTAL PART: MATERIALS AND METHODS

Surface micro-hardness measurements on contact surfaces of specimens (pins) made of experimental HA grades (contact surface roughness Ra = 0.1 - 0.12 µm) before and after friction on rotating titanium-aluminum alloy VT-3 counter bodies (disks, contact surface roughness Ra = 0.15 - 0.17 µm) were made using NanoSCAN-01 nano-hardnessmetre (Russia) by scratching the surfaces with different forces F_s. Tribological testing of square section samples (5x5 mm2) made of different grades of tool HA were performed on tribometre T-11 (Poland), which implemented a scheme of friction "pin on disk" widely used to simulate in the laboratory processes of friction when cutting metals [24],[25]. Measured and saved parameters were friction force F, the offset/inset of the indenter (pin) relative to the counter body (disk) Δ and the time of the experiment T. Studies were carried out at a constant speed of v=0.3 m/s (318 RPM, track radius 9 mm) and constant pressure P = 4.1 MPa, the sliding length was varied L = 100 - 1400 m. Measurements of the mass wear of the tested samples were carried out on the scales LV210-A (precision 0.0001 g) which are recommended for evaluation of mass wear of samples when tested according to the scheme "pin on disk" [26]. Roughness of rubbing surfaces after friction was measured using profilometre Abris-PM7 (Russia).

3. EXPERIMENTAL PART: RESULTS AND DISCUSSION

Comparison of surface micro-hardnesses for various materials was carried out by measuring the width of a scratch h left by diamond micro-indenter on the surface of the sample: the smaller was the width of the scratch under given value of the normal load F_s, the higher was the surface micro-hardness of the investigated material. The fragment of a scanned image of the surface of the specimen made of experimental HA grade 2.21 with scratches of different widths h from the various values of the normal load F_s as well as the curves of $h(F_s)$ dependences are presented in Figure 1.

Surface micro-hardness values of all experimental HA grades exceed the same parameter of basic standard grade VK8; the highest micro-hardness value is characteristic for 2-22 grade. It should be noted that surface micro-hardness measurements of materials 2-22 and 2-23 with a normal loads of less than 7.5 N left no significant changes of surface topography (scratches had not been observed) and, therefore, to evaluate surface micro-hardness by the width of the scratch left by ultrasonically oscillated indenter for these cases had not been possible.

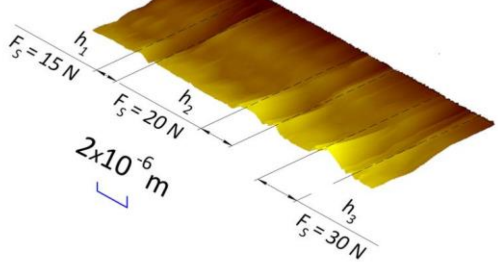

a)

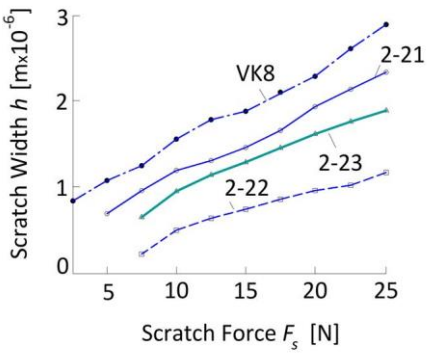

b)

Figure 1. The indenter surface scan on the specimen of 2-21 alloy after scratching (a) and curves of scratch width h dependences on normal load F_s for different HA grades (b)

The evolution in time curves of the friction coefficient f for all tested samples were of the similar character which can be divided into three characteristic stages: A – stage of the friction coefficient increasing; B – stage of the friction coefficient reducing; C – steady-state friction stage (Figure 2).

The stages A and B represent, in fact, running-in period for steady-state friction stage C. The duration of these two phases differs depending on the HA grade: the shortest time to reach steady-state friction stage C was characteristic for indenters made from experimental grades 2.21 and 2.22, the largest - for the basic standard grade VK8. The average friction coefficients on stable stage f_C for indenters made from experimental grades do not differ significantly, however, these coefficients exceed the same characteristic for alloy VK8. The comparison of fluctuations intensities of friction coefficients can be produced by the average amplitude of oscillations [27] or by r.m.s. deviation values σ_C at a stage of steady-state friction (Figure 2). The lowest fluctuations intensities of friction coefficients according to the parameter σ_C were observed for the alloys VK8 and 2-23.

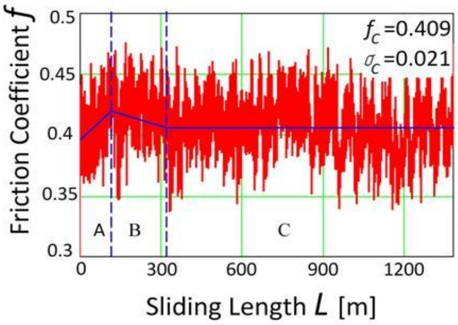

a)

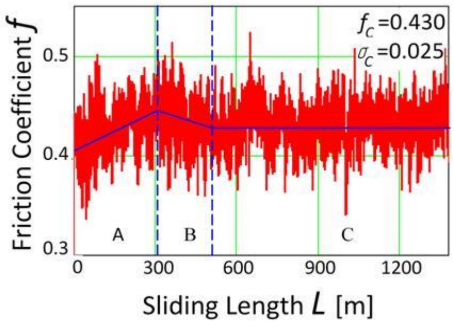

b)

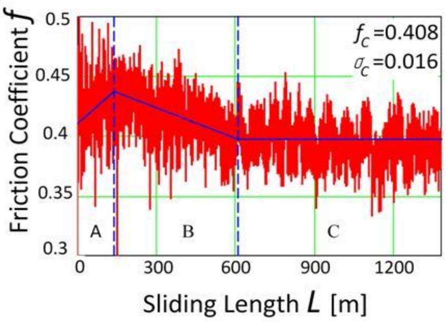

c)

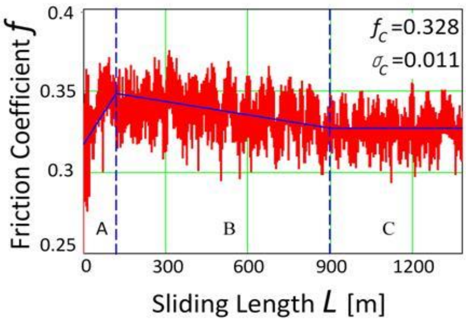

d)

Figure 2. Dependence of the friction coefficient f on the sliding length L: a – 2-21; b – 2-22; c – 2-23; d – VK8(basic)

The total friction force during friction without lubricant consists of adhesive and mechanical components [10],[14]. Therefore, higher friction coefficients and their considerable fluctuations observed in tests with experimental HA grades may have the following possible causes. Experimental alloys may have a higher propensity to adhesive junction formation with titanium-aluminum alloy and higher shear resistance of these junctions than basic alloy VK8. The second reason may be high shear resistance of the "third body" currently emerging in the contact areas during friction process and its rheological properties. Intensive processes of formation/destruction of adhesive junctions inevitably lead to high wear rates of rubbing bodies and change the geometry of contacting surfaces on micro level.

Analysis of the indenter offset/inset *Δ(L)* data allows to judge about the changing contacting surfaces geometry which occurs due to: *a)* comparatively soft counter body (disk) wear; *b)* hard indenter (pin) wear; *c)* the features of secondary surface structures self-organization and the formation of the "third body". Depending on the intensity of each of the above mentioned processes taking place in contact areas it can be observed removing (offset) of rubbing bodies or convergence (inset) of these bodies or near stable state [10]. It should be noted that in our previous studies dedicated to investigations of tribological characteristics of experimental HA grades based on tungsten carbide with modified cobalt binder under conditions of dry friction on disks made of structural steel the formation of the "third body" of a considerable thickness was fixed [28]. This phenomenon was conductive to decreasing of friction forces and contact temperature levels and obtained shielding effect reducing wear rates. The same phenomenon has been observed also while rubbing specimens made of some high speed steel grades [29]. Depending on the chemical composition of rubbing bodies and the level of thermal-mechanical activation the "third bodies" with different properties can be generated. The "third body" can perform either role of solid lubricant, or obtain shielding effect having its own significant shear resistance, or increase total wear rates due to additional abrasive wear. In all the experiments carried out in this study the convergence (inset) of indenter (pin) and counter body (disk) was observed, i.e. the processes of wear dominated over the processes of the "third bodies" formation. The Fig. 3 shows that the convergence (inset) of indenter (pin) and counter body (disk) for specimens made of experimental HA grades was going slower than for specimens made of basic grade VK8.

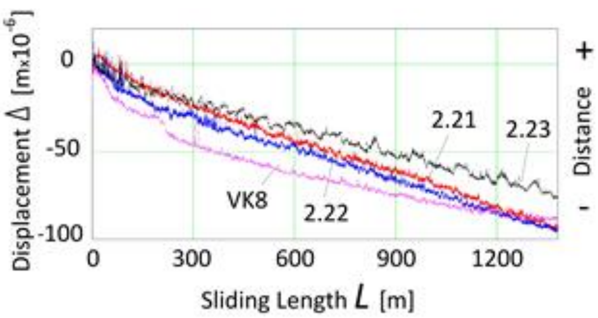

Figure 3. The dependencies *Δ(L)* for experimental and basic HA grades

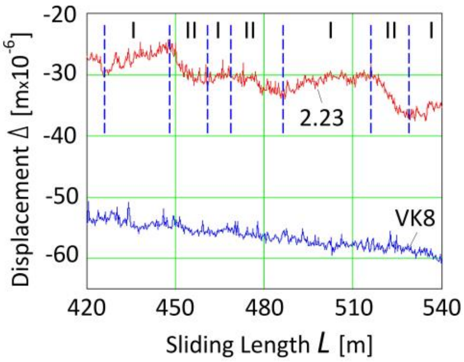

Figure 4. Comparative character of the curves *Δ(L)* for HA grades VK8 and 2.23

At the initial stage of the friction process (*L*<150 m) the curves *Δ(L)* are close enough to each other, and then diverge. Also at this stage the processes of friction for specimens made of experimental HA grades were accompanied by significant fluctuations of the displacement values; then the fluctuations were reduced. The maximum value of fluctuations was characteristic for specimens made of 2.23 experimental HA grade, for basic grade VK8 the fluctuations were of minimal value. It also should be noted that *Δ(L)* curves for specimens made of 2.23 experimental HA grade consist of two alternative phases: the first phase (I) of gradual rubbing bodies offset (fig. 4, plots I), the second phase (II) of gradual rubbing bodies inset (fig. 4, plots II). This process alternates over time, i.e. is quasi periodical in nature.

The plots of type I are a reflection of the thickness of the "third body" growth; during these periods the wear rates are of minimal value due to the removal of rubbing surfaces from direct contact. The friction force at these phases increases slightly due to significant shear resistance of the "third body" and actual contact area growth (fig. 5). Increase of the "third body" thickness is of non-linear character; kinetics of the growth may be best described by an exponential curve [28]. The plots of II type are indicative of the "third body" partial or total destruction and subsequent wear of rubbing bodies until the beginning of the next period of the "third body" growth; the friction force at these periods shows the downward trend (fig. 5). In the case of the most intense growth of the "third body" and high thickness of the intermediate "third body" layer observed for alloy 2.23, the resulting inset of indenter relative to counter body was of minimum value (fig. 3). Comparison of Δ*(L)* curves (fig. 3, 4) shows that friction processes for specimens made of experimental HA grades were accompanied by more intensive formation of the "third bodies" which were also thicker than for VK8. Stages of I and II types in Δ*(L)* curves for experimental HA grades 2.21 and 2.22 (not shown on fig. 4) were also observed, but they are less pronounced than for the alloy 2.23. Curves Δ*(L)* for basic alloy VK8 were comparatively smooth among all options to compare, indicating a clear predominance of destructive wear processes on the constructive processes of the "third body" formation and growth.

Let’s try to quantify and compare the "third body" formation/destruction processes for various HA grades having different formulations. Intensive formation of the "third body" with shielding properties is a factor that reduces the wear rates of rubbing bodies. Ideally, the intensity of the "third body" growth process should be close in value to the intensity of its destruction process, and then the geometry of the tribo contact changes would be minimal. Thus, it can be considered desirable such a “script” of the friction process, in which the maximum possible increase of the "third body" thickness (offset value) δ_I would be achieved in less time T_I and its destruction time T_{II} preceding direct contact of rubbing bodies attributed with wear would be the longest possible and accompanied by a smaller inset value δ_{II} (fig. 5).

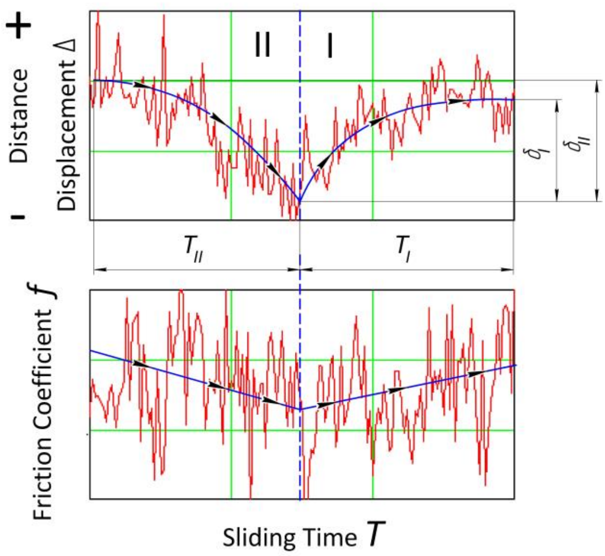

Figure 5. The characteristics of the "third body" formation/destruction processes

Then, to quantify and compare the efficiency of the "third body" formation/destruction processes to a first linear approximation, we introduce dimensionless parameter Ψ, specified as

$$\Psi \quad \frac{\delta_I}{T_I}\ \frac{T_{II}}{\delta_{II}}, \qquad (1)$$

where δ_I , δ_{II} – the offset/inset values during formation/destruction of the "third body", [μm]; T_I, T_{II} – the periods of time during which these movements occurred, [min].

The higher is the value of the parameter Ψ, the stronger the formation processes of the "third body" compensate for destruction processes. The maximum values for the parameter Ψ were characteristic for alloys 2.23 (Ψ = 14.2) and 2.21 (Ψ = 6.3), the smallest value – for basic alloy VK8 (Ψ = 1.9).

Cutting tool materials with high values of entropy S have a strong propensity for the rapid formation of the "third bodies" having considerable thickness, secondary structures generated during friction (cutting) deposit on the contact surfaces of indenters (tools) made of HSSs, remaining on it after the termination of the experiment and forming a semblance of wear resistant shielding coatings [29]. For experimental HA grades the "third bodies" fully collapsed when friction process was stopped, and the worn surfaces of indenters maintained metallic luster [28].

Some considerations about the character of adhesive (cohesive) junctions formed during friction can be made on the base of counter bodies tracks roughnesses measured perpendicular to the direction of sliding velocity: in case of stronger adhesive (cohesive) junctions on the surfaces of contacting bodies the roughness will be higher [10]. Dependencies of R_a and R_{max} roughness parameters on sliding length L are shown in Figure 6 which shows that the lowest roughness parameters have counter bodies tracks after friction interaction with indenters made of 2.21 and 2.23 alloys.

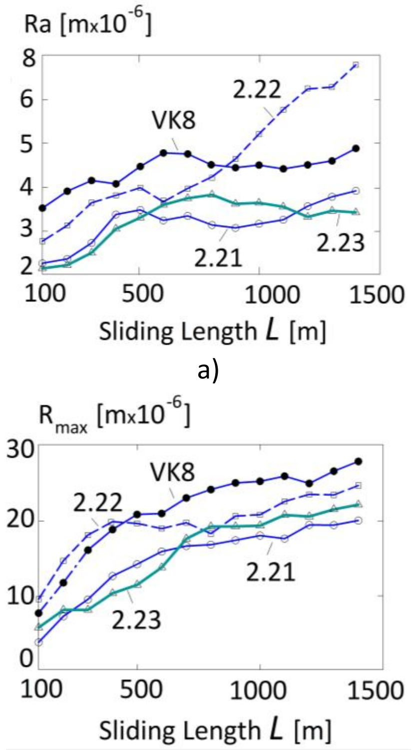

a)

b)

Figure 6. Dependencies of R_a and R_{max} roughness parameters on sliding length L

To evaluate the wear resistance of experimental HA grades under conditions of dry friction on titanium-aluminum alloy VT-3 mass loss measurements of indenters for each fixed value of sliding length L were made. Volumetric wear ΔV of samples was calculated by the formula:

$$\Delta V = \frac{m_1 - m_2}{\rho}, \quad (2)$$

where m_1, m_2 – sample masses before and after friction test; ρ – the density of the sample material.

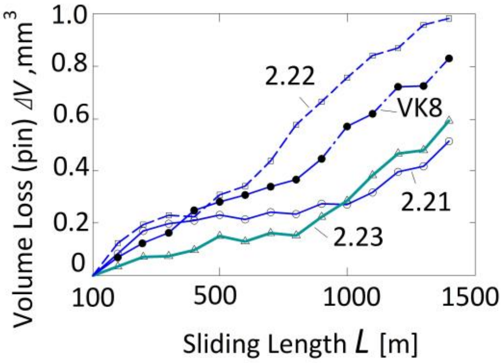

Figure 7. Wear curves for different HA grades.

The greatest volumetric wear ΔV, despite its high surface micro hardness (Fig. 1), was observed in samples made of alloy 2.22 (fig. 7). The process of friction for this HA grade was characterized by maximum values of average friction coefficient and its r.m.s. deviation (Fig. 2b), and also was accompanied by a significant changes of counter body and indenter contacting surfaces micro geometry (Fig. 3 and 4). These peculiarities indicate that the process of friction of indenters made of 2.22 HA grade on titanium-aluminum alloy VT-3 counter bodies was accompanied by strong adhesive junctions formation that led to the greatest wear rates among all tested HA grades. The lowest values of volumetric wear ΔV and minimal changes of the contacting surfaces micro geometry in comparison with basic standard grade VK8 were observed for 2.21 and 2.23 alloys. Higher values of friction coefficients for 2.21 and 2.23 HA grades can be explained by the features of the "third body" formation/destruction processes, as well as by the "third bodies" rheological properties: intermediate "third body" layers formed during friction have their own high shear resistance, but also have considerable shielding effect.

4. CONCLUSION

As a result of tribological tests of experimental tool hard alloy grades based on tungsten carbide with modified cobalt binder under conditions of dry friction on disks made of titanium-aluminum alloy VT-3 it was found that among the tested grades the best characteristics has alloy 2.23 which is characterized by the lowest average friction coefficient, the lowest surface roughness of counter body track after friction and the highest wear resistance. The friction couples of “hard alloy 2.23 *vs.* titanium-aluminum alloy VT3” type have significant propensity to the formation of secondary surface structures and specific features of self-organization in the friction areas leading to formation of the "third body" which protects contacting surfaces from wear due to considerable shielding effect and has its own significant shear resistance. Such properties of the "third body" can lead to reducing wear on the rake surface of the tool when cutting alloy VT-3 using cutting tools equipped with HA inserts made of 2.23 experimental grade, this consideration in the future to be verified experimentally.

REFERENCES

[1] A.A. Ryzhkin, V.E. Burlakova, D.V. Moiseev et al: Determination of the efficiency of high-entropy cutting tool materials, Journal of Friction and Wear, Vol. 37, No.1, pp. 47-54, 2016.

[2] Z. Zhao, J. Liu, H. Tang et al: Investigation on the mechanical properties of WC–Fe–Cu hard alloys, Journal of Alloys and Compounds, Vol. 632, pp. 729-734, 2015.

[3] Z. Zhao, J. Liu, H. Tang et al: Effect of Mo addition on the microstructure and properties of WC–Ni–Fe hard alloys, Journal of Alloys and Compounds, Vol. 646, pp. 155-160, 2015.

[4] J. Long, K. Li, F. Chen et al: Microstructure evolution of WC grains in WC–Co–Ni–Al alloys: Effect of binder phase composition, Journal of Alloys and Compounds, Vol. 710, pp. 338-348, 2017.

[5] A.A. Ryzhkin: *Synergetics of cutting tool materials wear processes, triboelectric aspect*, DGTU publ. house, Rostov-on-Don, in Russian, pp. 322, 2004.

[6] A.A. Ryzhkin, E.V. Fominoff and Y.A.Torop: Estimation of triboelectrical properties of high-speed steels, Vestnik DGTU, in Russian, Vol. 2, pp. 20-29, 2017.

[7] A.A. Ryzhkin, B. Ch. Meshi, A.I. Bokov et al: Hard alloy grades based on tungsten carbide: patent for invention №2531332, Russian Federation, MPK C22C29/08/, 2014.

[8] A.A. Ryzhkin , V.E. Burlakova, A.A. Novikova: Wear and performance of hard alloys, Russian Engineering Research, Vol. 38, No. 6, pp. 438-441, 2018.

[9] R. Liu, D. Li: Modification of Archard’s equation by taking account of elastic/pseudoelastic properties of materials, Wear, Vol. 251, pp. 956-964, 2001.

[10] I.V. Kregelskiy: *Basis of calculation for friction and wear*, Mashinostroenie, Moskva, in Russian, 1977.

[11] P.J. Blau: *Friction science and technology: from concepts to applications*, Taylor&Fransis Group LLC, pp. 421, 2009.

[12] P.J. Blau: Relationship between Knoop and scratch micro-identation hardness and implications for abrasive wear, in: D.O. Northwood, W.E. White and G.F. VanderVoort (Ed.): *Microstructural Science*, Vol. 12, ASM international, Materials Park, OH, pp. 293-313, 1985.

[13] A. Vencl, B. Gligorijević, B. Katavić et al: Abrasive Wear Resistance of the Iron- and WC-based Hardfaced Coatings Evaluated with Scratch Test Method, Tribology in Industry, Vol. 35, No. 2, 2013.

[14] B. Bhushan: *Modern tribology handbook,* CRC Press LLC, pp: 1691, 2001.

[15] J.F. Archard: Contact and Rubbing of Flat Surfaces, Journal of Applied Physics, Vol. 24, pp. 981-988. 1953.

[16] E. Rabinowicz: *Friction and Wear of Materials*, Wiley: Hoboken, NJ, USA, 1995.

[17] Y. S. Ahmed, G. Fox-Rabinovich, J. M. Paiva: Effect of Built-Up Edge Formation during Stable State of Wear in AISI 304 Stainless Steel on Machining Performance and Surface Integrity of the Machined Part, Materials, Vol. 10, 2017.

[18] S.C. Veldhuis, G.K. Dosbaeva, K. Yamamoto: Tribological compatibility and improvement productivity and surface integrity, Tribology International, Vol. 42, pp. 1004-1010, 2009.
[19] S. Atlati, B. Haddag, et al: Effect of local friction and contact nature on the Built-Up Edge formation process in machining ductile metals, Tribology International, Vol. 90, pp. 217–227, 2015.
[20] G.S. Fox-Rabinovich, J.M. Paiva, I. Gershman et al: Control of self-organized criticality through adaptive behavior of nano-structured thin film coatings, Entropy, Vol. 18, 2016.
[21] A. Brotzu, F. Felli, F. Marra: Mechanical properties of a TiAl-based alloy at room and high temperatures, Material Science and Technology, Vol. 34, pp. 1847-1853, 2018.
[22] C. De Formanoir, G. Martin, F. Prima et al: Micromechanical behavior and thermal stability of a dual-phase alpha plus alpha' titanium alloy produced by additive manufacturing, Acta Materialia, Vol. 162, pp.149-162, 2019.
[23] S. Qin, Z. Li, G. Guo et al: Analysis of Minimum Quantity Lubrication (MQL) for Different Coating Tools during Turning of TC11 Titanium Alloy, Materials, Vol. 9, 2016.
[24] J. Salguero, J. M. Vazquez-Martinez et al: Application of Pin-On-Disc Techniques for the Study of Tribological Interferences in the Dry Machining of A92024-T3 (Al–Cu) Alloys, Materials, Vol. 11, 2018.
[25] B.L. Strahin, G.L. Doll: Tribological coatings for improving cutting tool performance, Surface and Coatings Technology, Vol. 336, pp. 117-122, 2018.
[26] ASTM G99-17 *Standard Test Method for Wear Testing with a Pin-on-Disk Apparatus*, 2017.
[27] G. Liang, S. Schmauder, M. Lyu et al: An Investigation of the Influence of Initial Roughness on the Friction and Wear Behavior of Ground Surfaces, Materials, Vol. 11, 2018.
[28] E.V. Fominoff, C.G. Shuchev: Tribological Properties of Experimental Hard Alloys in Conditions of Friction on Structural Steel without Lubricant, MATEC-Web of Conferences, Vol. 226, 2018.
[29] A.A. Ryzhkin, E.V. Fominoff, C.G. Shuchev: Study on The Tribological Characteristics of High Entropy High Speed Steels In Conditions of Dry Friction On Structural Steel, Lecture Notes In MechanicaL Engineering, Part F4, pp. 1819-1827, 2019.

Serbian Tribology Society

SERBIATRIB '19

16th International Conference on Tribology

Faculty of Engineering University of Kragujevac

Kragujevac, Serbia, 15 – 17 May 2019

WEAR RESISTANCE PROPERTIES OF EPOXY ALUMINIUM MICROPARTICLE COMPOSITE

Sefiu Adekunle BELLO[1, *], Johnson Olumuyiwa AGUNSOYE[2], Jeleel Adekunle ADEBISI[3], Nasirudeen Kolawole RAJI[4], Suleiman Bolaji HASSAN[2]

[1]Department of Materials Science and Engineering Kwara State University, Malete, Nigeria,
[2]Department of Metallurgical and Materials Engineering, University of Lagos, Nigeria,
[3]Department of Metallurgical and Materials Engineering, University of Ilorin, Nigeria,
[4]Department of Metallurgical Engineering, Yaba College of Technology, Lagos, Nigeria,
*Corresponding author: belloshaafiu@gmail.com or sefiu.bello@kwasu.edu.ng

Abstract: *Present priority of light materials for enhancing automobile safety and fuel efficiency creates a premise for developing new materials with optimum combination of lightness and better or comparative properties to replace existing heavy alloys for transportation applications. Previous authors' study reveals development of epoxy aluminium composite with investigation of mechanical properties and its targeted application as an automobile bumper but the wear resistance of the composite has not been reported. This study investigates wear resistance properties of epoxy containing 10% by weight of aluminium microparticles. The composite was produced from epoxy resin (MAX 1618 A) cured with hardener (MAX 1618 B) at 2:1 volume mix ratio through in-situ polymerisation. Firstly, wear rates (volume loss per unit time) were measured as a function of the applied load. Then, the wear rates (mass loss per sliding distance) were examined as a function of the applied load, velocity and % weight of aluminium particles. Worn-out surfaces of examined samples were tracked morphologically. Result obtained indicated that the applied load, sliding speed and percentage by weight are all significant factors influencing the wear resistance of the epoxy composites with the model, P value of 0.049≤0.05. The sliding velocity of β value = 0.011 contributed to increase in the wear rate than the applied load having lower β value (0.001). Addition of aluminium particles (β value = -0.003) to the epoxy lowered the wear rate. This implies that an increase in the wt% of aluminium particle added to the epoxy enhances the wear resistance of the composites. SEM study affirms the wear mechanism by crack nucleation which is characterised with continual propagation, deflection and pining. A greater damage observed on the surface of epoxy polymer justifies its higher wear rates in comparison with those of the composite.*

Keywords: *Epoxy, aluminum, load, sliding distance, wear rate.*

1. INTRODUCTION

Epoxy polymeric composites have been found useful for many applications because of their better combination of mechanical properties when compared with their counterparts such as heavy alloy and metal matrix composites. Besides optimum combination of mechanical properties, ease of formability in shape detailing which is a function of a reduction in the number of individuals parts and overall automobile weights has also favoured the epoxy polymeric composites [1-4].

Globally, efforts have been made to reduce the weight of automobiles parts such as bumper using light structural polymer matrix composites. This is to enhance the pedestrians' safety on accidental collision with vehicles and to reduce the fuel consumption. In designing a bumper beam; safety, performance, weight, size, cost, environmental issues and appearance are taken into considerations. Low impact test at 4.0 km/h using longitudinal pendulum, high speed test at 8 km/h and pedestrian impact test using a leg form impactor through finite element modellings are the three safety criteria used by European car manufacturers [5, 6]. Based on these, bumper materials should be light, tough and strong. A bumper system contains three parts, namely: fascia, bumper beam and bumper damp. The fascia is for aesthetics and aerodynamic force reduction; bumper beam is the major beam structure that absorbs kinetic energy due to collision and the bumper damp helps in preventing the vibration of the car structures. The bumper beam needs to be strong, ductile and tough. Strength increases the car safety abilities and helps in load distribution to various components but lowers the damping ability. Flexural strength helps in preventing beam from plastic region while the ductility/toughness aids the damping abilities. Besides prerequisites mechanical properties, wear resistance forms part of requirement of automobile bumper because the bumper is not used in isolation, it is attached to the frontal and rear parts of automobiles at point of installation. Based on unavoidable contact of the bumper with the anchoring material, wear knowledge of bumper materials is inevitable in the bumper design and fabrication. Previous work of this author and his team in a published article [7] reveals mechanical properties of epoxy aluminium composites and its possible selection for automobile bumper application. However, this study is focused on wear resistance properties of epoxy containing 10% aluminium microparticles.

2. MATERIALS AND METHODS

Epoxy/aluminium composites used in this work was produced from epoxy resin (MAX 1618 A), hardener (MAX 1618 B) and absolute ethanol. Both the resin and hardener were purchased from Polymer Composite Institute, Canada via a local chemical vendor at Ojota Lagos, Nigeria. A weighed quantity of aluminium (10% of epoxy resin) was added to ethanol in a measuring cylinder and agitated for 5 minutes to dissolve particle clusters before adding to epoxy resin in a reaction flask. The mixture was stirred mechanically for 20 minutes and heated at 100˚C and stirred on a Stuart heating mantle to evaporate ethanol. Then, the mixture was degassed in a vacuuming process at 150 mmHg for 30 minutes after which a weighed quantity of hardener (50% of epoxy resin) was added to the degassed mixture and gently stirred until the gelation of the mixture began and the composite blend was poured into a metallic mould whose cavity formed a representative sample for the wear test. The wear resistance property of 50 x 10 x 6 mm^3 epoxy samples were investigated using a central circular disc wear testing machine with P 60 SiC coarse emery paper. Initial mass (m_o) of each sample was determined using the Pioneer weighing scale. The 10 x 6 mm^2 sample surface firmly fixed to the wear rig was placed on the emery paper at 50 mm from the center of the disc. While the sample was kept at 50 mm from the centre of the disc under applied load of 9 N, the disc with emery paper was made to rotate against the sample surface at a speed of 125 mms^{-1} for 20 s. New mass (m_1) of the sample was taken after it was demounted from the rig. The process was repeated first, by gradually increasing the period of rotation of the disc from 30 seconds to 3 minutes at 30 second intervals while the load was kept constant. Second, the applied load was increased to 25 N at 4 N intervals. Mass of the sample in each case was measured and recorded. At the end of each run, the wear debris was removed from the surface of the emery paper with hard brush. The mass loss due to friction, volume and wear rate were estimated using Equations 1-3.

$$Mass\ loss \quad initial\ mass\ m_0 \quad final\ mass\ m_1 \tag{1}$$

$$Volume\ loss \quad \frac{mass\ loss}{density\ of\ the\ sample} \tag{2}$$

$$Wear\ rate \quad \frac{total\ volume\ loss}{total\ wear\ duration} \tag{3}$$

3. RESULTS AND DISCUSSION

3.1 Wear resistance of epoxy aluminium composites

Wear rate of epoxy/Almp composites were evaluated using volume loss-per unit time and mass loss-per unit sliding distance approaches. Figure 1 shows the wear rate (volume loss-per time) of epoxy and epoxy/10Almp composites at different applied loads, ranging from 9 to 25 N. It is understood from Figure 1 that the wear rate increased with an increment in applied loads. Similar observation was earlier being made in [4, 8]. The increment could be attributed to increased cutting efficiency as the applied load increased. With an increase in loads, materials under study were pressed more firmly on emery paper placed on the disc. The firm grip of the samples on the disc by the wear pin increased the friction between the sample and the emery paper, leading to higher cutting efficiency of the emery paper during the wear investigation. Results of SEM examination of the worn-out surfaces of the tested samples display severity of the surface wear in form of different trench networks due to wear induced crack initiation, propagation and growths. Continual long trenches seen in Plate 1 are explained by ease of propagation of wear induced cracks within the epoxy matrix. Since unfilled epoxy is very soft and less stiff because of absence of second phase particles, it has low strength to inhibit the crack propagation. Presence of firmly bonded second phase particles within epoxy/10Almp composites impinged and blocked the cracks and prevented their easy advancement within the composites. This causes differences in trench geometries in Plate 2 which are described as crack deflection or twisting.

In the volume-per unit time wear rate approach, the applied loads are the influential factor that affects the wear rate since experiment was performed at constant velocity (0.65 ms^{-1}) and sliding distance (200 m), effect of loads (predictor/independent variable) on wear rate (response) was studied at 95 % confidence level using linear regression model involving full factorial experimental design. Equations 4-7 present the design of matrices for predictor variable, regression coefficients and responses in line with [9], found in [10].

$$x \quad [9:4:25] \tag{4}$$

$$x_p \quad [9:.04:25] \tag{5}$$

$$coeff \quad polyfit(x, y, 1) \tag{6}$$

$$y_p \quad polyval(coeff, x_p) \tag{7}$$

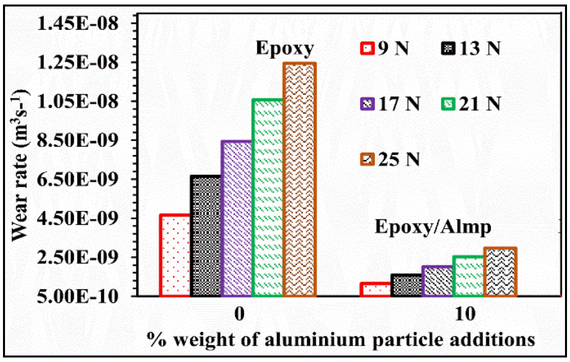

Figure 1. Wear rate of epoxy/Almp and epoxy/Alnp composites

Figure 2 shows the plot of the modelled and experimental data. Relationship between wear rate (response) of epoxy/Almp composites and the applied loads (predictor variable) is explained by the model. A function describing the mono-variate regression model is presented in Equation 8. The regression coefficient of determination for this model is 0.9992 (see Table 1). The deduction from this is that 99.92 % of experimental wear rate are explained by the model. However, mean of residuals (-7.60exp-13) reveals goodness of the data fit due to absence of the systematic error from response determination. The model exhibits a good predictability. Residuals between predicted and actual values of epoxy/Almp composites wear rate are shown in Table 2.

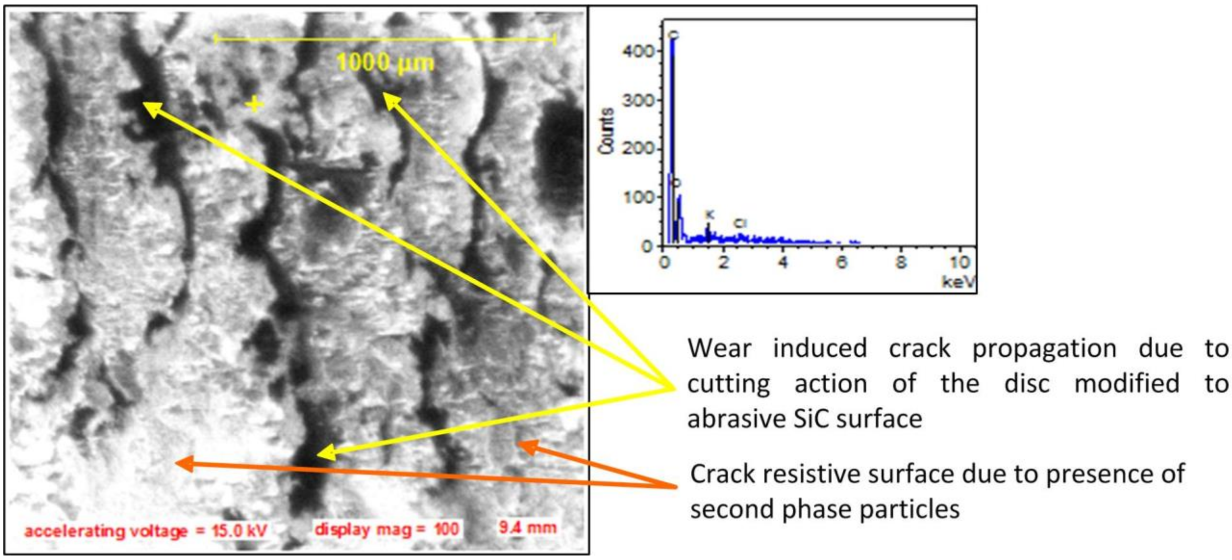

Plate 1. SEM/EDX of worn-out surface of the epoxy matrix

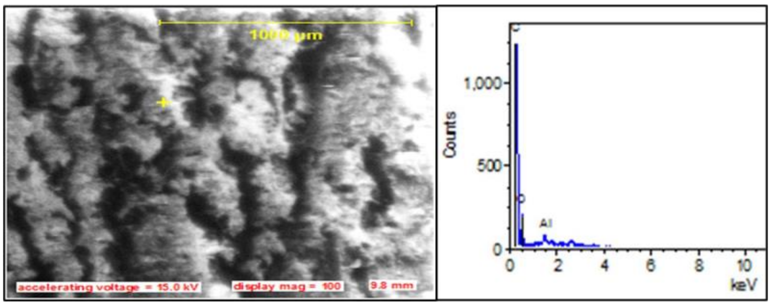

Plate 2. SEM/EDX of worn-out surface of epoxy/10Almp composites

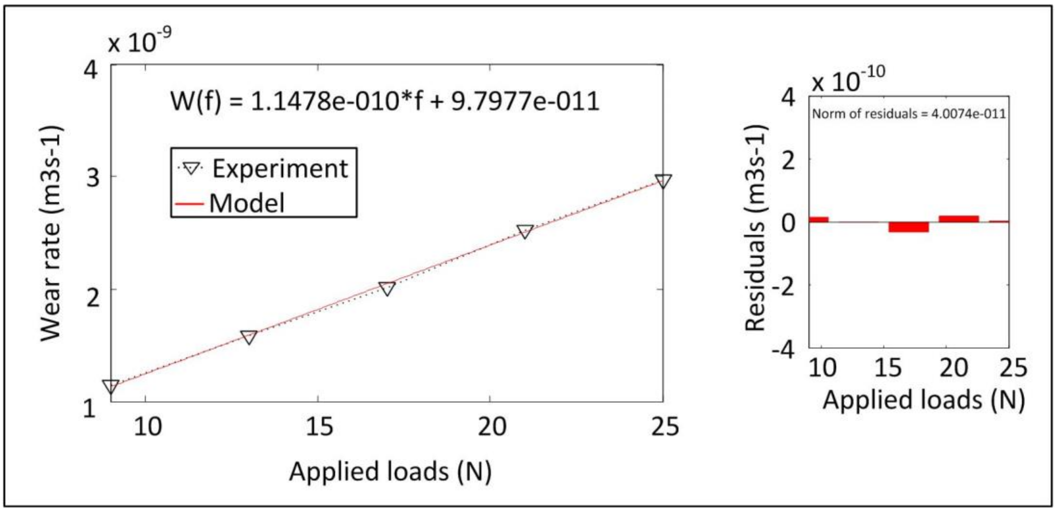

Figure 2. Regression model prediction of wear rate for epoxy/Almp composites

$$W \quad f_{\;Epoxy/Almp\,composites} \quad 1.1478x10^{\;10} f \quad 9.7877x10^{\;11} \tag{8}$$

Table 1. ANOVA of epoxy/Almp composites wear rate

Sum of squares		Mean	Model summary
Regression	Residuals	Residuals	R square
2.13607E-16	1.60588E-21	-7.60E-13	0.999238708

Table 2. Confirmation of experiment and validation of epoxy/Almp composites wear rate

Order	Independent variable	Response ((m^3s^{-1})		
	Applied load, f (N)	Actual values	Predicted values	Residual
1	9	1.14E-09	1.131E-09	-9.00E-12
2	13	1.59E-09	1.59012E-09	1.20E-13
3	17	2.02E-09	2.04924E-09	2.92E-11
4	21	2.53E-09	2.50836E-09	-2.16E-11
5	25	2.97E-09	2.96748E-09	-2.52E-12

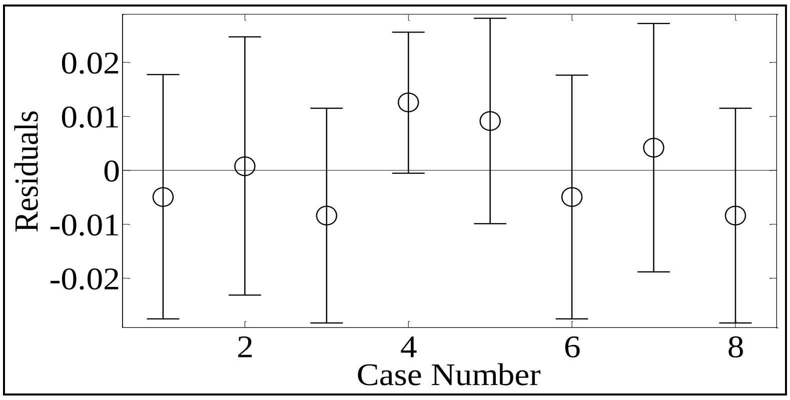

Figure 3. Co-plot of residuals and residual intervals for epoxy/Almp composites wear rate (W)

Table 3. Design layout and response data for wear behaviour of epoxy/Almp composites

Order	Applied loads, f (N)	Speed of rotation v (ms^{-1})	A_m	Wear rate (W) (f, v, A_m) (gm^{-1})
1	9	0.65	0	0.020667
2	25	0.65	0	0.04352
3	9	1.3	0	0.02445
4	25	1.3	0	0.06253
5	9	0.65	10	0.007951
6	25	0.65	10	0.010975
7	9	1.3	10	0.010252
8	25	1.3	10	0.014792
Am – weight of aluminium micro particles				

Table 4. Pearson correlation of dependent and independent variables for epoxy/Almp composites wear rate

W- wear rate; f – applied load; A_m - weight of aluminium micro particles; v – speed of rotation of the disc	Variables	W(A_m,v,f)	F	A_m	V
	W(A_m,v,f)	1.000	0.477	-0.747	0.201
	f	0.477	1.000	0.000	0.000
	A_m	-0.747	0.000	1.000	0.000
	v	0.201	0.000	0.000	1.000

Table 5. ANOVA of the wear rate of epoxy/Almp composites

Standard order	Model	Sum of squares	Df	Mean Square	F	Significance	R^2
1	Regression	0.002	3	0.001	6.313	0.049	
2	Residual	0.001	4	0.000			
3	Total	0.003	7				
4	Summary						0.826
Df – degree of freedom; F – Fisher's value; R^2 – regression coefficient of determination							

Table 6. Regression coefficients (β) characterising the model function for epoxy/Almp composites wear rate

Standard order	Predictors	B	Standardised Error	Standardised β	95 % confidence interval for β		Tolerance	VIF
					Lower Bound	Upper Bound		
1	(Constant)	0.009	0.015		-0.032	0.050		
2	f	0.001	0.000	0.477	0.000	0.002	1.000	1.000
3	A_m	-0.003	0.001	-0.747	-0.005	-0.001	1.000	1.000
4	V	0.011	0.012	0.201	-0.021	0.043	1.000	1.000
Key: f - applied load; A_m - weight of aluminium micro particles; v – speed of disc rotation; VIF - Variance inflation factor								

Table 7. Model evaluation parameters for epoxy/Almp composites wear rate

	Minimum	Maximum	Mean	Standard deviation
Mahalalabonis Distance	2.625	2.625	2.625	0.000
Cook's Distance	0.003	0.702	0.250	0.226
Standardised residual	-1.120	1.676	0.000	1.069

$$W \; A_m, f, v \; _{Almp} \quad 1 \quad _2A_m \quad _3f \quad _4v \qquad (9)$$

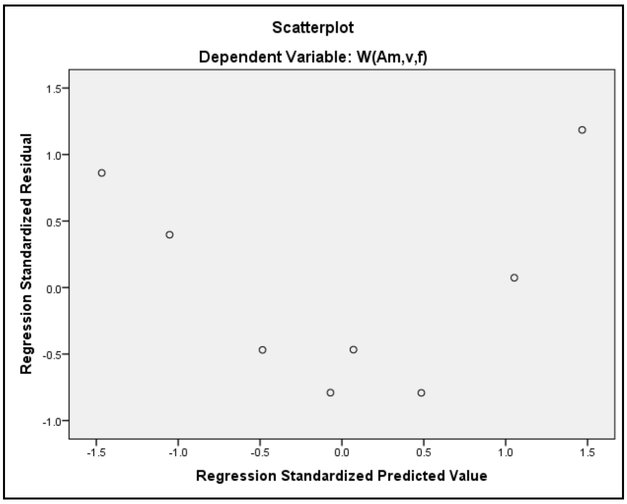

Figure 4. Standardised residuals for epoxy/Almp composites wear rate

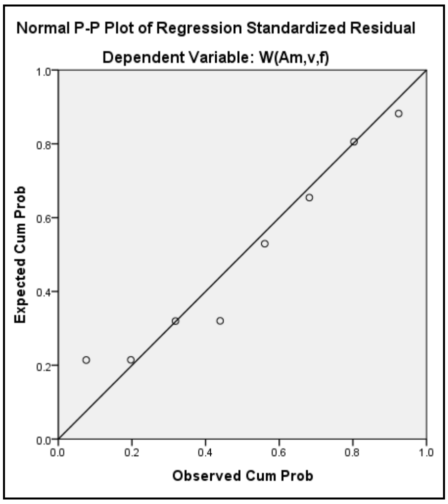

Figure 5. Expected and observed cumulative probabilities for epoxy/Almp composites wear rate

Table 8. Result of confirmation of experiment and validation epoxy/Almp composites wear rate

Standard order	Wear rate (gm^{-1})		
	Experiment	Model	Residuals
1	0.020667	0.0256	-0.0049
2	0.04352	0.0427	0.0008
3	0.02445	0.0328	-0.0084
4	0.06253	0.05	0.0126
5	0.007951	-0.0012	0.0091
6	0.010975	0.0159	-0.005
7	0.010252	0.006	0.0042
8	0.014792	0.0232	-0.0084

Mass loss-per sliding distance wear rate of epoxy/10Almp was modelled as a function of three independent/predictor variables, percentage weight of Almp (Am) additions, speed (v) and applied load (f) at two different levels. The model was built using full factorials design of experiments (2^3 = 8) at 95 % confidence level, with alpha = 0.05. The design layout for the model is presented in Table 3. Relationship between dependent variable, wear rate (W) and independent variables; f, v and A_m in Table 4 shows that f and A_m are statistically significant in prediction of W.

Correlation coefficient of v (0.201) less than 0.3 as reported by Pallant [11] indicates a weak relationship between W and v. Evaluating the interaction between v, A_m and f, their correlation coefficient is 0.000 indicating no relationship between them. This is excellent; it implies that linear multi-interaction among independent variables in prediction of response (W) is obeyed. The last three columns of Table 5 indicate model Fisher value of 6.313, meaning that there is a very low chance that noise could occur in this model; prob>F value of 0.054 approximated to 0.05 indicating that every term of this model is statistically significant in the prediction of responses and R^2 is equal to 0.826. This implies that 82.6 % of the data can be explained by the model.

Tolerance and variance inflation factor (VIF) values of 1 each, for all independent variables which is higher than 0.1 and less than 10 is a confirmation of obedience to multicollinearity of the independent variables f, v and A_m. Neglecting the negative sign in the front of the standardised β in Table 6, A_m (0.747) has largest contribution to the prediction of the response (W), followed by f (0.477). These observations imply that the model gives a reasonable explanation on the relationship between the predictor variables and the response. This agrees with a report in [2]. The co-plot of residuals and their intervals in Figure 3 demonstrates that all residuals at each case or level ranges from negative through zero to positive values, affirming that no outlier is found in the response matrix, that is, no response value is much higher or lower than expected values.

This agrees with standardised residual plot in Figure 4 which according to Tabachanick and Fiddell (2001) found in [11], the standardised residuals should fall between -3.3 and 3.3. Also, the mean Cook's distance (0.250) which is less than one affirms absence of an outlier in the model. The scatter plot in Figure 5 which shows the data distribution along the diagonal line through the origin is a confirmation of little difference between the predicted and actual values. The mean Mahalabonis' distance (2.625) in Table 7 which is lower than 16.27 assigned to any linear regression involving three independent variables [11] shows that the prediction of the response (W) by this model is free from any critical case that may require additional attention. Substitution of β in Table 6 into Equation 9 gives the regression function for obtaining the response, the predicted values of the epoxy/Almp composites wear rate (W) as shown in Table 8.

3.0 CONCLUSIONS

Based on the result of investigation, the following conclusion can be made:

[1] There were 177.8 and 160.6 % increases in the wear rates of epoxy polymer and epoxy aluminium composites, respectively when the applied load increased from 9 to 25N.

[2] Smaller percentage wear rate of the epoxy composite is attributed to addition of aluminium particles to epoxy.

[3] Regression coefficients of determination for both analyses are 99.92 and 82.6 % which show good coverage of input data.

[4] Absence of outlier and critical case in the regression analyses establishes that both the models are appropriate for prediction of the wear rates of epoxy/aluminium composites.

[5] The continual trench-geometry observed on the worn-out surface of the epoxy polymer indicates a greater damage to the surface in comparison with that of the epoxy polymer.

[6] There is an agreement between the wear rates and worn-out surface geometry of the examined materials.

ACKNOWLEDGEMENT

Author show their appreciation to Mr Rasheed Jimoh for his support towards successful completion of this research.

REFERENCES

[1] F. Asuke, M. Abdulwahab, V. S. Aigbodion, O. S. I. Fayomi, O. Aponbiede; Egyptian Journal of Basic and Applied Sciences. Vol. 1, No. 1, pp. 67-70, 2014.

[2] C. U. Atuanya, V. S. Aigbodion, S. C. Nwigbo, Materials & Design, Vol. 53, No. pp. 65-73, 2014.

[3] J. O. Agunsoye, V. S. Aigbodion, Results in Physics, Vol. 3, No. pp. 187-194, 2013.

[4] J. O. Agunsoye, S. A. Bello, L. **B**ello, M. M. Idehenre, Advances in Production Engineering & Management. Vol. 11, No. 1, pp. 5-14, 2016.

[5] J. A. Carroll, A. H. Barrow, B J , B. Robinson, *Client Project Report CPR1825 Pedestrian Legform Test Area Assessment Final Report*, Transport Research Laboratory, European Commission, DG Enterprise, Europe, 2014.

[6] M. M. Davoodi, S. M. Sapuan, D. Ahmad, A. Aidy, A. Khalina, M. Jonoobi, Materials & Design. Vol. 32, No. 10, pp. 4857-4865, 2011.

[7] S. A. Bello, J. O. Agunsoye, J. A. Adebisi, R. G. Adeyemo, S. B. Hassan; Journal of King Saud University - Science. Vol. in press, No. pp. 2018.

[8] J. O. Agunsoye, S. A. Bello, S. I. Talabi, A. A. Yekinni, R. I. A., O. A. D., I. T. E.; Tribology in Industry. Vol. 37, No. 1, pp. 107-116, 2015.

[9] J. P. I. William, *Introduction to MATLAB 6 for Engineers*, McGraw-Hill, America, 1998.

[10] J. O. Agunsoye, S. A. Bello, L. O. Adetola; Journal of King Saud University - Engineering Sciences. Vol. in press, No. pp. 2017.

[11] J. Pallant, *SPSS Survival Manual*, Allen & Unwin, Australian, 2005.

Serbian Tribology Society

SERBIATRIB '19

16th International Conference on Tribology

Faculty of Engineering University of Kragujevac

Kragujevac, Serbia, 15 – 17 May 2019

WEAR SIMULATION OF THE POLYMER BASED COMPOSITE SLIDING BEARINGS BY MEANS OF ANSYS

Miloš STANKOVIĆ[1], Aleksandar MARINKOVIĆ[2], Nenad KOLAREVIĆ[3]

[1]Inovation Center of the Faculty of the Mechanical Engineering, Serbia, mstankovic@mas.bg.ac.rs

[2]Faculty of the Mechanical Engineering, Serbia, amarinkovic@mas.bg.ac.rs

[3]Faculty of the Mechanical Engineering, Serbia, nkolarevic@mas.bg.ac.rs

*Corresponding author: mstankovic@mas.bg.ac.rs

Abstract: *Polymer based composite sliding bearings are increasingly applied in many industries, due to their economic (usually low cost of production) and technical (good tribological properties) benefits. In order to predict their life cycle, it is necessary to perform numerous experiments and evaluate their wear rate. This is generally quite expensive and time consuming.*

By applying only one series of the experiments and determining Archard's wear coefficient, and embedding it into the code of the Ansys software, it is possible to simulate the wear, and thus save the time and the financial resources. This paper explains the procedure of the wear simulation in case of known Archard's coefficient, for sliding bearings made of PTFE polyamide composite material in contact with shaft of steel. The output of the simulation is the contact pressure in relation of time and the amount of worn volume for 3 revolutions of the shaft.

Keywords: *wear simulation, polymer sliding bearings, Archard's coefficient, Ansys.*

1. INTRODUCTION

Sliding or a plane bearings are increasingly applied in various industries, due to their simplicity in production and economic advantages. If compared to roller bearings, they are significantly cheaper to produce. Making sliding bearings of polymer materials leads to the further evolution, since they are light weighted, and usually have low friction coefficient in contact with steel. They could run dry or initially lubricated, which makes them applicable in the "clean industries" (pharmaceutical, food etc.).

Wear calculations are very important in order to predict the life cycle of a certain component, and thus schedule the forehand replacement or prevent the failure. Wear tests are usually expensive and time consuming, so the alternative approaches were introduced. One of the youngest is the numerical calculation. Hand by hand with the evolution of the computer technology, the numerical methods were developing. They started and took very important place in strain/stress analysis, but recently their application expands to the wear simulations.

Although the idea of the wear calculations dates from the mid of the 20th century [1], the real breakthrough happened during the '90s by authors Podra and Anderson ([2], [3]). Later at 2010, Anderson gave a detailed summery in subject of wear simulation, its application and constraints [4]. Benabdallah and Olender [5] performed 2D wear simulation of POM. By means of pin-on-disc configurations they obtained necessary input values. The development of an inclination in the wearing profile of the pin was predicted by the simulation. They used adaptive mesh and different working regimes: v = 0.1..1 m/s, s = 20..80 km and p = 1..10 Mpa.

2. PRINCIPLES OF THE WEAR SIMULATION

Analysing the literature it is noticed that the most common approach to simulate the wearing process is the one that applies the Archard´s wear formula:

$$V \quad K \frac{L\ F}{H}$$

Where stands: ΔV-worn volume, L-sliding distance, F-radial load, and H hardness of the softer material in contact (in this case PTFE polyamide).

Applying this formula, the wear could be simulated by FEM. In this case, it was performed in software ANSYS 18.1.

2.1 Determination of the input data for the wear simulation

In order to perform numerical simulation of the wearing process, it is necessary to obtain input data. Some of these data are read from the producer's catalogue, while the others are determined by experimental research.

The examined bearings are made of PTFE polyamide which characteristics are given in Table 1.

Table 1: PTFE Polyamide sliding bearing´s characteristics

Permissible load, N/mm^2 (dynamic/static)	40/80
Permissible sliding velocity, m/s	1
Friction coefficient	0.06..0.15
Temperature range °C	-30..+110
Density kg/m^3	1380

But beyond these characteristics, it is necessary to define Young´s modulus and Poisons ratio of the PTFE polyamide, which are according to the literature ([6], [7]):

$$E\text{=}2100\ \text{N/mm}^2$$
$$\nu\text{=}0.4$$

The most demanding part of experimental research is to determine Archard´s wear coefficient K. Detailed steps and results regarding to this topic were processed and published in previous articles [8]. Wear coefficient in case of PTFE polyamide is:

$$K = 1.2196\cdot10^{-6}$$

Micro-hardness of the examined material H should also be determined experimentally. According to the referent literature [8], this it is done by Micro-Vickers method. By means of the micro Vickers hardness tester TH710, this value is determined to be:

$$H = 10\ \text{kg/mm}^3 = 98.07\cdot10^6\ \text{N/m}^3$$

Other input values such are: sliding distance L, sliding velocity v, and contact pressure p, are defined with respect to working regime, pv-characteristics of the specimen bearing and referent literature [5]. These values are:

$$L = 20000\ \text{m}$$
$$p = 1\ \text{MPa}$$
$$v\text{= }1\ \text{m/s}$$

3. NUMERICAL SIMULATION SETUP

The numerical simulation is performed in "Transient Analysis", module of the software ANSYS 18.1, which executes time dependent phenomena. It is necessary to define contact properties in the tribo-pair. In this case, the contact is defined as a frictional between one rigid (shaft) and one flexible body (bearing), with friction coefficient 0.8, which is also confirmed experimentally. Additional contact properties between the shaft and the sample are defined in a custom code. These properties are Archard's coefficient and the sample's hardness, exponents m and n, that comprehend the influence of the contact pressure and sliding velocity. It was simulated 3 full revolutions of the shaft in contact with the sample. In order to provide more data for analysis, 15 sub-steps were created (five steps per revolution).

4. RESULTS

The results of the numerical simulation of wear are contact pressure (Figure 1), readable in each of 15 steps, and the volume of the sample at the beginning and the end of the process of wearing. Contact pressure is also determined by applying Herzian formula, and the results were consistent.

At the Figure 2, there could be noted three pressure segments: 6.05 to 6.03, 6.01 to 5.99 and 5.97 to 5.95. Each pressure segment corresponds to the one separate revolution of the shaft. There is observed a decrease in contact pressure, which is explained by the material removal.

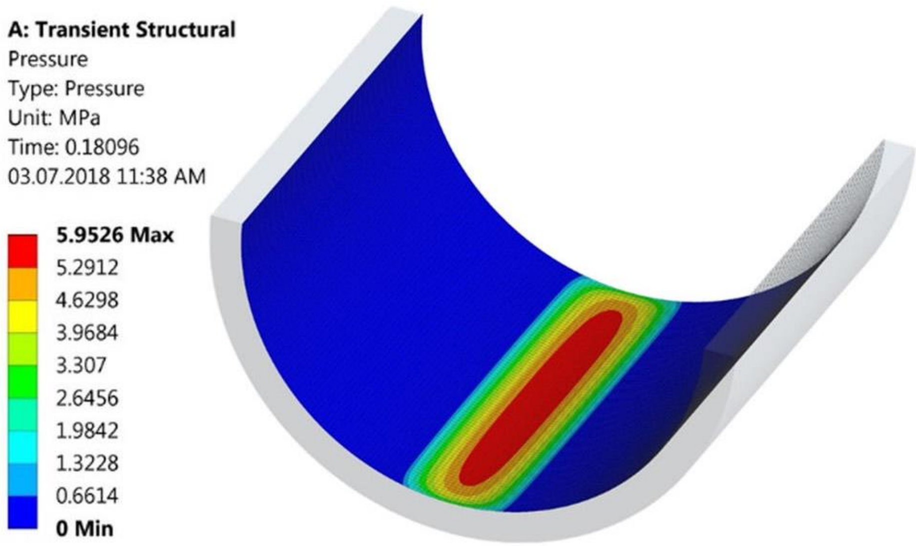

Figure 1. Calculated contact pressure

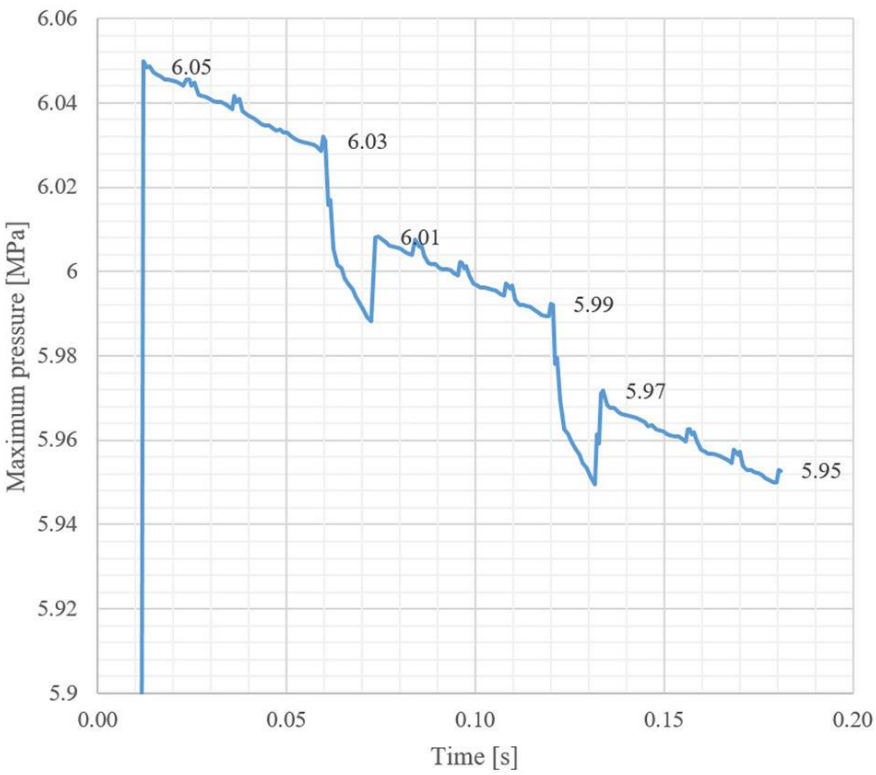

Figure 2. The pressure decrease during 3 full revolutions of the shaf

Between the segments, there are also spotted sharp decreases of the contact pressure (6.03 to 6.01 and 5.99 to 5.97), which are caused by the increase of contact surface with every next revolution. Initially, the contact between two different size cylinders is line, but due to the material removal, the line transfers to the surface with an increasing trend with every next revolution. Due to this increase of the contact surface, the pressure between two revolutions sharply decreases. The quantitative amount of the wear is given through calculated volumes of the sample before and after wearing. These volumes are respectively 947.8 and 947.61 mm^3, which gives 0.19 mm^3 in difference. Since the number of the revolutions in the experiments is cca. 285000, the calculated worn volume is not comparable to the experiment. The three revolutions are simply not enough to compare with the experiment, especially if taken into account that the wearing process is not uniform in time.

5. CONCLUSIONS

In this paper it was presented the result of the numerical simulation of wear, in case of the sliding bearing / shaft contact. The outputs of the calculation are contact pressure, its diagram over time and volume before and after the wearing. Contact pressure is confirmed in high correlation with the analytical (Herzian) calculation.

It was noted the constant decrease of the contact pressure, which is in correlation with the wearing process.

Since the numerical calculation is highly strenuous for the computer, it was limited to only three revolutions of the shaft. Hence, the result was not comparable to the experiment. The possible solution is to simplify the model to 2D.

REFERENCES

[1] R. Holm: Electric Contacts, Almqvist and Wiksells Boktryckeri, Uppsala, 1946.

[2] P. Podra, S. Andersson: Wear simulation with the Winkler surface model, Wear, Vol. 207, pp. 79–85, 1997.

[3] P. Podra, S. Andersson: Simulating sliding wear with finite element method, Tribology International, Vol. 32, pp. 71–81, 1999.

[4] S. Andersson, Wear Simulation, Advanced Knowledge Application in Practice, Igor Fuerstner (Ed.), 2010.

[5] H. Benabdallah, D. Olender: Finite element simulation of the wear of polyoxymethylene in pin-on-disc configuration, Wear 261 (2006), pp 1213–1224.

[6] Professional Plastics, Mechanical Properties of Plastic Materials, available at: https://www.professionalplastics.com/professionalplastics/MechanicalPropertiesofPlastics.pdf .

[7] Li J., “Mechanical Properties of a Polyamide 6-Reinforced PTFE Composite”, Mechanics of Composite Materials, Vol. 45, No. 3, 2009, pp. 287-292, 2009.

[8] M. Stanković, A. Marinković, A. Grbović, Ž. Mišković, B. Rosić, R. Mitrović, (2019) "Determination of Archard’s wear coefficient and wear simulation of sliding bearings", Industrial Lubrication and Tribology, Vol. 71, Issue 1, pp. 119-125, 2019.

[9] B. Bhushan: Introduction to Tribology, A John Wiley & Sons, 2013.

Serbian Tribology Society

SERBIATRIB '19

16th International Conference on Tribology

Faculty of Engineering University of Kragujevac

Kragujevac, Serbia, 15 – 17 May 2019

THE EFFECT OF CRYOGENIC TREATMENTS ON PITTING CORROSION SUSCEPTIBILITY OF AA5083-H111 IN 3.5% NaCl ENVIRONMENT

Husnu GERENGI[1]*, Ilyas UYGUR[1], Mesut YILDIZ[1], Doğancan UZ[1],

[1]Corrosion Research Laboratory, Department of Mechanical Engineering, Faculty of Engineering, Duzce University, 81620, Duzce, Turkey,

*Corresponding author: husnugerengi@gmail.com

Abstract: *Application of aluminium alloys is increasing in all industries due to its combined properties of low weight, good mechanical resistance, thermal conductivity, electrical conductivity, high strength, and good corrosion resistance. In particular, AA5083-H111 alloys have been successfully used in the maritime sector. Unlike purely surface treatments, cryogenic treatment is an inexpensive one-time process that influences the core properties of the components. Cryogenic treatment has recently been introduced to Al alloys. Although the main mechanisms are still ambiguous, considerable improvements on mechanical properties are well noted. However, the effect of cryogenic treatment on the corrosion of Al alloys is limited.*

This study investigated the effect of shallow cryogenic treatment (-80 °C) on the corrosion of 5083-H111 aluminium alloy, which is used particularly in the shipbuilding industry. Plates of 6-mm thickness exposed to a 3.5% NaCl environment were evaluated via Brinell hardness measurements, Electrochemical Impedance Spectroscopy (EIS) and surface monitoring methods including atomic force microscopy (AFM) and optical profilometry (OP) applied before and after the effect of cryogenic treatment.

Results indicated that the duration time of cryogenic treatment (24 h, 36 h and 48 h) had little effect on changing the hardness values and corrosion response of AA5083-H111 alloy in the 3.5% NaCl environment.

Keywords: *AA5083, corrosion, cryogenic, hardness, AFM*

1. INTRODUCTION

The mechanical properties of aluminium, the most abundant element of the earth's crust, can be improved by alloying it with other metals. Aluminium and its alloys are the most widely produced among the non-ferrous metals due to their lightness, processability, high corrosion resistance, and capability of being recycled. Recently, various methods such as aging, heat treatment and cryogenic treatment have been applied to increase the strength of aluminium alloys and improve their mechanical properties.

The properties of materials show significant improvements with the application of cryogenic treatment in its two forms as deep and shallow cryogenic treatment. Shallow cryogenic treatment is more common and is applied to materials at up to -90 C. The deep cryogenic process is applied to the material at temperatures below -90 C [1]. With cryogenic treatment, increases have been determined in the mechanical properties of materials such as yield, tensile strength, fatigue, impact strength, hardness, corrosion resistance [2], ductility, toughness and modulus of elasticity.

The 5083 aluminium-magnesium alloys, which have high corrosion resistance and moderate strength, are widely used in the shipbuilding industry in single- or multiple-hull high-speed ferries, cryogenics, transportation equipment and armor plates [3-5]. Because the environments where the 5083 Al-Mg alloys are used are severe, their properties need to be improved. These alloys are hardened only by cold treatment [6].

An H-designated temper is applied to develop the mechanical properties of the 5083 Al-Mg alloys, which are among those of the 5XXX series with the highest magnesium content. In the H111 temper designation, the first digit after H indicates strain-hardened only, the second digit indicates the degree of strain hardening (1/8 hard) and the last digit indicates the variation of the two-digit temper [7]. The elements of Cr and Mn in the composition of 5083-H111 control the stress corrosion of the alloy and increase its mechanical properties. The 5083-H111 is widely used in automobile production, aerospace parts and machine production [8].

In the present study, cryogenic treatment was applied to 5083 Al-Mg alloy at -80 ^{o}C for 24, 36 and 48 h, and Brinell hardness tests were performed. After cryogenic treatment, the corrosion resistance of the metal in a 3.5% NaCl medium was investigated by using Electrochemical Impedance Spectroscopy (EIS). After the corrosion tests, AFM and OP methods were applied to examine surface morphologies

2. MATERIALS AND EXPERIMENTAL PROCEDURE

2.1 Materials and Chemicals

The studied 5083-H111 aluminium alloy was supplied from ALRO S.A., Romania. The chemical composition (wt %) of the metal is listed in Table 1. The metal samples for corrosion and surface morphology studies were prepared following the method previously described by the authors. The corrosion environment was prepared using NaCl obtained from Sigma-Aldrich.

2.2 Corrosion Measurements

Electrochemical Impedance Spectroscopy (EIS) experiments were done using a Gamry instrument, Reference 600. All the electrochemical corrosion studies were conducted at room temperature using a three-electrode cell in which a Pt plate and Ag/AgCl were used as the counter and reference electrodes, respectively. The working electrodes (i.e., 5083-H111 samples) were embedded in epoxy resin with only 0.785 cm^2 exposed to the corrosive solution (3.5% NaCl). Before EIS measurement, the open circuit potential (OCP) was measured for a 2-h period in order to achieve a steady-state potential. The EIS measurements were carried out in a frequency range of 100 kHz–0.1 Hz with an applied AC signal of 10 mV. The equivalent circuit simulation program (ZSimpwin 3.21) was used for data analysis, the equivalent circuit synthesis and the experimental data fitting. In order to obtain a reproducible result, experiments were repeated seven times under the same conditions and the closest values presented as the result.

2.3 Hardness Testing

The DIGIROCK-RB hardness tester (Fig. 1) was used to calculate the Brinell hardness of each sample and the average of seven repeated measurements was taken. A load of 60 kg was applied to determine the hardness of the samples using an 8-mm-diameter ball indenter with a 3-s dwell time.

Table 1. Chemical composition of aluminium 5083-H111

	Si	Fe	Cu	Mn	Mg	Cr	Zn	Ni	Ti	Sn	Zr	Al
AA5083-H111	0.075	0.404	0.031	0.276	4.300	0.081	0.012	0.007	0.018	<0.002	<0.005	94.796

Figure 1. Hardness testing equipment

2.4 Surface Morphological Screening

After electrochemical measurements for all studied conditions, the AA5083-H111 surface morphologies were examined [9] by means of the AFM (PARKSYSTEMS, Model: XE-100E) and OP (Phaseview, Model: Zeescope) (Fig. 2).

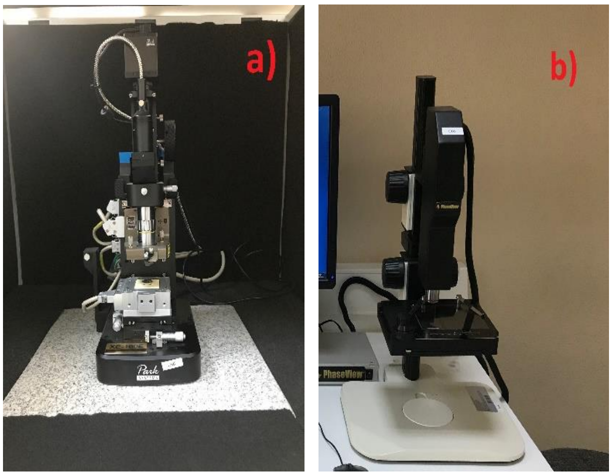

Figure 2. Equipment for AFM (a) and OP (b)

3. RESULTS AND DISCUSSION

3.1 EIS Measurements

The impedance method provides information about the kinetics of the electrode processes and simultaneously about the surface properties of the investigated systems [10]. Figure 3 presents the EIS results recorded for the AA5083-H111 alloy samples without and with 24, 36 and 48 h shallow cryogenic treatment (-80 ^{o}C) exposed to 3.5% NaCl solution. The EIS results are shown in Fig. 3 with (a) Nyquist, (b) Phase angle, and (c) Bode modulus representations. In order to obtain relevant electrochemical parameters, an equivalent circuit diagram, as shown in Fig. 4, was selected for fitting the obtained impedance results. The goodness-of-fit parameter (variance, σ^2) for all selected experimental data was not greater than 2.1×10^{-3}.

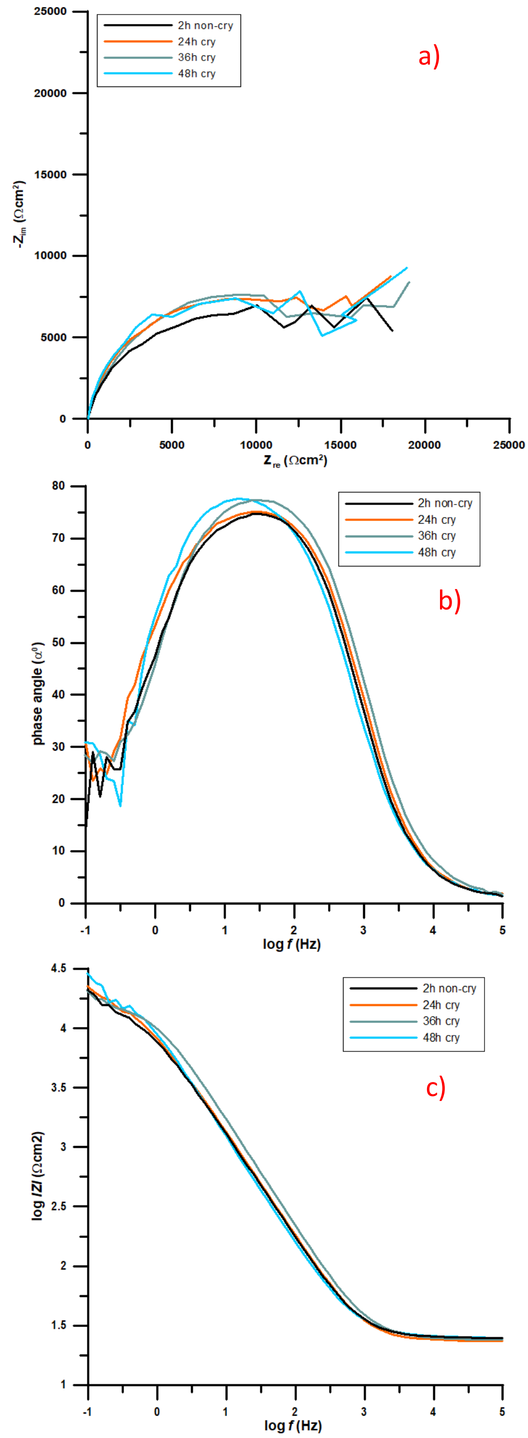

Figure 3. Experimental and fitted impedance of AA5083-H111 alloy samples without and with 24, 36 and 48 h shallow cryogenic treatment exposed to 3.5% NaCl

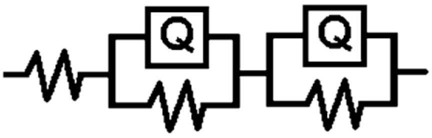

Figure 4. Equivalent circuit used for EIS analysis

The circuit R(QR)(QR) was recently used in our previous study [11]. The meaning of the elements in this circuit is as follows, respectively, for the solution resistance (R_s), charge transfer resistance (R_{ct}) and film resistance (R_f) to be derived. The Q parameter denotes the constant phase element (CPE) and was used to compensate for the roughness and the non-uniformity of the studied metal electrodes; Q_f and Q_{dl} represent the capacitance for the surface film and double layer. All the derived electrochemical parameters are listed in Table 2.

It is clear from Fig. 3a and Table 2 that there was no significant change in the R_{ct} values with the cryogenic treatment or the duration of the process.

The increase in the R_f value indicated that the cryogenic process had created an oxide film on the metal surface. However, this increase was not directly proportional to the duration of the cryogenic treatment process.

The R_p (R_{ct}+R_f) value was found to have increased from 33448 to 33984 Ω.cm^2 after 48 h of cryogenic treatment.

These small changes seemed not to depend much on the duration time of the cryogenic treatment. In general, the R_P values were increased due to the small increases in R_{ct} and R_f.

3.2 Hardness Testing

The hardness of all AA5083-H111 alloy samples was tested before the EIS experiments and a correlation was reported between the hardness and corrosion resistance [12,13]. The hardness results are presented in Fig. 5. The hardness results indicated that there was very little difference in the data obtained depending on the time. The difference was 2.8 Brinell between the average hardness values of the metal samples cryogenically treated for 48 h and those not treated. This value shows that the cryogenic treatment process did not have a significant effect on the hardness of the AA5083-H111 alloy.

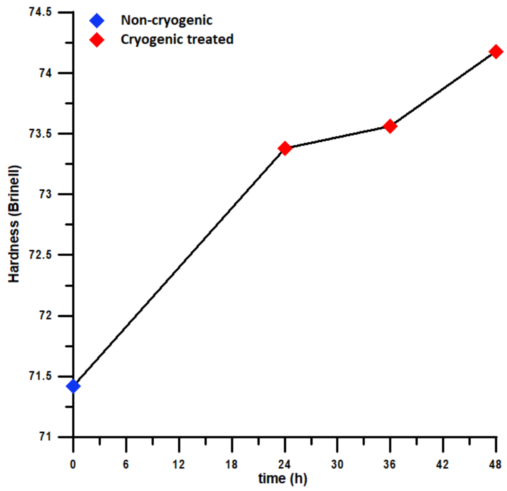

Figure 5. Surface hardness of AA5083-H111 alloy before and after 24-, 36- and 48-h cryogenic treatment

3.3 Surface Morphological Screening

The surfaces of the AA5083-H111 samples with (24, 36 and 48 h) or without cryogenic treatment were examined with AFM following the EIS measurements.

Table 3. AFM results (horizontal axis)

	5083-H111	
	R_a (nm)	R_z (nm)
Without cry treat	47.874	213.921
After 24 h cry treat	75.650	315.969
After 36 h cry treat	126.872	403.466
After 48 h cry treat	183.892	731.526

Table 2. EIS results of AA5083-H111 in the 3.5% NaCl environment.

Investigated system	R_s (Ω.cm^2)	Y_{01} (Ω^{-1}s^{2}cm^{-2})x10^{-3}	n 1	R_{ct} (Ω.cm^2)	Y_{02} (Ω^{-1}s^{2}cm^{-2})x10^{-3}	n 2	R_f (Ω.cm^2)	R_p (Ω.cm^2)
Without cry treat.	18.60	0.153	0.7810	24954	0.118	0.9127	8494	33448
After 24 h cry treat.	18.86	0.162	0.7925	25310	0.018	0.9338	9248	34558
After 36 h cry treat.	18.28	0.027	0.8796	25650	0.213	0.9659	9424	35074
After 48 h cry treat.	19.62	0.0096	0.7936	24771	0.027	0.9879	9213	33984

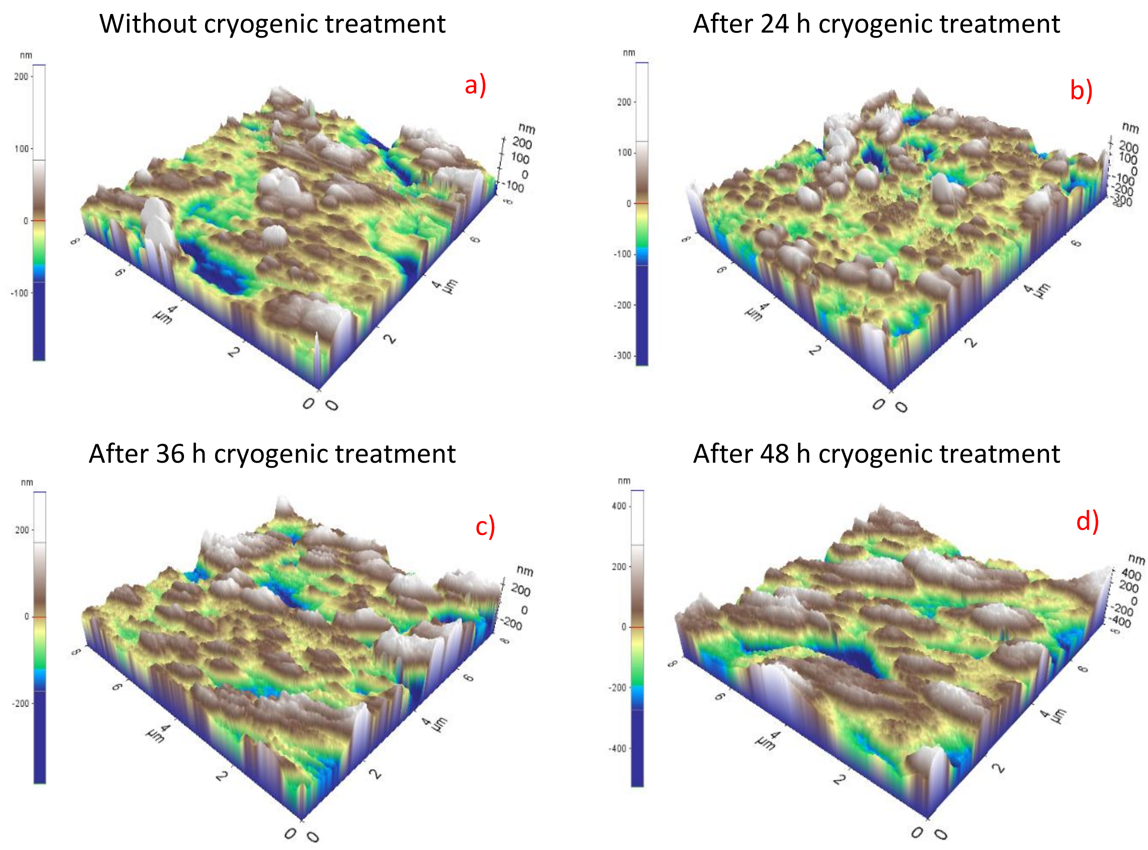

Figure 6. AFM analyses of AA5083-H111 after EIS measurements.

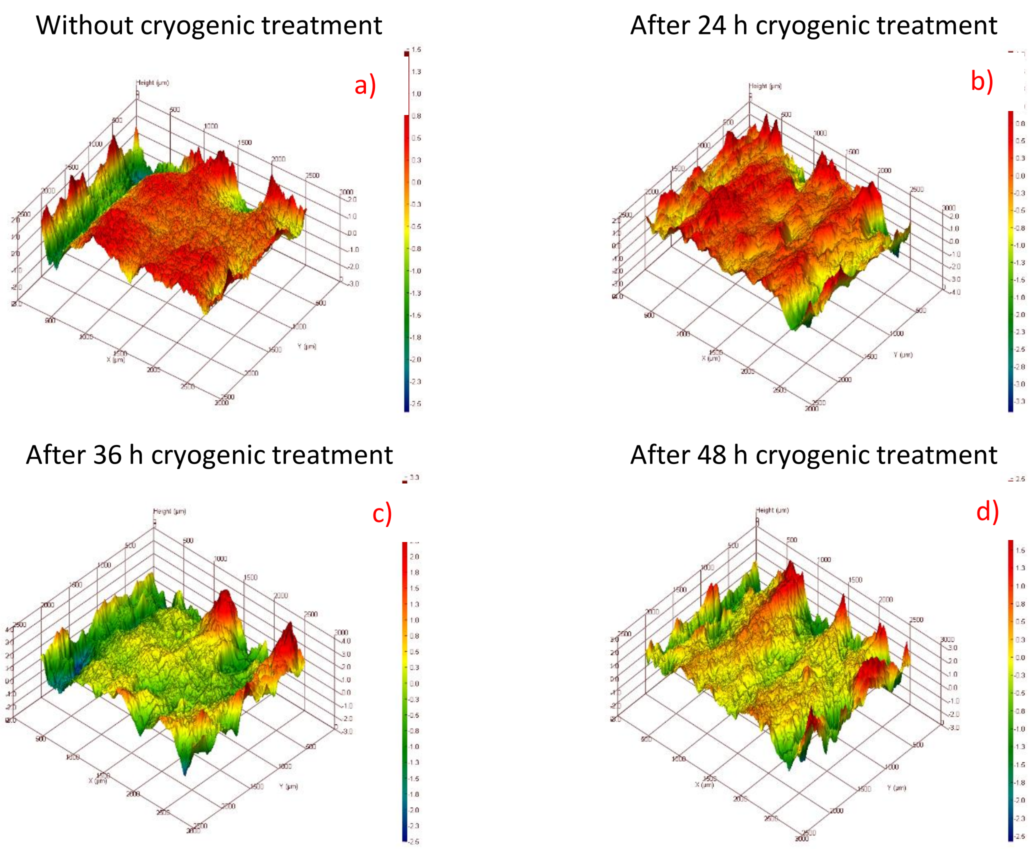

Figure 7. OP analyses of AA5083-H111 after EIS measurements.

The average roughness of the AA5083-H111 sample surfaces was obtained by statistical analysis of the AFM images. For AFM image processing, the zero point of height corresponded to the plane surface (defined by the software), and the Z-scale showed both higher and lower features on the surface. The average roughness (R_a) and root-mean-square roughness (R_z) were calculated by the equations reported in [14].

The AFM images for the cryogenically treated and untreated samples are shown in Figs. 6a-6d. The average roughness of the non-treated surfaces was about 48 nm and as the time of the cryogenic process was increased from 24 h to 36 h and 48 h, this value increased respectively from 76 to 127 and 183 nm. The results are presented in Table 3. According to these EIS data, the cryogenic process formed an oxide film on the metal surface and protected the metal against corrosion. However, this oxide layer was not stable. Therefore, the roughness on the metal surface increased after the EIS measurements.

Table 4. OP results after EIS measurements.

AA5083-H111		
	R_a (µm)	R_z (µm)
Without cry treat	0.07935	0.5173
After 24 h cry treat	0.1325	0.6587
After 36 h cry treat	0.1437	0.8998
After 48 h cry treat	0.1557	0.8496

The OP results were similar to the AFM findings (Figs. 7a-7d). The root-mean-square roughness (R_z) value also increased with the cryogenic treatment duration time (Table 4).

4. CONCLUSION

Investigations were carried out on the corrosion of AA5083-H111 in 3.5% NaCl solution and resulted in the following conclusions:

- The AA5083-H111 was highly resistant to corrosion in a 3.5% NaCl environment.
- Shallow cryogenic treatment (-80 ^{o}C) had no significant improvement effect on the corrosion of AA5083-H111 in 3.5% NaCl solution.
- There was a meaningful correlation between the EIS values and the hardness results. The findings obtained by both methods showed little change as the duration of the cryogenic process was increased.
- Results of the EIS measurements revealed that the charge transfer resistance increased with the duration of cryogenic treatment. However, this change was not extreme.
- The AFM and OP images revealed that the cryogenic treatment had changed the surface morphology of AA5083-H111. As the cryogenic treatment process time was increased, more roughness was observed on the metal surface after EIS measurements. In order to better explain this event, long-term studies should be conducted using Dynamic Electrochemical Impedance Spectroscopy (DEIS) in order to carry out time-based impedance analysis.
- The effect of deep cryogenic treatment on the improvement of corrosion of AA5083-H111 in 3.5% NaCl solution should also be investigated.
- According to these EIS data, the cryogenic process had caused an oxide film to form on the metal surface which protected the metal against corrosion. However, this oxide layer was not stable. This finding should be investigated using XRD and other methods.

ACKNOWLEDGEMENTS

The authors gratefully acknowledge the financial support of this work by the Duzce University Research Fund (DUBAP).

REFERENCES

[1] A.R. Jha: *Cryogenic Technology and Applications,* Elsevier Academic Press, USA, 2006.

[2] I. Uygur, H. Gerengi, Y. Arslan, M. Kurtay: The effects of cryogenic treatment on the corrosion of AISI D3 steel, Materials Research, Vol. 18, No. 3, pp. 569-574, 2015.

[3] B. Gungor, E. Kaluc, E. Taban, A. SIK: Mechanical and microstructural properties of robotic cold metal transfer (CMT)

welded 5083-H111 and 6082-T651 aluminum alloys, Materials and Design, Vol. 54, pp. 207–211, 2014.

[4] B. Gungor, E. Kaluc, E. Taban, A. SIK: Mechanical, fatigue and microstructural properties of friction stir welded 5083-H111 and 6082-T651 aluminum alloys, Materials and Design, Vol. 56, pp. 84–90, 2014.

[5] G.E. Totten, S. Mackenzie: *Handbook of Aluminum. vol 1. Physical Metallurgy and Processes*, Marcel Dekker Inc, USA, 2003.

[6] K. Stambekova, H.M. Lin, J.Y. Uan: Surface modification of 5083 Al alloy by electrical discharge alloying processing with a 75 mass % Si–Fe alloy electrode, Applied Surface Science, Vol. 258, No. 10, pp. 4483–4488, 2012.

[7] G. Akçay: *Effect Of Friction Stır Processıng on Fracture Toughness and Crack Growth Behaviour of Fusion Welded 5083 Grade Alumınum Plates*, MSc Thesis, Master Of Science in Metallurgical And Materials Engineering Department, Middle East Technical University, Ankara, 2015.

[8] M. Dilek: *Mechanical Properties of Different Aluminum Alloys Joined By Friction Stir Welding*, MSc Thesis, Department of Mechanical Engineering, Institute of Natural and Applied Sciences, Çukurova University, Adana, 2006.

[9] H. Gerengi, G. Bereket, M. Kurtay: A morphological and electrochemical comparison of the corrosion process of aluminum alloys under simulated acid rain conditions, Journal of the Taiwan Institute of Chemical Engineers, Vol. 58, pp. 509-516, 2016.

[10] M.A. Amin, K.f. Khaled: Copper corrosion inhibition in O_2-saturated H_2SO_4 solutions, Corrosion Science, Vol. 52, No. 4, pp. 1194-1204, 2010.

[11] M.M. Solomon, H. Gerengi, T. Kaya, E. Kaya, S.A. Umoren: Synergistic inhibition of St37 steel corrosion in 15% H_2SO_4 solution by chitosan and iodide ion additives, Cellulose, Vol. 24, No. 2, pp 931–950, 2017.

[12] L. Zhang, H. Peng, Q. Qin, Q. Fan, S. Bao, Y. Wen: Effects of annealing on hardness and corrosion resistance of 60NiTi film deposited by magnetron sputtering, Journal of Alloys and Compounds, Vol. 746, pp. 45-53, 2018.

[13] B. Zhu, C. Zanella: Hardness and corrosion behaviour of anodised Al-Si produced by rheocasting, Materials & Design, Vol. 173, pp. 107764, 2019.

[14] J. Li, L. Ecco, A. Ahniyaz, J. Pan: Probing electrochemical mechanism of polyaniline and CeO_2 nanoparticles in alkyd coating with *in-situ* electrochemical-AFM and IRAS, Progress in Organic Coatings, Vol. 132, pp. 399-408, 2019.

FRICTION OF ULTRA-HIGH-MOLECULAR-WEIGHT POLYETHYLENE, MODIFIED WITH CARBON NANOTUBES

Kiril NIKOLOV[1], Mara KANDEVA[2,3] Lubomir DIMITROV[1]

[1]Faculty of Mechanical Engineering, Technical University – Sofia, 8 Kl. Ohridski Blvd, 1000 Sofia, Bulgaria

[2]Faculty of Industrial Technology, Tribology Center, Technical University – Sofia, 8 Kl. Ohridski Blvd, 1000 Sofia, Bulgaria

[3] South Ural State University, 76 Prospekt Lenina, Chelyabinsk, Russia

*Corresponding author: knikolov90@gmail.com

Abstract: *The present study investigates the coefficient of friction of new composites based on UHMWPE with the addition of different percentages of carbon nanotubes (CNTs) - 0.5%, 0.75%, 1.0% and 1.5%. UHMWPE samples with carbon nanotubes, samples of 0.5%, 0.75%, 1.0% and 1.5% carbon nanotubes (UHMWPE-CNTs) and samples with the same carbon nanotube content were made, but with carbon nanotubes subjected to Electroless Nickel Composite Coating with nanoparticles of SiC (UHMWPE-NiCNTs). The coefficient of friction is investigated with a tribometer in a kinematic scheme "Thumb-Disc" without lubricant in a high-alloy steel frame with hardness HRC=56.9 and roughness Ra=2.35 µm. All samples were tested under the same friction conditions - friction path, sliding speed, roughness of the counterpart and samples, ambient temperature. Results and regularities of the effect of carbon nanotubes UHMWPE-CNTs and UHMWPE-NiCNTs on the coefficient of friction at different normal loads are obtained. The micro-hardness of the materials under investigation was measured and its relationship to the percentage of CNTs and NiCNTs and to the coefficient of friction was analyzed. It was found that the highest micro-hardness belongs to the materials with 1.5% carbon nanotubes having a composite nickel plating (UHMWPE-1.5NiCNT).*

This study and the results are related to the implementation on contract: ДН 07/28-15.12.2016 "Research and creation of new wear-resistant coatings using composites and nanomaterials", funded by the National Science Fund at the Ministry of Education and Science, Bulgaria.

Keywords: *tribology, friction, UHMWPE, carbon nanotubes, composite materials*

1. INTRODUCTION

The main priority of tribology as interdisciplinary science and technology is to increase the energy efficiency and reliability of the machines. It is known that 30% of energy losses in the world are due to friction and 80% of failures in machines belong to friction compounds [1-5].

One of the methods for reducing friction and wear is the development of new composites and coatings with physico-mechanical characteristics and properties, providing low tangential stresses and high wear resistance of friction contacts. A specific feature of the tribological processes is that they occur in the thin surface layers of the contacts, they depend significantly on the operating modes and they change over time [6-10].

The development of modern industry is characterized by a wide variety and intensification of machine operating modes - increasing power, which means high speeds, loads and temperatures, vibration, abrasion, erosion and other extreme conditions. In many of the operating conditions, liquid lubricants are inapplicable and the tribo systems work in "*dry*" mode. In such cases, dry lubricants are used which are characterized by the anisotropy of their mechanical properties in tangential and normal directions. One such interesting material is ultra-high molecular weight polyethylene (UHMWPE), which has a number of advantages as a tribological material. Its specific molecular structure defines its antifriction properties and belonging to the group of self-lubricating materials with high abrasion resistance under conditions of abrasion and chemically aggressive environments. As a tribological material, UHMWPE has a wide range of applications - in low-revving and periodically operating nodes, guides and gears, in the presence of vibrations and vibration loads, in the presence of abrasive particles and others. Its low thermal conductivity is a flaw that limits some of its applications. One of the methods to improve the mechanical and tribological characteristics of UHMWPE is to introduce into its volume nano-sized particles having different shapes, sizes, concentration and nature [11-15].

The purpose of this paper is to study the effect of carbon nanotubes concentration in UHMWPE on the coefficient of friction without lubricant at different normal loads.

2. Materials

The composite samples under investigation are based on ultra-high molecular weight polyethylene (UHMWPE) with two types of non-oriented carbon nanotubes with different percentages (by mass). Nine (9) types of samples were prepared in two pieces of each type: samples (UHMWPE) without carbon nanotubes; samples (UHMWPE-CNTs) containing 0.5%, 0.75%, 1%, and 1.5% carbon nanotubes; samples (UHMWPE-NiCNTs) containing 0.5%, 1% and 1.5% carbon nanotubes with Nickel-Phosphorus Coating (Ni-P) applied by the method of electroless plating. The carbon nanotubes (CNTs) are multi-walled (MWCNTs) with a mean diameter of 10÷40 nm, length 1÷25 µm, specific surface area 150÷250 m^2/g and 99% purity. In order to increase the cohesive forces of interaction between the carbon nanotubes and the UHMWPE matrix and, accordingly, to improve the functional properties of the composite material, nickel-phosphor coating (Ni-P).

The new composite material obtained by sintering in a cylindrical press "*piston-cylinder*" (Fig. 1) after pre-homogenization in the following mode: pressure - 200 bar, sintering temperature - 185°C, sintering time - 30 min.

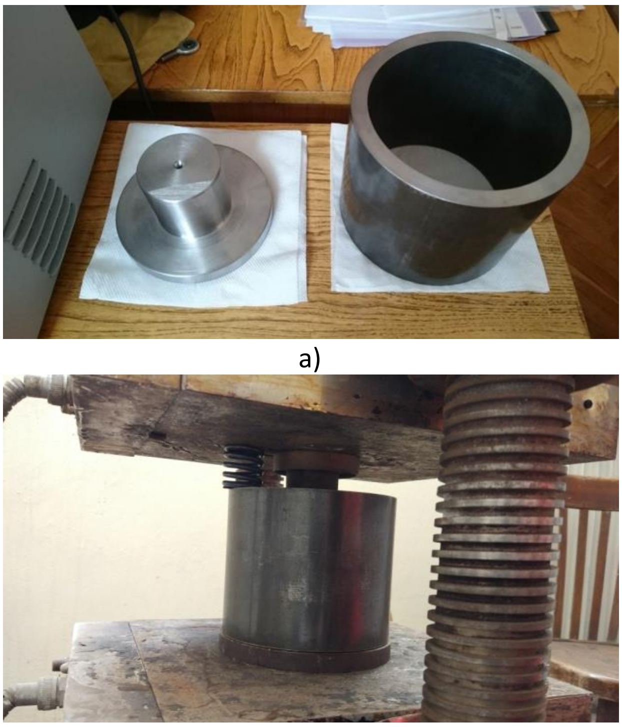

Figure 1. a) Piston and cylinder of cylindrical press; b) Cylindrical press for obtaining UHMWPE composites by sintering

The resulting blanks have the following dimensions - diameter 124 mm and thickness 15 mm – Fig. 2.

Figure 2. Picture of a disk blank with a diameter of 124 mm from composite UHMWPE-0.75CNTs: a) face, b) side

From the disk blanks samples are produced having a cubic shape with dimensions 15x15x15 mm. All specimens are prepared with the same roughness Ra=0.71÷0.98 μm. The roughness of the surface is measured by taking profileogram using a profilometer „TESA Rugosurf 10 - 10G".

Table 1. Hardness of the test samples

№	Sample	Average Hardness, MPa
1	UHMWPE-0CNTs	54.24
2	UHMWPE-0.5CNTs	53.38
3	UHMWPE-0.75CNTs	49.74
4	UHMWPE-1.0CNTs	48.84
5	UHMWPE-1.5CNTs	44.11
6	UHMWPE-0.5NiCNTs	55.12
7	UHMWPE-1.0NiCNTs	68.16
8	UHMWPE-1.5NiCNTs	77.10

Microhardness of the samples was measured by the Vickers method using a microhardness tester FISCHERSCOPE® H100. Table 1 shows the average hardness of the test pieces.

Designations of the samples include an Arabic number that indicates the percentage of carbon nanotubes without nickel-phosphorous coating (CNTs) and nickel-plated carbon nanotubes (NiCNs).

3. Device and methodology

The kinetic coefficient of friction is investigated using "*UHMWPE-Steel*" tribosystem under conditions of sliding without lubricant ("*dry*" friction). The study was performed with the device on kinematic scheme "*thumb-disk*" with the functional diagram shown in Fig. 3.

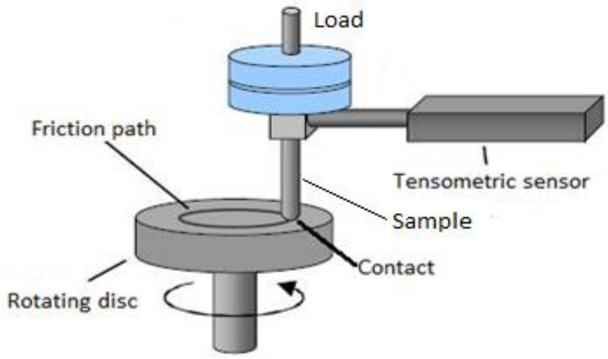

Figure 3. Scheme of the „*Thumb-Disk*" device

The fixed thumb represents the test specimen and the rotating disc is a high-alloy steel plate with hardness HRC56,9 and roughness Ra=2.35 μm. The friction force T is measured with an accuracy of 0.1 N with a dynamometer attached to the sample holder. The normal load P is set in the center of the specimen by means of weights or with a lever system mounted on the fixed sample holder. The coefficient of friction μ is calculated according to the law of Leonardo-Amonton as the ratio of the measured friction force T and the normal load P:

$$\mu = \frac{T}{P} \quad (1)$$

The methodology consists in measuring the friction force for each sample under the same friction - load modes P_1=60 N; P_2=80 N; P_3=100N; P_4=120 N, rotation speed n=94 min^{-1} (sliding speed v=0.83 m/s), ambient temperature 24^{o}C and calculating the coefficient of friction using formula (1).

4. Results and analysis

According to the described method, results were obtained for the friction force and the coefficient of friction at different loads. Figures 4-7 show graphically the friction coefficient dependence on the percentage of uncoated carbon nanotubes and nickel-coated carbon nanotubes, respectively, for the four load types.

The figures show that the presence of carbon nanotubes in UHMWPE influences the coefficient of friction (COF). This influence is not unambiguous, it depends on three factors: the percentage of nanoparticles, their modification with nickel-phosphorus coating and the value of the normal load.

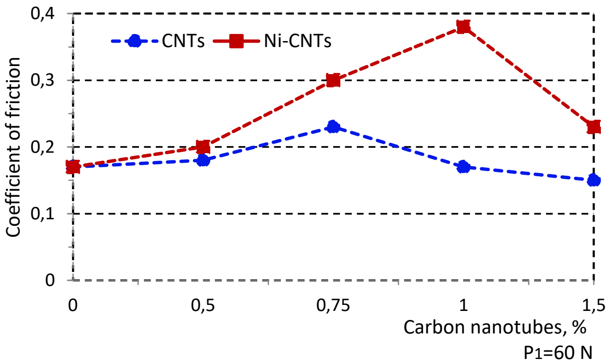

Figure 4. Friction coefficient change from the percentage of CNTs and NiCNTs at load P_1 = 60 N

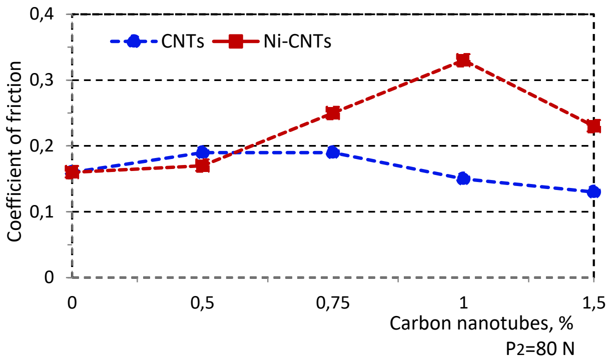

Figure 5. Friction coefficient change from the percentage of CNTs and NiCNTs at load P_2 = 80 N

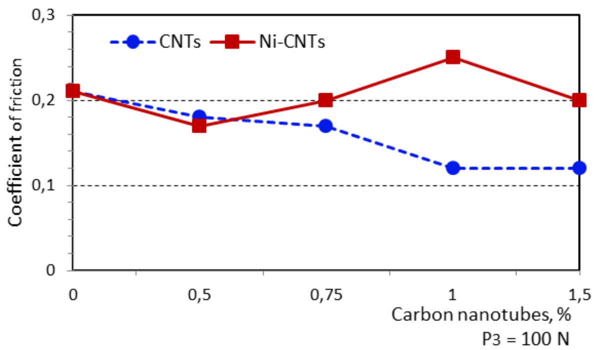

Figure 6. Friction coefficient change from the percentage of CNTs and NiCNTs at load P_3 = 100 N

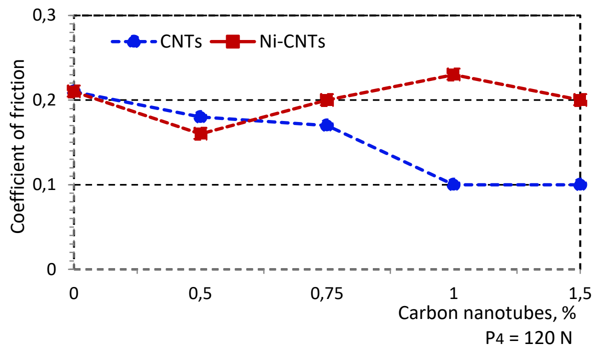

Figure 7. Friction coefficient change from the percentage of CNTs and NiCNTs at load P_4 = 120 N

For materials modified with carbon nanotubes without nickel-plated (CNTs), for the same load, COF dependence on the percentage of nanoparticles is non-linear. At low loads P_1=60N and P_2=80 N COF increases to 0.75% CNTs and reaches values higher than COF of non-nanoparticulate materials. When increasing the percentage of CNTs (1.0-1.5%) COF decreases smoothly and reaches values less than those of non-nanoparticulate material (Fig.4, Fig.5). At a higher load in the range P_3 = 100N and P_4 = 120N COF has a one-way change with an increase in the CNTs content - it decreases nonlinearly and there are always lower values than those of UHMWPE without nanoparticles (Fig.6, Fig.7). At these load values for CNTs content = 1% and 1,5%, the coefficient of friction takes the same minimum values, i.e. the coefficient of friction is of a sustained nature.

In the presence of nickel-coated carbon nanotubes (NiCNs), COF has a higher value than COF for NiCNs for all their percentages and for all normal loads. In this case, the COF dependence on the percentage of nanoparticles also has a nonlinear character - with an increase in the nanoparticle content, COF increases, reaches a maximum in NiCNTs - 1%, then decreases and reaches a higher COF value as with the non-nanoparticulate material. It is noteworthy that the maximum COF has different values for the different loads but always this maximum is observed for the same percentage of nanoparticles - 1% NiCNTs. At high loads - P_3=100N and P_4=120N, the curve has a wavy character with pronounced minimum and maximum. The minimum coefficient of friction is at 0.5% Ni-CNTs.

From the obtained results it was found that a maximum value of the friction coefficient μ=0.38 was observed in the friction of UHMWPE-1.0NiCNTs materials, i.e. materials doped with 1% nickel-plated carbon nanoparticles at least load P_1 = 60 N.

The smallest friction coefficient μ=0.1 is observed at the highest load P_4=120 N for nanotubes doped without nickel-phosphorous coating - UHMWPE-1.0CNTs and UHMWPE-1.5CNTs, i.e. the materials containing 1% and 1.5% carbon nanoparticles.

Figures 8 and 9 show COF diagrams for the same load P at different percentages of carbon nanotubes, respectively, with and without nickel coating.

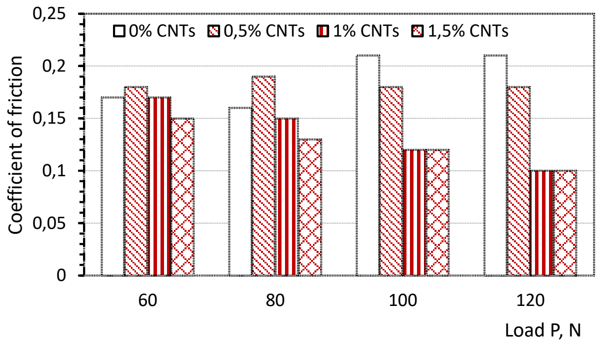

Figure 8. Diagram of COF for the same load P at different percentages of carbon nanotubes CNTs

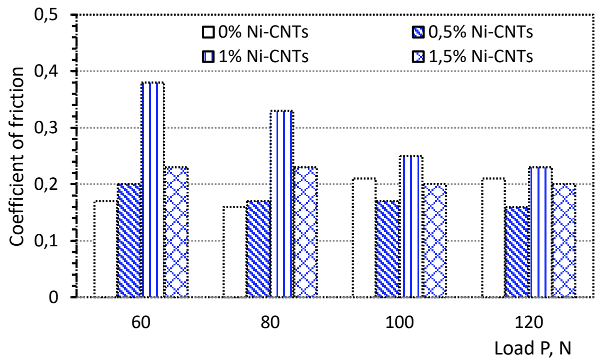

Figure 9. Diagram of COF for the same load P at different percentages of carbon nanotubes NiCNTs

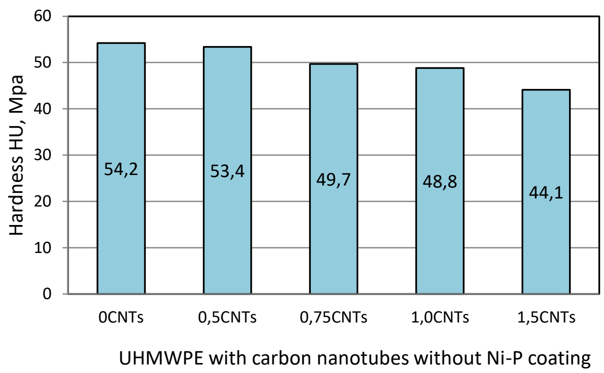

Figure 9. Hardness of UHMWPE with carbon nanotubes without nickel-phosphorous coating

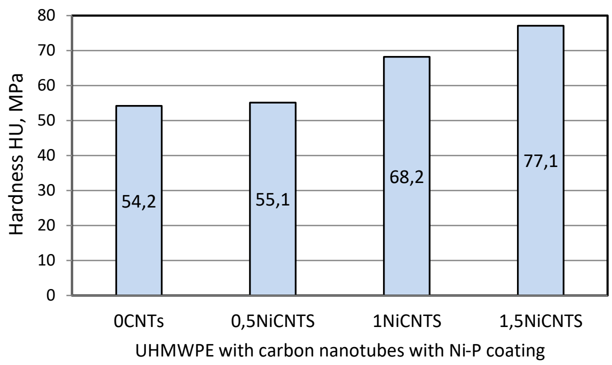

Figure 10. Hardness of UHMWPE with carbon nanotubes with nickel-phosphorous coating

Figures 10 and 11 show UHMWPE hardness graphs with different carbon nanotube contents, respectively, with and without a nickel-phosphor coating.

The analysis of the results on diagrams in Figures 8 and 9 shows that with increasing the load on materials without nanotubes COF increases with the increasing load.

It is clear from Figures 10 and 11 that when alloying with carbon nanotubes with a nickel-phosphorus coating, the UHMWPE hardness rises by 1.42 times in comparison to its non-nanoparticle hardness. The alloying of UHMWPE with uncoated carbon nanotubes does not increase hardness, on the contrary, a slight decrease is observed with an increase in the percentage content.

The obtained results can be interpreted on the basis of generally accepted in tribology molecular-deformation theory of friction [3]. According to this theory, friction is the result of two interdependent processes: a molecular interaction in the microcontacts that determines the adhesion component of the friction and the contact deformations defining the friction deformation component. The forces of molecular interaction depend mainly on the physico-chemical properties of the surface layers in the contact, the temperature, the transfer of material into the contact from one surface to the other, the presence of reinforcement, new structures and vary within certain limits. These forces resist the mutual movement of the bodies and influence contact deformations. The deformation component of the friction is composed of normal and tangential deformations of the contact spots. It mainly depends on the load, physico-mechanical characteristics of the surface layers and can increase or decrease with the increasing of the normal load. The division of the coefficient of friction in two components - adhesion and deformation has a contingent character. Under different modes of friction - load, speed, temperature, one or the other component can dominate, both influencing each other. The increase in COF with the increasing of the load on the material without nanotubes can be explained by the increase of the deformation component by friction as a result of sinking of the microroughnesses in the surface layers, increasing the number of contact areas and the actual contact area with a high contact pressure as a result of plastic deformation. For small content of nanoparticles - 0.5% with and without nickel coating the friction coefficient has a stable character, i.e. it has almost the same values for different loads, but its value is greater for nickel-plated nanoparticle materials. With a nanoparticle content of 1% and 1.5%, the friction coefficient decreases with increasing the normal load. This is probably due to the reduction of plastic deformation and the flow of elastic and elasto-plastic contact deformations as well as the reduction of the adhesive component.The high COF value for nickel-phosphorus-coated nanotubes is due to an increase in the friction deformation component, in particular an increase in tangential contact deformities due to the increased rigidity of the composite material, containing such particles (Fig. 11).

5. CONCLUSION

In the current work a comparative study was carried out of the coefficient of friction without lubrication of new composite materials based on UHMWPE, containing two types of carbon nanotubes - uncoated CNTs and carbon nanotubes having a coating of nickel-phosphorus coating by the electroless method NiCNTs.

The main work results are limited to:

It has been found the influence on the coefficient of friction of three factors: carbon nanotube percentage, loading and presence of Ni-P coating on nanotubes.

The effect of the carbon nanotube percentage with and without nickel-phosphorus coating on the UHMWPE hardness was determined.

The dependence of COF on carbon nanotubes percentage CNTs and NiCNTs is non-linear and unambiguous and depends on the normal load. In nanoparticle composites CNTs at low loads COF increased to 0.75% CNTs and reached values higher than COF of non-nanoparticulate materials UHMWPE-0CNTs. With an increase in the percentage of CNTs (1.0-1.5%) COF decreases smoothly and reaches values less than those of non-nanoparticulate material. At a higher load COF decreases nonlinearly and always has values smaller than those of UHMWPE without nanoparticles.

In the presence of nickel-coated carbon nanotubes (NiCNs), COF has a higher value than COF for non-coated CNTs for all their percentages and all normal load values. With an increase in the nanoparticle content, COF increases reaching a maximum for Ni-CNTs - 1%, then decreases and reaches a higher COF value of non-nanoparticulate materials.

The smallest friction coefficient μ = 0,1 is observed at the highest load P4 = 120 N for nanotubes doped without nickel-phosphor coating: UHMWPE-1.0CNTs and UHMWPE-1.5CNTs, i.e. materials containing 1% and 1.5% carbon nanoparticles.

The highest coefficient of friction - μ = 0.38 is observed in the friction of UHMWPE-1.0NiCNTs, i.e. materials doped with 1% nickel-plated carbon nanoparticles at least P_1 = 60 N.

REFERENCES

[1] M. Kandeva, V. Kamburov, Zadorozhnaya, E., Kalitchin, Zh., Abrasion Wear of Electroless Nickel Composite Coatings Modified with Boron Nitride Nanoparticles, Journal of Environmental Protection and Ecology, Vol. 19, No. 4, pp. 1690-1703, 2018.

[2] P. Martin: Introduction to Surface Engineering and Functionally Engineered Materials. Hoboken: John Wiley & Sons, 2011.

[3] K, Holmberg, A. Matthews: Coatings Tribology: Properties, Mechanisms, Techniques and Applications in Surface Engineering. Amsterdam: Elsevier, 2009.

[4] M. Kandeva, AL. Vencl, D. Karastoyanov: Advanced Tribological Coatings for Heavy-Duty Applications: Case Studies, Academy Publishing House, Sofia, Bulgaria, p. 147, 2016.

[5] A. Vencl, Optimization of The Deposition Parameters of Thick Atmospheric Plasma Spray Coatings. – J Balk Tribol Assoc, Vol. 18, No. 3, p. 405, 2012.

[6] M. Kandeva: The Contact Approach in Engineering Tribology, Technical University of Sofia, ISBN: 978-954-438-986-4, p. 505 2012.

[7] R. Dimitrova, Electroless nickel coatings on silicon carbide particles using two nickel salts in alkaline solution, International Working Conference ’’Total Quality Management – Advanced and Intelligent Approaches’’, 2–5 June, 2015, Belgrade, Serbia.

[8] J.A. Kaleicheva, Z.K. Karaguiozova, Electroless Composite Nickel Coatings rengthening with TiN Nanoparticles Plated on Ductile Cast Iron, Novel Trends in Production Devices and Systems, Materials Science Forum, Vol. 919, pp. 52-58, 2018. doi: 10.4028/www.scientific.net/MSF.919.52

[9] L. Dimitrov, “Principles of Mechanical Engineering Design”, Second Revised and Expanded Edition, University Textbook, ISBN: 978-954-580-257-7, pp. 128-144, 2009.

[10] A.V. Maksimkin, V.D. Danilov, F.S. Senatov, L.K. Olifirov, S.D. Kaloshkin, Wear performance of bulk oriented nanocomposites UHMWPE/FMWCNT and metal-polymer composite sliding bearings, Wear, Vol. 392–393, pp. 167–173, 2017.

[11] B. Chang, H. Akil, R. Nasir, A. Khan, "Optimization on wear performance of UHMWPE composites using response surface methodology", Tribology International, Vol. 88, pp. 252–262, 2015.

[12] I. Chang, J. Chou, "A molecular analysis of carbon nanotori formation", JOURNAL OF APPLIED PHYSICS, Vol. 112, p. 063523, 2012.

[13] M. Kandeva, V. Kamburov, L. Dimitrov, K. Nikolov, Abrasive Wear of Ultra-High-Molecular-Weight Polyethylene (UHMWPE), Modified with Carbon Nanotubes (CNTS)", Journal of the Balkan Tribological Association, 2019.

[14] T. Bakalova, L. Svobodová, K. Borůvková, P. Louda, L. Voleský, "The influence of nanoadditives on the tribological properties of process fluids", Journal of Physics: Conference Series, Vol. 709, Iss. 1, 2016.

[15] S. Banerjee, S. Naha, P. Ishwar, "Molecular simulation of the carbon nanotube growth mode during catalytic synthesis", 2008.

Serbian Tribology Society

SERBIATRIB '19

16th International Conference on Tribology

Faculty of Engineering University of Kragujevac

Kragujevac, Serbia, 15 – 17 May 2019

MORI-TANAKA METHOD IN CHARACTERISATION OF COMPOSITE STRUCTURES

Vukasin SLAVKOVIC[1], Nikola PALIC[1,*], Varun SHARMA[1], Nenad GRUJOVIC[1], Fatima ZIVIC[1]
[1]University of Kragujevac, Faculty of Engineering, Kragujevac, Serbia
vukasinsl@gmail.com, , varun.eu@gmail.com, gruja@kg.ac.rs, zivic@kg.ac.rs
*Corresponding author: nikpa2112@gmail.com

Abstract: *This paper describes the theory of the dependence of the tribological characteristics of the material (coefficient of friction and wear) and the mechanical properties of the material (Poisson's ratio and modulus of elasticity). A special focus is placed on the characteristics of composite materials which are difficult to predict by mechanical and tribological characteristics. Relationship between effective values of friction coefficient and wear and modulus of elasticity is given for composites. Mori-Tanaka homogenization method is applied in calculation of modulus of elasticity and Poisson's ratio, and their dependencies, for composites with spherical particles.*

Keywords: *Mori-Tanaka method, homogenisation, composites, friction coefficient*

1. INTRODUCTION

It is well known that tribological characteristics of materials such as friction coefficient and wear of materials are very important for tribological applications. When it comes to composite materials, the situation undermines the inhomogeneity of the material itself. As we know, composite materials consist of two or more materials. Each of them has separate material characteristics, and effective material characteristics can be determined by different experimental techniques (tensile test, pressure, indentation) [1]. When creating the composites themselves, it is necessary to take into account the material characteristics of the new material. By predicting the material characteristics of the composite, we can further predict the tribological characteristics. Determination of material properties requires the use of knowledge in mathematics, mechanics, and material science [2]. For the purpose of predicting the material characteristics of composites, different methods have been studied, such as Mori-Tanaka method, Hashin-Shtrikman bounds, Lielens method, Self-consistent scheme [3], as well as fem modeling [4].

The characterization of composite materials is a very complex area. Particularly complex is the homogenization of hybrid composites that comprise several materials with different material characteristics. Depending on the nature of the composite materials, there may be materials with a matrix and various types of inclusion, such as spherical particles, fiber particles, as well as multilayer materials and woven fiber composites. Mori-Tanaka method represents fast and efficient homogenisation method and provides reliable material properties. By using this method, it is possible to study composite materials by determining the parameters, such as volume fraction of the matrix and inclusion, shape and size of inclusion, types of layers and features in multilayer composites. It is realised in order to obtain the most favorable characteristics of the material from different aspects. Such methods are particularly important in the prediction of material parameters and mechanical characteristics of new micro composite materials. This paper deals with a relationship between the tribological characteristics of the material (friction coefficient and wear) and the mechanical properties of the material (Poisson's ratio and modulus of elasticity).

2. FRICTION COEFFICIENT AND WEAR OF COMPOSITES

The friction coefficient is related to two components: adhesion (due to the force of molecular interaction of contact surfaces) and deformation component. By increasing the modulus of elasticity, the surface strength of the material increases, and consequently the deformation component of the friction coefficient decreases. By increasing the material's elasticity modulus, the contact surface of the sample and the element with which this material is in contact decreases, and thus reduces the adhesive force of attraction between interactive surfaces. As a result, the friction coefficient will decrease.

The functionally graded material can be in the form or in the form of a mono component material with an elastic gradient, caused, for example, by an uneven distribution of residual tensions. Both types of sorted material are widely used in tribo-compounds.

2.1 The law of mixtures in the calculation of the friction coefficient and wear

In case of fibers as reinforcements, the friction coefficient μ can be given by [5]:

$$\mu = \frac{F}{W} = \frac{F_f + F_m}{W_f + W_m} \quad (1)$$

where W is normal load, F is tangential force, suffixes f and m denote fiber and matrix, respectively. The following equations are hypothesized:

$$A_f = V_f A \quad (2)$$

$$A_m = V_m A = 1 - V_f A \quad (3)$$

where A is the nominal area of contact, V_f and V_m are the volume fractions of the fibers and matrix, respectively. Under certain conditions, (e.g. in absence of fibers peel-off), shear strain γA_f is equal to γA_m:

$$\gamma A_f = \gamma A_m \quad (4)$$

If GA_f and GA_m, the moduli of rigidity of materials underneath the contacting surface, are equal, then the shear stress τ becomes constant, that is:

$$\tau_f = \frac{F_f}{A_f} = \tau_m = \frac{F_f}{A_f} \quad (5)$$

where:

$$F_f = V_f F \quad (6)$$

$$F_m = V_m F \quad (7)$$

By using the relationship $W = W_f + W_m$, the following equations can be obtained:

$$\frac{F}{\mu} = \frac{F_f}{\mu_f} + \frac{F_m}{\mu_m} \quad (8)$$

$$\frac{1}{\mu} = V_f \frac{1}{\mu_f} + V_m \frac{1}{\mu_m} \quad (9)$$

From this equation we are able to calculate the effective friction coefficient μ of composite material strengthened by the fibers when the friction coefficients of the fibers μ_f, and of the matrix, μ_m, are given.

When the composite material strengthened by the fibers is hybrid-reinforced with two fibers f_1 and f_2, the law of mixtures in the calculation of the friction coefficient is given by [5]:

$$\frac{1}{\mu} = V_{f1} \frac{1}{\mu_{f1}} + V_{f2} \frac{1}{\mu_{f2}} + V_m \frac{1}{\mu_m} \quad (10)$$

$$V_{f1} + V_{f2} + V_m = 1 \quad (11)$$

The wear volume (W) is proportional to the contact area (A) and the sliding distance (S), as in:

$$W = A*S*C \tag{12}$$

where C is a non-dimensional wear coefficient defined as a function of CS and a non-dimensional contact stress ($\frac{P}{E}$), where E is the elastic modulus of the material:

$$C = fun(CS, \frac{P}{E}) \tag{13}$$

Cross shear ratio (CS) was defined as the frictional work component perpendicular to the principal molecular orientation direction ($E_{cross-shear}$), divided by the total frictional work (E_{total}) [6]:

$$CS = \frac{E_{cross-shear}}{E_{total}} \tag{14}$$

3. FINITE ELEMENT METHOD IN CHARACTERISATION OF MECHANICAL PROPERTIES FOR COMPOSITE MATERIALS

The finite element method (FEM) can efficiently support simulation of experimental testing of composite structures. When simulating the compressive test by using the finite element method, one can clearly conclude that the friction that occurs between the surface of the sample and the compression plate has a slight influence on the deformation in the direction of the compression plate operation. From this, it can be concluded that the experimentally determined modulus of elasticity is valid.

Unlike the previous, the friction affects the lateral deformation of the sample on the contact surface. The greater the friction coefficient, the smaller Poisson coefficient. In order for the test results to be relevant, the contact surfaces should be polished or lubricated [7].

3.1 Determination of the material properties of composite (Mori-Tanaka method)

Micro-mechanics of materials is the analysis of composite or heterogeneous materials at the level of the individual constituents, commonly used for nano and biomedical materials. As a multidisciplinary area, it covers mechanical, electrical, and in general thermodynamic behavior. Composites comprise different phases throughout the structure, and these can be of completely different mechanical and physical properties. Microstructural properties of such materials can be modeled with isotropic behavior, but in reality they exhibit anisotropy due to different relevant properties within one structure. Anisotropic material models are available for linear elasticity. In the nonlinear regime, the modeling is often restricted to orthotropic material models, which do not capture the physics for all heterogeneous materials. Micro-mechanics goal is to predict the anisotropic response of the heterogeneous material based on the geometries and properties of the individual phases, aiming at homogenization. Micro-mechanical analysis is the discipline that requires the theoretical framework and the related tools. There are two different approaches or methods in micro-mechanics: analytical and numerical approaches. Analytical methods of continuum micro-mechanics are Voigt method, Reuss method, Strength of Materials (SOM), Vanishing Fiber Diameter (VFD), Composite Cylinder Assemblage (CCA), Hashin-Shtrikman Bounds, Self-Consistent Scheme and Mori-Tanaka method. Numerical approaches to continuum micro-mechanics are Finite Element Analysis (FEA), Mechanics of Structure Genome (MSG), Generalized Method of Cells (GMC), and Fast Fourier Transforms (FFT) [8], [9].

For homogenization of the composite and determination of effective mechanical characteristics by the Mori-Tanaka method, it is necessary to set the input parameters that characterize the matrix and inclusion. These are Poisson's' ratio, modulus of elasticity and volume fraction for each individual. The obtained effective characteristics of the material can be validated by using standard mechanical tests, like tensile test (Fig. 1), pressure test, indentation test, etc.

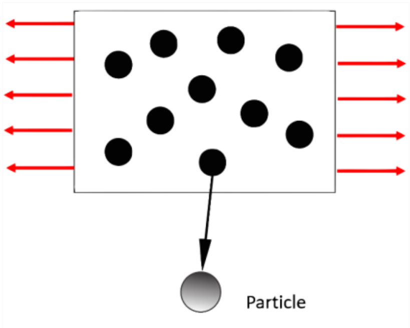

Figure 1. Composite structure – Matrix with spherical inclusion loaded with tension

Based on Eshelby solution fundamental results in ellipsoidal inclusion, the total strain induced by the appearance of Eigenstrain is uniform. The uniform strain field inside inclusion can be expressed as a function of the Eigenstrain per:

$$\varepsilon = S\varepsilon^{*} \tag{15}$$

Where S is fourth order Eshelby tensor. Eshelby tensor depends on the material properties and the shape of the inclusion (cylindrical or spherical). Analytical expressions can be found for isotropic linear materials for some specific shapes. Fourth order Eshelby tensor is given by:

$$S \quad \begin{matrix} S_{1111} & S_{1122} & S_{1133} & 0 & 0 & 0 \\ S_{2211} & S_{2222} & S_{2233} & 0 & 0 & 0 \\ S_{3311} & S_{3322} & S_{3333} & 0 & 0 & 0 \\ 0 & 0 & 0 & 2S_{1212} & 0 & 0 \\ 0 & 0 & 0 & 0 & 2S_{1313} & 0 \\ 0 & 0 & 0 & 0 & 0 & 2S_{2323} \end{matrix} \tag{16}$$

The effective modulus requires the definition of the strain concentration tensor **A**. In order to calculate the effective modulus the Mori-Tanaka approximation has been chosen. The expression of the strain concentration tensors are identified as:

$$\boldsymbol{A}_r = \boldsymbol{T}_r\left(\sum_{r=0}^{N} c_r \boldsymbol{T}_r\right)^{-1} \tag{17}$$

$$\boldsymbol{A}_0 = \frac{1}{c_0}\left(\boldsymbol{I} - \sum_{r=1}^{N} c_r \boldsymbol{T}_r\right)^{-1} \tag{18}$$

The effective stiffness tensor is obtained from the expression of the concentration tensors as:

$$\boldsymbol{L} = \sum_{r=0}^{N} c_r \boldsymbol{L}_r \boldsymbol{A}_r \tag{19}$$

Taking an isotropic stiffness tensor it is possible to obtain effective values respectively:

$$\lambda_{ef} = L_{12} \tag{20}$$

$$\mu_{ef} = \frac{1}{2}(L_{11} - L_{12}) \tag{21}$$

$$E_{ef} = \frac{\mu_{ef}(3\lambda_{ef} + 2\mu_{ef})}{\lambda_{ef} + \mu_{ef}} \tag{22}$$

$$\nu_{ef} = \frac{\lambda_{ef}}{2(\lambda_{ef} + \mu_{ef})} \tag{23}$$

$$\kappa_{ef} = \frac{3\lambda_{ef} + 2\mu_{ef}}{3} \tag{24}$$

The aim of this study was to obtain effective properties of the fiber composite as a function of Young's modulus varying from 7 to 110 GPa using simplified Mori-Tanaka method, whereas the structure is shown in Fig. 1. We applied simplified Mori-Tanaka method to obtain analytical dependences between Young modulus of elasticity, shear modulus and Poisson's ratio and relationship to matrix and inclusion properties, and results are given in Figs 2-5.

Table 1. Material properties of composite material

Material constants	E (GPa)	ν (-)	c (-)
Matrix	207e9	0.3	0.34
Inclusion	from 7e9 to 110e9	0.26	$1 - c_m$

Numerical calculations were realised for composites with spherical and cylindrical particles and fibers. Obtained results are homogenized values, or effective values, of Young modulus and Poisson's coefficient for composite structure.

It can be seen that there is significant difference between values of Young modulus and Poisson's ration for matrix material, reinforcement material and the composite structure, indicating that effective values must be included in characterisation of composites. These results can be further used to predict the tribological characteristics of the composite material because the coefficient of friction and wear depends directly on material parameters such provided by Mori-Tanaka method and numerical solving of the homogenization problem of composite materials.

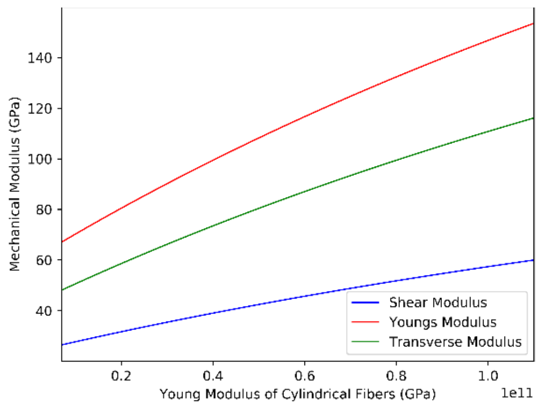

Figure 2. Effective mechanical modulus of composite (Young modulus, shear modulus and transverse modulus) as the function of Young modulus of cylindrical fibers as reinforcements

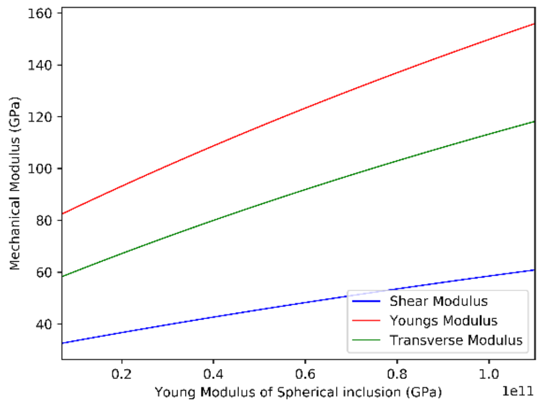

Figure 3. Effective mechanical modulus of composite (Young modulus, shear modulus and transverse modulus) as the function of Young modulus of spherical particles as reinforcements

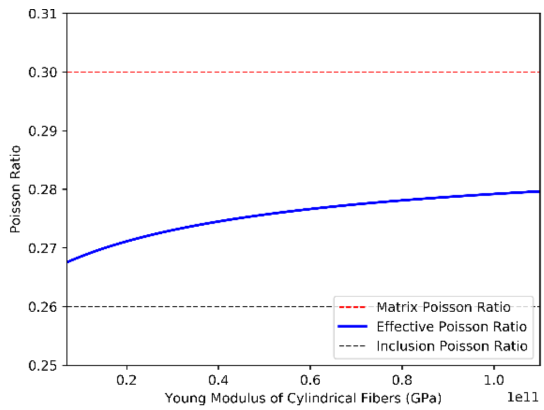

Figure 4. Poisson's ratio as the function of Young modulus of cylindrical fibers as reinforcements

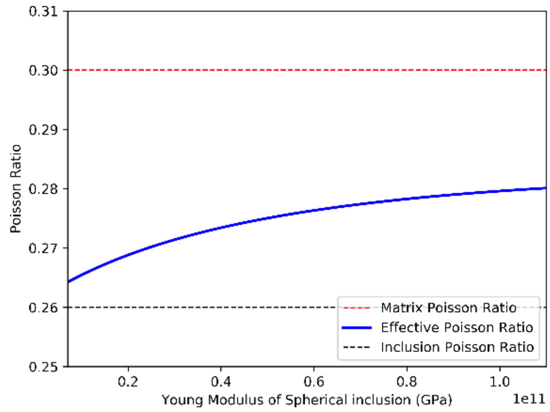

Figure 5. Poisson's ratio as the function of Young modulus of spherical particles as reinforcements

4. CONCLUSION

Material parameters such as the Young modulus of elasticity and the Poisson's ratio have a direct relationship with tribological properties. In order to predict the behaviour of coefficient of friction and wear of composite material, it is necessary to determine effective material characteristics. Mori – Tanaka method, together with finite element analysis, is efficient approach that can provide necessary properties, such as Young modulus of elasticity over range of loading. These effective values can be further used in characterisation of tribological behaviour of composites.

ACKNOWLEDGEMENT

This work was funded by the SELECTA (No. 642642) H2020-MSCA-ITN-2014 project.

REFERENCES

[1] G. Guillonneau, G. Kermouche, S. Bec, J. L. Loubet: Determination of mechanical properties by nanoindentation independently of indentation depth measurement, Journal of Materials Research, Cambridge University Press (CUP), pp. 2551-2560, 2012.

[2] S. Kurukuri: A Review of Homogenization Techniques for Heterogeneous Materials, Advanced Mechanics of Materials and Structures Graduate School in Structural Engineering Bauhaus Universität, Weimar, Germany, Term Paper, March 2004.

[3] B. Klusemann, B. Svendsen: Homogenization methods for multi-phase elastic composites: Comparisons and benchmarks, Technische mechanik, pp. 374 – 386, 2010.
[4] B. Duleba, L. Dulebová, E. Spišák: Simulation and evaluation of carbon/epoxy composite systems using FEM and tensile test, Modelling of Mechanical and Mechatronic Systems MMaMS 2014, Procedia Engineering, Vol. 96, pp. 70 – 74, 2014.
[5] T. Tsukizoe, N. Ohmae: Friction and Wear of Advanced Composite Materials, Fibre Science and Technology, Vol. 18, pp. 265-286, 1983.
[6] A. Abdelgaied, J. Fisher, L. M. Jennings: A Comprehensive Combined Experimental and Computational Framework for Pre-clinical Wear Simulation of Total Knee Replacements, Journal of the Mechanical Behavior of Biomedical Materials, 2017.
[7] O. Orella, J. Vuorinena, J. Jokinena, H. Kettunenb, P. Hytönenb, J. Turunenb, M. Kanervaa: Characterization of elastic constants of anisotropic composites in compression using digital image correlation, Composite Structures, Vol. 185, pp 176–185, 2018.
[8] V.P. Tran, S. Brisard, J. Guilleminot, K. Sab: Mori-Tanaka estimates of the effective elastic properties of stress-gradient composites, International Journal of Solids and Structures, 2018.
[9] L. Liu, Z. Huang: Anoteon Mori -Tanaka's method, Acta Mechanica Solida Sinica, Vol. 27, No. 3, June, 2014.

Serbian Tribology Society

SERBIATRIB '19

16th International Conference on Tribology

Faculty of Engineering University of Kragujevac

Kragujevac, Serbia, 15 – 17 May 2019

ANALYSIS ON THE CORROSION RATE CHANGES OF AISI 410 STAINLESS STEEL SUBMITTED TO ABRASION-CORROSION IN SIMULATED MARINE CONDITIONS

Gerardo A. RODRÍGUEZ-BRAVO[1], Manuel VITE-TORRES[1,*], Jesús G. GODÍNEZ SALCEDO[2]
[1]Instituto Politécnico Nacional SEPI ESIME Zacatenco, Ciudad de México, México
[2] Instituto Politécnico Nacional SEPI ESIQIE Zacatenco, Ciudad de México, México
*Corresponding author: drmanuelvite9@hotmail.com

Abstract: Due to its diversity of applications in mechanical components such as; turbines, valves and pumps, AISI 410 stainless steel is exposed to combined conditions of mechanical and electrochemical wear. Basic studies on the wear resistance of this martensitic stainless steel have already been carried out, but it still necessary to delve into the tribocorrosion perspective, analyzing the effect of the combined wear forms since it is still been a phenomenon not completely understood. This work presents an analysis on the changes in the electrochemical response of AISI 410 stainless steel in marine abrasion-corrosion conditions, using a novel test rig based on ASTM G105-16 wet abrasion apparatus configuration, with an adapted electrochemical cell. The material was submitted to polarization resistance (Rp), and anodic potentidynamic polarization tests, in both conditions; pure corrosion and abrasion-corrosion. Substitute ocean water (aqueous media), and silica sand (abrasive particles) were used to recreate the agressive marine environment.
Potentiodynamic polarization test results do not show a passivation zone of the material when it is submerged in the media. The material does not present a good corrosion resistance under pure corrosion condition contrary to abrasion-corrosion. In addition SEM images analysis sample surface was carried out for each test. Micrograph shows the dominant wear mechanisms are produced by mechanical work.

Keywords: *Tribocorrosion, martensitic, stainless, steel, abrasion-corrosion, AISI 410.*

1. INTRODUCTION

Martensitic stainless steels are essentially Fe-Cr-C metallic alloys. These kinds of alloys are used in mechanical components that require a good mechanical performance and also a moderate corrosion resistance [1]. Stainless steel AISI 410 is the martensitic steel with greater availability in the market and the easiest to obtain, also has a low cost compared with other stainless steels. This alloy is commonly used in applicatios such as pump axis and valvs parts for the hydrocarbon extraction industry, aircraft engines parts, gas turbines, chemical plants, energy generetion equipment, and some components for the marine industry [2]. Due to its diverse uses and applications it is easy to find AISI 410 stainless steel exposed to tribocorrosion.

Tribocorrosion is defined as the transformation process of a material due to electrochemical degradation (corrosion) and mechanical wear simultaneously happening in contacting surfaces with relative motion between them. Rarely the tribocorrosion effect is just the sum of mechanical wear plus corrosive wear, but generally it is higher (synergistic interaction) or lower (antagonistic interaction) [3]. Two main forms of tribocorrosion can be found in literature: erosion-corrosion and abrasion-corrosion, and can be generated by various mechanisms like sliding, fretting, rolling, or impingement. Every one of these mechanisms can have its own variations [4].

To evaluate corrosion rate when a metallic material is probed in tribocorrosion conditions, generally electrochemical techniques are applied (i.e. Open circuit potential, TAFEL plot, polarization resistance, and anodic potentiodynamic polarization) in combination with standard tribological tests [5].

Martensitic steels, including AISI 410, have been probe in different conditions, for example: Pure corrosion [1], [2], erosion [6], and also in some tribocorrosion conditions like erosion-corrosion [7]. In previous works abrasion-corrosion has been evaluated in martensitic stainless steels using the pin on disk and the ball on disk tribometer configuration (two body unidirectional sliding to generate mechanical wear in a corrosive media) combined with the electrochemical techniques to evaluate accelerated corrosion [8], [9]. But even though the AISI 410 martensitic stainless steel has application in components used in marine environments, there are not enough information available about its performance when is submitted to tribocorrosion conditions similar to marine ones.

This work focus on the analysis on the corrosion rate changes of stainless steel AISI 410 when it is exposed to abrasion-corrosion (three-body unidirectional sliding) compared with pure corrosion in a simulated marine environment, in order to evaluate the material performance, and using a novel tribocorrosion test rig developed by the IPN ESIME Zacatenco tribology group to simulate the mentioned work conditions.

2. TEST RIG AND MATERIALS

Elements used during experimentation to reproduce work conditions in marine environment were: a potentiostat, an abrasion-corrosion test rig, substitute ocean water as corrosive media, silica sand particles as abrasive agent, and as work material: samples of commercial AISI 410 stainless steel.

In the following subjects, the most important aspects of each element are detailed.

2.1 Experimental arrengment and abrasion-corrosion tribotester details

Experimental arrengment used in this work consist in a test rig design, with some characteristics based in the machine configuration called “wet sand/rubber wheel“ that is used to perform wet abrasion tests [10], but adapted to a work cell that allows to perform electrochemical tests to evaluate corrosion rate using a potentiostat-galvanostat (Fig. 1).

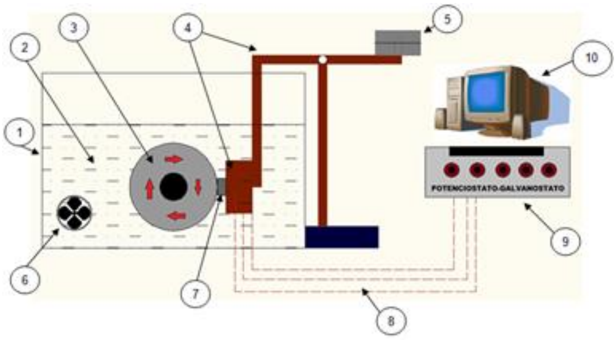

Figure 1. Test rig components and configuration: 1. Electrochemical cel; 2. Abrasive-corrosive aqueous media; 3. Counter body; 4. Sample holder and load applier; 5. Weight; 6. Media mixer; 7. Metallic sample; 8. Electrode cables; 9. Potentiostat-galvanostat; 10. Data processing software.

Similar machine configurations, where a sample (work body) is presented against a sliding counter body in the presence of an abrasive agent between (third body), have been used in previous works [11][12].

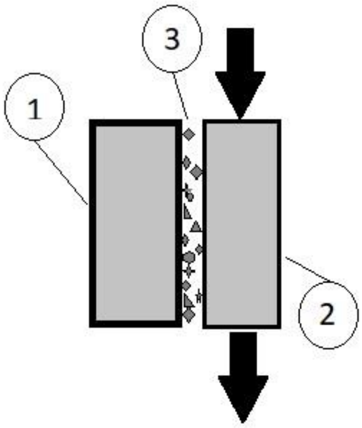

Figure 2. Schematic representation of contact configuration: 1. Work body; 2. Rubber wheel (softer unidirectional sliding body); 3. Silica sand particles suspended in synthetic seawater (abrasive slurry).

For the present work the counter body is a rubber wheel that has a softer surface than the metallic sample so the contact does not produce any damage in the work body; the only function of the counter body is to apply a load and move the silica sand particles in one direction to evaluate their effect in the corrosion rate (Fig. 2).

2.2 Metallic samples

Samples where obtainden from a round bar of comercial AISI 410 stainless steel with a 210 HV vickers hardness. The material was analyzed by electron difraction spectrometry (EDS) to determine if chemical composition corresponds to the proposed steel (Table 1).

Table 1. Chemical composition of AISI 410 stainless steel according to data sheet [13].

Element	Maximun Concentration (%)
C	0.08 – 0.15
Mn	1.0
S	.030
P	.040
Si	1.0
Cr	11.5 – 13.5
Ni	0.75
C	0.08 – 0.15

Results of EDS analysis indicate that the obtained material corresponds to AISI 410 martensitic stainless steel as shown in Fig. 3 and Table 2.

Table 2. Element concentration according to EDS analysis of samples.

Element Line	*Weight %*	*Atom %*
Si K	0.49	0.96
S K	0.03	0.12
Cr K	12.10	12.81
Mn K	0.39	0.39
Fe K	86.95	85.71
Total	100.00	100.00

Geometry of the metallic sample (working electrode) was determinated with the aim of obtain a 1 cm^2 work surface, to have a better control of parameters during electrochemical measurements. Instead of the commonly used Sturated Calomel (KCl), and graffite electrodes; two metallic rings made of the same working material (AISI 410 stainless steel) were asigned as reference electrode and counter electrode [14].

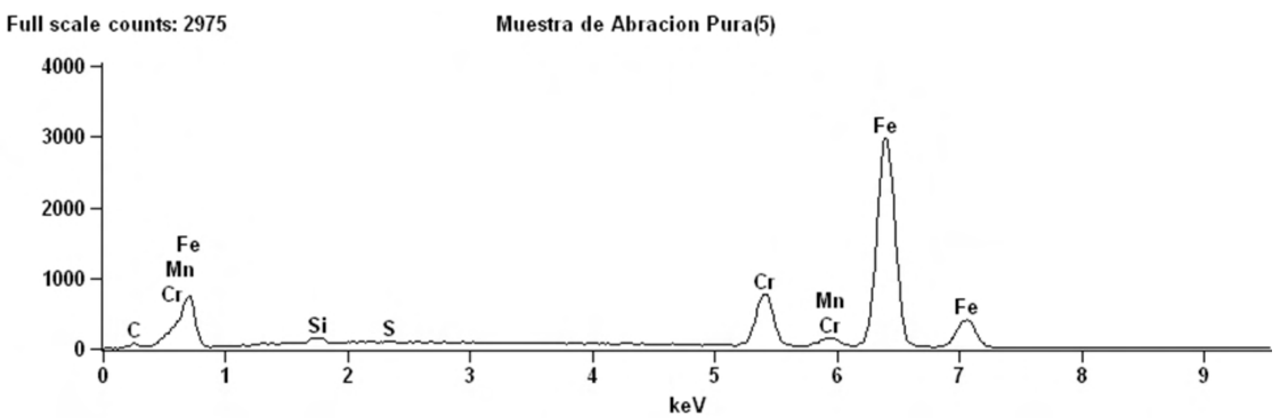

Figure 3. Spectre obtained from EDS analysis of AISI 410 stainless steel.

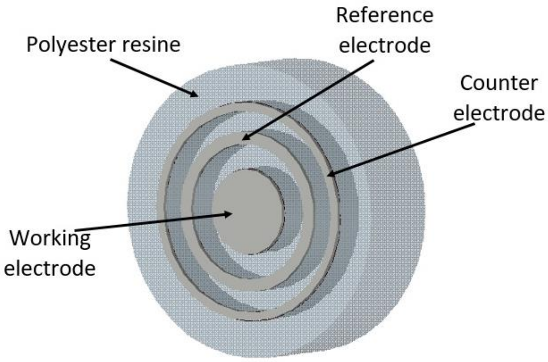

Figure 4. Schematic representation of sample and electrodes mounted on polyester resine.

Electrodes were mounted in polyester resine as shown in Fig. 4 in order to let the test rig counter body to mantain sliding contact with the working electrode, without affect the reference and counter electrodes [15].

2.3 Abrasive particles

Silica sand (SiO_2) was used to represent seaground abrasive particles. Characterization of sand particles was made using scanning electron microscopy (SEM) to determine morphology, laser annalysis to calculate average size, and nano identation to calculate hardness. Results of particle characterization showns a sharp edges particles, with average size of 176 µm, and hardeness of 789.5 Vickers.

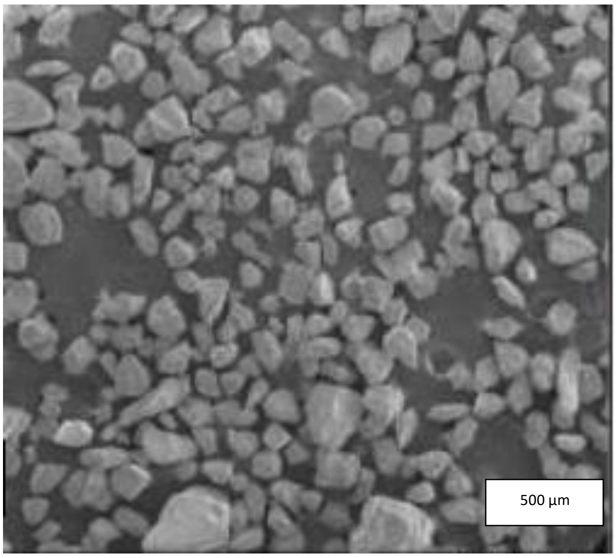

Figure 5. SEM image of SiO_2 particles.

2.4 Corrosive aqueous media

Substitute ocean water was used as corrosive media to simulate marine conditions. It is a solution with content of inorganic salts in representative proportions and concentrations of seawater. Its preparation is normalized by ASTM International [16]. Table 3 shows concentration of chemical compounds used to prepare substitute ocean water. Aqueous media was stabilized in an 8.2 pH.

Table 3. Chemical compounds in substitute ocean water according to norm ASTM D1141-98(2013).

Compound	Concentration (gr/l)
NaCl	24.53
$MgCl_2$	5.20
Na_2SO_4	4.09
$CaCl_2$	1.16
KCl	0.695
$NaHCO_3$	0.201
KBr	0.101
H_3BO_3	0.027
$SrCl_2$	0.025
NaF	0.003

3. Methodology

Two samples of AISI 410 were tested with three electrochemical techniques to evaluate corrosion. Techniques used in this experimental procedure were: Open circuit measurement to determine corrosion potential (E_{Corr}), Polarization resistance (Rp) to calculate corrosion rate, and potentiodynamic anodic polarization to analyse and compare the characteristic sample polarization plot generated. Each technique was performed in two conditions: Pure corrosion, and abrasion-corrosion. Both conditions were recreated in 1 L of substitute ocean water. Parameters controlled to recreate each work conditions were: Abrasive particle concentration (Apc, gr), Counter body load (load, N), and sliding velocity (Sv, m/min). Table 4 shows parameter values established for each test.

Table 4. Test parameters

Sample ID	Performed Test	Tests condition	Parameters value	
AISI410-1	Ocm	Pure corrosion	No abrasive particles or sliding contact.	
	Rp			
	Pap			
AISI410-2	Ocm	Abrasion-corrosion	150 gr	Apc
	Rp		2.5 N	Load
	Pap		30 m/min	Sv

Polarization resistance technique serves to measure corrosion rates and generally is expressed in mill-inches per year (mpy). This technique consist in perform a scanning trough a potential range very close to the (E_{Corr}). The potential range used for the experiment was ±20 mV. Resulting current is plotted versus potential, and then is related to the corrosion rate as can be seen in Equation 1:

$$(\text{mpy}) = \frac{0.13\ \text{Icorr}\ (\text{E.W.})}{d} \qquad (1)$$

were "I_{corr}" is the measured corrosion current density (μA/cm^2), "E.W." is the equivalent weight of the corroding specie, and "d" is the density of the material (gr/cm^2).

Potentiodynamic anodic polarization tests also consist in a potential scanning were the potential is plotted against the current density but with a wider range of voltage. This tests generate a polarization plot that can yield information such as: ability of the material to passivate, potential region in which the material remains passive, identify potential regions of the material and calculate corrosion rate in a certain one [17]. For this work the potential sweep was -200 mV to +1600 mV from the E_{Corr}.

After the tests both samples were analysed using SEM to determine prevalent wear mechanisms.

4. RESULTS AND DISCUSSION

Comparison of open circuit measurements, as can be observed in Fig. 6, shows how in abrasion-corrosion condition, with the presence of the abrasive slurry generated by the substitute ocean water mixed with SiO_2 particles, the open circuit potential gets a value between -0.359 and -0.059 mV showing instability in its behaviour, while in the pure corrosion condition values are stables between -0.357 and -0.441 mV. This is an indicator of reactivity decrease in the sample-media interface due to the presence of abrasive slurry in the sample surface.

The Rp tests results confirm a decrease on the corrosion rate in a 87 % taken it into 1.4 mpy (miles per year). Decreasing of corrosion rate value confirm the difficult to made the electron exchange between electrodes when the mechanical wear is occurring. The corrosion rate is an average of four "Rp" technique repetitions in each sample and it can be observed in Fig. 7.

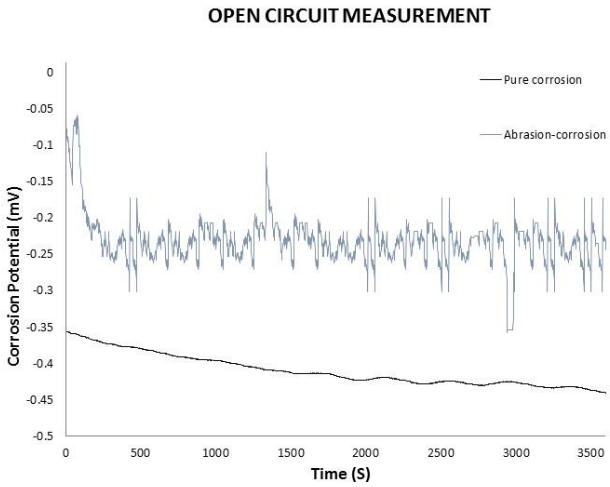

Figure 6. Open circuit plots of AISI 410 stainless steel in both conditions.

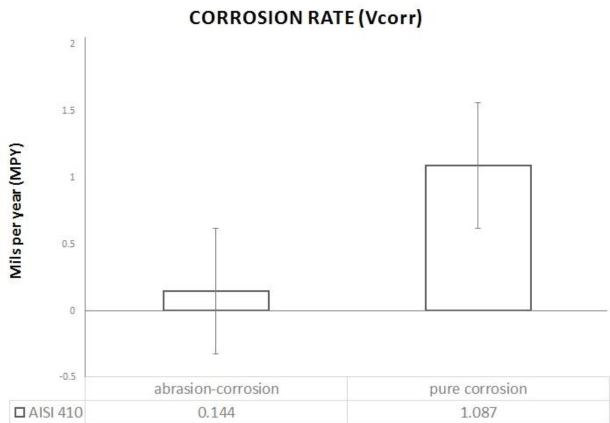

Figure 7. Corrosion rate comparison between work conditions.

Potentiodynamic anodic polarization plots, showed in Fig. 8, are graphic representations of material electrochemical response in media. In pure corrosion condition, it cannot be seen a well-marked passivation zone. This is an indicator of a low corrosion resistance in seawater. By the other hand an unstable behavior can be observed in the abrasion-corrosion condition. This can be attributed to the interference produced by the abrasive slurry present between electrodes. Decrease in the corrosion rate in this condition can be confirmed by the low current density observed in the plot.

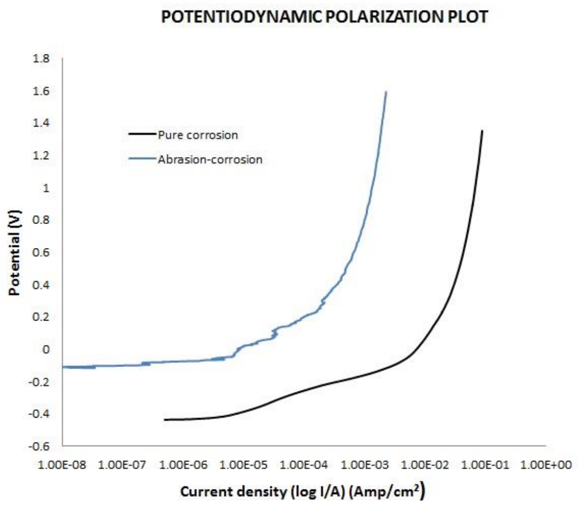

Figure 8. Anodic potentiodynamic polarization plot comparison between work conditions.

Wear mechanisms occurring during potentiodynamic anodic polarization (in both work conditions) can be observed in the next images. Figure 9 shows zones were, the increase of electric potential (1.2 Volts over the open circuit potential), caused a detachment of material from the sample surface. In a close up of one of the pitting holes, produced by detach of material, signs of intergranular corrosion can be seen. This can be caused by sensitization of the oxide layer in grain boundaries, phenomenon that have been correlated with pitting corrosion of martensitic stainless steels in previous studies [18].

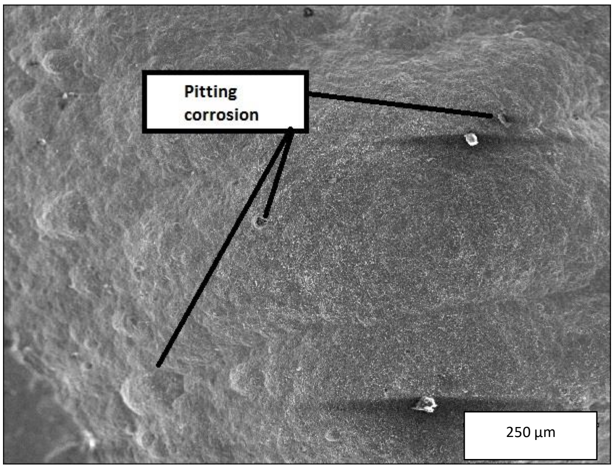

Figure 9. SEM View of wear scars generated in pure corrosion condition.

The last micrograph, showed in Fig. 11, presents the mechanisms found in abrasion-corrosion tests. As can be observed the pitting corrosion traces are no longer visible; instead, only scars produced by the mechanical action of abrasive particles can be appreciated. This is an evidence of the corrosion rate decrease measured with the polarization resistance tests.

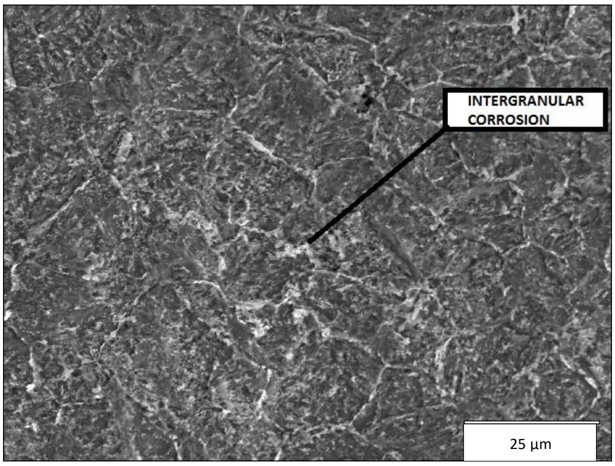

Figure 10. SEM view of intergranular corrosion mechanism, occurring during pure corrosion test.

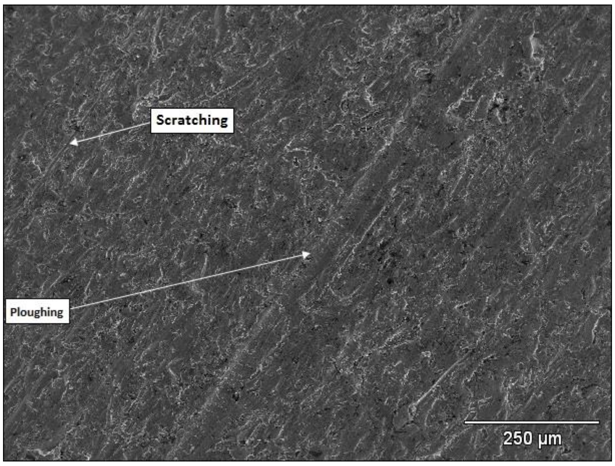

Figure 11. SEM view of wear scars generated in abrasion-corrosion condition.

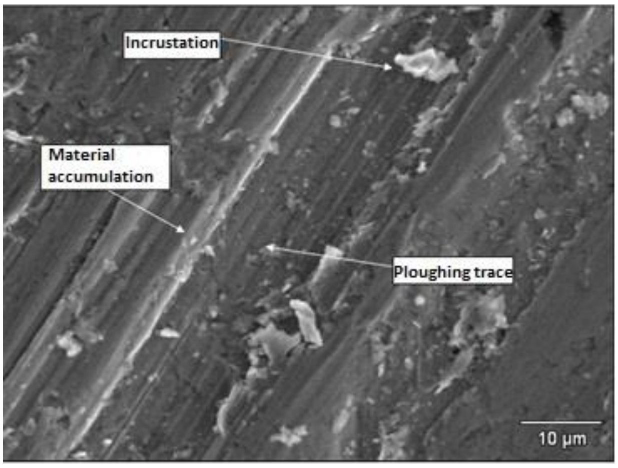

Figure 12. Close up of ploughing trace.

Ploughing and scratching are the main forms of wear presents in the sample surface, generating material accumulation in the edges of the scars. Also some incrustations of abrasive particles were found as can be seen in Fig. 12.

5. CONCLUSIONS

Results indicate that:

AISI 410 steel does not have good resistance to corrosion in an aggressive environment such as seawater, so its use is not recommended under these conditions.

Steel did not present a passivation zone in the analyzed graphs, but media mixed with abrasive particles inhibited the effect of corrosion; this is a antagonistic effect of the abrasion-corrosion phenomenon.

When AISI 410 stainless steel is subjected to the phenomenon of 'wet abrasion-corrosion', using synthetic seawater as a medium and SiO2 as an abrasive particle, mechanical wear predominates over corrosion.

It becomes a priority to implement chemical tests for the identification of corrosion products and also determinate the mechanisms that are causing the reduction in corrosion rate.

ACKNOWLEDGEMENT

Thanks to the tribology research group from IPN SEPI ESIME Zacatenco and to the corrosion laboratory team of the IPN ESIQIE Zacatenco for all the equipment and materials used during the develop of this work, also IPN-COFAA for the economic support for the presentation of this work in the international conference on tribology Serbiatrib ’19 at the University of Kragujevac, Serbia.

REFERENCES

[1] H.C. Paul D. Krell, Shengxi Li, “Synergistic effect of temperature and HCl concentration on the degradation of AISI 410 stainless steel,” *Corros. Sci.*, vol. 122, pp. 41–52, 2017.

[2] R.T. Loto, “Study of the corrosion behaviour of S32101 duplex and 410 martensitic stainless steel for application in oil refinery distillation systems,” *J. Mater. Res. Technol.*, vol. 6, no. 3, pp. 203–212, 2017.

[3] D. Landolt, S. Mischler, *Tribocorrosion of passive metals and coatings*. Sawston, Cambridge, UK.: Woodhead Publishing, 2011.

[4] A.I. Muoz, N. Espallargas, “Tribocorrosion mechanisms in sliding contacts,” in *Tribocorrosion of Passive Metals and Coatings*, 2011, pp. 118–152.

[5] D. Landolt, S. Mischler, M. Stemp, “Electrochemical methods in tribocorrosion: A critical appraisal,” *Electrochim. Acta*, vol. 46, no. 24–25, pp. 3913–3929, 2001.

[6] L.A. Espitia, L. Varela, C.E. Pinedo, A.P. Tschiptschin, “Cavitation erosion resistance of low temperature plasma nitrided martensitic stainless steel,” *Wear*, vol. 301, no. 1–2, pp. 449–456, 2013.

[7] D. López, A.P. Tschiptschin, N.A. Falleiros, “Sinergismo Erosión-Corrosión En Un Acero Inoxidable Martensítico Aisi 410: Erosion-Corrosion Synergism of an Aisi 410 Martensitic Stainless Steel,” *Dyna*, vol. 76, no. 159, pp. 53–60, 2009.

[8] A. Dalmau, W. Rmili, C. Richard, A. Igual–Muñoz, “Tribocorrosion behavior of new martensitic stainless steels in sodium chloride solution,” *Wear*, vol. 368–369, pp. 146–155, 2016.

[9] A. Dalmau, C. Richard, A. Igual – Muñoz, “Degradation mechanisms in martensitic stainless steels: Wear, corrosion and tribocorrosion appraisal,” *Tribol. Int.*, vol. 121, no. December 2017, pp. 167–179, 2018.

[10] ASTM G105-16, “Standard Test Method for Conducting Wet Sand/Rubber Wheel Abrasion Tests,” West Conshohocken,PA., 2016.

[11] M.B. Santos, W.S. Labiapari, M.A.N. Ardila, W. M. Da Silva, J.D.B. De Mello, “Abrasion-corrosion: New insights from force measurements,” *Wear*, vol. 332–333, pp. 1206–1214, 2015.

[12] G.B. Stachowiak, M. Salasi, W.D.A. Rickard, and G. W. Stachowiak, “The effects of particle angularity on low-stress three-body abrasion-corrosion of 316L stainless steel,” *Corros. Sci.*, vol. 111, pp. 690–702, 2016.

[13] “Specification Sheet: Alloy 410.” [Online]. Available: https://www.sandmeyersteel.com/images/410-Spec-Sheet.pdf.

[14] Princeton Applied Research Center, “Electrochemistry and Corrosion: Overview and Techniques,” TN, USA., 2017.

[15] C. Sedano-de la Rosa, M. Vite-Torres, J.G. Godínez-Salcedo, E.A. Gallardo-Hernández, R. Cuamatzi-Melendez, L.I. Farfán-Cabrera, “Erosion-corrosion of X-52 steel pipe under turbulent swirling impinging jets,” *Wear*, vol. 376–377, pp. 549–556, 2017.

[16] ASTM D1141-98(2013), "Standard Practice for the Preparation of Substitute Ocean Water," West Conshohocken, PA., 2013.
[17] B.N. Popov, "Basics of Corrosion Measurements," *Corros. Eng.*, no. 865, pp. 181–237, 2015.
[18] I. Taji, M.H. Moayed, M. Mirjalili, "Correlation between sensitisation and pitting corrosion of AISI 403 martensitic stainless steel," *Corros. Sci.*, vol. 92, pp. 301–308, 2015.

Serbian Tribology Society

SERBIATRIB '19

16th International Conference on Tribology

Faculty of Engineering University of Kragujevac

Kragujevac, Serbia, 15 – 17 May 2019

SURFACE ROUGHNESS QUALITY, FRICTION AND WEAR OF PARTS OBTAINED ON 3D PRINTER

Bogdan NEDIĆ[1*], Lazar SLAVKOVIĆ[1], Stefan ĐURIĆ[1], Dragan ADAMOVIĆ[1], Slobodan MITROVIĆ[1]

[1]Faculty of engineering University of Kragujevac, Serbia

*nedic@kg.ac.rs

Abstract: *The achievement of the required roughness of the surface (today known as surface texture) is of great importance in obtaining the required characteristics of the parts from the aspect of reduction of friction and wear. The most common methods for obtaining the required roughness, or surface textrure, are laser treatment and micro-processing by milling. 3D printingis increasingly being used to produce parts of wide range of applications. In order to obtain the neccessary surface texture, the use of 3D printing technology compared to traditional technologies is faster, more flexible and cheaper. So far, a small number of studies have been related to the surface characteristics of parts produced by 3D printing.Therefore, all the researches in this field in order to improve the friction and wear characteristics have significant role.This work provides an insight into the research of tribological characteristics of surface of samples made from polymers which are most commonly used materials in 3D printing technologies. The surface roughness, friction and wear are measured using tribometer and experimental method „Block-on-Disk". The results shows significant differences in measured values in the tested materials, which demand further researches in order to.*

Keywords: *3D printing tribology, friction, wear, surface roughness quality*

1. INTRODUCTION

Roughness determines the performance of the part because it plays a significant role in determining how the parts interact with the environment. In terms of the surfaces of the engineering materials, roughness is thought to be detrimental to the performance of the part. In tribology, rough surfaces commonly have higher friction coefficients than smooth surfaces and wear faster. For this reason, the surface structure is closely related to the friction and wear properties of the surface [1].

Kovan et al. pointed out that the strength of the adhesive bond connection between the 3D printed parts is affected by the surface roughness. It has been determined that layer thickness and printing orientation in 3D printed parts have significant effects on adhesion strength. In the case of low layer thicknesses, the layer produced on the side edge has the highest adhesive strength, whereas in the high layer thickness, the horizontal layer has the highest adhesive strength [3].

Three-dimensional printing is a production method that uses only digital technology to produce pieces, as opposed to machining methods such as turning, milling, drilling, etc., in which the material is cut out. Although the focus of 3D printing technologies has been developed primarily for prototype purposes, it has become possible to fabricate metallic structures and a much wider variety of functional parts, with increased emphasis on mechanical properties [2, 3].

Fused Deposition Modelling (FDM) is the most widely used technology in this production method which is also called additive manufacturing. FDM has many advantages, such as the use of cheap materials, the lack of expensive equipment, and the ability to create complex geometry. However, FDM has limitations, such as roughness on the surfaces. Methods that will remove these constraints and achieve better surface quality have been studied by many researchers [7, 8, 10].

Griguras and Kramar examined the hybrid production process of 3D printing and milling. To enhance the surface quality of the part, the outer surface of the parts produced by 3D printing is milled. By using a larger nozzle size, the production time is shortened and obtained the same surface quality [3].

Dewey and Ulutan researched the use of CO2 laser polishing as an adjunct post-treatment to FDM-produced PLA parts to improve the surface features of the products. In their study, instead of reducing the layer thickness in 3D printing, the total processing time could be reduced without sacrificing surface quality. In addition, larger layer thicknesses and lasers have shown that the surface could be processed rapidly [3, 5].

Maidin et al. have tried to improve the surface characteristics of the FDM specimen by applying ultrasonic vibration in their work. As a result of the study, it was found that the best surface quality was obtained with a 21 kHz frequency applied during FDM production [3].

These hybrid processes, which combine machining, laser and ultrasonic processes with FDM processes, result in better surface quality. However, in all of these methods, machinery and production costs significantly increase. For this reason, the effect of the printing parameters on the surface properties of the different printing parameters has been investigated by many researchers, as it is known that the printing parameters affect the surface properties of the 3D printed parts.

Many autors are searched the surface roughness and wear of PLA models fabricated by 3D printing technique. It is found that surface roughness decreased with increasing material melting temperature and wear increases [3 - 6].

2. EXPERIMENTAL METHODOLOGY

In this work, surface roughness measurement specimens were manufactured using a WANHAO Duplicator i3 plus printer by two samples from the PLA, ABS+ and PETG material of 1.75 mm diameter produced by Devil Design, Poland. The 3D printer is capable of producing a model with dimensions of 200x 200x180 mm with a positioning accuracy of 12 µm for X and Y axes and 0,4 µm for Z axis.

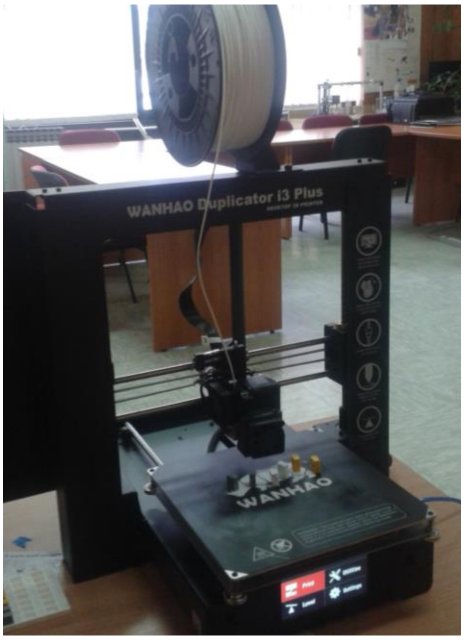

Figure 1. WANHAO 3D printer

Conditions of the experiment are presented in Table 1. The dimensions of the samples were 11 x 6.3 x 15 mm and that is shown on Figure 2.

Table 1. Conditions of the experiment

Materials	PLA	ABS+	PETG
Layer thicknesses, mm	0.15	0.15	0.15
Fill density, %	100	100	100
Print speed, mm/s	35	35	35
Printing temperature, ^{o}C	220	200	230
Bed temperature, ^{o}C	70	50	90

With specially prepared 3D printing codes, for all samples; 3 shells were used around the sample and on the upper and lower surface, and the inside of the sample was printed using the specified printing angles (-45°/+45°) and 100% infill ratio. In this paper, all samples were manufactured in the same printing orientation (upright position). Investigating the effect of other printing orientations (flatwise and edgewise) on surface roughness will be extremely useful for engineering applications.

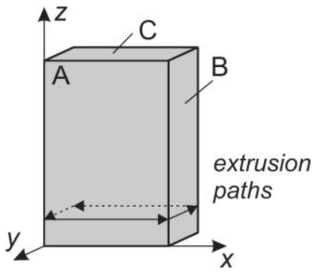

Figure 2. Sample

Surface roughness Ra and other parameters surfaces roughness are measures by device computerized measuring device Talysurf-6, which allows complex monitoring of the contact surfaces, figure 3.

Figure 3. Talisurf-6

Figure 4 shows the rectangular sample details and the measuring direction. Measuring direction the is perpendicular 90˚ to the building direction for all samples identical.

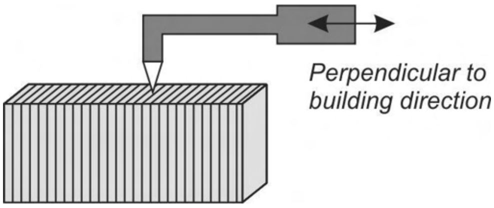

Figure 4. Sample area B and measuring direction surfaces roughness Ra

Research was carried out with materials of PLA, ABS+ and PETG [11].

PLA material is a biodegradable thermoplastic which is derived from renewable resources, such as cornstarch, sugar cane. This makes PLA the most environmentally friendly material in the domain of 3D printing. PLA is tough, though it has the feature of a little brittle. When printing, PLA is odorless, low shrinkage, good rigidity, excellent gloss of printed object, no heated print bed necessary, high printing speed, available in rich colors [11].

PLA Filament is normally extruded at around 190-220℃, with printing speed as 50-60 mm/s. Opening the fan near the extruding nozzle is usually recommended to speed up the cooling down.

ABS+ material is generally very durable and strong, slightly flexible and quite resistant to heat. It has good shock absorbing properties and great plastic properties. It solidifies quickly, durable and difficult to break, ideal for mechanical parts.

ABS Filament is generally operated at the temperature around 210-250℃. Because of the feature of ABS material, ABS Filament cools down quickly, so 3D Printer need a heated print bed(around 110℃) to process ABS filament, in order to prevent warping or cracking of the printed object. ABS filament is better printed in a well ventilated area.

PETG filament is a close to PET (Polyethylene terephthalate) filament. PETG is a new updated version that has enhanced properties. It has minimal shrinkage and warping.

PETG filament has good flexible strength more than ABS filament. The filament is super transparent with a glossy finish. PETG filament is also environmentally friendly and recyclable. PETG is known for it's transparency and clarity. It has great chemical resistance with good acidic and alkalic resistance.

The ideal print temperature is between 220°C – 250°C. The filament has easy adhesion, so it can be printed on acrylic, glass, polyimide (Kapton) tape, blue tape, and others. A heated bed is not required.

Tribological investigations of the friction coefficient and wear surface layer were performed on the TPD-93 tribometer "Block-on-disc", with contact at a line with disc made of 50CrMo4 of hardness 240 HB, Figure 5.

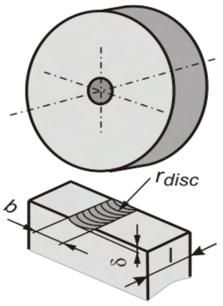

Figure 5. Contact elements "Block-on-disk"

The tribometer TR-95 perform contact condition variations in terms of shape, dimension and material of the contact elements, the normal load contact and sliding speed. Normal load was 20, 50 and 80 N and the sliding speed 0.25 m/s and 0.75 m/s. Total slip route was 150 m.

3. EXPERIMENTAL RESULTS

After finishing the production of samples (from all materials) on 3D printer, roughness measurement is done in the middle of surface B (with repeated measurement). Figures 6, 7 and 8 show the results of the foughness parameter Ra, the appearance of the obtained surface and the surface profile. Figure 9 shows a histogram with values of Ra of all samples.

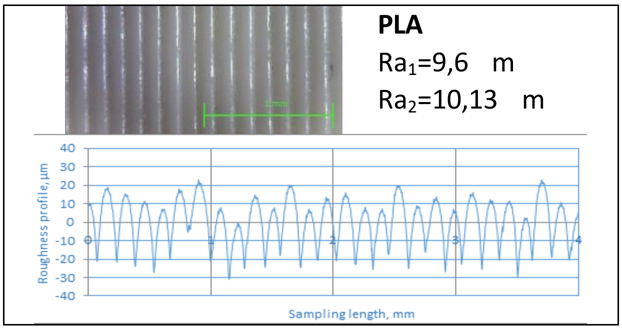

Figure 6. Surface profile of sample PLA

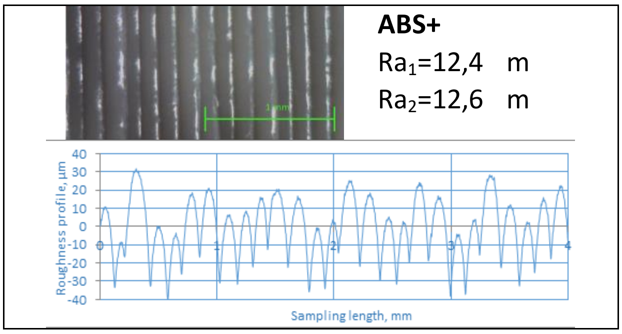

Figure 7. Surface profile of sample ABS+

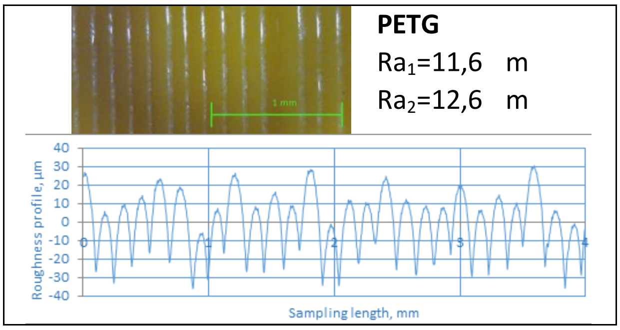

Figure 8. Surface profile of sample PETG

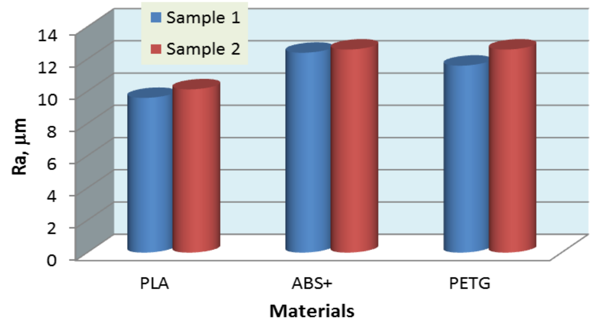

Figure 9. Surface roughness

By analysing the shape of the surfaces obtained by 3D printing, the unevenness profiles and values of Ra, it can be concluded that there are differences between the samples and that the smallest roughness has samples of PLA material. Furthermore, it can be noticed that in the samples of ABS+ and PETG materials, there is an unequal distribution of the material with the occurrence of local increase and decrease in the height of unevenness.

Measurement of tribological properties, both coefficient of friction and wear of samples was performed on the tribometer TPD-95 and the results are shown in Tables 2 and 3. The experiment was performed with two slip speeds and three normal loads.

Table 2. Friction coefficient

Fn, N	v=0.25 m/s			v=0.75 m/s		
	PLA	ABS+	PETG	PLA	ABS+	PETG
20	0.26	0.43	0.24	0.30	0.44	0.26
50	0.16	0.33	0.19	0.19	0.30	0.20
80	0.14	0.28	0.15	0.12	0.25	0.17

During the experiment the coefficient quickly reached a value that was approximately constant. Figure 10 shows the change in the friction coefficient over time for all three measured materials at a speed of 25 m/s and with a normal load of 50 N.

Figures 11 and 12 show the values of the friction coefficient depending on the type of material, the slip speed and the normal load. It can be concluded that with increasing normal load in all materials there is a significant reduction in the coefficient of friction. That coefficient it almost does not depend on the slip spreed. The highest coefficient of friction is for ABS+, while PETG is slightly higher than PLA.

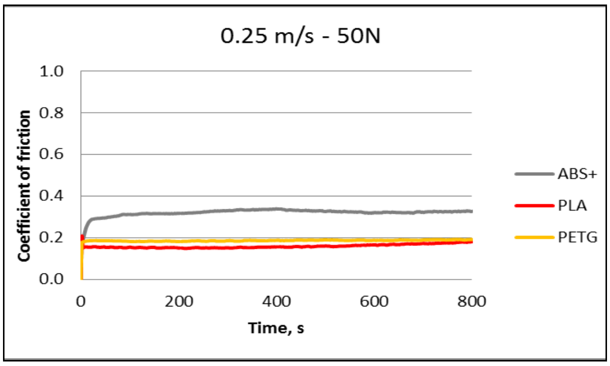

Figure 10. Change friction coefficient for materijals

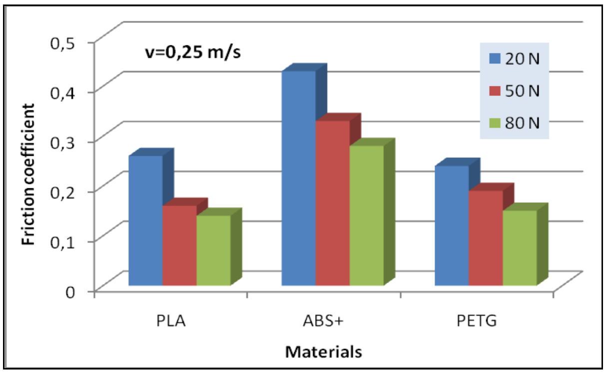

Figure 11. Friction coefficient for v=0,25 m/s

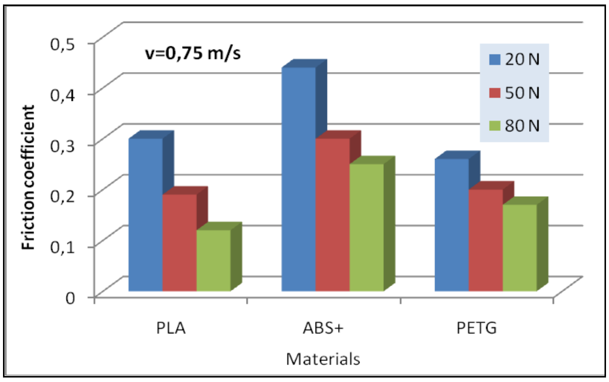

Figure 12. Friction coefficient for v=0,75 m/s

Measurement of the width of wear on the blocks after testing was performed on UIM-21 microscope. Tables 3, 4 and 5 show worn surfaces of tested blocks for different materials and different normal loads, tested at speed of 0.75 m/s. Table 6 shows all the values of the width of the wear on the blocks.

Table 3. Wear sample PLA, v=0,75 m/s

20 N	50 N	80 N
	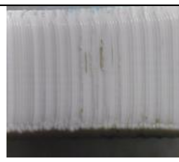	
h=1 mm	h=1,2 mm	h=2,2 mm

Table 4. Wear sample ABS+, v=0,75 m/s

20 N	50 N	80 N
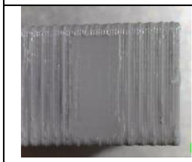		
h=2,43 mm	h=3,73 mm	h=4,34 mm

Table 5. Wear sample PETG, v=0,75 m/s

20 N	50 N	80 N
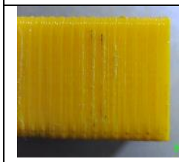	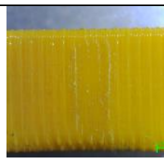	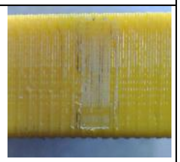
h=1,3 mm	h=1,68 mm	h=2,48 mm

Table 6. Wear samples, mm

Fn, N	v=0.25 m/s			v=0.75 m/s		
	PLA	ABS+	PETG	PLA	ABS+	PETG
20	0,8	1,45	1,19	1	2,43	1,3
50	1	2,88	1,41	1,2	3,73	1,68
80	1,3	3,62	2,1	2,2	4,34	2,48

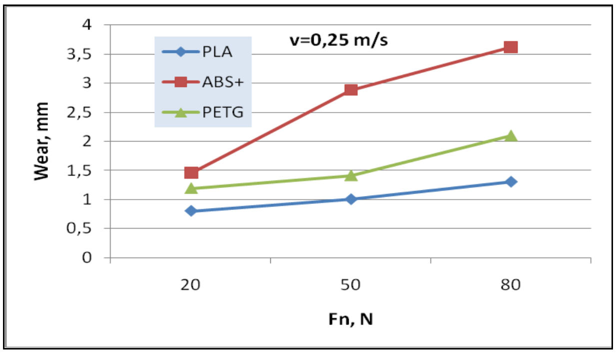

Figure 13. Wear block for v=0,25 m/s

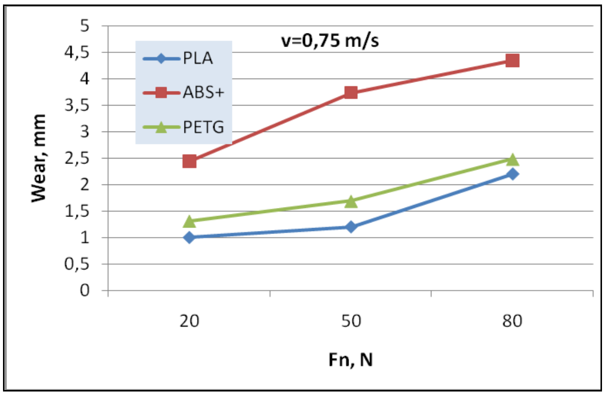

Figure 14. Wear block for v=0,75 m/s

Figures 13 and 14 show dependence of the wear width on the tested samples from the normal load, slip speed and material. It can be seen that the wear of the samples increases with increasing load as well as with increasing speed. The highest wear has ABS+ then PETG and PLA has the lowest wear.

4. CONCLUSION

The analysis of the obtained results of testing the tribological characteristics of the tested materials which are used as filament for 3D printing indicates that there are significant differences. This means material selection for 3D printing technology plays an important role from the aspects of surface roughness (topography), friction and wear and attention should be paid for it. The development and application of tribo-materials [9] significantly contributes to the expansion of the 3D printing area and its intensive development.

ACKNOWLEDGEMENT

This paper is part of project **TR35034,** funded by the Ministry of Education, Science and Technological Development of Serbia.

REFERENCES

[1] Y. Hong, P. Zhang, K.H. lee, C.-H. Lee: Friction and wear of textured surfaces produced by 3D printing, SCIENCE CHINA Technological Sciences, Vol. 60, p. 1400, 2017.

[2] S. Perepelkina, P. Kovalenko, R. Pechenko, K. Makhmudova: Investigation of Friction Coefficient of Various Polymers Used in Rapid Prototyping Technologies with Different Settings of 3D Printing, Tribology in Industry, Vol. 39, No. 4, pp. 519-526, 2017.

[3] V. Kovan, T. Tezel, E. S. Topal, H. E. Camurlu: Printing Parameters Effect on Surface Characteristics of 3D Printed PLA Materials, International Scientific Journal "Machines. Technologies. Materials.", No. 7, P.P. 266-269, 2018.

[4] W. Pawlak, Wear And Coefficient of Friction of PLA-Graphite Composite in 3D Printing Technology, in: *24th International Conference Engineering Mechanics 2018*, Svratka, Czech Republic, 14-17.05.2018, pp. 649–652, 2018.

[5] M.S. Alsoufi, A.E. Elsayed: How Surface Roughness Performance of Printed Parts Manufactured by Desktop FDM 3D Printer with PLA+ is Influenced by Measuring Direction, American Journal of Mechanical Engineering, Vol. 5, No. 5, pp. 211-222, 2017.

[6] M.S. Alsoufi, A.E. Elsayed: Surface Roughness Quality and Dimensional Accuracy—A Comprehensive Analysis of 100% Infill Printed Parts Fabricated by a Personal/Desktop Cost-Effective FDM 3D Printer, Materials Sciences and Applications, Vol. 9, pp. 11-40, 2018.

[7] B.C. Eddine, A. Chaparala: A *Study on the Surface Topography and Dimensional Accuracy of Fused Deposition Modeling, The Effects of Surface Orientation and Different Print Settings,* Master Thesis, Halmstad University, Halmstad, 2017.

[8] W. Musiał, J. Haracewiat, K. Kozłowicz: Assessment of the texture and topographic features of a surface produced by the 3D printing process, Advanced Technologies in Mechanics, Vol. 2, No. 3(4), pp. 35-45, 2015.

[9] 3D Printing, *EU_brochure_tribo_filamenti 3Dprint_web.pdf,* www.igus.eu/tribo-printing, accessed 12.04.2019.

[10] G. Krolczyk, P. Raos, S. Legutko, Experimental analysis of surface roughness and surface texture of machined and fused deposition modelled parts, Tehnički vjesnik, Vol. 21, No. 1, pp. 217-221, 2014.

[11] http://ziro3d.com/, accessed 12.04.2019.

Serbian Tribology Society

SERBIATRIB '19

16th International Conference on Tribology

Faculty of Engineering
University of Kragujevac

Kragujevac, Serbia, 15 – 17 May 2019

APPLICATION OF TAGUCHI METHOD IN THE OPTIMIZATION OF ZINC BASED COMPOSITE

Nenad MILORADOVIĆ[1,*], Blaža STOJANOVIĆ[1], Slobodan MITROVIĆ[1], Sandra VELIČKOVIĆ[1]
[1]University of Kragujevac, Faculty of Engineering, Kragujevac, Serbia
*Corresponding author: mnenad@kg.ac.rs

Abstract: *Tribological behaviour of composite with the ZA-27 alloy base reinforced by 5% SiC is considered in this paper. The optimization of tribological behaviour was conducted using the Taguchi method. Composite was prepared by the compocasting procedure. Tribological experiments were carried out using a block on disc tribometer with the variation of three different load values (10, 20 and 30 N), three sliding speed values (0.25, 0.5 and 1 m/s) and sliding distance value of 600 m. All the experiments were conducted under dry sliding test conditions. The analysis of the wear rate was executed using the ANOVA method of analysis. The sliding speed has the greatest impact on the wear rate (81.72%), then the SiC content (11.07%), and the least the contact load (5.07%).*

Keywords: *ZA27 alloy based composites, wear behaviour, Taguchi method*

1. INTRODUCTION

The high aluminium containing zinc alloys, known generally as ZA-27, which are commonly used in a variety of applications, have good physical, mechanical and tribological properties. It is suitable for producing castings of different shapes and sizes.

Over the last few decades, many researchers have used different approaches to improve the properties of ZA-27 alloy and its composite materials. Thus, composite materials have emerged which can be used to make components with great wear resistance such as engine bearings, pistons, piston rings and cylinder liners.

The sliding wear performance of zinc based alloy reinforced with SiC particles in dry and lubricated conditions was studied in [1]. Research has confirmed that dimensional stability and wear resistance of the composites were improved Effects of SiC particles reinforcement were investigated for different loads and sliding distances [2, 3]. The authors have discovered that the composites exhibited a lower wear rate compared to the unreinforced alloy specimens in testing conditions.

The mechanical behaviour of ZA-27 alloy and hybrid composites reinforced with 3 wt.% graphite and 0-9 wt.% silicon carbide particles was described by Kiran et al. [4]. It has been concluded that these hybrid composites are suitable for making the journal bearings.

The positive effects of SiC reinforcement were pointed out in [5, 6]. The experiments were performed on a block-on-disc tribometer under dry sliding conditions.

Tribological properties of a hybrid composite based on zinc-aluminium ZA27/SiC/Gr were investigated by Mitrović et al [7]. The wear volumes of the alloy and the composite were determined by varying the normal loads and sliding speeds. The tested sample contained 5% of SiC and 3% Gr particles.

The corrosion behaviour and artificial aging of ZA27/SiC composites synthesized via compocasting with addition of 1, 3, 5 and 10% SiC particles in the matrix alloy was studied in [8, 9].

2. DESIGN OF EXPERIMENTS

The tested composite material was successfully prepared using the compocasting procedure. Microstructure of ZA-27 alloy is given in Fig. 1 and microstructure of ZA-27/5%SiC composite is displayed in Fig. 2

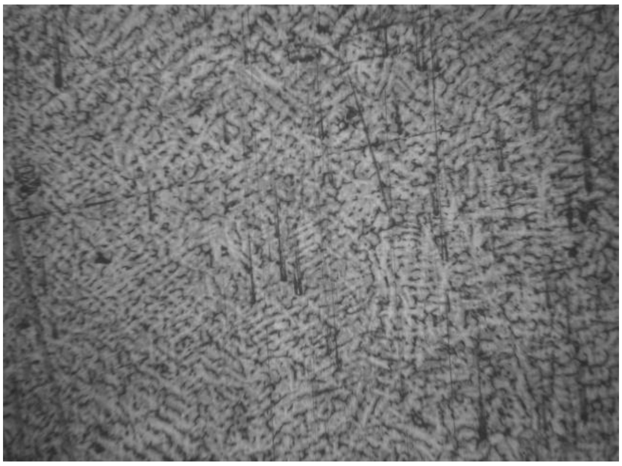

Figure 1. Metallographic structure of ZA-27 alloy

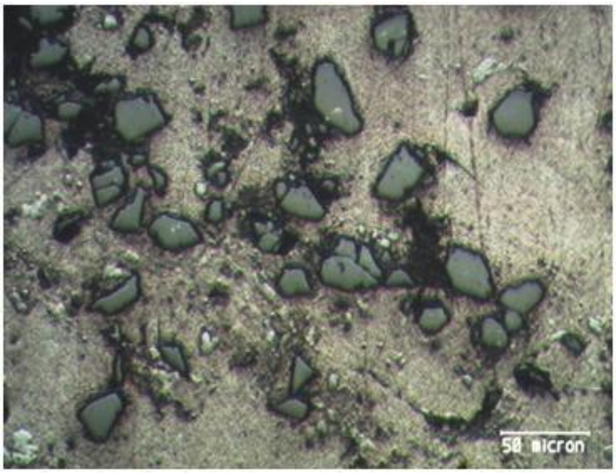

Figure 2 Metallographic structure of ZA-27/5%SiC composite

Microstructure of ZA-27 alloy and obtained ZA-27/5%SiC composite were observed by metallurgy microscope.

The wear rate of the ZA-27/5%SiC composite and ZA-27 alloy were analyzed for different values of contact load (10 N, 20 N and 30 N), sliding speed (0.25 m/s, 0.50 m/s and 1.0 m/s) and constant sliding distance of 600 m. The main factors influencing the wear rate (control factors) are: (A) SiC content, (B) the contact load and (C) the sliding speed. Factors and their levels are shown in Table 1.

Table 1. Levels for various control factors

Control factors	Units	Level I	Level II	Level III
(A) SiC	%	0	5	
(B) Load	N	10	20	30
(C) Sliding speed	m/s	0.25	0.5	1.0

An orthogonal matrix L18 obtained by application of the Taguchi mixed level design was used in experimental design, Table 2. The statistical tool Minitab 18 was used to form the orthogonal matrix.

Generally, there are three types of S/N ratio: ”smaller is better”, ”larger is better”, and ”nominal is best”, which are used for measurement of quality [10, 11]. Characteristic S/N ratio ” smaller is better” was implemented for analysis of the wear rate in the paper. The equation for calculating S/N ratio for Taguchi characteristic ”smaller is better” can be calculated through the equation [12-15]:

$$S/N = -10 log \frac{1}{n} \quad y^2 \quad , \tag{1}$$

where: S/N is the signal-to-noise ratio, n is the repetition number of each trial and y_i is the result of the *i*-th experiment for each trial.

The S/N ratio for each level of influencing parameters is calculated based on the S/N analysis. The statistical analysis of variable is used to consider parameters statistically worth. The optimal combination of parameters can be predicted.

Experimental values for wear rate are obtained by using orthogonal array for different factors’ combinations and they are given in Table 2. Table 2 also shows the values of S/N ratio of wear rate.

3. RESULTS AND DISCUSSION

The influence of control parameters, such as SiC content in composite, contact load and sliding speed was confirmed by the S/N ratio analysis.

3.1 S/N Ratio Analysis

Process parameter settings with the highest S/N ratio always yield the optimum quality with minimum variance. The control parameter with the strongest influence was determined by the difference between the maximum and minimum value of the mean of S/N ratios. Higher the difference between the mean of S/N ratios, the more influential will be the control parameter.

Table 3. Response table for signal to noise ratios for "smaller is better"

Level	SiC	Load	Sliding speed
1	-8.414	-6.371	-3.066
2	-6.154	-7.240	-8.501
3		-8.242	-10.285
Delta	2.260	1.871	7.219
Rank	2	3	1

The influence of control parameters on mean of wear rate is presented in Table 3. Based on ranking, it may be observed that the value of sliding speed is the most dominant parameter influencing the wear rate, followed by the SiC content. The contact load exerts the least influence on the wear rate.

Figure 3 shows a graph of the main effects of the influence of the various testing parameters on the wear rate. In the main effect plot, if the line for a particular parameter is near horizontal, then the parameter has no significant effect. In contrast, a parameter for which the line has the highest inclination has the most significant effect. In this case, the sliding speed has the greatest influence on the wear rate, followed by the SiC content, while the contact load has the smallest influence.

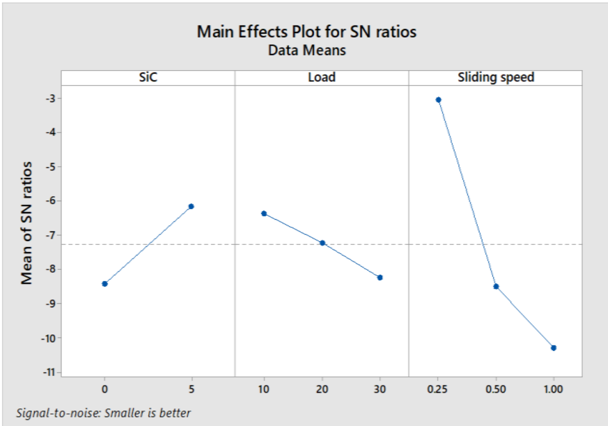

Figure 3. Main effect plots for means for the wear rate

Table 2. Experimental design using L18 orthogonal array

L18	SiC, %	Load, N	Sliding speed, m/s	Wear rate, mm^3x10^{-3}/m	S/N ratio, dB
1	0	10	0.25	1.329	-2.4705
2	0	20	0.25	1.603	-4.0987
3	0	30	0.25	2.029	-6.1456
4	0	10	0.50	2.706	-8.6466
5	0	20	0.50	2.907	-9.2689
6	0	30	0.50	3.202	-10.1084
7	0	10	1.00	3.299	-10.3676
8	0	20	1.00	3.812	-11.6231
9	0	30	1.00	4.466	-12.9984
10	5	10	0.25	1.096	-0.7962
11	5	20	0.25	1.253	-1.9590
12	5	30	0.25	1.401	-2.9288
13	5	10	0.50	2.323	-7.3210
14	5	20	0.50	2.383	-7.5425
15	5	30	0.50	2.547	-8.1206
16	5	10	1.00	2.699	-8.6241
17	5	20	1.00	2.801	-8.9463
18	5	30	1.00	2.868	-9.1516

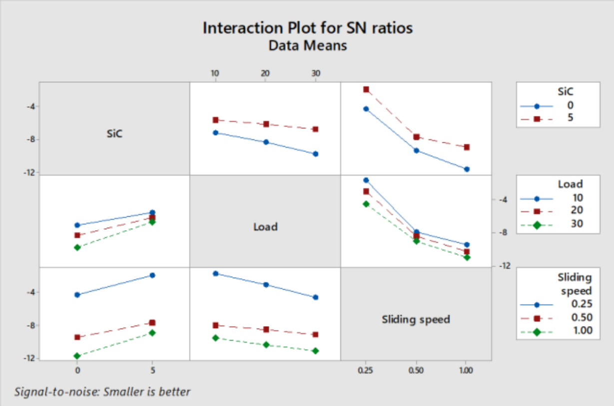

Figure 4. Interaction plot for means for the wear rate

The Figure 4 shows the interactions between some parameters and their mutual influence on wear rate for ZA-27/5% SiC and ZA-27.

3.2 Analysis of variance results for the wear rate

Experimental results were processed by using analysis of variance (ANOVA). This method is used for testing the influence of considered parameters (SiC content, contact load and sliding speed) on the wear rate. By performing analysis of variance, it can be decided which independent factor dominates over the other and the percentage contribution of that particular independent variable.

Table 4 shows the ANOVA results for the wear rate for three factors and interactions of those factors. This analysis is carried out for a significance level of α=0.05, i.e. for a confidence level of 95%. Sources with a P-value less than 0.05 were considered to have a statistically significant contribution to the performance measures. In Table 4 the last column shows the percentage contribution (Pr) of each parameter on the total variation indicating their degree of influence on the result.

From Table 4 it may be seen that the sliding speed has the greatest influence on the wear rate (81.72%). The SiC content (11.07%) and contact load (5.07%) have smaller influence on wear rate.

As interactions are concerned, the biggest influence is attributed to Load*Sliding speed (0.83%). The impact of other interactions is smaller.

Figures 5 to 7 show 2D and 3D diagrams of dependence between the wear rate and the influencing parameters (SiC content, contact load and sliding speed).

Table 4. Analysis of Variance for S/N ratios for wear rate (DF – Degrees of freedom, Seq SS – Sum of squares, Adj SS – Adjusted sum of squares, Adj MS – Adjusted mean of squares, F – ratio, P – value, Pr – Percentage of contribution)

Source	DF	Seq SS	Adj SS	Adj MS	F	P	Pr%
SiC	1	22.979	22.979	22.9793	319.92	0.000	11.07
Load	2	10.522	10.522	5.2612	73.25	0.001	5.07
Sliding speed	2	169.659	169.659	84.8293	1181.01	0.000	81.72
SiC*Load	2	1.561	1.561	0.7803	10.86	0.024	0.75
SiC*Sliding speed	2	0.884	0.884	0.4419	6.15	0.060	0.43
Load*Sliding speed	4	1.714	1.714	0.4284	5.96	0.056	0.83
Residual Error	4	0.287	0.287	0.0718			0.14
Total	17	207.606					100.00

a)

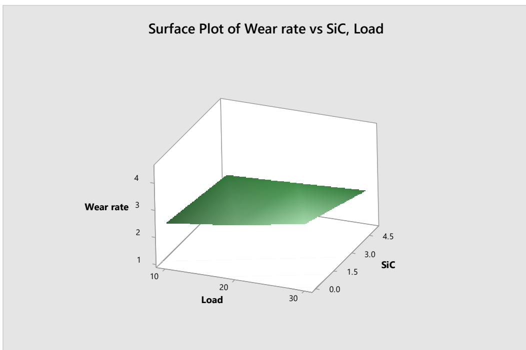

b)

Figure 5. a) Contour plot and b) Surface plot for dependence between wear rate of the %SiC and load

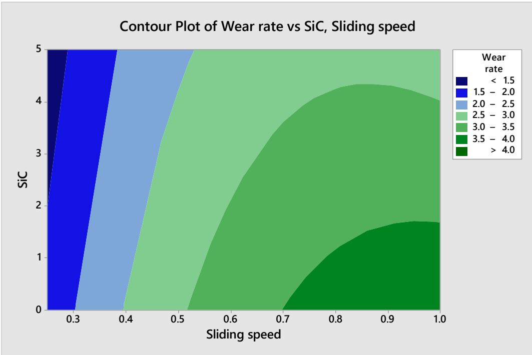

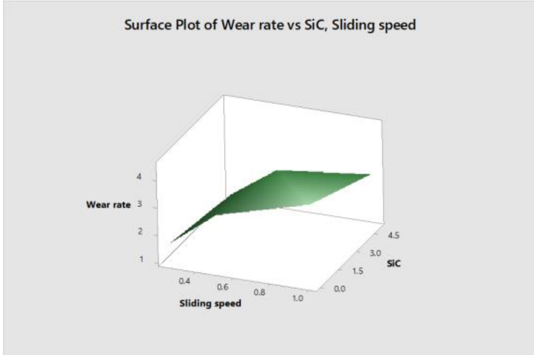

a) b)

Figure 6. a) Contour plot and b) Surface plot for dependence between wear rate of the %SiC and sliding speed

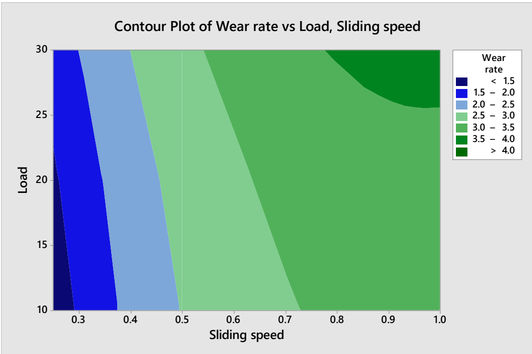

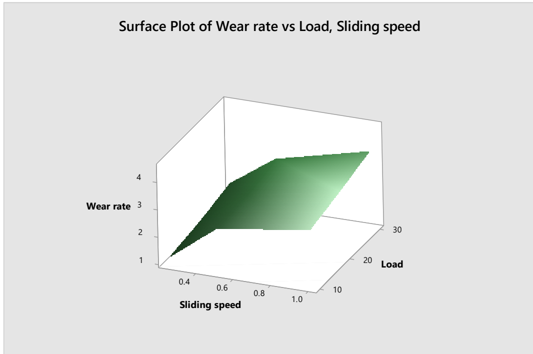

a) b)

Figure 7. a) Contour plot and b) Surface plot for dependence between wear rate of the load and sliding speed

3.3 Multiple regression model

Multiple linear regression model has been developed using statistical software “MINITAB 18”. This model gives the ratio between parameters and responds by setting linear equation for the observed data. Regression equation generated this way establishes the connection between significant parameters obtained by ANOVA analysis, i.e. SiC content, contact load and sliding speed. The regression equation developed for S/N ratio of wear rate is as follows [13-15]:

$$\begin{aligned} &Wear\ rate = 0.951 - 0.1329\,SiC + \\ &+0.0255\,Load + 2.324\,Sliding\ speed \end{aligned} \tag{2}$$

$$\begin{aligned} &S = 0.391162\,R\text{-}Sq = 85.09\% \\ &R\text{-}Sq(adj) = 81.89\% \end{aligned} \tag{3}$$

Equation (3) shows that the wear rate increases with the increase of the contact load and the sliding speed and decreases with increase of the SiC content.

4. CONCLUSION

Taguchi design method may be used for analysis of wear problem in composite materials with ZA-27 alloy base. Based on the analyses, the following conclusions can be drawn:

- The parameter design of the Taguchi method provides a simple, systematic, and efficient methodology for the optimization of the wear test parameters.
- The ANOVA shows that the greatest impact on the wear rate has the sliding speed (81.72%), then the SiC content (11.07%), and the least the contact load (5.07%). The impact of interaction is considerably smaller.
- The estimated S/N ratio using the optimal testing parameters for wear rate was calculated, and a good agreement between the predicted and actual wear rates was observed for a confidence level of 99.5%.

- By the use of MINITAB program, the corresponding equation for the wear rate with the high coefficient of regression was formulated.

ACKNOWLEDGEMENT

This paper presents the results obtained during research within the framework of the project TR 35021, supported by the Ministry of Education, Science and Technological Development of the Republic of Serbia.

REFERENCES

[1] B.K. Prasad: Investigation into sliding wear performance of zinc-based alloy reinforced with SiC particles in dry and lubricated conditions, Wear, Vol. 262, No. 3-4, pp. 262-273, 2007.

[2] S. C. Sharma, B. M. Girish, R. Kramath, B. M. Satish: Effect of SiC particle reinforcement on the unlubricated sliding wear behavior of ZA-27 alloy composites, Wear, Vol 213, No. 1-2, pp. 33-40, 1997.

[3] B. K. Prasad: Influence of some material and experimental parameters on the sliding wear behaviour of a zinc-based alloy, its composite and a bronze, Wear, Vol. 254, No. 1-2, pp. 35-46, 2003.

[4] T.S. Kiran, M. Prasanna Kumar, S. Basavarajappa, B. M. Vishwanatha: Mechanical properties of as-cast ZA-27/Gr/SiCp hybrid composite for the application of journal bearing, Journal of Engineering Science and Technology, Vol. 8, No. 5, pp. 557-565, 2013.

[5] N. Miloradovic, B. Stojanovic:, Tribological behaviour of ZA27/10SiC/1Gr hybrid composite, Journal of the Balkan Tribological Association, Vol. 19, No. 1, pp. 97-105, 2013.

[6] N. Miloradović, B. Stojanović, R. Nikolić, N. Gubeljak: Analysis of wear properties of Zn-based composites using the Taguchi method, Materials Testing, Vol.60, No.3, pp. 265-272, 2018.

[7] S. Mitrović, M. Babić, N. Miloradović, I. Bobić, B. Stojanović, D. Džunić, M. Pantić: Wear Characteristics of Hybrid Composites Based on ZA27 Alloy Reinforced With Silicon Carbide and Graphite Particles, Tribology in Industry, Vol. 36, No. 2, pp. 204-210, 2014.

[8] B. Bobić, I. Bobić, A. Vencl, M. Babić, S. Mitrović: Corrosion Behavior of Compocasted ZA27/SiCp Composites in Sodium Chloride Solution, Tribology in Industry, Vol. 38, No. 1, pp. 115-120, 2016.

[9] I. Bobić, M. Babić, A. Vencl , B. Bobić, S. Mitrović: Artificial aging of thixocast ZA27 alloy and particulate ZA27/SiCp composites, International Journal of Materials Research, Vol. 104, No 10, pp.954-965, 2013.

[10] S Veličković, B. Stojanović, M. Babić, A. Vencl, I. Bobić, G. Vadászné Bognár, F. Vučetić: Parametric optimization of the aluminium nanocomposites wear rate, Journal of the Brazilian Society of Mechanical Sciences and Engineering, Vol.41, No.1, pp. 1-10, 2019.

[11] B. Stojanović, A. Venc, I. Bobić, S. Miladinović, J. Skerlić: Experimental optimisation of the tribological behaviour of Al/SiC/Gr hybrid composites based on Taguchi's method and artificial neural network, Journal of the Brazilian Society of Mechanical Sciences and Engineering, Vol.40, No.311, pp. 1-14, 2018.

[12] S. Veličković, B. Stojanović, M. Babić, I. Bobić: Optimization of tribological properties of aluminum hybrid composites using Taguchi design; Journal of composite materials, Vol. 51, No. 17. pp. 2505–2515, 2017.

[13] B. Stojanovic, J. Blagojević, M. Babic, S. Veličković, S. Miladinovic, Optimization of hybrid aluminum composites wear using Taguchi method and artificial neural network, Industrial Lubrication and Tribology, Vol. 69, No. 6, pp. 1005-1015, 2017.

[14] B. Stojanovic, M. Babic, S. Veličković, J. Blagojević: Tribological behavior of aluminum hybrid composites studied by application of factorial techniques, Tribology Transactions, Vol. 59, No. 3, pp. 522-529, 2016.

[15] R. K. Roy, *Design of Experiments Using the TaguchiApproach: 16 Steps to Product and Process Improvement*. Wiley-Interscience, NewYork, 2001.

Serbian Tribology Society

SERBIATRIB '19

16th International Conference on Tribology

Faculty of Engineering
University of Kragujevac

Kragujevac, Serbia, 15 – 17 May 2019

TRIBOLOGICAL CONSIDERATIONS ON RWL 34 TOOLS STEEL

Mihai DEMIAN[1], Claudiu NICOLICESCU[1,*], Gabriela DEMIAN[1]
[1]University of Craiova, Faculty of Mechanics, Department of Engineering and Management of the Technological Systems, Drobeta-Turnu Severin, Romania, mihaidemian@yahoo.com; gabrielademian@yahoo.com
*Corresponding author: nicolicescu_claudiu@yahoo.com

Abstract: *The paper presents an analyze of the tribological testing on the RWL 34 tools steels in diffrent stages: untreated, hardened and hardened and tempered. The wear tests were made by ball on disk, which is an oscilating sliding method. Two types of materials were used for the counterbody balls, namely: steel (100Cr6) and alumina (Al2O3). The coefficients of friction, worn track sections, worn cap diameters and samples wear rates at diffrent loads (4 and 6 N) were measured. A comparation between all three stages of the material and parameters of the wear tests was made.*

Keywords: *tool steel, heat treatment, micro hardness, coefficient of friction, wear rate, worn track section*

1. INTRODUCTION

For grinding tea plants, knives of different shapes and sizes can be used. Metallic materials used in the manufacture of knives from milling mills have high carbon content to ensure adequate hardness. So we have a tool steel that has alloying elements such as chrome, molybdenum, vanadium, silicon, manganese, etc.[1]
To cut the dried plants, the knife has a high rotational speed and the cut of the knife from the grinder is strongly required. Due to the high rotational speed of the die knives and the permanent contact between the tool cutter and grinding material, the wear resistance of the cutter knife must be high. It is known that wear resistance is high hardness on the parts analyzed, so a high carbon content and a structure with high hardness.

Taking into account the working conditions, the grinding material, it is necessary that the hardness of the material from which the knife is made is as great and the resilience and ductility as possible. This is possible if the structural component is martensitic. It requires a very fine martensite, and this can be achieved by applying a heat treatment applied to the mill knife after being brought to shape and size.

The final heat treatments are applied to the products in order to obtain the necessary mechanical characteristics for use in service. Final heat treatments can be volumetric when heating and cooling takes place throughout the workpiece volume, or may be superficial when heating and cooling takes place to a certain depth [2].

In the case of mill knives analyzed due to the small dimensions, in particular the thickness, the heat treatment is in the volume (volumetric).

In Fig. 1 are presented the shapes of the mill blades from which were taken samples for this study.

Figure 1. The shapes of the mill blades analyzed

The final thermal treatment applied to obtain the martensitic structure is the martensite hardening and the annealing. Martensitic hardening applies to most steels can be applied to non-ferrous alloys or cast iron. The aim of heat treatments for martensite hardening is to obtain the martensitic structure that is a non-equilibrium constituent.

Annealing is necessary to reduce the tensions in the material even if hardness and resilience could decrease, increase ductility. The main purpose of heat annealing is to decompose the constituents out of balance, as martensite, into constituents closer to equilibrium such as annealing martensite. With structural transformations, partial and total internal tensions are also eliminated [4,5].

2. MATERIALS AND EXPERIMENTAL DETAILS

The material used for the research is sintered steel RWL34 with the composition presented in Table 1.

Table 1. Concentration in chemical elements

C [%]	Cr [%]	Mo [%]	Si [%]	Mn [%]	V [%]
1	13	4	0.5	0.5	0.2

According to the manufacturers of this steel, the heat treatment chart shows three important temperatures [6-11]:

- Austenitizing, temperature between 1050-1080^0 Celsius;
- Fast cooling, temperature between -16 and -18^0 degrees Celsius;
- Anneling treatment, temperature between 150-200^0 Celsius

The austenitization and cooling time below zero degrees Celsius is of the order of a few minutes and the anneling time of about 2 hours.

For the tribological tests a CSM Instruments tribometer was used and were set up the following parameters: method: ball on disk; material of the balls: 100Cr6 and Al_2O_3; diameter of the ball: 6 mm; acquisition: linear mode; amplitude: 6.00 [mm]; max lin. speed: 12.00 [cm/s]; normal load: 4 and 6 [N]; stop condition: 50.00 [m]; acquisition rate: 10.0 [hz]; temperature: 25.00 [°C]; Atmosphere: Air; humidity: 30.00 [%]. In order to study the worn track section and the worn cap diameter were used a Surtronic 25+ profilometer and a Nikon MA100 microscope equipped with NIS ELEMENTS software.

3. RESULTS AND DISCUSSIONS

In Fig. 2-13 are presented worn track sections respectively worn cap of the counter ball. All the microscopic images were at 75x magnitude.

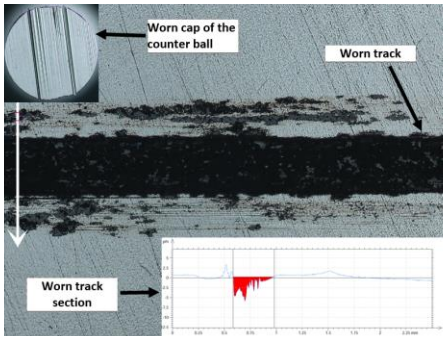

Figure 2. Tribological results of the RWL 34 steel against 100Cr6 ball (F=4N, untreated)

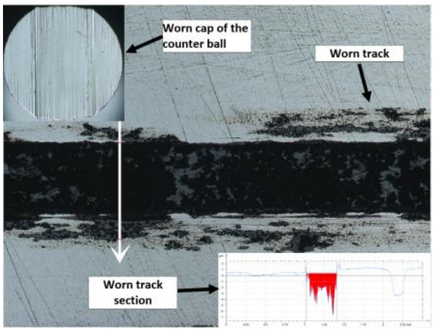

Figure 3. Tribological results of the RWL 34 steel against 100Cr6 ball (F=6N, untreated)

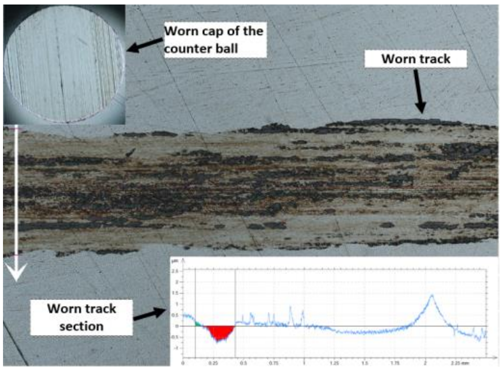

Figure 4. Tribological results of the RWL 34 steel against 100Cr6 ball (F=4N, hardened)

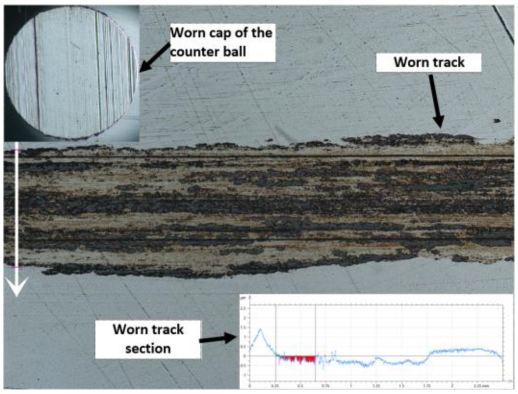

Figure 5. Tribological results of the RWL 34 steel against 100Cr6 ball (F=6N, hardened)

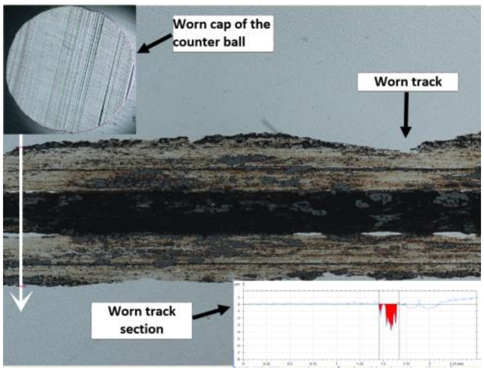

Figure 6. Tribological results of the RWL 34 steel against 100Cr6 ball (F=4N, hardened and tempered)

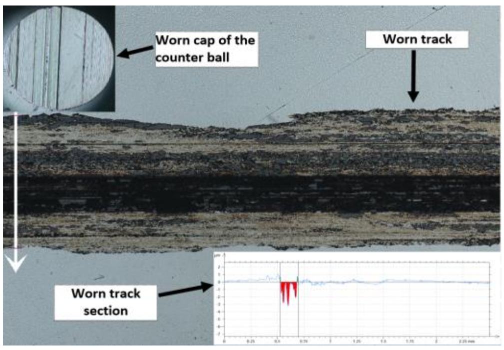

Figure 7. Tribological results of the RWL 34 steel against 100Cr6 ball (F=6N, hardened and tempered)

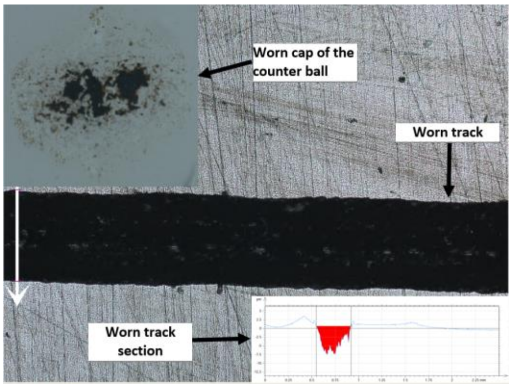

Figure 8. Tribological results of the RWL 34 steel against Al_2O_3 ball (F=4N, untreated)

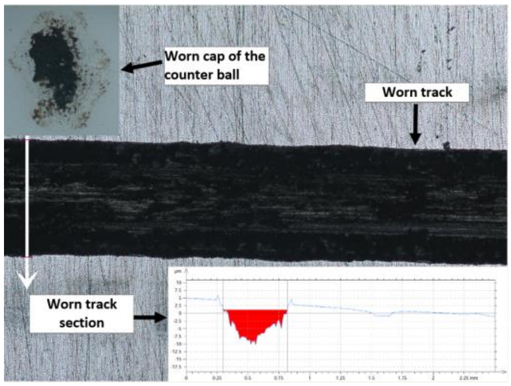

Figure 9. Tribological results of the RWL 34 steel against Al_2O_3 ball (F=6N, untreated)

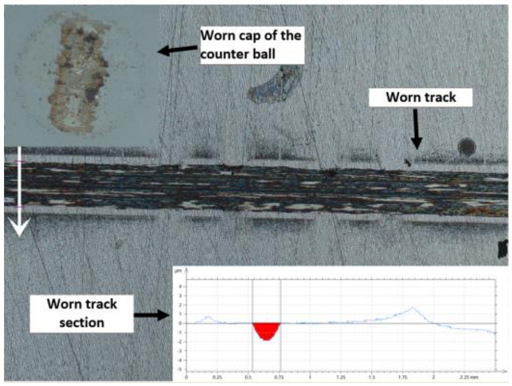

Figure 10. Tribological results of the RWL 34 steel against Al_2O_3 ball (F=4N, hardened)

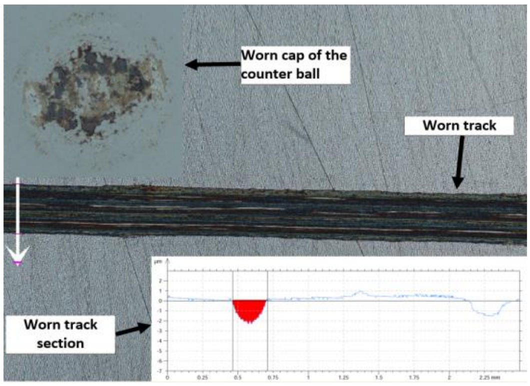

Figure 11. Tribological results of the RWL 34 steel against Al_2O_3 ball (F=6N, hardened)

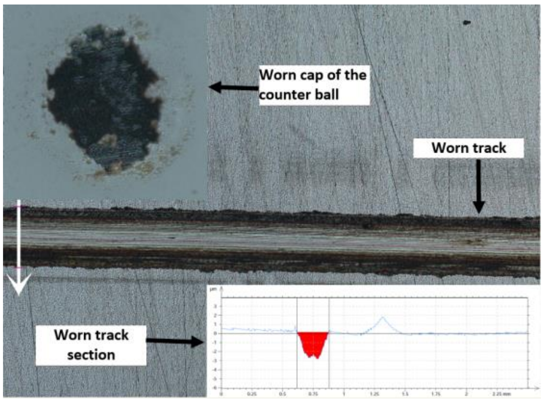

Figure 12. Tribological results of the RWL 34 steel against Al_2O_3 ball (F=4N, hardened and tempered)

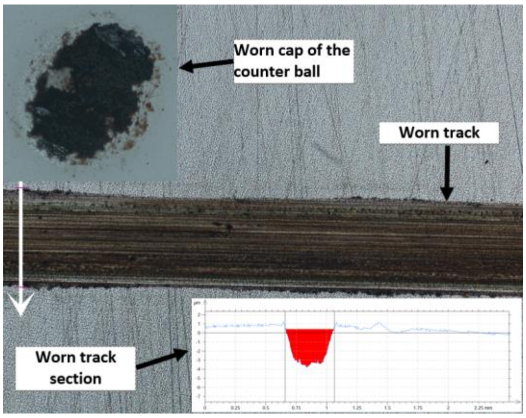

Figure 13. Tribological results of the RWL 34 steel against Al_2O_3 ball (F=6N, hardened and tempered)

In the Table 2-5 there are presented the values of the tribological parameters of the samples using the two types of the counterbody balls.

Table 2. Evolution of the worn track sections

Sample	Force [N]	Worn track section [µm^2]	
		100Cr6	Al_2O_3
untreated	4N	876.4	2088.8
	6N	1125.2	3181.4
hardened	4N	60.4	345.6
	6N	57.32	412
hardened nd tempered	4N	304.8	520.2
	6N	132.54	1143.8

Table 3. Evolution of the coefficients of friction

Sample	Force [N]	Coefficient of friction	
		100Cr6	Al_2O_3
untreated	4N	0.348	0.476
	6N	0.332	0.471
hardened	4N	0.320	0.466
	6N	0.297	0.462
hardened and tempered	4N	0.355	0.490
	6N	0.317	0.533

Table 4. Evolution of the wear rates of the samples

Sample	Force [N]	Wear rates [mm^3/n/m] *10^{-5}	
		100Cr6	Al_2O_3
untreated	4N	2.6290	6.2660
	6N	2.2500	6.3620
hardened	4N	0.1812	1.0370
	6N	0.1146	0.8239
hardened and tempered	4N	0.9143	1.5600
	6N	0.2651	2.2870

Table 5. Evolution of the wear rates of the counterbody balls

Sample	Force [N]	Wear rates of the ball[mm^3/n/m] *10^{-6}	
		100Cr6	Al_2O_3
untreated	4N	8.3530	0.7070
	6N	6.3090	0.8832
hardened	4N	6.5410	0.1215
	6N	4.9950	0.1049
hardened and tempered	4N	8.3610	0.2017
	6N	5.6820	0.3015

As it can be seen from fig.2-13, the worn track sections of the samples using Al_2O_3 as counter body ball are more clearly comparative with those were was used 100Cr6 counterbody ball. It is an advantage in the process of measure the worn track section with the profilometer. Also, the width of the worn obtained with Al_2O_3 balls are lower and uniform comparative with the worn obtained with 100Cr6 ball, which is irregular and present material debris from the ball. After the tribological tests, the counterbody balls made from 100Cr6 present a flat surface due to the scraping by the sample material, which is the cause of the high width of the resulting worn track section of the sample.

The forces used in the tribological tests influence the wear parameters and the higher value for the coefficient of friction was attained for the sample hardened and tempered, tested with a force equal to 6N and Al_2O_3 counter body ball. As it can be seen in Table 5, the wear rates of the Al_2O_3 ball are increase with the increasing of the load.

4. CONCLUSIONS

The experimental research leads to the following conclusions:

- The characteristics of the material used for milling knives after the heat treatment applied are in accordance with the expectations;
- Due to the presence of the debris which act as a counterbody, the values of coefficients of the friction are irregular in the case of 100Cr6 ball;
- In this moment milling knives subjected to the heat treatments from the present paper are in exploitation and will be monitored for an eventually modification of the heat treatment parameters or heat treatment cycle.

REFERENCES

[1] C. Dumitrescu, R. Saban: *Metalurgie fizica. Tratamente termice*, Fair Parteners Publisher, 2001.

[2] D. Bunea, R. Saban & others: *Alegerea si tratamentele termice ale materialelor metalice*, Didactic and pedagogical publishing house, 1996.

[3] E. Badisch, C. Katsich, H. Winkelmann, F. Franek, ManishRoy: Wear behaviour of hardfaced Fe-Cr-C alloy and austenitic steel under 2-body and 3-body conditions at elevated temperature, Tribology International Vol. 43, pp. 1234–1244, 2010.

[4] T. Dulamita, T. Vasile: *Tratamente termice si termochimice*, Didactic and pedagogical publishing house, 1978.

[5] T. Dulamita, I. Gherghescu: *Oteluri de scule-proprietati, tratamente termice*, Tehnic Publisher, 1990.

[6] http://www.finetools.ro/RWL34-40-38-500

[7] http://damasteel.se/our-steel-alloys/

[8] http://www.zknives.com/knives/steels/rwl-34.shtml

[9] https://www.jatagan.eu/en/blades-and-steel/rwl-34-4x38x250-mm

[10] https://www.bladeforums.com/threads/spyderco-high-performance-blade-steels.1245724/

[11] http://michaelwest.dk/knive/rwl34-datasheet.pdf

Serbian Tribology Society

SERBIATRIB '19

16th International Conference on Tribology

Faculty of Engineering University of Kragujevac

Kragujevac, Serbia, 15 – 17 May 2019

TRIBOLOGICAL BEHAVIOUR OF A356/SIC NANOCOMPOSITE

Sandra VELIČKOVIĆ[1,*], Blaža STOJANOVIĆ[1], Aleksandar VENCL[2,3], Miroslav BABIĆ[1] Dragan DŽUNIĆ[1], Marko PANTIĆ[1], Veljko ŠLJIVIĆ[2],

[1]Faculty of Engineering University of Kragujevac, Kragujevac, Serbia

[2]University of Belgrade, Faculty of Mechanical Engineering, Belgrade, Serbia

[3]South Ural State University, Chelyabinsk, Russia

*Corresponding author: e-mail sandrav@kg.ac.rs

Abstract: *The paper presents tribological behaviour of aluminium nanocomposite A356/SiC produced by the compocasting process with mechanical alloying preprocessing (ball milling). Tribological tests were performed on tribometer with block-on-disc contact geometry under lubricated sliding conditions. Influence of amount of silicon carbide reinforcement (0, 0.2, 0.3 and 0.5 wt.%) on wear rate was investigated in the following testing conditions: sliding speed of 0.25 and 1.0 m/s, normal load of 40 N and 100 N and at sliding distance of 1000 m. Analysis of worn surface of nanocomposites was performed by using SEM equipped with EDS.*

Keywords: *nanocomposite, wear rate, silicon carbide, aluminium.*

1. INTRODUCTION

Over the last investigation of decades, nanocomposites with a metal base has been in the focus of researchers In order to find materials with the best combination of characteristics such as durability, high strength, low weight and low density. Today, due to their good properties, such as high strength and weight ratio, excellent corrosion resistance and erosion, Al-SiC nanocomposites have attracted great attention for numerous engineering applications in the automotive, military and aerospace industries [1-4]. The mentioned industries set aluminum as the basic material for the nanocomposite. In addition to the mentioned features, another advantage of using aluminum is from an ecological point of view, more precisely, components made of aluminum alloys can be easily recycled. Nanocomposites consist of a base that can be metal, ceramic or a kind of polymer, and reinforcements that can be in the form of fibers, particles or whiskers with a size up to 100 nm [5]. An exceptional class of materials are nanocomposites with an aluminum base due to their unique combinations of mechanical and tribological properties [3]. Aluminum reinforced with various particles such as carbides (SiC, B_4C, TiC), oxide (Al_2O_3, TiO_2) is suitable for different engineering purposes.

Researchers tend to use various techniques in the process of obtaining materials, variation in the content and size of the reinforcement, in simulation of real working conditions of the elements, and analysis of mechanical and tribological properties, in order of understanding the behavior of materials, and thus find the material that will respond to the task.

Yaghobizadeh O et. al for production of aluminum nanocomposites by stir casting method for applied a coating of SiC particles with aluminium in order to avoid dangerous chemical reactions with the A356 base. SiC particles with a size of 80 nm were used as an reinforcement while the size of the aluminium base particles was 50 µm. They examined the influence of the content of the SiC reinforcement in nanocomposites from 0% to 5% volume fractions, as well as the influence of temperature in the production of nanocomposites of 800°C and 850°C on strength, hardness and flexibility.

Based on the results of experiments, they concluded that generally the hardness of the samples casted at 850°C was higher than the hardness of the samples casted at 800°C. In general, they have found that by increasing the amount of SiC particles in the nanocomposite, the hardness, flexibility and ultimate tensile strength increase for the samples casted at 850°C. Then, on the basis of the SEM analysis, good particle distribution was observed which is the effect of the particle coating process. Also, they found that it is very difficult to prevent agglomeration, which they observed when testing one material, because the particles are very small [6].

Yun-hui Du et. al. in their investigations of the nanocomposites with ca Al-1.5wt.%Si aluminum alloy observed that the distribution of SiC particles significantly influences the characteristics of the composite [7]. For the study they used particles with an average particle size of 20 µm, and the volume fraction of SiC particles in the base alloy was 4.25 vol.%. In order to prove that, they have developed electromagnetic mechanical stirring and by SEM analysis, they have shown that composites can be produced with a uniform distribution of reinforcing particles by a newly created apparatus. The difference between the volume fraction of the SiC particles, at the top of the ingot and that at the bottom are both ~ 0.04 vol.%, is very small and it can be considered that uniform distribution is achieved. They achieved an significant improvement in tensile strength by about 51% and reduced the porosity of the composite. A good distribution of SiC particles in the A356 alloy without agglomeration was also demonstrated by Wu S. and others [8]. They used β-SiC particles with an average size of 40 nm, while the average size of aluminum powder was 30 µm. By application of the new complex method for obtaining the nanocomposite, the molten-metal process combined with high-energy ball milling and ultrasonic vibration methods, it was and demonstrated the improvement of the mechanical properties of the nanocomposite in relation to the basic alloy.

A higher percentage of silicon carbide reinforcement content in aluminum base for the production of nanocomposites by the stir-casting method was studied by Ashok Kumar R. and Krishnakumar T. S. The authors investigated tribological and mechanical properties of the nanocomposite with the Al 6063 base reinforced with SiC particles (0, 4, 8, 12 and 16 wt.%) with average size of 60 nm. They considered the influence of the mixing rate (400, 500 and 600 rpm) in the production of the nanocomposite on the wear and micro-hardness of the nanocomposite. Based on the analysis of the microstructure with the use of SEM, they came to the conclusion that the particles were well distributed in the base but only up to 12 wt.% SiC, and at the same time this nanocomposite showed improved mechanical and tribological characteristics.

While, when adding 16 wt.% SiC, they observed a decrease in the micro-hardness values which is the effect of forming of nanoparticles agglomeration, as well as the porosity of the nanocomposite [9].

A Prasad Reddy et. al., in addition of the silicon carbide reinforcement, also used graphite in the nanocomposite to examine the effect of applied normal load and abrasive grit particle size on two-body abrasion wear behaviour of hybrid nanocomposite. For base material AA6061 aluminum alloy was used, while the content of the reinforcement in the nanocomposite was 2 wt.% SiC and 2 wt.% Gr with an average particle size of 50 nm and 500 nm respectively. Ultrasonic-assisted stirring technique under protective argon atmosphere was used to produce nanocomposites.

The highest value of micro-hardness had a nanocomposite with 2 wt.% SiC while the hybrid nanocomposite had the best wear resistance. They concluded that the wear rate is minimal at a smaller size of abrasive grit paper, and that it is higher in coarse-sized grit paper [10]. Nidhi Sharma and Syed Nasimul Alam [11] investigated the behavior of the nanocomposite due to surface treatment. By analyzing nanocomposites with Al_2O_3 and SiO_2 base with graphite nanoplatelets (xGnP) and multiwalled carbon nanotubes (MWCNT) reinforcements they concluded that wear is influenced by geometric parameters such as the texture of the abrasive surface and the contact surface. They, also, found that SiO_2-xGnP/MWCNT composites had better wear resistance compared to Al_2O_3-xGnP/MWCNT composites. In recent years, researchers in addition to experimental tests have applied various statistical methods to plan the experiment, analyze the results, shortened the time and number of experimental performances and most importantly used them to predict the behavior of new materials [12, 13].

The aim of this study is to investigate the effect of the reinforcement on the wear of the nanocomposite in comparison with the base alloy, by applying a modified method for production of nanocomposite. The contribution of this paper is the application of a very small percentage of the reinforcement content in the A356 base.

2. MATERIAL AND EXPERIMENTAL DETAILS

2.1 Preparation of nanocomposite

In this paper, the hypoeutectic alloy A356 (AlSi7Mg0.3) was used as the base material, the chemical composition of which is shown in Table 1. The nanoparticles of silicon carbide with an average size of about 50 nm with a different weight fraction were used as a reinforcement material in aluminium alloy. The particles of silicon carbide are selected as an reinforcement because they are very common in composites with a metal base.

Prefabrication process implies mechanical alloying procedure of matrix alloy chip particles along with SiC reinforcement particles in order to reduce the generation of larger clusters before infiltration in the semi-solid alloy during the compocasting process. The prefabrication process was realised using the Turbula Type 2TC Mixer with three-dimensional eccentric movement. Mechanical alloying was carried out at a speed of 500 rpm and a time of 1 hour for each fraction of the shavings-nanopowder mixture. Then a compocasting process was carried out, which is described in [14].

It is important to note that the samples are thermally processed according to the so-called T6 regime. For these materials, mentioned regime consisted of 5 hours of heating under liquid conditions at 540°C, with subsequent quenching in water, followed with artificial aging that implies heating the samples at 160° C for 6 hours and quenching in water.

2.2 Specimen preparation

The metallographic investigation of the microstructure was done due to surface analysis of the prepared samples of nanocomposite and the basic alloy. The samples prepared from cast nanocomposite were polished with sandpaper of P1000, P2000 and P3000 granulation, with approximately the same parameter values: polishing time and polishing speed.

Table 1. Chemical composition of A356 alloy (wt.%)

Chemical element	Si	Cu	Mg	Mn	Fe	Zn	Ni	Ti	Al
Element content (wt.%)	7.20	0.02	0.25	0.01	0.18	0.01	0.02	0.11	the rest

Figure 1. Polisher with mark MetaServ 250

Then polishing the surfaces was performed by an emulsion with abrasive grains of 1 µm. Preparation of samples on this polisher is simple because it provides the possibility of cooling with water supply by means of a water jet, thus preventing surface heating.

The surface appearance after the sample preparation is shown in Figure 2.

2.3 Tribological testing

In order to investigate the tribological characteristics of nanocomposite, tests were performed on a computer-supported tribrometer TPD 95, with block-on-disc contact geometry. The tests were carried out under lubrication conditions in accordance with the ASTM G77-83 standard. The contact pair consists of a disc with diameter 60 mm and width of 10 mm and block with size of 6×16×12 mm. The block materials are the tested aluminum nanocomposites, while 42CrMo4 steel, with hardness of 50-55 HRC, was used for the disc material. Contact between the elements of the tribomechanical system is line contact. Outputs that can be tracked in addition to wear and friction coefficient are lubricant temperature, contact temperature as well as sliding distance. Surface roughness measurements for tribological testing were performed on the computerized measuring device Talysurf 6. The surface roughness of the blocks and discs was approximately Ra = 0.2 and 0.4 µm, respectively.

Tribological tests of A356 aluminum alloy and aluminum nanocomposites were carried out under lubrication conditions on a sliding distance of 1000 m. The lubricant used in this experimental test was a gear oil, viscosity of which is 220 mm^2/s. In the realization of tribological tests factors: load (40 N and 100 N) and sliding speed (0.25 m/s and 1 m/s) were varied to monitor the behavior of the material. Also, the content of the reinforcement particles in the base alloy was varied (0.2 wt.% SiC, 0.3 wt.% SiC and 0.5 wt.% SiC). Figure 3 shows a tribometer used for experimental testing of the nanocomposite.

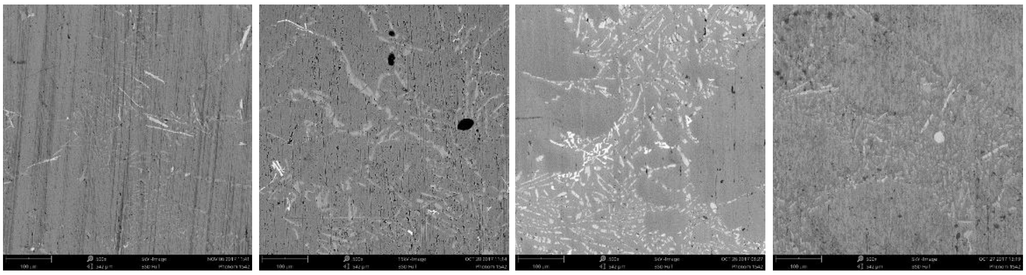

a) b) c) d)

Figure 2. Surface of nanocomposite with magnification x500 a) A356, b) A356/0.2 wt.% SiC, c) A356/0.3 wt.% SiC and d) A356/0.5 wt.% SiC

Figure 3. Tribometer testing

After the completed tests, the worn surface of the samples was observed using a scanning electron microscope and an EDS analysis was performed to determine the chemical composition of the nanocomposite.

3. RESULTS AND DISCUSSION

The results of tribological tests of the nanocomposite and A356 base material are shown in the following diagrams (Figs. 4-7). The effect of the silicon carbide reinforcement in the A356 alloy was studied by monitoring the wear of the material, as well as analyzing the worn surfaces using SEM and EDS analysis.

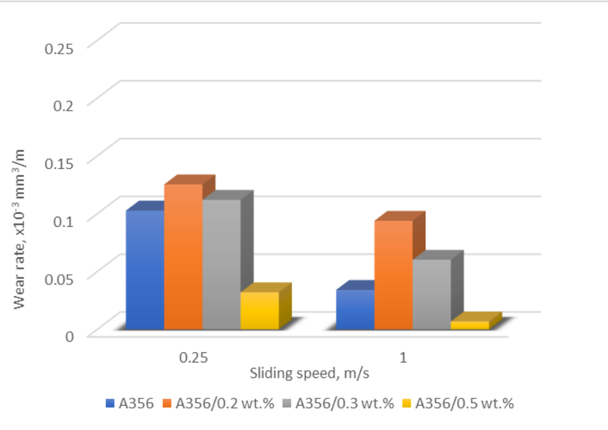

Figure 4. Wear rate at load of 40 N

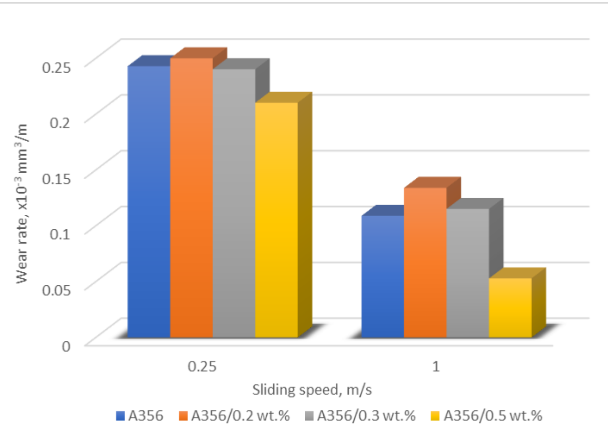

Figure 5. Wear rate at load of 100 N

Forming of the diagrams is based on the measurement of the wear track after 1000 m and the calculation of the wear rate. By comparing the diagrams (figures 4 and 5), the wear rate increases with an increase of load from 40 N to 100 N for all tested materials. This finding is in accordance with the literature data for dry sliding conditions [15-21]. The increase of wear rate is particularly present in the nanocomposite A356/0.5 wt.% SiC at a sliding speed of 0.25 m/s. Then, by increasement of sliding speed wearing rate is reduced, which is justified by the fact that in this test at a higher sliding speed for loads of 40 N and 100 N there was mixed lubrication. Increase in the wear value of the nanocomposites with 0.2 and 0.3 wt.% SiC reinforcement in relation to the base alloy is probably due to the existence of structural imperfections, most likely porosity, which is characteristic for nanocomposites [9, 22-24]. The influence of the reinforcement content on the wear rate, in this study, is the smallest. It is concluded that the improvement of wear resistance occurs only with the content of 0.5 wt.% SiC reinforcement compared to the base alloy of the nanocomposite. The assumption is that an insufficient amount of silicon carbide particles was used in the base to achieve a reinforcement of the base. Also, it can be said that in the nanocomposite with 0.5 wt.% SiC reinforcement, the percentage of the reinforcement is sufficient to annul-cancel the influence of the structural imperfection existence. The same conclusion can be made when it comes to a load of 100 N.

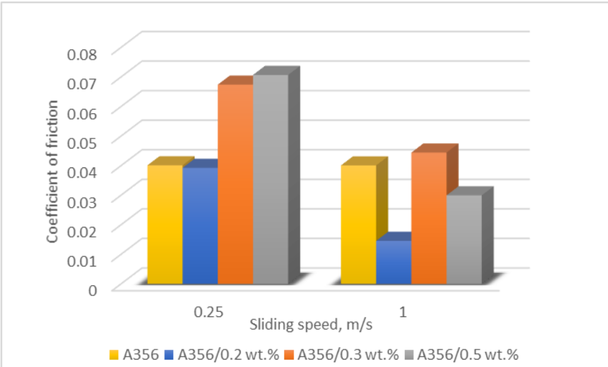

Figure 6. Friction coefficient at load of 40 N

Regarding to the friction coefficient, it is noted that with the increase of sliding speed the friction coefficient decreases, for each observed material individually, which is expected. For the influence of the load, the dependence of the tested materials cannot be observed, because on the basis of the friction coefficient value it is noticed that there was mixed lubrication. In this type of lubrication, it happens that in some segments of the contact there is a separation of the contact surfaces.

This type of lubrication occurs in gear pairs, ball and roller bearings, and even with conventional bearings [25].

By analyzing the experimental results, the dependence between the reinforcement content and the friction coefficient cannot be established. What can be observed from the diagram is that with the increase of the load, the friction coefficient increases, but only at a sliding speed of 0.25 m/s for materials A356 and A356/0.5wt.% SiC. While at a 1 m/s sliding speed, it is observed that the friction coefficient decreases with increasement of the load. The consequence of the difference in friction coefficients is definitely the existence of structural imperfections, which is confirmed by the large differences in the measured values of the friction coefficient.

After tribological testing, wear tracks of tested materials were observed using SEM analysis. Figure 8 shows the wear tracks of the A356 base material (Fig. 8a) and the nanocomposite with 0.5 wt.% SiC (figure 8b) formed under test conditions of F = 100 N and v = 0.25 m/s.

In the previous figures of the worn surfaces of the observed samples, the grooves who follow the sliding direction can be observed. The worn surfaces of the tested materials contain white and gray tracks in certain areas, suggesting the transfer of material from the steel disk to the tested block. White tracks represent iron oxide in the surface layer of the nanocomposite. This phenomenon is present in all investigated nanocomposites and base alloy. By observing the morphology of the worn surfaces, it is noted that the grooves that occur during sliding are parallel to the sliding direction, which indicates that the abrasion wear is present. In addition to abrasion, adhesion appears as the dominant wear mechanism in the investigation of these materials. Comparison of results with the investigation of other researchers is not possible because they performed tribological testing of nanocomposites in conditions without lubrication.

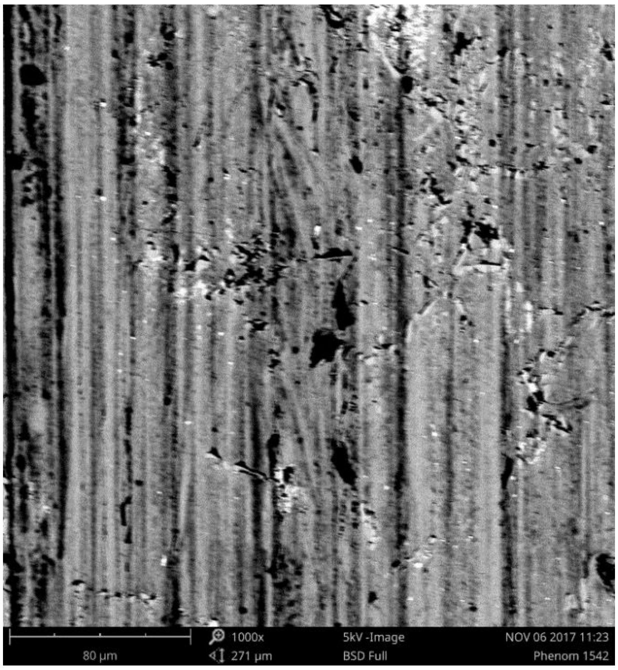

a)

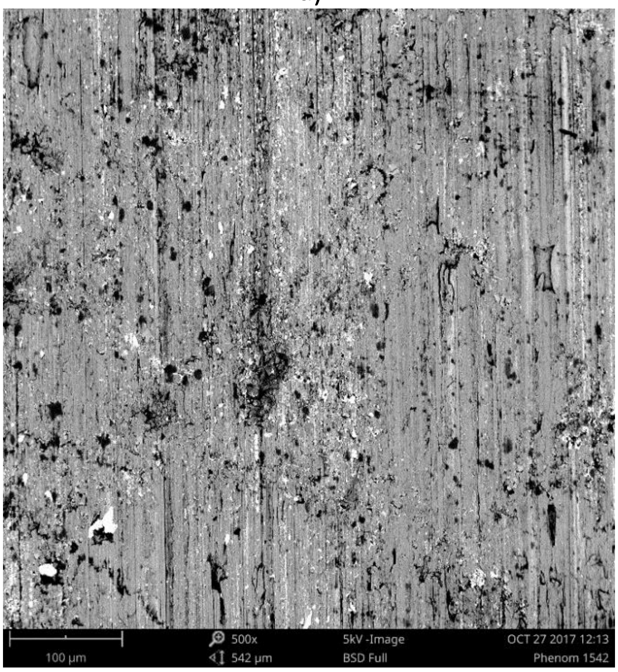

b)

Figure 8. Worn surface of: (a) matrix alloy A356 and (b) nanocomposites with 0.5 wt.% SiC

The presence of nanoparticles led to a reduction in wear which was conclude also in [26] because it was observed that the number and depth of the grooves were smaller in the nanocomposite A356/0.5 wt.% SiC compared to the base alloy. Similar results on the behavior of composites with aluminum base and reinforced with SiC nano particles, have been published in [27,28].

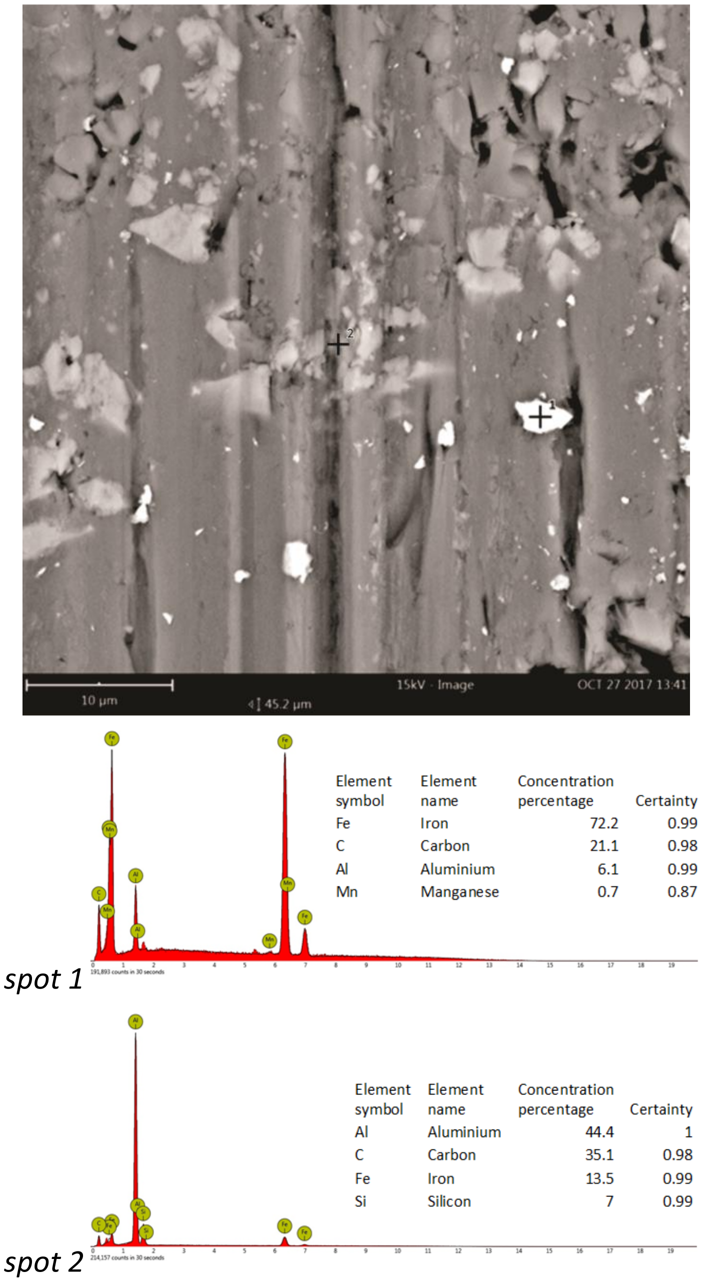

Figure 9. EDS analysis of the wear track of A356/0.5wt.% of nano-SiC

The EDS analysis was done in the wear track of the nanocomposite (Fig. 9), which was created under testing conditions of load of 40 n and sliding speed of 0.25 m/s. The EDS analysis confirmed that the brighter surfaces on the worn surface beside the aluminum element contain a significant amount of iron. This confirms that there is a tranfer of material moving from the steel disk to the tested blocks.

4. CONCLUSION

Aluminum composites reinforced with silicon carbide nano particles were produced by a modified compocasting process with different wt.% of SiC particles in the A356 base alloy. Experimental testing was carried out on a block-on-disc tribometer under lubrication conditions to examine the effect of the reinforcement on the tribological characteristics of the nanocomposite. Based on this research, the following conclusions can be made:

- Nanocomposites are successfully prepared by a modified compocasting process.
- The content of ceramic particles of silicon carbide in the A356 alloy should only be above 0.3 wt.%, in order to improve the wear resistance of the

nanocomposite regarding to the base alloy. More precisely, in the nanocomposite with 0.5wt.% SiC, the effect of the reinforcement has diminished the existing structural irregularities which can be observed based on the wear.

- The dependence of the effect of the reinforcing particles on the friction coefficient of the material could not be established. The only thing that can be noted is that the increase in the sliding speed decreases the friction coefficient for each material that was investigated.
- An analysis of the surface surfaces with SEM and EDS nanocomposites revealed abrasion as the main wearing mechanism, which is characterized by the formation of grooves. Furthermore, based on the transfer of material from the disc to the tested samples, it is concluded that besides abrasion there is, also, adhesion.
- The future investigations will focus on precise determination of the density and porosity of the materials in order to confirm the results that are obtained.

ACKNOWLEDGEMENT

This work has been performed as a part of activities within the Projects TR 35021 and TR 34028. These projects are supported by the Republic of Serbia, Ministry of Education, Science and Technological Development, whose financial help is gratefully acknowledged. Collaboration through the bilateral Project No. 451-03-02294/2015-09/9 and TÉT_16-1-2016-0164 between Republic of Serbia and Hungary is also acknowledged

REFERENCES

[1] H. Tazari, M.H. Siadati: Synthesis and mechanical properties of aluminum alloy 5083/SiCnp nanocomposites, Journal of Alloys and Compounds, Vol. 729, pp. 960-969, 2017.

[2] L.K. Singh, A. Bhadauria, S. Jana, T. Lah: Effect of Sintering Temperature and Heating Rate on Crystallite Size, Densification Behaviour and Mechanical Properties of Al-MWCNT Nanocomposite Consolidated via Spark Plasma Sintering, Acta Metallurgica Sinica, Vol. 31, pp. 1019–1030, 2018.

[3] S. Veličković, S. Garić, B. Stojanović, A. Vencl: Tribological properties of aluminium matrix nanocomposites, Applied Engineering Letters, Vol. 1, No. 3, pp. 72-79, 2016.

[4] I. Manivannan, S. Ranganathan, S. Gopalakannan, S. Suresh, K. Nagakarthigan, R. Jubendradass: Tribological and surface behavior of silicon carbide reinforced aluminum matrix nanocomposite, Materials Surfaces & Interfaces, Vol. 8, pp. 127–136, 2017.

[5] J.P. Davim, C.A. Charitidis (Eds.): Nanocomposites materials, manufacturing and engineering, Springer Heidelberg New York Dordrecht London, 2013.

[6] O. Yaghobizadeh, H.R. Baharvandi, A.R. Ahmadi E. Aghaei: Development of the Properties of Al/SiC Nano-Composite Fabricated by Stir Cast Method by Means of Coating SiC Particles with Al, Silicon, Vol. 11, No. 2, pp. 643–649, 2018.

[7] Y. Du, P. Zhang, W. Zhang, Y. Wang: Distribution of SiC particles in semisolid electromagnetic-mechanical stir-casting Al-SiC composite , China foundry, Vol. 15, No. 5, pp. 351-357, 2018.

[8] S. Wu, D. Yuan, S. Lü, K. Hu, P. An: Nano-SiCp particles distribution and mechanical properties of Al-matrix composites prepared by stir casting and ultrasonic treatment, China Foundry, Vol. 15, No. 3, pp. 203-209, 2018.

[9] R. Ashok Kumar, T.S. Krishnakumar: Casting and characterization of Al6063/SiC nano composites produced using stir casting method, Materials Today: Proceedings, Vol. 5, No. 11, pp. 23853–23862, 2018.

[10] A. Prasad Reddy, P. Vamsi Krishna, R.N. Rao: Two-body abrasive wear behaviour of AA6061-2SiC-2Gr hybrid nanocomposite fabricated through ultrasonically assisted stir casting, Journal of Composite Materials, Online First, 2019.

[11] N. Sharma, S.N. Alam: Influence of Surface Roughness on Wear Behaviour of Ceramic Nanocomposites, Materials Today: Proceedings, Vol. 5, No.14, pp. 28051–28060, 2018.

[12] K.K. Ikpambese, E.A. Lawrence: Comparative Analysis of Multiple Linear Regression and Artificial Neural Network for Predicting Friction and Wear of Automotive Brake Pads Produced from Palm Kernel Shell, Tribology in Industry, Vol. 40, No. 4 pp. 565-573, 2018.

[13] T. Varol, A. Canakci, S. Ozsahin: Prediction of effect of reinforcement content, flake size and flake time on the density and hardness of flake AA2024-SiC nanocomposites using neural networks, Journal of Alloys and Compounds, Vol. 739, pp. 1005-1014, 2018.

[14] S. Veličković, B. Stojanović, M. Babić, A. Vencl, I. Bobić, G. Vadászné Bognár, F. Vučetić: Parametric optimization of the aluminium nanocomposites wear rate, Journal of the Brazilian Society of Mechanical Sciences and Engineering, Vol. 41, No. 19, pp. 1-10, 2019.

[15] E.M. Sharifi, F. Karimzadeh: Wear behaviour of aluminium matrix hybrid nanocomposites fabricated by powder metallurgy, Wear, Vol. 271, No. 7-8, pp. 1072–1079, 2011.

[16] N. Nemati, R. Khosroshahi, M. Emamy, A. Zolriasatein: Investigation of microstructure, hardness and wear properties of Al-4.5 wt.% Cu–TiC nanocomposites produced by mechanical milling, Materials & Design, Vol. 32, No. 7, pp. 3718–3729, 2011.

[17] M.K. Abbass, M..J. Fouad: Study of wear behavior of aluminum alloy matrix nanocomposites fabricated by powder technology, Engineering and Technology Journal, Vol. 32, No. 7, pp. 1720–1732, 2014.

[18] D. Jeyasimman, R. Narayanasamy, R. Ponalagusamy, V. Anandakrishnan, M. Kamaraj: The effects of various reinforcements on dry sliding wear behaviour of AA 6061 nanocomposites, Materials & Design, Vol. 64, pp. 783–793, 2014.

[19] M. Karbalaei Akbari, S. Rajabi, K. Shirvanimoghaddam, H.R. Baharvandi: Wear and friction behavior of nanosized TiB_2 and TiO_2 particle-reinforced casting A356 aluminum nanocomposites: A comparative study focusing on particle capture in matrix, Journal of Composite Materials, Vol. 49, No. 29, pp. 3665–3681, 2015.

[20] K.K. Ekka, S.R. Varun Chauhan: Dry sliding wear characteristics of SiC and Al_2O_3 nanoparticulate aluminium matrix composite using Taguchi technique, Arabian Journal for Science and Engineering, Vol. 40, No. 2, pp. 571–581, 2015.

[21] I.E. Kalashnikov, L.K. Bolotova, L.I. Kobeleva, P. A. Bykov, A. G.Kolmakov: Wear products that form during tribological tests of aluminum-matrix composite materials, Russian Metallurgy, Vol. 2015, No. 4, pp. 285–289, 2015.

[22] H. Ezatpour, S. Sajjadi, M. Sabzevar, Y. Huang: Investigation of microstructure and mechanical properties of Al6061-nanocomposite fabricated by stir casting, Materials & Design, Vol. 55, pp. 921-928, 2014.

[23] A. Mazahery, M. Ostadshabani: Investigation on mechanical properties of nano-Al2O3-reinforced aluminum matrix composites, Journal of Composite Materials, Vol. 45, No. 24, pp. 2579-2586, 2011.

[24] M. Karbalaei Akbari, H.R. Baharvandi, O. Mirzaee: Nano-sized aluminum oxide reinforced commercial casting A356 alloy matrix: Evaluation of hardness, wear resistance and compressive strength focusing on particle distribution in aluminum matrix, Composites Part B: Engineering, Vol. 52, pp. 262-268, 2013.

[25] M. Babić, Monitoring of lubricating oil, Faculty of mechanical engineering, Jugoslavian tribology society, Kragujevac, 2004 (in Serbian).

[26] I. Manivannan, S. Ranganathan, S. Gopalakannan, S. Suresh, K. Nagakarthigan, R. Jubendradas: Tribological and surface behavior of silicon carbide reinforced aluminum matrix nanocomposite, Surfaces and Interfaces, Vol. 8, pp. 127-136, 2017.

[27] N. Singh, M.I.U. Haq, A. Raina, A. Anand, V. Kumar, S.M. Sharma: Synthesis and tribological investigation of Al-SiC based nano hybrid composite, Alexandria Engineering Journal, Vol. 57, No. 3, pp. 1323-1330, 2017.

[28] M. Moazami-Goudarzi, F. Akhlaghi: Wear behavior of Al 5252 alloy reinforced with micrometric and nanometric SiC particles, Tribology International, Vol. 102, pp. 28-37, 2016.

Serbian Tribology Society

SERBIATRIB '19

16th International Conference on Tribology

Faculty of Engineering
University of Kragujevac

Kragujevac, Serbia, 15 – 17 May 2019

ALUMINIUM METAL MATRIX COMPOSITE SINTERING WITH ELECTROLESS METALLIZED COMPONENTS

Valentin KAMBUROV, Rayna DIMITROVA, Antonio NIKOLOV, Mara KANDEVA, Anton MIHAYLOV
Technical University of Sofia, Bulgaria
*Corresponding author: vvk@tu-sofia.bg

Abstract: *In this work was studied the creation possibilities of Aluminium Metal Matrix Composite (AlMMC) with joint electroless co-metallized matrix and non-metallic components. The metal matrix is aluminium alloy (AlSi9Cu3) turnings preliminary Ni-Cu-P coated at the same time as the reinforcing phase thereafter mixed and sintered together. Different types of non-metallic reinforcement and un-reinforcement phases are used to create the sintered composites with aluminium powder, silicon carbide microparticles and carbon nanotubes (CNTs). A comparative analysis of the morphology, hardness and the elemental composition of the obtained composite materials were presented; also tribological research was performed.*

Keywords *aluminium metal matrix composites, electroless metallization, tribology, wear resistance, sintering.*

1. INTRODUCTION

Aluminium Metal Matrix Composites (AlMMC) offer significant potential for use in the automotive and aviation engineering due to their light weight and good mechanical properties coupled with improved wear resistance [1, 2]. Compared to casting, powder metallurgy has the advantage of being able to produce hypereutectic Al-Si alloys with a high percentage reinforcing phase, which enhances the wear resistance of the produced materials and significantly alters their mechanical properties [3, 4].

The aluminium matrix of most of the structural composites is based on wrought or cast alloy composition containing Cu, Si and / or Mg, and relatively rarely Zn [5, 6]. When composing AlMMC, hard ceramic particles with sharp edges of Al_2O_3, SiC or $ZrSiO_4$ spherical particles and some industrial waste such as fly ash with non-sharp morphology are traditionally used as a reinforcing phase [7]. Carbon nanotubes (CNTs) are a suitable material for the production of Aluminium Metal Matrix Composites by powder metallurgy [8]. Sometimes the carbon nanotubes perform the function of the un-reinforcing phase. To improve the wetting of the non-metallic components of the composite materials (especially in the presence of a liquid phase) and to create better adhesion bonds with the aluminium matrix, electroless metallization of the reinforcing phase is often applied [9-12].

The purpose of the work is to investigate the possibility of creation of Aluminium Metal Matrix Composites based on aluminium turnings and both electroless metsllization (Ni-Cu-P) of the Aluminium Alloy Metal Matrix and reinforcing / un-reinforcing components.

Aluminium alloy turnings (AlSi8Cu3) and three different types of neutral, reinforcing and un-reinforcing material are used to create a co-metallized sintered composite. The three types used materials are as follows: aluminium powder, silicon carbide microparticles and carbon nanotubes (CNTs).

2. MATERIALS AND METHODS

A cast aluminium alloy (EN AB-AlSi8Cu3) is used to produce the aluminium turnings with cross-sectional dimensions of about 0.1 mm x 0.05 mm. The mechanical properties of the basic aluminium alloy EN AB-46200 (DIN 226) are as follows: Brinell hardness 82; yield strength $Rp_{0.2}$ = 130 MPa; ultimate tensile strength R_m = 210 Mpa; with density 2.8 g/cm^3, melting onset (Solidus) 540^{O}C, melting completion (Liquidus) 620^{O}C.

The aluminium powder's size is max. 100 m, stabilized with 2% fat, 90% base substance. The Silicon carbide is 7-10 µm fraction and it is mixed with aluminium powder in a 1: 1 ratio.

The carbon nanotubes (CNTs) had an average diameter of 10-40 nm and a length of 1.0 - 25 m, a purity by weight 93% and a specific surface area 150 – 250 m^2/g.

2.1 Electroless Ni-Cu-P of the Components

All components for sintered composite material, after appropriate surface preparation, are chemically nickel-copper plated / coated.

The solution for electroless ultrasonic treatment for realization of the Ni–Cu-P coating procedure [13, 14] contains, as follows: nickel chloride ($NiCl_2.6H_2O$) - 25-40 g/l; copper sulphate ($NiSO_4.6H_2O$) – 10-25 g/l; ammonium citrate $(NH_4)_2C_6H_6O_7.H_2O$ - 50-80 g/l; sodium citrate ($Na_3C_6H_5O_7..2H_2O$) - 30-50 g/l; and sodium hypophosphate ($NaH_2PO_2.H_2O$) - 10-20 g/l.

The preparation of CNTs includes surface cleaning in acetone (CH_3COCH_3) and surface modification containing the following stages: oxidization in concentrated nitric acid (HNO_3); sensibilization and chemical activation in solution, containing $PdCl_2$ and $SnCl_2$ dissolved in 3M hydrochloric acid (HCl).

The result from the fiber modification and the removal of the oxide layer from the aluminium powder is the creation of a low pH at the dispersion phase surface and accordingly the reduction of the total pH of the metallization suspension.

After electromagnetic stirring the suspension for the plating, along with the activated aluminium powder / SiC / CNTs has a pH value of 5.

The suspension is alkalized with ammonia to pH 9-10 under ultrasonic treatment. The alkalysis of the suspension with ammonia results in a gradual initiation of an exothermic reaction at room temperature resulting in an intense release of hydrogen in the form of bubbles. This reaction is maintained by the treatment in an ultrasonic bath without the need for further heating of the suspension.

The degreased aluminium turnings (AlSi8Cu3) are added to the carbon nanotubes or aluminium powder suspension with a started release of hydrogen, and is waited until the ultrasonic bath reaction is complete. The dense suspension containing the aluminium turnings is transferred from the bath for ultrasonic treatment to electromagnetic stirring.

The suspension is diluted with a new solution and stirred intensive at 1800 rpm. The reaction may be accelerated and the metallization re-started by further heating to 70-80^{O}C. The color of the suspension with light aluminium alloy turns gradually darkens. After the completion of the metallization, the suspension is colored in black due to the deposited nickel-copper-phosphor coating and the surface of the aluminium turnings.

After the completion of the co-nickel-copper metallization of the disperse phase and the aluminium turnings, they are filtered through a filter paper ("blue strip"). After an air drying, the metallized components of the composite material are pulverized to a powder state.

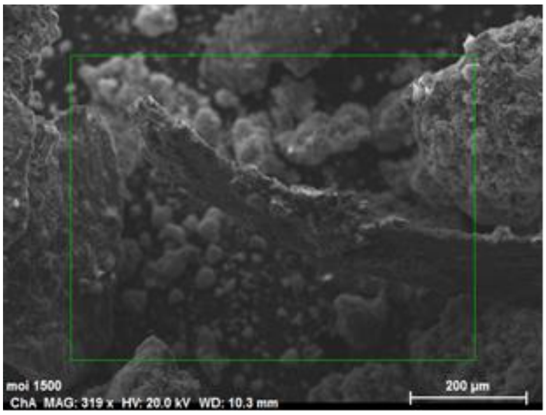

a)

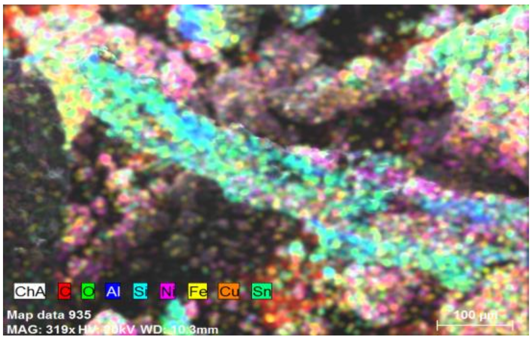

b)

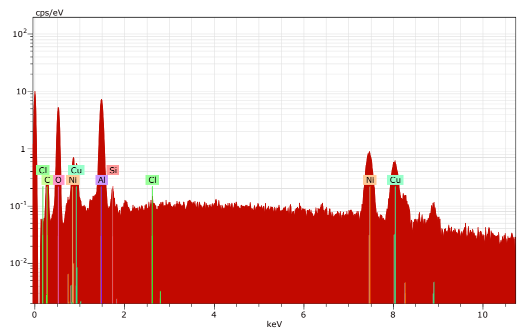

c)

Figure 1. Co-metallized (NI-Cu-P) aluminium alloy (AlSi8Cu3) turnings and CNTs: (a) Scanning electron microscopy; (b) EDX mapping; (c) EDX spectrum

From the Energy Dispersive X-ray EDX analysis (EDX) shown in Figure 1c it can be seen that when co-metallization with the described ultrasonic treatment solution, the nickel and copper peaks are almost equal, which implies the coating of all sintering components with a copper-nickel-based alloy.

2.2 Sintering of Aluminium Metal Matrix Composites

The production of samples for hardness and wear resistance testing from the co-metallized dispersed phase and aluminium alloy turnings involves several major steps: blending, cold compaction at 300 MPa, and sintering at 540 °C for 4 hours in an argon atmosphere. This heating results in a swelling effect and the emergence of fine drops of molten metal on the surface of the samples due to the formation of small amounts of the supersolidus liquid phase from the basic metal alloy matrix (Fig. 2a).

After the sintering, cooling of air and age hardening is also performed on the produced composites, carried out at a temperature of 140-170^{O}C for 10-14 hours.

The sintering material is a matrix of an aluminium alloy turnings of 8% and up to 18% by weight of a reinforcing / un-reinforcing phase. Before the cold compaction, about 1% lubricant Zn stearate is added to the metallized mixture and homogenized by an intensive agitation. No lubricant is added to the CNTs sintering mixtures, because they themselves act as a lubricant.

a)

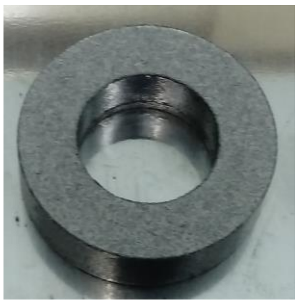

b)

c)

Figure 2. Sintered co-metallized AlMMC with: (a) aluminium powder; (b) silicon carbide microparticles; (c) carbon nanotubes (CNTs)

The samples for wear resistance and hardness testing are rings with an inside diameter of 23 mm, an outer diameter of 42 mm and a height of 10 mm. Due to the high reinforcing / un-reinforcing components strength, the sintered composites have a different color (Fig. 2) and different densities.

Because of its different density, the Brinell hardness is conducted according to ISO 6506-1: 2014 with two load types 24.52 N and 49.03 N at a 1 mm diameter steel ball on the Zwick 4350, Germany.

The tests of the co-metallized AlMMC tribological parameters were performed on the tribometer with a “disc-roll” contact geometry (Fig. 3).

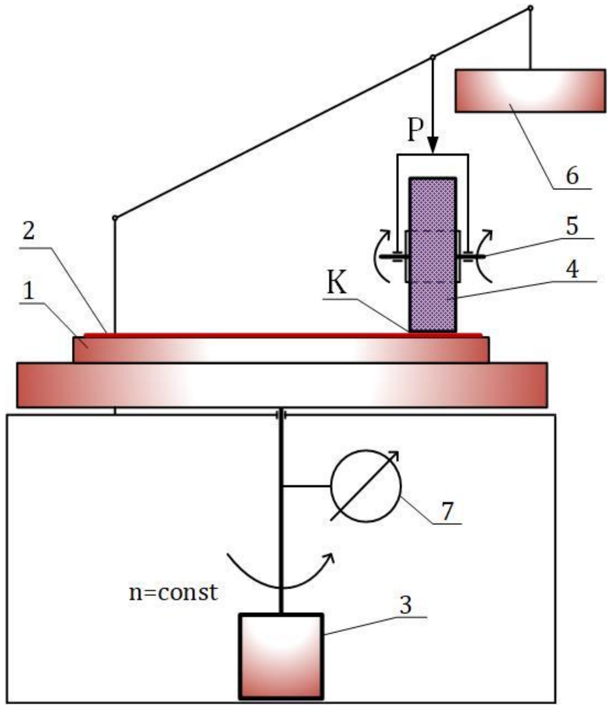

Figure 3. The scheme of “disc-roll” tribometer

The test specimen 4 forms a contact (*K*) with an abrasive surface 2, which is disposed on a horizontal disk 1. The disc 1 rotates around its central vertical axis with a constant frequency ***n***, which is supplied by an electric motor 3. The number of revolutions (*N*) is measured by cyclometer 7.

The test specimen 4 is a disc that rotates freely about a horizontal axis 5. The axes of rotation of the disk 1 and of the sample 4 are two cross axes. An abrasive wear on the cylindrical surface of the specimen occurs in the contact surface (*K*). The contact load (*P*) is provided by weight 6 on the axis 5. The test specimen 4 has the following dimensions: outer diameter Ø 43 mm inside diameter Ø 23.5 mm and contact width 10 mm. The nominal contact area between the abrasive surface and the sample is about 10 mm^2. The linear sliding speed of the center of gravity of the contact surface is 0.239 m/s.

Abrasive wear is calculated as a mass loss, i.e. as a difference between the initial mass of the sample and its mass after given number of abrasion cycles (*N*), counted by the cyclometer. Before and after testing, the mass of co-metallized AlMMC disc is measured by the electronic balance with accuracy of 0.1 mg. Normal contact load of 250 g (2.45 N) is constant for all tests and co-metallized AlMMC. The sliding distance (***S***) is calculated from the following equation

$$S \quad 2 \quad N \qquad (1)$$

where: ***r*** = 35 mm is the distance between the rotational axis of disc sample and mass centre of the contact area, and *N* is the number of abrasion cycles.

The wear resistance I is calculated according to the formula

$$I \quad \rho.A_a S/m \qquad (2)$$

where: ρ is the density of the composite material, A_a - the nominal contact surface, and *m* - the measured mass wear.

3. TESTING AND RESULTS

3.1 Morphology and Structure of the AlMM Composites

Results from Scanning Electron Microscopy of fracture of sintered co-metallized AlMMC with 18% by weight of aluminium powder are shown in Fig. 4. The photos are show globalized during the sintering aluminium powder (with a melting point of 660^{O}C) between regions with a locally crystallized supersolidus liquid phase (Fig. 4a).

The EDX microanalysis show the presence of the elements Ni and Cu (Fig. 4b, c), which prove the committed nickel-copper coating.

Results from Scanning Electron Microscopy of fracture of sintered co-metallized AlMMC with 18 % silicon carbide and aluminium powder in a ratio of (1:1) are shown in Fig. 5. The silicon carbide particles with their typical sharp edges located in the aluminium alloy matrix are clearly shown on the photos (Fig. 5a).

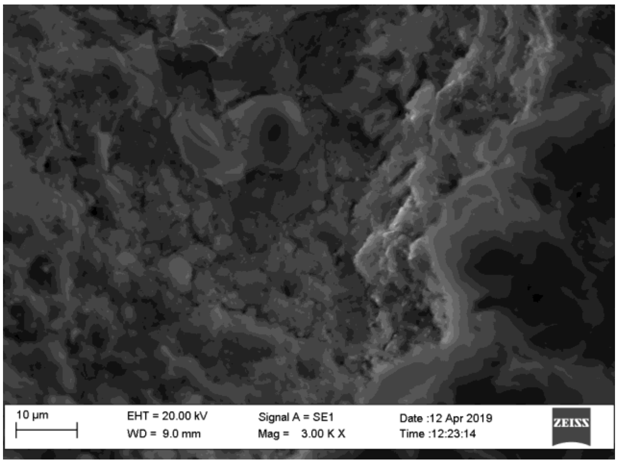

a)

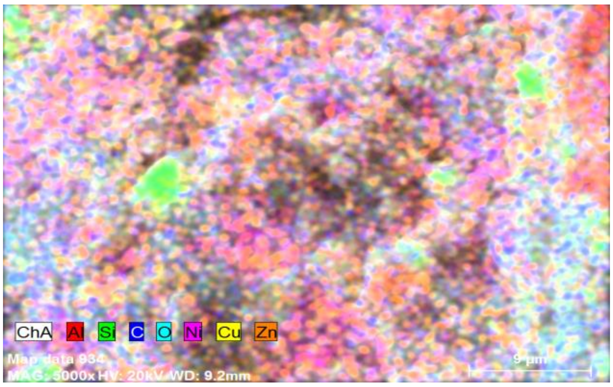

b)

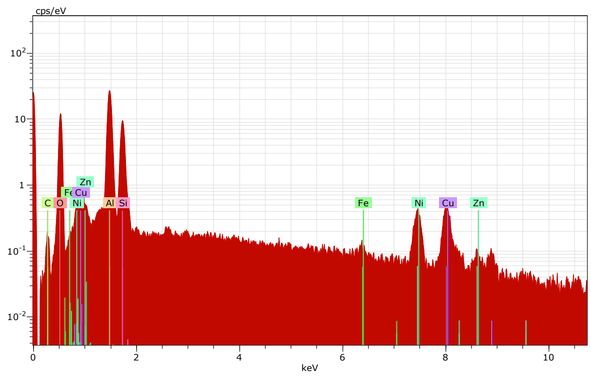

c)

Figure 4. Sintered co-metallized (NI-Cu-P) AlMMC with 18% aluminium powder: (a) SEM magnification 3 000; (b) EDX mapping; (c) EDX spectrum

The EDX microanalysis shows the presence of the elements Ni and Cu (Fig. 5b, c), which prove the committed nickel-copper coating.

Results from Scanning Electron Microscopy of fracture of sintered co-metallized AlMMC with 8 % carbon nanotubes are shown in Fig. 6.

The metallized carbon nanotubes in the aluminium matrix can be distinguished only at large magnitudes from 30 000 to 50 000 times. Distinct CNTs can be distinguished in the cluster beads formed shown In the Figure 6a. Those clusters are seen as separate balls with a scratchy surface at smaller magnitude (Fig. 6b).

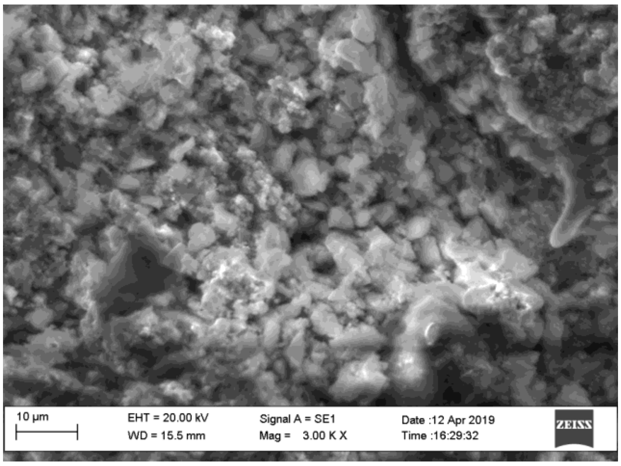

a)

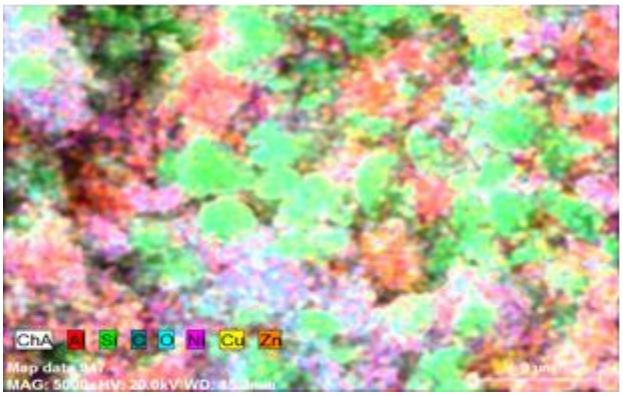

b)

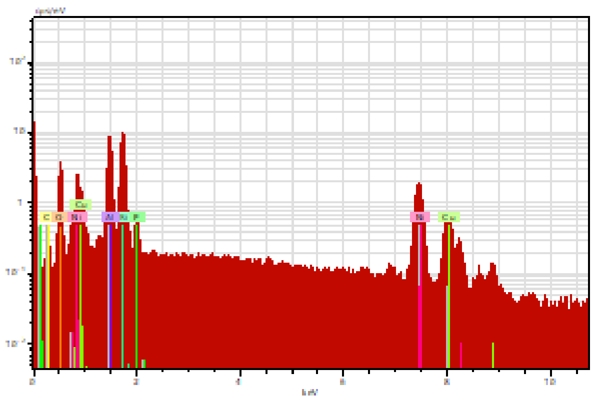

c)

Figure 5. Sintered co-metallized (NI-Cu-P) AlMMC with 18% SiC and Al powder: (a) SEM magnification 3 000; (b) EDX mapping; (c) EDX spectrum

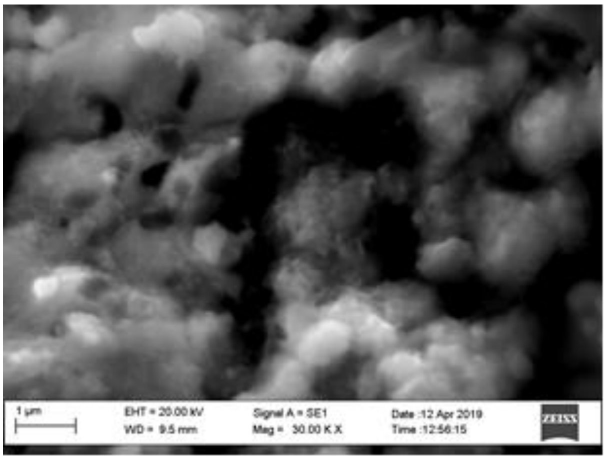

a)

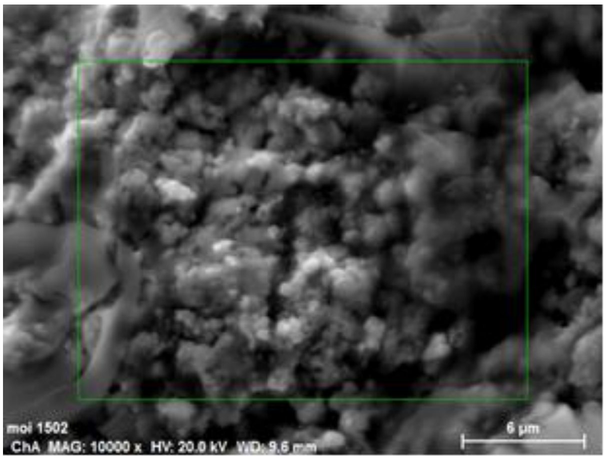

b)

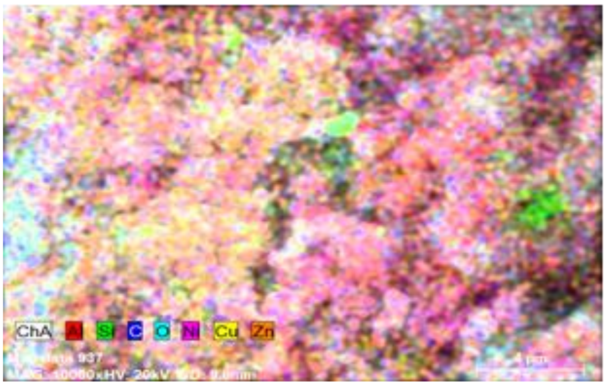

c)

Figure 6. Sintered co-metallized (NI-Cu-P) AlMMC with 18% CNTs: (a) SEM magnification 30 000; (b) EDX magnification 10 000; (c) EDX mapping

3.2 Results from AlMM Composites Hardness

Table 1 shows the results from the density determination and the hardness testing (mean values and standard deviation S_{HB}) of the sintered co-metallized AlMMC composites with different type and quantity of neutral, reinforced and un-reinforced components.

Table 1. Results of the hardness testing and density of sintered co-metallized AlMMC

Sintered material	Density, g/cm^3	Hardness HBS	
		Mean value	S_{HB}
Al turnings only (№1)	1.76	$25.6\ ^{1.86}_{1.94}$	0.40
Al turnings only Ni-Cu (№2)	2.29	$30.7\ ^{3.90}_{4.80}$	1.22
Al +8% powder Ni-Cu (№3)	2.50	$46.3\ ^{3.99}_{5.01}$	1.20
Al +18% powder Ni-Cu (№4)	2.54	$43.7\ ^{3.82}_{4.58}$	1.19
Al + 8% SiC Ni-Cu (№5)	2.22	$53.4\ ^{8.30}_{1.60}$	1.49
Al + 18% SiC Ni-Cu (№6)	2.26	$51.0\ ^{4.10}_{3.50}$	0.88
Al + 4% CNTs Ni-Cu (№10)	1.87	$19.7\ ^{5.48}_{4.82}$	1.05
Al + 8% CNTs Ni-Cu (№8)	1.77	$11.0\ ^{2.84}_{1.46}$	0.49
8% CNTs temp. Ni-Cu (№13)	1.78	$18.1\ ^{5.59}_{3.21}$	1.10

The density and the hardness of sintered co-metallized AlMMC composites depends on the type and the percentage of the metallised dispersed phase (Table 1). The Ni-Cu coating of aluminium turnings leads to a 20% increase in the hardness, but also to an increase in the non-uniformity of the composite structure.

Insertting the neutral aluminium powder to the aluminium turnings increases the hardness with 70-80% and improves the interfacial bonding in the sintered composite.

Highest hardness values have related to ceramic reinforcement composites (silicon carbide and aluminium powder SiC and Al powder) in which a double increase was observed. The excessive increase in the percentage of the reinforcement phase from 8 % to 18 % leads not only to a slight decrease in the hardness and the density, but also to a degradation of the turnings' interfacial bonding into the common aluminium alloy matrix.

Lowest values of the mechanical parameters and the density is accounted in the sintered co-metallized AlMMC with CNTs. Their comparison with other composites and their behavior during the wear resistance and hardness test shows that the CNTs to a large extent preserved their original structure in the aluminium alloy matrix and they did not break into soot during the compaction at 300 MPa.

The evaluation of this behavior, determination of their friction coefficient and finding more suitable sintering modes are a subject to future research on improving the mechanical behavior of those AlMMC.

3.3 Results from AlMM Composites Tribological Properties

For a reference sample is selected a sintered material only from aluminium turnings.

On the graphs of Figure 7 and Figure 8 there are shown the results from the determination of the mass wear rate and wear resistance of sintered co-metallized AlMMC composites with neutral and reinforcing components.

The lowest wear rate (Fig. 7) and highest wear resistance (Fig. 8) was demonstrated by the sintered co-metallized AlMMC with 8 % Al powder. They are with increased wear resistance by about 50% compared to the reference sample of aluminium turnings.

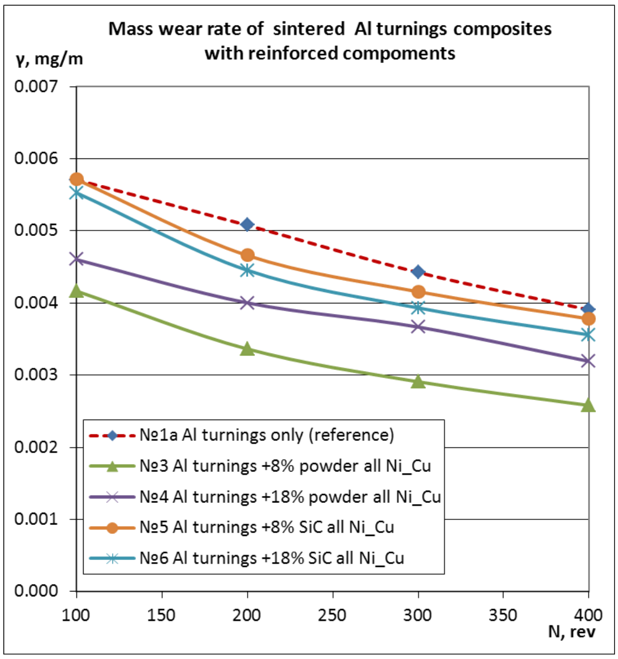

Figure 7. Variation of mass wear rate with the number of friction cycles for AlMMC specimens with reinforcing components

On the graphs of Figure 9 and Figure 10 there are shown the results from the determination of the mass wear rate and the wear resistance of sintered co-metallized AlMMC composites with CNTs.

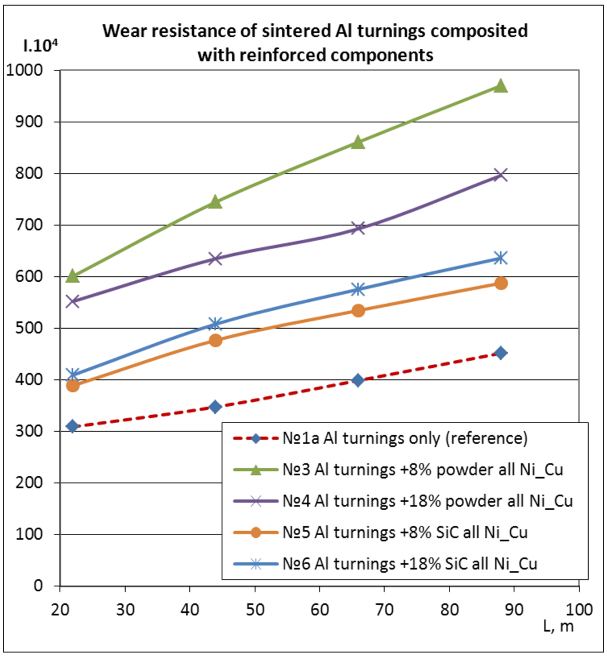

Figure 8. Variations of abrasive wear resistance of AlMMC specimens with reinforcing components

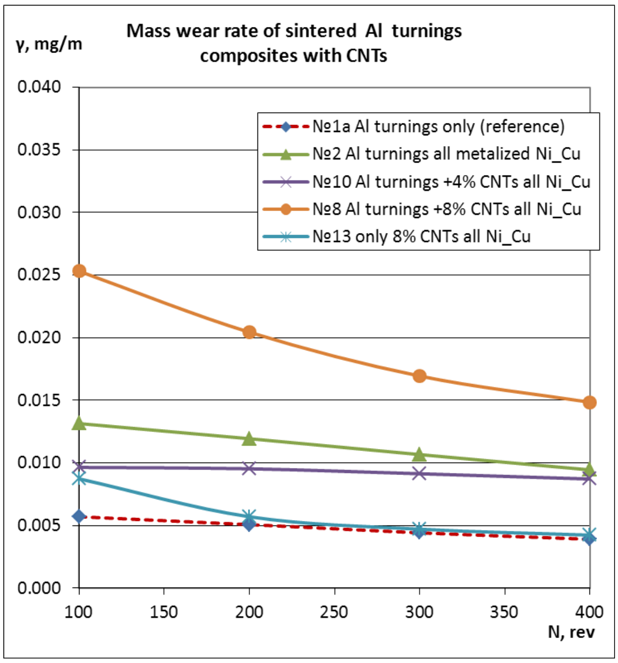

Figure 9. Variation of mass wear rate with the number of friction cycles for AlMMC specimens with CNTs

The highest wear rate is related to AlMMC composites with 8 % CNTs (Fig. 9). The next increase in their percentage ratio results in an instability and a disintegration of the sintered under the specified parameters composite.

The behavior of the sintered co-metallized AlMMC un-reinforced with CNTs shows, that due to the metallization, they have retained their structure and they did not decay to soot during the compaction. However, this results in an instability of the composite material and it does not allow the integration of a higher percentage of CNTs into the aluminium alloy matrix.

The metal-metal composite of metallized (Ni-Cu) aluminium turnings without an additional phase also increases the wear rate and decrease the wear resistance compared to the reference sample (Figs. 9 and 10).

Best performance demonstrates the specimen of Ni-Cu metallized carbon fiber CNTs (without aluminium turnings) (Fig. 10), obtained by additional heating during the electroless metallization. It has a wear resistance commensurate with that of the reference sample, but probably it has a very different coefficient of contact friction.

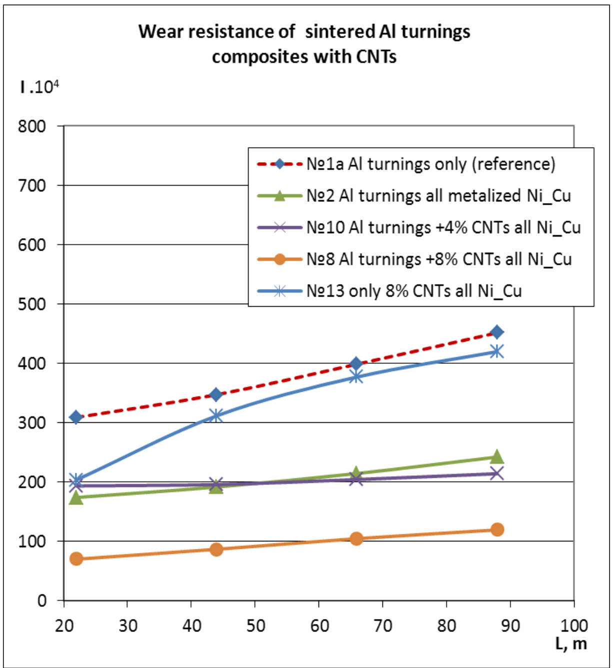

Figure 10. Variations of abrasive wear resistance of AlMMC specimens with with CNTs

On Figure 11 the sintered co-metallized AlMMC composites are compared to the reference sample in regard to their relative abrasion wear resistance.

The AlMMC with reinforcing components have 100-120% increase in wear resistance compared to the reference sample. The AlMMC with neutral components have only 20-40% increase in their wear resistance.

The AlMMC with CNTs have 40-50% decrease in their wear resistance. The specimen from only metallized 8% CNTs without aluminium turnings has a wear resistance commensurate with that of the reference sample.

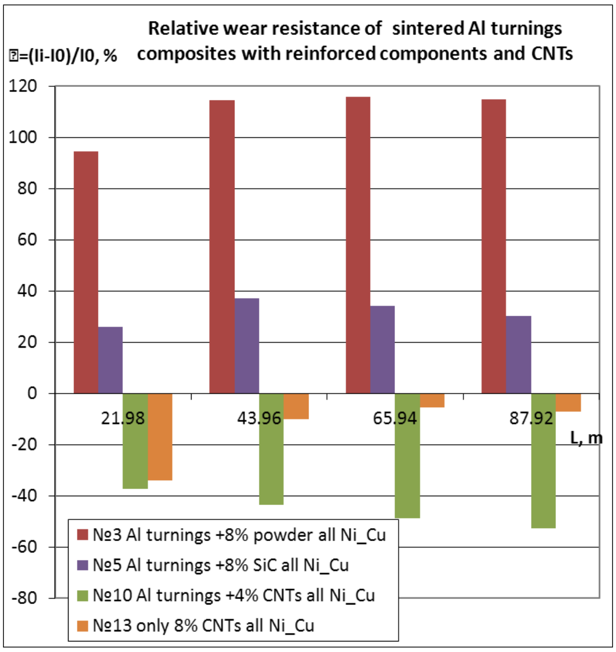

Figure 11. Relative wear resistance change of co-metallized AlMMC specimens with reinforcing components and with CNTs

4. CONCLUSIONS

1. It has been found that the addition of a neutral phase with another fractional composition to the aluminium turnings (in this case aluminium powder) significantly improves the interfacial bonding, the hardness and the wear resistance of the sintered co-metallized AlMMC composites.

2. Co-metallized ceramic reinforced AlMMC demonstrate a double increase in hardness, but the excessive increase in the percentage of the ceramic reinforcement results in a deterioration of the turnings bonding into the common aluminium alloy matrix.

3. Sintered co-metallized AlMMC composites un-reinforced with CNTs demonstrate the lowest density, mechanical and tribological performance. Their behavior during the test and scanning electron microscopy shows that through to the metallization CNTs have retained their fibrous structure after the cold compaction.

4. It has been proven that it is possible to sinter composite material only from

electroless metallized CNTs obtained by further heating of the solution described in the work. The specimen from metallized CNTs has a wear resistance commensurate with that of the reference sample, but is likely to have a very different coefficient of contact friction.

ACKNOWLEDGEMENT

The authors would like to thank to Assoc. Prof. S. Valkanov, Department of Materials Science and Technology, Technical University – Sofia, for his invaluable help in carrying out the SEM and EDX analysis. The authors would like to thank the Research and Development Sector at the Technical University of Sofia for the financial support.

REFERENCES

[1] Th. Schubert, T. Weißgärber, B. Kieback, H. Balzer, H.C. Neubing, U. Baum, R. Braun: P/M Aluminium Structural Parts for Automotive Application, Proc. of Euro Euro PM2004, EPMA, Shrewsbury, UK (2004), Vol. 5, 627.

[2] A. Pohl: High Wear Resistance Parts of Sintered Aluminium for the Automotive Application, in: *Proc. of Euro PM2005*, EPMA in Prague, Shrewsbury: EPMA, pp. 199-204, 2005.

[3] A. Dudhmande, Th. Schubert, M. Balasubramanian, B. Kieback: Sintering and properties of new P/M Aluminium Alloys and Composites, Euro PM2005, Metal Matrix Composites, EPMA, pp. 301-306, 2005.

[4] S. Müller, Th. Schubert, F. Fiedler, R. Stein, B. Kieback, L. Deters: Properties of Sintered P/M Aluminium Composites, Euro Euro International Powder Metallurgy Congress and Exhibition PM 2011, Barcelona, 2011.

[5] M. Babic, S. Mitrovic, I. Bobic: Tribological properties of composites with substrate made of ZA-*27 alloy reinforced by the graphite particles*, Tribology in Industry, Vol. 29, No. 34, pp. 3-8, 2007.

[6] S. Mitrovic, M. Babic, B. Stojanovic, N. Miloradovic, M. Pantic, D. Dzunic, Tribological Potencial of Hybrid Composites Based on Zinc and Alluminium Alloys Reinforced with SiC and Graphite Particles, Tribology in Industry, Vol. 34, No.4, pp. 177-185, 2012.

[7] P.K. Rohatgi, R.Q Guo, H. Iksan, E.J. Borchelt, R. Asthana: Pressure infiltration technique for synthesis of aluminum-fly ash particulate composite, Materials Science and Engineering, Vol. A 244, pp. 22-30, 1998.

[8] A. Agarwal, S.R. Bakshi, D. Lahiri: *Carbon nanotubes: Reinforced metal matrix composites*, CRC Press Taylor & Francis group, p. 296, 2011.

[9] R. Dimitrova, M. Kandeva, V. Kamburov, M. Jordanov: Mechanical and tribological characteristics of hardfaced dispersive reinforced aluminium metal matrix layers, Journal of the Balkan Tribological Association Vol. 23, No. 4, pp. 641-652, 2017.

[10] R. Dimitrova, M. Kandeva, V. Kamburov, Mechanical and tribological characteristics of TIG hardfaced dispersive layer by reinforced with particles extruded aluminium, Tribology in Industry Journal, Vol. 38, No. 1, pp. 9-19, 2017.

[11] V. Kamburov, R. Dimitrova, M. Kandeva: Introduction of nickel coated on silicon carbide particles in aluminium metal matrix hardfaced by MIG/TIG processes on precoated flux layer, Tribology in Industry, Vol. 40, No.1, pp. 73-80, 2018.

[12] M. Kandeva, V. Kamburov, E. Zadorozhnaya, Zh. Kalitchin: Abrasion Wear of Electroless Nickel Composite Coatings Modified with Boron Nitride Nanoparticles, Journal of Environmental Protection and Ecology, Vol. 19, No. 4, pp. 1690-1703, 2018.

[13] R. Dimitrova, Electroless nickel coatings on silicon carbide particles using two nickel salts in alkaline solution, International Working Conference ''TQM – Advanced and Intelligent Approaches'', Belgrade, Serbia, 2015.

[14] V. Kamburov, R. Dimitrova, K. Nikolov: Electroless nickel coating of carbon microfibres and nanotubes intended for a reinforcing phase in Metal/Polymer matrix composites, Oxidation Communications Journal, Vol. 42, No. 1, pp. 63–73, 2019.

Serbian Tribology Society

SERBIATRIB '19

16th International Conference on Tribology

Faculty of Engineering
University of Kragujevac

Kragujevac, Serbia, 15 – 17 May 2019

COMPUTER AIDED GEOMETRIC DESIGN IN MODELLING OF 3D TEXTILE COMPOSITES

Varun SHARMA[1]*, Fatima ZIVIC[1], Nenad GRUJOVIC[1], Zivana JOVANOVIC[1]
[1]University of Kragujevac, Faculty of Engineering, Kragujevac, Serbia
zivic@kg.ac.rs, gruja@kg.ac.rs, zixi90@gmail.com
*Corresponding author: varun.eu@gmail.com

Abstract: *Orthogonal three-dimensional textile composite was evaluated by using numerical simulation. Three-dimensional (3D) geometry models were created (angle interlock and layer to layer), with 48 % and 53 % overall volume fractions. Warp, weft and binder were adjusted according to the yarn spacing, width, and height. Finite element numerical simulation was realised by using multistep linear static test for general behaviour. Both models were evaluated based on the calculated stress and strain values. Internal yarn architecture and overall volume fractions both have significant influence on the mechanical behaviour of the composite.*

Keywords: *Textile composite, fiber reinforcement, Computer-aided geometric design, CAGD, FEM modelling, Stress, Strain.*

1. INTRODUCTION

Composite materials represent a combination of two or more phases that usually have different physical and mechanical properties at micro and macro scale. Altogether different materials combined together within composite structure, usually exhibit distinctively different properties than each of the constituents. Composites can be made with different structural shapes and sizes of reinforcements within the matrix, such as particulate inclusions, fibers or hybrid composites with several types of reinforcements. Textile composite, or laminate composites with different directions of laminates combinations, have emerged as attractive materials due to their application in aerospace, marine, transportation, and construction industries [1, 2]. They comprise yarns, which are anisotropic in nature and have lower modulus than fiber materials. Traditional laminated composites involve high labour cost and can exhibit delamination which can limit their application [2]. Development and selection of material combination from a wide range of composite structures is complex process. One current trend in textile engineering is to develop advanced composites using low cost, "out of autoclave" (OOA) manufacturing techniques. Instead of processing route that involves industrial autoclave, OOA provides material curing, desired fiber content and voids elimination via other techniques without use of autoclave (vacuum, pressure, or heat). The focus is to create advanced weaving architecture [7].

Efficient methods in design of composite structures engage computer modelling, simulation and numerical analysis of loading and structure responses in terms of resulting mechanical properties. Some of the techniques like Computer Aided Geometric Design (CAGD) that deals with mathematical description of shapes have been used in research of such structures. Design of 3D volumes aimed at 2D and 3D textile structures have been studied [1]. In combination with numerical simulation, development of textile composite structures can be efficiently supported. Modelling software is capable to create different 3D models by variations of weave type and yarns. Fabric compaction and yarn waviness are very important for final deformation properties of the composite and their overall mechanical properties [4, 5]. Additionally, three-dimensional (3D) printing is an additive manufacturing process that can rapidly fabricate samples of different geometries and structures, in order to experimentally study influence of different geometrical design on composite behaviour [11]. Numerical simulation is also powerful technique to study the influence of structural changes within the composite structure, on its mechanical behaviour. Usually, for 2D textile composites, idealised cells are applied in finite elements modelling (FEM) to determine stress – strain response. However, in case of 3D composite structures, such approach showed rather large differences from real cases and accordingly other approaches to finite element analysis (FEA) have been tried, such as voxel-based FEA or continuum damage model [3]. Voxel-based finite element meshing use labeled voxel information, such as computer tomography (CT) scan images, or some other digital images, and convert it to a finite element. Definition of the label is directly linked to different constituent materials within composite. That way, 3d volume model can be created that has close resemblance to the real material structure. Continuum damage models, for fiber reinforced composites, have been developed focused on the onset of intralaminar failure and its evolution until structure collapse, as well as the governing failure mechanisms.

Multi-scale modelling also has been proposed for the investigation of textile composites, such as based on Voronoi tessellation [6]. Homogenisation models that are often used for the characterisation of composites are not well suited for textile composites where geometry and internal architecture governs the stress and strain responses [6, 7]. Mechanical properties of the woven composites with complex 3D structures are significantly influenced by the distribution of different regions within the composite, such as the regions with increased resin content, or waviness [7]. Zones with binding sites represent initiation sites for damage, under all loading conditions, for all woven composites [7]. Different numerical simulation approaches provide different degree of similarity to real mechanical responses of textile composites. Idealised geometry is the most rapid way to predict internal structural behaviour. However, more complex methods, such as Digital Element Method which is focused on compaction process and analytical method that consider undulation of fill, warp and binder yarns, provided better geometry prediction [8]. Resulting elastic properties for all these approaches were similar. Architecture of reinforcements can be observed at micro-scale (fibers and matrix), meso-scale and macro-scale (usually considered as homogenous material) [9].

Three-dimensional modelling allows monitoring of friction and wear of fibers at multiscale level [12]. Computer Aided Geometric Design (CAGD) enabled investigation of different combinations of matrices and reinforcement material in order to obtain composites with the best tribomechanical characteristics, both at micro and macro level [13].

This paper deals with the design of three-dimensional textile composite with different volume fractions in two different geometrical variations. Numerical simulation, by using finite element method (FEM) was realised to obtain stress-strain responses. First model in

3d weave type was created based on angle interlock geometry, with 48 % overall volume fraction. Second model was created in layer to layer format, with 53 % overall volume fraction. Both of the 3D models were simulated under compressive loading. For numerical simulations, simple linear static set was performed with multi set options by using the laminated composite modelling concepts. Open source software TexGen was used for the design and development of three dimensional geometrical model. FEMAP with Nastran (structural package) software was used for the conversion of partial differential equations into finite element code.

2. GENERAL TYPES OF TEXTILE COMPOSITES

General types of textile composites, with their properties are described in Table 1.

Textile composites have arrangement of weft, warp and binder sets, as shown in Fig. 1.

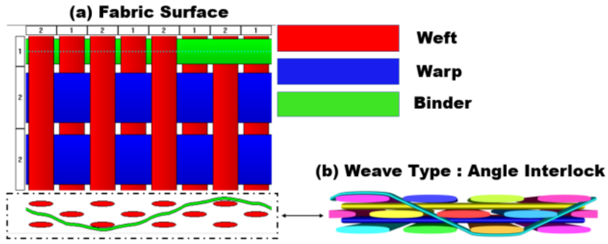

Figure 1. Schematic Representation of orthogonal 3D Woven Fabric Showing (a) Unit cell with tessellation; (b) 3D Weave type: Angle Interlock

They formed tessellations with proper sequence depending on the composite type. Figure 1 illustrates the orthogonal 3D woven fabric in angle interlock form. This model was created in open source software called TexGen. Spacing, width, height, and ratio of binder yarn were set according to real case properties.

Table 1. General types of textile composite and their main properties [1-4]

Type	Woven	Braided	Knitted	biaxial
Main property	- High delamination, resistance	- High Impact resistance	- Elastic, high productivity, low cost - Different types of geometric structures can be made	- Good Quality - Damage tolerance - Good peel strength - Reduced delamination
Angle	- Warp and weft yarns are oriented at 0 and 90 respectively. - Characterised by the repeating pattern of interlacing in warp and weft yarn direction	- Yarns interlacing is not set at 0 and 90 degree - Many forms can be made; one of yarn is set in one direction at some angle and the other half is in opposite direction		Made in three directions: - One in vertical direction (Weft) - Two in diagonal (warp) - 0 and 60 degree
Properties of simple 2D, plain, twill, satin weaves				
Advantages	- Balanced and unbalanced weaves - Open and closed packing - High out of plane strength - Good strength - Anisotropic stability	- Suitable for near net shape structure - Useful in cross sectional shapes such as nozzles, cones	- Low level of fiber packing density - High extendibility	- Quasi Isotropic at macro scale
Drawbacks	- Lower extendibility - Lower deep molding	- Low fiber fractions - Decreased in-plane mechanical properties	- Brittle fiber due to lot of twisting during knitting; may break easily	
Processing	- Vacuum injection process for thermoset matrix - Hybrid yarn technique for thermoplastic matrix	Made by orthogonally interlacing set of yarns	- 3D printing based on geometry model	Warp, weft and binder yarns are stitched together by chain stitch

3. NUMERICAL SIMULATION

Accuracy of modelling is based on material model and element geometry. TexGen software can be used to create 2D and 3D weave model. Unit cell can be assigned to the yarn in a number of different ways. In this work, TexGen software was used for the design of two different three-dimensional weave patterns (Table 2).

Table 1. Parameters of 3D weave pattern model

Parameter	Weft yarns	Warp yarns	Binder yarns
Yarns	4		
Number of yarns layers	3		
Yarn spacing	1	1	0.5
Yarn width	0.8	0.8	0.4
Yarn height	0.1	0.1	0.05
Power ellipse section power	0.6	0.6	0.6
Total number of yarns in warp direction	3	-	-
Ratio of binder yarns	1	-	-

Two different weave models were created, with properties given in Table 2: 1) angle interlock and 2) layer to layer. In case of angle interlock, binder goes in a fixed pattern from top to bottom. Number of weft yarns and weft layers are linked. In case of layer to layer, binder yarn is in stack whereas binder path is selected interactively. Damage and failure behaviour of 2D woven composites have been investigated by using multiscale progressive modelling [10]. TexGen software can create voxel mesh, comparable to the finite element mesh in terms of elastic properties, and local stress field evaluation [9]. First, STEP file was exported from TexGen software and further processed in FEMAP software using the meshing toolbox. As stated above, two varied geometrical model, Angle interlock with 48 % overall volume fraction and Layer to layer with 53 % overall volume fraction, were simulated under compression. Element size was restricted to 0.186, with a total of 10863 and 308892 solid tetrahedral parabolic 10 Node elements, assigned to both models. Both models were simulated with multi step structural static analysis and properties are given in Table 3, as implemented in X, Y, and Z directions. 3D orthotropic material orientation was assigned to the geometry.

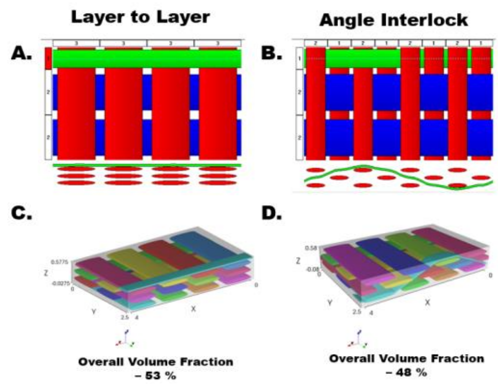

Figure 2. Schematic Representation of textile Composite in 2-Dimensional vie: A) Layer to Layer Format, B) Angle Interlock; and in 3D view: C) overall volume fractions of 53% and D) overall volume fractions of 48%

Linear stress analysis of 3D textile laminate composite was done. At the beginning of the numerical simulation, layup creation was done, followed by generation of the second layup for layers definition. Afterwards, mesh fitting was done and linear static test was realised to obtain stress – strain values. Geometry scale factor was set to mm scale at the beginning of the numerical simulation. 3D orthotropic material was adopted.

Table 2. Table of material properties for constituents and yarn [3]

	E_{11} (GPa)	E_{22} (GPa)	$V_{12} = V_{23}$	V_{23}	$G_{12} = G_{23}$	G_{23} (GPa)	S_{11} (MPa)	S_{22} (MPa)	$S_{12} = S_{13}$ (MPa)	S_{23} (MPa)
Carbon Fiber	238	13	0.20	0.25	13	6	4620	-	-	-
Epoxy Resin MVR 444	3.1	3.1	0.35	0.35	1.2	1.2	77.6	77.6	61.5	61.5
Yarn	167	8.1	0.24	0.37	4.5	3.0	3234	36.4	53.8	61.5

Density, modulus of elasticity in respective directions, and shear modulus were defined as given in Table 3. Poisson's ratio was taken from FEMAP material library for materials given in Table 3. Warp, weft and binder were distinguished in the modelling by giving the upper, lower and middle name with varied thicknesses at different angle starting from 0 – 45 degrees. FEMAP has the possibility to create the laminate's equivalent properties, number of layers and thickness related to plane properties which are usually bending and flexural properties. After sorting out the layers position and thickness, symmetric option was used. Similar approach was applied for the reinforcement fiber by adjusting the thickness and angle. For material orientation direction, Cartesian coordinate system was used. The Nastran bulk data was set to small field.

Upper surface of the geometrical model was loaded with 50 N load, as shown in Fig. 3. Bottom surface was fixed without any translational and rotational degrees of freedom.

Layer to layer and angle interlock geometrical models were evaluated based on the numerical values of stress and strain. Maximum shear stress and maximum principal stress contours, for layer to layer and angle interlock geometrical models are shown in Fig. 4. Model with 53 % volume fraction experienced higher magnitude of stress - strain values in X, Y and Z directions respectively. This is resulting from the amount of fibers and yarns within the structure that increased capability for extension in comparison to model with 48 %. Overall maximum shear stress showed similar behaviour in XY, YZ and ZX directions.

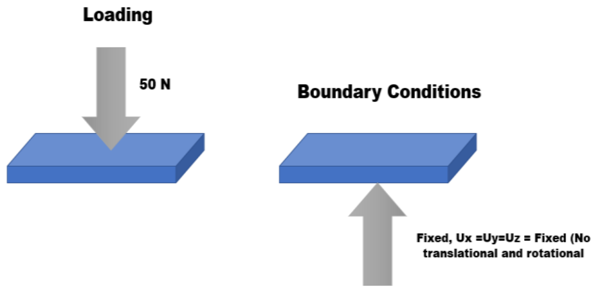

Figure 3. Loading (left) and boundary conditions (right) during uniaxial compressive testing

Results of stress – strain numerical calculations are shown in Fig. 5. Strain as the function of stress is shown for different volume fractions. It can be seen that the highest stress was exhibited for 48% volume fraction.

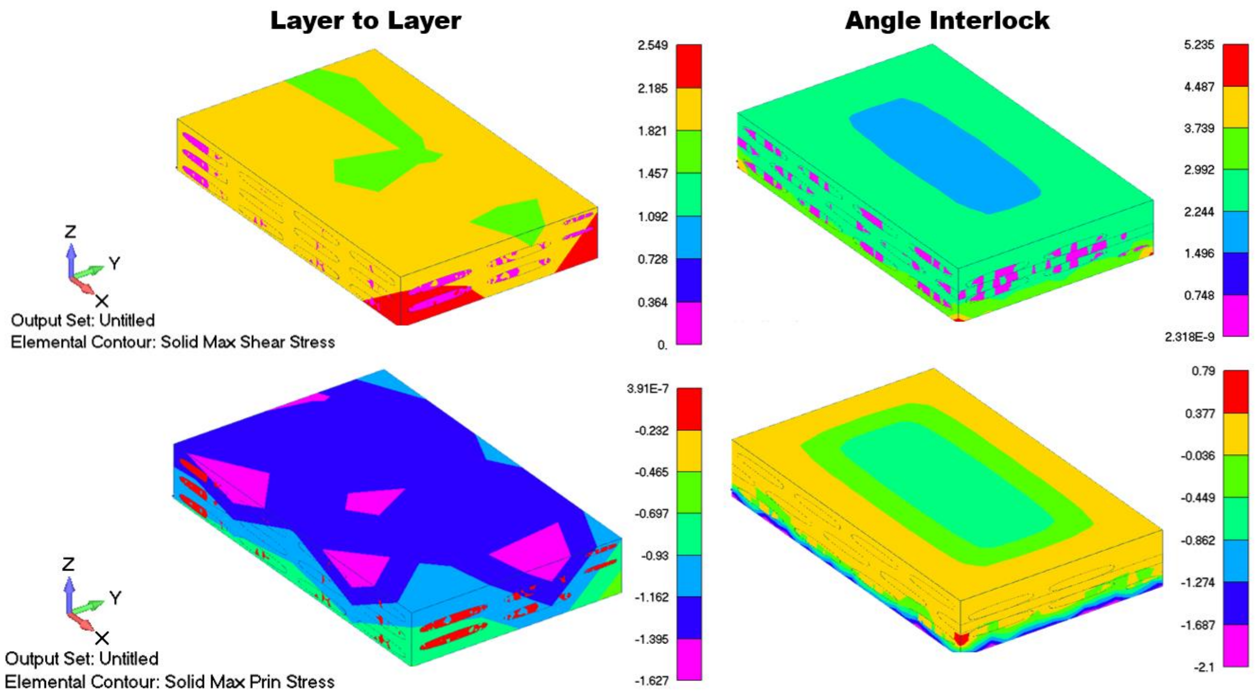

Figure 4. Upper row shows maximum shear stress contours [MPa] for layer to layer and angle interlock geometrical models. The bottom row shows maximum principal stress contours [MPa

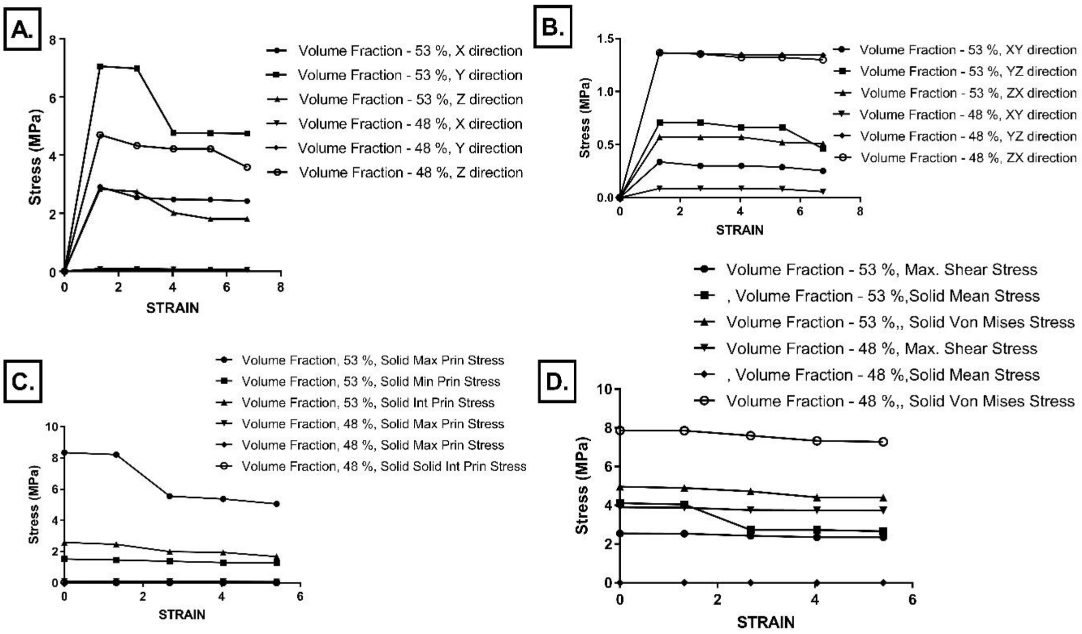

Figure 5. Stress - strain curves in: A) X, Y, Z directions and B) XY, YZ and ZX directions; C) Maximum, minimum and solid principal stress; D) Maximum shear, mean, and Von Mises stress

4. CONCLUSION

Three-dimensional textile composite was evaluated by using computer aided geometric modelling. Two different models having geometrical variation in 3D weave type was developed. Two types of textile composites (Angle interlock and Layer to layer) were model, and warp, weft and binder adjustments. Geometrical models were imported to finite element solver to perform multi set linear static test under compressive load. Results showed that overall volume fractions have significant influence on mechanical properties of the textile composites, especially influenced by the 3D arrangement of reinforcements.

ACKNOWLEDGEMENT

This work was supported by SELECTA project (No. 642642) H2020-MSCA-ITN-2014.

REFERENCES

[1] S. Adanur, T. Liao: 3D modelling of textile composite preforms. Composites Part B, Vol. 29B, pp. 787–793, 1997.

[2] S.Adanur: *Welling Sears Handbook of Industrial Textile*, Technomic, Lancaster, PA, 1995.

[3] S.D. Green, M.Y. Matveev, A.C. Long, D. Ivanov, S.R. Hallett: Mechanical modelling of 3D woven composites considering realistic unit, Composite Structures, Vol. 118, pp. 284–293, 2014.

[4] B.N. Cox, M.S. Dadkhah, W.L. Morris: On the tensile failure of 3D woven composites, Compos Part A: Appl. Sci. Manuf, Vol. 27, pp. 447–58, 1996.

[5] Y. Mahadik, S.R. Hallett: Effect of fabric compaction and yarn waviness on 3D woven composite compressive properties, Compos Part A: Appl. Sci. Manuf, Vol. 42, pp. 1592–600, 2011.

[6] B. El Said, D. Ivanov, A.C. Long, S.R. Hallett: Multi-scale modelling of strongly heterogeneous 3D composite structures using spatial Voronoi tessellation, Journal of the Mechanics and Physics of Solids, Vol. 88, pp. 50–71, 2016.

[7] S. Dai, P.R. Cunningham, S. Marshall, C. Silva: Influence of fibre architecture on the tensile, compressive and flexural behaviour of 3D woven composites, Composites: Part A, Vol. 69, pp. 195–207, 2015.

[8] N. Isart, B. El Said, D.S. Ivanov, S.R. Hallett, J.A. Mayugo, N. Blanco: Internal geometric modelling of 3D woven composites: A comparison between different approaches, Composite Structures, Vol. 132, pp. 1219–1230, 2015.

[9] A. Doitrand, C. Fagiano, F.-X. Irisarri, M. Hirsekorn: Comparison between voxel and consistent meso-scale models of woven composites, Composites: Part A, Vol. 73, pp. 143–154, 2015.

[10] L. Wang, J. Wu, C. Chen, C. Zheng, B. Li, S.C. Joshi, K. Zhou: Progressive failure analysis of 2D woven composites at the meso-micro scale, Composite Structures, 2017.

[11] S. Fafenrot, M. Korger, A. Ehrmann: Mechanical properties of composites from textiles and three-dimensional printed materials, Mechanical and Physical Testing of Biocomposites, Fibre-Reinforced Composites and Hybrid Composites Woodhead Publishing Series in Composites Science and Engineering, pp. 409-425, 2019.

[12] M. Arjmandi, M. Ramezani: Finite element modelling of sliding wear in three-dimensional textile hydrogel composites, Tribology International, Vol. 133, pp. 88-100, 2019.

[13] D.K. Patel, A.M. Waas, C.-F. Yen: Compressive response of hybrid 3D woven textile composites (H3DWTCs): An experimentally validated computational model, Journal of the Mechanics and Physics of Solids, Vol. 122, pp. 381-405, 2019.

Serbian Tribology Society

SERBIATRIB '19

16th International Conference on Tribology

Faculty of Engineering
University of Kragujevac

Kragujevac, Serbia, 15 – 17 May 2019

EMERGENCE OF CONTACT FILMS DURING FRICTION. GEOTRIBOLOGICAL FILMS

Emilia ASSENOVA[1*], Evgenia KOZHOUKHAROVA [2]
[1]Society of Bulgarian Tribologists, Sofia, Bulgaria, emiass@abv.bg
[2]Geological Institute of the BAS, Sofia, Bulgaria, ekozhoukharova@abv.bg
*Corresponding author: emiass@abv.bg

Abstract: *Focusing on frictional surfaces contact interaction study, tribology comprises, beside the well-known friction/wear problems, the research on the genesis, characteristics and functioning of the films formed by the interacting materials in the contact zone. Self-building films occur as natural formations in frictional pairs, such as the secondary protective films, the frictional films formed at the selective transfer during friction, and the geotribofilms between adjacent geological rock plates in the Earth's crust. The paper focusses on the creation of geotribofilms, especially of the mica schist films acting as lubricating films in the shear zones of friction between rock plates. Specifics of geotribological processes and products are the wide extent of scales, which they cover, and the possibility for history time tracking of the entire development of the object.*

Keywords: *friction films, variety of tribology scale levels, geotribological friction films*

1. INTRODUCTION

Concentrating on the contact interaction of frictional surfaces, tribology comprises the study of the contact or the third or body. Surface interaction controls and manages the functioning of practically every mechanism and device through the friction in contact pairs. Friction - a resistance to movement - is a global natural phenomenon of energy transformation and dissipation during the joint action of two surfaces in contact. It represents the processes of deformation and damaging in tribo-couple surface layers. Through managing friction, tribology affects our quality of life.

Friction results of two opposite and simultaneous trends: accumulation of potential energy by the deformable contact and release (dissipation) of that energy. The first one defines the effect of deformation and leads to plastic deformation and damage. The second trend defines the heat effect of friction. Both trends reveal the mechanisms of transformation and dissipation of energy during friction. [1] The high pressures together with shift deformation (i.e. the main components of the friction process), deliver immense energy to the material, and high reaction velocities. [2]. This offers great potential for the utilization of tribology.

The most popular tribological studies are on friction, wear, and on the inserted in the contact coatings and lubricating layers. The emerged during friction films covering the contact surfaces belong to the self-building films. The study of the emergence, the mechanisms of creation and the characteristics of films of material between contacting bodies, and the consequences of film destruction of a film, which are usually manifested by severe friction and wear. Film formation between any pair of sliding objects is a natural phenomenon, a part of the self-regulation and self-organization, aiming protection of the systems' life, which can occur without human intervention. Film formation might be the fundamental mechanism preventing the extremely high shear rates at the interface between two sliding objects. [3]

In the fight for longevity and reliability of the tribosystems, against the disadvantages of friction [4], tribology considers the emergence of films between solid frictional surfaces in the contact evolution in diverse exemplary applications. Self-building films emerge based on the self-organization and synergy in the contact zone [1], and occur in mechanical and non-mechanical tribosystems. Numerous examples are known, like the secondary surface protective films [5,6], the frictional films formed at the selective transfer of material during friction [2,7-12], and the geotribofilms between adjacent geological rock plates in the Earth's crust which control the friction process [13,14]. Geotribology embraces contact processes on the most wide-ranging in scales: from micro/nano- level in the crystal lattice of rocks to mega- or geological level in the contact zones of Earth's crust geological plates, hence the study of geotribofilms is extremely interesting also in the quest of basic resemblance and similarity between friction on various scale level. [15,16]

The paper focusses on the creation of geotribofilms, especially of the mica schists films in the shear zones of friction between rock plates acting as lubricating films.

2. FRICTIONAL FILMS IN NON-MECHANICAL AND INORGANIC TRIBOSYSTEMS. GEOTRIBOFILMS.

The mechanical tribosystems with interacting metal surfaces (machines and mechanisms on the scale-level of everyday life), are subject to the most common tribology research. Non-mechanical sliding systems are not so popular in tribology; however, they provide many interesting examples of film formation during friction [2,3,13,14]. For instance, studies of the movement between adjacent geological plates on the surface of the earth reveal that a thin layer of fragmented rock and water forms between contacting rock plates. [13,14] Chemical reactions between rock and water under high temperatures (about 600°C) and pressures (about 100 MPa) improve the lubricating function of the material in this layer [2,3,13,15,16]. Laboratory tests confirm that sliding friction inducts emergence of a self-building film of fragmented rock at the interface with solid rock. A pair of self-sealing layers attached to both rock surfaces prevent the leakage of water necessary for the lubricating action of the layer of fragmented rock and water [3,13,14]. The thickness of the layer of fragmented rock is between 1 - 100 m, however it is insignificant when compared to the extent of geological plates and these layers can be classified as 'films' [3]. Sliding on a geological scale is controlled by the properties of these lubricating films, and this hints on a fundamental similarity between friction on different scale levels.

The example with geotribological films chosen in the paper refers also to another peculiarity and importance: geotribological products offer the opportunity to observe rests and relics of the whole period of the formation the object. The geotribological objects allow time tracking of the processes of the entire development: from the initial moment, passing through the changes and modifications, up to the ending of the process with new crystallizations.

3. TRIBOMETAMORPHIC MICA SCHISTS AS A LUBRICANT IN THE TECTONIC ZONES OF FRICTION

The chosen example comes from the inorganic nature, namely from the study of friction in the multiple shear zones of friction created in the Earth's crust during tectonic movements.

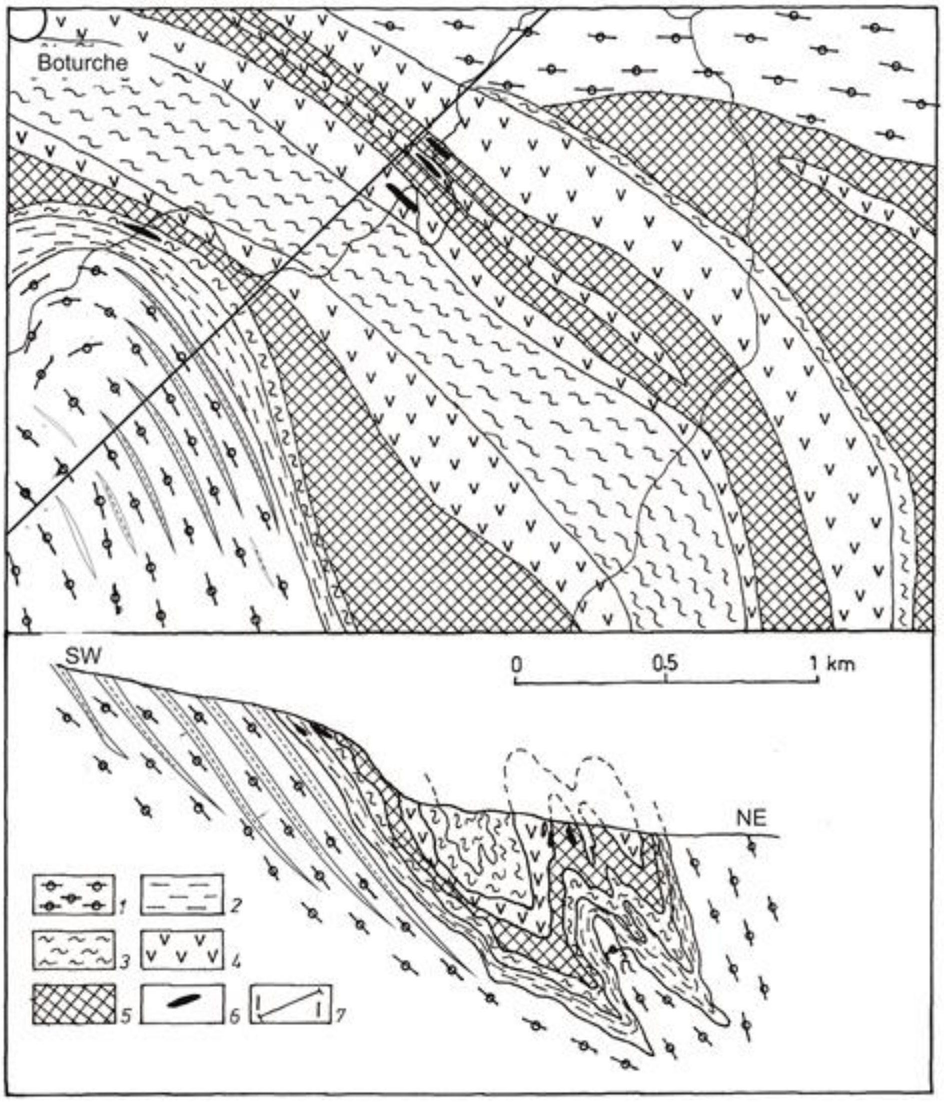

Figure 1. a. Geological map of a region in the Eastern Rhodopes, Bulgaria;

b. Section line I-I (magnified)

1. Porphiroblastic gneisses with thin films of mica schists; 2. Deformed gneisses;

3. Mica schists; 4. Amphibolites; 5. Serpentinites; 6. Amphibolitized eclogites; 7. Section line I-I

The mica schists are metamorphic rocks that form either by crystallization of fine-grained pelitic (clay or mud) sediments during regional metamorphism, or by the tribological processes in the shear zones of friction.

Mica schists are platy rocks and consist of micas (biotite, muskovite), feldspar, and quartz. They may define a planar texture (foliation – arrangement in planes) or a linear texture (lineation – for the minerals built long flakes in one direction). Schists form layers alternated with gneisses, marbles, and quartzites in the metamorphic complexes.

Mica schists form also in the shear zones of friction, which arise during tectonic movements and locate alongside lithological contacts - the boundaries between rocks of different mineral composition, with different physico-mechanical and rheological properties, and hence reacting in a particular of way to deformations. They represent the weak places in the rock complex, where there is most often a rupture and genesis of tribozones. Secondary shear zones may also occur parallel to the main zone (Figure 1) in a homogeneous rock due to the irregularity of stress in the rock formations.

The rock plates are moving along the shear zones, so friction occurs resulting in a process of deformation and disintegration of the rocks manifested as bending, cataclasis and mylonitization. At the same time, in the crystal lattice of the minerals also occur elastic and plastic deformations and appear defects: vacancies, dislocations and cracks, which lead to the complete decomposition of the mineral to molecular and atomic level. Mylonitization in the tribological zones of friction goes through elastic and plastic deformation of minerals, appearance of defects in the crystal lattice up to complete decomposition of the minerals to molecular and atomic level. The newly created tribomaterial is similar to the fine-grained pelitic sediments.

The mechano-chemical and tribochemical processes in the tribozone cause a rapid increase in temperature, pressure and chemical activation of the components in the restricted space of the zone, resulting in recrystallization of the crushed material and occurring of new metamorphic product. Some rocks such as granites and gneiss are composed mainly of quartz and feldspars (plagioclase and orthoclase), the latter rich in aluminum Al and silicon Si. These brittle minerals disintegrate quickly in the shear zones of friction. Due to the high temperatures and in the presence of water penetrating the zones, nuclear crystallization of muscovite is initiated in the disintegrated material. When rocks are basic (rich in Fe and Mg), biotite, chlorite, talc and antigorite, which also have a flaky appearance, are formed instead of muscovite.

Flaky minerals form thin monomineral films, which adhere to the surfaces of the tribozones, and if the disintegrated material is of larger quantity, they can form layers of rocks – schists, parallel to the main tribological zone (Figure 1), which contain new feldspars and quartz. The surfaces of the tribological zones covered with mica or schists favor the sliding of the rock plates or blocks, and thus play the role of lubricants in the subsequent tectonic movements.

A typical example of creation of mica schists as a result of tectonic friction was observed in the Eastern Rhodopes - the Bela River [17]. A zone of mica shale is formed on the steep contact between gneisses and a varied rock formation. They contain relics of feldspar clusters, evidence of their tribogenesis. These rocks now mark the main tribological zone of friction between heterogeneous rock formations. Parallel to the main zone in the gneiss substrate, parallel schists zones occur that gradually fall away, disappearing away from the contact.

4. CONCLUSION

1. Film formation between any pair of sliding objects is a natural phenomenon related to the tribosystem's striving to preserve its integrity and life through self-organization and synergy in the tribosystem ;
2. Self-building films occur during friction in mechanical and non-mechanical tribosystems;
3. Specifics of the geological non-mechanical systems, i.e. of the geotriboproducts, are the following:

   = Contact processes in geotribology develop on the most wide-scales: from micro/nano- level to mega- or geological level;

   = Geotribological objects allow time tracking of the processes of the entire development of the object;
4. The rocks deform, destruct, desintegrate and transform into fine grained materials in the shear zones of friction. A nuclear crystallization take place due to increased temperature in the tribozones of friction;
5. The destructed gneisses transform into muscovite mica schists with similar chemical composition;
6. As they are films on the contact surfaces, mica schists favour the tectonic movements playing the role of a lubricant.

REFERENCES

[1] S. V. Fedorov, E Assenova: Synergy and Self-organization in Tribosystem’s evolution.

Energy Model of Friction, IOP Conf. Ser.: Mater. Sci. Eng, Vol. 295, 2018.

[2] N.S. Enikolopyan et al: Investigation of the Structure of the Surface Layer of Polyethylene in Polymerization Filled Perlite, Dokladi (Proceedings) of the Academy of Science of the SU, Vol. 269, No.1, pp. 140-143, 1983.

[3] G.W. Stachowiak, A. Batchelor, *Engineering Tribology*, 4th Edition, Butterworth-Heinemann, 2013.

[4] E. Assenova, V. Majstorovic, A. Vencl, M. Kandeva: Green Tribology and Quality of Life, in: *International Convention on Quality 2012,* 05-07.06.2012, Belgrade, Serbia, Vol. 40, No. 2, pp. 32-38, 2012.

[5] L.I. Bershadskii: On the Self-organization and Concepts of Wear-resistance in Tribosystems, Trenie i Iznos (the Russian Friction and Wear) Vol. 13, pp. 1077-1094, 1992.

[6] L.I. Bershadskii, B.I. Kostetskii: The General Concept in Tribology, Trenie i Iznos (the Russian Friction and Wear), Vol. 14, pp. 6-18, 1993.

[7] D.N. Garkunov, *No-wear Effect Under Friction: Hydrogen Wear of Metals*. Moscow Agricultural Academy Press, Moscow, 2007.

[8] N. Manolov , E. Assenova, K. Danev: Über die Modellierung von selbstorganisierenden Tribosystemen", Seminar "Neue Prinzipien und Prüfmethoden in der Tribotechnik", Zwickau, 1989.

[9] G.P. Shpenkov, *Friction Surface Phenomena*, Tribology Series, 29, Ed. D. Dowson, Elsevier, 1995.

[10] E. Assenova, M. Kandeva: Self-organization Aspects in Tribosystems, in: *Proc. Int. Conference ROTRIB'03, Galati, 2003*, In: The Annals of the University "Dunarea de Jos", Fascicle 8, Tribology, 2003.

[11] E. Assenova, G. Polzer, Dr. Tsermaa, M. Kandeva: Smart Coatings and Green Tribology. ID 885, in: *5th World Tribology Congress*, Torino, 2013.

[12] E. Assenova, G. Polzer, Dr. Tsermaa, M. Kandeva: The Effect of Selective Transfer of Materials between Tribological Surfaces, in: *Proc. 19th Int. Colloquium Tribology*, Esslingen/Ostfildern, Germany, 2014.

[13] N.H. Sleep, M.L. Blanpied: Creep, Compaction and the Weak Rheology of Major Faults, Nature, Vol. 359, pp. 687-692, 1992.

[14] E. Kozhoukharova: The Tribometamorphic Mica Schists as a Lubricant in the Tectonic Zones of Friction, Papers from the 8th National Conference with International Participation BULTRIB '2011, Sofia, in: *Tribological Journal BULTRIB*, Vol. 2, pp. 298-304, 2012.

[15] E. Kozhoukharova: Application of Tribo-principles in Geology. An example for Tribochemical Genesis of Eclogites, in: *6th Intern. Conference on Tribology Balkantrib '08*, Sozopol, Bulgaria, 2008.

[16] E. Kozhoukharova: Geotribology – a new view on the tectonometamotphism, R.Bul. Geol. Soc., Vol. 77, No. 2-3, pp. 51-60, 2016.

[17] E. Kozhoukharova: Eclogitized layered serpentinites in the East Rhodope block, C. R. Acad. Bulg. Sci, Vol. 49, No. 6, pp. 69–71, 1996.

Serbian Tribology Society

SERBIATRIB '19

16th International Conference on Tribology

Faculty of Engineering University of Kragujevac

Kragujevac, Serbia, 15 – 17 May 2019

ASSESSMENT OF TRIBOLOGICAL BEHAVIOUR OF ZA-27 ZINC-ALUMINIUM ALLOY BASED NANOCOMPOSITE

Dragan DžUNIĆ[1], Marko PANTIĆ[1,2,*], Slobodan MITROVIĆ[1], Miroslav BABIĆ[1], Suzana PETROVIĆ SAVIĆ[1], Aleksandar ĐORĐEVIĆ[1], Aleksandra KOKIĆ ARSIĆ[2]

[1]University of Kragujevac, Faculty of Engineering, Kragujevac, Serbia (Calibri 12 pt, Center)

[2]Higher Technical Professional School in Zvečan, Zvečan, Serbia

*Corresponding author: pantic@kg.ac.rs

Abstract: *Mechanical and tribological investigation of obtained nanocomposites is presented in this paper. As matrix material, well known tribological zinc-aluminium alloy, ZA-27 was used. Nanocomposites were obtained by compocasting procedure, while as reinforcement Al_2O_3 nanoparticles with average size of 20-30 nm was used. Nanocomposites with three different volume fractions were obtained. In order to get insight in structure and mechanical properties of obtained nanocomposites density and hardness measurements were performed. Tribological properties of tested materials were investigated using block-on-disc tribometer in dry sliding conditions with variation three different values of sliding speed and normal load. Wear tracks that were generated as a result of dry sliding process were analysed using optical and scanning electron with EDS microscope.*

Keywords: *ZA-27 alloy, nanocomposite, Al_2O_3 nanoparticles, dry sliding, friction, wear, MML*

1. INTRODUCTION

Material properties improvement is a subject of constant efforts of numerous researchers from round the world. One of the most applicable techniques to improve the material properties is obtaining composites and creating material that has different properties from origin material. Metal are wide used, mostly, due to their good mechanical properties, but improving their origin properties is an elusive goal. Common metal matrix composites have been obtained through reinforcing light metals with ceramics, in order to maintain good metallic properties (Yield strength) and get them closer properties of ceramic materials, such as great strength and thermal stability. This composite finds their application in automotive industry [1, 2].

In comparison to the micro composites there are many problems that have to be solved in order to obtain optimal nanocomposite: nanoparticles tends to agglomeration, strengthening mechanism is different, properties of nanoparticles are different than same micro particles and finally nanocomposites are much harder for examination [3]. The biggest challenges in order to obtain proper nanocomposite material are dispersion of reinforcement particles in matrix alloy, reactivity, thermal stability, wettability and price.

ZA-27 has been already known tribological alloy with wide industrial application since it has very good combination of strength, toughness and stiffness. Due to their good bearing properties it is widely used for plain bearing that operates in low load and sliding speeds conditions [4]. However, major limitation in application of these alloys is deterioration of mechanical properties on elevated temperatures above 100°C [5, 6]. Reinforcing ZA-27 alloy with ceramic particles should improve their tribological properties, thermal stability and operation temperature as well.

Nanocomposites presented in this paper were obtained using compocasting technique, due to its simplicity, flexibility and cost effectiveness, which proved to be very successful in producing micro composites [4, 7-12]. Regarding that this paper presents experimental investigation of obtained nanocomposites, based on ZA-27 alloy reinforced with Al_2O_3 nanoparticles, using compocasting technique.

2. MATERIAL

ZA-27 is the ASTM B68 standard label for zinc-aluminium alloy, which contain 25-27% of aluminium, 2-2.5% of copper, 0.0015-0.02 % of magnesium, while balance is reserved for zinc. ZA-27 was used as base alloy for obtaining nanocomposites, reinforced with Al_2O_3 nanoparticles with 1, 3 and 5% of volume fraction in matrix alloy. Average size of Al_2O_3 nanoparticles was 20-30 nm. Obtained nanocomposites were produced using compocasting technique that was conducted thought casting and hot pressing phase. Casting phase implies matrix alloy furnace melting on temperature above 570°C, then cooling down in furnace on temperature around 475°C in order to achieve semi-solid state. At this temperature mixing process starts to homogenize the mixture. At the beginning mixing speed is 50 rpm which continuously increases for 5 minutes and when mixing speed of 500 rpm is achieved infiltration of nanoparticles starts. After intensive mixing under 1000 rpm for 15 minutes obtained nanocomposites were poured in moulds that were pre-heated at 350°C. Second phase of compocasting procedure was hot pressing at 350°C and applied load of 250 MPa.

Samples preparation implied cutting, grinding and polishing under controlled condition in order to avoid temperature increase and deterioration of nanocomposite mechanical properties.

3. EXPERIMENT

Structural, mechanical and tribological experiments were performed using various laboratory equipment. Structural properties were expressed through density measurement results using Archimedes principle, while mechanical properties were examined hardness tests.

Friction and wear properties were obtained using block-on-disc tribometer, under dry sliding conditions, varying sliding speed (0.25, 0.5 and 1 m/s) and normal load (10, 20 and 30 N). Sliding distance was constant, i.e. 300m for all tribological experiments. Blocks were prepared from obtained nanocomposites and ZA-27 alloy, while steel disc were used as counter material. Detail schematic representation of tribological testing apparatus is presented elsewhere [4]. Obtained wear tracks as result of sliding process were examined using optical and scanning electron microscopy. All results from nanocomposite material testing were compared to the ZA-27 matrix alloy results. All experiments were repeated at least three times and presented values are mostly averaged values.

4. RESULTS AND DISCUSSION

Density of obtained nanocomposites and compared to the matrix ZA-27 alloy are presented on Fig. 1. Results are presented showing average values with error bars. Density measurements were performed on eight samples from each material. Measured values were analysed and averaged and presented thought histogram bars.

From presented histogram it is noticeable that highest average hardness belong to nanocomposite reinforced with 1 vol. % of Al_2O_3 nanoparticles, but due to wide range in which hardness value oscillates it is very hard to conclude that it is the nanocomposite without structural irregularities.

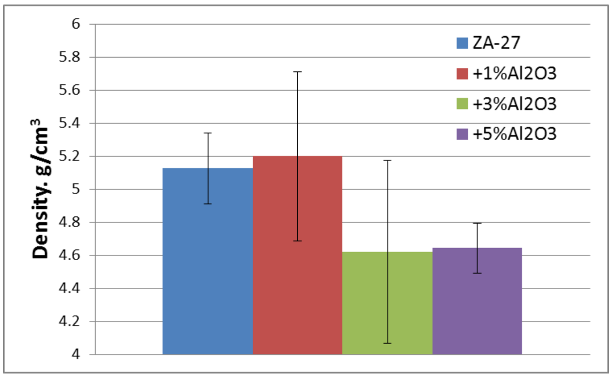

Figure 1. Density of obtained nanocomposites in comparison to the matrix ZA-27 alloy

Reasonable explanation for this result would be that there were samples with uniform distribution of reinforcement nanoparticles and samples with structural irregularities, such as agglomeration and porosity, as well. Since density of Al2O3 as a material is lower than ZA-27 alloy, it is logical that nanocomposite material has slightly lower density than ZA-27 alloy. Higher density is probably a result of hot pressing within the second phase of compocasting procedure.

In the present nanocomposites it is very hard to obtain information regarding distribution of Al_2O_3 nanoparticles within the matrix material, since matrix alloy contain large % of aluminium as constitutional material. Using SEM and EDS for microstructural analysis will not be able to distinguish alumina reinforcement from aluminium as constituent of the matrix alloy.

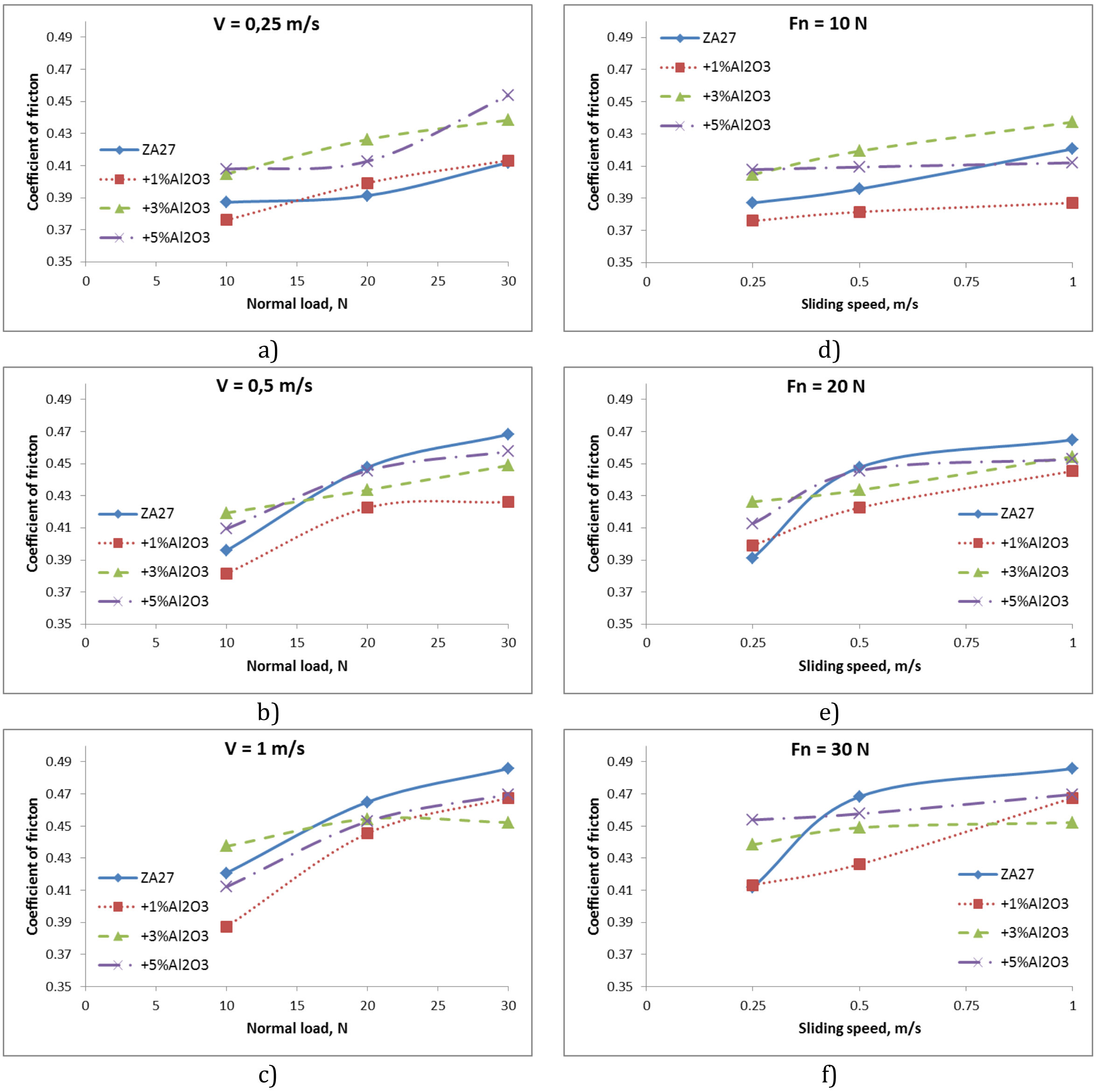

Figure 2. Coefficient of friction of obtained nanocomposites and matrix ZA-27 alloy in comparison to normal load (a, b, c) and to sliding speed (d, e, f)

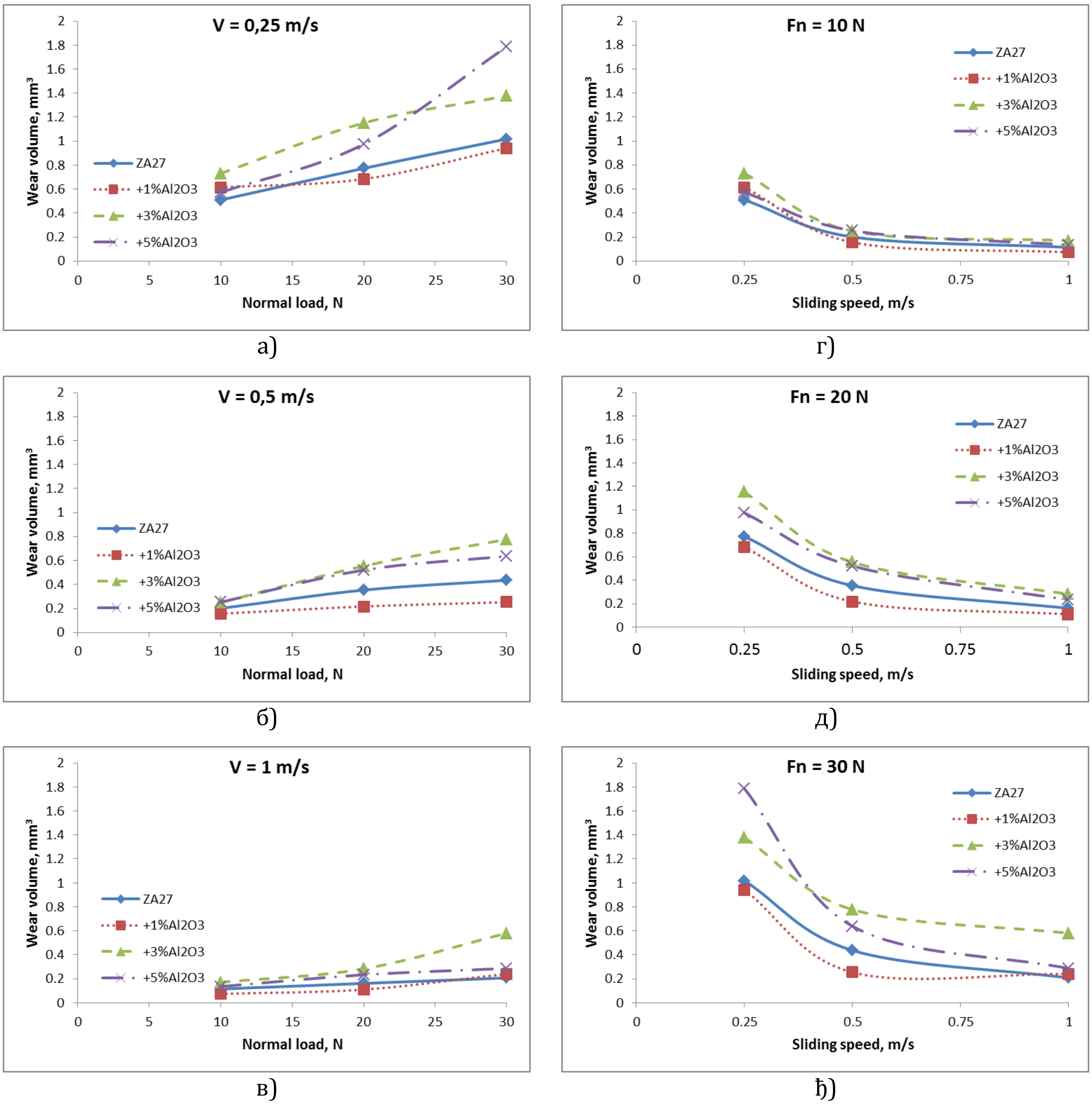

Figure 4. Wear volume of obtained nanocomposites and matrix ZA-27 alloy in comparison to normal load (a, b, c) and to sliding speed (d, e, f)

Hardness was measured using Vickers diamond tip with applied load of 50 N and those results are presented in Table 1. It is noticeable that hardness decreases with increase of volume fraction of nanoparticle reinforcement. Also, density measurement results are in correlation with hardness measurement results, except for nanocomposite reinforced with 1 vol. %.

Table 1. Hardness measurement results

	Material	Hardness, HV_5
1	ZA-27	122
2	ZA-27 + 1 vol.% Al_2O_3	114
3	ZA-27 + 3 vol.% Al_2O_3	105
4	ZA-27 + 5 vol.% Al_2O_3	102

Generally in theory presence of reinforcement nanoparticles within matrix material should improve the mechanical properties of the same though nano-recrystallization during casting [13, 14] and/or through limitation of dislocation movement [15-17]. In this both improvement methods could be countermanded with presence of structural irregularities, especially with porosity, which is obviously present within nanocomposites reinforced with 3 and 5% of reinforcement nanoparticles. When porosity is present within material structure, dislocation, generated as a result in thermal expansion difference of matrix and reinforcement, will move toward trapped gas bubbles that will contribute lower harness in comparison to the matrix alloy [18, 19].

Coefficient of friction values of matrix ZA-27 alloy and obtained nanocomposites in comparison to the sliding speed and normal load are presented on Figure 2. Presented coefficient of friction is related to the steady state values. In both cases, coefficient of friction increases with increase of sliding speed and normal load value. It is logical that coefficient of friction rises with increase of normal load, but increase with increase of sliding speed is result of contact temperature increase. Since all obtained coefficient of friction values are close to each other, it could be concluded that coefficient of friction is independent from reinforcement volume fraction value and that on micro and macro level nanoparticles has no influence on friction.

Structural irregularities have negative influence on wear resistance since nanoparticles agglomerates under normal and tangential load will be crushed into the fine abrasive particles that easily abrades both materials due to much higher hardness of reinforcement particles. Abraded steel disc is presented on Figure 3, while fine grooves are noticeable within the wear track surrounding adhesion pits (Figure 3).

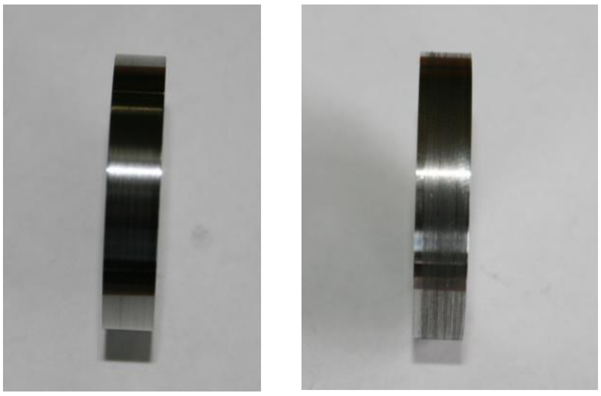

Figure 3. Disc appearance before and after sliding

Wear properties are expressed through wear volume value that is calculated from measured wear track width and already known geometry of the block (Figure 4).

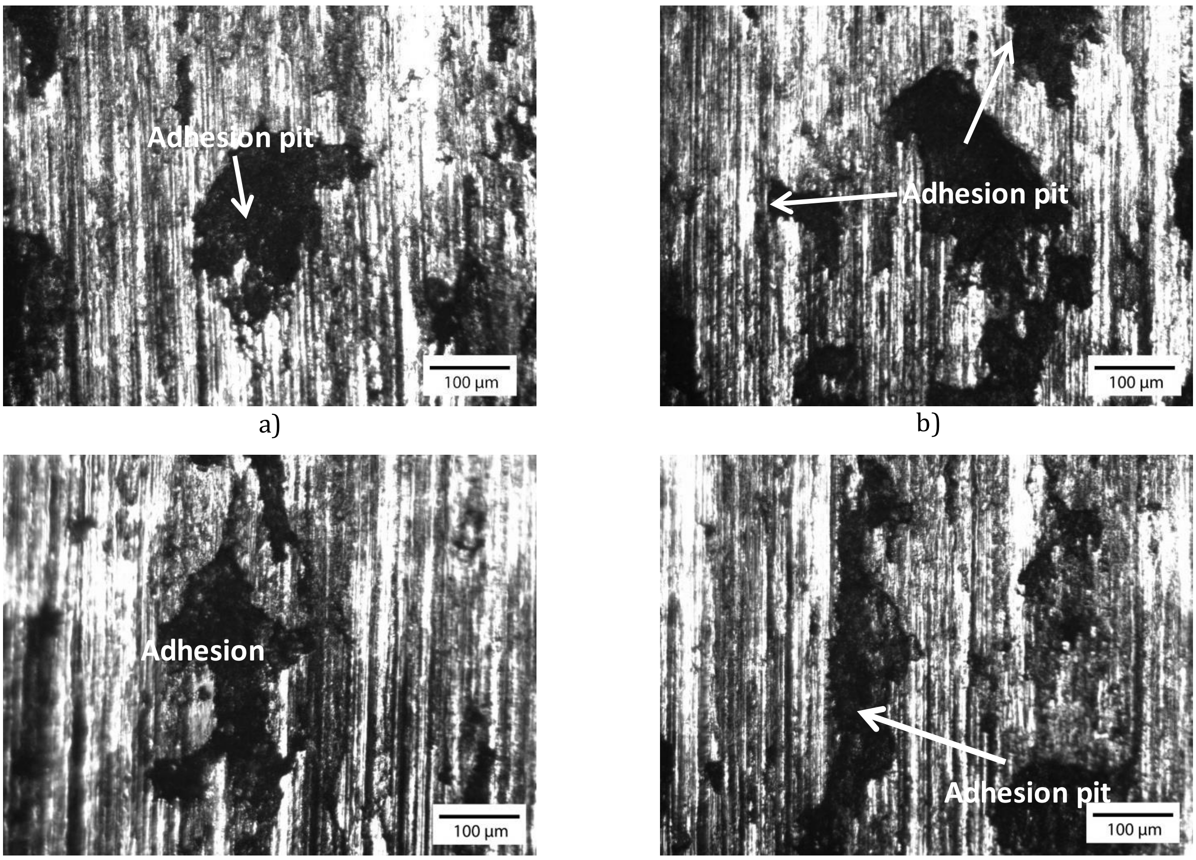

Figure 5. Optical microscopy of obtained wear track for matrix Za-27 alloy and nanocomposites a) ZA-27, b) ZA-27+1% Al_2O_3, c) ZA-27+3% Al_2O_3, d) ZA-27+5% Al_2O_3 (v=0.5 m/s; F=20 N).

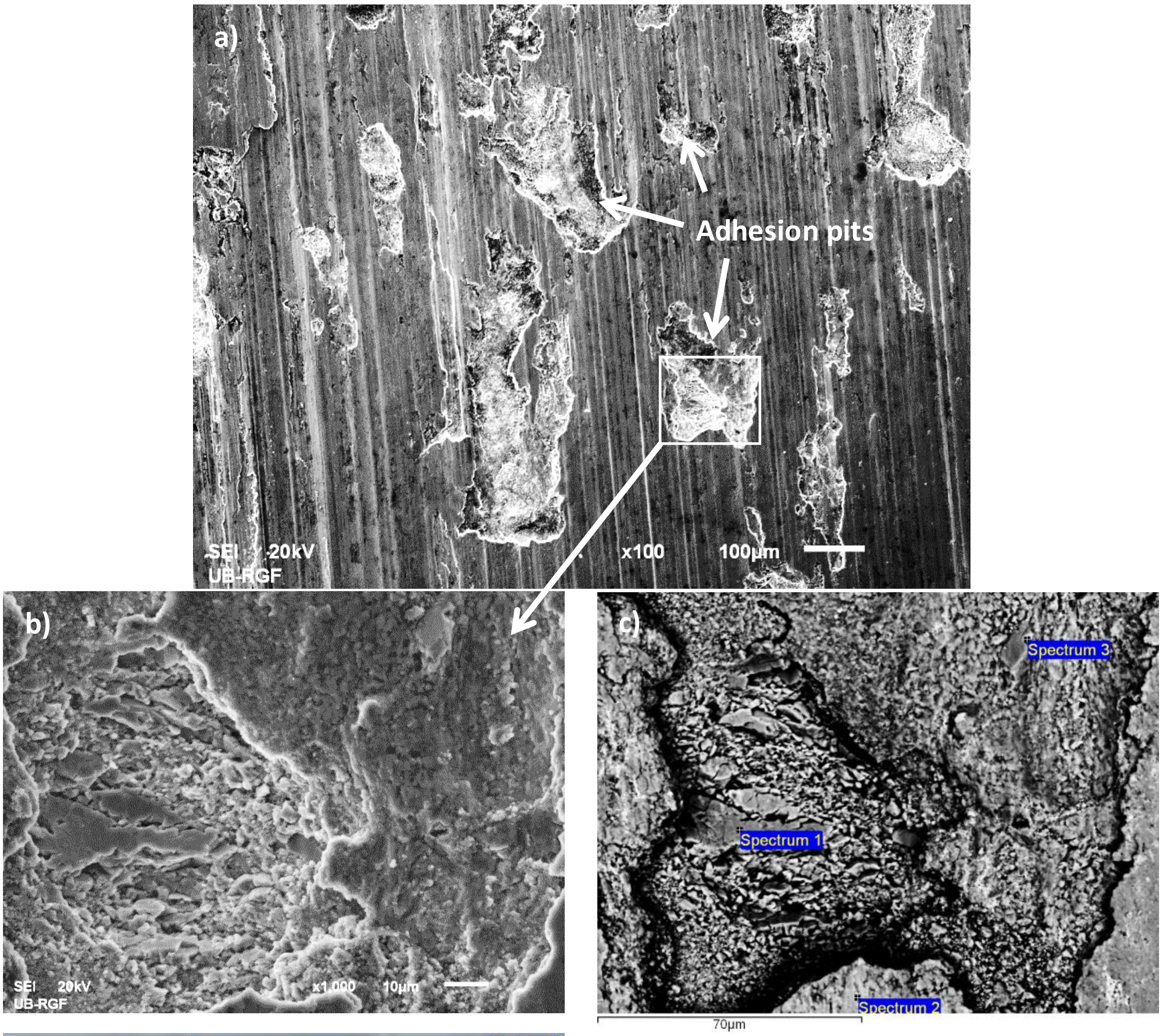

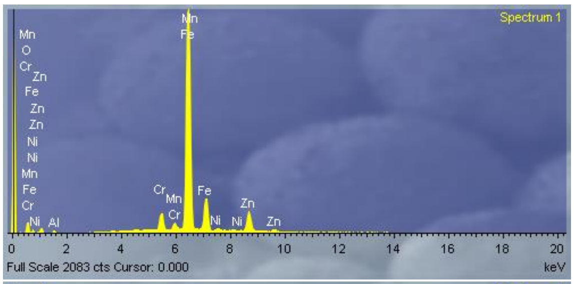

O – 2.04
Al – 0.37
Cr – 3.34
Mn – 1.40
Fe – 75.89
Ni – 1.38
Zn – 15.58
Total 100.00
Values in wt.%

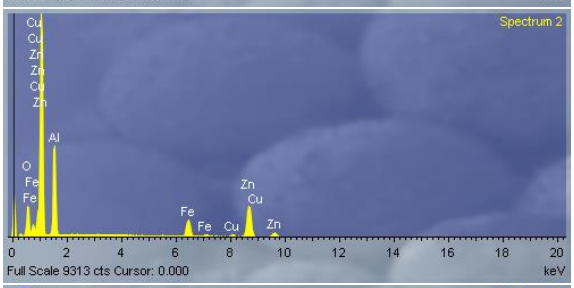

O – 14.35
Al – 23.08
Fe – 10.27
Cu – 2.19
Zn – 50.11
Total 100.00
Values in wt.%

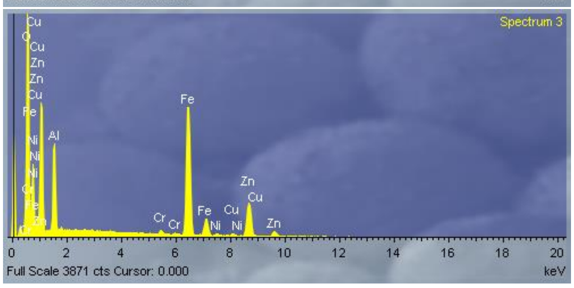

O – 30.68
Al – 8.63
Cr – 0.79
Fe – 34.62
Ni – 0.65
Cu – 1.09
Zn – 23.54
Total 100.00
Values in wt.%

Figure 6. SEM and EDS analysis a) wear track of nanocomposite rainforced with 1%Al_2O_3 (a), b) enlarged adhesion pit; c) adhesion pit EDS analysis.

With increase of normal load wear volume increases, but with increase of sliding speed wear volume decreases. It is noticeable that wear volume of nanocomposite reinforced with 1 vol. % of Al_2O_3 nanoparticles is close to the value of wear volume of matrix ZA-27 alloy and in many combinations of sliding parameters nanocomposite expresses slightly better wear resistance than matrix alloy. This result is in correlation with density and hardness results. Despite lower hardness in comparison to the matrix alloy, 1 vol. % of reinforcement proved to be enough to improve wear properties of nanocomposite material, which is not the case for nanocomposites that are reinforced with 3 and 5 vol. % of reinforcement nanoparticles. In case of nanocomposites reinforced with 3 and 5 vol.% of Al_2O_3 nanoparticles, presence of structural irregularities have detrimental effect on wear resistance.

Wear tracks of were examined using optical and scanning electron microscopy. Wear tracks appearance obtained using optical microscope are presented on figure 5. Analysing presented wear tracks it is noticeable that adhesion is present as adhesion pits within the wear track that are surrounded with parallel groves that indicated on abrasion process. Adhesion pits are different in shape and size and mainly depends of material structure in surface and subsurface layer. Adhesion pits are present within the wear track of all tested materials, their number is increased in wear tracks of tested nanocomposites. In case of presence of hard particles in surface and subsurface layer, in surrounding material initial crack could occur as result of sliding process and tangential forces [20]. Also, adhesion pits could be result of hard phase detachment [4]. Abrasion occurs in mild sliding conditions, delamination and material detachment is reserved for transient phases, while under higher loads oxide layers are generated [21].

More detailed analysis of adhesion pits was performed using scanning electron microscope with energy dispersive spectre (Figure 6). EDS analysis of wear tracks and observed adhesion pits revealed presence of Fe that originate from steel disc. Presence of iron and oxygen in contact layer of tested materials suggest that during dry sliding oxide layer generates. Both contact materials react with oxygen from air. With increase of sliding speed, contact temperature raises that favours oxidation process and as a result oxide layer on the both contact surfaces will become thicker. Due to direct contact of oxidized MML arises (Mechanically Mixed Layer - Layer) [22, 23]. Presence of MML on contact surface protects origin surface from the direct contact with counterbody material and regarding that lead to lower wear of tested material with increase of sliding speed. Obtained wear results of tested material are in the corresponding with mentioned assumption, since wear volume decreases with increase of sliding speed regardless the value of applied load.

Based on EDS analysis of noticed pits within obtained wear tracks it is possible to conclude that mentioned pits are pits in MML layer that was generated on the contact surface of tested materials. Detached material from MML layer become wear debris and in that moment third body abrasion occurs.

5. CONCLUSION

Nanocomposite materials were obtained on a base of zinc aluminium alloy ZA-27, that has been already proved tribological material. Nanocomposites were obtained using Al2O3 nanoparticles (average size 20-30 nm) as reinforcement in different volume fractions 1, 3 and 5. Prepared samples were mechanically and tribologicaly analysed, and based on that results following could be concluded:

Structural irregularities such as agglomeration and porosity are noticed in obtained nanocomposites which directly influences on density and hardness, witch decreases with increase of volume fraction of reinforcement.

Presence of nanoparticles within the material structure has no influence on the frictional properties of nanocomposites, since in all testing conditions coefficient of friction of tested material has close values to each other.

Optical and scanning electron microscopy of obtained wear tracks revealed that dominant wear mechanisms were abrasion and adhesion, due to presence of adhesion pits that are surrounded with grooves parallel to the sliding direction.

SEM and EDS analysis of obtained wear tracks indicate on the presence of MML on the contact surfaces, that protects contact surface of tested materials from direct contact with counter body and on that way leads to lower wear. Thickness of MML increases with increase of sliding speed.

ACKNOWLEDGEMENT

This paper is a result of the researches within the project TR35021 financed by the Ministry of Science and Technological development of the Republic of Serbia.

REFERENCES

[1] A. Vencl, A. Rac, New wear resistant Al based materials and their application in automotive industry, Mobility & Vehicles Mechanics (MVM), 30, Special Edition, pp. 115-139, 2004.

[2] A. Vencl, A. Rac, I. Bobić, Tribological behaviour of Al-based MMCs and their application in automotive industry, Tribology in Industry, vol. 26, no. 3-4, pp. 31-38, 2004.

[3] F. He, 'Ceramic nanoparticles in metal matrix composites', Ceramic nanocomposites, Woodhead Publishing Limited (2013) 185-207.

[4] M. Babic, M. Slobodan, D. Džunic, B. Jeremic, I. Bobic, 'Tribological Behavior of Composites Based on ZA-27 Alloy Reinforced with Graphite Particles', Tribol Lett, vol. 37, no. 2, pp. 401-410, 2010.

[5] S. Tjong, F. Chen, 'Wear behavior of As-cast ZnAl27/SiC particulate metal-matrix composites under lubricated sliding condition', Metall and Mat Trans A, vol. 28, no. 9, pp. 1951-1955, 1997.

[6] T. Chen, C. Yuan, M. Fu, Y. Ma, Y. Li, Y. Hao, 'In situ silicon particle reinforced ZA-27 composites: Part 1 – Microstructures and tensile properties', Materials Science and Technology, vol. 24, no. 11, pp. 1321-1332, 2008.

[7] B. Bobic, M. Babic, S. Mitrovic, N. Ilic, I. Bobic, M. Jovanovic, 'Microstructure and mechanical properties of Zn25Al3Cu based composites with large Al2O3 particles at room and elevated temperatures', IJMR, vol. 101, no. 12, pp. 1524-1531, 2010.

[8] M. Babić, A. Vencl, S. Mitrović, I. Bobić, 'Influence of T4 Heat Treatment on Tribological Behavior of ZA-27 Alloy Under Lubricated Sliding Condition', Tribology Letters, vol. 36, no. 2, pp. 125-134, 2009.

[9] I. Bobić, M. Babić, A. Vencl, B. Bobić, S. Mitrović, Artificial aging of thixocast ZA-27 alloy and particulate ZA-27/SiCp composites, International Journal of Materials Research, vol. 104, no. 10, pp. 954-965, 2013.

[10] B. Bobić, S. Mitrović, M. Babić, A. Vencl, I. Bobić, Corrosion behaviour of the as-cast and heat-treated ZA-27 alloy, Tribology in Industry, vol. 33, no. 2, pp. 87-93, 2011.

[11] A. Vencl, I. Bobić, M.T. Jovanović, M. Babić, S. Mitrović, Microstructural and tribological properties of A356 Al-Si alloy reinforced with Al2O3 particles, Tribology Letters, vol. 32, no. 3, pp. 159-170, 2008.

[12] B. Stojanović, M. Babić, N. Miloradović, S. Mitrović, 'Tribological behaviour of a356/10SiC/3gr hybrid composite in dry-sliding conditions', Materials and technology, vol. 49, no. 1, pp. 117-121, 2015.

[13] P. Salehikahrizsangi, F. Karimzadeh, M. Enayati, M. Abbasi, 'Investigation of the effects of grain size and nano-sized reinforcements on tribological properties of Ti6Al4V alloy', Wear, vol. 305, no. 1-2, pp. 51-57, 2013.

[14] M. Shen, X. Wang, C. Li, M. Zhang, X. Hu, M. Zheng, K. Wu, 'Effect of submicron size SiC particles on microstructure and mechanical properties of AZ31B magnesium matrix composites', Materials & Design, vol. 54, pp. 436-442, 2014.

[15] S. Mishra, S. Biswas, A. Satapathy, 'A study on processing, characterization and erosion wear behavior of silicon carbide particle filled ZA-27 metal matrix composites', Materials & Design, vol. 55, pp. 958-965, 2014.

[16] M. Farvizi, T. Ebadzadeh, M. Vaezi, H. Kim, A. Simchi, 'Effect of nano Al2O3 addition on mechanical properties and wear behavior of NiTi intermetallic', Materials & Design, vol. 51, pp. 375-382, 2013.

[17] M. Tavoosi, F. Karimzadeh, M. Enayati, 'Wear behaviour of Al–Al2O3 nanocomposites prepared by mechanical alloying and hot

pressing', Materials Science and Technology, vol. 26, no. 9, pp. 1114-1119, 2010.

[18] M. Karbalaei Akbari, H. Baharvandi, O. Mirzaee, 'Nano-sized aluminum oxide reinforced commercial casting A356 alloy matrix: Evaluation of hardness, wear resistance and compressive strength focusing on particle distribution in aluminum matrix', Composites Part B: Engineering, vol. 52, pp. 262-268, 2013.

[19] A. Mazahery, M. Ostadshabani, 'Investigation on mechanical properties of nano-Al2O3-reinforced aluminum matrix composites', Journal of Composite Materials, vol. 45, no. 24, pp. 2579-2586, 2011.

[20] R. Deuis, C. Subramanian, J. Yellup, 'Dry sliding wear of aluminium composites—A review', Composites Science and Technology, vol. 57, no. 4, pp. 415-435, 1997.

[21] S. Natarajan, R. Narayanasamy, S. Kumaresh Babu, G. Dinesh, B. Anil Kumar, K. Sivaprasad, 'Sliding wear behaviour of Al 6063/TiB2 in situ composites at elevated temperatures', Materials & Design, vol. 30, no. 7, pp. 2521-2531, 2009.

[22] M. Srinivasan, C. Loganathan, M. Kamaraj, Q. Nguyen, M. Gupta, R. Narayanasamy, 'Sliding wear behaviour of AZ31B magnesium alloy and nano-composite', Transactions of Nonferrous Metals Society of China, vol. 22, no. 1, pp. 60-65, 2012.

[23] A. Alizadeh, E. Taheri-Nassaj, 'Mechanical properties and wear behavior of Al–2wt.% Cu alloy composites reinforced by B4C nanoparticles and fabricated by mechanical milling and hot extrusion', Materials Characterization, vol. 67, pp. 119-128, 2012.

Serbian Tribology Society

SERBIATRIB '19

16th International Conference on Tribology

Faculty of Engineering University of Kragujevac

Kragujevac, Serbia, 15 – 17 May 2019

FRICTION MODELING IN SIMULATING BALLISTIC IMPACT. A REVIEW

George Ghiocel OJOC[1,2], Catalin PIRVU[3], Simona BADEA[4], Lorena DELEANU[1]
[1]"Dunarea de Jos" University of Galati, Galati, Romania
[2]Maritime University Constanta, Romania
[3]INCAS - National Institute for Aerospace Research "Elie Carafoli", Bucharest, Romania
[4]Scientific Research Center for CBRN Defense and Ecology, Bucharest, Romania
*Corresponding author: lorena.deleanu@ugal.ro

Abstract: This paper presents a review on using friction coefficient in modelling ballistic impact. The are discussed on friction introduced in modelling the impact at different levels: micro (fiber and yarns), meso (woven or unidirectional fabrics) and macro (layered or equivalent monoblock structures). Recent works simulating the impact projectile - target, done at different levels (micro, meso, macro) pointed out the influence of friction coefficient between bodies in contact. In all cited references, the friction coefficient is kept constant, even if experimental studies proved that it has different values for different sliding speeds, especially for contact metal - polymer as in the impact of aramid fabric armor.

Keywords: *friction coefficient, impact velocity.*

1. INTRODUCTION

Myshkin et al [1] discussed the influence of load and velocity on the friction coefficient and graphically resumed (Fig. 1) the research studies of [2], [3], [4], [5], but for low velocity, from 0.1 m/s to 2 m/s, values that are far bellow the values charactering the impact velocity of projectiles (100...1000 m/s). Also, the load influences the value of friction coefficient of the same couple of materials in dry conditions.

When the projectile is arrested by the target, the friction coefficient is not constant, having values for high, medium and low velocities, also depending on the temperature between the moving contact surfaces. Also, high friction occurs when projectile is deformed on or into the target.

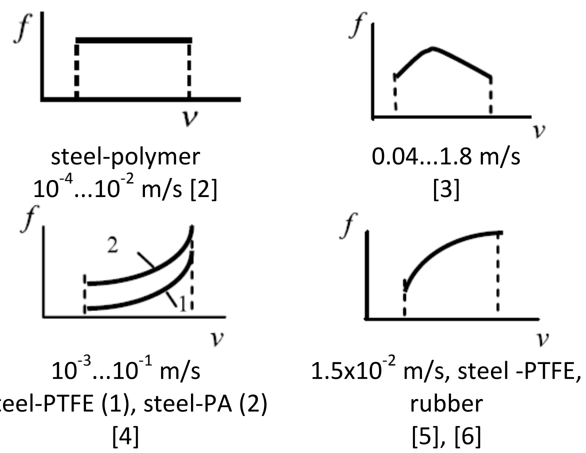

Figure 1. Variants of the dependence of friction coefficient on sliding velocity, Steel - polymer

Many engineering designs are based on considering friction coefficient as a constant of materials in contact, thus, independent of velocity, load, temperature, size of contact. This is acceptable as long as the tribolayers do not change their mechanical and thermal characteristics. It is difficult to impossible to practically separate the effect of these factors. Also, the impact is characterized by very dramatic failure processes, overlapping on friction and measuring the energy dissipated by friction alone is still quite an adventure.

Sliding friction steel-polymer may be discussed taking into account the mechanical an thermal influences:

- at low velocity, thermal effect is reduced but the effect of adhesion and viscous resistance, especially under higher load, could make the value of friction coefficient higher and with big oscillations,

- at high velocity, elastic characteristics are more influent and the value of friction coefficient will depends only slightly on velocity or it will decrease with the increasing velocity; frequently, the application involving high velocity contact last less time and thermal effect could be neglectable,

- for medium velocity between bodies in contact, visco-elastic and thermal effects are present, most of the polymers sliding on steel having a maximum value of the friction coefficient.

This qualitative analysis is difficult to put into practice, that is limiting these three domains with actual values for velocity, even at laboratory scale.

Stachowiak [7] mentioned the exerimental work of Ettles [8] in 1987 for pointing out that polymers like LPDE, PP and PA had a maximum value for friction coefficient in the range of o.3...8 m/s (close to 1 or even above 1), after that this value decreasing dramatically, but tests were done under 100 m/s, value that is at the lower level for ballistic impact. Another study done by Bueche and Flom [9] in 1958 for steel sliding against unlubricated plexiglass at different temperatures reveals that above 5 m/s the friction coefficient is not influenced by the temperature.

2. FACTORS AFFECTING FRICTION WHEN A PROJECTILE HITS A TARGET

Based on the principal of conservation of energy and the relation given by Nilakantan et al. [10 Nilakantan, 2015] for the energy transformations that occur during the projectile-fabric impact, the follwoing energy balance may be written:

$$E_{projectile}^{initial} = E_{projectile}^{residual} \quad E_{\mathrm{fabric}}^{\mathrm{internal}} \quad E_{fabric}^{kinetic} \quad E_{fabric}^{friction} \quad E_{projectil}^{deformation} \quad E_{projectil\ \ fabric}^{friction} \quad E_{fabric}^{miscellanous} \tag{1}$$

The loss of projectile kinetic energy is equal to the summation of the three main fabric energy dissipating mechanisms:

- fabric internal energy due to tensile yarn elongation,

- fabric kinetic energy due to projectile-fabric momentum transfer, and

- frictional energy due to inter-filament, inter-yarn, and projectile-fabric frictional sliding interactions.

Internal energy due to other deformations such as yarn transverse compression and yarn shearing are usually much smaller than that due to tensile straining especially for anisotropic fibers, such as aramid. Other miscellaneous energy losses, such as acoustic and heat, are relatively very small in some application, including for individual armors, and can be neglected, but for heavy threats should be taken into account

The factors affecting friction in impact process include:

- materials of the bodies in impact (projectile, target), by their mechanical and thermal characteristics,

- size and structure of target (metallic, fibre, ceramics)

- size and shape of the projectile

velocity and mass of the projectile

Thus, friction should be analyzed for particular cases of impact.

During the projectile impact with the target, friction process could have different aspects:

- friction between projectile and target without penetration (the projectile is rebonded); friction is initiated in a layered target, but with small displacements, reducing the influence of friction in energy dissipation,

- friction between the projectile and the broken layers and the consequently friction between layers that are laterally tensioned (delamination with friction after).

For the similar projectile, the target could be designed against penetration using different materials and even combinations of them.

Protection systems could made of steel (monoblock or sheets), fabrics manufactured from woven or unidirectional polymeric fibres gained the interest in protecting individuals, usually in layers, also ceramic plate are introduced rarely alone, often in addition to first ones [11]. When impacting the target, friction depends on materials in contact and, especially for fibres, on their arrangement (2D and 3D woven, unidirectional etc.) and coating, if the structure is layered or monoblock (for transparent windows) etc.

Introduction of friction in simulation of impacts has to be done for the particular case of interest.

In simulations, friction was introduced for micro, meso and macro level.

Sockalingam [12] published a review analyzing all these levels in order to finally discussed the complex multi-scale system of fabrics, woven or not, taking into account the structural hierarchy of the materials, anisotropic material behavior, projectile–fabric interactions, impact velocity and boundary conditions and also the friction between contacting bodies.

Frictional mechanisms, including fiber breakage at the yarn cross-overs, flattening and rupture of fibers and yarn pull out, are also physically observed.40

Unlike aramid fibers, the melting temperature of PE is low (110...145 °C). Prevorsek et al. [13] reported that the projectile-fiber frictional interactions result in an increase in temperature on the projectile-target interface, above the melting point of this PE fiber. Due to the short time of ballistic impact, the temperature rise is limited to a small region and its effects on the target performance are not significant, even if, locally, the polymer is soften to molten.

3. FRICTION BETWEEN FIBERS

The micro level simulation of the impact implies model for a fiber or a yarn.

The apparent friction (defined as the ratio of lateral scratch force to normal indentation force) is reported to increase up to 300% higher than the aramid yarn–yarn friction of 0.2–0.3. Apparent fiber–fiber and yarn–yarn friction are an important energy dissipative mechanisms due to increased apparent friction associated with these fibres [14].

Sockalingam et al. [15] simulated the behavior of a fiber under impact taking into account a friction coefficient of 0.2, mesh size of 1.8 m, fiber length 500 mm, but introducing friction, the tensile stress near the contact with the projectile may increase, even if impact energy is now dissipated also by friction.

The fiber friction with the contacting bodies (projectile and other fibres) and mechanical and thermal properties play a substantial role in slowing down the projectile, bullet deformation and arrest. The friction coefficient of aramid fibers is higher as compared to UHMWPE fibers, which are slicky, highly oriented, high strength and exibit lower friction. The low friction in fabrics, in layered arrangement, is overcome by adding higher-friction coatings (polymeric foil of PE or other thermoplastic polymers, having the thickness of microns) to the ballistic fabric surface. Also, more rigid matrix for fabrics [16] (like polyvinyl butyral or other similar for helmets) improve the ballistic resistance.

One factor that influences the ballistic resistance is the friction between fibers during projectile penetration. Controlled friction between fibers is desirable to slow down and deform the projectile. If friction between fibers is too high, one fiber will make the other fiber to fail during projectile penetration and reduces the resistance of the whole protection system. If fiber-to-fiber friction is too low, the material will not offer any resistance.

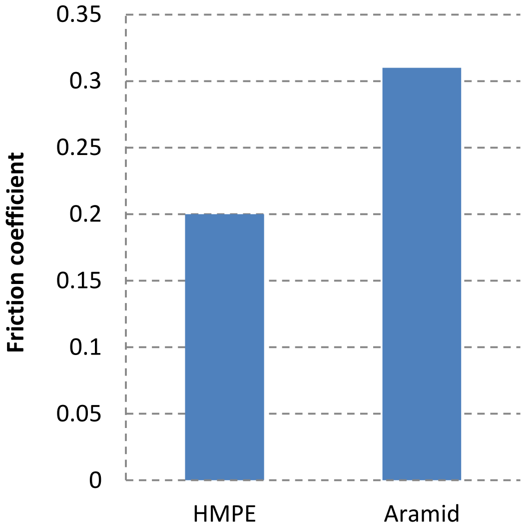

Figure 2. Coefficient of friction for yarn-to-yarn moving contact [17]

In fabrics, friction is increased by changing the fiber orientation (for instance, fabrics are composed by two, three or four layers, with unidirectional fibers, arranged at relative angles [0°,90°,45°,-45°]), by a coating at fiber level or fabric level, by bonding very thin foils on the fabrics (sometimes on each layer). Quilting/sewing with yarns of lower properties, at regular intervals of the unidirectional yarns, increases fiber-to-fiber friction, as they maintain the fibers and the yarns in contact.

The frictional properties of projectile-to-fiber interaction may be modified by adding a suitable polymer coating, during the manufacturing of the protection system. Both woven and non-woven aramid and HDPE plied materials have an increased ballistic resistance for a certain number of threats. If the coating is not adequately selected, it will increase the weight and stiffness of ballistic material without improving its ballistic resistance of individual armor [17].

When the projectile is passing through layer after layer, more and more fibers become engaged with the bullet and increase the friction, sufficient enough to slow it down, especially when the bullet is strongly deforming.

Rebouillat et al. [18] investigated the tribological properties of the Kevlar 29 woven fabric and its yarns. They measured the friction between several Kevlar 29 fabrics and between their Kevlar 29 yarns, with different surface treatments, under various sliding speeds and the inter-yarn friction coefficients was in the ranged of 0.2 and 0.4. No significant change of the inter-yarn friction coefficient occurred as the sliding velocity increased from 96 mm/min to 600 mm/min, but friction varied significantly as the sliding speed increased.

Each type of high performance ballistic fiber have particular characteristics. Aramid fibers have higher fiber-to-fiber friction than HMPE fibers (Fig. 2), making the bullet outer jacket to crack easier. HMPE fibers have non-linear viscoelastic properties, which help to arrest bullet fragments better than aramid fibers (that could be consider linear when compared). Using layers of high friction material at the front and capturing fragmented bullets by HMPE offers a lighter weight solution to stop the bullet at a lower weight than either a 100% aramid or 100% HMPE fiber individual armor [17]. The effect of increasing friction by coating or combining different types of fibers is far from being explained as there is a synergic response of the new designed protection system and simulation and tests could reveal influences far from being linear or added one to another (Fig.3).

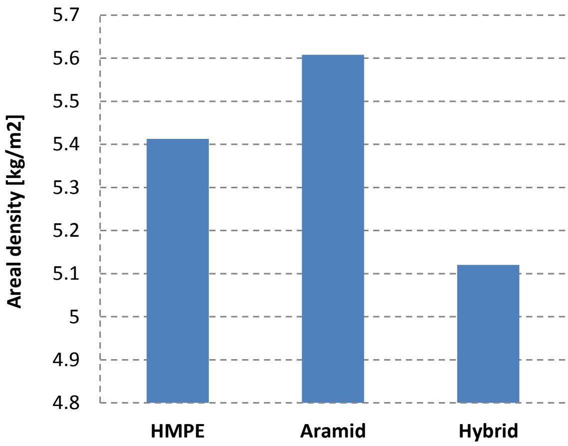

Figure 3. Effect of hybrid protection system for an individual armor level NIJ IIIA [17]

For protection systems made of fabrics, the frictional energy dissipated during the impact is a non-linear energy absorption mechanism. Friction mechanisms include friction due to slippage of yarns, interaction of adjacent layers and interaction projectile-target. Many factors influence the amount of energy dissipated by friction, including the contacting yarns, armor boundary conditions allowing or restricting yarn motion. Bhatnagar [17] concluded that, at lower impact velocities, elongation, abrasion and fibrillation of fibers are more important in arresting the projectile.

The energy absorbed during the impact is mainly due to the compression of the yarns around the projectile and the dissipated energy due to the friction between the yarns [19]. The presence of this type of perforation versus shear plugging in dry fabrics and laminates is highly affected by the projectile nose shape [20].

The final mechanism, common to all projectile types and most material systems is friction and is simply the energy required to push the projectile through the crater created by either hole expansion or plugging. The frictional load is related to the length of penetrator in contact with the panel, the in-plane compressive stresses acting on the penetrator and the coefficient of friction between penetrator and composite [17].

Friction in Fabrics

Mechanical properties of a fabric are different from the constitutive yarns, due to its complex arrangement. Yarn crimp, friction and yarns' interaction change the response of a fabric to a particular threat. Cunniff [21] discussed the loss of efficiency in going from a fibre to a yarn, from a yarn to a fabric, and from a single fabric layer to multi-layer packs. He concluded that yarn slippage may lead to the loss of efficiency and performance degradation in a loosely woven fabric or a fabric with low yarn-to-yarn friction.

Considering the geometry of the weave, balanced fabrics (plaine, for instance) absorb more energy than non-balanced ones (twill or satin), but o more dens weaving induce a process of yarn degradation, the bending induce by the weave reducing the mechanical characteristics of yarns.

In studies published by Lee et al. [22] and Rudov-Clark et al. [23] degradation of glass yarn properties during the weaving process of three-dimensional fabrics is discussed. The weaving damage mainly influences the yarn strength, reducing it by up to 30% due to the high abrasion of the filaments. The tensile modulus of the yarns was found to be less affected by weaving.

Lim et al. [24] developed a finite-element model of ballistic impact on Twaron fabric. A non-linear, explicit, 3D finite-element was used for simulating the behavior of the fabric under high-velocity impact. The fabric is modeled using membrane elements. Suitable material properties to account for its viscoelastic nature are obtained through mathematical manipulation of the three-element spring-dashpot model and by using available experimental data. The ballistic limit, residual velocity, energy absorption and transverse deflection profiles of the fabric are predicted and compared to those from tests.

Lim et al. [19] studied two-ply fabrics impacted by the same projectile geometries. They concluded that while target performance is highly affected by the projectile nose-shape, the influence diminishes in the thicker panels. They also observed that while failure throughrupture and friction is more evident on the impact face, bowing is more amplified on the back-face of the target (Fig. 4).

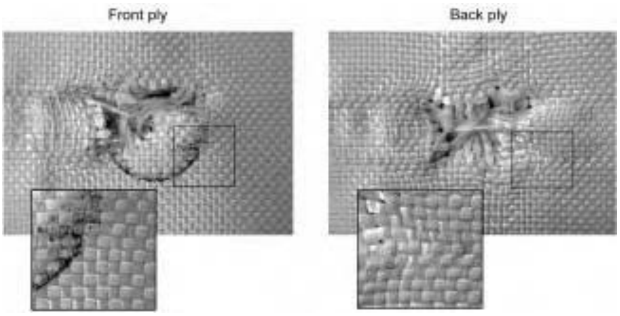

Figure 4. Increase in bowing of the yarns on the backside of the target [19]

Recent studies [19], [24] have included the effect of transverse yarn interactions and have found that these interactions can significantly influence the results from ballistic response models. The description of single ply fabric deformation is given to serve as an illustrative example to point out some of the fundamental physical mechanisms observed that influence the ballistic performance of fabrics. Material properties, fabric structure, projectile geometry, impact velocity, multiple ply interaction, far field boundary conditions and friction all play a role. Although many authors attempt to describe these mechanisms individually, it should be noted that many of the individual mechanisms have been reported in a coupled manner (i.e. multiple ply ballistic panels impacted by different geometry projectiles at varying velocities). As such, it is difficult to isolate each mechanism; therefore, further research in this aspect is needed.

The failure modes of aramid fibers are splitting and fibrillation, but also shearing, thinning (Fig. 5, [25]). PBO fiber also shows similar behavior as the aramid one. Nylon-66 fiber exhibits melting. The UHMWPE fiber, such as Spectra, exhibits straining, kinking due to the strain, as well as snap-back of fibers after breakage. The evidence of melting was also observed for Spectra fibers. To explain this phenomenon, the following two opposite arguments were reported: a) the melting is due to the heat generated from the target-projectile friction, during the penetration, b) adiabatic heating effect after the penetration.

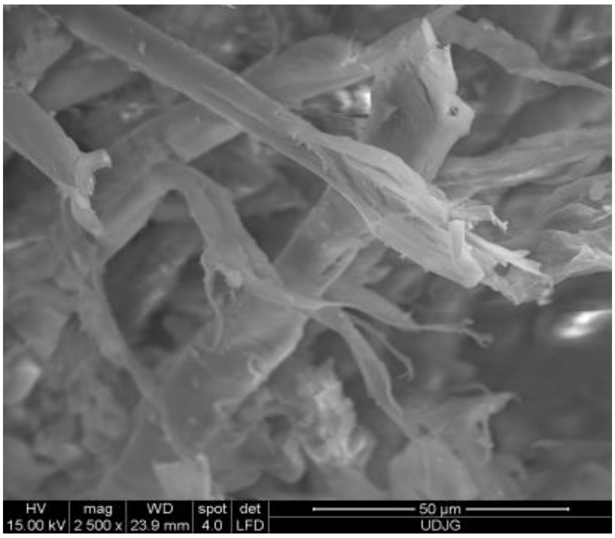

Figure 5. Typical failures of aramid fibers, after a ballistic impact with a 9mm FMJ on 24 layers of fabric SB1, bonden with PVB [25], [26]

In ballistic resistant structures, filament yarns are used to absorb projectile impact force. The logic behind the use of filaments is to present a network of high modulus, high strength fiber structure components that individually extend the entire breadth or length of the structure into which a ballistic impact is directed.

Sockalingam et al. [27] modeled the yarn as a system of fibres, including the effect of intra-yarn friction The sensitivity of friction between the fibers is studied by choosing a small and a high value of the coefficient of friction and the predicted force displacement curves are shown in Fig. 6b.

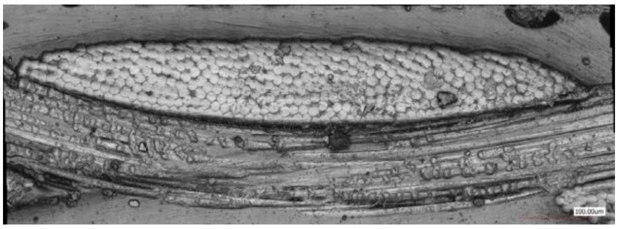

a) Actual yarn formed by aramid fibers (unloaded)

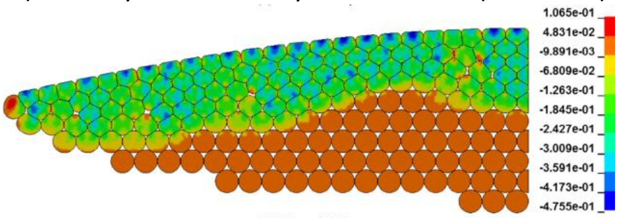

b) Contours of compressive strains at 324 m/s impact at the moment 7x10-5 s

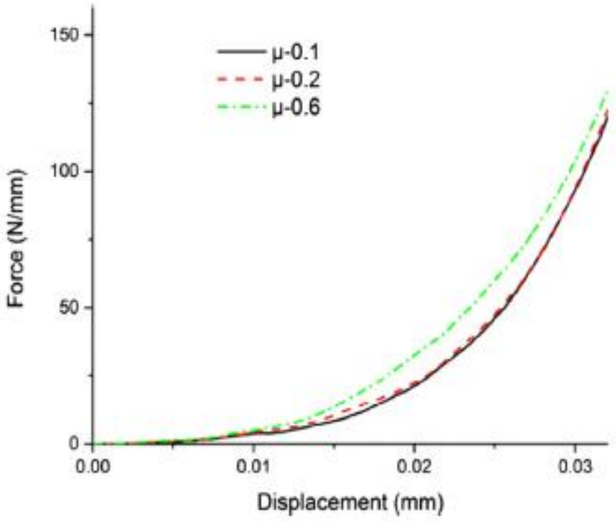

c) Influence of friction coefficient value

Figure 6. Tow transverse compression response of Kevlar KM2 fibers, using an anisotropic constitutive model [27]

The numerical predictions indicate there may be a dependence on the friction coefficient in the finite strain regime with a higher force required to compress the fibers with larger friction coefficient (Fig. 6c).

Among findings during this development, it was clear that significant advantage exists where HPPE/ECPE fibers are 5.5 denier or finer. Disadvantage was observed when fiber blends with PBO present were tested because of the very low frictional characteristics of these fibers [28].

Duan et al. [29] developed a finite-element model to study the influence of friction during ballistic impact of a rigid sphere on a square woven fabric that was firmly fixed along its four edges. Projectile-fabric friction and yarn-yarn friction were investigated and from the modeling result indicates that friction dramatically affects the local fabric structure at the impact region by hindering the lateral mobility of principal yarns. Reduction of lateral yarn mobility allows the projectile to load and break more yarns so that fabric possessing a high level of friction absorbs more energy than fabric with no friction. The projectile-fabric friction delays yarn breakage by distributing the maximum stress along the periphery of the projectile-fabric contact zone. The delay of yarn breakage substantially increases the fabric energy absorption during the later stages of the impact. The yarn-yarn friction hinders the relative motion between yarns and, thus, resists de-crimping of fabric weave tightness. It induces the fabric to fail earlier during the impact process. The overall influence of projectile-fabric friction and yarn-

inter-fiber friction coefficient increases up to a critical value. Beyond that point, ballistic strength decreases slightly as the inter-fiber friction coefficient increases. The inter-fiber friction also changes the ballistic perforation mechanisms. The effect of the friction behavior of fibers and yarns is twofold in an opposite manner. Inter-fiber friction reduces yarn mobility and reduces the outward movement of principal yarns from the impact center. As a result, more yarns participate in resisting the projectile, which improves the ballistic performance of the fabric. On the other hand, inter-fiber friction restricts the relative motion between fibers that, in turn, generates a higher fiber stress wave at the vicinity of a failed fiber element.

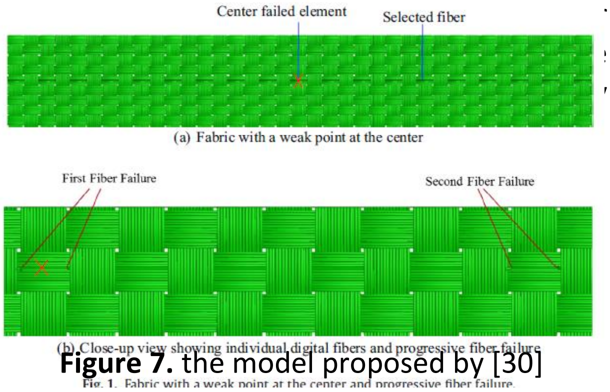

Figure 7. the model proposed by [30]

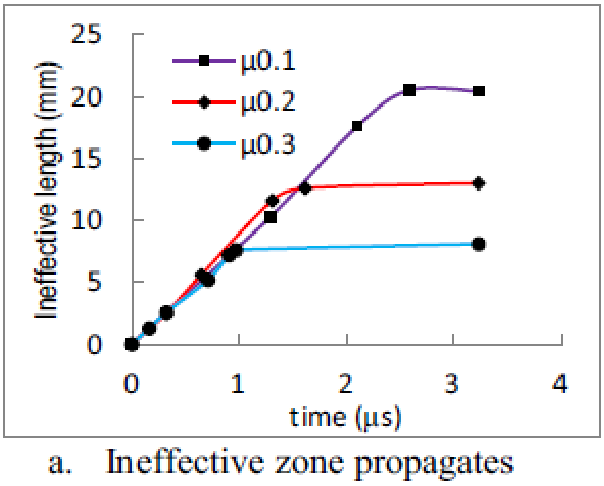

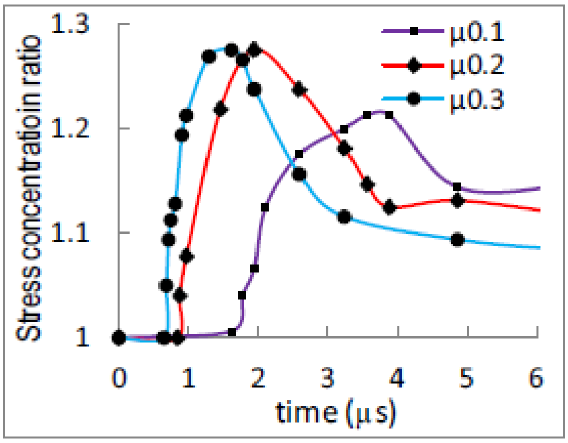

Figure 8. Stress concentration ratio depending on friction coeffient value [30]

processes of Kevlar KM2 fabrics are simulated using a fiber (micro) level. In this model, each yarn is discretized into many fibers and each fiber is divided into many rod elements. Relations of ballistic limits and inter-fiber friction coefficients are presented. In these simulations the ballistic limit improves as the

Inter-fiber friction coefficients of 0.3 or greater are also applied in the numerical simulations. Results indicate employment of a larger friction coefficient causes fiber damage to propagate not only in the longitudinal direction, but also in the transverse direction. The damage mechanism is explained as follows: As a fiber element breaks, a portion of the load originally supported by the broken fiber is transferred to its neighboring fibers through inter-fiber friction, generating stress concentration (overload) in the neighboring fibers (Fig. 8). If the stress of a neighboring fiber is greater than its fiber strength, the neighboring fiber will fail, resulting in trans-fiber failure propagation. This could further propagate into the surrounding neighboring fibers and trigger trans-fiber failure in a yarn. Cracks in the fabric demonstrate the consequence of this progressive trans-fiber damage propagation. Numerical results indicate trans-fiber damage propagation is more pronounced in fabrics with increased inter-fiber friction.

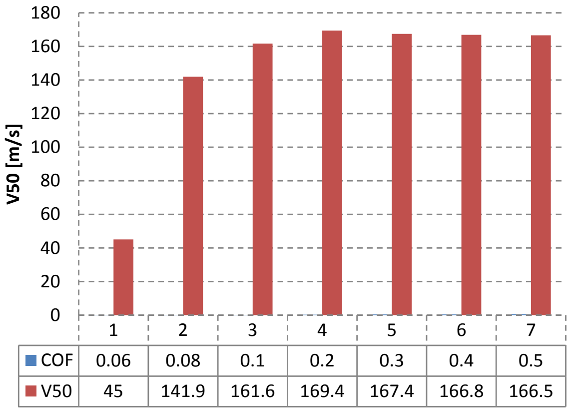

Figure 9. Effect of friction coefficient on V50 in simulations on the V_{50}, the experimental value being $V_{50\ experimental}$=132.9 m/s

Table 1. Numbers of failed yarns after impact

Friction coefficient	0.06	0.1	0.3	0.5
Number of failed wefts	0	2	4	6
Number of failed warps	0	2	4	6

Duan [31] derived from numerical simulations, the ballistic resistances of fabrics at various interfiber friction levels (Fig.9). In order to examine the role of friction during ballistic impact of high-strength fabric structures, a model the ballistic impact of a rigid sphere into a square patch of plain-weave fabric. Two types of boundary conditions were applied on the fabric: four edges clamped and two opposite edges clamped. Simple Coulomb friction was introduced between yarns at crossovers and between the projectile and the fabric. Results show that the friction contributed to delaying fabric failure and increasing impact load (Fig. 10). The delay of fabric failure and increase of impact load allowed the fabric for absorbing more energy. Fabric boundary condition is a factor that influenced the effect of friction. The fabric more effectively reduced the projectile residual velocity when only two edges were clamped.

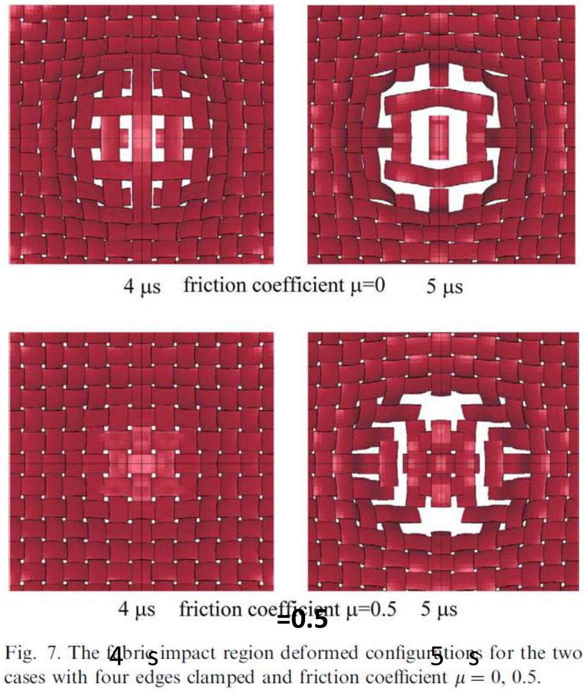

Figure 10. The impacted region of the fabric, at two moments, all edges fixed [31]

Only impact velocity and residual velocity of the projectile are measured in ballistic impact experiments. The role of friction during an impact process, is hard to resolve through experimentation only. This is because it is very difficult or even impossible to obtain detailed information on fabric deformation and failure. For a better understanding of the ballistic impact of fabric structures, analytical or numerical models are necessary. The role of friction during the ballistic impact is explored by comparing the fabric deformation, impact load, and energy absorption capacity at different friction conditions, the failed yarns (Table 1).

A case was modeled where a friction coefficient μ=0.5 was used for both the yarn–yarn friction and the projectile–fabric friction.

Figure 11 presents the fabric deformation at different moments. As the impact process continued, the transverse deflection of the principal yarns (those yarns in direct contact with the projectile) propagated away from the impact region. The interaction between yarns at crossovers caused the secondary yarns (those yarns not directly in contact with the projectile, but having been twisted or/and displaced) to deflect out of the fabric plane. This caused the transverse deflection to become pyramidal in shape. The transverse deflection wave front formed a square with its four corners located at the two cross principal yarns that passed through the impact center. At 6 μs, the transverse deflection wave front did not reach the fixed edges, but the fabric had been broken at the impact region. Eventually, the projectile perforated the fabric and moved away at a constant velocity; the fabric sprung back and, at 8 μs, the transverse deflection became conical in shape as indicated by its largely circular base

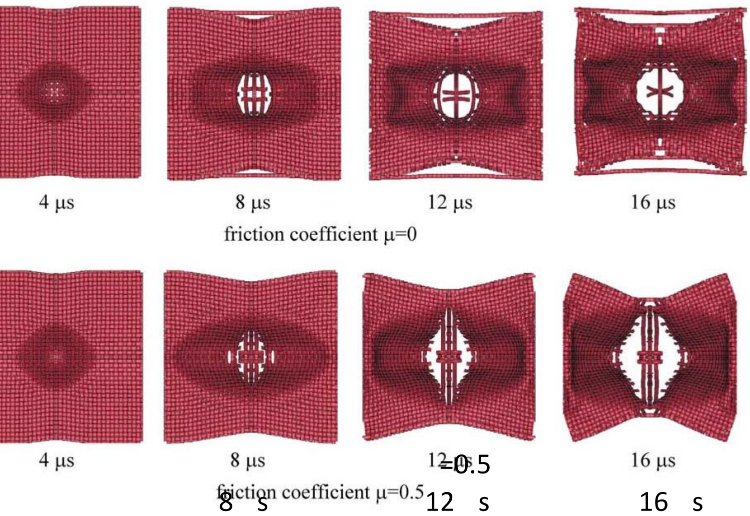

Figure 11. Different moments for two cases: without friction (=0) and with friction (=0.5)

Wilde et al. [32] observed similar pyramidal- and conical- shape deformations during their photographic investigation of high-speed missile impact on a nylon fabric. Pirvu also reported piramidal shape during a test with 9 mm FMJ, with impact velocity of 400 m/s (Fig. 12).

The boundary conditions significantly affected the fabric deformation. With the same friction condition, the fabric with four edges clamped slowed down the projectile more quickly than the fabric with two edges clamped; however, the fabric with two edges clamped more effectively reduced the residual velocity of the projectile.

Figure 12. layers of LFT SB1, 9 mm FMJ, 400 m/s, fast camera image [26]

This is because the time needed for the projectile to perforate the fabric was much less if four edges of the fabric were clamped. with the same friction condition, the fabric energy absorption capacity was much higher if only two edges of the fabric were clamped. With the same boundary conditions, the fabric energy absorption capacity was higher when consider μ=0.5. The friction effect was different at different boundary conditions; the friction increased the fabric energy absorption capacity by 11% when four edges of the fabric were clamped, whereas it increased the fabric energy absorption capacity by 24% when two edges of the fabric were clamped. The result suggests that fabric boundary condition is a factor that influenced the friction effect.

Wang [30] concluded that the ineffective zone length after first fiber breakage is related to the inter-fiber friction coefficient, for the simulation with impact velocity in the range 63 m/s...142 m/s, with spherical projectile. A lower friction coefficient yields a larger ineffective zone. A higher friction coefficient results in a higher stress concentration ratio. Fragment length after a progressive fiber failure is inverse proportional to the inter-fiber friction coefficient. Trans-fiber damage propagation occurs when the inter-fiber friction is high, which generates yarn failure or fabric cracks. In simulations, V50 increases with an increase of the friction coefficient until a critical value is reached. Beyond this point, V50 is insensitive to friction coefficients and decreases slightly as the friction coefficient continues to increase. Fabric damage starts from fiber cut and fibrilations along the principal yarns. As impact proceeds, high fiber stress in the impact area develops and more and more fibers fail. Perforation follows. If the inter-fiber friction coefficient is smaller than the critical inter-fiber friction coefficient, perforation is primarily due to fiber fragmentation propagating along the principal yarns. If the friction coefficient is greater than the critical friction coefficient, trans-fiber and trans-yarn damage propagates in the transverse direction. This induces more yarn failure in the perforation process. Numerical results are approximately 25% higher than experimental results.

Ionescu et al. [33] did simulations with isotropic layers, having the mechanical properties of aramid yarns on longitudinal axis. The virtual residual velocities was obtained for a range of impact velocities of 150...400 m/s (Fig. 13). The model run without friction has produced the highest value of the top head bullet velocity after impact for each case. The friction becomes important in energy balance of the impact when the layers are broken. When the projectile velocity is not enough for destroying the layers (at least one), the projectile is rebound, the influence of friction being noticed on a reduced time interval. These cases suggest that friction increases V_{50}, with 10...40 m/s, at least for the studied range of initial velocity of the bullet and the bullet residual velocity is lowered.

Figure 14 [33] revealed the different behavior of the bullet and stratified panel when using different values for the friction coefficient between layers.

The selection of friction coefficient values seems to be realistic, especially for bullet-layer COF(b-l)=0.3 and for friction between two layers COF(l-l) 0.2...0.4. Images from simulations (Fig. 14) could be compared to the experimental ones and parameters that better described the layer failure could be used for future more complex simulation.

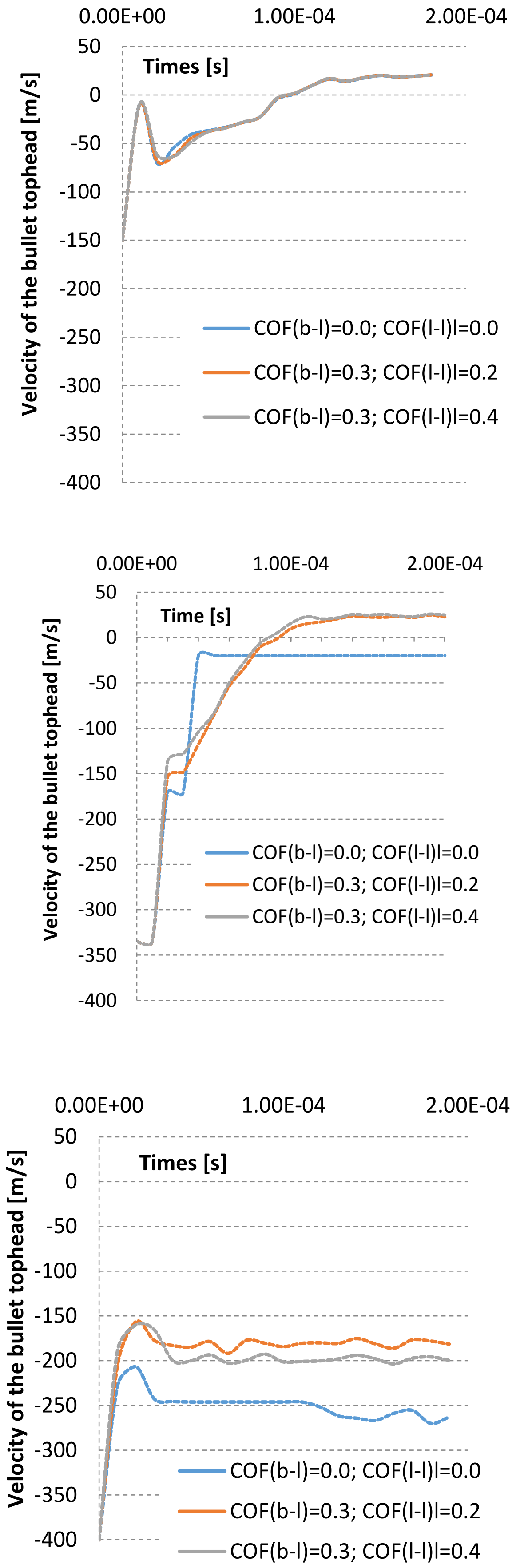

Figure 13. Macro model of the 4 layers made of virtual material with isotropic characteristics and values close to longitudinal ones of aramid yarns

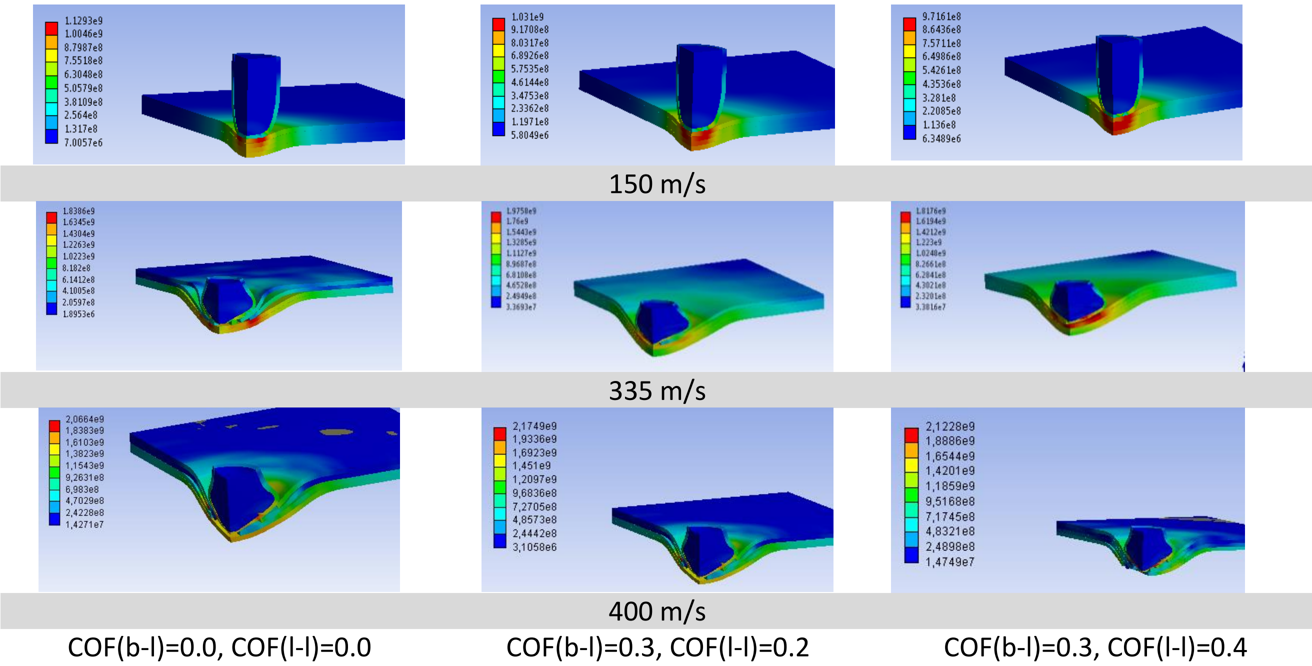

Figure 14. Influence of friction coefficient, for the same moment of simulation, t=3x10^{-5} s

The validation could imply the number of broken layers, the residual velocity (that could be measured), the backface signature, the number of broken yarns etc.

Grujicic et al. [34] used a simple penalty-based algorithm for modeling yarn/yarn and projectile/fabric interactions. A Coulomb model was for friction as a viscous model of friction was not yet supported by the dedicated soft. Two frictional cases were considered: a) both the yarn/yarn friction coefficient $_{y/y}$ and the projectile/fabric friction coefficient $_{p/f}$ are set to 0.5, and b) no friction, meaning $_{y/y}$= $_{p/f}$ =0. Boundary conditions consider all four fabric edges are fixed. The aramid yarn (Kevlar 129) has orthotropic linear elastic characteristics, Examples of the temporal evolution of deformation within the fabric obtained using the yarn-level FEM analysis and the unit-cell based FEM analysis are displayed in Fig. 15.

For the no-friction case, yarns were substantially displaced in the in-plane directions, away from the center of impact. Thus, the friction at the yarn crossovers provides resistance to the relative tangential motion of the yarns, while such resistance is absent in the no-friction case. In the no-friction case, yarns impacted by the projectile are pushed outward, a fewer number of yarns are broken and the projectile manages to penetrate the fabric mainly by "wedging" through it.

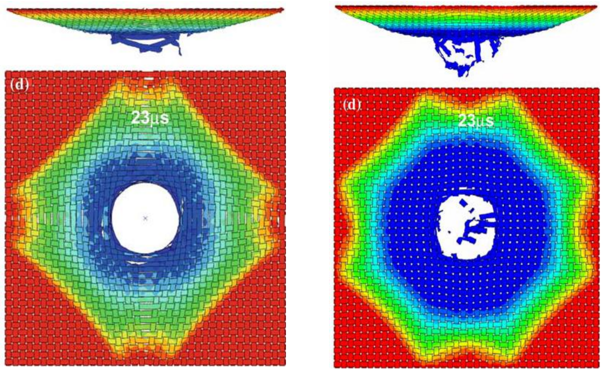

$_{p/f}$ = 0 $_{p/f}$ = 0.5

Figure 15. The deformation in the fabric for the yarn-level FEM model Contour bands correspond to different values of the displacements normal to the fabric surface [35]

Ojoc et al. [35] simulated the behavior of unidirectional fabrics, with isotropic yarns (similar to aramid ones) under the impact of a 9 mm bullet. The yarns of a layer were perpendicularly to the direction of yarns in the previous layer (0°,90°,0°,90°). The friction coefficient was constant, $_{projectile\text{-}yarn}$=0.3 and $_{projectile\text{-}yarn}$=0.4. For all these cases, the impact velocity was varied between 100 and 400 [m/s] with an increment of 100 m/s, in order to understand how the panel is damaged.

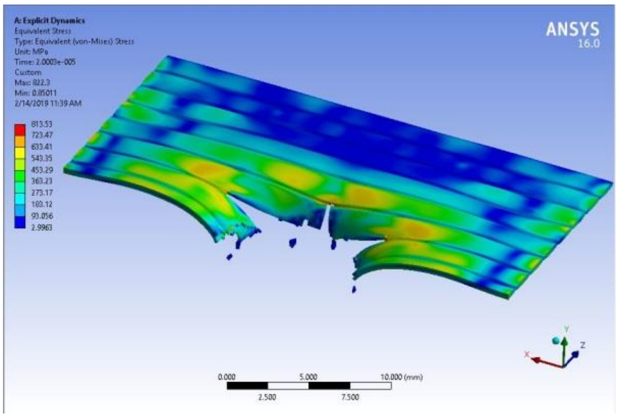

Layer 1

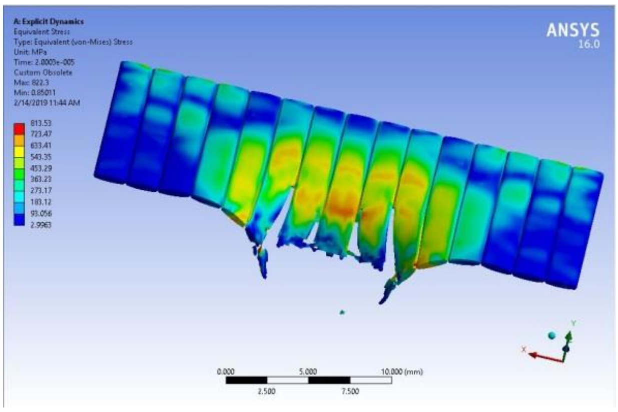

Layer 2

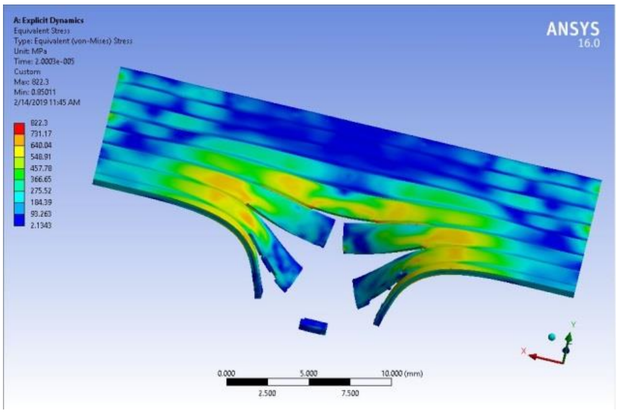

Layer 3

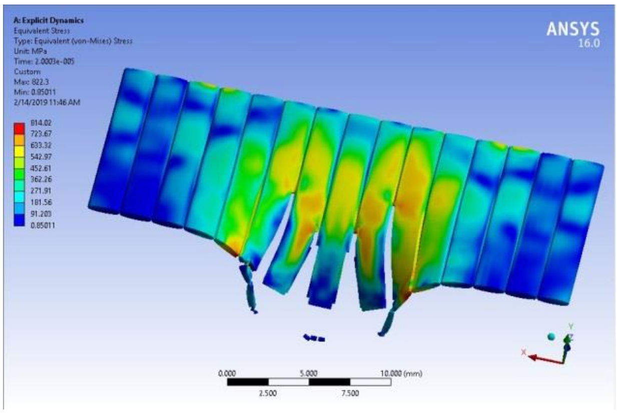

Layer 4

Figure 16. Impact simulated on four layers made of unidirectional yrans, at moment t=2 10^{-5} s impact velocity 400 m/m, the bullet being transparent [34]

For the four layer package, for lower velocities, the residual velocity has a lower percentage of the impact velocity, but at high speeds (Fig. 16), for this package, the reduction of the residual velocity from the impact velocity is even lower (2.7% at v_0=300 m/s and only 1.75% at v_0=400 m/s).

In the absence of friction the projectile can wedge through the fabric, while in the presence of friction more yarn failure is required before the projectile can reach its residual velocity.

Nilakantan et al. [36], [37] simulated the impact of a fabric, using a static frictional coefficient of 0.18 for the yarn to yarn contact and 0.18 for the projectile to yarn contact algorithms. The thickness of the warp and fill yarns is 0.115 mm and the total fabric thickness at the cross-over locations is 0.23 mm. The yarn count in both warp and fill directions is 34 yarns per inch. Two impact velocities of 100 m/s and 200 m/s are selected. While the projectile is penetrating through a hole in the fabric which is smaller than the projectile's diameter, the frictional energy dissipated by the projectile-yarn interaction rises to its maximum level. While the fabric is springing back after complete projectile penetration, the frictional energy dissipated by yarn-yarn sliding interactions rises to its maximum level.

4. CONCLUSION

Recent works simulating the impact projectile - target, done at different levels (micro, meso, macro) pointed out the influence of friction coefficient between bodies in contact. In all cited references, the friction coefficient is kept constant, even if experimental studies proved that it has different values for different sliding speeds, especially for contact metal - polymer as in the impact of aramid fabric armor.

ACKNOWLEDGEMENT

This paper was supported by a grant of the Romanian Ministery of Research and

Innovation, CCCDI-UEFISCDI, project no. PN-III-P1-1.2-PCCCDI-2017-0404/31PCCDI/2018, within PNCDI III and by Doctorale School for Mechanical and Industrial Engineering of “Dunarea de Jos” University of Galati.

REFERENCES

[1] N.K. Myshkin, M.I. Petrokovets, A.V. Koval: Tribology of polymers: Adhesion, friction, wear, and mass-transfer, Tribology International, Vol. 38, pp. 910–921, 2005.

[2] K. Shooter, R.H. Thomas: Frictional properties of some plastics. Research, Vol. 2, pp. 533-539, 1952.

[3] T. Fort: Adsorption and boundary friction of polymer surfaces, Journal of Physical Chemistry, Vol. 66, pp. 1136-1143, 1962.

[4] N.S. White: Small oil-free bearings. Journal of research of the National Institute of Standards and Technology, Vol. 57, pp. 185-189, 1956.

[5] G.M. Bartenev, V.V. Lavrentev: *Friction and wear of polymers*, Elsevier; p. 212, Amsterdam, 1981.

[6] D.G. Flom, N.T. Porile: Effect of temperature and hight-speed sliding on the friction of teflon on teflon, Nature, Vol. 175, pp. 682-685, 1955.

[7] G. W. Stachowiak, A.W. Batchelor: *Engineering tribology*, Butterworth-Heinemann, Team Lrn., 2005.

[8] C.M. McC. Ettles: Polymer and Elastomer Friction in the Thermal Control Regime, ASLE Transactions, Vol. 30, pp. 149-159, 1987

[9] A.M. Bueche, D.G. Flom: Surface Friction and Dynamic Mechanical Properties of Polymers, Wear, Vol. 2, pp. 168-182, 1958/1959.

[10] G. Nilakantan, R. L. Merrill, M. Keefe, J.W. Gillespie Jr., E.D. Wetzel: Experimental investigation of the role of frictional yarn pull-out and windowing on the probabilistic impact response of Kevlar fabrics, Composites: Part B Vol. 68, pp. 215–229, 2015.

[11] Opportunities in Protection Materials Science and Technology for Future Army Applications, ISBN 978-0-309-21285-4, 2011.

[12] S. Sockalingam, S. C. Chowdhury, J. W. Gillespie Jr., M. Keefe: Recent advances in modeling and experiments of Kevlar ballistic fibrils, fibers, yarns and flexible woven textile fabrics – a review, Textile Research Journal, Vol. 87, No. 8, pp. 984–1010, 2017.

[13] D. Prevorsek: `Spectra: *The lastest entry in the field of high-performance fibers*., in Lewin, M. and Preston, J. (eds) *Handbook of Fiber Science and Technology*, High Technology Fibers Part D, Marcel Dekker, Vol. 3, p. 17, 1996.

[14] Q.P. McAllister, J.W. Gillespie Jr., M.R. Van Landingham: The influence of surface microstructure on the scratch characteristics of Kevlar fibers, Journal of Materials Science; Vol. 48: pp. 1292–1302, 2013.

[15] S. Sockalingam, J. W Gillespie Jr, M. Keefe: Influence of multiaxial loading on the failure of Kevlar KM2 single fiber, Textile Research Journal, Vol. 88,No. 5, pp. 483–498, 2018.

[16] M. Sava, A. Hadăr, I. Părăuşanu, H.A. Petrescu, F. Baciu, S.M. Marinel: Validation of the numerical model of single-layer composites reinforced with carbon fiber and aramid, AIP Conference Proceedings 1738 (1), 480080.

[17] A. Bhatnagar: *Lightweight ballistic composites*, CRC Press, Boca Raton Boston New York, 2006.

[18] S. Rebouillat: Tribological properties of woven para-aramid fabrics and their constituent yarns, Journal of Material Science, Vol. 33, pp. 3293-3301, 1998.

[19] C.T. Lim, V.B.C. Tan, C.H. Cheong: Perforation of high-strength double-ply fabric system by varying shaped projectiles. International Journal of Impact Engineering, Vol. 27, No. 6, pp. 577-591, 2002.

[20] V. B. C. Tan, K. J. L. Khoo: `Perforation of flexible laminates by projectiles of different geometry,' International Journal of Impact Engineering, Vol. 31, pp. 793-810, 2005.

[21] P. M. Cunniff: `An Analysis of the System Effects in Woven Fabric Under Ballistic Impact, Textile Research Journal, Vol. 62, No. 9, pp. 495-509, 1992.

[22] L. Lee, S. Rudov-Clark, A.P. Mouritz, M.K. Bannister, I. Herszberg: `Effect of weaving damage on the tensile properties of three-dimensional woven composites,' Composite Structures, Vol. 57, pp. 405-413, 2002.

[23] S. Rudov-Clark, A.P. Mouritz, L. Lee, M. K. Bannister `Fibre damage in the manufacture of advanced three-dimensional woven composites,' Composites: Part A, Vol. 34, pp. 963-970, 2003.

[24] C.T. Lim, V.P.W. Shim, Y.H. Ng: Finite-element modeling of the ballistic impact of fabric armor, International Journal of Impact Engineering, Vol. 28, pp. 13-31, 2003.

[25] Ballistic material handbook, Teijin, available at: https://www.teijinaramid.com/wp-content/uploads/2018/03/TEIJ_Handbook_Ballistics_2018_WEB.pdf, accessed at 21.04.2019.

[26] C. Pirvu: Contributions on numerical and experimental study of ballistic packages made of aramid fibers (in Romanian) PhD thesis, Dunarea de Jos University, 2015.
[27] S. Sockalingam, J.W. Gillespie Jr., M. Keefe: On the transverse compression response of Kevlar KM2 using fiber-level finite element model, International Journal of Solids and Structures, Vol. 51, pp. 2504–2517, 2014.
[28] H.L. Thomas: `Needle-Punched Non-Woven Fabric for Fragmentation Protection', 14th International Conference on Composite Materials, Society of Manufacturing Engineers, July 14-18, 2003.
[29] Y. Duan, M. Keefe, T.A. Bogetti, B.A. Cheeseman: `Modeling friction effects on the ballistic impact behavior of a single-ply high-strength fabric, International Journal of Impact Engineering, Vol. 31, No. 8, pp. 996-1012, 2005.
[30] Y. Wang, Y. Miao, L. Huang, D. Swenson, C.-F. Yen, J. Yu, J. Q. Zheng: Effect of the inter-fiber friction on fiber damage propagation and ballistic limit of 2-D woven fabrics under a fully confined boundary condition, International Journal of Impact Engineering, Vol. 97, pp. 66–78, 2016.
[31] Y. Duan, M. Keefe, T.A. Bogetti, B.A. Cheeseman: `Modeling the role of friction during ballistic impact of a high-strength plain-weave fabric,' Composite Structures, Vol. 68, No. 3, pp. 331-337, 2005.
[32] A. Wilde, D. Roylance, J.M. Rogers: `Photographic investigation of high-speed missile impact upon nylon fabric, Part 1: Energy absorption and cone radial velocity in fabric,' Textile Research Journal, Vol. 12, pp. 753-761, 1973.
[33] T.F. Ionescu, C. Pirvu, S. Badea, C. Georgescu, L. Deleanu: The Influence of Friction Characteristics in Simulating the Impact Bullet - Stratified Materials, 15th International Conference on Tribology, Kragujevac, Serbia, 17 – 19 May 2017.
[34] W.C.M. Grujicic, B. Æ T. He, B. A. Cheeseman: Development and verification of a meso-scale based dynamic material model for plain-woven single-ply ballistic fabric J Mater Sci, Vol. 43, pp. 6301–6323, 2008.
[35] G. G. Ojoc, L. Oancea, Catalin Pirvu, S. Sandu, L. Deleanu, Modeling of Impact on Multiple Layers with Unidirectional Yarns, Scientific Conference of Doctoral Schools, Dunarea de Jos University of Galati, 2019.
[36] G. Nilakantan, R. L. Merrill, M. Keefe, J.W. Gillespie Jr., E.D. Wetzel: Experimental investigation of the role of frictional yarn pull-out and windowing on the probabilistic impact response of kevlar fabrics, Composites: Part B Vol. 68, pp. 215–229, 2015.
[37] G. Nilakantn, M. Keefe, T. A. Bogetti, J.W. Gillespie Jr.: Multiscale modeling of the impact of textile fabrics based on hybrid element analysis, International Journal of Impact Engineering , Vol. 37, pp. 1056-1071, 2010.

Surface Engineering and Coating Tribology

16th International Conference on Tribology – SERBIATRIB '19

15 – 17 May 2019, Kragujevac, Serbia

Serbian Tribology Society

SERBIATRIB '19

16th International Conference on Tribology

Faculty of Engineering University of Kragujevac

Kragujevac, Serbia, 15 – 17 May 2019

FAILURE OF DIAMOND-LIKE CARBON (DLC) COATINGS IN AUTOMOBILE ENGINES – A REVIEW

Funsho Olaitan KOLAWOLE[1,2,*], André Paulo TSCHIPTSCHIN[1], Shola Kolade KOLAWOLE[3,4], Marco Antonio RAMIREZ R[5]

[1]Departamento de Engenharia Metalúrgica e de Materiais, Universidade de São Paulo, Sao Paulo, Brazil, fkopresido@yahoo.com; antschip@usp.br

[2]Department of Materials and Metallurgical Engineering, Federal University, Oye-Ekiti, Nigeria, fkopresido@yahoo.com

[3]National Agency for Science and Engineering Infrastructure, Abuja, Nigeria, sholak190e@yahoo.com

[4]Materials Science and Engineering, African University of Science and Technology, Abuja, Nigeria, sholak190e@yahoo.com

[5]Instituto de Pesquisa e Desenvolvimento, Universidade do Vale do Paraiba, São Jose dos Campos, Brazil, marco.macrol@gmail.com

*Corresponding author: fkopresido@yahoo.com

Abstract: *Diamond-like carbon (DLC) coatings have become very attractive for various industrial applications, such as cutting tools, automotive engines, biomedical implants, micro-electromechanical devices (MEMS). Due to their surface energies and ability to interact with lubricants to form surface protective films, good adhesion with substrate, increased wear resistance, improved electrical conductivity, decreased internal compressive stresses during deposition and thermal stability there are used in automobile components. In the automobile industry, DLC coatings are usually applied on combustion engine components such as piston, tappet, camshaft, piston rings and gudgeon pin, valve stem and head and rocker arm. DLC coatings helps in reducing friction and wear of the moving parts. However, there are challenges facing the use of DLC coated components during service, which are; internal compressive stresses, low adhesion and low thermal stability leading to failures such as rolling contact fatigue, micro-pitting, delamination, oxidation and scuffing. Hardness and internal compressive stress increase with increasing* sp^3 *content* (sp^3/sp^2) *ratio in DLCs. Internal compressive stress for DLC coatings > 1GPa in tribological applications is not good, due to the elastic strain energy that drives fractures along the coating/substrate interface, leading to delamination through blistering. The addition of non-metals (Si, N, F or O) or metals (W, Cr, Ta, Ti, Mo or Cu) can improve thermal stability of DLC up to about 500* ^oC*. Above, 500* ^oC *transformation of sp3 to sp2 begins to occur leading to graphitization. The addition of metals increases the interfacial fracture toughness and moderates the internal stress by creating two (2) interface; substrate/adhesion layer interface and adhesion layer/functional coating interface. This present paper will discuss the various failures that occur on DLC coatings such as internal compressive stresses, low adhesion and low thermal stability of non-metal and metal doped DLC coatings, regarding their applications in automobile engines. The effect of annealing conditions, tribological properties of non-metal and metal doped DLC, effect of sp3/sp2 ratio, and possible ways of reducing these failures on DLC coatings be discussed also.*

Keywords: *automobile industry, diamond-like carbon, energy consumption, internal compressive stresses, low adhesion, low thermal stability.*

1. INTRODUCTION

In the automotive industry the use of coatings which possess long-term stability having low friction coefficients and low wear rates at temperatures up to 500 ^{o}C are important for current developments, such as higher power densities, downsizing or the use of low-viscosity oils [1]. The use of diamond-like carbon (DLC) coatings are increasingly used in the automobile industry, mostly the hydrogenated amorphous carbon (a-C:H) coatings, even the hydrogen-free ta-C coatings are also gaining attention up to about 350 ^{o}C [2,3,4]. Incorporating additional elements can be used to modify DLC and increase the heat resistance of DLC coatings [5].

DLC coatings are commonly used for automotive engine parts (engine block, cylinder head, cylinders, crankshaft, connecting rods, pistons, sparks plug, fuel injectors, intake and exhaust valves, camshaft and belt) [6]. The main reason DLC coatings are used in automotive engine parts is simply due to the fact that it is a low friction coating, other reasons are; to circumvent the problems when using low viscosity oils, friction and wear resistance, constant change in oil additives and to reduce the use of anti-wear additives like Zinc dialkyldithiophosphates (ZDDP) [6]. It has been reported that DLC coatings reduces friction up to 30% in lubricated contact compared to steel/steel contact [7]. Energy lost to friction in a passenger car has been estimate as 33% [7].

2. ENGINE OPERATIONAL CONDITIONS

During the last 20 years, diminishing oil reserves and global warming has brought the awareness for the need to have a fuel-efficient and environmentally friendly transportation system. In this same period, automotive and lubrication engineers have intensified their efforts to reduce energy losses due to friction, rolling resistance, and cooling systems and to thereby boost the efficiency of the next-generation engines [8]. The main target of the automotive industry as they produce luxury cars to attract customers is to cutdown on extra weight and fuel consumption [9]. High temperature is one of the causes of valve failure in internal combustion engine, which are also subjected to cyclic loading. Failure on the surface is as a result of elastic and plastic deformation, fatigue micro-crack and spalling [10]. These failures lead to increase in friction and wear on engine components, consequently causing high fuel consumption in engines of vehicles. Although, increase in the operational temperature of an automotive engine has some advantages, due to the fact that it directly influences the elements that bring about losses in the engine and effectiveness of the cooling system, and the formation of emissions gas in the engine. Increase in temperature raises the engine oil temperature and in turn lowers frictional losses in the engine, leading to an improved fuel efficiency [11].

Erdemir and Holmberg, 2015 [8] carried out a compressive study on energy consumption due to friction in motored vehicles. In automotive engines, rolling contact fatigue, micro-pitting, oxidation and scuffing are the tribology challenges encountered during operating conditions due to friction and wear [12]. The use of DLCs can overcome these challenges except for the issue of oxidation. This is due to the high temperature (150 to 180^{o}C) involved, if exposed to high temperatures at operating conditions of the engine, they would be prone to oxidation [12].

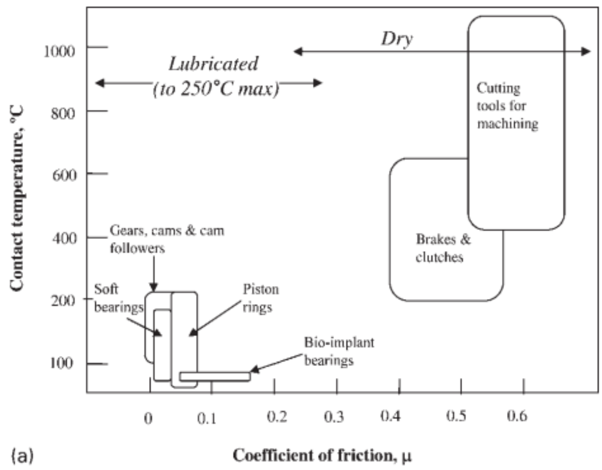

Figure 1. Friction–temperature regimes [12]

The temperature regimes for automobile lubricated engine components is 250°C (maximum) as seen in Figure 1. A decrease in friction coefficient and wear resistance of DLC films occurs with increase in temperature between 100 – 300 °C [13]. Piston ring coatings are required to resist a combination of surface degradation effects that encompass both chemical and mechanical processes. Since boundary lubrication occurs at the extreme displacement of the piston ring cylinder liner contact, the durability of the top piston ring requires resistance to wear [12].

2.1 Internal compressive stress and low adhesion

Internal compressive stress increases with increasing sp3 content (sp3/sp2) ratio. The effect of internal compressive stress is shown in Figure 2 for both hydrogenated and non-hydrogenated DLCs. High internal compressive stress value of 1 GPa are a potential achilles heel for DLCs in tribological applications which leads to the elastic strain energy that drives fractures along the coating/substrate interface and leads to coating delamination, sometimes via blistering [14]. Poor DLC coating adherence is an issue irrespective of the substrate. DLCs show variable adherence to Co–Cr–Mo, Ti–6Al–4V, cemented carbides, high speed steels, through hardened and stainless steels. To minimise this effect, coating architectures of the type shown in Figure 3 are invoked to locally moderate internal stress and increase interfacial fracture toughness. Here, at least one bond or adhesion layer is placed between the substrate and the multifunctional carbon coating. Accordingly, there are interface 1 (substrate/adhesion layer) and interface 2 (adhesion layer/functional coating). Either interface is a potential source for crack initiation and growth [12]. While, DLC coating adherence might be deemed satisfactory following scratch adhesion testing, such materials can nonetheless demonstrate poor adherence in various tribological applications. A further factor needs to be taken into account: the initiation and propagation of fractures due to fatigue stress cycling [12]. This effect can be studied using high cycle surface elastic contact indentation testing of the kind reported by Ledrappier et al. (2008) [15].

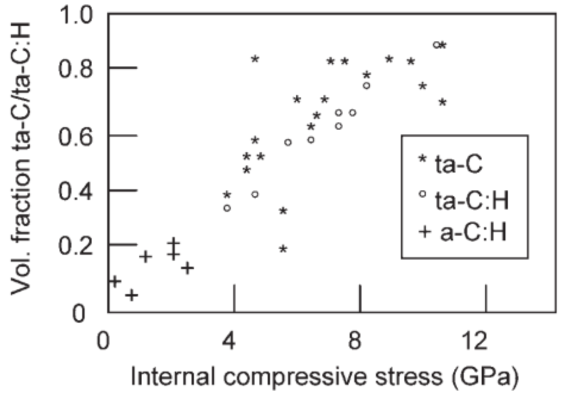

Figure 2. Variation of internal stress for ta-C and ta-C:H coatings as function of ta-C (sp^3) content.

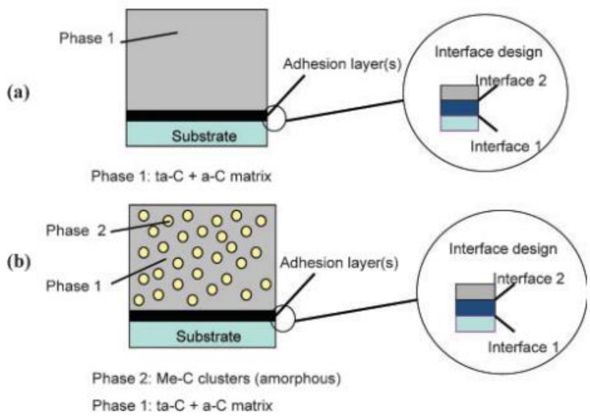

Figure 3. Typical non-hydrogenated DLC coating architectures (a) pure carbon multifunctional coating; (b) metal or non-metal doped carbon multifunctional coating [16]

2.2 Low thermal stability of non-metal and metal doped DLC coatings

It is very important to know the operating temperature range for an automobile engine in a passenger car in order to ensure that the provided coatings can withstand the effect of the maximum operating temperature. Studies have shown that several researchers have reported different operating temperatures; 85 to 155°C [17], maximum of 180°C [9], 250 to 300°C [18] and 750 °C to 950 °C [10]. Another author mentioned that the normal operating temperature conditions for an automotive engine is 80 – 100 °C, while some experimental studies have used as low as 22 °C and as high as 500 °C [19]. Thermal stability (under vacuum) for hydrogen-free ta-C films deposited by CVAE are much more thermally stable than a-C:H films deposited by PACVD [20]. It was published in 1977 that the hardness of ta-C does not drop up to about 600 °C under vacuum [21].

It was observed that thin films in the thickness range of several tens of nm are stable up to at least 400 °C with only a very small graphitization under vacuum [22]. Investigations on very thin films (1.5 nm) showed that changes observed in the Raman peak position and ID/IG of the 300 °C annealed samples (time 60 min) are not attributable to graphitization. The ta-C film at 300 °C showed only more sp2 clustering and not a reduction in sp3 content [23]. Oxidation for diamond films in air started at about 640 °C [24]. Different graphite grades have been investigated and results showed that almost no oxidation at 330 °C for 1 h, while at 530 °C had a significant oxidation rate depending on the graphite grade [25]. The starting temperature of oxidation for a-C and ta-C films varied depending on structure. It has been shown that for a-C and ta-C films deposited by FCVAE, the oxidation behavior depends strongly on the sp3 content [26].

3. FAILURE OF DLC COATED AUTOMOBILE COMPONENTS.

Failure modes for 100Cr6 rollers are summarised in the schematic diagram (Figure 4). Failure of the uncoated 100Cr6 rollers is usually due to the occurrence of large, rolling contact fatigue (RCF) pits, which resembled those classified as type IIIA [12]. In addition, smooth wear also prevail, which is evident from the polishing away of the original surface grinding marks. RCF pitting was typically observed after several hundred hours of testing and also affected some of the coated rollers being classified as types IIIA and IIIB failures, although the size (surface areas) of these particular rolling contact fatigue failures were approximately 30–50% smaller than those observed for the uncoated rollers [12]. In some cases, RCF pitting was initiated after shorter times than those observed for the uncoated materials. An unexpected mode of failure was that due to micropitting (mode type IV). This mechanism prevailed to a varying extent on all the coatings tested, but did not cause complete coating failure. Coating delamination is a serious problem, there are three kinds of failure modes, types IA, IB and IIB (Figure 4) [12,27]. On the W-doped DLC (Cr–W–C:H), type IA and IIB caused delamination of the nanolayers that comprised the architecture of this coating. The type IA or IB failure modes took place for the Cr2N and CrNznC coatings, either along interface 1 or interface 2 (as seen in Figure 3) [12]. None of these delamination failure modes affected the more uniformly structured W-doped DLC (W–C:H). Here, eventual failure is rate controlled through microabrasion and a feature of this wear is the formation of banding patterns shown in Figure 5.

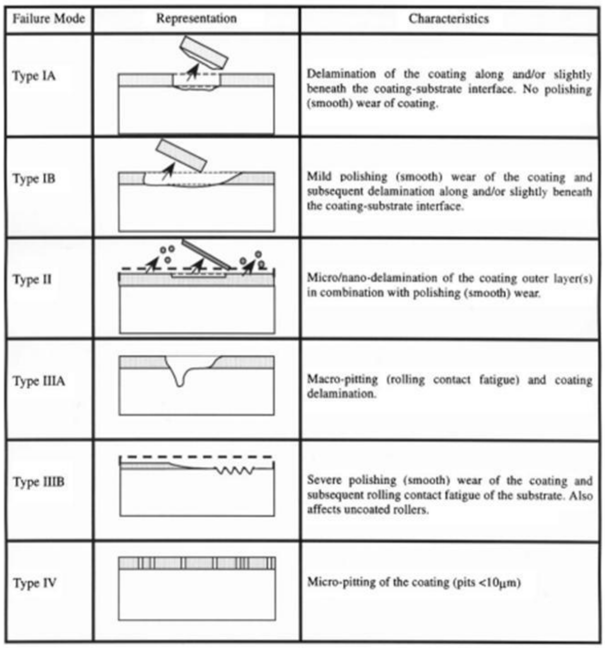

Figure 4. Principal failure modes of hard coated bearing surfaces observed during high pressure lubricated contacts [27]

Two types of carbon coating, one based on non-hydrogenated a-C and the other based on ta-C, were applied to 100Cr6 substrates and subjected to the same rolling/sliding contact described earlier. Here, a simple base oil containing no specific additive package was used. For both kinds of carbon coated 100Cr6, type IA coating delamination took place after a relatively few test cycles (Figure 6) [12].

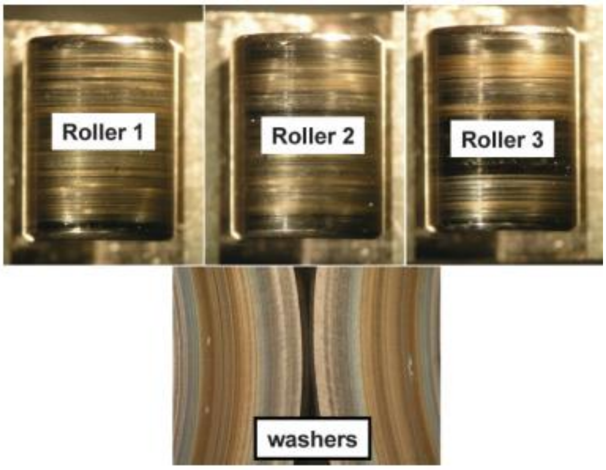

Figure 5. Microabrasion of W doped DLC (W-C:H: type B) coating on 100Cr6 test bearing rolls and corresponding uncoated washers.

Figure 6. Delamination failure of ta-C DLC coating on 100Cr6.

The effect was studied more carefully and it was demonstrated that the delamination phenomenon, although exhibiting wide scatter, followed an S–N behaviour that is typical of fatigue (Figure 7).

This suggests that crack propagation along interfaces 1 or 2 (Fig. 3) occurs at a rate that depends upon the magnitude of the change in stress per unit cycle and the total number of stress cycle reversals, this means crack growth is due to a fatigue mechanism.

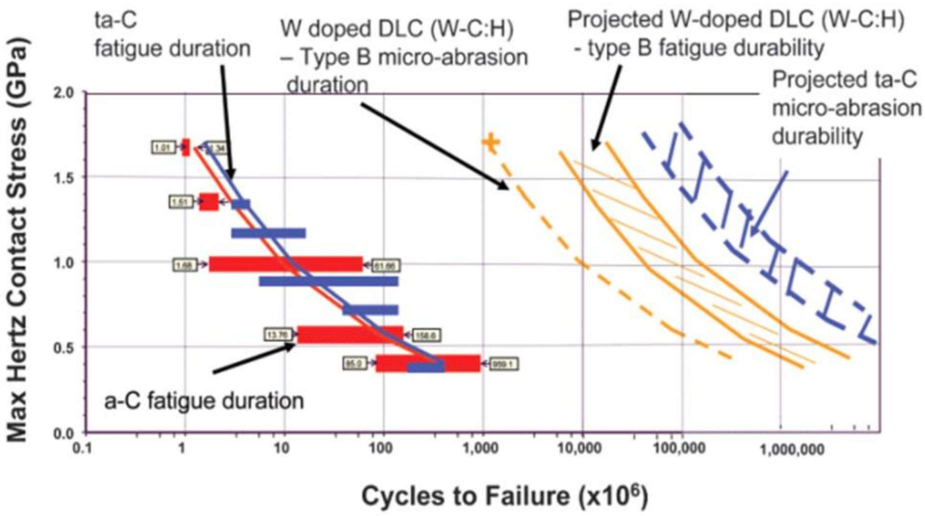

Figure 7. Coating life for indicated carbon coatings on 100Cr6 and their failure mechanisms.

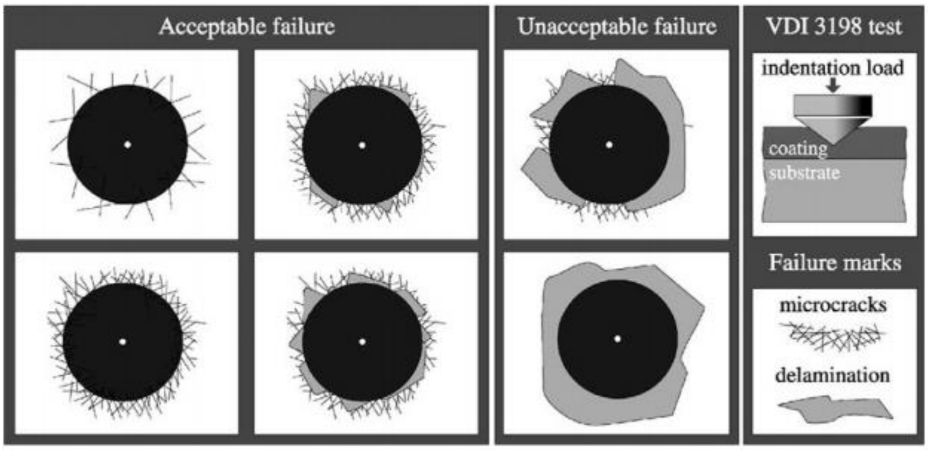

Figure 8. The principle of the VDI 3198 indentation test.

Accordingly, fatigue delamination and microabrasion processes are competing failure modes for carbon based coatings in this application. For the non-hydrogenated a-C and ta-C enriched carbon coatings, failure was dominated by delamination in Figure 7, while the hydrogenated W-doped DLC type B failures, contained lower internal stress (approximately 800 MPa), compared to (approximately 3 Gpa) for the ta-C coatings failed progressively by a process of microabrasion (Figure 5). If delamination fatigue failures could be mitigated for non-hydrogenated a-C and ta-C enriched carbon coatings by significantly reducing internal stress, then more durable coated 100Cr6 with projected life cycles moving towards the right hand side in Figure 7 [12].

The result of adhesion quality of the DLC film on Inconel Alloy 718 samples resulted to be very good according to the VDI 3198 standard (see Fig. 8), which are classifies into acceptable and unacceptable failure for delamination fault. Some very small radial cracking of the film can be observed on the samples around the indentation region [28].

4. IMPROVEMENT OF DLC COATINGS FOR AUTOMOBILE APPLICATION.

Different modified DLC coatings have been investigated with regard to their mechanical and tribological properties up to 550 °C. The results of these investigations form a basis for being able to define friction- and wear-reducing DLC coatings for automotive components for use at higher temperatures (Figure 9a & 9b) [5].

4.1 Effect of annealing on the thermal stability of DLC coatings.

DLC coatings are usually associated with internal stresses, which affects the tribological properties and thermal stability of the coatings. Annealing is always used to reduce the internal stress in DLC coatings. Annealing ta-C up to 800 °C reduces the internal stress to an insignificant value (Figure 10) [21,26]. However, annealing DLCs above 500 °C reduces the thermal stability. Figure 11, shows two carbon films deposited with different bias voltages, the lower hardness film having a lower sp3 fraction. Two (2) decades later it was revealed that the mechanical properties, hardness and elastic modulus remain almost stable with annealing up to 850 °C for ta-C coatings with sp3 content of 85% [21,26].

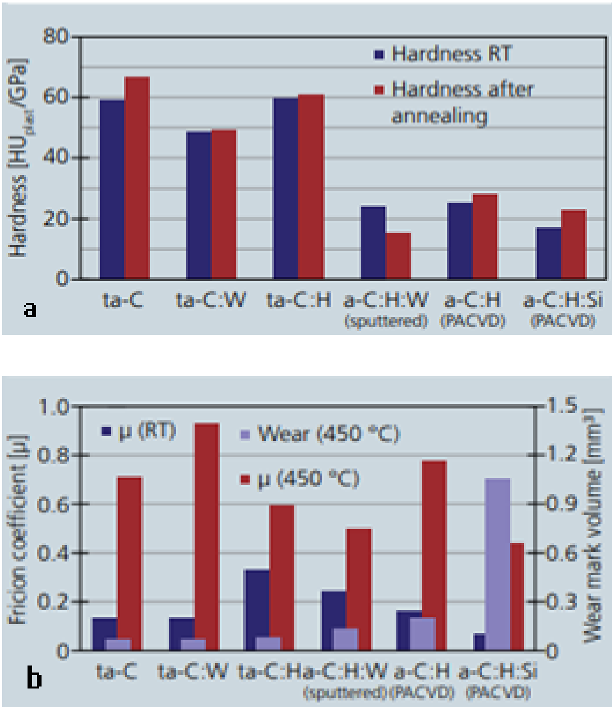

Figure 9. (a) Hardness before and after annealing, (b) Friction coefficients and wear rates after the at room temperature and at 450°C

During the annealing process a clustering of the sp2 bonded carbon atoms occurs first [30,31], and the sp3 content is not affected. That process results in the change of some physical properties, and a reduction in compressive stress [30].

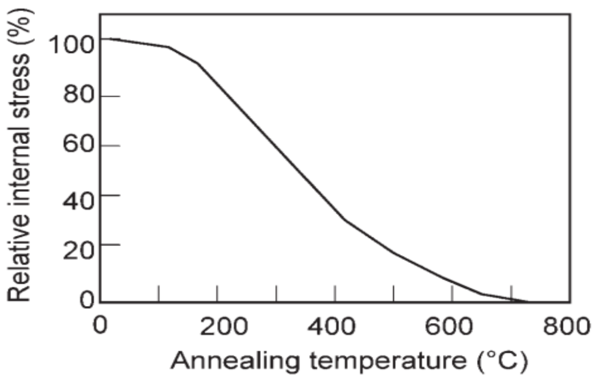

Figure 10. Relative internal stress (%) against annealing temperature (°C) for ta-C coatings deposited at room temperature [12]

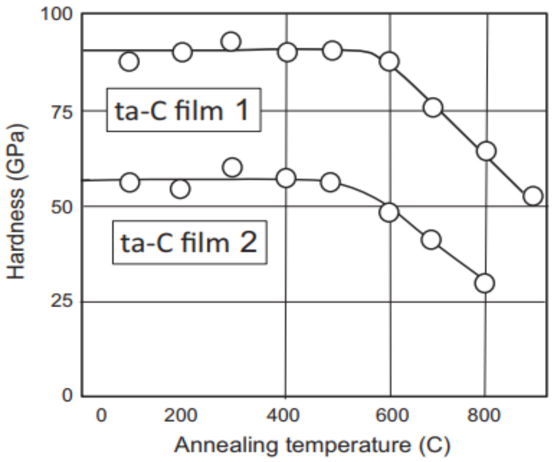

Figure 11. Micro hardness versus annealing temperature for ta-C films deposited using DCVAE with different bias voltages [21]

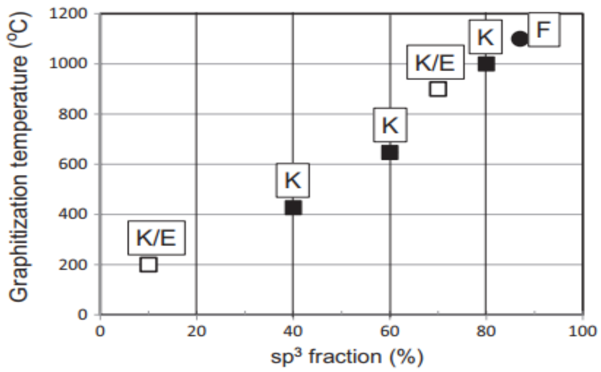

Figure 12. Graphitization temperature for a-C films versus the sp3 fraction [30,31]

At higher temperatures graphitization begins, Figure 12, shows the graphitization temperature for a-C films having different sp3 fractions, deposited by argon ion beam sputtering (IBS), mass-selected carbon ion beam (MSIB) deposition, pulsed-laser deposition (PLD), and filtered arc (FCVAE) deposition [23]. In Figure 12, points K/E are estimated values for low sp3 (IBS) and high sp3 (PLD) films, points K is measured values for MSIB film and point F is an FCVAE film [30,31]. The best thermal stability, up to approximately 1100 °C, was shown by the film with the highest sp3 fraction, deposited by FCVAE. By 1200 °C the sp3 fraction of this coating was decreased to 20% [30]. The confirmation of a strong correlation exists between the sp3 fraction and the graphitic transformation temperature by the investigations of the evolution of bonding structures of a-C films and the electrical resistivity during laser annealing [32]. Figure 13 shows the plot of loss in film thickness against annealing temperature for films (initial thickness of 450 nm). It can be observed that films with higher sp3 fraction retain their structure up to 500 °C, and a lower rate of material loss during heat treatment. The oxidation rate (thickness loss) becomes significant only above 500 °C for the taC film, whereas the a-C films with the low sp3 content begins to lose thickness above 450 °C and almost completely at 475 °C. The friction torque of the valve train for various surfaces as a function of the rotation speed (Figure 14). Using ta-C coating gave a reduction of 45% in the friction torque at 2000 rpm compared to the standard phosphated surface treatment [23].

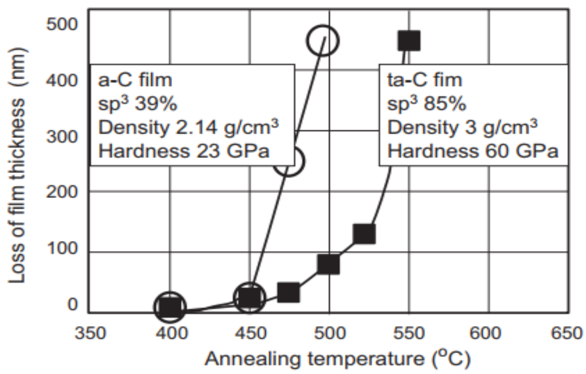

Figure 13. Shows loss in film thickness as a function of annealing temperature in air for 2 h, for a-C and ta-C film deposited by FCVAE [26]

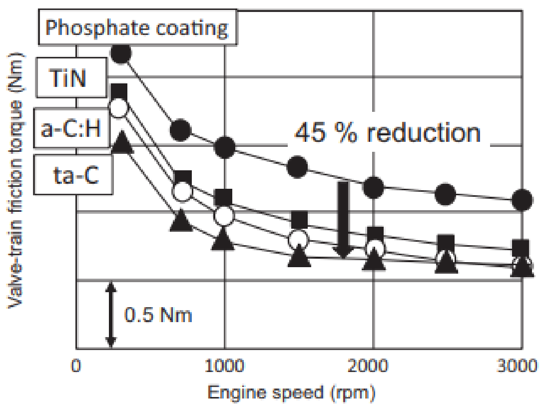

Figure 14. Friction torque of the valve train for various surfaces as a function of the rotation speed [23]

4.2 Non-Metal and metal doping of DLC coatings

Metal-doped DLC (Me-DLC) coatings usually exhibit higher thermal stability than non-doped DLC up to annealing temperatures of 500°C, which was revealed by X-ray diffraction, transmission electron microscopy, and Raman spectroscopy.

Annealing temperature above 500°C, losing high amount of hydrogen from the Me-DLC coatings, causing breakdown and structural collapse of the coatings at high temperature, which may be due to breaking of C-H bonds. Thereby, the C-C networks become graphite-like, leading to the formation of volatile C-O and metal oxides phases [33]. Since 1971, DLC has been widely used in automotive industry, this is simply due to their excellent tribological properties such as low friction, wear and corrosion resistance, high hardness, high thermal and chemical stability. Non-doped hydrogenated DLC coating has low resistance to wear in lubricating oils containing MoDTC, this is due to the decomposition and chemical reactions that formed oxides and nano-crystallites [34]. Si-doped DLC coating produces anti-wear film which is stronger in the presence of additives in lubricants but weaker in the absence of additives. Raman spectroscopy is used to characterize the tribo-chemical process for the DLC coatings in the presence of additives in lubricants. PVD process was used to deposit tungsten-doped diamond-like carbon (a-C:H/W) on AISI 52100 bearing steel [34].

It has been observed that addition of Mo delays graphitization up to 400°C in air and at 500°C in low pressure atmospheres, the addition of Mo_2S leads to an increase in the thermal stability by a decrease in the graphitization rate. Molybdenum oxides act as abrasive particles providing hardness and stability at high temperatures, simultaneously damaging the formed tribolayer which promotes lubrication. MoO_3 above 500°C become volatile so at high temperatures the coefficient of friction will change due to formation of a new tribolayer, which helps to decrease the friction. Mo-DLC coatings tends to form a granular pattern (onion-like) structure whose density is reduced as the carbon content increases in the matrix, while reducing hardness. An industrial sized Hauzer HTC 1000-4 PVD coating machine which combines UBM (Unbalanced magnetron) and HIPIMS (High power impulse magnetron sputtering) was used for the deposition [35]. Mo-doped diamond-like carbon coatings were deposited by closed field unbalanced magnetron sputtering to determine their mechanical and blood compatibility properties. The undoped and Mo-doped DLC coatings were analysed by Raman spectra, Atomic force microscopy, and temperature-dependent frictional wear testing. The obtained results indicated that the Mo-DLC coatings with low Mo concentration was a more efficient protective coating with reduced residual stress, increased cohesive strength and good wear resistance at temperature of 500°C [33].

5. CONCLUSION

In conclusion, the need of DLC coatings for automobile engine components were discussed, engine operational conditions, internal compressive stress and low adhesion, low thermal stability of non-metal and metal doped DLC coatings, failure of DLC coated automobile components, Improvement of DLC coatings for automobile application, effect of annealing on the thermal stability of DLC coatings, non-metal and metal doping of DLC coatings were also discussed. The challenges faced with the use of DLC coated components during service, which are; internal compressive stress, low adhesion and low thermal stability, which leads to failure of engine components such as rolling contact fatigue, micro-pitting, delamination, oxidation and scuffing. Internal compressive stress can be reduced by annealing, adhesion can be improved by the use of substrate/adhesion layer and adhesion layer/ coating interface, while low thermal stability can be overcome by non-metal and metal doping of DLC. These solutions reduce the failure of DLC coatings and make them suitable for coating automobile engine components.

ACKNOWLEDGEMENT

The authors would like to thank, Petroluem Technology Development Fund (PTDF) for its financial support.

REFERENCES

[1] H.M. Mobarak, M. Chowdhury: Tribological performance of hydrogenated amorphous carbon (a-C:H) DLC coating when lubricated with biodegradeable vegetal canola oil, Tribology in Industry, Vol. 36, No. 2, pp. 163-171, 2014.

[2] S.D.A. Lawes, M.E. Fitzpatrick, S.V. Hainsworth: Evaluation of the tribological properties of DLC for engine applications, Journal of physics D: Applied physics, Vol. 40, pp. 5427-5437, 2007.

[3] A. Matthews, S.S. Eskildsen: Engineering applications for diamond-like carbon, Diamond Related Materials, Vol. 3, No. 4-6, pp. 902–911, 1994.

[4] C.P.O. Treutler: Industrial Use of Plasma-Deposited Coatings for Components of Automotive Fuel Injection Systems, Surface & Coatings Technology, Vol. 200, No. 5-6, pp. 1969-1975, 2005.

[5] M. Keunecke, M. Weber: 2015 Fraunhofer IST https://www.ist.fraunhofer.deFraunhofer,Institute for Surface Engineering and Thin Films IST | Bienroder Weg 54 E | 38108 Braunschweig | Germany, 2015.

[6] D. Sniderman: Coatings and engineering are shaping tomorrow' s world, Tribology & Lubrication Technology, pp. 52-63, 2016.

[7] K. Holmberg, P. Andersson, A. Erdemir: Tribology International Global energy consumption due to friction in passenger cars. Tribiology International, Vol. 47, pp. 221–234, 2012.

[8] A. Erdemir, K. Holmberg: Energy consumption due to friction in motored vehicles and low-friction coatings to reduce it, In S.C. Cha, A. Erdemir (Eds.) *Coating technology for vehicle applications*, Cham, Switzerland, Springer International Publishing AG, pp. 10-11, 2015.

[9] H. Allmaier, C. Priestner, D.E. Sander, F.M. Reich: Friction in automotive engines. Tribology in Engineering, pp. 149 – 184, 2013.

[10] A. Pandey, R.K. Mandloi: Effects of high temperature on the microstructure of automotive engine valves. International journal of engineering research and applications, Vol. 4, No. 3, pp. 122-126, 2014.

[11] H.H. Pang, C.J. Brace: Review of engine cooling technologies for modern engines, Journal of automobile engineering, Vol. 218, pp. 1-7, 2004.

[12] P.A. Dearnley, A. Neville, S. Turner, H. Scheibe, R. Tietema, R. Tap, R., M. Stüber, P. Hovsepian, A. Layyous, B. Stenbom: Coatings tribology drivers for high density plasma technologies, Surface Engineering, Vol. 26, No. 2, pp. 80-96, 2017.

[13] A. Grill: Review of the tribology of diamond-like carbon,Wear, Vol. 168, pp. 143-153, 1993.

[14] X.L. Peng, T.W. Clyne: Residual stress and debonding of DLC films on metallic substrates, Diamond Related Materials, Vol. 7, No. 7, pp. 944–950, 1998.

[15] F. Ledrappier, L. Houze, C. Heau: A comparison of the tribology of tetrahedral amorphous carbon and hydrogenated amorphous carbon, *Proceedings 16th International Colloquium on Tribology, Esslingen*, Germany, January, TAE, 2008.

[16] J. Robertson: Diamond-like amorphous carbon, Materials Science and Engineering, Vol. R37, pp. 129–281, 2002.

[17] M. Tuner: *Combustion of alternative vehicle fuels in internal combustion engine. A report on engine performance from combustion of alternative fuels based on literature review*, Lund University, Department of Energy Sciences, Division of Combustion Engines, pp. 1 – 39,2015.

[18] R.H. Magnusdottir: *Engine preheating before ignition*, A M.Sc. Thesis, Faculty of Engineering, University of Iceland, pp. 1-36, 2007.

[19] R. Zahid, H.H. Masjuki, M. Varman, R.A. Mufti, M.A. Kalam, M. Gulzar: Effect of lubricant formulations on the tribological performance of self-mated doped DLC contacts: A review. Tribology Letters, Vol. 58, No. 32, pp. 1-28, 2015.

[20] N. Khamnualthong, K. Siangchaew, P. Limsuwan: Influence of thermal heating on diamond-like carbon film properties prepared by filtered cathodic arc, Thin Solid Films, Vol. 544, pp. 477–481, 2013.

[21] V.E. Strel'nitskij, S.I. Vakula, N.N. Matjushenko, Ukrainian Journal of Physics, Vol. 22, pp. 431–433 (Russian), 1977.

[22] B.K. Tay, D. Sheeja, S.P. Lau, X. Shi, B.C. Seet, Y.C. Yeo: Time and temperature-dependent changes in the structural properties of tetrahedral amorphous carbon films, Surface & Coatings Technology, Vol. 130, No. 2-3, pp. 248–251, 2000.

[23] J. Vetter: 60 years of DLC coatings: Historical highlights and technical review of cathodic arc processes to synthesize various DLC types,

and their evolution for industrial applications. Surface & Coatings Technology, Vol. 257, pp. 213-240, 2014.
[24] J.-C. Pu, S.-F. Wang, J.C. Sung: High-temperature oxidation behaviors of CVD diamond films, Applied Surface Science, Vol. 256, No. 3, pp. 668–673, 2009.
[25] M. Balden, K.U. Klages, W. Jacob, J. Roth: Oxidation erosion of graphite in air between 600 and 1000 K, Journal of Nuclear Materials, Vol. 341, pp. 31 – 44, 2005.
[26] S. Anders, J.W. Ager III, G.M. Pharr, T.Y. Tsui, I.G. Brown: Heat treatment of cathodic arc deposited amorphous hard carbon films, Thin Solid Films, Vol. 308–309, pp. 186–190, 1997.
[27] D. Yonekura, R.J. Chittenden, P.A. Dearnley: Wear mechanisms of steel roller bearings protected by thin, hard and low friction coatings, Wear, Vol. 259, pp. 779–788, 2005.
[28] M.A. Ramírez-R, P.C. Silva, E.J. Corat, V.J. Trava-Airoldi: An evaluation of the tribological characteristics of DLC films grown on Inconel Alloy 718 using the Active Screen Plasma technique in a Pulsed-DC PECVD system, Surface & Coatings Technology, Vol. 284, pp. 235–239, 2015.
[29] S. Anders, J. Díaz, J.W. Ager III, R.Y. Lo, D.B. Bogy: Thermal stability of amorphous hard carbon films produced by cathodic arc deposition, Applied Physics Letters, Vol. 71, No. 23, pp. 3367–3369, 1997.
[30] A.C. Ferrari, B. Kleinsorge, N.A. Morrison, A. Hart: Stress reduction and bond stability during thermal annealing of tetrahedral amorphous carbon, Journal Applied Physics, Vol. 85, No. 10, pp. 7191–7719, 1999.
[31] R. Kalish, Y. Lifshitz, K. Nugent, S. Prawer: Thermal stability and relaxation in diamond-like-carbon. A Raman study of films with different sp3sp3 fractions (ta-C to a-C), Applied Physics Letter, Vol. 74, No. 20, pp. 2936–2938, 1999.
[32] N. Xu, S.H. Tsang, E.H.T. Teo, X. Wang, C.M. Ng, B.K. Tay: Effect of initial sp3 content on bonding structure evolution of amorphous carbon upon pulsed laser annealing, Diamond Related Material, Vol. 30, pp. 48–52, 2012.
[33] K.Y. Fu, Y.F. Mei, M.Y. Fu, X.Y. Liu, P.K. Chu: Thermal stability of metal-doped diamond-like carbon fabricated by dual plasma deposition, Diamond & Related Materials, Vol. 14, pp. 1489-1493, 2005.
[34] L. Yang, A. Neville, A. Brown, P. Ransom, A. Morina: Friction reduction mechanisms in boundary lubricated W-doped DLC coatings, Tribology International, Vol. 70, pp. 26-33, 2014.
[35] I.C. Muller, J. Sharp, W.M. Rainforth, P. Hovsepian, A. Ehiasarian: Tribological response and characterization of Mo-W doped-DLC coating, Wear, Vol. 376-377, pp. 1622-1629, 2017.

Serbian Tribology Society

SERBIATRIB '19

16th International Conference on Tribology

Faculty of Engineering
University of Kragujevac

Kragujevac, Serbia, 15 – 17 May 2019

MANUFACTURING NANOCOMPOSITE COATINGS AND WEAR EVALUATION IN CERMETS

Matheus A. DA CUNHA[1], Waleska C. GUAGLIANONI[1], Bruno F.A. BEZERRA[1], Felipe V. DE CAMARGO[1,2,*], Carlos P. BERGMANN[1]

[1]Federal University of Rio Grande do Sul, Porto Alegre, Brazil
[2]University of Bologna, Bologna, Italy
*Corresponding author: fevannucchi@gmail.com

Abstract: *This work investigates the wear rate of a cermet from a NiCr alloy that is added at 5 wt% to cobalt carbide. This carbide was milled for 3, 6 and 12 hours in a high energy mill to obtain different sizes of nanometer-scale crystallites, and high velocity oxygen fuel thermal spraying (HVOF) was used to deposit the coating onto a metal substrate. The feedstocks used to obtain the coating were characterized via morphology through scanning electron microscopy (SEM), crystallite size, and crystalline phases by X-ray diffraction (XRD) as well as particle size analysis. The coatings were evaluated for microstructure (optical microscope), Vickers hardness and thickness, and wear was performed by means of solid particle erosion and Ball-on-disc tests. The results showed that the crystallite size of WCCo significantly decreased in the first milling hours. The coatings milled for 3 hours and 12 hours showed a mass loss for the erosive test of approximately 50% less than the commercial coating at the 30° angle. For erosion, at 90° angle, the coating with lower mass loss was the compound milled for 3h. All cobalt carbide compositions displayed an improved behavior relative to that of samples made from the commercial feedstock.*

Keywords: *WCCo/NiCr coatings, Thermal spraying, Tribology, Wear, Erosion.*

1. INTRODUCTION

The preparation and modification of the surfaces of mechanical components that perform specific functions in an application, generally without significantly changing the dimensions of the components, are of great importance in the study of surface engineering. Surface engineering deals with the application of traditional or innovative technology to modify the properties of components and materials, creating a new composite material that combines the desirable characteristics of the surface and the base material in the same piece [1].

One way of modifying the properties of the surfaces is by depositing a coating using thermal spray techniques, which consists of a group of processes where metallic or non-metallic materials are sprayed in a molten or semi-molten condition on a prepared substrate forming a coating. The coating material may initially be in the form of powder, rod or wire and the formed coatings may be applied to provide wear resistance, electrical or thermal insulation or conductivity [2].

Several metallic and non-metallic alloys have been developed to be deposited through thermal sprinkling techniques. Cermet coatings consist of a mixture of a ductile metal matrix that may be pure or in a blend composed of Ni, Cr or Co with WC or Cr_3C_2 particles dispersed within the metal matrix [3]. Nickel-based cermets are widely used industrially because of their superior mechanical strength as well as corrosion, erosion, and abrasion resistance. They are easy to manufacture, have lower production costs and the ability to coat substrates with any geometric design [4]. The wear resistance of the material is controlled by the proportion of carbide particles dispersed in the matrix, the carbide size and the hardness. These coatings require particles that can resist to wear. The best thermal deposition technique for coatings with these characteristics is HVOF spraying [5].

Most studies on WCCo coatings employ raw materials on traditional scales [6-8]. The literature does not present investigations on coatings that use nanostructured NiCr and WCCo together and in their composition. The performance of these coatings can be altered if one of these materials is used on the nanometer scale, in a way that the physical and mechanical properties of the materials become superior due to the high volumetric fraction of atoms present in the grain boundary due to the reduced size of the nanometer scale [9].

It is in this context that the present investigation is conducted, aiming to obtain raw materials based on WCCo/NiCr to constitute coatings through HVOF spraying and subsequent evaluation of the wear resistance in different techniques, thus pointing out optimal coating process parameters for the attainment of an enhanced performance of the composite against wear.

2. MATERIALS AND METHODS

The cermet consists of nickel-chromium (NiCr) and tungsten carbide-cobalt (WCCo) supplied by Sulzer Metco and sold commercially as Diamalloy 2001 and Woka 3652. Table 1 shows the chemical composition of these materials according to the manufacturer [10, 11].

The high energy milling of WCCo was performed with a planetary mill using tempered steel milling bowl and AISI 52100 steel spherical milling bodies that are 10 mm diameter. The milling speed was 450 rpm using ethyl alcohol to cover the system. The milling times ranged from 15 min to 12 hours. After this step, the sample was dried at 50°C [12].

Table 1. Chemical composition of NiCr (Diamalloy 2001 [10]) and WCCo (Woka 3652 [11])

Material	Composition (%)					
NiCr	**Ni**	**Cr**	**B**	**Si**	**C**	**Fe**
	Balance	17.0	3.5	4.0	1.0	4.0
WCCo	**W**	**Co**	**Cr**	**C**	**Fe**	**-**
	Balance	8.5-11.5	3.4-4.6	4.8-5.6	0.2	-

The morphological analysis of the powders was carried using a scanning electron microscope (SEM) with a tungsten filament, and the crystalline phases were characterized via X-Ray spectroscopy. The instrument was equipped with a graphite monochromator and Cu-Kα radiation (λ = 1.5406). Crystallite sizes of the tungsten carbide in commercial form and after milling were determined via XRD technique using the Scherrer equation (Eq. 1):

$$D = (k.\lambda)/\beta.\cos(\theta) \quad (1)$$

where D is the average dimension of crystallites; K is the Scherrer constant (usually assumed to be 1); λ is the wavelength of the X-ray source; and β is the integral breadth of a reflection (in radians) located at 2θ.

The manufacture used 95 wt% NiCr with 5 wt% WCCo. The powders were in the commercial form, and the process used 3 milling times (3, 6, and 12 h). The samples were mixed and agglomerated with 10% polyvinyl acetate. The heat treatment occurred in a 600°C oven with an argon atmosphere for 3 hours.

The coating deposited on on AISI 310 stainless steel was obtained via HVOF. The deposition parameters [13] are 0.385 L/min of kerosene flow, 58.2 and 0.3 mm^3/h of oxygen and feed flow, respectively, 300 mm of spraying distance and a 4 inches nozzle.

The coatings were evaluated for their microstructure and microhardness after thermal deposition. Samples were cut in a cross section after which they were sanded and polished. The microstructure was analyzed with a camera-embedded microscope. The Vickers microhardness tests employed a 3 N load for 10 seconds. Five indentations were made in the matrix region and another 5 were made in the carbide region.

The erosive wear tests were based on ASTM G76-13 [14]. The tests were performed at room temperature with 600 grams of erodent mass (electrofused alumina) and erodent impact velocity in the coating was approximately 30 m/s. The incidence angles between the surface of the coating and the erodent evaluated were 30° and 90°. Wear was determined by the difference between the final mass and the initial mass of the parts.

The tribological test was performed with a tribometer, providing both the wear rate of the coating and the coefficient of friction between the parts. The ball-on-disc test was performed according to ASTM G99 [15]. Three tests were performed for each group to evaluate wear rate. The test was conducted with alumina spheres after applying loads of 10 N, 15 N and 20 N with a linear velocity of 3.0 cm/s (without lubricant) and a distance of 33 m [16].

The wear rate was obtained based on the volume removed from the coating surface after tribological testing, dividing the worn volume (obtained with a contact profile model) by the product of the applied load and the distance.

3. RESULTS

The reduction of crystallite size as a function of milling time is shown in Figure 1, where samples submitted to milling for a few minutes did not present significant changes in their crystallite size, but the greatest variations were obtained with samples at 3 and 6 hours. Carbide milled for 12 hours has a crystallite size that is very close to sample milled for 6 hours. This small variation might occur because the material reaches the saturation point of deformation of the crystalline lattice at the atomic level and because of the increase in the density of defects in the crystalline lattice – a characteristic feature of the high energy milling process [17]. A recovery phenomenon can also occur during long milling times, where the density of defects in the crystalline lattice is reduced [18].

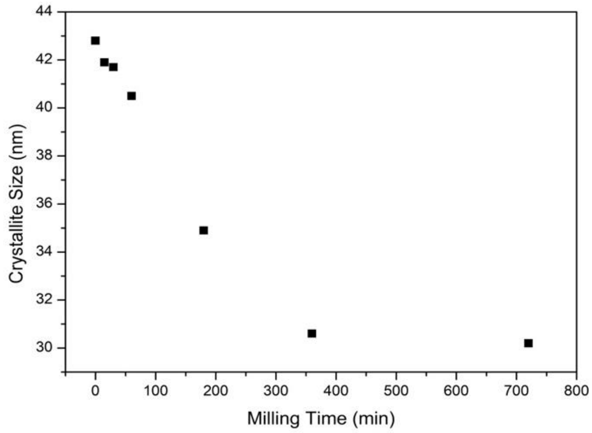

Figure 1. Crystallite size of WCCo as a function of milling time

Different crystallite size values can be found in similar studies when using distinct weight ratio of milling bodies to powder [17], or due to different milling rotation speeds [19].

XRD analysis did not show new phases even after milling. However, it is possible to see in Figure 2 that grinding broadened the diffraction peaks of the carbides. The crystallite size is refined and the internal strain has increased as a result of this enlargement.

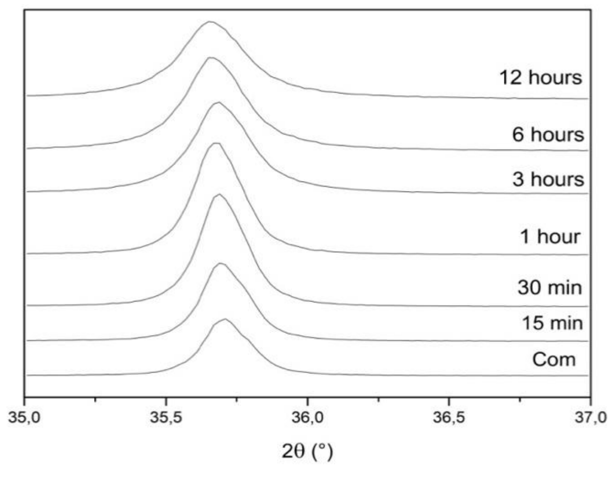

Figure 2. X-ray diffraction patterns of the first peaks of the commercial WCCo samples after different grinding times

The amplification of the diffraction peaks of carbide with increasing grinding time indicates a reduction of the crystallite size [20]. The peak shifted to the left suggesting insertion of tensile stress in the crystalline structure [21]. This behavior has been seen by other researchers using low [22] and long grinding times [17].

Figure 3a to 3d show scanning electron microscope (SEM) images upon addition of 5% WCCo to the NiCr alloy, illustrating that most of the ground fraction adhered to the surface of the NiCr alloy.

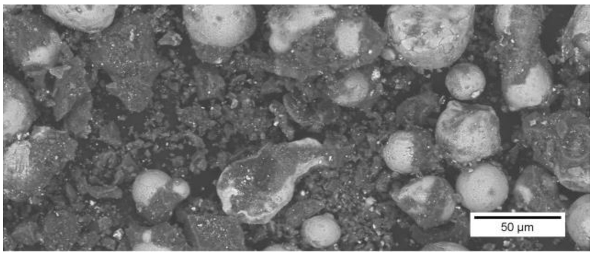

(a)

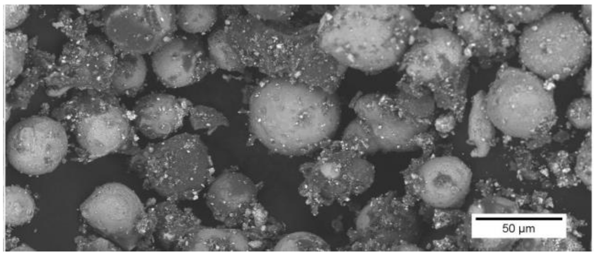

(b)

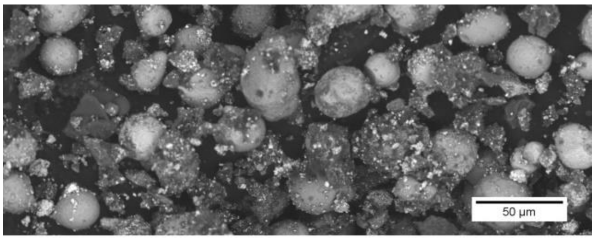

(c)

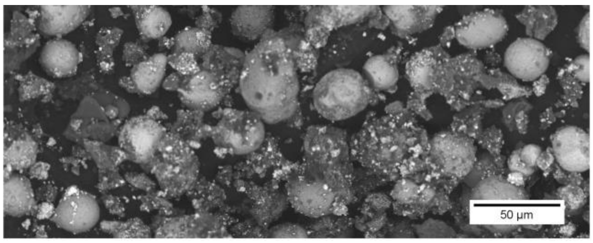

(d)

Figure 3. WCCo-NiCr with 5% WCCo (500x): commercial (a); with WCCo grinding for 3 hours (b); 6 hours (c); and 12 hours (d)

Figure 4a to 4d show the microstructure of coatings obtained by thermal spraying for all 5 % WCCo/NiCr samples. The coating layer is formed with NiCr (light part of the images) and carbides (dark regions). The coatings made with WCCo milled for 6 and 12 hours showed relatively greater thickness than the other samples. The coatings formed via carbide grinding for 3 hours or for 12 hours showed more dispersed carbides in the metal matrix.

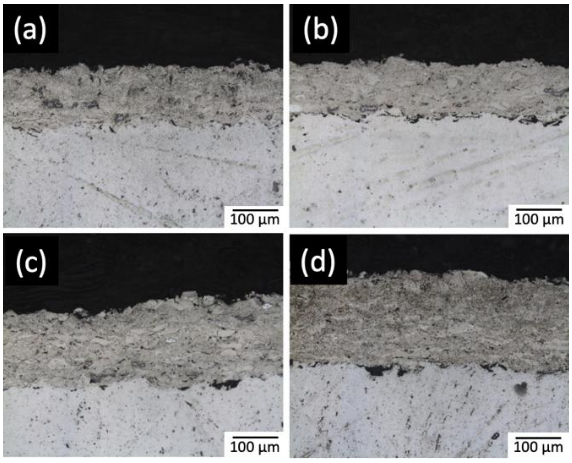

Figure 4. Microstructure of the cross section of the WCCo-NiCr alloy coating with 5% WCCo (200x): commercial (a); with WCCo processed for 3 hours (b); for 6 hours (c); and for 12 hours (d)

The average thicknesses for coatings obtained by HVOF with 5% WCCo added to the NiCr were measured 5 times along two pieces of each coating. The commercial coating and the ones with WCCo milled for 3, 6 and 12 hours had, respectively, 130 ± 12, 134 ± 8, 206 ± 7 and 194 ± 9 mm.

The microhardness measurements were performed in the matrix and the carbides regions. The average values for commercial coating and the ones with WCCo milled for 3, 6 and 12 hours had, respectively, are 423 ± 7, 403 ± 8, 406 ± 7 and 409 ± 4 HV for the matrix, and 876 ± 22, 637 ± 11, 823 ± 14 and 598 ± 12 HV for the carbide.

Figure 5a shows that the presence of small grains and the well-defined shape of the four indentation edges are observed in the indentation region in the point with the highest microhardness value (823 HV) for the coating. On the other hand, Figure 5b shows the indentation performed in the region of the matrix of the coating formed with WCCo for 3 hours. The microhardness value (403 HV) indicates that this region of the coating is more ductile. The indentation has elongated diagonals, which validates the lower hardness value of the coating. Similar hardness results were attained by other researchers [23].

Table 2 shows the mass loss for the erosion test of coatings obtained with 5% WCCo and the results of the wear rate obtained with the ball-on-disc test with normal loads of 10 N, 15 N and 20 N.

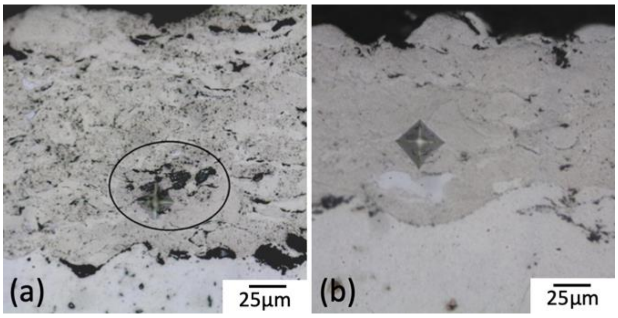

Figure 5. (a) Indentation in the carbide region for the WCCo-NiCr alloy with 5% WCCo grinding for 6 hours (500x); and (b) on the matrix for coating WCCo-NiCr with 5% WCCo grinding for 3 hours (500x)

Table 2. Erosive wear (at 30 ° and 90 °) and tribological tests for normal loads of 10 N, 15 N and 20 N in coatings with 5 wt% WCCo in different sizes of crystallites

Wear		5% WCCo comm.	5% WCCo (3 h)	5% WCCo (6 h)	5% WCCo (12 h)
Erosion (g)	30°	0.102 ± 0.004	0.052 ± 0.002	0.086 ± 0.019	0.052 ± 0.002
	90°	0.068 ± 0.007	0.065 ± 0.011	0.079 ± 0.007	0.091 ± 0.002
Tribology (mm^3/Nm)	10 N	1.73 ± 0.44	1.09 ± 0.15	1.51 ± 0.16	1.10 ± 0.14
	15 N	1.32 ± 0.29	0.91 ± 0.29	1.18 ± 0.12	0.70 ± 0.17
	20 N	2.33 ± 0.19	1.73 ± 0.17	1.26 ± 0.21	0.95 ± 0.21

In tests conducted at an angle of 30°, the coatings obtained with grinded WCCo had less mass loss than the ones with commercial WCCo. The coatings composed of WCCo grinded for 3 and 12 hours showed similar performance and 50% lower mass loss than the commercial coating, because the second had a smaller crystallite size.

The coatings formed with commercial WCCo and milled 6 hours presented higher erosive wear at 30° than at 90°, showing ductile material behavior. On the other hand, the coatings with WCCo milled for 3 and 12 hours demonstrated greater mass loss at 90°, indicating a fragile behavior. Rateick et al. [24] studied the mechanism present in the erosive wear of a cermet WC-Co, observing that the fragile and ductile nature of WC-Co cermets (rigid carbides embedded in a soft matrix) make it difficult to predict the effect of erodent particles and the impact angle on the erosion rate and the erosion mechanism, once results showed both weak and fragile responses.

The smaller erosions at 30° after 3 and 12 hours of milling are attributed to the fact that the carbides are better dispersed in the NiCr matrix, which favors the endurance of the material under such impact angle.

It is possible to see that for all normal loads the commercial specimen presented the worst performance regarding resistance to wear due to the fact of presenting larger crystallite size. By analyzing only the results of the tests with a load of 20 N, it can be seen that the wear rate decreased as the size of the crystallite decreased and consequently the coating containing the carbide benefited for 12 hours obtained the lowest rate of wear.

For the tests carried out with a normal load of 15 N, the coating containing the smallest crystallite size (WCCo 12 hours) also presented the highest resistance to wear. It can be seen that the tested coatings with WCCo milled for 3 hours and 6 hours showed a reversal in their wear resistance behavior, which can be attributed to better dispersion of the carbide in the coating providing a lower wear rate.

For the tests carried out with a load of 10 N it was observed that the coatings composed of carbides benefited for 3 and 12 hours had practically the same rate of wear, that is, the coatings were the most resistant to wear. Due to the better distribution of the carbides along the coating, the WCCo sample at 3 hours showed a lower wear rate than the other samples.

4. CONCLUSIONS

Coatings obtained with 5% WCCo milled for 3 hours and 12 hours showed the most dispersed carbides in their matrix. On the other hand, in coatings with 5% WCCo milled for 6 hours and in the commercial form, the carbides were observed in concentrated areas.

Erosive wear for a 30° angle of attack was higher for 5% WCCo milled for 6 hours and in the commercial form. At the same erodent impact angle, the 5% WCCo 3-hour-milled coating presented in the erosion test a 50% lower mass loss than the commercial coating, demonstrating that in order to improve the wear resistance of this coating, unduly long millings are dispensable.

The higher erosive wear at 30° than at 90° of coatings formed with commercial WCCo and milled 6 hours, demonstrates the predominantly ductile behavior of the material. Instead, when milled for 3 and 12 hours, greater mass losses are identified at 90°, indicating a fragile behavior.

Tribology ball-on-disc tests showed that coatings from 5% WCCo commercial had the highest wear rates independently of the loads applied. On the other hand, coatings that had 5% WCCo grinded for 12 hours had the lowest wear rate for normal loads of 15N and 20N and the carbide coating grinded for 3 hours obtained the lowest wear rate with a normal load of 10 N.

ACKNOWLEDGEMENT

This work was supported by the Brazilian National Agency for Petroleum, Natural Gas and Biofuels - ANP (Project 2.20.1003 (40)) and performed in collaboration with Rijeza Metallurgy Co., which was responsible for the HVOF thermal spraying of the coatings.

REFERENCES

[1] T. Bell: Surface engineering: past, present, and future, Surface Engineering, Vol. 6, pp. 31-40, 1990.

[2] American Welding Society, *Thermal Spraying: Practice, Theory, and Application*, 1985.

[3] D. Toma, W. Brandl, G. Marginean: Wear and corrosion behaviour of thermally sprayed cermet coatings, Surface and Coatings Technology, Vol. 138, pp. 149-158, 2001.

[4] P.K. Gupta, A.N. Tiwari, B.K. Agrawal: Electrodeposition and mechanical properties of nickel-tungsten carbide composites, Transactions of the Japan Institute of Metals, Vol. 23, pp. 320-327, 1989.

[5] J. Nerz, B. Kushner, A. Rotolico: Microstructural evaluation of tungsten carbide-cobalt coatings, Journal of Thermal Spray Technology, Vol. 1, pp. 147-152, 1992.

[6] M. Jafari, M.H. Enayati, M. Salehi, S.M. Nahvi, C.G. Park: Comparison between oxidation kinetics of HVOF sprayed WC–12Co and WC–10Co–4Cr coatings, International Journal of Refractory Metals and Hard Materials, Vol. 41, pp. 78-84, 2013.

[7] M. Xie, S. Zhang, M. Li: Comparative investigation on HVOF sprayed carbide-based coatings, Applied Surface Science, Vol. 273, pp. 799-805, 2013.

[8] P. Chivavibul, M. Watanabe, S. Kuroda, K. Shinoda: Effects of carbide size and Co content on the microstructure and mechanical properties of HVOF-sprayed WC–Co coatings, Surface and Coatings Technology, Vol. 202, pp. 509-521, 2007.

[9] A.S. Edelstein, R.C. Cammaratra: *Nanomaterials: Synthesis, Properties and Applications*, Second Edition, Taylor & Francis, UK, 1998.

[10] Diamalloy 2001 Material Product Data Sheet, DSMTS-0026.7 – Nickel and Cobalt Self-Fluxing Alloys, Oerlikon Metco, 2016.

[11] Woka 3652 Material Product Data Sheet, DSMTS-0025.12 – 86WC-10Co-4Cr Agglomerated and Sintered Powders, Oerlikon Metco, 2017.

[12] M.I. Dvornik, A.V. Zaytsev: Research of surfaces and interfaces increasing during planetary ball milling of nanostructured tungsten carbide/cobalt powder, International Journal of Refractory Metals and Hard Materials, Vol. 36, pp. 271-277, 2013.

[13] W. Zhou, K. Zhou, Y. Li, C. Deng, K. Zeng: High temperature wear performance of HVOF-sprayed Cr3C2-WC-NiCoCrMo and Cr3C2-NiCr hardmetal coatings, Applied Surface Science, Vol. 416, pp. 33-44, 2017.

[14] ASTM G76-13 *Standard Test Method for Conducting Erosion Tests by Solid Particle Impingement Using Gas Jets*, 2013.

[15] ASTM G99-17, *Standard Test Method for Wear Testing with a Pin-on-Disk Apparatus*, 2017.

[16] R. Ahmed, O. Ali, N.H. Faisal, N.M. Al-Anazi, S. Al-Mutairi, F.L. Toma, L.M. Berger, A. Potthoff, M.F.A. Goosen: Sliding wear investigation of suspension sprayed WC–Co nanocomposite coatings, Wear, Vol. 322, pp. 133-150, 2015.

[17] M.H. Enayati, G.R. Aryanpour, A. Ebnonnasir: Production of nanostructured WC–Co powder by ball milling, International Journal of Refractory Metals and Hard Materials, Vol. 27, pp. 159-163, 2009.

[18] W. Dawihl: Transition Metal Carbides and Nitrides, Angewandte Chemie, Vol. 84, pp. 960-960, 1972.

[19] K. Mandel, L. Krüger, C. Schimpf: Particle properties of submicron-sized WC–12Co processed by planetary ball milling, International Journal of Refractory Metals and Hard Materials, Vol. 42, pp. 200-204, 2014.

[20] C. Suryanarayana: Mechanical alloying and milling, Progress in Materials Science, Vol. 46, pp. 1-184, 2001.

[21] B.D. Cullity, S.R. Stock: *Elements of X-ray Diffraction*, Pearson Education, London, 2013.

[22] R.M. Raihanuzzaman, T.S. Jeong, R. Ghomashchi, Z. Xie, S.-J. Hong: Characterization of short-duration high-energy ball milled WC–Co powders and subsequent consolidations, Journal of Alloys and Compounds, Vol. 615, pp. S564-S568, 2014.

[23] J.K.N. Murthy, B. Venkataraman: Abrasive wear behaviour of WC–CoCr and Cr3C2–20(NiCr) deposited by HVOF and detonation spray processes, Surface and Coatings Technology, Vol. 200, pp. 2642-2652, 2006.

[24] R.G. Rateick, K.R. Karasek, A.J. Cunningham, K.C. Goretta, J.L. Routbort: Solid-particle erosion of tungsten carbide/cobalt cermet and hardened 440C stainless steel—A comparison, Wear, Vol. 261, pp. 773-778, 2006.

Serbian Tribology Society

SERBIATRIB '19

16th International Conference on Tribology

Faculty of Engineering University of Kragujevac

Kragujevac, Serbia, 15 – 17 May 2019

RESEARCH OF TRIBOLOGICAL CHARACTERISTICS OF ADI IN CONTACT WITH MODIFICIETED MATERIALS WITH DIFFERENT COATTINGS

Dušan JEŠIĆ[1], Pavel KOVAČ[2*], Dragan Rodić[2], Borislav SAVKOVIĆ[2], Dražen SARJANOVIĆ[3], Željko ALEKSIĆ[4]

[1]Tehnološko menadžerska Akademija, Novi Sad, Srbija, dusanjesic@hotmail.com

[2]Univerzitet U Novom Sadu, Fakultet tehničkih nauka, Srbija, pkovac@uns.ac.rs; rodicdr@uns.ac.rs, savkovic@uns.ac.rs;

[3] Srbijagas, Novi Sad, Srbija, aleksic@srbijagas.com

[3] Sarda-Mont. Doo, Milića Rakić 7, Beograd, Srbija, sarjanovicd@gmail.com

Abstract: *The existing level of application of hard coatings due to relatively high deposition temperatures is largely limited to the tool area. However, special interest deserves the possibility of applying contemporary PDV procedures for the conversion of constructional steels used for the manufacture of elements of the most varied tribomehanical sistems.Friction and wear behavior of different types of nodular cast irons in contact with carbon steel were studied. The lubricated sliding line contact was performed on the Pin and Disk tribometer. Value of wear were determined by PQ index. Pins were made of carbon steel without and with three types of coating (TiN, TiZrN, TiAIN) on the tool rake surface.*

Keywords: *Friction, wear, coating, sliding contact, PQ index.*

1. INTRODUCTION

Tribological properties of materials can be determined by measuring the friction force (friction or energy aspect) and by measuring the magnitude of any wear parameter of the critical element of tribo-mechanical system [1, 2].

The value of the friction force in the contact zone as well as the value of wear parameter of the critical element of tribo-mechanical system after the certain time of contact duration, depends upon numerous factors that are defining the conductions under which contact is realized (loading, sliding velocity, type of lubricant, surface integrity, etc.) [3, 4].

Comparing of tribological properties of two different materials during contact with, for instance, any steel has to be realized under the constant condition [5, 6].

In this paper friction and wear properties of two types of nodular cast iron EN-GJS-500-7 NL500 and EH GJS700-2 NL700 are compared by measuring the friction force and PQ index as wear parameters during contact with carbon steel and different type of coating.

Friction coefficients obtained within the range of 0.02 to 0.9 [1].

2. EXPERIMENTAL PROCEDURE

In this experimental investigation the geometry of line contact was realized on tribometer Pin and Disk TPD-93. Disks as specimens were made of both type of nodular cast irons heat treated in different ways, and (Tins were made of carbon steel without and with three types of coating (TiN, TiZrN, TiAIN) on the face surface [7].

The Table 1 shows chemical compositions and hardness of nodular cast irons NL500 and NL700 together with thermal treatment conditions.

Friction force and loading measurement is realized by strain gauges transducer and monitoring technique which include Amplifier and Recorder.

Wear intensity is determined by PQ index which indicates quantity od wear products in the sample of lubricant PQ index is measured by PQ Particle Quantifier PQ 2000 Model 501 (Swansea Tribology Centre).

Measuring of the friction force was performed in the experimental operations in which the contact between Block and Disk was realized with the three value of normal loading Fn (5 daN; 10 daN and 20 daN) and with the three sledding velocities.

Measuring of PQ index was performed in the experimental operations in which the contact between Pin and Disk was realized with the normal loading Fn=20 daN and the sliding speed v = 1.3 m / s.

Lubrication in the experimental operations was done with oil type POLAR 32K. The realized thickness of the oil film points to the phenomenon of the boundary lubrication.

The measured values of the friction force at the beginning and at the end of sliding (t = l min, t = 30min) were equal in all the experimental operations.

3. BASIC RESEARCH RESULTS

On the basis of the results of measurements of the friction force within the frame of the realized research program, was calculated friction coefficient as the function of the normal loading and sliding speed.

In Fig. 3 is illustrated the influence of the normal loading on the value of friction coefficient.

In Fig. 4 is presented the influence of the sliding velocity on the value of friction coefficient. Both Figures show that there is no big influence of the value of normal loading and sliding velocity on the value of the friction coefficient.

Table 1. Chemical compositions and hardness of nodular cast irons NL500 and NL700

Disk	Chemical composition in %								Ta [°C]	Ta [°C]/t [min]	Structural basisi
	C	Si	Mn	Mg	P	S	Cu	Wi			
NL500	3.85	2.9	0.075	0.035				1.5	900	520/60	Ferrite - pearlite
										390/30	
NL700	3.76	2.35	0.51		0.02	0.004	1.48	1.5		520/60	perlite
										390/30	

Hardnes of NI HB 194. After isothermal threatment HB 363

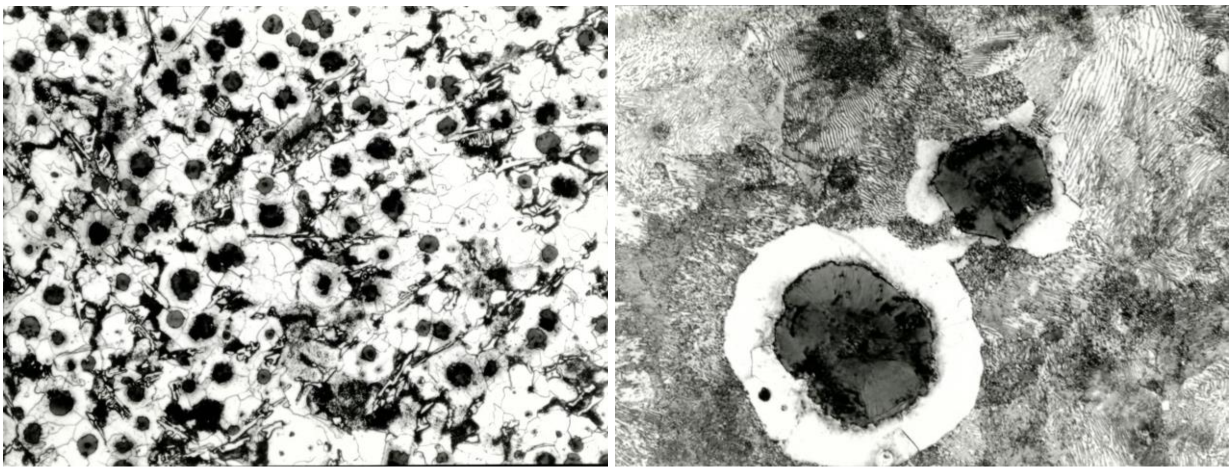

Figure 1. NL500 - The batch 5844-13.a) Increase 100x etched with HNO_3 2%, NL700 - The batch 5766-13. Increase 500x etched with HNO_3 2%

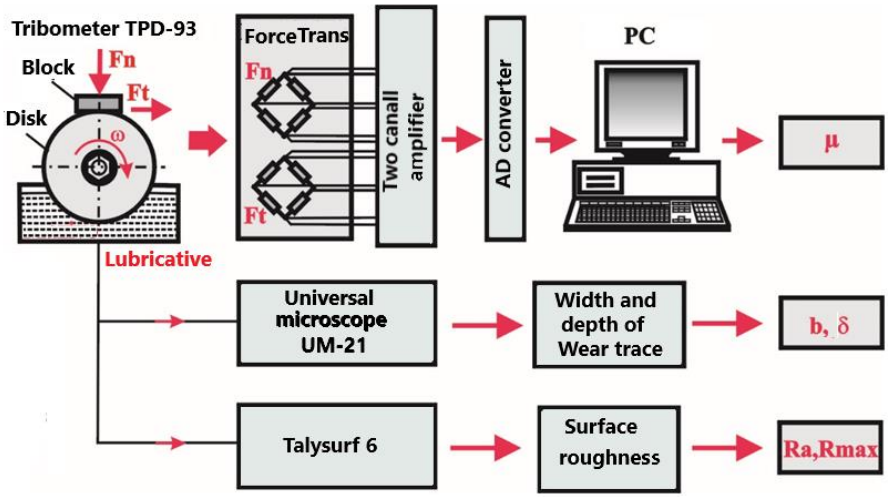

Figure 2. Tribology parameters measurement

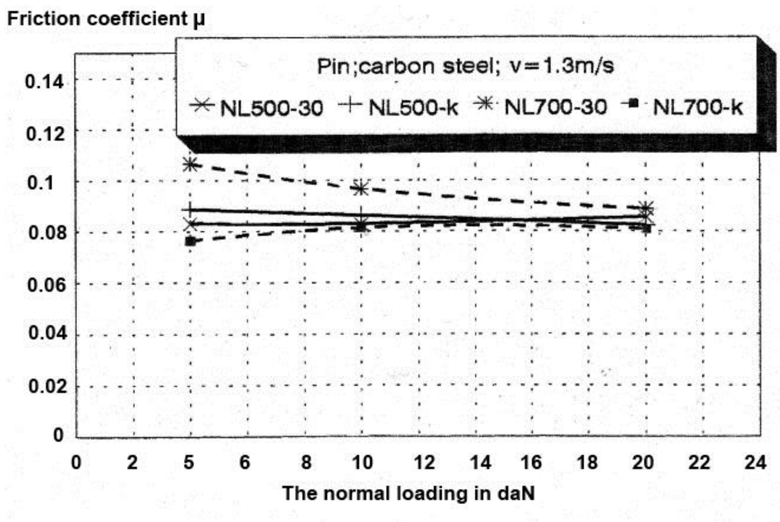

Figure 3. Friction coefficient as a function of the normal loading

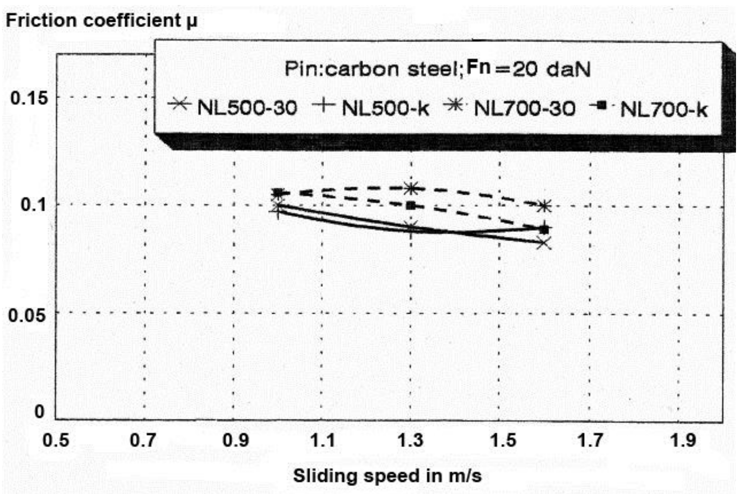

Figure 4. The friction coefficient as function of the sliding speed

The results of measurements of the friction force also show that the influence of the kind of heat treatment and type of nodular cast irons (disk material) on the value of friction coefficient is not small. From the aspect of the energy consumption for overcoming the friction in the tribo-mechanic systems, these differences in the value of friction force can be very significant.

Measuring of the friction force was also performed and in the experimental operation-sin in which the contact between Pins with three type of coatings (TiN, TiZrNn and TiAIN) and Disk was realized with the normal loading Fn=10 daN and the sliding speed v=1.3 m/s. Part of these results of measurements are shown in Fig. 4.

Results of measurements of the PQ indices, as a representative of quantity of the wear products produced during the realization of contact between the Pin and Disk for the period of 30 minutes, show that the intensity of wear of disk is greatly depends upon the type of nodular cast irons and the kind of their heat treatment.

It is known, that the value of the PQ index is directly proportional to the quantity of the wear particles that is contained in the sample of oil used for lubrication of the contact zone during the sliding of disk along the pin.

$$PQ \quad k \; q \tag{1}$$

Where is q - the quantity of wear particles which is contained in the sample of oil produced during contact between elements of tribo-mechanic system for t minutes.

In Figure 4 are shown values of the PQ indices expressed in percent's obtained by realization of the part of the experimental program that is related to the contact between Pin made of carbon steel and disks made of two type of nodular cast irons bettered by classical and isothermal procedure.

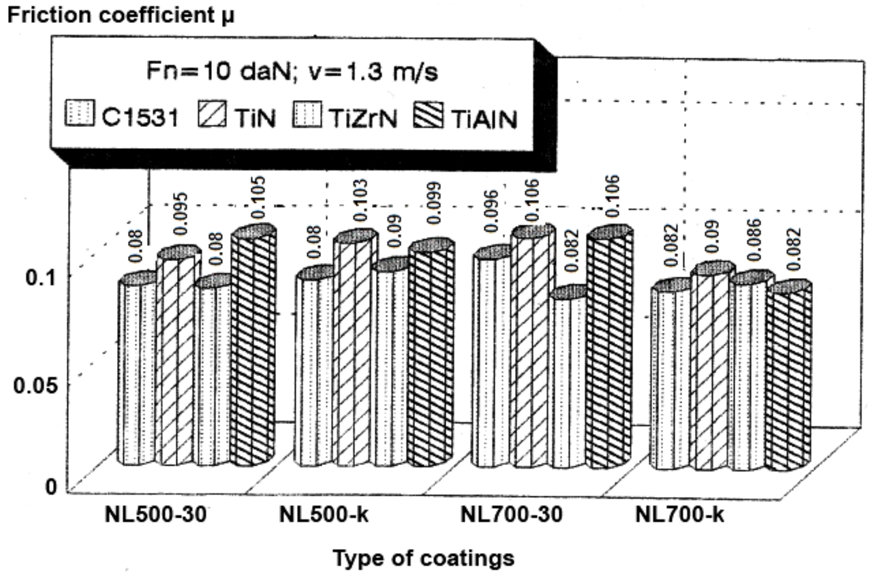

Figure 5. The friction coefficient as a function of the type of coatings

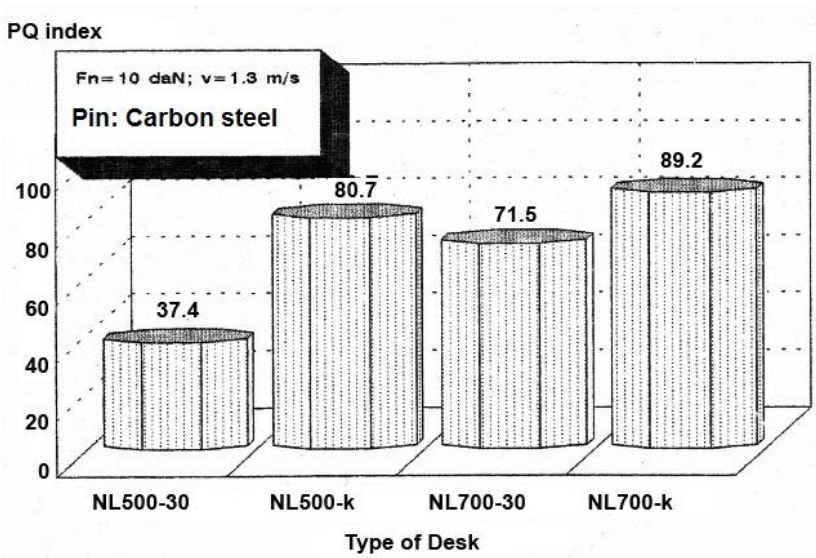

Figure 6. Values of the PQ indices for different type of disks

Results of the PQ indices measurements show that the tribological properties of disks, determined based on the magnitude of wear, are greatly influenced by the kind of betterment procedure and type of nodular cast irons.

If the wear intensity of the Disk is defined as the ratio between the quantity of wear particles obtained during the contact between it and the Pin, and the time of contact duration, and, on the other hand , the wear resistance is defined as the reciprocal value of the wear intensity, the following relations are valid:

$$I \quad \frac{Q}{t} \quad \frac{mg}{\min} \tag{2}$$

$$R \quad \frac{t}{Q} \quad \frac{\min}{mg} \tag{3}$$

$$I \quad \frac{P \; Q}{k \; t} \tag{4}$$

$$R \quad \frac{k \; t}{P \; Q} \tag{5}$$

The ratio between the wear intensity and wear resistance of Disks made of different materials or of the same material but heat treated under different conditions, is equal to the ratio of the respective values of the PQ indices.

4. CONCLUSION

Results obtained in this research point to the fact, before all, that friction and wear properties of nodular cast irons are relative and that they depend a great deal on the chosen criterion for their determination (friction coefficient or wear resistance).

The second conclusion is that the PQ index as a parameter of wear can be used as a relative value by which the resistance or intensity of wear of several material can be compared.

Friction and wear processes in the sliding contact depend much more upon the type of materials of tribo-elements and their heat treatment than loading and sliding velocity. The biggest influence on tribological properties of nodular cast iron has the condition of the isothermal betterment.

Friction coefficients obtained within the range of 0.02 to 0.9. Experimental investigations were carried out with a limiting lubrication of 25 ml.

REFERENCES

[1] B. Ivković, D. Ješić, N. Milić: Tribological characteristics of materials- Identification and measurement problem, Journal Friction and Wear, Vo1.14, No.4, 1993.

[2] J.K. Lancaster, Accelerated Wear Testing as an Aid to Failure Diagnosis and Material Selection, Tribology International, Vol.15, No.6, pp. 323-329, 1982.

[3] D. Golubović, P. Kovač, D. Ješić, M. Gostimirović, V. Pucovski: Wear intensity of different heat treated nodular iron, Metalurgija, Vol. 51, No. 4, pp. 518-520, 2012.

[4] D. Ješić, Tribological Properties of Nodular Cast Iron, Monography, Journal of the Balkan Tribological Association, Sofia, p. 125, 2000.

[5] D. Golubovic, P. Kovač, D. Jesic, M. Gostimirović: Tribological properties of ADI material, Journal of the Balkan Tribological Association, Vol. 18, No. 2, pp. 165-173, 2012.

[6] J. Zimba, D.J. Simbi, E. Navara, Austempered ductile iron: an alternative material for earth moving components, Cement & Concrete Composites, Vol. 25, No.6, pp. 643-649, 2003.

[7] D. Ješić, J. Pulić, P. Kovač, B. Savković, N. Kulundžić: Application of nodular castings in the modern industry of tribomechanical systems today and tomorrow, Journal of Production Engineering, Vol. 16, No. 1, pp. 55-58, 2013.

Serbian Tribology Society

SERBIATRIB '19

16th International Conference on Tribology

Faculty of Engineering University of Kragujevac

Kragujevac, Serbia, 15 – 17 May 2019

TRIBOLOGICAL PROPERTIES OF ALUMINA-ZIRCONIA COMPOSITE COATINGS PREPARED BY PLASMA SPRAYING

Jacob Shiby MATHEW[1,*], Liutauras MARCINAUSKAS[1,2], Mindaugas MILIEŠKA[2], Mitjan KALIN[3], Romualdas KĖŽELIS[2]

[1]Kaunas University of Technology, Department of Physics, LT- 51368 Kaunas, Lithuania
[2]Lithuanian Energy Institute, Plasma Processing Laboratory, LT-44403 Kaunas, Lithuania
[3]University of Ljubljana, Laboratory for Tribology and Interface Nanotechnology, 1000 Ljubljana, Slovenia
*Corresponding author: jacob.mathew@ktu.edu

Abstract: *The intent of this research was to determine the tribological trends of zirconia as an additive to a plasma-sprayed alumina coating matrix. For the deposition process, pure alumina and alumina-with-zirconia (5%, 10%) weight percentages were employed to be coated on steel substrates using an air-hydrogen plasma. The torch power was set to ~40 kW. The surface roughness for the alumina coatings were in the range from 2.6-3.2 µm and with additive percentages of zirconia, it was found to vary between 3.0-3.7 µm. XRD measurements indicated that the predominant phase in the alumina-zirconia coatings was tetragonal-ZrO_2 (t-ZrO_2) and with alumina, it was α-Al_2O_3 and γ-Al_2O_3. The tribological properties such as the friction coefficient and the wear-rate of the alumina-composite coatings had been inspected to evaluate its dependence on the type and concentration of the additive powders. An increase in friction-coefficient was observed with the addition of zirconia. The normalized wear rates were in the range of ~10^{-5} mm^3/Nm for the composite coatings with certain exceptions.*

Keywords: *Plasma Spraying, Zirconia, Alumina Composite Coating, Tribology.*

1. INTRODUCTION

Customarily, alumina is used as a ceramic coating due to its superior properties such as high hardness and strength, and prevailing wear resistance properties [1]. One of the more feasible ways to produce these coatings is by plasma spraying. The merits of using the plasma spraying technique are an increased flame temperature, proliferated particle velocity and a high degree of melting. This therefore, produces coatings with neat and expedient surface characteristics [2]. It was found that plasma-sprayed alumina had a friction coefficient ranging from 0.53 to 0.78 with varied counter-bodies and the normalized wear rates were found to span from 1.18 x 10^{-6} mm^3/Nm to 2.85 x 10^{-4} mm^3/Nm [3]. In another study it was obtained that the friction coefficient of alumina coatings had ranged from 0.6 to 0.8, the wear rates being from 1 x 10^{-5} to 3 x 10^{-5} mm^3/Nm [4]. In order to compliment the properties of alumina, it has been observed that a ceramic such as zirconia proliferates the toughness, dimensional stability as well the wear resistance, when added to the matrix [5]. It was estimated that with a 25 wt.% reinforcement of ZrO_2 into

Al_2O_3, the average friction coefficient was 0.45 for a vertical load of 30 N [6]. B. Liang et al. even demonstrated a condition wherein the friction dropped to ~0.2 with 70 wt.% of zirconia in the alumina-zirconia composite coating with a wear rate of ~3 x 10^{-5} mm^3/Nm, and in some other cases even half of the latter [5]. Therefore, to amalgamate both would be to derive at the least, a condition of superior hardness (alumina) and higher toughness (zirconia), which are imperative mechanical properties [5-6]. In this research here, we have employed zirconia additives into an alumina matrix to study the effect of the former's concentration on the tribological properties of the alumina-composite coatings.

2. EXPERIMENTAL

The coatings were deposited on stainless steel substrates (AISI 304L) using a direct current plasma torch operating at atmospheric pressure. The plasma torch herein was constructed at the Lithuanian Energy Institute [7]. The steel substrates *(s)* had dimensions of 40x10x1.5 mm. Additionally, they were subject to polishing and chemical-cleaning as a prerequisite. The steel substrates were positioned on a water-cooled sample holder. Air was employed as for both the primary gas with a total flow rate of 4.72 g/s, and the powder-carrier gas with a flow rate of 0.60 g/s. Hydrogen (0.1 g/s) was employed as the secondary gas. An Al bonding layer *(Al)* was employed to facilitate adhesion between the composite-coating and the substrate. The feedstock materials: Al_2O_3 *(A)* and ZrO_2 *(Z)* powders were from PRAXAIR Surface Technologies- USA, the specifications being ALO-101 and ZRO-113/114, respectively. The spraying distance was set at 70 mm. The coatings were deposited at a torch power of ~40 kW. The surface morphology was investigated by a scanning electron microscope (SEM) Hitachi S-3400N. The elemental composition of the coatings was determined by an energy dispersive X-ray spectroscopy (EDS) Bruker Quad 5040 spectrometer. The surface roughness was measured using a Mitutoyo Surftest-SJ-210-Ver2.00 profilometer. Structural characterization of the coatings was performed by X-ray diffractometry. Tribological properties of the samples were inspected using a CETR-UMT-2 ball-on-disc tribometer. For the tribological tests, an alumina ball of 10 mm diameter of grade 10 (99.5%), was used as a counter-body; the load being taken at 0.8 N. And, the wear was determined by a 3D-white light optical interferometer. We have herein employed three different types of coatings which are: pure alumina *(A)*, alumina with 5 wt.% of zirconia *(A5Z)* and alumina with 10 wt.% of zirconia *(A10Z)*, to gauge its tribological properties.

3. RESULTS AND DISCUSSIONS

The pure alumina coating had a morphology that was well spread but was rather wavy and disordered as seen from the figure 1a. It could be perceived that the coating was well adhered to the substrate with certain branch-like structures upholding it. The size of the irregular splat particles varied from 10-50 µm. With alumina-zirconia coating: *A5Z* (figure 1b), large globules could be observed with the addition of the additive, and the spread of the coating was rather non-uniform in nature. The size of the splats varied from 10-150 µm, and there was the presence of both fully-molten and semi-molten particles in the matrix. It could be seen with 10 wt.% of zirconia to the alumina matrix: *A10Z* (figure 1c), the globular formations had normalized. Nevertheless, both partially and fully-molten particle distributions could be discerned. Additionally, there were interfacial voids that could be perceived throughout the morphology of the composite matrix, and the size distribution was found to be close to the former case with the zirconia additive.

EDS analysis indicated that for *A5Z* and *A10Z* there was a 2-3 wt. % and 4-6 wt. % of zirconium, respectively after the plasma coating process. With the addition of zirconia to the alumina matrix with an R_a of 2.82 µm

(R_q= 3.54 µm), there was an overall increase in the surface roughness of the composite coatings. With *A5Z*, there was an increase up to 3.50 µm (R_q= 4.40 µm), and with *A10Z*, the value was recorded at 3.33 µm (R_q= 4.17 µm). With 10 wt.% of zirconia, there was a drop in the surface roughness (from 5 wt.%), due to the relatively uniform and finer morphology that was yielded.

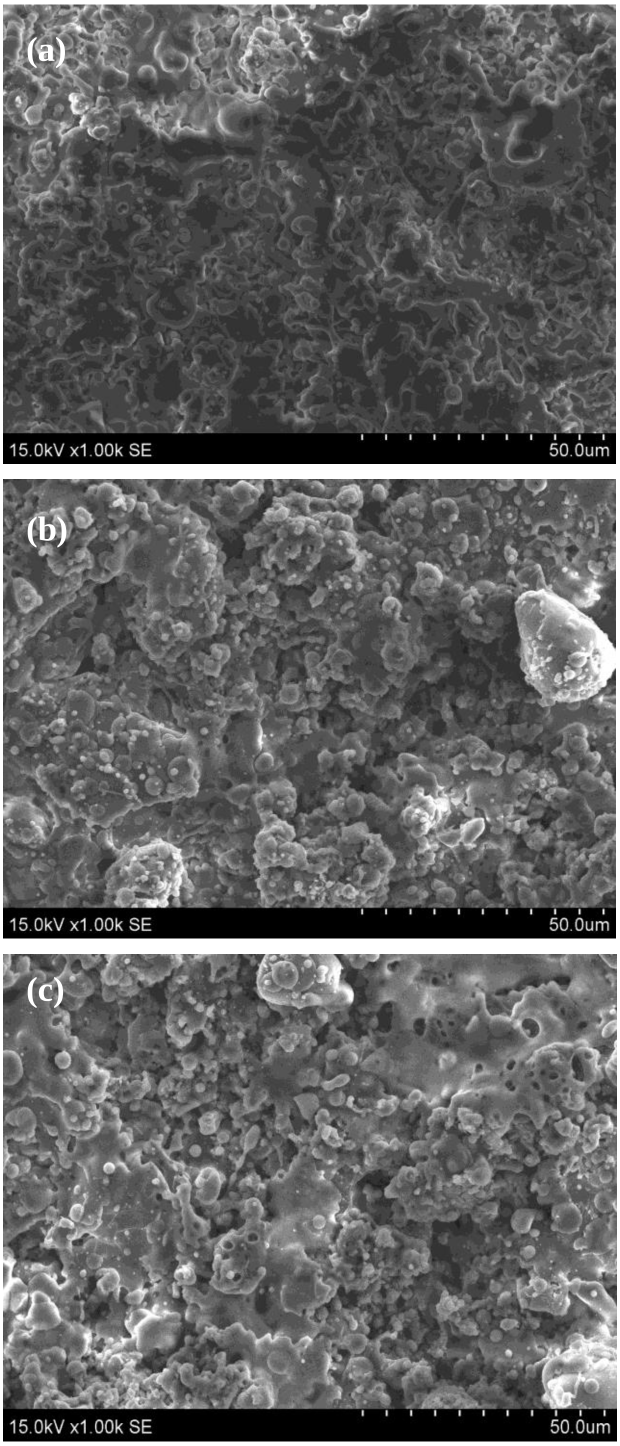

Figure 1. Surface morphology of (a) Al_2O_3, (b) Al_2O_3-5 wt.% ZrO_2 and, (c) Al_2O_3-10 wt.% ZrO_2 coatings

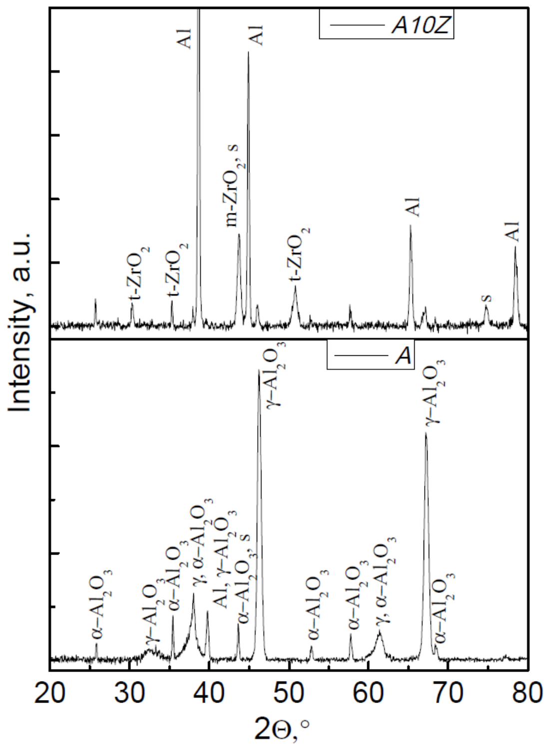

Figure 2. XRD pattern: Alumina *(A)* and Alumina-10 wt.% Zirconia coating *(A10Z)*

The XRD patterns pertaining to alumina *(A)* (see, figure 2) indicated predominantly the presence of rhombohedral α-Al_2O_3 and cubic γ-Al_2O_3 phases. The peaks at 25.84°, 35.42°, 43.63° etc., denoted the α-Al_2O_3 phase. The highest intensity peaks at 46.23° and 67.18° were found to be of γ-Al_2O_3. As regards the XRD pattern of the alumina-zirconia *A10Z* coatings: there was the presence of t-ZrO_2 (30.29°, 35.29°) and m-ZrO_2 (43.7°) phases, which was also similar to that of *A5Z*. Meanwhile, the intensities of the α-Al_2O_3 and γ-Al_2O_3 peaks were reduced with the additives.

As for the tribological properties of the coatings, the advancement of the friction coefficient with sliding distance for cases within the three types of coatings are presented herewith. As seen from the figure 3, alumina coatings *(A)* had the most stable steady-state and the lowest friction coefficient; for *A5Z* it was mid-level in terms of steady-state characteristics and the friction coefficient; with *A10Z* it was the highest. Gauging the average friction coefficient of the alumina coating *(A)*, it turned out to be 0.55 and for the cases with zirconia additives, it was found to be 0.65 and 0.74 for *A5Z* and *A10Z* coatings, respectively.

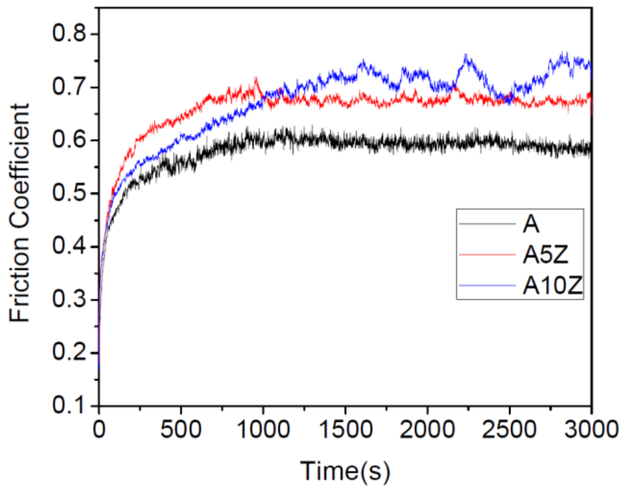

Figure 3. Friction coefficient curves for *A, A5Z* and *A10Z*

The normalized wear rate for *A* and *A5Z* coatings were found to be practically immeasurable, due to a mere plastic deformation, but with *A10Z*, it was found to be 2.64 x 10^{-5} mm^3/Nm. The reasons for the lowest friction coefficient and wear rate as in the pure alumina coatings could be mainly due to the presence of a strong phase: γ-Al_2O_3, brought forth due to the α→γ transformations from well-melted particles aiding a better surface morphology subject to efficient substrate cooling [7]. With respect to the alumina-zirconia *A5Z* coatings, the well-spread tetragonal phase which aids in the formation of a stronger and tougher matrix, could have been seen in application here [6]. With *A10Z*, the negative effect of both interfacial-voids and crevices as seen from the morphology, could have outweighed the tetragonal-phase effect as observed in the former, leading to a measurable wear and the highest friction coefficient in comparison. Therefore, the ideal concentration of the additive zirconia was estimated to be 5 wt.%, depicting exemplary friction characteristics and a neat wear-resistance from among the composite coatings.

4. CONCLUSION

The work herewith studied the tribological effect of zirconia as an additive (5, 10 wt.%) to a plasma-sprayed alumina matrix. It was demonstrated that the friction coefficient of the pure alumina coating was the least (0.55), and with 10 wt.% of zirconia, it was the highest (0.74). The normalized wear rate was the least for the condition with 5 wt.% of zirconia, just as with the pure alumina, whereas with *A10Z* it was the highest (2.64 x 10^{-5} mm^3/Nm). The tangible effect of the phases: γ-Al_2O_3 and t-ZrO_2, could be observed for its contribution toward the superior tribological properties subject to plasma-spray parameters, in the alumina-composite coatings.

REFERENCES

[1] X. Lu, S. Bhusal, G. He, D. Zhao, C. Zhang, A. Agarwal, Y. Chen: Efficacy of graphene nanoplatelets on splat morphology and microstructure of plasma sprayed alumina coatings, Surf. Coatings Technol, Vol. 366, pp. 54–61, 2019.

[2] S. Sathish, M. Geetha: Comparative study on corrosion behavior of plasma sprayed Al_2O_3, Trans. Nonferrous Met. Soc. China, Vol. 26, pp. 1336–1344, 2016.

[3] W. Deng, S. Li, G. Hou, X. Liu, X. Zhao, Y. An: Comparative study on wear behavior of plasma sprayed Al_2O_3 coatings sliding against different counterparts, Ceram. Int., Vol. 43, No. 9, pp. 6976–6986, 2017.

[4] A. Riedl, N. Schalk, C. Czettl, B. Sartory, C. Mitterer: Tribological properties of Al_2O_3 hard coatings modified by mechanical blasting and polishing post-treatment, Wear, Vol. 289, No. Supplement C, pp. 9–16, 2012.

[5] B. Liang, G. Zhang, H. Liao, C. Coddet, C. Ding: Friction and wear behavior of ZrO_2–Al_2O_3 composite coatings deposited by air plasma spraying: Correlation with physical and mechanical properties, Surf. Coatings Technol., Vol. 203, No. 20, pp. 3235–3242, 2009.

[6] R. Younes, M. A. Bradai, A. Sadeddine, Y. Mouadji, A. Bilek, A. Benabbas: Effect of TiO_2 and ZrO_2 reinforcements on properties of Al_2O_3 coatings fabricated by thermal flame spraying, Trans. Nonferrous Met. Soc. China, Vol. 26, No. 5, pp. 1345–1352, 2016.

[7] L. Marcinauskas, J. S. Mathew, M. Milieška, B. Thanigachalam, A. Kupec, R. Česnavičius, R. Kėželis, M. Kalin: Microstructure and tribological properties of plasma sprayed alumina and alumina-graphite coatings, Surf. Coatings Technol, Vol. 350, pp. 401–409, 2018.

Serbian Tribology Society

SERBIATRIB '19

16th International Conference on Tribology

Faculty of Engineering University of Kragujevac

Kragujevac, Serbia, 15 – 17 May 2019

WEAR RESISTANCE OF MULTI-COMPONENT COMPOSITE COATINGS APPLIED BY CONCENTRATING ENERGY FLOWS

M. KANDEVA[1,3*], T. PENYASHKI[2], G. KOSTADINOV[2], M. NIKOLOVA[4], T. GROZDANOVA[1]

[1]Faculty of Industrial Technology, Technical University, Sofia, Bulgaria
[2]Institute of Soil Science Agrotechnologies and Plant Protection "N. Pushkarov", Sofia, Bulgaria
[3] South Ural State University, Chelyabinsk, Russia
[4] University of Ruse "A. Kanchev", Russe, Bulgaria
*Corresponding author: e-mail: kandevam@gmail.com

Abstract: *In this work are presented the results of comparative tests of the abrasion wear characteristics and the wear resistance of new coatings from multi-component composite materials. The main objective of the study is to reveal the mechanisms of wear and optimization of the composition of multi-component materials to obtain high wear resistant coatings under conditions of abrasion and erosion. The coatings are applied by electrical spark deposition and gas-fuel spraying on carbon steel substrates. Composite mixtures of Cr-Ni-Co-B-Si-C, reinforced with micro-sized particles of boron and tungsten carbides, and titanium diboride in varying proportions are used for layering. Results were obtained for the influence of microgeometric parameters, the composition and microstructure of coatings on their wear resistance and on the characteristics of the wear at different loads under dry abrasive friction. It has been found that the resulting coatings have a 20-50% higher wear resistance than the conventional materials used. The compositions of layering materials and the process parameters of the two methods have been determined, at which maximum wear resistance of the coated samples is obtained.*

Keywords: *tribology, coatings, composite materials, carbides, abrasion wear, structure, wear resistance*

1. INTRODUCTION

One of the most promising directions for enhancing the reliability and durability of equipment and technique is the modification of the working surfaces of the rapidly wearing parts and products and the creation of surface layers with high mechanical and tribo-technical characteristics. The diversity and complexity of the processes and operating conditions and friction in which wear takes place have led to the creation of numerous methods and means of coatings, on the basis of which various apparatus and equipment were developed [1,2,3]. Each of these methods has certain drawbacks and advantages that make it more or less suitable for the various specific uses.

Gas Flame Spraying (GFS) [4,5,6,7,8] and Electrical spark deposition (ESD) [9-12] are of the most versatile, lightweight and affordable methods for applying wear-resistant coatings. Both methods are realized by converting the layering material into molten particles, which are applied at high speed to the surface of the coated article and bonded thereto. The

coatings applied by these methods have lower characteristics and properties as compared for example with the Physical and Chemical vapor deposition - PVD or CVD methods, but the latter require significant investments in expensive equipment and technologies and specially trained operators. ESD and GFS are simple, environmentally friendly methods with simple, affordable and portable equipment easy technology that does not require pre-treatment and are universal - they allow the local application of coatings from any and on any all conductive materials, and GFS - and on non-conducting - wood, plastics and others.
Because of their simplicity and universality versatility, ESD and GFS are not only more widespread but also significantly cheaper and fully accessible to most consumers.

One of the main problems of gas thermal spray coatings is their porosity, lack of homogeneity on account of poor agglomeration of powder particles, high roughness of surface and low adhesion to substrate. These result in insufficient corrosion and wear resistance of such coatings [4,5,7,9]. Increasing the efficiency of the GFS and ESD coatings is related to the development of new materials and technologies to increase adhesion, uniformity and wear-resistance of coatings, as well as the hardness of the contact surfaces. In this connection, the aim of the present work is to develop new materials for GFS and ESD coatings, to study of the nature and the regularities of the wear of coatings obtained with these materials and to optimize of the materials composition and of the processes parameters for obtaining new coatings with increased wear resistance and triboefficiency.

2. EXPERIMENTAL. MATERIALS AND METHODS

2.1. Apparatus for applying coatings

GFS is carried out using a Super Jet-S-Eutalloy oxy-acetylene thermal spray torch which provides very precise anti-wear protective coatings thanks to its sensitive controls- Fig. 1 [6].

Figure 1. Device for manual gas fuel deposition (Reproduced by permission of Castolin Eutectic [6]

Parameters of application modes: Combustion gases: Acetylene, Oxygen
Fuel / Oxygen ratio (/ O_2),% - 45-55
Pressure of O_2 -4 bars
Acetylene pressure - 0.7 bar
Spray distance, mm – ≈ 20-30 mm
Angle of impact, degree - 90;
Powder flow rate, g / min - 20-25
Preheating –to 300-350 degrees C^0
Flame temperature: ≈3000 °C

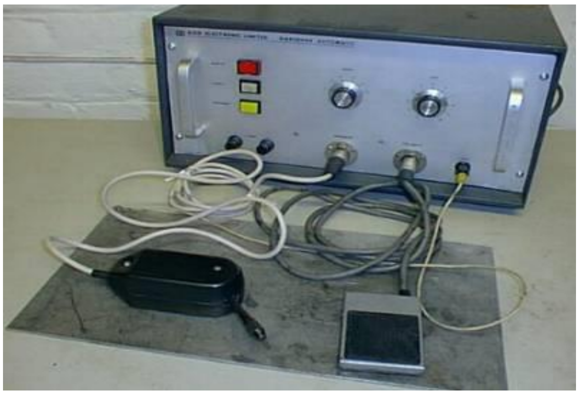

Figure 2. Device for Manual electrical discharge deposition with vibrating electrode "Harddege" - England, USA

The ESD is performed by a hand-held apparatus with vibrating movement of the electrode "Hardedge" (Fig.2) with the following parameters: Short circuit current - 0.2÷2A, Voltage - 80V, Capacity -5-100µF, oscillation frequency of the vibrator - 100 Hz. The individual layering modes are numbered from 1 to 6 in order of increase of pulse energy. In this work were used regimes with single pulse energy $E_i=C.U^2/2=0.03\div0.3J$. The individual layering modes are numbered from 1 to 6 in the order of increase of pulse energy given in Table 1.

Table 1. Regimes for ESD whit vibrating electrode

№ of regimes	Single pulse energy, J
1	$E_1 \approx 0.02$
2	$E_2 \approx 0.03$
3	$E_3 \approx 0.05$
4	$E_4 \approx 0.06$
5	$E_5 \approx 0.16$
6	$E_6 \approx 0.3$

2.2. Materials and Methods

Substrate.

Model plates of carbon steel with 0,45%C - (45) with hardness 190-210HB, and of steel 210Cr12 heat treated to a hardness of HRC 59–61 with sizes 10×10×4 mm and polished to a roughness *Ra*=0.63µm are used for substrate. The chemical composition of these steels is given in Table 2.

Table 2. Chemical composition of substrate plates.

Element,%	Steel 210Cr12	steel 45
C	1.9-2.2	0.42-0.5
Cr	11-12	Up to 0.25
Si	0.1-0.4	0,17-0,37
Mn	0.15- 0.45	0,5-0,8
Ni	up to 0.35	up to 0.25
Mo	up to 0.2	-
W	up to 0.2	-
Ti	up to 0.03	-
Cu	up to 0.3	up to 0.25
V	up to 0.15	-
P	up to 0.03	up to 0.04
S	up to 0.03	up to 0.04

Table 3. Chemical composition of the bonding metal powder mixtures and of initial compositions whit addition of WC.

Designation/Element %	NW	KW
C	0.6	1.5
S	2.9	1.5
Cr	12	23
Fe	3.9	0.5
B	3.6	1.5
Ni	Balance	30
Co	-	42
∑ %	55	45
WC	45	55

Coating materials

Two types of metal powder compositions Ni-Cr-B-Si-Fe-C and Co-Cr-Ni-B-Si-C with trademarks NP60 [6] - based on Ni, and 10612[6] - based on Co as bonding phases of the powder compositions are defined and used. To these has been added tungsten carbide in the proportions and with the inscriptions NW and KW given in Table 3.

The introduction into the composition of the materials of the self-fluxing additives (B, Si, C, etc.) is one way to maximize the storage of the beneficial properties of the individual components of layering material in the coating [13-17]. The securing the necessary performance characteristics and adhesion of the surface layer in the present work is solved by the using of Co, Ni, Cr forming unlimited solutions in the iron [14-16,18,19]. According to the data for the mutual solubility of the metals and the compounds [14-16,18-20], taking into account the principles established for the selection of the bonding and wear-resistant components and using the wettability data of the difficult compounds and alloys, the following compositions of powder mixtures were having selected and formulated to provide the effective forming a wear-resistant layers on the steel surfaces:

(1)NWT10B10 - 80%NW+ 10%B_4C+10%TiB_2.

(2)NWW15T20- 65% NW +15% WK8 + 20% TiB_2. (WK8 is hard alloy with 92%WC and 8%Co).

(3)NWW15B10T20 - 55%NW +15%WK8 + 10%B_4C + 20%TiB_2;

(4)NWW10T10B10 - 70%NW+10%WK8 +10%B_4C + 10%TiB_2.

(5)NWW10T20B20 - 50% NW + 10% WK8+ 20% B_4C+ 20%TiB_2.

(6)NWT20B20 - 60% NW +20%B_4C+ 20%TiB_2.

(7)KWB10- 90% KW + 10%B_4C.

(8)KWT10B10-80%KW + 10%B_4C + 10%TiB_2.

The high hard components B_4C, TiB_2, and WC [9,10,14] are selected for to provide both high wear resistance, such and obtaining of new additional wear-resistant compounds and phases in the process of forming the coatings.

Boron carbide B_4C is a super hard material with extremely high wear resistance and abrasion resistance but is brittle. The introduction of the less fragile and rigid components titanium diboride - TiB_2 and tungsten carbide- WC eliminates this issue. It's very high hardness, wear resistance and chemical resistance distinguishes TiB_2.

By literature data compared with the carbide, the boride bonds are more difficult to decompose and is expected TiB_2 to be stored in the layer to a higher degree than of WC or TiC. TiB_2 and WC, in addition to abrasive wear, are also resistant to impact loads.

Carbide mixtures of WC + 8% Co - WK8 are added in order to increase the amount of WC and of Co in the composition of the powder compositions and of the electrodes. Composite materials of B_4C, TiB_2, and WC are selected for to provide both high wear resistance, such and obtaining of new additional wear-resistant compounds and phases in the process of forming the coatings.

Initially, base mixtures with designations "NW and KW" according (Table 2), were milled to a 45±5 μm and are homogenized. After this the wear-resistant compounds B_4C, WK8 and TiB_2 with grain size 20 ± 5 μm in respective weight ratios were added to base mixtures.

Laminating electrodes for ESD with a diameter of 1÷1.5mm are obtained by electrically discharge cutting from monolithic plates, prepared by the methods of powder metallurgy. Coatings of carbide composite electrode materials from 16%TiC +4.5 %(Ta, Nb) C +10.5%Co +WC, studied and developed earlier [21,22] with indications respectively P25 were used as reference for comparison with the resulting coatings from the new electrodes.

Appropriate ratios between the base phases NW and KW and the composition and amount of the wear-resistant phases in the powder compositions should be established based on the results obtained from the tribological tests.

Methodology of measurements.

- Balance WPS 180/C/2, which has 0.0001g sensitivity, was used to determine the mass loss of tested samples.
- The surface roughness Ra, μm and thickness B, μm of the resulting coatings are measured by using profilometer - AR-132B (China) and Pocket Leptoskop 2021 Fe (Germany). Density, uniformity and morphology of coatings were monitored by a VT-300 (Germany) digital microscope.
- The initial indicative determination of the surface hardness of the coatings was performed with hardometer Al 150A (Germany).
- The microstructure of the coatings has been studied by optical microscopy on cross-sectional sections by metallographic Optical microscopy (Epytip 2, Carl Zeiss Jena).
- The tribological properties and wear resistance of the coatings are investigated by comparative tests of friction with tribotester type "Thumb -disk" under dry surface friction with hard-fixed abrasive particles – Fig.3. The wear characteristics test method consists in measuring the mass wear m of the samples for a specific friction path L (friction cycles) under constant conditions - load P and glide speed V.

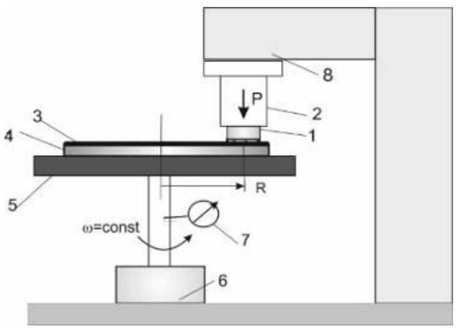

Figure 3. Tribotester type 'Thumb –disk'

Calculated are the following wear characteristics:

- *mass loss*, [mg]:

$$m=m_o - m_i \quad (1)$$

- *wear rate,* [mg/min]:

$$\gamma = m/t \quad (2)$$

- *wear intensity*, [mg/m]:

$$i_e = m/L \quad (3)$$

- *wear resistance*, [m/mg]:

$$I=1/i_e = L/m \quad (4)$$

Table 4 gives the experimental conditions for testing the wear of the test coatings.

Table 4. Parameters of the experiment in studying the wear of the tested GFS and ESD coatings

№	Parameter	Value (GFS)	Value (ESD)
1	Normal load	100 N	5N
2	Nominal contact area	2.25 cm^2	2.25 cm^2
3	Nominal contact pressure	44.4 N/cm^2	2.22 N/cm^2
4	Speed of rotation	95 min^{-1}	212 min^{-1}
5	Distance between the axis of rotation and the center of the contact site	80 mm	-
6	The friction path of the center of the contact site	238.64 m	42.68 m
7	Friction time	5 min	-
8	Sliding speed of the contact center site	0.8 m/s	0.8 m/s
9	Ambient temperature	20^oC	21^oC
10	Abrasive surface	Corund P 120	Corund P 320

3. RESULTS AND DISCUSSION

3.1 Coating characterization

Initially, in a wide range of values of technological parameters with each of the tested materials were applayed coatings on steel substrates. After visual comparative evaluation of the uniformity, density, roughness, grain size of porosity of the resulting coatings, for each test material were selected conditions suitable for deposition, in which hard are obtained dence, uniform and fine-grained coatings.

ESD Coatings

With the various materials used were obtained similar in structure and composition coatings, but with a different quality characteristics and properties. The results obtained show that at ESD with the multi-component carbide alloys the coatings have high density and uniformity and with acceptable for the practical use roughness, which in many cases do not require further processing. A transfer coefficient by 12-18% higher than that at ESD with the conventional hard alloys type P25 was achieved, and the mass gain of the cathode is up to 1.8 times higher than that of the electrodes based of tungsten carbide. The minimum and maximum values (borders) of the thickness δ, of surface roughness Ra, and microhardness HV of coatings, obtained from the studied electrodes at the different used values of parameters of regimens for ESD is shown in Tables 5 and 6. The obtained results of vibration ESD show that the increase of the energy of the impulses (in the direction from mode 1 to mode 6 - Table 2) leads to an increasing in the thickness of the obtained coatings, but significantly increase and their roughness and unevenness. The maximum thickness at which is obtained a relatively uniform coating with surface roughness up to Ra=3÷4µm is in the range of 45÷50µm at regime № 5 with pulse energy E5 =0.16J. From the results obtained at ESD and onto the both steels it was found that at the NWW15T20 electrodes, the thickness of the coatings is higher. Moreover, the increase in the amount of bonding metals in the electrode composition allows us to create coatings with a greater thickness. The higher thickness of the coatings can be explained by the presence of bonding metals forming unlimited solid solution with the substrate material and by the presence of boron and silicon, which slows down the formation of oxide films and have a positive effect on the continuity and the increase of the thickness of the coating. In addition, the introduction of the boron reduces the erosion resistance of the alloying electrode, as a result of which the transport of electrode material to the surface to be processed is increased [14]. In all investigated coatings, the hardness of the white layer is higher than that of the substrate and varies too widely (Tables 6 and 7). However, the microhardness of coatings applied by vibration ESD with the new electrodes is up to 10-15% higher than that obtained with P25 electrodes. The highest values of HV to 18GPa were obtained at coatings from electrodes KWB10T10 and NWW15B10T20 in ESD on steel 210Cr12. The highest coefficient of increase in the hardness after the ESD, however, was observed in the unhardened steel 45 - K=3.8÷6 times increase in HV, while for hardened tool steel 210Cr12 the coefficient is 1.4÷2.

GFS coatings

The thickness of GFS coatings is in the range 150÷350µm, the roughness Ra - 5÷15µm, and the hardness HRC of the various materials varies within the range 60÷75.

The results of the study showed that the surface layers are a inhomogeneous, non uniforms, similar in form and structure with acceptable repeatability of the qualitative characteristics. All layers are to some extent porous. The reason for this is the presence of non melted particles of the hard phases remaining in the lamellae of the coating obtained, as well as of the unfilled spaces between the lamellae due to their incomplete bonding to each other in the heat-sealing process. Figure 4 shows the microstructure of the coatings from KWT10B10 compositions on st.45.

In the middle (Fig.4a) (which divides the image into two parts) is visible a diffusion white layer - a mixture of the layers and the substrate - and is most likely amorphous. Above it, in most areas of the coating, dark (almost black) spherical phases are visible - grains of approximate size of 15-30µm, which are undissolved and non-melted carbides and borides.

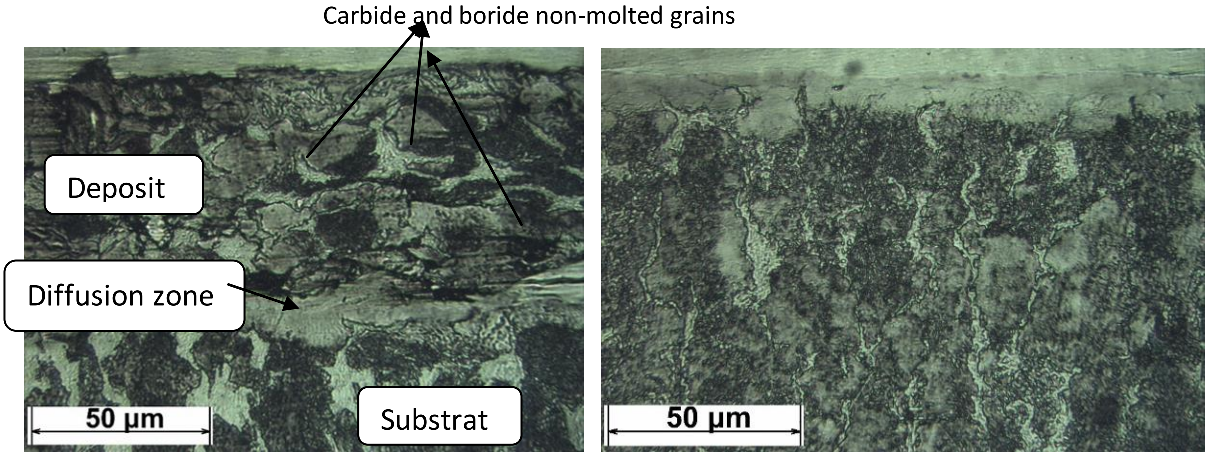

a) GFS - Coating material KWT10B10 b) ESD - coating material KWT10B10

Figure 4. Cros- section microphotographs of microstructure of coatings applied by GFS – a), and by ESD – b) on steel 45

Table 5. Range of change of parameters of tested coatings obtained with ESD with vibrating apparatus on 210Cr12 steel, E_i=0.03 ÷0.3J

№	Electrode	Ra, µm	δ, µm	Hv, GPa	Coeff. of hardening
1	P25	1.8 ч4.2	10- 40	10ч16	1.2÷1.9
2	NWW15T20	2.5ч6.5	15ч80	11ч15	1.4÷1.7
3	NWW15B10T20	2.5ч7.2	15ч80	12ч17	1.4÷2
4	KWB10	2- 6.2	12-80	12-17	1.4÷2
5	KWT10B10	2.5-6.5	15-70	12-18	1.4÷2.1

Table 6. Range of change of parameters of tested coatings obtained with ESD with vibrating apparatus on 45 steel, E_i=0.03ч0.3J

№	Electrode	Ra, µm	δ, µm	Hv, GPa	Coeff. of hardening
1	P25	1.8÷4.2	13- 40	6÷13	3÷6.5
2	NW15T20	2.5÷6.5	20÷90	6÷13	3÷6.5
3	NW15B10T20	2.5÷6.5	20÷70	6÷14	3.5÷7
4	KWB10T10	2.6÷6.5	16÷80	7÷15	3.5÷7

The bright areas between them are probably a multi-metal solid solution based on Co- Ni-Cr-B-Si and the larger long grey areas at the top of the surface form a metal matrix incorporating part of the melted carbides and borides during the transfer.
The ESD coating - Fig. 4b represents a white uniform and homogeneous layer with a thickness to 20-25 microns.

3.2 Wear resistance of the coatings obtained

GFS Coatings

In Tables 7 and Fig. 5-7 are given the results of the comparative experimental studies of the influence of the composition powder materials on the tribo-technical properties of the resulting GFS coatings.

The results obtained show that the wear of the layered samples is 5-12 times lower than that of the uncoated steel 45 and on coated steel 210Cr12 – 3 -6 times lower.
Similar is the amendment in wear rate, wear intensity and wear resistance of coatings – Table 7 and 8.

The comparison of the wear of the layered specimens shows that coated with the materials KWB10 and KWT10B10 specimens from steel 45 have 1.2 to 1.7 times lower wear than that at the analogous materials NWT10B10 and NWW10T10B10 and respectively higher wear resistance. Coated with this materials specimens from steel 210Cr12 have 1.1 to 1.3 times lower wear than that at the analogous materials NWT10B10 and NWW10T10B10. The good wetting of carbide in the cobalt matrix contributes to the high cohesion strength of the resulting metal ceramics. Wear analysis shows that the presence of B_4C, TiB_2 and WC in the powder compositions is the main reason for the higher wear resistance of these coatings. Apparently, the combination of TiB_2 and B_4C and WC additives in the powder composition allowed to use the full advantages of each of the individual component and to receive higher wear resistance of the layered surfaces compared to that obtained with only WC - TiB_2 or with WC-Co. However, with the increase of the B_4C and TiB_2 content from 10% to 20%, the difference in wear of the layered and non-coated samples sharply decreases.

Table 7. Parameters of wear of test samples with GFS coatings on steel 45 – s = 238.64m

№	Coating designation	Mass loss, mg	Wear rate mg/min	Intensity, mg/m	Wear Resistance, m/mg
1	NWT10B10	158.2	31.60	66.3×10^{-2}	1.50
2	NWW10T10B10	105.3	21.10	44.4×10^{-2}	2.30
3	NWW10T20B20	142.5	28.50	59.7×10^{-2}	1.70
4	KWB10	91.2	18.20	38.2×10^{-2}	2.60
5	KWT10	98.4	19.7	41.6×10^{-2}	2.42
6	KWT10B10	90.8	18.20	38.0×10^{-2}	2.60
7	Substrat steel 45	1089.5	217.90	456×10^{-2}	0.22

Table 8. Parameters of wear of test samples with GFS coatings on steel 210Cr12 – s = 238.64m

Coating designation	Mass loss, mg	Wear rate, mg/min	Intensity, mg/m	Wear resistance, m/mg
NWW10B10T10	91.8	18.30	0.386	2.60
NW B20T20	138.6	27.70	0.58	1.70
NWB10T10	107.8	21.60	0.45	2.22
KWB10	88.2	17.40	0.37	2.70
KWB10T10	83.7	16.70	0.35	2.85
Substratest.210Cr12	563.6	112.70	2.36	0.42

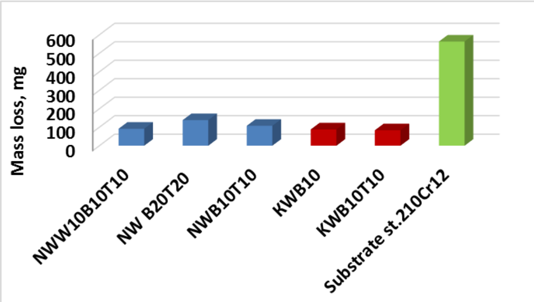

Figure 5. Wear of GFS coatings on steel 210Cr

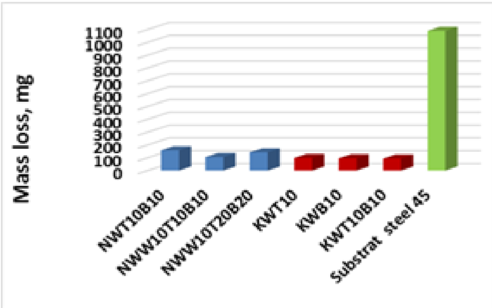

Figure 6. Wear of GFS coatings on steel 45

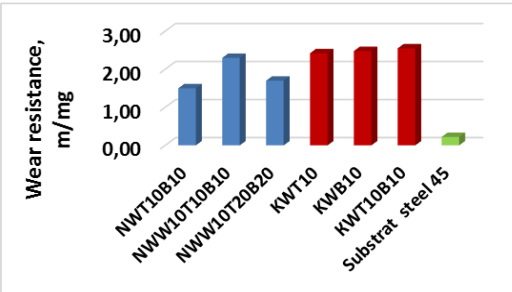

Figure 7. Comparative wear resistance of the GFS coatings on steel 45

Obviously, the higher concentration of these materials results in a weakening of the connections of the individual grains with the metal matrix in the coating, which results in tear, the more that, the breakaway high hard particles abrasively act on the surface of the coating, and further contributing to the increased wear.

Powder compositions KWT10B10, KWB10 and NWW10T10B10 are emerging as promising materials for high-performance coatings.

ESD coatings

In Tables 9 and Fig. 8 are given the results of the comparative experimental studies of the influence of the materials and the ESD regimes on the wear of the resulting coatings.

From the results it was established that the coated samples have 2-6 times lower wear than those of uncoated samples, and up to 1.5 times smaller than the deposited samples with electrode P25. Similar is the change in wear rate, wear intensity and wear resistance of coatings - Table 9. The lowest wear at ESD with electrode KWB10T10 and NWW15B10T20 samples is obtained in the pulse energy modes E_i = 0.05-0.06 J, while at electrode NWW15T20 the lowest wear is obtained at E_6 = 0.3 J.

Table 9. Parameters of wear of ESD test samples at 200 friction cycles (42.6m)

№	Pattern, Electrode / Designation, regime	Mass loss, mg	Wear rate, g/min	Intensity, mg/m	Wear resistance, m/mg
1	NWW15B10T20/steel 45, E_2=0.03J,	8.7	9.1	20.0 x 10^{-2}	5
2	NWW15T20/steel 210Cr12 hardened, E_3=0.05J	10.3	10.7	24.2 x 10^{-2}	4.13
3	NWW15T20/steel 45, E_3=0.05J	12.6	13.1	29.6 x 10^{-2}	3.3
4	NWW15T20 /steel 210Cr12 hardened, E_6=0.3J	5.1	5.3	12.0 x 10^{-2}	8.35
5	NWW15B10T20/steel 45, E_6=0.3J	7.6	7.9	17.8 x 10^{-2}	5.62
6	NWW15T20 /steel 45, E_6=0.3J	7.5	7.8	17.6 x 10^{-2}	5.68
7	NWW15B10T20/steel 45, E_3=0.05J	5.0	5.2	11.7 x 10^{-2}	8.87
8	NWW15B10T20/steel 45, E_5=0.16J	6.9	7.17	16.1 x 10^{-2}	6.21
9	NWW15B10T20 /steel 45, E_4=0.06J	6.5	6.8	15.2 x 10^{-2}	6.56
10	NWW15B10T20 /st.210Cr12 hardened, E_6=0.3J	6.5	6.8	15.3 x 10^{-2}	6.55
11	KWB10T10/st.210Cr12, E_5=0.16J	4.4	4,7	10.3 x 10^{-2}	9,7
12	KWB10T10/st.45, E_3=0.05J	4,8	5	11.4 x 10^{-2}	8,87
13	P25/st45, E_5=0.16J	9.8	10.2	23.0 x 10^{-2}	4.35
14	P25/steel 210Cr12, E_5=0.16J	8.9	9.2	20.8 x 10^{-2}	4.5
15	Conventional layering material 602P/steel 45, E_5=0.16J	10.4	10.81	24.8 x 10^{-2}	4.03
16	Steel 210Cr12 hardened	19.7	20.6	46.1 x 10^{-2}	2.17
17	Steel 45	29.3	30.68	68.7 x 10^{-2}	1.46

As can be seen from Fig. 8 the effect of ESD differs according to the different sliding distances. The highest values of the effect of ESD were observed in the second part of the curve of wear - after the initial smoothing of the friction surfaces. High wear resistance is ensured by the homogeneous fine-grained structure of the electrical-spark coatings and of the combination of TiB_2 and B_4C and WC additives in the composition of the electrodes.

The comparison of the effect of using the new electrodes by both methods shows that at the vibration ESD the effect at both studied steels is lower than those at GFS.

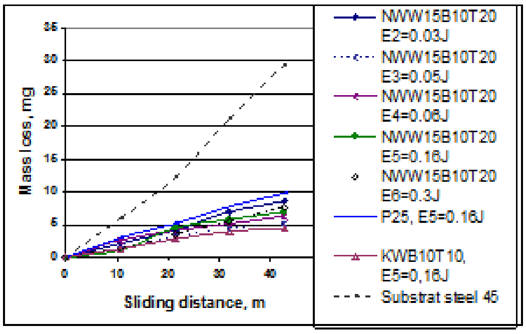

a) Mass loss vs. sliding distance for coatings from electrode NW15B10T20 on 45 steel

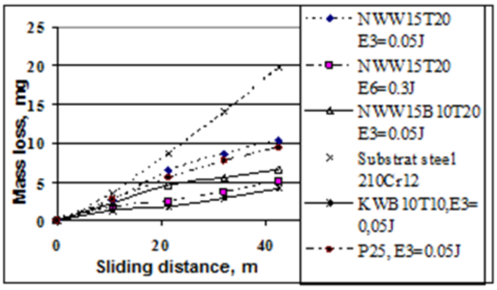

b) Mass loss vs. sliding distance for coatings from electrode NW15T20 on 45 steel

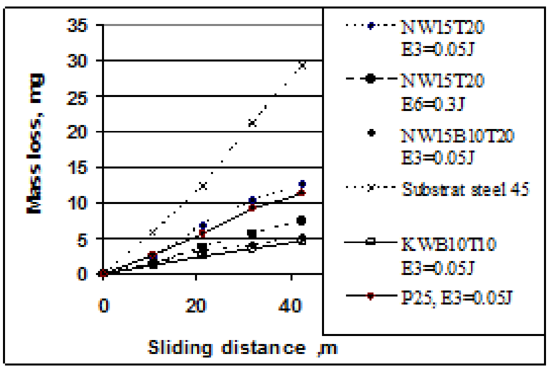

c) Mass loss vs. sliding distance for coatings on 210r12 steel

Figure 8. Mass loss vs. sliding distance of the tested coatings

While at GFS the lowest wear for the two tested steels has the coatings from KWB10T10 and NWW10B10T10, then at the ESD lowest wear rates show the coatings with increased content of the high-hard components - NWW15B10T20 and KWB10T10.

Due to the lower roughness, better uniformity and the absence of thermal impact on the substrate the ESD is more suitable for the initial layering of parts and tools with high demands on surface accuracy and quality. GFS due to the higher coating thickness - is more suitable for restoring the shape and dimensions of worn out parts.

The resulting coatings from KWB10T10 and NWW10B10T10 show higher wear-resistance in friction and abrasion, than the others studied materials, than those obtained with conventional materials and then the substrate and they may be efficiently used to strengthen rapidly wearing parts and tools of steels 45 and 210Cr12 and for protection of steel parts for severe wear applications.

4. CONCLUSIONS

Carbide composite multiphase materials have been made based on mixtures of Co-Cr-Ni-B-Si with WC, TiB_2 and B_4C in varying percentages; by ESD and GFS are received dense coatings with wear resistance over five times higher than that of non-coated surfaces.

The influence of the energy parameters of the vibration ESD processes on the roughness, thickness and abrasion wear of coatings obtained was investigated.

Experimentally, the limit values of the energy of the pulses are determined by which dense and even coatings with acceptable roughness are obtained with the new electrode materials. The conditions and processing parameters for ESD, at which has been obtained the lowest wear of coated steel have been determined.

Increasing the content of B_4C and TiB_2 additives over 10 to 20% in the Ni based materials, at GFS coatings result to a reduction, and in ESD coatings - to an increasing of their wear resistance.

The least wear is at the ESD coatings from KWB10T10 and NWW15B10T20 electrodes, and at GFS - of coatings from KWB10T10 and NWW10B10T10 materials.

The resulting coatings show higher wear-resistance in abrasive friction than the substrate and then those obtained with conventional materials, and they may be efficiently used to strengthen rapidly wearing parts and for protection of steel parts for severe wear applications.

These coatings reduce the wear intensity to a greater extent than the coatings of conventional tungsten hard alloys, slow down of wear development over time, and can be used to increase the durability of friction steel surfaces as well as parts subjected to abrasion wear.

The resulting dependencies can be used to control and manage the basic parameters and the tribological properties of the molded wear-resistant coatings and to develop technologies for the lamination of specific details and articles.

ACKNOWLEDGMENT

The present work is based on researches that are funded from the Bulgarian National Science Fund of the Ministry of Education and Science under the project "Research and Development of New Wear - Resistant Coatings Using Compositional and Nano Materials " – ДН 07/28.

REFERENCES

[1] I.I. Berkovich, D.G. Gromakovsky: *Tribology, physical fundamentals of mechanics and technical applications*, D.G. Grom, (Ed), akovsky, Samara,pp. 268, 2000.

[2] R.J. Wood, K.M. Roy: Tribology of thermal-sprayed coatings, in: Roy, Manish (Eds), *Surface Engineering for Enhanced Performance against Wear*, Springer-Verlag Wien, pp. 1-43, 2013.

[3] T.G. Penyashki: Types of coatings and methods for their deposition on the machine tools. Some guidelines for selecting suitable materials and methods for coatings. Tribological Journal Bultrib, pp. 258–286, 2011.

[4] L. Pawlowski: *The Science and Engineering of Thermal Spray Coatings*, Chichester: John Wiley & Sons, England, 2008.

[5] G. Barsukov, V.V. Barabash, A.YU. RodicheV, O. Kozhus: Technology of Powder Coatings Application by Gas-Flame Spraying Using Oxyhydrogen Flame, Materials Science Forum, Vol. 906, pp. 80-87, 2017.

[6] Broshures available at: https://www.flamespray.org, https://syscoat.com, http://www.linde-gas.com, https://www.castolin.com/, http://remoterm.com/

[7] I. Peichev, M. Kandeva: Characterizing of composite coatings deposited through gas-thermal super sound stream (HVOF-process) at different technological regimes, in: Proceedings of the 11th International Conference on Tribology "BULTRIB 2012", Sofia,pp. 187-197, 2012.

[8] An Introduction to Thermal Spray, Brochure, Oerlikon Metco, Winterthur, available at: http://www.oerlikon.com/metco

[9] G.V. Samsonov, A.D. Verkhoturov, G.A. Bovkun, V.S. Sychev: *Electrospark alloying of metal surfaces*, Kiev, Naukova Dumka, pp. 220, 1976.

[10] A.E. Gitlevich, V.V. Mikhailov et al.: *Electrospark alloying of metal surfaces, Chisinau*, Stinitsa, pp. 198p, 1985.

[11] R.N. Johnson, G.L. Sheldon: Advances in the electrospark deposition coating process: Journal of Vacuum Science & Technology A, Vol. 4, No. 6, pp. 2740-2746, 1986.

[12] G.A. Bovkun, Z.I. Vladkova, V. Molyar, T. Penyashki, Yu.G. Tkachenko: Research hardening of steels at a local electrospark depostion of metal carbides, Surface Engineering and Applied Electrochemistry, Vol. 1, pp. 10-12, 1988.

[13] K.A. Habib, D.L. Cano, C.T. Caudet, M.S. Damra, I. Cervera, J. Bellés, P. Ortells: Influence of Al_2O_3 Particle Size on Microstructure, Mechanical Properties and Abrasive Wear Behavior of Flame-Sprayed and Remelted NiCrBSi Coatings, Journal of Materials Engineering and Performance, Vol. 26, No. 4, pp. 1647 -1656, 2017.

[14] V. Nikolenko, A.D. Verkhoturov, N.A. Syui: Generation and study of new electrode materials with self-fluxing additives to improve the efficiency of mechanical

electrospark alloying, Surface Engineering and Applied Electrochemistry, Vol. 51, No.1, pp. 38-45, 2015.
[15] M.A. Garrido, A. Rico, M.T. Gómez, J.E. Fernández-Rico, J. Rodríguez: Tribological and Oxidative Behavior of Thermally Sprayed NiCrBSi Coatings, Journal of Thermal Spray Technology, Vol. 26, No. 3, pp. 517- 529, 2017.
[16] S. Houdková, E. Smazalová, M. Vostřák, J. Schubert: Properties of NiCrBSi Coating, as Sprayed and Remelted by Different Technologies, Surf. Coat. Technol., Vol. 253, pp. 14-26, 2014.
[17] F. Fanicchia, D.A. Axinte, J. Kell, G. Brewster, A.D. Norton: Combustion Flame Spray of CoNiCrAlY&YSZ coatings, Surface and Coatings Technology, pp. 546-557, 2017.
[18] J. Schubert, Š. Houdková, M. Kašparová, Z. Česánek: Effect of Co content on the properties of HVOF sprayed coatings based on tungsten carbide, in: *Proceedings of 21st International Conference on Metallurgy and Materials – Metal 2012*, Brno, Czech Republic, 23-25.05.2012, pp. 1086-1091, 2012.
[19] D. Alontseva, S. Missevra, A. Russakova: Characteristics of Structure and Properties of Plasma-Detonated Ni-Cr and Co-Cr Based Powder Alloys Coatings, Journal of Materials Science and Engineering A, Vol. 3, No. 1, pp. 41-49, 2013.
[20] A.E. Kudryashov, A.Yu. Potanin, D.N. Lebedev et all: Structure and properties of Cr–Al–Si–B coatings produced by pulsed electrospark deposition on a nickel alloy, Surface & Coatings Technology, Vol. 285, pp. 278–288, 2016.
[21] T. Penyashki, G. Kostadinov, I. Mortev, E. Dimitrova: Microstructures and wear properties of WC, TiN, and TiC based cermet coatings deposited on 210Cr12 and 45 carbon steel by contactless electrospark process, Tribological Journal BULTRIB, Vol. 6, pp. 154-167, 2016.
[22] T. Penyashki, G. Kostadinov, I. Mortev, E. Dimitrova: Improving the Surface Properties of Steel 210Cr12 by Non-Contact Electrical Spark Deposition with Electrodes Based of WC and TiC, Journal of the Balkan Tribological Association, Vol. 23, No 1, pp. 69–81, 2017.

Serbian Tribology Society

SERBIATRIB '19

16th International Conference on Tribology

Faculty of Engineering University of Kragujevac

Kragujevac, Serbia, 15 – 17 May 2019

TRIBOLOGICAL BEHAVIOUR AND CORROSION IMPROVEMENT OF THE CHROMIUM COATED PISTON RINGS BY GRAPHENE OXIDE

Doğuş ÖZKAN[1], Yaman ERARSLAN[2], Cem KINCAL[3], Egemen SULUKAN[1]

[1]National Defense University, Turkish Naval Academy, Turkey, dozkan@dho.edu.tr/esulukan@dho.edu.tr
[2]Yıldız Technical University, Turkey, erarslan@yildiz.edu.tr
[3]Istanbul Technical University, Turkey, kincal@itu.edu.tr

Abstract: *Corrosion and wear protection of metal surfaces is an important phenomenon in industrial applications in order to prevent material losses from the surfaces. Graphene is a material which synthesized from the graphite or growth via chemical vapor deposition (CVD) as a single layer of carbon atoms with hexagonal lattice structure and sp2 covalent bonding. Graphene oxide (GO) is one form of the graphene-based materials and is highly promising for corrosion inhibition. To date, corrosion protection of this material has been widely investigated as a sheet on copper or nickel surface. However, to the best of our knowledge, anti-wear reduction of this material has not been investigated especially under lubricated condition. In this paper, chromium coated piston ring was coated GO by CVD at ambient pressure furnace. Optical microscope, scanning electron microscope (SEM/EDX), atomic force microscope (AFM) and Raman analysis were used to characterize the GO coatings. Corrosion resistance of the coatings was evaluated by SP-150 potentiostat galvanostat with 0.5 and 1 M sulphuric acid solutions and wear behaviour of the coating was evaluated by tribometer tests under lubricated condition. Results showed that GO significantly reduced the corrosion rate of ring at extreme corrosive media when compared to chromium ring. Furthermore, GO reacted with ZDDP and form tribofilm to provide wear resistance to ring, which resulted in very effective wear protection because of no wear scar observation on the ring surface.*

Keywords: *Graphene oxide, corrosion inhibition, piston rings coatings, tribofilm, ZDDP.*

1. INTRODUCTION

Piston rings used in internal combustion engines are one of the important application fields of coatings [1, 2]. Chromium (Cr)/chromium nitride (CrN), phosphate (P), diamond-like carbon (DLC) are the coating types and thanks to its good wear and corrosion resistance, Cr is the most commonly used one [3, 4]. Especially, top rings which run at higher pressures and thermal stress due to the combustion process are coated with Cr by physical vapor deposition (PVD) [5, 6]. Cr coating provides wear and corrosion resistance to ring that slides against cylinder liner under boundary lubricating and corrosive conditions due to high contact pressures versus low speed and combustion residues of fuels, respectively [7, 8]. Over the last few years, due to its good hydrophobic structure, graphene oxide (GO) has been investigated to be a corrosion resistant coating by many researches [9-12]. In this study, corrosion resistance and tribological behaviour of CVD grown GO on Cr coated steel piston ring was investigated by corrosion and tribometer tests. Results showed that GO coated piston ring introduced superior corrosion and wear resistance than Cr coated piston ring.

2. MATERIALS AND METHODS

Corrosion resistance of the Cr and GO coated steel rings were evaluated via electrochemistry method. Tribological performance of the coatings was carried out with tribometer tests under lubricated condition. Microscopic and spectroscopic methods were used to characterize tribochemical and morphological changes.

2.1 Sample Preparation and Coating Process

Grey cast iron cylinder liner samples (9.5 mm x 12 mm x 8 mm) were used to counter surface for Cr and GO coated rings with the typical composition of % 93.95 Fe, % 3 C, % 0.3 P, % 0.15 V, % 0.6 Mn, % 2 Si in weight, 270 HV microhardness, and root mean square surface roughness of (Rq) 353.8 nm. Cr ring samples cut from the piston ring in 15 mm length and they had approximately 100 µm coating thickness with Rq=62.4 nm. The hardness of the coatings was measured to be 16 GPa and elastic modulus of the Cr ring was 275 GPa. Cr ring coated with graphene oxide under continuous Ar, H2 flow in ambient pressure CVD set up. Graphene oxide growth was triggered by the letting of CH4 into the tube with a rate of 10 sccm for 20 minutes.

2.2 Characterization of GO coating

Optical microscope (Nikon LV-150), SEM-EDX (Zeiss ultra plus Fe-SEM equipped with Bruker XFlash 5010 EDX detector with 123 eV resolution), AFM (Nanosurf Flex-5), and Raman (Renishaw Invia, equipped with 532 nm laser) were used to morphological and chemical characterization of the GO.

2.3 Corrosion and tribometer test conditions

A commercial tribometer was used to friction and wear performance characterization under boundary lubrication condition using fully formulated SAE 5W40 grade lubricating oil. 60 N normal force was applied to sample surfaces and sliding distance was 72.6 meters with 0.055 m/s sliding speed, respectively.

The maximum contact pressures were calculated using elliptical Hertzian contact theory (see Eq. 1).

$$P_{max} = \frac{L}{a.b} \quad (1)$$

The minimum film thickness and lambda ratio for boundary lubricating condition were calculated by Eq. 2 and 3, respectively.

$$h_{min} = 3.63x\frac{(\alpha.E')^{0.49}\left(\frac{\eta_0 U}{E'}\right)^{0.68}}{(W/E')^{0.073}}(1 - e^{-0.68k} \quad (2)$$

$$\lambda_{min} = \frac{h_{min}}{(R_{qb}^2 + R_{qs}^2)^{1/2}} \quad (3)$$

The calculated maximum Hertzian contact pressure of the Cr and GO coatings was 0.19 GPa. In addition, the calculated minimum film thickness of the coatings was 63.30 and the lambda ratios were 0.18. Quantitative determination of the corrosion rates was evaluated via Tafel curve analysis. Corrosion rates were extracted by plotting the logarithm of the current density (I) vs. the electrode potential (V) from the Tafel plots. Corrosion rates (CR) were evaluated by Eq. 4.

$$CR = \frac{I_{corr}xKxEW}{\rho xA}, \text{(mm/year)} \quad (4)$$

3. RESULTS

Fig. 1 shows a morphological and chemical analysis of the coatings by an optical microscope and Raman analysis. Blue oxidized surface was observed with an optical microscope (see Fig. 1(a)) and Raman analysis confirmed GO coating on the Cr surface with the D peak showing disorders at 1350 cm-1, G peak at 1583 cm^{-1} (assigned to the E2g phonon vibrational mode of C sp2 atoms) and 2D peak at 2702 cm^{-1} (see Fig. 1 (b)) [13-15]. In addition, weak CrO peak was detected at 660 cm^{-1} in Raman spectra.

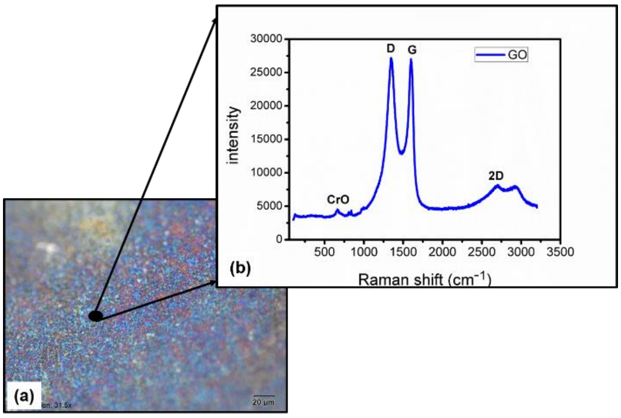

Figure 1. Microscopic and spectroscopic analysis of the GO coating (a) optical microscope analysis, (b) Raman analysis

Table 1 shows corrosion test results and for the 0.5 M solution Cr coating had 6.19 mm/year corrosion rate with 78.73 μA/cm^2 corrosion current (i_{corr}) while GO coating had 0.11 mm/year CR and 1.41 μA/cm^2 i_{corr}. When looking at the 1 M solution results, CR of GO was 0.16 mm/year with 2.11 μA/cm^2 i_{corr} and CR of Cr coating increased to 7.84 mm/year with 99.69 μA/cm^2 i_{corr}.

Table 1. Corrosion test results of the Cr and GO coated rings

	0,5 M H_2SO_4		**1 M H_2SO_4**	
	Cr Coated Ring	**GO Coated Ring**	**Cr Coated Ring**	**GO Coated Ring**
E_{corr} (mV)	-465.98	-461.46	-444.72	-449.55
I_{corr} (μA/cm^2)	**78.73**	**1.41**	**99.69**	**2.11**
$β_a$ (mV)	82.3	52.8	68.6	56.9
$β_c$ (mV)	98.3	132.8	98.4	142.2
Rp (ohm)	**224**	**10596**	**162**	**7409**
CR (mm/year)	**6.19**	**0.11**	**7.84**	**0.16**

Figure 2 shows friction coefficient results (COF) of Cr and GO coated ring. The average COF of Cr ring was 0.14 and the average COF of GO coated ring was 0.12. When looking the wear resistance of the Cr and GO coatings shown in Fig. 3, no wear scar was observed on GO surface while abrasive wear scars (labelled with red arrows) can be seen on the Cr surface.

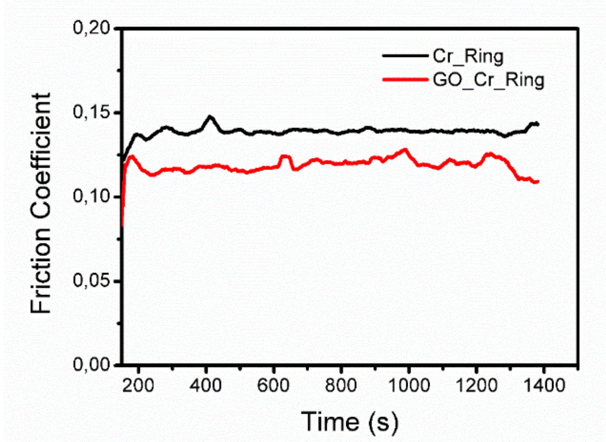

Figure 2. Friction coefficients of the Cr and GO coatings

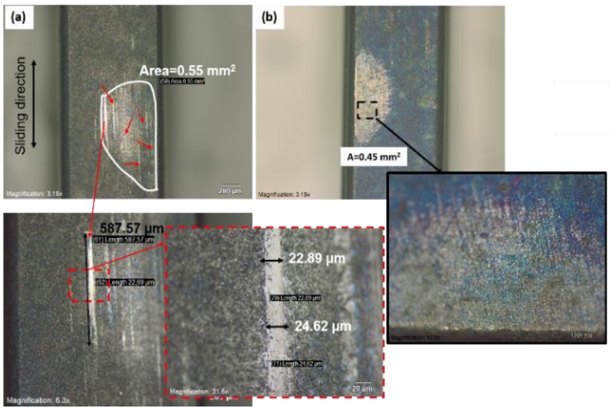

Figure 3. Optical microscopy analysis of the contact area, (a) Cr ring surface with abrasive wear scars, (b) GO coated ring with no abrasive wear scars

4. CONCLUSION

In this paper, we demonstrated a large scale directly grown GO on Cr surface via CVD method that can be a good candidate for commercial corrosion protective applications with a very low cost (only CH4, H2, and Ar gas consumption) and an excellent corrosion resistance. Furthermore, GO provided excellent wear resistance to the Cr surface, therefore, it can be a good application for piston rings of internal combustion engines.

ACKNOWLEDGEMENT

The authors would like to thank Dr. Barış Yağcı from KUYTAM of Koç University for Raman and SEM/EDX analysis and Dr.Batuhan Gündoğdu from National Defence University, Turkish Naval Academy for filtering code generation of friction force signals.

REFERENCES

[1] J. Lin, R. Wei, D.C. Bitsis, P.M. Lee, Development and evaluation of low friction TiSiCN nanocomposite coatings for piston ring applications, Surface and Coatings Technology, Vol. 298, pp. 121-131, 2016.

[2] B. Zabala, A. Igartua, X. Fernández, C. Priestner, H. Ofner, O. Knaus, M. Abramczuk, P. Tribotte, F. Girot, E. Roman, R. Nevshupa: Friction and wear of a piston ring/cylinder liner at the top dead centre: Experimental study and modelling, Tribology International, Vol. 106, pp. 23-33, 2017.

[3] T. Higuchi, Y. Mabuchi, H. Ichihara, T. Murata, M. Moronuki: Development of Hydrogen-Free Diamond-Like Carbon Coating for Piston Rings, Tribology Online, Vol. 12, No. 3, 2017.

[4] C. Friedrich, G. Berg, E. Broszeit, F. Rick, J. Holland: PVD CrxN coatings for tribological application on piston rings, Surface and Coatings Technology, Vol. 97, pp. 661-668, 1997.

[5] M. Priest, C.M. Taylor: Automobile engine tribology approaching the surface, Wear, Vol. 241, pp. 193–203, 2000.

[6] P. Lauda: Applications of thin coatings in automotive industry, J Achieve Materials Manufacturing Engineering, Vol. 24, pp. 51–56, 2007.

[7] L.C. Martin, O. Ajayi, A. Erdemir, G.R. Fenskea, R. Wei: Effect of microstructure and thickness on the friction and wear behavior of CrN coatings, Wear, Vol. 302, pp. 963–971, 2013.

[8] T. Haque, A. Morina, A. Neville, S.S. Arrowsmith: Tribochemical interactions of friction modifier and antiwear additives with CrN coating under boundary lubrication conditions, Journal of Tribology, Vol. 30, No. 4, pp. 042302-042302-12, 2008.

[9] A.K. Geim, K.S. Novoselov: The Rise of Graphene, Nature Materials, Vol.6, pp. 183–191, 2007.

[10] O. Penkov, H.J. Kim, H.J. Kim, D.E. Kim, Tribology of Graphene: A Review, International Journal of Precision Engineering and Manufacturing, Vol. 15, No. 3, pp. 577-585, 2014.

[11] P. Avouris, C. Dimitrakopoulos: Graphene: Synthesis and Applications, Materials Today, Vol. 15, No. 3, pp. 86-97, 2012.

[12] R.K. Singh Raman, A. Tiwari: Graphene: The Thinnest Known Coating for Corrosion Protection, Journal of the Minerals, Metals & Materials Society, Vol. 66, No. 4, pp. 637–642, 2014.

[13] N.T. Kirkland, T. Schiller, N. Medhekar, N. Birbilis: Exploring graphene as a corrosion protection barrier, Corrosion Science, Vol. 56, pp. 1-4, 2012.

[14] B.P. Singh, S. Nayak, K.K. Nanda, B.K. Jena, S. Bhattacharjee, L. Besra: The production of a corrosion resistant graphene reinforced composite coating on copper by electrophoretic deposition, Carbon, Vol. 61, pp. 47-56, 2013.

[15] M.V. Stanković, I. Jevremović, I. Jung, K.Y. Rhee: Electrochemical study of corrosion behaviour of graphene coatings on copper and aluminium in a chloride solution, Carbon, Vol. 75, pp. 335-344, 2014.

[16] S. Pavan, A.S. Ramanan: A study on corrosion resistant graphene films on low alloy steel, Applied Nanoscience, Vol. 6, pp. 1175-1181, 2016.

Serbian Tribology Society

SERBIATRIB '19

16th International Conference on Tribology

Faculty of Engineering University of Kragujevac

Kragujevac, Serbia, 15 – 17 May 2019

CONSIDERATIONS FOR THE SELECTION OF MATERIALS FOR ELECTRICAL SPARK AND GAS FLAME SPRAYING DEPOSITION ON STRUCTURAL STEELS

T. PENYASHKI[1*], M. KANDEVA[2,3], G. KOSTADINOV[1], E. DIMITROVA[1], I. MORTEV[1]

[1]Institute of Soil Science Agrotechnologies and Plant Protection "N. Pushkarov", Agricultural Academy – Sofia, Bulgaria
[2]Faculty of Industrial Technology, Tribology Center, Technical University – Sofia, Bulgaria,
[3] South Ural State University, 76 Prospekt Lenina, Chelyabinsk, Russia
* Corresponding author: peniashki@abv.bg

Abstract: *The aim of the present work is to identify and formulate the basic principles and approaches for the selection of materials for electrical spark and gas-flame stratification of structural steels. For this purpose, have been examined:*
-The characteristic features and physical foundations of the two methods, the changes in the composition and structure of the coating materials in the transfer process and in the formation of the coatings and the general similarities and differences.
- The regularities of formation and qualitative characteristics and properties of the coatings obtained, depending on the process parameters of the coating mode and the layering material.
- The interrelation between: the process parameters of the application system; the coating material; the quality characteristics, the composition, the structure of the coatings; the mechanical and the tribological properties of the coatings.
The requirements for coatings have been formulated for various loads and wear cases and on this basis the requirements for the layering materials are determined by the two methods. Appropriate materials and compositions are specified for various cases of friction and wear. The main approaches to the selection of the layering materials are described.

Keywords: *electrical discharge deposition, gas flame spraying coatings, laminating materials, wears resistance.*

1. INTRODUCTION

The need to increase the complexity, power and efficiency of the technical systems has led to a sharp increase in the social and economic importance of processes related to friction and wear and the providing high wear resistance to the work surface of the bodies. Increasing of wear resistance in the largest extent is achieved through the development of new, environmentally friendly technologies for the deposition of highly effective and reliable coatings for the protection and hardening of metal products. The coating applied to the working surfaces of the parts is a quite versatile and easy means by which it is possible a new approach to the problems of improving the properties of the materials, increasing their working capacity and controlling the friction or cutting processes.

Most of the existing methods and technologies for applying wear-resistant coatings however are realized through complicated and expensive equipment and require high investment. Because of its simplicity and versatility the electrical spark - ESD and gas flame spraying – GFS with their accessible and portable equipment, easy technology and a universality are not only more widespread, but also significantly cheaper, and fully accessible to most consumers [1-5, 6-8].

The common feature of both methods is that the coatings are obtained by transferring the coating materials onto the substrate mainly in liquid and semi-solid (softened phases) as a result of high temperature impact with concentrated energy streams - electro-spark plasma discharge channel and gas-flame jet. Diffusion processes flow in the "substrate - coating" boundary at the methods of thermal impact, are formed chemical compounds, solid solutions and new phases, and the structural construction changes and occurs a transition zone in which runs a grouping of various atoms and reducing of the differences in the properties of the pair materials[1.2, 6-8] .

This ensures a stronger connection with the base than the other methods and makes them more suitable for working with high and variable impact loads. The effectiveness of these two methods for applying coatings is determined by the use of deposition materials, which must ensure, on the one hand, the technological effectiveness of the coating process, and on the other, a high level of physical, and operational properties of the surface.

The wrong choice of material for the application of wear-resistant coatings does not allow obtaining a satisfactory combination of the required level of performance characteristics of tribosystems with acceptable process ability, maintainability and cost-effectiveness of the processes of manufacturing and repairing parts. Numerous and various data are available in the literature on studying of the structure, composition and properties of wear-resistant coatings applied by both methods [1-5,6-8,9-17] and many others. There the basic principles of the formation of the coating are given, and numerous data on their properties, the nature, and type of wear and tear in different conditions, and the results of their application taking into account the 1.3 to 10 and more times the increase in durability. Nevertheless, the processes and the wear mechanism under different friction conditions are still not well understood and there is insufficient data on the relationship between the type and nature of the wear and the physico-chemical and physico-mechanical properties of the coatings.

There are no developed criteria for the selection of materials and layering regimes, and the famous criteria and experimental data do not solve the problem of obtaining quality coatings with high physico-chemical and performance properties. These makes it difficult for the development of a common methodology and recommendations for selecting a coating material and their application in practice. These limits more widespread use of these two so light and accessible methods as a means of extending the life of the products and of machines, and the economy of labor, energy, and materials. In order to improve the efficiency of ESD and GFS, it is necessary to select special materials for obtaining coatings with enhanced quality characteristics and properties and for direct and multi-purpose intended.

In this regard, the aim of the present work is to identify and formulate some basic considerations, principles, and approaches in the selection of materials for electro-spark ESD and gas-flame spraying GFS deposition of structural steels.

2. CHARACTERISTICS OF THE TWO METHODS

Electrical spark deposition / ESD / is the easiest, simplest, cheapest, most versatile and effective means of locally application of a wear-resistant coatings of various uses with different functions on the work surface of rapidly of wearing parts and tools. The main advantages of the ESD process compared to other existing coating methods are the simplicity and accessibility of the technology, the cheap and compact equipment, the low cost of materials and the low energy intensity of the process. The ESD makes it possible to apply the coatings in strictly defined locations without the need for means and measures to protect the rest of the surface of the product. The Electrical spark coating has a high adhesion strength to the substrate, a lack of heating and deformation of the material of the substrate, possibility of use and operation without additional mechanical treatment. The method is based on the use of short-term pulsed plasma discharges with controlled energy in the air environment, accompanied by electrical erosion and polar transfer of material from the depositing electrode (anode) on the article cathode. The formation of the layer occurs under conditions of local short-term operation at high temperatures (above 10000 °C) and pressures. As a result of the electric spark discharges occurs melting and evaporation of the particles of the electrodes which, with extremely high speed, strike and stick to the surface of the laminated product. The formation of a hardened surface layer and coating at ESD is a result of complex plasma-chemical, thermal, and mechano-thermal processes occurring on the local surface areas of the workpiece under the influence of the energy of a spark discharge. Diffusion and chemical interaction between the materials of the anode, the cathode and the surrounding medium accurate, and fixed high-temperature states, extremely unbalanced phases, and structures that sharply change the physico-chemical properties of the surface layer are obtained. A coating with a new relief and structure with different from the initial state surface properties is formed which are controlled over a wide range by changing the parameters of the spark discharge and the composition of the electrode material [6-8, 13-17].

The short duration of the electrical impulse of -5-500 µs leads to an extremely fast hardening of the deposited material, which results in a new structured coating showing unique tribological and corrosion efficiency. The method allows the application of coatings with a thickness usually of 3-200µm from any and on any conductive materials, but most often used are hard-alloy composite materials based on WC, TiC and TiN. The hardness of the applied super dispersed top white layer reaches 20.103MPa and the shelf life of the laminated articles increases 1.5-4 and more times [16-21].

Depending on the layering modes and the materials of the electrodes, coatings can be obtained with predetermined qualitative characteristics, composition, structure, and properties. With an increase in the energy of the single pulse E (current, voltage, capacity, pulse duration), and the pulse frequency, the transfer from the electrode increases, the thickness increases, but also the roughness and the unevenness of the coatings [6-8, 14, 15, 16, 21-23].

The amount of amorphous phase's decreases due to the elevated surface temperature of the cathode reduces the cooling rate of the molten and evaporated particles of electrode material, which activates the transition from the metastable amorphous to the thermodynamically stable crystalline phase. The process does not require special cameras, booths, or operator protection, does not release hazardous waste, smoke or waste water, and is attractive to a very wide range of applications to of strengthening of any rapid wearing tools, working bodies and parts of metallic materials.

The main disadvantage of electrospark hardening is that with an increase in the thickness of the applied coating, its roughness increases, which negatively affects its performance properties.

3. GAS-FLAME SPRAYING

Gas-flame spraying GFS is realized by converting the casting material into molten particles which are applied at high speed to the surface of the coated article and bonded thereto. The application is carried out by means of a torch in which the inserted coating material is introduced and mixed with the burning gas. The molten particles are applied at a rate of 100-150m/s and adhere to the surface of the substrate to form the coating.

The particles carried by the flame stream pass into a plastic and semi-plastic state and after contact with the substrate due to the high kinetic energy, they deform, to form thin flaps of different shapes.

Through this method, coatings with high hardness and wear resistance of all materials on non-metallic and metal surfaces with thickness up to several millimeters are applied. These coatings usually require additional treatment because they are uneven and high roughness. Due to the substrate heating in the application process and the need for post-processing, GFS significantly complicates the technology of layering the cutting tools and heat-treated parts and is therefore mainly applied to unprocessed steel parts of structural carbon and alloy steels.

GFS methods have very broad possibilities both for restoration of worn parts and for production of new ones with predetermined surface properties independent of the properties of the base material. The relatively low speeds of the sprayed particles and the high content of oxides in the coatings formed by the gas-flame method, however, reduce their quality.

A variety of GFS are technologies and devices for high-speed supersonic flame plating systems (HVOF), where the leakage gas stream is 3 to 5 times the sound velocity. With these systems, thick and dense coatings with low porosity and high adhesion strength high bond strength due to the large kinetic energy of the particles are obtained [2,5,11,25-27]. Their thickness may vary between 100μm and 1mm and above, depending on the type of the layered material, as typical thicknesses are in the range 120-500μm [5,11,27].

The main parameters of the process determining the quality, composition, structure and properties of the coatings are: the thermal power emitted in the working jet (Gas flow temperature is - 3000 - 3500˚C); type, pressure and consumption of the working and transport gases; granulometric composition, consumption, particulate form of the starting powder; angle and way of delivery of the powder; roughness, purity and surface temperature of the substrate; type of the surrounding environment [1, 2, 5,11,27].

In spite of the established legalities in the literature between the technological, micro-structural and operational parameters, due to the complexity of the processes and the variety of thermal spray technologies and coatings, there is not yet a generic model with which to plan the technological conditions for to produce coatings with predefined properties.

The comparative characteristics of the coatings obtained by the two methods are given in Table 1.

In the manner of transferring the layered material onto the substrate, these two methods are similar, but there are also significant differences. At ESD material was transferred to a liquid, solid (softened) and vapor phases at a rate of the particles with an order of magnitude higher than those at GFS.

The same is mixed with the locally melted micro spot of the substrate to form a surface layer of a mixture of the two materials, new compounds and phases derived from their chemical interaction and from the reactions with the materials from the environment. The coating-substrate bond is diffusion and metallurgical. Adhesion is at the strength level of the substrate. Due to the extremely high cooling rate of the resulting coating has a superdispersed structure reaching to the metallic glass. Its thickness in the most frequent cases is limited - up to 100μm. As a result, a new layer is obtained which is different properties - increased hardness, wear - and corrosion resistance, etc., controlled extensively by the parameters of the spark plasma discharges and the material of the electrodes.

In the case of GPL, the material is transferred to the liquid and softened phases. On the "layer-substrate" borderline is obtained diffusion layer but is absent superdispersed and amorphous non-porous structure, smaller is the degree of mixing of the two materials, and to obtain an acceptable adhesion is necessary pre-heating of the substrate. However, the thickness of the coating can be up to 2 mm, much higher than the ECD, which gives priority to this method of restoring worn surfaces. The roughness of the resulting coatings is higher and in most cases they require further processing.

Table. 1. Comparative characteristics of the coatings obtained by ESD and GFS methods

Energy Source	Tempe rature ^{0}C	Mini-mum area of heating [mm^2]	Maximum energy den-sity in the heated spot [W/mm^2]	Coatings			
				Thickness [μm] Roughnes [μm]	Hardness	Coating properties	Surface to be treated. Size and shape of the part
Gas flame	3000 ÷ 3500	≈1	5 x 10^2	50÷1300 5÷30	HRC 30-÷70	wear-, corrosion-resistant, heat-resistant	local application, dimensions and form of the part are not limited
Electro-spark discharg e	5000 ÷ 15000	≈1 x 10^{-6}	10^6÷10^{9}	5÷500 1÷12	HV 7÷18GPa		

Figure 1. Correlation scheme "layering mode and material - wear resistance"

ESD is better suited for preliminary surface modification and the GFS- for recovery and in this sense, the two methods complement each other.

4. FACTORS DETERMINING THE DURABILITY OF THE COATED PRODUCT:

In both methods, the durability and exploitation properties of the layered products depend on the simultaneous action and mutual influence of a large number of factors, which are divided into three main groups:

- Factors relating to the layering conditions - the layering mode parameters, the layering material, the coating application scheme, etc.;
- Factors relating to the layered products - material, type, shape and dimensions of the work parts, the significance and degree of impact on the machine's working, productivity and operating resources etc.;
- Factors resulting from operating conditions - speed, type, nature and size of the mechanical loads, temperature, type of friction, presence of cooling, type and nature of prevailing wear and degree of admissible wear, impact of the environment in the exploitation process, and for friction pairs - the material and type of the conjugate detail.

In both methods, the composition, the structure and the properties of the deposited coatings depend on the type, composition, and structure of the deposited and of the substrate materials and the parameters of the application regime. Their interconnection is given schematically in Fig 1.

It can be seen from the diagram that in both methods the main factor is the type of material to be laid. From the selection of the material combined with the parameters of its application regime, the properties of the coatings depend - and hence their wear resistance. Of the above factors depends the choice of both the material and the method of coating. If it is not known how this complex affects any of the determinant properties, it is not possible to determine the appropriate type of layering material for one or another article.

5. REQUIREMENTS FOR COATINGS AND COATING MATERIALS

In the process of wear, the contacting surfaces must successfully resist on plastic deformations, on shearing of micro-volumes from the material, on the penetration of solid abrasive particles in surface (particles from the external environment, separated particles or growths during adhesion), as well as and against effects of aggressive media and temperatures. Depending on the specific conditions of use, wear-resistant coatings must meet a variety of different requirements. In some cases, high resistance to abrasion wear is required, in others high resistance to heat load, in third - high chemical resistance, etc. In most cases, coatings require a complex of properties that ensure long-term performance of the product under certain operating conditions, the main ones being:

- High wear resistance and maintenance of consumer properties over the entire range of temperature, pressure, or chemical aggressiveness in the working area;
- High micro-hardness is a basic requirement that reflects the resistance of the abrasion-resistant coating;
- Tensile strength and toughness reflect the ability of the coating to withstand stresses and deformations in working conditions, to absorb mechanical energy under dynamic loads, not to break under the influence of high pressure on its surface, to prevent the formation and development of cracks in variable conditions loads, impacts and vibrations;
- Chemical and corrosion resistance, heat resistance, thermal conductivity, low coefficient of friction;
- Technological and economic requirements
- They affect the parameters and the properties of the coating depending on its deposition process, the possibility of obtaining coatings with high quality characteristics - low roughness, high density and uniformity, necessary thickness for the concrete case , with predefined properties, composition , structure and morphology, and the ability to control and evaluate the process. They are crucial in terms of process performance and its cost, the minimizing the cost of parts and coatings at maximizing product durability and productivity;
- An important condition is also the formation of a strong connection between the base and the coating. The nature of the base materials and the particles of the coating and their energy state during bonding are determinant factors for the formation of a strong bond.

5.1. Requirements for coating materials

Additional requirements for coating materials according to the layering processes.

The operability and efficiency of the coated detail can be ensured only if coating material has sufficient hardness, strength, wear resistance, temperature resistance and thermal conductivity and in addition, according to the particularities of the two methods, the following qualities:

- Low degree of oxidation in the transmission process;

ESD and AFS are accompanied by rapid specific chemical-thermal phenomena, occurring at high local temperatures and pressures. These conditions require the laminating material to be less susceptible to high-temperature oxidation processes or to use self-lubricating additives in order for to prevent the formation of oxide and nitride phases, which cause brittleness of the applied layer, [1-3,10,11,25,27-30].

- Possible lower melting temperature (under GFS) of the bonding mass;
- Full or high solubility of the bonding metals in the iron - which is a guarantee of a strong bond with the substrate;
- Resistance to high temperatures and a tendency to form intermetallic compounds, borides, carbides and nitrides in the course of formation of the coating.
- -Smaller grain sizes of the high-hard phases to aid and facilitate their melting;
- At ESD - small grain sizes, up to several microns, contributing to obtaining the ultra-dispersive and amorphous structures.

5.2. Considerations in selecting the composition of the coating materials

For the correct choice of the layering material it is necessary to consider the interconnections: product for coating - operating conditions - laminating material - coating method and process parameters - topography, composition and structure of the coating - physico-chemical and mechanical properties of the coating - wear resistance and performance of the covered surface- Fig. 2.

If for the parts working in conditions of static load, the main criterion in evaluating the coated layer, is its wear-resistant, for the products working under dynamic load conditions, is essential this layer to acquires a strength of fatigue and impact strength. Therefore, for the numerous and different operating conditions of different products, it is necessary to create different materials and different composition, structure and morphology coatings.

Just as well as there are no universal constructive or tool materials, there is no and universal coating materials. Traditionally, pure metals and metal alloys are used as deposition materials.

To achieve high adhesion of the coating to the substrate and efficient formation of the layer, the components of the laminating material must form solid solutions or intermetallic compounds with the substrate material and have a thermal expansion coefficient close to it. As most suitable for coatings, most authors [1-3,6,7,9,10,11,15,24,27,28,30,31] and many others indicate Ni, Co, Fe, Cr, Mo, W Cu, Al, Fe, and their alloys. The metals Ni, Co, Cr, Mo, W form with Fe limited and unlimited solid solutions and intermetalides. These metals form intermetallic phases with iron, and carbide phases, therefore so that the probability of increasing the hardness and wear resistance of the layer is high and therefore these metals may be included in the composition of the laminating materials.

The most widely used coatings are chromium-nickel alloys that provide resistance to high-temperature corrosion [1-3, 24, 28, 30-32]. Special attention to the selection of the brazing metals in the composition of the electrodes and powders is separated on chromium Cr. Chromium has a higher wear resistance than iron and particularly high wear resistance in various aggressive environments. Iron and chromium have unlimited solubility in solid and liquid state, regardless of temperature. Most researchers have found that a number of solid solutions are formed in the iron-chromium alloy.

According to some researchers [6,7,9,10,12,15,22,24,29,30,33], the combination of Cr with Ni contributes to the formation of more carbides in the layer and an increase in wear resistance. The heat action on the substrate in the presence of nickel may cause both the solid solution of Ni in the γ - Fe, and the formation of additional compounds of the type of FeNi3, and in the presence and B is possible, and formation of Fe_3Ni_3B.

According to most researchers [1,3,5,7,9,10,22,30,31,33], the Ni and Co metals provide a high density of the layers, forming limited and unlimited hard solutions with Fe and intermetalides.

The Cr has a less complete electronic envelope and therefore has a higher carbon affinity in steels to form carbides, which increase the hardness of the layer as opposed to Ni and Co, which in the presence of Fe do not form carbides. The presence of Co in the steels and alloys leads to high stiffness, corrosion resistance and high resistance to wear. Cobalt is a valuable alloying element for high-speed tool steels.

Combined with chromium, a high hardness of alloy steels is achieved. When creating layering materials, it is also necessary to take into account the influence of the environment and the ability to form carbides and borides directly onto the substrate. For this reason, technological additives such as B, Si, C, Al_2O_3, Cu, C, Al and others can be incorporated into the material composition with different purposes. For example, the introduction of B, Si, C reduces the formation of oxides, and at ESD also reduces the erosion resistance of the laminating electrodes [22, 35-38,39].

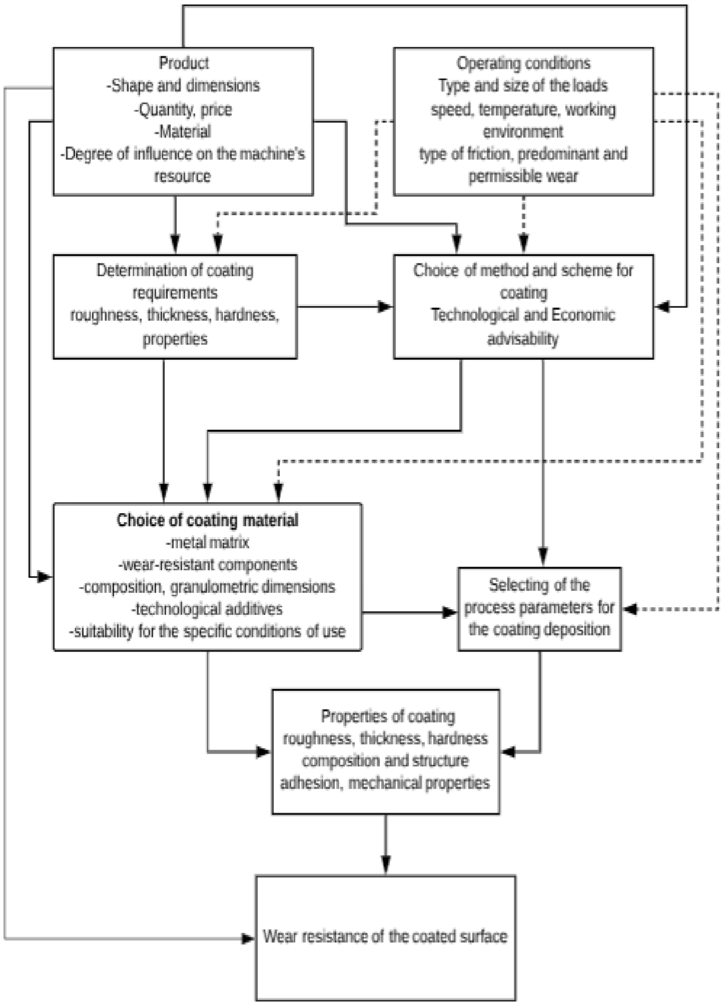

Figure 2. An algorithm for selecting a suitable coating material

At the same time, the boron serves as a donor for the formation of wear-resistant borides in the layer, the carbon - as an anti-decarburization during the transfer process, and for the additional formation of dispersed carbides in the process of forming the coating. Cu contributes to reducing the size of the grains in the layer; Aluminum increases the yield strength limit and, because of its low melting temperature, helps to increase the transfer to the substrate. Due to their good wear and corrosion resistance, Ni-C-rB-Si-based alloys are commonly used in the GFS on steels [35-40]. Essential elements in these compositions are B and Si. These elements have several functions: they reduce the melting temperature of Ni by several hundred degrees - from 1450 to 1000 °C. They form a low melting point boron silicate, which flows to the surface and protects the melt pool from oxidation. Further, they promote wetting of the substrate by reducing Ni, Co, Fe and Cr oxides, controlling surface tension and fluidity of the melt .The low melting point of NiCrBSi alloys as well as the fluxing effect of the Si and B allows these materials to be deposited by flame spray followed by fusing and welding the powders. An increase in the amount of chromium, boron and carbon increases the amount of solid carbides and borides, respectively [15, 35-40].

In addition to nickel-based, higher wear-resistant cobalt-based metal alloys Co-Ni-Cr-B-Si can also be used. In this case, in order to increase the bond strength and the degree of melting of high-hard phases, a higher heat capacity of the flame jet at the GFS is required, and at the ESD process, impulse parameters will depend on the quality requirements of the coatings. In spite of such widespread use of Ni-Cr-B-Si alloys in thermal spraying, their abrasive wear resistance is still not fully understood.

The insufficient wear resistance of metal coatings leads to the need to use new materials for the ESD and GFS. The development of chemistry and nanotechnology allows us to accept the particularly high performance of complex coatings, from composite materials that have unique properties. According to most of the authors, the future is of the compositional coatings. These are multi-component multi-phase coatings from several of the above materials - mixtures and solid solutions of metals and metal-like compounds - mainly carbides, borides, nitrides and oxides of difficult metals. They are the most common combination of two or several heterogeneous materials. In the hardened surface layer, it is necessary to ensure sufficient ductility, high hardness, and strength. These requirements can be realized only in the composite coating, organizing a hardened layer consisting of a plastic base (matrix) with solid inclusions.

For a metal matrix Ni-Cr-B-Si and Co-Ni-Cr-B-Si alloys are most suitable - for the latter more appropriate is the HVOF method. Besides Ni, Cr, Si, Co and B, these alloys may contain Fe, C and sometimes Mo, W, Cu.

Experience has proved these alloys are a good choice for components in the presence of hard particles. Higher hardness and abrasion resistance is ensured with additions of hard-alloy compounds [15,22,2,35-40].

In the selection and optimization of the composition of the laminating material should also take into account the change in its properties in the process of the ESD and the GFS. In most cases, the issues about the choice of solid phases can be successfully resolved using components of the difficult compounds of metals of IV-VI groups of the periodic system with boron, carbon, nitrogen and other non-metals. High wear-resistant components in the composition of the composite material are most suitable: WC, TiC, TiN, Cr_2C_3. The authors of this paper also recommend TiB_2 in combination with WC and ultra-hard B4C.

Tungsten carbide based alloys with TiC are of high strength and hardness, they have the widest application in the production of various tools and in the application of wear-resistant coatings on metals. TiC is widely used for wear-resistant coatings on cutting tools. Titanium carbide is recommended because of its wide range of homogeneity, high hardness, temperature resistance and wear resistance. [7,13,15,22,23,31,33,34,42,43].

TiN has the lowest friction coefficient and the highest resistance to wear. Furthermore, it is chemically least active with respect to iron and copper and can be an excellent barrier against adhesion and diffusion wear and is the most common in practice material for applying wear-resistant coatings on metal cutting tools of high-speed steels [13-15,21-23,41-43].

Titanium diboride is distinguished by its very high hardness, abrasion resistance and chemical resistance[41,42]. Boron carbide B_4C is a super hard material with extremely high abrasion resistance and abrasion resistance.

Conventional tungsten carbide alloys can be added in order to increase the amount of WC and cobalt. The WC and TiB_2, in addition to abrasive wear, are also resistant to impact loads [6,7,15,22,31,34,41,42].

Table 2 gives some recommended powder formulations designed and tested by the authors suitable for wear-resistant coatings on steels.

The microstructure of the coatings obtained with the above materials contains besides the metal matrix and different amounts of solid carbides and borides. [5,10,11,12,24,26,39].

Coating composite material consisting of particles of the metal alloy on and or particles of high wear resistance compounds – WC-TiB_2, B_4C is of particular interest since the hard particles as incorporated in the metal alloy matrix give high hardness (1800-2000HV) to the coatings. The test results of these coatings obtained by blending powder mixtures [11,26,39] show that wear sharply reduces and takes up to twice smaller values than those of the coatings of conventional materials without the presence of added our materials. High hard additives in the volume of the coating forming an internal contact network with high strength characteristics, which provide a high resistance of the coating against destruction by scratching action of the abrasive particles.

Table 2. Conditional designation of the coating and suitable powder chemical composition (% by weight)

№	Designation	Chemical composition of powders, wt. %
1	602P - Ni-Cr-B-Si-Fe-C and tungsten carbide.	Cr: 13.2; Si: 3.98; B: 2.79; Fe: 4.6; Co: 0.03; C: 0.63; **Ni: Balance**
2	10611W- Co-Ni-Cr-B-Si and tungsten carbide.	(45% (1.5% C, 1.5% Si, 23% Cr, 0.5% Fe, 42% Co, 30% Ni,1.5% B) + 55% WC)
3	6P50W	Cr: 13.15; Si: 4.28; B: 2.87; Fe: 0.04; Ni: 29.6; Co: 0.04;C: 0.58; **WC+ 12%Co : Balance**
4	WC–12Co,	Co: 12; C: 5.4; Fe: < 0.1; Ni: < 0.1; **WC: Balance**
5	602P–6P50W–(WC–12Co)-(B_4C - TiB_2)	Mixture ratio (1:1:1: 0,3)
6	NWW10T20B10	60% (55% (0.6% C, 2.86% Si, 12% Cr, 3.94% Fe, 77%Ni, 3.6% B) + 45% WC) + 10% WK8 + 10% B_4C + 20%TiB_2.
7	NWW10T10B10 (based on 602P)	70% (55% (0.6% C, 2.86% Si, 12% Cr, 3.94% Fe, 0%Co, 77% Ni, 3.6% B) + 45% WC) +10% WK8 + 10% B_4C + 10% TiB2 (WK8 is hard alloy with 92% WC and 8% Co).
8	KWT10B10 (based on 10612)	80% (45% (1.5% C, 1.5% Si, 23% Cr, 0.5% Fe, 42% Co, 30%Ni, 1.5% B) + 55% WC) + 10% B_4C + 10% TiB_2.

6. DISCUSSE AND FINDINGS IN RELATION TO COATING MATERIAL STRUCTURE

Analyzing the surface hardening, it should be noted that, by increasing the hardness, we reduce the ductility, which reduces the danger of adhesion sticking and micro-welding of the conjugated surfaces, on the one hand. On the other hand, a decrease in plasticity increases the sensitivity to local high pressures, which can even lead to local destruction of the surface.

To reduce the brittleness of the coating and increase the performance of the electrospark and GFS processes, it is advisable to increase the metal binder [3,7,22,28,29,32,39] . The metal bond material must wet the refractory phase of the composite, since in this case the wear-resistant particle is enveloped by a low-melting component, which ensures good adhesion to the alloyed surface.

The metal matrix improves and adhesion with the substrate because at the moment of impact of the particles there is an exothermic reaction that is accompanied by a self-binding. The appropriate amount of the plasticizer phase depends on the chemical and physical properties of the wear-resistant phase and the substrate material and should be optimized for the various difficult-to-wear compounds. If the material of the plasticized phase does not wet the particles of hard phases, the amount it should be higher.

Very important is the determination of the amount of high hard supplements. In a large quantity over 70%, they do not adhere firmly to the substrate and the wear resistance of the coating decreases. This is due to the insufficiently high temperatures reached in the flame of the acetylene torch to melt (albeit only partially) the carbide particles and to embed in the coating.

For example, in the coatings made of the powder NWW10T20B10 [39],only about half of quantity W, Ti and B was found, indicating that about half of the mechanically added to the starting powder WC, TiB_2 and B_4C particles (with a concentration of 40 wt%) do not participate in the construction of the gas-flame coatings.

At ESD, however, due to the high temperatures of the process, the amount of high-hard additives in coating is a pretty greater.

Considering that these additives increase the hardness but also the brittleness of the coating and the specificity of the ESD transfer, the optimal concentration of the bonding mass should be in the range of 12-25% for coatings of different uses, and for thick coatings - 20-40%. [6,7,8,13-16,22,23,33,43]. The composition and particle size is chosen depending on the type of the material to be laid, the desired coating properties and the type of the coating apparatus.

For dust of metals and alloys, the most authors are recommended that particle sizes be between 45μm and 105μm, and for powders of hard-wearing oxides and carbides between 10μm and 40μm [1,3,4, 5,10,12,24,25,27,29].

In practice, such layers deposited on steel substrates can be used to increase hardness and wear resistance during high load and friction conditions of in abrasive environments as well as for corrosion-resistant workpieces. Obtaining a dense and uniform coating with each of the materials used requires certain parameters of the application modes.

Table 3. Methods of surface modification and increased durability depending on operating conditions defining the type of predominant wear.

Workingconditions causing predominant wear	***Basic methods and materials for surface modification and increased durability***
Friction with low contact pressures low, medium and high speeds	*Solid antifriction alloys and composites. Improving the surface relief, increased hardness and abrasion resistance - thin and medium single- and multilayer coatings of wear-resistant materials with low coefficient of friction and high smoothness- applied by ESD - with composite electrode materials based on (W, Ti) C, TiC-TiN, TiCN, TiB_2-TiAl with bonding metals Co, Cr, Ni, Mo and different technological additives(Cu, Al_2O_3,B,C); GFS with Ni-Cr-B-Si alloys different technological additives of WC-Co hard alloys, compositions KWW10T10B10 and NWW10T20B20;*
The presence of solid particles and elements causing abrasive wear	*Improving relief and an increase in surface hardness - medium and large single-and multi-layer coatings of hard and abrasive resistant materials - hard alloys- WC-Co, (W, Ti)C, TiCN-II layer, compositions KWT10B10 and NWW10T20B20 applied by ESD, compositions; KWT10B10, NWW10T10B10, 6P50W- by GFS and HVOF methods.*
Adhesive interaction between contacting materials	*Creating a chemical resistance layers to the material of the conjugated detail – hard alloys based on TiN + Al_2O_3, WC-TiC-TiN, TiB_2-TiAl, (W,Ti)C-TiCN+ B_4C, KWW10T20B10 - applied by ESD ; compositions KWT10B10, NWW10T10B10, 602P-10611W–(WC–12Co)-(B_4C - TiB_2)- Mixtures , 6P50W- by GFS and HVOF methods.*
Fixed, variable force and high shock workloads	*Increase in surface hardness, toughness and strength characteristics and improve relief - medium and large single and multilayer coatings of high hard and rubbery materials - hard alloys, WC-B_4C, TiC + TiN, TiC-B_4 C, Ni-Cr-Si-B, TiB_2 - BN, WC-B_4C applied by EH, plasma and gas or electrochemical lamination. Increase in surface hardness, toughness and strength characteristics and improve relief - by medium and large single and multilayer coatings of high hard and rubbery materials - hard alloy based onWC, WC-TiB2,Ni-Cr-Si-B-Fe, , NWW20T10, KWW10T10 applied by ESD,; 602P , 10611W, KWW10T10 ,602P–6P50W – applayed by GFS or HVOF.*
Thermal stresses	*Thin and medium-sized single-and multilayer coatings from temperature-and chemical-resistant materials with a thermal conductivity close to that of the substrate – Co- Cr, hard alloys based on TiN, TiC- TiN+ Al_2O_3, TiAlN, TiC-TiAlN, TiC-TiB_2+B4C, TiB_2-TiAl, - obtained by ESD; 10611, KWW10T10B10, NWW10T10B10 etc- by GFS or HVOF.*
Work in chemically aggressive environments	*Create a layer of thin and medium-sized one-and multilayer coatings of chemically resistant materials – Cr-Ni-Co, hard alloys based on TiC – TiN+ Al2O3, (W,Ti)C -TiB_2, WC-TiB2–B_4C,-obtained by ESD; 10611, Fe-Cr-Al-Mo, KWW10T10B10, Mixture 602P–6P50W–(WC–12Co)+(B_4C - TiB_2), Co-Ni-Cr-B-Si alloy and tungsten carbide. etc.*

To create the necessary physicochemical and mechanical properties of the surface layer for a variety of operating conditions, we need to control the processes involved in depositing the coatings. One of the possible ways to increase productivity and wear resistance of the

ESD coatings is to create amorphous and nanostructured phases. The unique wear resistance, high rigidity and plasticity, good performance of the amorphous and nanostructured alloys are related to the relaxation character of their physical and mechanical properties and are a prerequisite for the appearance of such properties in the electrospray coating.

It was found [40,44,45] that the structure of the electrode material strongly affects the composition, structure and properties of the coating (hardness, modulus of elasticity, roughness, coefficient of friction, wear resistance). When using a nano-structured electrode, the carbide phase (Ti, W) C + W_2C content in the coating increases from 60 to 95%, resulting in an increase in hardness, and the friction coefficient decreases from 0.7 to 0.3.

The lack of reliable scientific data on the properties of coatings with amorphous and nanocrystalline structures, the small number of scientific developments in the field of wear-resistant coatings using amorphous and nanostructural materials, as well as the set of thermophysical and physico-mechanical properties of these alloys, make the obtaining of coatings of such structures a complicated but necessary scientific and technological task.

Table 3 gives the recommended ways of surface modification and coating materials to increase durability according to the operating conditions that determine the type of prevailing wear. From the table is visible that much of the recommended materials combine several qualities.

7. CONCLUSIONS

The hardening methods under consideration have both advantages and certain disadvantages. Their use for parts and tools requires both the improvement of specific technological processes, and at the same time to search for new high effective applying materials taking into account the specifics of their behavior in the process of-of transfer onto the substrate and the knowledge of the complex influence of the materials on the properties and morphology of the coatings, together with the peculiarities and the parameters of the ESD and GFS regimes. Therefore, the development of an effective, fairly simples and economical to industrial production materials improving wear resistance remains an urgent scientific and practical task.

Choice of suitable laminating materials for the particular case should be performed in the following sequence: analysis of the material, shape and dimensions of the product; analysis of the working conditions of the product - prevailing wear and its causes; formulation of the requirements for the coating in order to provide the necessary complex of exploitation properties; determination of possible methods to provide the necessary complex of operational characteristics of coatings; analysis of the relation between the morphology, the composition, the structure and wear and tear, operational reliability and durability of the layered surface, choice of highly resistant and friction materials for coatings and process parameters for their deposition.

Factors influencing the properties of the coatings and the durability of the plastered products have been identified and on this basis the basic requirements for the composition, structure and properties of the coatings and the plastering materials are formulated and certain recommended materials for wear-resistant coatings for different operating conditions are justified.

Based on existing scientific and technical literature:

- it has been found that in order to increase the wear resistance of ESD and GFS coatings it is necessary to use composite materials by adding high solid carbides, borides and nitrides of W, Ti, Cr etc. to the used metal alloys in the type and quantities according to the specific operating conditions;
- indicated are compositions of laminating materials specified for different operating conditions.
- these materials should be applied by appropriate regimes according to the chosen method.

ACKNOWLEDGMENT

The present work is based on researches that are funded from the Bulgarian National Science Fund of the Ministry of Education and Science under the project "Research and Development of New Wear - Resistant Coatings Using Compositional and Nano Materials”.

REFERENCES

[1] L. Pawlowski: *The Science and Engineering of Thermal Spray Coatings*, Chichester: John Wiley & Sons, England, p. 656, 2008.
[2] *An Introduction to Thermal Spray*: Brochure, Oerlikon Metco, Winterthur, 2015.
[3] M.A. Belotserkovskiy: Tribotechnical Characteristics of Gas-flame Coatings: Friction and Wear, Vol. 21, No. 5, p. 534, 2000 (in Russian).
[4] *White Paper of ASM,* International Thermal Spray Society. www.tss.asminternational.org.
[5] Broshures: https://www.flamespray.org, https://syscoat.com, http://www.linde-gas.com, https://www.castolin.com,http://remoterm.com/
[6] G.V. Samsonov, A.D. Verkhoturov, G.A. Bovkun, V.S. Sychev: *Electrospark alloying of metal Surfaces*, Kiev, Naukova Dumka, p. 220, 1976 (in Russian).
[7] A.E. Gitlevich, V.V. Mikhailov et al: *Electrospark, alloying of metal surfaces*, Chisinau, Stinitsa, p. 198, 1985, (in Russian).
[8] R.N. Johnson, G.L. Sheldon: Advances in the electrospark deposition coating process, Journal of Vacuum Science & Technology A, Vol. 4, No. 6, pp. 2740-2746, 1986.
[9] R.J. Wood, K.M. Roy: *Surface Engineering for Enhanced Performance against Wear*. Springer -Verlag Wien 2013. Editors: Roy, Manish. Chapter1-Tribology of thermal-sprayed coatings. pp. 1-43.
[10] G. Barsukov, V.V. Barabash, A.Yu. Rodichev, O. Kozhus: Technology of Powder Coatings Application by Gas-flame Spraying Using Oxyhydrogen Flame, Materials Science Forum, Vol. 906, pp. 80-87, 2017 (in Russian).
[11] I. Peichev, M. Kandeva: Characterizing of Composite Coatings Deposited through Gas-thermal Super Sound Stream (HVOF-Process) at Different Technological Regimes. In: Proceedings of the 12th International Conference on Tribology ‘BULTRIB 2012’, Sofia, pp. 187-197, 2012.
[12] J.Davis (ed.): *Handbook of thermal spray technology*, ASM International, Materials Park, OH, pp. 3-13, 2004.
[13] T.G. Peniashki: Types of coatings and Methodsfor their deposition on the machinetools.Some guidelines for selecting suitable materials and methods for coatings. Tribological Journal Bultrib, pp. 258–286, 2011.
[14] T. Penyashki, G. Kostadinov, I. Mortev, E. Dimitrova: Improving the Surface Properties of Steel 210Cr12 by Non-Contact Electrical Spark Deposition with Electrodes Based of WC and TiC. Journal of the Balkan Tribological Association, Vol. 23, No. 1, pp. 69–81, 2017.
[15] V. Nikolenko, A. D.Verkhoturov, N. Syui: A. Generation and study of new electrode materials with self-fluxing additives to improve the efficiency of mechanical electrospark alloying. Surface Engineering and Applied Electrochemistry, Vol. 51, No. 1, pp. 38–45, 2015.
[16] T.G. Penyashki, G.D. Kostadinov: Enhancing durability and resources agricultural machinery using electrospark hardening. Agricultural Engineering (Bulgaria), No. 4-6, pp. 48-55, 2013.
[17] V.N. Gadalov, D.N. Romanenko, I.M. Goryakin, YU.P. Kamyshnikov, V.I. Shkodkin: Local selective application of electrophysical coatings to metalworking tools. Strengthening technologies and coatings. (Uprochnyayushchiye tekhnologii i pokrytiya). No. 4, pp. 33-36, 2008.
[18] E.A. Brown, G.L. Sheldon, A.E. Bayoumi: A parametric study of improving tool life by electrospark deposition. Wear, Vol. 138, Iss. 1–2, pp. 137-151, 1990.
[19] K.R.C. Soma Raju, N.H. Faisal, D.S. Rao, S.V. Joshi, G. Sundararajan: Electro-spark coatings for enhanced performance of twist drills. Surface & Coatings Technology, Vol. 202, pp. 1636, 2008.
[20] V.N. Gadalov, R.E. Abashkin, Yu.V. Boldyrev, E.F. Balabaeva, A.I. Lytkin: Cutting-tool wear and hardening of high-speed steel by local electrospark coating application. Russian Engineering Research, Vol. 29, Iss. 4, p. 419, 2009.
[21] G.A. Bovkun, Z.I. Vladkova, V. Molyar, T. Penyashki, Yu.G. Tkachenko: Research hardening of steels at a local electrospark depostion of metal carbides, Surface Engineering and Aplied Electrochemistry, No. 1, pp. 10-12, 1988 (in Russian).
[22] A.D. Verkhoturov, S.V. Nikolenko: Classification, development and creation of

electrode materials for electrospark alloying, Strengthening technologies and coatings, (Klassifikatsii, razrabotka i sozdanie élektrodnykh materialov dlya élektroiskrovogo legirovaniya), Uprochnyayushtie tekhnologii i pokrytiya, No. 2, pp. 13-22, 2010 (in Russian).

[23] T. Penyashki, G. Kostadinov, I. Mortev, E. Dimitrova: Microstructures and wear properties of WC, TiN, and TiC based cermet coatings deposited on 210Cr12 and 45 carbon steel by contactless electrospark process, Tribological Journal BULTRIB, Vol. 6, pp. 154-167, 2016.

[24] Pl. Petrov: Mechanical Characteristics and Structure of Gas-thermal Coatings form Powders on Ni Base PNKH-10 and PNKH-14 (1050-00 and 1060-00) at Gas-chemical Coating of Fuel Mixture from Propane-Butane and Oxygen. Proceedings of the Union of Scientists, Series ‘Technical Sciences’, pp. 67-71, 2017 (in Bulgarian).

[25] G. Barbezat, A.R. Nicol, A. Sickinger: Abrasion, Erosion and Scuffing Resistance of Carbide and Oxide Ceramic Thermal Sprayed Coatings for Different Applications, Wear, Vol. 162–164 (Part A), p. 529, 1993.

[26] M. Kandeva, I. Peichev, A. Dimitrova: Wear of composite coatings deposited through gasthermal super sound stream (hvof-process), Tribological Journal BULTRIB, Vol. 11, pp. 198-203, 2012.

[27] M.Oksa, E. Turunen, T. Suhonen, T. Varis, S.-P. Hannula: Optimization and characterization of high velocity oxy-fuel sprayed coatings: Techniques, materials and applications. Coatings, Vol. 1, No 1, pp. 17-52, 2011.

[28] V.N. Korenev, V.V. Barabash, A.V. Semenov: The Bonding Strength of Powder Coatings in Gas-flame Spraying with the Hydrogen–Oxygen Flame. Journal Welding International, Vol. 31, No. 4, pp. 333-336, 2017 (in Russian).

[29] V.N. Korenev, V. N. Khromov: Improving the Adhesion Strength of Gas-flame Coatings. In:Advanced Coating Technology: a Collective Monograph (Ed. A. V. Kiricheka). Spectrum Publishing House, Moscow, pp. 85–160, 2012 (in Russian).

[30] D. Alontseva, S. Missevra, A. Russakova: Characteristics of Structure and Properties of Plasma Detonated Ni-Cr and Co-Cr Based Powder Alloys Coatings: Journal of Materials Science and Engineering A 3. (1), pp. 41-49, 2013.

[31] L.M. Demidenko: *High-fire-resistant Composite Coatings*. Metallurgy, Moscow, 1979, p. 216 (in Russian).

[32] J.Schubert, Š. Houdková, M. Kašparová, Z. Česánek: Effect of Co content on the properties of HVOF sprayed coatings based on tungsten carbide. in Proceedings of 21st International Conference on Metallurgy and Materials – Metal 2012, Brno (Czech Republic), 23-25.05.2012, pp. 1086-1091.

[33] A.D Verkhoturov, I.A. Podchernyaeva, L.F.Pryadko, F. F.Egorov: *Electrode materials for electrospark alloying*, M. Nauka, 1988, 224 p. (in Russian)

[34] G.V.Samsonov, A.P.Epik: *Refractory coatings*, M. Metallurgiya, 1973,p. 400, (in Russian).

[35] K.A. Habib, D.L.Cano, C.T. Caudet, J. Bellés, P. Ortells: Influence of Al2O3 Particle Size on Microstructure, Mechanical Properties and Abrasive Wear Behavior of Flame-Sprayed and Remelted NiCrBSi Coatings. Journal of Materials Engineering and Performance, Iss. 4, pp. 1-10, 2017.

[36] M.A. Garrido, A. Rico, M.T. Gómez, J.E. Fernández-Rico, J. Rodríguez: Tribological and Oxidative Behavior of Thermally Sprayed NiCrBSi Coatings, Journal of Thermal Spray Technology, Vol. 26, No. 3, pp.517-529, 2017.

[37] S. Houdková, E. Smazalová, M. Vostřák, J. Schubert: Properties of NiCrBSi Coating, as Sprayed and Remelted by Different Technologies, *Surf. Coat. Technol.*, Vol. 253, pp. 14-26, 2014.

[38] F. Fanicchia, D.A. Axinte, J. Kell, G. Brewster, A.D. Norton: Combustion Flame Spray of CoNiCrAl coatings, Surface and Coatings Technology, Vol. 315, pp. 546-557, 2017. DOI: 10.1016/j.surfcoat.2017.01.070

[39] T. Penyashki, G. Kostadinov, D. Radev, M. Kandeva: Comparative studies of tribological characteristics of carbon steels with gas flame coatings from new multi-component carbide composite materials. oxidation communications, Vol. 42, No. 1, pp. 74–89, 2019.

[40] A.E. Kudryashov, A.Yu. Potanin, D.N. Lebedev, et al: Structure and properties of Cr–Al–Si–B coatings produced by pulsed electrospark deposition on a nickel alloy. Surface & Coatings Technology, Vol. 285, pp. 278–288, 2016.

[41] V.F. Labunets, L.G. Voroshnin, M. V. Kindarchuk: *Wear-resistant Boride Coatings*. Technique, Kiev, 1989, p. 158 (in Russian).

[42] G.V. Samsonov, I. M. Vinitskiy: *Refractory Compounds*. Metallurgy, Moscow, 1976.

[43] T. Penyashki, G. Kostadinov, M. Kandeva: Investigation of the properties of non-tungsten electro-spark coatings on high speed Steel, in Proceedings of BALTTRIB'2017 edited by prof. J. Padgurskase. Published by Aleksandras Stulginskis University.
[44] V.N. Khromov: Studies of wear-resistant electro-spark coatings with nanocrystalline and amorphous structures. Strengthening technologies and coatings, Vol. 72, No. 12, pp. pp. 18–21, 2010.
[45] I.S. Kuznetsov: Electro-sparking treatment with electrodes from amorphous and nano-crystalline alloys of cutting parts Tr. GOSNITI, T. 108, pp. 230–233, 2011.

Serbian Tribology Society

SERBIATRIB '19

16th International Conference on Tribology

Faculty of Engineering University of Kragujevac

Kragujevac, Serbia, 15 – 17 May 2019

SURFACE TEXTURING FOR TRIBOLOGICAL APPLICATIONS: A REVIEW

Aleksandar VENCL[1,2], Lozica IVANOVIĆ[3,*], Blaža STOJANOVIĆ[3], Elena ZADOROZHNAYA[2], Slavica MILADINOVIĆ[3], Petr SVOBODA[4]

[1]University of Belgrade, Faculty of Mechanical Engineering, Belgrade, Serbia
[2]South Ural State University, Chelyabinsk, Russia
[3]Faculty of Engineering, University of Kragujevac, Kragujevac, Serbia
[4]Brno University of Technology, Brno, Czech Republic
*Corresponding author: lozica@kg.ac.rs

Abstract: *Surface texturing is one of the surface modification techniques which deliberately change the texture of the surface, in order to improve, among other things, its tribological performance. This is obtained through different patterns, which can be on micro or nano scale, created on the contact surfaces. The performance of a textured surface depends on the shape, geometry and pattern of the surface texture and the operating condition of the components in contact. There is a number of various techniques for surface texturing, among which laser surface texturing is most often used. The different surface texture shapes, different textured area ratios and patterns, different lubrication regimes with different contact geometries and materials have been subject of theoretical and experimental research for many years. This paper reviews the state-of-the-art of researches that consider various surface texturing for tribological application, as well as its effect on performance enhancement. Conclusions of this paper may provide guidance for optimal design of surface textures in practical engineering applications.*

Keywords: *review, surface texturing, lubrication, friction, wear.*

1. INTRODUCTION

Surface texturing can be defined in several ways. In a broad sense, it can be defined as any process that artificially changes the texture of the surface. In many cases these changes are inspired by nature [1]. Defined like this, surface texturing can be obtained through some coating deposition (adding of the material) or some surface modification (without adding of the material) technique [2]. In the present review, the surface texturing will be defined as "any surface modification process that produce multiple engineered surface features of appropriate shape, geometry and pattern, which are intentionally made in order to improve the performance". It can be performed either as a micro and nano asperities (protrusions) or micro and nano holes (dimples), Fig. 1, with the latter being more popular.

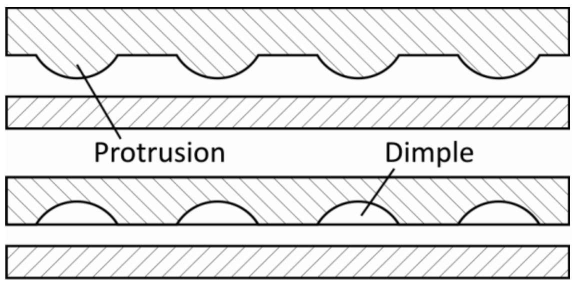

Figure 1. Different principle of intentionally made surface texturing with some surface modification technique

The earliest known commercial application of surface texturing for tribological applications is the honing of the cylinder liner [3]. Surface texturing is also known to be used in magnetic storage devices [4], as well as in MEMS devices [5] for overcoming adhesion and stiction. Surface texture in the automotive applications is mainly applied in reciprocating sliding surfaces and piston/cylinder arrangements [6,7]. This idea is also promoted in mechanical seals and sliding bearings [8-11]. Surface texturing is one of the most effective methods for tool wear reduction and improvement of tool life in the modern machining process, and thus enhancing the final product quality [12]. Biomedicine is the latest field in which surface texturing is implemented. The laser texture presents excellent results for adaptations to the biological performance of biomedical polymers. Improvement of the cellular activity on the implant surface constitutes the primary objective of the surface texture technique in biomedical applications [13].

2. SURFACE TEXTURING TECHNIQUES

The development of advanced engineering materials and precise design requirements limits the use of conventional processing methods, so the nonconventional machining processes, also known as advanced machining processes were developed. A variety of these process is being used in the industry, such as chemical, electrochemical and electro discharge machining, abrasive jet and abrasive water jet machining, ultrasonic machining, laser beam, electron beam, ion beam and plasma beam machining, each of them having their own limitations [14]. Some of these machining techniques are successfully applied in surface texturing for tribological applications. Surface modification techniques used to enhance tribological performance, through surface texturing, covers: removing material technologies, material displacement technologies, and self-forming methods, all being well described and reviewed by Coblas et al. [15].

Various techniques of surface texturing were developed over the years for enhancing tribological performance. The most promising and the most frequently used technique seems to be laser surface texturing. Its principle can be explained as a removal of material by an ablation process, i.e. by an excessive heating, melting and evaporation or sublimation of the substrate material in contact with laser beam [16]. Desired texture geometry can be obtained by utilizing the scanning optical systems so as to position the laser beam on the workpiece along a predefined trajectory. The laser surface texturing owes its effectiveness and efficiency to the laser technology utilised, due to it being rapid and permitting shorter processing times. Furthermore it is eco-friendly and due to its excellent accuracy permits strict control of the shape and size of the micro-dimples, allowing realization of optimum designs. Its ability to control energy density enables the laser to safely process hardened steels, ceramics, and polymers as well as crystalline structures [9,16].

There are also other techniques of surface texturing, and some of them are suitable for mass production, but they usually require large, expensive facilities, can show process-related draw-backs, and are not always suitable for flexible production. One of them is vibrorolling technique recommendable as a substitute for a variety of conventional, environmentally harmful techniques [17]. The vibrorolling principle is based on the transfer of hard indenter shape (pattering) on the work piece surface, by plastic deformation. Other techniques include lithography and anisotropic etching [18], photochemical etching (masking by photolithography followed by chemical etching) [19], photolithography combined with electrolytic etching process [20], focused ion beam milling [21] and abrasive jet machining [22], etc. The frequency of laser surface texturing usage compared to others techniques is presented in Table 1. It also shows the frequency of other research conditions in 40 papers, published in the last 20 years, whose research topic was surface texturing for tribological applications.

Table 1. Review of the research conditions and their representation in the surface texturing for tribological application literature

Research condition		Reference	Total number*
Surface texturing technique	Laser surface texturing	[6], [7], [8], [10], [23], [24], [25], [26], [27], [28], [29], [30], [31], [32], [33], [34], [35], [36], [37], [38], [39], [40], [41]	23
	Other techniques	[18], [19], [20], [21], [22], [42], [43], [44], [45], [46], [47]	11
Type of contact	Conformal (lower kinematic pairs)	[6], [7], [8], [10], [20], [21], [25], [26], [27], [28], [29], [33], [34], [35], [36], [38], [40], [41], [43], [44], [45], [47], [48], [49], [50], [51]	26
	Nonconformal (higher kinematic pairs)	[6], [18], [19], [22], [23], [24], [27], [30], [31], [32], [37], [39], [40], [42], [46], [52], [53]	17
Lubrication regime	Unlubricated conditions	[21], [22], [30], [31], [39], [42]	6
	Boundary and mixed lubrication	[6], [7], [10], [18], [23], [24], [26], [28], [29], [30], [32], [33], [34], [35], [36], [37], [40], [41], [43], [44], [47], [51]	22
	Full fluid-film lubrication	[8], [19], [20], [25], [27], [28], [34], [36], [38], [40], [43], [45], [46], [48], [49], [50], [52], [53]	18
Methodology of research	Theoretical researches and simulations	[8], [45], [48], [49], [50], [51] [52], [53]	8
	Experimental researches	[6], [7], [8], [10], [18], [19], [20], [21], [22], [23], [24], [25], [26], [27], [28], [29], [30], [31], [32], [33], [34], [35], [36], [37], [38], [39], [40], [41], [42], [43], [44], [45], [46], [47]	34

*Total number of references in each group of research conditions differs from 40 because in some references more than one research condition of the same group is investigated. In addition, references with simulations usually do not have the surface texturing technique defined

3. INFLUENCE OF SURFACE TEXTURING ON TRIBOLOGICAL PROPERTIES

A large number of studies have shown that the presence of artificial texturing on the surface of the kinematic pair improves their tribological properties, i.e. decrease the friction and increase the wear resistance. Among these two characteristics, the coefficient of friction is the object of interest in almost all of the studies, while the wear is investigated in only few studies. As already emphasized texturing effects are mainly beneficial, but there are studies which show the increase of coefficient of friction [6,35,43] or wear [18,54]. As an example, shot peening process leading to the creation of surface textures can cause the reduction in fatigue life of rolling/sliding concentrated contacts under mixed lubrication [55]. However, shot peening treatment followed by polishing can increase the film thickness during the start-up add reduce the asperity interactions. Further attempts have been also made to understand the effects of modified surface topography on the fatigue life of heavily loaded concentrated contacts [56].

The analysis of the Table 1 shows that the majority of surface texturing techniques use laser beam, and that most of the studies from Table 1 are experimental. The latter one can be attributed to the complexity of the phenomena and the inability of analytically describing them in many instances. However, it has been shown that the virtual texturing process and simulations [52] and theoretical mathematical models [57] can be considered as a tool for designing textured surfaces. In addition, optimization of testing conditions, such as surface texture geometrical parameters, through the design of experiments (DoE) approach [35] is also used in studies in order to reduce the necessary testing time.

The frequency of conformal (plane contact) or nonconformal (point and line contact) type of contact in reviewed papers is similar, although the conformal type of contact is more frequent (Table 1). Tribological system with nonconformal contact enable reduction of friction due to a fact that initial wear generation allows a transition of lubricated conditions from the high friction boundary lubrication to the lower friction mixed lubrication regime. The above-mentioned phenomenon is beneficial assuming that the potential of accelerated wear is acceptable in that application [11]. The regime of lubrication and the method of surface texturing highly influence the tribological behaviours of textured concentrated contacts [58,59].

A review of surface texturing on various tribological pairs has revealed that most of the studies were conducted under the boundary or mixed lubrication conditions (Table 1). The frequency of full fluid-film lubrication conditions is little bit smaller, while the unlubricated contacts were investigated in only few studies. It was shown that in full fluid-film and mixed lubrication regime, surface textures can serve as storage pockets for lubricant, generating additional micro-hydrodynamic pressure and thus reducing the contact between the surfaces. In addition, wear debris can be trapped in the artificially made dimples, reducing the effect of three-body abrasion, especially under boundary lubrication or in unlubricated conditions [11].

Influence of surface texturing on tribological properties is analysed through the influence of texture shape, texture geometry and texture pattern. It is also important to realise that this influence sometimes is not the same with conformal and nonconformal contacts or with full fluid-film lubricated, mixed or boundary lubricated or unlubricated conditions. The preview of the used texture shapes, their orientations and arrangements (arrays) and other research conditions of the selected experimental literature published in the last 20 years, whose research topic was surface texturing for tribological applications, is presented in Table 2.

3.1 Influence of surface texture shape

The mostly used texture shape is circular dimple, but hemispherical, elliptical, ellipsoidal, triangular, square and rectangular dimples, as well as different grooves are also applied and investigated. Some of them are presented in Figure 2.

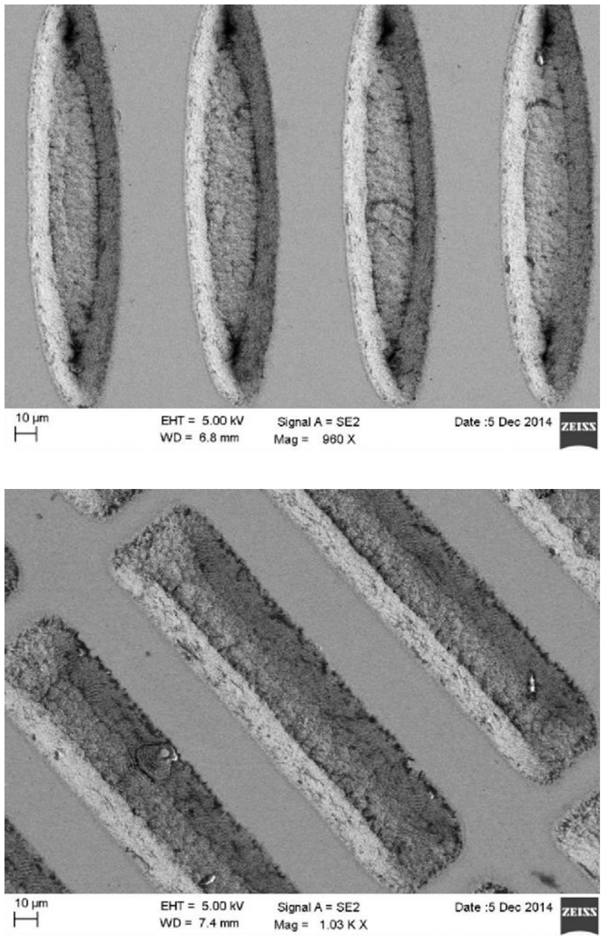

Figure 2. Representation of two different laser surface texture shapes, i.e. elliptical and rectangular dimple; high magnification SEM images [33]

The effect of the texture shapes is relatively complex to investigate, since the shapes should have similar ratio between surface dimensions and depth of the dimple/groove (aspect ratio), as well as similar area under the texture (texture density). For this reason, there are only few papers that review the effect of texture shape on tribological properties in experimental conditions. All of them are in full fluid-film or boundary/mixed lubrication conditions. Qiu and Khonsari [10] tested laser surface textured system with conformal contact and in unidirectional sliding and mainly boundary lubrication conditions.

Table 2. Preview of the selected experimental literature published in the last 20 years, whose research topic was surface texturing for tribological application (references are ordered according to the publication year)

Reference	Year	Surface texturing technique	Textured material (counter-body material)	Texture shape (orientation/array)	Contact type	Type of motion	Lubrication regime (lubricant)
Dumitru et al. [23]	2000	Laser surface texturing	Steel disc (WC-Co ball)	Circular dimples (square array)	Nonconformal (ball-on-disc)	Unidirectional sliding	Boundary and mixed lubrication (lubricating oil)
Wang et al. [25]	2001	Laser surface texturing	SiC disc (SiC ring)	Circular dimples (hexagonal array)	Conformal (ring-on-disc)	Unidirectional sliding	Full fluid-film lubrication (water)
Ryk et al. [6]	2002	Laser surface texturing	Chrome coated steel block (cast iron plate)	Hemispherical dimples	Conformal (block-on-plate)	Reciprocating sliding	Boundary and mixed lubrication (engine oil)
			Nitrided steel piston ring (cast iron cylinder)		Nonconformal (ring-on-cylinder)		
Pettersson and Jacobson [18]	2004	Lithography combined with anisotropic etching	WC/C coated textured silicon plate (bearing steel ball)	Square dimples (longitudinal and 30° inclined)	Nonconformal (ball-on-plate)	Reciprocating sliding	Boundary and mixed lubrication (base oil)
				Grooves (longitudinal and transversal)			
Costa and Hutchings [19]	2007	Lithography combined with chemical etching	Steel plate (aluminium cylinder)	Circular dimples (square array)	Nonconformal (cylinder-on-plate)	Reciprocating sliding	Full fluid-film lubrication (base oil)
				Grooves (longitudinal, inclined and transversal)			
				Chevron dimples (longitudinal and transversal)			
Marchetto et al. [21]	2008	Focused ion beam milling	Silicon plate (flat silicon AFM probe)	Grooves (transversal)	Conformal (pin-on-plate)	Unidirectional sliding	Unlubricated conditions
Yuan et al. [20]	2011	Lithography combined with electrolytic etching	Cast iron plate (cast iron plate)	Grooves (longitudinal, 30°, 45° and 60° inclined and transversal)	Conformal (plate-on-plate)	Reciprocating sliding	Full fluid-film lubrication (engine oil)
Qiu and Khonsari [10]	2011	Laser surface texturing	Hardened stainless steel ring (hardened stainless steel ring)	Circular dimples (square array)	Conformal (plate-on-plate)	Unidirectional sliding	Boundary and mixed lubrication (lubricating oil)
				Elliptical dimples (longitudinal and transversal)			

Table 2. *Continued*

Reference	Year	Surface texturing technique	Textured material (counter-body material)	Texture shape (orientation/array)	Contact type	Type of motion	Lubrication regime (lubricant)
Hu and Hu [26]	2012	Laser surface texturing	Aluminium alloy disc (steel cylindrical pin)	Circular dimples (hexagonal array)	Conformal (pin-on-disc)	Unidirectional sliding	Boundary and mixed lubrication (lubricating oil)
Segu et al. [27]	2013	Laser surface texturing	Steel cylindrical pin (steel disc)	Circular and elliptical (transversal) dimples combination	Conformal (pin-on-disc)	Unidirectional sliding	Full fluid-film lubrication (lubricating oil)
			Steel disc (steel ball)		Nonconformal (ball-on-disc)		
Braun et al. [28]	2014	Laser surface texturing	Steel cylindrical pin (steel disc)	Circular dimples (hexagonal array)	Conformal (pin-on-disc)	Unidirectional sliding	Boundary and mixed lubrication (base oil)
							Full fluid-film lubrication (base oil)
Li et al. [29]	2014	Laser surface texturing	Copper disc (steel cylindrical pin)	Hemispherical dimples (square array)	Conformal (pin-on-disc)	Unidirectional sliding	Boundary and mixed lubrication (lubricating oil)
Wang et al. [30]	2015	Laser surface texturing	Steel plate (steel ball)	Grooves (longitudinal and transversal)	Nonconformal (ball-on-plate)	Reciprocating sliding	Unlubricated conditions
							Boundary and mixed lubrication (lubricating oil)
Mohd Iqbal et al. [31]	2015	Laser surface texturing	Steel disc (steel ball)	Circular dimples (hexagonal array)	Nonconformal (ball-on-disc)	Unidirectional sliding	Unlubricated conditions
Lu et al. [32]	2016	Laser surface texturing	Steel plate (bearing steel roller)	Square dimples (square array)	Nonconformal (cylinder-on-plate)	Reciprocating sliding	Boundary and mixed lubrication (base oil)
Ancona et al. [33]	2017	Laser surface texturing	Steel truncated ball pin (aluminium alloy disc)	Rectangular dimples	Conformal (pin-on-disc)	Unidirectional sliding	Boundary and mixed lubrication (lubricating oil)
				Elliptical dimples			
Schneider at al. [34]	2017	Laser surface texturing	Steel disc (steel cylindrical pin)	Hemispherical dimples (square, hexagonal and random array)	Conformal (pin-on-disc)	Unidirectional sliding	Boundary and mixed lubrication (lubricating oil)
							Full fluid-film lubrication (lubricating oil)
Lenart et al. [22]	2018	Abrasive jet machining	Steel disc (steel ball)	Circular dimples (square array)	Nonconformal (ball-on-disc)	Reciprocating sliding	Unlubricated conditions
			Steel disc (WC ball)				

They investigated the influence of circular and elliptical (longitudinally and transversally oriented) dimples on the coefficient of friction under variable loads and speeds. All dimpled surfaces had texture density of 40 %, and dimples aspect ratio around 0.1. The results show that the longitudinally oriented (same as the sliding direction) elliptical dimples provide a significantly lower coefficient of friction compared to the circular dimple, especially under higher load.

Somehow similar conclusions were obtained by Yu et al. [45]. They investigated the influence of circular, square and elliptical dimples on the coefficient of friction of the system with conformal contact, in reciprocating sliding and full fluid-film lubrication conditions. The texturing method was photoelectrolytic etching, i.e. masking by photolithography followed by electrolytic etching. Mean contact pressure was from 0.5 to 1.0 MPa, and a maximum sliding speed was within a stroke of 0.21 – 2.1 m/s. Lubricant was commercial engine oil. All textures had two variants of texture density, i.e. 2.6 and 10.4 %. It was found that the elliptical dimples provide the lowest coefficient of friction, but in this case the orientation of the elliptical dimples was transversal, i.e. opposite to the sliding direction. The difference of the coefficient of friction values between square dimples and circular dimples is not obvious and it can also be seen that as the test load increases, the differences between all three dimple shapes become smaller. In addition, the influence between texture shapes is noticed only in the variant of texture density of 10.4 %. Samples with texture density of 2.6 %, regardless of the shape of the texture, showed similar coefficient of friction values.

In the study by Costa and Hutchings [19], it was also showed that the shape of the texture has very small influence on the maximum film thickness values in the full fluid-film lubrication conditions. They investigated three different shapes with different orientation, i.e. grooves (longitudinally, inclined and transversally oriented) and circular and chevron (longitudinally and transversally oriented) dimples. The texturing method was photochemical etching, i.e. masking by photolithography followed by chemical etching. Reciprocating sliding tests were carried out in nonconformal (cylinder-on-plate) contact and full fluid-film lubrication conditions. Lubricant was base lubricating oil (without additives), and Hertz contact pressure was from 9 to 24 MPa.

3.2 Influence of surface texture geometry

Texture geometry influence is mainly analysed through the dimensions and texture density, i.e. through two dimensionless parameters:

- aspect ratio $\varepsilon = h_p/2r_p$, where h_p is dimple depth and r_p is dimple radius,
- texture density $S_p = S_t/S$, where S_t is the total textured area and S is the total surface area

There are a large number of studies that investigate the influence of surface texture geometry on tribological properties, so only the experimental studies were reviewed. The majority of them are in full fluid-film or boundary/mixed lubrication conditions. Only two of them were in unlubricated contact conditions, which was insufficient to make some general conclusions.

As far as aspect ratio is concerned, there is agreement in the literature that an optimum can be found around 0.1 [6,10,34], even though there are examples in which aspect ratio influence is dependent on operation conditions. As example, Yuan et al. [20] investigated the influence of grooves depth on the coefficient of friction of the system with conformal contact, in reciprocating sliding and full fluid-film lubrication conditions. The texturing method was lithography combined with electrolytic etching. Three different contact pressures were used, i.e. 0.12, 0.25 and 0.5 MPa, and a maximum sliding speed was within a stroke of 0.21 – 2.1 m/s. Lubricant was commercial engine oil. All specimens were textured with grooves of the same width of 100 mm, and the same texture density of 10 %, but with two different depths (7 and 19 µm). It was found that under low contact pressure, the grooves with the depth of 7 µm show lower coefficient of friction values than those with the depth of 19 µm. On the other hand, under higher contact pressure the relation is opposite, i.e. the grooves with the depth of 19 µm show lower coefficient of friction values than those with the depth of 7 µm.

There are also studies which show that the aspect ratio does not have significant influence on tribological properties. In the previously described study by Yu et al. [45], it was showed that, in conformal contact and full fluid-film lubrication conditions, texture densities in the range from 2.6 to 22.9 % and aspect ratios in the range from 0.02 to 0.08, regardless the shape of the texture (elliptical, square and circular dimples), do not have noticeable influence on the coefficient of friction values. Somehow similar conclusions were obtained by Costa and Hutchings [19], also previously described. Results of their study showed that, in nonconformal contact and full fluid-film lubrication conditions, texture densities in the range from 2 to 24 % and aspect ratios in the range from 0.02 to 0.1, regardless the shape of the texture (grooves, and circular and chevron dimples) or its orientation (longitudinal, inclined and transversal orientation), had very little effect on the coefficient of friction values, as well as on the maximum film thickness values.

Another important parameter whose influence in improving tribological properties is also often analysed is the texture density. Some studies show that the tribological properties are improved as the texture density increase [10,27], while the other show that the influence is opposite [25,26], i.e. that the tribological properties are improved as the texture density decrease. Qiu and Khonsari [10] tested a system with conformal contact and mainly under boundary lubrication conditions. They investigated three texture densities (26, 41 and 58 %) of the circular dimples with an aspect ratio of approximately 0.1, and showed that the lowest coefficient of friction is obtained with texture density of 58 %. Similarly to this, Segu et al. [27] tested a system with conformal contact and mainly under full fluid-film lubrication conditions. They investigated four texture densities (5, 7, 12 and 20 %) of the circular and elliptical dimples combination with aspect ratio of approximately 0.02, and showed that the lowest coefficient of friction is obtained with a texture density of 20 %. On the other hand, Wang et al. [25] tested a system with conformal contact and under full fluid-film lubrication conditions. They investigated four texture densities (2.8, 4.9, 8.7 and 11 %) of the circular dimples with aspect ratio of approximately 0.06, and showed that the lowest coefficient of friction is obtained with a texture density of 2.8 %. Similarly to this, Hu and Hu [26] tested a system with conformal contact and mainly under mixed lubrication conditions. They investigated three texture densities (8.5, 17 and 35 %) of the circular dimples with aspect ratio of approximately 0.3, and showed that the lowest coefficient of friction is obtained with a texture density of 8.5 %.

There are also studies which show that there is always an optimal value of the texture density, regarding its influence on tribological properties. Schneider et al. [34] investigated the system with conformal contact, in unidirectional sliding and under two lubricated conditions (full fluid-film lubrication and mixed lubrication conditions). The texturing method was laser surface texturing. A normal contact pressure of 3 MPa was applied, and a sliding speed was varied from 0.04 to 2 m/s. Lubricant was commercial synthetic lubricating oil. They investigated four texture densities (5, 10, 20 and 30 %) of the hexagonally oriented hemispherical dimples with aspect ratio of 0.1, and showed that the lowest coefficient of friction is obtained with a texture density of 10 %. Similarly to this, Li et al. [29] tested system with conformal contact and under mixed and boundary lubrication conditions. They investigated three texture densities (5, 13 and 35 %) of the hemispherical dimples with aspect ratio of 0.01, and showed that the lowest coefficient of friction is obtained with a texture density of 13 %.

3.3 Influence of surface texture pattern

Texture pattern used in the reviewed papers differ in orientation and in arrangement (array). Orientation is consider in relation to the sliding direction, so we have: longitudinal orientation (same as the sliding direction), transversal orientation (opposite to the sliding direction), and inclined orientation (inclined to the sliding direction). Arrangement is generally: square, hexagonal or random array (Fig. 3). Similarly to the previous two influences, only experimental studies were reviewed.

Pettersson and Jacobson [18] investigated the influence of grooves and square dimples orientation on the coefficient of friction and wear of the system with nonconformal contact, in reciprocating sliding and under mixed lubrication conditions. The texturing method was lithography combined with anisotropic etching. A normal load of 5 N was applied, resulting to a Hertzian pressure of around 680 MPa. Lubricant was base lubricating oil (without additives). The samples that were compared were textured with grooves and square dimples of the same width of 20 µm, depth of 5 µm, and a texture density of 25 %. Grooves were tested in two sliding orientations, i.e. longitudinal and transversal orientation, as well as square dimples, i.e. longitudinal and 30° inclined orientation. It was found that grooves with transversal orientation show better friction and wear behaviour than the grooves with longitudinal orientation, i.e. low and stable coefficient of friction of around 0.05 is achieved, while there was no noticeable wear on textured surface or on the counter-body. Similar behaviour was noticed for the square dimples, i.e. when the square dimples pattern was inclined by 30° from the sliding direction, the coefficient of friction also became very stable and low (around 0.05), while the wear was negligible.

The positive influence of the transversal orientation of the grooves over the longitudinal orientation is also shown in the investigation performed by Wang et al. [30]. They investigated the influence of groove's orientation (longitudinal or transversal) on the coefficient of friction and wear of the system with nonconformal contact, in reciprocating sliding and under two lubricated conditions (unlubricated and mixed lubrication). The texturing method was laser surface texturing. A normal load of 2 N was applied, and a sliding speed was 5 mm/s. Lubricant was commercial synthetic lubricating oil. All samples were textured with grooves of the same width and depth of approximately 0.2 µm. The texture density was approximately 40 %. In both testing conditions (unlubricated and mixed lubrication), it was found that grooves with transversal orientation give lower coefficient of friction values than the grooves with longitudinal orientation. In unlubricated contact conditions, the average coefficient of friction values were 0.34, 0.33 and 0.29 for untextured, longitudinal grooves and transversal grooves, respectively. The average value for the transversal grooves represents a reduction of 14.9 % compared to the untextured surface. In addition, in unlubricated contact conditions, wear of this sample was lower than the wear of other two samples. In mixed lubrication conditions, average coefficient of friction values were 0.13, 0.09 and 0.08 for untextured, longitudinal grooves and transversal grooves, respectively. The average value for the textured surface presents a reduction of 33 % (for longitudinal grooves) or 38 % (for transversal groove) compared to the untextured surface.

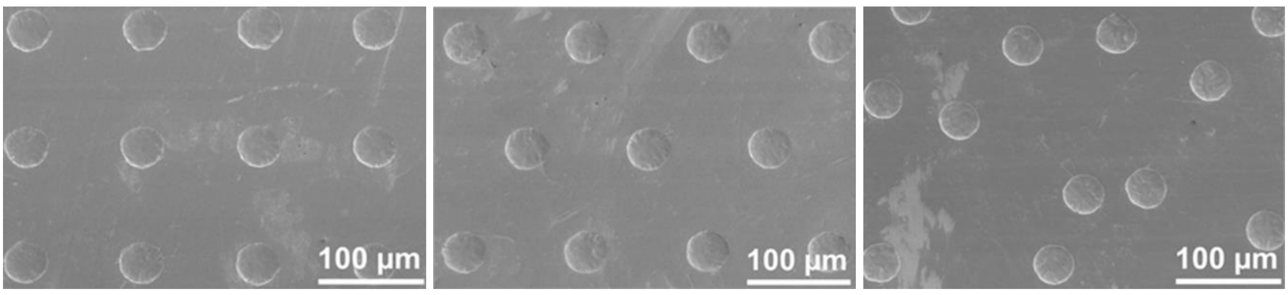

Figure 3. Representation of three different laser surface texture arrangements, i.e. square, hexagonal and random arrangement; SEM images [34]

The effect of orientation is not always so unambiguous and there are cases in which longitudinal grooves are better than transversal grooves, or in which the orientation has no effect on tribological characteristics. Results of the previously described study of Yuan et al. [20] showed that, in conformal contact and full fluid-film lubrication conditions, the transversally oriented grooves provided lower coefficient of friction values than the inclined or longitudinally oriented grooves only at lower loads and for grooves with lower depth of 7 μm. On the other hand, under higher contact pressure, longitudinally oriented grooves with the higher depth of 19 μm, provided lower coefficient of friction values than the inclined or transversally oriented grooves. Similarly to this, results of the previously described study of Qiu and Khonsari [10] showed that, in conformal contact and boundary lubrication conditions, the longitudinally oriented elliptical dimples provided a lower coefficient of friction than the transversally oriented.

On the other hand, Costa and Hutchings [19] showed that, in nonconformal contact and full fluid-film lubrication conditions, orientation (longitudinal, inclined or transversal) of the grooves and chevron dimples did not have noticeable influence on the maximum film thickness values. Nakano et al. [43] also showed that there is no influence of the grooves orientation on the coefficient of friction values. They investigated the influence of grooves of longitudinal and transversal orientation in a system with conformal contact, in reciprocating sliding under two lubricated conditions (full fluid-film lubrication and mixed lubrication). The texturing methods were milling and shot blasting combined with photolithography. Two different contact pressures was used, i.e. 1 and 6 MPa, and average sliding speed was within a range of 0.08 – 1 m/s. Lubricant was commercial lubricating oil. Two types of grooves were textured. The first group was grooves of 500 μm width, 45 – 50 μm depth and texture density of 50 %, and the second group was grooves of 60 μm width, 6 – 10 μm depth and texture density of approximately 67 %.

Similarly to the orientation influence, the different arrangements can also have some influence on tribological properties or that influence can be rather negligible. As an example, Schneider et al. [34], in the previously described study, investigated the influence of hemispherical dimples arrangement (square, hexagonal and random) on the coefficient of friction of the system with conformal contact, in unidirectional sliding and under two lubricated conditions (full fluid-film lubrication and mixed lubrication). The dimples aspect ratio was 0.1 and texture density was 10 %. It was shown that, among the dimple arrangements tested, the hexagonal one resulted in the largest reduction in coefficient of friction values compared to the untextured surface. The other two arrangements (square and random) show similar coefficient of friction values. On the other hand, Nakano et al. [43], in the previously described study, showed that there is no difference between square and hexagonal arrangements of the circular dimples. Dimples had diameter of 60 μm, depth of 6 – 10 μm and texture density of approximately 35 %.

4. CONCLUSIONS

Surface texturing is widely used in recent years in the process of improving the tribological properties of materials. This paper reviews the state-of-the-art of researches that consider various surface texturing for tribological applications, as well as its effect on performance enhancement. The most frequently used technique of surface texturing for enhancing tribological performance is laser surface texturing, and the majority of the researches were experimental.

Influence of surface texturing on tribological properties in most cases is analysed through the influence of texture shape, texture geometry and texture pattern in various research conditions, such as type of contact (conformal and nonconformal), lubrication regime (full fluid-film lubricated, mixed or boundary lubricated or unlubricated), normal load, sliding speed, temperature, lubricant type and viscosity, etc.

It was shown that in full fluid-film and mixed lubrication regime, surface textures can serve as storage pockets for lubricant, generating additional micro-hydrodynamic pressure and thus reducing the contact between the surfaces. On the other hand, under boundary lubrication or in unlubricated conditions, wear debris can be trapped in the artificially made dimples, reducing the effect of three-body abrasion.

Surface texture shape can have a significant influence on tribological properties, but there are also situations in which texture shape does not have any influence. Similar conclusions can be made for the influence of surface texture geometry and texture pattern. Therefore, it is evident that in many cases the surface texturing benefits may be better utilised when the design of surface texturing is optimised and applied to specific contact pairs. Design of experiments (DoE) approach offer such a possibility to optimise the testing condition and to reduce the necessary testing time.

ACKNOWLEDGEMENT

This work has been performed as a part of activities within the projects TR 35033, TR 34028 and TR 35021. These projects are supported by the Republic of Serbia, Ministry of Education, Science and Technological Development, whose financial help is gratefully acknowledged. Elena Zadorozhnaya acknowledges the project financially supported by the Ministry of Education and Science of the Russian Federation (grant No 9.7881.2017/8.9). Petr Svoboda acknowledges the project FSI-S-17-4415, financially supported by the Ministry of Education, Youth and Sports of Czech Republic. Collaboration through the CEEPUS network CIII-BG-0703 is also acknowledged.

REFERENCES

[1] L. Ivanović, A. Vencl, B. Stojanović, B. Marković: Biomimetics design for tribological applications, Tribology in Industry, Vol. 40, No. 3, pp. 448-456, 2018.

[2] M. Kandeva-Ivanova, A. Vencl, D. Karastoyanov: *Advanced Tribological Coatings for Heavy-Duty Applications: Case Studies*, Prof. Marin Drinov Publishing House of Bulgarian Academy of Sciences, Sofia, 2016.

[3] E. Willis: Surface finish in relation to cylinder liners, Wear, Vol. 109, No. 1-4, pp. 351-366, 1986.

[4] U.P. Hausmann, P. Joerges, J. Heinzl, F.E. Talke: Nano-texturing of magnetic recording sliders via laser ablation, Microsystem Technologies, Vol. 15, No. 10-11, pp. 1747-1751, 2009.

[5] K. Komvopoulos: Adhesion and friction forces in microelectromechanical systems: Mechanisms, measurement, surface modification techniques, and adhesion theory, Journal of Adhesion Science and Technology, Vol. 17, No. 4, pp. 477-517, 2003.

[6] G. Ryk, Y. Kligerman, I. Etsion: Experimental investigation of laser surface texturing for reciprocating automotive components, Tribology Transactions, Vol. 45, No. 4, pp. 444-449, 2002.

[7] G. Ryk, Y. Kligerman, I. Etsion, A. Shinkarenko: Experimental investigation of partial laser surface texturing for piston-ring friction reduction, Tribology Transactions, Vol. 48, No. 4, pp. 583-588, 2005.

[8] I. Etsion, Y. Kligerman, G. Halperin: Analytical and experimental investigation of laser-textured mechanical seal faces, Tribology Transactions, Vol. 42, No. 3, pp. 511-516, 1999.

[9] I. Etsion: State of the art in laser surface texturing, Journal of Tribology, Vol. 127, No. 1, pp. 248-253, 2005.

[10] Y. Qiu, M.M. Khonsari: Experimental investigation of tribological performance of laser textured stainless steel rings, Tribology International, Vol. 44, No. 5, pp. 635-644, 2011.

[11] T. Ibatan, M.S. Uddin, M.A.K.Chowdhury: Recent development on surface texturing in enhancing tribological performance of bearing sliders, Surface and Coatings Technology, Vol. 272, pp. 102-120, 2015.

[12] P. Šugár, J. Šugárová, M. Frnčík: Laser surface texturing of tool steel: Textured surfaces quality evaluation, Open Engineering, Vol. 6, No. 1, pp. 90-97, 2016.

[13] A. Riveiro, A.L.B. Maçon, J. del Val, R. Comesaña, J. Pou: Laser surface texturing of polymers for biomedical applications, Frontiers in Physics, Vol. 6, Paper 16, 2018.

[14] M.J. Madou: *Fundamentals of Microfabrication and Nanotechnology, Volume II*, CRC Press, Boca Raton, 2011.

[15] D.G. Coblas, A. Fatu, A. Maoui, M. Hajjam: Manufacturing textured surfaces: State of art

and recent developments, Proceedings of the Institution of Mechanical Engineers, Part J: Journal of Engineering Tribology, Vol. 229, No. 1, pp. 3-29, 2015.
[16] G. Dumitru: Surface texturing by laser ablation, in: Q.J. Wang, Y.-W. Chung (Eds.): *Encyclopedia of Tribology*, Springer, New York, pp. 3498-3505, 2013.
[17] V.P. Bulatov, V.A. Krasny, Y.G. Schneider: Basics of machining methods to yield wear- and fretting-resistive surfaces, having regular roughness patterns, Wear, Vol. 208, No. 1-2, pp. 132-137, 1997.
[18] U. Pettersson, S. Jacobson: Friction and wear properties of micro textured DLC coated surfaces in boundary lubricated sliding, Tribology Letters, Vol. 17, No. 3, pp. 553-559, 2004.
[19] H.L. Costa, I.M. Hutchings: Hydrodynamic lubrication of textured steel surfaces under reciprocating sliding conditions, Tribology International, Vol. 40, No. 8, pp. 1227-1238, 2007.
[20] S. Yuan, W. Huang, X. Wang: Orientation effects of micro-grooves on sliding surfaces, Tribology International, Vol. 44, No. 9, pp. 1047-1054, 2011.
[21] D. Marchetto, A. Rota, L. Calabri, G.C. Gazzadi, C. Menozzi, S. Valeri: AFM investigation of tribological properties of nano-patterned silicon surface, Wear, Vol. 265, No. 5-6, pp. 577-582, 2008.
[22] A. Lenart, P. Pawlus, S. Wos, A. Dzierwa: The effect of surface texturing on dry gross fretting, Lubricants, Vol. 6, No. 4, Paper 92, 2018.
[23] G. Dumitru, V. Romano, H.P. Weber, H. Haefke, Y. Gerbig, E. Pflüger: Laser microstructuring of steel surfaces for tribological applications, Applied Physics A, Vol. 70, No. 4, pp. 485-487, 2000.
[24] T.V. Kononenko, S.V. Garnov, S.M. Pimenov, V.I. Konov, V. Romano, B. Borsos, H.P. Weber: Laser ablation and micropatterning of thin TiN coatings, Applied Physics A, Vol. 71, No. 6, pp. 627-631, 2000.
[25] X. Wang, K. Kato, K. Adachi, K. Aizawa: The effect of laser texturing of SiC surface on the critical load for the transition of water lubrication mode from hydrodynamic to mixed, Tribology International, Vol. 34, No. 10, pp. 703-711, 2001.
[26] T. Hu, L. Hu: The study of tribological properties of laser-textured surface of 2024 aluminium alloy under boundary lubrication, Lubrication Science, Vol. 24, No. 2, pp. 84-93, 2012.
[27] D.Z. Segu, S.G. Choi, J.h. Choi, S.S. Kim: The effect of multi-scale laser textured surface on lubrication regime, Applied Surface Science, Vol. 270, pp. 58-63, 2013.
[28] D. Braun, C. Greiner, J. Schneider, P. Gumbsch: Efficiency of laser surface texturing in the reduction of friction under mixed lubrication, Tribology International, Vol. 77, pp. 142-147, 2014.
[29] K. Li, Z. Yao, Y. Hu, W. Gu: Friction and wear performance of laser peen textured surface under starved lubrication, Tribology International, Vol. 77, pp. 97-105, 2014.
[30] Z. Wang, Q. Zhao, C. Wang: Reduction of friction of metals using laser-induced periodic surface nanostructures, Micromachines, Vol. 6, No. 11, pp. 1606-1616, 2015.
[31] K.Y. Mohd Iqbal, D.Z. Segu, H. Pyung, J.H. Kim, S.S. Kim: Surface texturing for low friction mechanical components, Journal of the Korean Society of Tribologists and Lubrication Engineers, Vol. 31, No. 6, pp. 287-293, 2015.
[32] P. Lu, R.J.K. Wood, M.G. Gee, L. Wang, W. Pfleging: The friction reducing effect of square-shaped surface textures under lubricated line-contacts – An experimental study, Lubricants, Vol. 4, No. 3, Paper 26, 2016.
[33] A. Ancona, G.S. Joshi, A. Volpe, M. Scaraggi, P.M. Lugarà, G. Carbone: Non-uniform laser surface texturing of an un-tapered square pad for tribological applications, Lubricants, Vol. 5, No. 4, Paper 41, 2017.
[34] J. Schneider, D. Braun, C. Greiner: Laser textured surfaces for mixed lubrication: Influence of aspect ratio, textured area and dimple arrangement, Lubricants, Vol. 5, No. 3, Paper 32, 2017.
[35] B. Meylan, F. Saeidi, K. Wasmer: Effect of surface texturing on cast iron reciprocating against steel under cyclic loading in boundary and mixed lubrication conditions, Lubricants, Vol. 6, No. 1, Paper 2, 2018.
[36] Kovalchenko, O. Ajayi, A. Erdemir, G. Fenske, I. Etsion: The effect of laser surface texturing on transitions in lubrication regimes during unidirectional sliding contact, Tribology International, Vol. 38, No. 3, pp. 219-225, 2005.
[37] P. Andersson, J. Koskinen, S. Varjus, Y. Gerbig, H. Haefke, S. Georgiou, B. Zhmud, W. Buss: Microlubrication effect by laser-textured steel surfaces, Wear, Vol. 262, No. 3-4, pp. 369-379, 2007.
[38] L.M. Vilhena, B. Podgornik, J. Vižintin, J. Možina: Influence of texturing parameters and contact conditions on tribological behaviour of

laser textured surfaces, Meccanica, Vol. 46, No. 3, pp. 567-575, 2011.
[39] D. Bhaduri, A. Batal, S.S. Dimov, Z. Zhang, H. Dong, M. Fallqvist, R. M'Saoubi: On design and tribological behaviour of laser textured surfaces, Procedia CIRP, Vol. 60, pp. 20-25, 2017.
[40] Š. Houdková, P. Šperka, M. Repka, J. Martan, D. Moskal: Shifted laser surface texturing for bearings applications, Journal of Physics: Conference Series, Vol. 843, Paper 012076, 2017.
[41] H. Kasem, O. Stav, P. Grützmacher, C. Gachot: Effect of low depth surface texturing on friction reduction in lubricated sliding contact, Lubricants, Vol. 6, No. 3, Paper 62, 2018.
[42] E.-S. Yoon, R.A. Singh, H. Kong, B. Kim, D.-H. Kim, H.E. Jeong, K.Y. Suh: Tribological properties of bio-mimetic nano-patterned polymeric surfaces on silicon wafer, Tribology Letters, Vol. 21, No. 1, pp. 31-37, 2006.
[43] M. Nakano, A. Korenaga, A. Korenaga, K. Miyake, T. Murakami, Y. Ando, H. Usami, S. Sasaki: Applying micro-texture to cast iron surfaces to reduce the friction coefficient under lubricated conditions, Tribology Letters, Vol. 28, No. 2, pp. 131-137, 2007.
[44] M. Nakano, K. Miyake, A. Korenaga, S. Sasaki, Y. Ando: Tribological properties of patterned NiFe-covered Si surfaces, Tribology Letters, Vol. 35, No. 2, pp. 133-139, 2009.
[45] H. Yu, H. Deng, W. Huang, X. Wang: The effect of dimple shapes on friction of parallel surfaces, Proceedings of the Institution of Mechanical Engineers, Part J: Journal of Engineering Tribology, Vol. 225, No. 8, pp. 693-703, 2011.
[46] A. Zavos, P.G. Nikolakopoulos: Tribological characterization of smooth and artificially textured coated surfaces using block-on-ring tests, FME Transactions, Vol. 43, No. 3, pp. 191-197, 2015.
[47] M.H. Sulaiman, P. Christiansen, N. Bay: The influence of tool texture on friction and lubrication in strip reduction testing, Lubricants, Vol. 5, No. 1, Paper 3, 2017.
[48] M. Qiu, A. Delic, B. Raeymaekers: The effect of texture shape on the load-carrying capacity of gas-lubricated parallel slider bearings, Tribology Letters, Vol. 48, No. 3, pp. 315-327, 2012.
[49] H. Yu, X. Wang, F. Zhou: Geometric shape effects of surface texture on the generation of hydrodynamic pressure between conformal contacting surfaces, Tribology Letters, Vol. 37, No. 2, pp. 123-130, 2010.
[50] K. Li, D. Jing, J. Hu, X. Ding, Z. Yao: Numerical investigation of the tribological performance of micro-dimple textured surfaces under hydrodynamic lubrication, Beilstein Journal of Nanotechnology, Vol. 8, pp. 2324-2338, 2017.
[51] D. Bijani, E.L. Deladi, A. Akchurin, M.B. De Rooij, D.J. Schipper: The influence of surface texturing on the frictional behaviour of parallel sliding lubricated surfaces under conditions of mixed lubrication, Lubricants, Vol. 6, No. 4, Paper 91, 2018.
[52] N. Ren, T. Nanbu, Y. Yasuda, D. Zhu, Q. Wang: Micro textures in concentrated-conformal-contact lubrication: Effect of distribution patterns, Tribology Letters, Vol. 28, No. 3, pp. 275-285, 2007.
[53] Y. Ohue, H. Tanaka: Effect of surface texturing on lubricating condition under point contact using numerical analysis, Engineering, Vol. 5, No. 4, pp. 379-385, 2013.
[54] H. Yu, W. Huang, X. Wang: Dimple patterns design for different circumstances, Lubrication Science, Vol. 25, No. 2, pp. 67-78, 2013.
[55] M. Vrbka, I. Křupka, P. Svoboda, P. Šperka, T. Návrat, M. Hartl, J. Nohava: Effect of shot peening on rolling contact fatigue and lubricant film thickness within mixed lubricated non-conformal rolling/sliding contacts, Tribology International, Vol. 44, No. 12, pp. 1726-1735, 2011.
[56] M. Vrbka, I. Křupka, O. Šamánek, P. Svoboda, M. Vaverka, M. Hartl: Effect of surface texturing on lubrication film formation and rolling contact fatigue within mixed lubricated non-conformal contacts, Meccanica, Vol. 46, No. 3, pp. 491-498, 2011.
[57] Yu. Rozhdestvensky, E. Zadorozhnaya, S. Cherneyko: Mathematical model for calculating thrust bearing with laser texturing of bearing surface, Bulletin of the South Ural State University, Series: Mathematical Modelling, Programming & Computer Software, Vol. 8, No. 1, pp. 5-24, 2015 in Russian.
[58] I. Krupka, M. Hartl, P. Svoboda: Effects of surface topography on lubrication film formation within elastohydrodynamic and mixed lubricated non-conformal contacts, Proceedings of the Institution of Mechanical Engineers, Part J: Journal of Engineering Tribology, Vol. 224, No. 8, pp. 713-722, 2010.
[59] I. Krupka, P. Svoboda, M. Hartl: Effect of surface topography on mixed lubrication film formation during start up under rolling/sliding conditions, Tribology International, Vol. 43, No. 5-6, pp. 1035-1042, 2010.

Serbian Tribology Society

SERBIATRIB '19

16th International Conference on Tribology

Faculty of Engineering
University of Kragujevac

Kragujevac, Serbia, 15 – 17 May 2019

TRIBOLOGICAL AND QUICK THERMAL EVALUATION OF PROTECTIVE COATINGS FOR AEROSPACE AND METALLURGY

Victor MANOLIU[1*], Sorin DIMITRIU[2], Mihail BOTAN[1], Gheorghe IONESCU[1], Radu Robert PITICESCU[3], George Catalin CRISTEA[1], Alina DRAGOMIRESCU[1]

[1]National Institute for Aerospace Research "Elie Carafoli" - INCAS, Bucharest, Romania,
[2]Academy of Romanian Scientists, Bucharest, Romania
[3]National Research & Development Institute for Non-Ferrous and Rare Metals - IMNR, Bucharest, Romania
*Corresponding author: manoliu.victor@incas.ro

Abstract: *Hot parts of turbo engines as well as those working in extreme conditions in the metallurgical industry are subject to complex loads, leading to wear factors that sometimes work together: temperature, thermal shock, erosion, corrosion, sliding friction, etc.*

The paper presents the types of protective structures developed, techniques used, methods of testing, investigation and results.

Protective materials used are from the class of ceramics such as M/MeCrAlY/ $ZrO_2 \cdot Y_2O_3$ (CaO, MgO, CeO), Me/NiCrAlY/Y_2O_3-Yb_2O_3-GdO_3-Nd_2O_3-ZrO_2/ZrB_2 and other variants, as well as the type of complex alloys associated with Cu support. The techniques used for creating protection layers are EB-PVD coating or WIG welding.

By tribological or extreme thermal testing on a facility design and made within INCAS, it was verified experimentally the basic properties of the protected structures.

Stand tests made on real components, successfully validate the materials and technology solutions we designed.

Keywords: *Tribology, coating, EB-PVD, high temperature, multiplex structure*

1. INTRODUCTION

The protection systems imposed as a solution to increase the life of some components from aircraft due to the limitation imposed by the thermo-mechanical properties of the materials but as well as a necessity in the other related fields. The effects which appear further to the degradations as corrosion at high temperatures, oxidation, erosion with pyrolyzed particles, wear, thermal degradation by overheating, and thermal fatigue, which are known further to the functional conditions can be minimize by protection coatings. The protection ceramic layers, thermal barrier coatings (TBC) are used both in aero spatial industry and in the machine building industry, metallurgy, power systems and electronics.

For aerospace industry two types of protection systems are used: TBC and FGM (functionally graded materials). Thermal

barrier coatings are thin layers of ceramic composites based on Zr, Al, Ti, B, Gd, etc. deposited on a metallic support [1].
So, a system of thermal barrier layers is formed from a high alloy metallic support resistant at temperature, a bonding layer an oxide layer - TGO (thermally grown oxide) and an external thermal resistant layer. Together the TBC and metallic support form a complex system of materials [3].

For metallurgical industry a protection system associated to some extreme stressed parts as tuyere from steel plants is formed from a metallic support, usually electrolytic cooper and a complex alloy based on Ni and Co which are deposited by an electric welding technology in protective atmosphere, argon inert gas – WIG (wolfram inert gas) [4].

The paper also shows, the conceive method and the installation made by authors to evidence the behaviour of the multiplex protective structures against the most perturbing wear factor – thermal shock.

The wear factors associated to the tuyere are: temperatures > 1000° C, quick thermal shock, erosion, hot corrosion, and metal liquid contact.

2. MATERIALS AND OBTAINING METHOD

2.1 Materials

The materials used for hot parts of aero engines are:

1. Duplex layers - $MeCrAlY/ZrO_2 20\%Y_2O_3$
2. Triplex FGM type
3. Triplex layers type: $MeCrAlY/MeCrAlY 90\% + Al_2O_3\ 10\%/ ZrO_2Y_2O_3$
4. $NiCoCrAlY/ Al_2O_3 /ZrO_2Y_2O_3$
5. $NiCoCrAlY/ Al_2O_3 +ZrO_2Y_2O_3/ ZrO_2Y_2O_3$
6. $NiCoCrAlY/ZrO_2Y_2O_3$ Nano
7. Duplex $NiCoCrAlY/ZrO_2Y_2O_3\ CeO_2$, $NiCoCrAlY/ ZrO_2Y_2O_3\ TiO_2$
8. $Me/NiCrAlY/Y_2O_3$-Yb_2O_3-GdO_3-Nd_2O_3-ZrO_2/ZrB_2 [5,6]

The materials used for the experimental program of the protective coatings are complex alloys:

- Ni, Cr, Si, B, Fe
- Ni, Cr, Si, B, Mo [7]

2.2 Obtaining method

The methods used in the case of the thermal barrier layers resistant at wear for the hot parts of aircraft are:

- Air plasma spray (APS)
- Non-conventional methods: PVD – Physical Vapor Deposition; cathodic deposited pulverization (sputtering)
- Wolfram inert gas equipment - WIG

3. SPECIMEN

In figures 1, 2 and 3 are presented, for aircraft industry the specimen support (fig. 1), the specimen no.9 - $NiCrAlY/Al_2O_3 + ZrO_2Y_2O_3$ before being tested (fig. 2) and the same specimen after being tested at 800° C (fig. 3). [5,6,7,8].

Figure 1. Specimen support for aircraft industry

Figure 2. Specimen for aircraft industry before being tested – C9 - $NiCrAlY/Al_2O_3 + ZrO_2Y_2O_3$

Figure 3. Specimen C9 - $NiCrAlY/Al_2O_3$+ $ZrO_2Y_2O_3$ for aircraft industry after being tested at 800°C

In figures 4, 5 and 6 are presented, the specimen support (fig. 4) for the metallurgical industry, the specimen Cu/Casto TIG (cooper and silver alloy) before being tested (fig. 5) and the same specimen after being tested at T=1000° C (fig. 6) [4,6].

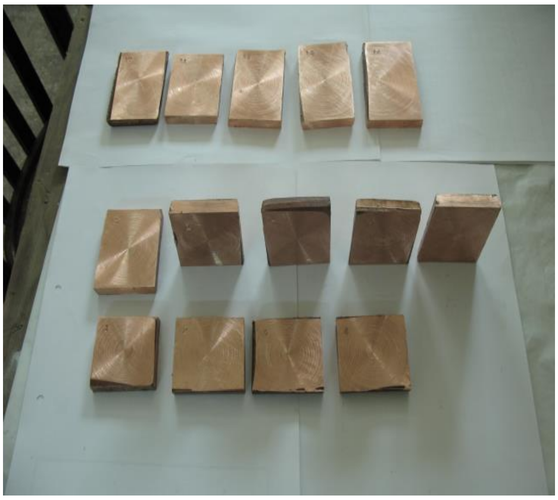

Figure 4. Specimen support for metallurgical industry

Figure 5. Specimen for metallurgical industry before being tested - Cu/Casto TIG (cooper and silver alloy x3)

4. TESTS

4.1. Thermal shock test

For aircraft industry the main tests are the quick thermal shock tests [2].

The main parameters of the QTS-2 installation, conceived, designed and manufactured by INCAS are:

- heating temperature 1300°C
- heat up thermal shock 10 s
- dwell time – about 300 s
- cooling time – 60 s
- max cooling air pressure 9 bar
- cycle duration – 6 minutes

Figure 6 shows the QTS-2 – quick thermal shock installation and figure 7 shows a graphic of a test at 1200° C [3,8].

Figure 6. Quick thermal shock installation – Patent number 127339

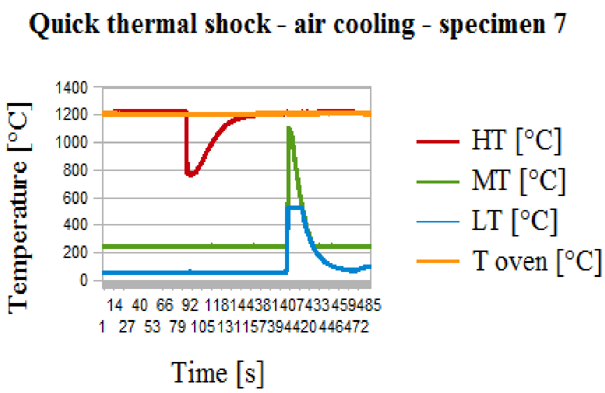

Figure 7. Quick thermal shock test graphics – heating at 1200° C, air cooling

4.2. Tribological tests

Tribological tests were performed under dry conditions using block on ring installation. For the ring we used the bearing sleeve of the Timken A4138 series. The steel block is provided with a nimonic support coated with a bonding layer (NiCrAlY) a ceramic oxide layer (Y_2O_3-Yb_2O_3-GbO_3-Nd_2O_3-ZrO_2) and an external ZrB2 layer. The tests were performed with universal tribometer CETR UMT-3 Bruker.

In Figure 8 is presented the Universal tribometer CETR-UMT-3 Bruker bloc on ring module.

Figure 8. Universal tribometer CETR-UMT-3 Bruker bloc on ring module

The testing method as per ASTM G77-98 standard allows the determination of the sliding wear for different materials with block on ring module. The test result is measured in volume diminution in mm³ both for block and ring. The collecting data are: F_x – friction force; F_z – normal force; T – testing time; Z_1 – the vertical position to determine the depth of wear, COF – friction coefficient.

The study was performed on a ceramic powder based on zirconia, used as TBC and sprayed on nimonic metallic support.

In Table 1 are presented the parameters used in the tests.

Table 1. Testing parameters used

Loading force, F [N]	Sliding length, L [m]	Sliding speed [m/s]	Speed [rot/min]	Testing time [s]
10	1000	0.25	136.42	3999.96
		0.50	272.84	2000.04
		0.75	409.26	1333.32

In Figure 9 is presented the COF variation of three speeds.

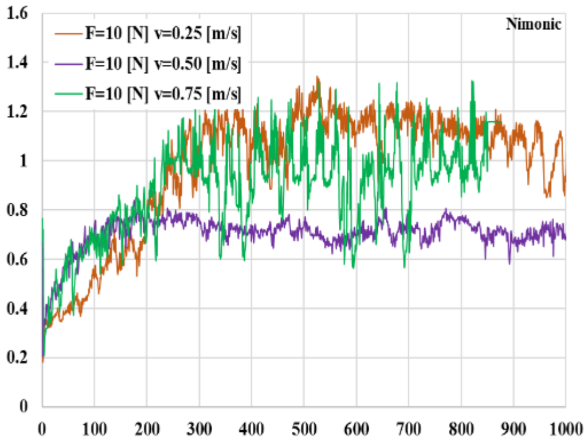

Figure 9. COF variation of three speeds

For the three speeds tested the graphic of the friction coefficient presents a slight decrease in the incipient stage, about 1% of the sliding length, after that an increase of the friction coefficient and then the stabilization of the value at the end of the test.

In figure 10 is presented COF variation of the specimen coated with NiCrAlY/Y_2O_3-Yb_2O_3-GbO_3-Nd_2O_3-ZrO_2/ ZrB_2.

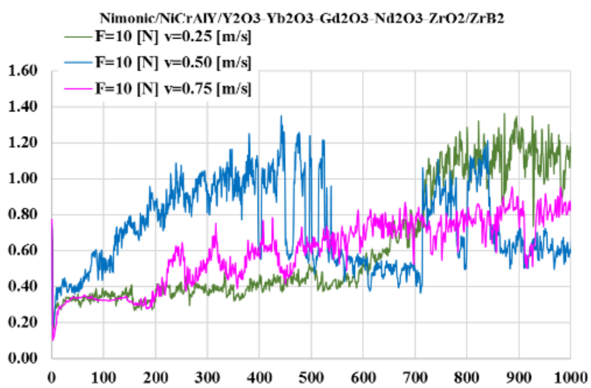

Figure 10. Friction coefficient variation for the tested specimens - Nimonic coated with NiCrAlY/ Y_2O_3-Yb_2O_3-GbO_3-Nd_2O_3-ZrO_2/ ZrB_2

At the minimum testing speed, the graphic of the friction coefficient shows a stable wear at the beginning, from 0 to 600 m and an increase for the rest of the test up to 1.3.

Taking into account the parameters of this study (sliding length and loading force) and the recent studies of the wear parameters, the following mathematical expression for wear rate is:

$$Wm = \frac{\Delta m(mg)}{\quad} \qquad (1)$$

Where:

- Δm [mg] loss of mass after testing,
- F [N] loading force,
- L [m] sliding length.

Table 2. Mass loss of the specimen with and without coatings

Materials	Sliding speed [m/s]	Initial mass [g]	Final mass [g]	Mass loss, Δm [mg]
NIMONIC (without coating)	0.25	9.1652	9.1644	0.8
	0.50	10.2081	10.2071	1.0
	0.75	10.0719	10.0712	0.7
NIMONIC + NiCrAlY/ Y_2O_3-Yb_2O_3-GbO_3-Nd_2O_3-ZrO_2/ ZrB_2	0.25	9.0401	9.0390	1.1
	0.50	9.0179	9.0176	0.3
	0.75	9.0876	9.0868	0.8

5. REAL PARTS

In figures 11 and 14 are presented a burning chamber for an aircraft engine before and after coating with duplex ceramic layers.

Figure 11. Part for aircraft industry - burning chamber before coating

Figure 12. Burning chamber after coating

In figures 13 and 14 are presented a tuyere for metallurgical industry before and after coating with special alloy based on Ni and Cr.

Figure 13. Part for metallurgical industry – tuyere before coating

Figure 14. Tuyere after coating

6. CONCLUSIONS

- Some aimed parts from aeronautics (hot parts of turbo engines) and metallurgy (tuyere, lance tip) presents similitudes of the wear factors - high temperatures, thermal shock, erosion, corrosion, etc.
- The support materials of the aimed parts are different (super alloys for turbo engines and electrolytic copper for tuyere) and as consequence specific solutions for the protective layers are imposed -

ceramic multilayer for turbo engines and complex alloys from compositional point of view for the tuyeres.

- The quick thermal shock test is fundamental to establish the ranking of the protective elaborated solutions.
- Quick thermal shock installation (and the associated method), conceived and achieved by INCAS is reliable, versatile, function in semiautomatic regime and can display all the parameters of the test in real time - oven temperature, temperature of the specimen surface inside and outside of the oven, air cooling pressure, heating time, cooling time, etc.
- The tuyeres with selecting protection present a superior endurance in function with 10-15% in relation to those without protection.

REFERENCES

[1] E. Adelpour: Thermal Barrier Coating for Gas Turbine Engine, NASA/TM—1999-209453, October 1999 39/12, pp. 28-31, 1987.

[2] A. Bolcavage, A. Feuerstein, J. Foster, P. Moore: Thermal Shock Testing of Thermal Barrier Coating/Bondcoat Systems, in: *Journal of Materials Engineering and Performance*, Vol. 13, No. 4, pp. 389–397, August 2004.

[3] V. Manoliu, N. Constantin, Gh. Ionescu, A. Stefan: Protective ceramic coating for aircraft engines, in: *Reliability and Diagnostics of Transport Structures and Means 2002*, Pardubice - Czech Republic, 26-27 09. 2002.

[4] Gh. Ionescu: Shear testing up to 1000° C to determine the adherence between layers of nickel complex alloys and copper support, in: *European Union Research Project ARI HPRI* - CT -2002-00185.

[5] G. Cosmeleata, M. Branzei, V. Manoliu, A. Stefan: Plasma sprayed thermal barrier coatings, in: *International Conference EUROMAT 2003*, Geneva 1-5 09. 2003.

[6] V. Manoliu, G. Cosmeleata, A. Stefan, Gh. Ionescu: Multilayered ceramics within the cogenerate system in the power industry, in: *6 International Symposium of Croatian Metallurgical Society SHMD’2004*, Šibenik, Solaris Holiday Resort, Croatia. 20-24. 06. 2004.

[7] V. Manoliu, A. Stefan, S. Gaman, G. Cosmeleata. I. Ivan: Multifunctional protection in metallurgy, in: *8 International Symposium of Croatian Metallurgical Society SHMD’ 2008*, Šibenik, Croatia, 2008.

[8] S. Dumitriu, V. Manoliu, Gh. Ionescu, A. Stefan, M. Botan, A. Dragomirescu: Triplex coatings in extreme thermal conditions, in: *23 International Conference on materials and Technology*, Slovenia, 27-30. 09. 2015.

Serbian Tribology Society

SERBIATRIB '19

16th International Conference on Tribology

Faculty of Engineering University of Kragujevac

Kragujevac, Serbia, 15 – 17 May 2019

STICKING AND GALLING PHENOMENA IN EJECTION PROCESS OF COATED CORE PINS FROM Al-Si-Cu ALLOY CASTING

Pal TEREK [1, *], Lazar KOVAČEVIĆ [1], Aleksandar MILETIĆ [1], Dragan KUKURUZOVIĆ [1], Branko ŠKORIĆ [1], Aljaž DRNOVŠEK [2], Peter PANJAN [2]

[1] University of Novi Sad, Faculty of technical sciences, Novi Sad, Serbia

[2] Jožef Stefan Institute, Ljubljana, Slovenia

*Corresponding author: palterek@uns.ac.rs

Abstract: *Wear of high pressure die casting (HPDC) tools used for processing of aluminum alloys is nowadays successfully reduced by application of physical vapor deposited (PVD) coatings. Although the coated tool parts are inert to cast alloy and resist erosion, their performance and endurance are dependent on cast alloy sticking and galling phenomena which occur during casting ejection. Considering that knowledge about these specific wear mechanisms is the driving force for development of coatings for HPDC tools, further research is required on this topic. To study wear phenomena of duplex CrN and TiAlN coatings in contact with Al-Si-Cu alloy ejection test is employed. The coatings were produced with different roughness. Before and after the tests, samples were evaluated by profilometry and different microscopy techniques. Cross sectional analyses of pin-casting assemblies revealed that pin and casting form a completely interlocked contact. Intermetallic phases of Al-Si-Cu alloy more intensively precipitate on the pin surfaces than the aluminum matrix. For both coatings it was found that the shape of the ejection curve and values of ejection force depend on the roughness of pin samples. After the ejection, as a result of sticking and galling, a thin layer of cast alloy remained on all investigated samples. Its morphology reveals the pin release mechanisms, sticking effects and type of sliding wear. For rough samples, as a result of ploughing and adhesion the cast alloy remained inside the grooves on the surface. Such release process requires less load but induce a stick slip effect that promotes adhesion. On smooth samples random islands of sticking layer are observed which mostly consist of Al-Si-Cu alloy intermetallic phases. On these samples, cast alloy agglomerates on nodular coating defects which promotes thickening of a built-up layer and wrenching of defects. The post polished samples exhibited the thinnest built-up but required the highest forces for ejection.*

Keywords: *HPDC, aluminum alloy, tool wear, PVD coating, surface roughness, sticking, galling*

1. INTRODUCTION

The erosion, corrosion, soldering and thermal fatigue wear of HPDC tools, for casting of aluminum alloys, is nowadays successfully reduced by application of duplex PVD coatings [1,2]. Although PVD hard coatings display high inertness to molten aluminum alloys, the cast alloy still sticks (mechanically or metallurgically) to coating surfaces. That process together with cast alloy galling cause difficulties in casting ejection and affect casting quality and productivity [3]. Therefore, proper exploitation and further development of these protective layers requires further research for deeper understanding of these wear phenomena. Surface topography controlled by pre and post treatment of coated surfaces greatly affect the performance, durability and cost of HPDC tools [1,3]. However, this topic is rarely addressed in the investigations from the field and it is even less concerned in industry.

Soldering can be evaluated by practical (industrial) and laboratory experiments [2,4]. Evaluation of coatings performance in industrial environment provides information about the specific production case (tool) [2]. However, it is usually not appropriate for analysis of a single wear mechanism [4]. On the other side, laboratory experiments allow isolation of specific wear mechanism, isolation of target parameters and better control of experimental conditions. Therefore, laboratory experiments are better suited for fundamental investigations of coatings wear mechanisms.

In this work the improved ejection test is employed for the evaluation of sticking and galling mechanisms of two the most used PVD coatings for HPDC tools (CrN, TiAlN), which were prepared to different roughnesses.

2. MATERIALS AND EXPERIMENTAL

Investigation concerned the performance of CrN and TiAlN PVD duplex coatings produced to a different degree of surface roughness. Cylindrical pin-shaped samples (ϕ15×100 mm) and disc samples (ϕ20×5 mm) were produced of quenched and tempered EN X27CrMoV51 hot-working tool steel (hardness of 42 HRC ± 1). Samples were prepared to three degrees of surface roughness by procedures regularly employed in production of HPDC tool parts. The steel samples were subjected to plasma nitriding which was followed by polishing (compound layer removal) and coating deposition. Plasma nitriding was performed using ION-25I (IonTech) unit, CrN coating was deposited by BAI730 (Balzers) termionic arc ion plating system and TiAlN coating by CC800/7 (CemeCon) unbalanced magnetron sputtering system. After coatings deposition a group of samples was subjected to post-deposition polishing. All polishing treatments were performed by 6 and 3 µm granulation diamond paste.

Sample denotation contains the type of the coatings (CrN or TiAlN) and suffixes which indicate the surface treatment of the samples: Rough-R; smooth-S; post deposition polished-PP.

Cast alloy soldering (sticking) tendency was evaluated by laboratory test, the improved ejection test. In this test, pin sample is used as a core for production of simple casting with a hole. Figure 1 schematically presents the employed test. As a result of a casting process a pin-casting assembly is obtained. Using a tensile testing machine ZDM 5/91 (VEB) the pin sample is ejected from the casting and a force displacement diagram is recorded (ejection curve). This test imitates the process of core removal from a casting produced by high pressure die casting technology. Therefore, the force recorded during the test carry information about the soldering tendency of cast alloy. Details about this test are given in our previous works [3,4].

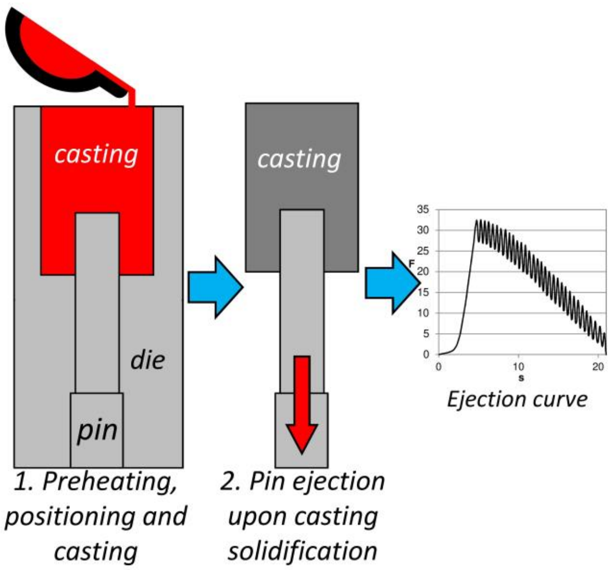

Figure 1. Schematic illustration of the employed ejection test

Casting process was performed by gravity melt pouring of EN AC-46200 alloy, at temperature of 730 °C, into a specially designed steel die, preheated to temperature of 320 °C. After each casting (solidification) cycle, the process is repeated for next sample.

Surface topography of samples was acquired by 3-D stylus profilometer (Taylor

Hobson Talysurf). Instrumented hardness tester H100C (Fischerscope) was employed for the evaluation of mechanical properties of layers and thin coatings, applying 50 and 100 mN indentation loads. Average values of hardness were determined from twelve repetitive measurements.

After the ejection tests samples surfaces and cross section were evaluated by confocal optical microscope Axio CSM700 (Zeiss), Focused ion beam (FIB) Helios Nanolab 650i (Fei) and scanning electron microscope (SEM) Ultra Plus (Zeiss). Both FIB and SEM devices are equipped with energy dispersive spectroscopy (EDS).

Table 1. Pin samples surface roughness

Sample group	S_a [µm]	S_{sk}	S_{dr} [%]
Rough samples (R)			
CrN-R	0.231	-0.863	0.055
TiAlN-R	0.214	0.878	0.157
Smooth samples (S)			
CrN-S	0.066	0.296	0.21
TiAlN-S	0.095	4.820	0.363
Post deposition polished samples (PP)			
CrN-PP	0.029	-1.087	0.020
TiAlN-PP	0.078	-1.750	0.016

3. RESULTS AND DISCUSSION

Plasma nitriding process of EN X27CrMoV51 steel pins resulted with 90 µm thick nitrided layer with maximum hardness of 1300 $HV_{0.01}$. The thickness of investigated duplex CrN coating was 2.7 µm and its hardness was 2735 $HV_{0.05}$. TiAlN coating was 3.4 µm thick and exhibited hardness od 3340 $HV_{0.05}$. Samples surface roughness parameters are presented in Table 1. It can be seen that all groups of the investigated samples belong to the group of very low surface roughness which are applied for HPDC tools of highest quality. Difference in S_a between the smooth and post deposition polished samples is small, however a significant change in morphology is evident by a considerable change in S_{sk} parameter. This is the most pronounced for post deposition polished samples. For these samples S_{sk} parameter indicate that the polishing treatment induced formation cavities on the surface as a consequence of nodular defects wrenching [3].

Figure 2 presents the most representative cross sections of pin-casting assemblies, before the ejection process. It can be seen that eutectic phase and other intermetallic phases of Al-Si-Cu alloy more intensively precipitate in proximity of the pin surface than the aluminum alloy matrix (Figure 2. a). For both coatings it was found that the pin casting contact is mostly established through different intermetalic phases which grow from the coating surfaces (Figure 2. b). Most of the intermetallics form a sharp interface with coated surfaces, which suggests a firm bond established between them (Figure 2. c). Such findings are not reported in the literature, yet. Cross sectional analysis also revealed that the pin and the casting exhibited a completely interlocked contact. Cast alloy closely follows the micro surface irregularities like grinding grooves and growth defects [3]. All these findings are typical for both types of investigated coatings.

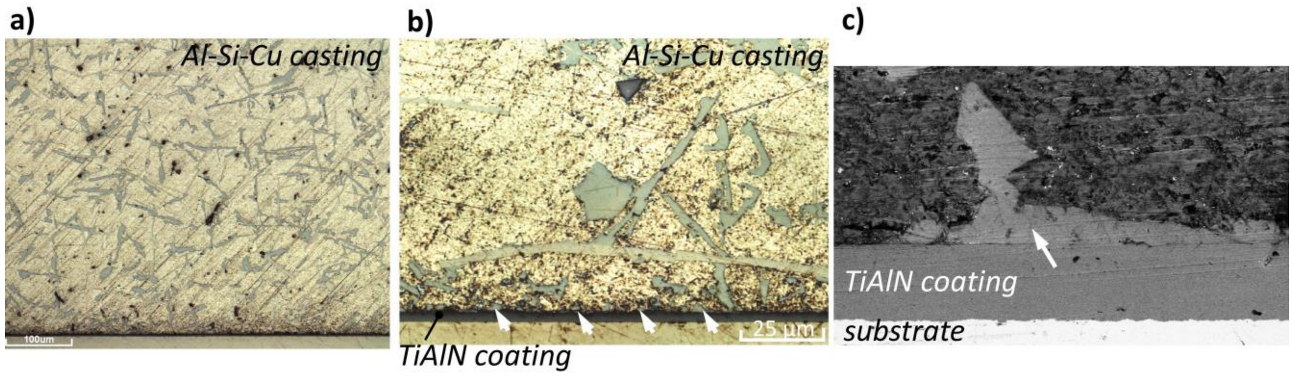

Figure 2. Cross section of pin-casting assembly before the ejection test of TiAlN-R sample, arrows indicate intermetallic of Al-Si-Cu alloy that precipitated on the coated surface, a) and b) CFM images of cross sections; c) SEM image of typical intermetallic phase that precipitate on coated surface

Figure 3 presents the most representative ejection curves of samples with different roughness. For the rough group (R) of samples, a sawtooth shape of the ejection curve typically appears. The sawtooth shape is a consequence of the stick-slip effect caused by two phenomena. One is the casting sliding over the pin surface covered with a built-up layer. The other is the repetitive ploughing of highest pin asperities through cast alloy [3]. The smooth (S) and post polished (PP) samples displayed higher maximal ejection force than the rough samples and their ejection curves are almost smooth and linearly decreasing. The stick-slip effect is absent for smooth and post polished samples. However, their higher ejection force is a consequence of increased adhesion of cast alloy promoted by high tangential force [5].

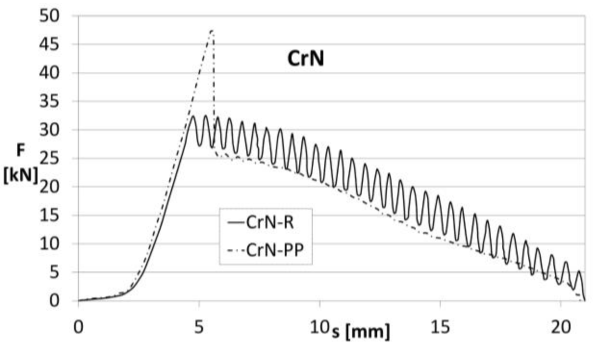

Figure 3. Ejection curves of CrN-R and CrN-PP samples

After the ejection process, cast alloy built-up layer was found on the sample surfaces of both kind of coatings. The built-up layer forms due to sticking of cast alloy, due to galling process, and due to the combination of these two. Morphology of the cast alloy built-up layer can reveal the release mechanisms, sticking effects and type of sliding wear. Figure 4 presents the surface of CrN-R sample. It can be seen, that the built-up on rough samples is mostly located in the grinding grooves and it is redistributed on the side of the groove, opposite to the ejection direction (Figure 4. c). Considering that initially the pin-casting contact was completely interlocked and that the space in grinding groove is limited, remained material in the groove could only be cut off the casting. Another typical form of a built-up is agglomeration of cast alloy around the coating nodular defects (circled in Figure 4. b and d). This is typical for all kind of samples which have nodular defects rough and smooth. Such features form due to the ploughing of higher nodular defects through casting material. The built-up in the grinding grooves together with those around nodular defects, or high asperities, contribute to effects which hamper the pin sliding, inducing the stick-slip effect [3]. During sliding, due to the effects of galling the built-up easily thickens on the layer formed during the initial release of the pin.

The appearance of TiAlN-PP sample after the ejection test is presented in Figure 5. As can be seen the built-up is distributed almost evenly over the whole pin surface. Generally, on surfaces of smooth and post polished pins the built-up layer is thinner. On pin regions which were shallow in the casting, thin

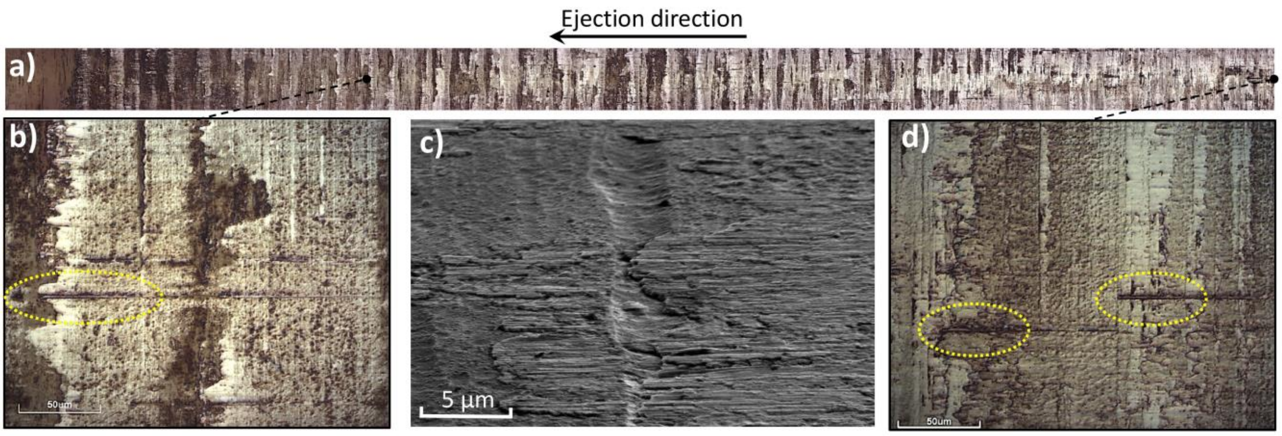

Figure 4. Surface of CrN-H sample after the ejection test: a) CFM panorama view along the sample; b) detail of built-up on the pin 5 mm deep in the casting; c) SEM image of typical built-up in a grinding groove; d) CFM image of built-up in the location 20 mm deep in the casting; circled areas are nodular defects with agglomerated built-up

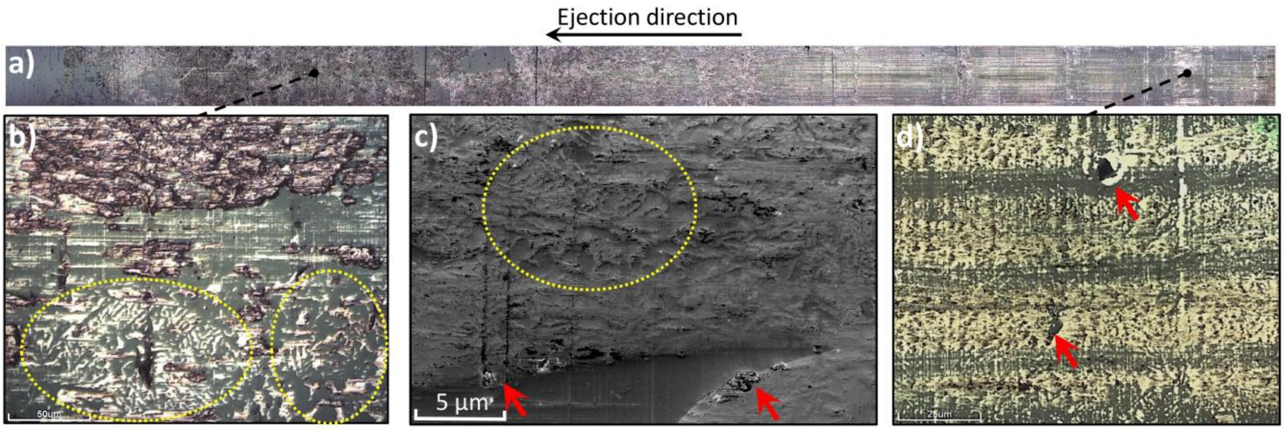

Figure 5. Surface of TiAlN-PP sample after the ejection test: a) CFM panorama view along the sample; b) detail of built-up on the pin 3 mm deep in the casting; c) SEM image of typical built-up on a smooth surface; d) CFM image of a built-up in the location ~18 mm deep in the casting; circled areas in the images indicate sticking layer in form of “chinese-script”, arrows indicate the crater defects filled with

built-up layers have typical shape of “chinese-scripts” (Figure 5. b). These shapes are also typical for intermetallic phases from the cast Al-Si-Cu alloy, which mostly contain Al and Fe (Figure 2. b and c). The number of built-up layers with these shapes agree with the amount of cast alloy intermetalics that precipitate on pin surfaces (Figure 2.). The EDS analysis (not presented here) confirmed that small islands of built-up layers mainly consists of Al-Si-Fe intermetallics. Therefore, it is believed that this kind of built-up forms due to better sticking of cast alloy intermetallics to PVD coatings than its aluminum matrix. The built-up on pin regions positioned deeper in the casting, has the morphology characteristic for wear caused by galling (Figure 5d). In these regions the morphology of a sticking layer, formed in the initial release of the pin, is changed by material transfer from casting to pin, which increases the built-up thickness. Therefore, for the pin regions positioned deeper in the casting the built-up morphology is not representing the sticking (soldering) processes. For post deposition polished samples (PP), a characteristic feature is that cast alloy also agglomerates in coating crater defects (Figure 5. c and d). This occurs on coating defects formed during deposition and on those created (wrenched) by polishing (Figure 5. c and d). Beside their tribological effects, the coating growth defects have large influence on coatings deterioration by corrosion in aluminum alloys [6].

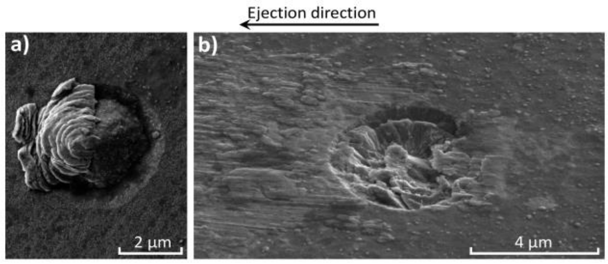

Figure 6. FIB-SEM images of details on CrN-S sample: a) nodular defect with agglomerated cast alloy, b) nodular defect wrenched during sliding

Figure 6 presents two typical phenomena that occur during sliding of coated pins over the casting surface. These micrographs give better prospective on the ploughing phenomena presented in the images of Figure 4 d. Intensive ploughing of highest coating nodular defects induces agglomeration of cast alloy in front of the defect (Figure 6. a). This process enhances the adhesion, increases the friction, which means that higher stress is put on nodular defect. This process can lead to two scenarios. If this stress reaches the shearing strength of a defect, the defect will crack (Figure 6. b). If the stress reaches the strength of bond between the defect and the substrate, the defect will be wrenched out and a cavity defect is formed. In subsequent casting cycles the locations of both cases would lead to the substrate corrosion through growth defects. Such process greatly endangers the coatings integrity because it induces coating cracking and spallation from the substrate which on longer runs puts the coated HPDC tool out of the service [1,6].

4. CONCLUSIONS

From the investigation presented in this paper the following conclusion are drawn.

- The pin and the casting form a completely interlocked contact which is mostly established through eutectic and other intermetallic phases of Al-Si-Cu alloy.
- Shape of the ejection curve depends on the roughness of pin samples. Ejection of rough samples is characterized by prominent stick-slip effect which results with a sawtooth shape of the ejection curves. Smooth and post polished coated samples ejects under higher loads because of the enhanced adhesion of cast alloy to smooth surfaces.
- CrN and TiAlN coatings displayed similar behavior in term of the effects of surface roughness and morphology on sticking and galling processes.
- Although, the rough surfaces exhibit lower ejection force the built-up agglomerates in grinding grooves and it further easily builds up by mechanisms of adhesive wear. During the sliding in process of casting ejection, nodular coating defects agglomerate cast alloy around them. This hampers the ejection process and cause nodular defects cracking or wrenching.
- Intermetallic phases from Al-Si-Cu cast alloy have higher tendency of sticking to coated surfaces than the aluminium matrix. The morphology of such sticking layers, have typical shape of “chinese-scripts”.
- The evaluation of pure sticking phenomena by ejection test is difficult on cylindrical samples because the galling process during the pin ejection covers the built-up layer formed by sticking of cast alloy.
- The morphology of coating growth defects can be significantly changed in casting ejection processes. This in the following casting cycle can change the coating performance and even induce coating deterioration.

ACKNOWLEDGEMENT

This work was financially supported by the Serbian Ministry of Education, Science and Technological Development grant III-45006 and by the Provincial Secretariat for Higher Education and Scientific Research of Vojvodina, Serbia grant 114-451-2192/2016-02. Special thanks to Termometal d.o.o. (Ada, Serbia) for samples fabrication and heat treatment.

REFERENCES

[1] S.B. Abusuilik, Pre-, intermediate, and post-treatment of hard coatings to improve their performance for forming and cutting tools, Surf. Coatings Technol., Vol. 284, pp. 384–395., 2015.

[2] L. Kovačević, P. Terek, A. Miletić, D. Kukuruzović, B. Škorić, P. Panjan, Industrial evaluation of duplex PVD hard coatings for HPDC, J. Brazilian Soc. Mech. Sci. Eng., Vol. 40, pp. 271-279, 2018

[3] P. Terek, L. Kovačević, A. Miletić, P. Panjan, S. Baloš, B. Škorić, D. Kakaš, Effects of die core treatments and surface finishes on the sticking and galling tendency of Al–Si alloy casting during ejection, Wear, Vol. 356–357, pp. 122–134., 2016

[4] P. Terek, L. Kovačević, A. Miletić, D. Kukuruzović, S. Baloš, B. Škorić, Improved ejection test for evaluation of soldering tendency of cast alloy to die core materials, J. Mater. Process. Technol., Vol. 266, pp. 114–124, 2019

[5] B. Bhushan, Adhesion and stiction: Mechanisms, measurement techniques, and methods for reduction, J. Vac. Sci. Technol. B., Vol. 21, pp. 2262-2296, 2003

[6] A. Persson, J. Bergström, Influence of deposition temperature and time during PVD coating of CrN on corrosive wear in liquid aluminium, Surf. Coatings Technol.,Vol. 147, pp. 42–47., 2001

Serbian Tribology Society

SERBIATRIB '19

16th International Conference on Tribology

Faculty of Engineering University of Kragujevac

Kragujevac, Serbia, 15 – 17 May 2019

ANOVA AND REGRESSION MODEL OF SLURRY EROSION PARAMETERS OF A POLYMERIC SPRAY- PAINT FILMS

Mahmoud HESHMAT[a], **Yasser ABDELRHMAN**[a]

[a] Mechanical Engineering Department, Faculty of Engineering, Assiut University, Assiut 71516, Egypt

Abstract: *In this paper, slurry erosion behavior of a polymeric paint film coated on steel and impacted with silica was investigated. The investigated coating was commercially available as 'Kendo' which are used in automobile paint systems to provide protection to both mechanical and corrosive damage. Slurry erosion tests were conducted on the samples to investigate the effect of the common slurry erosion parameters: slurry concentration, impact angle, and impact velocity on the mass loss of the paint material as response. ANOVA was used to study the contribution of the individual parameters, and regression equations were developed to predict the response (mass loss). The results revealed that the slurry erosion was found to be increased by increasing the slurry concentration and impact velocity. In addition, the increase in the impact angle resulted the increase of erosion until the angle reaches 66^o. Moreover, ANOVA analysis illustrated that slurry concentration and impact angle are the significant influencing parameters on the mass loss of the paint material, contributing of impact velocity was less significant. A linear regression model was developed based on the ANOVA results. The developed regression models were validated with the experimental results and found to be feasible.*

Keywords: *Slurry erosion; ANOVA; Regression; Automobile paint coatings, Kendo spray-paint*

1. INTRODUCTION

Erosion is a form of damage occurs on the surface of impacted materials, experienced by a solid body. When the solid body is laden by a fluid and impinges the surface of the material, in this case it is called slurry erosion. Nowadays, slurry erosion becomes a serious problem in many industrial applications because of the performance, reliability, and service life time of slurry equipment. Some of the industrial applications which have severe impact of slurry erosion problems are petroleum tubing and equipment system, solid-liquid hydrotranspotration systems, coal liquefaction plants and industrial boilers, hydraulic turbines, airplanes engines and bodies and so on [1]–[6].

Coatings and surface heat treatments techniques are very common methods used to protect the surface of materials against the erosion and corrosion damages [7]–[11]. In the field of means of transportation such as airplanes, railways, cars, etc., designers seek to protect the outer surfaces of these bodies from the impact of dust on them while traveling at high speeds, and protect them from the impact of corrosive damage. To protect these surfaces from mechanical and electrochemical corrosion, many techniques are used to increase the surface resistance against erosion such as carburizing, boronizing, High Velocity Oxygen Fuel (HVOF) thermal spray coating, etc. [7], [10]–[17]. The studies that used these techniques might enable to reduce the erosion rate and increasing the surface hardness, however, using these techniques are still expensive, and needs exclusive equipment and takes long-time to perform. Moreover, using these techniques pollutes the environment and have many risks on the workers. In addition, they are not suitable for complex shapes such as the external parts of vehicles bodies.

Alternatively, manufacturers utilize polymer paints as an easy and cheap method and, meanwhile they provide acceptable resistance to both mechanical and corrosive damages [18]. However, due to the variety of polymer paints types which are used in this industry, these paints should be, firstly, studied and investigated against the erosion and corrosion tests before they approved for use. The main common factors that affect the paint of vehicles, for example, the impact velocity, concentration of dust/solid particles, and impact angle. Therefore, in this study, the focus will be on these factors to investigate the significant of each factor on the mass loss of paint using experimental analysis and Analysis of variance (ANOVA) technique.

(ANOVA) is a widely used technique in the field of statistics being the appropriate procedure for testing the equality of several means. The objective of the ANOVA procedure lies mainly in estimating and testing hypotheses about the treatment effect parameters. The usual t- test cannot be used to test the joint hypothesis that the true partial slope coefficients are zero simultaneously.

In this paper, we use The Whirling- Arm Slurry Erosion Test Rig (WASET) which was designed by Aboul-Kasem et al. [19], [20] to investigate the impact of the three factors, namely slurry concentration, impact angle, and impact velocity at different levels on the mass loss of a polymer spry-pain material, commercially known as “Kendo”. Then, we use the results to identify the significant factors affecting the mass loss of a polymer spry-pain. We apply ANOVA to reach our objective and the significant factors comprise the independent factors of the developed regression model hereafter. The discrepancies between the experimental results and the developed regression model are calculated to test the model validity.

The remainder of the paper is organized as follows. Section 2 demonstrates the experimental work; section 3 gives the results and analysis; section 4 presents the discussion.

2. EXPERIMENTAL DETAILS

2.1 Test-rig description

The Whirling- Arm Slurry Erosion Test Rig (WASET) shown in Fig. 1 is used to investigate the slurry erosion parameters which are the impact angle, concentration, and impact velocity on the mass loss of the paint material. The full description of the device can be found in [10], [11], [19], [20]. The main units of the used device are the slurry unit, the specimen rotational unit, and the vacuum unit. The solid-particles with tape water are mixed in the slurry tank, then this mixture is going to another slurry tank (small one) inside the vacuum chamber. This small tank should be kept full of slurry all the time to let the falling velocity of the slurry is constant, v_1 = 1.67 m/s. The other horizontal component of impact velocity is coming from the specimen rotational unit, v_2. Therefore, the resultant impact velocity, v, will come from both of v_1 and v_2, as shown from Fig. 2. The impact angle, ϑ $(= \vartheta_o + \acute{\vartheta})$, is measured from the plan of the specimen to the vector of the resultant impact velocity, v. The vacuum unit is used to reduce the aerodynamic effect during the rotation of the specimens inside the chamber, all other details and descriptions can be found in these researches [19], [20].

2.2 Impact angle versus the exposure time

The most important difference in this new designed device (WASET) is the comparison process among the impact angles. In this apparatus, it is not correct to compare among the impact angles versus a constant exposure time, as shown in Fig. 2. The amount of erodent (solid particles) which strikes the surface of specimen is differ from impact angle to another, when they subjecting to the same test time. Therefore, a set of mathematical calculations are carried out to find a relation between the mass of erodent which will strike the specimen as a function of the impact angle and the exposure time; the following equation shows this relationship:

$$m_p = L\sin(\vartheta_o) A_n \frac{L\cos(\vartheta_o)\, Q}{DN} C_w \rho_w \quad (1)$$

Where,

ϑ_o: the angle between the top surface of specimen and the horizontal plane.

L: is the length of wear specimen surface, m

A_n: is the area of orifice, m^2

C_w: is the weight fraction of solid particles in water

ρ_w: is the water density, kg / m^3

D: is the rotational diameter of the wear specimen, m

Q: is the volume flow rate of slurry, m^3/min., and

N: is the rotational speed of the wear specimen, rpm.

This equation is used to adapt the corresponding test time at different impact angles. At these test times, all wear specimens will be subjected to the same amount of erodent (solid particles).

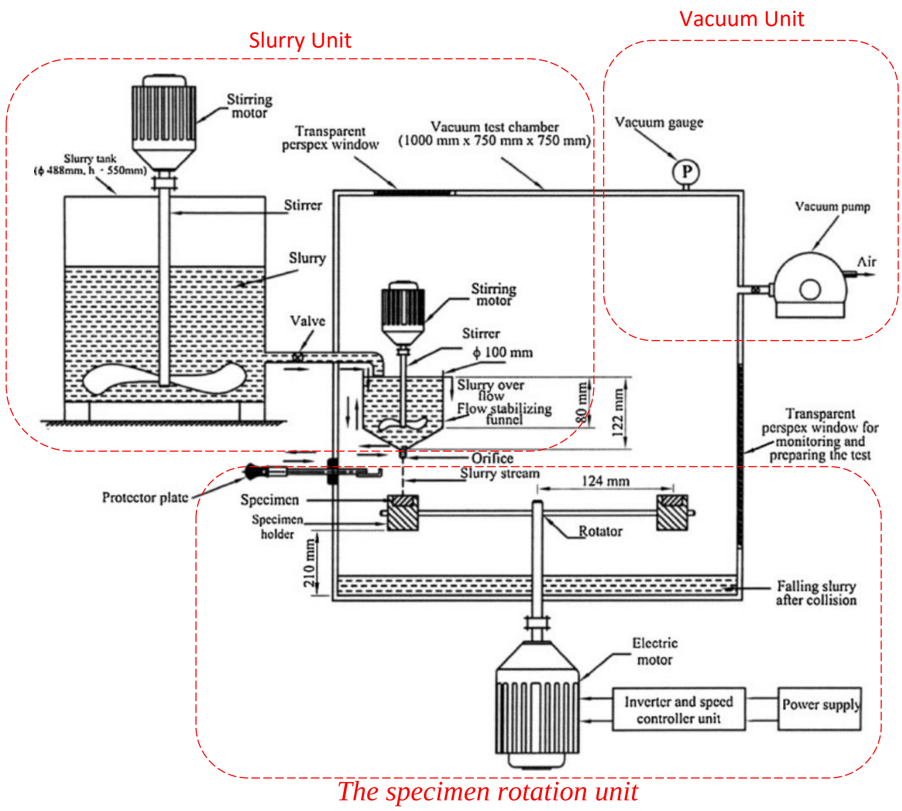

Figure 1. Schematic diagram of the used slurry erosion apparatus

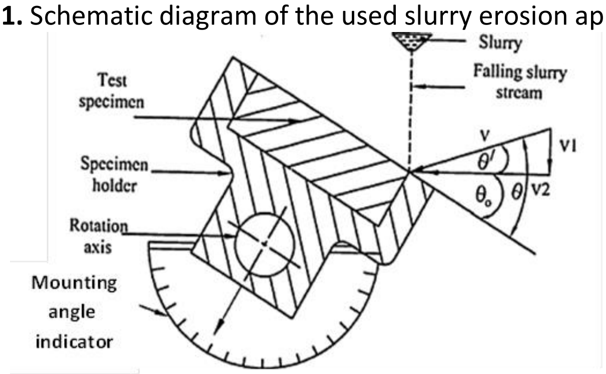

Figure 2. Impact velocity and impact angle

As a conclusion for this part, if the specimens are subjected to the same mass of erodent, say m_p=1.8729 g, then the test times corresponding to some common impact angles, are given in Table 1.

Table 1. Test Times Corresponding to Different Impact Angles for the Same Mass of Erodent (m_p=1.8729 g)

ϑ, deg.	Mass of erodent m_p, g	Corresponding test time, t (min.)
15	1.8729	4.12 = 00:04:07
30	1.8729	2.06 = 00:02:03
45	1.8729	1.44 = 00:01:26
60	1.8729	1.17 = 00:01:10
75	1.8729	1.04 = 00:01:02
90	1.8729	1.00 = 00:01:00

2.3 Painting process

The slurry erosion of the polymeric paint - films was examined through photographing the eroded areas and weighting the mass loss of paint. The used coating is known commercially as "Kendo spray-paint". The test coupons were 10 x 10 x 23 mm^3 steel blocks. The top surface of each block (10 x 23 mm^2) was exposed to polishing process until the surface roughness, R_a, reached about 0.3 µm. After cleaning each block by acetone, a hand spraying was employed from certain fixed height to form a uniform coating thickness, this technique was confirmed by Mehidi et al., [21] and Parslow et al., [22]. Then the test coupons were examined using an optical microscope to ensure the consistency of paint thickness.

As the properties of the used solid particles in erosion studies are very important [18], then, many precautions were taken during this study to let the factor of solid particles properties not included and its effect is constant during all experiments. From these precautions, a single source of solid particles was used, new and fresh particles were used for every experiment to avoid any change in the size due to degradation of particles, the size of used particles was fixed and it was 250 – 355 µm. The used fluid in this study was tap water at room temperature, and the concentration of slurry was 1 wt. %, if not stated unlike that. Finally, specimens were cleaned and weighted before and after each experiment and the average of two mass-losses of two specimens had been reported at each test condition.

3. RESULTS AND ANALYSIS

Table 2 reveals the obtained results with different levels of all studied factors. First, we present the response plots, then the ANOVA results, after that the linear regression models and its evaluation.

Table 2. The results of mass loss under different levels of the studied factors

Trial No.	Concentration	Speed	Angle	Mass loss
1	1	15	10	0.00
2	1	15	20	0.10
3	1	15	30	0.20
4	1	15	45	0.30
5	1	15	60	0.60
6	1	15	75	0.70
7	1	15	90	0.85
8	1	5	30	0.10
9	1	5	45	0.10
10	1	5	60	0.20
11	1	5	90	0.20
12	1	10	30	0.10
13	1	10	45	0.20
14	1	10	60	0.20
15	1	10	90	0.30
16	1	15	30	0.10
17	1	15	45	0.10
18	1	15	60	0.20
19	1	15	90	0.20
20	2	15	30	0.25
21	2	15	45	0.30
22	2	15	60	0.35
23	2	15	90	0.40
24	3	15	30	0.30
25	3	15	45	0.35
26	3	15	60	0.40
27	3	15	90	0.50
28	5	15	30	0.50
29	5	15	45	0.70
30	5	15	60	0.90
31	5	15	90	1.10

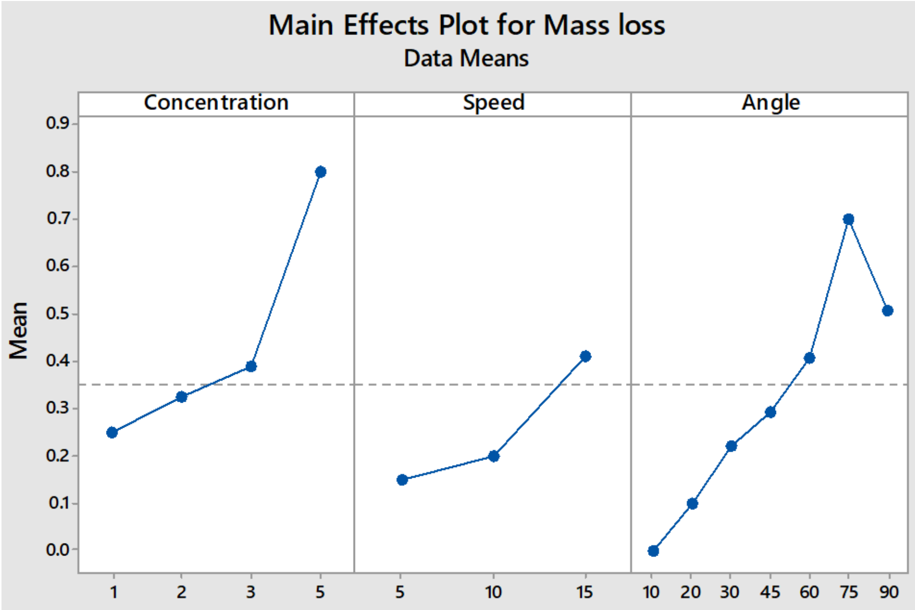

Figure 3. The main effect of the slurry concentration, speed, and impact angle on the mass loss

Table 4. Comparison between the obtained results and the experimental results

	Impact angle	Slurry concentration	Mass loss (Experimental)	Mass loss (from model)	Error (%)
1	45	1	0.1	0.19	-9
2	60	2	0.35	0.39	-4
3	30	3	0.3	0.35	-5
4	60	5	0.9	0.91	-1

3.1 Response plots

Figure 3 depicts the main effect of the studied factors on the response namely the mass loss. The observation of response plots depicts that the increase in the erosion factors increases the erosion rate. By increasing the speed and concentration of slurry, the mass loss is increased drastically, while increasing the impact angle results in increase the mass loss till maximum value, at impact angle 66^{o}, further increase in the impact angle has not such effect. This observation is quite consistent with the study of Joshi et al. [21], but they used the slurry pot erosion test.

3.2 ANOVA

In this section, we statistically test if the impact angle has a significant effect on the mass loss or not. Table 3 concludes the ANOVA of the experiments done in terms of the impact angle and the mass loss. It can be concluded that the impact angle and slurry concentration have a significant impact on the mass loss. However, the speed has no significant effect on the mass loss.

Table 3. ANOVA of the impact angle and the mass loss

Factor	SS	DOF	F-value	p-value
Speed	0.08766	2	1.93	0.172
Angle	0.62544	6	4.59	0.005
Concentration	0.69794	3	10.25	0.000
Error	0.43121	19		

3.3 Linear regression model

We generate a regression model between the slurry concentration, impact angle and the mass loss. The resulted regression model was developed using MINITAB, and it is as follow:

$$Mass\,loss \quad 0.1671 \quad 0.1217\,Concetration \quad 0.00524\,Angle \qquad (2)$$

The coefficient of slurry concentration is the highest, followed by the impact angle. The interaction effect is negligible, and this confirms the results of the experiments.

In order to validate the regression model, confirmation tests were conducted as shown in table 4. The prediction error is calculated as the difference between the experimental value and the predicted value. The error is quite acceptable for such weight- sensitive experiments. Thus, the developed model is considered to be feasible to predict the slurry erosion values within the range of the experimental conditions.

4. DISCUSSION

From the slurry erosion experiments, it is clear that concentration of slurry has a significant influence on the mass loss, by increasing the concentration of slurry, the number of impacting solid particles is increased. Therefore, the number of impacts will be increased causing higher damage on the surface, and this damage is leading to an aggressive mass loss. The impact velocity had the same trend of slurry concentration but with no significance on the mass loss. By increasing the impact velocity, the mean of mass loss is increased also, this may be interpreted in light of the kinetic energy of the impacting. As it is known that the kinetic energy is proportional with square velocity. Therefore, the impacting velocity increases the impacting force leading to deeper indentation, microcutting or ploughing of the solid particles in the surface material, depending on the accompanied mechanism at the impact angle, causing the increase in the mass loss [16], [23]. However, the effect of the impact angle has not the same trend, in the beginning the mass loss is increased by increasing the impact angle till the maximum value at the impact angle 66^{o}, but further increase in the impact angle has not such effect. The peak mass loss at this impact angle indicating the semi-ductile nature of the studied painting material [24].

5. CONCLUSIONS

This paper presented a slurry erosion experimental and statistical study. The statistical analysis illustrated that the concentration and impact angle are the significant factors; however, the speed is not significant. Moreover, slurry concentration has the most significant effect on the erosion of the painted specimens. The experimental results showed that the peak erosion occur at the angle of 66^{o}. A regression model was developed to predict the mass loss with the significant factors, and it was validated to be feasible to calculate and predict the mass loss under different values of concentration and impact angles.

REFERENCES

[1] Q. Fang, P.S. Sidky, M.G. Hocking: Microripple formation and removal mechanism of ceramic materials by solid-liquid slurry erosion, Wear, Vol. 223, No. 1–2, pp. 93–101, 1998.

[2] S. Lathabai, D.C. Pender: Microstructural influence in slurry erosion of ceramics, Wear, Vol. 189, No. 1–2, pp. 122–135, 1995.

[3] Y. Li, G.T. Burstein, I.M. Hutchings: The influence of corrosion on the erosion of aluminium by aqueous silica slurries, Wear, Vol. 186–187, pp. 515–522, 1995.

[4] Y. Iwai, K. Nambu: Slurry wear properties of pump lining materials, Wear, Vol. 210, No. 1–2, pp. 211–219, 1997.

[5] W. Tsai, J.A.C. Humphrey, I. Cornet, A.V. Levy: Experimental measurement of accelerated erosion in a slurry pot tester, Wear, Vol. 68, No. 3, pp. 289–303, 1981.

[6] B. Staniša, V. Ivušić: Erosion behaviour and mechanisms for steam turbine rotor blades, Wear, Vol. 186–187, pp. 395–400, 1995.

[7] P. Salehikahrizsangi, K. Raeissi, F. Karimzadeh, L. Calabrese, S. Patane, E. Proverbio: Erosion-corrosion behavior of highly hydrophobic hierarchical nickel coatings, Colloids Surfaces A Physicochem. Eng. Asp., Vol. 558, pp. 446–454, 2018.

[8] H.J. Amarendra et al: Combined Slurry and Cavitation Erosion Resistance of Hvof Thermal Spray Coated Stainless Steel, Mater. Today Proc., Vol. 4, No. 2, pp. 465–470, 2017.

[9] K. Girisha, K.V. Sreenivas Rao, C. Durga Prasad: Slurry Erosion Resistance of Martenistic Stainless Steel with Plasma Sprayed Al2O3-40%TiO2Coatings, Mater. Today Proc., Vol. 5, No. 2, pp. 7388–7393, 2018.

[10] Y.M. Abd-Elrhman, A. Abouel-Kasem, K.M. Emara, S.M. Ahmed: Effect of Impact Angle on Slurry Erosion Behavior and Mechanisms of Carburized AISI 5117 Steel, J. Tribol., Vol. 136, No. 1, p. 011106, 2013.

[11] Y. Abdelrhman, A. Abouel-Kasem, K. Emara, S. Ahmed: The effect of boronizing heat treatment on the slurry erosion of AISI 5117, Ind. Lubr. Tribol., Vol. 70, No. 7, pp. 1176–1186, 2018.

[12] K. Yang, J. Rong, C. Liu, H. Zhao, S. Tao, C. Ding: Study on erosion-wear behavior and mechanism of plasma-sprayed alumina-based coatings by a novel slurry injection method, Tribol. Int., Vol. 93, pp. 29–35, 2016.

[13] K.V. Sreenivasa Rao, C.S. Ramesh, K.G. Girisha, Y.D. Rakesh: Slurry Erosive Wear Behavior of Plasma Sprayed Cr2O3Coatings on Steel Substrates, Mater. Today Proc., Vol. 4, No. 9, pp. 10283–10287, 2017.

[14] S. Hong, Y. Wu, W. Gao, J. Zhang, Y. Zheng, Y. Zheng: Slurry erosion-corrosion resistance and microbial corrosion electrochemical characteristics of HVOF sprayed WC-10Co-4Cr coating for offshore hydraulic machinery, Int. J. Refract. Met. Hard Mater., Vol. 74, pp. 7–13, 2018.

[15] V. Javaheri, D. Porter, V.T. Kuokkala: Slurry erosion of steel – Review of tests, mechanisms and materials, Wear, Vol. 408–409, pp. 248–273, 2018.

[16] V. Javaheri, D. Porter, V.T. Kuokkala: Slurry erosion of steel – Review of tests, mechanisms and materials, Wear, Vol. 408–409. Elsevier, pp. 248–273, 2018.

[17] A.K. Rai, A. Kumar, T. Staubli: Hydro-abrasive erosion in Pelton buckets: Classification and field study, Wear, Vol. 392–393, pp. 8–20, 2017.

[18] K.L. Rutherford, R.I. Trezona, A.C. Ramamurthy, I.M. Hutchings: The abrasive and erosive wear of polymeric paint films, Wear, Vol. 203–204, pp. 325–334, 1997.

[19] A. Abouel-Kasem, Y.M. Abd-elrhman, K.M. Emara, S.M. Ahmed: Design and Performance of Slurry Erosion Tester, J. Tribol., Vol. 132, No. 2, p. 021601, 2010.

[20] Y.M. Abd-Elrahman, A. Abouel-Kasem, S.M. Ahmed, K.M. Emara: Stepwise Erosion as a Method for Investigating the Wear Mechanisms at Different Impact Angles in Slurry Erosion, J. Tribol., Vol. 136, No. 2, p. 021608, 2014.

[21] M.N. Noui-Mehidi, L.J. W. Graham, J. Wu, B.V. Nguyen, S. Smith: Study of erosion behaviour of paint layers for multilayer paint technique applications in slurry erosion, Wear, Vol. 264, No. 7–8, pp. 737–743, 2008.

[22] G.I. Parslow, D.J. Stephenson, I.E. Strutt, S. Tetlow: Paint layer erosion resistance behaviour for use in a multilayer paint erosion indication technique, Wear, Vol. 212, No. 1, pp. 103–109, 1997.

[23] T. Alam, Z.N. Farhat: Slurry erosion surface damage under normal impact for pipeline steels, Eng. Fail. Ana*l.*, Vol. 90, pp. 116–128, 2018.

[24] A.G. Joshi, M.P. Kumar, S. Basavarajappa: Influence of Al2O3 Filler on Slurry Erosion Behavior of Glass/Epoxy Composites, Procedia Mater. Sci., Vol. 5, pp. 863–872, 2014.

Serbian Tribology Society

SERBIATRIB '19

16th International Conference on Tribology

Faculty of Engineering University of Kragujevac

Kragujevac, Serbia, 15 – 17 May 2019

SURFACE BASE EFFECTS ON ZINC COATING CHARACTERISTICS

Desimir Jovanović[1], Bogdan NEDIĆ[1*], Jelena BARALIĆ[3]
[1]Zastava Arms Inc, Kragujevac, Serbia
[2]Faculty of engineering University of Kragujevac, Serbia, *nedic@kg.ac.rs
[3]Fakultet tehničkih nauka u Čačku, Univerzitet u Kragujevcu, Čačak, Serbia

Abstract: *Galvanic zinc coating applied in addition to perform appropriate performances of the base material surface such as corrosion resistance, chemical stability, required aesthetic impression etc. Galvanic zinc coating examinations are focused mostly on Zn connection with the base material, while we have poor data about the influence of the surface on the characteristics of the coating. Previous final processing has a large impact on the physical and mechanical properties and coating structure. This paper presents the results of research on the properties of zinc coatings deposition on the surface obtained by various final processing with different hardness and topography.*

Keywords*: galvanic zinc coating, hardness, topography*

1. INTRODUCTION

We have very poor research of the influence of processing procedure type and previous processing operations such as surfaces preparation wear coating. The surfaces that were processed obtained by various methods of processing may have a various structure. That could be noticed when exploitation period starts. Therefore, we can say that the surface layer characteristics are formed as a result of different processing conditions in the technological series of final parts production.

The main parameters that are arising from technological process can be divided into two groups. First, these are parameters related to the material properties: composition, structure, stress state, etc.., While the other parameters related to the macro and micro geometric area (geometric parameters) [1, 2]. That points that the problem is very complex and it has to be researched.

Zinc coatings are mostly used to protect steel surfaces from corrosion. Electrochemical zinc coatings may have different morphology and texture. Majority of studies conducted relating to the impact of standard parameters during the subsidence of the coatings such as current density, temperature, bath composition [3-7]. On the other hand the importance of steel base surface preparation was less considered. Researching influence on base conditions for deposition of zinc coatings mechanically polished [8-9] or electrochemical [10-11]. It shows that the morphology and texture of the coating on the surfaces are significantly different.

Surface finishing has a large impact upon the physically - mechanical properties and structure of the surface base. This paper research the influence of the previous surface processing and coating thickness on the mechanical and chemical properties of the zinc coating.

2. EXPERIMENTAL INVESTIGATION

The basis for coating deposited steel Č5730 was selected (according to GOST 30HN2FA 1). Selected steel is used for making shooting arms barrels.(Table 1) shows the chemical composition of the base. Testing samples are tiles 15 x 10 x 6.3 mm dimension (ASTM G 77). The samples were produced by milling. Heat treatment performs improvement on different hardness. Final processing of samples was carried out in several ways, with multiple modes of grinding, polishing, and sanding. In this way different characteristics of the surface layer and different samples surface topography were obtained.

Micro-geometry of coating surface was recorded on a computerized measuring device Talysurf-6, which allows complex monitoring of the contact surfaces.
Using this measuring system we have got the information about the initial micro-geometry of the samples contact surfaces.

Table 1. Chemical composition of the basics Č5730 **(**GOST: 30HN2FA 1)

	element	chemical composition %
1.	C	0.27-0.34
2.	Mn	0.30-0.60
3.	Si	0.17-0.37
4.	Ni	2.0-2.4
5.	Cr	0.60-0.90
6.	Mo	0.20-0.30
7.	V	0.10-0.18
8.	S	max 0.025
9.	P	max 0.025
10	Cu	max 0.25

Application of metal coatings was carried out at the electroplating operational of the factory "Zastava Arms" in Kragujevac. Table 2 shows the characteristics of the base material where coating was applied.

Zinc coatings are deposited in the progra-mmed mode by direct current, according to requested experiment plan. During the deposition process, direct current parameters are strictly controlled and regulated within the specific limits. The anodes which are made of lead with 10% tin were used.

Zinc coating was performed as follows:

- alkaline without cyanides degreasing with industrial detergent,
- flush water wash-out,
- pickling in diluted hydrochloric acid in the ratio 1:1,
- wash-out,
- electro-chemical coating of zinc,
    - coating on room temperature,
    - electric power I = 3 A/dm^2
    - illumination in 2% HNO_3 dilution during 50 seconds,
- flush water wash-out,
- drying by hot air.

Table 2. Surface samples characteristics

Sample No	Processing type	Ra, μm	Base hardness, HRC
10	grinding	0.818	38
11		0.719	29
12		0.844	19
13		0.920	37
20	polishing	0.197	25
21		0.185	38
30	sandblasting	1.570	35

The zinc coating was carried out by placing the samples in a vertical position, in same direction. The sample was marked on the upper side with "A" (Figure 1). Measurement of local thickness of the zinc coating was carried out on 15 points with the pattern of the sample shown in Figure 1.

Characteristics of the (mean of thickness and roughness) deposited coatings are given in Table 3.

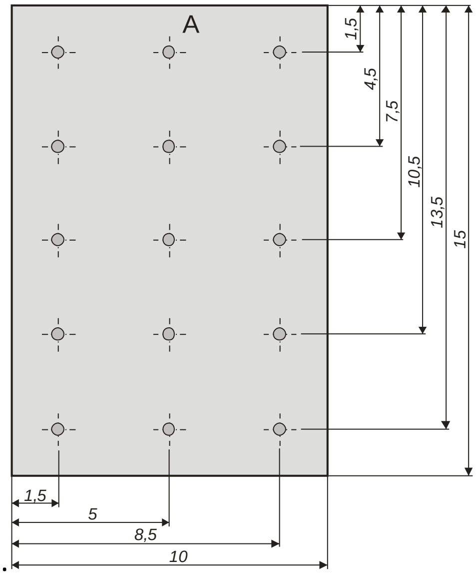

Figure 1. Scheme of coating thickness measuring points

Table 3. Coating characteristics

	Sample No.	Ra, µm	Coating thickness, µm
1	10	1.070	9.85
2	11	1.120	18.90
3	12	1.130	23.87
4	13	1.540	20.16
5	20	0.667	16.57
6	21	0.610	21.62
7	30	2.010	11.26

Figure 2, shows the topography of coatings for samples 13, 20 and 30.

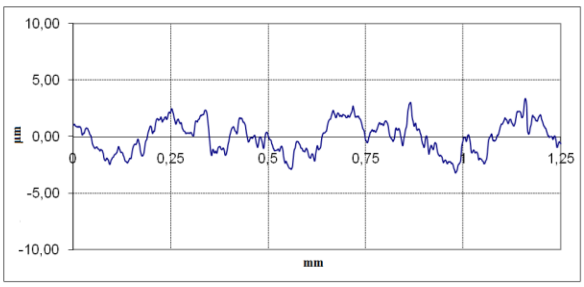

Sample 13

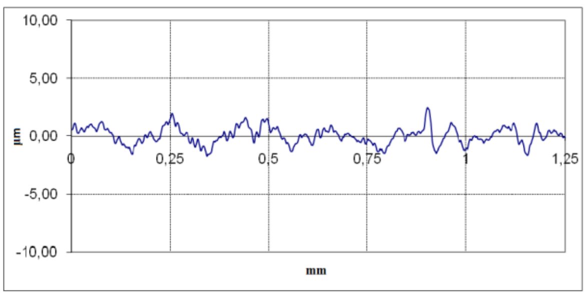

Sample 20

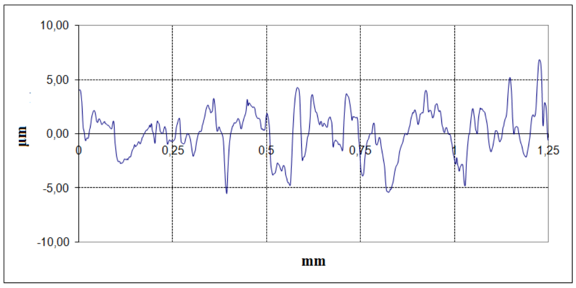

Sample 30

Figure 2. Topography after applying the coating

Figure 3 shows the appearance of the samples before and after coating.

Sample 13

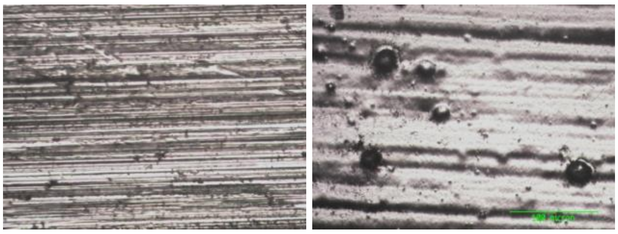

Before the coating After the coating

Sample 20

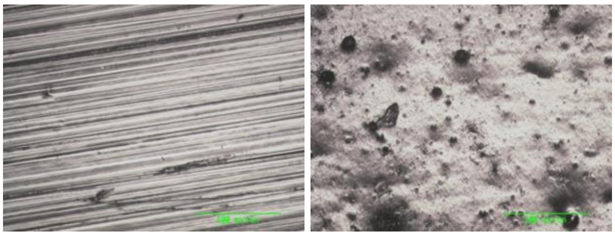

Before the coating After the coating

Sample 30

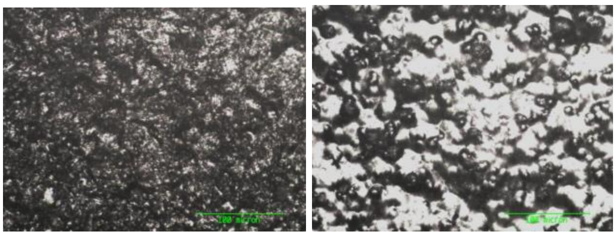

Before the coating After the coating

Figure 3. Look of the of samples before and after the coating

3. RESULTS ANALYSIS

Exterior checking was conducted for all samples first. The look of the coating was monitored visually in daylight, at an angle of 45 º. Coating surface for all samples is shiny and smooth. There are no dendrites, burnt and uncovered surfaces.

Zinc coating thickness was measured at 15 locations according to plan in Figure 1. The graph, Figure 4, shows the distribution of coating thickness on the sample surface, based on measurement results. According to those graphics we can concluded that the thickness along width and length of the sample is varied and uneven. The highest values of coating thickness were measured in the central part of the sample at the length of 13.5 mm from the edge. The edge of the sample is marked with "A". This is the point that marks the top of the sample during zinc coating.

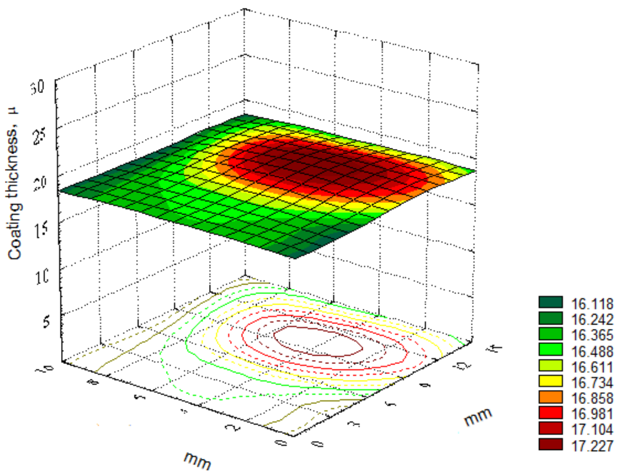

Figure 4. Schedule of coating thickness

Test of coatings adherence was carried out by warming, according to ISO 2819-1980. Terms of examination:

- Samples heating temperature T = 200^{0}C (according to T = 180^0-200^0 C),
- Warm-up time 1 hour.
- Wetting by cold water flash.

After heating according to required standard conditions samples are exposed to cold water flash. Coating must remain unchanged. The separation of the coating from the substrate must not be allowed.

The samples that were tested are in accordance to standard. Adhesion of the zinc coatings is good; there is no significant changing of zinc coating that could indicate the separation of the coating from the base metal surface (Figure 5).

Corrosion stability of zinc was determined by samples monitoring over time exposure to a solution of 3% Na Cl, in accordance with ASTM B117-64 method. The samples that were examined had different characteristics (roughness and hardness of the base, and the coating thickness), Table 2 The results of corrosion stability monitoring of zinc coating shows that there was no corrosion, so we cannot establish a connection between the parameters of the previous processing and corrosion resistance (Figure 6).

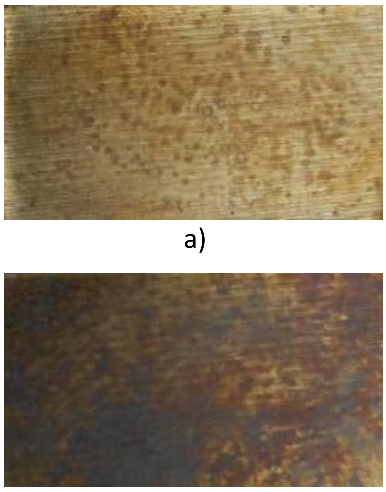

a)

b)

Figure 5. Appearance of samples after the original heating a) and cooling b)

Figure 6. The appearance of the coating after the corrosion resistance tests

The width of wear track on the block was measured by tribological tests on tribometre block-on-disk. On that way zinc coating wear resistance was determined (Figure 7).

Wear testing of coatings was performed on tribometre TR-95 with a contact block-on-disk at the Centre for metal cutting and the tribology of the Faculty of Engineering Sciences in Kragujevac. The tribometer TR-95 perform contact condition variations in terms of shape, dimension and material of the contact elements, the normal load contact and sliding speed. The tests may be conducted with using of lubrication or without them. The development of wearing process on the block appears by formatting and expansion as significant trace of wear. Normal load was 10 N and the sliding speed 0.25 m / s, 0.5 m / s and 1 m / s. Total slip route was 150 m. Tests have been realized with the boundary lubrication with mineral hydraulic oil Hidrovisk HD46. High coefficient of the friction which is usual measured with tribometer TR-95, avoided by using lubricants.

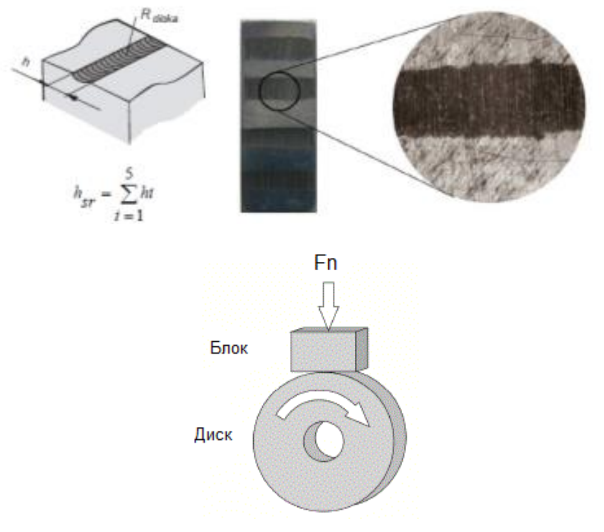

Figure 7. Trace of wear on the block

The initial nominal line contact between the disk and the block due to wear development process becomes a specific contact on the surface. This contact results as destruction of such materials, primarily in the surface layer of the block (Figure 8). Changing in wear track width has the same character for all tested samples; only difference was their wear level.

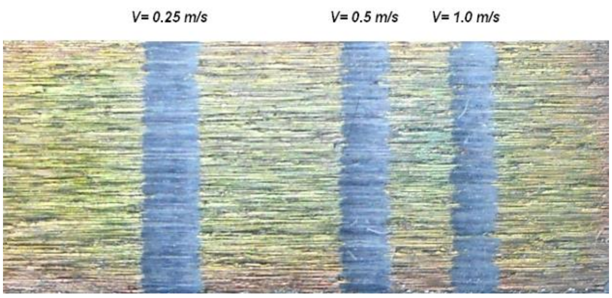

Figure 8. Wear track width on the block

The wearing process is characterized by achieving a certain level such as stabilization and slow growth wear track width during the test period. The contact (sliding velocity, normal force) individual and cumulative histogram of wear track width changes. Based on the measuring results of the wear track width on the block has been created, depending on the conditions (Fig. 9). Maximal wear track width of suit matches to minimal sliding speed.

The samples with different characteristics (roughness and hardness of the base, the coating thickness) were tested. Observing the histogram, Figure 7, it can be concluded that the surface roughness between samples before and after the application of the zinc coating and wear track width of the block cannot establish a connection. Also we cannot establish a connection between the technologies of processing of samples (grinding, sanding, etc...) with wear track width.

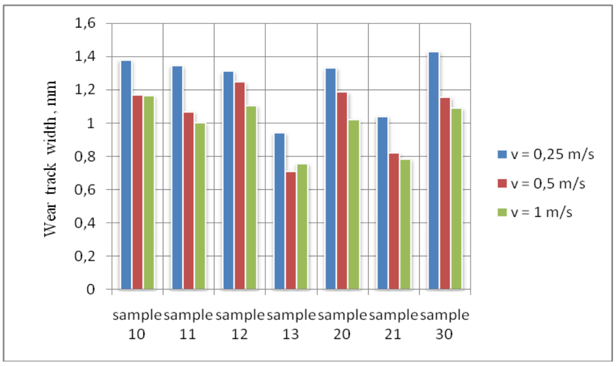

Figure 9. Wear track width of the block

Minimum wear was in samples 13 and 21, for samples with high surface hardness and high coating thickness. The greatest wear was in samples 30, 10 and 12. Sample 12 has the lowest hardness and samples 30 and 10 the least thickness of the zinc coating.

4. CONCLUSION

The investigated coatings of different thicknesses were applied on samples with varying topography and hardness. The results achieved by visual examination, results of corrosion resistance and adhesion of zinc coatings on base metal, showed that they are in accordance with standards. It means that we have optimal preparation and coatings technology.

The testing results shows that coating leads on significant surface topography changes (roughness increase) but it does not affect other characteristics of the zinc coating. The results show that there is dependence between the base hardness, coating thickness and wear track width during tribological tests. Establishment of correlative connections is possible by realization of numerous experiments.

ACKNOWLEDGEMENT

This paper is part of project **TR35034,** funded by the Ministry of Education, Science and Technological Development of Serbia.

REFERENCES

[1] В.М. Зинченко: *Технологическая наследственность при изготовлении деталей*, Технология металлов, 2007. № 5,

[2] П.И. Ящерицын: *Технологическое наследованиеэксплуатационных параметров деталей машин*. Справочник, Инженерный журнал № 9, 2004,

[3] B. Nedić**,** D. Jovanović**,** G. Lakić-Globočki: Scratch Testing of Zn Coating Surfaces, in: *Proceedings: 34th International conference on production engineering*, Niš, 2011.

[4] Raeissi, Saatchi, Golozar, Szpunar: Effect of surface preparation on zinc electrodeposited texture, Surface & Coating Tehnology, Vol. 197, 2005,

[5] K. Deblauwe, A. Deboeck, J. Bollen, W. Timmermans: Influence of processing parameters on the texture of pure zinc electrodeposited coating on steel, in: *Proceeding of the 12th International Conference on Textures of Materials (ICOTOM-12)*, Montreal, Quebec, Canada, 9–13 08.1999, pp. 1293-1298, 1999.

[6] S.H. Hong, J.B. Kim, S.K. Lee: The Role of Textures in the Corrosion Resistance of Electrogalvanized Zn Coatings, Materials Science Forum, Vol. 408–412, pp. 1025-1030, 2002.

[7] S.Ch.H. Kim: Initial and recrystallization textures and microstructures of Zn electrodeposits, in: *Proceeding of the 12th International Conference on Textures of Materials (ICOTOM 12)*, Montreal, Quebec, Canada, 09–13 08.1999, pp. 956-960, 1999.

[8] D. Vasilakopoulos, M. Bouroushian, N. Spyrellis: Texture and Morphology of Zinc Electrodeposited from an Acid Sulphate Bath, Transactions of the IMF, Vol. 79, No. 3, pp. 107-111, 2001.

[9] M. Ye, J.L. Delplancke, G. Berton, L. Segers, R. Winand: Characterization and adhesion strength study of Zn coatings electrodeposited on steel substrates, Surface and Coating Technology, Vol. 105, No. 1-2, pp. 184-188, 1998.

[10] H. Yan, J. Downes, P.J. Boden, S.J. Harris: A Model for Nanolaminated Growth Patterns in Zn and Zn-Co Electrodeposits, Journal of the Electrochemical Society, Vol. 143, No. 5, pp. 1577-1583, 1996.

[11] H. Park, J.A. Szpunar: The influence of deposition parameters on texture in electrogalvanized zinc coatings, in: *Proceeding of the 12th International Conference on Textures of Materials (ICOTOM 12)*, Montreal Quebec, L Canada, 09–13 08.1999, pp. 1421-1426, 1999.

[12] Standard ISO 2819-1980

[13] Standard ASTM B117

[14] Standard ISO 4539

Serbian Tribology Society

SERBIATRIB '19

16th International Conference on Tribology

Faculty of Engineering University of Kragujevac

Kragujevac, Serbia, 15 – 17 May 2019

STUDY ON FRETTING CORROSION OF TIN-COATED ELECTRICAL CONTACTS

Sándor KOVÁCS[1], Péter MARGITAI[2], Alexandra GÁL[2], Szabolcs SZÁVAI[3,*], Péter RÓZSAHEGYI[2]
[1]Institute of Physical Metallurgy, Metalforming and Nanotechnology, University of Miskolc, Miskolc, Hungary
[2]Bay Zoltán Nonprofit Ltd. for Applied Research, Miskolc, Hungary
[3]Institute of Machine and Product Design, University of Miskolc, Miskolc, Hungary
*Corresponding author: szabolcs.szavai@bayzoltan.hu

Abstract: *: The examination of the failure of electric connectors of electric powered vehicles is at the forefront of current vehicle developments, because the connector's operating time increases significantly in comparison with internal combustion engine vehicles. It was observed that the low amplitude fretting corrosion plays the most important role in failure, so the lifetime of the failure process is decisive in the life span of the connector. Typically, the failure of an electrical connector in terms of product is an increase in electrical resistance that can even cause malfunction of the drive within the product expected lifetime because of the generated Joule heat that causes temperature rise.*
The aim of our work is to study the fretting corrosion process in a given geometry and material quality of electrical connection by experiment and numerical model.
In the experimental test, an experimental construction was set which simulated contact properties of the built-in connectors. Tests for failure-life were performed as a function of the clamping force of the mating members and the amplitude of the relative displacement of the contact surfaces, of which magnitude can be typically for fretting. The change in resistance at the contact surface was measured and examined when this value reached the limit value for failure, thus determining the life span for fretting corrosion.
The experimental set-up was then modelled by finite element method. The purely elastic FE model made it possible to model the gradual removal of the material for given force-amplitude-frequency values by using the Archard's theory. The valid wear coefficient was searched that creates the same wear crater in the calculation as in the measurements.
Then, using the measured data, the FE analysis revealed the mechanical stress conditions, the electrical current flow conditions, and the resulting thermal conditions during the wear process both on and below the contact surface, which provides additional information on the details of the fretting corrosion process.

Keywords: *fretting, corrosion, wear, failure, FE analysis, lifetime*

1. INTRODUCTION

As regards the electrical connectors of cooling fans used in electric cars, the results of the standard lifetime testing procedures used in the case of internal combustion vehicles are not relevant, as the operating times of the connectors are significantly higher. Consequently, the expected lifetime of the connectors will be higher in the standards of electric automotive industry under development than in the internal combustion specifications. This requires the introduction of accelerated standardized lifetime tests.

In our work, one of the main factors influencing the lifetime of the connector, the fretting corrosion process, was studied using experimental and numerical tools to develop the testing standards for electric cars with the help of this knowledge. When the contact surfaces have oscillatory displacement at small sliding amplitude (smaller than 100 μm), electrical insulating oxidation products are continuously generated at the contact surfaces and cause fretting corrosion [1–6]. When fretting corrosion occurs, the contact resistance is increased, resulting in malfunction of the electronic devices. And the fretting corrosion has a chance because the small sliding amplitudes occur when the electric cars are operating.

The geometry and the material quality of the investigated connector were given in advance which was used by the cooperating automotive company for cooling fans.

In a first step, a simple geometry physical simulation was constructed in which a point contact properties are formed that corresponds to the average mechanical stress on the line contact surfaces of the electrical connector calculated by Hertz theory. The material was the same: industrial purity tin coated industrial purity copper.

The end-of-life phenomenon was determined with the help of a collaborative industrial partner, defined by a limit value for transition electrical resistance on the contact surface. In the first step, the limit value for the connector was assumed to be 10 mΩ. This value was converted according to the contact area of the experimental design. Thus, in our physical fretting simulation the electrical resistance was measured until the limit value of the transition electrical resistance was reached and then the process was stopped.

Vincent et al. [6] investigated the fretting sliding transition from partial slip to gross slip for electrical contacts with noble and non-noble material coatings. They reported that if the displacement amplitude becomes higher than the *transition value*, the generalized gross slip condition activates debris formation over the whole contact surface, resulting in unstable electrical resistance for non-noble material coatings. When the displacement amplitude is lower than the transition value then the partial slip regime occurs. Partial slip causes an annular slip area on the outer periphery and a stick zone in the center area where slip does not occur. The stick zone in the center has metal-to-metal contact and therefore the electrical resistance remains low in a stable way during the lifetime. So it is possible to achieve an infinite lifetime of the electrical connector. In contrast, when a gross slip occurs, slip occurs over the entire contact area and oxide debris is created in the entire area. As a result, the electrical resistance rapidly increases with the number of cycles.

Noble material coatings can only extend the lifetime of the electrical contacts. Wearing-out of the substrate coating material caused high and unstable electrical resistance [6].

To obtain as much information about the transition value of the amplitude and the changes in the lifespan as we can, the amplitude and the clamping force between the mating parts were varied and the lifetime was detected for each measurement. Also the effect of previous aging of the materials of connectors was studied.

In order to obtain more detailed data about of the degradation phenomenon a FEM numerical model was created. The built FEM model was a coupled structural-electrical-thermal model which was also able to the modelling of wear. The modelled geometry was the geometry of the physical simulation which is a contact of a surface of a hemisphere and a surface flat block. Also, for the electrical calculation, the measured transition electrical resistance were used.

The basis of the wear modelling was the Archard's equation. The calculation's time requirement of wear simulation was so high that an acceleration method was used which was implemented in the Archard's equation. The model was validated by the comparison of the measured and calculated wear depth and width.

2. EXPERIMENTAL PROCEDURES

A specific electrical connector of cooling fans used in electric cars was studied which can be seen with its CAD model in Fig.1. These are industrial purity copper connectors coated by 3μm thick industrial purity tin layer.

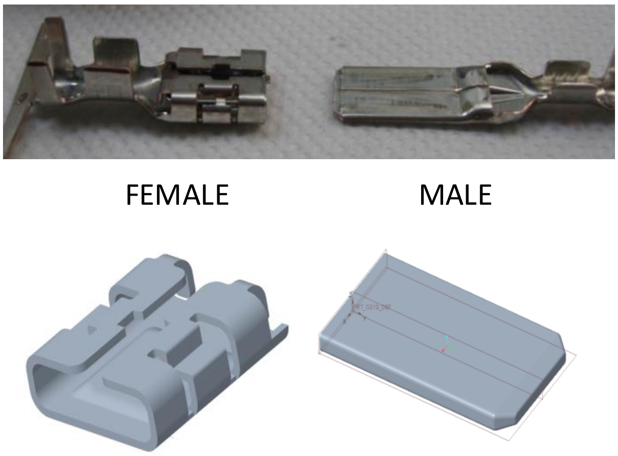

Figure 1. Female and male parts of the electrical connector of cooling fans and its CAD model

In order to study the contact properties, specimens with simpler geometry and with the same material and coating as in the electrical connectors were used for fretting experiments. The aim of the experiment was to compare the resistance values of the test specimens produced by the male terminal of connectors at different amplitudes and clamping forces as a function of the number of cycles. Knowing this information, lifetime graphs similar to strain-cycles curves were determined based on different parameters.

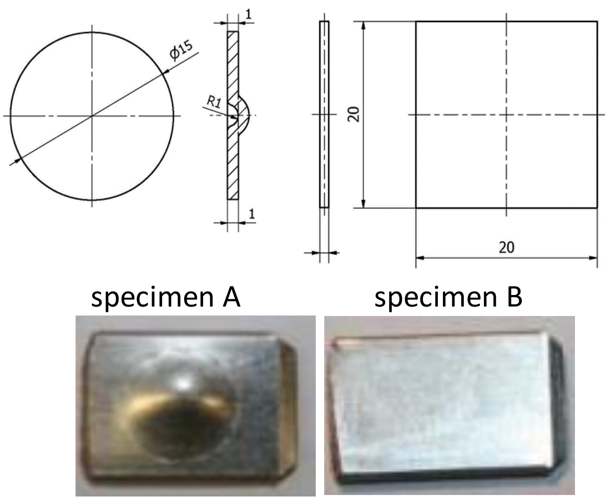

Figure 2. A and B parts of the contact specimen of the fretting experiments

The test specimens were prepared as shown in Fig.2. The relatively large surface of male terminal of connector provides the opportunity to form the required specimens (specimen A and B). The A specimens were embossed by a steel ball with R1 = 5 mm diameter (in Fig. 2). Then the specimen A was attached to the test equipment by soldering to avoid the unwanted vibration and backlash of the specimen. After the test, the soldered specimen can be removed without destruction and a new specimen can be fixed. The specimen B was cut from the male connector as it can be seen in Fig. 2. Specimen B was attached to the copper sample holder using screws.

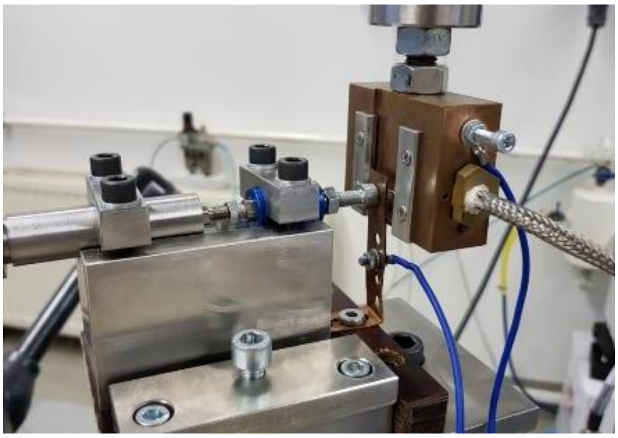

Figure 3. E10000 electrodynamic test equipment with the developed fretting test holders

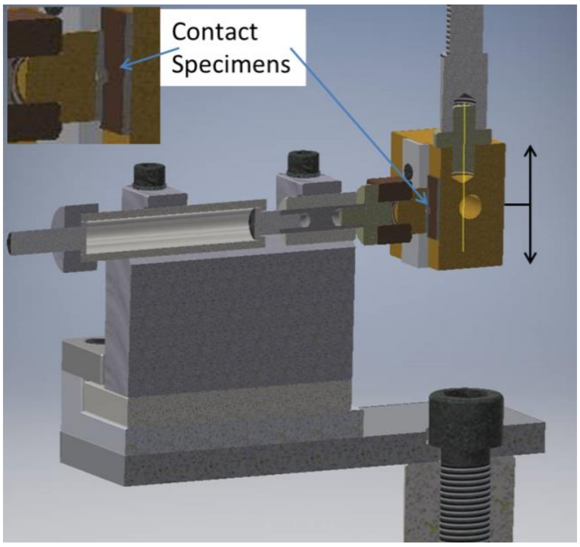

Figure 4. Schematic illustration of E10000 electrodynamic test equipment

The test equipment The tests are carried out on the E10000 electrodynamic test equipment with the developed fretting test holders as it can be seen in Fig. 3 and 4. The soldered horizontal part was created the uniaxial clamping force between the specimen A and B. The copper sample holder moved vertically in accordance with the given frequency and amplitude. The specimens are electrically insulated from the rest of the equipment so the electrical resistance change can be measured (Figs. 3-4).

Electrical resistance measurement is performed using a Keithley 2410 resistance meter. Temperature measurement was also carried out on the specimens during the fretting tests by thermocouples.

The lifetime test plan was:

- In the first series of tests, they were carried out with a force of 5N at room temperature (23˚C) with a relative humidity of 50% at a frequency of 30 Hz. The variable parameter was the amplitude.
- In the second series of tests, the effect of the compressive force was tested up to a pressure of 10 N.
- In the third series of tests, aged specimens were examined. Aging was done at 140 °C for 14 days.

In addition, development of the wear track was studied by measuring the surface roughness using Altisurf surface profiler with CL2 chromatic confocal sensor and the dimensions of the crater created by the wear track using a microscope. For this purpose, measurements were made up to different parts of the previously measured number of failure cycles, and the craters thus obtained were examined by surface profiler. The selected test parameters were 10 µm amplitude, 30 Hz frequency, 5 N load, 23 C ambient temperature and 50% humidity. In this case, the maximum number of cycles was 35620, at which we reached the critical value of the electrical resistance of failure. An additional 5 measurements were made up to 1/6, 2/6, 3/6, 4/6, 5/6 of the maximum cycle count.

2.1 Evaluation procedure for lifetime experiments

In the experiments, electrical resistance-cycles graphs were recorded. The actual electrical resistance values cannot be accurately determined even with the electrical resistance measured on the wires and connections During the electrical resistance measurement, only the electrical resistance change is recorded, which was used to determine the cycle value of the failure, i.e. when the critical resistance value is reached.

The value of the critical electrical resistance for each sample is different, depending on the size of the contact surface. Therefore, for each specimen, the extent of the critical resistance change was determined individually, based on the measured contact surface after the test, calculated by the following equation:

$$\boldsymbol{R}_{\mathbf{crit}} = \boldsymbol{R}_{\mathbf{1}} * \frac{\boldsymbol{A}_{\mathbf{terminal}}}{\boldsymbol{A}_{\mathbf{specimen}}} \tag{1}$$

R_1 is equal to 10 mΩ. A_{specimen} is the measured contact area on the specimen which varies in size around 0.09 mm^2 as a function of the test amplitude and cycle number. A_{terminal} is the measured contact area on the terminal of the electrical connector of which size is around 2.91 mm^2. Thereby, the critical electrical resistance to be measured on the surface is increased from the required 10 mΩ to more than 300 mΩ.

Knowing the defined critical resistance values, the critical cycle number for the test amplitude can be read from the electrical resistance - cycle number diagrams obtained from the experiments.

3. COUPLED NUMERICAL MODEL

FE analysis of contact properties of specimens of fretting experiments was carried out. The finite element model was a coupled model containing structural, wear, thermal and electrical analysis. The modelled geometry of specimens can be seen in Fig. 5. However, to save calculation time, only a small part of bodies of specimens were modelled around the contact area where the contact exerts its effect. In that parts of the bodies, a mesh were created as it can be seen in Fig. 5. The mating surfaces are smooth and the FEM was quasi-static.

There were 3 µm thick tin layers on mating surfaces while the material of other element in the body is copper. Because of the elastic model is more conservative and the calculation time was shorter than the elasto-plastic model the elastic model was used for this study.

Mechanical properties of industrial purity copper:

- Young's modulus: 117000 MPa
- Poisson ratio: 0.33
- Density: 8960 kg/m^3

Mechanical properties of industrial purity tin:

- Young's modulus: 41600 MPa
- Poisson ratio: 0.33
- Density: 7310 kg/m^3

Boundary conditions:

- The nodes on the bottom surface of the part of specimen B are fixed
- The motion parallel to the mating surface and the clamping force were defined on one node on the upper surface of the part of specimen A
- The friction coefficient between the mating surfaces 0.15
- There was no buckling of the parts of the bodies which was ensured by links defined on the side nodes

The boundary condition can be seen in Fig. 5 where the fixing is marked with green arrows, the motion definition with pink arrows and the clamping force definition with orange arrow. The clamping force was 5N. The motion was defined by sine curve where amplitude 10 µm and frequency 30 Hz.

Electrical properties of the coupled model:

- Specific resistance of copper: $1.68 \cdot 10^{-8}$ Ωm
- Specific resistance of tin: $1.09 \cdot 10^{-7}$ Ωm

Boundary conditions:

- 0V potential sinks defined on the nodes of the upper surface of the part of specimen A
- 25 piece of point current source are defined on bottom surface of the part of specimen B, 4 mA in each of them
- 20 mΩ was the assumed contact electrical resistance between the mating surface.

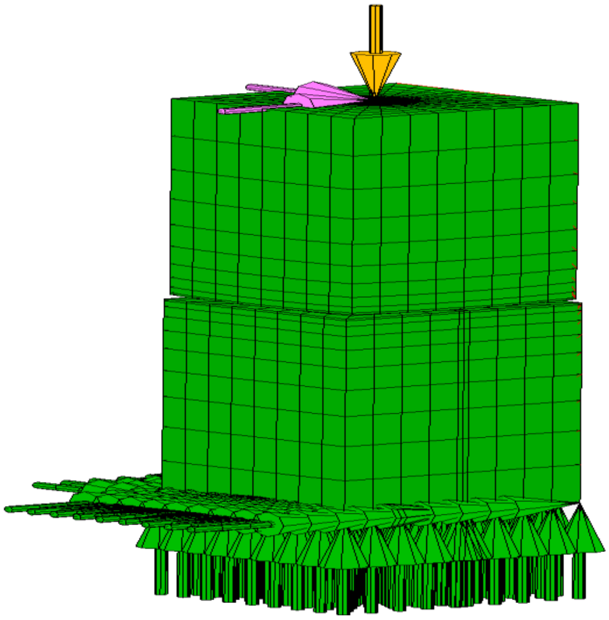

Figure 5. Meshed parts of the specimens A and B with structural boundary conditions

The electrical boundary condition can be seen in Fig. 6 where 0V potential sinks is marked with green arrows and electrical sources with purple arrows.

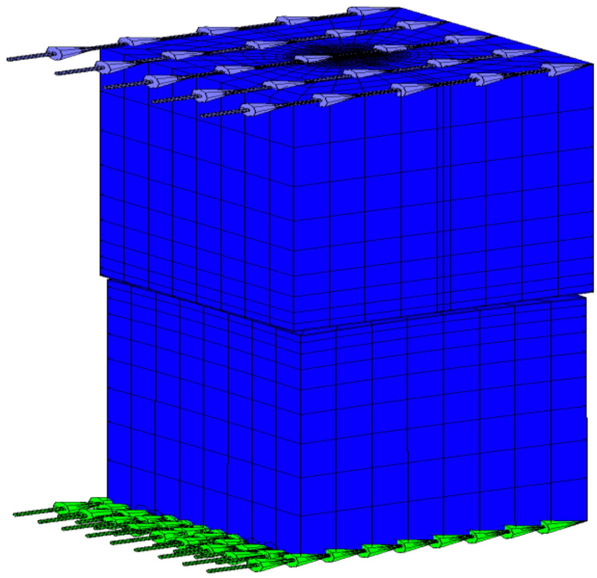

Figure 6. Meshed parts of the specimens A and B with electrical boundary conditions (sources and sinks)

Thermal properties of the coupled model:

- Thermal conduction of copper: 400 W/(m·K)
- Thermal conduction of tin: 67 W/(m·K)
- Specific heat capacity of copper: 385 J/(kg·K)
- Specific heat capacity of tin: 210 J/(kg·K)
- Transition thermal conduction between the mating surfaces: 10000 W/(m·K)

The given value of transition thermal conduction is an overestimation of the real value which was unknown before the examination.

The initial condition was 293 K. With the exception of the mating surfaces, there was not heat transfer through boundary surfaces on both bodies.

The frictional heat and the Joule heat were calculated together with the heat transfer.

For numerical simulations MSC Marc finite-element software was used.

Wear was modelled by Archard's equation. This equation is the most widely used for adhesive and abrasive wearing simulation [7-16]. MSC Marc implements wear by moving the nodes of the contact surface to the direction of wear with the extent of the wear depth.

The wear depth can be calculated by the next time-dependent equation based on the Archard's equation [7]:

$$\dot{w}^* = k \cdot \sigma \cdot v_{\mathrm{rel}} \tag{2}$$

where $\dot{w}^*$ [mm/s] wear rate (temporal change in wear depth), k[mm^3/(Nm)] is the specific wear rate, σ[MPa] is the normal stress on the contacting surface and v_{rel}[m/s] is the relative velocity in a mating point of the contact surfaces. The exact value of k was determined by comparison with validation measurements.

For reducing the time consuming of the coupled model an acceleration technique was used for the wear model where the increase of the wear depth calculated for a step was multiplied by a factor. In case of the acceleration method, the (3) equation was used to calculate the position change of the nodes of the contact surface due to wear in each time step:

$$\boldsymbol{x_{n+1}} = \boldsymbol{x_n} + \boldsymbol{f} \cdot \boldsymbol{\dot{w}^*} \cdot \boldsymbol{\Delta t} \tag{3}$$

where x_n [mm] and x_{n+1} [mm] are the position of a node in n-th and (n+1)-th time step, f [-] is the acceleration factor, $\dot{w}^*$[mm/s] wear rate (temporal change in wear depth), Δt[s] is the time step of the FEM calculation.

4. RESULTS AND DISCUSSION

4.1 Experimental results

The experimental lifetime tests were performed for given force, ambient temperature, frequency, amplitude and the electrical resistance data were recorded as it can be seen in Fig. 7. When the magnitude of the resistance change belonging to the failure phenomenon was reached, the test was stopped. After measuring the wear trace, the value of the exact critical electrical resistance of the failure is determined based on Eq. (1). The lifetime of the critical resistance was then determined inversely from the diagrams similar to Fig. 7 obtained from the measurements. This allowed us to determine a point on the strain-cycles-like amplitude-cycle curve.

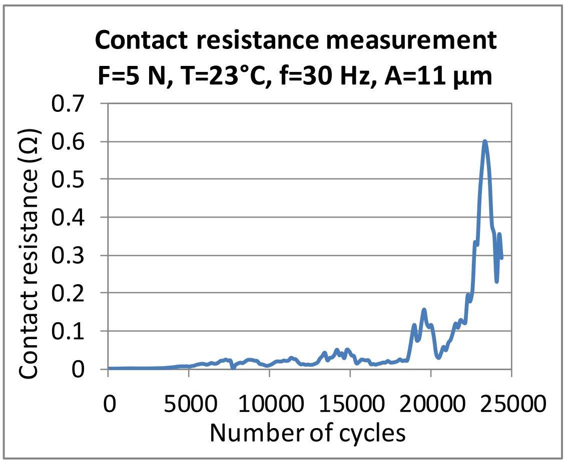

Figure 7. Measured electrical resistance as a function of the number of cycles for fixed parameters

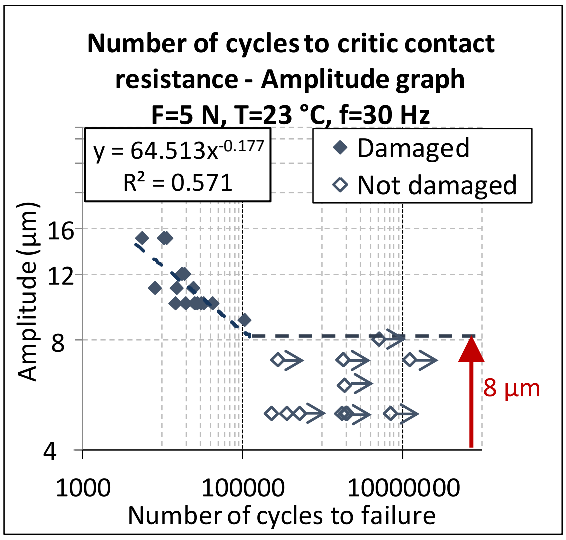

Figure 8. Lifetime diagram for fixed force temperature and frequency

According to the test plan, only the amplitude was changed with fixed force, frequency, humidity and ambient temperature in the first measurement series. The resulting amplitude-cycle lifetime curve can be seen in Fig. 8. As it can be seen, there is an 8 μm limit amplitude value below which the failure phenomenon does not occur.

In case of the second measurement series, the clamping force was increased. The resulted lifetime diagrams can be seen in Fig. 9-10. Fig. 10 clearly shows that with increased power, lifetime was increased. Also the limit amplitude belongs to "infinite" lifetime was increased with the clamping force.

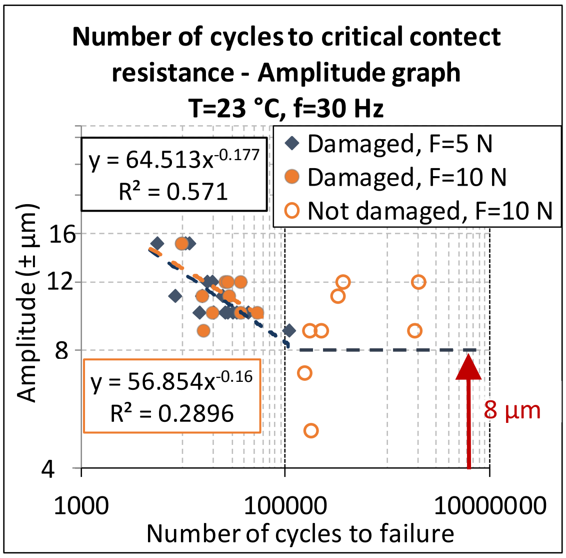

Figure 9. Lifetime diagram in case of 5 N and 10 N clamping force (logarithmic scale)

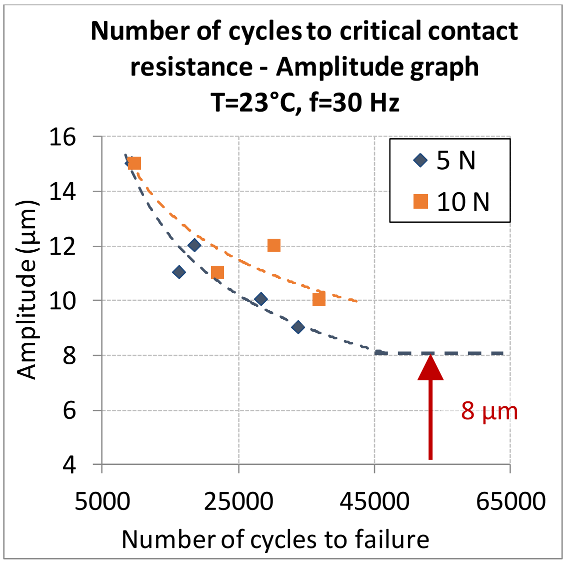

Figure 10. Lifetime diagram in case of 5 N and 10 N clamping force

In case of the third measurement series, the lifetime results of aged specimens were compared to results of the first measurement series where the clamping force was 5 N. The resulted lifetime diagrams can be seen in Figs. 11-12. The results are indicated that the aging process decreasing the lifetime of the electrical connectors. After 14 day aging the decreasing of the lifetime was so large that the limit amplitude belongs to "infinite life" was become less than 4 μm.

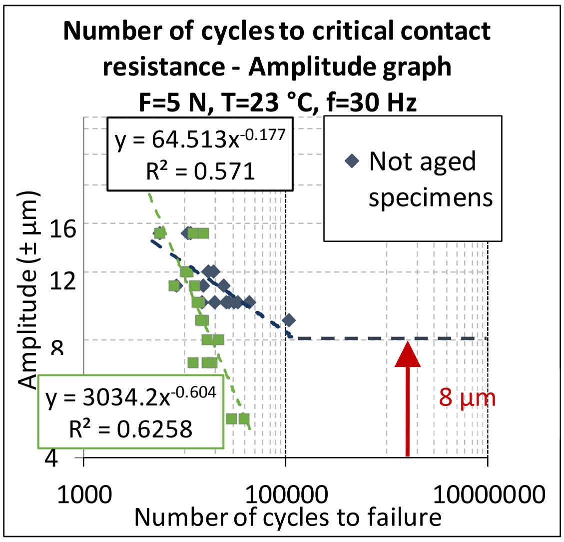

Figure 11. Comparison of the lifetime curves of aged and without aged specimens

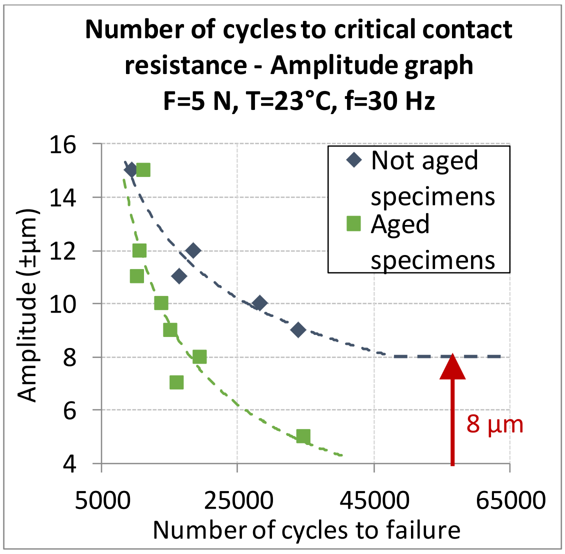

Figure 12. Comparison of the lifetime curves of aged and without aged specimens

For later validation of the coupled FEM model, wear traces were examined by surface profiler as the wear trace evolved. The maximum cycle was obtained by the previous lifetime measurements which was equal to 35620. And additional 5 measurements were made up to 1/6, 2/6, 3/6, 4/6, 5/6 of the maximum cycle count.

It was found that the wear depth has already been reached 11 μm at sixth of the total lifetime which depth is more than three time bigger than the thickness of the tin coating layer. Only the specimens B of each measurement was taken into account for validation because of its plain geometry since the wear depth can be more accurately determined. These results can be seen in Fig. 13-15.

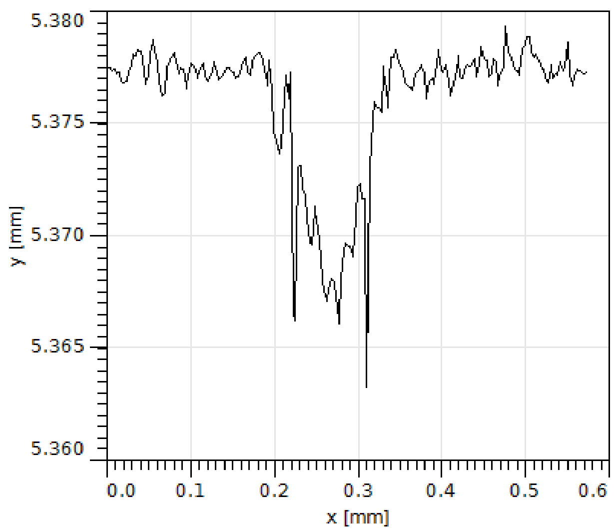

Figure 13. Wear depth measured by surface profiler for sixth of lifetime of given force (5 N), temperature (23 °C), humidity (50%) and frequency (30 Hz)

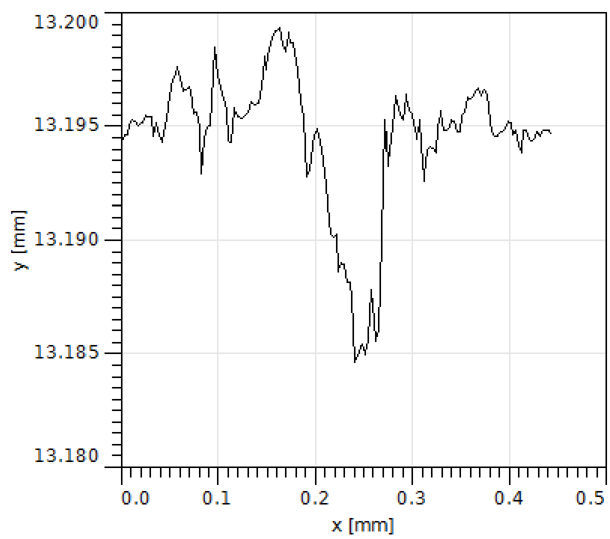

Figure 14. Wear depth measured by surface profiler for half of lifetime of given force (5 N), temperature (23 °C), humidity (50%) and frequency (30 Hz)

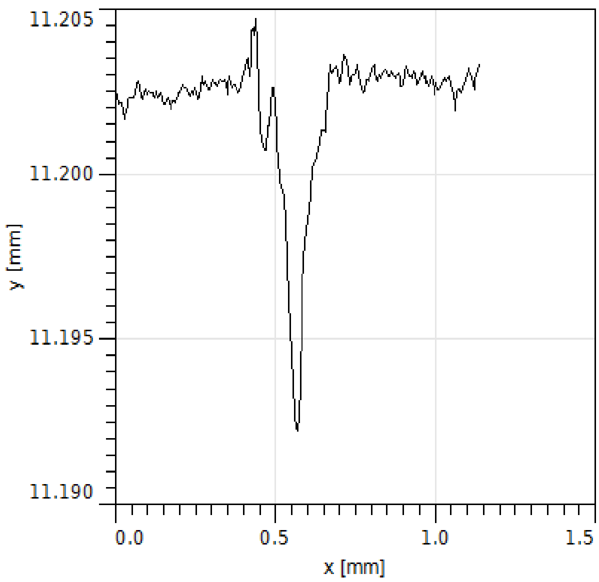

Figure 15. Wear depth measured by surface profiler for total lifetime of given force (5 N), temperature (23 °C), humidity (50%) and frequency (30 Hz)

As it can be seen in Table 1, the diameters and areas of the wear traces are also stabilized around a constant value very fast as the number of cycles increased.

It is assumed that after the fast fretting wear, the oxidation process of the copper-copper contact takes over the role until the failure phenomenon is reached. In this second period, the extent of wear is negligible because of the wear trace geometry and the debris accumulation between the contacting surfaces.

Table 1. Sizes of wear traces measured by optical microscope in case of measurements carried out different part of the total lifetime

	1/6 of lifetime	**1/2 of lifetime**	**Total lifetime**
#Cycles	5937	17 810	35620
Length of trace	382 μm	419,5 μm	419,2 μm
Width of trace	304 μm	279,5 μm	276,3 μm
Area	0,09241 mm^2	0,09561 mm^2	0,09493 mm^2
Wear trace (100x zoom)			

4.2 Result of numerical calculation

With the help of FEM numerical analysis the wear stage of the fretting corrosion was studied. So the total number of cycles was 5937 in this case.

Half model was used for the calculation with a symmetry plain which lays in the middle of the meshed parts of specimens parallel to the relative movement.

First, the coupled FEM model was validated by the measured sizes of the wear craters. The wear depth was measured by surface profiler. For the latitude measurements of wear trace optical microscope was used since the wear under 3 μm is difficult to identify with surface profiler due to the adhered debris and the surface roughness of the same size. By contrast, the areas affected by the contact with the optical microscope are well identifiable.

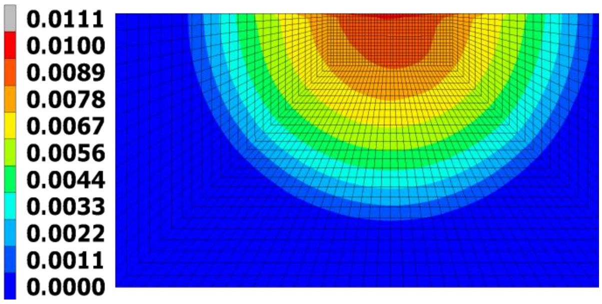

Figure 16. Calculated wear depth of the specimen B as the numver of cycles is 5937^{th}

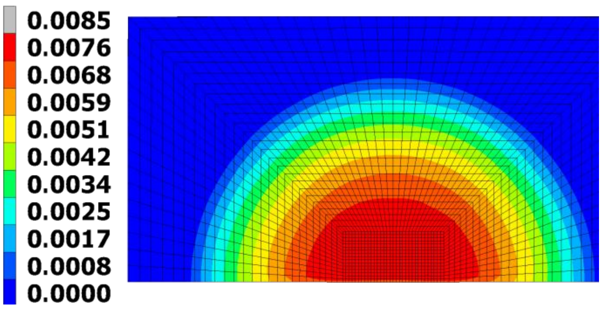

Figure 17. Calculated wear depth of the specimen A as the number of cycles is 5937^{th}

In the end of the validation procedure the obtained specific wear rate (*k*) for the contacting materials was $1.4 \cdot 10^{-3}$ $mm^3/(Nm)$. The obtained length of the trace was 483 μm and the width was 237 μm for the B part of the specimens which is quite comparable with the measured values in the Table 1. As it can be seen in Fig. 16, the calculated wear depth is the same with the results of the surface profiler.

Structural analysis was carried out by the validated model. The changes of the distribution of the normal stress on the mating surface can be seen in Figs. 18-21. It can be seen that contact surface was increased and the structure of the distribution of the maximum normal stress changed significantly.

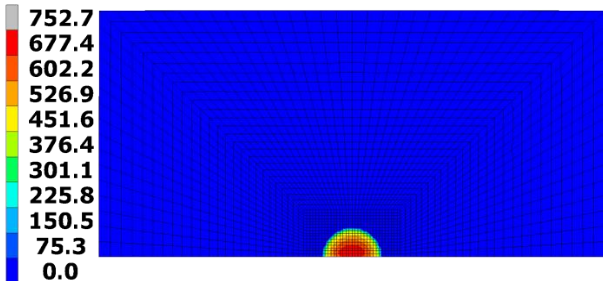

Figure 18. Normal stress distribution on the mating surface in the beginning of the wear process

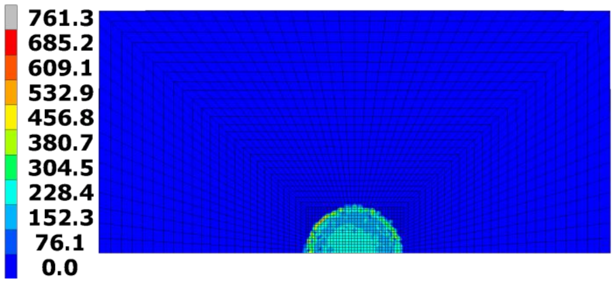

Figure 19. Normal stress distribution on the mating surface in the 25^{th} cycle

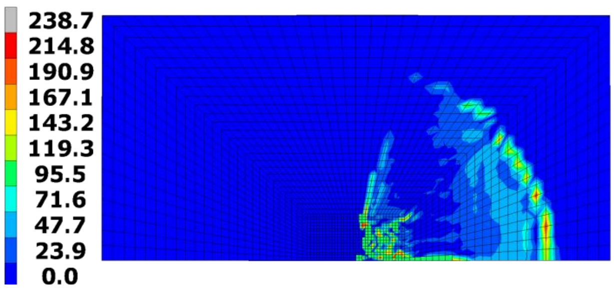

Figure 20. Normal stress distribution on the mating surface in the 5919^{th} cycle

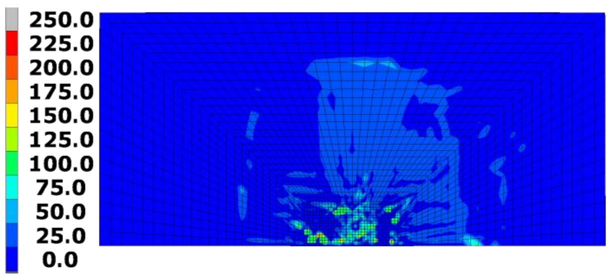

Figure 21. Normal stress distribution on the mating surface in the 5937^{th} cycle

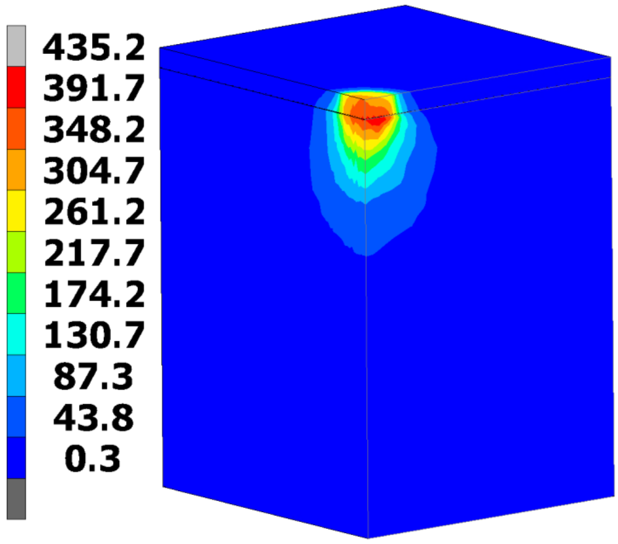

Figure 22. Von Mises stress distribution in specimen B in the beginning of the wear process

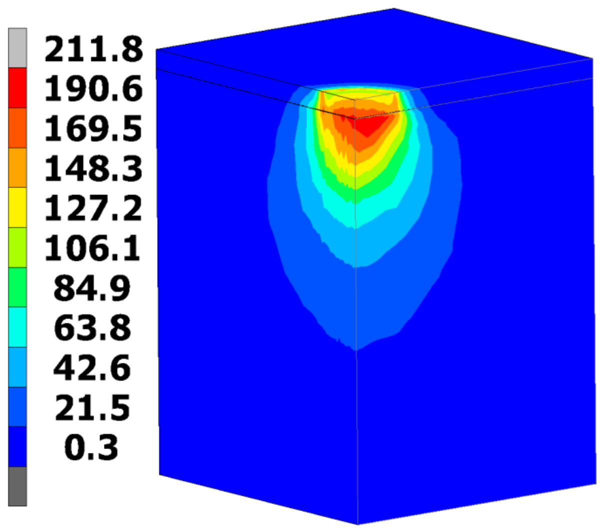

Figure 23. Von Mises stress distribution in specimen B in the 25th cycle

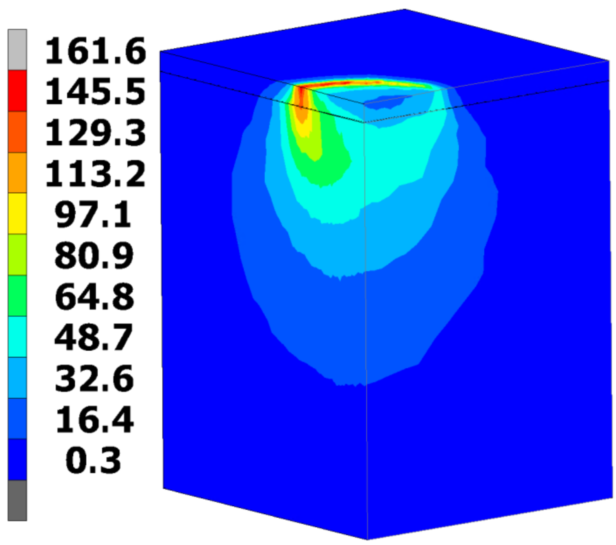

Figure 24. Von Mises stress distribution in specimen B in the 188th cycle

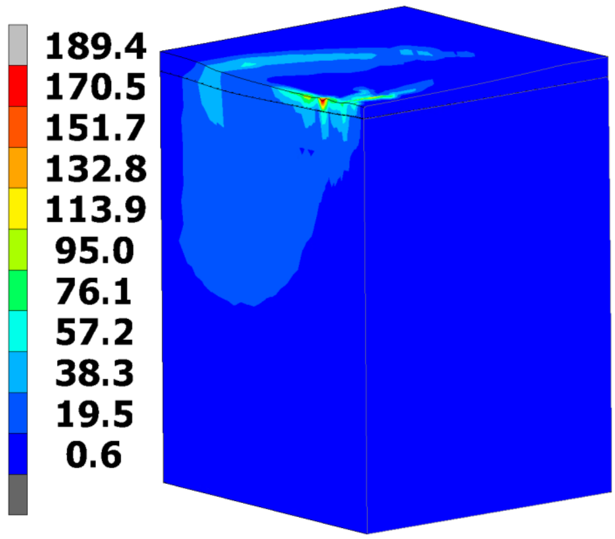

Figure 25. Von Mises stress distribution in specimen B in the 5919th cycle

The changes of the distribution of the Von Mises stress inside of the specimen B can be seen in Figs. 22-26. In the beginning of the process, until 180th-200th cycle, the maximum of Von Mises stress locates under the mating surface inside of the body.

In case of the first cycles, the Von Mises stress reaches its maximum value below the mating surfaces of 25 μm which is much larger distance than the thickness of tin layer (Figs. 22-23).

However, in case of larger cycles, the maximum of the Von Mises stress moves to the mating surface (Figs. 24-26). This phenomenon accelerates the crack initiation and propagation in the surface layers, i.e. the contact fatigue, and tearing of small pieces out of the body.

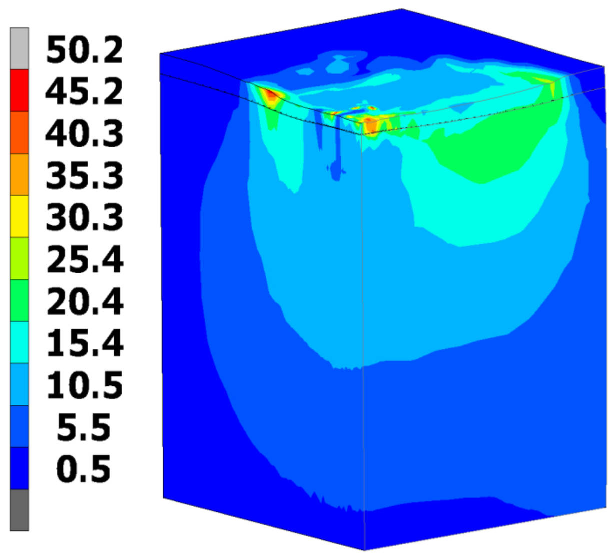

Figure 26. Von Mises stress distribution in specimen B in the 5937th cycle

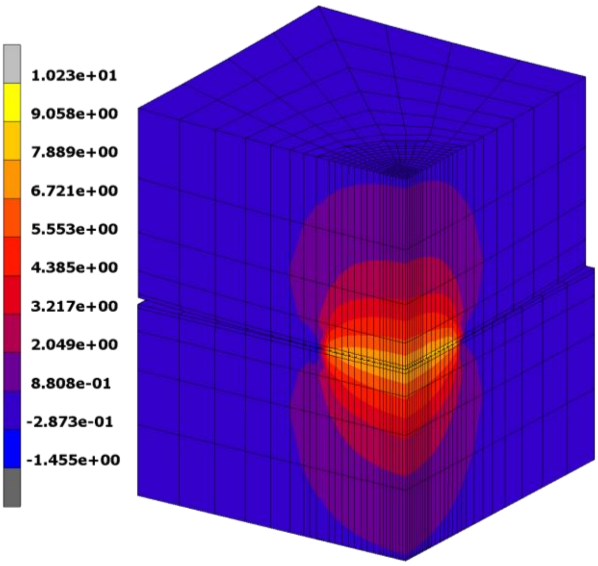

Figure 27. Current density distribution in the beginning of the wear process

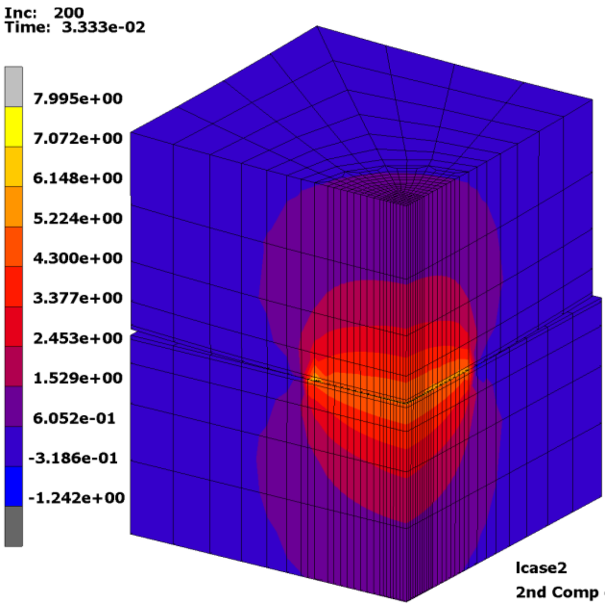

Figure 28. Current density distribution in the 5937th cycle

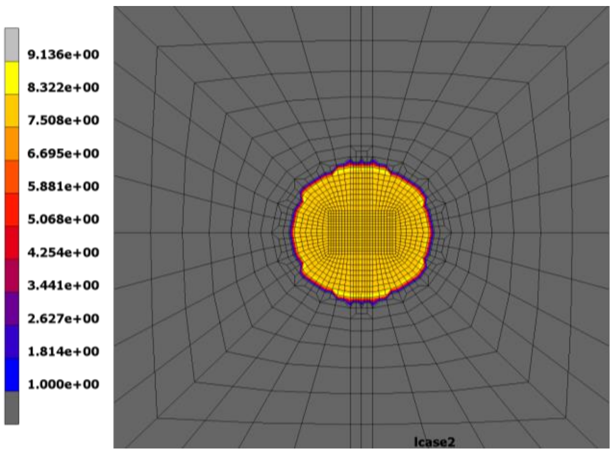

Figure 29. Current density distribution on the contact surface in the beginning of the wear process

The electrical analysis can be seen in Figs. 27-29. It can be seen that in the wear stage of the lifetime, the area where the current flows between the two contact bodies is equal to the contact area. In the initial phase, the current density in this area is evenly distributed, only with the exception of a 9 µm band on the boundary (Fig. 29).

The thermal analysis showed that there is only 3 °C temperature rise in the experimental specimens which distribution is quasi-homogeneous, even with the consideration of the Joule and friction heat. This result coincides with the results of temperature measurements performed during the experiments.

5. CONCLUSION

In this work, a procedure was developed comprising of experimental and numerical calculation methods to analyse the ability of fretting corrosion failure of electrical connectors of cooling fans used in electrical cars.

In order to better understand of the contact conditions of the electrical connector, test specimens were made from material of the connector and carried out fretting experiments with them.

Lifetime curves similar to the short cycle fatigue strain-cycle diagram were determined by electrical resistance measurements during fretting tests. In these diagrams, amplitude-cycle relationships are determined in case of fixed parameters.

In our case, it was found that there was a value similar to the endurance limit in the case of amplitude, where practically endless life belongs to the value smaller than this limit. The effect of the load force and the pre-aging on the lifetime curves were examined. Lifetime was increased with increasing load, while aging was significantly reduced lifetime and amplitude limit for practically endless life.

In addition, the evolution of the fretting wear process was examined by measuring the sizes of the wear trace as a function of the number of cycles within a given lifetime. In our study, it was found that a 10-11 µm deep crater was worn out quickly compared to the total lifetime, and then the corrosion of the resulting copper-copper contact surface led to the failure of the electrical connector. The fretting wear process takes place during the sixth life, and then no significant wear can be detected.

Numerical coupled FEM model was built that allowed us to carry out structural, wear, electrical, thermal analysis in the knowledge of the measured transition electrical resistance increase. The coupled model was validated using the measurements of crater size of the wear process and determined the specific wear rate for the particular case.

Structural analysis of the validation measurements was shown the change in the contact trace and movement of points of maximum of Von Mises stress from inside the body to the surface as fretting cycles increase, which accelerates contact fatigue and tearing out of small particles from the surface. It was found that after 3-4% of number of cycles of the fast-wear, the maximum Von Mises stress is already on the contact surface, accelerating the formation of debris.

Examining the distribution of the current density of the validation measurements, it was found that the size of the A-spot was the same as that of the contact area and was distributed quasi-uniformly on this area in the initial cycles.

The temperature analysis showed that 3 °C temperature increase in the test specimens occurred during the whole lifetime, confirmed by measurements.

Complementing of our examining procedure by the thermodynamic analysis of corrosion and metallurgical processes can be used to create a knowledge base for the contact conditions of the tested electrical connectors, which can be used to develop accelerated standardized lifetime tests for the electric car industry.

ACKNOWLEDGEMENT

This research was supported by Bilateral Serbian-Hungarian project TÉT_16-1-2016-0164, the Bolyai Fellowship of the Hungarian Academy of Sciences, the únkp-18-4 new national excellence program of the Ministry of Human Capacities and National Research, Development and Innovation Office - NKFIH, K115701 project, titled „Some selected problems in computational mechanics” furthermore by the European Union and the Hungarian State, co-financed by the European Regional Development Fund in the framework of the GINOP-2.2.1-15-2017-00090 project, titled „E-mobility from Miskolc: Improvement of Coolant Pump and Engine Cooling Fan Taking into Account the Higher Quality Requirements in Electric Vehicles”.

REFERENCES

[1] J. Laporte, O. Perrinet, S. Fouvry: Prediction of the electrical contact resistance endurance of silver-plated coatings subject to fretting wear using a friction energy density approach, Wear, Vol. 330-333, pp. 170–181, 2015.

[2] X.Y. Ji, Y.P. Wu, B.H. Lu, V.C. Pascucci: Fretting corrosion degradation of non-noble metal coated contact surfaces: a theoretical model, Tribol. Int., Vol. 97, pp. 31–37, 2016.

[3] P. Jedrzejczyk, S. Chad, S. Fouvry, P. Chalandon: Impact of the nickel interlayer on the electrical resistance of tin–tin interface submitted to fretting loading, Surf. Coat. Technol., Vol. 203, pp. 1624–1628, 2009.

[4] W. Ren, P. Wang, Y. Fu, C. Pan, J. Song: Effects of temperature on fretting corrosion behaviors of gold-plated copper alloy electrical contacts, Tribol. Int., Vol. 83, pp. 1–11, 2015.

[5] T.S.N.S. Narayanan, Y.W. Park, K.Y. Lee: Fretting corrosion of lubricated tin plated copper alloy contacts: effect of temperature, Tribol. Int., Vol. 41, pp. 87–102, 2008.

[6] S. Hannel, S. Fouvry, Ph. Kapsa, L. Vincent: The fretting sliding transition as a criterion for electrical contact performance, Wear, Vol. 249, pp. 761–770, 2001.

[7] J.F. Archard: Contact and rubbing of flat surfaces, J. Appl. Phys., Vol. 24, pp. 981–988, 1953.

[8] J.M.J. Challen, P.P.L.B. Oxley, B.S.B. Hockenhull: Prediction of Archard's wear coefficient for metallic sliding friction assuming a low cycle fatigue wear mechanism, Wear, Vol. 111, No. 3, pp. 275–288, 1986.

[9] L. Rodriguez-Tembleque, R. Abascal, M.H. Aliabadi: A boundary elements formulation for 3D fretting-wear problem, Eng. Analysis Bound. Elem., Vol. 35, pp. 935–943, 2011.
[10] I.R. McColl, J. Ding, S.B. Leen: Finite element simulation and experimental validation of fretting wear, Wear, Vol. 256, pp. 1114–1127, 2004.
[11] J. Ding, I.R. McColl, S.B. Leen, P.H. Shipway: A finite element based approach to simulating the effects of debris on fretting wear. Wear, Vol. 263, pp. 481–491, 2007.
[12] P.H. Shipway, E.J. Williams, S.B. Leen, J. Ding: A multi-scale model for fretting wear with oxidation-debris effects, Proc. Inst. Mech. Eng. Part J, J. Eng. Tribol., Vol. 223, pp. 1019–1031, 2009.
[13] A. Cruzado, S. B. Leen, M. A. Urchegui, X. Gómez: Finite element simulation of fretting wear and fatigue in thin steel wires, International Journal of Fatigue, Vol. 55, pp. 7-21, 2013.
[14] N. Ohmae, T. Tzukizoe, Wear, Vol. 27 p. 281, 1974.
[15] P. Kennedy, L. Stallings, M. B. Peterson, ASLE Trans., Vol. 27, p. 305, 1984.
[16] S. Siiderberg, T. Colvin, K. Salama, 0. Vingsbo, J. Eng. Mater. Technol., Vol. 108, p. 153, 1986.
[17] S. Soderberg, U. Bryggman, T. McCullough, Wear, Vol. 110, p. 19, 1986.

Serbian Tribology Society

SERBIATRIB '19

16th International Conference on Tribology

Faculty of Engineering University of Kragujevac

Kragujevac, Serbia, 15 – 17 May 2019

EVALUATION OF SOLDERING RESISTANCE OF CrAlN COATINGS INTENDED FOR APPLICATION ON HIGH PRESSURE DIE CASTING TOOLS

Dragan KUKURUZOVIĆ*[1], Pal TEREK[1], Lazar KOVAČEVIĆ[1], Branko ŠKORIĆ[1], Aleksandar MILETIĆ[1], Peter PANJAN [2], Miha ČEKADA[2]

[1]University of Novi Sad, Faculty of technical sciences, Trg Dositeja Obradovića 6, 21000, Novi Sad, Serbia, kukuruzovic@uns.ac.rs

[2]Jožef Stefan Institute, Ljubljana, Slovenia

*Corresponding author: kukuruzovic@uns.ac.rs

Abstract: *During high-pressure die casting (HPDC) of aluminum alloys the tool surfaces are exposed to extreme conditions as high temperatures, molten metal impact at high velocities, high pressure, corrosive environment, alternate heating and cooling cycles and abrasive wear. In such conditions tool surfaces suffer from thermal fatigue, erosion and soldering wear. As a result of tool wear, machine downtime and tool maintenance increases which cause significant financial losses. To reduce these losses and to extend the tool life, HPDC tool surfaces are submitted to plasma diffusion treatments and deposition of PVD (Physical Vapor Deposition) coatings. Therefore, in this study, the performance of duplex CrAlN coatings with three different chemical compositions was evaluated. The performance of the coatings was investigated in term of its soldering tendency to Al-Si-Cu alloy, using a detachment test. This test involves formation of a cylindrical casting on flat coated surfaces which is detached after the solidification and a required force is recorded. After detachment the analyses of contact surfaces reveal the soldering mechanisms and a sticking tendency of cast alloy toward investigated surfaces. For these purposes we employed 3D profilometry and different microscopy techniques. The cast alloy is kept in contact with the investigated coatings for four predetermined periods of time. The scanning electron microscopy (SEM), on all coatings, revealed the remnants of cast alloy (solder) after detachment tests and also a prominent coating delamination. The soldered area for different coatings has the same trend for different periods of contact with molten alloy. However, the amount of coatings delaminated area is different and closely correlates with samples detachment force. Higher detachment force is addressed to larger coating delamination area. It was found that the chemical composition of investigated coatings has modest influence on the soldering phenomena.*

Keywords: *HPDC tool, aluminum alloy, duplex treatment, PVD coatings, soldering*

1. INTRODUCTION

HPDC is a mass production process in which molten metal is injected into steel die (tool) at high velocities and employing high pressures. Rapid casting solidification is achieved by cooling lines in the tool walls. The process is used for casting aluminum, magnesium and zinc alloys. HPDC products are applied for wide variety of applications and can be found in everyday life all around us. Typical representatives of casted aluminum are parts of different devices, housings for mobile phones, engine parts, decorative parts, structural car parts, etc.

During the HPDC process, tool is exposed to extreme environment which cause thermal shock, oxidation, erosion, corrosion and soldering [1]. Cast alloy soldering represent one of the greatest issues in modern HPDC industry because it reduces both casting quality and process productivity [2]. In a soldering process cast alloy (casting) “welds” to the surface of the metallic die and forms a firm bond between them [3]. Such process hampers the casting ejection, cause defects on casting surfaces, damages the HPDC tool surfaces and endanger it integrity. All these effects beside the shortening of a die life increase machine downtime due to increased tool maintenance.

The cast alloy soldering is prevented by spraying of a liquid lubricant on die surfaces before each casting cycle. Considering that HPDC is a mass production process, significant amount of lubricant during is used in this production process. The amount of used lubricant takes a serious part in production costs by this technology. Additionally, excessive use of lubricant has harmful influence on the environment.

In order to reduce negative effect of a lubricant, numerous studies have been conducted in the field. One group of investigations directed toward application of permanent protective layers on tool surfaces to improve their corrosion and soldering resistance [1, 4]. For these purposes, different types of surface treatments were investigated. The most successful treatments so far are conducted by plasma processes, such as plasma nitriding, coating deposition by PVD processes and combination of these, the duplex treatments [4].

This study aimed to investigate the interaction of Al-Si-Cu alloy with duplex treated hot-working tool steel surfaces, using a detachment test. Focus was on the bonding (detachment) force achieved between the casting and the sample and on the soldering effects on coated surfaces. It was assumed that different compositions of CrAlN nanolayered coatings would display different performance under soldering conditions.

2. MATERIALS AND EXPERIMENTAL

Disc shaped samples (ϕ30 x 5 mm) used in this experiment were produced of EN X27CrMoV51 hot-working tool steel in a quenched and double tempered condition. Samples (contact) surfaces were submitted to grinding by sandpapers of different grades (grits), from the roughest to the finest (360, 500, 1000 and 2000). After surface preparation, plasma nitriding was carried out in an industrial nitriding unit ION-25I (IonTech) equipped with a pulsed plasma generator. Nitriding was conducted for 12 h at a temperature of 510 °C using a gas ratio of H_2:N_2=3:1, and by applying a 0.6 duty cycle. The compound layer that formed during the plasma nitriding process on the sample contact surface was removed before the deposition of the CrAlN coatings. The compound layer was removed by diamond paste polishing technique using 3 µm paste granulation. The removal was done in order to produce duplex layers with high adhesion and high heat resistance.

Nanolayered CrAlN coating was deposited using an industrial DC-magnetron sputtering system CC800/9 (CemeCon). The coating was produced with three different chemical compositions. Different compositions were obtained employing a special approach with triangular sputtering targets. The whole process of a nanolayered architecture required four targets. Two regular rectangular targets one Cr and one Al, and to triangular-segmental Cr/Al targets. Different composition is achieved at different heights in the chamber. The deposition process was performed using a 2-fold samples rotation. The sample denotations are as follows. The coating with balanced chemical composition is denoted as CrAlN, the coating with higher aluminum content as CrAlN-Al and the coating with higher chromium content as CrAlN-Cr.

The coating thickness was determined using a standard ball cratering test. The coatings adhesion was evaluated by Rockwell HRC test applying a force of 150 N. Surface topography of samples was acquired by 3-D stylus profilometer Talysurf (Taylor Hobson). Topographic measurements were analyzed by Mountainsmap and a Scanning Probe Image Processing software-SPIP (Image Metrology) software.

A laboratory test was employed for soldering evaluation, the detachment test. This test involves formation of a cylindrical casting on flat coated surfaces which is after the solidification detached from the surface. During detachment a force that is needed for casting detachment is measured and it represents a soldering tendency of paired materials.

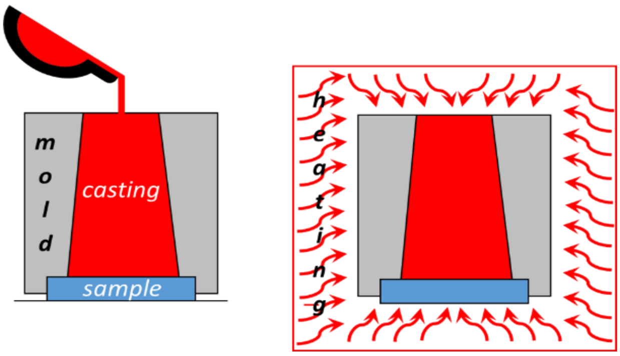

Figure 1. Schematic illustration of casting process

For casting experiment, the mold was made from castable heat-resistant refractory, based on Al_2O_3 ceramic. The schematic of the casting process is given in Figure 1. Before the casting process molds were preheated to 550 °C and samples to 300 °C. Casting process is performed by gravity pouring of molten Al-Si-Cu alloy (EN AB-46000) into the cavity. The cast alloy temperature was chosen to be 750 °C to achieve better flowability. The contact surface between the sample and the molten aluminum was set at ϕ22 mm. Considering the casting solidification, experiments were performed in two setups. In first setup, after pouring one group of samples was left immediately to solidify in ambient air, the so called 0-delay experiments. In second setup, after the pouring, the mold was placed in a furnace (heated to 700 °C), kept there for 10, 30 and 60 min to delay the solidification and afterwards taken out to allow casting to solidify in ambient air. These experiments were named 10; 30; 60 - delay experiments. The second group of experiments basically simulates a larger number of casting cycles which occur in industrial HPDC process.

A ZGIM 500 tensile tester was used to perform the detachment test and to measure the force needed to separate the casting from the coated samples.

After the test, both sample and casting surfaces were analyzed using digital camera D3200 (Canon), light optical microscope (LOM) Orthoplan (Leitz), Scanning Electron Microscope TH3030 (Hitachi). Image analyses of the surfaces with the built-up were also performed SPIP software,

3. RESULTS AND DISCUSIONS

The properties of investigated coatings are presented in Table 1. Although the coatings were deposited in a same production batch they resulted with different thickness. This is attributed to the effect of position (height) in deposition chamber. The number of coating defect varies from sample to sample. In Table 1. the average number of the area that is covered by coating defects and the average number of coating defects are given. The roughness of produced coatings is quite similar while the highest roughness of CrAlN-Cr coating is attributed to the highest density of average coating defects (crater and nodular). Figure 2 shows the results of HRC adhesion test. All produced coatings exhibited very good adhesion. CrAlN-Al coating has the best adhesion achieving HF1 level, while CrAlN coating exhibited HF2 and CrAlN-Cr coating the HF3 level of adhesion. The highest adhesion of CrAlN-Al coating is attributed to higher ductility achieved by thicker AlN nanolayers. The obtained levels adhesion and the observed coating ductility make these coatings appropriate for application on HPDC tools.

Figure 3 presents the values of detachment force recorded for investigated coatings which were subjected to different experimental setups. Detachment (sticking) force should be a measure of bonding strength achieved between casting and coating.

Table 1. Properties of Investigated coatings

Sample	Coating thickness [µm]	Sq [µm]	Coating defects density [num/mm^2]	Area of coating defects [nm^2]
CrAlN	5,7	0,192	185	119.7
CrAlN-Al	4,9	0,193	144	173.5
CrAlN-Cr	7,1	0,269	204	155.5

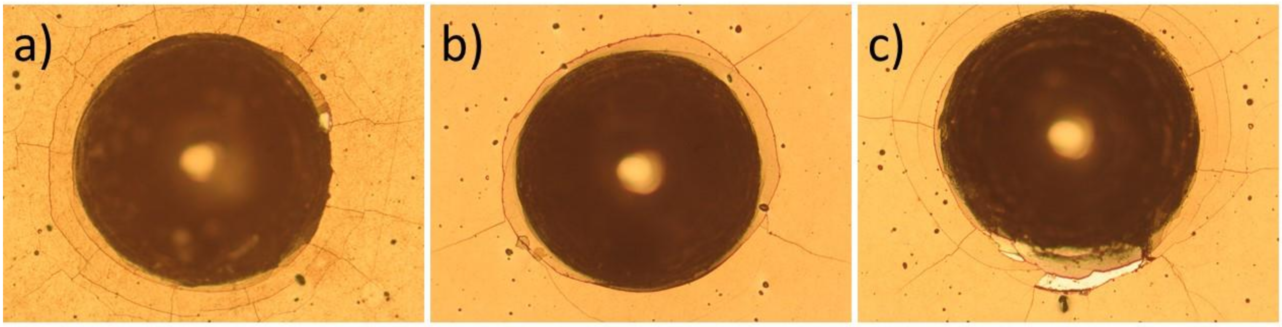

Figure 2. Results of Rockwell HRC adhesion test, a) CrAlN, b) CrAlN-Al and c) CrAlN-Cr coating

However, the sample surfaces indicate few different wear mechanisms which all have their contribution to the value of detachment force. These different components are: the bonding strength achieved between the casting and the coating, cohesive strength of soldered aluminum alloy and coating-substrate adhesion.

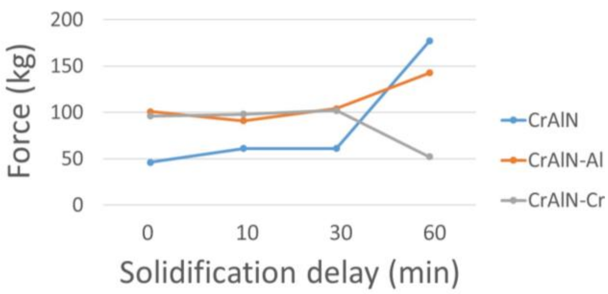

Figure 3. Detachment forces recorded for investigated coatings. Different experimental setups (period of contact with molten alloy) are presented on abscissa, 1= 0 min; 2 = 10 min; 3 = 30 min; and 4 = 60 min

For most of the investigated range of solidification delay periods CrAlN coating displayed the lowest ejection force. In the range of solidification delay from 0 to 30 min the values of detachment force determined for all investigated coatings does not change considerably with delay periods. For the experiment of 60 min solidification delay, the previously established trends completely change. CrAlN exhibit approximately three times higher detachment force, CrAlN-Al a slight increase and CrAlN-Cr coating exhibit almost double decrease of detachment force. Such results are mostly in agreement with results of cast alloy soldered areas and coating detachment areas, that are presented in paper.

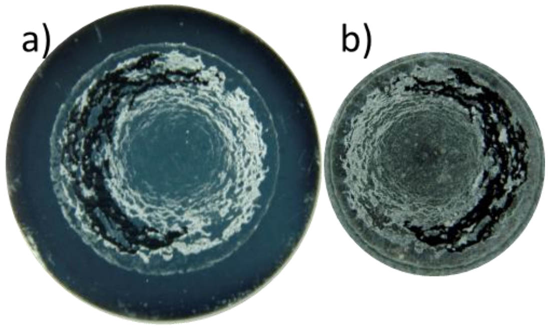

Figure 4. Appearance of CrAlN-Al 30min of solidification delay, a) sample and b) casting contact surfaces after detachment test

The appearance of coated sample surfaces and corresponding castings, after detachment tests, provide additional information about the soldering process. Using this information, the obtained detachment force can be explained and the inherent soldering mechanisms can be revealed. Figure 4 present a macroscopic image of the most representative coated sample (Figure 4 a) and its corresponding detached casting surface (Figure 4 b). The features on both elements correspond to each other. This is obvious when the images are specifically oriented to forms a mirror reflection of each other, see Figure 4. On both surfaces distinctive features can evidence the soldering process. LOM analysis revealed two distinctive soldering mechanisms. The first is that the cast alloy remained on coated surface in form of a soldering layer. The second is the coating detachment that occurred in these tests. Soldering layer can be seen as bright area, and spallation as dark area on the images of Figure 4. Analysis conducted on both coated sample and corresponding casting provide information on soldering processes that have detrimental effects which cause coating detachment from steel substrate surface.

In order to confirm typical wear features detected by LOM, after detachment test the coated samples were submitted to SEM and energy dispersive spectroscopy (EDS) analysis, Figure 5. In Figure 5a, a wider area with different kind of coating damage is presented. In that image a soldered layer can be clearly distinguished from detached coating and the intact coating area. All these features were confirmed by EDS analyses enclosed in the figure. The location shown in Figure 5b is an area with intact coating layer. However, the area nearby is the area where coating detachment occurred. At the area with intact coating, soldering is not detected, which agrees with findings published in literature that ceramic coatings do not wet with liquid aluminum alloy [5]. However, this does not agree with the fact that soldering layer can be found on a considerable area of coated samples, as shown in Figures 4 a and 5 a. The inherent coating delamination and soldering mechanisms were not revealed in this analysis.

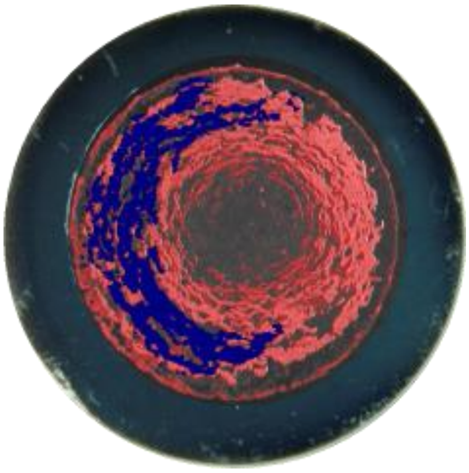

Figure 6. Representative image analysis, CrAlN-Al 30min

In order to quantify the soldering and coating detachment that occurred on the coated samples software image analyses were conducted. Detection of different wear features is helped by coupling the findings from SEM and LOM analysis. In Figure 6, the process of image analysis is presented on example of CrAlN-Al sample in 30 min experiment delayed solidification experiment. In presented image the red color represents the area of soldering and the blue color represents the color of the detached coating area from the substrate.

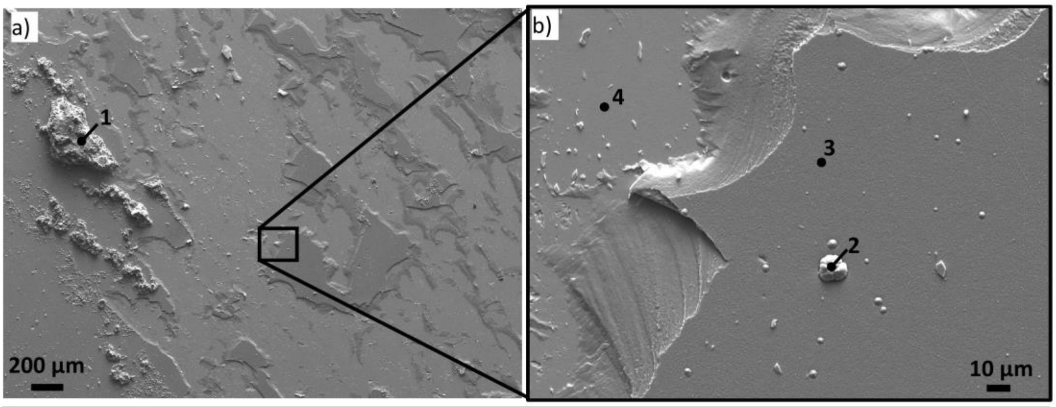

	Chemical composition [%]									
Spectrum	N [%]	O [%]	Al [%]	Cr	Fe	Si	Mo	V	C	Mn
1	-	3.22	52.81	16.52	15.49	0.91	-	-	8.9	2.13
2	24.58	1.84	8.6	64.61	0.38	-	-	-		-
3	22.13	1.62	9.22	67.04	-	-	-	-	-	-
4	3.19	-	-	5.49	86.51	1.08	1.16	0.33	2.24	-

Figure 5. SEM images of CrAlN-Cr sample subjected to 0 min delayed solidification, a) area with coating detachment and soldering; b) area with coating detachment, table presents EDS composition analysis

Figures 7 and 8 presents the quantitative results of image analysis used in soldering evaluation. There the areal coverage by cast alloy solder and detached (delaminated) coating area are presented for two experimental setups (30 and 60 min). For 30 min solidification delay, the amount of soldering and coating delamination closely correlates with measured detachment force presented in Figure 3. However, the amount of coating delamination has higher degree of correlation. The increase of detachment force is linked with more intensive coating delamination. This is obvious because the bond achieved between the coating and the substrate should be higher than one between the cast alloy and ceramic coating. CrAlN coating displayed the best performance in 30 min delayed solidification experiment.

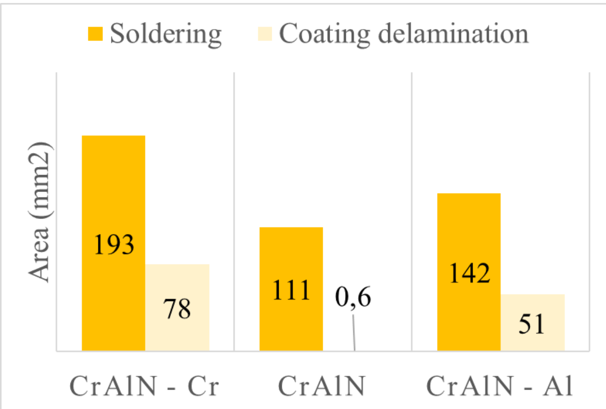

Figure 7. Areal coverage by soldering and area of coating delamination for 30 min delayed solidification

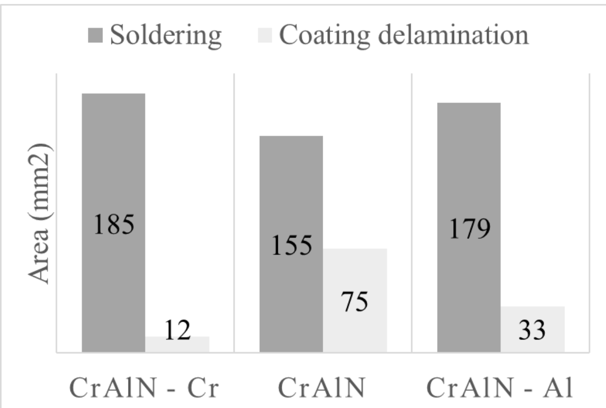

Figure 8. Areal coverage by soldering and area of coating delamination for 60 min delayed solidification

The quantitative results obtained for 60 min delayed solidification (Figure 8) display a similar trend of soldering area which is obtained for 30 min delay (Figure 7), but completely different values of coating delamination. However, once again, the coating delamination area has very good correlation with the detachment force. Such finding undoubtedly confirm that the value of detachment force dominantly depends on amount of coating delamination. CrAlN-Cr coating exhibited the best behavior in 60 min delayed solidification experiments.

A complete change of trends, in detachment force and areal coverage, between different coatings evaluated in 30 and 60 min delay experiments, remained unclear. We believe that such diversity in results can be explained by difference in the amount of coating growth defects between the same kind of samples which are used in different experiments (experimental points). In this investigation the coating defects density was not detailly monitored for every single sample.

4. CONCLUSIONS

From presented study the following conclusions are drawn.

- The investigated nanolayered CrAlN duplex coatings, of all three chemical composition, have appropriate properties for application on HPDC tools.
- For all investigated coatings and all experimental conditions, cast alloy soldering and coating spallation (detachment) was detected.
- The soldering mechanism and mechanisms that led to coatings deterioration (detachment from substrates) were not revealed in this study.
- CrAlN coating with balanced composition of Cr and Al, in most of the experimental conditions (contact durations with aluminum alloy) exhibited the lowest detachment force and smallest areas covered with cast alloy soldering. However, for the most severe experimental condition CrAlN coating with higher Cr content

displayed the smallest ejection force and coating spallation.

- The observed scatter of results obtained for two experimental points (delay periods) are addressed to the effects of coatings growth defects whose quantity were not monitored for every single sample in this investigation.
- The area of coatings delamination during detachment test has good correlation with samples detachment force. Such correlation was not found for the areal coverage by cast alloy solder.

The applied experimental method provides a new prospect on the evaluation of coatings soldering tendency. Its advantages are simplicity and a potential to acquire quantitative data on soldering resistance. However, some of techniques used in method have to be improved.

ACKNOWLEDGEMENT

This work was financially supported by the Serbian Ministry of Education, Science and Technological Development grant III-45006 and by the Provincial Secretariat for Higher Education and Scientific Research of Vojvodina, Serbia grant 114-451-2192/2016-02. We acknowledge GasTeh d.o.o. (Indjija, Serbia) for samples fabrication and Termometal d.o.o. (Ada, Serbia) for heat treatment

REFERENCES

[1] Z.W. Chen, M.Z. Jahedi: Die erosion and its effect on soldering formation in high pressure die casting of aluminium alloys, Mater. Des., Vol. 20, No. 6, pp. 303–309, 1999.

[2] P. Terek, L. Kovačević, A. Miletić, P. Panjan, S. Baloš, B. Škorić, D. Kakaš: Effects of die core treatments and surface finishes on the sticking and galling tendency of Al–Si alloy casting during ejection, Wear, Vol. 356–357, pp. 122–134, 2016.

[3] F. Gobber, A. Pisa, D. Ugues, S. Lombardo, E. Fracchia, M. Rosso: Study of the Effect of Surface—Roughness of Dies and Tooling for HPDC on Soldering, Light Metals, pp. 977–981. 2018.

[4] I. Peter, M. Rosso, F.S. Gobber: Study of protective coatings for aluminum die casting molds, Appl. Surf. Sci, Vol. 358, pp. 563–571, 2015.

[5] A. Salman, B.L. Gabbitas, P. Cao, D.L. Zhang: The performance of thermally sprayed titanium based composite coatings in molten aluminium, Surf. Coatings Technol, Vol. 205, No. 21–22, pp. 5000–5008, 2011.

[6] M. Rosso, I. Peter, F.S. Gobber: Overview of heat treatment and surface engineering, influences of surface finishing on hot-work tool steel, Int. J. Microstruct. Mater. Prop, Vol. 10, nNo. 1, p. 3, 2015.

Tribology of
Machine Elements and Systems

16th International Conference on Tribology – SERBIATRIB '19

15 – 17 May 2019, Kragujevac, Serbia

Serbian Tribology Society

SERBIATRIB '19

16th International Conference on Tribology

Faculty of Engineering University of Kragujevac

Kragujevac, Serbia, 15 – 17 May 2019

EVALUATION OF THE KINETIC FRICTION COEFFICIENT BY USING „DISC-BLOCK" FRICTION PAIR OF DIFFERENT WOODEN SAMPLES

Djordje VUKELIC[1,]*, Zeljko SANTOSI[1], Mario SOKAC[1], Igor BUDAK[1], Tomislav SARIC[2], Goran SIMUNOVIC[2], Branko TADIC[3]

[1]University of Novi Sad, Faculty of Technical Sciences, Novi Sad, Serbia

[2]Josip Juraj Strossmayer University of Osijek, Mechanical Engineering Faculty, Slavonski Brod, Croatia

[3]University of Kragujevac, Faculty of Engineering, Kragujevac, Serbia

*Corresponding author: vukelic@uns.ac.rs

Abstract: *The paper presents the measurement results of the kinetic friction coefficient on wooden specimens. The measurements were carried out according to the „disc-block" friction pair method. Blocks and discs are made of five different types of wood - beech, ash, oak, pine, and fir. Experimental investigations were performed for different values of disc speed (rpm) and with different normal loads on the block. The obtained results indicate that the contact pairs of wood with higher surface hardness have higher values of the kinetic friction coefficient and vice versa. The values of the kinetic friction coefficient had approximately constant values for different experimental conditions with the tendency of a slight decrease while increasing normal load and the speed (number of rpm).*

Keywords: *friction, wood, kinetic friction coefficient, „disc-block" friction pair.*

1. INTRODUCTION

Wood is a natural, heterogeneous, and hygroscopic material characterized by a number of positive properties, such as easier machining, acceptable price, low thermal conductivity, etc. [1]. In order to predict the behaviour of the wood under different exploitation conditions, and to take its advantages and eliminate disadvantages, first of all, one should be well familiarized with its aesthetic, technological, mechanical and physical properties. Knowledge of tribological properties is one of the main prerequisites for the proper exploitation of contact pairs made of wood [2].

Friction is a complex phenomenon that occurs between contacting surfaces. Experiments indicate the functional dependence of friction from a different number of parameters, such as materials, velocity, contact pressures, temperature, normal load, humidity, surface preparation, etc. Friction and wear contact pairs are held in complex exploitation conditions. In most cases, in various moving elements, friction is undesirable and harmful occurrence, and a considerable amount of mechanical energy is used to overcome the friction force [3]. As a result of friction on the contact surfaces, it leads to wear and increased heat between materials in contact [4].

The tribological characteristics of the elements of tribomechanical systems can be quantified by the intensity of the friction force, i.e., the friction coefficient [5].

Two types of friction coefficients can be distinguished [6]:

- static friction coefficient (μ_s) - represents the friction opposing the onset of relative motion (impending motion),
- kinetic friction coefficient (μ_k) - represents the friction opposing the continuance of relative motion once that motion has started.

Friction coefficients are defined as [6]:

$$\mu_s = F_s / F_n \quad (1)$$

$$\mu_k = F_k / F_n \quad (2)$$

where F_s is the force just sufficient to prevent the relative motion between two bodies, F_k is the force needed to maintain relative motion between two bodies, and F_n is the force normal to the interface between the sliding bodies.

Friction is an important factor to be taken into account when different types of wooden materials are utilized or processed. Friction coefficients depend on the moisture content of the wood, surface roughness of the wood, and the characteristics of the opposing surface. They vary little with different types of wood. Static friction coefficient is generally greater than those of kinetic friction, and the latter depend somewhat on the sliding speed. Kinetic friction coefficients vary only slightly with speed when the wood moisture content is less than about 20%; at high moisture content, the kinetic friction coefficient decreases substantially as speed increases [7].

Several investigations on friction of wood-based materials have been published.

Desaguliers presented data which yield coefficients of friction for unlubricated sliding of wood on wood between 0.35-0.5. Coulomb measured static friction coefficients from 0.43 to 0.67 for various samples of unlubricated wood sliding against wood, and found that lubrication with tallow reduced the values to 0.1-0.2. Bowden and Tabor reported a value of 0.6 for dry wood sliding on steel, while Rabinowicz provided data ranging from 0.45 to 0.5 for wood sliding on steel [8].

Further, Blau [6] presented friction coefficients for different wood. The values of the static friction coefficient ware in the range of 0.25 to 0.7, and the values of the kinetic friction coefficient ware in the range of 0.19 to 0.5. Glass and Zelinka [7] reported kinetic friction coefficients for different types of wood. Coefficients of kinetic friction for smooth, dry wood against hard, smooth surfaces commonly range from 0.3 to 0.5; at intermediate moisture content, 0.5 to 0.7; and near fiber saturation, 0.7 to 0.9. Seki et al. [9] evaluated the friction characteristics of wood during deformation processing with relatively high levels of pressure. The nominal friction coefficient remained at almost constant value during sliding, or it increased slightly immediately after sliding was started under each testing condition. Seki et al. [10] measured friction coefficient between metal tools and phenol formaldehyde resin-impregnated wood specimens during compression in the tangential direction at high pressure. The static friction coefficient decreased with an increase in the phenol formaldehyde resin concentration. Pitenis et al. [11] measured friction for various wood blocks sliding on a wood surface. The values of the static friction coefficient were in the range of 0.35 to 0.72. The values of static friction coefficient under dry, clean, smooth, and sanded conditions were 0.72±0.04. Eliminating sanding from the experimental procedure lowers the static friction coefficient (0.44±0.04), and introducing fine Olive wood sawdust on the sliding surfaces achieves an average static friction coefficient of 0.35±0.03. When sliding blocks are used with roughly cut surfaces sullied by the natural oils, those static friction coefficients were 0.25±0.03. Aira et al. [12] reported preliminary results of static and kinetic friction coefficients for softwood (scots pine). Friction coefficients between transverse surfaces were roughly twice as the friction coefficients between radial surfaces. Xu et al. [13] measured friction coefficients of solid wood for a “wood–wood” frictional pair under varying wood grain. The results showed that the friction coefficients of the solid wood increased linearly with the arithmetic mean deviation of the surface profile - Ra. Sathre and Gorman [14] determined the static and kinematic friction coefficient at three load stress levels for maple bearings treated. Without the presence of lubricants, static friction coefficient had a value of about 0.45 while a kinetic friction coefficient had a value of about 0.35.

Unlike with previous research, the aim of this study is to determine the kinetic friction coefficients of samples made from different types of wood, as well as for different values of normal load and speed (rpm).

2. MATERIALS AND METHODS

For the experimental investigations (Figure 1) a tribometer is used to test the tribomechanical properties of various materials, in conditions with and without lubricant.

Figure 1. Tribometer used for evaluation of the kinetic friction coefficient

Measurements of kinetic friction coefficient were carried out on a „disc-block" friction pair. Figure 2 shows the scheme for wear testing using „disc-block" friction pair on a tribometer. The contact between two surfaces is achieved on 2D line. During measurements different values of normal load on the block (F_n) and the number of disc rotations (n) were used and values of the kinetic friction coefficient for different contact pairs were obtained.

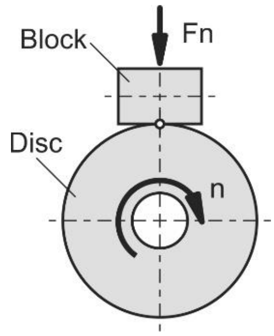

Figure 2. Scheme for wear testing using „disc-block" friction pair

Disc and block samples, used for carrying out experimental investigations, were made of five different types of wood - beech, ash and oak classified as hardwoods as well as two softwoods pine and fir. The geometry of the disk and the block are shown in Figure 3.

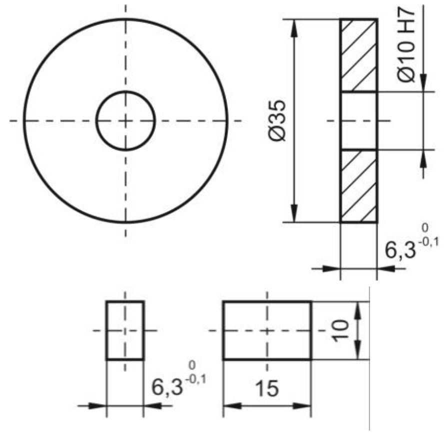

Figure 3. Geometry of disk and block

Before conduction the test, few steps were required in order to control the measurement conditions. First, raw woods (for all samples) were dried in a furnace to a moisture content of <3%. This is required due to the possibility of formation of small cracks or deformation on the surface of the wooden samples prior to their drying. After drying a total of 30 samples were made for each type of wood. Next, the physical and mechanical properties of all samples were measured. The mean arithmetic values and standard deviations of the physical and mechanical properties of the samples are shown in Table 1.

Table 1. Mean arithmetic values and standard deviations (SD) values of all samples

Characteristics	Beech		Ash		Oak		Pine		Fir	
	Mean	SD	Mean	SD	Mean	SD	Mean	SD	Mean	SD
Hardness HB	77	1.554	76	1.734	75	1.943	35	2.212	39	2.256
Modulus of elasticity E (GPa)	17	0.567	14	0.854	12	0.934	12	0.954	11	1.031
Tensile strength Rm (N/mm^2)	142	2.211	182	2.781	102	2.397	112	3.279	86	2.989
Roughness Ra (µm)	1.604	0.005	1.605	0.006	1.606	0.005	1.603	0.009	1.604	0.008

Table 2. The mean arithmetic values of the kinematic friction coefficient and standard deviation

Contact type	*n* (rpm)	F_n (N)									
		10		15		20		25		30	
		$\bar{\mu}$	σ_μ	$\bar{\mu}$	σ_μ	$\bar{\mu}$	σ_μ	$\bar{\mu}$	σ_μ	$\bar{\mu}$	σ_μ
Beech-beech	100	0.36	0.008	0.35	0.009	0.35	0.007	0.35	0.011	0.35	0.009
	120	0.35	0.008	0.35	0.009	0.35	0.009	0.35	0.010	0.35	0.008
	140	0.35	0.009	0.35	0.007	0.35	0.010	0.35	0.009	0.35	0.011
	160	0.35	0.010	0.35	0.010	0.35	0.009	0.34	0.011	0.34	0.010
	180	0.34	0.010	0.34	0.010	0.34	0.009	0.34	0.011	0.33	0.010
Ash-ash	100	0.35	0.008	0.34	0.009	0.34	0.007	0.34	0.011	0.33	0.009
	120	0.34	0.008	0.34	0.007	0.34	0.009	0.34	0.010	0.33	0.008
	140	0.34	0.007	0.34	0.008	0.34	0.010	0.33	0.009	0.33	0.009
	160	0.34	0.010	0.34	0.010	0.34	0.008	0.33	0.011	0.32	0.010
	180	0.34	0.010	0.34	0.010	0.33	0.009	0.32	0.010	0.32	0.007
Oak-oak	100	0.31	0.008	0.30	0.011	0.29	0.007	0.29	0.011	0.29	0.009
	120	0.30	0.008	0.29	0.009	0.29	0.009	0.29	0.010	0.29	0.011
	140	0.29	0.009	0.29	0.009	0.29	0.011	0.29	0.009	0.28	0.011
	160	0.29	0.010	0.29	0.011	0.29	0.009	0.28	0.011	0.28	0.010
	180	0.29	0.010	0.29	0.010	0.29	0.011	0.28	0.010	0.27	0.010
Pine-pine	100	0.24	0.012	0.23	0.009	0.22	0.007	0.21	0.011	0.21	0.009
	120	0.23	0.008	0.22	0.009	0.22	0.009	0.21	0.010	0.21	0.011
	140	0.22	0.009	0.22	0.009	0.22	0.011	0.21	0.009	0.21	0.011
	160	0.22	0.011	0.22	0.011	0.22	0.011	0.21	0.011	0.20	0.011
	180	0.21	0.011	0.21	0.011	0.21	0.010	0.20	0.010	0.20	0.012
Fir-fir	100	0.23	0.012	0.22	0.007	0.21	0.007	0.20	0.011	0.19	0.009
	120	0.22	0.011	0.21	0.009	0.20	0.009	0.19	0.008	0.19	0.010
	140	0.21	0.009	0.20	0.009	0.19	0.010	0.19	0.009	0.19	0.008
	160	0.20	0.011	0.20	0.010	0.19	0.009	0.19	0.010	0.19	0.011
	180	0.20	0.009	0.19	0.009	0.19	0.009	0.19	0.009	0.18	0.008

3. RESULTS

Experimental investigations were carried out for five different normal load values (F_n=10, 15, 20, 25, 30 N), and five different disc speeds (n=100, 120, 140, 160, 180 rpm). The actual values of the kinetic friction coefficient were recorded for 60 seconds for each measurement. Investigations were carried out at a constant temperature of 23°C, the pressure of 1 bar, and humidity of 55% for all samples. For each value of rpm and normal load a total of 30 measurements of the kinetic friction coefficient were captured. The mean arithmetic values of the kinetic friction coefficient and standard deviations are shown in Table 2 and Figure 4.

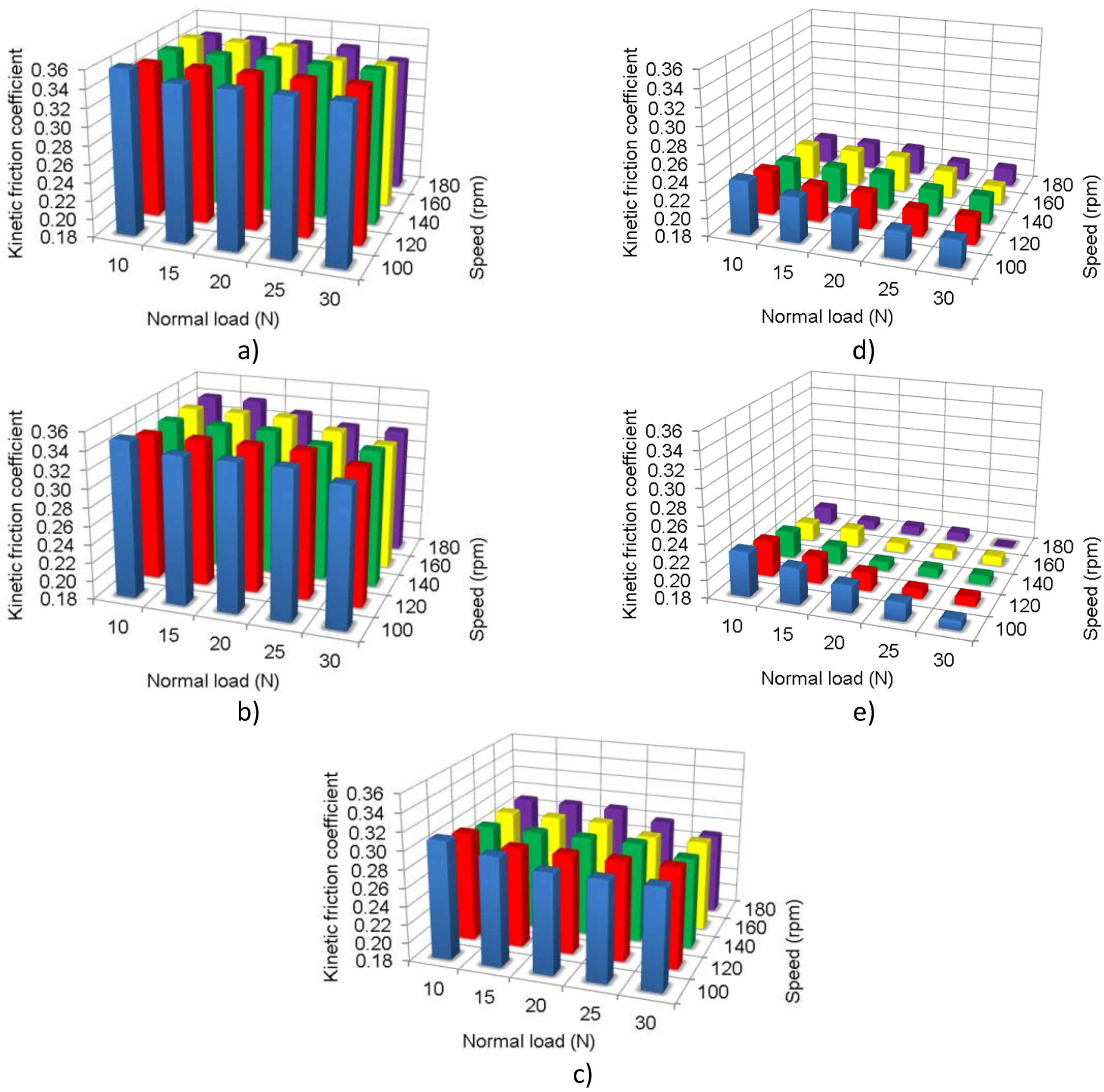

Figure 4. The mean arithmetic values of the kinetic friction coefficient for different values of normal load and speed (rpm): a) contact pair beech-beech, b) contact pair ash-ash, c) contact pair oak-oak, d) contact pair pine-pine, ande) contact pair fir-fir

For different contact pairs different kinetic friction coefficients are evaluated, as follows:

- The contact pair beech-beech has the mean value of the kinetic friction coefficient in the range of 0.33 to 0.36,
- The contact pair ash-ash has the mean value of the kinetic friction coefficient in the range of 0.32 to 0.35,
- The contact pair oak-oak has the mean value of the kinetic friction coefficient in the range of 0.27 to 0.31,
- The contact pair pine-pine has the mean value of the kinetic friction coefficient in the range of 0.20 to 0.24,
- The contact pair fir-fir has the mean value of the kinetic friction coefficient in the range of 0.18 to 0.23.

The higher values of the kinetic friction coefficient were obtained for wood characterized by higher hardness and modulus of elasticity, and vice versa. The kinetic friction coefficient has the highest values for beech wood and the lowest values for fir wood samples.

For all contact types, the mean values of the kinetic friction coefficient have:

- The highest values for the smallest number of rpm and the lowest value of the normal load,
- The lowest values for the maximum number of rpm and the maximum value of the normal load.

The mean value of the kinetic friction coefficient for certain speeds (rpm) has approximately constant value, with a slight tendency to decrease when increasing the normal load.

The mean values of the kinetic friction coefficient have a mild tendency of reduction with the increased speed for identical values of normal load.

4. CONCLUSION

Due to current trends which move towards the development and use of the tribomechanical systems without lubricant or with its minimum use, the experimental research has been carried out without the presence of a lubricant.

The mean value of the kinetic friction coefficient of contact pairs made from different types of wood ranges from 0.18 to 0.36. Higher values of the kinetic friction coefficient for contact pairs made of hardwood were obtained. For all contact pairs, it can be noticed that the kinetic friction coefficient has approximately a constant value with a low dissipation. In accordance to this, kinetic friction coefficient has a slight tendency to decrease at a higher speed (rpm) and the higher normal load.

The future research will focus on the measurements of the kinetic friction coefficient of contact pairs made of other types of wood that have different mechanical and physical characteristics, and under different experimental conditions (contact types, micro kinetic parameters, different speeds, normal loads, etc.).

REFERENCES

[1] B. Luo, L. Li, M. Xu, H. Liu, F. Xing: Analysis of Static Friction Coefficient Between Work-piece and Rubber Belt in Sanding Wood-Based Panel, BioResources, Vol. 9, No. 4, pp. 7372-7381, 2014.

[2] W. Yin, Z. Liu, P. Tian, D. Tao, Y. Meng, Z. Han, Y. Tian: Tribological properties of wood as a cellular fiber - reinforced composite, Biotribology, Vol. 5, pp. 67-73, 2016.

[3] P. Beer: In situ examinations of the friction properties of chromium coated tools in contact with wet wood, Tribology Letters, Vol. 18, No. 3, pp. 373–376, 2005.

[4] R. Bendikiene, G. Keturakis: The influence of technical characteristics of wood milling tools on its wear performance, Journal of Wood Science, Vol. 63, No. 6, pp. 606-614, 2017.

[5] M. Ciavarella: Modeling and simulation in tribology across scales: An overview, Tribology International, Vol. 125, pp. 169-199, 2018.

[6] P.J. Blau: The significance and use of the friction coefficient, Tribology International, Vol. 34, No. 9, pp. 585-591, 2001.

[7] V. S. Glass, L. S. Zelinka: Moisture Relations and Physical Properties of Wood, in R. J. Ross (Ed.), Wood Handbook: Wood as an Engineering Material, Madison, Wisconsin, pp. 1-19, 2010.

[8] I.M. Hutchings: Leonardo da Vinci’s studies of friction, Wear, Vol. 360-361, pp. 51-66, 2016.

[9] M. Seki, H. Sugimoto, T. Miki, K. Kanayama, Y. Furuta: Wood friction characteristics during exposure to high pressure: influence of wood/metal tool surface finishing conditions, Journal of Wood Science, Vol. 59, No. 1, pp. 10–16, 2013.

[10] M. Seki, S. Tanaka, T. Miki, I. Shigematsu, K. Kanayama: Friction characteristics between metal tool and wood impregnated with phenol formaldehyde (PF) resin during exposure to high pressure, Journal of Wood Science, Vol. 62, No. 3, pp. 233–241, 2016.

[11] A.A. Pitenis, D. Dowson, G.W. Sawyer: Leonardo da Vinci’s Friction Experiments: An Old Story Acknowledged and Repeated, Tribology Letters, Vol. 56, No. 3, pp. 509-515, 2014.

[12] J.R. Aira, F. Arriaga, G. Iniguez-Gonzalez, J. Crespo: Static and kinetic friction coefficients of Scots pine (Pinus sylvestris L.), parallel and perpendicular to grain direction, Materiales de Construccion, Vol. 64, No. 315, pp. e030, 2014.

[13] M. Xu, L. Li, M. Wang, B. Luo: Effects of Surface Roughness and Wood Grain on the Friction Coefficient of Wooden Materials for Wood–Wood Frictional Pair, Tribology Transactions, Vol. 57, No. 5, pp. 871–878, 2014.

[14] R. Sathre, T. Gorman: Improving the performance of wooden journal, Forest Products Journal, Vol. 55, No. 11, pp. 41-47, 2005.

Serbian Tribology Society

SERBIATRIB '19

16th International Conference on Tribology

Faculty of Engineering University of Kragujevac

Kragujevac, Serbia, 15 – 17 May 2019

DETERMINATION OF FRICTION AND WEAR BEHAVIOR OF ORGANIC DUSTS REINFORCED WITH THE BRAKE PADS BY USING TAGUCHI METHOD

Hasan ÖKTEM[1], Ilyas UYGUR[2], Gulsah AKINCIOĞLU[2], Sitki AKINCIOĞLU[2]

[1] Kocaeli University, Kocaeli, Turkey,

[2] Duzce University, Duzce/Turkey,

*Corresponding author:ilyasuygur@duzce.edu.tr

Abstract: *Brake pads play a major role in braking systems controlling the motions of automobiles. There are dozens of different friction materials in the brake pads. The braking performance of the brake pad depends on the content and amount of these powders. In recent years, importance has also been attached to the environmental friendliness of dust. In this study, the brake pad is manufactured with the addition of 3.5 % walnut shell dusts. The walnut shell dusts have been preferred in order to benefit from the local resources of our country. Hardness, density, water and oil absorption tests were applied to the brake pads. A specially designed tester was used for wear friction tests. Friction-wear tests were planned with Taguchi orthogonal L18 test set. Experiments were carried out by applying a pressure of 2 MPa. Variable temperature, speed and braking number are used. Due to the long duration of braking tests and high cost, the Taguchi optimization (Taguchi L18) method has been used to make the tests more efficient. The results obtained were compared with a commercial brake pad sample. The friction coefficient values of the commercial brake pad sample and the walnut added sample are similar. The friction coefficients obtained from the tester are in accordance with SAE J-661 standards.*

Keywords: *Brake pads, walnut shell dust, wear and friction, Taguchi method*

1. INTRODUCTION

The development of the automobile sector has increased studies on the brake pads. One of the most important parts of the braking system of automobiles is the brake pad, which is a composite material containing dozens of different materials. [1]. It is therefore possible to produce brake pads with very different contents. Powder materials in the components affect the braking performance of the brake pads [2]. In recent years, the search for natural dust additives has increased, especially after it has been found that asbestos fibers are harmful to human health [3]. It is also expected to be environmentally friendly as well as a good brake from an ideal brake pad. In their work, researchers examined the performance of brake pads that they produced using natural and environmentally friendly materials. Organic materials such as wollastonite, vermiculite, mica, basalt fiber, chopped glass fiber, ceramic fiber, rock wool, polyester and aramid fibers used in place of asbestos have similar performance characteristics [4]. Furthermore, agricultural, natural remnants and wastes have commenced to be used as new and inexpensive materials in the development of brake pads [5]. There are studies in the literature that are made with agricultural products such as banana shell, rice husk, hazelnut shell. [5-8].

In this study, walnut shell dust, which is harmless to the environment and health, was used as additive material in brake pads (W sample). A specially designed tester was used for wear friction tests. Friction-wear tests were planned with Taguchi orthogonal L18 test set. Experiments were carried out by applying a pressure of 2 MPa. Variable temperature, speed and braking number are used. Due to the long duration of braking tests and high cost, the Taguchi optimization (Taguchi L18) method has been used to make the tests more efficient. The results obtained were compared with a commercial brake pad sample (C sample).

2. MATERIAL AND METHODS

Brake pads are made of walnut shell dust which is added to 3.5% powder in addition to 17 different powder materials. Brake pads are produced by hot pressing. Load and temperature applied during the pressing of the brake pads is important for properly obtaining the pad. The production of the pads was carried out at a pressure of 100 kg / cm² at 180 ° C for 6 minutes. Brake pads are shown in Figure 1.

Figure 1. Brake pad sample

The hardness tests were carried out using a Shore D hardness tester. The water and oil absorption performances were investigated by keeping the brake pads in water and oil for 24 hours. The densities of the brake piercing samples were also measured according to the Archimedes principle. A specially designed device is used for wear and friction performances of the samples. The Taguchi L18 method was used to save time and experiment time. Special design friction wear tester shown in Figure 2.

Figure 2. Special design test device

The factors and levels determined for the Taguchi method are given in Table 1.

Table 1. Factors and levels with Taguchi L_{18} method

Factor Name	Factor	Unit	Values		Levels				
A	Temp.	(C°)	6	30	60	90	125	155	205
B	Speed	(rev/min)	3	300	600	900	-	-	-
C	Brake numbers	Num-ber	3	100	200	500	-	-	-

The experiment sequences designed by Taguchi L_{18} method are given in Table 2.

Table 2. Taguchi orthogonal with L18 experiment sequences

Exp. no	A	B	C
1	1	1	1
2	1	2	2
3	1	3	3
4	2	1	1
5	2	2	2
6	2	3	3
7	3	1	2
8	3	2	3
9	3	3	1
10	4	1	3
11	4	2	1
12	4	3	2
13	5	1	2
14	5	2	3
15	5	3	1
16	6	1	3
17	6	2	1
18	6	3	2

3. RESULTS

The measured hardness values and densities of brake pad samples; walnut (W) and Commercial (C) after standing in water adsorption (WA) and in oil adsorption (OA) are given in Table 3.

Table 3. The hardness (Shore D) and density values of samples

Samp-les	Hardnes s	After WA	After OA	Density (gr/cm^3)
W	88	84	87	2,340
C	86	82	85	2,470

According to the table, the first hardness value of the Walnut-added sample is higher than the hardness of the commercial pad. It can be said that Walnut shell additives increase hardness. After the water and oil absorption, the hardness values of both pad samples decreased. The hardness values of the pads waiting in the water have decreased more than the pads waiting in the oil. This can be explained by the fact that the density of the water is less than the density of the oil. Due to the low density of water, it penetrated more into the samples. Moreover, it can be said that the walnut shell sample absorbs more water because it has less density than the commercial sample. The same situation is observed in the weight changes of the brake pads. Table 4 shows the weight changes of the samples waiting in the water.

Table 4. Weight changes in water

Samp-les	First Weights (gr)	Weight Changes after 24 hours in water (gr.)	Weight Changes (%)
W	250,235	250,727	0,20
C	225,024	225,450	0,19

Table 5 shows the weight changes of the samples waiting in the oil. The weight of the W sample is further increased. Walnut-added sample has more oil absorption. It can be said that it absorbs more oil because its density is less than that of commercial (C) sample.

The results of the friction coefficient obtained according to the Taguchi L18 are given in Table 6.

Table 5. Weight changes in oil

Samp-les	First Weights (gr.)	Weight Changes in oil (gr.)	Weight Changes (%)
W	252,640	253,622	0,39
C	250,677	251,533	0,34

Table 6. The results of the friction coefficient obtained according to the Taguchi L18

Exp.no	Factors			Friction Coef.	S/N Ratio
	A	B	C		
1	1	1	1	0,475	6,466
2	1	2	2	0,469	6,577
3	1	3	3	0,492	6,161
4	2	1	1	0,515	5,764
5	2	2	2	0,488	6,232
6	2	3	3	0,514	5,781
7	3	1	2	0,528	5,547
8	3	2	3	0,530	5,514
9	3	3	1	0,522	5,647
10	4	1	3	0,499	6,038
11	4	2	1	0,505	5,934
12	4	3	2	0,503	5,969
13	5	1	2	0,462	6,707
14	5	2	3	0,480	6,375
15	5	3	1	0,480	6,375
16	6	1	3	0,468	6,595
17	6	2	1	0,480	6,375
18	6	3	2	0,470	6,558

The results in Table 6 were obtained between 0.462 and 0.530 μ. The results of this friction coefficient obtained according to the Taguchi L18 formula comply with the SAE J661 standard. According to 18 different tests applied in different parameters, all values of friction coefficient are suitable for "G" and "H" class. The test results obtained by the Taguchi Method are evaluated by converting them to the signal / noise (S / N) ratio. The Noise Factor is needed to select the optimal values for their variability, by determining these causes or factors, in order to reduce the variability resulting from ordinary or system causes. These factors that create variability are called noise factor [9]. The value with the smallest S / N ratio is calculated and analyzed differently according to the value of the best, the greatest value is best, the nominal value is best, and the quality value is targeted [10]. According to these results, it can be said that it is appropriate to use walnut dust in brake pads because the friction coefficient values are in the appropriate range according to the standards. The graph of the resultant table for the average friction coefficient and S / N ratio for the W-coded brake pad is shown in Figure 3.

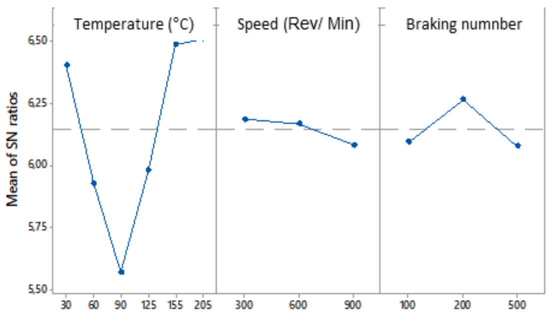

Figure 3. The effect of the factors on the friction coefficient and the S / N ratio for the W sample

The nominal level $A_4B_2C_1$ was determined when the control factors of the friction coefficient results of the W sample were examined. The nominal friction coefficient value was found to be 0.505 µ. Verification test was conducted to determine the accuracy of the results obtained. The friction coefficient verification test results by the Taguchi method of the test specimens are given in Table 7.

Table 7. Nominal friction coefficients and verification test results

Sam-ples	Nominal Levels	Taguchi method Friction coefficient (µ)	
		Experimental result (µ)	Predictions (µ)
W	$A_4B_2C_1$	0,505	0,503

According to the verification test results for the determination of the accuracy of the predicted values by the Taguchi method, the method yielded reliable results. According to the results obtained, friction coefficient results of brake pads can be optimized by Taguchi method.

4. CONCLUSION

As a result of this work, adding the walnut shell dust on brake pads were produced in real dimensions. As a result of friction and wear tests carried out on a specially designed test device, friction coefficient values according to the standards have been obtained. Also, according to the verification test results for the determination of the accuracy of the predicted values by the Taguchi method, the method yielded reliable results. Moreover, friction coefficient results of brake pads can be optimized by Taguchi method.

ACKNOWLEDGEMENT

This study was supported by the Scientific Research Project Unit of Duzce University (DÜBAP-2015/72).

REFERENCES

[1] D. Chan, G. Stachowiak: Review of automotive brake friction materials, In *Proceedings of the Institution of Mechanical Engineers, Part D: Journal of Automobile Engineering,* Vol. 218, pp. 953-966, 2004.

[2] K. Liew, U. Nirmal: Frictional performance evaluation of newly designed brake pad materials, Materials & Design, Vol. 48, pp. 25-33, 2013.

[3] M. Jacko, P. Tsang, S. Rhee: Automotive friction materials evolution during the past decade, Wear*,* Vol. 100, pp. 503-515, 1984.

[4] P. J. Blau: Compositions, functions, and testing of friction brake materials and their additives, Oak Ridge National Lab., TN (US)2001.

[5] U. Idris, V. Aigbodion, I. Abubakar, C. Nwoye: Eco-friendly asbestos free brake-pad: Using banana peels, Journal of King Saud University-Engineering Sciences*,* Vol. 27, pp. 185-192, 2015.

[6] S. Qi, Z. Fu, R. Yun, S. Jiang, X. Zheng, Y. Lu: Effects of walnut shells on friction and wear performance of eco-friendly brake friction composites, In *Proceedings of the Institution of Mechanical Engineers, Part J: Journal of Engineering Tribology,* Vol. 228, pp. 511-520, 2014.

[7] N. A. Ademoh, A. I. Olabisi: Development and evaluation of maize husks (asbestos-free)

based brake pad, Development, Vol. 5, pp.67-80, 2015.

[8] D. Yawas, S. Aku, S. Amaren: Morphology and properties of periwinkle shell asbestos-free brake pad, Journal of King Saud University-Engineering Sciences, Vol. 28, pp. 103-109, 2016.

[9] D. Taylan: *An application of Taguchi experimental design*, MSc thesiss, Süleyman Demirel University, Isparta, Turkey, 2009.

[10] M. Şirvancı: Quality for Experimental Design: Taguchi approach: Literatür, Ankara, 1997.

Serbian Tribology Society

SERBIATRIB '19

16th International Conference on Tribology

Faculty of Engineering
University of Kragujevac

Kragujevac, Serbia, 15 – 17 May 2019

STUDY THE STRUCTURAL PROBLEM IN THE BRAKE SYSTEM APPLYING A DIFFERENT PRESSURE FUNCTIONS

Nadica STOJANOVIC[1,*], Oday I. ABDULLAH[2,3], Josef SCHLATTMANN[3], Ivan GRUJIC[1], Jasna GLISOVIC[1]

[1]University of Kragujevac, Faculty of Engineering, Department for Motor Vehicles and Motors, Serbia

[2]Dept. of Energy Engineering, College of Engineering, University of Baghdad, Iraq

[3]Hamburg University of Technology, Germany

*Corresponding author: nadica.stojanovic@kg.ac.rs

Abstract: *During every braking process, the wear in the contacting surfaces of brake disc and brake pads will be occurred. Therefore, it's very important to investigate the effective parameters on the wear mechanism of the contacting surfaces, this is necessary because of the lifetime of the elements of brake is proportional directly with the rate of wear.*

In this research paper, the influence of the applied pressure function by which brake pads act on the brake disc is investigated using finite element method. Three different functions of pressure were applied which are: constant, linear and exponential. 3D model has been developed in order to analyze the penetration in the contacting surfaces of the elements of brake system. The results presented the variation of penetration with braking time. Furthermore, the results illustrated the distributions of the contact pressure in the friction pair (inner and outer sides) at any instant during the braking process.

Also, it was found that the values of stress at the end of the braking process (regardless of the contact area) were the same for all functions of the applied pressure. The differences in the stresses occurred when applied different function of pressure function during the braking process.

Keywords: *brake system, wear problem, finite element method, penetration effect, stress analysis.*

1. INTRODUCTION

In order to improve the understanding of the tribological characteristics of the braking system, it is necessary to compute the pressure distribution in the contacting surfaces (between the braking disc and braking pads). In order to observe what is happening in every moment during the braking process with minimum cost and time, therefore numerical analysis is the optimal way to find the solution of such complex problem.

The analysis of the thermo-elastic interaction that occur in the interface between the disc and pads is very complex, because of there are many parameters affect the barking process such as surface structure, material properties, degree of cooling, sliding speed etc. [1].

This differences that exist in elements of brake system, are making an obstacle for consistency and repeatability of results. The microscopic tests are necessary to investigate the contact geometry, surface composition and mechanical characteristics in contact zone.

The most effective factors on the wear ratio are the properties of the selected material for the braking disc, besides that it should take into the consideration the price of the materials [2].

The distribution of the contact pressure in the contacting surfaces is considered the significant factor that specify the magnitude and distribution thermal stresses that generated during the sliding process [3].

It is necessary that the pressure distribution in the contact area is uniform as much as possible, in order of braking system life prolonging.

Abu Bakar и Ouyang [4] has a goal to obtain the uniform pressure distribution on the contact surface, as well as the lowest possible values of the pressures in the contact. Four different models have been tested, and for each model are obtained different values for the contact pressure, as well as for the pressure distribution. The dynamic contact pressure distribution in the disc brake system remains impossible to measure through experimental methods. This makes numerical analysis using finite element method an indispensable alternative tool to predict the contact pressure during the braking process [5]. By developing technology and current commercial software packages that are capable of predicting more realistic results of contact pressure distributions.

In the research of Sarip et al. [6], it was presented that the friction material compressibility is important in pressure distribution analysis of brake, where the high value of Young's modulus has a negative effect on the distribution of contact pressure. In addition to these literatures, there are other studies which investigated the effect of the brake pad surface topography on the the contact pressure distribution [7]. Also, there is a little difference in the contact pressure for pads with and without damping shims. The test results also proved that the change in brake-line pressure results in different contact pressure distributions, when the brake-line pressure increases the maximum contact pressure increases too, and vice-versa. The worn pads will be produced more concentrated contact pressure than the new sets of pads, where highest contact pressure appeared at the outer border region of brake pads. Earlier research's Stojanovic et al. showed that highest values for the penetration occurred on the outer side of the disc, which is directly related with the pressure that occurred in the contact area [8].

The results of Belhocine and Bouchetara were showed that temperature field and stress field in the process of braking phase was fully coupled. The temperature, Von Mises stress, total deformations of the disc and contact pressures of the pads are higher than disc, because the thermal stresses are added to mechanical stress which caused the crack propagation and fracture of the bowl and wears in the disc and pads [9].

The aim of the research paper is to investigate deeply the influence of the function of applied pressure on the contact pressure distribution during the braking process. Where, it was applied different functions of the applied pressure. The results presented the distribution of the penetration and stresses at any time of braking. The thermal stresses are not disused in this research paper.

2. STATE OF THE PROBLEM

In this section will be introduced the initial and boundary conditions. The values of applied pressure, angular velocity and friction coefficient are obtained experimentally [10]. The conditions of test of a vehicle were in ambient temperature of 22 $^{\circ}$C. The vehicle is moving at a speed of 80 km/h then should be barked to stop. This means that the initial angular velocity is equal to 71.12 rad/s. Figure 1 shows the model of the brake system with all parts. The applied pressure affects both pads with the same intensity.

Friction in most mechanical element is undesirable phenomenon; however in the brake system is considered useful to achieve the task of brake, therefore without friction the vehicle could not be stopped. The contact pair, between disc and the brake pads is realized friction. The value of the coefficient of friction is 0.288.

Figure 1. Disc brake components [11]

In this paper, three different analyses have been performed, when the pressure for each analysis has been applied based on different function as shown in Figure 2.

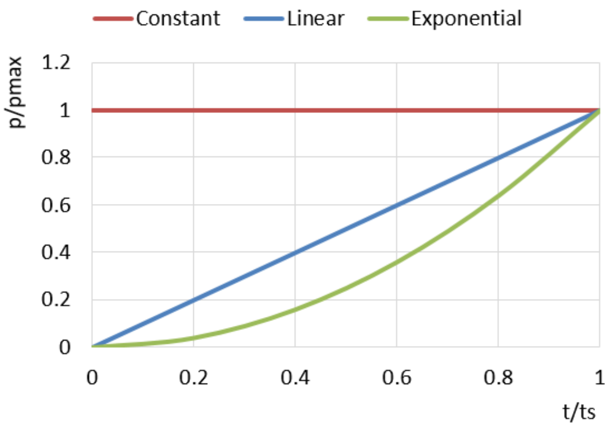

Figure 2. The functions of applied pressures

The maximum value of the pressure is the equal for all three cases. Equation 1 represents the function of the linear applied pressure, while Equation 2 represents the function of the exponential applied pressure. Where, the third case, the applied pressure is constant during the braking process. Values of the speed and the friction coefficient are the same for all three cases, as well and other boundaries. Also, the characteristics of materials for the braking disc and pads are the same for all cases; Table 1 lists the properties of materials of the brake system.

$$p \quad t \ 0.254 \quad 3 \ 10^{16} \tag{1}$$

$$p \quad t^2 \ 0.0508 \quad t \ 4 \ 10^{16} \quad 2 \ 10^{15} \tag{2}$$

The mesh type which used to build the finite element model is hexahedra. In the contact of pads and the disc the mesh size is very fine, and will be coarser when go away from the contact area. Number of elements and nodes are listed in Table 3.

Table 1. Material properties of the brake disc and brake pads [10]

	Density (kgm^{-3})	Young's modulus (GPa)	Poison ratio (-)
Disc	7100	118	0.32
Pads	2300	20	0.3

Using tetrahedral mesh it does not take much time for mesh defining, while its needs more time when used the hexahedra mesh type. It's necessary to select the suitable element size, when used the hexahedra mesh type. The advantage for hexahedra is to obtain accurate results of stress, without using very fine mesh [12].

As the nonlinearity present in frictional contact, an extra attention is necessary to be paid about the contact algorithms and their input parameters. For surface-to-surface contact elements, the program offers several different contact algorithms [13]:

- Penalty method uses a contact "spring" to establish a relationship between the two contact surfaces. The spring stiffness is called the contact stiffness;

$$F_n \quad k_n x_p \tag{3}$$

where F_n is contact force, k_n is contact stiffness and x_p is the distance between two existing nodes or separate contact bodies (penetration or gap), as shown in Figure 3.

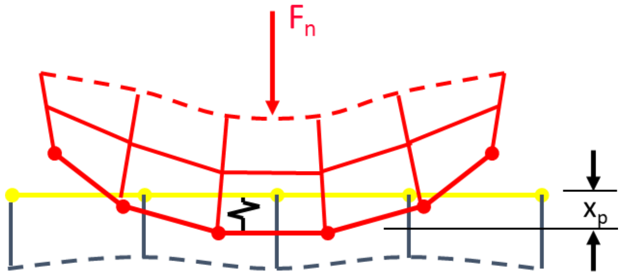

Figure 3. Contact between two parts [14]

- Augmented Lagrangian method is an iterative series of penalty methods. The contact tractions (pressure and frictional stresses) are augmented during equilibrium iterations so that the final penetration is smaller than the allowable tolerance. Compared to the penalty method, the augmented Lagrangian method usually leads to better conditioning and is less sensitive to the magnitude of the contact stiffness;

$$F_n \quad k_n x_p \tag{4}$$

where is Lagrange multiplier component.

- Lagrange multiplier on contact normal and penalty on tangent - enforces zero penetration when contact is closed and "zero slip" when sticking contact occurs. This method adds contact traction to the model as additional degrees of freedom and requires additional iterations to stabilize contact condition It often increases the computational cost compared to the augmented Lagrangian method;
- Pure Lagrange multiplier on contact normal and tangent - enforces zero penetration when contact is closed and “zero slip” when sticking contact occurs. This algorithm does not require contact stiffness. Instead it requires chattering control parameters. This method adds contact traction to the model as additional degrees of freedom and requires additional iterations to the stabilized contact conditions. It often increases the computational cost compared to the augmented Lagrangian method, and
- Internal multipoint constraint (MPC) is used in conjunction with bonded contact and no separation contact to model several types of contact assemblies and kinematic constraints.

In defining the coefficient of friction, it was used Augmented Lagrange algorithm. Figure 4 shows the finite element model of the brake system using the element hexahedra. It was selected a fine mesh in the contact area between the brake disc and brake pads where supposed the highest stresses will be occurred, the mesh size is very fine at the contacting surfaces and then will be more coarse when moving away from the contact area through the thickness of disc surface.

The advantage to select the hexahedra is to obtain the accurate results (stresses) with not very fine mesh [15]. The elements are used for contact elastic model in this analysis are listed in Table 2. The primary mesh is hexahedra, but due to the complexity of the model, the tetrahedral mesh has appeared in some places, in doing so, the accuracy of the results will be not reduced. For the contact surfaces, the mesh type is hexahedra. The DOFs from Table 2 that are used in this analysis, these elements can have other DOFs but they aren’t used in this analysis. The contact surfaces are surfaces of the brake pads and the target surfaces are surfaces of the brake disc. The finite element model which used to achieve the numerical analyses is the same for all three cases, as listed in Table 3.

Table 2. The type of elements and description [16]

Title	Description	Degrees of freedom	Illustration
SOLID186	3-D 20-Node Structural Solid 20 nodes 3-D space	Displacement in *x*, *y* and *z* axis	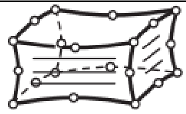
SOLID187	3-D 10-Node Tetrahedral Structural Solid 10 nodes 3-D space	Displacement in *x*, *y* and *z* axis	
CONTA174	3-D 8-Node Surface-to-Surface Contact 8 nodes 3-D space	Displacement in *x*, *y* and *z* axis	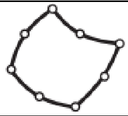
TARGE170	Contact 3-D Target Segment 8 nodes 3-D space	Displacement in *x*, *y* and *z* axis	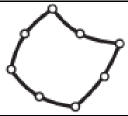
SURF154	3-D Structural Surface Effect 4 to 8 nodes 3-D space	Displacement in *x*, *y* and *z* axis	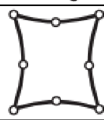
COBIN14	Combination Spring-Damper 2 nodes 3-D space	Displacement and rotation in *x*, *y* and *z* axis	

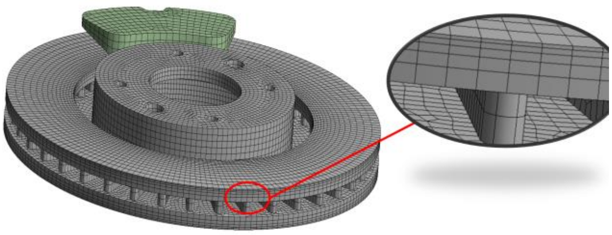

Figure 4. The finite element model of the brake system

Table 3. Number of finite elements and number of nodes

		Number of nodes	Number of elements
Disc		206956	59781
Pad			
Initial case	Inside	2640	434
	Outside	2673	440

3. RESULTS AND DISCUSIONS

3.1 Linear Applied pressure

This section presents the results of the contact pressure when applied a linear function of the pressure. Figure 5 illustrates the variation of the highest of contact pressure on the inner and outer sides of the pads. It can be noticed that the contact pressure appeared only on the inner side at the initial period, later on the contact pressure starts rising after 0.75 s of the braking process. It can be seen that the values of the contact pressure on the inner side grown approximated linearly with time until reach the maximum value at the end of the braking process. While, the contact pressure on the outer side increased directly to the peak value at t = 1.3 s, and after that the contact pressure decreased to the final value at the end of the braking process. It can be observed that the values of the contact pressure on the outer side are higher than those occurred on the inner side the reason of these is the umbrella effect. It can be seen from the results that the values of contact pressure at the outer location are higher than the applied pressure except at the beginning period. Also, the values of contact pressure at the inner location are higher than the applied pressure during all the period of braking process, where the contact pressure at the inner location is approximately double of the applied pressure at end of the braking process, while the contact pressure at the outer location is approximately 3.5 times of the applied pressure. Efficiency of such braking system is very good, because vehicle with such braking system will have a small stopping distance. From Figure 5 it can be seen that on the outer side of the disc, impact loads spear, which further can cause system failure.

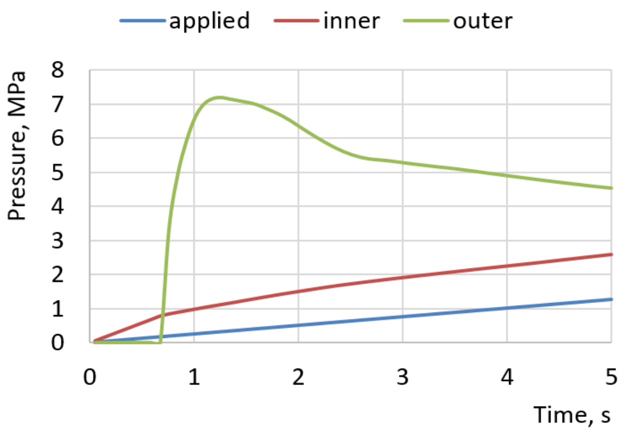

Figure 5. The variation the contact pressure at different locations when applied linear pressure

Figures 6 and 7 show the distribution of penetration on the inner and outer sides of the friction pair during the braking period. It was found that the highest values of the penetration occurred on the outer side, because, the penetration is proportional directly to contact pressure. The maximum values of the penetration on the inner side occurred at the end of braking period (t=5 s). However, penetration on the inner side of the friction pair, increased approximately linear with time. While on the outer side, the maximum value of penetration occurred after 1.3 s, and then decreased to the final value at the end of period. It can be seen, that the penetration zone in the inner side was dominant, while on the outer side the penetration area was limited. The reason behind the existing difference in the contact pressure between the inner and outer sides is this is the consequence of the umbrella effect.

3.2 Constant Pressure

When applied a constant pressure on the braking disc, the contact pressure on the contact surfaces will not change with time as shown in Figure 8. The results showed that the contact pressure on the outer side is higher than those occurred in the inner side. In each case, the values of obtained contact pressures

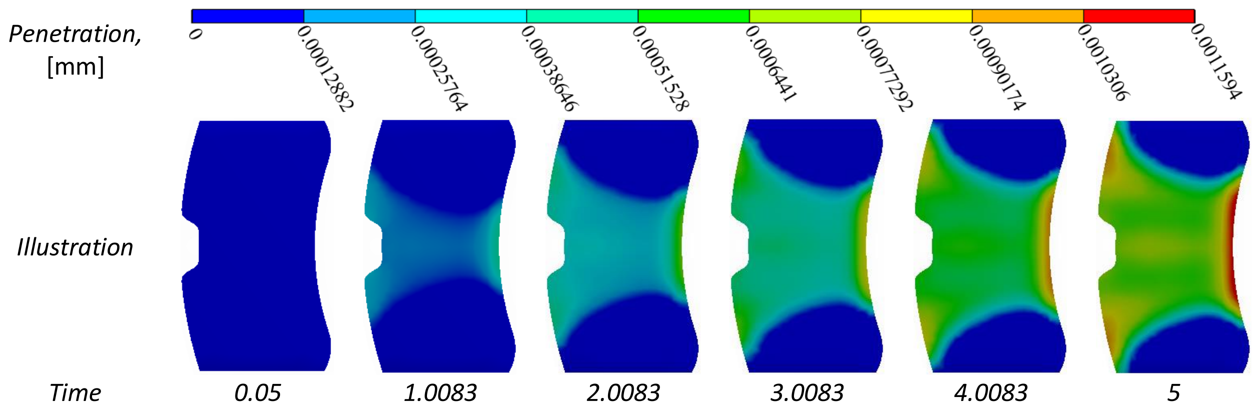

Figure 6. Penetration over the time on the inner side of the friction pair

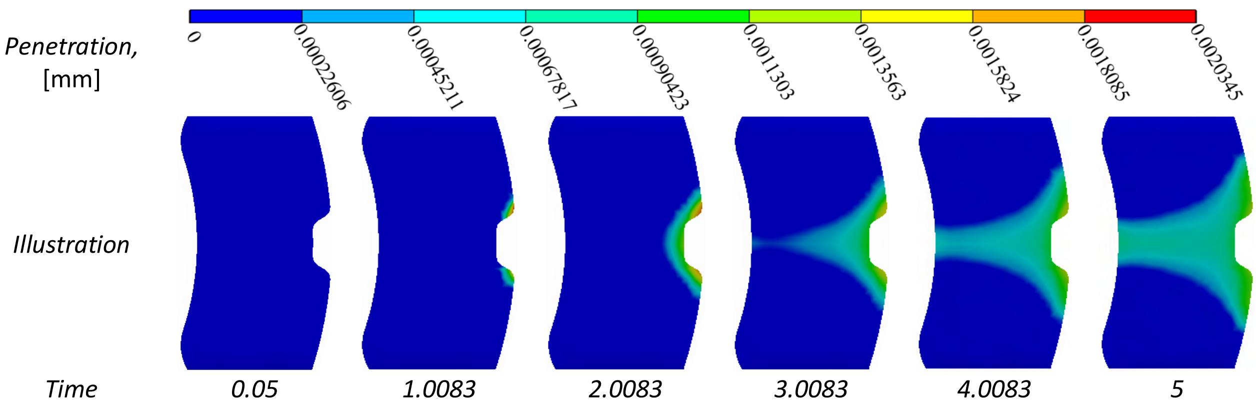

Figure 7. Penetration over the time on the outer side of the friction pair

are higher than applied pressure, and which it's directly depends on the coefficient of friction and size of contact surfaces. It was found at any instant during the braking process that the contact pressure at the inner location is approximately double of the applied pressure, while the contact pressure at the outer location is approximately 3.2 times of the applied pressure.

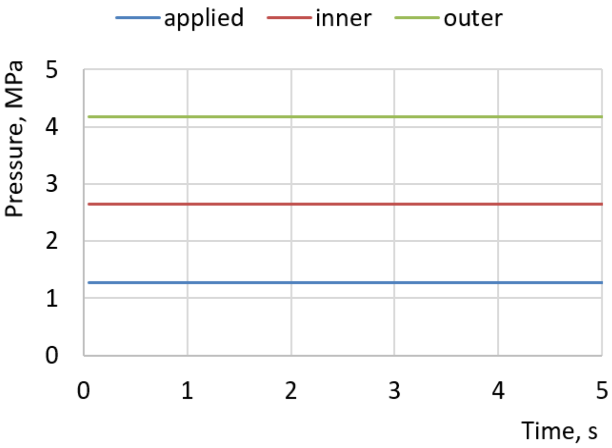

Figure 8. Obtained pressures for constant pressure

It was observed that the values of penetration on the outer side are higher those in the inner side as shown in Figures 9 and 10. However, it is interested results which obtained, where the maximum value of the penetration is approximately the same on the both sides but the distribution is different. The penetration focused in the outer side on area that is smaller than those in the inner side.

3.3 Exponential pressure

In this case the pressure was applied as exponential function during the braking time. Figure 11 exhibits the contact pressures when applied pressure as exponential function. The maximum contact pressure appeared in outer side and the minimum one on the inner side. It can be seen the big different in the behaviour of contact pressure between the inner and outer sides. Where at the inner side, the contact stresses increases gradually from low value at the beginning of the braking period to the high value at the end of period. While, at the outer side, the contact stresses started with huge increasing after 1.8 s of the beginning of the braking period to the high value (maximum) and then decreased to the low value at the end of period. It's clear that the behaviours of the contact pressure relative to the applied pressure are similar to the case when applied a linear function of pressure.

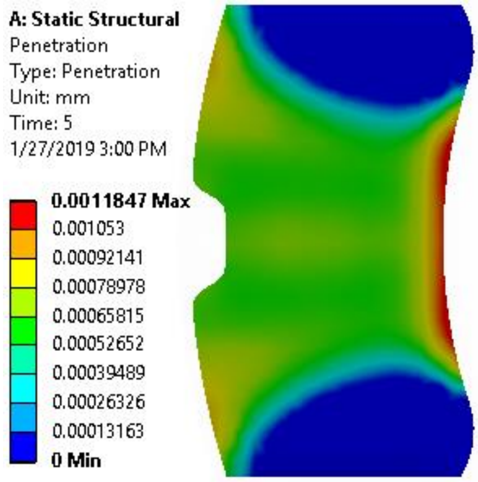

Figure 9. Penetration on the inner contact of the friction pair

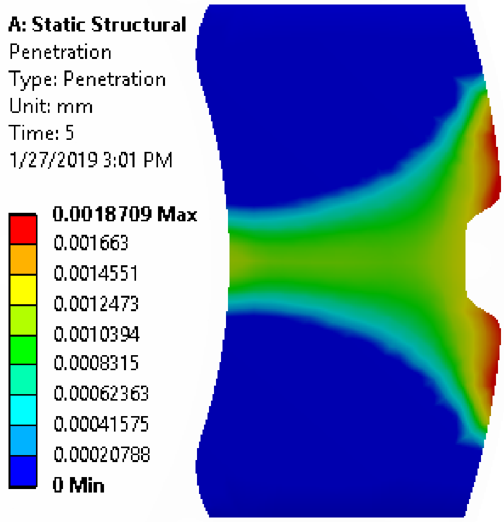

Figure 10. Penetration on the outer contact of the friction pair

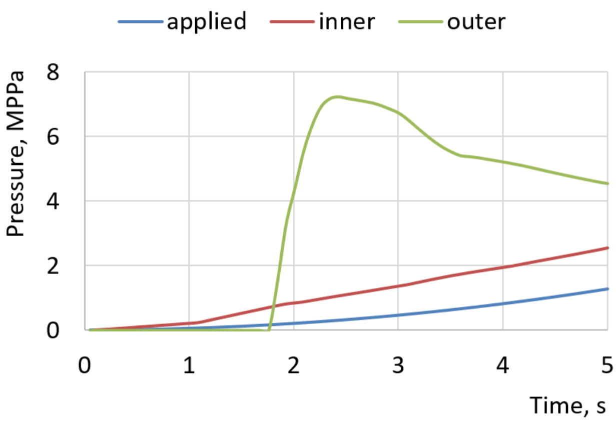

Figure 11. The contact pressures when applied pressure as exponential function

In the first two seconds, the penetration doesn't appeared on the outer contact, but after the time passed (3 s) the maximum value of penetration appeared as shown in Figures 12 and 13. After that the penetration decreased to the finial value at the end of the braking process. It can be noticed that the maximum value in mentioned cases occurred on the outer contact. The values of the penetration and contact pressure that occurred on the inner contact of the friction pair were very small. Figure 14 illustrates the distribution of penetration on the brake pads acting on the disc at the beginning and at t = 1.0083 s.

3.4 Stresses Analysis

Also, in this numerical analysis, it was computed the stresses that generated during the sliding period. Figure 15 shows the variation of Stresses during the braking process at different locations of brake system. It can be seen during the complete period of braking at the inner side (disc and pad), that the maximum stresses generated when applied a constant pressure. While at the outer side, the maximum stresses generated when applied the linear and exponential function for pressure.

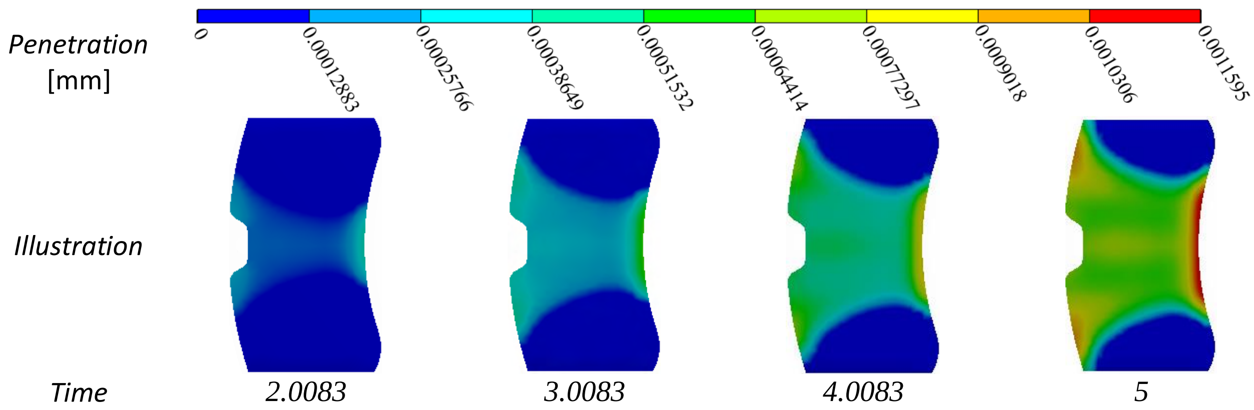

Figure 12. Penetration on the inner contact of friction pair during time

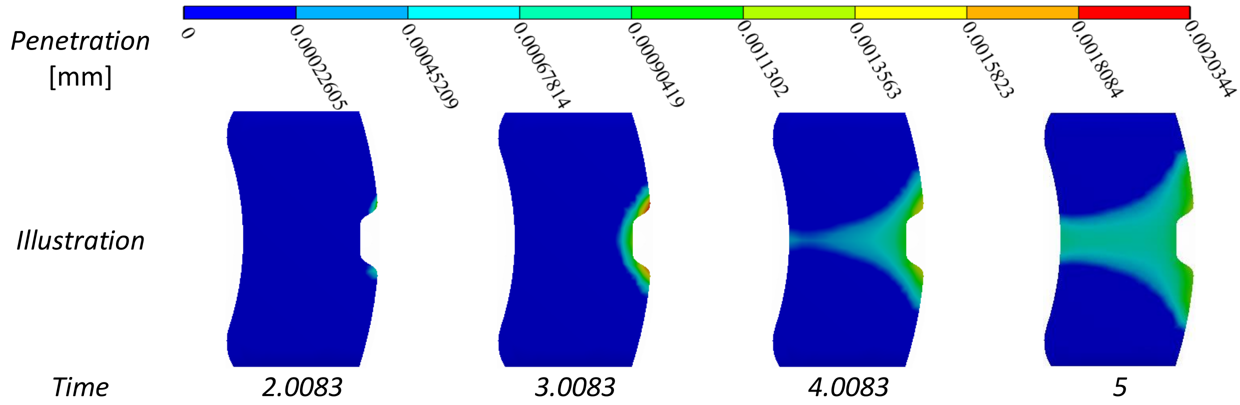

Figure 13. Penetration on the outer contact of friction pair during time

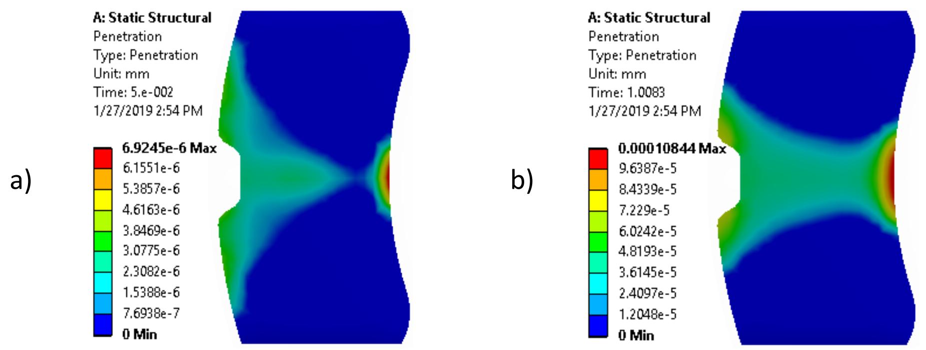

Figure 14. Penetration on a) the inner and b) outer contact pair at the beginning of applied pressure

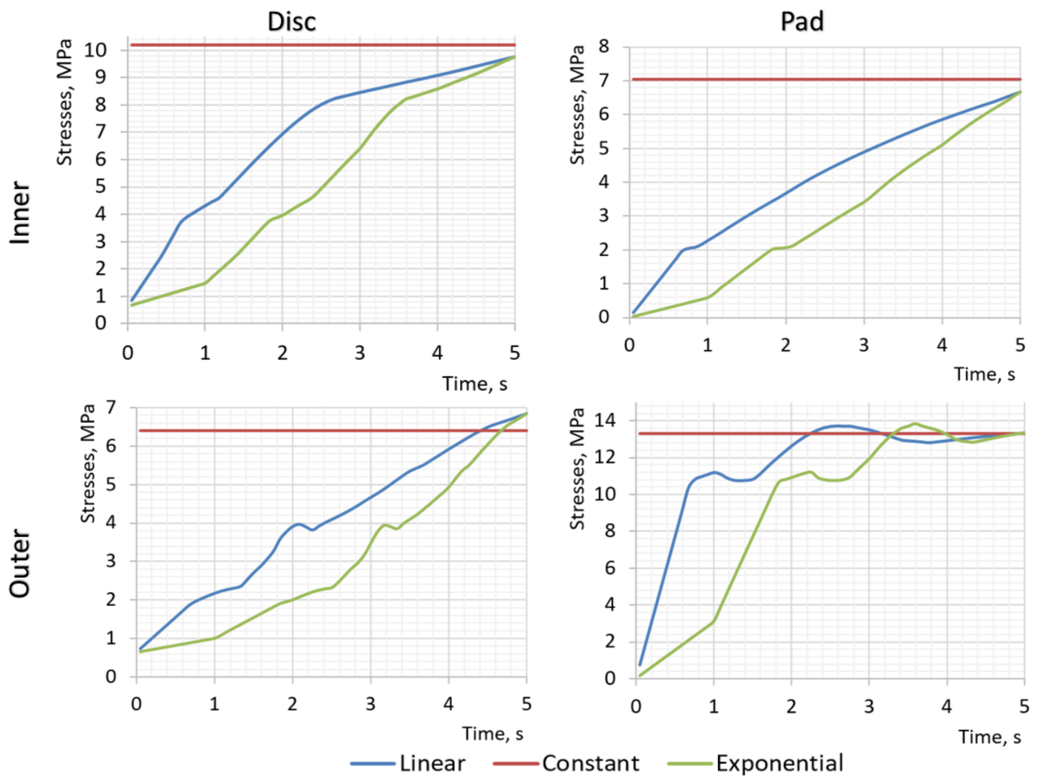

Figure 15. Variation of von-Misses Stresses during the braking process at different locations of brake system

In general when we compare the two cases of the applied pressure (linear and exponential), it can be noticed that the values of stresses when applied the linear function of pressure are higher than those generated when applied the exponential function.

By observing Figure 15, it can be noticed, that the outer pad was exposed to fluctuating stresses over the time, when applied the pressure as linear or exponential function, and this is lead to appear the maximum penetration.

In the inner side, it can be seen that the stresses when applied the linear and exponential functions are lower than those when applied the constant pressure. While at the outer side, the stresses when applied the linear and exponential functions exceeded the stresses of constant pressure function at some period during the braking process.

Besides all of that, the highest values of Von-misses stresses occurred at the outer side of the braking disc, which is the consequence of the umbrella effect [17].

During the process of the brake design, it should be paid more attention about the level of stresses that expected, where it must be lower than the allowable stresses of the selected materials.

4. CONCLUSIONS AND REMARKS

In this research paper, it was developed a numerical approach to investigate the effect of the applied pressure function on the magnitude and distribution of the contact pressure and penetration of the contacting surface of the brake system. It was applied three different functions which are contact, linear increasing with time and exponential.

It was found that the highest values of contact pressures and penetration appeared on the outer contact side when applied the pressure as exponential and linear functions. While, the lowest values of penetration appeared on the contact surfaces when applied a constant pressure.

The highest pressure values in the contact surfaces appeared in case of linear function almost at the beginning within the period from 0.75 to 1.3 s. While, for the exponential function occurred within the period from 1.8 to 2.4 s. In the third case study, when applied a constant pressure, it was found that the contact pressures were constant at any instant during the braking process.

Also, it was found that the maximum stresses appeared in the outer pad because of the pad is from one side pressed by pistons, and from the outer by the disc, which is consequence of the umbrella effect. While, in the inner side the maximum stresses occurred in the disc. The reason of this result is constructive nature of the disc brake.

The values of contact pressure between pads and the disc of any case are much higher than those of applied pressure of any functions. This is very good point, because the vehicle that has such braking system and that is manufactured from materials such as in this paper, will have very short stopping time (shortest stopping distance). As result of this, the safety of traffic participants will not be disturbed.

This research is preliminary research that will be followed by further research that will study deeply all the effective factors on the behaviour and performance of the brake system in order to find the optimum design.

ACKNOWLEDGEMENT

This paper was realized within the framework of the project "The research of vehicle safety as part of a cybernetic system: Driver-Vehicle-Environment", ref. no. TR35041, funded by the Ministry of Education, Science and Technological Development of the Republic of Serbia.

Also, the authors would like to thank the System Technology and Mechanical Design Methodology Group / Hamburg University of Technology to support this research paper.

REFERENCES

[1] Rensselaer Polytechnic Institute, available at: http://www.ewp.rpi.edu/hartford/~ernesto/F2013/FWLM/StudProj/Feist/Feist-TPR.pdf, accessed: 27.01.2017.

[2] P. N. Gunjal, D.S Galhe, H. Mishra: Selection of the disc brake material using pin on disc apparatus, International Journal of Innovations in Engineering Research and Technology, Vol. 2, No. 11, pp. 8-11, 2015.

[3] O. I. Abdullah, J. Schlattmann, H. Jobair, N. E. Beliardouh, H. Kaleli: Thermal stress analysis of dry friction clutches, Industrial Lubrication and Tribology, 2018.

[4] A.R. Abu Bakar, H. Ouyang: Prediction of disc brake contact pressure distributions by finite element analysis, Jurnal Teknologi, Vol. 43, No. 1, pp. 21-36, 2005.

[5] Sensor Products Inc., available at: https://www.sensorprod.com/news/white-papers/2006_npm/index.php, accessed: 27.01.2019.

[6] S. Sarip, A. J. Day, P. Olley, H. S. Qi: Analysis of temperature and pressure distribution in brake disc for regenerative braking, In: *Proceedings of the Conference on Flexible Automation and Intelligent Manufacturing*, FAIM2009, Teesside, UK, pp. 1 – 8.

[7] A. R. Abu Bakar, H. Ouyang, J. E. Siegel: Brake pad surface topography part I: contact pressure distribution, SAE International, 2005-01-3941, 2005.

[8] N. Stojanovic, J. Glisovic, B. Stojanovic, I. Grujic: Numerical analysis of tribomechanical system brake disc-pad for heavy duty vehicles, In: *Proceedings of the Conference on IX International Conference "Heavy Machinery-HM 2017",* Zlatibor, 28 June – 1 July, pp. D.57 – D.64, 2017.

[9] A. Belhocine, M. Bouchetara: Temperature and thermal stresses of vehicles gray cast brake, Journal of Applied Research and Technology, Vol. 11, pp. 674-682, 2013.

[10] J. Glišović: *Teorijska I eksperimentalna istraživanja visokofrekvetne buke disk kočnica*, Doktorska disertacija, Fakultet inženjerskih nauka, Kragujevac, 2012.

[11] Imagenesmi, available at: https://www.imagenesmi.com/im%C3%A1genes/brake-grinding-noise-4a.html, accessed: 07.03.2019.

[12] ANSYS, available at: https://support.ansys.com/staticassets/ANSYS/staticassets/resourcelibrary/confpaper/2004-Int-ANSYS-Conf-9.PDF, accessed: 26.12.2018.

[13] ANSYS Contact Technology Guide, ANSYS Release 12.1 Documentation, ANSYS, Inc.

[14] Finite Element Analysis Standards, available at: http://www-eng.lbl.gov/~als/FEA/ANSYS_V9_INFO/Workbench_Simulation_9.0_Nonlin/ppt/AWS90_Struc

tural_Nonlin_Ch03_Contact.ppt, accessed: 26.12.2018.
[15] ANSYS, available at: https://support.ansys.com/staticassets/ANSYS/staticassets/resourcelibrary/confpaper/2004-Int-ANSYS-Conf-9.PDF, accessed: 26.12.2018.
[16] ANSYS Mechanical APDL Element Reference, ANSYS 15.0 Documentation, ANSYS, Inc.
[17] N. Stojanović, J.Glišović: Structural and thermal analysis of heavy vehicles' disc brakes, Mobility & Vehicle Mechanics, Vol. 42, No. 1, pp. 9-16, 2016.

Serbian Tribology Society

SERBIATRIB '19

16th International Conference on Tribology

Faculty of Engineering University of Kragujevac

Kragujevac, Serbia, 15 – 17 May 2019

THREE-DIMENSIONAL SIMULATION OF THE THERMAL PROBLEM IN FRICTION CLUTCHES USING FINITE ELEMENT TECHNIQUE

Laith A. SABRI[1], Josef SCHLATTMANN[2], Oday I. ABDULLAH[3,2]*
Nesser Eddine BELIARDOUH[4], Emilia ASSENOVA[5]
[1]Case Western Reserve University, USA
[2]Hamburg University of Technology, Hamburg, Germany
[3]University of Baghdad, Baghdad, Iraq,
[4]Badji Mokhtar University of Annaba, Annaba, Algeria
[5]Society of Bulgarian Tribologists, Sofia, Bulgaria
*Corresponding author: oday.abdullah@tuhh.de

Abstract: *This research paper presents a new numerical model of the single disc clutch that works under the dry conditions, whereas this model simulates the actual model in terms of geometry. It was overcome the difficulties that which faced the researchers in the previous literatures to build the three dimensional model of friction clutch. It was investigated deeply the thermal problem that occurred during the sliding period when the friction clutch starts to transfer the torque. In this paper, the finite element technique was applied to implement the thermal analysis. The developed finite element model was verified by comparing the obtained results with results of the other researchers that used different approaches. Moreover, the influence of the sliding speed on the thermal behaviour of the clutch disc has been studied.*

Keywords: *Dry friction, friction clutch, thermal problem, finite element method*

1. INTRODUCTION

The main resource of the failures and damages in the contacting surfaces and the reduction in the performance of the automotive brakes and clutches can be attributed to the excessive temperature that will be appeared during the first stage of engagement due to the sliding between the contacting parts. These excessive temperatures will be leaded to produce high thermal stresses. These stresses are considered the main reason to appear the cracks and the permanent deformations in the surfaces of the element of clutch system. Finally, these blemishes will be reduced the lifetime of the friction clutch system. In order to reduce the percentage of clutch failure before expected lifetime, it should be find out the distributions of temperatures during the engagements and what are the effective factors on the thermal problem of the friction clutches during the early stage of engagement. It can be seen the main parts of the friction clutch disc that are responsible to transfer the torque from engine to gearbox in Figure 1.

Most of researchers investigated numerically the friction clutch system were they used the two dimensional models (axisymmetric) to obtain the thermal behaviour during the sliding period. They overcame the complexities of the clutch geometry by reduce the thermal problem from three dimensions to the two dimensions. It was obtained the distributions of temperature and contact pressure with an acceptable degree of accuracy [1-12].

While the other researchers who obtained the analytical solution, the supposed some assumptions to reduce the complexities of the problem. One of these assumptions is to reduce the thermal problem from three-dimension problem to the one-dimension problem. Because of the difficulties to obtain the analytical solution in the two-dimension or three-dimension [13-24].

On the other hand, the experimental solution as we know it is very expensive as well it takes a long time to build any test rig device. Therefore, the numerical solution among all available solutions is considered the most suitable to reduce the time and cost of computations, this is in case where the mathematical model was built in the right way taking into consideration the influence of all effective factor on the system under working conditions.

The aim of this research is to develop a new solution based on the approximation approach (finite element method) of the thermal problem in the dry friction clutches that appeared during the sliding. Whereas, the developed approach in this work takes into account all the complexities of geometries that are existing in the clutch parts. The results present the temperatures distributions of all elements of the clutch system in the whole period of sliding of a single engagement.

2. STATEMENT OF THE PROBLEM

Through the early period of engegement (sliding period, $0 \le t \le t_s$), most kinetic energy will be transferred into heat. In this research paper, It has been supposed that all friction energy will be consumed and will be converted into heat energy. It can be written the form of total frictional heat generated during the sliding as follows [9],

$$Q_t(r,t) = \mu p V_s; \quad 0 \le t \le t_s \qquad (1)$$

Where, $V_s = \omega_s r$

V_s: Sliding speed

ω_s: Angular sliding speed [rad/sec].

It was assumed that the angular sliding speed decrease linearly with time as following,

$$\omega_s(t) = \omega_o\left(1 - \frac{t}{t_s}\right), \quad 0 \le t \le t_s \qquad (2)$$

ω_o: Initial angular sliding speed of the friction clutch (t_s=0).The frictional heat generated on the surfaces of clutch disc at any instant of sliding is,

$$Q_c(r,t) = f_c \mu p r \omega_o\left(1 - \frac{t}{t_s}\right); \ 0 \le t \le t_s \qquad (3)$$

f_c: Heat partition factor that determine the amount of frictional heat which enter into the clutch disc, pressure plate and flywheel.

It has been assumed that the materials of the pressure plate and flywheel are the same, therefore the heat partition factor is [12]

$$f_c = \frac{\sqrt{K_c \rho_c c_c}}{\sqrt{K_c \rho_c c_c} + \sqrt{K_f \rho_f c_f}} + \frac{\sqrt{K_c \rho_c c_c}}{\sqrt{K_c \rho_c c_c} + \sqrt{K_p \rho_p c_p}} \qquad (4)$$

K: thermal conductivity

ρ: Density

c: Specific heat.

It was indexed all parameters of the axial cushion with *cu*, friction material with *c*, flywheel with *f* and pressure plate with *p*.

The difference in speeds between the flywheel and the pressure plate from one side and the friction clutch disc from the other side will lead to generate a high amount of frictional heat. The heat dissipation will be occurred by conduction between the parts of the clutch system and by convection to the surrounding environment. The time of the sliding of the friction system is very short, therefore the effect of radiation is ignored.

The first step is to build the geometry (three-dimensional) of the clutch system based on the real dimension by using Solidworks2018. The next step is to export the model of the clutch system to Ansys/workbench 18 to find the results of the thermal problem.

It can be written the parabolic heat conduction equation in the cylindrical coordinate system to find the temperature field of the friction clutch components as following (Fig. 2):

$$\frac{\partial^2 T}{\partial r^2}+\frac{1}{r}\frac{\partial T}{\partial r}+\frac{1}{r^2}\frac{\partial^2 T}{\partial \vartheta^2}+\frac{\partial^2 T}{\partial z^2}=\frac{1}{\alpha}\frac{\partial T}{\partial t} \quad (5)$$

r: Radial coordinate [m]
ϑ: Circumferential coordinate [rad]
z: Aaxial coordinate [m]
α: Thermal diffusivity ($\alpha=k/\rho\, c$)

On the exposed surfaces of the friction clutch models, the convection takes place. It was assumed that the coefficient of heat transfer is independent of temperature. The boundary conditions and initial conditions of the case study of the friction clutch are shown in Figure 3. The initial temperature is,

$$T(r,\vartheta,z,0)=T_i \quad (6)$$

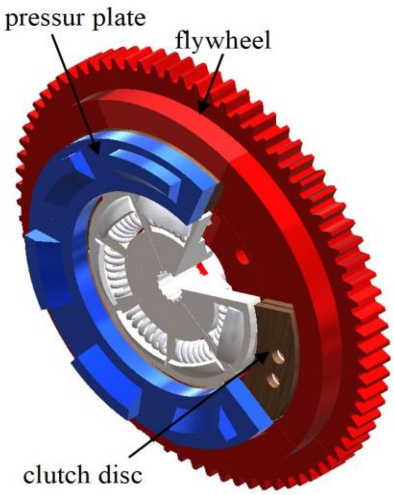

Figure 1. The main components of the frictional clutch system

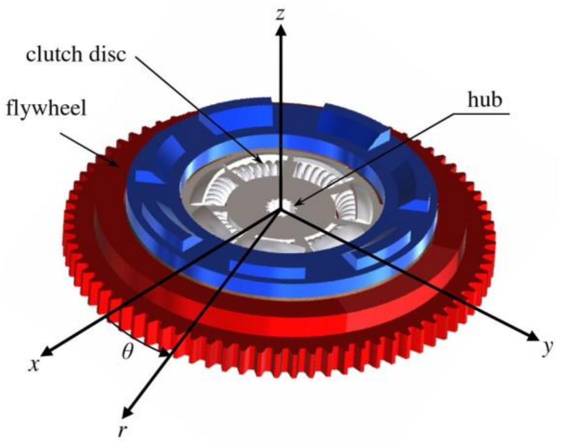

Figure 2. Three-dimensional model of frictional clutch system

(single-disc with two effective faces)

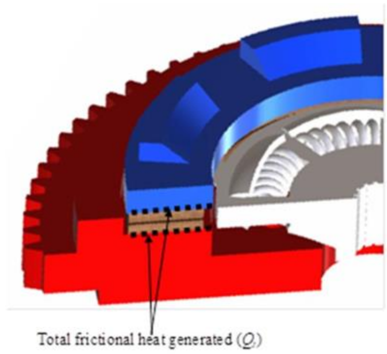

Figure 3. The thermal load on the contacting surface of clutch system

3. FINITE ELEMENT FORMULATION

This section presents the details to build the finite element model and the assumptions that are necessary to achieve the numerical analysis. The transient solution is involved time dependent function of the heat transfer.

The temperature will be changed in a unit volume of a specific material will be resisted by the thermal mass that depends on density (ρ) and specific heat (c). It can be expressed the finite element form of the transient problem as [25]

$$[C]\{\dot{T}\}+[K]\{T\}=\{F\} \quad (7)$$

Where,
[C]: Specific heat matrix
[K]: Conductivity matrix
{T}: Vector of nodal temperatures
{$\dot{T}$}: Derivative of temperature with time ($\dot{T}=\partial T/\partial t$)
{F}: Applied heat flows.

The mesh element that selected to build the finite element model is considered the effective key to obtain the accurate results of temperature distribution. It was used Crank-Nicolson method as an unconditionally stable scheme. In this research paper, Ansys/workbench was to study the transient conduction problem of the friction clutch system under the dry condition.

It was assumed the thermal load based on the theory of design (uniform wear) for the friction clutches. This means that the thermal load is uniform over the contacting surfaces at any instant of time during the sliding phase. All materials properties are used in this analysis are supposed to be homogeneous and isotropic. Also, the properties of materials are temperature-independent. Table 1 lists all material properties and operational parameters of the case study. The value of the heat transfer coefficient which used to achieve the numerical computation was 40.89 W/m^{2}K [2] and assumed to be a constant over all exposed surfaces. In the analysis, the intial temperture for the entire system is 300K.

Table 1. Operational parameters and material properties of the friction clutch system [4]

Parameters	Values
Inner radius, r_c and r_{cu} [m]	0.06
Outer radius, r_c and r_{cu} [m]	0.0792
Thickness of axial cushion, [m]	0.004
Inner radius, r_p [m]	0.06
Outer radius, r_p[m]	0.091
Thickness of pressure plate, [m]	0.01
Inner radius of flywheel, [m]	0.0485
Outer radius of flywheel, [m]	0.097
Thickness of flywheel, [m]	0.0194
Applied pressure, p_a [MPa]	1
μ	0.3
ω_o [rad/sec]	295
No. of friction surfaces, n	2
ρ_c [kg/m^3]	1000
ρ_{cu}, ρ_f, ρ_p [kg/m^3]	7200
c_c [J/kg K]	1400
c_{cu}, c_f, c_p [J/kg K]	450
K_c [W/mK]	0.75
K_{cu}, K_f, K_p [W/mK]	56
t_s [s]	0.4

Figure 4 illustrates a sector of the three-dimensional finite element model of the assembly of the flywheel, clutch disc and pressure plate. Owing to the symmetry of the geotry and load, it was used only a sector of the total model in order to reduce the computation time. The element (SOLID90) was selected to build the finite element model, where this element contains 20 nodes with a single degree of freedom which is temperature. This element has compatible with temperature shapes and it's very suitable to the model which has curved boundaries.

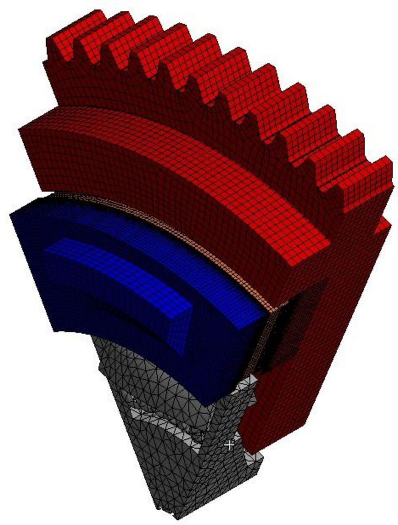

Figure 4. Finite element model of the clutch system (sector)

It was accomplished study of the mesh sensitivity in order to select the optimal mesh based computational accuracy point of view.

4. RESULTS AND DISCUSSIONS

I was achieved the finite element analysis based on the developed model of the dry friction clutch using Ansys/APDL to study the temperature field during the sliding time ur

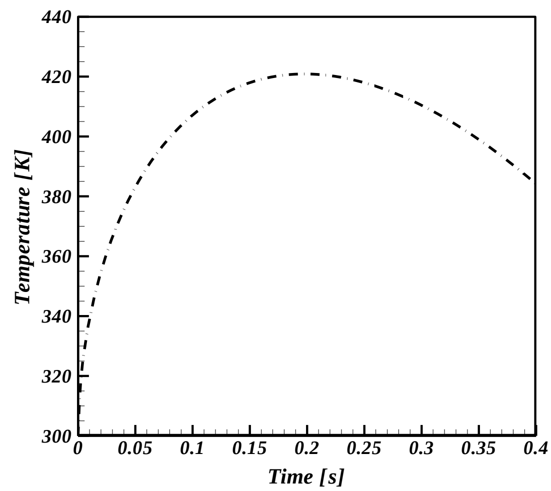

Figure 5. The maximum temperature of the friction clutch system during the sliding period

Figure 5 illustrates the highest temperature during the sliding period in the components of the friction clutch. It can be seen that the temperature increased from the initial condition (t_s=0) to the maximum value that occurred at approximately the mid time of heating phase (t_s=0.25s), later on the temperature decreased with time to end of the heating phase. The maximum difference in temperature ($T_{max.}$-T_i) occurred at the mid time of heating phase (t_s =0.2) which was (420.8 K).

The contours of the temperature field of the friction clutch disc, flywheel and pressure plate at different intervals of sliding time are shown in Figures 6. It can be noticed that the distribution of temperatures is approximately uniform on the contacting surfaces. These results were obtained based on the thermal load that calculated when assumed that the rate of wear is uniform (old friction clutch) over the contacting surfaces. In other words, the thermal load (the frictional heat) was generated uniformly at the interface between the contacting surfaces.

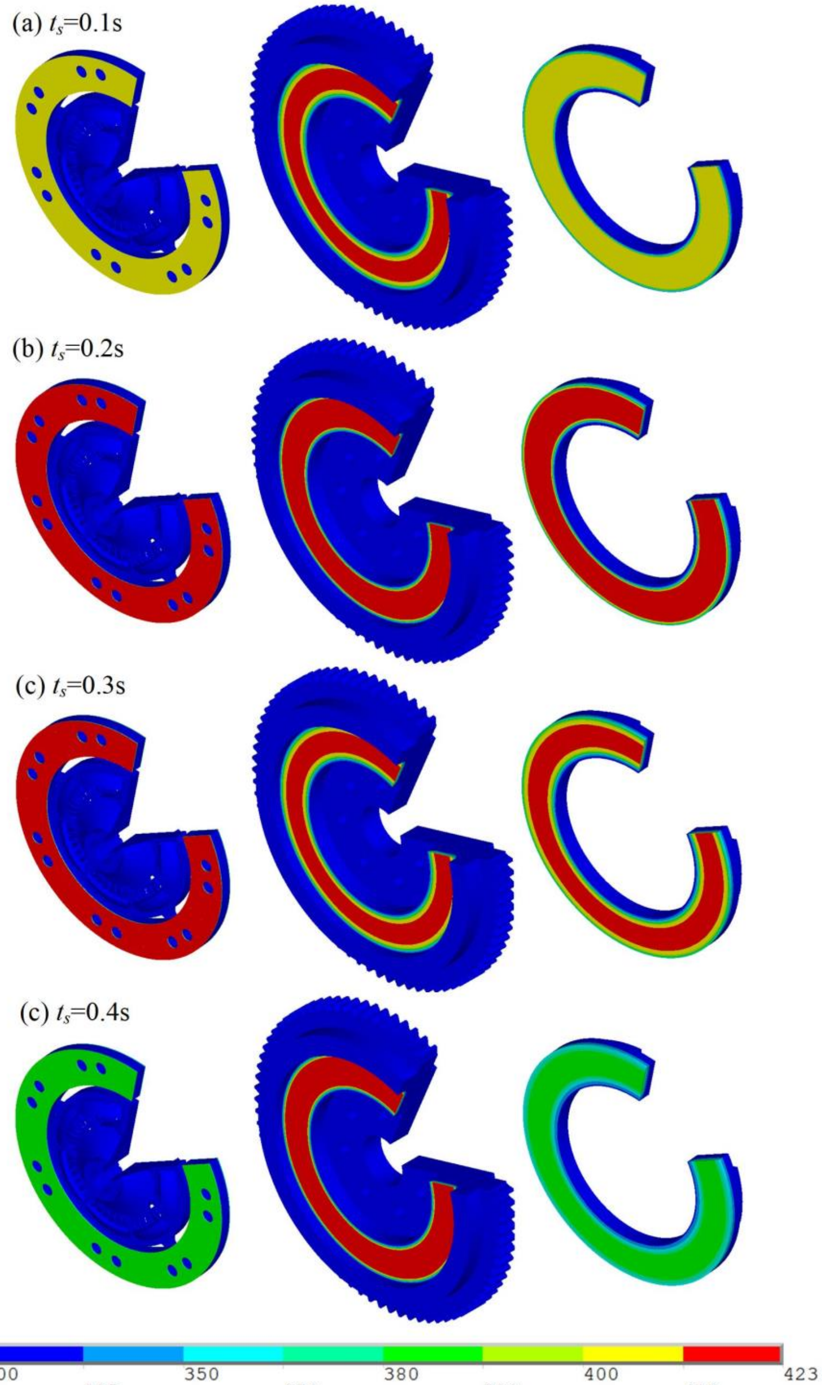

Figure 6. Distributions of temperature of the friction clutch system at different time of sliding period

5. CONCLUSIONS AND REMARKS

In this work, a significant numerical approach was introduced to solve accurately the thermal problem of the friction clutch system with one disc when both sides were effective. The analysis covered the sliding time within a single engagement. It was built 3dimensional finite element model to obtain the temperature distribution during the whole period of sliding.

The results proved the validity of the developed model, where the temperature was distributed uniformly over the surfaces of contact during the heating phase. The results showed that the maximum temperature occurred at approximately the mid time of the heating phase. In general, it has been observed that the highest temperature generated at the interface between the contacting elements. The thermal influences decreased when going toward the depth of clutch disc (friction material) to a minimum value approximately zero at midpoint of thickness.

Building this finite element model is considered very important forward step to explore the solution of more complex problems. Where, this paper is a preliminary investigation and will be followed by other future researches that will be investigated deeply the unsymmetrical load problem, effect of surface roughness, damaged contacting surfaces etc.

REFERENCES

[1] O.I. Abdullah, J. Schlattmann, A. Senatore, A. M. Al-Shabib: Investigation of thermoelastic problem of multiple-disc friction clutches applying different thermal loads, Heat and Mass Transfer, Vol. 54, No. 11, pp. 3461–3471, 2018.

[2] O.I. Abdullah, J. Schlattmann, M.H. Majeed, and L.A. Sabri: The Distribution of Frictional Heat Generated Between the Contacting Surfaces of the Friction Clutch System, International Journal on Interactive Design and Manufacturing, 2018.

[3] O.I. Abdullah, J. Schlattmann, M.H. Majeed, and L.A. Sabri: The Temperatures Distributions of a Single-Disc Clutches Using Heat Partitioning and Total Heat Generated Approaches, Case Studies in Thermal Engineering, Vol. 11, pp. 43-54, 2018.

[4] O.I. Abdullah, J. Schlattmann: Thermoelastic Analysis of Grooved Friction Clutches Using Finite Element Method, Tribology Transactions, Vol. 60, No. 6, pp. 1011-1021, 2017.

[5] O.I. Abdullah, J. Schlattmann: Thermal Behavior of Friction Clutch Disc Based on Uniform Pressure and Uniform Wear Assumptions, Friction, Vol. 4, No. 3, pp. 1-10, 2016.

[6] O.I. Abdullah, J. Schlattmann: Temperature Analysis of A Pin-On-Disc Tribology Test Using Experimental and Numerical Approaches, Friction, Vol. 4, No. 2, pp. 1-9, 2016.

[7] O.I. Abdullah, M.J. Akhtar, J. Schlattmann: Investigation of Thermo-Elastic Behavior of Multidisk Clutches, Journal of Tribology, Vol. 137, No. 1, pp. 1-9, 2015.

[8] O.I. Abdullah, J. Schlattmann: An Investigation into the Thermal Behavior of the Grooved Dry Friction Clutch, Journal of Tribology, Vol. 136, No. 3, pp. 1-6, 2014.

[9] O.I. Abdullah, J. Schlattmann: Computation of Surface Temperatures and Energy Dissipation in Dry Friction Clutches for Varying Torque with Time, International Journal of Automotive Technology, Vol. 15, No. 5, pp. 733-740, 2014.

[10] O.I. Abdullah, J. Schlattmann, A.M. Al-Shabibi: Thermo-Mechanical Analysis of the Dry Clutches Under Different Boundary Conditions, Journal of Tribology in Industry, Vol. 36, No. 2, pp. 172-180, 2014.

[11] O.I. Abdullah, J. Schlattmann, A. M. Al-Shabibi: Stresses and Deformations Analysis of a Dry Friction Clutch System, Tribology in Industry, Vol. 35, No. 2, pp. 155-162, 2013.

[12] O.I. Abdullah, J. Schlattmann: Finite Element Analysis of Temperature Field in Automotive Dry Friction Clutch, Tribology in Industry, Vol. 34, No. 4, pp. 206-216, 2012.

[13] K. Topczewska: Analytical model for investigation of the effect of friction power on the thermal stresses in friction elements of brakes, Journal of Theoretical and Applied Mechanics, Vol. 56, No. 4, pp. 1017-1027, 2018.

[14] K. Topczewska: Temperature distribution in a brake disc with variable contact pressure, Technical Issues, Vol. 2016, No. 1, pp. 90-95, 2016.

[15] K. Topczewska: Frictional heating with time-dependent specific power of friction, acta mechanica et automatica, Vol. 11, No. 2, pp. 111-115, 2017.

[16] K. Topczewska: The temperature of a brake disc during frictional heating with linear distribution of the contact pressure, Technical Issues, Vol. 2016, No. 3, pp. 113-119, 2016.
[17] K. Topczewska: Analytical model for investigation of the effect of friction power on the thermal stresses in friction elements of brakes, Journal of Theoretical and Applied Mechanics, Vol. 56, No. 4, pp. 1017-1027, 2018.
[18] K. Stevens, M. Tirovic: Heat dissipation from a stationary brake disc, Part 1: Analytical modelling and experimental investigations, Proceedings of the Institution of Mechanical Engineers, Part C: Journal of Mechanical Engineering Science, Vol. 232, No. 9, pp. 1707-1733, 2018.
[19] A. Yevtushenko, M. Kuciej, K. Topczewska: Analytical model for investigation of the effect of friction power on temperature in the disk brake, Advances in Mechanical Engineering, Vol. 9, No. 12, 2017.
[20] A.A. Yevtushenko, P. Grzes: Mutual influence of the sliding velocity and temperature in frictional heating of the thermally nonlinear disc brake, International Journal of Thermal Sciences, Vol. 102, pp. 254-262, 2016.
[21] A.M. Al-Shabibi: Solution of heat conduction problem in automotive clutch and brake systems, In *ASME 2008 Heat Transfer Summer Conference collocated with the Fluids Engineering, Energy Sustainability, and 3rd Energy Nanotechnology Conferences*, pp.321-326. American Society of Mechanical Engineers, 2008.
[22] A.M. Al-Shabibi, J.R. Barber: Transient solution of 2-D TEI problem using reduced order models, SAE transactions, pp. 1244-1248, 2001.
[23] A.M. Al-Shabibi: Solution of a Non-Linear Heat Conduction Problem, In *Automotive Clutch and Brake Systems. In ASME 2009 Heat Transfer Summer Conference collocated with the InterPACK09 and 3rd Energy Sustainability Conferences*, pp. 415-419 American Society of Mechanical Engineers, January 2009.
[24] A.M. Al-Shabibi: Solution for transient heat conduction problem with low Biot number, 9th International Conference on Heat Transfer, Fluid Mechanics and Thermodynamics, 2012.
[25] J. N. Reddy, D. K. Gartling: *The finite element method in heat transfer and fluid dynamics*, CRC press, 2010.

Serbian Tribology Society

SERBIATRIB '19

16th International Conference on Tribology

Faculty of Engineering University of Kragujevac

Kragujevac, Serbia, 15 – 17 May 2019

ASSESSMENTS FOR THE COUPLING OF SUPERPARAMAGNETIC PARTICLES

Farshed KARIMOV
Institute of Geology, Earthquake Engineering and Seismology,
Academy of Sciences of the Republic of Tajikistan
*Corresponding author: fkarim@mail.tj

Abstract: *The physical analytical conditions for coupling of superparamagnetic particles have been regarded in the present paper. The cases of two interacting superparamagnetic particles and superparamagnetic particle with another one being in single domain state were investigated. Assessments have been made for the critical period of magnetic moments' oscillations, determining the coupling of superparamagnetic particles. Some conclusions about the role of external magnetic field in this coupling were outlined.*

Keywords: *tribological technology, ferrofluids, superparamagnetic particles, magnetostatics interactions, coupling*

1. INTRODUCTION

The quality of ferrofluids, composing the wide basics of tribology, as a colloidal solution with fine ferro- and ferrimagnetic particles of 1-10 nm linear dimensions by the order of magnitude, is sufficiently dependent on the type of these particles and their interactions [1,2]. These particles normally are in superparamagnetic state and their agglomeration in clusters, chains, couples under the magnetostatics interactions depends both on material micro structure, magnetic properties, geometrical parameters and environmental factors such as temperature and external magnetic field. Thermal activation creates two main types of magnetic moment oscillations and rotations in SP particles. One is called internal, stipulated by the thermal fluctuations, another is called external, stipulated by the rotation of a particle as a whole [1].

As far as the energetical barriers for the in-phase and antiphase magnetic moments' fluctuations are different of each other the physical conditions for the agglomeration turn up different as well [3].

The physical conditions for the agglomeration of superparamagnetic (SP) particles through the magnetostatics interaction is under the consideration in the present work regarding in-phase and antiphase thermal activation fluctuation modes of their magnetic moments.

2. OBJECTIVES

The objective of the present study is to find out the critical conditions for the agglomeration of superparamagnetic particles with taking into account of in-phase and antiphase modes of thermally activated fluctuations of their magnetic moments.

The knowledge about these conditions is supposed to be important for the further progress in designing of high quality ferrofluids for the tribological technical and technological applications.

2.1 Methods

To analyze the SP particles' magnetostatics interactions the states of these particles, their geometrical and physical parameters are taken into account according to the classical representations [1,2,4].

As far as the shape of the particles under the present study is assumed for the simplicity to be spherical, the magnetostatics interaction between them is the same as for the magnetic dipoles. Two superparamagnetic particles with spherical shape, interacting magnetostatically, are under the consideration in the present study (see figure 1). Influence of magneto crystalline anisotropy is to be taken into account additionally.

The free energy of magnetic dipole interaction can be emphasized as the following:

$$W = \frac{\overrightarrow{\mu_1} \cdot \overrightarrow{\mu_2}}{|\overrightarrow{d}|^3} - \frac{3(\overrightarrow{\mu_1} \cdot \vec{d})(\overrightarrow{\mu_2} \cdot \vec{d})}{|\overrightarrow{d}|^5}, \qquad (1)$$

where vectors $\overrightarrow{\mu_1}$ and $\overrightarrow{\mu_2}$ are the particles' magnetic moments, $\vec{d}$ is the vector, connecting their centers in the right angular coordinate system $oxyz$ [1,4].

By means of writing down the components of all vectors in the formula (1) in the system $oxyz$ one can take the specific relations for the interaction energies for the cases of in-phase and antiphase rotations of the magnetic moments, emphasized in terms of the deflection angle from the initial equilibrium state.

For the analysis of the SP particles' movement the classical mechanics laws is applied with taking into account the interaction (1). For obtaining the results the relevant differential equation of the second order is under the solution with taking into account of the initial conditions.

3. COUPLING OF TWO SP PARTCILES

Couples of SP particles with in-phase and antiphase modes can be regarded as two interacting magnetic dipoles (figure 1). Magnetic moments in the coordinate system $oxyz$ for the in-phase mode can be represented in components as

$$\vec{\mu}_1\{\mu \sin\theta; 0; \mu\cos\theta\},$$

$$\vec{\mu}_2\{\mu \sin\theta; 0; \mu\cos\theta\},$$

where μ is the modulus of the moments $\overrightarrow{\mu_1}$ and $\overrightarrow{\mu_2}$, θ is the deflection angle $\vec{\mu}$ from oz axis. For the antiphase mode –

$$\vec{\mu}_1\{-\mu \sin\theta; 0; \mu\cos\theta\},$$

$$\vec{\mu}_2\{\mu \sin\theta; 0; \mu\cos\theta\}.$$

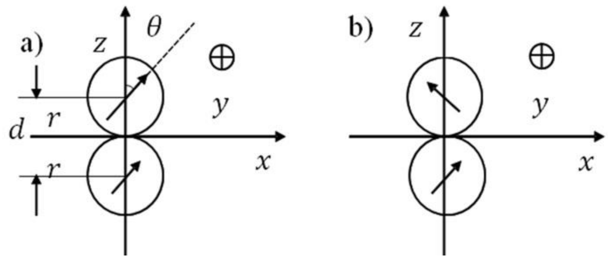

Figure 1. SP particles with in-phase (a) and antiphase (b) magnetic moments

Taking in mind that $\vec{d}$ has the only non-zero component d in oz one can write down the energy (1) for the in-phase and antiphase modes accordingly as

$$W_{\mathrm{a}} = W_0(1 - 3\cos^2\theta), \qquad (2)$$

$$W_{\mathrm{b}} = -W_0(1 + \cos^2\theta), \qquad (3)$$

where W_0 is the reference energy, equal to μ^2/d^3.

The energy barriers for these modes are represented in the figure 2.

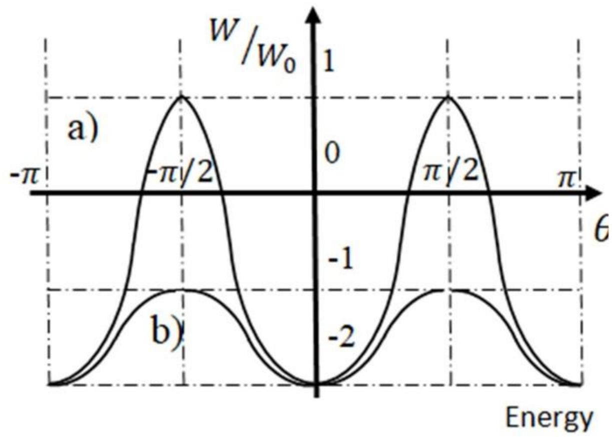

Figure 2. Energy barriers for in-phase (a) and antiphase (b) magnetic moments modes

As far as the particles with antiphase magnetic moments mode turn up always in the negative energy barrier the conditions for their agglomeration doesn't break and they remain in a coupling state. The particles with in-phase mode at the deflection angles θ (3) larger than $\theta_0 = \arccos \sqrt{3}/3$ and less than $\pi - \theta_0$ repel each other and therefore they can be principally disintegrated if the divergence distance between them will be sufficiently large.

According to the classical mechanics one can write the following equation for the movement of a particle in the time t taking in mind (3)

$$\frac{\mathrm{d}^2 z}{\mathrm{d}t^2} = -\frac{3\mu^2}{md^4} \cdot (1 + 3\cos 2\theta), \qquad (4)$$

where m is the mass of a particle and θ is oscillating with the round frequency ω: $\theta = \omega t$.

Equation (4) shows that the character the particles do move is dependent both on their magnetic interactions and inertia factor.

To find the conditions for the remaining particles' coupling state let's assume for simplicity that they don't move far from each other so that the divergence distance $\Delta d \ll 2r$.

4. CALCULATIONS

By solving the differential equation (4) under the initial conditions at $t = t_0$, when $\theta = \theta_0$, so that

$$z = r;\ \frac{\mathrm{d}z}{\mathrm{d}t} = 0,$$

we find the critical term for the frequency ω and relevant period of magnetic moment oscillations:

$$\tau_{cr} \cong 10 \cdot \sqrt{\rho \cdot \frac{r}{J}}, \qquad (5)$$

where ρ is the particles' material density.

For instance, for the particles with J = 500 Gs, $r = 10^{-6}$ cm, $\rho = 4\ \mathrm{g/cm^3}$ we obtain τ_{cr}= $4 \cdot 10^{-8}$ c. If to compare this value with the internal relaxation time for SP particles, equal to 10^{-9} c [1], we can conclude, that for this kind of thermal activation the agglomeration is stable. According to the term (5) the agglomeration and coupling of the SP particles remain if the frequency of magnetic moments rotation is enough high, i.e. the period is smaller than τ_{cr}. The physical meaning of the relation (5) obtained signifies that the agglomeration of a couple of SP particles for in-phase magnetic moments' oscillations will be realized for the particles with high enough inertia, i.e. having large density and volume impact, low enough magnetization, providing moderate repulsion between them. Otherwise, the particles detach on sufficient distance from each other and the probability for the restoring coupling and agglomeration has low probability, because of collisions with other particles and fluid flows carrying them away.

The energy barriers in SP particles besides of magnetostatics interactions is created also by magneto crystalline anisotropy [1,2,4]. Let's compare the impacts of magnetostatics interaction (1) and magnetic anisotropy free energies. From (1) and (2) for the maximum magnetostatics energy barrier we have

$$W_m = \frac{\pi J^2 V}{3}$$

and for the single axial magneto crystalline anisotropy –

$$W_K = KV,$$

where K is magneto crystalline anisotropy constant and V is a particle's volume.

Comparing the last equalities, we find that magnetostatics interactions prevail, if the following nonequality is fulfilling:

$$\pi J^2 > 3K.$$

Some examples for the assessments are in the table. One can notice that for some SP particles the magnetostatics plays more important role in determining the thermal activation of the magnetic moments than magneto crystalline anisotropy.

Table. Examples for the assessments of the magnetostatic and magnetocrystalline anisotropy free energies' impact

No	J, Gs	K, erg/cm^3	W_m / W_K
1	1000	$3 \cdot 10^6$	0.35
2	500	$5 \cdot 10^4$	2.13
3	1700	$4 \cdot 10^5$	7.57

5. COPUING OF SP AND SD PARTICLES

Let’s consider the case, when one of the coupling particles is in single domain (SD) state and another one is SP (figure 3). The magnetic moment of the first is pinned by the magneto crystalline anisotropy.

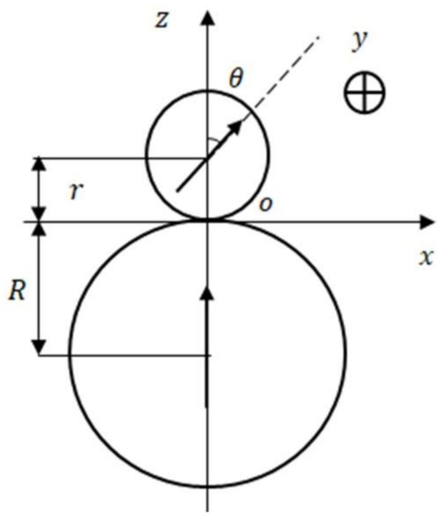

Figure 3. SD and SP particles.

The magnetic moments of the SD and SP partciles in components let’s write accordingly as the following:

$$\vec{\mu}_{SD}\{0,0,\mu_{SD}\cos\theta\},$$

$$\vec{\mu}_{SP}\{\mu_{SP}\sin\theta,0,\mu_{SP}\cos\theta\}.$$

Inserting these components in (1) leads to the impression for the magnetostatics energy of interaction:

$$\boldsymbol{W_1} = \frac{-3\boldsymbol{\mu_{SD}\mu_{SP}}\cos\boldsymbol{\vartheta}}{(\boldsymbol{r}+\boldsymbol{R})^3}. \qquad (\boldsymbol{6})$$

Like for the case of two SP particles by means of composing the equation for the SP particle’s movement (4) one can obtain the condition for the periods of SP particle oscillation, when coupling is conserving:

$$\tau_1 \le \pi\sqrt{\frac{2\rho r R}{3(\pi-2)J_{SD}J_{SP}}}. \qquad (7)$$

where J_{SD},J_{SP} are the magnetizations of the SD and SP partciles accordingly.

Than it follows from (7) that for the smaller SD and SP partciles, larger their magnetizations, more density of SP partcile the periods of oscillations for the coupling should be shorter.

For instance for the magnetizations J_{SP} = 500 Gs, J_{SD} = 1000 Gs, r = 10^{-7} cm, R = 10^{-5} cm, ρ = 4 g/cm^3 (7) gives, that critical period is about $5{\cdot}10^{-9}$c, i.e. five times exceeding the internal relaxation time for SP particles, equal to 10^{-9} c [1].

If to apply external magnetic field, directed along $\boldsymbol{oz}$ axis, the energy barriers for the SP particle’s magnetic moment equilibrium state will be deeper and therefore the average magnetic moment component along this axis will be larger increasing the attraction between SD and SP particles and promoting the coupling between these particles. If to compare the barriers of the magnetostatics energy in an external magnetic field $\boldsymbol{H}$ and single axis magneto crystalline one for the particle’s magnetic moment,

$$\boldsymbol{HJ} \ge \boldsymbol{K},$$

for instance, at $\boldsymbol{J}$ = 500 Gs, $\boldsymbol{K}$ = $5{\cdot}10^5$ erg/cm^3, we can find that the magnetic field, exceeding 100 Oe, plays sufficient role in the coupling of SP particles.

6. CONCLUSION

For the in-phase magnetic moments’ oscillations in SP spherical particles the terms for stable agglomeration of their couples are fulfilling if the particles have enough density, low magnetization and relatively large radius.

The conditions for the SP particles' agglomeration depends also on the acting temperature both trough magnetization getting down and thermal activation rising up.

In some cases the magnetostatics interactions prevail the impact of magneto crystalline anisotropy in magnetic moments’ oscillations in SP particles and in-phase oscillation modes’ are to be taken into the consideration in determining their agglomeration state.

An external magnetic field is able to reduce free energy barrier for the stability of SP partcile’s magnetic moment and therefore increase the probability of the coupling.

REFERENCES

[1] R. Rosensweig: *Ferrohydrodynamics*, Cambridge University Press, Cambridge, New York, 1985.
[2] S. Odenbach: Ferrofluids, in: K.H.J. Buschow (Ed.): *Handbook of magnetic materials*, Vol. 16. Hardbound, 2006.
[3] F.H. Karimov: The aggregation of superparamagnetic particles under in-phase and antiphase oscillations of their magnetic moments, in: *Proceedings of the 12th International Conference and School "Problems of Geocosmos"*, 8-12.10.2018, St. Petersburg, Russia, 2018, p. 71.
[4] L.D. Landau, E.M. Lifshitz: *Course of Theoretical Physics,* vol. 8. Electrodynamics of Continuous Media, Butterworth-Heinemann, 1979.

Serbian Tribology Society

SERBIATRIB '19

16th International Conference on Tribology

Faculty of Engineering University of Kragujevac

Kragujevac, Serbia, 15 – 17 May 2019

RESEARCH AND STUDIES ON FLEXIBLE TUBING WEARING

A. HAGIANU[1], I. NAE[1], G. C. IONESCU[1*], R. G. RIPEANU[1], A. DINITA[1], I. N. RAMADAN[1]

[1] Petroleum-Gas University of Ploiesti, Ploiesti, Romania,

Corresponding author: ionescu_g_r@yahoo.com

Abstract: *Flexible tubing (coiled tubing) demonstrated its capabilities and has been becoming nowadays a necessity in the oil and gas industry. Within the applications of flexible tubing have to be mentioned inclined drilling or horizontal drilling, cleaning clogged wells, interventions on wells both on production wells and during the drilling activities. The flexible tubing used in exploitation and/or operating the wells should meet the following requirements: tensile strength resistance collapse resistance, fatigue strength, corrosion resistance and resistance to fragilizant factors. In particular, the damages that may occur with respect to the functionality loss of flexible tubing are manifested by breakage or loss of tightness, excessive plastic deformation, bumping, and breakage. During the use of the flexible tubing in the well, it undergoes a series of stresses that lead to wear and degradation, changes in dimensional, geometric and mechanical characteristics. The paper presents the theoretical and experimental studies performed in order to establish the admissibility conditions regarding the mechanical and dimensional characteristics (shape deviations) of the material, the influence of working environments on the state of operation of the flexible tubing.*

Keywords: *flexible tubing, mechanical characteristics, geometric characteristics, corrosion, wear.*

1. ASPECTE GENERALE

For drilling equipment the tubing column is one of the key elements. The crisis of fossil fuels in parallel with the high demand of oil has been leading to deeper bore hole drilled in the search for this key resource as well as in the development of new drilling technologies as guided horizontal drilling, arborescent drilling. These challenging tasks are demonstrating that classic, segmented columns cannot be used since the threaded joint is not resisting to the high requirements of these applications. At the same time economical pressure to conduct in the shortest possible time the needed intervention at the wells such as cleaning, removing colmatation, rectification of the bore whole or extraction of damaged tools cannot be fulfilled with segmented columns [1].

The development of new materials and new welding technologies generated the opportunities for the development of flexible, flexible tubing (coiled tubing). In all the applications where it is used drilling, well interventions, the flexible tubing is reducing the time and consequently the operational costs of activities conducted.

In all the conducted activities on the flexible tubing is applied a lot of stress and in addition is prone to erosion and corrosion. All these are leading to wearing and sometimes modifications of its physical and geometrical properties. Thus it is obviously necessary that all the wearing factors to be considered, monitored and taken into calculation in order to establish properly the degree of flexible tubing wearing in order to analyse the risk of using it in further operations.

The main factors which affect flexible tubing wearing depend on well specific requirements (whole diameter, depth, deviation) as well as different operations required in the drilling process (acidulations boring, milling, transportation of special instrumentations packages, tools recovery, washing, circulation of different fluids etc.).

In this context this article presents the research conducted for establishing the mechanical characteristics of the flexible tubing used in the intervention equipment.

2. TYPES OF STRESS APPLIED TO FLEXIBLE TUBING

On the flexible tube there is applied at the same time and at the same operation a complex stress (Fig. 1), which generates an accelerate wearing and consequently decrease its operational life.

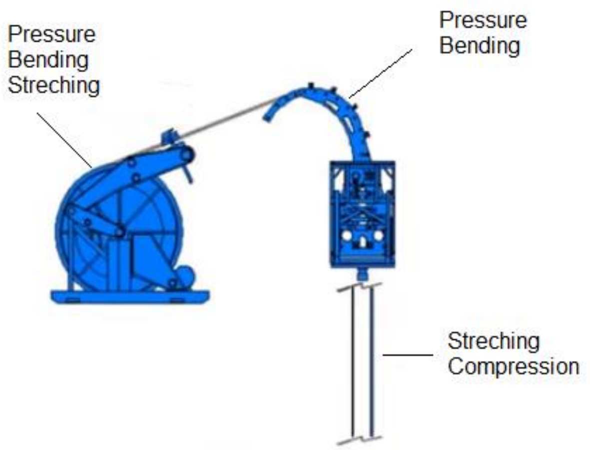

Figure 1. Types of stress applied to flexible tubing [1]

Every time when the flexible tube is coiled / uncoiled and is pushed/pulled through the injector it is affected by bending, compression, stretching as presented in Fig. 1. In addition, on the flexible tubing are acting pressure forces both from inside and outside.

Areas were the flexible tubing is stressed (bending, stretching, compression, traction, inside outside pressure) are presented in Fig. 2 as follows: introduction step (1, 2, 3), extraction step (4, 5, 6).

An operational cycle for the coiled tubing consists of all the phases required for fulfilling the operation staring with the uncoiling from the drum, insertion on the well bore, drilling, rectifying, washing, removing damaged parts etc., extraction from the bore well and coiling it on the drum as presented in Fig. 2. By following these operations there, it could be identified six bending steps as could be seen also in Fig. 2.

There should be mentioned that the stress applied to the flexible tubing should not be greater than the limits established by the producer for material. However, if these limits are overcome cold lead to a premature fatigue of the flexible tubing or even worst in its physical deformation making it unusable.

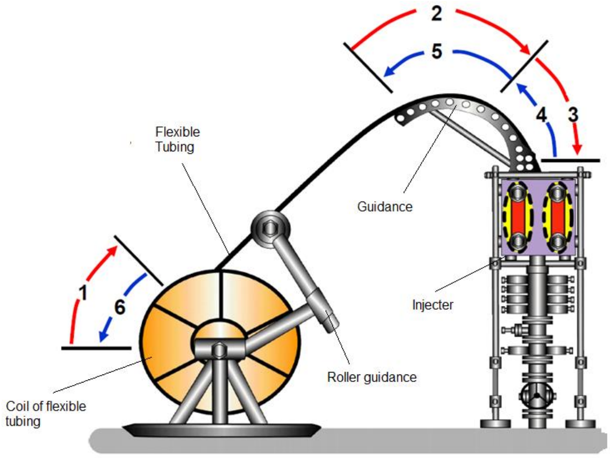

Figura 2. Flexible tube areas which are under cyclical bending stress [2]: Flexible tube introduction in well bore (1-2-3); Extraction of flexible tube from well bore (4-5-6).

In addition to the stress factor described previously there are other factors which contribute to the flexible tubing wearing: corrosion generated by the liquid medium from the well bore (salty water, different non neutral PH liquids, etc.) and erosion due to the touching the walls of bore well and due to mineral particles existing in the liquid working medium.

Taking into account all the stress, corrosion and erosion factors and assessing their impact on the flexible tubing there it could be established the wearing degree as well as the risk coefficient for using the coiled tubing in further applications. Consequently, research and studies regarding coiled tubing wearing are very important in establishing its operational life and thus avoiding accidents with human and financial losses.

3. ESTABLISHMENT OF EXPERIMANTAL DETERMINATION PROGRAME

The experimental determination programme has the goal to establish mechanical and geometrical (shape deformations) of coiled tubing. In addition in order to establish the impact of corrosion on flexible tubing there was conducted experimental research using different liquids used in the drilling or intervention processes.

Input data used for conducting the planned tests as well as the output data (measurement results, calculation based on output measurements) are presented in Fig. 3.

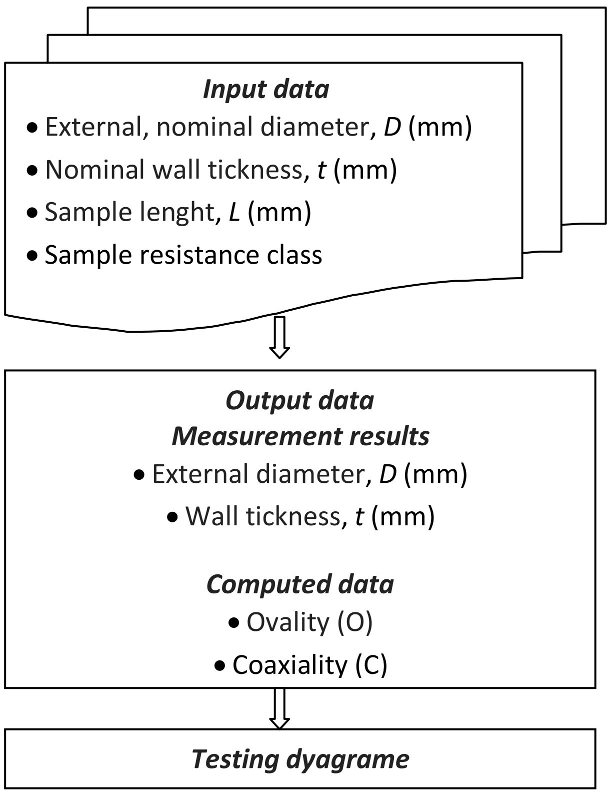

Figure 3. Establishment of testing conditions for flexible tubing.

The programme of experimental research encompasses the tests as are presented in Table 1.

The classification of samples used in the programme of experimental testing is presented in Table 2.

Table 1. Programme of experimental research

Type of test/ determination	Characteristic specifications
Determination of geometrical characteristics of studied flexible tubing	• External nominal diameter, *D* (mm) • Nominal thickness of wall, *t* (mm) • Sample length, *L* (mm) • Ovality (O) • Coaxiality (C)
stretching testing of flexible tubing	• Tensile strength (R_m) • Yield strength (R_c) • Elongation after breaking (A)
Corrosion tests for flexible tubing	• Polarization resistance (R_p) • Corrosion potential (E_{corr}) • Corrosion current density (I_{corr}) • Corrosion rates (C_{rr}).

Table 2. Classification of samples used in the programme of experimental testing

Sample	Marking on the testing sample	Number of functional hours
P1	P1/1	New flexible tubing (0 operational functioning hours)
	P1/2	
	P1/3	
P2	P2/1	Tubing with 30 full operation conducted
	P2/2	
	P2/3	

In Table 3 are presented the geometrical characteristics of tested samples.

Table 3. Geometrical characteristics of tested samples

Tested sample (D = 1½ in) (*D* = 38,10 mm)	
External nominal diameter, *D* (mm)	38,1
Nominal wall thickness, *t* (mm)	2.76
Length of sample, (mm)	400

The tested flexible tubing was made off A 606 steel, this material presents a high resistance to atmospheric corrosion [3]. According to ASTM standard, chemical composition and main mechanical characteristics are as presented in Tables 4 and 5.

Table 4. Steel A606, chemical composition [3]

Steel standard	Chemical composition (%), max.		
	C	Mn	S
A606	0.26	1.30	0.06

Table 5. Material A606 – mechanical characteristics [3]

Steel standard	mechanical characteristics, min.		
	Tensile strength, MPa (ksi)	Yield strength, MPa (ksi)	Elongation %
A606	450 (65)	310 (45)	22

3.1 Establishment of geometric characteristics of flexible tubing

In order to establish the testing parameters for the experiments to be conducted first step is to identify testing sample as presented in Fig. 4. The measurements are conducted in six measurement planes (1, 2, 3, 4, 5, 6), equally distributed on the tube generator at 2D distance one for other. In each measurement plane will be conducted 8 measurements on the circumference (A, B, C, D, E, F, G, H) – angular these points being placed at 45^0.

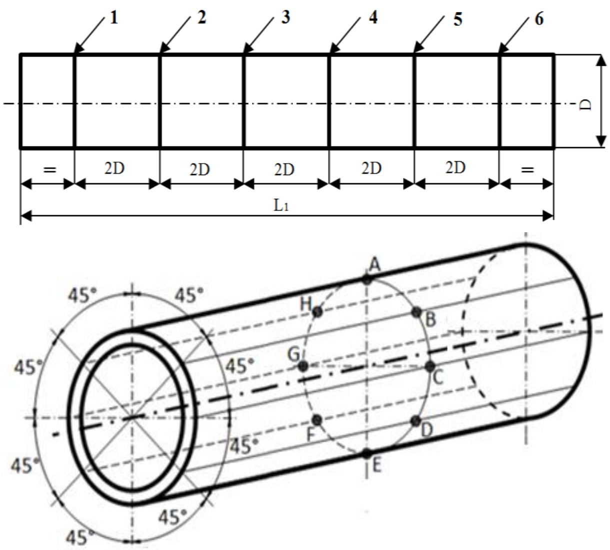

Figure 4. Establishment of geometrical characteristics of test samples:

D –external diameter; L_1 – minimum length of tested sample; *1, 2, 3, 4, 5,6* – five areas in plane for each being measured external diameter, and wall thickness.

The dimensions of external diameters and wall thickness according to the catalogue data are presented in Table 6 [4].

Table 6. External diameters and wall thickness [4]

External diameter (D)		Wall thickness (t) (mm)
(inch)	(mm)	
1,000	25,40	2,41 - 3,17
1,250	31,75	2,41 - 3,96
1,500	38,10	2,59 – 4,77

Hereunder is presented the methodology of measurements conducted on samples from P1 and P2 classes.

First set of measurements are conducted in order to verify external diameter of tubing (*D*) in each measurement plane (1, 2, 3, 4, 5, 6) and on each position established on the circumference (A-E, B-F, C-G, D-H). The same measurements are conducted for wall thickness (*t*) in each measurement plane (1, 2, 3, 4, 5, 6) and on each position established on the circumference (A-E, B-F, C-G, D-H). The obtained results for sample P1/1 are presented in Tables 7 and 8.

Table 7. Measured values of external diameter

Measured values of external diameter, *D* (mm) – sample P1/1						
Position	"1"	"2"	**"3"**	**"4"**	"5"	"6"
A-E	37.51	37.56	37.56	**37.58**	37.61	37.66
B-F	37.85	37.76	37.96	**37.78**	37.92	37.84
C-G	37.75	37.74	37.99	**37.85**	37.7	37.71
D-H	37.51	37.52	37.74	**37.33**	37.67	37.87
Average	37.655	37.645	37.813	**37.635**	37.725	37.77

Table 8. Measured “t “values and calculated values of “E “and” O” for sample for P1/1

Measured “t“ values and calculated values of “E“ and ”O” for sample for P1/1						
Position	"1"	"2"	**"3"**	**"4"**	"5"	"6"
"A"	2.72	2.70	**2.67**	**2.67**	2.74	2.66
"C"	2.63	2.68	**2.67**	**2.60**	2.62	2.66
"E"	2.60	2.68	**2.62**	**2.62**	2.66	2.69
"G"	2.67	2.69	**2.60**	**2.68**	2.60	2.67
Average	2.65	2.68	**2.64**	**2.64**	2.65	2.67
Excentricity (%)	$E = [(t_{Max} - t_{Min}) / t_{med}] \times 100$					5.243
Ovality (%)	$O = [(D_{Max} - D_{Min}) / D_{med}] \times 100$					1.752

Measurements of the flexible tubing was conducted by using the ultrasonic portable measurement device, OLYMPUS 38DL Plus, which is capable of measuring thickness from 0,1 up to 635,0 mm. Based on the obtained results were calculated eccentricity (*E*) and ovality (*O*) according to the relationship presented in Table 8.

Based on measured parameters for sample P1 and P2 there were established the variations of diameters for each measurement plane (1, 2, 3, 4, 5, 6) and on each point of circumference (A-E, B-F, C-G, D-H). The obtained graph for P1/1 is presented in Fig. 5.

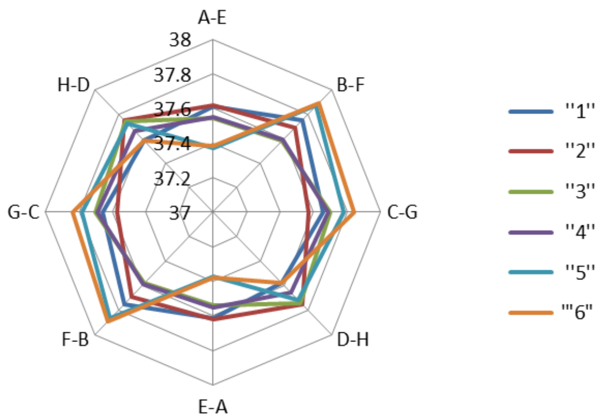

Figure 5. The variations of external diameters (D) for sample for P1/2

The geometric characteristics of flexible tubing have an important impact on its behaviour during the exploitations since a smaller external diameter or a smaller thickness of the wall are possible areas of flexible tube breaking.

3.2 Stretch testing of the flexible tubing

In real life the flexible tubing is under various types of stress which are almost impossible to be reproduced in laboratory. Usually the tests conducted in laboratory are verifying one by one different types of stretch, thus the monoaxial stretch is one of the most important tests [3].

The stretching test is conducted applying an axial growing force to a sample of material usually until the sample is breaking. To the entire period of testing data related to sample elongation correlated with the applied force are recorded. For the conducted tests was used the Walter Bay LF300 universal testing device. This equipment is designed to be used for both static and dynamic tests having the capacity of applying a force 300 in static regime and ± 250 kN with a frequency of up to la 20 Hz regime and is presented in Fig. 6.

Figure 6. Walter Bay universal testing equipment.

The tests were conducted on the two samples P1 (new flexible tubing) and P2 (30 cycles conducted) and the samples are presented in Fig. 7.

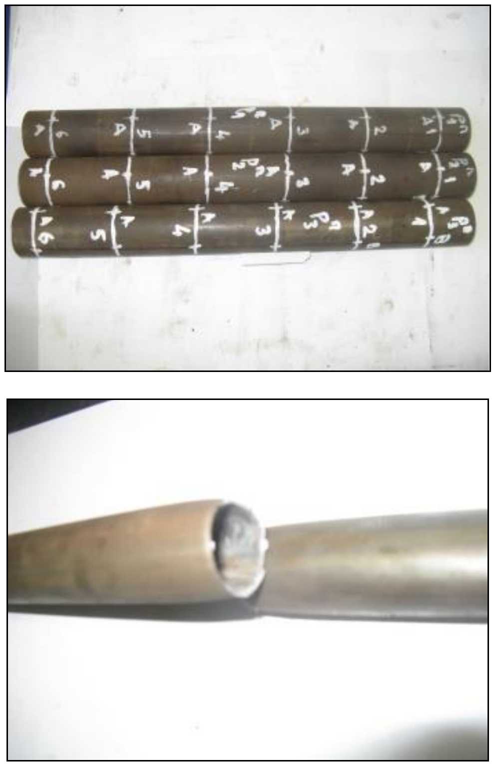

Figure 7. Tested samples

The results obtained after testing the samples are presented in Table 9.

Table 9. Strength measured values for the samples of flexible tubing.

Sample	Measured values
Sample P1 –Flexible tubing 0 hours of operations	
P1/1	D_{med} = 37.66 mm; t_{med} = 2.67 mm; S_0 = 104.28 mm^2
	R_m = 637MPa; R_c = 608 MPa; A = 21.9 %
P1/2	D_{med} = 37.63 mm; t_{med} = 2.725 mm; S_0 = 106.301 mm^2
	R_m = 633 MPa; R_c = 582 MPa; A = 21.4 %
P1/3	D_{med} = 37.68 mm; t_{med} = 2. 71mm; S_0 = 104.397 mm^2
	R_m = 633 MPa; R_c = 582 MPa; A = 22.8 %
Sample P2 – Flexible tubing with 30 cycles of operations	
P2/1	D_{med} = 37.88 mm; t_{med} = 2.765 mm; S_0 = 107.22 mm^2
	R_m = 620 MPa; R_c = 598 MPa; A = 17.61 %
P2/2	D_{med} = 37.835 mm; t_{med} = 2.82 mm; S_0 = 107.22 mm^2
	R_m = 611 MPa; Rc = 588 MPa; A = 20.48 %
P2/3	D_{med} = 37.77 mm; t_{med} = 2.775 mm; S_0 = 106.63 mm^2
	R_m = 620 MPa; R_c = 588 MPa; A = 20.9 %

In the Table 9 were used the following notations: D_{med} – average of measured diameters; t_{med} – average of wall thickness; S_0 – surface of breaking surface; R_m – tensile strength; R_c – yield strength ; A – elongation at breaking.

According to the obtained results it could be established that plasticity index (A – elongation) in lower at P2 samples that at P1 samples, while breaking resistance and limit of flow does not have significant variations.

These results shows that the material of which the flexible tubing is made of is going through a process of cold hardening due to the complex stress generated by operational use (stretching, compression, stretching combined with internal pressure, bending combined with internal pressure and external pressure due to roller guidance's from the injection head).

In regard with the geometry (*D*, *t*) of the samples used another important observation is that the tested samples broken in the areas of variations of diameter and thickness where these two parameters had the minimum value.

3.2 Corrosion testing of flexible tubing material

The corrosion resistance was tested on six samples taken from flexible tubing (three form the new and 3 from the one with 30 operational cycles).

The samples were taken both from area were the flexible tube was welded and area without any weld as presented in Figure 8. The cutting of samples was conducted in less intensive regimes in order to avoid introduction of additional stress in the structure of material.

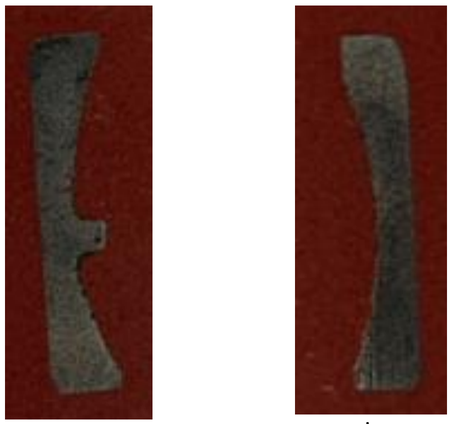

a b

Figure 8. Samples to be tested:
a – from welded area; b – area without weld.

The sample surface which should be in contact with the liquid was rectified and polished with abrasive material with a granulation of 600 Mesh. The liquid used for testing was the liquid taken from a functional well and has the chemical composition presented in Table 10.

Table 10. Well liquid chemical composition

Components	Measured value	U.M.
pH	7.2 at 15.9 ^{0}C	unit. pH
Calcium	2450	mg/L
Magnesium	1020	mg/L
Sodium	30100	mg/L
Sulphate (SO4)	64.8	mg/L
Chlorate (Cl^-)	56800	mg/L
Bicarbonates (HCO3)	296	mg/L

The pH was measured with PHM201 MeterLab (Radiometer) with a combined electrode Ag/AgCl. For testing was used the Volta Lab PGZ 100 potențiostate and an electrochemical cell according ASTM G5. The electrochemical cell consists of a glass vessel, a Haber-Luggin capillary installed on a special fixture, two graphite electrodes in series as counter, a reference electrode made of saturated Calomel and the third one which was the sample. The setting is presented in Fig. 9.

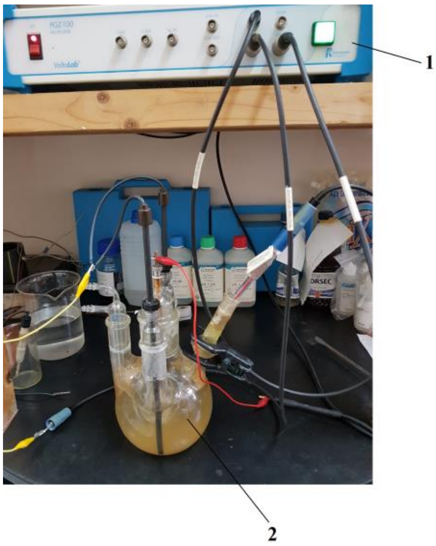

Figure 9. The experimental testing used for testing the corrosion:

1 –Volta Lab PGZ 100 potentiostate;
2 – Electrochemical cell.

The holder of the sample was made of Teflon with an opening with the surface of 1 cm^2 through this opening the sample getting in contact with the well liquid. In front of the opening was fixed the capillary tube.

There were acquired the polarization curves and Evens diagrams containing Tafel lines. From these outputs there were established polarization resistance (R_p), corrosion potential (E_{corr}), corrosion current densities (i_{corr}), and corrosion rates (C_{rr}). The results are presented in Figs. 10-13 and Table 11. For the polarization curves the limits of balancing were between -1 and 1V with a speed of 1mV/sec.

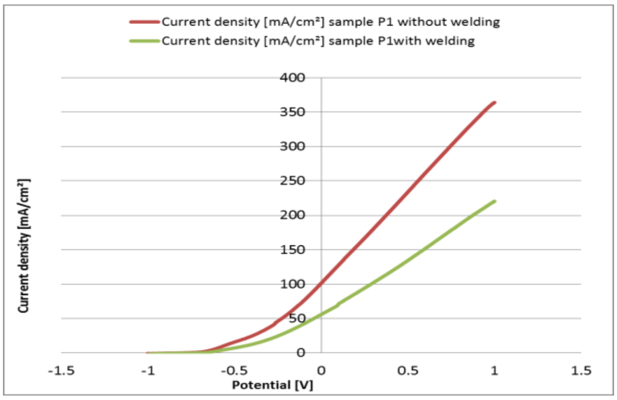

Figure 10. Variation of current density in regard with potential for the not used flexible tube sample

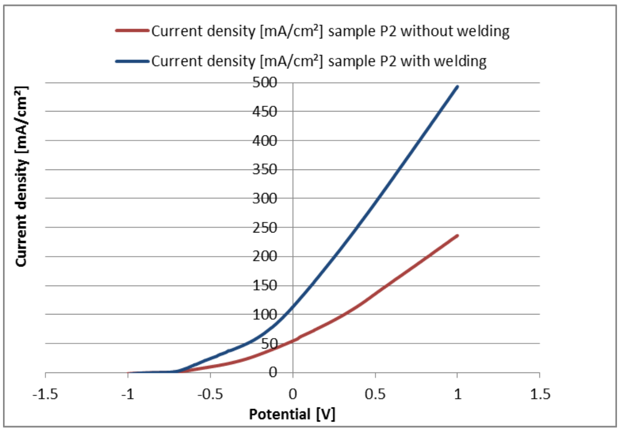

Figure 11. Variation of current density in regard with potential for the sample taken from flexible tube with 30 cycles of use.

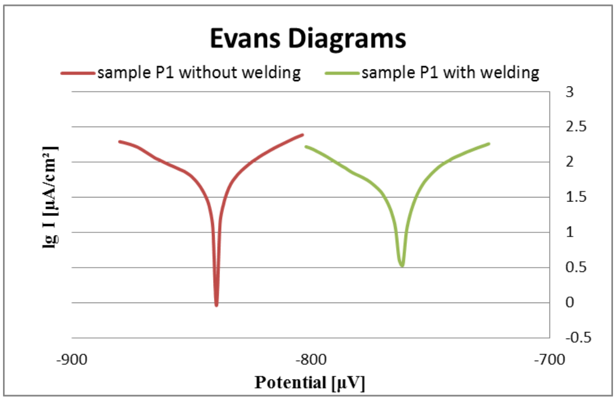

Figura 12. Evans diagram for the not used flexible tube sample

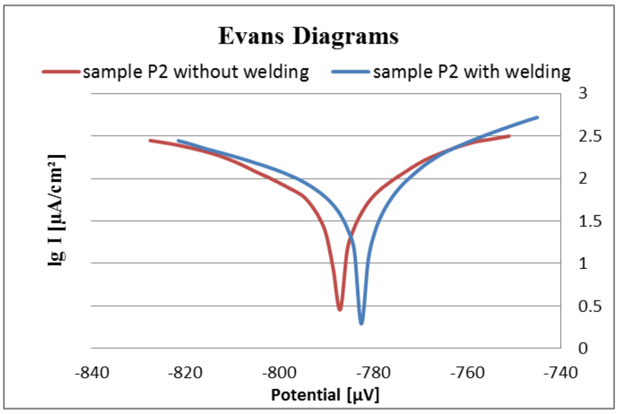

Figure 13. Evans diagram potential for the sample taken from flexible tube with 30 cycles of use

Table 11. Results of experimental testing

Sample Type	R_p ($\Omega.cm^2$)	E_{corr} (mV)	i_{corr} ($\mu A/cm^2$)	C_{rr} (µm/year)
P1/2	191.900	-839.0	39.724	461.600
P1/3	239.130	-761.8	27.772	322.700
P2/2	134.840	-787.0	40.368	469.100
P2/3	121,630	-782,4	64,643	751,200

The conducted tests show that the samples present a good resistance to corrosion in the medium specific to the wells; however, the values of i_{corr} should be at lower level and R_p should be at high values in order to obtain these results.

Taking into consideration the criterion described previously we could observe that samples taken from the new flexible tubing P1/3, are more resistant to corrosion than the sample P1/2. This behaviour could be explained due to the fact that the chosen welding material is more resistant to the corrosion, or the welded areas were treated after welding. The same behaviour could be observed studying corrosion rates for the two samples.

The sample taken from the flexible tubing with 30 cycles of operational use we could observe a different behaviour; the sample with welding on it P2/3, had a higher rate of corrosion that one with no welding on it P2/2. This could be explained by the fact that during the 30 operational cycles conducted, the surface treatment was eroded / corroded and the welded area is less resistant than the other one.

A coil of flexible tubing is used an average of 80 cycles/year, and a working cycle with an average of 12 hours duration. When is not used in operations, the flexible tubing is also affected by atmospheric corrosion. A reliable monitoring system of flexible tubing wearing must take into consideration the effect of atmospheric corrosion on the flexible tubing state of health.

In order to establish the corrosion velocity in atmospheric conditions there were taken three samples from the flexible tubing P1. The weight of each of the three samples was recorded and samples were introduced in well liquid. Samples were taken out of the liquid and let in a controlled temperature room at 15 ^{0}C for 7 days. After that the weight of the samples was recorded and the corrosion rate was determined according to NACE SP0775-2018-SG standard [8]. Using this method the corrosion rate calculated was C_{rr} air = 0.154 mm/an.

Taking into consideration the statistical data regarding operational use and time of sitting on standby and being affected by atmospheric corrosion there it was obtained a corrosion rate of C_{rr} tubing = 0,214 mm/year (C_{rr} P2/3 = 751.200 mm/year (Table 11) and C_{rr} air = 0.154 mm/year).

It could be observed that traces of well liquid which remain on the flexible tubing could severely affect speed of corrosion consequently it is highly recommended to clean the liquid from the tubing both from inside and outside.

4. CONCLUSIONS

Flexible tubing used in well related operations is prone to complex stress which could lead to its premature wearing, consequently to reduce the operational life. Some of the first indications of flexible tubing wearing are the modification of tubing geometry. These local modifications also depend on the quality of injection system, and different length of the wells operated. When used for deep wells (over 3000 m) due to friction with well bore walls and elongation generated by its own weight the diameter and wall thickness of flexible tubing are smaller and the danger of breaking it is higher.

Simultaneous stretching and pressure stress accelerates the wearing of flexible tubing and consequently reduce its operational life. In addition when it is used for horizontal applications the friction with well bore walls increases consequently the force for pushing/puling the tools are greater and the elongation increases.

In order to develop a reliable system for assessing the wearing of flexible tubing one first step to be considered is the monitoring the modifications occurred in geometry of tubing: external nominal diameter (*D),* wall thickness *(T),* ovality *(O)*. When considered the corrosion then the thickness of the tubing wall is also decreasing significantly.

As monitoring methods to be used there could be mentioned the followings:

a) Periodic visual verifications looking for geometrical modifications.
b) Periodic measurement of flexible tubing wall thickness (the measurement should be conducted on different segments in order to avoid mistakes).
c) Periodic measurement of flexible tubing coil weight and length (this situation gives a better information on corrosion and elongation).

REFERENCES

[1] https://en.wikipedia.org/wiki/China_National Petroleum_Corporation accessed: 18.09.2018.

[2] https://wildwell.com/wp-content/uploads/Coiled-Tubing.pdf.

[3] ASTM A 606 Standard Specification for Steel, Sheet and Strip, High-Strength, Low-Alloy, Hot-Rolled and Cold-Rolled, with Improved Atmospheric Corrosion Resistance.

[4] https://www.nov.com/WorkArea/DownloadAsset.aspx?id=28541.

[5] C. Besleaga, V. Dumitru, L.M. Trinca, A.C. Popa, Popa, C.C. Negrila, L. Kolodziejczyk, C.R. Luculescu, G.C. Ionescu, R.G. Ripeanu, A. Vladescu: Mechanical, Corrosion and Biological Properties of Room-Temperature Sputtered Aluminium Nitride Films with Dissimilar Nanostructure, Nanomaterials Vol. 7, No. 11, pp.1-26, 2017, doi: 10.3390/nano7110394

[6] C. Dudu, R.G. Ripeanu, A.C. Drumeanu, A. Dinita, A.M. Lospa: Evaluation of the corrosion wear speed of different equipment in the water injection treatment plant, The 10th International Conference of Product Design, Robotics, Advanced Mechanical &Mechatronic Systems and Innovation Conference (PRASIC 18), 8-9 November 2018, Brasov, Romania, 2018.

[7] ASTM G5-14e1, Standard Reference Test Method for Making Potentiodynamic Anodic Polarization Measurements, ASTM International, West Conshohocken, PA, 2014.

[8] NACE SP0775-2018-SG "Preparation, Installation, Analysis, and Interpretation of Corrosion Coupons in Oilfield Operations" NACE International, 15835 Park Ten Place, Houston, TX 77084.

Serbian Tribology Society

SERBIATRIB '19

16th International Conference on Tribology

Faculty of Engineering
University of Kragujevac

Kragujevac, Serbia, 15 – 17 May 2019

INVESTIGATION OF DYNAMIC FRICTION COEFFICIENT IN BRAKE SYSTEMS

Pavel KOVALENKO[1,*], Svetlana PEREPELKINA[1]
[1]ITMO University, Saint Petersburg, Russian Federation
*Corresponding author: kovalenko_p.p@mail.ru

Abstract: *In this paper, the research of friction coefficient changes in the tribopairs carbon-fiber-reinforced silicon carbide (C/SiC) – steel 37Cr4 and C/SiC – steel C22 used in cars brake systems was carried out for the selection of suitable materials and conditions of usage that provide a vehicle with high performance and safety of braking. Brakes made of C/SiC are very effective in sport cars, but they are expensive, which makes it impossible to use such materials for design of both pads and discs in the brake systems of trucks and off-road vehicles. The main goal of this work was to choose the most suitable material for manufacturing of brake discs interacting with C/SiC pads in order to decrease the cost of brake systems without decreasing their performance. According to the results of the research, the tribopair C/SiC – steel C22 could be used in heavy loaded trucks and massive off-road vehicles.*

Keywords: *dynamic friction coefficient, carbon-fiber-reinforced silicon carbide, tribological properties, wear, design of brake systems.*

1. INTRODUCTION

Brakes are one of the most significant parts in any vehicles, such as cars, trucks, trains and aircrafts [1, 2]. Disk brake is the most common type of brakes. It is based on the use of friction between the elements of the brake. These brakes usually consist of brake pads that can be pressed to a brake disc connected to the wheel [3]. Cast iron is widely used for manufacturing of such brakes. This material has good thermal conductivity and anti-vibration capacity [3]. The disadvantage of cast iron brakes is high level of noise and wear rate.

Various materials are used for manufacturing of brake pads. The efficiency of these brake systems depends mostly on the tribological properties of the materials used, as well as on the conditions of their usage [3]. A wide range of research has been carried out on ceramic composite materials and their tribological and mechanical properties for better understanding of the behaviour of such materials in braking systems [2].

In this paper, the experimental research of metallic and ceramic materials was carried out in order to select the optimal tribopairs that could be used for manufacturing of brake systems for trucks and off-road vehicles providing them with high safety and efficiency without increasing the cost.

2. MATERIALS FOR BRAKES

Materials for brake pads can be classified into semi-metallic, metallic, organic and ceramic types [4].

Metallic pads are noisy and produce a lot of dust. Wear rate of such brakes is high [5].

Nowadays, brakes manufacturers use some organic and non-asbestos materials in order to decrease the negative ecological impact and produce environment-friendly brakes [6-10]. These brakes produce less noise, but wear rate is also high.

C/SiC composites are used in braking systems, because they have a lot of advantages, such as low density, high temperature resistance, good tribological properties and low wear rate [11, 12]. The disadvantage of such brakes is their cost. Ceramic composites are expensive. Also, the tribological properties of ceramic pads depend on the temperature. The influence of the temperature in brake systems on the friction processes was studied by V. Dygalo et al. in [13] and N. Benhassine et al. in [14].

Another important issue for brakes is vibrations and their influence on the contact pressure and area, since friction between the elements of brakes depends on these parameters, and, therefore, such effects should be considered during the design process [15, 16]. Also, the contact area and, therefore, the tribological properties depend on the initial surface roughness and the accuracy of manufacturing and assembling of brake system elements [17-19].

3. EXPERIMENTAL RESEARCH

A wide range of measurement machines and methods has been developed for investigation of tribological properties [20].

In this paper, the experimental research of the materials for the design of brakes was carried out with the use of the universal friction machine MTU-1 that is based on a vertical milling machine “JMD-X1” and contains the original friction assembly unit that allows us to save the parallelism of the contacted surfaces [21, 22].

The scheme of the experiment was plate-on-plate. The lower samples were made of C/SiC, the upper samples were made of two types of steel: C22 and 37Cr4. The rotational speed of the upper sample was 300 and 650 rpm, whereas the lower sample was fixed. No lubricants were used. The load on the upper sample was 150, 400 and 600 N. The influence of braking pressure and braking speed on the tribological properties of C/SiC in brakes was investigated by Fan et al. in [23]. Dynamic friction coefficient was measured and analysed during the experiments.

The first set of experiments was carried out during 10 minutes for the tribopairs C/SiC – steel 37Cr4 with the following conditions: rotational speed was 300 rpm, starting load was 400 N.

Figure 1 shows the photographs of the samples after the first experiment.

Figure 1. C/SiC (left) and 37Cr4 (right) samples after the first experiment

In figure 2, the graph of friction coefficient versus time for the tribopair C/SiC – steel 37Cr4 during the first experiment is shown.

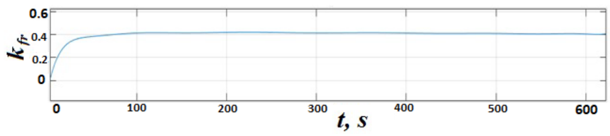

Figure 2. Graph of friction coefficient versus time during the first experiment

As can be seen from the graph in figure 2, the running-in of a friction pair occurs rather quickly, and at a small load the dynamic friction coefficient, having reached a plateau at the level of approximately 0.4, does not depend on time. This indicates a slight destruction of the surface layer and minimal wear.

The second set of experiments was carried out during 15 minutes for the tribopairs C/SiC – steel C22 with the following conditions: rotational speed was 300 rpm, starting load was 150 N.

In Figure 3 the samples after the second experiment are shown.

Figure 3. Steel C22 (left) and C/SiC (right) samples after the second experiment

In Figure 4, the graph of friction coefficient versus time for the tribopair C/SiC – steel C22 during the second experiment is presented.

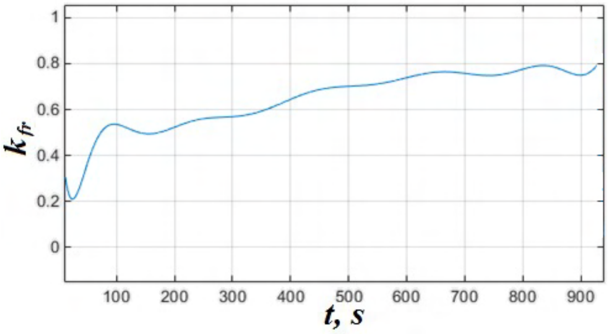

Figure 4. Graph of friction coefficient versus time during the second experiment

Figure 5. C/SiC (left) and Steel 37Cr4 (right) samples after the third experiment

It can be noticed from the graph in figure 4 that this tribopair at the beginning of the experiment behaves unstably, which is associated with a low hardness of C22. Surface running-in is observed during the entire experiment. Plastic deformation is observed on the surface of the sample made of C22, which increases the friction coefficient. The wear rate of such a pair will be high enough, the average coefficient of friction is 0.6.

The third set of experiments was carried out for the tribopairs C/SiC – steel 37Cr4 with the following conditions: rotational speed was 650 rpm, starting load was 600 N.

In Figure 5 the samples after the third experiment are shown.

In Figure 6, the graph of friction coefficient versus time for the tribopair C/SiC – steel 37Cr4 during the third experiment is presented.

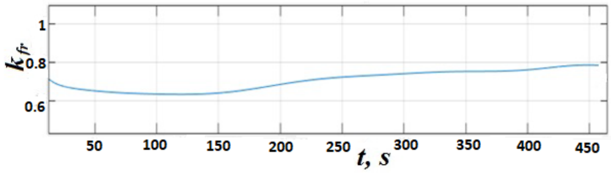

Figure 6. Graph of friction coefficient versus time during the third experiment

It can be observed from the graph that after the running-in, the oxide films are destroyed, the particles of oxides are dispersed and act as an additional abrasive without leaving the contact zone, which leads to the continuing growth of the friction coefficient. The average coefficient of friction is 0.75.

The last set of experiments was carried out during 15 minutes for the tribopairs C/SiC – steel C22 with the following conditions: rotational speed was 650 rpm, starting load was 600 N.

In Figure 7 the samples after the last experiment are presented.

Figure 7. C/SiC (left) and Steel C22 (right) samples after the last experiment

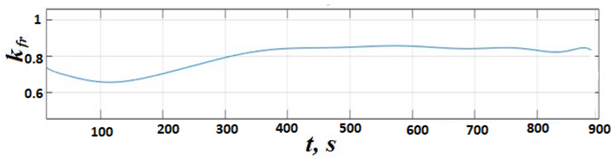

Figure 8. Graph of friction coefficient versus time during the last experiment

In Figure 8, the graph of friction coefficient versus time for the tribopair C/SiC – steel C22 during the last experiment is shown.

The graph in Fig. 8 shows that this tribopair after running-in also has an increase in the coefficient of friction, which is associated with the destruction of the surface layer. Further, wear particles act as abrasive, but the friction coefficient has small changes. The average coefficient of friction is 0.8.

4. CONCLUSION

The results of the experiment show that friction coefficient in the tribopair C/SiC – steel 37Cr4 increased in the beginning and then remained virtually constant during the experiment whereas in the tribopair C/SiC – steel C22 it increased during the whole experiment. This could be explained by the fact that in the second tribopair wear particles do not leave the contact area and charge the material acting as an abrasive. However, friction coefficient in the tribopair C/SiC – steel C22 is greater than friction coefficient in the tribopair C/SiC – steel 37Cr4, which means that use of steel C22 can help us reduce the braking distance, but wear of braking system parts is higher in that case.

REFERENCES

[1] Z. Wang, J. Han, J. P. Domblesky, Z. Li, X. Fan, X. Liu: Crack propagation and microstructural transformation on the friction surface of a high-speed railway brake disc, Wear, Vol, 428–429, pp. 45–54, 2019.

[2] S. Fan et al.: Microstructure and tribological properties of advanced carbon/silicon carbide aircraft brake materials, Composites Science and Technology, Vol. 68, pp. 3002–3009, 2008.

[3] A. Borawski: Simulation Study of the Process of Friction in the Working Elements of a Car Braking System at Different Degrees of Wear, Acta Mechanica et Automatica, Vol.12, No.3, 2018.

[4] C. Pinca-Bretotean et al.: Friction and wear characteristic of organic brake pads material, IOP Conf. Series: Materials Science and Engineering, Vol. 477, paper 012009, 2019.

[5] X. Xiao, Y. Yin, J. Bao, L. Lu, X. Feng: Review on the friction and wear of brake materials, Advances in Mechanical Engineering, Vol. 8, pp. 1–10, 2016.

[6] M. Kandeva, V. Balabanov, E. Zadorozhnaya, Zh. Kalitchin, P. Svoboda: Environmental protection by self-organisation of tribosystems with self-lubricating materials in dry friction. Part I. Investigations at different loads, Journal of Environmental Protection and Ecology, Vol. 18, No. 3, pp. 1050-1069, 2017.

[7] G. Akıncıoglu, H. Öktem, I. Uygur, S. Akıncıoglu: Determination of Friction-Wear Performance and Properties of Eco-Friendly Brake Pads Reinforced with Hazelnut Shell and Boron Dusts, Arabian Journal for Science and Engineering, Vol. 43, pp. 4727–4737, 2018.

[8] K.K. Ikpambese, E.A. Lawrence: Comparative Analysis of Multiple Linear Regression and Artificial Neural Network for Predicting Friction and Wear of Automotive Brake Pads Produced from Palm Kernel Shell, Tribology in Industry, Vol. 40, No. 4, pp. 565-573, 2018.

[9] B. Dan-asabe, A. Stephen: Mathematical Modelling and Optimization of the Compressive Strength, Hardness and Density of a Periwinkle-Palm Kernel and Phenolic Resin Composite Brake Pad, Tribology in Industry, Vol. 40, No. 1, pp. 108-116, 2018.

[10] Y. Lyu, J. Wahlström, M. Tu, U. Olofsson: A Friction, Wear and Emission Tribometer Study of Non-Asbestos Organic Pins Sliding Against AlSiC MMC Discs, Tribology in Industry, Vol. 40, No. 2, pp. 274-282, 2018.

[11] S. Fan et al.: Wear mechanisms of the C/SiC brake materials, Tribology International, Vol. 44, pp. 25–28, 2011.

[12] G. Byeong-Choon, C. In-Sik: Microstructural Analysis and Wear Performance of Carbon-Fiber-Reinforced SiC Composite for Brake Pads, Materials, 10, 701, 2017.

[13] V. Dygalo, I. Zhukov: The thermal loading estimation of the friction pairs of a vehicle automated brake system, IOP Conf. Series: Materials Science and Engineering, Vol. 386, paper 012012, 2018.

[14] N. Benhassine, A. Haiahem, B. Bou-Said: A comparative study of the transient thermomechanical behavior of friction of the ceramic brake discs: Temperature field effect, Journal of Mechanical Science and Technology, Vol. 33, Issue 1, pp. 233–240, 2019.

[15] G.M. Ismailov, A.E. Tyurin: Experimental study of frictional vibrations under dry friction

conditions, Tribology in Industry, Vol. 40, No. 3, pp. 392-400, 2018.
[16] A.E. Tyurin, G.M. Ismailov, E.V. Beloenko, A.V. Baranov: Monitoring vibrations and microdisplacement for "pin on disc" tribology studies, Journal of Physics: Conference Series, Vol. 803, No. 1, paper 012167, 2017.
[17] G. Riva, G. Perricone, J. Wahlström: Simulation of Contact Area and Pressure Dependence of Initial Surface Roughness for Cermet-Coated Discs Used in Disc Brakes, Tribology in Industry, Vol. 41, No. 1, pp. 1–13, 2019.
[18] M. Bolotov, I. Grachev, E. Kudashov: Investigation of parts assembly error, taking into account the deviation of the shape of their surfaces, MATEC Web of Conferences, 224, paper 01098, 2018.
[19] M.A. Bolotov, V.A. Pechenin: Model of precision parts assembly, in: *Proceedings of the International Conference of DAAAM Baltic Industrial Engineering*, 2016-April, Tallinn, Estonia, pp. 98-103.
[20] A.Y. Grigoriev, D.M. Gutsev, A.P. Zozulya, I.N. Kovaliova, V.G. Kudritskii, N.K. Myshkin, M.S. Semenyuk: Reciprocating MTU-2K7 millitribometer, Journal of Friction and Wear, Vol. 35, No. 6, pp. 455-459, 2014.
[21] S. Perepelkina, P. Kovalenko, R. Pechenko: Investigation of Tribological Properties of Metallic Materials with the Use of the Universal Friction Machine “MTU-1", Procedia Engineering, Vol. 176, pp. 301-309, 2017.
[22] S. Perepelkina, P. Kovalenko, R. Pechenko, K. Makhmudova: Investigation of friction coefficient of various polymers used in rapid prototyping technologies with different settings of 3D printing, Tribology in Industry, Vol. 39, No. 4, pp. 519-526, 2017.
[23] S. Fan et al.: Effect of braking pressure and braking speed on the tribological properties of C/SiC aircraft brake materials, Composites Science and Technology, Vol. 70, pp. 959–965, 2010.

Serbian Tribology Society

SERBIATRIB '19

16th International Conference on Tribology

Faculty of Engineering University of Kragujevac

Kragujevac, Serbia, 15 – 17 May 2019

ANALYSIS OF EFFICIENCY OF A NEW TWO STAGE CYCLOID DRIVE CONCEPT

Miloš MATEJIĆ[1,*], Mirko BLAGOJEVIĆ[1], Nenad KOSTIĆ[1], Nenad PETROVIĆ[1], Nenad MARJANOVIĆ[1]

[1]University of Kragujevac Faculty of Engineering, Kragujevac, Serbia

*Corresponding author: mmatejic@kg.ac.rs

Abstract: *Cycloid drives are part of a new generation of planetary gear trains. These reducers have massively appeared in the second half of the 20th century. Research on the subject of cycloid drives is an interesting subject in the field of mechanical power transmissions due to its wide use and price range which is similar to other types of conventional, planetary, and other types of reducers.*

This paper gives an analysis of efficiency of a new two stage cycloid drive concept. The efficiency analysis takes into consideration the losses due to friction in the bearing cam surface of the shaft, on the central gear rollers and the output rollers. The efficiency of the new concept of cycloid drive is given for different standard power values. In order to assess the efficiency of the new concept of the two stage cycloid drive a comparative analysis was conducted with a standard concept of two stage cycloid drive. The paper concludes with suggestions as well as possible directions for further research.

Keywords: *two stage cycloid drive, new concept, friction, losses, efficiency*

1. INTRODUCTION

One of the newest types of planetary power transmissions are definitely cyclod reducers. The cyclod reducer was invented and patented by German engineer *Lorenz Branen*,[1]. He also started production line of the cyclod reducers. Cyclod reducers are experiencing mass expansion in the second half of the 20th century. Nowadays there is a growing number of manufacturers, as well as a wider range of concepts of these mechanical power transmissions. Since then, to this day, cyclo reducers have been a very attractive subject for research in the field of mechanical gearboxes due to their wide range of applications, and because of the price ranges that resemble to other gearboxes types (conventional, planetary, etc.).

One of the most important characteristics of the gearbox is its efficiency. The first mathematical formulation of the cycloid reducer efficiency is presented in the book *Planetary Transmissions*,[2]. Based on the mathematical model presented in the book [2], *Malhotra* made a new model for determining the cycloid reducer efficiency taking into account the power losses on each cylinder of the central gear unit individually, as well as on each output roller individually [3]. *Kosse* has been investigating how is efficiency affected by the multiplication of the input torque,[4]. In the paper [5], a comparative analysis of the experimental and theoretical determination of the cycloid reducer efficiency was given, and on the basis of the obtained results, a new mathematical model was developed for determining the cycloid reducer efficiency [5,6]. *Blagojević* et al. examined the influence of friction coefficients variation on the cycloid reducer efficiency,[7]. *Neagoe* and a group of authors carried out experimental tests on the efficiency of the non-pin wheel concept of cycloid reducer,[8]. *Zah* was defined the procedure for the thermal analysis of the cyclod reducer,[9]. *Tonoli* studied the influence of the non-lubricating regime on the cycloid reducer efficiency,[10]. *Mihailidis* performed an experimental lubrication test for a cyclod reducer,[11]. *Blagojevic* et al. experimentally verified the method for determining cycloid reducer efficiency which was given by Kudrijavcev,[12].

In this paper the results of the theoretical determination of the new concept double-stage cycloid reducer is presented. That new cycloid reducer concept is given in the paper [13]. At the end of the paper, a comparative analysis between the new double-stage cycloid reducer efficiency and the existing solutions of the world's leading companies is presented.

2. EFFICIENCY OF THE NEW TWO STAGE CYCLOID DRIVE CONCEPT

The cycloid reducer efficiency analysis is a complex and attractive task, both for science and for engineering practice. This problem becomes much more complicated if multi-stage cycloid reducers are observed or, in turn, cycloid reducers have concepts that are different from commercial ones. This topic is still an insufficiently explored aspect of cycloidal power transmissions. Efficiency determination of the cycloid reducers in all theoretical models is based on the determination of power losses in the contacts of certain elements of the cycloid reducers due to the friction of sliding, or rolling. These losses occur in contact between the following elements:

- **Power loss due to friction in the bearing on the eccentric cam.** Power loss in the bearing on the eccentric cam depends on the size and type of bearing, the size of the roller bodies, the friction coefficient of the bearing, the intensity of the force on the eccentric cuff and angular velocity.

- **Power loss due to friction between the output rollers and the openings in the cycloid gear.** In the contacts between the output rollers and the opening in the cycloid gear, the rolling friction is mostly present, so the power losses are very small at this point.

- **Power loss due to friction between the teeth of the cycloid gear and the central gear.** In the contacts between the cycloid gear and the central gear, as well as in the contacts between the openings on the cycloid gear and the output rollers, the dominant is rolling friction.

- **Power loss due to friction between the output rollers and the output pins.** Output rollers are most often directly mounted on the matching axes of the output mechanism, so in this contact there are losses due to sliding friction. The variables that directly affect the power losses in this contact are: the diameter of the output pin, the sliding friction coefficient, the slip speed and the output force.

- **Power loss due to friction between the central gear rollers and its pins.** As the number of contacts of the central gear rollers and its pins large, here the greatest power losses occur due to slip friction. The greatest impact on power losses is: the pin diameter (inner diameter of the central gear roller), the sliding friction coefficient, the sliding velocity and the normal force.

The new concept of the double-stage cycloid reducer differs from the conventional concepts in that one gearbox is used for each of the transmission rates. The *CAD* model of the new concept of two stage cycloid reducer is given in Figure 1.

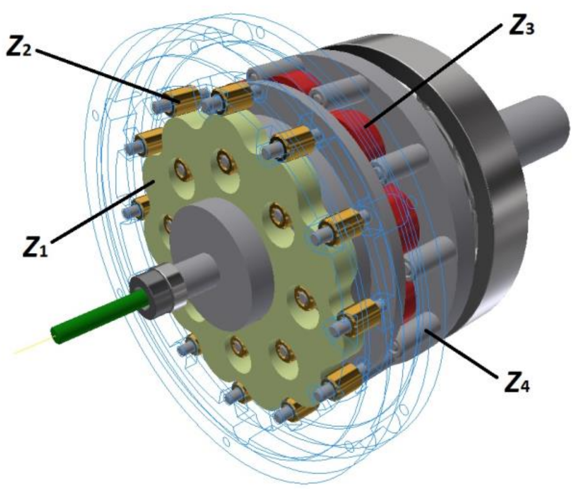

Figure 1. Double stage cycloid reducer new concept

In figure 1 are marked: z_1 – cycloid gear of first stage, z_2 – central gear of first stage, z_3 – cycloid gear of second stage and z_4 – central gear of second stage.

A modified Kudrijavcev's method was used to determine the efficiency of the double stage cycloid reducer new concept,[2]. The expression for determining the efficiency by this method is:

$$\eta = \frac{1-\psi_I}{1+z_1\psi_I}\cdot\frac{1-\psi_{II}}{1+z_3\psi_{II}}, \tag{1}$$

where are: η – double stage cycloid reducer new concept efficiency, z_1 – number of teeth of first stage cycloid gear, ψ_I – power losses in first reduction stage, z_3 – number of teeth of second stage cycloid gear and ψ_{II} – power losses on second reduction stage.

Power losses of first reduction stage can be calculated by equation:

$$\psi_I = \psi_{I1} + \psi_{I2} + \psi_{I3}, \tag{2}$$

where are: ψ_{I1} – power loss due to friction on the central gear rollers, ψ_{I2} – power loss due to friction on the output rollers and ψ_{I3} – power loss due to friction on the eccentric cam bearing.

The power losses for the second reduction stage are calculated in the same way as for the first reduction stage (it is used same type of equation). The difference is in the value of the losses, which occurs as a result of the of different forces effect related to first reduction stage. Determination of the individual values of losses is described in detail in the literature, [12]. The described equations refer to the determination of the nominal double stage cycloid reducer new concept efficiency under previously defined working conditions.

3. EFFICENCY DETERMINATION APPLICATION

For the purposes of this research, the application was developed in the software package *Autodesk INVENTOR 2019*. The application is based on the principles presented in the second chapter of this paper as well as on the mathematical model presented in the author's previous work [12]. The user application form for determining the efficiency of double stage cycloid reducer new concept is shown in Figure 2.

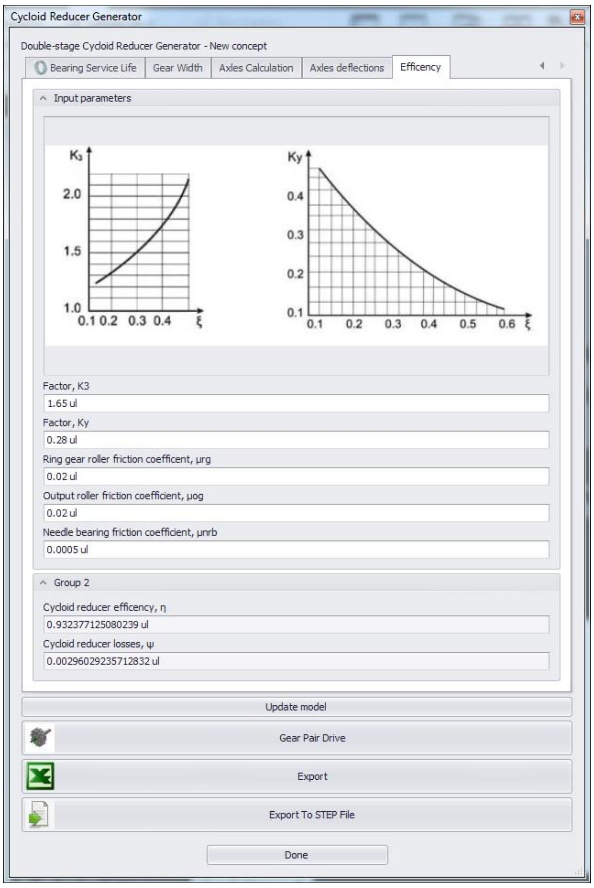

Figure 2. Application form for determining the efficiency of double stage cycloid reducer new concept

The user form for the nominal efficiency calculation of the two-stage cycloid reducer new concept is divided into two parts. The first part refers to the input of the input parameters, while the second part refers to the calculated efficiency parameters. The application is used by the user form to enter the selected values of the factors based on the diagram from the upper part of the form, which are determined according to the predefined working conditions, as well as the friction coefficients between the individual elements of the cycloid reducer. Factors K_3 and K_y are determined based on choice of the cycloid profile correction factor ξ, while the friction coefficients between the elements of the cycloid reducer are determined based on the selected material of the elements, as well as on the basis of the lubricant used in the cycloid reducer.

4. ACHIEVED RESULTS ANALYSES

Double stage cycloid reducer new concept has been analyzed for three various rotations per minute on the input shaft: n_{in}=750 min^{-1}, n_{in}=1450 min^{-1} and n_{in}=3600 min^{-1}. In the same manner, the three various transmission ratios was used, which are approximated by standard catalogue values, u=121, 165 and 231, [14-16]. Efficiency simulations for cycloid reducer are conducted for standard power values: 0,25; 0,55; 0,75; 1,5; 3; 5,5; 7,5 and 15 kW. Other parameters of cycloid reducer are adopted form literature,[2,5,6,12,13].

In figure 3 is shown efficiency for double stage cycloid reducer new concept at n_{in}=750 min^{-1} on the input shaft.

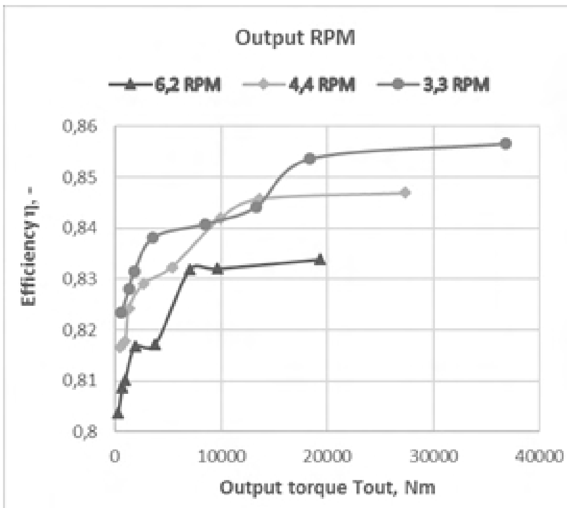

Figure 3. Efficiency diagram for 750 RPM of input shaft

The curve with triangles represents double stage cycloid reducer new concept having an approximately transmission ratio equal to the catalog of u=121; the curve with rhombuses is a gear ratio with a transmission ratio of u=165, while the curve with circles represents a gear ratio with a transmission ratio of approximately u=231. From Figure 3, it can be noticed that the gears with the lowest transmission ratio (u=121) have the lowest efficiency. The reducers with a transmission ratio of u=165 have a slightly higher efficiency while the reducers with a transmission ratio of u=231 have the highest efficiency.

In figure 4 is shown efficiency for double stage cycloid reducer new concept at n_{in}=1450 min^{-1} on the input shaft.

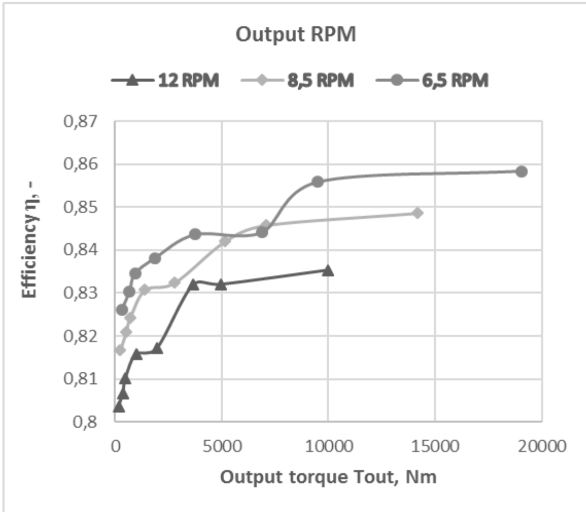

Figure 4. Efficiency diagram for 1450 RPM of input shaft

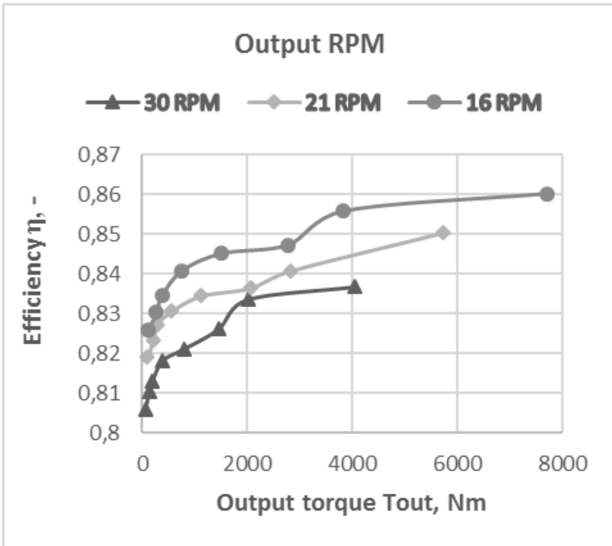

Figure 5. Efficiency diagram for 3600 RPM of input shaft

Figure 4 shows that the curves for the same transmission ratios are very similar to those of the curves shown in Figure 3. In general, the efficiency at the input shaft speed of n_{in} =1450 min^{-1} is 1 to 2% higher than the transmission ratio for the input shaft speed of n_{in} =750 min^{-1}.

In figure 5 is shown efficiency for double stage cycloid reducer new concept at n_{in}=3600 min^{-1} on the input shaft.

Figure 5 shows that the curve shapes for the same transmission ratio are very similar to the curve shapes in Figure 4. In general, the efficiency at the input shaft speed of n_{in}=3600 min^{-1} is 0.5 to 1.5% higher than transmission ratio for the input shaft speed of n_{in}=1450 min^{-1}.

5. CONCLUSION

This paper presents a methodology for efficiency determination of double stage cycloid reducer new concept. A theoretical model for determining cycloid reducer efficiency is based on the Kudrijavcev's model,[2]. In order to automate the process of determining the cycloid reducer efficiency, an application was developed in the *CAD* software *Autodesk INVENTOR 2019*.

The simulations result of determining the efficiency of double stage cycloid reducer new concept differ from the catalog results [14-17] in the interval from 2% to 5%. In according to manufacturer Nabtesco, the obtained results of cycloid reducer efficiency are from 0% to 2% greater than the catalog values. In according to Sumitomo manufacturer, the obtained results are 0% to 5% lower for double stage cycloid reducer new concept.

In the further steps of this research, it is planned to manufacture a series of new two-stage cycloidal reducers and to carry out experimental tests.

ACKNOWLEDGEMENT

This paper is a result of TR33015 and TR32036 project of the Ministry of education, science and technological development, in Serbia. The projects are titled "Research and development of a Serbian zero-net energy house", and "Development of software for solving the coupled multi-physical problems" respectively. We would like to thank the Ministry of education, science and technological development on their financial support during this research.

REFERENCES

[1] L. K. Brarren: Gear transmission, U.S. Patent 1,694,031, December 4th, 1928.

[2] V.N. Kudrijavcev: *Planetary Transmissions* (in Russian), Moscow, 1966.

[3] S. K. Malhotra, M. A. Parameswaran: Analysis of a cycloid speed reducer, Mechanism and Machine Theory, Vol. 18, No. 6, pp. 491-499, 1983.

[4] V. Kosse: Using hysteresis loop and torsional shock loading to assess damping and efficiency of cyclodrives, *4th International Congress on Sound and Vibration-ICSV14*, 9-12.07.2007, Cairns, Australia, pp. 1-8, 2007.

[5] P. Davoli, C. Gorla, F. Rosa, C. Longoni, F. Chiozzi, A. Samarani: Theoretical and experimental analysis of a cycloidal speed reducer, *10th ASME International power transmission and gearing conference*, 4-7.09.2007, Las Vegas, USA, 2007.

[6] C. Gorla, P. Davoli, F. Rosa, F. Chiozzi, A. Samarani: Theoretical and experimental analysis of a cycloidal speed reducer, Journal of Mechanisms, Transmissions and Automation in Design, Vol. 130, 2008.

[7] M. Blagojevic, M. Kocic, N. Marjanovic, B. Stojanovic, Z. Djordjevic, L. Ivanovic, V. Marjanovic: Influence of the friction on the cycloidal speed reducer efficiency, Journal of the Balkan Tribological Association, Vol. 18, No. 2, pp. 217-227, 2012.

[8] M. Neagoe, D. Diaconescu, C. Jaliu, L. Pascale, R. Saulescu, S. Sisca: On a new cycloidal planetary gear used to fit mechatronic systems of res, *11th International Conference Optimization of Electrical and Electronic Equipment-OPTIM 2008*, 22-24.05.2008, Brasov, Romania, pp. 439-448, 2008.

[9] M. Zah, D. Lates, V. Csibi: Thermal calculation for planetary cycloidal gears with bolts, Acta Universitatis Sapientiae-Electrical & Mechanical Engineering, Vol. 4, pp. 103-110, 2012.

[10] A. Tonoli, N. Amati, F. Impinna, J. G. Detoni, S. Ruzimov, E. Gasparin, K. Abdivakhidov: Influence of dry friction on the irreversibility of cycloidal speed reducer, World Tribology

Congress, 8-13.09.2013, Turin, Italy, Vol. 5, pp. 1-4, 2013.
[11] A. Mihailidis, E. Athanasopoulos, E. Okkas: Efficiency of a cycloid reducer, International Gear Conference, 26-28.08.2014, Lyon, France, Vol. 2, pp. 794-803, 2014.
[12] M. Blagojević, M. Matejić, N. Kostić, N. Petrović, N. Marjanović, B. Stojanović: Theoretical and experimental testing of plastic cycloid reducer efficiency in dry conditions, Journal of the Balkan Tribological Association, Vol.23, No.2, pp. 367-375, 2017.
[13] M. Blagojevic, N. Marjanovic, Z. Djordjevic, B. Stojanovic, A. Disic: A new design of a two-stage cycloidal speed reducer, Journal of Mechanical Design, Vol. 133, No. 8, 2011.
[14] Sumitomo Drive Technologies: Cyclo Drive 6000 Gearmotors & Speed Reducers, catalogue, 2019.
[15] Sumitomo Drive Technologies: Fine Cyclo Zero Backslash Precision Gearboxes, catalogue, 2018.
[16] Nabtesco: Precision Reduction Gear RV / E Series / C Series / Original Series /, catalogue 2019.
[17] Nabtesco: Precision Reduction Gear RV / N Series /, catalogue 2019.

Serbian Tribology Society

SERBIATRIB '19

16th International Conference on Tribology

Faculty of Engineering
University of Kragujevac

Kragujevac, Serbia, 15 – 17 May 2019

EFFECT OF CASHEW NUT SHELL LIQUID (CNSL) ON TRIBOLOGICAL BEHAVIOR OF BRAKE PAD COMPOSITE

Harun YANAR[1], Gencaga PURCEK[1,*], H. Huseyin AYAR[2]
[1]Department of Mechanical Engineering, Karadeniz Technical University, Trabzon, Turkey,
[2]Metisafe® Cleanroom and Biosafety Systems, Ankara, Turkey
*purcek@ktu.edu.tr

Abstract: *Effect of CNSL addition as a friction modifier on the wear characteristics and mechanical properties of non-asbestos composites brake pad was investigated. For this purpose, the content of CNSL in the matrix structure was only changed in the range of 0 - 5 wt.% and six different compositions were prepared. Only the amount of resin were changed, other ingredients in the mixture were keept constant. The brake-pad samples were tested for their friction and wear behavior on a pin-on-disk type test configuration according to the NF F 11-292 French standard. It was observed that coefficient of friction of composite decreased with increasing CNSL contents up to 2wt % level, above which coefficient of friction increased. Specific wear rate however, linearly decreased with increasing the amount of CNSL content in the matrix. On the other hand, CNSL addition to the composite matrix decreased the some mechanical properties such as hadness, compressive strength and elastic module of sample, while increased the compressibility values.*

Keywords: *Composite brake pad/shoes, Friction material, CNSL ingredient*

1. INTRODUCTION

Friction materials for trains and automobiles are important parts of the vehicle to slow down and stop the vehicle safely. The characteristics of the brake pad / shoes used as friction material are directly affecting the braking performance of the vehicles. Therefore, they should have effective braking performance under different variable conditions such as speed, temperature, humidity and pedal pressure. In last decades, these commercial products have been produced in the form of composite structure consisting of more than 10 ingredients instead of the single friction materials produced from cast iron in order to achieve the best combination of performance properties of friction materials at a broad variety of braking circumstances [1]. All these ingredients added in the brake pad composite material have an effect on the friction or physical properties of the brake pads. Therefore, type and amount of each ingredient must be selected correctly in the matrix structure of the brake pads. These additives used were collected in four classes of materials named as fiber, binder, friction modifier and space filler according to their effects on the friction and wear performance of brake pad [2].

Increasing demand to produce faster and more powerful vehicles has also dramatically changed the desired performance outputs from the brake friction materials. Many researchers have extensively studied the effects of types and amounts of these ingredients on the friction and wear performance of friction materials in recent years [3-6]. However, in the literature, very limited studies have been undertaken regarding the effect of CNSL additions into the brake pad matrix structure on the mechanical and tribological properties of the brake pad [7]. The purpose of this study is to investigate the effect of CNSL addition on the friction characteristic and mechanical properties of non-asbestos brake pad composite. For this purpose, with five different CNSL content was chosen to be 1, 2, 3, 4 and 5 wt.%. In the present work, periodic braking test according to the NF F 11-292 French standard was conducted on the specimens to analyze their tribological performance. Some mechanical tests were also performed to determine the mechanical properties of composite brake pad samples. Also, scanning electron microscopy (SEM) and 3D surface analysing were used in order to elucudate the wear mechanisms.

2. MATERIAL AND METHODOLOGY

The composition of the composite sample is given in the Table 1. All samples consist of seven constituents; binder (phenolic resin), filler (barite), fiber (rockwool and kevlar), lubricant (graphite) and friction modifier (CNSL) and abrasive (magnetite). Only the concentration of the binder (resin) and friction modifier (CNSL) were changed while the concentration of other ingredient were kept constant to be 80 wt.% in all compositions. The CNSL was added into the composite between 1 - 5wt% by replacing phenolic resin in the pad formulation. All ingredients were mixed for 5 min in a high-speed blender to ensure macroscopic homogenization of the mixture. Subsequently, about 10 g of the mixture was compressed under the pressure of 50 bar into a compression mold pre-heated to 90 °C. Temperature of the mold was then increased to 150 °C, and the samples were cured in the mold under a pressure of 50 bar for 10 min. Finally, post-curing was carried out by using an electrical resistance furnace at 200 °C for 20 min to achieve curing all of the resin into the matrix. All samples produced were then polished with 1000 and 2000 grit SiC papers to attain surface smoothness. Surface hardness of the test samples was measured by a hardness tester (Rockwell Mettest-HT) with a 19.3 mm ball-indenter under the maximum load of 60 kg. The compressive strength and elastic modulus (E) of the samples was determined using a tension / compression test machine (Instron 3382) with cylindrical test samples having the diameter of 20 mm and the thickness of 15 mm. The elastic module (E) of the samples was determined by using the Eq. 1 given below.

A specific pin-on-disc type test system was used to perform friction and wear tests of the brake pad samples. The sample size for friction test was 20 mm in diameter and 15 mm in thickness. The counter disc was made of AISI 52100 steel with the surface roughness (Ra) of about 0.05 mm and hardness of 55-58 HRC. The disc rotated at the speed of 2800 rpm corresponding to the sliding speed of 26 $m.s^{-1}$ (95 km/h). During braking, the 80 kg normal load (corresponding to about 0.8 MPa) was applied to the samples by means of hydraulic cylinder for 20 s and then removed for 150 s. This is called one cycle and this was repeated fifteen times for the testing of each sample. Friction force and coefficient of friction (CoF) was recorded during the tests depending on time. The specific wear rate ($\boldsymbol{Q}$) of the samples was determined by using the Eq. 2 given below. After tribological tests, the worn surfaces of the samples were scanned using a 3D surface profilometer and examined by scanning electron microscopy (SEM) to analyze the wear characteristic of the samples in detail.

$$E = \frac{F\,(N)}{\pi R^2} \mathrm{x}\ \frac{Lo}{\Delta l} \qquad (1)$$

Where;

E: Elastic Modulus (MPa)
F: Applied load (N)
R: Radius of the sample (mm)
Lo: Initial thickness of the sample (mm)
Δl: The thickness change (mm)

$$Q = \frac{m\,(g)\,.\,10^{\wedge}6}{X\,.\,F\,(N)\,.V\left(\frac{m}{s}\right).\,\mu\,.\,t\,(s)\,.\,\rho\,\left(\frac{g}{cm3}\right)} \quad (2)$$

Where;

Q: Specific wear rate (cm^3/MJ)
m: Weight Loss (g)
X: Number of braking period
F: Applied Normal Load (N)
V: Test speed (m/s)
µ: Average coefficient of friction
t: Braking time in one period (s)
ρ: Density of sample (g/cm^3)

Table 1. Composition of the investigated composite samples.

Element	Composition (wt.%)					
	Base	S1	S2	S3	S4	S5
Phenolic Resin	20	19	18	17	16	15
CNSL	0	1	2	3	4	5
Others	80					

3. RESULTS AND DISCUSSION

3.1 Physical and mechanical properties

Hardness values, compressive strength, compressibility test results and elastic modules of the friction materials are given in Table 2.

Table 2. Physical and mechanical properties of the composite samples.

	Base	S1	S2	S3	S4	S5
Density (g/cm3)	2,05	2,05	2,05	2,05	2,05	2,05
Hardness (HRX)	97	91	88	87	84	82
Compressive Strength (MPa)	128	157	155	150	140	125
Compressibility (µm)	87	92	97	95	113	122
E-Module (MPa)	1520	1290	1180	1150	1070	995

Change in the amount of CNSL affected the physical and mechanical properties of a friction material. Compressive strength and hardness values of the samples decreased generally with increasing CNSL content in the matrix structure, while the compressibility test values increased. This is an expected result. Because the addition of CNSL was balanced only by reducing the same amount of phenolic resin in the matrix. The decrease in the amount of phenolic resin which bonds all ingredients of the brake pad caused to weaken the binding effect. This resulted in a reduction in the mechanical properties of the friction materials.

3.2 Friction and wear behavior

Variation of friction coefficient of the samples with number of braking cycle are presented in Fig. 1. The average friction coefficient values taken from these curves calculated after the 15 cycles friction test are given in the Fig. 2. The results in these figures demonstrated that addition of CNSL as a friction modifier in the main matrix structure resulted in a significant change in the coefficient of friction of the CNSL-free sample. The friction coefficient of the base sample changed over 15 braking cycles. It was about 0.21 in the first braking period and reached to about 0.32 after the 15th braking period. On the other hand, fluctuation was observed at every loading period of friction test for base sample (Fig. 1.) Addition of CNSL in all contents reduced the average coefficient of friction (~0.27) of the base sample. The average friction coefficient was obtained as 0.17 after 1 wt.% CNSL addition and reached to a minimum value of 0.13 with the 2 wt.% CNSL addition. However, when the CNSL content was chosen more than 2 wt.%, friction coefficient start increasing. Average friction coefficient was determined to be 0.18 for the sample having 5 wt% CNSL content. In addition, it was observed that the samples with varying CNSL content have smooth friction coefficient curves during each braking period and 15 braking test cycles.

As can be seen in Fig. 2, addition of CNSL into matrix brought about a reduction in the specific wear rate of composite samples after the 15 cycles braking tests. Unlike the friction coefficient of the samples, their specific wear rate decreased linearly with increasing CNSL content in the matrix structure. The reduction in the amount of specific wear can be explained in terms of increasing in the contact surface area between the sample and the rotating disc. As the contact surface increases, more homogeneous and relatively low wear takes place as also clearly understood from the SEM and 3D images of the worn surfaces of sample (Fig. 3). As seen in Fig.3, primary and secondary plateaus formation controlling the wear of materials were observed on the worn surfaces of all composite samples. However, distribution of these plateaus on the worn surface varied according to the CNSL content of the samples. As seen in Fig. 3, a thick layer of wear debris that generally consists of degraded or melted organic materials was observed on the worn surface of base sample. In general, the debris layer which loosely adhered to the bulk of the composite underneath breaks away from the worn surface and/or transferred to the counter disc surface. The fluctuation observed in the friction coefficient and more wear of the base sample can be associated with this situation. The worn surface is very smooth with increasing CNSL content. As the CNSL ratio increased, the modulus of elasticity of the composite increased and resulted in larger contact surface between the disc and tested sample. This contributed to the dissipation of heat generated at the rubbing surface over the entire surface and resulted in more uniform wear of samples including CNSL.

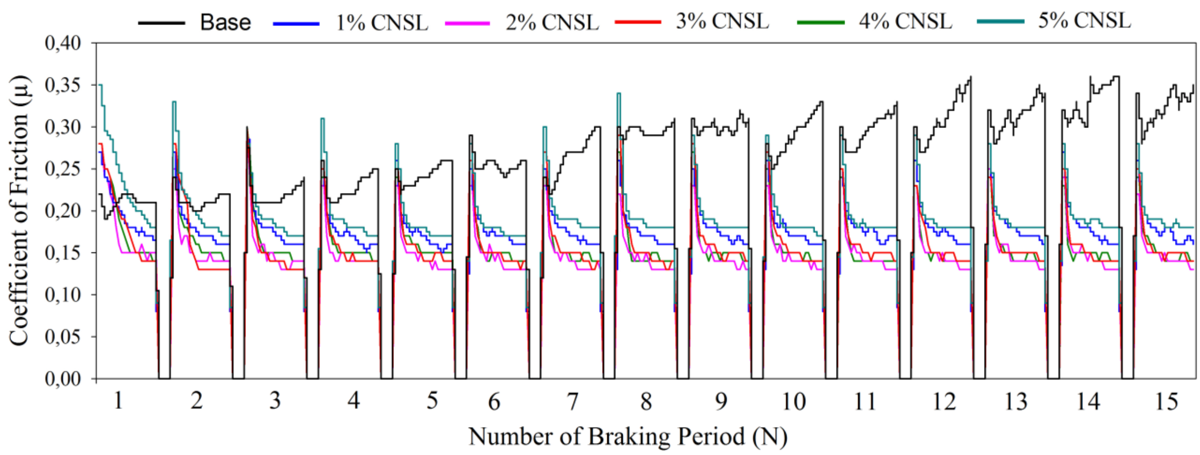

Figure 1. The change of coefficient of friction as a function of number of braking for all friction composites.

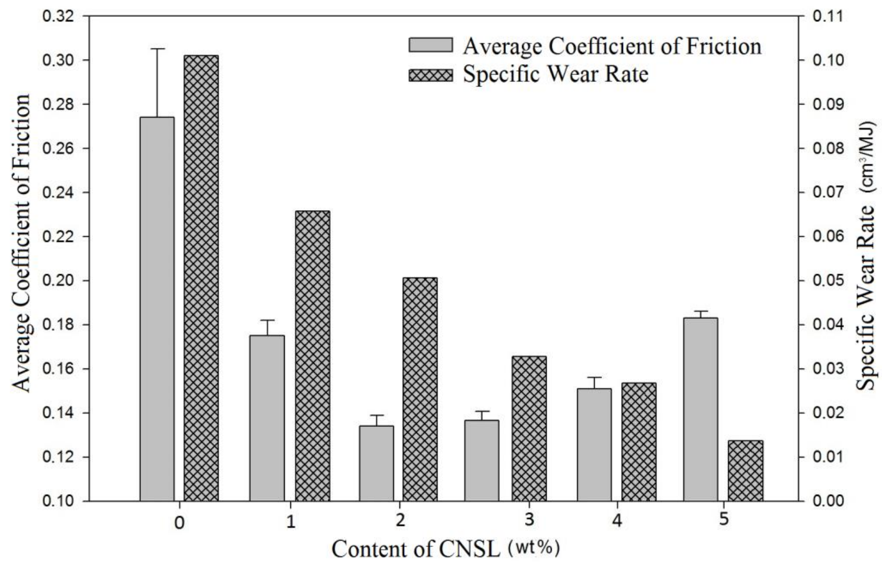

Figure 2. Average coeffient of friction and specific wear rate of composite sample with variying content of CNSL.

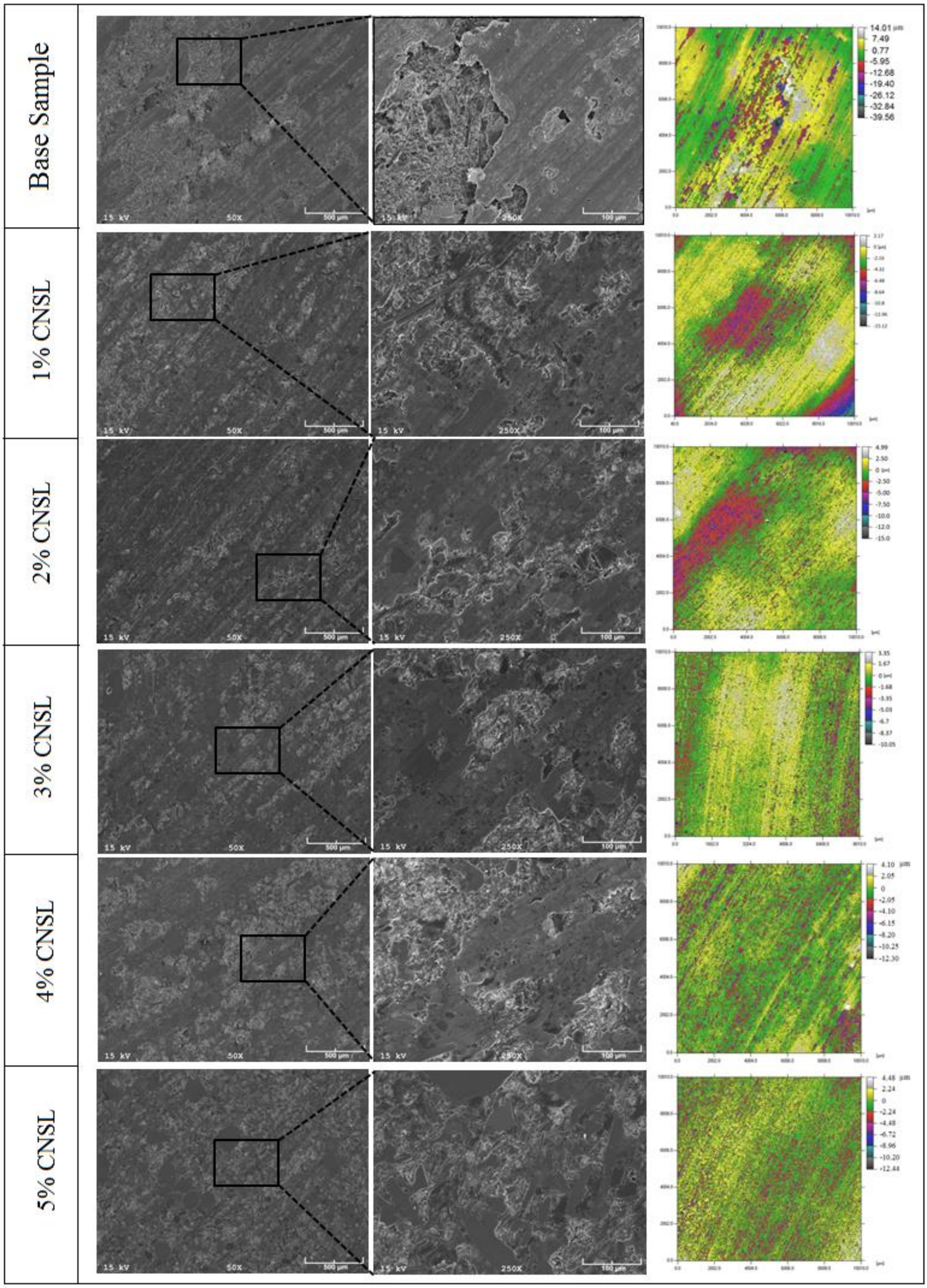

Figure 3. SEM images and 3D topographic view of worn surface of composite sample sample having different amount of CNSL.

4. CONCLUSIONS

- As the CNSL content in the main matrix structure increases, compressibility, hardness and elasticity modulus of the composite sample decrease while confine and unconfine compressibility values increase.
- Average coefficient of friction of base composite sample were determined to be 0.27 duruing the 15 cycles braking test. A parabolic decrease was observed in the average friction coefficient values of composite sample with increasing CNSL content up to 2.0%, above which it start increasing.
- The stability of the friction coefficient changed during the wear tests with increasing the CNSL content. Base composite sample (CNSL-free sample) has a poor friction stability with high amount of fluctuations in friction coefficient values. The best frictional stability was obtained in the composite sample having 5 wt.% CNSL.
- The wear resistance of sample increases with increasing the CNSL content due to better surface contact between the sample and rotating disk.
- The roughness (or waviness) of worn surface of composite samples increased with decreasing the CNSL content in the matrix due to thier high elastic modulus.
- The composite mixture having the highest amount of CNSL (5 wt.%) was proposed to be the most appropriate one considering the mechanical properties and wear behavior of composite sample.

ACKNOWLEDGEMENT

Thanks to the METISASE Co., Ankara, Turkey, for its support during the experimental studies.

REFERENCES

[1] M.H. Cho, S.J. Kim, D. Kim, and H. Jang: Effects of ingredients on tribological characteristics of a brake lining: an experimental case study, Wear, Vol. 258, pp. 1682-1687, 2005.

[2] Y. Lu: A combinatorial approach for automotive friction materials: effects of ingredients on friction performance, Composites Science and Technology, pp. 591-598, 2006.

[3] H. Jang, K. Ko, S. J. Kim, R.H. Bash and J. W. Fash: The effect of metal fibers on the friction performance of automotive brake friction materials, Wear, Vol. 256, pp. 406-414, 2004.

[4] U. S. Hong, S. L. Jung, K. H. Cho, M. H. Cho, S. J. Kim and H, Jang: Wear mechanism of multiphase friction materials with different phenolic resin matrices, Wear, Vol. 266, pp. 739-744, 2009.

[5] N. Dureja, J. Bijwe and P. V. Gurunath: Role of Type and amount of resin on performance behavior of non-asbestos organic friction materials, Journal of reinforced plastics and composites, Vol. 28, No. 4, pp. 489-497, 2009.

[6] M. H. Cho, J. Ju, S. J. Kim and H. Jang: Tribological properties of solid lubricants (graphite, Sb2S3, MoS2) for automotive brake friction materials, Wear, Vol. 260, pp. 855-860, 2006.

[7] Y. C. Kim, M. H. Cho, S. J. Kim and H. Jang: The effect of phenolic resin, potassium titanate and CNSL on the tribological properties or brake friction materials, Wear, Vol. 264, pp. 204-210, 2008.

Serbian Tribology Society

SERBIATRIB '19

16th International Conference on Tribology

Faculty of Engineering University of Kragujevac

Kragujevac, Serbia, 15 – 17 May 2019

STUDY OF THE INFLUENCE OF ABRASIVE PARTICLES ON A JOURNAL BEARING WITH A SOFT COATING (PB-CU-AL) UNDER BOUNDARY LUBRICATION CONDITIONS

A. HERNÁNDEZ-PEÑA[1,*], E.A. GALLARDO-HERNANDEZ[1], L.I.F. CABRERA[2], M. VITE-TORRES[1]

[1]Instituto Politécnico Nacional, SEPI-Escuela Superior de Ingeniería Mecánica y Eléctrica, Unidad Zacatenco, Grupo de Tribología, Col. Lindavista, C.P. 07738, Ciudad de México, México.

[2]Tecnológico de Monterrey, Campus Puebla, Escuela de Ingeniería y Ciencias, Vía Atlixcáyotl No. 2301, Reserva Territorial Atlixcáyotl, 72453, Puebla, Puebla, México.

*Corresponding author: andys400@hotmail.com

Abstract: *Some times operating conditions, namely, misalignment, overheating and the start/stop of engine generate boundary lubrication conditions increasing wear of journal bearings (JBs). Thus, debris are a consequence of wear and fatigue either from JBs or other lubricated mechanical components. Debris are commonly immersed in the oil and recirculated through the entire lubrication system interacting with all the lubricated mechanical elements and accelerating wear rate due to three-body abrasion. The aim of this work is to evaluate the effects of abrasive particles on the wear behaviour of sections of an actual JB coated with a soft alloy (Pb-Cu-Al) by replicating boundary lubrication in JBs using a micro-scale abrasion test set-up. Steel balls were used to replicate the shaft counter face for the tests. Initially, the tests were carried out with a slurry prepared with distilled water and SiC micro-particles at a concentration of 20% vol. On the other hand, a SAE 10W-30 engine oil was blended with SiC micro-particles at different concentrations to replicate an engine oil contaminated with abrasive particles. The slurry was tested at 26°C while the contaminated oil was tried at two different oil temperatures (26 and 100°C). The wear scars produced were measured and analysed by optical microscopy, SEM and contact profilometry. It was found that clean oil generated higher wear than oil contaminated with SiC particles at different concentrations since a layer of SiC particles was generated on the scars by embedment of many particles in the soft coating. It acted as protective layer for the JB's coating reducing wear. However, it generated significant wear in the ball surface.*

Keywords: *Journal bearings, oil contaminated abrasion, pure oily sliding wear, wear rate and abrasive particles.*

1. INTRODUCTION

Journal bearings (JBs) are components used to support a rotary shaft with a load applied, allowing relative motion between both elements (bearing and shaft) with relative low friction [1]. The motion is facilitated by a thin film of lubricant generating low friction by means of hydrodynamic lubrication conditions. The lubricant characteristics, conditions, texture, and coatings are the main parameters for consideration in the design and performance of these components. The operation of JBs is preferably expected to be under hydrodynamic lubrication regime (HL). However, operating situations, such as overheating, misalignment, oil ageing and debris generate premature damage due to wear caused by the transition from hydrodynamic to mixed, or even, boundary lubrication situations. Wear of JBs can be a consequence of corrosion, abrasion, adhesion, fatigue, cavitation, fretting and erosion [2, 3]. Nonetheless, the most common wear types in JBs are adhesive and abrasive wear produced by rupture of hydrodynamic film achieving the boundary lubrication regime. Also, the interaction with free abrasive particles (debris) in the oil causes damage in both the JB and the shaft. Severe damage of JBs and shafts results in machine shutdown and accidents, producing undesired high costs of maintenance and production stops [4].

There are two types of abrasion occurring in JBs: two-body abrasion and three-body abrasion. In two-body abrasion, the material is removed from the JB´s surface by hard protuberances on the shaft´s surface meanwhile three-body abrasion is generated by free hard particles (debris) that can roll and abrade both surfaces [5]. It happens commonly since much debris are immersed in the oil as a product from wear of other components, including those from JBs and shaft. To have a considerable effect of debris on wear of JBs, those particles should be larger than the minimum lubricant film thickness expected between the JB and the shaft [6].

In some research works [7-9], debris made of Fe, Al, Sn, Cu, Ag, SiC, SiN, silicates, and sand micro-particles have been found immersed at different concentrations in used engine oils. The hardness of such particles is in the range from 40 to 1300 HV depending of each material. As a reference, about 85 mg/kg of debris concentration was reported for an oil used in a four-cylinder engine during 100 hours in a bench test at a controlled temperature in the range of 88 and 110°C. [10].

The performance of JBs is mainly related to the material´s properties, namely, thermal conductivity, flexible conformability and debris embeddability [11-14]. Thermal conductivity refers to the intrinsic ability of a material to transfer or conduct heat. Flexible conformability is the ability to be deformed according to the shaft surface topographical characteristics meanwhile embeddability is referred to the capability of the material for trapping hard particles in the bearing surface to avoid damage caused by three-body abrasion for both the JB and the crankshaft. Embeddability is usually achieved in JBs by using soft coatings at the surface. However, soft coatings are highly susceptible to be damaged by two-body abrasion under boundary lubrication conditions [15, 16]. It usually produces abrasive and adhesive wear patterns. Adhesive wear is mainly ascribed to the chemical compatibility of the metallic surfaces in sliding contact producing high adhesion forces and seizure of JB material [15, 16]. Incompatibility between the steel shaft and the JB surface may be expected under boundary lubrication conditions (high loads, low speed, low viscosity of oil, etc.) producing increased wear and high friction coefficients.

Nowadays, most of commercial JBs are made of steel backs coated with an alloy made of Sb, Sn and Pb, which is named as “babbitt” alloy. There are two types of babbitt alloys, Sn-based and Pb-based alloys. The benefits of these coatings are related to properties, such as good chemical compatibility with steel shafts, good embeddability, low friction coefficient, ability to accommodate with small shaft misalignment and being a protective and/or sacrificial layer for scuffing (severe abrasion). Scuffing is expected to be produced in the running-in period and lubricant starvation [17-21].

In several studies, the tribological performance of JBs has been investigated by using different methodologies and testers, the most common being the pin-on-disk tester, full-scale test rigs and the block-on-ring tester [3, 22-25]. Also, experimental tests combined with simulation works have been used to investigate wear caused by metal-to-metal sliding contact in the start-stop process in JBs [6, 26-28].

According to the literature reported about wear of JBs, the effects of hard particles acting as contaminant in engine oil on the wear behaviour of JBs with soft coatings has been scarcely studied. Sep et al. [6] carried out tests of JBs in a test rig (ZAN research rig) using an oil (SAE 40) clean and contaminated with hard aluminium oxide powder (spherical micro-particles with a diameter of 21μm). The test bench allowed trying complete conventional JBs under lubricated conditions including contaminant particles. Overall, they found that wear of JBs is increased when the oil is contaminated with hard particles in comparison with clean oil [6]. In other research work, Gebretsadik et al. [29] studied the embeddability of JBs with a soft overlaying made of Pb-Free by full-scale tests using an engine oil (SAE 10W 30) contaminated with SiC particles at 95°C. The results suggested that three-body abrasion is mainly influenced by the variation of the lubricant film thickness at the different operating conditions (rotational speed of the shaft, dynamic loads and misalignment) [29].

This paper aims to contribute within a study of the effects of micro-abrasive particles on the wear behaviour of a commercial JB with a soft coating (Pb-based lining alloy (Babbitt)) under boundary lubrication conditions. To restrict effects of variations in parameters, such as sliding speed and distance, shaft misalignments, vibrations, oil temperature, as well as to accelerate the wear test and have an accurate control of the boundary lubrication regime conditions, an approaching test using a micro-abrasion tester was developed and used. The method has been demonstrated to be effective to reproduce wear features occurred in actual JBs in lubricated condition, generating small wear scars with defined geometry by saving time, lowering testing cost and allowing accurate wear scar measurements in comparison with other wear test techniques for JBs [30]. Steel balls were conditioned and used to reproduce the characteristics of typical shafts. Initially, as a reference to evaluate the pure effect of the abrasive particles on wear of the JBs and steel shaft material, conventional micro-abrasion tests [30-33] were carried out for JB samples using a slurry made of SiC micro-particles suspended in distilled water. Finally, tests were conducted under boundary lubrication regime using different concentrations of abrasive particles (SiC micro-particles) suspended in an engine oil (EO) at 26 and 100°C, respectively.

2. TESTS CHARACTERISTICS

2.1 Test set-up

Figure 1 shows a schematic view of the test set-up used. A micro-scale abrasion tester (TE-66) was adapted to perform the abrasive wear tests. The tribometer is equipped with a pivoted L-Shaped arm. Together the arm and the counterbalance allow the application of a predefined normal load between the steel ball and the JB by using dead weights.

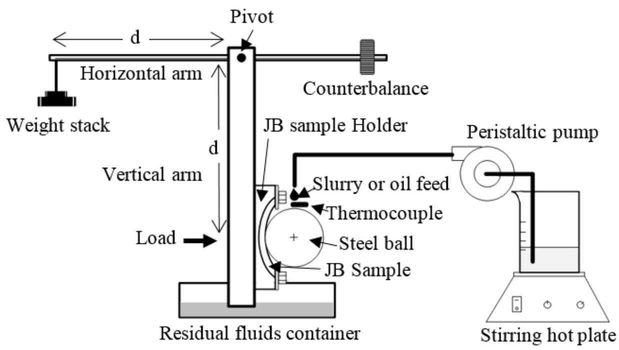

Figure 1. Schematic view of the tester arrangement.

A specimen cut from the JB is mounted in the arm by using a special holder while a steel ball sample is fixed between two coaxial shafts with auto-alignment, enabling the tangential contact of the ball and sample. The steel ball is rotated at constant speed and specified cycles by an electric motor. A stirring hot plate with a magnetic agitator was incorporated in the test arrangement to keep suspended the abrasive particles either in oil (contaminated oil) or distilled water (slurry) in a beaker and to heat up the temperature of the oil simultaneously.

A peristaltic pump is used to move the fluids from the beaker to the sliding contact region. The oil temperature is monitored in the dripping region exactly located upper the ball through a thermocouple.

2.2 Test samples

An actual automotive JB was sectioned to obtain samples with adequate geometry for the tests. The JB tested was made by two different coatings (a lining and an overlaying) on the steel substrate. The chemical composition of each coating was estimated through EDS analysis, see Table 1. Also, the thickness and elastic modulus were measured by Scanning Electron Microscopy (SEM) and instrumented nanoindentation tests, respectively. The results from the characterizations can be seen in Fig. 2a and Table 2.

Table 1. Chemical composition of the coating of JB

JB sample	Chemical composition (wt%)					
	C	O	Al	Fe	Cu	Pb
Overlaying	-	13.2	0.6	-	3.8	82.4
Lining	-	-	1.1	-	98.9	-
Substrate	4.7	-	0.5	94.8	-	-

Table 2. Mechanical properties of the specimens.

Sample	Steel ball	JB	
		Overlaying	Lining
Hardness (HV)	848 ± 17	10.7 ± 3.8	92.1 ± 6.4
E (GPa)	200 ± 10	7.85 ± 2.8	61.9 ±2.5
Poisson´s ratio	0.27	0.44	0.34
Roughness (µm)	0.22 ± 0.02 Ra 0.35 ± 0.03 Ra	0.87 ± 0.1 Sa	-

The ball specimens tested were made of steel (AISI 52100) with 25.4 mm in diameter. The steel ball´s mechanical properties are also given in Table 2. In order to achieve two different ball roughness, one required for conventional micro-abrasion tests using slurry (about 0.3 µm) while the other required to replicate the roughness of actual shafts (around 0.2 µm) using oil for the tests, the balls were etched into 20% nital solution during 30 and 8 s, respectively. The highest roughness is required in conventional micro-abrasion tests to allow abrasive particles being dragged along the contact interface [31-33]. Meanwhile, the lowest roughness is only to achieve an approached surface finishing suggested for actual crankshafts (0.20 – 0.25 µm Ra) through controlled pitting.

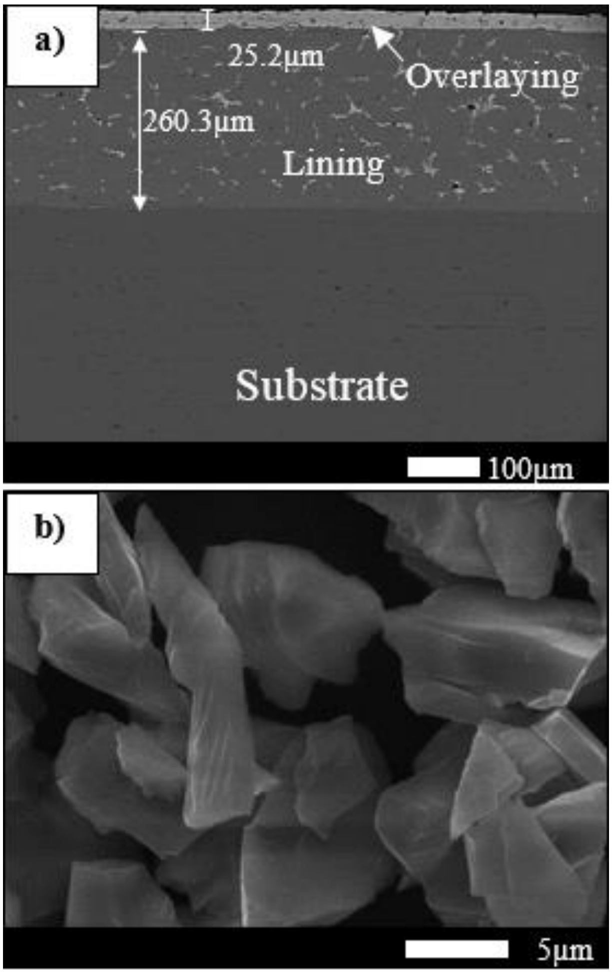

Figure 2. Electronic microscopy; a) SEM image from the cross-section of the sample; b) SEM image from the SiC particles tested.

The SiC particles were used to act as debris in the tests, with a mean particle size of 8 µm with angular shapes, as illustrated in Figure 2b. On the other hand, distilled water and a commercial engine oil (EO) with 10W-30 API SN/GF-5 specification were used to prepare the slurry and the contaminated oil samples, respectively. The EO viscosities were 112 and 12.4 cSt at 25 and 100°C, respectively.

2.3 Test procedure

The set of tests was established and carried out to examine the wear patterns and behaviour of the JB samples at different SiC micro-particles concentrations and temperatures. The tests conditions selected for the experiments are shown in Table 3.

Table 3. Test parameters.

Parameters	Micro-abrasive method	Micro-abrasive oily wear
Lubricant	Distilled water	EO
Normal force [N]	1	1
SiC particles concentration	20% [vol.]	0, 40, 80, 120, 160 [mg/kg]
Ball cycles	50, 100, 150 and 200	10 000
Sliding distance [m]	4, 8, 12, 16	798
Tangential sliding velocity [m/s]	0.11	0.22
Number of repetitions	3	3
Contact pressure [MPa]	110	110
Temperature [°C]	25	25, 100

Firstly, the micro-abrasive wear tests were carried out under parameters, namely, load, sliding velocity and abrasive slurry concentration specified in the classic micro-abrasion test reported for different materials in [3, 33]. The sliding distance was varied from 4 to 16 m (50, 100, 150 and 200 cycles) to evaluate the wear progression. For these tests, the steel ball sample was rotated every 50 cycles since it exhibited significant visual damage in the wear track in previous trials run after 50 cycles, which may influence the wear progression. Afterwards, wear tests were carried out using the clean EO and EO contaminated with SiC micro-particles at different concentrations (40, 80, 120, 160 mg/kg). These tests will be named as micro-abrasive oily wear tests in the following. The concentrations used were selected to approach the typical quantity of wear debris concentration found in used engine oils [10]. The oil samples were tested at 25 and 100 °C at the same load than that used for the micro-abrasive wear tests approaching the boundary lubrication regime. The regime was determined through the theory developed by Hamrock for elasto-hydrodynamic lubrication in elliptical conjunctions [34] and lambda ratio equations [35, 36]. These set of tests were carried out at a sliding speed of 0.22 m/s during 10,000 ball cycles to produce measurable and consistent wear scars.

3. RESULTS AND DISCUSSION

3.1. Damages on the journal surface

Micro-abrasive wear

The wear volume of scar was considered to have the shape illustrated in Figure 3a. Where a and b dimensions were measured by using optical microscopy while h was measured by using a contact profilometer obtaining the wear scar profile, as seen in Figure 3b.

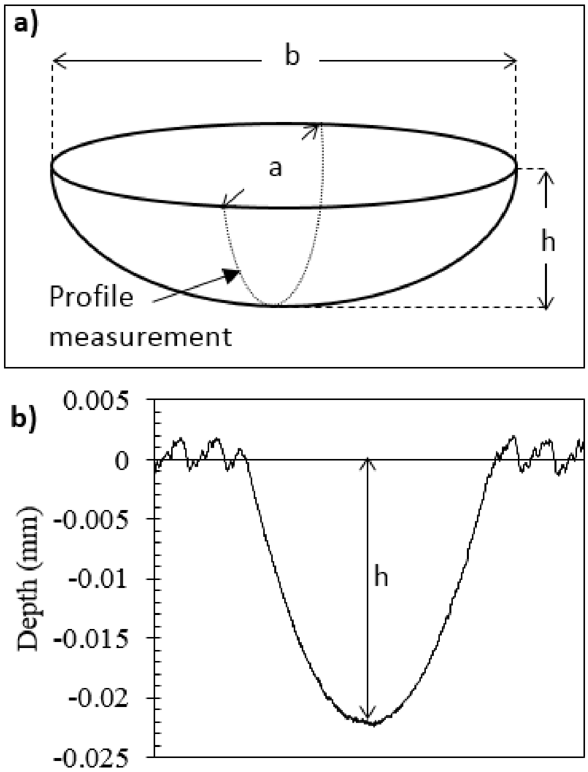

Figure 3. Measurement of wear scar; a) axes measurement, b) scar profile measurement

The wear scars had an elliptical shape due to the ball-on-concave flat sliding contact produced in these tests. Therefore, the Vwear and wear coefficient k were calculated by using Equations 1 and 2, respectively.

$$V_{Wear} = \frac{1}{6}(\pi * a * b * h) \tag{1}$$

$$k = \frac{V_{wear}}{S * P} \quad (2)$$

Where:
a = minor axis
b = mayor axis
h = wear scar depth
S = sliding distance
P = load

The micro-abrasion wear volumes obtained at for the sliding distances are showed in Figure 4. Wear volumes presented a proportional increase with sliding distance. Figure 5 shows a SEM image from a representative wear scar produced for a sliding distance of 16 m (200 cycles).

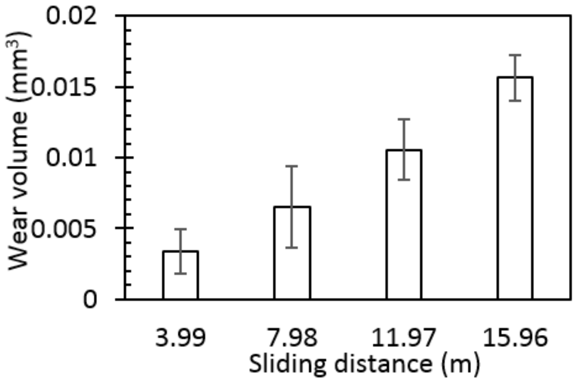

Figure 4. Wear volume obtained at different sliding distances by micro-abrasion tests using slurry.

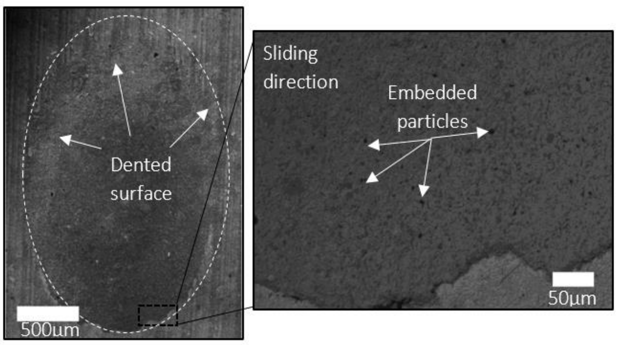

Figure 5. Example of SEM image from a wear scar produced by using slurry for 200 cycles.

All the scars produced by micro-abrasive wear exhibited similar wear patterns. The wear scar shows many embedded particles on the overlaying, which may be caused by the high embeddability of the coating. Besides, several indentations can be seen in the scar. The indentations and SiC embedment in the JB sample were produced by rolling and tumbling of the abrasive particles due to the ball sliding [6, 8, 29]. They are the main characteristics of rolling abrasion that can be considered as the predominant wear mechanism. Rolling abrasion mechanism is typically produced at large concentrations of hard particles at high contact pressures [37]. The accumulation and embedment of sic particles in the scar was confirmed by conducting EDS analysis.

Wear produced by using clean oil

The comparison of wear volumes obtained using clean oil at 25 and 100°C can be seen in Fig. 6. It can be seen a significant difference of wear volume obtained at both temperatures. It is attributed to the considerable oil viscosity reduction at 100°C, generating more reduced lubricating films conductive to more severe lubricated sliding wear.

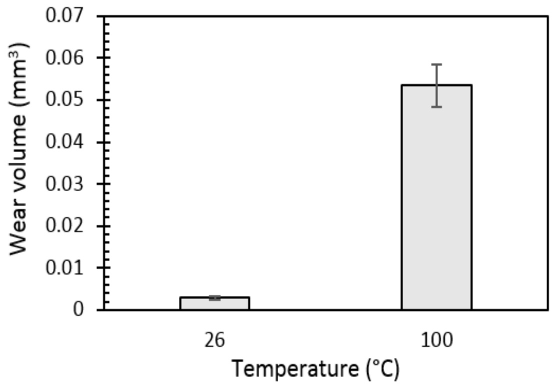

Figure 6. Wear volume by using clean oil

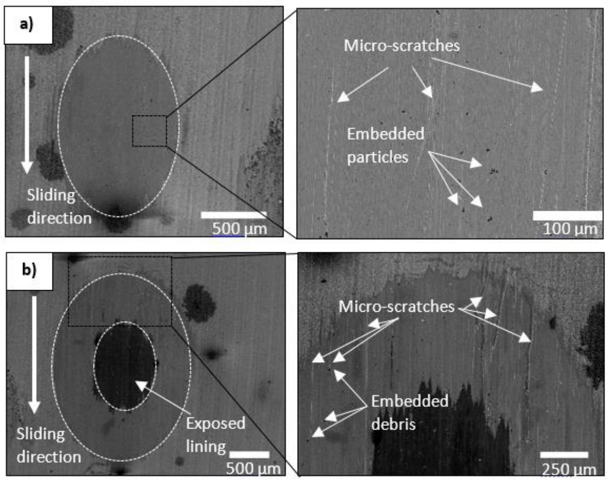

Figure 7. Example of a SEM image from a wear scar obtained by using clean oil at: a) 26 °C, b) 100 °C.

An example of a wear crater produced by using clean oil at both temperatures can be seen in Figures 7a-b. In contrast with the scars produced by micro-abrasion, the scars produced by using clean oil did not showed indentations, but they showed a shiny appearance produced mainly by polishing due to lubricated sliding wear. In addition, some micro-scratches were identified in the scar. They can be ascribed to three-body abrasion produced by wear particles detached from the JB by wear or two-body abrasion caused by large asperities of the ball. The wear produced at 25°C was evidently less severe than that produced at 100°C. It can be also seen in Figs. 7a-7b. The test at 25°C only generated wear on the overlaying (Fig. 7a) while the test at 100°C causes perforation of the overlaying generating wear on the lining material too (Fig. 7b).

Micro-abrasive oily wear

The comparison of wear volumes of scars produced using oil contaminated with different SiC concentrations are shown in Figures 8a-b. The plots present the evolution of wear volume with SiC concentration at 26 and 100°C, respectively. Figure 8a suggests that the lowest wear volume was obtained using a SiC concentration of 160 mg/kg at 26°C while Figure 8b suggests that the lowest wear volume was produced using a concentration of 120 mg/kg at 100°C.

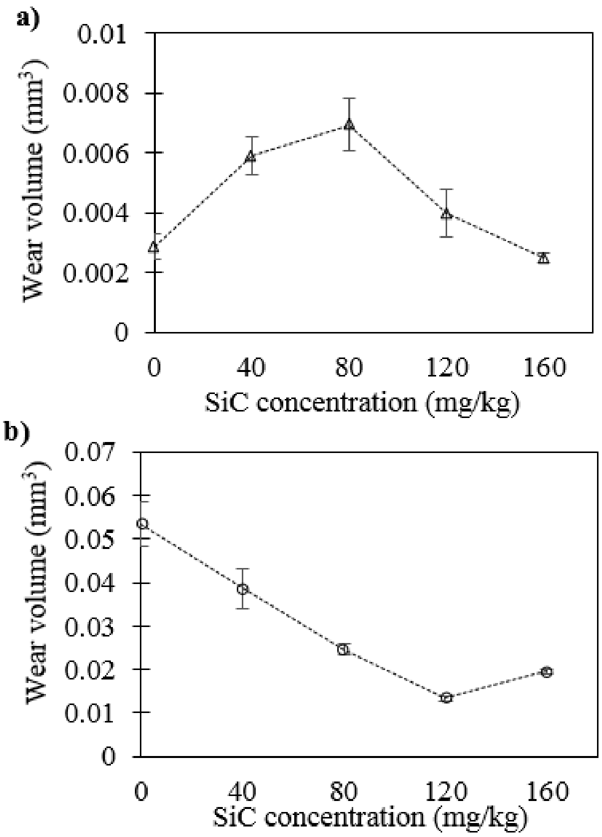

Figure 8. Wear volumes obtained from the micro-abrasive oily tests at: a) 25°C; b) 100°C.

In both Figures, the wear volume tended to decrease at high SiC concentrations in the oil. This phenomenon can be attributed to the formation of a layer made of many embedded SiC particles in the scar promoting a mechanical wear protection that decrease abrasive wear on the JB's surface.

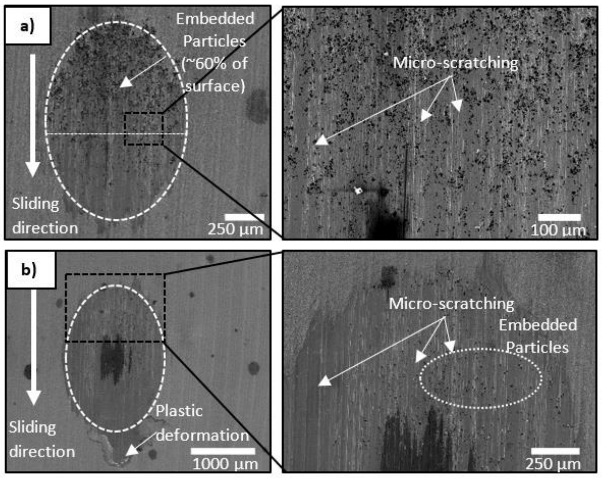

Figure 9. SEM image of wear scar of the micro-abrasive oily test using a SiC concentration of 80 mg/kg at; a) 26°C; b) 100°C.

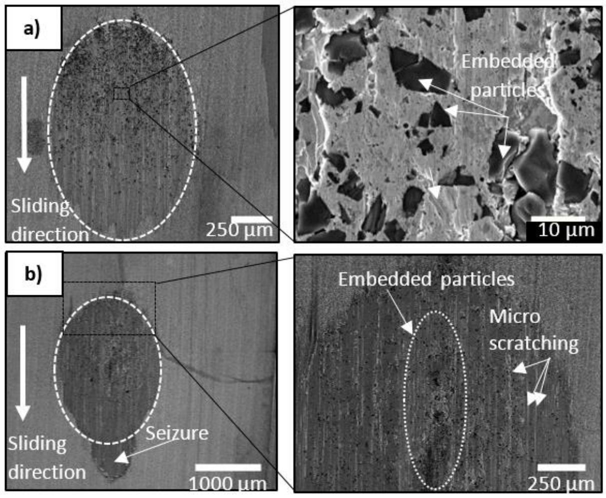

Figure 10. Example of a SEM image of wear scar obtained by a micro abrasive oily test using a SiC concentration of 160 mg/kg at: a) 26°C; b) 100 °C.

It is evidenced in Figures 9a-9b and 10a-10b where a lot of SiC particles were embedded on almost 60% of the JB sample's surface by using EDS analysis. SiC embedment and micro-scratching were the main wear patterns identified in all the scars. The highest wear volume was exhibited by the clean oil at 100°C and it was decreased with the increase in SiC concentration, as it can be seen in Figure 9b. It suggests that two-body abrasion generated by oily sliding wear is more critical than three-body abrasion for this coating. It means that the soft coating helps to reduce wear in the presence of debris, but it is very susceptible to wear by boundary lubrication situations.

3.2 DAMAGE ON THE STEEL BALL SURFACE

The wear produced in the ball by using clean oil was minimal, even it was not visible. In contrast, it was found that micro-abrasion produced in the JB samples by using both slurry and contaminated oil, in particular, at high SiC concentrations, caused severe damage on the steel ball surface.

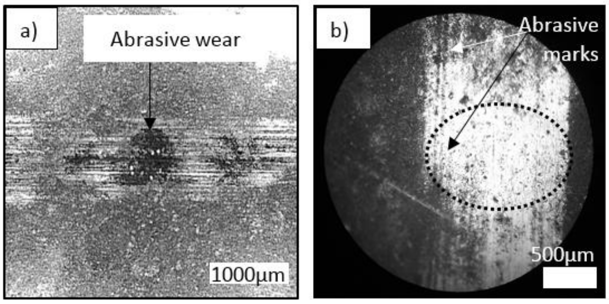

Figure 11. Examples of optical micrographs from a wear track on the ball surface produced by using: a) 80 mg/kg of SiC concentration; b) 160 mg/kg of SiC concentration.

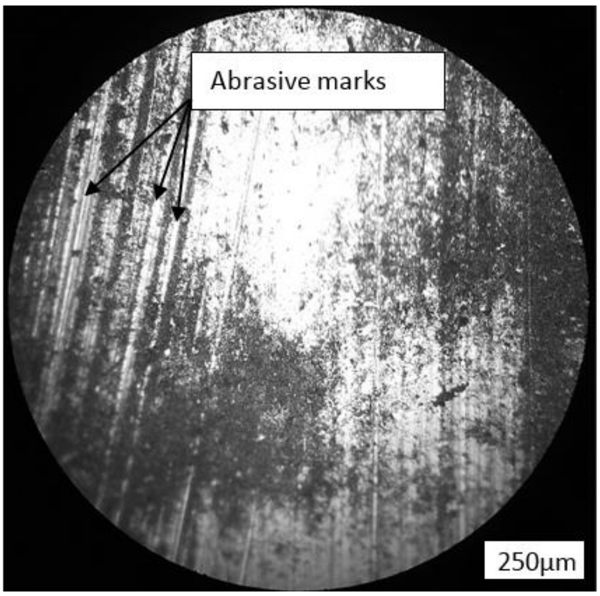

Figure 12. Example of an optical micrograph from a wear track produced on the steel ball surface using the contaminated oil sample at a SiC concentration of 160 mg/kg.

It generates wear tracks with visible abrasive marks, as it can be seen in Figures 11a-11c and 12. The most critical damage to the ball was produced by using slurry. However, contaminated oil at the higher SiC concentrations (80 to 160 mg/kg) generated significant wear tracks in the ball surface.

Pitting, grooving, ploughing and polishing were the main wear patterns exhibited at high SiC concentrations. These wear patterns can be considered as severe for shafts in actual applications.

Overall, the JB tested could prevent wear caused by debris in the oil but it may be very susceptible to be damaged by boundary lubrication situation such as engine start-stop, misalignments, overheating, etc., decreasing the JB's life and promoting premature failures. Although limiting wear by debris in JBs could be considered as positive, the embedment of debris in the soft coating can accelerate significantly wear in shafts. It perhaps generates more severe failures involving not only the JBs but also the shafts.

4. CONCLUSIONS

According to the findings in this work, it can be stated that clean oil generated higher wear than oil contaminated with SiC particles at different concentrations under boundary lubrication conditions. Also, the wear volumes were reduced even more with the increase in SiC concentration in the oil.

A layer of SiC particles was generated on the scars produced by using contaminated oil by embedment of many particles in the soft coating. It acted as protective layer for wear of the coating reducing wear volumes. However, the protective layer for the coating resulted as aggressive for the steel ball since the ball surface exhibited significant wear with severe abrasive marks.

The predominant wear mechanisms in JB samples tested with clean oil were slight abrasive marks and polishing meanwhile with oil contaminated with SiC particles exhibited patterns such as much particles embedment, micro-scratches, rolling abrasion and polishing.

ACKNOWLEDGEMENT

The authors would thank to CNMN-IPN for the nano-indentation tests and ESIQIE and IF-UNAM for the SEM facilities.

REFERENCES

[1] P.R.N. Childs, Journal bearings. In Mechanical Design Engineering Handbook, Elsevier Ltd, Butter worth Heinemann, United Kingdom, 2014, http://dx.doi.org/10.1016/B978-0-08-097759-1.00005-8.
[2] H. Singh, S.S. Sen, Wear in hydrodynamic journal bearings: a review, Int. J. Mod. Eng. Res., Vol. 4, No. 8, pp. 45–57, 2014.
[3] A. Vencl, A. Rac, Diesel engine crankshaft journal bearings failures: case study, Eng. Fail. Anal. Vol. 44, pp. 217–228, 2014, doi: 10.1016/j.engfailanal.2014.05.014
[4] Y. H.e, Z. Zhao, T. Luo, X. Lu, J. Luo. Failure analysis of journal bearing used in turboset of a power plant. Mater Des, Vol. 52, pp. 923–931, 2013.
[5] I. Hutchings, P. Shipway, 6 - Wear by hard particles, Editor(s): Ian Hutchings, Philip Shipway, Tribology (Second Edition), Butterworth-Heinemann, 2017, Pages 165-236, ISBN 9780081009109.
[6] J. Sep, A. Kucaba-Pietal, Experimental testing of journal bearings with two-component surface layer in the presence of an oil abrasive contaminant, Wear, Vol. 249, pp. 1090–1095, 2001.
[7] GK. Nikas. A state-of-the-art review on the effects of particulate contamination and related topics in machine-element contacts. Proc Inst Mech Eng Part JJ Eng Tribol, Vol. 224, pp. 453–479, 2010.
[8] MM. Khonsari, ER. Booser. Effect of contamination on the performance of hydrodynamic bearings. Proc Inst Mech Eng Part J J Eng Tribol., Vol. 220, pp. 419–428, 2006.
[9] M.H. Jones, Wear debris associated with diesel engine operation, Wear, Vol. 90, pp. 75– 88, 1983.
[10] Y. Zhang , J. Mao & Y. Xie, Engine Wear Monitoring with OLVF, Tribology Transactions, Vol. 54, No. 2, pp. 201-207, 2001, DOI: 10.1080/10402004.2010.534838
[11] H. Wu, Q. Bi, S. Zhu, J. Yang, W. Liu. Friction and wear properties of Babbitt alloy 16-16-2 under sea water environment, Tribol Int, Vol. 44, pp. 1161–7, 2011.
[12] AR. Lashin, M. Mossa, A. El-Bediwi, M. Kamal. Study of some physical properties of the rapidly solidified Sn–Sb–Cu–Zn alloys. Mater Des, Vol. 43, pp. 322–6, 2013.
[13] A. Zeren. Embeddability behaviour of tin-based bearing material in dry sliding. Mater Des, Vol. 28, pp. 2344–50, 2007.
[14] D. Zhang, J. K.L. Ho, G. Dong, H. Zhang, M. Hua. Tribological properties of Tin-based Babbitt bearing alloy with polyurethane coating under dry and starved lubrication conditions, Tribology International, Vol. 90, pp. 22-31, 2015, doi: 10.1016/j.triboint.2015.03.032
[15] A.E. Bravo, H.A. Durán, V.H. Jacobo, A. Ortiz, R. Schouwenaars, Towards new formulations for journal bearing alloys, Wear, Vol. 302, Iss. 1–2, pp. 1528-1535, 2013, doi: 10.1016/j.wear.2013.01.040.
[16] E. Rabinowicz: The Determination of the Compatibility of Metals Through Static Friction Tests, ASL E Transactions, Vol. 14, No. 3, pp. 198–205.
[17] Q. Wang & H. S. Cheng, A Mixed Lubrication Model for Journal Bearings with a Thin Soft Coating—Part I: Contact and Lubrication Analysis, Tribology Transactions, Vol. 38, No. 3, pp. 654-662, 1995, DOI: 10.1080/10402009508983455
[18] E. Feyzullahoglu, A. Zeren, M. Zeren. Tribological behaviour of tin-based materials and brass in oil lubricated conditions. Mater Des, Vol. 29, pp. 714–20, 2008.
[19] D. Tabor, The frictional properties of some white metal bearing alloys: the role of the matrix and the hard particles. J Appl Phys, Vol. 16, pp. 325–37, 1945.
[20] B.S. Ünlü. Investigation of tribological and mechanical properties of metal ¨ bearings. Bull Mater Sci, Vol. 32, pp. 451–7, 2009.
[21] M.Ö. Bora, O. Coban, T. Sinmazcelik, V. Günay, M. Zeren, Instrumented indentation and scratch testing evaluation of tribological properties of tin-based bearing materials. Mater Des, Vol. 31, pp. 2707–15, 2010.
[22] K.S. Pondicherry, F. Grün, I. Gódor, R. Bertram, M. Offenbecher, Applicability of ring-on-disc and pin-on-plate test methods for Cu–steel and Al–steel systems for large area conformal contacts, Lubr. Sci., Vol. 25, pp. 231–247, 2013, doi: 10.1002/ls.1187.
[23] F. Summera, F. Grüna, J. Schiffera, I. Gódora, I. Papadimitriou. Tribological study of crank

shaft bearing systems: comparison of forged steel and cast iron counterparts under start–stop operation, Wear, Vol. 338–339, pp. 232–241, 2015, doi: 10.1016/j.wear.2015.06.022.
[24] E. Feyzullahoglu, N. Sakiroglu, The wear of aluminium-based journal bearing materials under lubrication, Mater. Des., Vol. 31, pp. 2532–2539, 2010, doi: 10.1016/j.matdes.2009.11.037.
[25] H. Singh, M.S. Sethi, O.S. Bhatia, Wear rate analysis of hydrodynamic journal bearing in different conditions, Int. J. Mod. Eng. Res. Vol. 4, No. 10, pp. 60–69, 2014.
[26] D.E. Sander, H. Allmaier. Starting and stopping behavior of worn journal bearings. Tribology International, vol. 127, pp. 478-488, 2018, doi: 10.1016/j.triboint.2018.06.031
[27] X. Wang, L. Zhou, M. Huang, X. Yue, Q. Xu. Numerical investigation of journal misalignment on the static and dynamic characteristics of aerostatic journal bearings, Measurement, Vol. 128, pp. 314-324, 2018.
[28] J. Sep, L. Tomczewski, L. Galda, A. Dzierwa, The study on abrasive wear of grooved journal bearings, Wear, Vol. 376–377, pp. 54-62, 2017, doi: 10.1016/j.wear.2017.02.034.
[29] W. Daniel, Gebretsadik, J. Hardell, B. Prakash: Embeddability behaviour of some Pb-free engine bearing materials in the presence of abrasive particles in engine oil, Tribology - Materials, Surfaces & Interfaces, 2019, DOI: 10.1080/17515831.2019.157445
[30] L.I. Farfán-Cabrera, E.A. Gallardo-Hernández. Wear evaluation of journal bearings using an adapted micro-scale abrasion tester, Wear, Vol. 376-377, pp. 1841–1848, 2017.
[31] R.I. Trezona, I.M. Hutchings. Three-body abrasive wear testing of soft materials, Wear, Vol. 225–229, pp. 205–214, 1999, doi: 10.1016/S0043-1648(99) 00183-0.
[32] D.N. Allsopp, R.I. Trezona, I.M. Hutchings, The effects of ball surface condition in the micro-scale abrasive wear test, Tribol. Lett. Vol. 5, No. 4, pp. 259–264, 1998, doi: 10.1023/A:1019178716408.
[33] K.L. Rutherford, I.M. Hutchings, Theory and application of a micro-scale abrasive wear test, J. Test. Eval., Vol. 25, pp. 250–260, 1997, doi: 10.1520/ JTE11487J
[34] B.J. Hamrock, S.R. Schmid, B. Jacobson, Fundamentals of fluid film lubrication, Second Edition, Mercel Dekker Inc, New York, pp. 504–538, 2004.
[35] R.S. Fein, High pressure viscosity and EHL pressure-viscosity coefficient, In Tribology Data Handbook, CRC Press, Boca Raton, Fla, pp. 3–33, 1997.
[36] I.M. Hutchings, Tribology, friction and wear of engineering materials, First edition, Butterworth-Heinemann, pp. 58–73, 1992.
[37] K. Adachi, I.M. Hutchings, Wear mode-mapping for the micro-scale abrasion test, Wear, Vol. 255, pp. 23–29, 2003.

Serbian Tribology Society

SERBIATRIB '19

16th International Conference on Tribology

Faculty of Engineering
University of Kragujevac

Kragujevac, Serbia, 15 – 17 May 2019

OPTIMIZATION OF MECHANICAL LOSSES IN RECIPROCATING AIR COMPRESSOR WITH CYLINDER CONSISTING OF ALUMINUM ALLOY

Saša MILOJEVIĆ*, Dragan DŽUNIĆ, Dragan TARANOVIĆ, Radivoje PEŠIĆ, Slobodan MITROVIĆ
University of Kragujevac, Faculty of Engineering, Kragujevac, Republic of Serbia
*Saša Milojević: sasa.milojevic@kg.ac.rs

Abstract: *Transport is largely dependent on oil because the majority of transport vehicles are propelled by engines combusting petroleum products-hydrocarbon fuels. This particularly relates to road, air and water transport. Power losses in the internal combustion engines and other reciprocating machines are mainly engaged to overcome friction. If using aluminum alloys for producing of piston and cylinders in engines and compressors, the results are lower fuel consumption and exhaust emission, firstly because of lower weight and mechanical losses, too. The problems are poor tribological characteristics and lower strength of unprotected aluminum comparing with gray cast iron. For research purposes, the inner surface of cylinder which was produced of aluminum was reinforced by integrating tribological inserts. In this paper, the tribological properties of ferrous based reinforcements were analyzed and compared with aluminum alloy as a base material for cylinder liner and piston skirt in air brake compressor. The ball-on-plate CSM tribometer was used to carry out these tests under dry sliding conditions. In addition to tribological, have carried out and testing of experimental reciprocating compressor on the bench, in the laboratory for engines and compressors in Faculty of Engineering in Kragujevac.*

Keywords: *Aluminum, cylinder liner, friction, mechanical losses, reciprocating compressors, transport.*

1. INTRODUCTION

In the transport process, the input energy is converted into the movement of transport vehicles which provide the required spatial relocation of goods and persons. Therefore, transport is dependent on energy supply. Existing main energy resources are non-renewable and their stocks are constantly decreasing. Transport is the only major sector in the EU where greenhouse gas (GHG) emissions are still raising. Given to the mentioned facts there is the effort to make transport more efficient in the field of energy dependence [1-3].

The European Commission (EC) is working on the measures to reduction of GHG emissions from all sources and specific emission of carbon dioxide (CO_2) has limited proportional to fuel consumption.

Heavy-duty (HD) vehicles, trucks and buses are responsible for about a quarter of (CO_2) emissions from road transport in the EU and for about 6% of total EU emissions. There was not much progress in reduction of fuel consumption and thus exhaust emission starting from vehicle model EURO I (1992-1996) to EURO VI (since 2013) [4].

Because of the fact that all vehicles must give to reduction of fuel consumption and emission, the EU formed regulation for certification of all new registered HD vehicles. The main idea is to determinate which components of HD vehicles contributing to lowering mechanical efficiency and fuel consumption [4, 5].

As a contribution, we researched reduction of power demand of auxiliary devices on the engine, specifically in air compressor [6,7,8].

The air compressor in brake system of trucks and buses is two-stroke reciprocating machine which delivering air into pressure cylinders to feed the consumers as pneumatic brakes, clutch, gearbox and drivetrain, suspension system, actuators at engine, AdBlue injector, if exists inside of the exhaust system etc.

According to above facts, simplified model of pneumatic system for simulation of cylinder pressure, as well as the compressor power and measurement of the air consumption was given in Fig. 1.

In every moment of time, the air mass inside the pneumatic system we will determined by application of the ideal gas law, Eq. 1 and Eq. 2. Air temperature, air pressure and the cylinder volumes were main input values [8].

$$(p \cdot V)_R = R_{s,air} \cdot (m \cdot T_{avr})_{R,air} \qquad (1)$$

$$V_{air,tot,std} = \frac{m_{air,tot}}{\rho_{air,tot}} \qquad (2)$$

where is:

- $(p \cdot V)_R$ -Volume of air cylinder and pressure in cylinder;
- $(m \cdot T_{avr})_{R,air}$ -Air mass and average temperature in cylinder;
- $m_{air,tot}$ - Total air mass, cylinders brake front, brake rear, air suspension system, auxiliaries;
- $R_{s,air}$ - Specific gas constant for dry air, $287.1\, J \cdot (kg \cdot K)^{-1}$;
- $\rho_{air,std}$ - Density of dry air at standard conditions:
  $(20℃, 1.013\, bar); 1.204\, kg \cdot m^{-3}$
- $V_{air,tot,std}$- Total air content, mass unit of standard litres air; one litre of dry air at $(1\, bar, 20\ ℃)$; $[sl] = 0.001204\, kg$.

The air mass in reservoir is calculated in steps of one second, by applying the ideal gas law for dry air.

As example, when the reservoir pressure falls under the lower limit, e.g. $6\, bar$ the compressor is turned on, the reservoir pressure increases, and when the upper limit, e.g. $10\, bar$ is reached, the compressor is turned off. Then, compressed air is only taken off the reservoir, its pressure decreases until the lower limit, and the cycle restarts.

The $1\, Hz$ time course of the reservoir pressure can be calculated via Eq. 3.

$$p_R(t) = p_R(t - 1s) + \Delta p_R(t) \qquad (3)$$

where is:

- $p_R(t)$ -reservoir pressure at current time step (t);
- $p_R(t - 1s)$ -reservoir pressure at last time step $(t - 1s)$; and
- $\Delta p_R(t)$ -pressure change in actual time step.

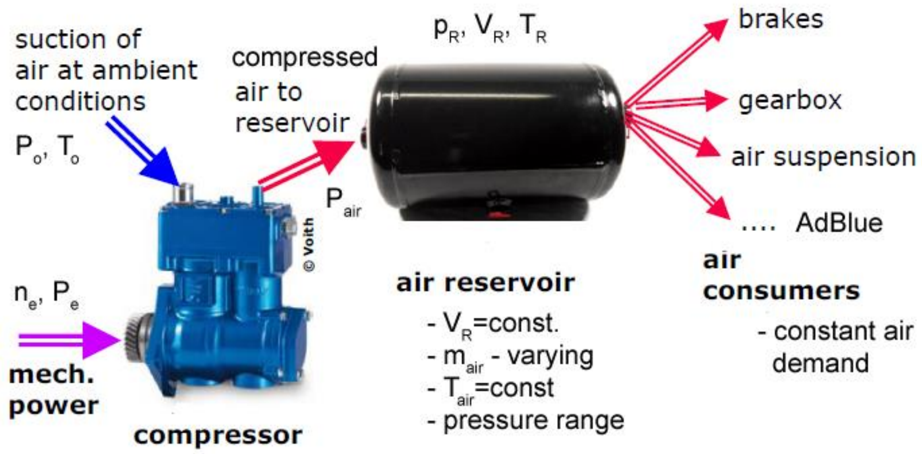

Figure 1. Simplified model for simulation of pneumatic system of a delivery truck (category N2)

2. TRIBOLOGICAL RESEARCHES AND RESULTS

With the aim to achieving strength as well as tribological characteristics similarly as in case of the application grey cast iron, we patented the cylinder of composite material for reciprocating air compressor with the reinforcements consisting of tribological materials.

For the purposes of the experiment, internal surface of the aluminum cylinder as base material matrix, (alloy EN AlSi10Mg), was modified by putting tribological reinforcements of cast iron that are arranged in the form of continuous pads, the plates or like discrete tribological plugs in the form of spheres (nodule), or particles spherical shape, as reinforcement [9].

Tribological tests were carried out at CSM tribometer with ball-on-plate contact pair for different normal loads and sliding speeds in dry conditions. Tribological tests are based on variation of three different normal loads $(0.3, 0.6\ and\ 0.9)\ N$ and sliding speeds, $(3, 9\ and\ 15)\ mm \cdot s^{-1}$. Duration of each test was $500\ cycles$ (distance of $1\ m$) acquisition rate $100\ Hz$ [10].

2.1 Optical microscopy analysis

Experiments were carried out with the base material for cylinders (aluminum alloy) and with the material for reinforcements made of cast iron [11,12].

More detail analysis of prepared samples, both of aluminum alloy and cast iron inclusions were performed using Phenom ProX Energy Dispersive Spectroscopy (EDS). EDS analysis results are presented on the Fig. 2 and 3 for base aluminum alloy and on the Fig. 4 and 5 for cast iron inserts.

Figure 2 presents EDS analysis of aluminum alloy and it noticeable that are present three phases, white one iron particles trapped in aluminum alloy as a result of grinding process. Lighter grey zones represent eutectic silicone, which is constituent element of the aluminum alloy, while dark grey represent pure aluminum, Fig. 3.

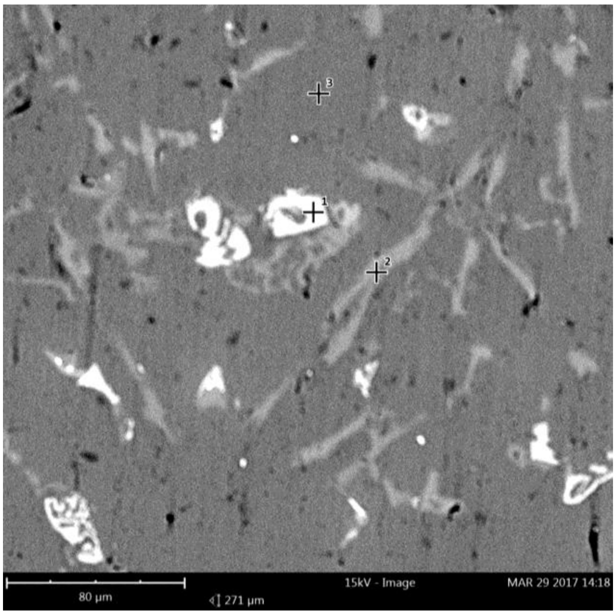

Figure 2. Prepared sample for EDS analysis of base aluminum alloy

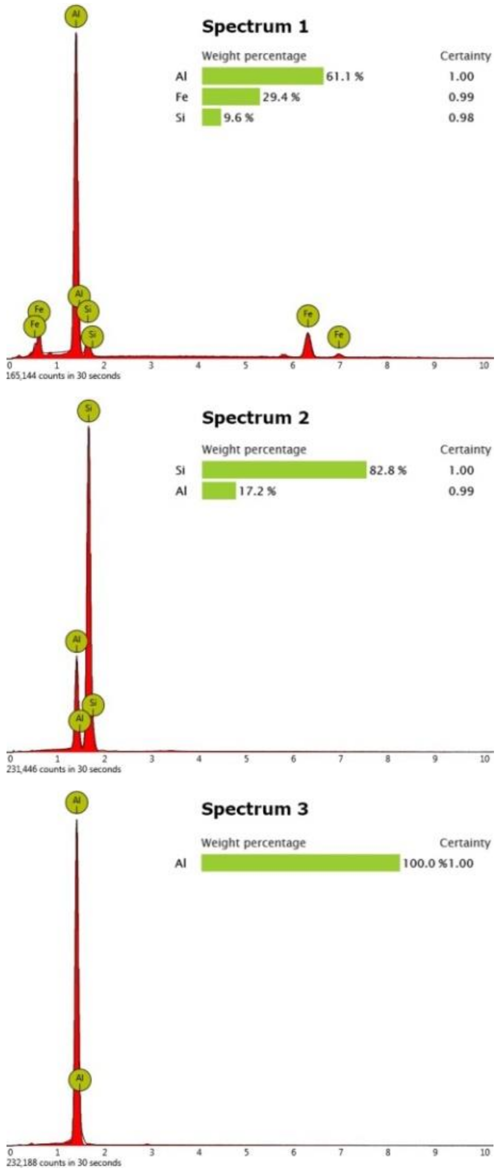

Figure 3. EDS analysis of base aluminum alloy

Fig. 4 and 5 represents EDS analysis of cast iron inserts, and it is noticeable that only two phases exist. Black phase represent graphite inclusions as is it is previously assumed based on optical microscopy. White phase represents pure iron, although graphite is present, which can be seen on spectrum 2.

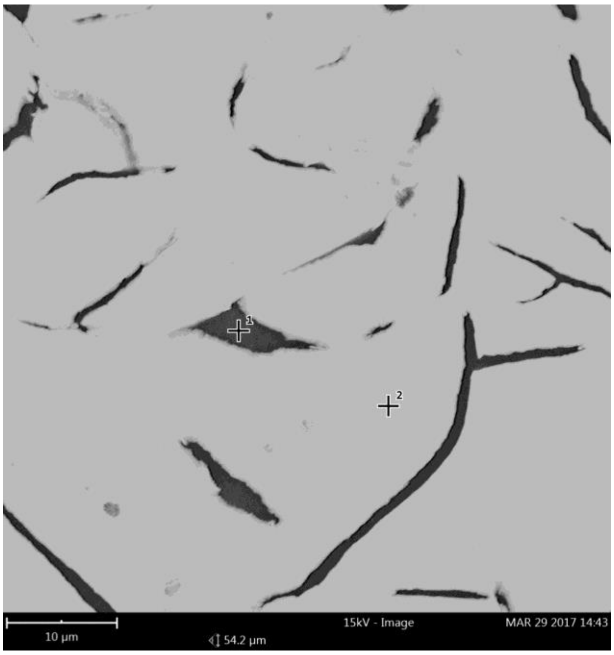

Figure 4. Prepared sample for EDS analysis of cast iron inserts

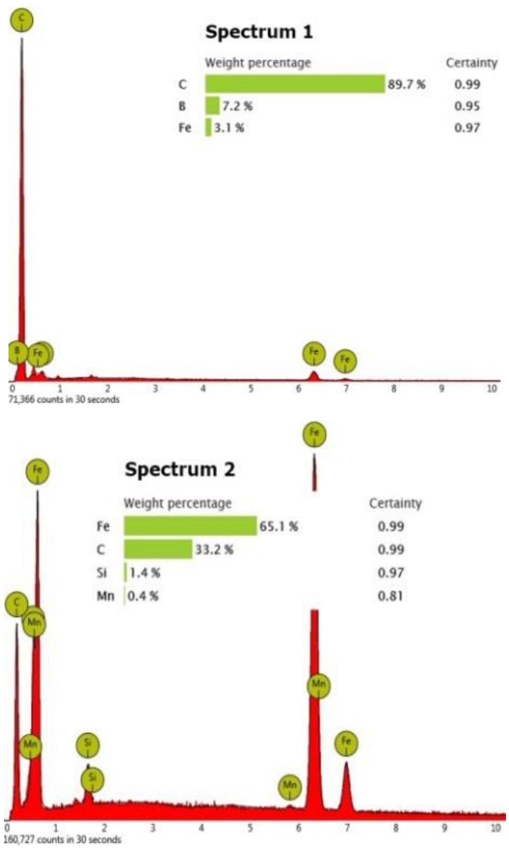

Figure 5. EDS analysis of cast iron inserts

Higher percentage of graphite in this phase is, also, result of grinding and polishing process that smears graphite inclusions all over the surface.

2.2 Coefficient of friction and penetration depth

Changes of COF and PD (ordinate) during sliding under low load conditions, depending on time, distance and numbers of cycles (abscissa) are shown in Fig. 6 for basic material (aluminum) and in Fig. 7 for tribological reinforcement. Due to the reciprocating motion of the needle of CSM tribometer between two end positions, the friction force was also changing direction during the test.

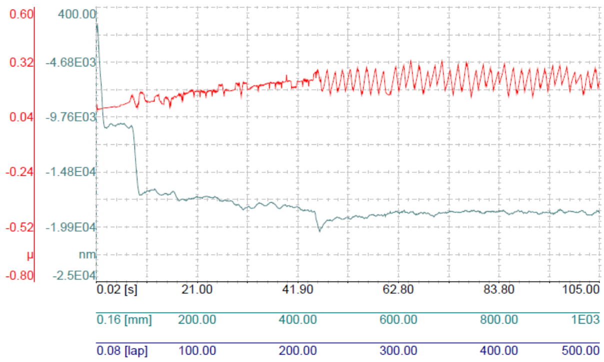

Figure 6. COF and PD for base material under ($F_N = 0.9\ N;\ V = 15\ mm \cdot s^{-1}$)

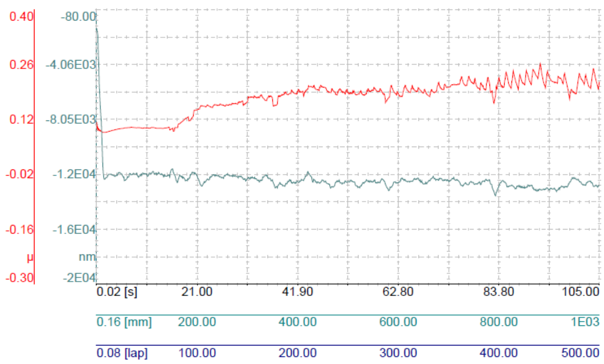

Figure 7. COF and PD for reinforcements under ($F_N = 0.9\ N;\ V = 15\ mm \cdot s^{-1}$)

Under higher load conditions and same sliding speed, a lower maximum value of COF of the reinforcement was recorded, Fig. 8. The obtained COF values is in the range (0.087-0.262) for the reinforcements, and (0.076-0.327) for the base material. The mean value of COF of the reinforcements is lower (0.176) than the value for base material (0.202).

It is noticeable that during wear testing of base material (aluminum alloy) COF sharply rises after a certain period of sliding as result of material transfer on counter body steel ball. After the material was transferred on the steel ball contact between transferred aluminum and aluminum as a base material was achieved, which result in increase of COF value. This process happens regardless the applied load, and it has cyclic nature, which indicates that transferred material on the counter body surface accumulates until it reaches critical size, that cannot bear tangential loads.

Penetration depth plot (Fig. 6 and Fig. 7) confirms this assumption. After reaching critical size, transferred material will fall off and process of transferring starts from the beginning.

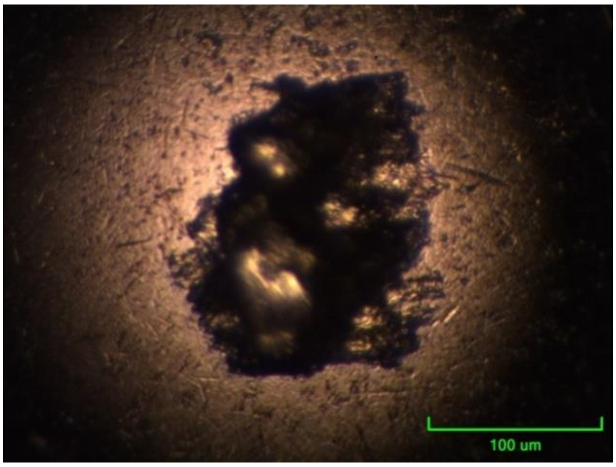

Figure 8. Optical microscopy of the counter body steel ball profile after sliding test with aluminum

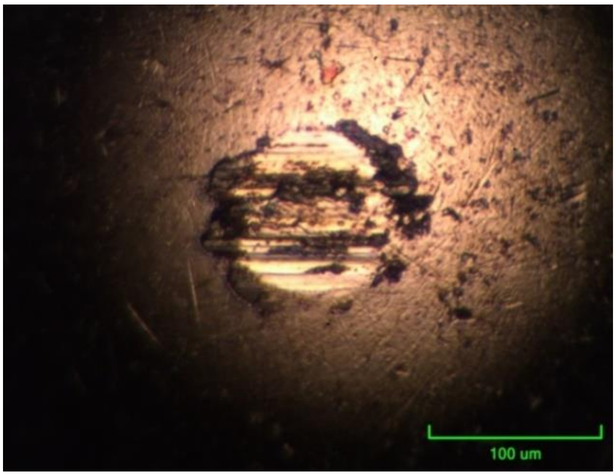

Figure 9. Optical microscopy of the counter body steel ball profile after sliding test with reinforcement (cast iron inserts)

In case of wear testing of cast iron inserts (reinforcements) no transfer material was observed, which is also confirmed by COF and penetration depth curves regarding applied load value. Both measured values, COF and penetration depth has almost constant averaged value during wear testing.

In addition to this conclusion, Fig. 8 clearly indicates accumulated transferred material on the counter body steel ball surface after sliding tests of base material (aluminum alloy) and no transferred material on counter bod surface after sliding test of reinforcement (cast iron), Fig. 9.

2.3 Wear analysis

Wear mechanisms based on examinations of worn surfaces by optical microscopy, were analyzed in comparison with trends of PD curves. Figure 10 and 11 present surface micrographs of base material and reinforcements after test under dry sliding, obtained for the same conditions of applied load and speed. It is noticeable that wear of aluminum is higher than cast iron sample due to transfer material and increase of COF which occurs for aluminum.

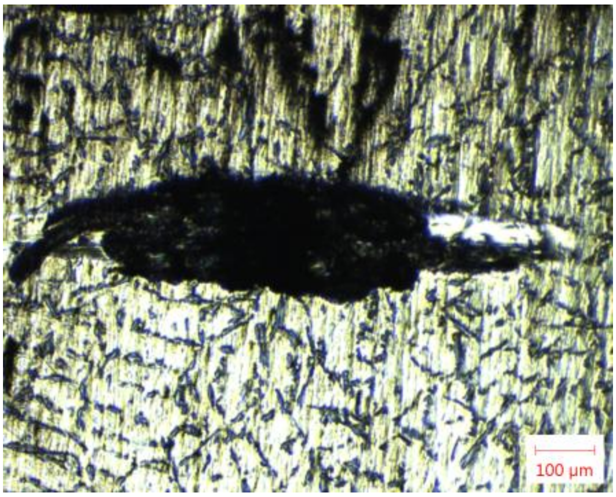

Figure 10. Surface micrographs of base material after dry sliding test under ($F_N = 0.9\ N;\ and\ V = 15\ mm \cdot s^{-1}$)

Prior wear tests, mechanical characterization of the prepared samples have been performed. Hardness tests were performed using CSM NHT2 nanoindenter, using Berkowich three sided diamond tip. Nine measurements for each tested material were done and averaged hardness values for base material and for reinforcement are 90 and 318 Vickers, respectively. Divergence in hardness values of tested materials indicates in better wear resistance of reinforcement in comparison to the base material.

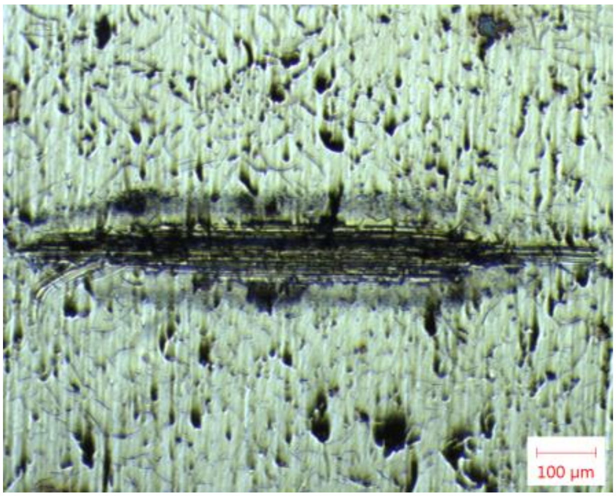

Figure 11. Surface micrographs of reinforcement after dry sliding test under ($F_N = 0.9\ N;\ and\ V = 15\ mm \cdot s^{-1}$)

Deep grooves in analyzed surfaces, indicates that the abrasive wear is the most dominant mechanism of wear for both tested materials, although transfer material on the counter body should not be neglected, especially for aluminum alloy.

Similar conclusions can also be made when testing materials at lower load and at the same sliding speed ($\mathrm{F_N} = 0{,}3\ \mathrm{N};\ \mathrm{V} = 15\ \mathrm{mm} \cdot \mathrm{s}^{-1}$) [11].

3. TEST RIG FOR MEASUREMENT OF LOSSES RELATED TO FRICTION IN AIR COMPRESSOR

Investigated reciprocating compressor, as an auxiliary device on the vehicle, drives the IC engine or an electric motor during its laboratory testing. When determining power (kW) of friction losses (P_m) using the indicator method, the indicated mean effective pressure (W_i) is determined with the help of pressure sensor which mounted in cylinder head, Fig. 12. The pressure inside the cylinder is captured by piezo-electric pressure transducer and the data is stored using data acquisition system. Effective compressor power (at the flywheel), (P_e) is analogous to it, the driving power, contrary to the IC engines. Indicated power (P_i) is less than the effective power for friction losses, that demanded to overcome mechanical losses in the compressor (friction in the cylinder, bearings, etc.), Eq. 4.

Figure 12. Photography of the experimental reciprocating air compressor

Use of the indicator method requires very high reproduction accuracies of the operating conditions, and thus of the friction conditions. For the most precise control and reproducibility of the boundary conditions, therefore, the oil and coolant pumps are replaced with external cooling system. The compressor is cooled by a fan. The detailed test rig setup for small air compressors is shown in Fig. 13 [13]. The compressor is connected with air reservoir and the pressure is maintained by using the automatic servo valve.

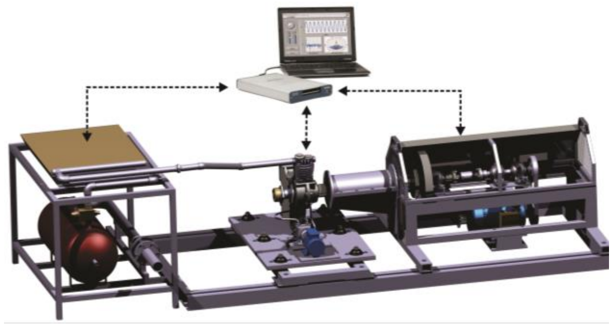

Figure 13. Test rig for small air compressors

Generally, over a period of time, performances of compressor reduce drastically. The causes are mainly such as wear and poor maintenance. Because of a periodic performance assessment is essential to minimize the cost of compressed air. To test performance of the compressor proposed the use of ACACA Protocol™ 2000 of the

Australian Commercial Air Compressor Association. Protocol defines standard test procedure for measuring of Free Air Delivery (FAD) of air compressor package.

FAD ($l \cdot min^{-1}$) is the volume flow rate of air (measured at ambient pressure and temperature and humidity) which has been compressed and delivered to the terminal discharge point of the air compressor package. It is a measure of the volume of air available for use at the exit point of the air compressor package.

The air flow is measured by pump up test method. The pump up test consists of operating the compressor at a constant speed and observing the time required to increase the pressure in the air receiver (cylinder of measured volume) from $6-8\ bar$ ie when the compressor is operating under load. The approximate air output of the compressor or FAD can then be calculated with application of the Eq. 4:

$$FAD = \frac{V_R \cdot (p_1 - p_2)}{p_o \cdot t} = \frac{2 \cdot V_R}{t} \quad (4)$$

where is:

- p_1, p_2 -Air cylinder pressure at start and at and of test, respectively;
- t -Pump up time taken to increase the pressure in the air cylinder from $p_1\ to\ p_2$, min; and
- p_o -Atmospheric pressure $p_0 = 100\ kPa\ (1\ bar)$.

Testing must need to be completed within twenty minutes after the compressor has reached normal operating temperature. After the results of 3 tests have been recorded, take the average and calculate FAD of compressor package in accordance with Protocol.

However the pump up test is a useful comparative measure and has been selected as being suitable to rate commercial air compressors for pump displacements, up to $600\ l \cdot min^{-1}$. Large compressors must be rated in accordance with standard ISO 1217.

Pump displacement ($\dot{V}_h, l \cdot min^{-1}$) is the theoretical volume of air that can be pumped by a reciprocating air compressor, if it was 100% efficient, Eq. 5:

$$\dot{V}_h = \frac{\pi d^2}{4} sN\ \ n_e 10^{-6} \quad (5)$$

where is:

- d, s -Cylinder diameter and stroke, mm;
- N -Number of cylinders;
- -1 for single acting and 2 for double acting cylinders; and
- n_e -Compressor speed, rpm.

4. CONCLUSIONS

The European Commission is working on the measures to reduction of greenhouse gases emissions from all sources. Because of the fact that all vehicles must give to reduction of fuel consumption and emission, the EU formed regulation for certification of all new registered HD vehicles. We researched reduction of power demand in air compressor as auxiliary device on the engine, by tribological optimization of their piston and cylinder.

The use of aluminum alloys for making parts of propulsion and mobile systems is important from the aspect of weight reduction, which directly affects the reduction of fuel consumption. On the other hand, the problems in application are lower strength and poor tribological characteristics of aluminum as well as aluminum constructions.

The problems of lower strength as well as the poor tribological characteristics of the cylinder for application in reciprocating air compressor for brake system of bus have solved by application aluminum matrix composite material. One of the constituents is aluminum alloy (EN AlSi10Mg) as the base material or matrix. Second constituent is being inserted into base material and serves as reinforcement which is made of cast iron in the form of particles of a spherical shape.

Presented results obtained during tests of materials from which consisting cylinder, shows that by transferring the contact between the piston rings and cylinder made of aluminum on the reinforcements, it is possible to reduce the friction and wear.

To test performance of the experimental compressor on test rig proposed the use of ACACA Protocol™ 2000. Protocol defines standard test procedure for measuring of free air delivery and pump displacement.

ACKNOWLEDGEMENT

The paper is a result of the research within the project TR 35041 financed by the Ministry of Science and Techno-logical Development of the Republic of Serbia.

REFERENCES

[1] T. Skrucany, S. Milojević, Š. Semanová, T. Čechovič, T. Figlus, F. Synák: The Energy Efficiency of Electric Energy as a Traction Used in Transport, Transport technic and technology, Vol. XIV, No. 2, pp. 9-14, 2018.

[2] S. Milojević, R. Pešić: CNG buses for clean and economical city transport, Int. J. Mobility and Vehicle Mechanics (MVM), Vol. 37, No. 4, pp. 57-71, 2011.

[3] S. Milojević, T. Skrucany, H. Milošević, D. Stanojević, M. Pantić, B. Stojanović: Alternative Drive Systems and Environmentally Friendly Public Passengers Transport, Applied Engineering Letters, Vol. 3, No. 3, pp. 105-113, 2018.

[4] European Commission. Climate Action, from *https://ec.europa.eu/clima/policies/transport/vehicles/heavy_en*, accessed on 13.04.2019.

[5] S. Milojević: Reconstruction of existing city buses on diesel fuel for drive on Hydrogen, Applied Engineering Letters, Vol. 1, No. 1, pp. 16-23, 2016.

[6] Pesic, S. Milojevic: Efficiency and Ecological Characteristics of a VCR Diesel Engine, Int. J. Automotive Technology, Vol. 14, No. 5, pp. 675-681, 2013.

[7] S. Milojević: Sustainable application of natural gas as engine fuel in city buses - Benefit and restrictions, Journal of Applied Engineering Science, Vol. 15, No. 1, pp. 81-88, 2017.

[8] D. Ninković, D. Taranović, S. Milojević, R. Pešić: *Modelling* Valve Dynamics and Flow in Reciprocating Compressors, Mobility & Vehicle Mechanics (MVM), Vol. 39, No. 3, pp. 47-63, 2013.

[9] S. Milojević, R. Pešić, D. Taranović: Tribological Principles of Constructing the Reciprocating Machines, Tribology in Industry, Vol. 37, No. 1, pp. 13-19, 2015.

[10] S. Milojevic, R. Pesic, D. Taranovic: Tribological optimization of reciprocating machines according to improving performance, Journal Balkan Tribological Association, Vol. 21, No. 3, pp. 690-699, 2015.

[11] S. Milojević, D. Džunić, D. Taranović, R. Pešić, S. Mitrović: Tribological Reinforcements for Cylinder Liner of Aluminum - Example Compressors for Brake Systems of Trucks and Buses, in: *15th International Conference on Tribology SERBIATRIB '17*, Kragujevac, 17 – 19 05. 2017, pp. 251-257, 2017.

[12] S. Milojević, D. Džunić, D. Taranović, R. Pešić, S. Mitrović: Experimental Determination of Tribological Characteristics of Composite Materials in use for Parts in Aluminum Air Compressor (Piston and Cylinder), in: *VII International Congress, Motor Vehicles & Motors 2018, Ecology - Vehicle and Road Safety - Efficiency*, Serbia, Kragujevac, 04-05 10.2018, pp. 383-392, 2018.

[13] D. Taranović, D. Ninković, A. Davinić, R. Pešić, J. Glišović, S. Milojević: Valve dynamics in reciprocating compressors for motor vehicles, Tehnički Vjesnik, Vol. 24, No. 2, pp. 314-319, 2017.

Serbian Tribology Society

SERBIATRIB '19

16th International Conference on Tribology

Faculty of Engineering
University of Kragujevac

Kragujevac, Serbia, 15 – 17 May 2019

MODELLING OF THERMOELASTIC PROCESSES AND TEMPERATURE DISTRIBUTION IN METAL TRIBOPAIRS DURING DRY FRICTION

Pavel KOVALENKO[1,]*, Svetlana PEREPELKINA[1], Vlada SEMENOVA[2]
[1]ITMO University, Saint Petersburg, Russian Federation
[2]Peter the Great St. Petersburg Polytechnic University, Russian Federation
*Corresponding author: kovalenko_p.p@mail.ru

Abstract: *In this paper, a model for calculation of the temperature distribution in the metal tribopair bar - plane in the conditions of dry friction is developed. A model for solving of the problem of thermoelasticity for a metal bar under uniaxial tension-compression is also proposed. A simulation of the interaction between the bar and the plane was carried out taking into consideration various conditions, such as ambient temperature and linear dimensions of the contacting pairs. The simulation results showed that the distribution of the thermal field nonlinearly depends on the linear dimensions of the body, but the frictional heating in the first counter-body can be compensated by small changes of the linear dimensions.*
When calculating the stress-strain state of the bar, a non-linear dependence of the stress in the bar was obtained, which is due to the presence of contact pressure.
The modelling results were proved experimentally with the use of the friction machine MTU-1.
The results of the work can help us predict frictional heating for metal tribopairs and decrease its negative consequences.

Keywords: *frictional heating, thermoelastic processes, distribution of the thermal field, stress-strain state of tribopair elements, uniaxial tension-compression.*

1. INTRODUCTION

In the process of friction, a sufficiently large part of the energy transforms to heat losses [1]. Energy dissipation processes, as a rule, lead to negative consequences, such as catastrophic wear, ignition of lubricant, etc. The theoretical description of the processes occurring in this case is extremely difficult, which is due to the nonlinearity of the processes, as well as taking into account a large number of factors affecting both the friction process and the energy transformation [1].

The thermal problem of friction was analyzed in [1-3]. The friction heat between sliding bodies can cause thermoelastic deformation that changes the contact pressure distribution. The sliding velocity that is higher than the critical velocity can cause the appearance of local high temperature areas called hot spots. These hot spots with high local stresses may cause material degradation, eventual failure and undesirable frictional vibrations [4-6]. Thermoelastic processes in composite materials were investigated in [7]. The results of these researches made it possible to achieve significant success in engineering calculations of non-stationary friction modes in brakes and friction devices with complex thermal conditions [8-12].

The development of theories based on simplified fundamental models that take into account the influence of wear, elasticity, phase transitions, etc. is of great importance.

In this paper, we propose a model for distribution of thermal fields in the volume of a solid body in dry friction conditions and a model for thermoelastic processes in a metal bar under uniaxial tension-compression during dry friction.

2. DISTRIBUTION OF THERMAL FIELDS

The basis of the simulation is the classical thermal conductivity equation:

$$h \quad b \quad c\dot{T}, h \quad k \quad T, \quad h \quad k\Delta T \ , \quad (1)$$

where h is the heat flux vector, b is the volumetric heat release, *c* is the volumetric heat capacity, k is the thermal conductivity coefficient. It must be taken into account that heat will be concentrated on the contact surface.

The initial conditions for equation (1) are the following:

$$T|_{O_1} \quad T_e, k \quad {}_n T|_{O_2} \qquad T_e \quad T ; \qquad (2)$$
$$T|_{t \ 0} \quad T_0 .$$

On the contactless surface of the body O_1, the ambient temperature is T_e. The heat flux β is specified on the contact part of the surface O_2. However, it can be expressed in terms of temperature difference and heat transfer coefficient .

To simplify the model, we assume that the volumetric heat capacity and thermal conductivity coefficient are constant.

The differential equation in partial derivatives with given boundary and initial conditions can be solved numerically by a variational method with an approximation by a system of coordinate functions. The method is based on a variation equation:

$$\int_V (k \quad T \quad b \quad cT)\delta T dV \quad \int_O \beta \quad k \ {}_n T \ \delta T dO \quad 0, \quad (3)$$

where δT is an arbitrary temperature increment.

Approximation of the solution with given coordinate functions:

$$T \quad \sum_{i \ 1}^{N} \theta_i(t) \ {}_i(r) \quad \theta^T \qquad {}^T\theta, \qquad (4)$$
$$\delta T \quad \delta\theta$$

We use matrix notation. Functions ${}_i$ are set by us. Variable functions θ_i should be defined.

Substituting (4) into (3) and taking into account arbitrariness of, we obtain the following:

$$C\dot{\Theta} \quad K\Theta \quad B(t), \qquad (5)$$

where

$$C \quad \int_V c \quad {}^T dV;$$
$$K \quad \int_V k \quad {}^T dV \quad \int_O k \quad {}_n \quad {}^T dO; \qquad (6)$$
$$B \quad \int_V b \ dV \quad \int_O dO.$$

In equation 6, C is the heat capacity matrix, K is the thermal conductivity matrix, B is the column of thermal loads.

When calculating the intensity of heat generation during friction contact, we use a simplified contact scheme (Fig. 1).

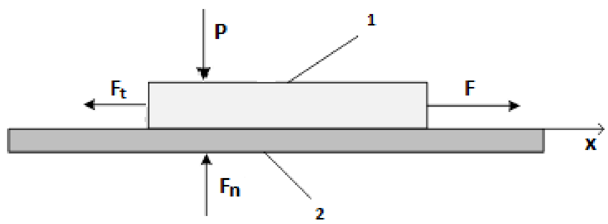

Figure 1. Bar on a rough plane

The bar moves on a plane under the action of force F, overcoming the force of dry friction F_t. The pressing force is equal to P, the normal reaction is F_n.

According to Coulomb's law:

$$F \quad F_n, \qquad (7)$$

where μ is friction coefficient. Since mechanical energy remains constant, all mechanical power is equal to heat generation. Thermal power per unit area could be defined as following:

$$b \quad \tau v, \qquad (8)$$

where τ is the tangential stress during friction, v is the velocity of the body.

In the contact of two bodies of the same material, the heat release is distributed approximately equally between both bodies.

The temperature distribution in the volume of the bar will be obtained by solving equation (5).

We take steel C22 as counter-bodies for initial data.

The number of functions N is 7. For steel C22: $k = 45.4$, W / (m·K), c = 460 J / m^3. Heat transfer coefficient between steel and air 30 W / (m^2 · K). Bar dimensions are the following: $L = 0{,}1$ m, $a_1 = 0{,}1$ m, $a_2 = 0{,}03$ m. The pressing force P is 150 N, friction coefficient is 0,55, the speed $v = 1$ m / s.

In Fig. 2, temperature versus time at the center T (L, t) and at the edges T (0, t) of the bar is shown.

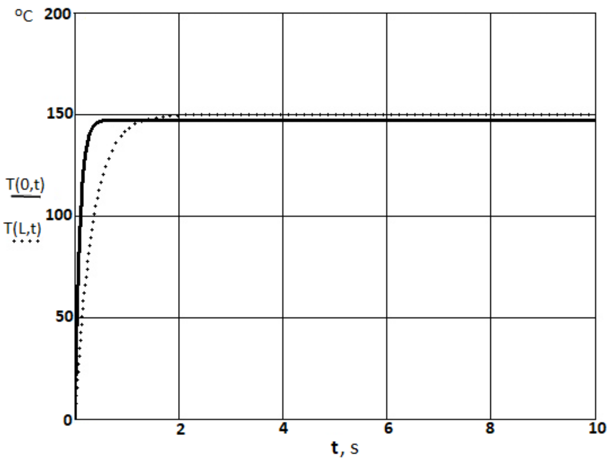

Figure 2. Temperature in the center of the bar (dotted line) and at the edges of the bar (solid line) versus time for steel C22

The graph shows that the temperature change is maximum at the beginning of the simulation, and the temperature graphs have approximately the same shape both in the center and at the edges of the bar.

3. EXPERIMENTAL RESEARCH

A set of experiments with samples made of steel C20E2C was carried out for the verification of the simulation.

The experiment was carried out with the use of a friction machine MTU-1 [13, 14]. The scheme of the experiment was plate-on-plate, the rotational speed was 150 rpm, the loading force was 150 N. Friction coefficient obtained experimentally is 0.55.

The obtained results were used for the simulation. The simulation results are presented in Fig. 3.

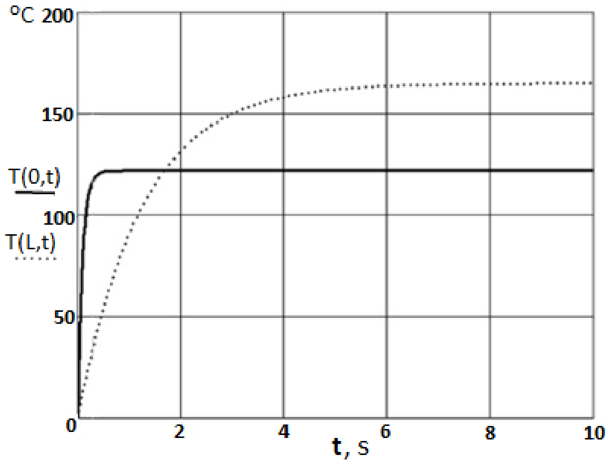

Figure 3. Temperature in the center of the bar (dotted line) and at the edges of the bar (solid line) versus time for steel C20E2C

In the center of the bar there is a real contact area where the interaction occurs with minimal loss of energy. The graph in figure 3 shows that the temperature changes in that area smoothly, which is probably due to energy dissipation to mechanical surface destruction, as well as to the occurrence and destruction of molecular bridges in tribopairs of similar materials.

The graph of temperature at the edges of the sample has a sharp jump at the beginning of the experiment, which is explained by the initial stage of running-in. There is no temperature flash in the contact zone. The absence of extremum is due to the fact that the model offers not a point distribution, but an integral distribution of the temperature field.

4. THERMOELASTIC PROCESSES

When moving the bar along the base (Fig. 1), we assume that the stress state of the bar is uniaxial, which means that the bar works for compression and tension. The equation for a straight rod with a combined thermomechanical action under tension-compression is well known [15, 16]:

$$
\begin{aligned}
&N \quad f \quad \rho\ \ddot{u}; \\
&N \quad E_1\, u \quad \alpha T\ ;
\end{aligned}
\tag{9}
$$

$$N(\ \ L) \quad 0; N(L) \quad f, \tag{10}$$

where N is the force directed along the x axis, is the transverse load, u (*x, t*) is deflection, is the density of the bar, is the stiffness of the bar for tension, is the coefficient of linear thermal expansion, is the temperature field distribution.

Since the load changes slowly and smoothly, the inertia forces can be neglected. In this regard, we obtain a quasistatic solution of the equation (9):

$$
\begin{aligned}
&N(x) \quad \int_{L}^{x} f dx; \\
&u \quad \int_{x}^{L} \frac{N}{E_1} \quad T\ dx.
\end{aligned}
\tag{11}
$$

To obtain the results of simulation, we substitute to the equation (11) the following data: tension stiffness $E_1 = 6 \cdot 10^8$ N, linear thermal expansion coefficient $\alpha = 1.1 \cdot 10^{-5}$ K^{-1}. The distribution of the temperature field T (*x*) = const = 90 ^{0}C (Fig. 2, 3).

The simulation results are presented in Fig. 4.

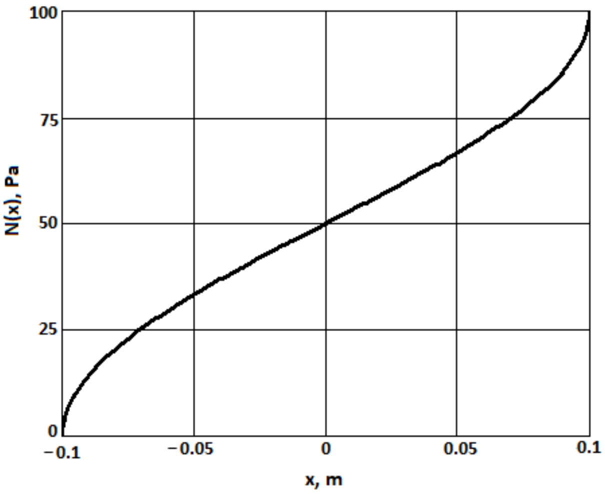

Figure 4. Stress distribution in the bar

It can be noticed from the graph in Fig. 4 that the deviation from the linear distribution is observed at the ends of the bar due to the presence of excessive contact pressure and, probably, elastic-plastic deformation at the edges of the bar.

5. CONCLUSION

When comparing fig. 2 and fig. 3, it can be concluded that the model can be used for simulation of the temperature distribution in the contact area during dry friction of metallic materials without taking into consideration the flash temperature rise. The difference between the results in figure 2 and figure 3 could be explained by the difference in the conditions of the experiments and initial data. The shape of the graphs proves that the model takes into consideration energy dissipation and temperature distribution in the contact area. The model uses characteristics of real metallic materials, such as heat capacity and thermal conductivity, and allow us to predict temperature distribution not only on the surface of the contacting bodies, but also in their volume.

The model for stress-strain state of the bar can be used for estimation of the influence of the frictional heating on the deformation of the elements of tribopairs during dry friction. The presence of elastic-plastic deformation at the edges of the bar can partially compensate the linear thermal expansion that occurs in the process of frictional heating during dry friction.

REFERENCES

[1] F.E. Kennedy: Frictional Heating and Contact Temperatures, in: B. Bhushan (Ed.): *Modern Tribology Handbook, Volume One: Principles of Tribology*, CRC Press LLC, 1997.

[2] S. Boutechebak, A. Azeb Ahmed: Analysis of a Dynamic Frictional Contact Problem for Thermo-Elastic-Viscoplastic Materials with Damage, Gen. Math. Notes, Vol. 19, No. 1, pp.60-77, 2013.

[3] P. Zagrodzki, K. B. Lam, E. Al Bahkali, J. R. Barber: Nonlinear Transient Behavior of a Sliding System with Frictionally Excited Thermoelastic Instability, Journal of Tribology, Vol. 123, pp. 699-708, 2001.

[4] B. Mostefa, B. Ali: Thermoelastic Analysis of Disk Brakes Rotor, American Journal of

Mechanical Engineering, Vol. 2, No. 4, pp. 103-113, 2014.

[5] A.E. Tyurin, G.M. Ismailov, E.V. Beloenko, A.V. Baranov: Monitoring vibrations and microdisplacement for "pin on disc" tribology studies, Journal of Physics: Conference Series, Vol. 803, No. 1, paper 012167, 2017.

[6] G.M. Ismailov, A.E. Tyurin: Experimental study of frictional vibrations under dry friction conditions, Tribology in Industry, Vol. 40, No. 3, pp. 392-400, 2018.

[7] Z.F. Baczynski: Dynamic thermoelastic processes in microperiodic composites. Journal of Thermal Stresses, Vol. 26, pp. 55-66, 2003.

[8] S.S. Kang, S.K. Cho: Thermal deformation and stress analysis of disk brakes by finite element method, Journal of Mechanical Science and Technology, Vol. 26, No. 7, pp. 2133-2137, 2012.

[9] V. Dygalo, I. Zhukov: The thermal loading estimation of the friction pairs of a vehicle automated brake system, IOP Conf. Series: Materials Science and Engineering, Vol. 386, paper 012012, 2018.

[10] Y. Rozhdestvensky, E. Zadorozhnaya: A simulation of the thermal state of heavily loaded tribo-units and its evaluation, Bulletin of the South Ural State University, Series: Mathematical Modelling, Programming and Computer Software, Vol. 7 No. 4, pp. 51-64, 2014.

[11] N. Benhassine, A. Haiahem, B. Bou-Said: A comparative study of the transient thermomechanical behavior of friction of the ceramic brake discs: Temperature field effect, Journal of Mechanical Science and Technology, Vol. 33, No. 1, pp. 233–240, 2019.

[12] O.I. Abdullah, J. Schlattmann: Finite Element Analysis of Temperature Field in Automotive Dry Friction Clutch, Tribology in Industry, Vol. 34, No. 4, pp. 206-216, 2012.

[13] S. Perepelkina, P. Kovalenko, R. Pechenko: Investigation of Tribological Properties of Metallic Materials with the Use of the Universal Friction Machine “MTU-1", Procedia Engineering, Vol. 176, pp. 301-309, 2017.

[14] P. Kovalenko, S. Perepelkina, T. Korakhanov: Investigation of tribological properties of friction pairs duralumin – fluoropolymer used for design and manufacturing of biomechatronic devices, Tribology in Industry, Vol. 39 No. 2, pp. 192-197, 2017.

[15] V.V. Eliseev: *Mechanics of elastic bodies,* SPbPU, Saint Petersburg, 2003 (in Russian).

[16] V.V. Eliseev: *Mechanics of a solid deformable body*, SPbPU, Saint Petersburg, 2006 (in Russian).

Serbian Tribology Society

SERBIATRIB '19

16th International Conference on Tribology

Faculty of Engineering University of Kragujevac

Kragujevac, Serbia, 15 – 17 May 2019

REPAIR OF A DAMAGED TURBOCHARGER

Svetislav Lj. MARKOVIĆ[1,*], Aleksandar MARINKOVIĆ[2], Bratislav STOJILJKOVIĆ[3], Goran DEVIĆ[4], Milan KLIPA[4], Vladimir PETROVIĆ[4]

[1] Technical College, Čačak, Serbia

[2] Faculty of Mechanical Engineering, Belgrade, Serbia

[3] Nikola Tesla Museum, Belgrade, Serbia

[4] JP EPS, RB Kolubara, Lazarevac, Serbia

*Corresponding author: svetom@mts.rs

Abstract: *The turbocharger is among the highest quality assemblies for modern internal combustion engines. Its contribution to engine operation is immeasurable – it increases the power output of the engine while indirectly reducing fuel consumption. Like all devices, turbochargers require quality maintenance as they are susceptible to failure. Faulty turbochargers are either repaired or replaced with new ones. Repair ensures substantial financial savings. The paper presents the consequences of damage to the turbocharger and the process of its repair.*

Keywords: *turbocharger, damage, repair.*

1. INTRODUCTION

Most failures of the turbocharger are due to problems occurring outside the device. If the turbocharger is faulty, apart from its repair or replacement, it is imperative to determine and eliminate the cause of failure to prevent its recurrence.

Figure 1 shows damage to the turbocharger caused by the entry of a foreign object into its housing. The foreign object has damaged the compressor wheel at the front i.e. inlet, leading to a partial fracture of its blades. Blade damage causes rotor imbalance as well as rapid wear to the bearings and seal rings. This results in increased lubricating oil consumption, power loss and black or white smoke coming from the exhaust pipe. Also, these problems are often accompanied by a squeaking sound, which clearly indicates turbocharger malfunction. Foreign objects may enter the inlet manifold: due to a damaged air filter, due to holes or cracks in the air hoses or worn-out hose clamps, or if the entire air supply system has not been properly cleaned during the previous servicing of the turbocharger [2].

Figure 1. Compressor wheel damaged by a foreign object

Figure 2. Compressor wheel damaged by a large foreign object

Before reinstalling the turbocharger, it is necessary to determine the routes of foreign object ingestion into the turbocharger in order to prevent recurring impact damage. To this end, the inlet manifold hoses should be inspected and washed, the hose clamps and the air filter should be checked for foreign objects and replaced as required. Otherwise, the turbocharger will suffer the same failure.

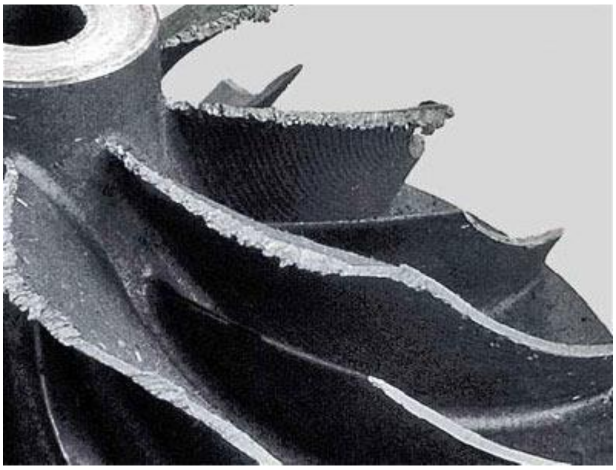

Figure 3. Compressor wheel damaged by dirt

Figure 4. Rotor damaged by foreign objects with soot build-up

Figure 5. Rotor damaged by foreign objects

2. DAMAGE TO THE TURBOCHARGER

After disassembly of the turbocharger, damage typical of a partial or complete blockage in the exhaust pipe has been identified. This type of blockage in the pipe causes a high exhaust gas pressure in the turbine housing. As exhaust gases cannot exit the engine freely, they push the turbocharger rotor forward to the compressor side. Therefore, on the front side of the turbine wheel, there are clearly visible marks of its unallowable wear against the flame guard, leading to turbocharger oil leaks. This failure is caused by a faulty (blocked) engine brake (a faulty brake cylinder or a clogged butterfly valve shaft) or by a foreign object blocking the exhaust pipe.

Before reinstalling the turbocharger, the cause of the failure (in this case, the faulty engine brake and/or blocked exhaust pipes) must be eliminated.

Figure 6. Damage to the turbocharger rotor due to blockage in the exhaust pipe

Wet oil found at the turbine inlet is a characteristic sign of a forced oil leak. The compressor housing is soiled with oil at the inlet; therefore, as the turbocharger sucks in air, the oil can only come from the breather. The inspection of the intake hose clearly shows that the leaking oil is working its way from the breather towards the turbocharger. Due to an engine problem, pressure builds up in the engine crankcase. Increased pressure raises the oil level in the crankcase, resulting in fresh oil at the breather. As the turbocharger is connected to the engine crankcase through the oil return pipe, the seal rings become overloaded with pressurised oil, which forces its way through them, eventually causing physical damage to them, resulting in the need for repair. In such failures, oil consumption is always higher due to an engine problem than due to a problem in the turbocharger. Therefore, this problem (increased oil consumption) cannot be solved only by turbocharger repair.

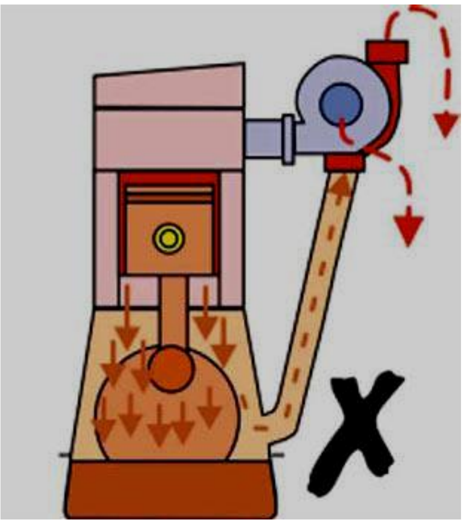

Figure 7. Effect of oil pressure in the engine crankcase on the turbocharger

The increased pressure in the crankcase is due to a variety of reasons:

1. The breather is clogged. The intake hose on the turbocharger is dry.
2. The oil return line which allows oil to drain from the turbocharger to the crankcase is bent, clogged, with a restricted flow. Normally, it must have an appropriate oil drain angle (±15 degrees from the vertical).
3. The air filter is dirty.
4. The internal pressure in the engine is too high, due to the wear of engine parts and assemblies (worn-out piston rings, cylinder liners and other parts of the engine).

The excessive oil pressure problem in the crankcase must be fixed before reinstalling a new or repaired turbocharger, since otherwise the problem will not be permanently solved.

After the core assembly of the turbocharger has been dismantled, high wear rates of the sliding surfaces of the bearings and the shaft have been found. Wear marks i.e. furrows in characteristic places, due to dirt in the lubricating oil, are clearly visible. The oil is contaminated with combustion by-products and shavings of engine parts. Depending on the degree of oil contamination, the gap between the bearings and the shaft increases over time, causing wear to the seal rings, imbalance of the turbocharger rotating assembly and even striking of the turbine and compressor wheel blades against the housing. The turbocharger consumes oil, the engine has no power, and black or white smoke appears at the exhaust outlet. When installing the hose with oil supply and return fittings, sealants must not be used because only original gaskets are permitted.

Figure 8. Radial bearings damaged by dirty oil

When performing major repairs of automobile engines, such as overhaul, leftover shavings may get into the oil and cause wear. Since the turbine rotor spins up to 50 times faster than other shafts on the engine, turbo wear is much higher and faster. After the overhaul, the engine crankcase should be thoroughly washed. Before reinstalling the turbocharger, the cause of the failure must be eliminated. It is necessary to replace both the oil and the oil filter and clean the engine crankcase to prevent recurring problems.

Figure 9. Damage to the turbocharger shaft caused by dirty oil

Figure 10. Damage to the turbocharger shaft due to lack of lubrication

In older types of turbochargers which do not have VSG valves, failure is caused by disruption in the fuel combustion system, due to which exhaust gas pressure and temperature exceed predetermined values. At high rotational speeds, the rotor material undergoes internal stress, which leads to blade fracture, and the turbocharger bearings cannot withstand such loads, resulting in frequent rotor impeller cracks. Turbochargers equipped with VSG valves are designed to operate at higher rotational speeds compared to the turbochargers without VSG valves. When the exhaust gas pressure in the turbocharger reaches the critical, maximum allowable value, the role of the VSG valve is to direct the exhaust gas flow out of the rotating zone of the rotor, thus reducing its rotational speed.

In the new generation of turbochargers having variable geometries, in addition to the abovementioned role, the electromagnetic valve regulates both the amount and pressure of exhaust gases during the operation. When the VSG valve is damaged or unprofessionally adjusted, the turbocharger rotor rotates at a rotational speed higher than the maximum limit. Therefore, the engine consumes more oil and loses power, and the turbocharger produces a characteristic squeaking sound. Often, the turbocharger rotor breaks due to internal load. In variable geometry turbochargers, there is damage to the rotor, the variable geometry and the central housing, and the only solution is to replace the turbocharger with a new one.

Figure 11. Typical fracture of the turbocharger impeller

Figure 12. Effect of high temperature on the turbocharger rotor

Figure 13. Cracks in the turbine housing due to a high exhaust gas temperature

3. REPAIR OF THE TURBOCHARGER

In practice, as a rule, successful repair of a turbine is possible only if its housing is not mechanically damaged. Repair generally involves replacement of the shaft coupled with the propellers, bearings and all seal components. This is the primary and cheapest repair.

When repairing the turbine, all its components are disassembled. They are usually rather dirty, which does not necessarily mean that they are damaged. However, soot build-up can block the stator blades. This is the cheapest intervention as there is no need for replacement of the turbine components. [1]

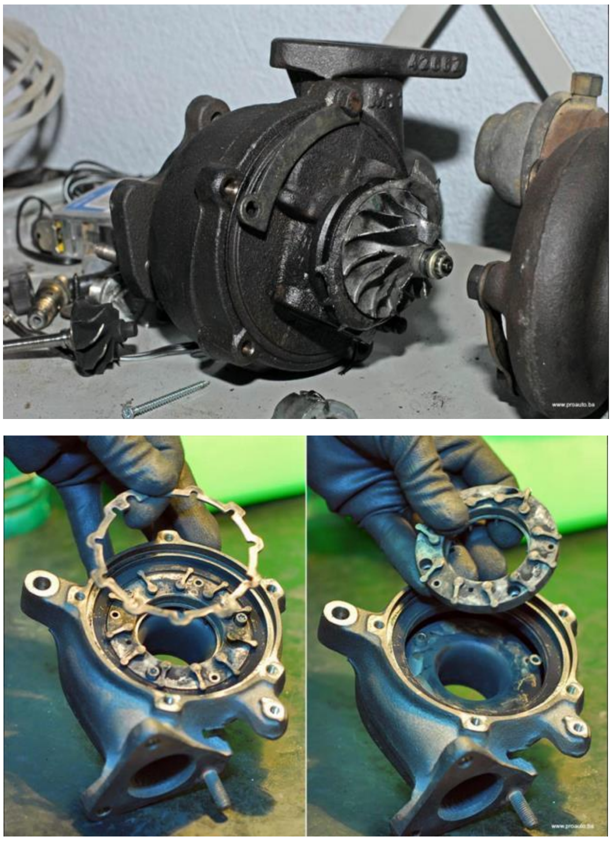

Figure 14. Turbine disassembly [1]

Before repair, all dismantled parts are thoroughly cleaned using a special liquid solvent, or petroleum, or a certain amount of a degreasing agent. After drying, they are subjected to sandblasting, which involves smoothing of large rough surfaces occurring due to mechanical operation, which may subsequently lead to undesirable effects. Since blasting is performed by quartz crystals of small grain size, all parts should be additionally washed in a solvent additive or in petroleum after the process. Also, they should be dried either with a soft cloth or simply under compressed air. It is only after these detailed cleaning and drying operations that certified service providers can determine the degree of repair needed.

Figure 15. Cleaning, degreasing and sandblasting [1]

Turbine failure is generally determined by visual inspection. The shaft with the blades on both sides is the most visible and, practically, the key part of the turbine. The blades on the side through which clean air passes are the most vulnerable. If any particle of dirt enters this area, at least one vane will become damaged, which will automatically lead to mass imbalance and unbalanced rotation. Such rotation will, by all means, cause damage to the nearest bearing in no time. If, for example, a stone or a piece of glass or some other hard object gets into this area, the entire section will be destroyed and the blades broken. This damage will probably result in a complete loss of symmetry in the shaft.

Similarly, the drive blades can suffer damage due to poor combustion and extremely high temperatures. The blades in such an operating environment erode over time, which reduces the operating life of the turbine.

Another reason for turbine damage is poor lubrication. The turbine shaft is lubricated with oil from the engine, and the oil also serves as a coolant. If for any reason lack of lubrication or oil starvation occurs, the bearings (bronze rings) will be the first to suffer damage. Also, due to increased temperatures and loss of balance during rotation, seal rings will become permanently damaged.

Figure 16. The most common types of damage [1]

Even in prolonged contact with lubricating oil, these rings will not be able to retain hot oil under pressure, and over time the oil will leave the lubrication area through them. Although damaged, the turbine can be reconditioned.

Any reconditioning operation after turbine disassembly involves the replacement of seal rings, bronze bearings and rubber seals. Well-equipped service providers use kits including the replacement components required during turbine disassembly. The turbine contains the so-called seal plate or housing cover, which is generally not replaced. In variable geometry turbines, the stator section should also be replaced in major overhauls. Undamaged components are reinstalled in the housing in reverse order.

Figure 17. Reconditioning of turbine parts [1]

When reinstalling the existing shaft and blades or installing new components, the assembly should be additionally balanced. It is only after this operation that the turbine can be assembled. Balancing is among the most sensitive processes during turbine reconditioning. It is performed only by trained service providers. Excess removal of the material during the balancing operation may cause permanent damage to the turbine.

Figure 18. Balancing of the shaft and blades [1]

4. CONCLUSION

Repair primarily serves to restore the operating performance of machine parts suffering surface damage (wear) and fracture. Rather than being disposed of as waste, worn-out and broken parts are repaired and reinstalled in mechanical structures instead of new spare parts. Repair has been widely applied for the following reasons: high competitiveness, struggle to make the maximum possible profit, and economic, energy-based and ecological crises. As repair of mechanical parts and structures requires expert knowledge in different fields (knowledge of materials, types of damage, mechanical engineering calculations, etc.), it cannot be performed by a single person, but by a well-balanced team of experts.

ACKNOWLEDGEMENT

This work has been performed within the project TR 35011. This project is supported by the Republic of Serbia, Ministry of Science and Technological Development, which financial help is gratefully acknowledged.

REFERENCES

[1] A. Huseinagić: *Savjeti – servisiranje turbopunjača*, Proauto, 2016.

[2] J. Csato: *Effects of prewhirl on the compressor of turbochargers*, Mobility and vehicle mechanics, Mašinski fakultet Univerziteta u Kragujevcu – Jugoslovensko društvo za motore i vozila, Kragujevac, Vol. 23, br. 2, 1997.

[3] S. Lj. Marković: *Regeneracija mašinskih delova i elemenata*, Visoka škola tehničkih strukovnih studija, Edicija „Akademija“,Čačak, 2017.

[4] *Postupak reparature turbokompresora*, Turboservis „Božec“, Čačak, 2017.

Serbian Tribology Society

SERBIATRIB '19

16th International Conference on Tribology

Faculty of Engineering University of Kragujevac

Kragujevac, Serbia, 15 – 17 May 2019

THE POSSIBILITY OF IMPROVING THE SAFETY OF TRAFFIC USING AN ADEQUATE SYSTEM FOR MAINTAINING THE VEHICLE'S CONTROL SYSTEM

Vojislav Krstić [1], Boris Antić[2]

[1,2] Faculty of transport and traffic engineering, University of Belgrade, Beograd, Serbia, vojislavkrstic33@gmail.com, mpeeric@gmail.com

Abstract: *Results of voluminous investigations of the control system reliability parameters, which were obtained by monitoring the behavior of the analyzed motor vehicle in the real exploitation conditions, from the aspect of failure occurrence of its motor engine, and with application of the corresponding scientific knowledge from the area of probability, mathematical statistics, systems theory and reliability theory, have served as a basis for finding the optimal periodicity of the control system maintenance, taking into account the criteria of maximal availability and minimal costs of its maintenance.*
Since the optimal periodicities of conducting the control system preventive maintenance, determined by criteria of maximal availability and minimal maintenance costs differ from each other, it was necessary to apply one of the multicriteria analysis methods.
The presented methodology of the multicriteria decision-making can be applied for obtaining the reliable value of optimal periodicity of conducting the preventive maintenance procedures also of other parts of the analyzed control system.

Keywords: *Safety of traffic using, Motor vehicle, Control system, Maintenance, Reliability, Availability, Costs*

1. INTRODUCTION

This work presents a possibility to find the optimal solution in the maintenance of the control system when the criteria functions are maximal availability and minimal maintenance costs. These two criteria lead to several solutions of the motor engine assembly maintenance; therefore, it was necessary to apply the multicriteria optimization.

By correct forming of the maintenance model it is possible to perform the optimization, namely to select the most favorable maintenance system. Such a problem can be solved if all the important requirements and restrictions are precisely determined. As the optimal periodicity of the preventive maintenance procedure of the analyzed control system, determined according to the criterion of the maximal availability differs from the optimal periodicity determined according to the criterion of the minimal costs, it is necessary to apply the multicriteria analysis methods and to determine the value of the required optimal periodicity, taking into account both mentioned optimization criteria. This actually is the basic goal of this work.

By the method of the compromise selection, the limits are determined of the optimal periodicity for the preventive maintenance procedure conducting, which correspond to extreme values of the adopted criterion functions. By applying the method of the multicriteria analysis, one determines the discrete value of this periodicity, whose exactness depends on selection of the discretization step of the analyzed time interval. Generally considering, the presented methodology of the multicriteria decision-making can be applied for obtaining the reliable value of the preventive maintenance procedure conducting periodicity of the technical systems. There one needs to know the availability of data, which are acquired by analysis of the control system during their operation and maintenance, based on which one can determine the indicators of their reliability, as well as the characteristics of their maintenance.

2. DETERMINATION OF PARAMETERS OF THE CONTROL SYSTEM RELIABILITY

Determination of the control system reliability distribution law represents the Basis for evaluation of its state, as well as for decision-making on when, i.e., after how many working hours, one should conduct procedures of the preventive maintenance. Determination of the most acceptable model of the reliability distribution, based on data on its behavior, from the aspect of irregularities appearance, is a complex task and it is solved by application of the corresponding algorithm [1], with application of the probability theory, mathematical statistics and the reliability theory [2].

Based on voluminous research of the control system behavior, in the real exploitation conditions, for a longer period of operation, in Table 1 are presented the working times until occurrence of failure and between the two consecutive failures.

Estimated values of the control system reliability indicators, based on data from Table 1, are determined using the known methodology [1] and presented in the table 2. Based values of deviation of the reliability theoretical values, obtained by testing the corresponding hypotheses by application of the known methodology [2], from results of the estimated values, obtained from the exploitation data (Table 1), one came up to the conclusion that the Weibull's two-parameter distribution, with the shape parameter 2.68 and scale parameter 450, was the most acceptable for the analyzed vehicle sample.

Table 1. The working times until occurrence of failure

Failure number (i)	Working time till failure (h)	Number of km passed till failure (km)	Failure number (i)	Working time till failure (h)	Number of km passed till failure (km)	Failure number (i)	Working time till failure (h)	Number of km passed till failure (km)
1	383	11496	13	472	14158	25	599	17963
2	394	11831	14	479	14373	26	637	17981
3	395	11863	15	480	14396	27	640	19100
4	399	11878	16	485	14563	28	655	19196
5	413	12382	17	492	14763	29	663	19638
6	426	12778	18	531	15938	30	671	19882
7	431	12935	19	547	16397	31	716	20125
8	440	13186	20	566	16967	32	788	21492
9	448	13431	21	573	17186	33	823	23651
10	459	13757	22	579	17384	34	880	24697
11	465	13952	23	591	17726	35	913	26391
12	466	13972	24	592	17752	36	913	27391

Table 2. Estimated values of the control system reliability indicators

Number, (i)	Time, (t_i)	Number of failures, $n(t_i)$	Frequency of failure occurrence, f (t_i)	Reliability, R (t_i)	Unreliability, F (t_i)	Failure intensity (t_i)
1	400	12	0,00245	0,5520	0,4480	0,00318
2	500	10	0,00204	0,3478	0,6522	0,00360
3	600	9	0,00184	0,1643	0,8357	0,00519
4	700	4	0,000816	0,0824	0,9176	0,00520
5	800	2	0,000408	0,0426	0,9574	0,00530
6	900	2	0,000408	0,0212	0,9788	0,01020

Table 3. Control system maintenance costs for various periodicities of its preventive maintenance

Maintenance frequency (h)	120	140	180	1120	1160	1200	1250	1300	1350	1400	1450
Costs of corrective maintenance (Ck)	3000	3000	3000	3000	3000	3000	3000	3000	3000	3000	3000
Costs of preventive maintenance (Cp)	600	600	600	600	600	600	600	600	600	600	600
Reliability R(t)	0,997	0,988	0,9831	0,9536	0,906	0,841	0,7599	0,6666	0,5663	0,4649	0,3679
$\int_0^T R(t)dt$	50	99,84	99,80	148,78	195,43	239,15	279,09	314,75	345,65	371,36	392,10
Total specific costs C(t)	14,11	7,40	6,50	5,86	5,11	4,01	4,32	4,41	4,63	5,25	5,55
$f_{i,,2}$	12,11	6,40	5,48	4,76	4,21	4,11	4,22	4,44	4,73	5,05	5,41

Adopting this reliability distribution law for the control system of the analyzed technical system, expressions for determination of the reliability function *R(t)*, the density function *f(t)* and failure intensity *(t)*, can be written in the following forms:

$$R(t) \quad e^{(\frac{t}{450})^{2,68}} \tag{1}$$

$$f(t) \quad \frac{2,68}{450} \; (\frac{t}{450})^{1,68} \;\; e^{(\frac{t}{4450})^{2,68}} \tag{2}$$

$$(t) \quad \frac{2,68}{450} \; (\frac{t}{450})^{1,68} \tag{3}$$

Based on the previous expressions, the optimal periodicity of the working time can be determined, after which either of the following should be performed: preventive inspections, preventive substitutions, repairs or general revisions, as well as providing the optimal values of spare parts stocks [3].

3. DETERMINATION OF THE CONTROL SYSTEM PREVENTIVE MAINTENANCE PERIODICITY BASED ON CRITERION OF THE MINIMAL MAINTENANCE COSTS

Providing for the required availability and reliability of the control system, with minimal maintenance costs, is possible if one correctly determines the periodicity interval of that maintenance [3].

The total control system maintenance costs can be expressed in the form [3]:

$$C(t) \quad \frac{C_k \quad (C_k \quad C_p) \;\; R(t)}{\int_0^T R(t)dt} \tag{4}$$

where: *C(t)* are the total specific maintenance costs; $C_k$are the corrective maintenance costs and C_p re the preventive maintenance costs.

By application of expression (4) for various periodicities of the control system maintenance, the values for the maintenance costs are obtained shown in Table 3.

Based on results shown in Table 3, one can conclude that the lowest maintenance costs of the analyzed technical system clutch are obtained for the maintenance periodicity of 1200 working hours.

4. DETERMINATION OF THE CONTROL SYSTEM PREVENTIVE MAINTENANCE PERIODICITY BASED ON CRITERION OF MAXIMAL AVAILABILITY

Since the most acceptable model of reliability, distribution is determined and since the time picture of the control system of the analyzed control system is completely known (time in operation, time spent on waiting to operate while in order, time spent while out of order), it is possible to apply the maintenance model based on availability [3]. By application of this model, the exploitational reliability of the control system, from the aspect of the frictional control system, can be determined by using the expression:

$$G(t) \quad \frac{t_p \quad t_{cr}}{t_p \quad t_{cr} \quad t_o \quad \dfrac{F(t)}{R(t)} \quad t_k} \qquad (5)$$

where: t - is the periodicity of maintenance; t_{cr} - is the time spent to operate while in order; t_p - is the time of preventive maintenance; t_k - is the time of corrective maintenance.

By varying the periodicity of preventive maintenance, one obtains the functional dependence based on which the optimal value of the preventive maintenance periodicity can be determined, based on the maximal availability criterion. Results of determination of availability, for various maintenance periodicities of the control system of the considered control system, are shown in Table 4.

Based on results shown in Table 4 and in Figure 2 it can be concluded that the highest availability of the analyzed control system, from the aspect of its clutch, is obtained for the maintenance periodicity of 1300 working hours.

5. DETERMINATION OF THE OPTIMAL PERIODICITY OF THE PREVENTIVE MAINTENANCE OF THE CONTROL SYSTEM BY APPLICATION OF THE MULTICRITERIA OPTIMIZATION

The value of the preventive maintenance periodicity of the analyzed control system lies between the times that correspond to maximal availability and to minimal costs. This period can be discretized. Each discrete value can be associated with considered concept of the preventive maintenance. In that way, one obtains the corresponding number of

Table 4. Motor vehicle availability as a function of its control system preventive maintenance periodicity

Maintenance periodicity (h)	1160	1200	1250	1300	1350	1400	1450
Working time t_r (h)	1160	1200	1250	1300	1350	1400	1450
Preventive maintenance time t_p (h)	20	20	20	20	20	20	20
Unreliability F	0,016	0,046	0,093	0,159	0,240	0,333	0,433
Reliability R	0,906	0,841	0,7599	0,6666	0,5663	0,4649	0,3679
Number of corrective maintenances between the two preventive ones	0,017	0,048	0,103	0,189	0,316	0,500	0,765
Time of corrective maintenance k_k (h)	1,03	2,92	6,21	11,35	18,96	30,01	45,95
Time spent on waiting while in order $t_{čr}$ (h)	30	45	60	75	90	105	120
Availability G(t)	0,983	0,984	0,985	0,986	0,981	0,978	0,977
$f_{I,,2}$	0,983	0,985	0,984	0,983	0,981	0,978	0,977

preventive maintenance variations, which differ from each other only in working time lengths after which the procedures of preventive maintenance are being conducted. Since the values of optimal periodicities of the considered clutch preventive maintenance, obtained by criterion of maximal availability and criterion of minimal costs differ from each other (parts 3 and 4 of this paper), in this part are presented results of determination of the periodicity by application of the multicriteria optimization method, which is known in literature as the MCDM (Multi Criteria Decision making) problem [5]. The basic characteristic of the MCDM problem, thus accordingly of the problem considered in this work, is that the best alternative is found in the sense of several attributes, simultaneously, or in the limited set of available alternatives.

In literature can be found a large number of multicriteria optimization methods [5]. One of the most frequently used methods is the Analytical Hierarchy Process [7]. The AHP method was developed based on the principle of decision making, human knowledge, as well as on data that are available to experts in the process of decision making. That process is a creative one, which is based on three main concepts: analytics, hierarchy and process [3].

The nature of the optimality criterion can be benefit wise and coastwise [6]. When the benefits optimality criterion is used, the higher its value is the better and vice versa. When the costs optimality criterion is used, the less their values are the better and vice versa.

The set of alternatives i is being represented by the set of alternative indices i = (1, … i, … I) where I is the total number of the considered alternatives. The problem is represented by matrix $F = [f_{ik}]_{,1\ K}$. Here f_{ik} denotes the optimality criterion k for alternative i. In the general case, the optimality criteria are of various natures; they have different values and different units. This means that the optimality criteria values, for alternative are not comparable. From that reason it is necessary to perform the normalization procedure by which all the values of f_{ik} are being mapped within interval [0, 1]. At present, a large number of the normalization types are being used[7]: simple, linear, vectorial, etc. regardless of which type of normalization is being used, different expressions are used for benefit wise and coastwise optimality criteria. When the vectorial normalization is applied, the decision making process can be represented by matrix $F = [f_{ik}]_{,1\ K}$, where $(f_{ik})_{,n}$ is the normalized value of the optimality criterion k for alternative i. To each considered alternative, certain value is being associated [7].

Normalization of values $f_{i,1}$ is being done by application of the expression for vectorial normalization and by application of the benefit wise optimality criterion. For solving the concrete task the following expressions can be used:

$$(f_{i,1})_n = f_{i,1} \Big/ \left(\sum_{i=1}^{7} (f_{i,1})^2\right)^{1/2} \tag{6}$$

$$(f_{i,2})_n = (1/f_{i,2}) \Big/ \left(\sum_{i=1}^{7} (1/f_{i,2})^2\right)^{1/2}. \tag{7}$$

The value of the factor based on which the best alternative of the maintenance periodicity a_i is being determined by application of the assumption that validities of the adopted optimization criteria (maximal availability and minimal maintenance costs) are equal and that they are set as normalized, what is the case in this concrete task, by application of the following expression [7]:

$$a_i = \frac{1}{k}\sum_{k=1}^{K}(f_{ik})_n = \frac{1}{2}\left((f_{i,1})_n + (f_{i,2})_n\right). \tag{8}$$

The optimal value of the periodicity of conducting the preventive maintenance of the motor vehicle's control system is within interval of 1200 to 1300 working hours, because the limits of that interval were obtained based on criterion of the control system maintenance minimal costs and criterion of the maximal availability in that interval.

Table 5. Availability of the motor vehicle from the aspect of its control system

Alternative number (i)	Control system maintenance periodicity (h)	Vehicle's availability (G) from the control system aspect	$f_{i,1}$	$(f_{i,,1})_n$	Total specific maintenance costs (C)	$f_{i,,2}$	$(f_{i,,2})_n$	a_i
1	1200	0,9841	0,9841	0,369	4,11	4,11	1,54	1,012
2	1210	0,9842	0,9842	0,364	4,19	4,19	2,80	1,554
3	1220	0,9843	0,9843	0,369	4,20	4,20	3,43	1,995
4	1230	0,9844	0,9844	0,369	4,24	4,24	3,43	2,096
5	1240	0,9845	0,9845	0,361	4,30	4,30	3,44	2,097
6	1250	0,9846	0,9846	0,362	4,32	4,32	3,45	2,098
7	1260	0,9847	0,9847	0,351	4,33	4,33	3,45	2,099
8	1270	0,9853	0,9853	0,353	4,35	4,35	3,45	2,026
9	1280	0,9854	0,9854	0,351	4,36	4,36	3,57	1,967
10	1290	0,9860	0,9860	0,346	4,39	4,39	3,27	1,896
11	1300	0,9863	0,9863	0,335	4,44	4,44	3,15	1,879

The interval is being divided into 11 equal parts (Table 5).

Elements of matrix F are being obtained in such a way that they are being made equal to values of the analyzed motor vehicle availability, from the aspect of its control system, for various periods of the preventive maintenance that correspond to individual alternatives ($f_{i,1}$) and by making them equal to values of the total control system maintenance costs for different periods of preventive maintenance that correspond to individual alternatives ($f_{i,2}$).

Based on data obtained by monitoring the analyzed control system, from the aspect of its control system, in real exploitation conditions, by application of expression (5) for determination of availability, obtained were the values of elements $f_{i,\ 1}$ (namely the availabilities) of matrix F, while by application of expression (4) for determination of the maintenance costs obtained were the values of elements $f_{i,2}$ (namely the maintenance costs) of matrix F (Table 5).

The best alternative is one for which the value of factor a_i has the highest value. The values of this factor, calculated by application of expression (8) are given in table 5 based on those values and by recognizing the aforementioned, it can be concluded that the optimal value of periodicity of conducting the preventive maintenance procedures of the analyzed control system, from the aspect of its control system, is after every 1260 working hours.

6. CONCLUSIONS

Results of voluminous investigations of the motor vehicle's control system reliability parameters, which were obtained by monitoring the behavior of the analyzed control system the real exploitation conditions, from the aspect of failure occurrence of its control system, and with application of the corresponding scientific knowledge from the area of probability., mathematical statistics, systems theory and reliability theory, have served as a basis for finding the optimal periodicity of the control system maintenance, taking into account the criteria of maximal availability and minimal costs of its maintenance.

Since the optimal periodicities of conducting the control system preventive maintenance, determined by criteria of maximal availability and minimal maintenance costs differ from each other, it was necessary to apply one of the multicriteria analysis methods and to determine the value of the required optimal periodicity of conducting the preventive maintenance procedures, taking into account both optimization criteria.

The value of optimal periodicity of

conducting the preventive maintenance procedures of a control system was determined according to maximal availability criterion to be 1200 working hours, while according to criterion of minimal maintenance costs that value was 1300 working hours.

By application of the multicriteria analysis the value of the required optimal periodicity of conducting the preventive maintenance procedures of a control system, with taking into account both optimization criteria, was 1260 working hours.

The presented methodology of the multicriteria decision-making can be applied for obtaining the reliable value of optimal periodicity of conducting the preventive maintenance procedures also of other parts of the analyzed control system. There one needs available data, which can be obtained by analysis and monitoringof the considered motor vehicle, this the reliability indicators of the system can be determined, as well as the characteristics of its maintenance.

REFERENCES

[1] BS5760 *British Standard - Part 2, Guide to the assessment of reliability, Reliability of systems, equipments and components*, 1981.

[2] S. Vukadinović: Elements of the Probability Theory and Mathematical Statistics, Economy Review, Belgrade (In Serbian), 1981.

[3] T.L. Saaty: How to Make a Decision: The Analytic Hierarchy Process, European Journal of Operational Research, Vol. 48, pp. 9-26, 1990.

[4] P. Kaur, S. Chakrabortyb: A New Approach to Vendor Selection Problem with Impact Factor as an Indirect Measure of Quality, Journal of Modern mathematics and Statistics, Vol. 1, No. 1, pp. 8-14, 2007.

[5] J. Puente, P. de la Fuente, R.P. Priore: ABC classification with uncertain data: a fuzzy model vs. A probabilistic model.*Applied* Artifical Intelligence, Vol. 16, No. 6, pp. 443-456, 2002.

[6] D. Milanović et al: *Management Information Systems*, Megatrend University, Belgrade, 2003.

[7] R. Ramanathan: ABC inventory classification with multiple-criteria using weighted linear optimization, Computers & Operations Resarch, Vol. 33, No. 3, pp. 695-700, 2006.

[8] S. Opricović: *Multicriteria Optimization*, Faculty of Civil Engineering, Belgrade (In Serbian), 1986.

[9] C.W. Chu, G.S. Liang, C.T. Liao: Controlling inventory by combining ABC analysis and fuzzy classification, Computers & Industrial Engineering, Vol. 55, No. 4, pp. 841-851, 2008.

[10] J.C. Pomerol, S. Barba - Romero: *Multicriterion Decision in Management: principles and Practice*., Kluwer Academic Publishers, 2000.

[11] Bass, S.M., &Kwakernaak, H. (1977). Rating and Ranking of multiple-aspect Alternatives using Fuzzy sets.*Automatica*, *3*(1), 47-58.

[12] D. Dubois, H. Prade: Decision –making under fuzziness, In M.M. Gupta, R.K. Ragade, R.R. Yager (Eds.), *Advances in Fuzzy set Theory and Applications*, North-Holland, pp. 279-302, 1972.

[13] K.P. Yoon, C.I. Hwang: *Multiple Attribute Decision Making: An Introduction (Quantitative Applications in the Social Sciences)*, Sage University Paper Inc, 1995.

[14] D. Pavličić: Normalization of Attribute Values in MADM the Conditions of Consistent Choice IV, DI and α, Yugoslav journal of operations research, Vol. 10, No. 1, pp. 109-122, 2000.

Serbian Tribology Society

SERBIATRIB '19

16th International Conference on Tribology

Faculty of Engineering University of Kragujevac

Kragujevac, Serbia, 15 – 17 May 2019

TRIBOLOGICAL ASPECTS OF WATER HYDRAULICS

Franc MAJDIČ*, Ervin STRMČNIK
Faculty of Mechanical Engineering, University of Ljubljana, Slovenia, EU
*Corresponding author: franc.majdic@fs.uni-lj.si

Abstract: *A clean and healthy environment must be an increasing priority. Different kinds of hydraulic fluids are in use nowadays. Unfortunately, the majority of them are harmful. The use of tap water as a hydraulic-pressure medium is one of the possible solutions. This study presents the research and development of different hydraulics components. Every research of a new water-hydraulic component starts with basic tribological investigations of different material pairs and their surfaces. Then follows the design and calculations of the hydraulics characteristics, the production of a prototype and its experimental investigations. The following water-hydraulic components, i.e., proportional control valve, hydraulic cylinder, piston pump, hydraulic accumulator, check valve and hydraulic motor, will be presented.*

Keywords: *water hydraulics, tribological pairs, friction, wear, proportional valve, cylinder, pump, accumulator, hydraulic motor*

1. INTRODUCTION

Fluids are the first and some of the most important components in power-control hydraulics (PCH). The main tasks of the most used traditional hydraulic fluid, mineral hydraulic oil, are: power transmission, lubrication, cooling, elimination of insoluble particles, preventing corrosion, preventing foaming, reducing internal leakage, water extraction, etc. In addition, it is available in large quantities. Unexpected outflows of hydraulic liquids, i.e., mineral oils, into the ground and even into underground drinking-water supplies are a frequent occurrence. One of today's major challenges to prevent harmful consequences for the environment is to use alternative, natural and biodegradable sources of hydraulic fluid. In power-control hydraulics there are two ways in which we can protect the environment. The first solution is to use a biodegradable oil [1-6] instead of a mineral oil, while the second – and better – solution is to use tap water instead of mineral oil. This solution is harmless to the environment, but it is very difficult to realize [7-9]. One reason being that only some relatively simple, conventional control valves exist on the market today. In spite of many years of water-hydraulics research, there is still insufficient understanding of the mechanisms and performance and, consequently, the available component designs. Some of the reasons lie in many of the specifics that water has compared to oil in hydraulic systems, which already affect the research and development phase, and later – in the long term – the performance of the water-hydraulic system. Some of these are described below and some are listed in Table 1. For example, for any research of water hydraulics in real-scale components, home-made components and test rigs are required, because they do not exist on the market. However, this is associated with costs and technical problems.

Table 1. Properties, the main advantages and disadvantages of water

Property	Advantage	Disadvantage
Low viscosity	Lower pressure losses	Higher leakage
High vapour pressure	-	Erosion during the cavitation
High compression modulus / high speed of sound	High / quick responses	Larger "water-hammer effect"
Corrosion protection	-	Poor – special materials are needed
Lubrication, lubrication film	-	Weak, special materials are needed
Thermal conductivity	High – fast heat transmission	-
Relative cost	Low	-
Environmental impact	No negative impact	-
Temperature range	-	Narrow temperature range: 2–50°C
Flash / ignition point	No fire hazard	-

The much lower viscosity of water compared to oil causes a high rate of leakage with clearances typical for oil, while reduced clearances result in excessive wear and high friction. Higher working temperatures, which are still common for oil hydraulics, i.e., around 70 or 80 °C, are hardly acceptable for water in hydraulic systems because of the evaporation at local contact spots [10]. In water, micro-organisms develop with time. This causes several problems with chemical changes to the water and the growth of algae, which results in sediments. The tribological properties of conventional materials (stainless steel) in water are unfavourable, while comparable material selection is poor, and their properties are unknown. For example, a new class of high-potential diamond-like-carbon materials [11-21] that showed excellent properties in a variety of conditions that are in many ways comparable to those in water hydraulics have not been investigated in detail for this application yet. Furthermore, another class of materials that has already confirmed excellent properties suitable also for water [22-29], i.e. ceramics, are probably too brittle for the required dynamic conditions in water hydraulics or are too expensive for precise manufacturing [30], but this has not been investigated either. Corrosion and cavitation are other well-known problems related to tribological performance and the life-time of components. Therefore, research into the chemical and tribological properties that affect the life and performance, as well as the dynamic characteristics, of water hydraulics, are required for the successful development of new components, which is necessary for the wider use of the water in power control hydraulics.

2. TRIBOLOGICAL INVSTIGATIONS WITH WATER

Different material pairs

In order to investigate the change in hydraulic parameters, in particular wear resistance and useful life, in selected hydraulic tests for different possible material combinations, model tribological tests were performed to make an initial or preliminary selection. Generally, stainless steel (SS) is the most typical and inexpensive material that is already used in several hydraulic parts and was thus reasonably the first-choice material. Other potential groups of materials include ceramics and polymers. Since ceramic materials are very costly and also have a low fracture toughness, they were not considered as being suitable materials for the real-scale tests with which we would like to compare materials in the later stages of this research. Therefore, they were not included as the "studied" material (disk) in the first screening tribological tests; however, a ceramic was used, at least as a counter-material, i.e. pin, which should also give us some indication of the tribological properties of the selected couples. Different commercially available polymeric materials were also considered. We selected those that can be used in water for a longer time period [14-16] and gave some promising tribological results in the past, and which are also easily commercially available and suggested by world-renowned producers. Thus, we selected two different types of materials from two groups of polymeric materials, i.e., polyetheretherketone (PEEK) and polyimide (PI). A commercially available PEEK (Victrex Europa GmbH, Germany) containing 30 % of carbon (CA30) and 30 % of glass (GL) fibres was used. Polyimides (Vespel) from Dupont™ without any addition (SP1) and containing 15 % of graphite fibres were also tested. The pin materials were SS (X105CrMo17), obtained from Aubert&Duval and hardened to 55 Hrc, and alumina ceramic balls (99.7 % purity, 10 mm diameter) from Hightech Ceram. In total, four types of polymeric materials and stainless steel were selected as the disc materials, while pins were made from the same stainless steel and alumina ceramics.

Figure 2 shows the measurement results for different material pairs lubricated with distilled water at room temperature. Compared to the polymeric materials, significantly higher friction values were measured in the contacts with SS discs, which were in the range 0.6–0.8. Other friction data show friction values between 0.13 and 0.28, which is 2–3 times less than with SS discs. With the exception of the pure polyimide (SP1), with all the other polymer discs, contacts with alumina pins resulted in a lower friction than against SS pins. However, these differences were not very high. Nevertheless, it should be noted that friction in the polyimide SP1/SS contact resulted in the second-lowest friction, i.e., about 0.16. This is important, because the polymeric material contains no additional components and is thus simpler and cheaper. Moreover, the SS pin is also the most preferred counter-material from a practical point of view. The lowest friction in this study was, however, obtained with the PEEK CA30/Al2O3 combination, where the friction was about 0.13.

Different surface properties and hard coatings

Despite the many new materials for highly loaded surfaces, still the most promising materials are stainless steels in combination with hard coatings.

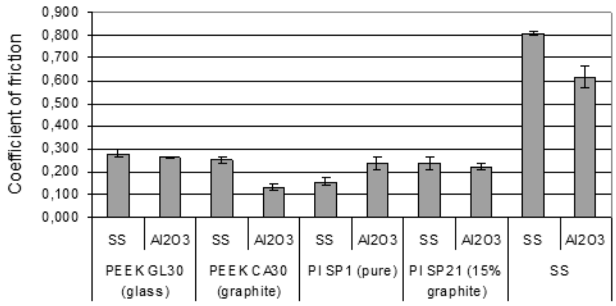

Figure 1. Coefficient of friction for different material pairs (four disc materials against two pin materials)

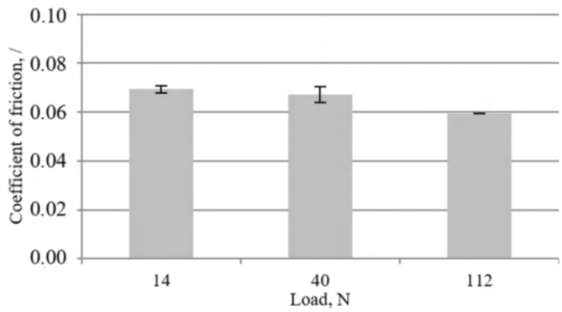

Figure 2. Coefficient of friction for DLC/AISI440 in water at three different loads

Figure 2 shows the COF of the SS/DLC lubricated with water for three different loads. The COF decreased when the load increased. It was also observed that the COF under water-lubricated conditions was slightly lower than the COF under oil-lubricated conditions [31]. As a general observation, the SS/DLC contact clearly provides a significantly lower coefficient of friction (Fig. 2) than the SS/SS contact (see Figs. 1 and 4).

3. NEW WATER-HYDRAULIC COMPONENTS

Through research in the Laboratory for Fluid Power and Control at the Faculty of Mechanical Engineering, University of

Ljubljana, some new water-hydraulic components were developed.

3.1 Proportional directional control valve

Despite the many years of research work in water hydraulics, there is still an insufficient understanding of the tribo-mechanical mechanisms and performances playing the most important roles in the application of components and systems for water PCH. High-pressure proportional 4/3 directional spool-sliding control valves are moreover widely used in the oil PCH, but for water PCH they are still almost wholly missing from the market [32]. That was the basic reason for our decision for the research, investigations and development of the new water 4/3 proportional directional control valve (Fig. 3) of the spool-sliding type [33].

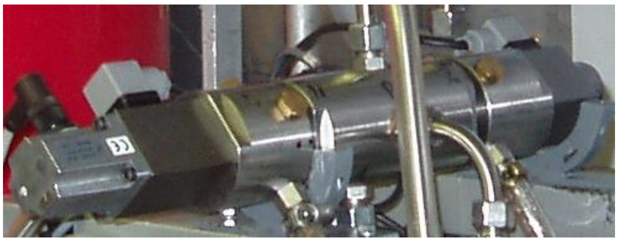

Figure 3. Prototype of proportional directional control valve for water hydraulics

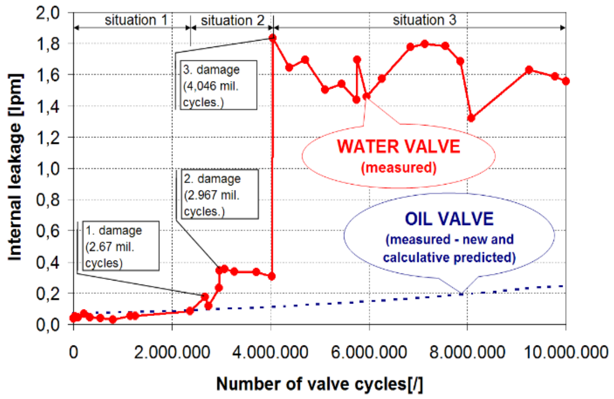

Figure 4. Measured values of the internal leakage of the water directional 4/3 proportional control valve during the whole lifetime test, depending on the number of switching cycles and the quality of the water filtering

Figure 4 shows the results of a long-term lifetime test of a proportional directional valve for water hydraulics. The situations were as follows: 1- single, by-pass filtering, 2 – without filtering, 3 – improved, double filtering (by-pass and pressure filter, both were 1 µm), the pressure was 160 bar, the flow was 20 l/min, the frequency was 5 Hz and the water temperature was 40°C. The leakage measured during the lifetime test of the water 4/3 proportional directional control valve oscillated, probably owing to the different positions of the spool (centric/eccentric, turned at different angles inside the sleeve). The measured leakage at the end of the testing procedure amounted to 1.55 lpm. The calculated, predicted internal leakage of a similar, oil 4/3 proportional directional control valve should be 0.24 lpm after 10 million cycles.

3.2 Hydraulic accumulator, piston type

The new water-hydraulic accumulator (Figure 5) was designed, manufactured and tested by the Laboratory for Power-Control Hydraulics. This water accumulator was constructed in such a manner that we could easily exchange its seals and/or study the tribological and hydraulic behaviour of the sliding contacts. The hydraulic accumulator with a 4-litres volume allowed a maximum working pressure of 390 bar. A prototype was manufactured and a certificate was acquired from the European Pressure Directive PED 97/23/EC. The piston type of water-hydraulic accumulator consists of the following parts (Fig. 1): piston with special seals and guides for gas and water, tube, piston rod, two end-covers, two pressure and two temperature sensors and a displacement sensor for the detection of the piston's position. The necessary additional equipment is a pre-set pressure-relief valve and two manually operated ball valves [33].

Figure 5. Prototype of a piston-type water-hydraulic accumulator

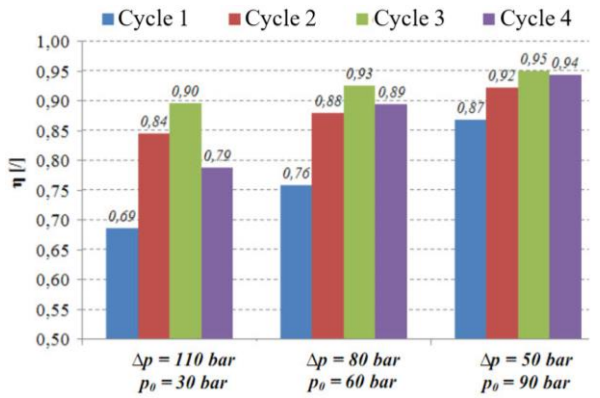

Figure 6. Influences of different nitrogen pre-filling pressures for all four cycles on the water-hydraulic accumulator efficiency

Figure 6 shows the pre-filling pressure effect of nitrogen on the efficiency of the accumulator measured in the water-hydraulic system. As can be seen, in all four cycles (different compression and expansion times) the efficiency rises with an increase of the nitrogen pre-filling pressure.

3.3 Modular hydraulic cylinder

A double-acting, double-rod hydraulic cylinder (Fig. 7) for using water as a hydraulic fluid was designed with the goal of investigating the static and dynamic performance of the hydraulic cylinder related to the specific working parameters and studying the tribological behaviour of various sealings and guidings [34]. The water-hydraulic cylinder has a modular design that has the easy exchange of one type of sealing and guiding with another.

Figure 7. A prototype of the double-acting, double-rod, water-hydraulic cylinder

Figure 8 shows the influence of the pressure difference between the A and B ports during the moving of the water-hydraulic cylinder rod with a constant velocity for three different inlet pressures and three different inlet flows for the water cylinder with a load of 163 kg in the horizontal position.

The lowest pressure difference between the A and B ports of the water cylinder with the sealing/guiding PTFE material was when moving the cylinder rod with a constant velocity, 3.7 bar occurred at 1 lpm and an inlet pressure of 70 bar. The highest pressure difference was also when moving the cylinder rod with a constant velocity, 12.1 bar at a flow of 22 lpm and an inlet pressure of 150 bar. The PTFE material used for sealing/guiding is very promising for water hydraulics [35].

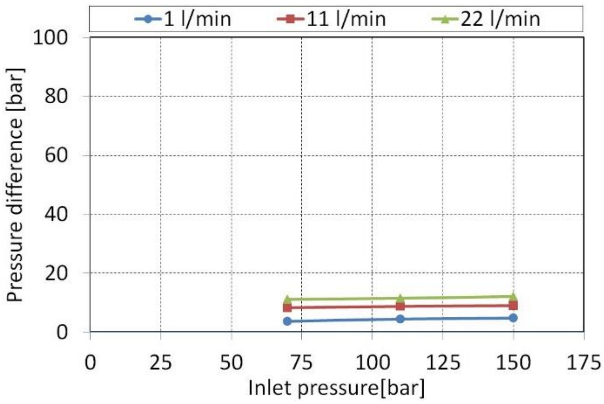

Figure 8. Friction due the pressure difference between the A and B ports of the water cylinder at the moment of moving the cylinder rod with a constant velocity for the hydraulic cylinder with a load of 163 kg in the horizontal position for different inlet pressures and different flows with sealing/guiding PTFE materials

3.4 Check valve

The check valve was designed (Fig. 9) in such a way that it can be simply and quickly disassembled [36]. Check valves consist of a housing made from two pieces, seat, closing element, guidance element and spring. The design of the valve allows researchers to experiment with different closing elements (ball, different conical elements, etc.) and different numbers of flow channels (from 1 to 6). Figure 10 shows the results for the fully-open slot.

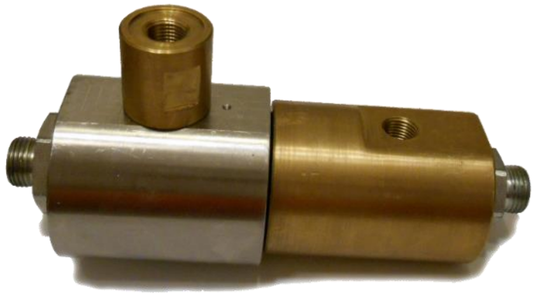

Figure 9. A prototype of the water-hydraulic check valve

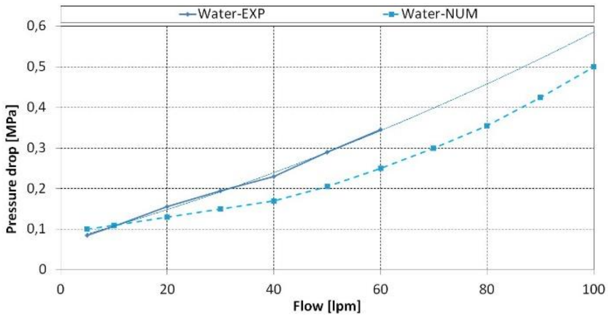

Figure 10. Comparison between experimental measurement (EXP) and numerical (NUM) simulations for the water check valve

Figure 10 shows the results of the experimental and numerical investigations of the water-hydraulic check valve for fully-opened slots. At a water flow of 60 lpm, 0.35 MPa of pressure drop was measured. The results of the numerical investigations show lower valves.

Hydraulic motor

A low-speed, high-torque, orbital hydraulic motor that converts the energy of a fluid under high pressure into the motion of a shaft of the hydraulic motor was developed. The important mechanical parts of the hydraulic motor are (1) the inner rotor, (2) the floating outer ring, and (3) the gerotor housing, as presented in Figure 11.

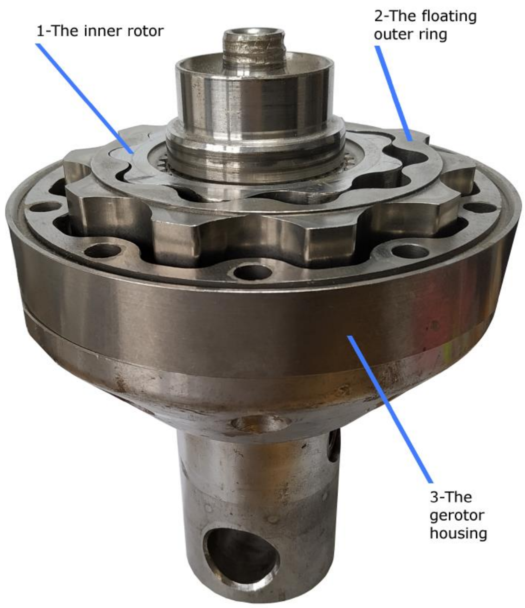

Figure 11. A prototype of a low-speed water-hydraulic motor

The modified hydraulic motor (steel/DLC contacts) satisfactorily operated for a few hours. The relatively high average total efficiency (up to 12.1%-green field) was observed at the higher rotational speeds, as shown in Figure 12, where one circle represents the average total efficiency at a specific operating point regarding the rotational speed and the pressure difference. The measurement included four physical quantities (p, pressure; n, rotational speed; M, torque; Q, flow rate), which are needed to calculate the total efficiency of the orbital hydraulic motor [37].

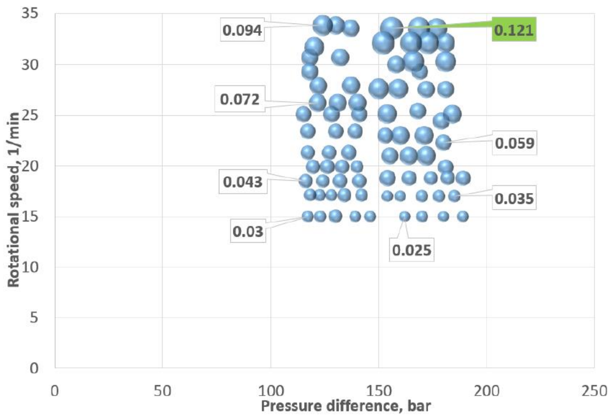

Figure 12. Total efficiency (value in label) of the modified hydraulic motor for water

4. CONCLUSION

The paper deals with the tribological aspects of water hydraulics. The key results can be summarized as follows:

- the material pair PEEK CA30/AL23 had the lowest coefficient of friction among the tested samples. The coefficient of friction in water was close to 0.1;
- the diamond-like-carbon coating reduced the coefficient of friction in water significantly;
- in-depth research and understanding of the tribological behaviour in different contacts leads to the development of new components in hydraulics (e.g., proportional directional control valve, accumulator, cylinder, check valve, hydraulic motor)

ACKNOWLEDGEMENT

For full support of this research we are sincerely grateful to Prof. Dr. Mitjan Kalin, Head of TINT.

The authors are also grateful to the Slovenian company Tajfun, the largest producer of forestry machinery in Europe, for their financial and technical support. For the financial support of this research, we are grateful to the Slovenian Research Agency.

REFERENCES

[1] W.J. Bartz: *Lubricants and the environment,* Tribology International, Vol. 31, pp. 35-47, 1998.

[2] M. Kalin, F. Majdič, J. Vižintin, J. Pezdirnik, I. Velkavrh: *Analyses of the Long-Term Performance And Tribological Bechaviour of an Axial Piston Pump Using Dimond-like-Carbon-Coated piston Shoes and Biodegradable Oil,* Journal of Tribology, Vol. 130, pp. 11013-18, 2008.

[3] A. Igartua, J. Aranzabe, J. Barriga, B. Rodriguez: *Tribological Study For The Application Of Biodegradable Lubricants In The Industry,* COST 516 Tribology Symposium Proceedings, *H. Ronkainen, K. Holmberg, eds., 1998, VTT, Espoo, p. 135-146.*

[4] M. Kalin, J. Vižintin: *A comparison of the tribological behaviour of steel/steel, steel/DLC and DLC/DLC contact when lubricated with mineral and biodegradable oils,* Wear, Vol. 261, No. 1, pp. 22-31, 2006.

[5] A. Adhvaryu, S.Z. Erhan, J.M. Perez: *Tribological studies of thermally and chemically modified vegetable oils for use as environmentally friendly lubricants,* Wear, Vol. 257, No. 3, pp. 359-367, 2004.

[6] M. Kalin, J. Vižintin: *The tribological performance of DLC-coated gears lubricated with biodegradable oil in various pinion/gear material combinations*, Wear, Vol. 259, pp. 1270-1280, 2005.

[7] W. Backe: *Water- or oil-hydraulics in the future, SICFP'99, Tampere, Finland, pp. 51–65, 1999.*

[8] E. Trostmann: *Water hydraulics control technology;* Lyngby, Technical University of Denmark, 1996.

[9] A.C.H. Tan, P.S.K. Chua, G.H. Lim: *Fault diagnosis of water hydraulic actuators under some simulated faults,* Journal of Materials Processing Technology, Vol. 138, No. 1, pp. 123-130, 2003.

[10] M. Kalin: *Influence of flash temperatures on the tribological behaviour in low-speed sliding,* a review, Mater. sci. eng., A Struct. mater. A374 (1/2), pp. 390-397, 2004.

[11] C. Donnet, A. Grill: *Friction control of diamond-like carbon coatings,* Surface and Coatings Technology 94-95, pp.456-462, 1997.

[12] J. Fontaine, C. Donnet, A. Grill, T.L. Mogne: *Tribochemistry between hydrogen and diamond-like carbon films,* Surface and Coatings Technology, Vol. 146-147, pp. 286-291, 2001.

[13] M. Kalin, J. Vižintin, J. Barriga, K. Vercammen, K. Van Acker, A. Arnšek: *The effect of doping elements and oil additives on the tribological performance of boundary-lubricated DLC/DLC contacts,* Tribology Letters, Vol. 17, pp. 679-688, 2004.

[14] A. Matthews, A. Leyland, K. Holmberg, H. Ronkainen: *Design aspects for advanced tribological surface coatings,* Surface and Coatings Technology, Vol. 100-101, pp. 1-6, 1998.

[15] M. Kalin, J. Vižintin, K. Vercammen, J. Barriga, A. Arnšek: *The lubrication of DLC coatings with mineral and biodegradable oils having different polar and saturation characteristics,* Surface and Coatings Technology, Vol. 200, pp. 4515-4522, 2006.

[16] S. Neville, A. Matthews: *A perspective on the optimisation of hard carbon and related coatings for engineering applications,* Thin Solid Films, Vol. 515, pp. 6619-6653, 2007.

[17] J. Andersson, R.A. Erck, A. Erdemir*: Friction of diamond-like carbon films in different atmospheres,* Wear 254, p. 1070-1075, 2003.

[18] M. Kalin, E. Roman, J. Vižintin: *The effect of temperature on the tribological mechanisms and reactivity of hydrogenated, amorphous diamond-like carbon coatings under oil-lubricated conditions,* Thin Solid Films, Vol. 515, pp. 3644-3652, 2007.

[19] I. Velkavrh, M. Kalin, J. Vižintin: *The performance and mechanisms of DLC-coated surfaces in contact with steel in boundary-lubrication conditions – a review,* Strojniški Vestnik – Journal of Mechanical Engineering, Vol. 54, pp. 189-206, 2008.

[20] J. Barriga, M. Kalin, K. Van Acker, K. Vercammen, A. Ortega, L. Leiaristi: *Tribological performance of titanium doped and pure DLC coatings combined with a synthetic bio-lubricant,* Wear, Vol. 261, No. 1, pp. 9-14, 2006.

[21] M. Kano: *Super low friction of DLC applied to engine cam follower lubricated with ester-containing oil,* Tribology International, Vol. 39, pp. 1682-1685, 2006.

[22] P. Andersson: *Water lubricated pin-on-disc tests with ceramics,* Wear, Vol. 154, pp. 37-47, 1992.

[23] F. Zhou, K. Adachi, K. Kato: *Sliding friction and wear property of a-C and a-CNx coatings against SiC balls in water,* Thin Solid Films, Vol. 514, No. 1, pp. 231-239, 2006.

[24] S. Novak, M. Kalin, T. Kosmac: *Chemical aspects of wear of alumina ceramics,* Wear, Vol. 250, No. 1/12, pp. 318-321.

[25] M. Kalin, J. Vižintin, S. Novak: *Effect of fretting conditions on the wear of silicon nitride against bearing steel,* Mater. sci. eng. A A220, pp. 191-199, 1996.

[26] B. Basu, J. Vleugels, M. Kalin, O. Van Der Biest: *Friction and wear behaviour of SiAlON ceramics under fretting Contacts,* Materials and Engineering A359, pp. 228-236, 2003.

[27] M. Kalin, S. Novak, J. Vižintin: *Wear and friction behaviour of alumina ceramics in aqueous solutions with different pH,* Wear, Vol. 254, pp. 1141-1146, 2003.

[28] J. Xu, K. Kato: *Formation of tribochemical layer of ceramics sliding in water and its role for low friction,* Wear, Vol. 245, pp. 61-75, 2000.

[29] S. Novak, G. Dražic, M. Kalin, J. Vižintin: *Interactions in silicon nitride ceramics vs. steel contact under fretting conditions,* Wear, Vol. 225/229, pp. 1276-1283, 1999.

[30] M. Kalin, S. Jahanmir: *Influence of roughness on wear transition in glass-infiltrated alumina,* Wear, Vol. 255, No. 1/6, pp. 669-676, 2003.

[31] E. Strmcnik, F. Majdic, M. Kalin: *Water-lubricated behaviour of AISI 440C stainless steel and a DLC coating for an orbital hydraulic motor application,* Tribology International, Vol. 131, pp. 128-136, 2019.

[32] K. Koskinen, T. Leino, H. Riipinen: *Sustainable development with water hydraulics – possibilities and challenges*, 7th International Symposium in Fluid Power, JFPS'08, Toyama, Japan, 2008.

[33] F. Majdič, A. Bombač: *Piston-Type Accumulator for Water Power-Control Hydraulics*, The 9th International Fluid Power Conference, 9. IFK, March 24-26, Aachen, Germany, 2014.

[34] F. Majdič, M. Kalin, A. Ljoki: *Cylinder seals in water and oil hydraulics.* V: Polytrib 2014: proceeding, 1st International Conference on Polymer Tribology, 11th - 12th September 2014, Bled, Slovenia. Ljubljana: Slovenian Society for Tribology, 2014.

[35] F. Majdič, J. Pezdirnik, M. Kalin: *Friction investigations in a water hydraulic cylinder.* 8th International fluid power conference (8. IFK), March 26-28, 2012 in Dresden: 8. IFK, Vol. 1, Symposium: Monday, March 26, 8th International Fluid Power Conference, March 26-28, 2012, Dresden. Dresden: Technische Universität, Institut für Fluidtechnik, pp. 345-356, 2012.

[36] F. Majdič: *Water hydraulic check valve researches*, The Fourteenth Scandinavian International Conference on Fluid Power, Tampere, Finland, May 20-22, 2015.

[37] E. Strmčnik, F. Majdič, M. Kalin: *Influence of a Diamond-Like Carbon-Coated Mechanical Part on the Operation of an Orbital Hydraulic Motor in Water,* Metals, Vol. 9, p. 466, 2019.

Serbian Tribology Society

SERBIATRIB '19

16th International Conference on Tribology

Faculty of Engineering
University of Kragujevac

Kragujevac, Serbia, 15 – 17 May 2019

DETERMINATION OF THE OPTIMAL VEHICLE MAINTENANCE STRATEGY AS ONE OF THE CONDITIONS OF IMPROVING THE SAFETY OF TRAFFIC

Vojislav KRSTIĆ [1], Boris ANTIĆ[2]

[1,2] Faculty of transport and traffic engineering, University of Belgrade, Beograd, Serbia,
bkrstic@kg.ac.rs, mpeeric@gmail.com

Apstract: *Two types of preventive maintenance are mostly used. First is preventive maintenance based on reliability information (on empirically defined distribution of possibility of work time until breakdown). By application of this type of preventive maintenance, maintenance procedure is planned in order to provide required level of reliability, most often by preventive replacements after a definite work periodicity. Other type of preventive maintenance is based on connection of information about reliability and information acquired in view of constant and systematic follow-up of vehicle (follow-up of selected parameters and indicators that with enough security show its condition).*

Strategy of total productive maintenance is based on statement that only by maintenance it is not possible to maintain projected level of reliability during exploitation, but it is necessary to have active participation of users and everyone who is in relation to the maintained vehicle.

Main application of so-called accelerated strategies of maintenance is not to conduct any activity of preventive maintenance if it is not economically justifiable.

Nowadays there is a tendency towards combined application of existing strategies of maintenance. The reason is placed in variety of maintained vehicles. Second reason is existence of flaws of current strategy for maintenance.

By application of knowledge based system, or so-called soft computing, we come to efficient methods used for treatment of problems while maintenance of technical systems, from the aspect of imprecision. One of such systems is fuzzy logic.

Essence of traditional and modern strategy of motor vehicle maintenance is analyzed. Special attention is given to modern strategy of motor vehicle maintenance.

Keywords: *vehicles, maintenance, fuzzy logic*

1. INTRODUCTION

Path of development of motor vehicle maintenance may be divided in several stages and they are as follows:

1. First (from the first usage of motor vehicles to 1950), which main essence is to remove breakdown when it appears;
2. Second (from 1950 to 1980), which main characteristics are lower maintenance costs, longer durability and greater disposability of motor vehicles;
3. Third (from 1980 and now), which main characteristics are better relation of effect and cost, longer duration, conservation, higher reliability and

disposability. Nowadays so-called classical strategies of maintenance are still dominating (corrective, preventive and its combination). Preventive maintenance is mostly performed according to time (vehicle is stopped – it does not transport, its technical state is defined, and necessary and planned replacements are done). Regarding primarily used techniques during maintenance management, several stages of its application may be noticed:

- First (fix the breakdown when it appears);
- Second (planning, introduction of system for planning and work control and introduction of information technology);
- Third (taking care of reliability and facilities for maintenance during projecting of motor vehicles, development and follow-up of the condition of maintenance equipment, elaboration of risk study, usage of expert systems and microcomputer network, application of methods for vehicle analysis from the aspect of failure occurrence – FTA, FMECA, planned experiment and introduction of flexible service systems).

In the area of motor vehicle maintenance, importance of application of the theory of reliability, from the 40s of the 19^{th} century, should be specially emphasized, esp. when it comes to defining regularity of breakdown appearance based on data about vehicle exploitation. Introduction of concept of integral logistic support and facilities of maintenance in the area of motor vehicle maintenance, during the 40s of the 19^{th} century, is also significant for the development of science and maintenance practice. Introducing previous mentioned scientific knowledge enabled introduction of the strategy of maintenance according to reliability and total productive maintenance in the 70s of the 19^{th} century.

Selection of maintenance procedures (preventive, corrective) that should be implemented during the motor vehicle maintenance, in order to provide their maximum reliability and disposability, is in literature often called conception of maintenance. Instead of term conception of maintenance, other terms are used as well: policy of maintenance, strategy of maintenance, system of maintenance. Nowadays many products are applied and their work is based on the fuzzy logic application.

It is performed in the field of forming fuzzy database, sample recognition, decision-making system, processing of native language, technology of development of fuzzy computers, fuzzy chips – fuzzy hardware, process and operation management in factories, realization of intelligent robots with the possibility to understand native language, understanding of scenes, with possibility to plan and control movement. It is performed in the field of usage of intelligent user's interface, cooperative work of people and robots, on adaptive fuzzy neuro systems, which can be adjusted to changeable conditions in the surrounding. Nowadays it is obvious that fuzzy logic can be applied in all fields of human performance.

Introduction of information system for easier acquisition and data processing during motor vehicle maintenance represents a great improvement in its maintenance system. It often occurs that objective conditions do not permit gathering of information necessary for statistic processing. If one bears in mind that gathering such information brings some expenditure, that is often a reason for impossibility to gather relevant information. In case when there are no high quality information, information that are incomplete and imprecise are used. It is a particular problem that is difficult to solve.

Application of knowledge-based system, so-called soft computing, enables efficient methods to treat the maintenance problem from the aspect of imprecision. One of such systems is fuzzy logic. Fuzzy logic is rarely used individually. Mostly its application is combined with neuro computing, genetic computing and expanding the possibility of expert systems. Application of fuzzy logic enabled many improvements, in large number of fields of human performance. Great possibilities of its application should be used in the systems of technical system maintenance. Objective of the work is a review of essence of classical and modern strategies of motor vehicle maintenance, with detailed review of fuzzy logic application during motor vehicle maintenance.

2. STRATEGIES OF MOTOR VEHICLE MAINTENANCE

At modern level of science and technology development, the greatest attention is dedicated to two strategies of maintenance 1 , and they are: maintenance according to reliability and total productive maintenance.

Methodology of maintenance according to reliability is based on modern scientific knowledge, mainly from the field of reliability and system science. Essence of this methodology is studying of vehicle behavior, mainly from the aspect of breakdown when used, with term and content adjustment of maintenance procedure. According to this methodology, maintenance is performed in view of recognition of reliability characteristics that are used for future state forecast, i.e. breakdown is foreseen. According to reliability characteristics of the vehicles, decisions about implementation of preventive maintenance are made (in order to prevent or postpone occurrence of sudden breakdown) and about procedure of corrective maintenance that is necessary to apply.

Main objectives of application of the methodology of maintenance according to reliability and safety of vehicles are:

- Providing reliability and safety of vehicles maintained on the level defined during development and production. When breakdown occurs, vehicle should be returned into primary level of reliability and safety.
- Gathering data about vehicle behaviour while used and taking over particular measures for improvement of its quality.

Previously mentioned objectives should be fulfilled with little costs (taking into account costs of maintenance and costs of occurrence of breakdown).

Application of methodology of total productive maintenance is based on the estimation of current condition of maintained vehicle. With application of this methodology it is provided to implement maintenance when it is necessary and not only when breakdown occurs, which resembles to the conception of preventive maintenance according to condition. In contrast to the conception of preventive maintenance according to condition, based on database of reliability, methodology of total productive maintenance is based on data from everyone who is in contact with the vehicle. For its application, it is necessary to have a domestic relation of experienced users towards to the vehicle. Implementation of this methodology does not exclude usage of reliability data, but it only insists on complete responsibility of all subjects that are in any way in contact with the vehicle.

During motor vehicle maintenance, the key problem is to avoid consequences of breakdown, but not prevent the occurrence of breakdown.

In existing literature from the field of maintenance, “advanced” strategies of maintenance are mentioned. By these strategies, it is tried to remove the flaws of other strategies. From these strategies, mostly are mentioned the following: PMO (Preventive Maintenance Optimization). Application of this strategy it is necessary to realize the following basic activities: defining of tasks of preventive maintenance; analysis of all breakdowns; analysis of consequences of arisen breakdown; definition of maintenance strategy. Objectives of application of this strategy are: rationalization of preventive maintenance procedure (implement only those that are appropriate and technically and economically justifiable, with optimization of periodic implementation); including equipment that enables maintenance according to condition; sharing of work on maintenance between maintainer and user.

Beside previously mentioned strategy, other strategies are mentioned in this group: statistic methods based on standard MILSTD2173 and method Cost Minimization Algorithm Program. It is envisaged 2 that in the future large application will have a so-called strategy of precise approach, based on removing of the cause of breakdown occurrence (if there is no cause for breakdown occurrence, breakdown will not happen), and then there is no need for maintenance. Such future is also envisaged for the strategy of total preventive maintenance (so that the vehicle itself implements adequate maintenance procedure).

3. PERFORMANCE INDICATORS OF THE VEHICLE MAINTENANCE SYSTEM

Nowadays it is spoken about successful system of motor vehicle maintenance if the following indicators are evident:

- Planned jobs in maintenance are much larger scale (over 90%), in relation to unplanned maintenance;
- Existing capacities for maintenance (equipment and personnel) are correctly engaged (usage of capacities is more than 70%);
- There is an optimum amount and assortment of spare parts and material in warehouse;
- Preventive maintenance is done when it is cheaper than corrective and without excluding exploitation vehicles;
- Planned activities of motor vehicle maintenance are done in due time;
- There is precise and accurate database necessary for realization of strategy of maintenance;
- Usage and maintenance of equipment is adequate;
- There is an adequate staff that participates in the realization of motor vehicle maintenance, with constant improvement of knowledge;
- There is maximum of people security that is involved in the realization of tasks of maintenance.
- Without usage of integral logistic support, esp. CMMS (Computerized Maintenance Management System), we cannot speak about possibility of application of modern strategies of motor vehicle maintenance.

Usage of information system for management of motor vehicle maintenance provides data necessary for application of modern strategy of maintenance. These data are useful for the realization of the following activities:

- Organization of maintenance jobs (type of jobs, plans, stop, costs, labor, equipment, material, spare parts, documentation);
- Labor arrangement (according to tasks, skill…);
- Realization of training, studying and giving instructions to staff working at motor vehicle maintenance;
- Generating of work order for realization of preventive maintenance, mainly in view of follow-up of all requirements for maintenance and given resources;
- Classification of maintenance tasks according to priorities, location...);
- Analysis of income and expenses;
- Selection of most suitable offer of spare parts and materials used for motor vehicle maintenance (owing to existing of data basis about manufacturers, quality and prices of spare parts and materials);
- Follow-up and analysis of breakdown of equipment used for maintenance;
- Realization of statistical analysis and data processing in order to acquire information that provide adequate management of maintenance;

- Increase of safety of personnel and equipment while motor vehicle maintenance;
- Follow-up of realization of taken obligations by adequate contracts about maintenance and realization of transport work.

According to acquired data by application of information system for maintenance management, analysis of adequacy of strategy for motor vehicle maintenance can be done (evaluation and defining of current problems when implemented).

Evaluation of the strategy for motor vehicles is done in view of responses to the following questions:

- Is preventive maintenance done in due time and what are the results of its realization?
- Are the plans and programs of preventive maintenance adequate (what is a relation between work on the realization of preventive and corrective maintenance, legality of appearance of corrective maintenance during time…)?
- For realization of which activities is most time spent?
- For realization of which activities of maintenance are most investments needed and what are the costs of maintenance?
- What is the scale of unrealized tasks of maintenance, esp. those that are taken over by contracts?
- What are the common problems in maintenance?

Information system for management of motor vehicle maintenance is satisfying if it does the following:

- Generates output documents in a useful way;
- Gives review of labor arrangement (according to tasks, skill…);
- Gives review of available equipment for motor vehicle maintenance (according to location, condition, belonging to organizational entireties, possibilities…);
- Gives review of available supplies (minimum and maximum level of supplies in parts, current condition in segments, locations);
- Gives work orders in a satisfactorily way;
- Analyze preventive maintenance procedure (needed resources);
- Gives feedback about effectiveness of done maintenance procedure and technical condition of motor vehicles.

In order to achieve maximum of effectiveness of usage of motor vehicles, in future there will be more attention given to their maintenance, both through improvement of maintenance system, and increased engagement of those who are involved in their development, production and exploitation.

Previously given activities may be expressed in a following way:

- Connection between manufacturer and user of equipment for maintenance with the manufacturers of motor vehicles;
- Application of adequate methodologies when defining strategy of motor vehicle maintenance, which shall give best results in given conditions;
- Application of adequate equipment for motor vehicle maintenance;
- Increase in implementation of IT in detection, diagnostics and foreseeing of breakdown (by usage of decision-making support system, expert's system, artificial intelligence….);
- Increased level of knowledge of all participants in motor vehicle maintenance;
- Application of strategy for motor vehicle maintenance without breakdown, primarily owing to removing cause of possible breakdown.

4. APPLICATION OF FUZZY LOGIC BY MOTOR VEHICLE MAINTENANCE

Words: indistinct, imprecise, undefined, indefinite, ambiguous, diffuse, vague, confused could be substituted by a single word.

It is a word fuzzy, which has an English origin. Professor of Computer Science at California University in Berkley, LoftiZadeh, is a founder of fuzzy logic.

He is considered to lay foundations for it in 1965. According to him, fuzzy logic can have two different meanings. In wider sense, fuzzy logic is a synonym for the theory of fuzzy groups, related to objects with vague borders measured by certain degree. In inner sense, fuzzy logic is a logic system that is an extension of classical logic. Essence of fuzzy logic is in many ways different from the essence of so-called traditional logic. Fuzzy logic uses the principle of incompatibility, which means tendency that with the increase of imprecision of statement it comes to its relevance. Fuzzy logic is multivalued logic that enables medium values defined between traditional opinions: true-false, yes-no, black-white etc. Fuzzy logic uses experiences of experts in the form of linguistic rules if-then, and mechanism of approximate reasoning is used as a control for definite case. Key aspect of application of fuzzy logic is development of theory which formalizes everyday informal opinion that can be used for computer programming.

In order to explain previously mentioned, we would shortly explain difference between fuzzy system and theory of possibility.

Those who do not recognize the essence and possibility of fuzzy logic application often ask the following question: “Can a process be controlled by using the vague method?” Where there was no perplexity about the answer to this question, fuzzy logic had turbulent development in almost all fields of human life. Nowadays, Japan is a leader in fuzzy logic application.

Fuzzy technology represents effort to imprecise information present and process by computer. That is a way to enable closer connection between man and computer. It enabled it to categorize to so-called humane technologies.

From Japan, by the professor from Tokyo Institute for Technology, Toshiro Terana, and professor from University for telecommunications in Osaka, KjodjiAsaia, there was an idea for broad usage of fuzzy logic as an engineer tool. Nowadays, fuzzy engineering has developed into a powerful scientific branch. In all segments of computing, fuzzy logic application is present today. Owing to its application, systems which use fuzzy technology within fuzzy database are realized, fuzzy systems for qualitative modeling, for fuzzy data analysis, fuzzy identification of system and data generalization, recognition of forms, fuzzy data analysis, fuzzy system for image process, development of intelligent interface and other computing fields.

Development of fuzzy idea is long-term, and its roots originate from far antique days, from Pluto and Aristotle. There are many famous persons, in a long chain of development of fuzzy idea, that contributed to the development of this idea, and on whose knowledge is based the learning of the founder of fuzzy logic and those who succeeded in implementation of its systems that have a base in fuzzy logic application. It is interesting that in that chain is the name of Verner Heisenberg, who defined the principle of uncertainty in 1927, and Max Black, who defined now called function of belonging in 1937. Professor Zadeh finally formulated theory of fuzzy logic, on which all developed systems are based. Basis of his theory is understanding that instead of rigorousness and tendency for greater precision of description and thinking about appearances, one should move in opposite direction, i.e. descriptions should be imprecise. Historical facts in development and application of fuzzy logic are also: development of first industrial fuzzy controller in London in 1974, first application of fuzzy controller for management of cement production in 1980. In 1987 began the work of first subway with fuzzy management. In 90s of the 19th century, many products whose work was based on application of fuzzy logic appeared on the market. Intensive work in this field was continued because of amazing results of application of fuzzy logic. It is about the field of forming intelligent users’ interface, cooperative work between people and robots, adaptive fuzzy neuro that can be adjusted to changeable conditions. Nowadays it is obvious that fuzzy logic may be applied in every field of human performance. Previously mentioned facts seem impressing.

If we wanted to tell something more about fuzzy logic shortly, we could tell the following: principle of humanity in engineering is necessity of application fuzzy engineering depends on how much engineer takes care about man when he develops each system. Principle of incompatibility is the more the realistic problem is viewed, the more its solution becomes fuzzy. Characteristics of fuzzy application, as a new approach to worlds are gradualness, imprecision, usage of qualitative description and expert's knowledge. Fuzzy technologies are humane technologies and represent relation between man and machine. Skill is received through practice, by learning and practicing. By using neuro technologies, training of computer systems can be done. By using fuzzy technologies expert's knowledge can be described and represented in a computer.

Advantages of application of fuzzy logic while maintenance of complex technical systems are:

a) Fuzzy logic is conceptually easy to understand, because its mathematical outline of fuzzy reasoning is simple;
b) Fuzzy logic is flexible – it is possible to correct analyzed system in each movement without need to return to start;
c) Fuzzy logic tolerates imprecise data, because it is based on existence of imprecise data;
d) Fuzzy logic may modulate linear functions, it is possible to create fuzzy system that may be adjusted to any set of input-output data;
e) Fuzzy logic may be used to describe expert's experience, for it leans on the experience of those who are excellent knowledge of analyzed system;
f) Fuzzy logic is based on native language, for its basis is human communication.

Common sense should be used while using fuzzy logic and apply it only then when it is possible to get effective solution – unless there is a simpler way to solve the set problem.

Classical logic uses phrases that are whether totally incorrect or completely correct. Fuzzy logic represents extension of classical logic. It actually represents multivalued logic. It means that phrase is with a definite level of correctness.

Group of elements with the *same* qualities is called classical - discreet group. It means that every element of discreet group belongs to that group 100%. Each element of discreet group belongs to that group with level from 1, on a scale from 0 to 1.

In fuzzy technologies, fuzzy group is a basic element for introduction and processing of imprecision. It represents extension and generalization of classical discreet group. That is actually a group of elements with similar qualities. Each element belongs to fuzzy group in a certain degree. By fuzzy function of belonging, level of belonging to some fuzzy group is described. With different levels of belonging, element can be placed in several groups. In that case, overlapping of intervals of confidence in those groups occurs. Input function of belonging can have discreet or continuating values. In continuating intervals of confidence, by means of parameters, function of belonging is defined. In the form of vectors, with definite number of parameters, discreet function of belonging is defined. In that case, it is necessary to specify range of confidence interval and level of each point.

Element of fuzzy group is each element in confidence interval with a definite degree of belonging. There are two questions while forming fuzzy groups: How many fuzzy groups are necessary and sufficient? How to choose definite function of belonging? Response to those questions is: by experience. Definite number of functions (false) of belonging can use program package Mat lab: triangular, trapezoid, linear, bell-like etc. In many cases standard functions of belonging are used: Z – type, - type (lambda), - type (pi), and S –

type. These functions are always normalized, so their maximum is always 1, and minimum 0. Since fuzzy groups are extension of classical groups, union, section or complement operational are used as modifiers of function of belonging. They are defined by operators. Union is defined by maximum operator, and section by minimum operator.

In fuzzy logic, linguistic objects are words, not numbers. Linguistic phrases represent relation between numeral representation of computer data and way of man's thinking .

For example, if variable quality of maintenance can have following values: good, bad, not bad, very good, more-less good, then the quality of maintenance is linguistic variable. In that case, good, bad, not bad, very good, more-less good are called values of linguistic variables or linguistic values. Also, more or less, similar phrases are called linguistic modifiers.

Group of rules where words describe solution to a problem is called base of rules or expert's rules. In order to easily understand, rules are written in adequate order.

Group of rules may be represented not only in form if-then, but in more compact presentation, in so-called relation form, or more compact in table linguistic form.

If input fuzzy variables are first input and second input, then this format is called linguistic fuzzy plan. Graphical format is used which shows curves of the functions of belonging (picture 1).

Mechanism of conclusion is a mechanism of approximate reasoning. It is a three-phase process: aggregation, activation and accumulation.

First step in solving some problem in fuzzy systems is fuzzification. It is a process that converts each numeral input data in a level of belonging, examining one or more functions of belonging. There is a level of belonging for each linguistic variable, applied on definite input size.

By aggregation there is a process of joining definite values of the function of belonging to the measured numerical value, that is, definition of confidence level (level of truth) of dome input numerical value has the belonging to given fuzzy group. Aggregation is equivalent to fuzzification when there is only one input. In every group, it can be realized with how much truthfulness each rule applies.

Activation is a conclusion made in a part of rule. It is actually deduction of conclusion. As an activated operator min or algebra product is used, mostly used methods of direct conclusion – Mamdani's methods. At those forms of conclusion, only true premises are taken into account. By application of these methods, fuzzy groups are in input and output. Takagi-Sugeno-Kang method does not differ from other methods of direct concluding, but there is a great difference in structure of fuzzy rules. There is a difference that in conclusion instead of fuzzy groups there is a linear function between input and output, Often used case is when linear coefficients are equal to zero and then function of belonging is known as singleton.

Accumulation consists of activating of conclusion that is accumulated by addition. As an accumulative operator max or algebra total is used. By approximate reasoning (e.g. min-max), it is necessary to emphasize which method is used.

During defuzzification, resulting fuzzy group converts into number. The following methods of defuzzification are used: 1. COG - Centre of gravity or COA - centriod of area. Output numeral value is abscise of the center of gravity of fuzzy group; 2. COGS - Centre of gravity method for singletons.This method has a relatively good computer complexity, and is differentiable in relation to singleton, which is useful in neurofuzzy systems; 3. BOA - Bisector of area; 4. MOM - Mean of maximum. Searching for the point which has max belonging is basis of intuitive access. If there are few maximums, then we search for the mean of maximum. This method disregards form of fuzzy group, but its computer complexity is good. It is often used in problems of recognition forms and classification; 5. LM - Leftmost maximum is greatest on RM - Rightmost maximum.

Next possibility is selection of largest maximum on right or left side. In case of robot movement management, it must be chosen between left and right, in order to avoid obstruct in front of him. Defuzzificator must choose one or other, and not something between. This method is indifferent to form of fuzzy group, but its computer complexity is small.

Fuzzy reasoning does not insist on sophisticated techniques of defuzzification. It requires great flexibility while forming rules, which is not a case when applied in automatic management, that is, in fuzzy control.

This analysis is done in order to see the influence of selection of function of belonging and its order, on output, or group of possible solutions. Two-dimensional table is caused by two inputs and one output. It can be drafted as a surface suitable for visual examination. Relation between one input and one output can be drafted as a graph of function. Graphs help when selecting functions of belonging and forming of rules. Surface form may be controlled to a certain degree by functions of belonging.

Fuzzy controller is a central part of configuration for management of motor vehicle. Fuzzy controller can be realized by program that is performed on PC and is connected to the process in a usual way, as in classical management. In that case, fuzzy controller is used for intelligent management, so that the knowledge of expert-operator is used in management. When it is necessary, fuzzy controller can be built as a microprocessor in smaller devices.

Possibilities of application of fuzzy logic are enormous. Let us mention some of examples of application of fuzzy controller on motor vehicles in Japan and Korea, countries that are leaders in practical application of fuzzy technologies.

Fuzzy brakes (Nissan): manages breaks in dangerous situations in view of speed and acceleration of vehicles, and in view of speed and acceleration of wheels.

Engine of the car (NOK, Nissan): manages fuel injection and ignition depending on condition of valve for fuel supply, oxygen flow, temperature of cooling water, number of rotationper minute, fuel volume, crankshaft, vibration of motor and pressure in absorb branch.

Transition system in car (Honda, Nisan, Subaru): selection of level of transition depending on motor pressure, way of driving and road conditions.

Management of vehicle movement (Isuzu, Nissan, Mitsubishi): adjust valve for fuel supply in view of speed and acceleration of vehicle.

Beside given examples of application of fuzzy management, there is also a large number of fuzzy management systems used on motor vehicle. Also, beside large application on motor vehicles, fuzzy controllers have found great implementation in medicine (diagnosis of illness), traffic (management of crossroads), house devices etc.

5. CONCLUSION

Two types of preventive maintenance are mostly used. First is preventive maintenance based on reliability information (on empirically defined distribution of possibility of work time until breakdown). By application of this type of preventive maintenance, maintenance procedure is planned in order to provide required level of reliability, most often by preventive replacements after a definite work periodicity. Other type of preventive maintenance is based on connection of information about reliability and information acquired in view of constant and systematic follow-up of vehicle (follow-up of selected parameters and indicators that with enough security show its condition).

Strategy of total productive maintenance is based on statement that only by maintenance it is not possible to maintain projected level of reliability during exploitation, but it is necessary to have active participation of users and everyone who is in relation to the maintained vehicle.

Main application of so-called accelerated strategies of maintenance is not to conduct any activity of preventive maintenance if it is not economically justifiable.

Nowadays there is a tendency towards combined application of existing strategies of maintenance. The reason is placed in variety of maintained vehicles. Second reason is existence of flaws of current strategy for maintenance.

Fuzzy logic application enables large advantage in many human activities. Large possibility of its application is to use in the systems of motor vehicle maintenance.

Aim of the work is a review, in the briefest form, of fuzzy logic base, some causes of uncertainty in the systems of motor vehicle maintenance and possibility of its application by maintenance.

In order to achieve maximum effectiveness of usage of motor vehicles, in future more attention will be given to their maintenance, both through improvement of maintenance system and increased engagement of those who participate in its development, production and exploitation.

Without integral logistic support, esp. information systems for management of maintenance, we cannot speak about possibility to apply modern strategy for vehicle maintenance.

By application of knowledge based system, or so-called soft computing, we come to efficient methods used for treatment of problems while maintenance of technical systems, from the aspect of imprecision. One of such systems is fuzzy logic. Fuzzy logic is rarely used individually. Mostly its application is combined with neuro computing, genetic computing and expanding the possibility of expert systems.

Application of fuzzy logic enabled many improvements, in large number of fields of human performance. Great possibilities of its application should be used in the systems of technical system maintenance.

Geometric model of management of process of preventive maintenance by fuzzy logic, which essence is showed in this work, should enable: defining of parameters in uncertainty of work of technical system; defining influence of specific parameters on the process of preventive maintenance of technical system; defining most influential parameter and order of activities that should be done, as defining moment to start preventive maintenance. Procedure of forming geometric model should be defined by maintenance manager, who is in authority of decision making about preventive maintenance of technical system.

Application of fuzzy logic during maintenance of technical system is justifiable by the fact that the model of maintenance is complex, esp. if it is taken into account that description of maintenance problem includes work and breakdown condition and also mid condition. By its application, we are closer to the goal of acquiring maximum readiness, effectiveness and minimal costs.

Essence of traditional and modern strategy of motor vehicle maintenance is analyzed. Special attention is given to modern strategy of motor vehicle maintenance.

REFERENCES

[1] R. Babuška: *Fuzzy and neural control*, Delft University of Technology, Netherlands, 2001.

[2] B. Krstić: Analysis of the vital parts of the engine vehicles on the base of the data from exploitation, *VII International scientific conference, Simulation Research in Automotive Engineering*, Lublin, Polska, 1999.

[3] B. Krstić: Determination of the optimal strategy for preventive maintenance the motor engine using policriterion optimization, International Journal for Vehicle Mechanics, Engines and Transportation Systems, Mobility Vehicles Mechanics, Vol. 29, No. 4, pp. 15-24, 2003.

[4] B. Krstić: Determination of the optimal strategy for preventive maintenance of the clutch motor vehicles using polycriterion optimization, *Third International Tribology Conference ITC 2004*, Z. Gora, Poland, 2004.

[5] B. Krstić: Analysis of the reliability of the motor vehicle brakes bands and

determination the optimal periodicity for their preventive maintenance, International Tribology Conference CONAT 2004, Brasov, 2004.

[6] BS5760 *British Standard - Part 2 Guide to the assessment of reliability, Reliability of systems, equipment and components*, 1981.

Tribology of Manufacturing Processes

16th International Conference on Tribology – SERBIATRIB '19

15 – 17 May 2019, Kragujevac, Serbia

Serbian Tribology Society

SERBIATRIB '19

16th International Conference on Tribology

Faculty of Engineering University of Kragujevac

Kragujevac, Serbia, 15 – 17 May 2019

THE POSSIBILITIES FOR APPLICATION OF NUMERICAL SIMULATION IN THE IRONING PROCESS OF THIN SHEETS

Milan T. ĐORĐEVIĆ[1*], Srbislav ALEKSANDROVIĆ[2], Vukić LAZIĆ[3], Dušan ARSIĆ[4], Aleksandar TODIĆ[5], Aleksandra PATARIĆ[6]

[1]Faculty of Technical Sciences University of Pristina, Kosovska Mitrovica, e-mail: milan.t.djordjevic@pr.ac.rs

[2]Faculty of Engineering University of Kragujevac, Kragujevac, e-mail: srba@kg.ac.rs

[3]Faculty of Engineering University of Kragujevac, Kragujevac, e-mail: vlazic@kg.ac.rs

[4]Faculty of Engineering University of Kragujevac, Kragujevac, e-mail: dusan.arsic@fink.rs

[5]Faculty of Technical Sciences University of Pristina, Kosovska Mitrovica, e-mail: aleksandar.todic@pr.ac.rs

[6]Institute for Technology of Nuclear and Other Mineral Raw Materials, Belgrade, e-mail: a.pataric@itnms.ac.rs

*Corresponding author: Milan T. Đorđević, e-mail (milan.t.djordjevic@pr.ac.rs)

Abstract: *In this research, results of experimental investigations and physical model were used as the input variables for numerical analysis of the ironing strip drawing process by application of lubricants. The numerical simulation was realized in the specialized applicative software Simufact.forming. By applying the software for the 3D modeling, a model of the tool element assembly was made, which served as the starting basis for numerical simulation by application of the Finite Element Method. Experimental values of the friction coefficient for each type of lubricants and the contact pressures were used for defining the contact conditions. Numerical simulation of the drawing process was done for each type of the contact conditions between the tool's elements and the thin sheet sample. After conducted tests comparison of experimental and numerical results of the drawing forces in different contact conditions was done. Comparison was done with taking into account appearance of galling due to difficult drawing process conditions. By comparation of numerical results to the experimental one it is possible to interpret what types of simplifications were adopted in creating the experimental physical-tribological model.*

Keywords: *strip drawing, ironing process, drawing force, numerical analysis.*

1. INTRODUCTION

Simulation of the production processes is applied in early design phases of both the new products and tools for their manufacturing [1]. Significant financial savings are realized and delays in products placing on the market are avoided by application of the physical and numerical modeling. Software, based on the Finite Element Method is used widely for optimization of the process parameters, eliminating the flaws during the material flowing, determination and minimizing the stresses in the tool, etc. Material's behavior during the forming process can be completely predicted by application of the corresponding software in the stress-strain analysis [2-4]. Analysis and simulation of the real processes can be done on cold and hot, by correction of tolerances between the die and the drawing tool, what directly influences the thin sheet thickness during the forming [5]. In that way, the higher degrees of drawing can be achieved without the appearance of destruction. Similarly, simulation results should lead to optimization of the process, so that fast and efficient reaction to market needs would be achieved [6]. Paper [7] also study the ironing of austenitic stainless steel cups by real experiment and FEM analysis. Aim of paper was to quantify the discrepancy (due to tool deformation) between nominal die–punch gap and real final wall thickness. As a result, the states of stress in the cup wall during and after drawing obtained by FEM are compared with results obtained by the analytical model. Since in processes of this kind the friction has the strong influence, in paper [8] is presented in details the procedure for determination of the friction coefficient between the tool and the thin sheet during the strip drawing process. Since the objective is to achieve resistance as least as possible, and by that the deformation forces in the ironing process, in paper [9] is presented an analysis of lubricants that are used in the multi-phase ironing process. It was concluded that the new group of ecological lubricants possesses somewhat better lubricating properties with respect to conventional lubricants (the zinc-phosphate layer, oil for deep drawing, etc.).

Within the experimental part of this work, the special attention was paid to lubricants that are used in the ironing process and to modern ecological lubricants [9]. The schematic is presented of the adopted physical model, as well as the used equipment, applied lubricants and the experimental results. They are used, together with the physical model, as the input variables for the numerical analysis of the strip deep drawing. The Finite Element Method simulation was done by the Simufact.forming software. Experimental values of the friction coefficient were used for definition of the contact conditions.

2. EXPERIMENTAL EQUIPMENT, PHYSICAL AND NUMERICAL MODEL

A special device that models the symmetrical contact between the thin sheet and the die in strip deep drawing was constructed for experimental investigations in this work, Figure 1, [10, 11].

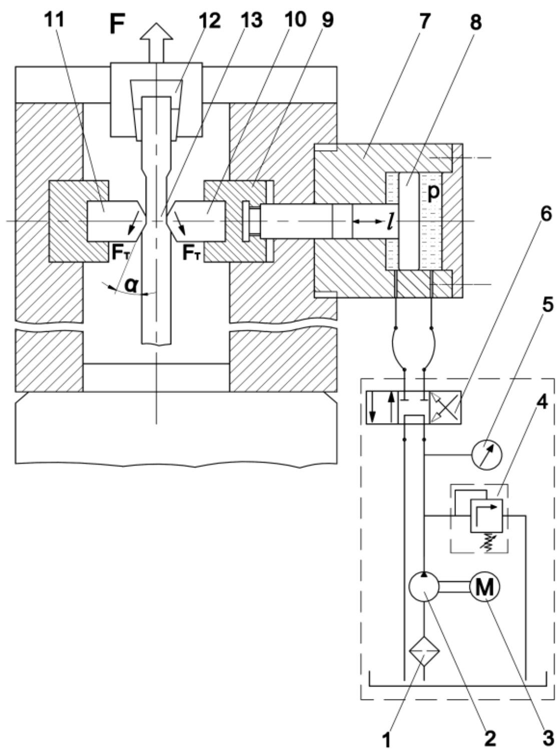

Figure 1. Block scheme of the experimental apparatus: 1-Filter, 2-Pump, 3-Driving motor, 4-Irreversible valve, 5-Manometer, 6-Two-position distributer, 7-Cylinder, 8-Piston of cylinder, 9-Holder with the T-groove, 10 and 11- Ironing die elements, 12-Jaws for sample camping, 13-Sample

The sheet strip is being placed into the clamping jaws 12 (Figure 1). The jaws with the sample are moving from the bottom upwards, by the holder of the mechanical part of the apparatus. The sample is being acted upon by the side elements 10 and 11, which simulate the die and perform the thinning. The moving sliding element 10 is placed into the holder with the T-groove 9, which is moving with the piston 8 of the hydro-cylinder 7. The sliding element 11 is fixed. Registering of the drawing force, during the drawing process, is done by the corresponding measurement chain at the total length of 40 mm.

2.1 Physical model

The physical model, used in this experiment, was realized based on previous research [10]. The applied model enables realization of high contact pressures.

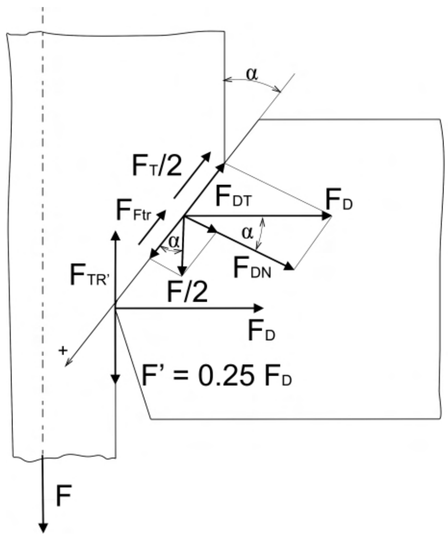

Figure 2. Tribological model-schematic of the forces' actions

The idea for realization of this experimental device was to determine the friction coefficient at the contact surface between the sliding elements and the sample (Fig. 2).

Calculation of the friction coefficient requires analysis of the forces that are acting at the inclined contact surface, as well as at the input portion of the sliding element (Fig. 2) [11]. The model is adjusted to the real process conditions by taking into account the friction forces (F_{TR}' and F'= $0.25 \cdot F_D$, Fig. 2b). Based on the scheme of the forces action (Fig. 2), one can compose the equilibrium equation. By solving equilibrium equation for one obtains the formula for the friction coefficient:

$$\frac{F \quad 2\ F_D \quad 0.25 \quad 2\ tg}{4\ F_D \quad F\ \ tg}. \qquad (1)$$

The mean values for friction coefficient for each type of lubricants and the compressive force, obtained by application of formula (1).

2.2 Numerical model

To be able to perform the simulation of a certain process of plastic forming, it is necessary to enter some input variables into the software for numerical simulation. Primarily, it is necessary to create the 3D model in the corresponding CAD software and adjust its format to formats offered by the numerical simulation software. Besides that, one needs to define the contact conditions between the sliding elements and the thin sheet strip, what was realized by entering the experimental values of the friction coefficient for each type of lubricant and each value of the sliding elements compressive force from Table 1 into the numerical simulation program.

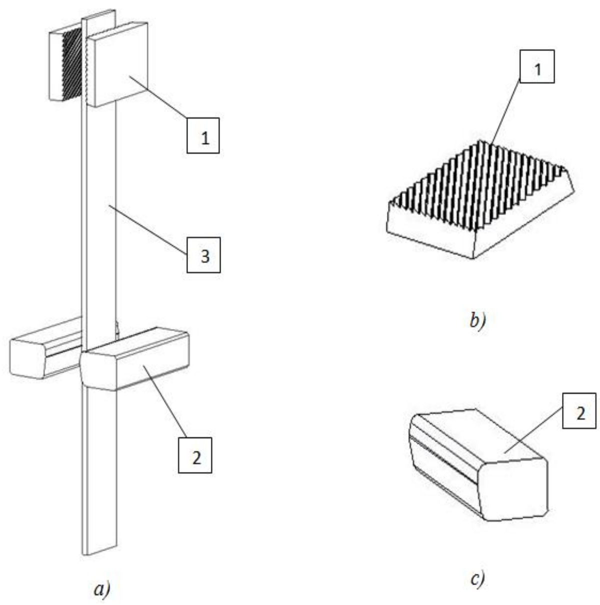

Figure 3. Numerical model after creating in the CAD program: 1-Clamping jaws, 2-ironing die elements, 3-thin sheet sample (DC04)

Table 1. Friction coefficient values for three values of compressive forces and four types lubricants

	Lubricant type	Compressive force, kN		
		10	**15**	**20**
Friction coefficient μ	L1 – The zinc-phosphate coating with oil	0.149	0.168	0.175
	L2 – Ecological single bath lubricant	0.132	0.144	0.154
	L3 – Grease based on MoS_2	0.153	0.160	0.164
	L4 – Oil for deep drawing	0.179	0.190	0.199

For this research case, the 3D CAD model was created in the 3D programming package CATIA V5 R18, while the numerical simulation was done in the specialized software for the plastic forming simulation Simufact.forming 2.1. The 3D model (Fig. 3) was created based on dimensions of real tools that are included in the process of strip drawing between the sliding elements according to the scheme shown in Fig. 2. The model was realized as the assembly consisting of the sliding elements, clamping platelets and the steel thin sheet strip DC04.

3. RESULTS

Within results of this physical-numerical experiment, the drawing forces, obtained in physical experiment were compared to forces obtained by numerical simulation. Diagrams of drawing forces obtained by physical experiment are presented first, Figs. 4 and 5. The obtained values of the drawing forces in the strip drawing process are different for all the types of lubricants and values of the compressive forces of the sliding elements. The largest values of the drawing forces were realized for the case of lubricant L4 (oil for deep drawing, Table 1) and L1 (phosphate layer with oil, Table 1) (Figs. 4a and 5a, respectively). Consequence of such large values is difficult contact conditions in applications of those lubricants, especially for drawing forces values of 15 kN and 20 kN (Fig. 4a). Besides that, the appearance of galling on the tool's sliders was noticed for those experimental conditions, what is a consequence of difficult sliding between the contact surfaces. That phenomenon directly causes increase of the drawing forces, especially for lubricant L4.

The lowest values of drawing forces were obtained in the case of single stage experiment of the new ecological lubricant L2, denoted as FL741 and lubricant L3 which represents oil based on MoS_2 (Figures 4b and 5b, respectively). Comparing to values of the drawing forces for other lubricants, one can conclude that the L2 lubricant exhibits the best lubricating properties, what is especially prominent in friction coefficient values (Table 1). Considering the drawing forces diagrams for various types of lubricants it could be assumed that the L2 lubricant has better properties than the conventional ones.

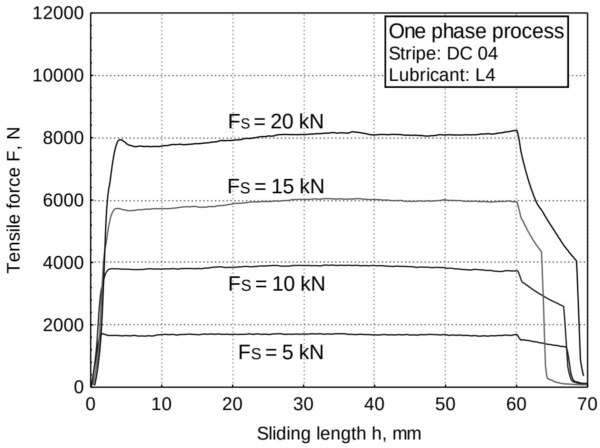

a)

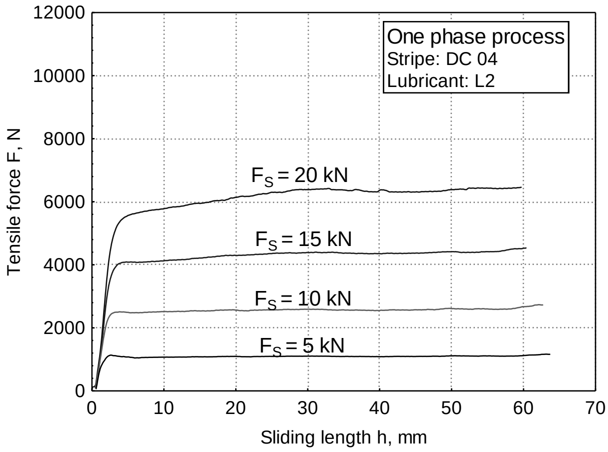

b)

Figure 4. Comparative presentation of drawing forces in experimental testing of lubricants: L4 (deep drawing oil); b) L2 (ecological lubricant)

Results of numerical analysis are in agreement with results of the physical experiment, to the great extent. This is the best illustrated for lubricant L4 where the highest values of the drawing forces were registered (Fig. 6a). Appearance of galling which was registered in physical experiment (lubricant L4) is manifested in numerical results by the high values of the drawing forces, especially at compressive forces of 15 kN and 20 kN. With increasing compressive force the appearance of galling is more prominent, since the squeezing of lubricant from the contact zone occurs.

The good correlation of experimental and numerical results was especially realized at higher values of the compressive forces of the sliding elements of 15 kN and 20 kN, for numerical experiments 15L1, 15L2, 15L3, 15L4, 20L2, 20L3.

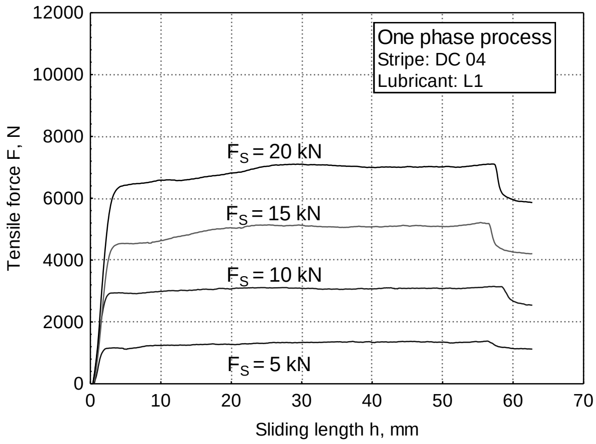

a)

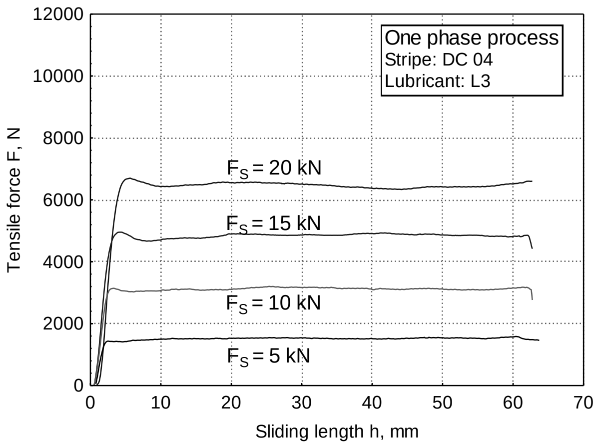

b)

Figure 5. Comparative presentation of drawing forces in experimental testing of lubricants: a) L1 (phosphate layer with oil); b) L3 (grease based on MoS_2)

The average value of the drawing force obtained by numerical experiment 15L1 was approximately 5 kN (Fig. 7a), while the drawing force obtained experimentally had the average value of about 5.1 kN, what can be noticed on diagram in Fig. 5a. Matching of drawing forces values obtained numerically and experimentally, was realized for numerical experiment 15L3. There, the average value of the drawing force obtained by numerical simulation was 4.96 kN (Fig. 6a), while experimental drawing force has negligibly lower value of 4.9 k N (Fig. 5b).

For numerical experiment 15L4, drawing forces have somewhat lower value of 5.85 kN (Fig. 6a) with respect to experimentally obtained value of 6.0 kN (Fig. 4a). Somewhat larger discrepancies between numerical and experimental results was noticed in the case of 15L2, where numerical simulation gave the average value of the drawing force of approximately 4.7 kN, while experimentally the value of about 4.2 N was obtained (Fig. 4b). This discrepancy can be ascribed to the error in the measurement chain during the drawing force recording in the physical experiment. Results of average values of drawing forces, obtained for the compressive force of the slider of 20 kN, are presented in Table 2.

Table 2. Average value of drawing forces for the force of 20kN

Experiment	Num.value, kN	Fig	Exp.value, kN	Fig
20L1	6.7	7a	6.85	5a
20L2	6.1	6b	6.2	4b
20L3	6.4	7b	6.5	5b
20L4	6.85	6a	8.05	4a

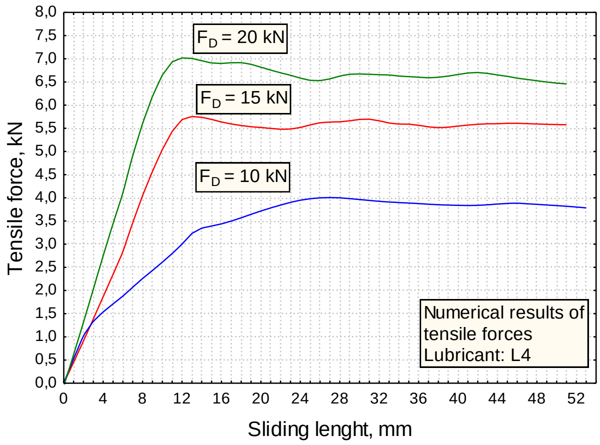

a)

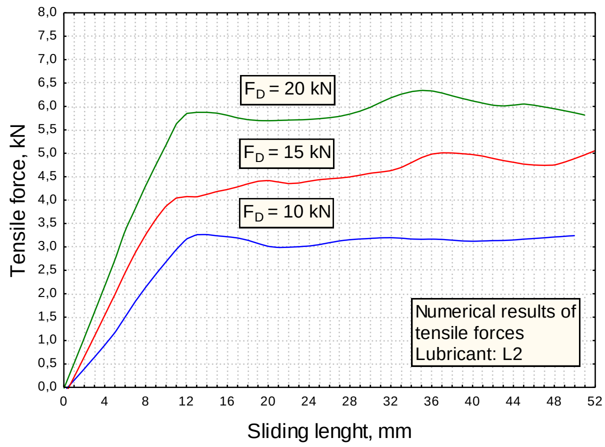

b)

Figure 6. Comparative presentation of the drawing forces obtained by numerical simulation of lubricants' applications. a) L4 (oil for deep drawing); b) L2 (ecological lubricant)

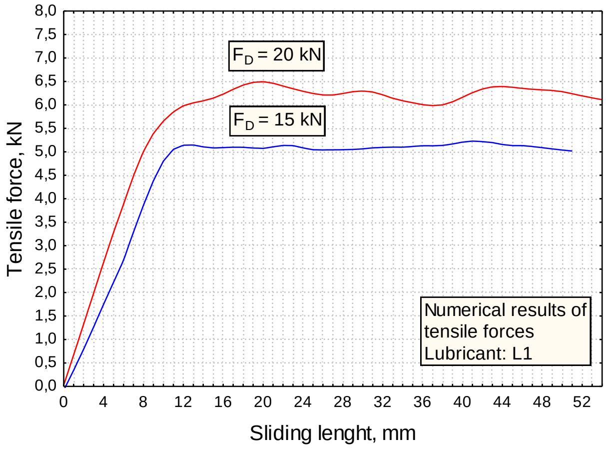

a)

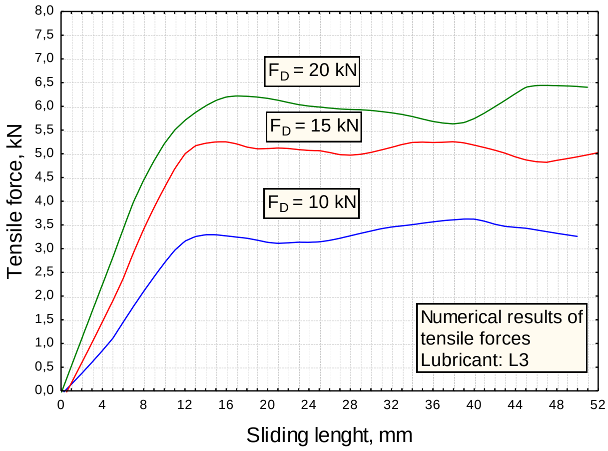

b)

Figure 7. Comparative presentation of the drawing forces obtained by numerical simulation of lubricants' applications. a) L1 (phosphate layer with oil); b) L3 (grease based on MoS_2)

Numerical and experimental results of average values of the drawing forces for experiments 20L1, 20L2 and 20L3 mainly have the similar values, so it could be concluded that there exist high correlation of the experimental and numerical results, what verifies that the numerical model was properly created. The only greater discrepancy between the experimentally and numerically obtained values of the drawing forces was for experiment 20L4. The high value of the drawing force of 8050 N (Fig. 4a) obtained in physical experiment is the consequence of difficult conditions for the sample sliding between the sliders, due to appearance of galling on sliders. That phenomenon results in very high friction coefficient due to worsen lubricating properties of lubricant L4. Subsequently, the drawing force must be greater to overcome the sliding resistance.

Influence of the contact conditions between the thin sheet strip and the sliding elements can be also monitored via the distribution of the effective stress (Figs. 8 and 9). Increasing of the compressive force of the sliding elements (10 and 20 kN) causes increase of stresses within the thin sheet strip, what is to be expected. Besides that, it is important to monitor the change of stresses for various lubricants for the same compressive force.

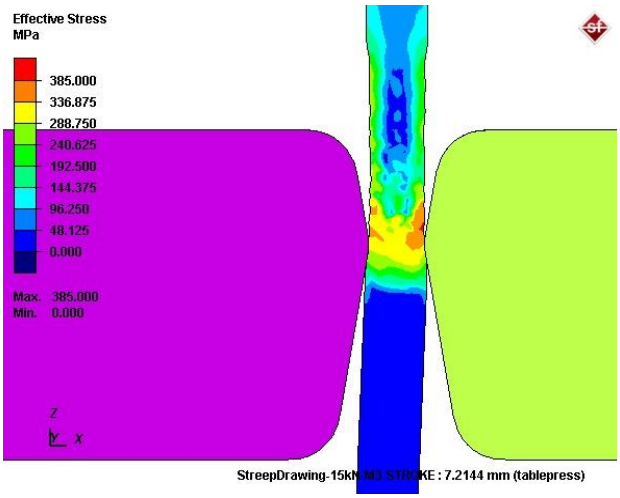

a)

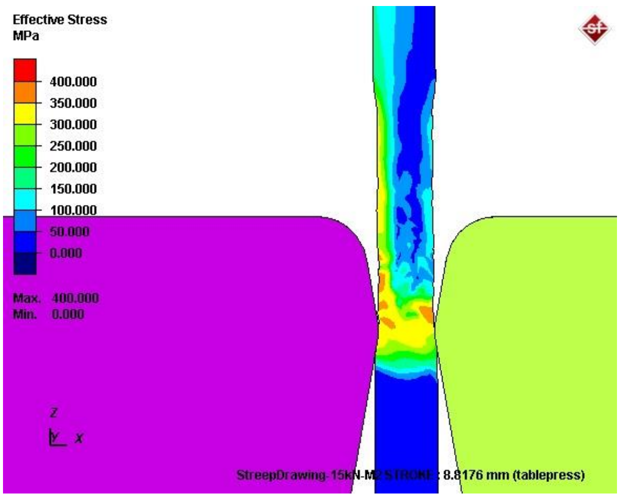

b)

Figure 8. Effective stress distribution in the thin sheet strip at compressive force of 15 kN for lubricants a) L2; b) L4

For the compressive force of 15 kN and lubricant L2 the maximum effective stress in the thin sheet strip amounts to 385 MPa (Figure 8a), while for the lubricant L4 it amounts to 400 MPa (Figure 8b). Increasing of the compressive force to 15 kN causes increase of the effective stresses. In this case, as well, the effective stresses values are lower for the lubricant L2

(410 MPa, Fig. 9a) with respect to lubricant L4 (435 MPa, Fig. 9b).

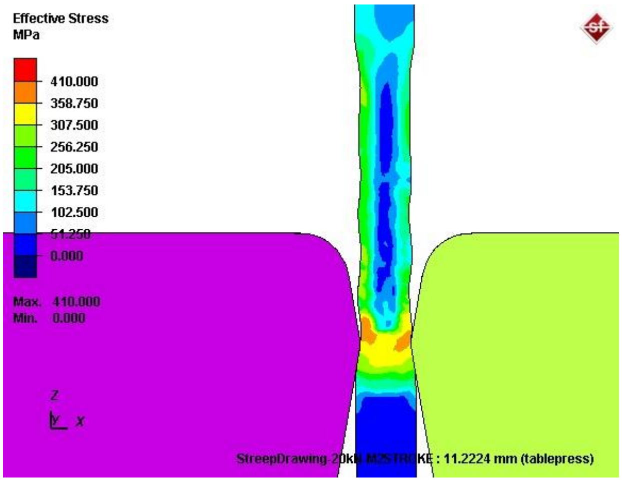

a)

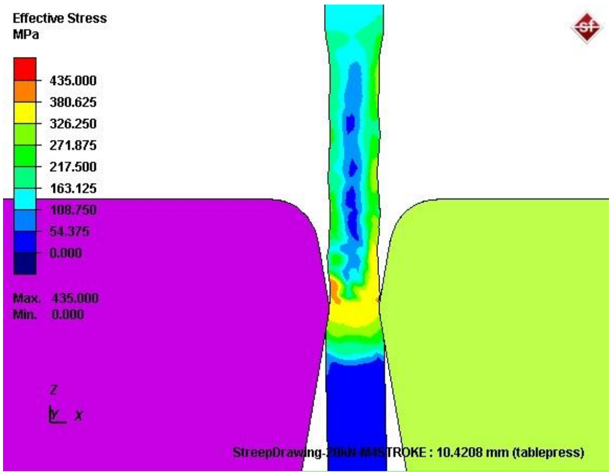

b)

Figure 9. Effective stress distribution in the thin sheet strip at compressive force of 20 kN for lubricants a) L2; b) L4

Increase of stresses, for the same value of the compressive force, is explained by the contact conditions between the sliding elements and the strip during the drawing process. For the lubricant L4 case, sliding is difficult because of worse lubricating conditions, squeezing of lubricant out of the contact zone and appearance of micro galling. Worse lubricating conditions with lubricant are being manifested by increase of the drawing force due to more difficult sliding between the contact elements, as it was already emphasized earlier (Figures 4a and 6a). The properties of lubricant L2, could be considered as very good, what is especially reflected in low values of the friction coefficient, drawing force, stress distribution in the material and absence of appearance of galling on the contact surfaces of the sliding elements.

4. CONCLUSION

In this paper are united two research approaches, physical modeling, realized by the laboratory experiment, and numerical simulation of the ironing drawing process. By analyzing the obtained results, one can say that the technique of physical modeling with help of the laboratory equipment and numerical simulation by application of the FEM can be successfully used in studying the thin sheet ironing strip drawing process.

The conclusions of these investigations can be summarized in following:

a) Physical experiment is necessary to define the precise input data for numerical analysis. In that way, it is possible to create the numerical model based on experimentally obtained values of the friction coefficient, real tool and working piece geometry, values of the compressive force of the tool elements that provide for thinning.
b) As a result of numerical simulation, the distributions of the effective stresses in the strip material were obtained, as well as values of the drawing (deformation) forces.
c) It is significant to compare values of the deformation forces obtained by physical experiment to values obtained by the numerical simulation. In that way, it is possible to compare applied contact conditions (lubricants) and estimate coincidence of experimentally and numerically obtained values of the deformation forces.
d) Analysis of stresses in the working piece wall, during the thin sheet strip drawing, requires precise values of the friction coefficient.

ACKNOWLEDGEMENT

The work reported in this paper was partially supported by the Serbian Ministry of Education, Science and Technological development, through contract TR34002.

REFERENCES

[1] D. Adamović, V. Mandić, M. Živković, Z. Gulišija, M. Stefanović, M. Topalović,

S. Aleksandrović: Numerical modelling of ironing process in tribology, Journal for technology and plasticity, Vol. 38, No. 2, pp. 109-123, 2013.

[2] S. K. Singh, V. Kumar, P. P. Reddy, A. K. Gupta: Finite element simulation of ironing process under warm conditions, Journal of Materials Processing Technology, Vol. 3, No. 1, pp. 71-78, 2014.

[3] D. M. Neto, M. C. Oliveira, J. L. Alves, L. F. Menezes: Influence of the plastic anisotropy modeling in the reverse deep drawing process simulation, Materials and Design, Vol. 60, pp. 368-379, 2014.

[4] T. Pepelnjak, G. Gantar, K. Kuzman: Numerical simulations in optimization of product and forming process, Journal of Materials Processing Technology, Vol. 115, pp. 122-126. 2001.

[5] Abdullah A. Dhaiban, M.-Emad S. Soliman, M. G. El-Sebaie: Finite element modeling and experimental results of brass elliptic cups using a new deep drawing process through conical dies, Journal of Materials Processing Technology, Vol. 214, pp. 828-838, 2014.

[6] M. Vrh, M. Halilovic, B. Starman, B. Stok, D. S. Comsa, D. Banabic: Capability of the BBC2008 yield criterion in predicting the earing profile in cup deep drawing simulations, European Journal of Mechanics A/Solids, Vol. 45, pp. 59-74, 2014.

[7] D. Delarbre, P. Montmitonnet: Experimental and numerical study of the ironing of stainless steel cups, Journal of Materials Processing Technology, Vol. 91, pp. 95-104, 1999.

[8] S. Aleksandrović, M. Djordjević, M. Stefanović, V. Lazić, D. Adamović, D. Arsić: Different ways of friction coefficient determination in stripe ironing test, Tribology in industry, Vol. 36, No. 3, pp. 293-299, 2014.

[9] M. Djordjević, S. Aleksandrović, V. Lazić, M. Stefanović, R. Nikolić, D. Arsić: Experimental analysis of influence of different lubricants types on the multi-phase ironing process, Materials Engineering, Vol. 20, No 3, pp. 147-152, 2013.

[10] M. Djordjević, V. Mandić, S. Aleksandrović, V. Lazić, D. Arsić: Experimental-numerical analysis of contact conditions influence on the ironing strip drawing process, Industrial lubrication and technology, Vol. 69, No. 4, pp. 464-470, 2017.

[11] P. Deneuville, R. Lecot: The study of friction in ironing process by physical and numerical modeling, Journal of Materials Processing Technology, Vol. 45, pp. 625-630, 1994.

Serbian Tribology Society

SERBIATRIB '19

16th International Conference on Tribology

Faculty of Engineering University of Kragujevac

Kragujevac, Serbia, 15 – 17 May 2019

EXPERIMENTAL STUDY ON THE FRICTION CHARACTERISTICS OF COTTON FABRICS WITH CLOTH TWILL 3/1 BEFORE AND AFTER FINISHING

Rayka CHINGOVA[1], Lyudmila TANEVA[2], Umme KAPANYK[3]

[1]South-West University "Neofit Rilski" - Blagoevgrad, Bulgaria, e-mail: raikach@abv.bg

[2]South-West University "Neofit Rilski" - Blagoevgrad, Bulgaria, e-mail: lusi_t@abv.bg

[3]South-West University "Neofit Rilski" - Blagoevgrad, Bulgaria, e-mail: umi12@abv.bg

Abstract: *This research shows some of the functional characteristics of the cotton fabrics all in the same cloth twill 3/1 in different direction of the cloth and under different pressure. The measurements are conducted according to the standard BDS EN ISO 8295:2006 using -meter MXD-02 made by Labthink, China. The tester allows the determination of the static and the dynamic coefficients of friction (COF). The tests are performed for both fabric sides (face and reverse), in different fabric directions, and under different pressure (200, 300 and 400 g). The speed of sliding has been constant -100 mm/min. Formulas for frictional characteristics specialized for fabrics have been used for the precise determination of the fraction behavior of the textile products – friction index n, friction parameter C and friction factor R. The connection between the friction force and the normal pressure is transformed to logarithmic relation:*

$$\frac{F_i}{B} \quad C.\ \frac{N_i}{B}^{\,n} \qquad \log\frac{F_i}{B} \quad \log C \quad n.\log\frac{N_i}{B}$$

i=1, 2,…m; B – contact area (m^2); C – friction parameter [Pa^{1-n}]; n – friction index (without dimension); N – normal pressure [N]; F – friction force [N]; m – number of conducted examinations.

The friction index n and the friction parameter C are calculated from the coefficients of the linear regression equation. The friction parameter and the friction index are used for the determination of the friction factor R.

Conducted examinations show the influence of the pressure on the friction characteristics of fabrics with the same composition (cotton), but made from yarns with different linear densities. The values of the friction characteristics depend also on the changing of the actual contact area which varies in the different fabric directions. The actual contact area is growing with the increase of the pressure that leads to the increase of the coefficient of friction in neutral state (at rest) and the coefficient of friction when sliding.

Keywords: *cotton fabric, friction, friction characteristics*

1. INTRODUCTION

Friction in weaves is defined as the resistance a weave encounters when changing its position relative to another solid body which touches it. Textile friction occurs between two or more textile surface areas, between a textile surface area and metal parts of sewing machines or cutting machines, ironing irons, as well as the human body, friction of upholstery furniture and furniture without upholstery, etc.

The subjective feeling of rubbing weaves between the thumb and forefinger of a person is called touch. This feeling is mainly related to the mechanical interaction between clothing and the human body. Human fingers are a sensitive tool for detecting small differences in friction of weaves.

In the field of sewing technology, friction occurs when the fabrics are cut, multi-layered cutting and subsequent separation, friction occurs when sewing clothing with metal sewing machine parts, packing and storing ready-made garments, etc. The friction of cloth on the same cloth, fabric on another cloth, or cloth on hard objects has a significant effect on its qualities such as wear and tear, as well as consumer comfort.

Cotton fabrics are the most commonly used ones. The reason for this is their special quality - it regulates the body heat, it does not cause allergies, it absorbs sweat from the body, etc. Cotton fabrics are strong and with low elasticity, resistant to bases, highly resistant to organic solvents, almost insect-free, etc. For the production of denim clothing, cotton fabrics with twill twill 3/1 are mainly used. Technological trends have been imposed on sewing raw cloth clothing and subsequent finishing operations to respond to fashion trends in cowboy fashion. Separately, readymade denim clothing is made of raw denim clothing.

2. MAIN HEADING

The study for the here presented work was carried out with 100% cotton (P) fabrics, with 3/1 cloth twill. Textiles tested have different characteristics. They are produced in "Strumatex" Textile Works - Blagoevgrad. Their parameters are shown in Table 1a and Table 1b. In the following tables the items are marked with letter A and different initials.

With the purpose of determining the friction parameter, friction factor, and friction index, values established as coefficients of friction at rest and friction when slipping were used when with MXD-02 from Labthink, China (1). Force meter 1 measures the friction force that occurs when sleigh 2 slides onto platform 3, which in turn moves forcefully along guide rail 4 (Fig. 1). The force-change graph is displayed on screen 6. It also displays the calculated friction coefficient at rest, the coefficient of drag friction, the speed of the platform and the mass of the sleigh.

Table 1a. Parameters of the tested cotton textiles

№	Item		Characteristics	
			Width	Specific weighting area
			mm	g/m^2
1.	Kiparis ready	A11	1510	247
2.	Kiparis raw	A12	1610	212
3.	Boro ready	A21	1510	282
4.	Boro raw	A22	1610	268
5.	Boby ready	A31	1510	261
6.	Boby raw	A32	1600	254

Table 1b. Parameters of the tested cotton textiles

№	Item	Characteristics			
		Linear density		Thickness	
		base	weft	base	weft
		tex	tex	no. threads/dm	no. threads/dm
1	A11	40	50	386	180
2	A12	40	50	355	178
3	A21	36	60	384	200
4	A22	40	60	355	200
5	A31	36	60	386	182
6	A32	36	60	355	176

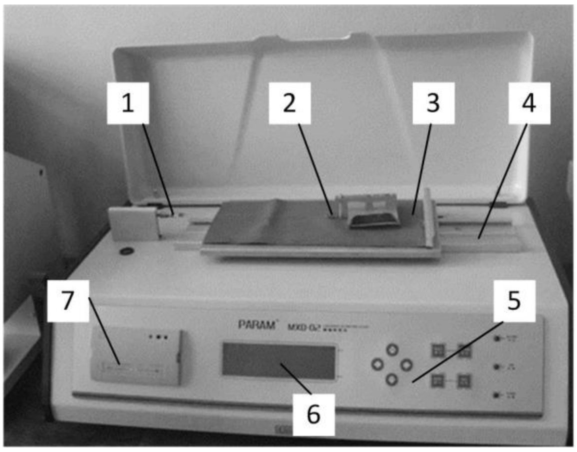

Figure 1. General appearance of device MXD-02

Force meter 1 measures the friction force that occurs when sleigh 2 slides onto platform 3, which in turn moves forcefully along guide rail 4 (Fig. 1). The force-change graph is displayed on screen 6. It also displays the calculated friction coefficient at rest, the coefficient of drag friction, the speed of the platform and the mass of the sleigh. The tester allows work to be performed based on different standards, as the hereby tests have been carried out according to BDS, ISO 8295: 2006.

Friction is done weave in weave, in different directions of the weaves on the face side of the two layers. Parameters and choice of standard are set by control panel 5. One layer of test weave is placed on the mobile platform 2 so that the direction of the base threads coincides with the direction of movement of the platform.

The second layer engages the sleigh in a selected direction - on a base, weft, and wreath. The friction coefficient at rest μ_0 is determined by the force taken into account in the test. At this point, the metal thread linking the force meter and the sleigh is stretched, then starts sliding on the platform. The instrument calculates the mean value of the studied coefficient of friction at sliding μ, as well as the mean deviation of μ_0 and μ. The numeric values visible on the screen can be printed with mini printer 7.

The results obtained for μ_0 and μ are shown in Table 2.

The literary study shows that there are no significant differences in frictional force [1, 4] in experiments with low sliding speeds of 10 to 500 mm / min. The main factor affecting the friction characteristics of the fabric is the weaves actual contact surface area of friction [2]. When in comes to the insignificant influence of the movement speed of friction surfaces relative to one another, the present study is carried out at a constant speed of 100 mm / min. Apart from this, most of the seamless manufacturing operations are at relatively slow speeds.

The relationship between friction force and normal load [2] is subject to logarithmic dependence:

$$\frac{F_i}{B} \quad C.\left(\frac{N_i}{B}\right)^n \text{ or } \log\frac{F_i}{B} \quad \log C \quad n.\log\frac{N_i}{B} \qquad (1)$$

i=1, 2,…m; B – contact surface area [m^2]; C – friction parameter (measured in [Pa^{1-n}]); n – friction index (no measurement); N – regular pressure [N]; F – friction force [N]; m – number of experimental observations.

Table 2. Coefficient of friction at rest and when sliding

Item	Sleigh weight	Coefficient of friction at rest		
	g	BFS-BFS	BFS-SFS	BFS-VFS
A11	200	0,959	0,918	0,787
	300	1,061	1,001	0,912
	400	1,177	1,073	1,101
A12	200	0,827	0,819	0,800
	300	0,905	0,933	0,936
	400	1,022	0,983	1,064
A21	200	0,861	0,938	0,880
	300	0,981	0,972	0,997
	400	1,121	1,120	1,155
A22	200	0,875	0,833	0,770
	300	1,033	0,921	0,934
	400	1,135	1,035	1,082
A31	200	0,880	0,816	0,752
	300	1,034	0,971	0,934
	400	1,191	1,102	1,108
A32	200	0,866	0,863	0,757
	300	0,965	0,968	0,915
	400	1,101	1,065	1,044
Item	Sleigh weight	Coefficient of friction when sliding		
	g	BFS-BFS	BFS-SFS	BFS-VFS
A11	200	0,744	0,658	0,641
	300	0,959	0,844	0,787
	400	1,096	1,031	1,000
A12	200	0,639	0,540	0,682
	300	0,795	0,722	0,850
	400	0,938	0,890	0,993
A21	200	0,738	0,661	0,665
	300	0,890	0,849	0,867
	400	1,100	1,000	1,056
A22	200	0,700	0,572	0,583
	300	0,861	0,771	0,778
	400	1,029	0,916	0,955
A31	200	0,682	0,605	0,566
	300	0,882	0,783	0,759
	400	1,060	0,944	0,942
A32	200	0,686	0,631	0,537
	300	0,823	0,802	0,745
	400	0,979	0,949	0,920

Abbreviations used in Table 2: BFS – base face side; WFS – weft face side; SFS – skew face side. The angle in the vertical direction is 45 °. The same abbreviations are used in the following tables and graphs in the text bel.

The studies of Apurba Das and team on textile materials blend cotton and polyester (C/ PE) in a different ratio, indicate that the logarithmic dependence approximates to a linear one [4].

For each of the tested textiles five tests were made. *Log* (F_i/B) and *log* (N_i/B) are determined in different directions and in change of pressure. Normal pressure changes. Further weight is added to the mass of the sleigh which is 200g. The mass of the test sample mounted on the sleigh is not taken into account as it is negligibly low.

The tests were carried out at an average air temperature of 22°C and an average humidity of 70%. The determination of the two parameters - friction index *n* and friction parameter *C* is performed by calculating $lg(F_i/B)$ and $lg(N_i/B)$ after calculation of normal Ni forces and friction forces F_i.

A linear regression equation of the type:

$$y=a+x.b \tag{2}$$

$$x= lg(N_i/B); \quad y= lg(F_i/B); \quad a=lgC; \quad b=n.$$

Frictional parameter *C* and frictional index *n* serve to determine the frictional factor *R*, also called compound coefficient of friction or correlation coefficient of friction [3] whose value is determined by the dependence:

$$R \quad \frac{C}{n} \tag{3}$$

Table 3a. Friction values at rest

Item	Direction of the textile	Friction characteristics at rest		
		index *n*	parameter *C*	factor *R*
		-	Pa^{1-n}	Pa^{1-n}
A11	BFS-BFS	1,292	0,306	0,237
	BFS-SFS	1,224	0,328	0,268
	BFS-VFS	1,476	0,110	0,075
A12	BFS-BFS	1,300	0,[illegible]5	0,196
	BFS-SFS	1,267	0,291	0,230
	BFS-VFS	1,410	0,843	0,598
A21	BFS-BFS	1,377	0,149	0,237
	BFS-SFS	1,245	0,355	0,285
	BFS-VFS	1,387	0,128	0,092
A22	BFS-BFS	1,378	0,202	0,237
	BFS-SFS	1,309	0,248	0,189
	BFS-VFS	1,490	0,084	0,056
A31	BFS-BFS	1,434	0,163	0,237
	BFS-SFS	1,433	0,130	0,091
	BFS-VFS	1,558	0,037	0,024
A32	BFS-BFS	1,341	0,233	0,237
	BFS-SFS	1,302	0,265	0,204
	BFS-VFS	1,464	0,130	0,089

Table 3b. Friction values when sliding

Item	Direction of the textile	Friction characteristics when sliding		
		index *n*	parameter *C*	factor *R*
		-	Pa^{1-n}	Pa^{1-n}
A11	BFS-BFS	1,563	0,083	0,351
	BFS-SFS	1,646	0,053	0,032
	BFS-VFS	1,633	0,110	0,067
A12	BFS-BFS	1,553	0,074	0,377
	BFS-SFS	1,721	0,034	0,020
	BFS-VFS	1,542	0,845	0,548
A21	BFS-BFS	1,568	0,0[illegible]	0,338
	BFS-SFS	1,599	0,064	0,040
	BFS-VFS	1,666	0,128	0,077
A22	BFS-BFS	1,553	0,081	0,342
	BFS-SFS	1,683	0,040	0,024
	BFS-VFS	1,712	0,084	0,049
A31	BFS-BFS	1,636	0,057	0,241
	BFS-SFS	1,641	0,050	0,030
	BFS-VFS	1,734	0,032	0,018
A32	BFS-BFS	1,509	0,094	0,397
	BFS-SFS	1,589	0,050	0,031
	BFS-VFS	1,779	0,130	0,073

The results of research on friction parameter, friction factor, and friction index for friction at rest and friction when slipping were shown in Table 3.

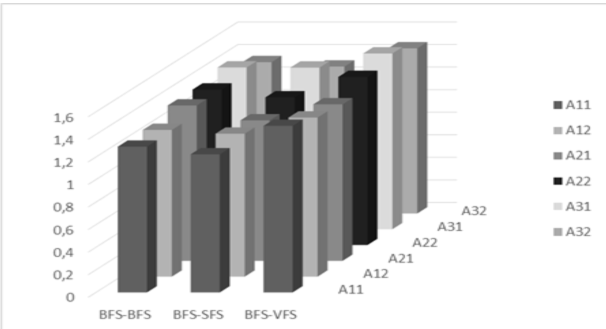

Figure 2. Influence of test direction on friction index *n* at rest

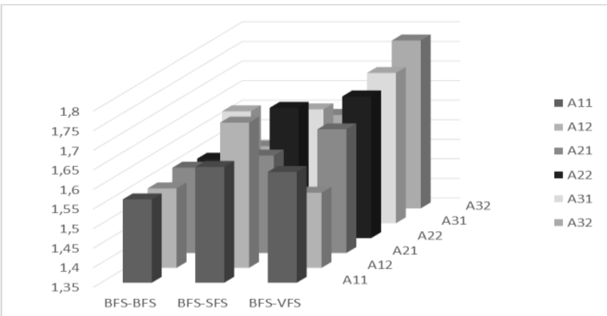

Figure 3. Influence of test direction on friction index *n* when sliding

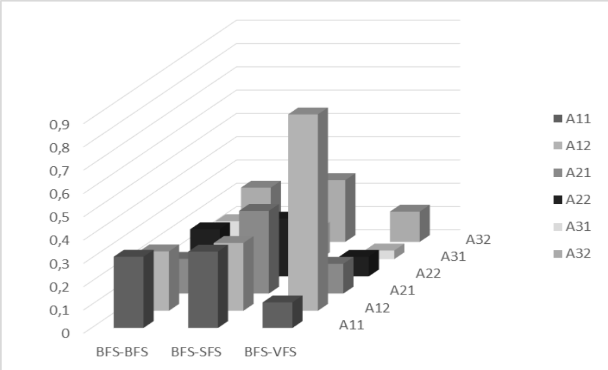

Figure 4. Influence of test direction on friction parameter *C* at rest

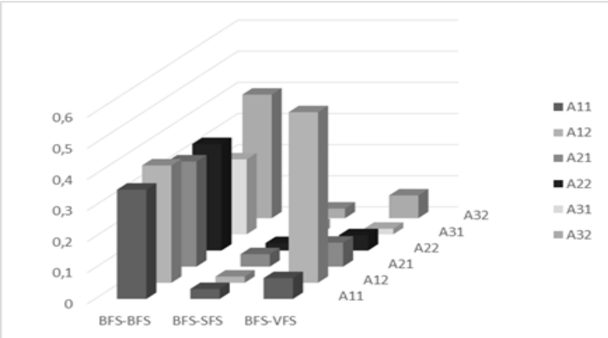

Figure 5. Influence of test direction on friction parameter *C* on sliding

Figures 2-5 visualize the experimental results for the friction index and friction factor, depending on the direct.

3. CONCLUSION

The conducted studies show the influence of pressure on the friction characteristics of weaves of the same composition, with the same weave, but with different thickness of the base and weft threads. Different values of frictional characteristics depend on the change in actual contact area, which varies in different directions. The actual contact area increases as the pressure increases, resulting in an increase in the coefficient of friction at rest and the coefficient of friction when sliding.

The friction index in the highest at face-facing direction for one layer and weft-facing direction for the other layer, both in the friction at rest and in the friction when sliding. In this direction - base face side - weft face front, the actual contact area increases due to increased contact areas of the base and weft threads of the two layers.

For articles A21 and A31, which are of the same thickness of the threads on base and weft sides but with different density of the weft threads, a difference in friction characteristics is also noted which is also due to the different real contact area of the friction surfaces.

Larger values for friction coefficients, both at rest and when sliding, are observed for finished fabrics than with raw cloth. In the raw cloth, the base and weft densities are lower than on the finished cloth, and hence the difference in the real size of the finished and the raw cloth.

The experimental results obtained here can serve as a basis for other scientific studies related to the fabrication of so-called "smart" garments, which use the friction of the layers of weave to produce electrical current. Additionally, the results obtained can serve as a basis for setting up textile machines. For the power analysis of machines in the sewing industry, these experimental results can also be used for their coefficients of friction when sliding and at rest.

REFERENCES

[1] G.D. Bhuvana, K. Raghunathan, V. Subramaniam: Studies on frictional behavior of chitosan coated fabrics. Autex Research Journal, Vol. 6, No. 4, pp. 216-222, 2006.

[2] D. Wilson: Study of Fabric-on-Fabric Dynamic Friction, Journal of Textile Institute & Industry, Vol. 1, No. 4, p2, 1964.

[3] B. Daniel, B. Hermann: *Mathematical Characterization of Frictional Properties*, A thesis in mathematics, Texas Tech University, 2003.

[4] A. Das, V.K Kothari, N. Vandana: A study on frictional characteristics of woven fabrics, Autex Research Journal, Vol. 5, No. 3, 2005.

Serbian Tribology Society

SERBIATRIB '19

16th International Conference on Tribology

Faculty of Engineering University of Kragujevac

Kragujevac, Serbia, 15 – 17 May 2019

EVALUATION OF HARDNESS IN CAST IRON: HOW SIMPLE IT IS !

Cristiano FRAGASSA[1,*], Matej BABIC[2], Ana PAVLOVIC[1]

[1] Department of Industrial Engineering, University of Bologna, Bologna, Italy

[2] Jožef Stefan Institute, Ljubljana, Slovenia

*Corresponding author: cristiano.fragassa@unibo.it

Abstract: *The accurate prediction of the mechanical properties of foundry alloys is a rather complex charge given the substantial variability of metallurgical conditions that can be created during casting even in the presence of minimal variations in the constituents and in the process parameters. In this study an application of intelligent methods, based on the machine learning, to the estimation of the hardness of a traditional spheroidal cast iron and a less common compact graphite cast iron is proposed. Microstructures are used as inputs to train the neural networks, while hardness is obtained as outputs. As general result, it is possible to admit that 'light' open source self-learning algorithms, combined with databases consisting of about 20-30 measures are already able to predict hardness properties with errors below 15%.*

Keywords: *Hardness prediction, Artificial Intelligence (AI), Machine Learning (ML), nodular/spheroidal cast iron (SGI), compact graphite cast iron (CGI), foundry process.*

1. INTRODUCTION

The family of cast irons consists of a large number of alloys, each one qualified by its own characteristics in terms of metallurgic composition, mechanical properties, surface resistance, and, ultimately, practical use. Perhaps, exactly for this variability, cast iron is one of the most used materials in industrial history and in the present by mankind [1].

The first attempts at producing cast iron in the Mediterranean basin can be traced back to over 1000 BC and tower ovens were found in Sweden, dated between 1150 and 1350.

Few modifications (as additives inoculation) are sufficient to produce materials with very different characteristics and applications, from the common gray iron to the high performing ductile cast iron.

This complexity in properties estimation is even more evident in the case of superficial features as the hardness. In this case, beyond all other aspects dealing with the overall variability of material characteristics, also additional considerations related to local effects in cooling start to be predominant.

However, limiting to the industrial purposes, often it would be sufficient to have quick indications regarding these properties, even if not extremely precise. In this study intelligent methods based on machine learning (ML) are proposed to estimate the hardness of a traditional spheroidal cast iron (SGI) and of a less common compact graphite cast iron (CGI).

Microstructural macroindicators, as, e.g., the quantity of graphite, ferrite, perlite in the alloy, acquired by microstructures, are used as inputs to train three (3) different ML algorithms, while hardness properties (in HB) are obtained as outputs.

Two datasets from tests were considered, one per each material, consisting of 25-30 samples, while comparisons were done by a direct correlations with the estimations.

2. EVALUATION METHODS

Several methods of ML can be conveniently considered. In the present work, according to preceding similar experiences, as detailed in [2], the following ones were preferred.

2.1 Random Forest (RF)

The RF is one of the most popular and extremely effective methods for solving the problems of machine learning, such as classification and regression [3].

A NN is a structure (network) consisting of a set of interconnected links (artificial neurons). Each link has a characteristic input / output and implements a local calculation or function. The output of any link is determined by the characteristics of its input / output, its relationship with other links, as well as external inputs, if any.

In terms of efficiency, it competes with support vector machines, neural networks and boosting, although it certainly does not lack its shortcomings. In appearance, the learning algorithm is very simple (in comparison with the learning algorithm of the support vector machines). The basic ideas laid down in Random Forest model (binary decision tree, bootstrapping aggregation or bagging, random subspace method and decorrelation).

2.2 Neural Network (NN)

The NN also represents a quite common strategy in problem solving. A NN can be used to build an efficient encryption system using a constantly changing key. The NNs offer a very powerful and general structure for representing a non-linear mapping of several input variables for several output variables. A NN can be considered as a suitable choice for functional forms used for encryption and decryption operations.

The NN topology is an important issue, since the application of the system depends on it. Therefore, since the application is a calculation problem, a multi-layered topology was used. Then, the NNs offer a very powerful and general structure for representing a non-linear mapping of several input variables for several output variables. The process of determining the values of these parameters on the basis of a data set is referred to as training or training, and therefore the data set is usually referred to as a training set. In particular, a NN can be considered as a suitable choice for functional forms used for encryption and decryption operations.

2.3 k-nearest neighbors (kNN)

The kNN is a non-parametric method used for classification and regression [5]. The input consists of the k closest training examples in the feature space. The output depends on whether k-NN is used for classification or regression.

In k-NN classification, the output is a class membership. An object is classified by a plurality vote of its neighbors, with the object being assigned to the class most common among its k nearest neighbors (k is a positive integer, typically small). If k = 1, then the object is simply assigned to the class of that single nearest neighbor. In k-NN regression, the output is the property value for the object. This value is the average of the values of its k nearest neighbors. The k-NN is a type of instance-based learning, or lazy learning, where the function is only approximated locally and all computation is deferred until classification. The k-NN algorithm is among the simplest of all machine learning algorithms. Both for classification and regression, a useful technique can be used to assign weight to the contributions of the neighbors, so that the nearer neighbors contribute more to the average than the more distant ones. For example, a common weighting scheme consists in giving each neighbor a weight of 1/d, where d is the distance to the neighbor.

The neighbors are taken from a set of objects for which the class (for k-NN classification) or the object property value (for k-NN regression) is known. This can be thought of as the training set for the algorithm, though no explicit training step is required. A peculiarity of the k-NN algorithm is that it is sensitive to the local structure of the data.

3. DATA ESTIMATIONS

Measures used in this investigation for training the ANNs derived from mechanical and tribological tests already discussed in details in previous works [6-8]. In particular, in accordance with [8] the datasets consist of 27 samples in SGI and 21 samples in CGI.

As input for training the ANN, the following metallographic parameters were chosen:

- Graphite
- Ferrite
- Perlite
- Grade of nodularity
- Grade of vermicularity

These data were provided in terms of single values estimated by micrographs: each sample (SGI and CGI) provided a specific set of 5 (five) values. Every set (21+27) of metallographic characteristics was combined with the related hardness property as measure by test.

ANN evaluations were implemented by Orange algorithms, an open source machine learning and data visualization system [9]. The ANN was learned by these data and provided outputs in terms of HB hardness. In particular, per each sample, it provided 3 (three) different estimations of hardness in accordance with the 3 (three) specific methods used:

- Random Forest (RF)
- Neural Network (NN)
- k-Nearest Neighbors (kNN)

These values are reported in table 1 and 2. Table 3 reports the related values of:

- mean (**μ**),
- standard (**σ**)
- relative standard (**$\sigma_{\%}$**) deviation
- Pearson correlation coefficient (**ρ_{xy}**)

In the way to show the overall variability of values and permit a comparison of methods.

Table 1. SGI Hardness as measured and estimated

N.	HB	RF	NN	kNN
1	165	182	168	181
2	166	174	171	171
3	167	178	178	173
4	168	182	182	169
5	169	182	171	168
6	171	182	182	169
7	171	182	182	166
8	173	171	182	171
9	173	182	184	165
10	174	181	178	167
11	176	204	184	165
12	178	182	181	165
13	178	181	182	171
14	180	176	206	183
15	181	178	178	169
16	181	173	173	165
17	182	178	178	171
18	182	173	171	165
19	182	178	171	171
20	183	184	206	180
21	184	180	176	176
22	185	169	182	169
23	186	190	204	180
24	190	185	206	180
25	204	206	206	206
26	206	183	190	180
27	206	204	204	180

Table 2. CGI Hardness as measured and estimated

N.	HB	RF	NN	kNN
1	132	148	137	137
2	136	141	141	139
3	137	145	145	142
4	139	142	136	136
5	141	142	144	142
6	142	147	144	141
7	142	151	156	147
8	144	142	149	141
9	144	142	145	137
10	145	132	137	137
11	146	150	149	147
12	147	147	132	132
13	147	147	151	151
14	147	147	151	151
15	148	150	147	132
16	149	147	156	144
17	150	146	148	146
18	150	142	147	142
19	151	147	147	147
20	151	147	147	147
21	156	147	151	141

Table 3. Mean (μ), standard deviation (σ) and relative standard ($\sigma_{\%}$) deviation, and, finally, the Pearson correlation coefficient (ρ_{xy}) for SGI and CGI hardness, as measured (HB) and estimated

	HB	RF	NN	kNN	
μ	180	182	184	173	SGI
σ	11	9	12	9	
$\sigma_{\%}$	6%	5%	7%	5%	
ρ_{xy}	1.00	0.46	0.59	0.56	
μ	144	145	146	142	CGI
σ	5	4	6	5	
$\sigma_{\%}$	4%	3%	4%	3%	
ρ_{xy}	1.00	0.17	0.43	0.28	

4. RESULTS

Measures and estimations can be graphically observed and compared in Figure 1 for SGI and CGI. In particular it can be observed the estimation provided by the *NN* method that, according to the Pearson correlation coefficients (ρ_{xy}) in Table 3 can be considered the most appropriate evaluation method. In fact, with value of 0.59 and 0.43 in the case of, respectively, SGI and CGI, it demonstrates a good (even not perfect) correlation between the experimental dataset and the estimated hardness.

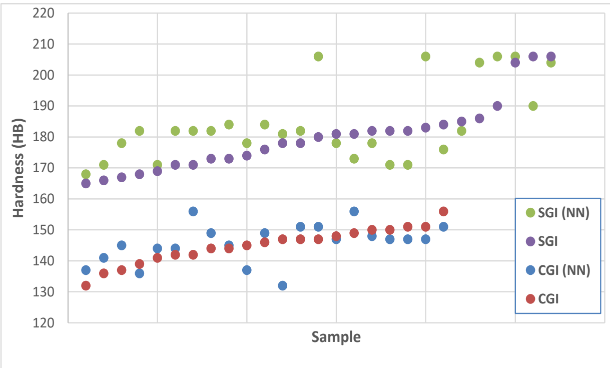

Figure 1. Measured and estimated hardness (HB) for SGI (up) and CGI (down)

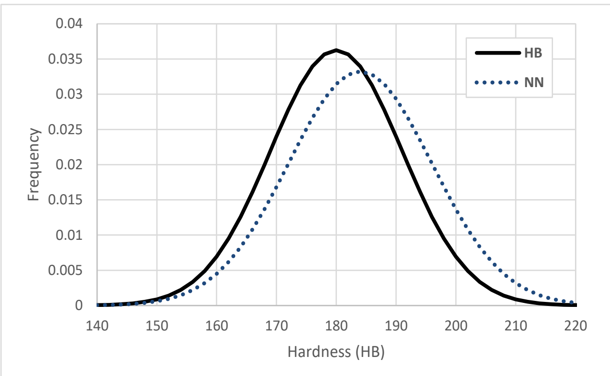

Figure 2. Overlapping between measures and estimations (in the case of SGI and NN)

This estimation by the NN method is able to guarantee a substantial coincidence on the average values of hardness (184 vs 180 in the case of SGI, 146 vs 144 for CGI) and its variability (e.g. in terms of relative standard deviations). It means that, as evident in Figure 2, there is a significant overlapping between the density distributions able to represent measures and estimations in terms of probability.

Moreover, all methods for Machine Learning under investigation seem able to provide an adequate estimation, especially when considered the real values. In Figure 3 it is shown, for instance in the case of SGI, the influence of the choice (MF, NN or kNN) in the estimation.

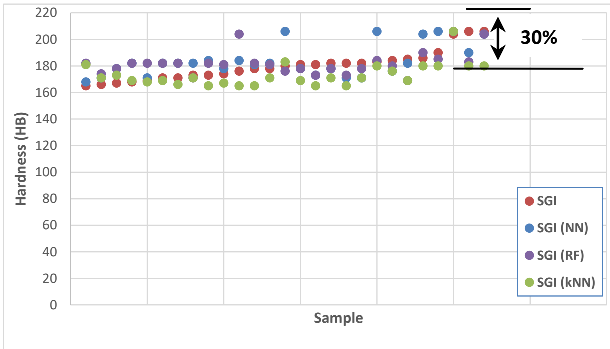

Figure 3. Comparison between the estimation methods (in the case of SGI)

In particular, in the graph it is possible to see how the variability in hardness predictions was limited within a range of 30% respect to the average measure. This result can be considered more than appropriate concerning that:

- Even if the specimens were extracted from the similar casting conditions, the experimental values were characterized by a certain intrinsic variability (σ = 11). This variability was transferred in the ANN evaluation even if with a tendency to a reduction.
- The use of ANN has not been optimized in this case, nor as structure or training. This choice is related to a specific strategy aiming at demonstrating the applicability of the ANN theory without entering in further details.

5. CONCLUSION

The present research deals with the use of Artificial Intelligence (AI) and Machine Learning (ML) in the prediction of hardness of spheroidal cast iron (SGI) and compact graphite cast iron (SGI). Results from previous experiments were used to train three ANNs, based on three different principles. Open source and easy accessible algorithms were used. Even if in the presence of a limited number of measures (20-30), the ANNs, independently of the specific network, were able to predict the hardness with an acceptable confidence (±15%).

It is believed that a greater accuracy could be easily achieved by: i) increasing the sample of measures on which the ANN is trained; ii) optimizing the ANN in terms of depth and quality of analysis (‘deep learning’), but also testing the opportunity to choose other methods of estimation (as Multiple Regression, Nearest Neighbors, Genetic Programming, Support Vector Machine…); iii) using microstructural information directly at a level of details.

ACKNOWLEDGEMENT

This research was implemented by the support of SCM Foundries, Italy, where the different samples of cast iron were produced. Special thanks to Giangiacomo Minak, Stefano Cucchetti and Giuseppe Lucisano.

REFERENCES

[1] C. Fragassa, G. Minak, A. Pavlovic: Tribological aspects of cast iron investigated via fracture toughness, Tribology in Industry, Vol. 38, No. 1, pp. 1-10, 2016.

[2] M. Babic, M. Calì, I. Nazarenko, C. Fragassa, S. Ekinovic, M. Mihaliková, M. Janjić, I. Belič: Surface Roughness Evaluation in Hardened Materials by Pattern Recognition Using Network Theory, International Journal on Interactive Design and Manufacturing, 2018.

[3] Y. Lin, J. Yongho: Random forests and adaptive nearest neighbors, Journal of the American Statistical Association, Vol. 101, No. 474, pp. 578–590, 2006.

[4] S. Jürgen: Deep learning in neural networks: An overview, Neural Networks, Vol. 61, pp. 85–117, 2015.

[5] S. Garcia, J. Derrac, J. Cano, F. Herrera: Prototype Selection for Nearest Neighbor Classification: Taxonomy and Empirical Study, IEEE Transactions on Pattern Analysis and Machine Intelligence, Vol. 34, No. 3, pp. 417–435, 2012.

[6] N. Radovic, A. Morri, C. Fragassa: A Study on the Tensile Behavior of Spheroidal and Compacted Graphite Cast Irons Based on Microstructural Analysis, in: *Proceeding of the 29th Danubia Adria Symposium on Experimental Solid Mechanics*, 26-29.09.2012, Belgrade, Serbia, pp. 164-170, 2012.

[7] C. Fragassa: Material selection in machine design: the change of cast iron for improving the high-quality in woodworking, *In Proceedings of the Institution of Mechanical Engineers, Part C: Journal of Mechanical Engineering Science*, Vol 231, No. 1, pp. 18-30, 2016.

[8] C. Fragassa, N. Radovic, A. Pavlovic, G. Minak: Comparison of mechanical properties in compacted and spheroidal graphite irons, Tribology in Industry, Vol. 38, No. 1, pp 49-59, 2016.

[9] https://orange.biolab.si

Serbian Tribology Society

SERBIATRIB '19

16th International Conference on Tribology

Faculty of Engineering University of Kragujevac

Kragujevac, Serbia, 15 – 17 May 2019

WEAR RESISTANCE UNDER DRY CONDITIONS OF DIFFERENT FILLER METALS USED FOR HARD FACING

Dušan ARSIĆ[1], Vukić LAZIĆ[1], Dragan DŽUNIĆ[1], Srbislav ALEKSANDROVIĆ[1], Milan ĐORĐEVIĆ[2], Milan UHRIČIK[3], Aleksandra ARSIĆ[4]

[1] Faculty of Engineering, University of Kragujevac, Sestre Janjić 6, 34000 Kragujevac, Serbia.
[2] Faculty of Technical Sciences, Knjaza Milosa 7, 28000 Kosovska Mitrovica, Serbia
[3] University of Žilina, Faculty of Mechanical Engineering, Univerzitna 8215/1, 010 26 Žilina, Slovakia.
[4] Faculty of Mechanical Engineering, Kraljice Marije 16, 11000 Belgrade, Serbia.
*Corresponding author: dusan.arsic@fink.rs

Abstract: *The aim of this paper is to show wear properties of different types of filler metals aimed for hard facing and exploitation in dry condition. Testing of wear resistance is done in laboratory on prepared samples/models in order to simulate real exploitation conditions. Samples were made by hard facing of carbon steel using 4 different filler metals. Hard facing was done by using MMA welding method in three layers with enough height so samples could be made. After samples were made, the hardness and microstructure of all zones of hard facing were determined. Testing of wear resistance is done using block on disc contact on samples made from pure weld metal. As a parameter for estimates of the wear resistance of models it was used volume of worn material in mm^3. Metallographic investigations and hardness measurements were used as additional parameter for drawing the conclusions.*

Keywords: *Hard facing, filler metals, hardness, microstructure, wear volume.*

1. INTRODUCTION

Numerous working parts of different technical systems are during the exploitation exposed to various types of complex wear processes. Since never one type of wear is dominant, it is very hard to determine which of the wear mechanisms lead to biggest damages. Usually, damages are consequences of coupled action of several wear mechanisms. That is why it is necessary to apply higher quality materials, which are resistant to wear and which can produce more working hours for the concrete machine part. On the other side, manufacturing of large parts with using of high-quality materials offten is very expensive. Than the problem could be solved by application of hard facing. Hard facing enables reparation of damaged parts or manufacturing of the new parts by depositing the high quality material on the cheaper material. In that way, one saves not only material and money, but also the time needed for revitalizing damaged parts, shortening the downtimes, etc [1]. There is many examples where hard facing was succesifully applied in order to achieve above mentioned goals such as: claddings for deep-hole drilling [2], rotary tiller blades [3], gears [4], mixer blades [5], etc.

In this paper, four different types of filler materials were used. These materials are aimed for hard facing of the parts exposed to intensive impact and abrasive wear, such as bucket teeth of excavator, parts for terrain leveling, mixer blades used in asphalt bases, teeth of stone mils, industrial gears, forging dies, etc [6]. During exploitation they are mainly in contact with various types of stones [7] and they are exposed to intensive wear what leads to surface damages.

2. EXPERIMENTAL PROCEDURE

Experimental testing of hard faced plates included preparation of samples for hardness measurement perpendicular to hard faced surface, investigation of microstructure of characteristic zones and samples from pure weld metal for tribological testing in order to determine wear resistance of hard faced layers.

2.1 Sample preparation

Samples were prepared from hard faced plates in Laboratory for welding and materials at Faculty of Engineering. Hard facing was done by manual metal arc welding method in three passes and three layers (Fig. 1). Filler metals were selected based on working conditions of the parts and properties that this kind of parts have to possess. All that imply that steel alloys with high carbon and chromium content can be good solution. The chemical composition of selected metals is given in table 1. Before welding plates were preheated at 300°C and hard facing was done according to parameters given in table 2.

Hard faced models are used to cut the blocks for tribological test (Fig. 1b) and metallographic samples – blocks out of them, as shown in Figure 1c. Height of the weld cladding was about 10-11 mm. Tribological test-wear resistance was determined on samples-prismatic blocks takken from pure hard facing, with dimensions shown in Fig. 1. Testing was done Laboratory for Tribology at Faculty of Engineering in Kragujevac by using tribometer TR-95 and realized "block on disc" contact.

Disc used in contact with tested samples was made of high speed tool steel, with diameter of 35 mm and thickness of 6.35 mm (the same as the width of 6.35 mm at test sample block as shown in Fig. 1). All samples were grounded and disc was grounded after each testing. Variables were the contact force and sliding speed. Since that the working parts hard faced with these filler metals work without lubricating, tribological tests were conducted under dry conditions.

Table 1. Chemical composition of base metal and filler metals [6]

Steel/Electrodes	Alloying elements [%]										Hardness, HRC/HV
	C	Si	Mn	P	S	Cr	Mo	W	Cu	CEV	
S355J0	0.2	0.5	1.4	0.035	0.035	-	-	-	0.55	0.47	≈ 24/240
E DUR 600 DIN 8555: E 6-UM-60	0.5	-	-	-	-	7.5	0.5	-	-	-	≈ 60/600
CrWC 600 DIN 8555: E 10-UM-60-C	4.0	-	-	-	-	26.0	-	4.0	-	-	≈ 60/600
INOX B 18/8/6*	0.12	0.8	7.0	-	-	19.0	9.0	-	-	-	-
E Mn17Cr13	0.6	-	16.5	-	-	13.5	-	-	-	-	≈ 48/500

Table 2. Hard facing parameters for the MMA welding procedure

BM thickness s [mm]	Electrode designation by producer	Electrode core diameter d_e [mm]	Hard facing current I [A]	Voltage U [V]	Hard facing speed v_z, [mm/s]	Driving energy q_l [J/cm]
10	E DUR 600	3.25	125	25.5	≈ 2.42	10539
	CrWC 600	3.25	130	26	≈ 1.95	13867
	INOX B 18/8/6	3.25	115	24.5	≈ 2.00	11270
	E Mn17 Cr13	3.25	135	26	≈ 2.50	11232

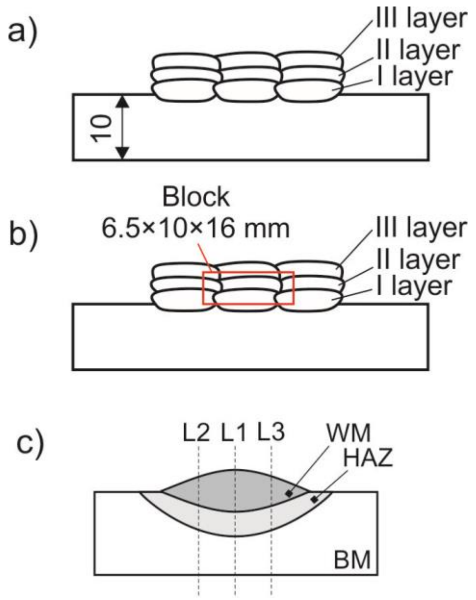

Figure 1. a) Order of layers deposition; b) blocks for tribological "block on disk" contact; c) metallographic ground slit

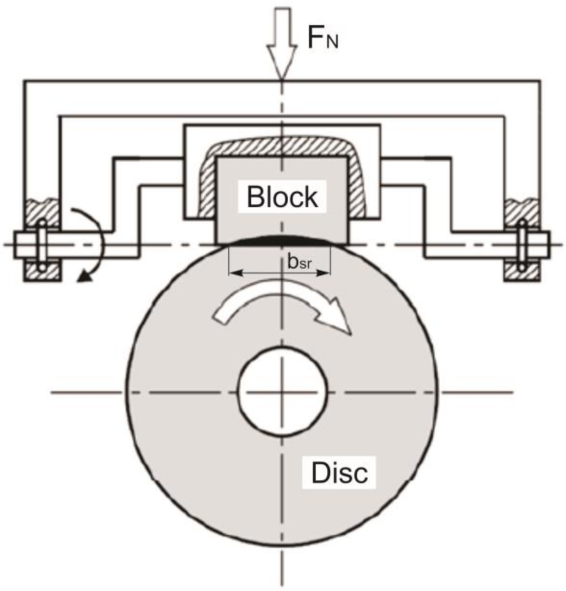

Figure 2. "block on disc" contact

Experiment assumed simulation of contact by using of three different sliding speeds (0.25 m/s, 0.5 m/s and 1 m/s) and three different loads (F_N = 50 N, F_N = 75 N i F_N = 100 N). Parameter for contact duration was sliding distance of 300 m. Parameters that were followed during process were wear volume and specific wear volume. The wear behavior of the block was monitored in terms of the wear track width, using the wear track width and the geometry of contact pair to determine the wear volume in mm^3 over the sliding distance.

Hardness has been measured on surfaces of metallographic samples in different directions. The same samples were used to estimate the microstructure of characteristic surfaced zones. Samples were chosen to be geometrically similar to hard faced part and they were made either of well weldable steel S355J0 (according to DIN: St St52-3U). Large number of parts in construction machinery is made of S355J0 steel, this is way this steel was used as base metal, but due to its poor wear resistance there is need for alloying or hard facing [8].

In Fig. 3 are shown 4 hard faced plates before cutting and one sample prepared for hardness measurement and microstructure estimation.

a)

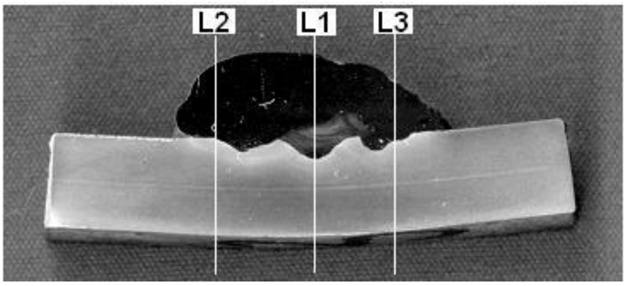

b)

Figure 3. Hard faced plates (a) and sample no. 3 prepared for hardness measurement

3. RESULTS

After testing, wear scar width of all samples were determined using microscope UIM 21 with magnification of 50×. Based on obtained values, the wear volume and specific wear volume was calculated, for sliding distance of 300 m. The results of wear volume obtained by experiment are shown in Figure 4 6 .

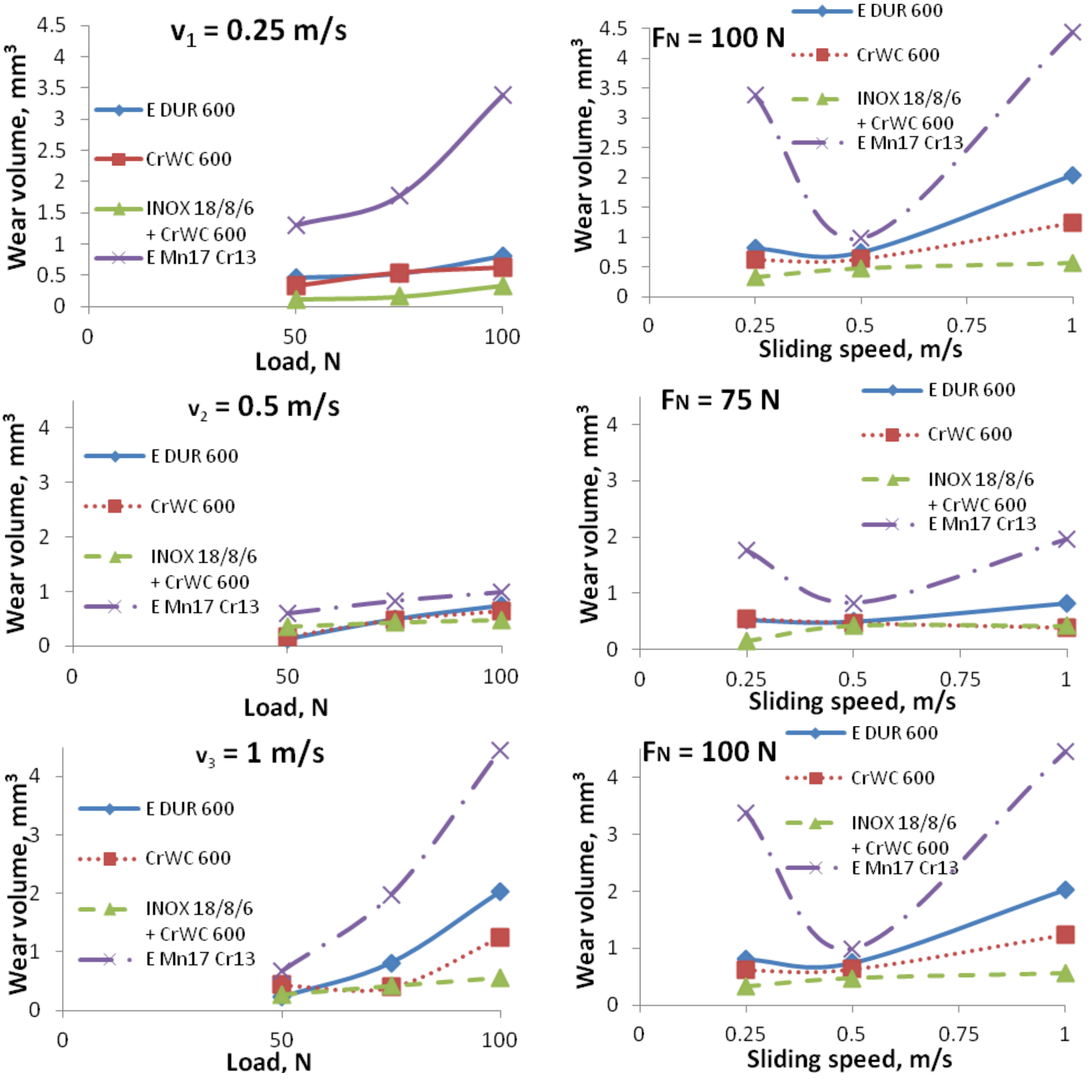

a) b)

Figure 3. Wear volume of the tested samples: a) at different sliding speeds and b) at different loads

Based on presented results it can be concluded that the best wear resistance has the filler metal designated as CrWC 600 (sample #3). The best results were obtained using all three sliding speeds of 0.25, 0.5 and 1 m/s and almost all used loads. The function of the interlayer is to absorb impacts during exploitation, as well as to replace preheating when it is impossible to apply it (while it is predicted by the welding technology). Samples #1 and #2 has a little bit lower wear resistance than Sample # 4. The worse wear properties have a filler metal with high manganese content – Sample #4. It should be taken into account that this filler metal is aimed for cold hardening because of hammering or exploitation (deformation induced the transformation of austenite into martensite), leading to an increase in hardness.

Hardness measurement was done by using Vickers method HV1 [9] along vertical line on hard faced sample. Obtained results are shown on diagrams at Fig. 4. Samples were prepared by water jet cutting in order to avoid overheating in cutting zone and potential change of structure. After cutting samples were grounded and polished. Hardness was measured along three vertical lines (as shown at Fig. 4).

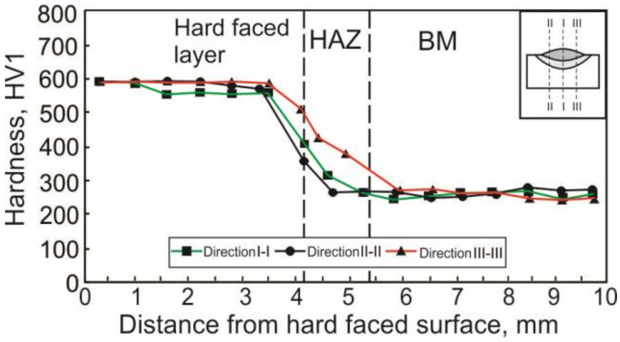

a) E DUR 600

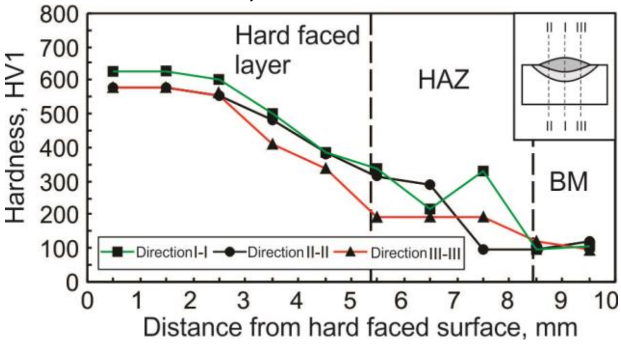

b) CrWC 600

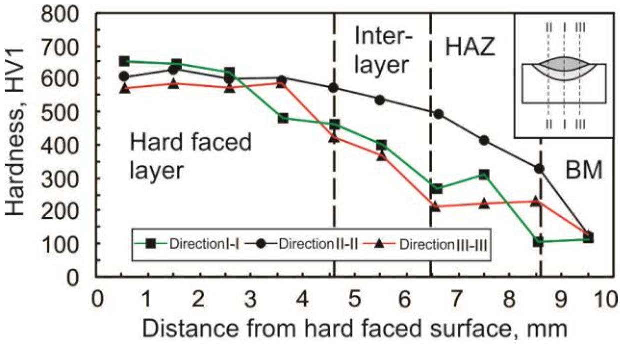

c) CrWC 600; Interlayer INOX B 18/8/6

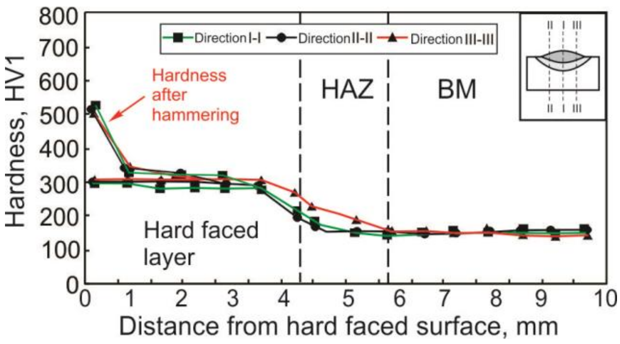

d) E Mn17 Cr13

Figure 4. Hardness distribution of four samples

Presented hardness distribution is showing that hardness of all samples is approximately 600 HV in the zone of filler metal and dropping when going down to the base metal. High hardness can reduce wear, but also beside hardness, microstructure of the hard facing has to be suitable. Microstructure found at these samples was mostly prominent dendrite casting structure with excreted carbides. Dendrites are formed due to high carbon content while carbides are formed in presence of Cr, Mo and W. High carbide hardness has positive effect on wear resistance, especially when they are uniformly distributed in metal matrix [10, 11].

4. CONCLUSION

Analyzing the results, it can be concluded that the best tribological properties and wear resistance have the filler metal designated as CrWC 600 (sample #3), deposited with or without an austenitic interlayer. The best results were obtained using all three sliding speeds of 0.25, 0.5 and 1 m/s and almost all used loads. In the case of other samples – #1 and #2 – the main conclusion is that their wear resistance is a little bit lower than that for Sample # 4. The worse wear properties have a filler metal with high manganese content – Sample #4. It should be taken into account that this filler metal is aimed for cold hardening because of hammering or exploitation (deformation induced the transformation of austenite into martensite), leading to an increase in hardness. However, the conclusion is that it also cannot drastically affect the tribological properties of this filler metal and that this filler metal should not be recommended for reparatory hard facing of parts exposed to intensive abrasive wear and impact loads.

ACKNOWLEDGEMENT

This research was partially financially supported by the Ministry of Education, Science and Technological development of Republic of Serbia through Grants TR 35021 and TR 35024. The authors are very grateful for this funding.

REFERENCES

[1] V. Lazić, R. Čukić, S. Aleksandrović, D. Milosavljević, D. Arsić, B. Nedeljković, M. Đorđević, Techno-economic justification of reparatory hard facing of various working parts of mechanical systems, Tribology in Industry, Vol. 36, No. 3, pp. 287-292, 2014.

[2] J. Truhan, R. Menon, F. LeClaire, J. Wallin, J. Qu, P. Blau, The Friction and Wear of Various Hard-face Claddings for Deep-hole Drilling, Wear, Vol. 263, pp. 234-239, 2007.

[3] A. Singh Kang, G. Singh Cheema, S. Singla, Wear Behavior of Hardfacings on Rotary Tiller Blades, Procedia Engineering, Vol. 97, pp. 1442-1451, 2014.

[4] S. Marković, Lj. Milović, A. Marinković, T. Lazović, Tribological Aspect of Selecting Filler Metal for Repair Surfacing of Gears by Hard Facing, Structural Integrity and Life, Vol. 11, No. 2, pp. 127-130, 2011.

[5] V. Lazić, M. Jovanović, D. Milosavljević, M. Mutavdžić, R. Čukić, Choosing of the Most Suitable Technology of Hard Facing of Mixer Blades Used in Asphalt Bases, Tribology in Industry, Vol. 30, No. 1&2, pp. 3-10, 2008.

[6] D. Arsić, V. Lazić, S. Mitrović, D. Džunić, S. Aleksandrović, M. Đorđević, B. Nedeljković, Tribological behavior of four types of filler metals for hard facing under dry conditions, Industrial Lubrication and Tribology, Vol. 68, No. 6, pp. 729-736, 2016.

[7] V. Lazić, D. Arsić, R. Nikolić, B. Hadzima, M. Mutavdžić, Experimental determination of mechanical characteristics of four types of stones and their influence on the construction machinery parts wear, Advanced Materials Research, Vol. 1100, pp. 178-184, 2015.

[8] N. Thongchitrugsa, A. Chianpairot, F. Hartung, G. Lothongkum, Effect of molybdenum on wear resistance of Cr-Nb Hard-faced S355JR steel, Materials Testing, Vol. 56 No. 3, pp. 191-197, 2014.

[9] ISO 6507-1:2018 Metallic materials – Vickers hardness test – Part 1: Test method.

[10] V., Lazić, D., Milosavljević, S., Aleksandrović, G., Bogdanović, B., Nedeljković:, Carbide type influence on tribological properties of the hard faced steel layer – part I – theoretical considerations, Tribology in Industry, Vol. 32, No. 2, pp. 11-20, 2010.

[11] V., Lazić, D., Milosavljević, S., Aleksandrović, G., Bogdanović, B., Nedeljković, Carbide type influence on tribological properties of the hard faced steel layer – part II – experimental results, Tribology in Industry, Vol. 32, No. 3, pp. 3-12, 2010.

SERBIATRIB '19

16th International Conference on Tribology

Serbian Tribology Society

Faculty of Engineering University of Kragujevac

Kragujevac, Serbia, 15 – 17 May 2019

OPTIMIZATION OF DRY TURNING PROCESS PARAMETERS USING TAGUCHI METHOD COMBINED WITH FUZZY LOGIC APPROACH

Mario DRAGIČEVIĆ[1,*], Edin BEGOVIĆ[2], Ivan PEKO[3]

[1]Univesity of Mostar, Faculty of Mechanical Engineering, Computing and Electrical Engineering, Mostar, B&H

[2]Univesity of Zenica, Faculty of Mechanical Engineering, Zenica, B&H

[3]AD Plastik d.d., Solin, Croatia

*Corresponding author: mario.dragicevic@fsre.sum.ba

Abstract: *In this paper, Taguchi method combined with fuzzy logic approach was used in order to define dry turning process parameters values that lead to minimal surface roughness. The surface roughness presents one of the most important criterions relating to proper choice of machining parameters during machining. Parameters that were being optimized here are cutting speed (v_c), depth of cut (a_p), feed rate (f) as well as workpiece steel material: St 50-2, C45 and 42CrMo4. The experiments were conducted using Taguchi's design of experiments. Orthogonal array L_9 (3^4) was selected for the four input parameters varied on the three levels. In this study it was found out that Taguchi method and fuzzy logic approach can be successfully employed to determine the optimal turning parameters values and to describe an influence of these parameters on the surface roughness response. Moreover, developed fuzzy logic model can be used for development of expert system that would enable better machining process control.*

Keywords: *dry turning, optimization, parameters, Taguchi, fuzzy logic*

1. INTRODUCTION

Green manufacturing is a basis of sustainable development strategy in machining industry that implies balancing between economical, ecological and sociological segment of production. Green machining in manufacturing industry requires changes in the type and quantity of resources, in the waste treatment, in the control of emissions CO_2, and in the quantity of manufactured products. The main goal of machining process is to get a high quality products in the short time. In achieving of that goal cutting fluids and machining input parameters have a main role. The problem of application conventional cutting fluids during machining processes are human health and environmental pollution problems. The solution in terms of switching to green manufacturing is hidden in application of alternative types of cooling, flushing and lubricating techniques. These techniques are minimum quantity lubrication (MQL), cooling with cold compressed air (CCA), cryogenic cooling (CL) with different gasses, high pressure cooling (HPC), minimum quantity lubrication and cooling (MQLC), near dry machining (NDM) or dry machining by using new cutting tools and coatings. Dry machining is an environmentally friendly technique which is successfully applied in machining processes.

The most important advantages of dry machining are in reducing of disposal and cleaning costs of cutting fluids, reducing of environmental pollution and no danger for health of operators. The elimination of CFs involves the loss of their positive effects, such as cooling, lubrication and chip flushing. Development of production in terms of transition to dry machining is followed by development of new cutting tool materials. Advanced cutting tool materials and tool coatings are necessary during dry machining but they are very expensive and increase the total machining costs. Some of these materials are: sintered diamond, sintered CBN, ceramics (Al_2O_3), cermets, cemented carbides etc. Coatings of cutting tools in dry machining replace function of conventional cutting fluids in the terms of decrease friction and temperature in the cutting zone. The lubricating function of coatings in dry machining can be replaced with the soft coatings or so-called self-lubricating coatings like molybdenum disulfide (MoS_2) or tungsten carbide/carbon (WC/C).

In each machining process so even in dry machining a surface roughness is one of the most used outputs that defines a quality of the final product. In this paper an investigation of the influence of input process parameters such as cutting speed, depth of cut, feed rate and type of workpiece material on the surface roughness output was conducted. Combined approach of Taguchi method and fuzzy logic technique was used to describe an influence of each process parameter on the surface roughness response and to define parameters values that lead to minimal surface roughness.

2. EXPERIMENTAL PROCEDURE

Experiments in this paper were carried out on a conventional PA-501A Potisje lathe with the ISO CNMG 120408-WG coated carbide insert of cutting tool. All experimental tests were carried out by dry machining. Machining process parameters that were considered in the experimentations are: cutting speed (v_c), depth of cut (a_p), feed rate (f) and type of workpiece material. These parameters were varied in the following ranges: cutting speed 58-162 m/min, depth of cut 1-3 mm, feed rate 0.107-0.321 mm/rev on three levels and workpiece material as follows St 50-2, C45, 42CrMo4 (Table 1). Measurements of the surface roughness parameter *Ra* were performed on a Perthometer M1 type (Mahr) profilometer, at three different locations. Experimental design matrix was defined in accordance with the standard Taguchi L9 (3^4) orthogonal array (Table 2). Experimental setup is presented in Figure 1.

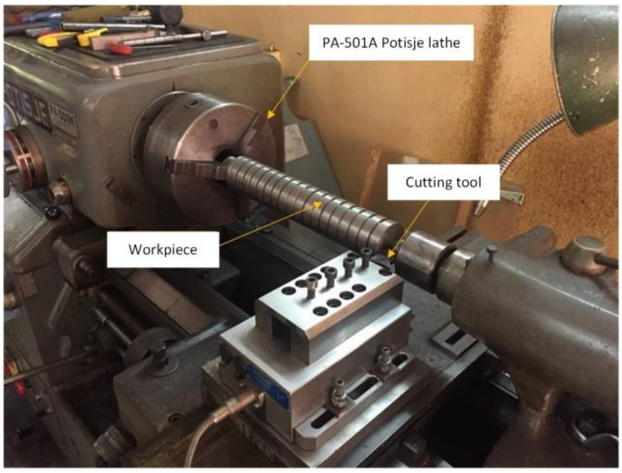

Figure 1. Experimental setup for dry turning

Table 1. Dry turning process parameters levels

Parameter/Level	Symbol	Level		
		1	2	3
Cutting speed v_c (m/min)	A	58	110	162
Depth of cut a_p (mm)	B	1	2	3
Feed rate f (mm/rev)	C	0.107	0.214	0.321
Workpiece material	D	St 50-2	C45	42CrMo4

3. METHODOLOGY

3.1 Taguchi method

Taguchi method is a simple and powerful tool for modelling, analysis and optimization of the machining process. In this method experimental data need to be transformed into signal-to-noise (*S/N*) ratio as the measure of the output quality characteristic. By *S/N* ratio it is possible to evaluate the effect of changing a particular input parameter on the analyzed process response. Depending on the criterion for the quality characteristic to be optimized, the *S/N* ratio can be divided into: smaller-the-better, larger-the-better, and nominal-the-better. Regardless of the category of the process response, the larger *S/N* ratio corresponds to the better process performance characteristic. Accordingly, process parameters levels that lead to optimal response have the highest *S/N* ratio values. Optimization of process response is performed by using the analysis of means (ANOM) and analysis of variance (ANOVA). The last step in the Taguchi optimization is conducting of the confirmation experiment that should verify optimal settings of variable process parameters [1, 2, 3].

Table 2. L9 orthogonal array and surface roughness results

Trial No.	Input parameters				Outputs	
	A	B	C	D	*Ra* (µm)	*S/N* (dB)
1.	1	1	1	1	1.88	-5.483
2.	1	2	2	2	1.17	-1.363
3.	1	3	3	3	1.36	-2.670
4.	2	1	2	3	0.95	0.445
5.	2	2	3	1	1.1	-0.827
6.	2	3	1	2	1.42	-3.045
7.	3	1	3	2	1.55	-3.806
8.	3	2	1	3	1.52	-3.636
9.	3	3	2	1	1.16	-1.289

3.2 Fuzzy logic

Fuzzy logic is an artificial intelligence method that is very useful for modelling complex processes where limited and imprecise informations and numerical data do not allow development of accurate mathematical models by using classical methods such as regression analysis. In these cases a fuzzy logic provides a way to better understand the process behaviour by allowing the functional mapping between input and output observations [4, 5]. Each fuzzy system consists of four components: the fuzzification module, the fuzzy inference module and the knowledge base and the defuzzification module. Fuzzification module converts numerical input data into linguistic variables by using different membership functions. There are various membership functions such as triangular, trapezoidal, Gaussian etc. These functions define how each point in the input and output space is mapped to a degree of membership value between 0 and 1. Fuzzy inference module uses knowledge base of membership functions and fuzzy IF-THEN rules to perform fuzzy reasoning and generate fuzzy linguistic output variables for corresponding inputs. Finally, the defuzzification module converts the aggregated fuzzy outputs into a non-fuzzy values [4, 5, 6].

4. RESULTS AND DISCUSSION

The process response values for all 9 experiments are used to calculate *S/N* ratio. In this case the goal is a minimization of the surface roughness and because of that *S/N* ratio smaller-the-better was used in calculations. Smaller-the-better *S/N* ratio can be defined as:

$$S/N = -10\log_{10}\left(\frac{1}{n}\sum_{i=1}^{n} y_i^2\right) \qquad (1)$$

where is *S/N* - signal-to-noise ratio, *n* - number of repetitions of the experiment, y_i - measured values of quality characteristic.

To analyze the effects of process parameters on surface roughness a main effects plot was generated. Main effects plot for S/*N* ratio of surface roughness is presented in Figure 2. Greater inclination of input parameter line defines a higher influence of that parameter on the surface roughness. Difference between maximal and minimal average of *S/N* ratio values determines the rank of parameters that affects the process response *Ra*. These values are listed in Table 3.

As it was already mentioned, the highest values of *S/N* ratio define input process parameters levels that together lead to the best process response characteristic. Based on

Figure 2 and Table 3 the optimal setting of process parameters that results with minimal surface roughness is identified as cutting speed 110 m/min, depth of cut 2 mm, feed rate 0.214 mm/rev and workpiece material 42CrMo4, represented as $A_2B_2C_2D_3$. This is marked in bold font in Table 3.

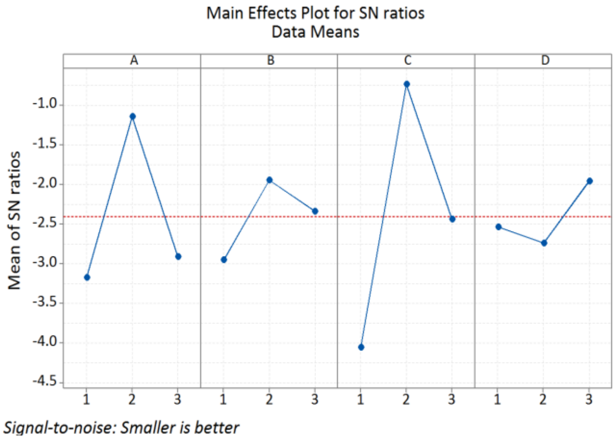

Figure 2. Main effects plot for *S/N* ratios of surface roughness

Table 3. Response table for *S/N* ratio, smaller is better

Level	Parameters			
	Cutting speed (v_c) A	Depth of cut (a_p) B	Feed rate (f) C	Workpiece material D
1	-3.1726	-2.9481	-4.0553	-2.5334
2	**-1.1427**	**-1.9428**	**-0.7358**	-2.7387
3	-2.9109	-2.3352	-2.4351	**-1.9540**
Delta	2.0299	1.0053	3.3195	0.7847
Rank	2	3	1	4

To estimate the significance of input parameters on surface roughness, analysis of variance (ANOVA) was performed. Because the experimentation with 4 parameters at 3 levels by using Taguchi L_9 OA does not provide enough data, firstly ANOVA pooling should be conducted. ANOVA pooling is a process of revision and re-estimation of ANOVA results in order to ignore an insignificant parameter whose contribution is less [7, 8]. In this case, from the Table 3 it is evident that workpiece material has the smallest influence on *S/N* ratio of surface roughness. Therefore, ANOVA pooling was done by exception that parameter (Table 4). From the pooled ANOVA it is obvious that feed rate is the most influential parameter that contributes towards *S/N* ratio by 62.67%. It is followed by cutting speed with contribution of 27.73% and depth of cut of 5.84%. This analysis was carried out in the MINITAB statistical software.

Table 4. ANOVA for *S/N* ratio of surface roughness (after pooling)

Source	DF	SS	MS	F	%
A	2	7.3153	3.6576	7.36	27.73
B	2	1.5402	0.7701	1.55	5.84
C	2	16.5316	8.2658	16.64	62.67
Error	2	0.9935	0.4968		3.77
Total	8	26.3805			

In the final step of Taguchi method it is obvious to conduct confirmation experiment to verify optimal process parameters settings ($A_2B_2C_2D_3$). Predicted and experimentally observed values of surface roughness at the optimum levels of process parameters are shown in Table 5.

Table 5. Results of confirmation experiment

	Taguchi optimal parameters settings			
	Prediction	Experiment		
Parameters levels	$A_2B_2C_2D_3$	$A_2B_2C_2D_3$		
Surface roughness *Ra* (µm)	0.753	*Ra1*	*Ra2*	*Ra3*
		0.76	0.73	0.77

Furtherly, in order to develop an expert system that would be used for better control of machining process a fuzzy logic modelling of surface roughness was performed. Mamdani fuzzy inference system was used to define relationship between variable (the most influential) process parameters (v_c, a_p and f) and surface roughness response. Structure of developed fuzzy logic system is shown in Figure 3.

For each input in fuzzy logic system three Gauss membership functions were used: low (L), medium (M) and high (H). On the other side six Gauss membership functions were used to describe an output of fuzzy logic system: low (L), low-medium (LM), medium (M), medium-high (MH) high (H) and very high (VH). These functions are shown in Figure 4.

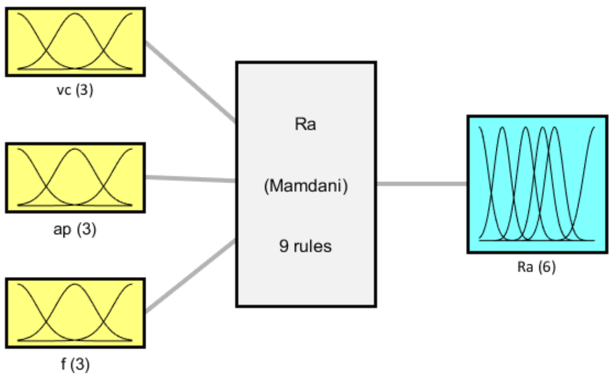

Figure 3. Structure of three inputs and one output fuzzy logic system

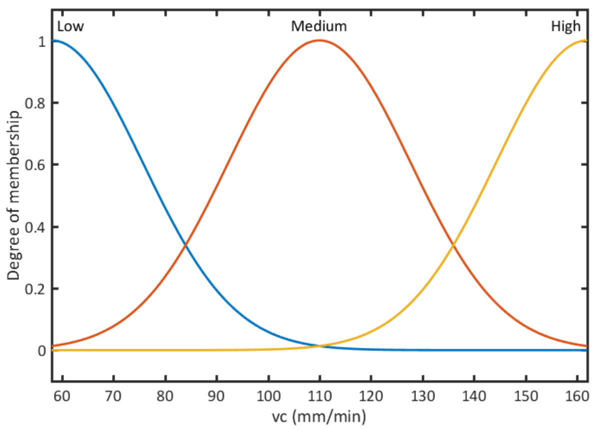

a)

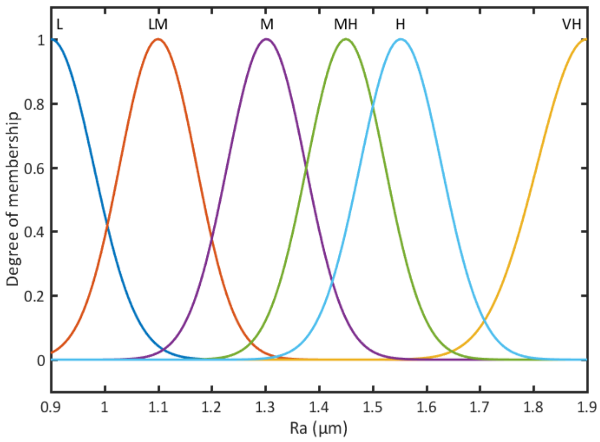

b)

Figure 4. Membership functions used for a) inputs (v_c, a_p, f), b) output (Ra)

To perform reasoning fuzzy logic system uses a set of fuzzy IF-THEN rules. In this case a set of nine IF-THEN rules were created to establish a relations between inputs and output. These rules are shown in Figure 5.

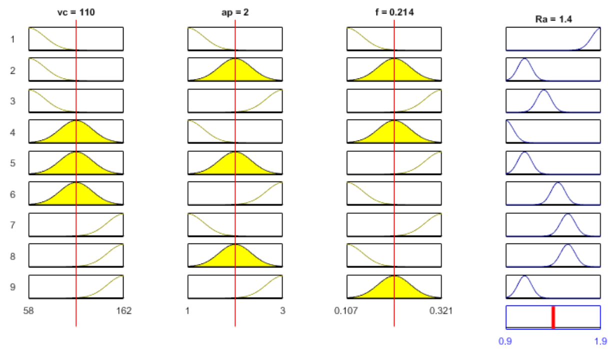

Figure 5. Graphical representation of fuzzy IF-THEN rules

Fuzzy inference process was conducted using MATLAB R2015 software toolbox with the following settings: and method: min, or method: max, implication: min, aggregation: max, defuzzification method: centroid.

Defuzzification module of developed fuzzy logic system converted fuzzy values of *Ra* into a non-fuzzy values. In order to verify prediction accuracy of generated fuzzy logic model, experimental and predicted values of surface roughness were compared. Mean absolute percentage error (MAPE) was used as comparison measure. MAPE of 3.14% proves a good prediction accuracy of developed fuzzy logic model. Comparison results, experimental and predicted surface roughness values and MAPE are shown in Figure 6.

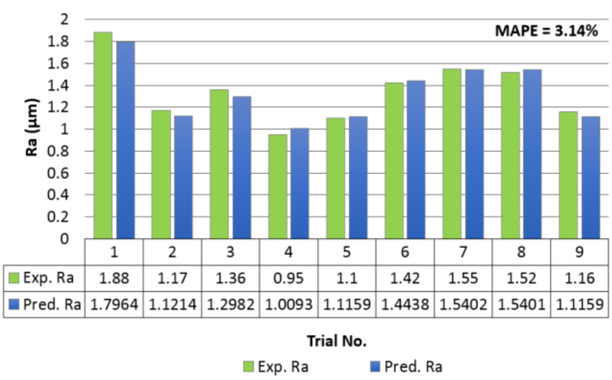

Figure 6. Comparison between experimental and predicted surface roughness values

Based on the developed and validated fuzzy logic model corresponding surface plots that show influence of input process parameters on the surface roughness were created and presented in Figure 7.

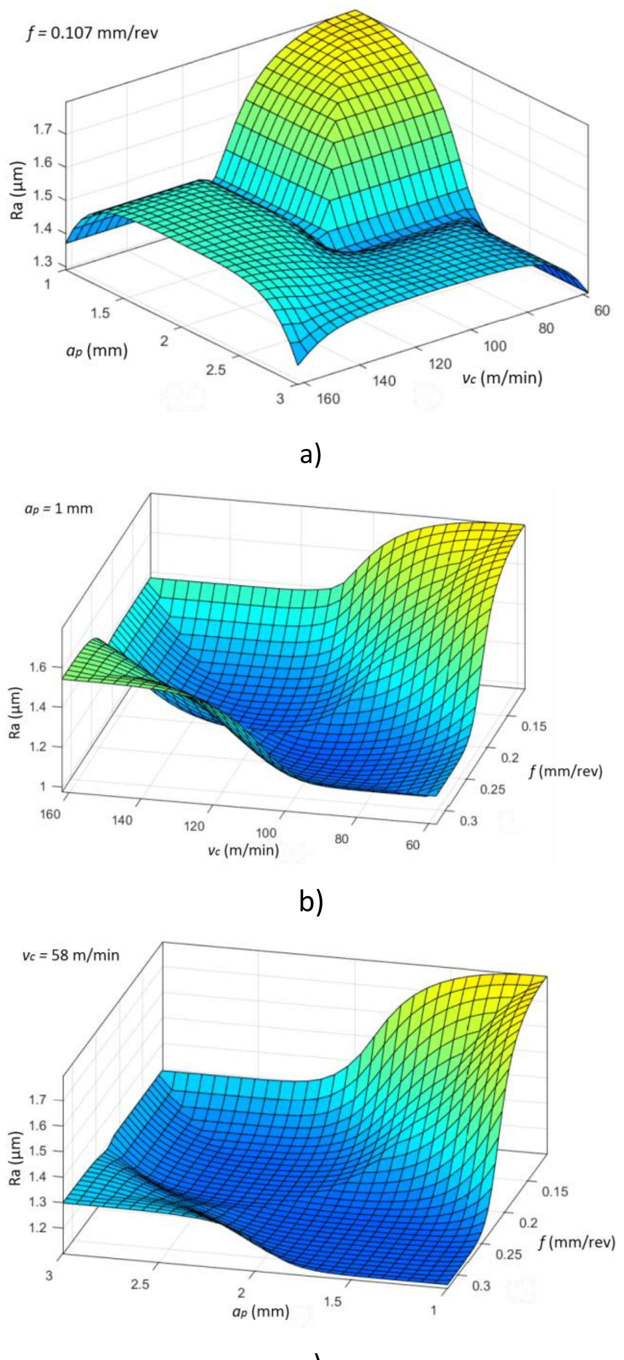

Figure 7. Effects of process parameters on surface roughness response

5. CONCLUSION

This paper presents an application of combined Taguchi-fuzzy logic approach for the optimization and analysis of surface roughness in dry turning machining process. Four different process parameters: cutting speed, depth of cut, feed rate and workpiece material were considered in experimentation according to Taguchi L_9 orthogonal array. From the conducted research, the following conclusions can be drawn:

- feed rate and cutting speed are the most significant parameters that affect the surface roughness variation, whereas the influence of the depth of cut and workpiece material is much smaller,
- it was observed that the cutting speed should be kept at the level 110 m/min, depth of cut 2 mm, feed rate 0.214 mm/rev and workpiece material should be 42CrMo4 to obtain minimal surface roughness,
- fuzzy logic method presents a good mechanism to describe an influence of significant variable dry turning process parameters on the surface roughness and to create an expert system that can be used furtherly in new experimentations and for better machining process control.

REFERENCES

[1] P. Ross: *Taguchi techniques for quality engineering*, McGraw Hill, 1988.

[2] M. Radovanović, L. Slatineanu, P. Janković, D. Petković, M. Madić: Taguchi Approach for the Optimization of Cutting Parameters in Finish Turning of Medical Stainless Steel, Applied Mechanics and Materials, Trans Tech Publications, Switzerland, Vol. 809-810, pp. 153-158, 2015.

[3] M. Madić, M. Radovanović, L. Slatineanu: Surface roughness optimization in CO_2 laser cutting by using Taguchi method, U.P.B. Sci. Bull., Series D, Vol. 75, No. 1, pp. 97-106, 2013.

[4] S. Sivarao, P. Brevern, N.S.M. El-Tayeb, V.C. Vengkatesh: GUI based Mamdani fuzzy inference system modelling to predict surface roughness in laser machining, International Journal of Electrical and Computer Sciences, Vol. 9, No. 9, pp. 37-43, 2009.

[5] M. Madić, M. Radovanović, Ž. Ćojbašić, B. Nedić, M. Gostimirović: Fuzzy Logic Approach for the Prediction of Dross Formation in CO_2 Laser Cutting of Mild Steel, Journal of Engineering Science and Technology Review, Vol. 8, No. 3, pp. 143-150, 2015.

[6] C.Z. Syn, M. Mokhtar, C.J. Feng, Y.H.P. Manurung: Approach to prediction of laser cutting quality by employing fuzzy expert system, Expert Systems with Applications, Vol. 38, No. 6, pp. 7558-7568, 2011.
[7] N. Senthikumar, J. Sudha, V. Muthukumar: A grey-fuzzy approach for optimizing machining parameters and the approach angle in turning AISI 1045 steel, Advances in Production Engineering & Management, Vol. 10, No. 4, pp. 195-208, 2015.
[8] Das Biswajit, S. Roy, R.N. Rai, S.C. Saha: Application of grey fuzzy logic for the optimization of CNC milling parameters for Al-4.5%Cu-TiC MMCs with multi-performance characteristics, Engineering Science and Technology, an International Journal, Vol. 19, No. 2, pp. 857-865, 2016.

Serbian Tribology Society

SERBIATRIB '19

16th International Conference on Tribology

Faculty of Engineering University of Kragujevac

Kragujevac, Serbia, 15 – 17 May 2019

ANALYSIS AND OPTIMIZATION OF SURFACE ROUGHNESS IN CO_2 LASER CUTTING OF P265GH STEEL

Miloš MADIĆ, Predrag JANKOVIĆ, Miroslav RADOVANOVIĆ, Dušan PETKOVIĆ
Faculty of Mechanical Engineering, Niš, Serbia
*Corresponding author: madic@masfak.ni.ac.rs

Abstract: *This paper is focused on the analysis and optimization of surface roughness obtained in CO_2 laser cutting of 4mm thick P265GH steel plate using oxygen as assist gas. For the purpose of experimental investigation central composite face-centered factorial design with 3 factors was realized. Assist gas pressure, cutting speed and nozzle diameter were considered as input controllable parameters and were systematically varied at 3 levels during the experimentation. Upon realization of experimental trials and measurements of surface roughness, second order non-linear mathematical model for the prediction of surface roughness was developed. Analysis of the developed model revealed the existence of significant parameter interaction effects. It has been observed that the effect of a given parameter on the surface roughness is varying and dependent on the settings of the other parameters. For each nozzle diameter a combination of assist gas pressure and cutting speed which yields minimal surface roughness was determined with the use of contour plots.*

Keywords: *CO_2 laser cutting, surface roughness, central composite design, mathematical model, P265GH steel*

1. INTRODUCTION

Laser cutting is one of the most widely used non-traditional contour cutting technologies in modern industry. The cutting process is achieved by concentrating high power and energy densities by focusing the laser beam on the workpiece material surface into a very small spot. Subsequently, the material being irradiated by the laser beam heats, melts and even evaporates in a fraction of a second. The removal of this molten and evaporated material is achieved by using the coaxial stream of assist gas, which type and pressure depend on the applied laser cutting method as well as the workpiece type and its thickness. Despite the simplicity of the process, multiple parameters affect the result in terms of cost, productivity, geometrical quality and surface quality. For a given material, some of them contribute to the melting, while others contribute to the removal of this molten material [1].

During the past years researchers, practitioners and scientists apply and combine different experimental methods, analytical and empirical approaches as well as mathematical and computational techniques and methods in order to analyze, model and control the cutting process and/or to obtain new insights about the laser cutting process. As the laser cutting process itself is a very complex process, often described as multi input multi output process, different laser cutting performances are being investigated. Related to the geometrical quality of cut, kerf width (top and bottom), kerf taper angle, perpendicularity deviation and dross adherence are widely investigated. Surface roughness, striation frequency, boundary layer separation point, drag line separation and erosion are often used as quality indicators of surface pattern. Size of the heat affected zone, micro-hardness, material removal rate, costs, cutting time are also some of the most important performance characteristics of the cutting process.

Great practical importance of surface roughness and its complex nature motivated the present research aimed at modeling and optimization of surface roughness in CO_2 laser cutting of a pressure vessel steel P265GH. To this aim, central composite face-centered factorial design with 3 parameters, such as assist gas pressure, cutting speed and nozzle diameter, was realized and the experimentally obtained data were used for surface roughness analysis, modeling and optimization.

2. EXPERIMENTAL SETUP AND DETAILS

The workpiece material used in the study was a 4 mm thick pressure vessel steel P265GH. This steel is carbon non-alloy steel designed for high temperature applications. Because of a good weldability it is widely used for manufacturing pressure vessels, piping elements, boilers, heat exchangers and similar components. From a plate the specimens with dimensions of 50 × 90 mm were cut using oxygen, Oxycut 3.5. In experimentation the following conditions were constant: CW operating mode, Gaussian distribution beam mode (TEM_{00}), laser power 1.3 kW, lens focal length of 127 mm, focal point position of 0 mm and standoff distance of 1 mm. On the other hand, three laser cutting parameters such as oxygen pressure (*p*), cutting speed (*v*) and nozzle diameter (d_n), were varied in accordance with the central composite face-centered factorial design. This type of central composite designs requires only 3 levels of each parameter during experimentation. The parameter levels used in the experiment are given in Table 1.

Table 1. Laser cutting parameter levels

Level	*p* (bar)	*v* (m/min)	d_n (mm)
-1	0.7	2.6	1.25
0	1.1	2.9	1.5
+1	1.5	3.2	2

In experiment, 8 trials in factorial points, 6 trials in axial (star) points and 3 trials in central point were conducted. In order to avoid bias, the experimental trials were performed at random. All trials were conducted in manufacturing environment using the Prima industry CO_2 laser cutting machine.

Surface roughness of cut edge was selected as the process response as its values are essential for characterization of the cut surface. It was assessed in terms of the average roughness (R_a). The measurements were made using digital, stylus type measuring instrument MahrSurf-XR1. The averaged value of three measurements taken along the cut at approximately in the middle of the workpiece thickness was recorded for each specimen. The surface roughness profile obtained in trial 10 (*p*=1.5 bar, *v*=2.9 m/min, d_n=1.5 mm) is given in Figure 1.

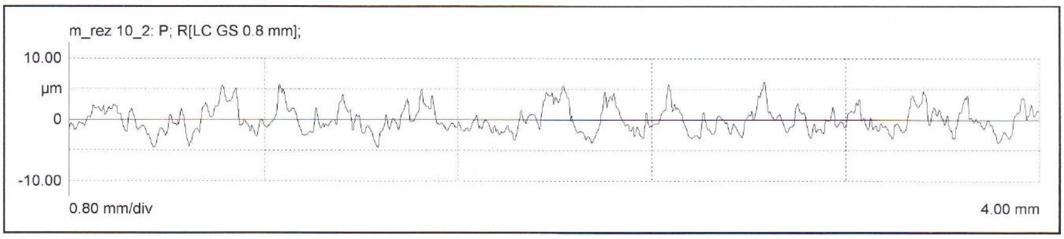

Roughness parameters - m_rez 10_2: P; R[LC GS 0.8 mm];	
Ra	1.663 µm
Rz	9.449 µm
Rmax	10.198 µm

Figure 1. Surface roughness profile (left) and measured surface roughness

3. RESULTS AND DISCUSSION

Based on experimentally measured values of surface roughness in all experimental trials the mathematical model relating the laser cutting parameters and surface roughness (R_a) was developed in the form of the second order polynomial equation:

$$\begin{aligned} &R_a \quad 1.53 \quad 0.11p \quad 0.15v \\ &0.41d_n \quad 0.34p^2 \quad 0.27v^2 \qquad\qquad . \quad (1) \\ &0.002d_n^2 \quad 0.13pv \quad 0.29pd_n \quad 0.43vd_n \end{aligned}$$

The coefficient of determination (R^2) value of 0.88 and mean average percentage error of about 10.2 % indicated that the model explained 88 % of the variability in surface roughness values and that the model has acceptable degree of accuracy. For the purpose of the analysis of the effects of laser cutting parameters on the surface roughness, 3 interaction graphs were developed (Figure 2).

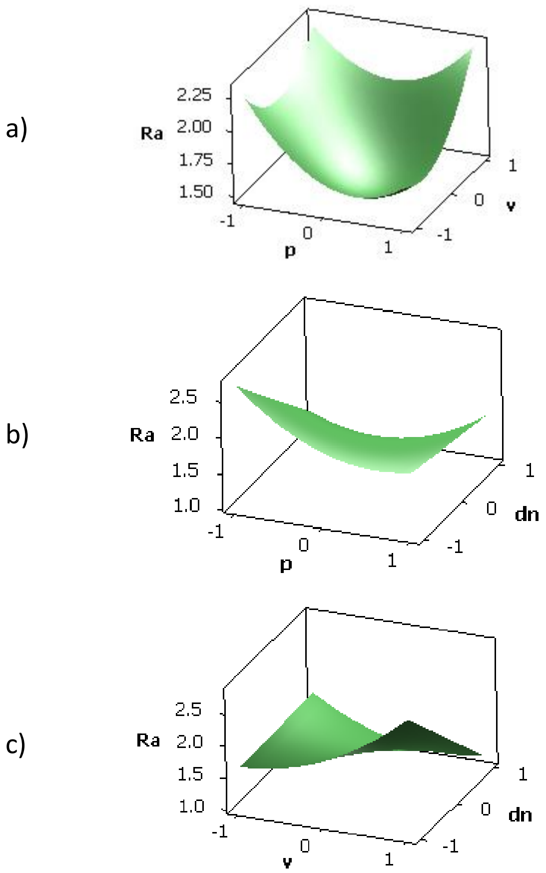

Figure 2. Interaction effects of the laser cutting parameters on the surface roughness

As could be observed from Figure 2a, for a given nozzle diameter, there exists an optimal combination of oxygen pressure and cutting speed which yields minimal surface roughness. For the selected intervals of change, for both parameters, positive and negative correlation between these parameters and surface roughness alter. From Figure 2b it could be observed that large nozzle diameters tend to produce smoother cut surfaces. This may be due to reduced jet velocities which prevent the turbulence of the melt or due to insensitivity of larger nozzles to minor misalignment and changes in oxygen supply pressure [2]. Figure 2c reveals that there exists a significant interaction effect between the cutting speed and nozzle diameter. Lower surface roughness values can be obtained in combination of low cutting speed and smaller nozzle diameter or in combination of high cutting speed and larger nozzle diameter. On the other hand, the roughest cut surface is obtained when using the smallest nozzle diameter and the highest cutting speed, which corresponds to the conditions of the least interaction time between the laser beam and workpiece material and low flow rate in the cutting zone which results in lower induced energy from exothermic reaction which, in addition to laser energy, is not sufficient to evacuate the molten metal cleanly and efficiently. Other possible reasons for this observation may be due to changes in kerf width, coupling efficiency and inclination angle of the cutting front due to cutting speed as well as increased oxygen jet velocities and possible turbulences. A nozzle with a small diameter creates difficulties in alignment and localizes the gas, resulting in a rough edge [3]. The interaction effect of these two parameters on the surface roughness is even more complex considering that the nozzle diameter may influence the cutting speed itself and that for a given workpiece material and thickness there exists an optimal nozzle diameter which gives the maximal cutting speed [4]. The change in the effect of the cutting speed on the surface roughness was also reported in the case of CO_2 laser cutting of P256GH steel with thickness of 6 mm [5].

The afore-given discussion indicates a very complex nature of surface roughness formation in CO_2 laser cutting of P256GH steel necessitating the careful selection of process parameters via process optimization. Given that the nozzle diameter is in essence discrete parameter which can have only a finite set of values, optimization of surface roughness with respect to other parameters can be performed using contour plots. The contour plot showing the change of surface roughness with respect to oxygen pressure and cutting speed for the nozzle diameter of 2 mm is given in Figure 3.

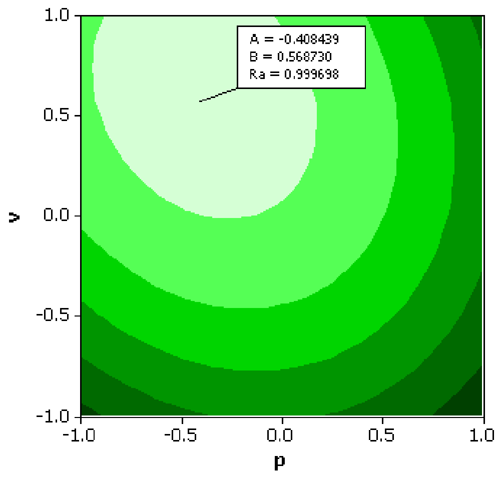

Figure 3. Contour plot of surface roughness

In Figure 3, A and B designate coded values of oxygen pressure and cutting speed. After transforming the coded values into real parameter values it could be observed that oxygen pressure of 0.94 bar and cutting speed of 3.07 m/min yield the minimal surface roughness of 1µm. In the case of using the smallest nozzle diameter (1.25mm), the combination of oxygen pressure of 1.4 bar and cutting speed of 2.61 m/min would yield the minimal surface roughness of 1.42 µm.

4. CONCLUSION

The conclusions drawn from the conducted study can be summarized by the following points:

- For the considered experimental hyper-space there exist significant interactions between laser cutting parameters which ultimately affect surface roughness formation.
- For each nozzle diameter there exists a certain combination of cutting speed and assist gas pressure which yield minimal surface roughness which belong to grade N7.
- The minimal surface roughness of 1µm can be obtained using the nozzle diameter of 2mm. Considering laser cutting costs, however, one should be kept in mind that an increase in the nozzle diameter by a factor of 2, increases the the assist gas flow rate by a factor of 4.

The developed surface roughness model can be used in line with other models as the functional constraint in the formulation of different laser cutting optimization problems.

ACKNOWLEDGEMENT

This work was carried out within the project TR 35034, financially supported by the Ministry of Science and Technological Development of the Republic of Serbia.

REFERENCES

[1] A. Riveiro, F. Quintero, M. Boutinguiza, J.D. Val, R. Comesaña, F. Lusquiños, J. Pou: Laser cutting: a review on the influence of assist gas, Materials, Vol. 12, No. 1, pp. 157, 2019.

[2] J. Powell: *CO_2 Laser Cutting*, Springer-Verlag, London, 1993.

[3] J. Ion: *Laser Processing of Engineering Materials: Principles, Procedure and Industrial Application*, Elsevier, 2005.

[4] W.M. Steen, J.N. Kamalu: Laser cutting, in: M. Bass (Ed.): *Materials Processing: Theory and Practices,* Imperial College of Science and Technology, London, pp.15-111, 1983.

[5] R. Kowalczyk, W. Zebala: Analysis of laser cutting speed influence on the surface quality and shape deviation of steel parts, Proceedings of the SPIE, Vol. 9290, id. 929011 9, 2014.

Serbian Tribology Society

SERBIATRIB '19

16th International Conference on Tribology

Faculty of Engineering University of Kragujevac

Kragujevac, Serbia, 15 – 17 May 2019

DETERMINATION OF CORRECTED PARAMETERS IN STRIP IRONING PROCESS WITH DOUBLE SIDE THINNING

S. ALEKSANDROVIĆ[1], S. ĐAČIĆ[2], M. ĐORĐEVIĆ[3], V. LAZIĆ[4], D. ARSIĆ[5]

[1]Faculty of Engineering, University of Kragujevac, Serbia, srba@kg.ac.rs
[2]Coal Mine, Pljevlja, Montenegro, djale@t-com.me
[3]Faculty of Technical Sciences Kosovska Mitrovica, University of Pristina, Serbia, milan.t.djordjevic@pr.ac.rs
[4]Faculty of Engineering, University of Kragujevac, Serbia, vlazic@kg.ac.rs
[5]Faculty of Engineering, University of Kragujevac, Serbia, cmz@fink.rs

Abstract: Determination of corrected main process parameters procedure in the strip ironing process with double side thinning, as well as appropriate experimental results are presented in this paper. Given is modified analysis for friction coefficient and contact pressure determination. Classical common so called "Schlosser model" is not suitable in many cases, and give unreal values for both of main process parameters. Formulas obtained here were verified in suitable examples which are, also, presented in the paper. Verification was performed on the base of experimental results. Realised was the single and four phase process of mild steel DC04 sheet stripes drawing. Stripes were 20 mm wide and 2.5 mm thick. Lateral force intensities were 5, 10 and 15 kN. Maximal obtained thinning deformation in one phase was about 17%. Appropriate lubrication with mineral oil and grease was used in conditions of lower speed of 20 mm/min.

Results shows that proposed corrected parameters enables more precise process monitoring and precise quantification of lateral force, contact pressure and thinning strain influence on friction.

Keywords: ***strip ironing test, corrected parameters, mild steel strips***

1. INTRODUCTION

Ironing is known as technological process which combine characteristics of sheet metal forming and bulk forming. Significance of ironing technology illustrate great interest of the researchers over the years. It is clearly visible in relatively small number of selected references ([1]–[18]) whose are representing short history of last four decades ironing researches. Main reason is probably great appliance of ironing forming process in modern industry. It is sufficiently to notice that by even ironing process industry produce more than two hundred billions pieces of well known product: beverage cans ([5], [7], [9]).

There are many researches of ironing process in literature. Only some of them are given here. Practically all cited references give tribological approach, mainly because ironing is most severe process in that sense. One of the significant tribological element is lubrication i.e. determination of the proper lubricants performance. In order to obtain tribological parameters and to quantify the performance of the individual lubricants, a different simulative tests has been developed. All the tests are modeling the process conditions in ironing, from old, now classic [1] to new ones ([12], [13]). All the tests considered mechanical models, parameters identification and experimental research of some selected factors influence on tribological phenomena's or specific parameters.

In papers [1] to [10] given were process analysis, modeling, parameters determination and particular experimental investigations of lubricants evaluation by friction coefficient determination mainly. In other cases used were specific materials, like in [3] and [4]. In [11] and [12] introduced was new test simulator and given were the results of tool characteristics influence on friction and lubrication. Papers [13] to [16] gives extensive researches of application of environmentally friendly lubricants. In papers [17] and [18] authors pays attention to some specific aspects of ironing process like acoustic emission, heat effects etc.

In this paper authors exposed are their own complete mechanical model and method for friction coefficient and contact pressure determination depending on drawing force, lateral force, tool and material sample geometry. Double sided strip reduction test was chosen in whole experiment. Conducted were extensive experimental investigations towards verifications of proposed procedures. With the reliable defined parameters can be perform different experimental investigations and, it is important, obtain more safer and precise results.

2. MECHANICAL MODEL OF ACTING FORCES

In this approach double sided thick strip reduction test was chosen like previously was mentioned. Figure 1 shows scheme of test tooling elements and main forces. The thick metal strip is being placed into the holding jaw. The jaw with the sample is moving in vertical direction, from down to up. On the sample acted drawing force F and two lateral (side) forces F_S which simulate the industrial tool die and perform the ironing. It is useful to notice that in Figure 1 are shown active lateral force and corresponding reactive forces. Also, it is important to notice for this model that existing of small vertical area which can be consider flat in first approximation (Figure 1 and 2).

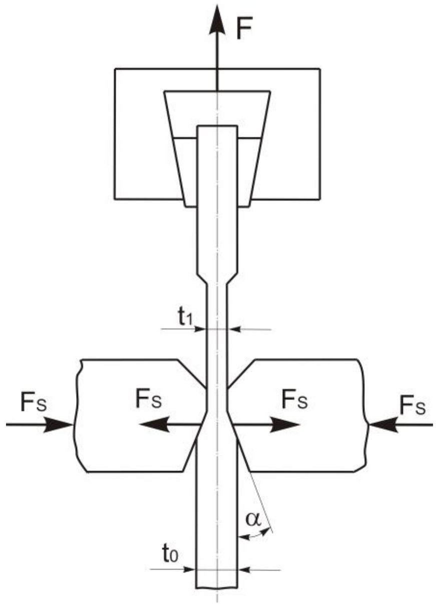

Figure 1. Test tooling elements

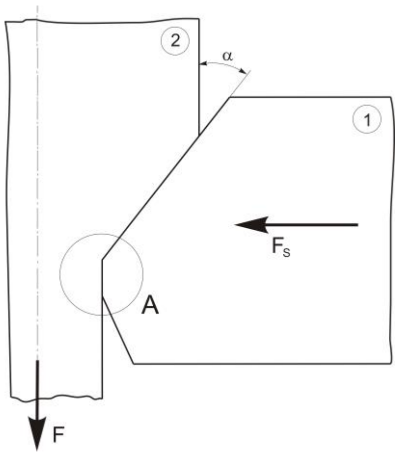

Figure 2. Contact zones

In real it is small arched surface of side element rounded edge i.e. part of cylindrical area with about 1 mm radius which is adopted here (Figure 3).

Forming and sliding process can be analyzed in two possible cases.

First case: ironing in conditions of very small deformation of thinning according to criteria:

$$s \quad \frac{s}{2} \quad \frac{s_0 \quad s_1}{2} \quad r\,1 \quad \cos \qquad (1)$$

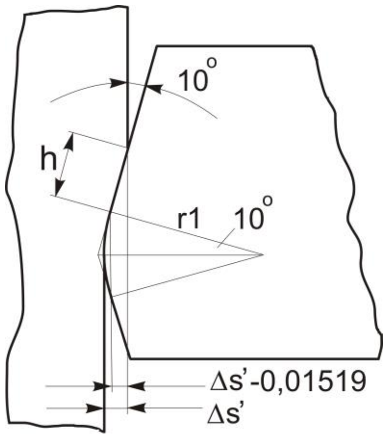

Figure 3. More realistic model

$$s \quad s_0 \quad s_1 \quad 2r\ 1 \quad \cos \qquad (2)$$

$$\frac{2r\ 1 \quad \cos}{s_0} 100,\ \% \qquad (3)$$

where s_0 is initial sheet thickness, s_1 is thickness after forming process, ε is percentage deformation. With here adopted values given are:

$$s \quad \frac{s}{2} \quad 0.0159 \qquad (4)$$

$$s \quad s_0 \quad s_1 \quad 0.03038 \qquad (5)$$

$$\frac{3.038}{s_0},\ \%\ ;\ for\ s_0 \quad 2.5\ mm \qquad 1.215\% \qquad (6)$$

Process is carry out in conditions of contact established on rounded surface only (Figure 3). There is no any flat contact. Mechanical model is very simple: drawing force **F**, two side forces $\mathbf{F_S}$ and two friction forces $\boldsymbol{\mu F_S}$ (Figure 3). Friction forces can be consider vertical (like adopted here) or inclined. Difference is negligible because angle **α** is relatively small and cosα≈1.

Second case: Ironing in conditions of flat area formation above small rounded area.

$$s \quad s_0 \quad s_1 \quad 2r\ 1 \quad \cos \qquad (7)$$

$$\frac{2r\ 1 \quad \cos}{s_0} 100,\ \% \qquad (8)$$

$$s \quad s_0 \quad s_1 \quad 0.03038 \qquad (9)$$

$$\frac{3.038}{s_0},\ \%\ ;\ if\ s_0 \quad 2.5\ mm \qquad 1.215\% \qquad (10)$$

So, sliding process and forces acting can be monitored now in two zones, rounded and flat.

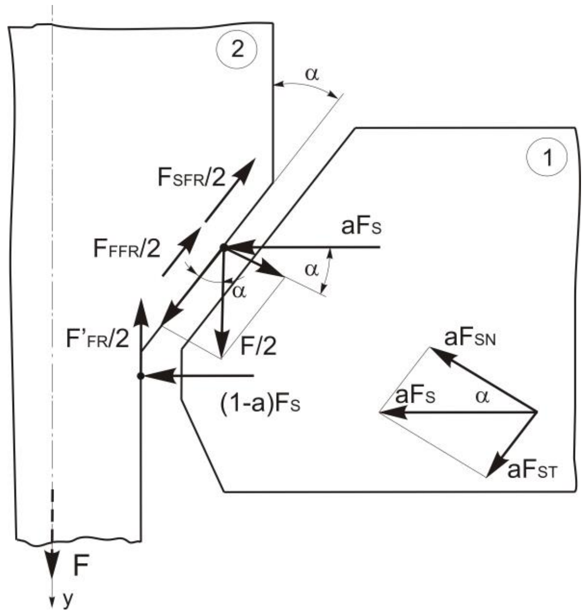

Figure 4. Mechanical model of right side forces acting

Mechanical model of acting forces is given in Figure 4 (for right side only). Can be assumed that side tool element 1 is slightly moved and his acting changed with the force $\mathbf{F_S}$. Distribution of force $\mathbf{F_S}$ between flat inclined and small near vertical surfaces determined by empirical parameter **a.** It was adopted **a=0.7** after analysis in [7]. Friction force $\mathbf{F_{SFR}}$ depends on normal component ($\mathbf{aF_{SN}}$) of side force part $\mathbf{aF_S}$. Force $\mathbf{F_{SFR}}$ acting on flat inclined surface. Force $\mathbf{F_{FFR}}$ depends on normal component of drawing force **F/2**. Friction force $\mathbf{F_{FR}}$´ depends on **(1-a)**$\mathbf{F_S}$ part of side force $\mathbf{F_S}$ which acting through small vertical surface. It is useful to notice that rounded area can be approximated by small vertical zone or not. That´s depends on particular case.

2.1 Friction coefficient determination

In first case of ironing (expressions (1) to (6)) three forces acting only, like is previously mentioned: drawing force and two friction forces, one on each side. If considered friction force is vertical coefficient of friction can be calculated by expression (11). Alternatively coefficient of friction can be calculated by expression (12) with negligible difference.

$$\frac{F}{2F_S} \qquad (11)$$

$$\frac{F}{2F_S \cos} \quad \frac{F}{2F_S \cos \frac{}{2}} \tag{12}$$

In second case (criteria in expressions (7) – (10)) for all acting forces on material sample (part 2, Figure 4) can be written equilibrium equations (13), (14), (15).

$$F_{iy} \quad 0 \tag{13}$$

$$F \quad F'_{FR} \quad F_{FFR} \cos \quad F_{SFR} \cos \quad 0 \tag{14}$$

$$\begin{gathered} F \quad 2 \quad 1 \quad a \, F_S \quad F \sin \quad \cos \\ 2 \quad aF_S \cos \quad \cos \quad 0 \end{gathered} \tag{15}$$

It is better to use complete force system (both sides of sample). After relatively simple mathematical transformations (16) can be obtained expression (17) i.e. coefficient of friction. If particular values of inclination angle (α=10^o) and parameter a=0.7 is considered ([8], [10]), can be obtained final expression for friction coefficient (18).

$$F \quad 2 \, 1 \quad a \, F_S \quad \frac{F}{2} \sin 2 \quad 2aF_S \cos^2 \tag{16}$$

$$\frac{F}{\frac{F}{2} \sin 2 \quad 2aF_S \cos^2 \quad 2 \, 1 \quad a \, F_S} \tag{17}$$

$$\frac{F}{0.17101F \quad 1.357785F_S \quad 0.6F_S} \tag{18}$$

Expressions (17) and (18) clearly shows that precise measuring of drawing force is essential for accurate determination of friction coefficient μ. Important also were: side force intensity, tool geometry and parameter a, but these are constant and previously set up values.

2.2 Procedure of contact pressure determination

According to previous consideration there exist two possible cases of ironing process, and that is related to contact pressure, also.

In first case there is no flat area (h=0, Figure 3) and consequently not exist corresponding forces (expression 19).

$$if \;\; h \quad 0 \;\; and \; A_1 \quad 0 \qquad F_{iA1} \quad 0 \tag{19}$$

$$p \quad \frac{F_S}{A_2} \quad \frac{F_S}{l \;\; b} \quad \frac{180}{} \frac{F_S}{r \;\; b} \tag{20}$$

$$A_2 \quad l \;\; b \quad {}_r \; r \;\; b \quad \frac{^o}{180} r \;\; b \tag{21}$$

$$l \quad \frac{10}{180} \quad 1 \quad 0.174533 \tag{22}$$

$$if \quad 10^o \; and \;\; r \quad 1mm \qquad p \quad \frac{5.73F_S}{b} \tag{23}$$

So, contact pressure p can be calculated by expression (20) where A_2 is rounded surface which depends on arch length **l** and sample width **b** (21). With particular values, **l** is given by (22) and **p** by (23).

In second case can be assume that area A_1 and area A_2 are joined and continuous ((24) –(27)), and there are acting normal components of drawing force (F/2 for one sample side) and lateral force F_S.

$$\begin{gathered} A_1 \quad h \;\; b \quad \frac{\frac{s_0 \quad s_1}{2} \quad r \; 1 \quad \cos}{\sin} \quad b \\ \frac{s_0 \quad s_1 \quad 2r \; 1 \quad \cos}{2 \sin} \quad b \end{gathered} \tag{24}$$

$$h \quad 2.879385 \, s_0 \quad s_1 \quad 0.08749 \tag{25}$$

$$A_2 \quad l \;\; b \quad {}_r \; r \;\; b \quad \frac{^o}{180} r \;\; b \tag{26}$$

$$l \quad \frac{10}{180} \quad 1 \quad 0.174533 \tag{27}$$

$$p \quad \frac{F_i}{A_1 \quad A_2} \quad \frac{\frac{F}{2} \sin \quad F_S \cos}{h \;\; b \quad l \;\; b} \tag{28}$$

$$p \quad \frac{F \sin^2 \quad F_S \sin 2}{b \;\; s_0 \quad s_1 \quad 2r \; 1 \quad \cos \quad \frac{}{90} r \sin} \tag{29}$$

$$p \quad \frac{0.03015F \quad 0.34202F_S}{b \;\; s_0 \quad s_1 \quad 0.0302302} \tag{30}$$

Pressure **p** can be calculated by starting expressions (28) and (29). Final expression is (30) for this particular case.

Can be notice here that small rounded area adopted like flat, inclined. This approximation is possible and reasonable because area A_2 is very small in comparison with A_1, and with lower significance in this case. Such approximation contributing to obtain simpler final expression for pressure **p**. Also, must be notice that approach like previous isn't reasonable for friction analysis in sliding process where two areas (A1 and A2) produce different friction forces each.

3. EXPERIMENTAL VERIFICATION
3.1 Oil lubrication example

Experimental verification of proposed approach, expressions i.e. formulas for coefficient of friction (**μ**) and contact pressure (**p**) presented were in this and next chapter.

Behind application of such formulas, monitoring and analysis of obtained results, given were results of comparison between new results and results obtained with classic, older formulas. Explanation of classic approach and classic formulas can be seen in [1], [5], [7] and [8].

All the details about experiment: equipment, tooling, material properties, geometry, lubricants properties, process properties etc. is not presented because of limited space here and can be fined in [7], [8] and [10].

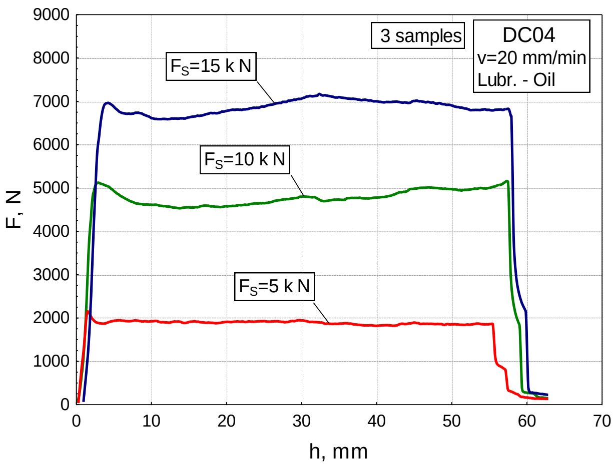

Figure 5. Force dependence on sliding length

Most important starting data gives dependencies of drawing (pulling) force on sliding length (sample travel). By using data acquisition system it is possible to obtain force dependence on sliding length in numerical form. That allows appliance of different formulas for friction coefficient (**μ**) and contact pressure (**p**) and obtaining corresponding dependencies during the ironing, i.e. sliding process. That also allows relatively simple comparison and evaluation of any particular approach.

Figure 5 shows force variation during the process for one phase ironing. Samples were deformed in one phase each, but with different lateral force F_S.

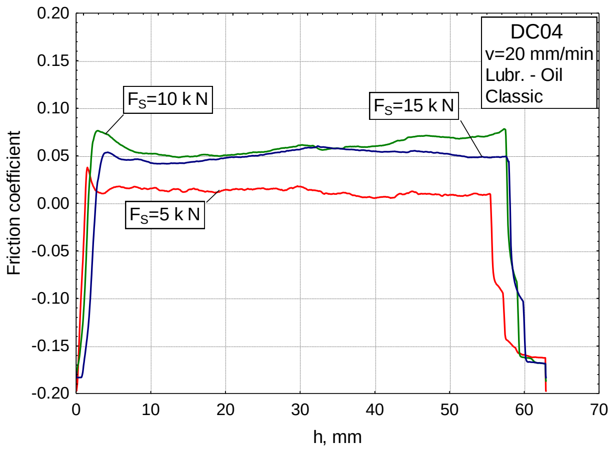

Figure 6. Friction coefficient dependence on sliding length

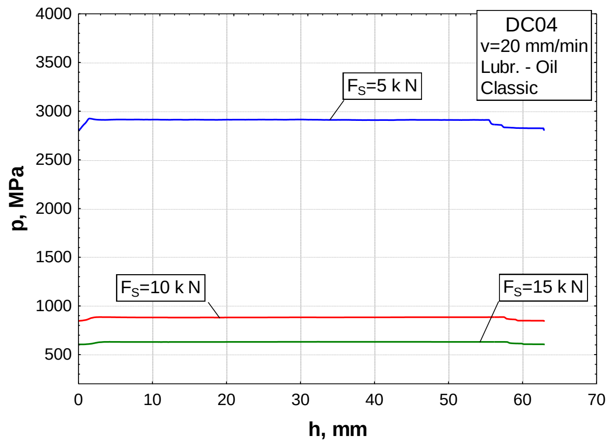

Figure 7. Pressure dependence on sliding length

Curves in figures 6 and 7 were obtained by application of classic formulas and can be seen that **μ** have very low values and pressure very high values in conditions of small deformations [7, 8, 10] i.e. lower intensity of side force F_S. Pressure **p** is near 3000 MPa and friction coefficient **μ** near zero which are unreal. In figures 8 and 9 shown are results of here proposed formulas. Values are much more realistic.

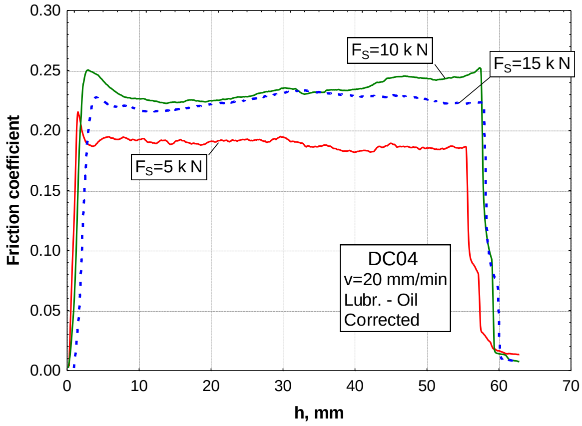

Figure 8. Friction coefficient dependence on sliding length

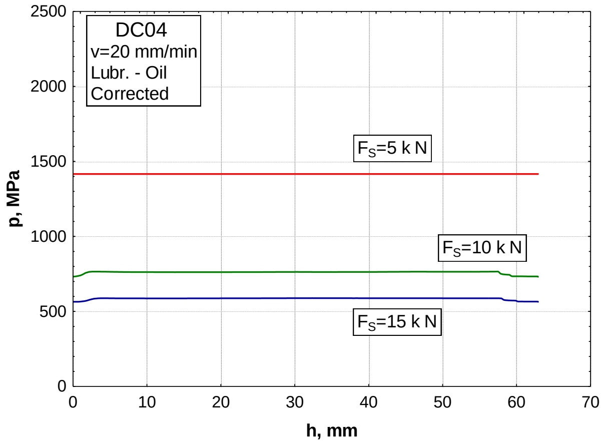

Figure 9. Pressure dependence on sliding length

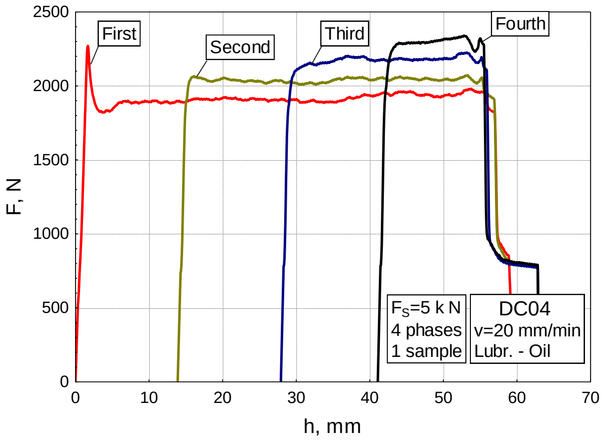

Figure 10. Force dependence on sliding length

Figure 10 illustrate second type of ironing process, multi phase sliding. On one and same sample makes four phase sliding process in conditions of side force F_S=5kN. Figures 11 and 12 gives results of classic formulas application with observations similar to previous case. In figures 13 and 14 shown are results of here proposed approach. Comments are like in previous case.

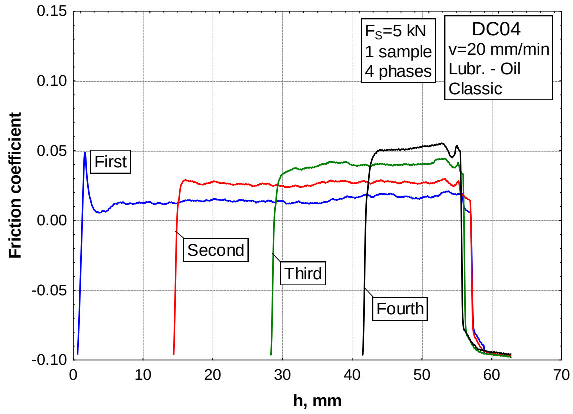

Figure 11. Friction coefficient dependence on sliding length

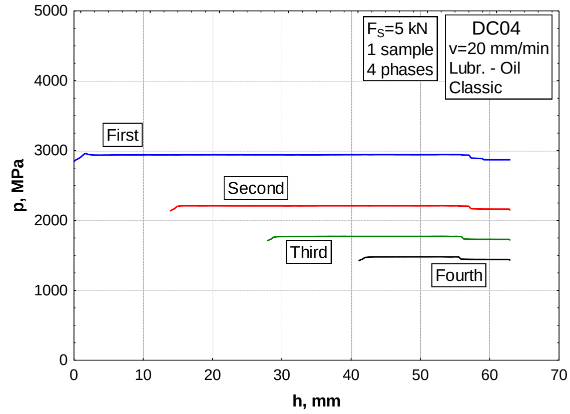

Figure 12. Pressure dependence on sliding length

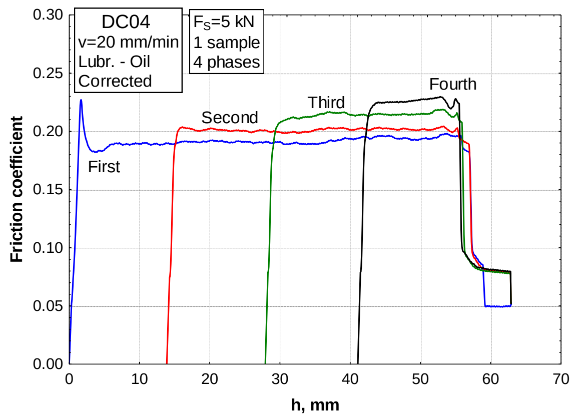

Figure 13. Friction coefficient dependence on sliding length

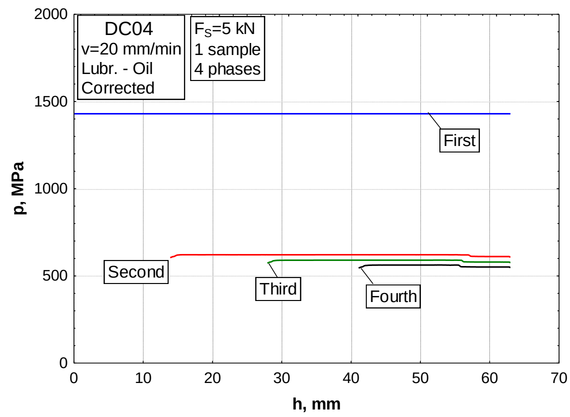

Figure 14. Pressure dependence on sliding length

3.2 Grease lubrication example

Figure 15 corresponds to figure 5. Different is only lubricant. There is appropriate grease [8, 10].

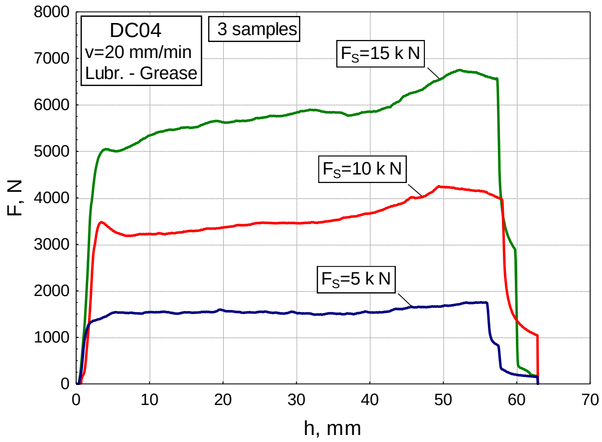

Figure 15. Force dependence on sliding length

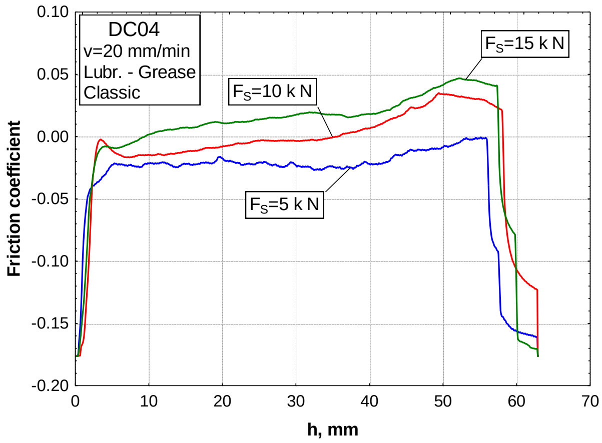

Figure 16. Friction coefficient dependence on sliding length

Classic formulas gives unacceptable results (coefficient of friction **μ**<0, and pressure **p**≈4500 MPa) in figures 16 and 18.

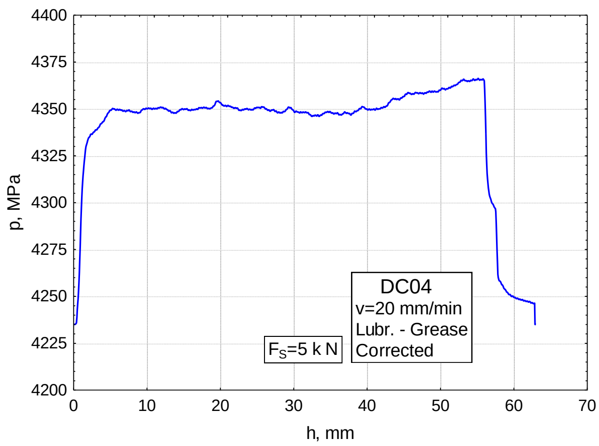

Figure 17. Pressure dependence on sliding length

In figure 17 are shown example where are illustrated small variation of pressure intensity. With appropriate scale it can be seen.

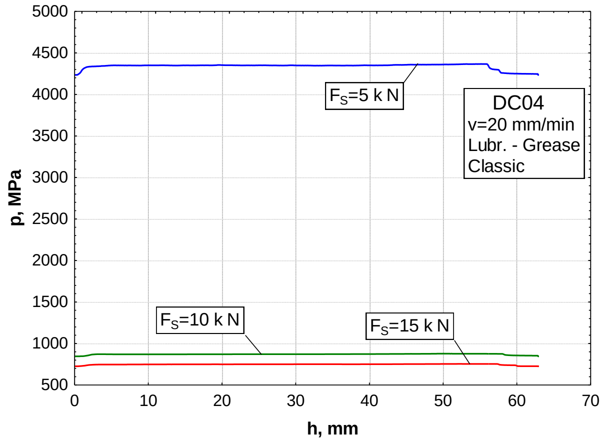

Figure 18. Pressure dependence on sliding length

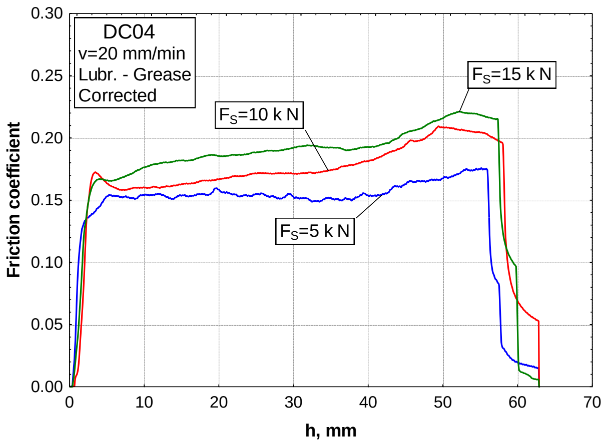

Figure 19. Friction coefficient dependence on sliding length

Results with new formulas is much better (Figs. 19 and 20).

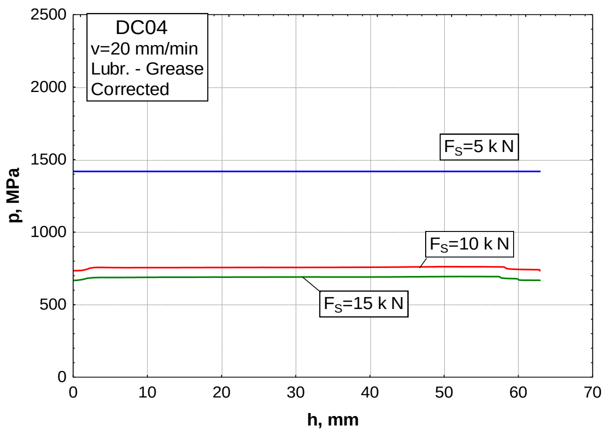

Figure 20. Pressure dependence on sliding length

Last example in this paper given are in figure 21 and corresponds to example in figure 10. Application of classic formulas gives in some cases negative values for friction coefficient and completely unreal values for pressure also (figure 22 and 23). It is clearly visible that results in figures 24 and 25 are more realistic.

4. CONCLUSION

Main goals in this research were: to establish mechanical model of ironing process with double side reduction , to define reliable expressions for coefficient of friction and contact pressure determination and evaluate applicability by experimental verification.

Obtained results presented in this paper, like others that's not presented here, clearly shows that proposed approach is acceptable, and it can be reliable support in next experimental investigations of ironing process. Also, it can help in common experiments like the evaluations of the quality of lubricants, evaluation of influence of different sample materials etc.

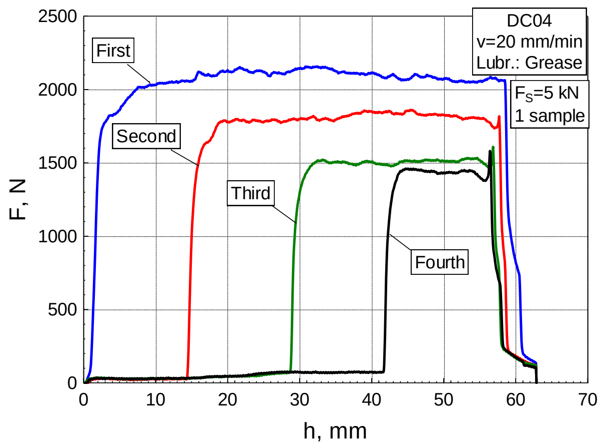

Figure 21. Force dependence on sliding length

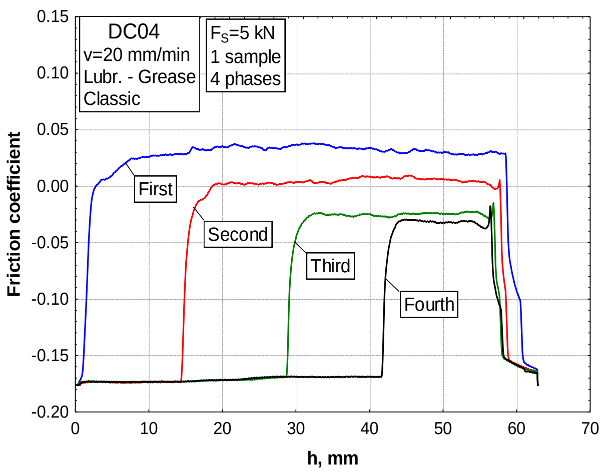

Figure 22. Friction coefficient dependence on sliding length

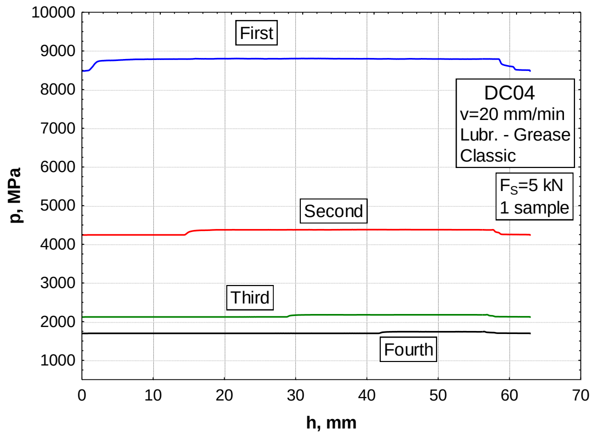

Figure 23. Pressure dependence on sliding length

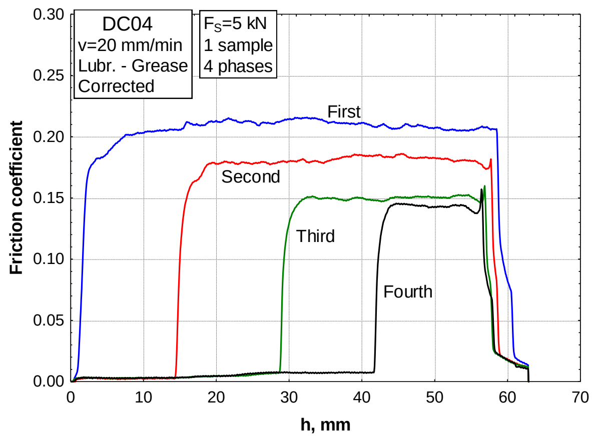

Figure 24. Friction coefficient dependence on sliding length

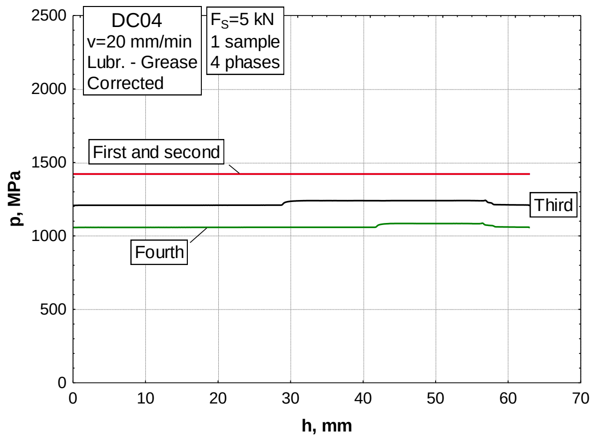

Figure 25. Pressure dependence on sliding length

ACKNOWLEDGEMENT

The experimental research with results reported in this paper was partially supported by the Ministry of Education, Science and Technological Development, Republic of Serbia through contract TR34002 and authors are very grateful for that.

REFERENCES

[1] D. Schlosser: Beeinflussung der Reibung beim Streifenziehen von austenitischem Blech: verschiedene Schmierstoffe und Werkzeuge aus gesinterten Hartstoffen, Bander Bleche Rohre, No. 7/8, pp. 302-306, 1975.

[2] P.Deneuville, R. Lecot: The study of friction in ironing process by physical and numerical modelling, Journal of Materials Processing Technology, Vol. 45, No. 1-4, pp. 625–630, 1994.

[3] J.L. Andreasen, N. Bay, M. Andersen, E. Christensen, N. Bjerrum: Screening the performance of lubricants for the ironing of stainless steel with a strip reduction test, Wear, Vol. 207, No. 1-2, pp. 1-5, 1997.

[4] H.C.E. Van der Aa, M.A.H. Van der Aa, P.J.G. Schreurs, F.P.T. Baaijens a, W.J. Van Veenen: An experimental and numerical study of the wall ironing process of polymer coated sheet metal, Mechanics of Materials, Vol. 32, No. 7, pp. 423-443, 2000.

[5] D. Adamovic, M. Stefanovic, V. Mandic: *Modelling of ironing process*, Faculty of Engineering, University of Kragujevac, 2012.

[6] M. Djordjević, S. Aleksandrović, V. Lazić, M. Stefanović, R. Nikolić, D. Arsić: Experimental analysis of influence of different lubricants types on the multi-phase ironing process, Materials Engineering - Materiálové inžinierstvo, Vol. 20, No. 3, pp. 147-152, 2013.

[7] S. Aleksandrović, M. Đorđević, M. Stefanović, V. Lazić, D. Adamović, D. Arsić: Different Ways of Friction Coefficient Determination in Stripe Ironing Test, Tribology in industry, Vol. 36, No. 3, pp. 293-299, 2014.

[8] S. Djacic S.: *Metal forming with double sided ironing*, Master thesis, Faculty of Engineering, University of Kragujevac, 2016.

[9] M. Djordjević, S. Aleksandrović, D. Arsić, V. Lazic: Experimental-numerical analysis of contact conditions influence on the ironing strip drawing process, Industrial lubrication and tribology, Vol. 69, No. 4, pp. 464-470, 2017.

[10] S. Aleksandrović, S. Đačić, M. Stefanović, M. Đorđević, V. Lazic, D. Arsić: Influence of process parameters on the friction coefficient in one and multi phase steel strip drawing ironing test, ACTA TECHNICA CORVINIENSIS – Bulletin of Engineering, Tome XI, Fascicule 2 , pp. 29-33, 2018.

[11] H. Sulaiman, P. Christiansen, N. Bay: Influence of tool texture on friction and lubrication in strip reduction, Procedia Engineering, No. 207, pp. 2263–2268, 2017.

[12] E. Ustunyagiz, C. Nielsen, P. Christiansen, P. Martins, N. Bay: Continuous Strip Reduction Test Simulating Tribological Conditions in Ironing, Procedia Engineering, No. 207, pp. 2286–2291, 2017.

[13] N. Bay et al: Environmentally benign tribo-systems for metal forming, CIRP Annals - Manufacturing Technology, Vol. 59, No. 2, pp. 760 – 780, 2010.

[14] Y.Sagisaka et al: Evaluation of Environmentally Friendly Lubricants for Cold Forging, Journal of Materials Processing Technology, Vol. 212, No. 9, pp. 1869–1874, 2012.

[15] M. Djordjevic, S. Aleksandrovic, V. Lazic, D. Arsic, M. Stefanovic, D. Milosavljevic: Two-phase ironing process in conditions of ecologic and classic lubricants application, in *Proceedings of the International conference on Tribology SERBIATRIB 2015*, 13.–15. 05., Belgrade, Serbia, pp. 407-413.

[16] M. Đorđević, D. Arsić, S. Aleksandrović, V. Lazić, D. Milosavljević, R. Nikolić: Comparative study of an environmentally friendly single-bath lubricant and conventional lubricants in a strip ironing test, Journal of Balkan Tribological Association, Vol. 22, No.1A-II, pp. 947-958, 2016.

[17] M. Moghadam, P. Christiansen, N. Bay: Detection of the onset of galling in strip reduction testing using acoustic emission, Procedia Engineering, No. 183, pp. 59–64, 2017.

[18] E. Ustunyagiz et al: A combined numerical and experimental approach for determining the contact temperature in an industrial ironing operation, Journal of Materials Processing Tech, No. 264, pp. 249–258, 2019.

Serbian Tribology Society

SERBIATRIB '19

16th International Conference on Tribology

Faculty of Engineering
University of Kragujevac

Kragujevac, Serbia, 15 – 17 May 2019

DEVICE FOR MACHINING NON-CIRCULAR GEARS

M. BOGDAN-ROTH[1], M. ROMANET[1], R. G. RIPEANU[1],
[1] Petroleum-Gas University of Ploiesti, Ploiesti, Romania,
rothinimagic@yahoo.com

Abstract: *If at first the non-circular wheels were treated as a hobby subject, their use now becomes ever larger. They are used in robotics, replacing cam mechanisms and lever mechanisms in the textile and agricultural industries.*

The paper presents a device used for the processing of non-circular gears, a device made according to my own design. For machining non-circular gears, it is necessary to make a toothed wheel on a CNC machine after which, with the designed device, it is possible to proceed to the processing of an unlimited number of wheels identical to the original wheel, which we will call the reference.

The device contains an operating rack that engages the reference wheel. The solid rack with the rack is mounted on the generator rack (tool). The two racks are fixed, with the indication that the tool performs both the main cutting movement and the intermittent radial feed motion.

The reference wheel and the semi-manufactured wheel move together (jointly) in engagement with the two racks. Taking into account the variable radius of the wheels (reference and green), the device is provided with a system of guides that allow the generation process to be carried out.

I appreciate that this device can be improved and adapted for machining non-circular toothed wheels with as many configurations as possible and with different gauges.

Keywords: *noncircular gear; gear manufacturing*

1. INTRODUCTION

The advantages of non-circular gears, as well as their great diversity and flexibility, are a serious alternative to replacing the classic mechanisms of obtaining variable gear ratios. Their kinematic and geometric complexity has limited the implementation of standardized algorithms for design but also for the adoption of performing teeth generation technologies.

The present paper provides an original solution for the construction of non-circular gears in large series production and mass by designing a specialized device for this purpose. For this, it is necessary to make a non-circular pattern wheel that is multiplied with this device. As such, the work is not subject to the design of non-circular gears.

The projected device allows to make the gears used in parallel axle gears with the spacing of fixed axles, obtained by rolling, with an evolving profile. Therefore, the non-circular wheels that can be made have an oval, elliptical and non-concave shape.

2. GENERAL CONSIDERATIONS REGARDING NON-CIRCULATING ROOTS

Non-circular gears justify their use through a wide range of advantages, such as:

Compact structure, rigidity, stability and high efficiency compared to cams or other mechanical transmission systems;

the possibility of making variable gear reports according to different motion laws, depending on their destination;

- may allow for a cyclical variation of movement, but non-cyclic variation laws may also be made by custom design;
- the use of a small number of kinematic elements to create a complex kinematics.

2.1 Types of non - circular gears

Considering the main characteristic of the non-circular gearing, namely the variation of the speed of the driven wheel, the following types of non-circular gears can be found: non-circular multithreaded toothed wheels where the driven wheel has different speeds; In this category also the eccentric circular wheels can enter.

Non-circular gears with continuous variable speed. They are most used, with a transmission ratio that varies according to a required law. In this category, logarithmic non-circular wheels can also be entered dividing (copying) the disc cutter, the module or a special profile with the cylindrical-front cutter, the same way or a special profile.

Figure 1. Logarithmic non-circular gears

- Rolling (rolling), with a worm gear module, comb knife or wheel knife.

The splitting process has the advantage of a low processing time and the disadvantage of a low precision, a feature that recommends them to operate at low peripheral speeds.

This is not a big impediment because the non-circular wheels are used in control mechanisms and work at low angular speeds.Non-circular concave shapes (e.g., logarithmic, concave complexes) can not be rolled.

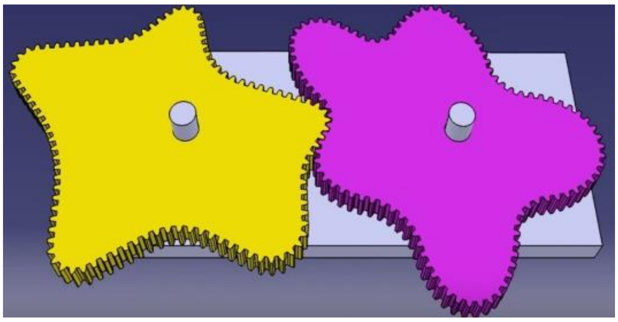

Figure 2. Non-circular wheels of complex shape

The advantage of the use of the rolling process is the advantage of the possibility of processing the tooth with an evolving tooth profile, a profile that gives precision in machining as well as economical machining processes.

3. PROJECTING THE NON-CROWN OVALE MODEL

From the start, we mention that we did not intend in this article to find a design algorithm for a non-circular wheel. It has been studied the possibility of making a wheel that can be used as a model for the projected device. For a quick and precise execution, a wheel made of four arches of sky, radius r18 and radius R78,033 as in the figure, equal two by two.

The adopted construction allows the evolving profile of module m=3 with an integer number of teeth on a circular arc of a certain radius, as in the figure. Highlights are for splitting cylinders.

We can see the shape of the different evolutionary profile on the two circular sectors of different division diameters.

The construction of the evolving profile used a program made in AutoLisp by the authors.

Generating the evolving profile for a non-circular wheel without concavities can be achieved by maintaining with the fixed axle of the wheel and displacement of the generator rack with the reference right tangential to the splitting right, as in Figs. 3 and 4 or maintaining the fixed generator rack and rotating the wheel with a variable distance from it to the tool, as was done in the design of the device.

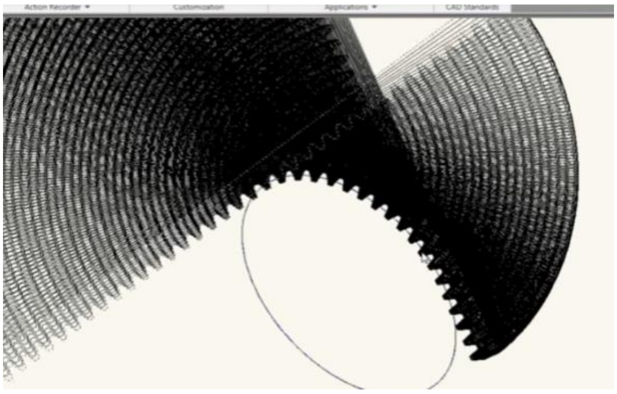

Figure 3. Generating Evolution

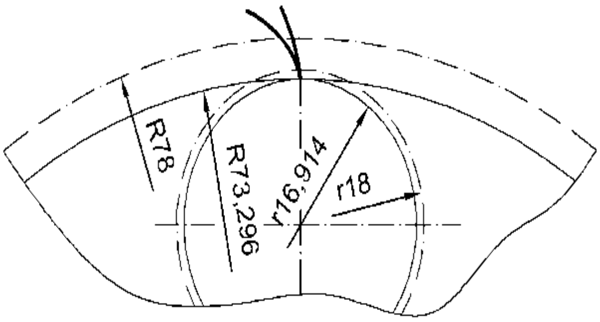

Figure 4. Different forms of evolution for different circles of the basic circle

The profile was generated in the engagement with a generating rack to take account of the shape of the evolutionary profile, different for different basic circles. In the picture, this phenomenon is noticed. It is noted that in the small toothed wheel sector, the foot ring is smaller than the base circle.

Generating the evolving profile for a non-circular wheel without concavities can be achieved by maintaining with the fixed axle of the wheel and displacement of the generator rack with the reference right tangential to the splitting right, as or maintaining the fixed generator rack and rotating the wheel with a variable distance from it to the tool, as was done in the design of the device.

The profile was generated in the engagement with a generating rack to take account of the shape of the evolutionary profile, different for different basic circles. In the picture, this phenomenon is noticed. It is noted that in the small toothed wheel sector, the foot ring is smaller than the base circle.

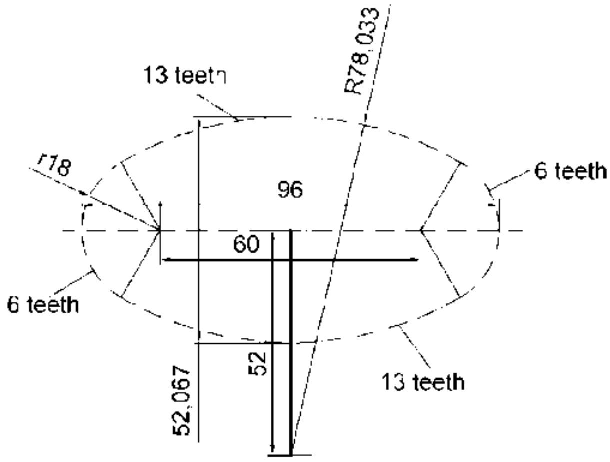

Figure 5. Geometrical elements for making the semifabrication of the metallic wheel

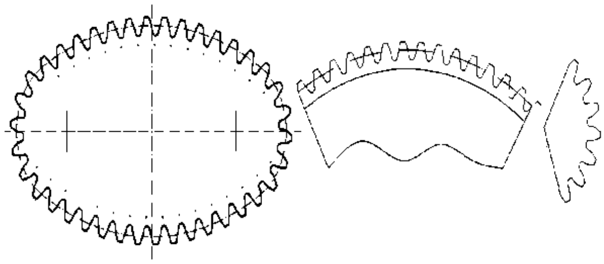

Figure 6. Gear sectors for making the model wheel

Between these two evolved circles must be extended with another curve, possibly with circular arcs.

4. PRESENTATION OF THE DEVICE

The component elements, sizes and subassemblies of the device are shown in the Figure 7.

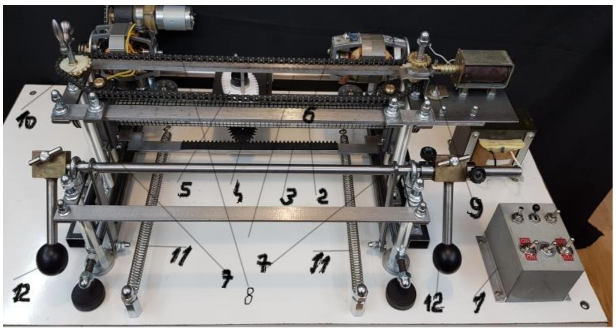

Figure 7. 1-bay, 2-blade tool, 3-rack reference, 4-wheel model,5-wheel gearing, 6-vertical feed mechanism, 7-transverse feed mechanism, for twin engagement; 8- longitudinal feed mechanism; 9-stroke mechanism for automatic vertical feed 10-manual vertical drop; 11- springs to keep in gear, 12-maneuvering handwheels

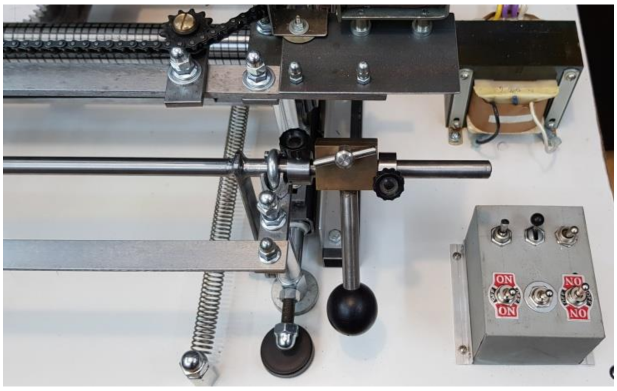

Figure 8. Command and power block

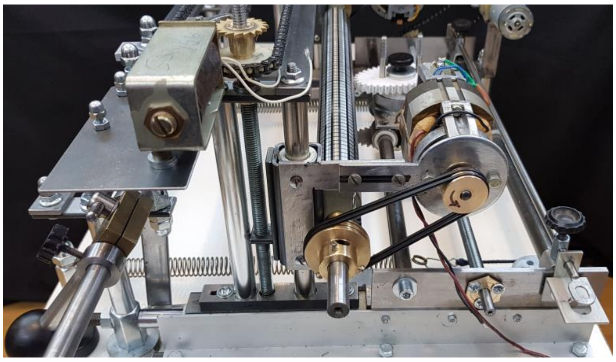

Figure 9. Mechanical transmission system for cutting tool operation

Figure 10. Mechanical transmission system for cutting tool operation

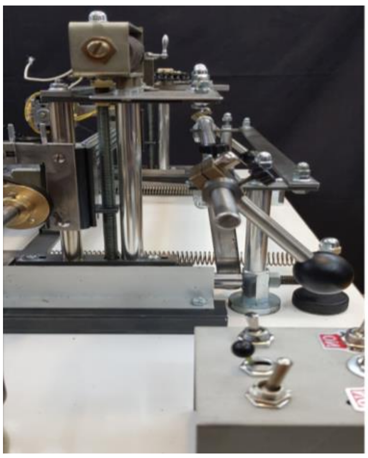

Figure 11. Screw mechanism for vertical vertical feed

5. DEVICE OPERATION

Device works on the principle of teething generation by rolling. It has the advantage that rack rails generate the profile of the tooth in accordance with the diameter of the basic circles of the different sectors of the semi-finished wheel.

The model wheel (4) was executed in order to achieve the longitudinal and transversal feed of the cermillary. This is monoblock or solidarized with the model wheel. The maintenance of the toothed wheel with the rack (3) is achieved by means of the springs (11) and the transverse feed shaft (7). The blade tool is a straight cutter with straight teeth with rack profile. The milling teeth are machined and detailed so that the cutting process performs a continuous movement of vertical movement during cutting and an intermittent radial feed motion for determining the depth of cutting at a passage.

After adjusting the depth of cut for a pass, the mechanical transmission system allows the rotating and displacement of the semi-finished wheel so that the cutting at the correct depth is achieved over the entire circumference.

This is carried out in a cyclical process performed with the automatic feed mechanism Fig. 11. The vertical drive mechanism of the cutting tool can be made manually or automatically and contains: a chain transmission required to move the scissors in a move on two vertical guides, without running the risk of locking by this inclination. The control and power block is shown in Fig. 8. Figure 9 is detailed with the cutting mechanism of the cutting tool.

6. CONCLUSION

The device allows the creation of a wheel or several wheels simultaneously having a model wheel in advance.

With this device, it is possible to make non-circular wheels without a device allowing the practical development of the theoretical evolution depending on the local curve radius of the model wheel and the semi-finished wheel.

The use of the device allows the making of non-circular toothed tooth profiles with hight roductivity.

Considering that the non-circular wheels are mainly used in control systems and that they are reduced in size, the device shown is suitable for such wheels, for large wheels it can be designed and redesigned according to the gauge of the wheel to be executed and the material it.

REFERENCES

[1] I. Florea, N. Rizea: Graphics of the involute profile for gear drawing, U.P.G. Ploieşti, Vol. LXII, No. 4B, pp. 7-12, 2010.

[2] M. Niculescu: Research on the design and generation of non-circular gears with applicability in the metallurgical industry, doctoral thesis summary, Galaţi, 2014.

[3] I. Florea, N. Rizea: Graphics of the involute profile for gear drawing, U.P.G. Ploieşti, vol. LXII, No. 4B, pp. 7-12, 2010.

[4] A. Jula, ş.a.: Design of Evolutionary Drives, Ed. Scrisul Românesc, Craiova, 1989 F.I. - Machine parts, U.P.G. Ploiesti, 2014.

[5] YouTube, available at: https://www.youtube.com/watch?v=dtkEyZwuwH4 https://www.youtube.com/watch?v=EcRTEgh4Z5M

Serbian Tribology Society

SERBIATRIB '19

16th International Conference on Tribology

Faculty of Engineering
University of Kragujevac

Kragujevac, Serbia, 15 – 17 May 2019

DISTRIBUTION NON-UNIFORMITY OF THE ACCUMULATED PLASTIC STRAIN AT 3D SIMULATION OF SINGLE AND MULTI-ANGLED ECAE PROCESSES USING A MOVABLE RAM-DIE

Valentin KAMBUROV[1]*, Antonio NIKOLOV[1], Rayna DIMITROVA[1], Vladimir SEMENOV[2], Bogdan GILEV[1]

[1]Technical University of Sofia, Bulgaria

[2] Ufa State Aviation Technical University, Ufa, Russia

*Corresponding author: vvk@tu-sofia.bg

Abstract: Four virtual schemes for realizing the Equal Channel Angular Extrusion (ECAE) using a movable ram-die with different geometries of their deformation spaces (extrusion angles) have been developed and considered. On the basis of the performed simulations using CAD/CAM software, the data on the mean values of effective strain and their distribution are processed depending on the contact friction between the tool and the work-piece. The selected modes are compared and analyzed in terms of effective strain means and their dependence on contact friction. It has been found that the single-angled ECAE-MRD modes allow for a greater mean values of the effective strain compared to multi-angled ECAE patterns. It has been proven that the strain distribution non-uniformity and the filling of the deformation space depend on the contact friction.

Keywords: *severe plastic deformation, equal channel angular extrusion, CAD/CAE software 3D simulation, contact friction.*

1. INTRODUCTION

The Equal Channel Extrusion (ECAE) has been invented in the 1970's and it has been described first in [1]. The various SPD processes and regimes aim and result in the development of the ultra-fine grained (UFG) and nanocrystalline (NC) structure in the deformed under their recrystallization temperature materials [2, 3]. The most widely used scheme for severe plastic deformations (SPD) is ECAE based on simple shear, concentrated in a relatively narrow deformation section, between the intersecting grooves of the channels [4, 5]. As a processing operation, ECAE presents several significant technological advantages, the most important of which is the development of uniform, severe and localized steady simple shear in the transverse cross sections of deformed work-pieces [5, 6].

A major disadvantage to apply the ECAE deformation schemes, besides the limited length of the billets [7], is the contact friction force emerging between the work-pieces and the die channel walls, which increases the surface tension, strongly altering the distribution of stress-strain state in the volume of the deformed body [8]. A solution to this problem is proposed by providing some movable parts of the deformation space - a moving ram-die and a fixed counter-support – ECAE-MRD [9, 10].

The present research introduces the results of a 3D simulation investigation, conducted to determine the distribution of the accumulated strains in an equal channel single and multi-angular extrusion with a movable ram-die and a counter-support as an effective technological scheme with limited friction forces. The deformation scheme and the tool equipment ensure a movable deformation space with two movable walls (ram-die) and a slightly mobile (related to two of the die-container walls) deformed work-piece.

The present research introduces the results of a 3D simulation investigation, conducted to determine the distribution of the accumulated strains in an equal channel single and multi-angular extrusion with a movable ram-die and a counter-support as an effective technological scheme with limited friction forces. The deformation scheme and the tool equipment ensure a movable deformation space with two movable walls of movable ram-die (ECAE-MRD) and a slightly mobile (related to two of the die-container walls) deformed work-piece.

2. MATERIALS AND METHODS

The three-dimensional modeling of the ECAE-MRD processes was performed at room temperature for a work-piece of deformable low-alloyed aluminum material having a cross-sectional dimension of 10.6 x 10.6 mm, a length of 70 mm (125 mm) and a ram-die movement speed of 5 mm/sec. The chosen lubricant is from package standard database with contact friction coefficient 0.05.

2.1 Virtual tool for Single-angled ECAE-MRD

The virtual tools to realize single-angled ECAE-MRD (Fig. 1) are composed from the following elements: die-container - 1; counter-support - 2; ram-die – 3; vertical channel - 4; -outlet calibration channel – 6. The vertical and calibration outlet channels are mutually intersecting (at an extrusion angle Φ), forming the zone of simple shear – 5 (Fig. 1). The virtual tools operate as follows: in the vertical channel 4 is placed the work-piece which, when moving the ram-die 2 downwards, is pushed (extruded) through the shear zone 5 in the outlet calibration channel 6. Extrusion is possible due to the counter-support 2 which closes the vertical channel 4. The processes of single angular extrusion with a movable ram-die and a rigid counter-support at different extrusion angles of channel crossing are simulated with the QForm VX 8.2.4 software (Fig. 1a and Fig. 1b).

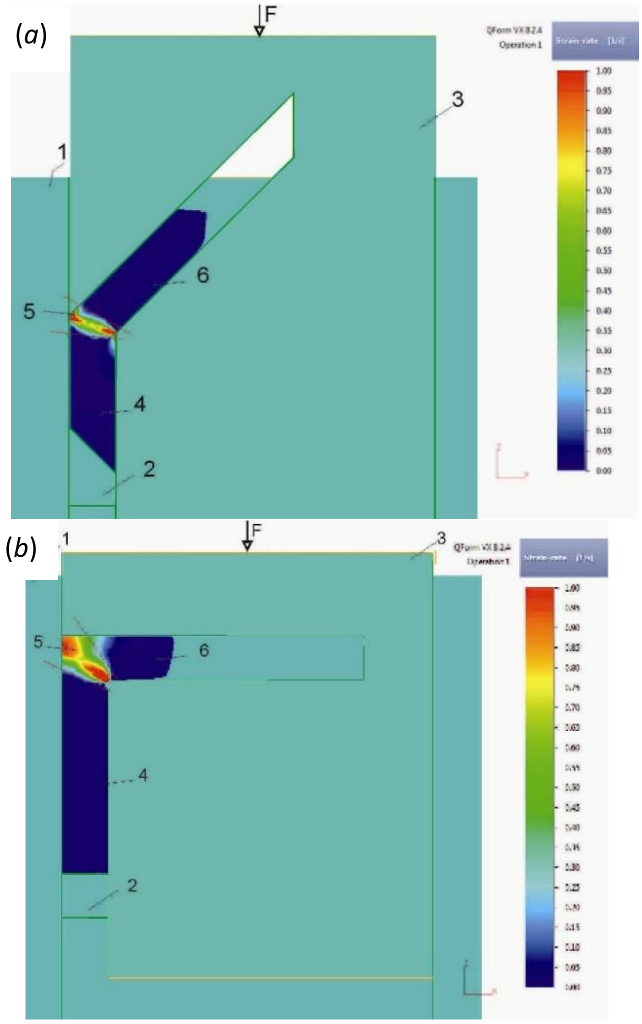

Figure 1. Virtual tool (QForm VX 8.2.4) for realizing single-angled ECAE-MRD, with strain rate distribution: (a) at an extrusion angle Φ=135^{O}; (b) at an extrusion angle Φ=90^{O}

Figure 1 shows the strain rate distribution in the scheme for realization of a single angular ECAE-MRD with an extrusion angle of intersection of the two channels: (a) Φ=135^{O} and (b) Φ=90^{O}.

2.2 Virtual tools for Multi-angled ECAE-MRD

The ECAE pattern with a movable ram-die can also be used to realize a multi-angular extrusion at intersection angles of 135^{O} for the channels. The processes of two-angled and four-angular equal channel extrusion with a movable ram-die were simulated with the QForm VX software (Figs. 2 and 3).

The virtual tool to realize a two-angled ECAE-MRD (Fig. 2) is composed of the following elements: die-container - 1; counter-support - 2; movable ram-die - 3. The deformation space is located in the ram-die and it consists of: a vertical channel - 4 (in which the work-piece is placed); and two crossed at an extrusion angle of 135^{O} channels - 6 and 7. The virtual tool for the two-angled ECAE operates as follows: a work-piece is placed in the vertical channel 4, moves through SPD zone 5 in the channel 7 after movement of the ram-die 3 downward, cross the deformation SPD zone 5A and enters the calibration channel 6 (Fig. 2 (a)).

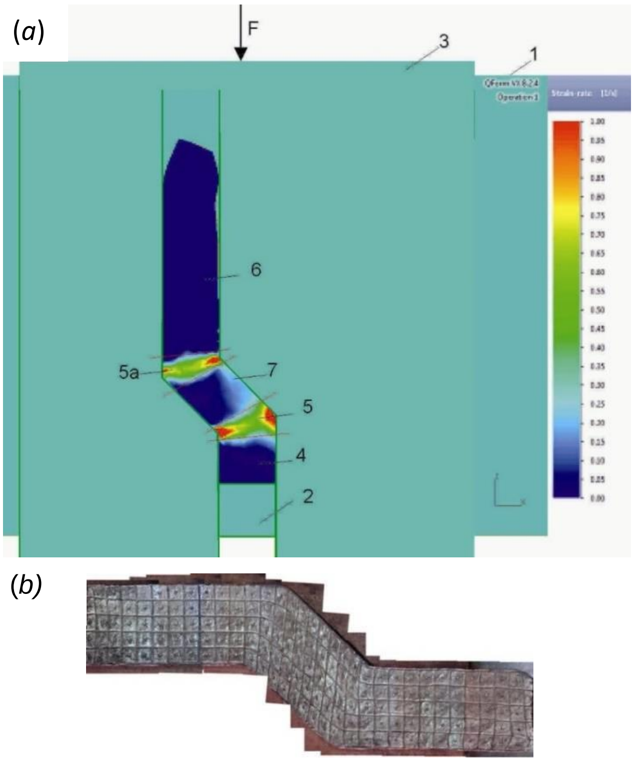

Figure 2. Two-angled ECAE-MRD at an extrusion angle Φ=135^{O}: (a) strain rate distribution (QForm VX 8.2.4); (b) deformed lead work-piece with a plotted coordinate grid

The virtual tool to realize a four-angled ECAE-MRD (Fig. 3) consists of the following elements: die-container - 1; counter-support - 2; movable ram-die - 3. The deformation space is located in the ram-die 3 and it consists of a vertical channel 4 (in which the metal work-piece is placed) and of crossed at an extrusion angle of 135^{O} channels - 7, 8, 9 and 6.

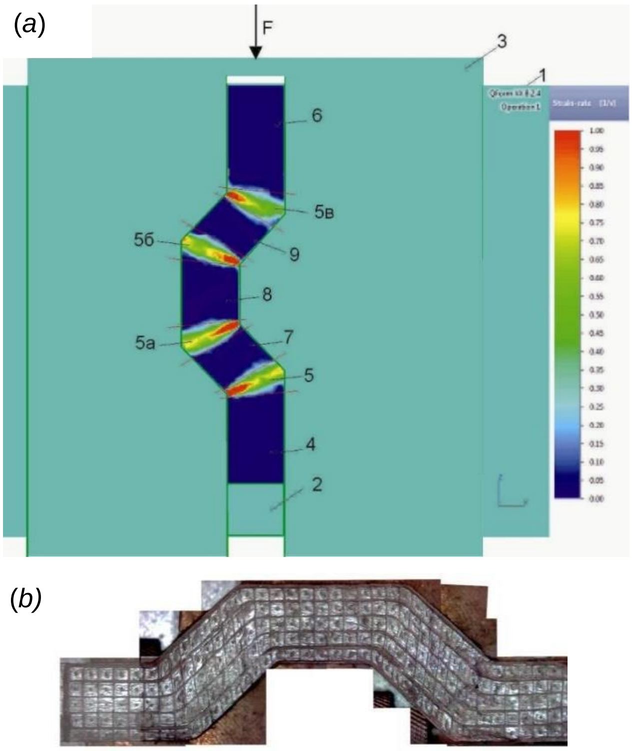

Figure 3. Four-angled ECAE-MRD at an extrusion angle Φ=135^{O}: (a) strain rate distribution (QForm VX 8.2.4); (b) deformed lead work-piece with a plotted coordinate grid

The virtual tool for a two-angled ECAE-MRD operates as follows: in the vertical channel 4 is placed the work-piece which, when moving the ram-die 3, is pushed out (extruded) and passes successively through the shear zone 5, the channel 7, the second shear zone 5a, the parallel channel 8, the third shear zone – 5b, the inclined channel - 9, the fourth deformation zone – 5c and finally entering the calibration channel - 6 (Fig. 2b)).

2.3 Determination of the Average Values of the Effective Strain

The magnitude of the equivalent effective plastic strain in single ECAE in a frictionless mode it was accepted to be determined according to the dependence [15]:

$$\varepsilon_{eff} = \frac{N}{\sqrt{3}}\left[2\cot\left(\frac{\Phi+\Psi}{2}\right)+\frac{\psi}{\sin\left(\frac{\Phi+\Psi}{2}\right)}\right] \quad (1)$$

where: ε_{eff} – the effective plastic strain, Φ is the extrusion angle between the two intersecting channels; Ψ is the die channel angle determined by the inner radius of curvature; N – the number of passes.

The mean values of the effective plastic strain obtained by a computer simulation (QForm VX 8.2.4) of the shown in Fig. 1, Fig. 2 and Fig. 3 schemes for single and multi-angled ECAE in the frictionless mode are given in Table 1. The values of the effective strain determined by formula (1) at Ψ=0 are given in brackets.

Table 1. Sample mean results of effective plastic strain from simulation of one-angled and multi-angled ECAE-MRD under frictionless conditions

Pass number x die channel angle	Effective plastic strain values - sample means of computer simulations under frictionless conditions (2) and - according to the formula (1) in brackets			
	One-angled x135°	**One-angled x90°**	**Two-angled x135°**	**Four-angled x135°**
First pass 1x135°	0.49 (0.48)	-	0.58 (0.48)	0.58 (0.48)
Pass 2x135° or 1x90°	0.97 (0.96)	1.00 (1.16)	1.00 (0.96)	1.01 (0.96)
Third pass 3x135°	1.48 (1.44)	-	1.44 (1.44)	1.54 (1.44)
Pass 4x135° or 2x90°	1.99 (1.92)	2.12 (2.31)	1.98 (1.92)	1.99 (1.92)

The close values for the effective strain obtained by calculation by the expression (1) and the computer simulation (Table 1) confirmed the claim that the deduced formula (1) does not take into account the contact friction and consequently the strain distribution uniformity [16].

The determination of the distribution of the plastic strain in the volume of the deformed work-piece is related not only to the averaging of the so-called sample mean, but also by determining their standard deviation values. In the numerical determination of the strain distribution non-uniformity it is accepted to use the standard deviation S_D or simply s:

$$S_d = s = \sqrt{\frac{1}{n-1}\sum_{i=1}^{n}\left(\varepsilon_i-\bar{\varepsilon}\right)^2} \quad (2)$$

where: n - the number of nodes in the cross-section (in this case n = 49); ε_i - the magnitude of effective plastic strain at certain nodes of the deformed body; $\bar{\varepsilon}$ - the sample mean of the plastic strain at all nodes of the selected cross section of the deformed body

$$\bar{\varepsilon} = \frac{1}{n}\sum_{i=1}^{n}\varepsilon_i . \quad (3)$$

The hypothesis will be examined whether the sampling averages of the effective strain for different ECAE-MRD (from the rows of Table 1) are equal [17]. For convenience, the two effective deformations obtained for different strain modes (Table 1) are denoted with X and Y , i.e. X for a deformation scheme (from Table 1), and Y for another deformation scheme (from Table 1). Then the difference between the two sample means is also normally distributed, i.e.:

$$Z_{\bar{X}-\bar{Y}} = \frac{(\bar{X}-\bar{Y})-(\mu_x-\mu_y)}{\sqrt{\frac{s_x^2}{n_x}+\frac{s_y^2}{n_y}}} \sim N(0,1) . \quad (4)$$

where: n_x n_y are the numbers of observations of the effective strains in those deformation modes - $n_X = n_Y$=49>30. If $Z_{\bar{X}-\bar{Y}} \in$ [-2.56, 2.56] it can be accepted with a confidence level) $\alpha = 0.01$ the basic hypothesis, i.e. that those the two sample means $\bar{X}$ and $\bar{Y}$ are equal.

3. SIMULATIONS AND RESULTS

3.1 Distribution of the Effective Strain in Single-angled ECAE-MRD at 135^{O}

In the computer simulation of a one-angled ECAE with a movable ram-die at an extrusion angle of 135° with contact friction, it was found that the deformed work-piece completely fills the deformation space. The effect of contact friction in the one angular (135^O) ECAE-MRD mode is also expressed in increasing the effective strain at the four corners of the deformed work-piece, with the middle section of the transverse cross-section being less deformed (Fig. 4).

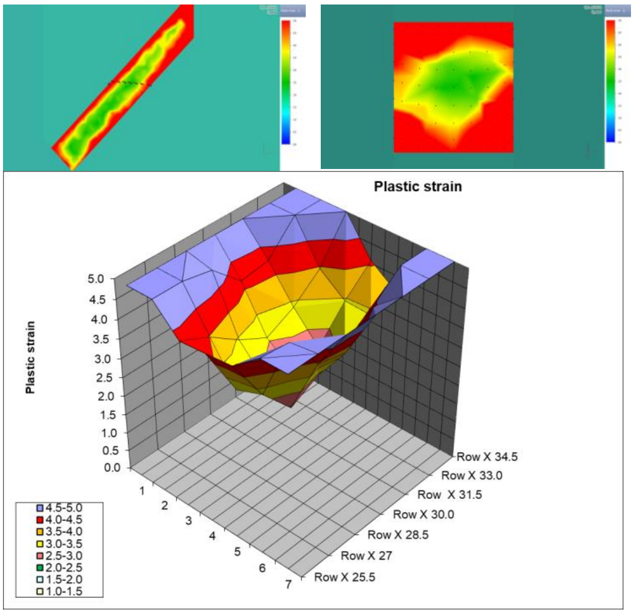

Figure 4. Effective plastic strain distribution (QForm VX 8.2.4) within the deformed by one-angled ECAE-MRD work-piece (at an extrusion angle $\boldsymbol{\Phi}$=135^O) after fourth pass (4x135^O)

The sample mean values of the effective strain after a second pass (2x135^O) is $\boldsymbol{\varepsilon_{eff}}$=2.37 (varies between $\boldsymbol{\varepsilon_{min}}$=1.16 in the middle and $\boldsymbol{\varepsilon_{max}}$=3.96), with a standard deviation of 1.43. After four passes (4x135^O), a similar distribution and an effect of the contact friction is recorded (Fig. 4). The sample mean values of the effective strain after the fourth pass increases and is $\boldsymbol{\varepsilon_{eff}}$=5.22 (ranges between $\boldsymbol{\varepsilon_{min}}$=3.15 in the middle and $\boldsymbol{\varepsilon_{max}}$=9.14), and the standard deviation increases to 2.08.

3.2 Distribution of the Effective Strain in Single-angled ECAE-MRD at 90^O

In the computer simulation of a one-angled ECAE with a movable ram-die at an extrusion angle of 90° with contact friction, it was found that the deformed work-piece filled the deformation space completely. The effect of the contact friction in the one-angled (90^O) ECAE-MRD diagram is also expressed in the increase of the effective strains from the outer wall of the deformed work-piece, the rest of the cross-section being less deformed. After the second pass (2x90^O), a similar effect of contact friction and symmetrical distribution on both sides is observed (Fig. 5).

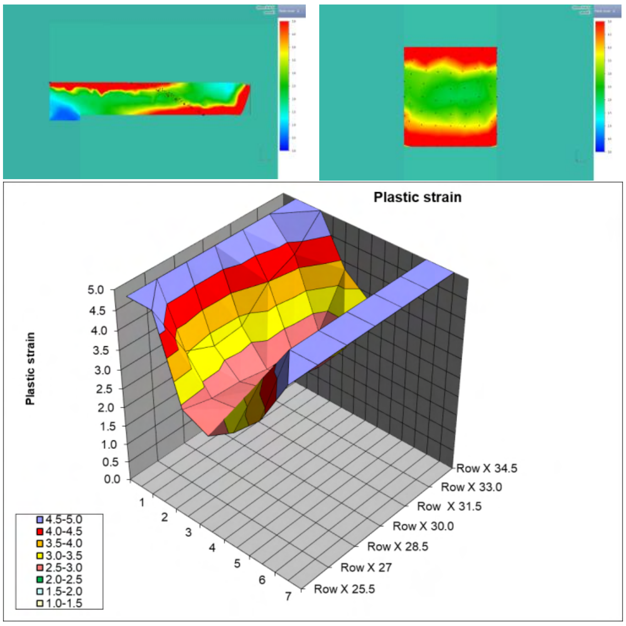

Figure 5. Effective plastic strain distribution (QForm VX 8.2.4) within the deformed by one-angled ECAE-MRD work-piece (at an extrusion angle $\boldsymbol{\Phi}$=90^O) after second pass (2x90^O)

The sample mean values of the effective strains after a second pass (1x90^O) is $\boldsymbol{\varepsilon_{eff}}$=2.21 (ranges between ε_{min}=1.06 and $\boldsymbol{\varepsilon_{max}}$=7.26), with a standard deviation of 1.92. The sample mean values of the effective strains after a second pass (Fig. 5) increases and is $\boldsymbol{\varepsilon_{eff}}$=4.87 (varies between $\boldsymbol{\varepsilon_{min}}$=2.69 and $\boldsymbol{\varepsilon_{max}}$=8.40) and the standard deviation increases insignificantly to 2.11.

3.3 Distribution of the Effective Strain in Two-angled ECAE-MRD at 135^O

From the representation of the effective strain in a computer simulation of a two-angled ECAE-MRD with contact friction reading at 2x135^O angles after a first transition (2x135^O) it is evident that they are unilaterally concentrated on one side of the deformed work-piece and after a second pass (4x135^O) – on both sides (Fig. 6).

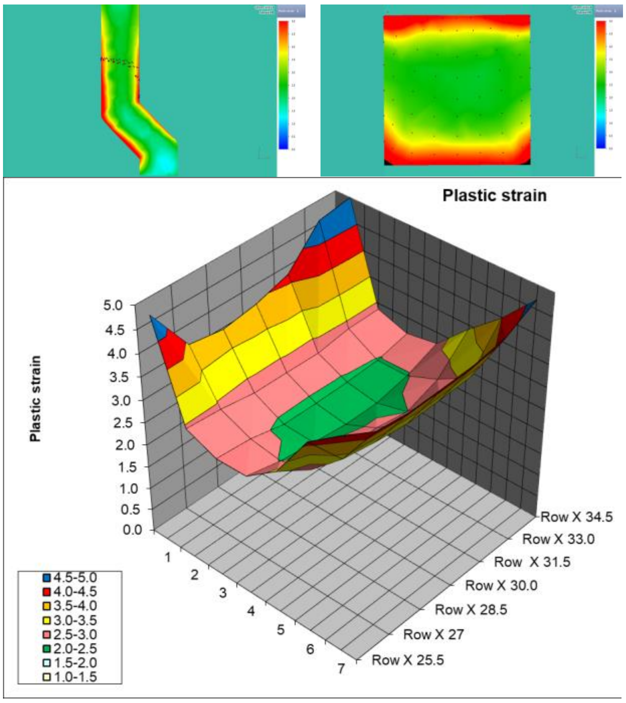

Figure 6. Effective plastic strain distribution (QForm VX 8.2.4) within the deformed by two-angled ECAE-MRD work-piece (at two extrusion angles Φ=135°) after second pass (4x135°)

The sample mean values of the effective strain after a second pass is $\boldsymbol{\varepsilon_{eff}}$=1.66 (varies between $\boldsymbol{\varepsilon_{min}}$=1.16 and $\boldsymbol{\varepsilon_{max}}$=3.40), with a standard deviation being relatively low 0.79. The sample mean values of the effective strain after the fourth pass (Fig. 6) increases and is $\boldsymbol{\varepsilon_{eff}}$=3.27 (varies between $\boldsymbol{\varepsilon_{min}}$=2.47 and $\boldsymbol{\varepsilon_{max}}$=4.61) and the strain distribution (the standard deviation) remains relatively low – 0.85.

3.4 Distribution of the Effective Strain in Four-angled ECAE-MRD at 135°

From the representation of the effective strain in a computer simulation of a four-angle ECAE-MRD with a contact friction reading at 4x135° angles, after crossing of the two (firs and second) shear zones (2x135°) shows that they are bilaterally concentrated, but it remains on both sides after crossing the remainder two (third and fourth) zones (4x135°) (Fig. 7).

The sample mean values of the effective strain after the first two zones is ε_{eff}=2.52 (ranges between $\boldsymbol{\varepsilon_{min}}$=1.37 and $\boldsymbol{\varepsilon_{max}}$=4.72), with a standard deviation of 1.22.

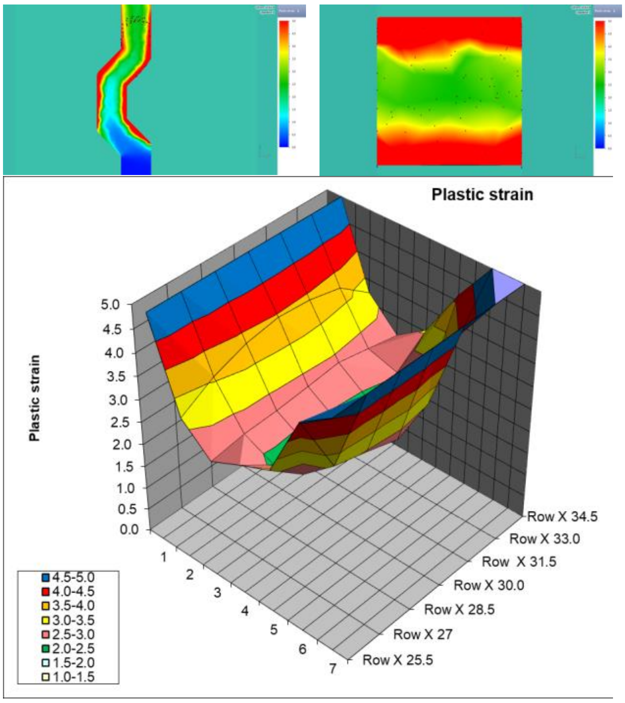

Figure 7. Effective plastic strain distribution (QForm VX 8.2.4) within the deformed by four-angled ECAE-MRD work-piece (at four extrusion angles **Φ**=135°) after single pass (4x135°)

The sample mean values of the effective strain after crossing and the fourth zone (Fig. 7) increases to $\boldsymbol{\varepsilon_{eff}}$=3.80 (ranges between $\boldsymbol{\varepsilon_{min}}$=2.45 and $\boldsymbol{\varepsilon_{max}}$=5.68) and the strain distribution (the standard deviation) is 1.36.

4. DISCUSSION

The results of the sample mean values of the effective strain, taking into account the contact friction shown in the modes of Fig. 1, Fig. 2 and Fig. 3 for single- and multi-angular ECAE-MRD with a contact friction reading are given in Table 2. Highest values of the accumulated effective strain at the same deformation angles were obtained with single-angled ECAE-MRD (90° and 135°) and the lowest were obtained for the two-angled ECAE-MRD (135°).

The determined effective strains in the selected deformation modes under contact friction conditions are 1.6 to 2.5 times higher than those obtained in the frictionless conditions (Table 1). The increase in the sample mean values of the effective strain by ECAE-MRD as well as the overall filling of the deformation space is due entirely to the contact friction between the deformed work-piece and the tool walls.

Table 2. Sample mean results $\overline{X}$ of effective strain from simulation of one-angled and multi-angled ECAE-MRD taking into account contact friction

Pass number x die channel angle	Effective plastic strain (sample means) taking into account friction			
	One-angled x135°	**One-angled x90°**	**Two-angled x135°**	**Four-angled x135°**
First pass 1x135°	0.96	-	1.05	1.25
Pass 2x135° or 1x90°	2.37	2.21	1.66	2.52
Third pass 3x135°	3.71	-	3.01	3.47
Pass 4x135° or 2x90°	5.22	4.87	3.27	3.80

The results of the determined strain distribution (the standard deviation) in the transverse cross section of the deformed bodies are given in Table 3. The highest non-uniformity of the effective strain is characterized by the single-angled ECAE-MRD mode at 90^{O} (Fig. 5) and the smallest – the two-angled ECAE-MRD (Fig. 6).

Table 3. Strain distribution uniformity of computer simulations taking into account friction expressed through standard deviation values $\mathbf{S_D}$

Pass number x die channel angle	Effective plastic strain (sample means) taking into account friction			
	One-angled x135°	**One-angled x90°**	**Two-angled x135°**	**Four-angled x135°**
First pass 1x135°	0.82	-	0.60	0.66
Pass 2x135° or 1x90°	1.43	1.92	0.79	1.22
Third pass 3x135°	1.76	-	1.17	1.40
Pass 4x135° or 2x90°	1.76	2.11	0.85	1.36

The increase in the standard deviation, i.e., the non-uniformity of the strains as a result of the contact friction reading varies with the various ECAE-MRD modes.

The observed value of $Z_{\overline{X}\,\overline{Y}}$ (Tables 4–7), by which we judge whether to accept the basic hypothesis of equality of sampling averages, i.e. if $Z_{\overline{X}\,\overline{Y}}$ is within the confidence interval [-2.56, 2.56], then the sample means are assumed to be equal. Otherwise it is assumed that they are not equal.

Table 4. Normalized difference $Z_{\overline{X}\,\overline{Y}}$ of sample means $\overline{X}$ and $\overline{Y}$ from the first pass $1x135^{O}$

First pass 1x135°	Two-angled 1x135°	Four-angled 1x135°
One-angled 1x135°	-0.86	-2.18
Two-angled 1x135°	-	-1.58

The comparisons of the sample means $\overline{X}$ of the first row of Table 2 (first transition 1x135°) are given in Table 4. They can be considered equal, because their $Z_{\overline{X}\,\overline{Y}}$ are within the range [-2.56, 2.56].

Table 5. Normalized difference $Z_{\overline{X}\,\overline{Y}}$ of sample means $\overline{X}$ and $\overline{Y}$ from the pass $2x135^{O}$ or $1x90^{O}$

Pass 2x135° or 1x90°	One-angled 1x90°	Two-angled 2x135°	Four-angled 2x135°
One-angled 2x135°	0.44	3.04	-0.57
One-angled 1x90°	-	2.27	-1.60
Two-angled 2x135°	-	-	-4.15

Table 6. Results of normalized difference $Z_{\overline{X}\,\overline{Y}}$ of sample means $\overline{X}$ and $\overline{Y}$ from the pass $3x135^{O}$

Third pass 3x135°	Two-angled 3x135°	Four-angled 3x135°
One-angled 3x135°	2.33	0.75
Two-angled 3x135°		-1.76

The comparisons of the second row of Table 2 (transition 2x135° or 1x90 °) are given in Table 5. They can be assumed to be equal (except for $\overline{X}$=1.66), because their respective values $Z_{\overline{X}\,\overline{Y}}$ are outside the range.

The comparisons from the sample averages $\overline{X}$ from the third row of Table 2 (transition 4x135° or 2x90°) are given in Table 5. They can be assumed to be equal because their $Z_{\overline{X}\,\overline{Y}}$ are within the range [-2.56, 2.56].

Table 7. Normalized difference $Z_{\overline{X}\,\overline{Y}}$ of sample means $\overline{X}$ and $\overline{Y}$ from the pass 4x135^{O} or 2x90^{O}

Pass 4x135° or 2x90°	One-angled 2x90°	Two-angled 4x135°	Four-angled 4x135°
One-angled 4x135°	0.83	6.07	3.99
One-angled 2x90°		4.91	2.97
Two-angled 4x135°			-2.33

The comparisons from the sample averages $\overline{X}$ of the fourth row of Table 2 (transition 4x135° or 2x90°) indicate that the first two (single-angled) and second two (multi-angled) can be considered equal.

5. CONCLUSIONS

1. It has been found that the single-angled ECAE-MRD modes allows for a greater mean values of the effective strain compared to multi-angled ECAE-MRD patterns at the same (resultant) value of their extrusion angles.
2. Using computer simulations, it is confirmed that the used dependence (1) for determining the effective strain does not take into account the contact friction and consequently caused by it the non-uniformity of the effective strain.
3. The determined values of ECAE-MRD accumulated effective strains with contact friction are 1.6 to 2.5 times higher than the values obtained in the simulation of the processes under the frictionless conditions.
4. It was found that contact friction rather than the type of the strain space of the ECAE modes under consideration is the main cause of the non-uniform distribution of effective strains, with the highest non-uniformity of the strains being considered in the single-angled ECAE-MRD mode at 90°, smaller – at the two-angled ECAE-MRD mode at 135°.
5. In the test for the equality of sample averages of effective strain (taking into account the contact friction) it was found that although the extrusion angles of the intersecting grooves in the ECAE are equal, it is not always the mean values of the effective strain that can be assumed to be equal.

ACKNOWLEDGEMENT

The authors thank the eng. N. Radeva and eng. A. Yordanov, who helped to perform the computer simulation with the specialized software product Quantor Form VX 8.2.4. The authors would like to thank the Research and Development Sector at the Technical University of Sofia for the financial support.

REFERENCES

[1] V.M. Segal: *The Method of Material Preparation for Subsequent Working,* Invention Certificate of the USSR No. 575892, 1977.

[2] V.M. Segal: *Equal channel angular extrusion: from macromechanics to structure formation*, Materials Science and Engineering 1999, A 271 (1-2): 322–333.

[3] G.J. Raab, R.Z. Valiev, T.C. Lowe, Y.T. Zhu: *Continuous processing of ultrafine grained Al by ECAP-Conform*, Materials Science and Engineering 2004, A 382, 30–34.

[4] R.Z. Valiev, T.G. Langdon: *Principles of equal-channel angular pressing as a processing tool for grain refinement*, Progress in materials science 51, 2006, 881-981.

[5] V.M. Segal, V.I. Reznikov, A.E. Drobyshevski, V.I. Kopylov: *Plastic working of metals by simple shear*, Russ. Metall. (Engl. Transl.) 1981, vol. 1, 99–105.

[6] J.G. Genov: *Energetic Interpretation of Limit Steady Forming of Sheet Metal*, Journal of Material Science and Technology (14, 2) 2006, ISSN 0861-9786, 75–86.

[7] V.M. Segal: *Engineering and commercialization of equal channel angular extrusion (ECAE)*, Materials Science and Engineering A 386 2004, 269–276.

[8] M. Kandeva: *The Contact Approach in Engineering Tribology*, Publishing House Technical University – Sofia, Sofia, 2012, 505 p. (in Bulgarian).

[9] A.A. Nikolov: *Construction schemes for severe plastic deformation of metals using equal channel angular extrusion*, PhD Thesis, Technical University of Sofia 2016, Sofia (in Bulgarian).

[10] V.V. Kamburov, V.I. Semenov, N.T. Tontchev, V.P. Mishev, A.A. Nikolov: *3D simulation by CAD/CAE software of the deformation process at equal channel angular extrusion with active friction forces*, XIV Int. Congress "Machines, Technologies, Materials 2017" Varna, 2017, Proceedings year I, Issue 6(6) vol. VI, 423-426.

[11] S. Letzkovska, P. Rahnev, J. Genov, K. Semenliyski: *Computer based equipment for measuring of limited deformation*, XXXVII Int. conf. on Information, Communication and Energy systems and Technologies, Niš 2002, Yugoslavia Proceedings of papers, vol.1, 168-169.

[12] K. Kamberov, G. Todorov, Sv. Stoev, B. Romanov: *Mechanical Strenght Test of Train Wheel Based on Virtual Prototyping*, Proceedings in Manufacturing Systems, 2015, vol. 10, issue 3, 99 – 104.

[13] N. Tontchev: Materials Science, Effective solutions and Technological variants, LAMBERT Academic Publishing, (2014) 142 p.

[14] N. Tontchev, Z. Cekerevac: *Approach and Application in Multicriteria Decision Support in the Field of Materials Science*, MEST Journal, (MEST, 2014, no. 118-29.

[15] Y. Iwahashi, J. Wang, Z. Horita, M. Nemoto, T. Langdon: *Principle of Equal-Channel Angular Pressing for the Processing Of Ultra-Fine Grained Materials*, Scr. Mater., 1996, 35, 143–146.

[16] F. Djavananroodi, B. Omranpour, M. Ebrahimi, M. Sedigli: *Designing of ECAP parameters based on strain distribution uniformity*, Chinese Materials Research Society, Progress in Natural Science: Materials International 2012, 22(5), 452-460, http://doi.org/10.1016/j.pnsc.2012.08.001.

[17] J.E. Freund: *Mathematical Statistics with Applications (eighth edition)*, Pearson Education Limited, 2014, ISBN 10: 1-292-02500-X.

Serbian Tribology Society

SERBIATRIB '19

16th International Conference on Tribology

Faculty of Engineering University of Kragujevac

Kragujevac, Serbia, 15 – 17 May 2019

THE INFLUENCE OF LASER MILLING PROCESS PARAMETERS ON DEPTH OF CUT AND SURFACE ROUGHNESS

Jelena BARALIĆ[1,*], Bogdan NEDIĆ[2], Stefan ĐURIĆ[2]

[1]Fakultet tehničkih nauka u Čačku, Univerzitet u Kragujevcu, Čačak, Srbija

[2]Fakultet inženjerskih nauka, Univerzitet u Kragujevcu, Kragujevac, Srbija

*Corresponding author: jelena.baralic@ftn.kg.ac.rs

Abstract: *Laser beam machining (LBM) is one of the lately most used nonconventional machining processes. It is based on melting and evaporation of processed material. It can be applied to almost a whole range of materials. Lately, it has been increasingly used for mark-engraving materials, as well as for milling less demanding 3D shapes. This paper presents the results of research on the possibility of laser milling of plexiglass. The influence of the cutting speed, laser power and the radial step on the machined surface roughness and depth of the cut was analyzed. It was concluded that increase in radial step and cutting speed causes lover values of the depth of cut. Laser milling with higher laser pover leads to higher values of depth of cut. Influence of mentioned laser machining parameters on surface roughness of machined surface is obvious, but it is necessary to realize more detail investigation on this subject.*

Keywords: *laser milling, depth of cut, surface roughness.*

1. INTRODUCTION

Unconventional processing methods have been developed to enable the machining of new materials, high strength and hardness and resistant to high temperatures. Some of these materials can not be machined by conventional machining methods at all, due to the appearance of very high processing forces and high stresses in the cutting zone. Laser machining is a good solution in these cases. The possibility of laser machining a certain material, depends primarily on material characteristics such as: thermal conductivity, specific heat and melting and boiling temperatures.

Laser cutting and engraving is nowadays very often applied machining in most manufacturing industries. With laser of various characteristics, almost all metal and non-metallic materials can be cut, welded, surface treated. Laser beam machining is now beeing increasingly used for engraving and milling of nonmetalic materials. Smaller power lasers are sufficient for this kind of machining. The nonmetalic materials have low thermal condustivity and thermal diffusion coefficients, but most of these materials have high absorptivity for the 10.6µm wavelenght radiation of CO_2 laser [1].

2. LASER BEAM MACHINING

Laser is the abbreviation of light amplification by stimulated emission of radiation [2]. Highly collimated, monochromatic and coherent light beam is generated and focused on a small spot on machined surface, resulting in very high power density (oko 10^6W/mm^2). A large number of laser machines, with different characteristics, are available today. Table 1 gives general types of the laser.

Table 1. Laser types

Laser type		Wavelenght, nm	Typical performance
Solid	Ruby	694	Pulsed, 5 W
	Nd-YAG	1064	Pulsed, CW, 1÷800 W
	Nd glass	1064	Pulsed, CW, 2 mW
Semiconductor	GaAs	800÷900	Pulsed, CW, 2÷10 mW
Molecular	CO_2	10.6µm	Pulsed, CW, <15 KW
Ion	Ar^+	330÷530	Pulsed, CW, 1W÷5 KW
	Excimer	200÷500	Pulsed
Neutral gas	He-Ne	633	CW, 20 mW

CO_2 laser is a molecular gas laser. Figure 1 shows CO_2 laser schematic.

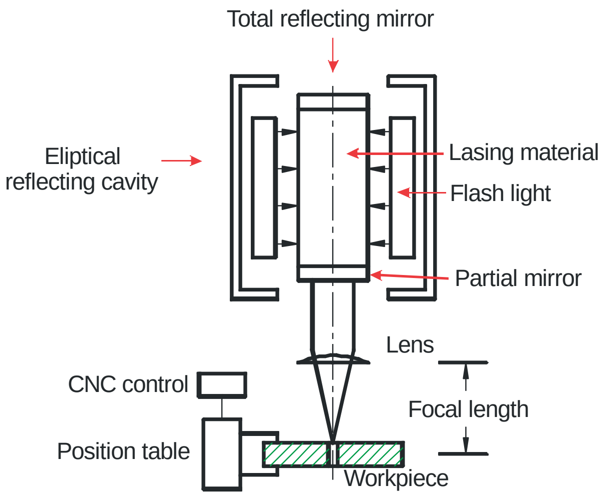

Figure 1. Laser beam mashining schematic

The laser tube is about 1000 mm long and a few tens of millimeters in diameter. A 10.6 µm wavelength laser beam passes through a partial mirror and then through a lens that focuses the laser beam on a small spot on the machined surface. Such a focused laser beam on the small spot on the surface of the machined object leads to the creation of an enormous amount of light and thermal energy, which leads to the melting and evaporation of any material, of any characteristic, and only in the laser beam action zone.

Laser milling is a new technology suitable for machining a wide range of materials (metals, glass, ceramics and plastics) by removing material in a layer-by-layer [3]. This technique involves the heating and melting of a material and material removal. This process depends on temperature developed on machined surface. It means that problems like micro cracks can commonly appear at heat affected zones.

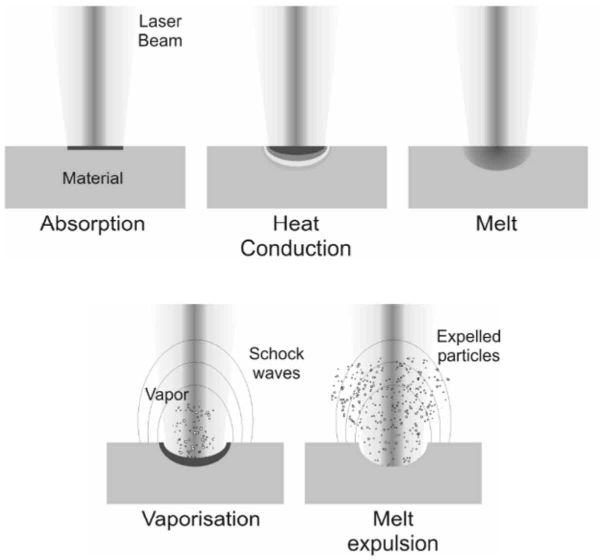

Figure 2. Laser milling phenomena [3]

When machining metals, the laser beam is heating, melting and evaporating the metal (metal sublimation), while in polymers the process is based on the rupturing of molecular chains (laser ablation), as shown in Figure 2.

The major disadvantage of the laser milling process is difficult achievement of vertical walls on shapes made by laser milling. Side walls that initially were meant to be vertical might end with a draft angle of 10° to 15°, depending on the size of the work area [4].

Laser milling is the removal of material from the top surface down to a specified depth. CO_2 lasers with 10.6 µm wavelength are primarily used for removal of non-metallic materials. The material type and laser power level determine the maximum depth of cut and speed of milling. Shallow milling-engraving is a faster process than deep milling. Also, lower density materials are faster engraved than higher density materials. Increasing laser power level increases laser milling speed. The non-metallic materials have low thermal conductivity and thermal diffusion coefficients, but most of these materials have high absorptive for the 10.6 µm wavelength radiation of CO_2 laser.

3. EXPERIMENTAL SETUP

Today, laser milling is mainly used to remove one layer of material, that is, it is used for engraving of the low depth contours. Machined material is in this case removed in one passage of the laser cutting head. There is very little research that investigates the laser machining parameters influence on the depth of cut in laser milling and roughness of the surface machined with laser milling. The aim of this study was to investigate the influence of cutting speed, laser power and radial step (step between two cutting laser head passes), on the depth of cut and surface roughness of machined surface with laser milling.

Experiments were performed on Laser Cut-1208 Laser CNC Machine, laser engraving machine. It is primarily intended for engraving and cutting of sheet non-metalic materials. The maximum laser power for this machine is 80 W.

The square shapes, 10x10 mm, were machined in 8 mm thick **PMMA** (polymethyl methacrylate - PLEXIGLASS), with laser milling. In the first part of the experiment, for each machined square, cutting speed and laser beam power were varied. The squares were made with several passes of the laser head in one layer. Cutting speed and laser power were varied during experiment. The radial step s_r between two passages of the laser head was constant and it was 0.02 mm. Depth of cut and surface roughness were measured. The appearance of the machined samples is given in Table 2.

In the second part of the experiment, the laser power was constant and amounted to 16 KW, while the cutting speed and the radial step were varied. The depth of cut and the roughness of the treated surface were also measured for thus obtained quadratic samples. The appearance of the samples obtained with these parameters of the laser milling process is given in Table 3.

Table 2. Machined samples-I

Radial step s_r = 0.02 mm				
V, mm/s	P, KW			
	16	24	32	40
100				
200				
300				

Table 3. Machined samples-II

Laser power P = 16 KW				
V, mm/s	s_r, mm			
	0.02	0.05	0.01	0.02
100				
150				
200				
250				
300				

4. THE RESULTS OF EXPERIMENTAL RESEARCH

As already mentioned, for samples obtained in both parts of the experiment, the depth of the cut and the roughness of the treated surface were measured. The depth of the cut was measured with a coordinate measuring machine with a measuring tap at several places. Surface roughness was also measured in several places, transverse with respect to the movement of the laser head. The mean values of the measured depth of cut and surface roughness are given in Table 4 and 5 respectively.

Table 4. Depth of cut and surface roughness in laser milling - I

Radial step s_r = 0.02 mm								
V [mm/s]	P , KW							
	16		24		32		40	
	h, mm	Ra, µm	h, mm	Ra, µm	h, mm	Ra, µm	h, mm	Ra, µm
100	0.59	18.4	1.453	8.9	4.109	/	5.977	/
200	0.24	15.1	0.24	26.3	0.24	42.7	0.24	40
300	0.121	11.7	0.121	13.3	0.121	22.9	0.121	42.5

Table 5. Depth of cut and surface roughness in laser milling - II

Laser power P = 16 , KW								
V [mm/s]	s_r , mm							
	0.02		0.05		0.1		0.2	
	h ,mm	Ra, µm	h, mm	Ra, µm	h, mm	Ra, µm	h, mm	Ra, µm
100	0.59	18.4	0.257	16.6	0.096	12.4	0.022	9.5
150	0.415	19.4	0.145	17.2	0.071	11.3	0.001	13.8
200	0.24	15.1	0.136	12.6	0.054	8.8	0.001	19.2
250	0.185	13.9	0.103	6.9	0.035	8.6	0.004	18.9
300	0.121	11.7	0.07	3.85	0.023	7.2	0.005	10.75

Based on the measured values for the depth of cut in laser milling - h, the following expressions were obtained:

$$h = 0.08 \cdot V^{-0.95} \cdot P^{2.37} , \qquad (1)$$

and

$$h = 3.06 \cdot V^{-1.24} \cdot s_r^{-1.05} . \qquad (2)$$

The dependence of the depth of cut - h on the cutting speed and the laser power has a correlation coefficient of 0.99 while the dependence of the depth of cut - h on the cutting speed and radial step has a coefficient of correlation of 0.988. This shows that the models represented by formulas (1) and (2) describe very well the dependence of the depth of cut on the parameters of the laser milling process. Unlike the cut depth, surface roughness could not be described satisfactorily by some simpler model.

The results shown in Tables 4 and 5 are shown graphically in the diagrams, Figures 3, 4, 5 and 6.

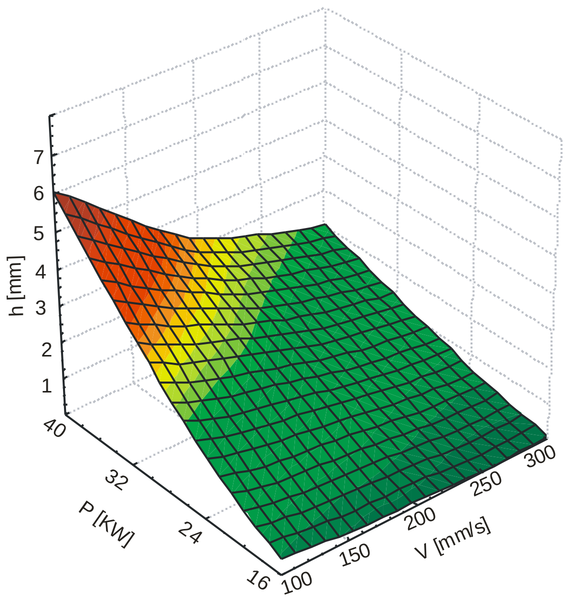

Figure 3. The laser power and cutting speed influence on the depth of cut

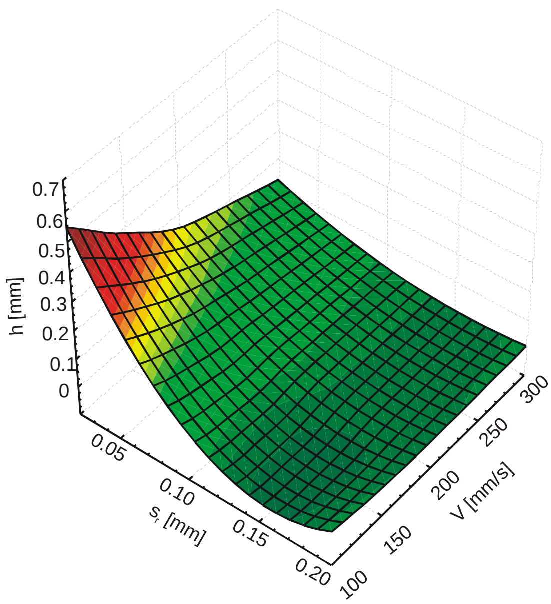

Figure 4. The radial step and cutting speed influence on the depth of cut

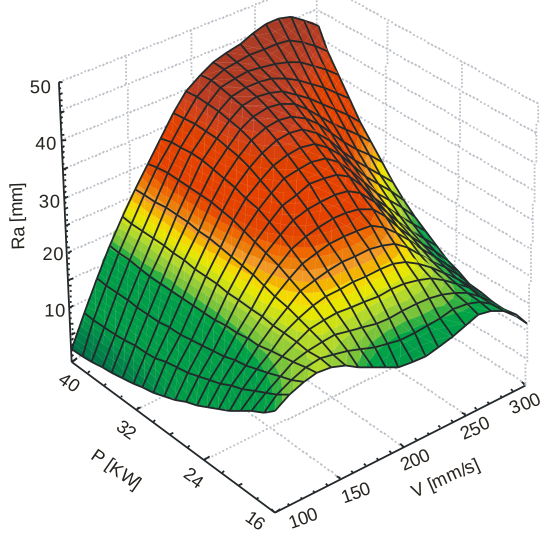

Figure 5. The laser power and cutting speed influence on the machined surface roughness

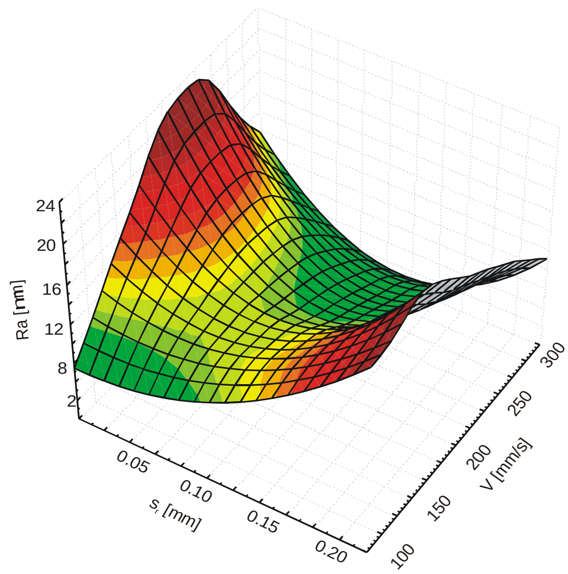

Figure 6. The radial step and cutting speed influence on the machined surface roughness

5. CONCLUSION

After measuring the depth of the cut and the roughness of the treated surface of the samples obtained in both parts of the experiment, it can be concluded that the selected parameters of the laser milling process have a significant influence on the depth of the cut and the roughness of the machined surface. In the laser milling with higher cutting speeds, a smaller depth of cut is achieved. The higher the laser beam's power, the greater the depth of the cut can be achieved. As the radial step increases, the cut depth decreases. These phenomena can be explained by the fact that with the increase in the energy of the laser beam, reduction of the cutting speed and the radial step, the amount of energy transferred to the unit of the machined material increases, which expedite the process of heating and melting of the material, and therefore the depth of the cut is higher.

The influence of machining parameters of laser milling on the surface roughness cannot be described by simple models. To define this addiction, more detailed research is needed.

ACKNOWLEDGEMENT

This paper is part of project TR35034, funded by the Ministry of Education, Science and Technological Development of Serbia.

REFERENCES

[1] B.H. Zhou, S.M. Mahdavian: Experimental and theoretical analyses of cutting nonmetalic materials by low power CO_2 laser, Journal of Materials Processing Technology, Vol. 146, pp. 188-192, 2004.

[2] H. El-Hofy: *Advanced Machining Processes - Nontraditional and Hybrid Machining*, Hassan McGraw-Hill, New York, 2005.

[3] J. C. Vasco, P. J. Bártolo: Processing conditions of laser micro-milling, in: *15th International Symposium on Electromachining*, Leiria, Portugal, 2007.

[4] Introduction to Laser Material Processing: http://www.elitebusinesssystems.com/intro-to-dlmp.pdf, acccessed 16.4.2019.

[5] *LaserCut-1208* - Machine documentation

[6] How CO_2 fiber laser cutting machine work: https://www.steeltailor.com/blog/how-co2-and-fiber-laser-cutting-machine-work/, accessed 08.09.2018.

[7] A.K. Dubey, V. Yadava: Laser beam machining – A review, International Journal of Machine Tools and Manufacture, Vol. 48, pp. 609-628, 2008.

[8] R.K. Hsu, S.M. Copley: Producting 3D shapes by laser milling, Journal of Egineering for Industry, Vol. 112, pp. 375-379, 1990.

[9] D. Lazarević, M. Radovanović: *Nekonvencio-nalne metode - Obrada metala odnošenjem*, Mašinski fakultet Niš, Niš, 1994.

Serbian Tribology Society

SERBIATRIB '19

16th International Conference on Tribology

Faculty of Engineering
University of Kragujevac

Kragujevac, Serbia, 15 – 17 May 2019

GENERATING AND CHARACTERISTIC OF SURFACES IN MECHANICAL MACHINING OF MICRO-PARTS

Branislav SREDANOVIC[1,*], Gordana GLOBOCKI-LAKIC[2], Damir GRGURAS[3], Davorin KRAMAR[4], Franci PUSAVEC[5]

[1, 2] University of Banjaluka, Faculty of Mechanical Engineering, Banjaluka, Bosnia and Herzegovina
[3, 4, 5] University of Ljubljana, Faculty of Mechanical Engineering, Ljubljana, Slovenia
*Corresponding author: branislav.sredanovic@mf.unibl.org

Abstract: *Development of micro-devices parts is intensified with developments in medical device and energetic industry. In production of micro-parts (micro-pump, micro-gears, micro-manipulators, etc.), a wide range of engineering materials is encountered. Strict requirements are set in terms of characteristic of micro-parts machined surfaces, such are low surface roughness, advanced tribological characteristic, etc. In this paper is analysed possibilities of different metallic materials mechanical micro-machining. The analysis includes the analysis of the generating and characteristics of the machined surfaces, and influence of a whole set of parameters on surface characteristic. The results showed the benefits of mechanical micro-machining and proved that it can achieve satisfactory results of the surface characteristics indicators.*

Keywords: *micro-parts, surfaces, machining, analysing*

1. INTRODUCTION

Micro-parts surface characteristic is the important properties regard to its functionality. The big problem in production of micro-parts is getting the appropriate machined surface roughness, because there are disproportion in range between dimensions, tolerations and surface roughness parameters. Industry of micro-devices and micro-parts is in expansion with growth of energetic sector, medical sector and automotive and aero industry. There are many mechanical and thermal methods for machining surface on metallic micro-parts, such are: laser beam machining, electro-discharge machining, forming, cutting, grinding, casting, and etc. Each of them have advantages and disadvantages.

In cutting technology, as mechanical method for production of metallic micro-parts, mains problem is caused by size effect. Size effect is caused by ratio between process parameters, tool geometry, workpiece structure and mechanical properties (Fig. 1).

Micro-milling, as mechanical micro-cutting technology, is increasingly used in tool and die industry because it can produce complex geometry with high-dimensional accuracy. Process of micro-cutting is done in range of elasticity of workpiece materials, which results in ploughing and sliding. This phenomena has big influence on generation and surface roughness on micro-parts. In this paper is analysed influence of different process parameters and workpiece properties on surface characteristic. Focus is on metallic materials such micro-milling of chromium-molybdenum tool steel AISI D2 (for production of mold and die) and Inconel 718 (for production of functional temperature loaded mechanical parts).

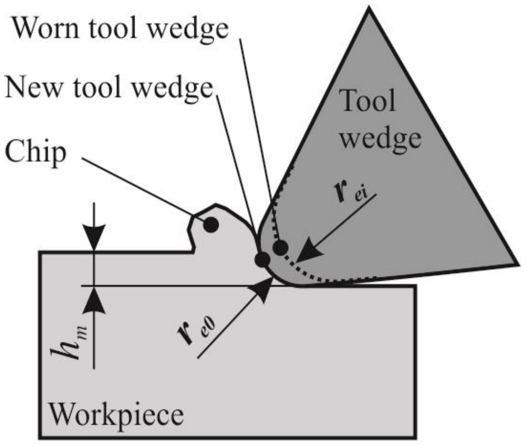

Figure 1. Size effect in mechanical machining

Bissasco et al. [1] analysed influence of tool geometric characteristics on surface roughness, in micro-milling of martensitic stainless steel, due the size effect. Aramcharoen et al. [2] analysed influence of size effect in micro-milling of hardened tool steel H13. Li [3] analysed tool wear and surface roughness in micro milling of SKD 61 steel (38 HRC), under different lubrication condition. They improved machinability by using MQL. Lee et al. [4], analyzed influence of cutting parameters on surface roughness and burrs. Based on experimental research, it was shown that the appropriate choice of parameters can reduce the surface roughness, and burrs on workpiece edge also. Similar studies are shown in [5]. In studies [6, 7] by Ucun et al., was investigated effect of cutting parameters, coating material and the built-up edge on the surface roughness in micro-milling of Inconel 718. They are concluded that coated tools are given better surface roughness performance. Kuram et al. [8] investigated the influences of cutting parameters on surface roughness and cutting forces, in micro-milling of Ti6Al4V alloy and Inconel 718. Lu et al. [9], analyzed the influencing of cutting condition and tool coats on output parameters in micro-milling of Inconel 718. Vazquez et al. [10] investegated influence of cooling and lubrication techniques in micro-milling of special alloy.

2. EXPERIMENTATION

Experiment measurement was performed on the tree axis high speed micro-milling centre Sodick MC430L (Figure 2) with hybrid bearing high speed spindle (maximum revolution 40.000 min^{-1}). The linear machine motors has resolution of 100 nm and accelerate up to 1 G. Machine is equipped MQL system. Cutting tool was two flute flat-end-mill by SECO, TiAlN layer coated. It has diameter is 600 µm, corner radius 0.05 mm, neck 8 mm and mounting diameter is 3 mm. Helix revolution angle is 7.25°, height 0.8 mm.

Figure 2. Experimental setup

In this analyse research was used two different workpiece materials. First, nickel-chromium based Inconel 718 supper-alloy, was used. This oxidation and high temperature resistant super-alloy has tensile strength 1350 MPa and hardness 40 HRc. Second workpiece material was cold work tool steel AISI D2, hardened to 62 HRC, with tensile strength 1100 MPa. Both materials are intended for micro-parts exposed to high temperature and mechanical loads.

Surface roughness was measured with optical 3D non-contact measuring device ALICONA InfiniteFocus (Figure 3). Measurement was based on photo recording of horizontal layers for every 10 nm, recognized the sharpest parts of captured image, and proceed the 3D micro-surface relief (Figure 4).

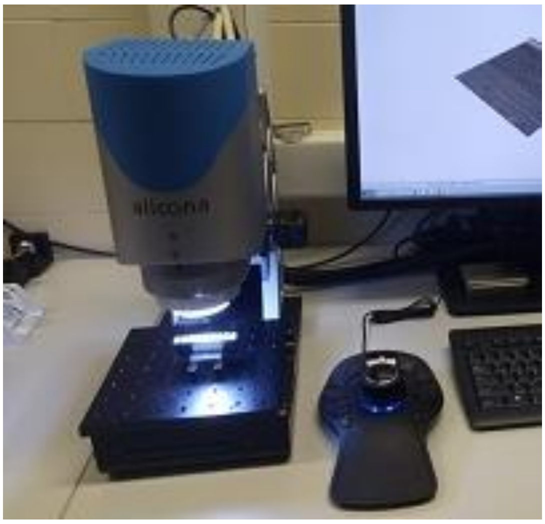

Figure 3. ALICONA measuring device

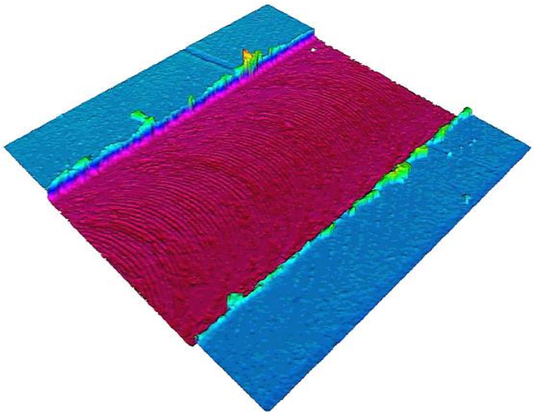

Figure 4. Formed measurable 3D model of micro-surface relief

Experiment was performed under MQL condition of lubricating. For all experiments cutting speed was v_c = 40 m/min. Other cutting parameters range was adopted by cutting tool manufactures.

3. RESULTS AND DISSCUSIONS

On Figure 5 is shown 3D scans of micro-machined channel in Inconel 718. On the same figure, on picture a) is shown relief of microchannel milled by use feed per tooth f_z = 0.012 mm and depth a_p = 0.01 mm, and b) micro-milled surface by same feed but depth a_p = 0.02 mm. Can be noted differences in generated surface on channel bottom. On bottoms can be noted cutting tool trace, and build-up edge on channel side. Height of build-up edge is higher on side where micro-mill cutter exits outside the channel. Also, can be concluded that generated surface is more plunged for higher values of cutting depth. Along channel, more intensive plunging of the workpiece material occurred at the entrance and exit of the milling micro-tool teeth. The reason for this is the reduction in the chip cross-section, which has the result of dominating the size effect. This phenomenon is caused by proportions of the thickness of the affected workpiece material by cutting wedge and cutting wedge radius, because edge is not ideal sharp. In this paper, follow up analysing of the parameters that describing the condition of the generated surface, such as the surface roughness and height of build on edge.

a)

b)

Figure 5. Scanned channel in Inconel 718

For both workpiece material is analysed the average surface roughness (R_a) and mean peak to valley height in ten points of roughness profile (R_z). This two surface roughness parameters was measured on four different points in each channel, after which their mean value was calculated. On each measuring point in channel, reference length was set along the channel.

On Figure 6 is shown influence of feed and depth of cutting on surface roughness parameters in micro-milling of Inconel 718. Can be concluded that surface roughness increase with increase of cutting parameters, except for set of lower cutting parameter values. High values of surface roughness for lower values of depth of cutting and feed were caused by phenomenon of size effect. In that case, values of feed wasn't provide a sufficient value of minimum chip cross-section that can be removed by cutting tool wedge. Similar conclusions can be obtained for the values of R_z (Figure 7).

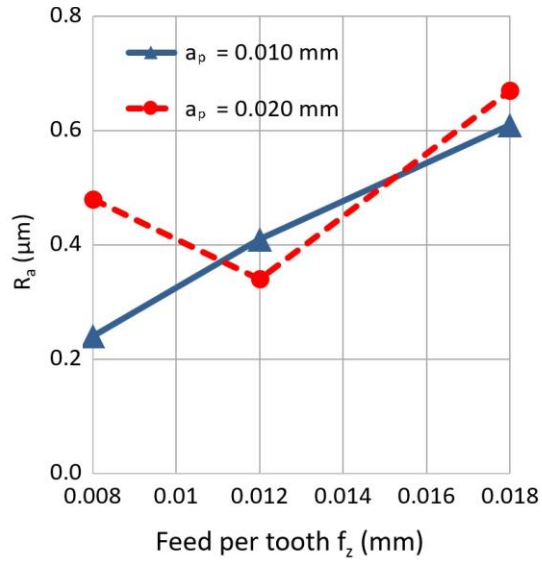

Figure 6. Average surface roughness (Ra) for Inconel 718

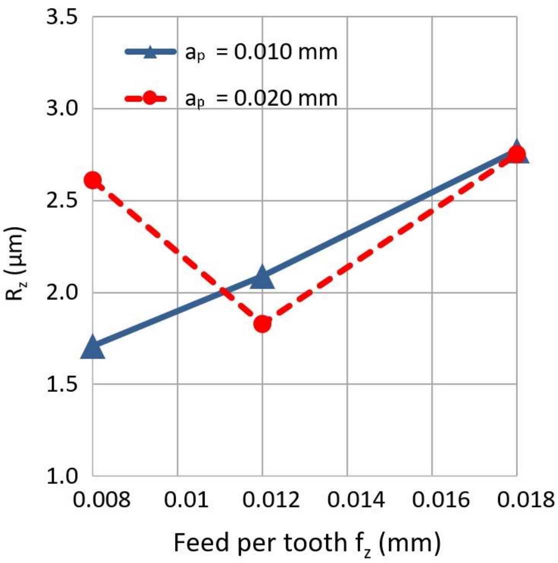

Figure 7. Average surface roughness in ten points (R_z) for Inconel 718

Based on graphs can be concluded that surface roughness parameters intensively increase with changing of feed, while the changing of depth of cutting leads to less change in values of surface roughness parameters. This variation of values is intensively for parameter R_a relative to parameter R_z.

On Figures 8 and 9 is shown values of surface roughness parameters after micro-milling of AISI D2. Can be concluded that R_a and R_z increase with increasing of feed and depth of cutting.

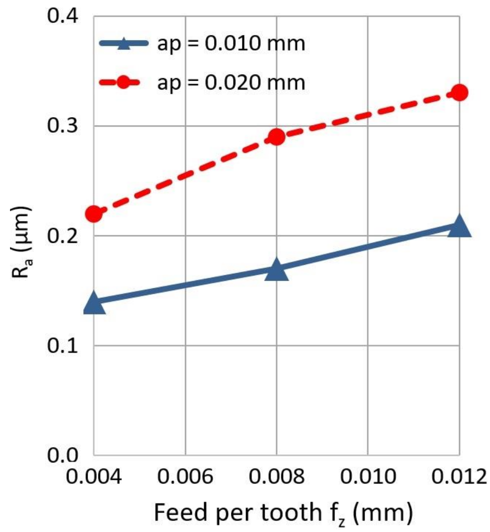

Figure 8. Average surface roughness (Ra) for AISI D2

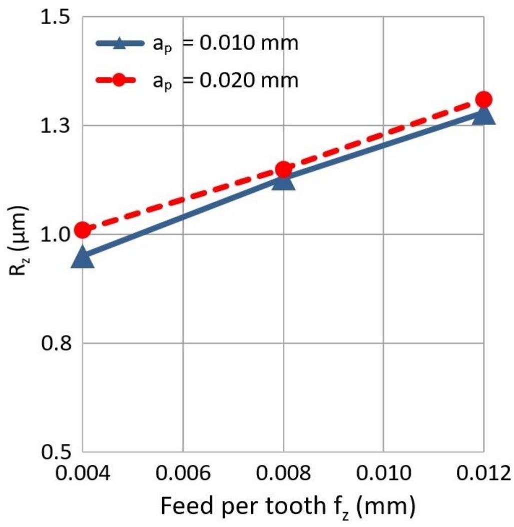

Figure 9. Average surface roughness in ten points (R_z) for AISI D2

In the case of micro-milling of AISI D2, fluctuations in the values of the surface roughness parameter at the lower values of feed are absent. Based on graphs can be concluded similar finding for this material. Values of both surface roughness parameters increase with increasing of depth of cutting and feed. In case of micro-milling of AISI D2, parameter R_a intensively increase with depth of cutting changing, while increasing of feed leads to relative lower increasing of R_a.

On Figure 10 is shown comparison of R_z parameters for different cutting conditions and different workpiece materials. Can be conclude that during micro-milling of AISI D2 obtained relative lower values of surface roughness than Inconel 718. The reason for this is a smaller workpiece material grain size, thereby avoiding the effect of the size effect and material ploughing.

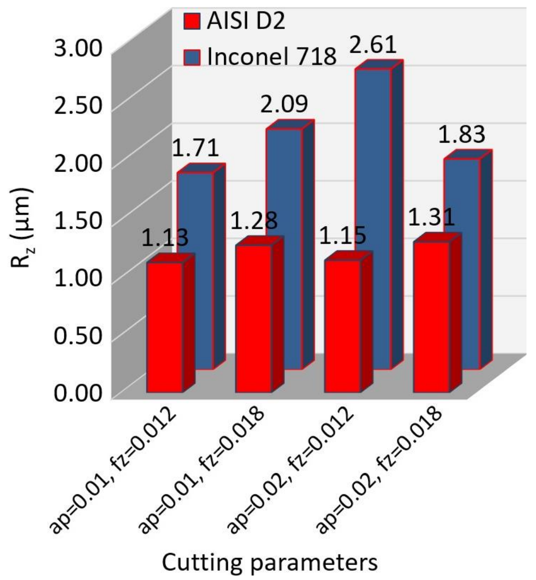

Figure 10. Surface roughness parameters for different workpiece materials

Variation of surface roughness during micro-milling, for different cutting condition and different material is shown on Figure 11.

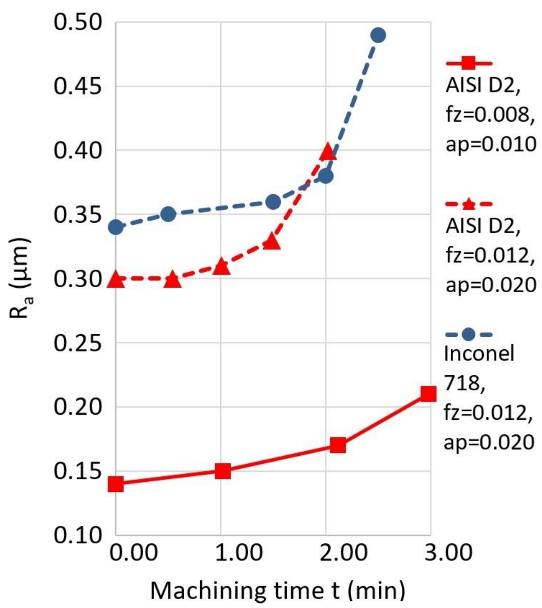

Figure 11. Increasing of surface roughness parameters during machining

Based on graph, can be concluded that surface roughness increases during machining time. Using of higher cutting parameters values leads to intensive tool wedge wear, and relative intensive decreasing of surface roughness. Increasing of surface roughness is results of intensive workpiece material ploughing, which caused with size effect. In that case, cutting tool tip was worn and its measure reaches values of minimal chip thickness.

Build up edge participates in the evaluation of the functionality of micro-part. For both materials height of build-up edge (B_w) was measured in for different points along channel, on its edge vertical side, where micro-milling tool tooth leaves the channel. Different points of measuring were coincided with the surface roughness measurement points. After evaluation, an arithmetic mean of heights was found.

On Figure 12 is shown values of build-up edge height (B_w) for different materials and cutting condition. Based on graph can be concluded that values of B_w increase with increasing of depth of cutting and feed. More intensive growth occurs with increasing of depth of cutting. Comparing the values for different materials, it is clearly noticed that there are higher values when micro-milling of AISI D2. Reason for this is relative higher tough of this material.

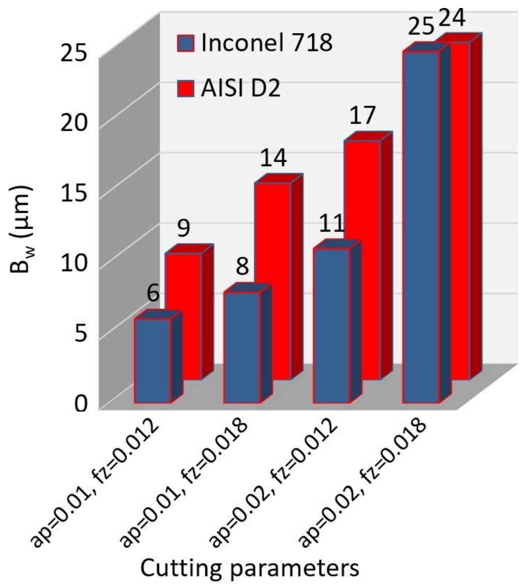

Figure 12. Built up edge for different workpiece materials

4. CONCLUSION

In this paper is presented study on characteristic of mechanical micro-machined surface for high alloyed metallic materials: AISI D2 hardened steel and nickel-chromium alloy Inconel 718. Both of workpiece materials are intended for production of high mechanical and temperature loaded micro-parts (micro-die, micro-pumps, micro-gears, etc.).

Generally, based on the presented research, can be concluded that micro-milling with, as mechanical process, can be used in production of micro-parts with very high surface quality. During micro-milling of AISI D2 obtained lower surface roughness, but during micro-milling of Inconel 718 obtained lower built-up edge high on workpiece. Greater impact on increasing of surface roughness, in micro-milling of Inconel 718, has feed. Greater impact on increasing of surface roughness, in micro-milling AISI D2, has depth of cutting. In fact, in micro-milling of Inconel 718, minimal values of analyzed surface roughness parameters R_a = 0.24 µm and R_z = 1.71 µm was reached with a_p = 0.010 mm and f_z = 0.008 mm. In micro-milling of AISI D2, for same cutting parameters, reached values of analyzed surface roughness parameters was R_a = 0.17 µm and R_z = 1.13 µm.

In future, will be performed additional research on mechanical micro-processing of different engineering materials. Aim of this research is development of database of adopted cutting condition in flexible micro-production of geometry complex, high quality and ultra-precision micro-parts.

ACKNOWLEDGEMENT

This paper is results of activities on interstate bilateral project, in cooperation between Department for management of production technologies at FME Ljubljana and Department for production and computer aided technologies at FME Banja Luka. The project is supported by ministries and governments of Republic of Slovenia and Republic of Srpska.

REFERENCES

[1] G. Bissacco, H. N. Hansen, L. De Chiffre: Size Effects on Surface Generation in Micro Milling of Hardened Tool Steel, CIRP Annals-Manufacturing Technology, Vol. 55, No. 1, pp. 1 – 4, 2006.

[2] A. Aramcharoen, P. T. Mativenga: Size Effect and Tool geometry in Micro-milling of Tool Steel, Precision Engineering, Vol. 33, pp. 402 – 407, 2009.

[3] K. M. Li, S. Y. Choub: Experimental evaluation of minimum quantity lubrication in near micro-milling, Journal of Materials Processing Technology, Vol. 210, pp. 2163 – 2170, 2010.

[4] K. Lee, D. A. Dornfeld: Micro-burr formation and minimization through process control, Precision Engineering, Vol. 29, pp. 246 -252, 2005.

[5] G. M. Schueler, J. Engmann, T. Marx, R. Haberland, J. C. Aurich: Burr Formation and Surface Characteristics in Micro-End Milling of Titanium Alloys, in: *Proceedings of the CIRP International Conference on Burrs*, 02. - 03.04.2010, Kaiserslautern, pp. 129 - 138.

[6] I. Ucun, K. Aslantas, B. Gockce, F. Bedir: Effect of tool coating materials on surface roughness in micromachining of Inconel 718 super alloy, P I Mech Eng B-J Eng. Vol. 288, No. 12, pp. 1550 - 1562, 2014.

[7] I. Ucun, K. Aslantas, B. Gockce, F. Bedir: The effect of minimum quantity lubrication and cryogenic pre-cooling on cutting performance in the micro milling of Inconel 718, P I Mech Eng B-J Eng, Vol. 229, No. 12, pp. 2134 – 2143, 2014.

[8] E Kuram, B. Ozcelik: Optimization of machining parameters during micro-milling of Ti6Al4V titanium alloy and Inconel 718 materials using Taguchi method, Proc IMechE Part B: J Engineering Manufacture, Vol. 231, No. 2, pp. 228–242, 2017.

[9] X. Lu, Z. Jia, H. Wang, L. Si, X. Wang: Surface roughness prediction model of micro-milling Inconel 718 with consideration of tool wear, Int. J. of Nanomanufacturing, Vol. 12, No. 1, pp. 93 – 108, 2016.

[10] E. Vazquez, J. Gomar, J. Ciurana, C.A. Rodríguez: Analyzing effects of cooling and lubrication conditions in micromilling of Ti6Al4V. J Clean Prod, Vol. 87, pp. 906-913, 2015.

Serbian Tribology Society

SERBIATRIB '19

16th International Conference on Tribology

Faculty of Engineering University of Kragujevac

Kragujevac, Serbia, 15 – 17 May 2019

ANALYSIS OF THE PROCESS PARAMETERS INFLUENCE ON THE CHANGE OF MEAN CONTACT PRESSURE IN IRONING PROCESS

Dragan ADAMOVIĆ[1]*, Jelena ŽIVKOVIĆ[1], Bogdan NEDIĆ[1], Fatima ŽIVIĆ[1], Slobodan MITROVIĆ[1], Miroslav ŽIVKOVIĆ[1],

[1] Faculty of Engineering, University of Kragujevac, Serbia

*Corresponding author: adam@kg.ac.rs

Abstract: *Friction that occurs in metal forming processes is significantly different from the friction in mechanical joints. Specific pressures in deep drawing with thinning of the wall thickness that occur on the contact surface between the deformed metal and the tool are very high and considerably exceed the yield stress of the workpiece. As a result of such high pressures there are significant changes in the friction conditions, the efficiency of the lubrication is reduced (the lubricant layer breaks and a direct contact of the surfaces occurs) and the wear process is intensified.*

This paper shows the analysis of the influence of different process parameters (the die angle, lubrication on die and punch, the punch surface roughness, tool material, etc.) on the mean contact pressure based on performed experimental tests on the model.

Keywords: *ironing, mean contact pressure, lubricant, tool material, roughness, steel sheet.*

1. INTRODUCTION

The occurence of friction in metal forming processes differs significantly from the friction that occurs in mechanical joints regarding the factors such as:

- High specific pressures (that exceed the yield stress of one of the metals in the contact pair),
- Large strain and hence the resulting difference in relation to the contact mechanisms,
- Continuous change of surfaces in contact,
- Function of lubrication, etc.

In metal forming processes the layers of the metal of a small hardness are shifting over the tool surface of substantially higher hardness, which is followed by release of energy of the contact pair that consists of a rigid and deformable body. In many cases, under the influence of significant pressures and corresponding high temperatures, the outer layers of the tool are deformed plastically, which is actually the occurence of the so-called plastic contact.

The specific pressures that occur on the contact surface between the deformed metal and the tool are very high and depend on the type of process and reach the values in the range of 100-3000 MPa, which means that they considerably exceed the yield stress of the workpiece and that they are close, and sometimes even higher, than the yield stress of the tool material. As a result of such high pressures there are significant changes in friction conditions, the efficiency of lubrication is reduced (the lubricant layer breaks and a direct contact of the surfaces occurs) which contributes to the intensification of the wear process.

2. DISTRIBUTION AND VALUES OF CONTACT PRESSURES

The load is one of the important values that characterizes friction. Therefore, all friction hypotheses usually give the dependence between the friction force and the normal force (load) where, so far, the friction science was taking into account the force under whose influence the contact elements were only elastically deformed (in terms of macro and not in terms of micro occurence). Friction has somewhat different character in case of metal forming processes, i.e., in such load conditions where one of the contact elements endures the final plastic deformation.

The process of cold deformation of most metals relates to the phenomenon of hardening (the process takes place below the recrystallization temperature). Based on this, metals can be classified using two basic mechanical models:

- Elasto-plastic model without hardening and
- Elasto-plastic model with hardening.

Hardening must be taken into account in the analysis of tribological phenomena because it is typical for this group of processes.

In metal forming processes a specific model of contact pairs consisting of a tool (rigid body) and deformed metal (plastic body) occurs. The pair tool-deformed metal has to be chosen in that way (with big difference in the resistance and hardness properties) to obtain a permanent deformations of workpiece at a given constant load that depends on the type of forming process. In contrast, the tool must not reach the plastic deformation at the same load (considering the strength and dimensions).

As a result of the fact that the pressure of one body (tool) to another (deformed material) is transmitted through micro-volumes of the actual contact, a complex stress state close to the state of three-axis pressure occurs, and in the points of actual contact there is a considerable exceeding of the yield stress and plastic deformation of the unevenness of the tool surface. With the increase in plastic deformation of the workpiece, the nominal surface area as well as the actual surface of plastic-shaped metal is growing, which causes a decrease in the value of normal pressures. On the other hand, the processes of shifting of workpiece layers over the tool surface are accompanied by significant shear stresses, and consequently a local increase in temperature occurs which results in a decrease of the yield stress in the micro-volume of the contact. Therefore, in the case of metal forming in macro sense, there is an elastic-plastic contact, and in a micro-volume a fully plastic contact can occur.

Considering these differences in load conditions, friction phenomena should be studied differently. Particularly significant importance should be given to the analysis and determination of the character of dependence between the friction force and the normal force in the area of higher pressures and finding out in which pressure area the *Amonton's* law is fulfilled, as well as the determination of other corrective quantitative relationships.

According to the studies carried out by Schey [1], dependence of the friction coefficient on the load has a nonlinear character, which means that the Amonton's law is not fulfilled, whereby it is characteristic that with the increase of the load the friction coefficient decreases (Figure 1).

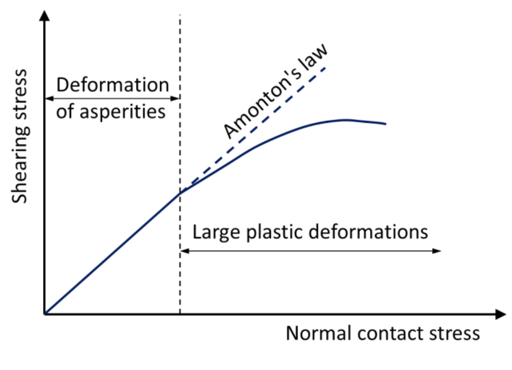

Figure 1. Amonton's law

Ziemba and Solski [2] found that in the general case, the curve that represents the dependence of the friction coefficient on the specific pressure can take the form shown in Figure 2, which means that in the field of low pressures the value of the friction coefficient decreases with increasing of the pressure, and in a certain area that dependence is linear. In the linear field of pressure, the friction coefficient does not depend on the load (it has a constant value), and at very high pressures there is a clear increase in its value.

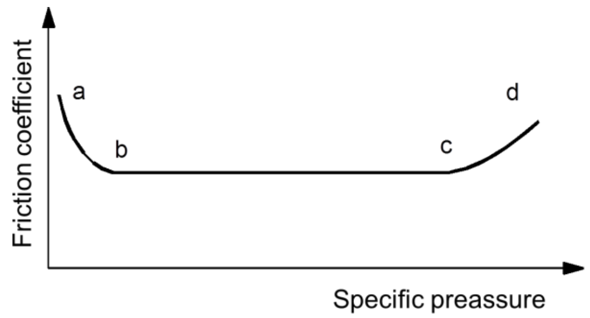

Figure 2. Dependence between friction coefficient and specific pressure [2]

Pavlov [3] examined the dependence of friction coefficient on the load during the rolling process and proved that together with the increase of the pressure the friction coefficient is decreasing. These tests, however, were related to the low pressure values. In the case of ironing process, the growth of the friction coefficient with increase of the pressure has been noted, with results referring to very high pressures (2000 MPa) which verifies the shape of the part of the general curve shown in Figure 2.

In this paper, presented results of friction analysis performed during the metal forming process show that the friction coefficient changes with increasing pressure, i.e., that the *Amonton's* law is not fulfilled in the entire load area. The friction coefficient is the proportionality coefficient and has a constant value independent of the load. After exceeding a certain load value, the dependence between F_{tr} and F_n is nonlinear and the friction coefficient (in the sense of *Amonton's* law) has no constant value and changes with increase of the pressure.

Decrease or, at very high pressures, increase of the friction coefficient with the increase of the pressure suggests that, in the case of higher loads, additional phenomena occurs which must be reflected on the friction law.

3. EXPERIMENTAL TESTS

The original strip ironing device has been developed at Faculty of Engineering, University of Kragujevac. It imitates the zone of contact with die and punch [4] with double-sided symmetry during modelling of ironing. This device enables the realisation of high contact pressures and respects physical and geometrical conditions of real process (material of die and punch, contact surfaces topography, different die angles α etc). The scheme of strip ironing device, with presentation of forces which act upon the workpiece, die and punch, as well as specimen shape is shown in Figure 3.

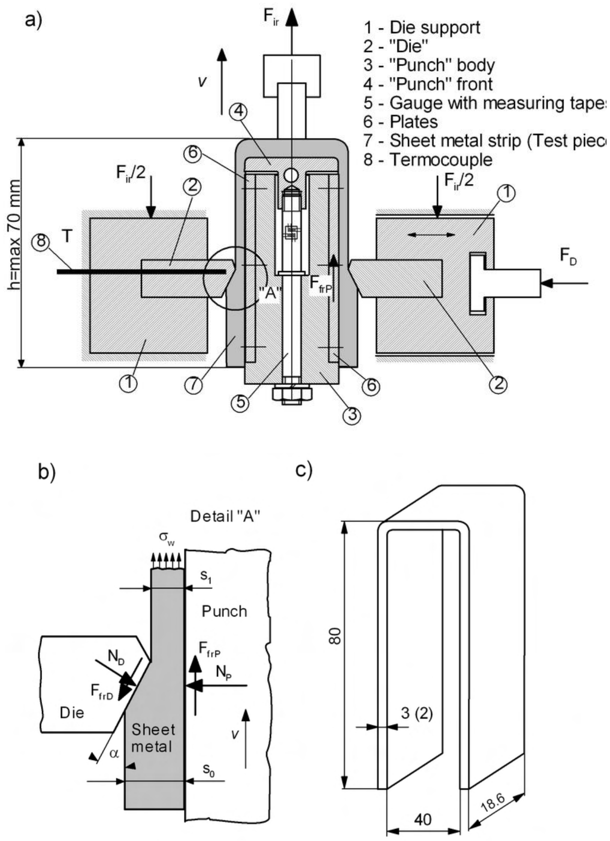

Figure 3. Scheme of strip ironing device with measuring chain for data acquisition (a), presentation of forces in deformation zone (b) and specimen shape (c)

Sheet metal strip 7 is bent (Figure 3c) and placed on the "punch". Dies 2 are placed in supports, whereat the left support is motionless, and the right one is movable together with the die.

The divided punch consists of body 3 and front 4 which are inter-connected by gauge with measuring tapes 5. The strip is ironed between dies due to the effects of force F_{ir} on the punch front. Throughout ironing, the outer surface of strip slides over die surface, which is inclined at an angle α. The inner surface of strip slides over plates 6, fixed onto the punch body. The main idea was to enable determination of friction coefficients, both on die side and on punch side at various contact conditions.

Total ironing force F_{ir} represents the sum of friction force F_{frP} between punch and workpiece, and force that acts upon the test specimen bottom, F_w, that is:

$$F_{iz} \quad F_{trI} \quad F_{z} \ . \qquad (1)$$

Mean contact pressure between die and sheet metal is the ratio between the normal force by which the die acts on the sheet metal, N_M, and the contact surface between die and the sheet metal S_k:

$$p_{sr} \quad \frac{N_M}{S_k} \quad \frac{2\ F_D\ \cos \quad \sin \quad F_{iz}\ \sin^2}{b \quad s_0 \quad s_1} \qquad (2)$$

Based on analysis of researches and preliminary investigations, the following factors were selected, which will be the subject of experimental researches, shown in Table 1.

Table 1. Properties of investigated material and investigation conditions

		Material	Mechanical properties	Surface characteristics
Tool	Die (D)	▪ TS (Tool steel) ▪ TS + Cr plate ▪ TS + TiN plate ▪ HM (Hard metal)	TS Hardness 60÷63HRC HM Hardness 1200HV30	R_a≈0.01 [µm] (N1)
	Punch plate (P)	▪ TS ▪ TS + Cr plate ▪ TS + TiN plate		R_a≈0.01 [µm] (N1), R_a≈0.01 [µm] (N3) and R_a≈0.4 [µm] (N5)
Workpiece		DC04 (EN10130) Thickness: 2.0 [mm] width: 18.6 [mm]	R_p=186 [MPa], R_m=283 [MPa] A_{80}=37.3 [%] n=0.2066, r=1.09009	R_a=0.92 [µm] R_p=3.62 [µm] R_v=5.11 [µm]
Reduction degree: 1÷55 [%]			Angle of die gradient: α = 5°, 10°, 15°, 20°	
Sliding path: max 70 [mm]			Investigation temperature: room temperature	
Ironing speed: 20 [mm/min]			Blank holding force (F_D): 8.7; 17.4; 26.1 [kN]	
Applied lubricants	On die side		L1, L2, L3	
	On punch side		L4	
TS – Tool steel (DIN17006: X165CrMoV12) HM – Hard metal, WG30 (DIN4990: G30) L1 – Lithium grease with additive of the molybdenum disulfide (Li+MoS_2) – Grease, L2 – Mineral emulsifying water-soluble oil with EP, anti-wear and lubricating additives – Oil, L3 – Mineral emulsifying agency – Paste, L4 – Non-emulsifying mineral oil with mild EP qualities – Oil (v = 45 [mm^2/s]),				

4. RESULTS OF EXPERIMENTAL TESTS

As shown, the mean contact pressure on the die side represents the ratio between the normal force by wich the die acts on the workpiece and the contact surface between the die and the workpiece (equation 2). From equation 2 it can be seen that the mean contact pressure will depend on the holding force, the die angle, the resulting deformation and the ironing force. As the drawing force, among other things, depends on the contact conditions, it is logical to conclude that the mean contact pressure, to a certain extent, will also depend on the achieved contact conditions. Since the drawing force changes very little on the sliding path, the mean contact pressure will also have an approximately constant value for the entire time of drawing (Figures 4 and 7).

Dependence of the mean contact pressure on the sliding path is shown in the Figure 4, where diagram is made for three characteristic holding forces. From the mentioned diagram it can be seen that the mean contact pressure decreases with increasing of holding force. This happens due to the fact that with the increase of the holding force, the contact surface between the die and the workpiece is growing.

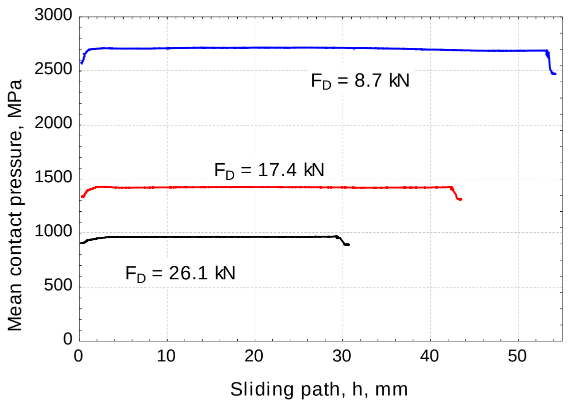

Figure 4. Dependence of mean contact pressure on the sliding path due to different holding forces

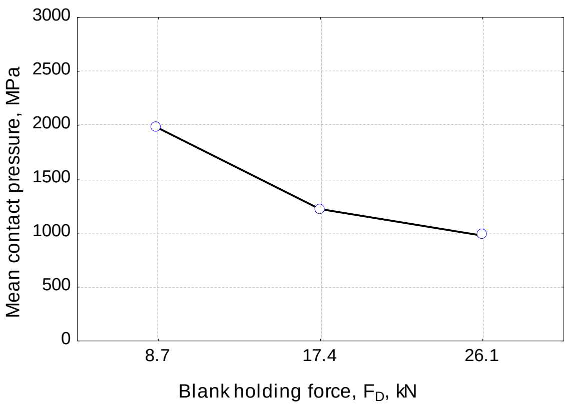

Figure 5. Change of mean contact pressure due to the holding force

The change of the mean contact pressure depending on the holding force is shown in Figure 5. With the increase of the holding force the mean contact pressure decreases more intensively at start, while with a further increase in the holding force the gradient of the pressure decreases considerably.

By increasing the holding force, at all die angles, the mean contact pressure decreases (Figure 6), wherein higher contact pressures correspond to greater angles. In the case of steel samples with the increase of holding force the differences in the pressure obtained with different die angles are decreasing (Figure 6).

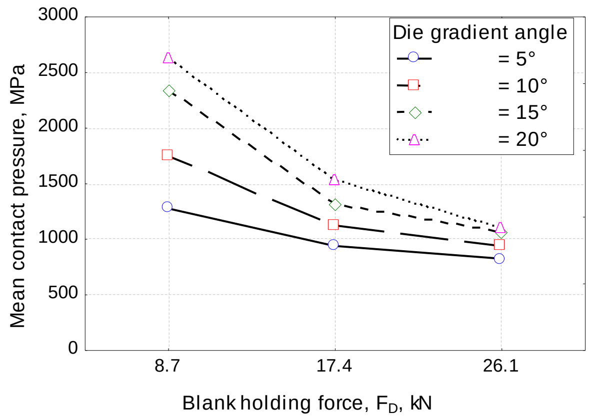

Figure 6. The change of the mean contact pressure due to the holding force at different die angles

As the die angle increases, as has already been said, the mean contact pressure increases. Dependence of p_{sr} on the sliding path for different angles , when the lubricant is on the die - L1, tool material – tool steel (TS), the roughness of the punch - N1, and the holding force - 8.7 kN is given in Figure 7.

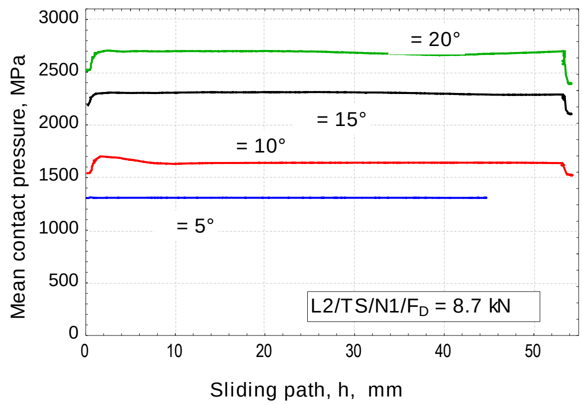

Figure 7. Dependence of the mean contact pressure on the sliding path at different die angles

Figure 8 shows the change of the mean contact pressure due to the die angle.

The influence of the lubrication type on the die on the value of the mean contact pressure is given in Figure 9. From the mentioned diagram it can be seen that in the case of all types of used lubricants almost the same values of p_{sr} are obtained, which points out to the small influence of the selected lubricants on the value of the mean contact pressure.

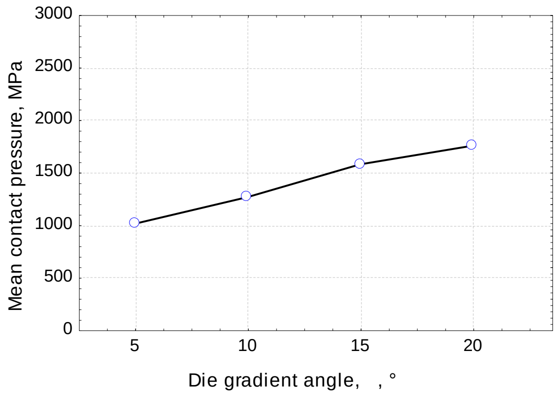

Figure 8. The change of the mean contact pressure due to the die angle

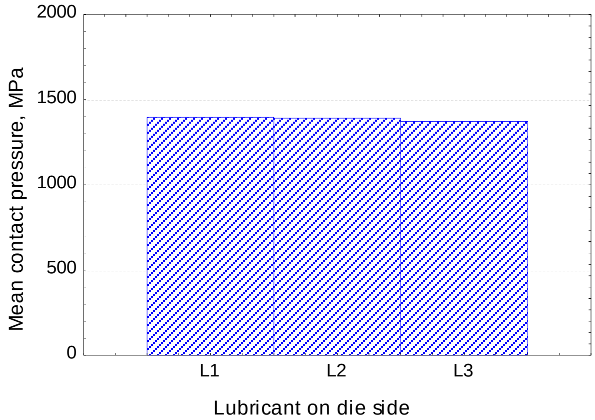

Figure 9. Dependence of the mean contact pressure on the lubricant type on the die

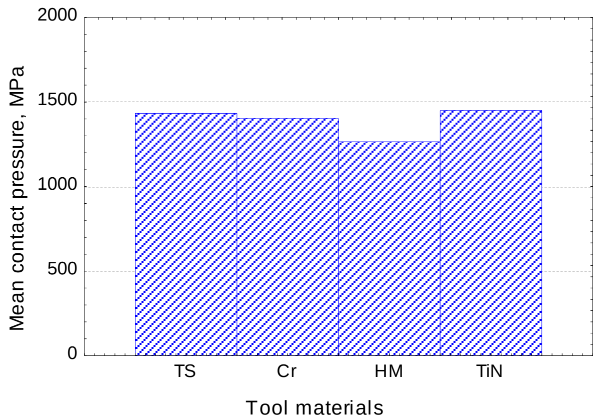

Figure 10. Dependence of the mean contact pressure on the tool material

The lowest value of the contact pressure is obtained by using tool made of hard metal, and somewhat higher values by using chromium-coated tools. The highest values of p_{sr} are obtained by using tools of alloyed tool steel and TiN coating (Figure 10).

As the roughness increases, there is a slight increase in the mean contact pressure, which is shown in Figure 11.

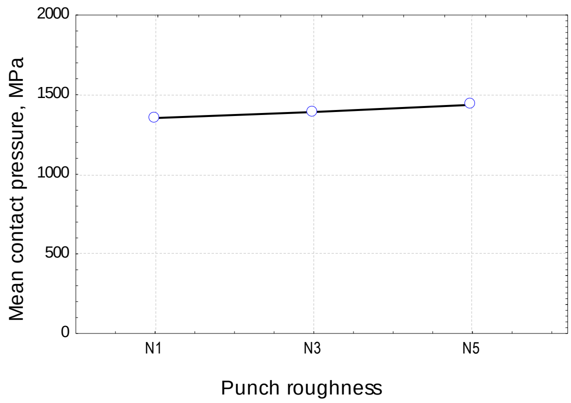

Figure 11. Dependence of the mean contact pressure on the roughness of the punch surface

Figures 12 to 14 show the dependence of the mean contact pressure on the die angle and the holding force for variations of different levels of the analyzed factors (lubricant on the die, tool material and roughness of the punch surface). In all combinations of the die angle and the holding force, approximately the same value of the mean contact pressure at all levels of lubricant on the die side are obtained. That indicates, as has already been said, a very small influence of the selected lubricants on the die to the value of p_{sr} (Figure 12).

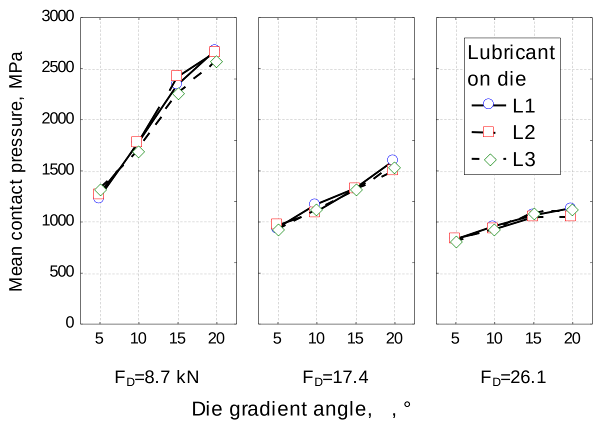

Figure 12. Change of the mean contact pressure due to the die angle and the holding force for different lubricant types on the die side

Diagrams in Figure 13 show that the lowest values of pressures are obtained with hard metal tools, and the highest values are obtained with tools made of tool steel and titanium nitride coating, for most of the levels of the die angles and the holding force. The influence of the punch surface roughness on the mean contact pressure, as shown in the diagrams in Figure 14, is very small.

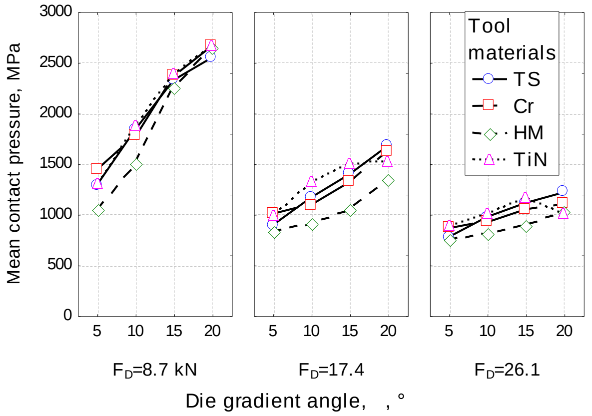

Figure 13. Change of the mean contact pressure due to the die angle and the holding force for different tool materials

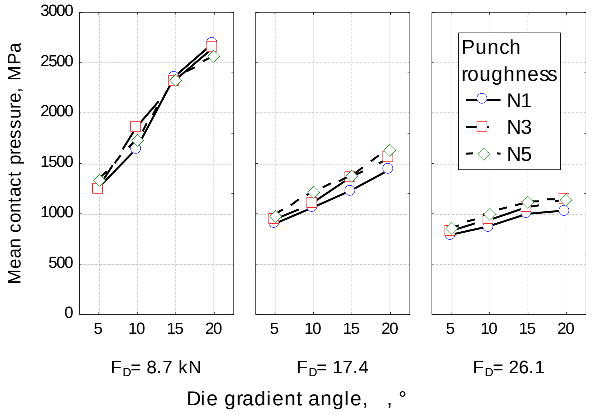

Figure 14. Change of the mean contact pressure due to the die angle and the holding force for different roughness of the punch surface

It has already been said that the mean contact pressure mainly depends on the holding force and the die angle, i.e., the degree of deformation, which is mostly determined by the angle and the force F_D. In Figures 15 and 16 dependence of the mean contact pressure on the degree of deformation at different die angles and the holding forces, respectively, are given. From these diagrams, the dependence between stress and deformation are clearly observed at different die angles (Figure 15) and the holding forces (Figure 16). It can be concluded that the highest mean contact pressures are obtained with the low holding forces and large die angle.

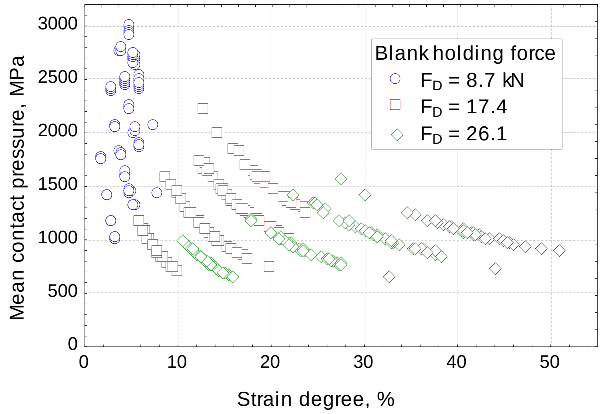

Figure 15. Dependence of the mean contact pressure on the degree of deformation at different die angles

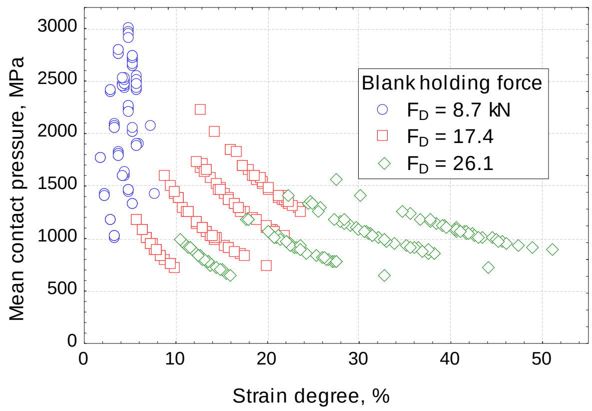

Figure 16. Dependence of the mean contact pressure on the degree of deformation at different holding forces

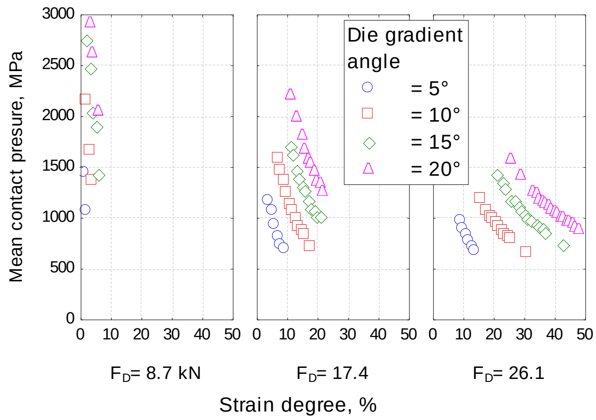

Figure 17. Dependence of the mean contact pressure on the degree of deformation at different holding forces and die angles

Previously described changes in the mean contact pressure due to the degree of deformation for different holding forces and the die angles could be presented in the form shown in Figures 17 and 18. In these diagrams, the points corresponding to the different values of holding force (Figure 17), and the die angle (Figure 18) are separated.

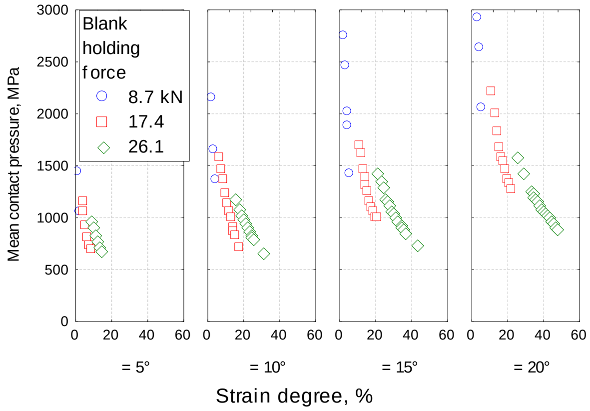

Figure 18. Dependence of the demium contact pressure on the degree of deformation at different die angles and the holding forces

5. CONCLUSION

The specific pressures that occur on the contact surface between the workpiece and the tool are very high and reach the value of the order of 400-3000 MPa, which means that their value significantly exceed the yield stress of one of the metals of the coupled pair, and it is close and sometimes even several times higher than the yield stress of the tool. As a result of such high pressures there are significant changes in friction conditions, the efficiency of lubrication is reduced (the lubricant layer breaks and a direct contact of the surfaces occurs) which contributes to the intensification of the wear process.

The mean contact pressure mainly depends on the holding force and the die angle, i.e., the degree of deformation, which is mostly determined by the die angle and the holding force.

ACKNOWLEDGEMENT

The part of this research is supported by Ministry of Education and Science, Republic of Serbia, Grant TR32036, TR34002 and TR35021.

REFERENCES

[1] A.J. Schey (Ed): *Metal Deformation Processes - Friction and Lubrication*, Marcel Dekker Inc., New York, 1970.

[2] P. Solski, S. Ziemba: *Zagadnienia tarcia suchego*, PWN, Warszawa, 1965.

[3] И.М. Павлов: *Теория прокатки, Металлургиздат*, Москва, 1950.

[4] D. Adamovic: *Behaviour of Materials in Contact in Cold Plastic Forming Processes with High Working Pressures*, Doctoral Thesis (in Serbian), the Faculty of mechanical Engineering in Kragujevac, Kragujevac, 2002.

Serbian Tribology Society

SERBIATRIB '19

16th International Conference on Tribology

Faculty of Engineering
University of Kragujevac

Kragujevac, Serbia, 15 – 17May 2019

PREDICTING CUTTING PARAMETERS BY APPLYING DEVELOPED NEURAL NETWORK AND LINEAR REGRESSION MODELS

Aleksandar ĐORĐEVIĆ[1], Milan ERIĆ[1,*], Miladin STEFANOVIĆ[1], Slobodan MITROVIĆ[1], Marko PANTIĆ[1,2], Aleksandra KOKIĆ ARSIĆ[2], Dragan DŽUNIĆ[1]

[1]University of Kragujevac Faculty of Engineering, Kragujevac, Serbia

[2]Higher Technical Professional School in Zvečan, Zvečan, Serbia

*Corresponding author: ericm@kg.ac.rs

Abstract: *The paper presents the methods for prediction of the cutting parameters. In order to test the workability of the material by process of scraping, from the aspect of the cutting temperature, an natural thermopar was placed just below the cutting edge of the plate. In this way, a simple, reliable, accurate and economical method for determining the workability of material by cutting is obtained. The feasibility study of several semi-finished products by applying the realized experiments was carried out. Different materials in processing with cutting discs with different coatings give different results, which are used to form neural network and linear regression models.*

Keywords: *cutting parameters, prediction model, neural networks, linear regression.*

1. INTRODUCTION

Scraping is a very widespread type of processing in the metalworking industry. It takes place in conditions that are very complex and to date completely undefined. Tribological phenomena on the cutting pin affect the reduction of the tool's stability, and this affects the increase in processing costs [1].

As a result of the complexity of occurrences on cutting tools, wear appears, and it is the main cause of the short life of tools. Defining the wear process can be based on: changes that occur on the tool, the object of processing, change of resistance or cutting temperature. Since many physical and chemical reactions occur in the cutting process and how they are directly related to the wear of the tool, and how they are highly dependent on the cutting temperature [2, 3], this is a study of the possible prediction model creation for cutting process parameters.

The aim of this paper is to establish a reliable prediction models through the application of the appropriate tools for prediction and measuring of the cutting parameters at the points in the body of the knife, and by determining the data necessary for studying the machining process. Checking the method and measuring chip for measuring the parameters in the knife body is done by parallel measurements of the mean temperature of the cutting by a natural thermopar. In this way, conditions are created for the development of adaptive prediction models for machining by cutting [4].

2. THE PREDICTION MODELS OVERVIEW AND INFLUENCE OF THE PROCESSING FACTOR ON THE CUTTING TEMPERATURE PARAMETER

In the last few decades, the application of computer systems and software tools, particularly those based on artificial intelligence, had a great influence on integration and general availability of the individual knowledge and experience of experts in the field of production engineering. This led to the development of expert systems intended for expert reasoning, evaluation and optimization of parameters within preparation and production activities [5].

For creation of the prediction model, various methods can be used that are grouped into several general categories [6]:

- mathematical (linear regression, statistical methods). The best known is the linear regression to link the values of different independent and dependent variables using a linear expression to predict the "new" values of the dependent variables.
- distant (distance learning). Distant methods are based on the concept of "distance between cases". Any two cases in the data set can be compared to determine the similarity measure, this is the equivalent of the distance (s) to the corresponding value, which is the case, the distance is smaller.
- Logical (decision tables, decision trees, classification rules). The most used logical decision-making method is the decision tree. In order to forecast a new case, the root of the tree is examined; the appropriate testing is carried out, based on the result of which the case moves to the lower to the corresponding branches of the tree. The process continues until the last node ("tree list") is completed, the value of the last node represents the estimated outcome of the tree.
- modern heuristic methods (neural networks (NN), fuzzy logic, genetic programming). These methods are based on the principles of heuristics, i.e. based on experience. They accelerate foresight processes and find a solution that are good enough in situations where the implementation of a detailed forecast is not practical and can require a longer search time.

In this paper, the developed models use neural networks as an artificial intelligence method and linear regression as a statistical method. NN have proven to be a very promising artificial intelligence method in many prediction applications [7, 8, 9], due to their ability to learn from the data set, their nonparametric nature and the ability to generalize [10, 11, 12]. Having this in mind, NN and linear regression have been applied to predict cutting temperature. Since, there are a number of factors that affect the cutting temperature, which are:

- the characteristics of the machining material (M) and tools (A),
- treatment with refrigerant and lubricant (H) and without refrigerant and lubricant (BH),
- Cooling system (SH) and type of coolant and lubricant (VS),
- Processing mode (RO) - step, cutting depth, cutting speed,
- Tool geometry (GA) - geometric elements and coordinates that define the shape and position of the cutting wedge and processing objects, and
- other processing conditions.

Knowing the character and degree of influence of the mentioned factors on cutting temperature θ i.e. the dependency (formula 1):

$$Q = f(M, A, H, BH, SH,\ VS, RO, GA) \quad (1)$$

This dependency creates the possibility of developing practical algorithms for optimization and adaptive management of production processes based on thermodynamic characteristics and temperature signals.

The contact temperature of the tool, sawdust and processing object is referred to as the mean cutting temperature θ_{mean}. The empirical term for the calculation of temperature in the cutting zones of the tribo-mechanical systems in which the cutting in the scraping process is realized as [13, 14] (formula 2):

$$\theta = C_\theta \delta^{xt} s^{yt} v^{zt} \prod_1^n K_i \tag{2}$$

where:

C, *k*, *i*, *z* - are constants and exponents that depend on the type and state of the processing material,
δ - cutting depth (mm),
s - step (mm / o), and
v - cutting speed (m / min).

Thermal phenomena (cutting temperature, heat generation, etc.) that occur in the narrower and wider area of the cutting zone are in direct and narrow correlation with the tool wear rate, the degree of workability of the machining material, the stability of the tools and a number of other characteristics, and effects of the production process. Almost the entire cutting force is transformed, as experimental testing shows, into heat energy. The generated heat passes from the cutting area to the sawdust, the tool, the processing object and the surrounding environment, and thus under the influence of a part of the heat passing on the tool, the hardness of the material of the cutting elements of the tool decreases, and leads to a gradual plastic deformation of the cutting blades, loss of cutting ability of the tool and sharpness reduction. (The process of gradual loss of cutting ability stimulates even intensive wear and periodic friction of cutting tool elements.)

Distribution of generated heat in the workpiece, the tool, material chip, and therefore the temperature of the elements on the working part of the tool, on the treated surface and in the sawdust, depends on the machining material (mechanical and chemical properties), cutting speed, cutting depth, tool geometry, cooling and lubricating means and a number of other factors [15, 16, 17].

In addition to the impact on tool durability, the generated heat or cutting temperature also affects the production process, the overall quality of the treated surface, the processing accuracy and other output effects of the process. Hence, testing, measuring, understanding and possible creation of prediction models of the size and arrangement of cutting temperatures in the tool and workpiece are of primary importance, since on the basis of these findings, optimal conditions and processing regimes, quality, productivity and cost-effectiveness of the process, stability of the tools can be determined.

The significance of measuring technique and the method of measuring cutting temperatures is primarily that these methods and techniques form the basis of the experimental method, which, in addition to analytic, is another general method for researching and detecting thermodynamic (temperature) laws in the narrower and wider cutting zone and the processing system in continent. One of the major goals, achieved by knowing these laws, is optimization and adaptive management of production processes.

3. FORMING A MEASURING CHAIN FOR THE TEMPERATURE MEASUREMENT IN THE KNIFE BODY

Measuring chain (system) includes a set of measurement devices and auxiliary devices interconnected, through the link channels, into one functional entity and connected to the measurement object, a control object, a control object, an object of analysis, or an object of research for generating, converting, displaying, storing, and use for certain purposes of measurement signals (measurement results) of one or more measuring sizes.

From this definition, two basic tasks of any measurement system arise:

- measuring the value of one or more given physical or other sizes and displaying the measurement results on an analog or digital display, a registry (printer or printer), or a signalizer.
- generation of signals or information on measured values in a form suitable for use for other purposes (automatic management and control of processing

processes, memory and storage of metering information, statistical processing of results, etc.).

3.1 Measuring instrumentation for the cutting temperature measurement

Measurement of cutting temperature (natural thermopar) was carried out on a turn according to the scheme of the measuring chain given in Figure 1.

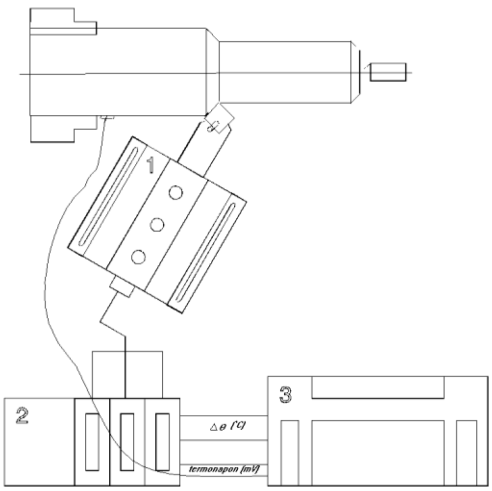

Figure 1. Measuring chain for measuring the cutting temperature

A four-channel printer "R-54" (position 3, figure 1) was used to record the signals. In the tool holder measurements, the KISTLER-9441 dynamometer (position 2 of Figure 1) was used, with the corresponding amplifier (position 2, figure 1).

To measure the temperature using a natural thermopar, the tool and the machining object were isolated from the machine. The natural thermocouple is not calibrated, due to its large complexity, the results of the temperature measurements by a natural thermocouple are expressed in mV.

The tool is a cutting knife CSDNR 2020K12 with a removable plate SPMX 12T3AP-75. Figure 5 shows a cutting board with basic dimensions. Tiles are coated with TiN, TiAlN, TiZrN, ZrN coatings.

All tests were carried out on the universal "Prvomajska" D-480lathe, with a power of 10 kW in the metal processing laboratory at the Faculty of Mechanical Engineering in Kragujevac.

4. PRELIMINARY MEASUREMENT OF THE TEMPERATURE IN THE SCRAPING WITH THE FORMED MEASURING CHAINS

Experimental tests were aimed to determining the change in cutting temperature in the knife body, depending on:

a - cutting speed in (m / min), respectively the corresponding speed n (rpm),

b - steps with (mm / o),

c - cutting depth δ (mm),

d - material processing objects,

e - coating of the cutting board.

The cutting mode parameters are:

a - cutting speed or corresponding speeds of 355, 450, 560, 710 rpm.

b - step 0.14, 0.2, 0.25 mm / o.

c - cutting depth 0.3, 0.5, 0.7 mm.

d - the largest part of the test was performed on the processing object of the C4730 in the improved state (273-300 HB). The workpiece obstruction is a half covertube (Material 1). Due to the inability to perform the same operation and measure resistance in laboratory conditions, external longitudinal treatment was performed. In order to ensure the same geometric parameters or an angle of attack, the dynamometer turning is also performed, which at the same time represents the tool carrier. In addition to this processing object, in order to compare the workability of materials in concrete conditions with different coatings on the tools, the surface treatment of the C4731.6 was performed, in the improved hardness of 230-280 HB (Material 2), and the head gears of the C5421, isothermal glow HB-120 forgings) (Material 3). All items of processing are pre-tested "bark" removed.

e - on the cutting plates of the corresponding geometry in the "Copper Institute" - Bor, application of a number of coatings was done, namely TiN, TiAlN, TiZrN, ZrN. The conducted tests were supposed to give a recommendation for the selection of the appropriate coating on the tool for carrying out a specific operation.

The experiment plan with the results of measuring the temperature rise ΔΘ (˚C) in the body of the knife and the thermonaphon of the natural thermo power (mean cutting temperature) are shown in the following tables.

Table 1 shows the results of the measurement of the temperature rise ΔΘ (˚C) for Material 1 (half cover) and all types of coatings. Cutting speed varies, i.e. number of revolutions n at a constant step (s = 0.2mm / o) and constant cutting depth (δ = 0.5mm). Cutting time is 0.5 min. The table also shows the temperature after cutting length (l) of 2 and 3 cm, due to comparison with the results of measurements in operations whose cutting time or cutting length is in this range. The results of the measurement of thermonaphones of a natural thermocouple are also shown for the coated TiAlN plate.

Table 1. Measurement of the temperature rise ΔΘ for material 1

coating type		t [min]	l [cm]	n [rPM]	temp [ΔΘ]
Without coatings	1	0.5	0	355	146
	1	0.5	0	450	151
	1	0.5	0	560	152
	1	0.5	0	710	154
	1	0.5	2	355	127
	1	0.5	2	450	132
	1	0.5	2	560	122
	1	0.5	2	710	112
	1	0.5	3	355	136
	1	0.5	3	450	140
	1	0.5	3	560	127
	1	0.5	3	710	121
ZrN	2	0.5	0	355	138
	2	0.5	0	450	145
	2	0.5	0	560	150
	2	0.5	0	710	156.5
	2	0.5	2	355	106
	2	0.5	2	450	108
	2	0.5	2	560	106
	2	0.5	2	710	102
	2	0.5	3	355	118
	2	0.5	3	450	119
	2	0.5	3	560	118
	2	0.5	3	710	115.5
TiN	3	0.5	0	355	143
	3	0.5	0	450	155
	3	0.5	0	560	158
	3	0.5	0	710	160
	3	0.5	2	355	109
	3	0.5	2	450	116
	3	0.5	2	560	112
	3	0.5	2	710	109
	3	0.5	3	355	125
	3	0.5	3	450	132
	3	0.5	3	560	127
	3	0.5	3	710	125
TiZrN	4	0.5	0	355	145
	4	0.5	0	450	147
	4	0.5	0	560	150
	4	0.5	0	710	152
	4	0.5	2	355	117
	4	0.5	2	450	119
	4	0.5	2	560	115
	4	0.5	2	710	114
	4	0.5	3	355	126
	4	0.5	3	450	128
	4	0.5	3	560	126
	4	0.5	3	710	124
TiAlN	5	0.5	0	355	146
	5	0.5	0	450	149
	5	0.5	0	560	151
	5	0.5	0	710	157
	5	0.5	2	355	117
	5	0.5	2	450	119
	5	0.5	2	560	115
	5	0.5	2	710	114
	5	0.5	3	355	126
	5	0.5	3	450	128
	5	0.5	3	560	126
	5	0.5	3	710	124

Based on the presented table application of prediction models is possible in order to predict cutting temperatures changes and degree of workability. Since degree of workability is calculated according to following (formula 3):

$$I_O = \frac{ref}{i} \quad (3)$$

where in:

Θ_{ref} - temperature of the etalon material,

Θ_i - temperature of the test material.

For the purpose of determining the workability index of the processing object material, a part of the obtained measurement results was obtained in the processing of various materials of the processing object with plates with different coatings. By accepting that the material is a reference material, it is easy to reach the workability index according to the previously defined form.

5. PREDICTION MODELS APPLICATION

Without involvement in the problem of the formation and development of the scarping process, it can be assumed that knowledge about cutting temperatures as well as their dependence on the processing conditions, and in combination with other factors, can determine the degree of workability of a material with sufficient precision by application of prediction models.

Based on a defined NN (Figure 2), the correlations coefficient R for the training, validation, testing group and the overall correlation coefficient between the predicted output values and the measured target values of cutting temperature are determined (see Figure 3).

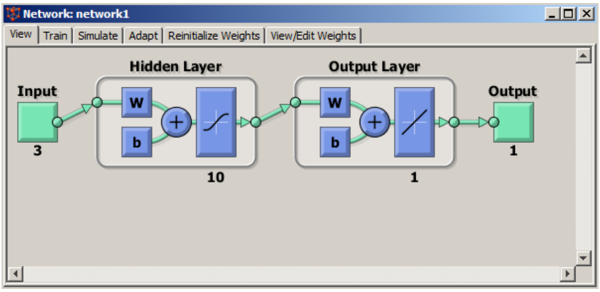

Figure 2. Defined neural network

According to the Figure 2, it may be concluded that in the input layer there are three neurons which correspond to the number of input parameters (coating type, cutting length, number of revolutions). Hidden layer has ten neurons and the output layer has only one layer, according to the output parameter (cutting temperature). Transfer function between hidden and output layer is tan-sigmoid, while transfer function between output layer and output is linear.

In the training set, with its regression line, linear correlation coefficient value is satisfactory equal to R = 0.99754. The same applies to the value of the correlation coefficient in the case of validation R = 0.97832. The value of the correlation coefficient in the case of testing is R = 0.95829, therefore the NN may be accepted as reliable for prediction of the cutting temperature and therefore prediction of workability index, since the total value of the correlation coefficient is R> 0.9. It may be concluded that there is a high correlation between the predicted output values and the measured target values.

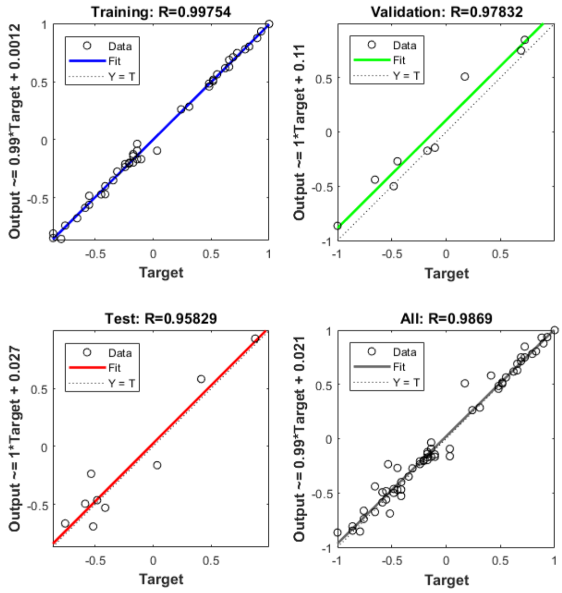

Figure 3. Correlation coefficients

Application of the linear regression model gave the following results presented in Table 2.

Table 2. Linear regression model summary

Model Summary		
Model	R	R Square
1	.743[a]	.552
a. Predictors: (Constant), coating type, l [cm], n [rev/min]		

Coefficients[a]						
Model		Unstandardized Coefficients		Standardized Coefficients	t	Sig.
		B	Std. Error	Beta		
1	(Constant)	146.635	6.881		21.309	.000
	coatings type	-.125	1.021	-.011	-.122	.903
	l [cm]	-9.609	1.158	-.743	-8.298	.000
	n [rev/min]	.000	.011	-.002	-.020	.984
a. Dependent Variable: temp [ΔΘ]						

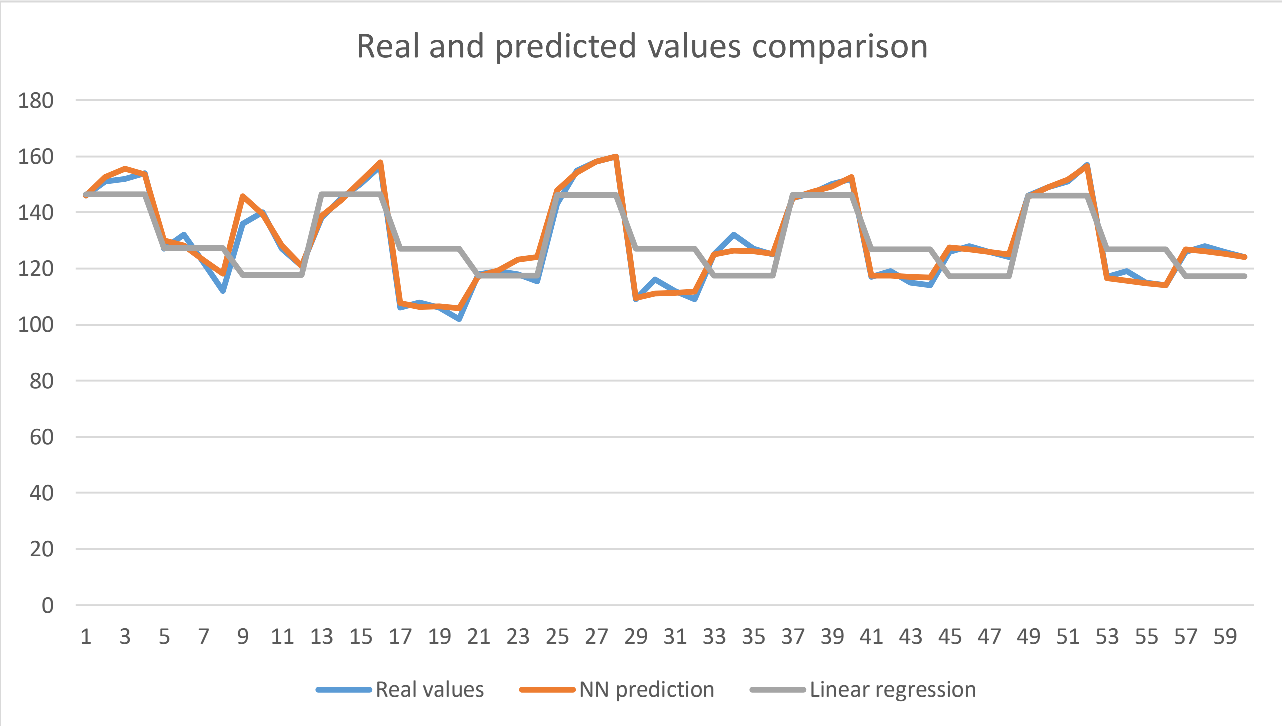

Figure 4. Comparisons between real and predicted values

Model show that the correlation coefficient between real and predicted values is R = 0.743.

Equationfor the prediction of cutting temperature values may be presented as (formula 4):

$$temp = 146.635 \quad 0.125 * c.t. \quad 9.609 * l \quad 0.0 * n \tag{4}$$

Comparisons of prediction results for both NN and linear regression models and real values have been presented on the Figure 4.

From the Figure 4 it may be concluded that NN prediction model gave better prediction results than the linear regression model. Based on this results NN may be used to predict degree of workability.

6. CONCLUSION

In this paper, authors have analyzed the possibility of application of NN and linear regression models for prediction of cutting temperatures, based on the few cutting parameters.

Based on the presented obtained prediction results, it can be concluded that the developed application provides the ability to predict the values of cutting temperature.

Information collected from natural thermopar may be used in order to obtain appropriate real temperature values, which are used for application of the NN and linear regression. Accordingly, decisions can be made, for the input parameters of cutting parameters, in order to obtain expected degree of workability.

ACKNOWLEDGEMENT

The paper has been fully supported by the Serbian Ministry of Education, Science and Technological Development under the projectsTR35021 and III44010.

REFERENCES

[1] B. Ivković: *Cutting theory (Teorija rezanja)*, Self-published edition, Kragujevac, 1991.

[2] D. Milikić: *New method for temperature measurement in cutting and the possibility of its technological and sensor application (Nova metoda za merenje temperature pri obradi rezanjem i mogućnosti njene tehnološke i senzorske primene)*, PhD dissertation, Faculty of Technical Sciences, Novi Sad, 1980.

[3] M. Gostimirović, M. Kovač, D. Milikić: Temperature method for determining the stability function of the cutting tool during grinding and milling (Temperaturska metoda za određivanje funkcije postojanosti reznog

alata pri struganju i glodanju), MMA'90, Novi Sad, 1990.
[4] J. Stanić: *Technological measuring systems (Tehnološki merni sistemi)*, Faculty of Mechanical Engineering, Belgrade, 1985.
[5] K. Priddy, P. Keller: *Artificial neural networks*, SPIE, Bellingham, Wash, 2005
[6] Z. Michalewicz: *Adaptive business intelligence*, Springer, Berlin, 2007.
[7] P. Chang, Y. Wang, C. Tsai: Evolving neural network for printed circuit board sales forecasting, Expert Systems With Applications, Vol. 29, No. 1, 2005.
[8] K. Sriraman, H. Strauss, S. Brahimi, S. Chromik, J. Szpunar, J. Osborne, S. Yue: Tribological behavior of electrodeposited Zn, Zn–Ni, Cd and Cd–Ti coatings on low carbon steel substrates, Tribology International, Vol. 56, 2012.
[9] L. Sziráki, E. Kuzmann, K. Papp, C. Chisholm, M. El-Sharif, K. Havancsák: Electrochemical behavior of amorphous electrodeposited chromium coatings, Materials Chemistry and Physics, Vol. 133, 2012.
[10] C. Feng, X. Wang: Surface roughness predictive modeling: neural networks versus regression, IIE Transactions, Vol. 35, No. 1, 2003.
[11] B. Ahn, S. Cho, C. Kim: The integrated methodology of rough set theory and artificial neural network for business failure prediction, Expert Systems With Applications, Vol. 18, No. 2, 2000.
[12] A. Abrahams, E. Coupey, E. Zhong, R. Barkhi, P. Manasantivongs: Audience targeting by B-to-B advertisement classification: A neural network approach, Expert Systems With Applications, Vol. 40, No. 8, 2013.
[13] N. A. Abukhshim, P. T. Mativenga, M. Aslam Sheikh: Heat generation and temperature prediction in metal cutting: A review and implications for high speed machining, International Journal of Machine Tools and Manufacture, Vol. 46, No. 7-8, pp. 782-800, 2006.
[14] J. Stanić: *The theory of metal processing I (Teorija obrade metala I)*, Faculty of Mechanical Engineering, Belgrade, 1989.
[15] J. Stanić, M. Kalajdzić, R. Kovačević: *Measuring technique in metal cutting technology (Merna tehnika u tehnologiji obrade metala rezanjem)*, Gradjevinska knjiga, Belgrade, 1983.
[16] D. Vukelja: *Cutting thermodynamics (Termodinamika rezanja)*, Gradjevinska knjiga, Belgrade, 1990.
[17] S. Zahar, M. Milošević, S. Karalazić: *Mean cutting temperature for steel processing, Metal processing and tribology 1*, Kragujevac, 1974.

Serbian Tribology Society

SERBIATRIB '19

16th International Conference on Tribology

Faculty of Engineering
University of Kragujevac

Kragujevac, Serbia, 15 – 17 May 2019

FABRICATION OF SILICON CARBIDE REINFORCED ALUMINIUM FOAMS USING FRICTION STIR PROCESSING ROUTE

Ioannis PAPANTONIOU[1], Nikolaos VAXEVANIDIS[2,*], Dimitrios MANOLAKOS[1]

[1] Laboratory of Manufacturing Technology, School of Mechanical Engineering, National Technical University of Athens, 9 Heroon Polytechniou Street, 15780, Zografos, Greece

[2]Laboratory of Manufacturing Processes and Machine Tools (LMProMaT), School of Paedagogical and Technological Education, (ASPETE), Greece

*Corresponding author: vaxev@aspete.gr

Abstract: *Microcellular materials and specifically metallic foams have attracted the attention of scientific community due to the advanced combination of particular properties that they offer, compared to solid metals. These combined properties make them revolutionary materials for applications requiring more than one function such as high stiffness, fire protection and sound insulation. The present research focuses on the development of a method of producing composite metallic foam localized regions on metallic parts using a friction stir processing route (FSP). This route consists of friction stir processing passes for the integration of the foaming and the stabilizing/reinforcing agents in the aluminium matrix (precursor specimens) and a separate foaming stage at a laboratory furnace. More specifically, a mix of microsized particles of silicon carbide (stabilizing/reinforcing agent) and titanium hydride (foaming agent) were dispersed on bulk aluminium alloy AA5083–H111 using FSP. The integration of the mix was achieved via grooves which were constructed along the plate, parallel to the rolling direction. The parameters investigated during the experimental procedure were the groove geometry and the number of FSP passes. The analysed outcomes were the dispersion of carbide particles in the stir zone of the precursor and the porous structure and morphology of the composite foamed aluminium. The results were correlated with hardness evolution in both precursor and final foamed specimens.*

Keywords: *Friction Stir Processing, porous materials, aluminium foams, composite metal matrix foams, silicon carbide, localized foamed structures.*

1. INTRODUCTION

The highly increasing demand for lightweight and at the same time high strength materials suitable for automotive, railway, aerospace and shipbuilding industries resulted in the growth of research and industrial applications of different type of hybrid materials. Cellular and microcellular materials are among a new class of hybrid materials and are found in everyday uses. Applications range from light-weight construction and packaging to thermal insulation, vibration damping, and chemical filtration [1]. Metallic cellular materials, namely metal foams, merit the use of cellular materials and are becoming a new very promising class of engineering materials. Metal foams offer unique properties, compared to solid metals. Such unique properties are their high strength to weight ratio, high energy absorption capacity, large specific surface, high gas and liquid permeability, and low thermal conductivity [2]. Thus, metallic foams can be used as single elements, as a core of sandwich panels, as filler materials of hollow structures in multi-functional hybrid construction elements, for energy absorption, sound absorption, vibration damping and heat dissipation [3].

The use of metal foams depends on their basic characteristics such as porosity, cell structure and cell morphology homogeneity [4]. Metal foams are expected to be used as components in automotive, aerospace and marine industries, where the large strength and stiffness to weight ratios and the safety are crucial issues [5,6].

Friction stir process (FSP) is a surface modifying technique which involves the generation of friction heat and intense plastic flow. During FSP a rotating tool with pin and shoulder is inserted in a single piece of material for microstructural modification and traversed along the desired line to cover the region of interest. FSP was developed from the basic principles of friction stir welding (FSW), which is a solid-state bonding process [7,8]. The FSP has been used for fabricating metal matrix composites with uniformly dispersed reinforcing particles owing to its high mixing ability [9-11].

Hangai et al. [12,13] introduced the application of FSP for manufacturing aluminum foams. The proposed method utilized FSP on AA1050 and AA4045 to produce precursor specimens. Firstly, two aluminum plates were stacked with the blowing agent and the stabilizing agent between the plates. Then, FSP passes were carried out to mix the mixture of blowing and stabilization agent into the aluminum plates and to create precursors which were heat treated afterward at a separate foaming process. Papantoniou et al. manufactured AA5083/nano-γAl_2O_3 [14] and AA5083/ MWCNT [15] reinforced composite foams at localized regions using a novel single aluminium plate process.

The main goal of the present study was to produce silicon carbide reinforced Al-foam regions on a single AA5083 plate. The silicon carbide microsized particles aimed to reinforce and to stabilize the porous structure of the final composite foam. Process parameters in this paper have been set with the intention to find a correlation among the composite metal foam foaming process, the microstructure evolution and the hardness distribution.

2. MATERIALS AND METHODS

2.1 Materials

The selected base metal was the AA5083-H111 in plates of 6 mm thickness. The selection of the specific alloy was due to two significant reasons: i) firstly the AA5083 is a not-heat treatable alloy; thus the mechanical properties after the FSP are not degraded [14], ii) secondly the high presence of the alloying element magnesium is expected to improve the wetting of the reinforcing particles [16]. Microsized Silicon carbide particles (Alfa Aesar, 325 mesh, 99.5%) were used as reinforcing and stabilizing material. Commercially available titanium hydride powder (with particle diameter < 45 μm) was used as a blowing agent.

2.2 FSP based manufacturing procedure

Friction stir processing experiments were carried out using a modified milling machine. The FSW tool was made of heat-treated steel; it consisted of a flat shoulder and a cylindrical threaded pin. The diameter of the shoulder was 22.19 mm, the diameter of the pin was 5mm and its height was 4.2 mm. The height of the pin determines the thickness of the layer that will be enhanced with the ceramic and the foaming particles.

Initially, FSP tests were carried out without any addition of reinforcing particles in order to define the optimum parameters that result in a defect-free stir zone, consisted of good material mixing and refined microstructure. The optimum adopted operational FSP parameters for the precursor specimens without nanoparticle reinforcement resulted from preliminary experiments that their presentation beyond of the scope of this paper. These experiments indicated the requisition for applicability of 1000 rpm rotational speed combined with 13 mm/min transverse speed.

The first stage of the manufacturing procedure was the machining of the grooves (Figure 1i). The grooves were machined parallel to the rolling direction of the plates and were aligned with the center line of the rotating pin.

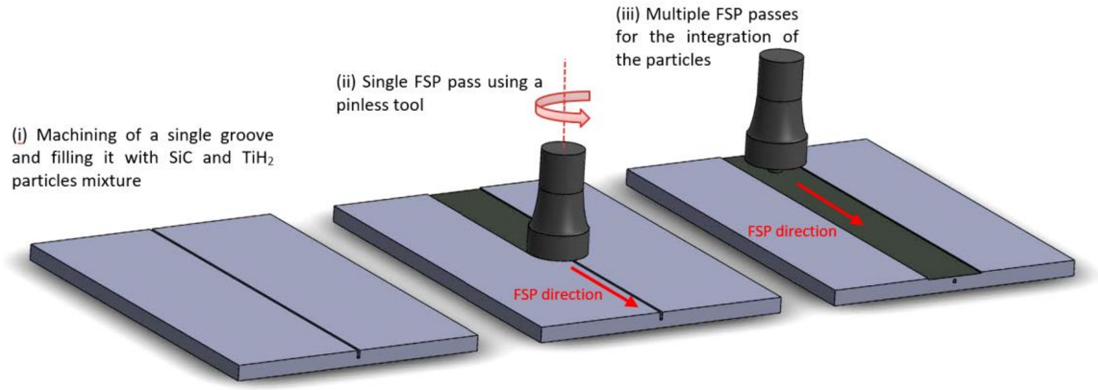

Figure 1. Precursor FSP manufacturing process

Two groove geometries have been used during the present study. The first geometry had a cross section of 1 mm width and 2.9 mm depth whether the second geometry had a cross section of 1 mm width with 3.9 mm depth.

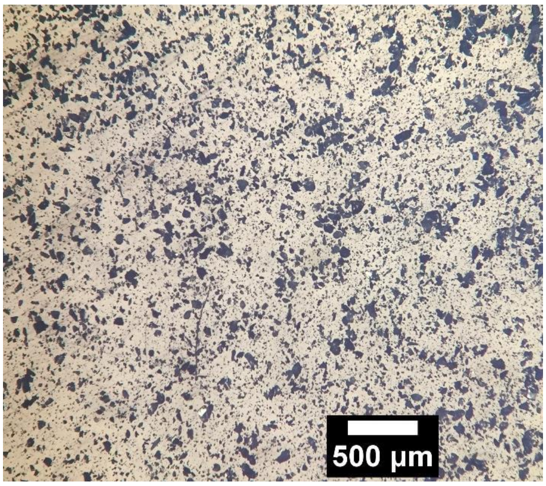

Figure 2. Micrograph (dark-field) of TiH_2 and SiC particles after the powder mixing stage

The precursor specimens were manufactured by mixing blowing agent powder (0.6% w/w TiH_2) and reinforcing/stabilizing silicon carbide microsized particles (4.0% w/w SiC) (Figure 2). The mixture of TiH_2 and SiC particles was firstly mixed for thirty minutes in a powder mixer and was then inserted carefully in the grooves and was pressed down, so as to fill them in a uniform manner.

To prevent ejection of the powder during the process, the groove was initially covered, using a pinless tool, by a single FSP pass (Figure 1ii). After covering the groove, multiple passes were carried out sequentially in the same direction and in such a way so as not to allow samples to cool down to room temperature between the passes (Figure 1iii). According to literature, increasing the number of FSP passes results in a more uniform nanoparticle distribution in the nugget [17]. Two, three, five and eight FSP passes were performed for each groove geometry.

2.3 Foaming Process

All the precursor samples were thermally treated in a preheated electric inductive oven, at a temperature range above liquidus, to induce the foaming process. The samples were held at a temperature of 750°C for five minutes. After the foaming process, the foamed specimens were air cooled to room temperature. An especially designed setup was used to characterize the free expansion behavior of the specimens during the foaming stage. The setup consisted of a ceramic-glass window at the front side of the furnace and a high definition camera mounted at a close distance behind the glass. The camera was connected to a computer for recording images. Using this setup, we were able to monitor the foaming process in all the experiments. The foaming time used was five minutes in order to observe all the foaming stages (growth, peak, coarsening and decay). Due to the fact that the porous structure was at localized regions; the calculation of the foaming efficiency of the foamed areas needed a different approach. Thus, for the estimation of the foaming efficiency, the specimen thickness increment corresponding to the initial specimen thickness was calculated by analysing the images from the camera using the open-source image processing software ImageJ (Figure 3).

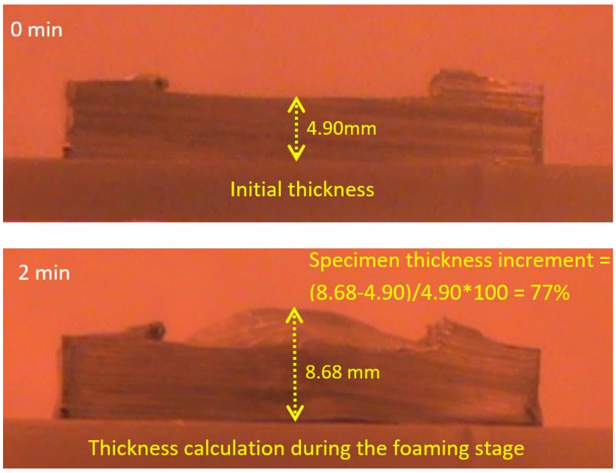

Figure 3. Specimen thickness increment calculation during the foaming stage (foaming efficiency estimation)

2.4 Metallurgical inspection

Specimens were created at different typical foaming times (e.g. peak, decay) in order to examine the porous structure. Cross-sections of the specimens were cut using a cut-off machine and processed by Electro Discharge Machining (EDM) to visualize the interior structure, without introducing any smearing effects in the porous structure.

Precursor specimens and foamed samples from each set of the experiment were polished with a suspension of 0.05 μm colloidal silica and then etched. Finally, the specimens were examined macroscopically by using a Leica MZ6 optical stereoscope, while microscopic observations were carried out by the optical microscope Leica DMILM.

2.5 Large-Scale Specimen

After obtaining the parameters that resulted in the optimum foamed specimen, a large-scale specimen was manufactured and analysed. For the manufacturing of the specimen, three grooves were machined in parallel and in close distance so as the stir-zones to be consecutive but not overlapped. Metallurgical inspection was also performed in this specimen and the microstructural observations were correlated to hardness distribution for both precursor and foamed specimens.

3. RESULTS AND DISCUSSION

3.1 Foaming Efficiency Results

Figure 4 illustrates the specimen thickness increment diagram (which is linked to the foaming efficiency) combined for all the specimens. From the diagram the following remarks were drawn. Firstly, it should be noted that the specimens with the two FSP passes introduced the lowest foaming efficiency. This correlates with the qualitative results obtained from the metallographic analysis of the cross-section of the precursor specimen in both specimens with different groove depths. Figure 5 illustrates stereoscopic images of the etched stir-zones of the two FSP passes precursor specimens. The ceramic particles were not found to be well distributed in the stir zones and large agglomerated areas in the center of the nuggets can be identified.

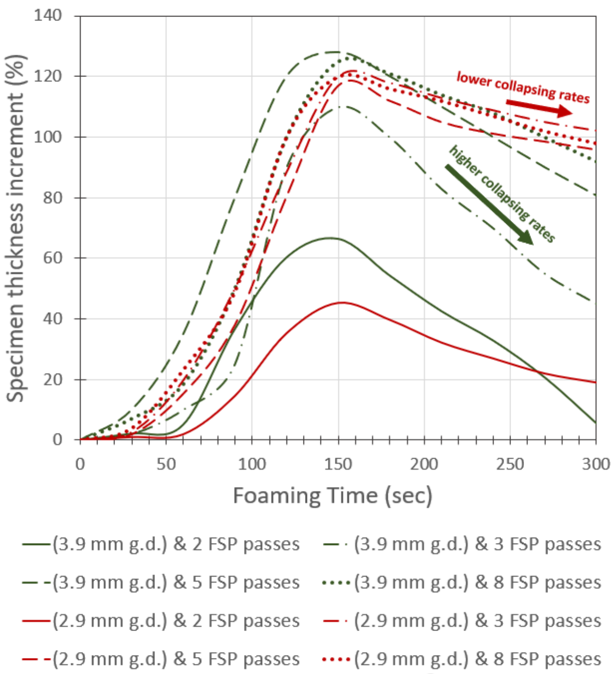

Figure 4. Specimen thickness increment-time diagram for different set of parameters during the foaming stage (g.d.: grooves depth)

The maximum foaming efficiency for all the other specimens was found to be in close values, even though the specimens with the larger groove depth had higher amounts of foaming TiH_2 particles due to the larger groove volume. The important outcome of this diagram is that the specimens with the deeper groove introduced a higher rate of collapsing than the specimens with the shorter groove. This can be attributed to the higher amount of the hard silicon carbide particles on the deeper groove that were not uniformly dispersed in the nugget during the FSP passes. This can be observed also from the stereoscopic image of Figure 6 where the higher volume groove introduced a non-uniform stir-zone with many areas of agglomerated particles. The deficiency of stabilizing agents led to higher collapsing rates.

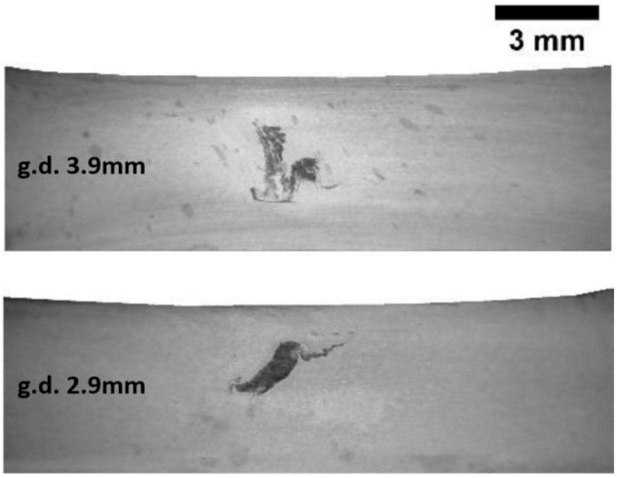

Figure 5. Macrographs of the cross-section of the specimens with 2 FSP passes for the two different groove depths

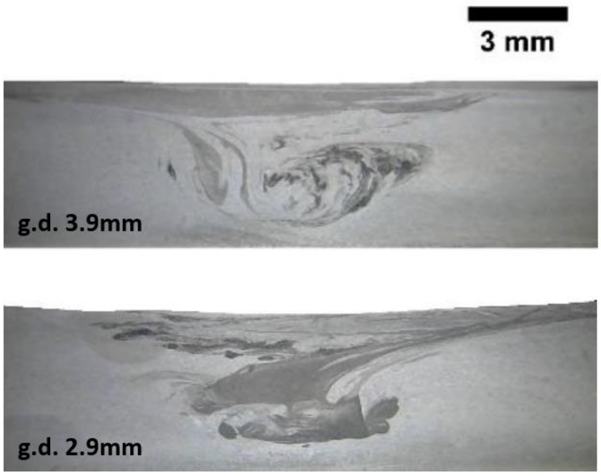

Figure 6. Macrographs of the cross-section of the specimens with 8 FSP passes for the two different groove depths

3.2 Large-Scale Specimen Results

For the large-scale specimen, three parallel grooves using the lower volume groove geometry were manufactured. Three FSP passes for each groove were chosen firstly due to the research outcome that for two and higher FSP passes the foaming efficiency was found to stay stable (Figure 4) and secondly for applicability reasons of the process. Figure 7a illustrates large scale specimens foamed at different foaming times. At the first specimen the foam has finished the nucleation and growth stage and has reached its peak. At the second and the third specimen the pores have started to coarse and merge and the structure gradually collapses and decays. Figure 7b shows the cross-section of the precursor specimen.

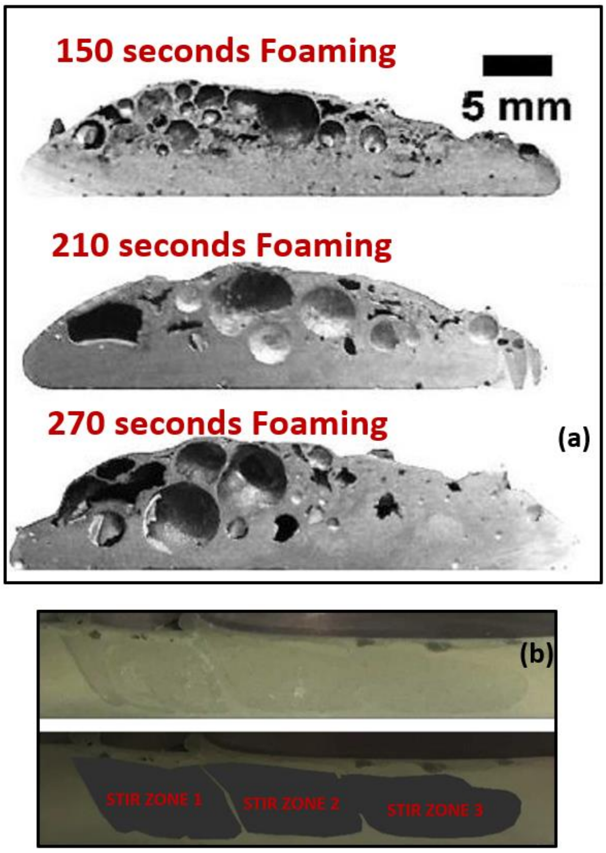

Figure 7. Large-Scale Specimens: a) Foamed specimens at different foaming times/stages (nucleation-growth-peak, coarsening, decay), b) Macrograph of precursor cross-section

Figure 9 illustrates optical microscopy images (dark field) of different regions of the large-scale precursor specimen. The distribution of the silicon carbide particles inside the stir zone appears to be totally homogeneous without introducing large agglomeration areas. On the foamed specimens the foam structure presented non-interconnected cellular morphology as it was expected and the foamed samples were characterized by dense strut and close-packed grains on the cell wall surface. The silicon carbide particles remained well distributed in the foamed matrix (Figure 10a-b) enhancing the stabilizing and reinforcing of the foamed region. Furthermore, on the ligament regions, most of the particles appear to protrude on the solid-air interfaces (indicated with red arrows in Figure 10b). The micrographs from the etched foamed specimen illustrated struts with a dendritic, relatively coarse-grained microstructure (Figure 10b-c).

The hardness evaluation of the large-scale foamed specimen, across the perpendicular axis of friction stir process, revealed a mean value of hardness evolution about 85-87 HV outside the stir-zone and inside the stir-zone the values fluctuated from 119 to 126 HV (Figure 8a).

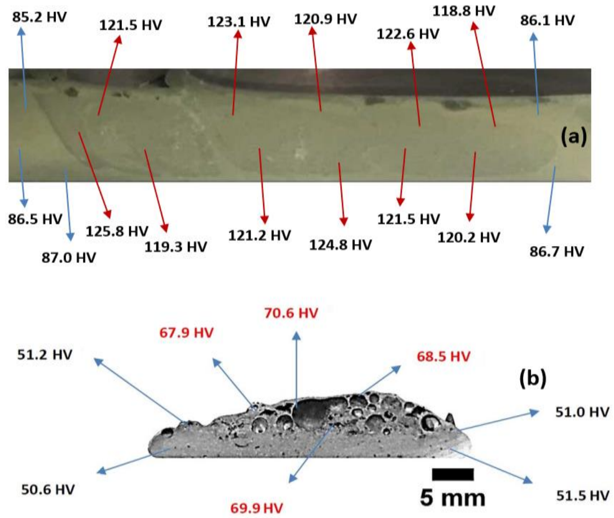

Figure 8. Variation of the hardness distribution along the cross section of: a) the FSPed precursor specimen, b) the foamed (at its peak) specimen

The increase is attributed to the presence of the hard microsized silicon carbide particles and to the Orowan mechanism where silicon carbide particles act as barriers.

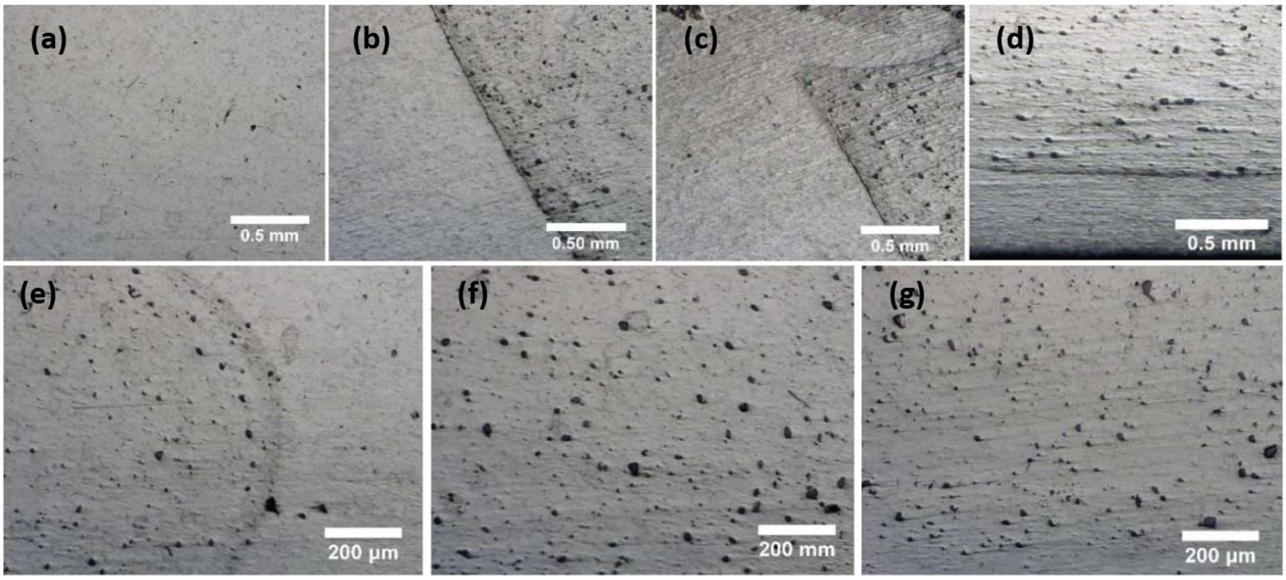

Figure 9. Optical microscopy (dark field) images of the precursor specimen on different regions: a) outside the reinforced stir-zone, b-e) interface of stir-zone and TMAZ, f-g) inside the stir zone

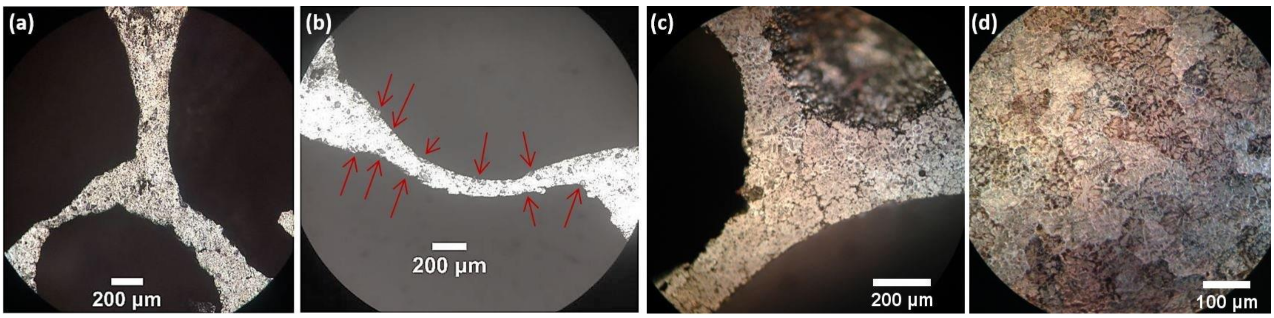

Figure 10. Interpore microstructure and texture evolution of ligaments: a) white field optical microscopy image, b) dark field optical microscopy image (red arrows indicate particles protruding on the solid-air interfaces of the foam cells), c - d) white field optical microscopy images of etched specimens

Figure 8b illustrates the variations of hardness distribution along the foamed (at its peak - 150 seconds) specimen. Outside the foamed stir-zone the microhardness distribution presented values in the range of 50-52 HV; whilst inside the foamed stir-zone the microhardness fluctuated from 68 to 71 HV. The decrease of the values in the foamed specimen corresponding to the precursor is caused by the intense grain growth (Figure 10d) and the elimination of the dislocations (which were created after strain hardening, H111) during the foaming process.

4. CONCLUSION

In the present work, a very promising method of manufacturing localized AA5083 – silicon carbide composite foam using Friction Stir Process was presented and the following concluding remarks can be drawn:

- Using friction stir process route, scope production of localized composite metal foam was successfully accomplished
- The optimum foaming efficiency resulted from three FSP passes (minimum) and the lower volume groove geometry.
- The higher volume groove geometry resulted in a non-uniform stabilizing particle (SiC) distribution in the precursor and this led to a higher collapsing rate during the foaming stage.
- The hardness measurements indicated a decrease in the values of the foamed specimen, corresponding the precursor specimen, which is attributed mainly to the intense grain growth during the foaming stage. Furthermore, the values inside the precursor and the foamed specimen stir-zones presented higher values in comparison to the areas outside the stir-zone.

Conclusively, the main novelty of the suggested method stems from the fact that foam structures can be obtained in different regions of the same metallic plate. The porosity, as well as the mechanical properties of the foamed structure can be controlled by the nature and the volume fraction of the foaming and the stabilization/reinforcing agent.

ACKNOWLEDGEMENTS

Prof. N.M. Vaxevanidis acknowledges financial support for the dissemination of this work from the *Special Account for Research of ASPETE* through the funding program "*Strengthening ASPETE's research*".

REFERENCES

[1] L. Gibson, M. Ashby: *Cellular Solids, Structure and Properties*, 2nd ed., Cambridge University Press, Cambridge, UK, 1997.

[2] M. Ashby, A. Evans, N. Fleck, L. Gibson, J. Hutchinson, H. Wadley: *Metal Foams: A Design Guide*, Butterworth-Heinemann, USA, 2000.

[3] B. Smith, S. Szyniszewski, J. Hajjar, B. Schafer, S. Arwade: Steel foam for structures: A review of applications, manufacturing and material properties, Journal of Constructional Steel Research, Vol. 71, pp. 1-10, 2012.

[4] B.A. Gama, T.A. Bogetti, B.K. Fink, C.J. Yue, D.T. Claar, H.H. Eiferte, J.W. Gillespie: Aluminum foam integral armor: a new dimension in armor design, Compos Struct, Vol. 52, pp. 381-395, 2001.

[5] J. Banhart: Manufacture, characterization and application of cellular metals and metal foams, Progr Mater Sci, Vol. 46, pp. 559-632, 2001.

[6] A.P. Mouritz, E. Gellert, P. Burchill, K. Challis: Review of advanced composite structures for naval ships and submarines, Compos Struct, Vol. 53, pp. 21-42, 2001.

[7] R.S. Mishra, Z.Y. Ma: Friction stir welding and processing, Mater Sci Eng R, Vol. 50, pp. 1-78, 2005.

[8] Z.Y. Ma: Friction Stir Processing Technology: A Review, Metall Mater Trans, Vol. 39A, pp. 642-658, 2008.

[9] D.J. Shindo, A.R. Rivera, L.E. Murr: Shape optimization for tool wear in the friction-stir welding of cast Al359-20% SiC MMC, J Mater Sci, Vol. 37, pp. 4999-5005, 2002.

[10] M. Yang, C. Xu, C. Wu: Fabrication of AA6061/Al2O3 nano ceramic particle reinforced composite coating by using friction stir processing, J Mater Sci, Vol 45, pp. 4431-4438, 2010.

[11] D.I. Pantelis, P.N. Karakizis, N.M. Daniolos, C.A. Charitidis, E.P Koumoulos, D.A. Dragatogiannis: Microstructural study and mechanical properties of dissimilar friction stir welded AA5083-H111 and AA6082-T6 reinforced with SiC nanoparticles, Mat Man Proc, Vol 31, pp. 264-274, 2016.
[12] Y. Hangai, T. Utsunomiya: Fabrication of Porous Aluminum by Friction Stir Processing, Metall Mater Trans, Vol. 40A, pp. 275-277, 2009.
[13] Y. Hangai, T. Utsunomiya, M. Hasegawa: Effect of tool rotating rate on foaming properties of porous aluminum fabricated by using friction stir processing, J Materials Proc Tech, Vol. 210, pp. 288-292, 2010.
[14] I. Papantoniou, E. Kyriakopoulou, D. Pantelis, A. Athanasiou-Ioannou, D. Manolakos: Manufacturing process of AA5083/nano-γAl2O3 localized composite metal foam fabricated by friction stir processing route (FSP) and microstructural characterization, Journal of Materials Science, Vol. 53, pp. 3817-3835, 2018.
[15] I. Papantoniou, H. Kyriakopoulou, D. Pantelis, D. Manolakos: Fabrication of MWCNT-reinforced Al composite local foams using friction stir processing route, Int J Adv Manuf Technol, Vol. 53, pp. 3817-3835, 2018.
[16] J. Hashim, L. Looney, M.S.J. Hashmi: The wettability of SiC particles by molten aluminium alloy, Journal of Materials Processing Technology, Vol. 119, pp. 324-328, 2001.
[17] D. Storjohann, O. Barabash, S. David, P. Sklad, E. Bloom, S. Babu: Fusion and friction stir welding of aluminium metal matrix composites, Metall Mater Trans, Vol. 36A, pp. 3237-3247, 2005.

Lubricants and Lubrication

16th International Conference on Tribology – SERBIATRIB '19

15 – 17 May 2019, Kragujevac, Serbia

Serbian Tribology Society

SERBIATRIB '19

16th International Conference on Tribology

Faculty of Engineering University of Kragujevac

Kragujevac, Serbia, 15 – 17 May 2019

RESULTS OF EXPERIMENTAL RESEARCH PHYSICAL-CHEMICAL CHARACTERISTICS OIL FROM ENGINES OF VEHICLES

Sreten PERIC[1*], Radovan RADOVANOVIC[2], Bogdan NEDIC[3], Mihael BUCKO[1]

[1]University of Defence in Belgrade, Military Academy, Belgrade, Serbia, sretenperic@yahoo.com

[2]University of Criminal Investigation and Police Studies, Belgrade, Serbia, radovan.radovanovic@kpu.edu.rs

[3]University of Kragujevac, Faculty of Engineering, Kragujevac, Serbia, nedic@kg.ac.rs

*Corresponding author: sretenperic@yahoo.com

Abstract: *In the study of ways to reduce the friction losses of internal combustion (IC) engines, investigations of losses from elements in the piston assembly, the bearing system, and the valve train system are paramount. Mechanical and thermodynamic losses, wear and the emissions caused by lubricating oil combustion are principally influenced by the tribological behaviour of the piston assembly. The tribological performance of piston rings in reciprocating IC engines can only be fully understood when both lubrication and wear are considered in combination.*

This paper deals with physical-chemical tests that are part of the oil analysis and are used to access the condition of the system. Furthermore, the results of experimental research on the physical-chemical properties of the oil sampled from engines of the vehicles are shown.

Keywords: *engine, engine oil, oil analysis, tribomechanical system, maintenance.*

1. INTRODUCTION

Modern reciprocating internal combustion (IC) engines have to meet today's requirements of lower fuel consumption and very low emissions. To reach these objectives, the trend towards increased specific load and power in engine development assumes greater importance. Smaller and lighter engines will be used increasingly for propulsion systems [1].

It is known that the piston assembly of heavy-duty diesel engines is a significant source of friction. It has been reported that the piston rings account for a significant portion of the total friction losses of an engine [2]. Typical percentages in the literature may vary from 20-30 % [3] up to 50-60 % [4]. Constructive measures such as lowering the tension of piston rings lead to decreased friction losses and wear rates but they also lead to increased oil consumption, emissions, and thermodynamic losses as a result of blow-by [1]. Much theoretical [5-8] and experimental [4, 9-12] work on the piston/cylinder assembly exists in the literature.

Traditional materials and surface treatments may not be adequate to address the issues towards improved reliability, higher performance and reduced oil consumption and emissions [13]. A coating on the piston may offer advantages such as friction reduction and better scuffing resistance and wear protection [14], while reduced clearance due to the coating thickness may improve oil consumption and engine noise.

The tribological conditions within engines as a real tribomechanical system are quite complex and are conditioned to a large extent by the characteristics of used lubricant. Complexities of the conditions are determined by temperature of the elements in contact, current properties of the used lubricant, external load in reference to specific pressures in contact zone, dynamic nature of contact creating.

The piston assembly tribosystem of reciprocating engines is: the cylinder liner, piston and piston rings, lubricating oil, and crankcase air. There are three major sources of engine friction losses: piston rings/cylinder liners, valve train and engine bearing. Among these parts, the cam/tappet contacts, which are the major source of valve train friction, have been thought to operate in both the boundary and elastohydrodynamic regime [15,16].

Lubrication between piston rings and cylinder liner to reduce friction losses is a critical area for improvement [17-19]. Piston, piston rings and cylinder bore are a coupled system with properties governed by the interaction of gases and inertial forces as well as by the lubrication regime (hydrodynamic, mixed, boundary) [20].

The subject of testing in this paper is the experimental determination of property changes of engine oil during operation depending on the dynamic properties of loads.

This part presents the results of testing of physical-chemical properties of engine oil which was sampled from engines of vehicles used in real conditions of exploitation.

Experimental testing of physical-chemical properties included determining: viscosity at 40 and 100°C, determining viscosity index, flash point and TBN (Total base number).

2. EXPERIMENTAL TESTING OF THE PHYSICAL AND CHEMICAL PROPERTIES OF ENGINE OIL

The physical-chemical properties (Table 1) of the engine oil were examined in accordance with standard methods. The analysis was performed using both fresh oil and oil used in the engines of vehicles. Allowed quantities of certain elements in used engine oil and allowed values of deviations in physical-chemical properties of new and used oil are given in Table 2.

Table 1. The tests and standards of tested the physical-chemical properties of oil

Properties	Standards
Kinematic viscosity, mm^2/s	SRPS B.H8.022
Viscosity Index	SRPS B.H8.024
Flash Point (C)	ISO 2592
Pour Point (C)	ISO 3016
Water Content, mas.%	ASTM D 95
Total Base Number (TBN), mgKOH/g	ASTM D 2896
Fe Content, %	ASS
Cu Content, %	ASS

Table 2. Allowed values of deviations in physical-chemical properties of oil

Physical-chemical properties of oil and wearing products	Maximum deviation allowed
Viscosity at 40 C (mm^2/s)	20%
Viscosity at 100 C (mm^2/s)	20%
Viscosity index (%)	5 %
Total base number (TBN) (mg KOH/g)	decrease to 50%
Flash point (C)	20 %
Water content (%)	0.2 %
Wear products – Fe content, ppm(μg/g)	100 ppm
Wear products – Cu content, ppm(μg/g)	50 ppm

Table 3. Used engine oil in tested vehicles [21]

Engine oil from engine of A vehicle	
SAE classification	API classification
SAE 15W-40	API SG/CE
Engine oil from engine of B vehicle	
SAE classification	API classification
SAE 30/S3	-

Table 4. Results of zero samples of used engine oil [21]

Physical-chemical characteristic	Type of engine oil	
	SAE 15W-40	SAE 30/S3
Color	3.0	3.0
Density (g/cm^3)	0.88	0.90
Viscosity at 40 C (mm^2/s)	104.8	104.6
Viscosity at 100 C (mm^2/s)	14.1	11.6
Viscosity Index	–	–
Flash Point (C)	230	240
TBN (mg KOH/g)	10.5	9.8

The results of experimental testing of physical-chemical properties are presented in Table 5. Experimental testing was carried out in accordance with manufacturer specifications and proper standards by using the necessary testing equipment.

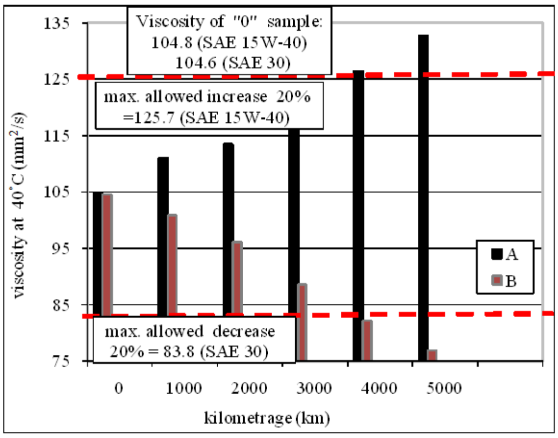

Figure 1. Change of the Viscosity at 40°C [21]

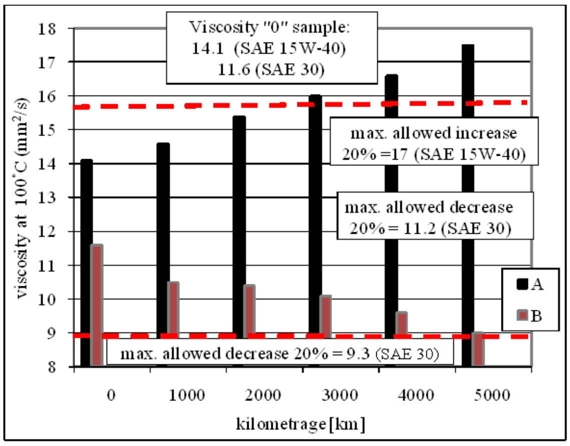

Figure 2. Change of the Viscosity at 100°C [21]

Figure 1 shows viscosity change of the tested oil at 40°C, while Figure 2 – viscosity change at 100°C. An increase in viscosity at 40°C is evident for A vehicle, exceeding the limit of 20%. The decrease in viscosity at 40°C is evident for B vehicle, exceeding the limit of 20%. The increase in viscosity indicates a process of oil oxidation as well or oil contamination with water and dirt, as well as wears products [22]. If a change in the oil viscosity is detected, subsequent analysis of the oil can identify the cause of the disturbance of its properties.

Table 5. Results of testing samples of used engine oil from tested vehicles [21]

Sample		Vehicles	
		A	B
Viscosity at 100 C,mm^2/s	0	14.1	11.6
	1	14.6	10.5
	2	15.4	10.4
	3	16.0	10.1
	4	16.6	9.6
	5	17.5	9.0
Viscosity at 40 C, mm^2/s	0	104.8	104.6
	1	111	100.9
	2	113.5	96.1
	3	119.4	88.6
	4	126.4	82.2
	5	132.7	76.9
Viscosity Index	0	135	100
	1	129	97
	2	122	95
	3	119	91
	4	116	87
	5	112	84
Flash Point, C	0	230	240
	1	220	193
	2	208	177
	3	205	159
	4	197	143
	5	192	128
TBN, mgKOH/g	0	10.5	9.8
	1	9.1	9.4
	2	7.2	8.4
	3	6.5	7.8
	4	6.1	6.6
	5	5.2	6.2
Fe Content (ppm)	1	98.4	17.9
	2	123	40.9
	3	137	86.7
	4	149	132
	5	165	261
Cu Content (ppm)	1	4.9	3.3
	2	5.9	3.8
	3	6.7	6
	4	7.3	8.1
	5	7.9	9.7

The viscosity index is an empirical number which shows how the viscosity of some oils changes by increasing or decreasing the temperature. High viscosity index shows relatively small tendency of viscosity to change upon influence of certain temperature, as oppose of low viscosity index which shows greater viscosity change with temperature. Change of engine oil viscosity index is shown in the Fig. 3. A decrease in the viscosity index oil is evident for both vehicles, exceeding the limit of 5%.

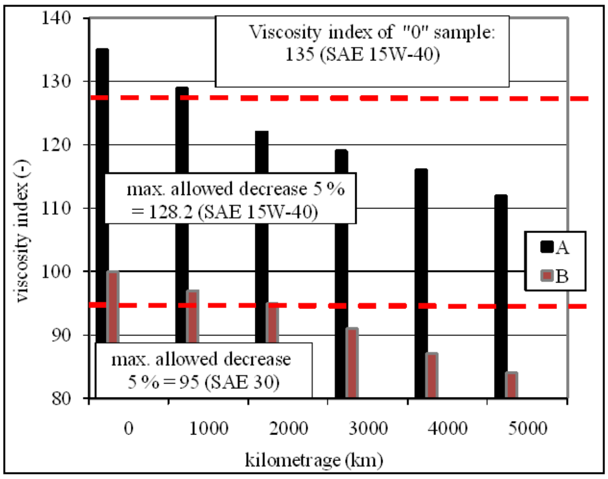

Figure 3. Change of viscosity index [21]

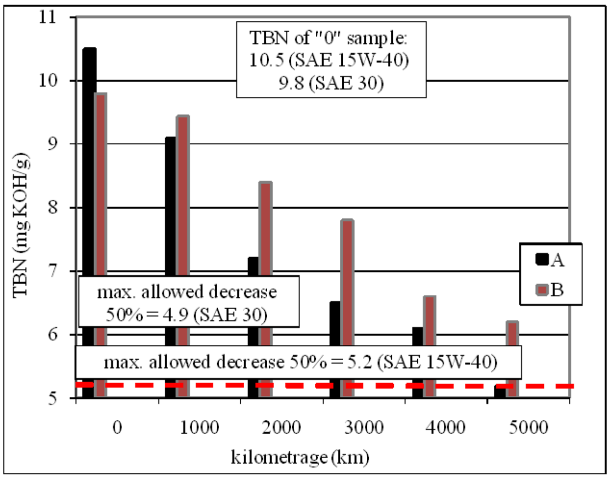

Figure 4. Change of TBN [21]

Total base number is a measure of reserve alkaline additives put into lubricants to neutralize acids, to retard oxidation and corrosion, enhance lubricity, improve viscosity characteristic and reduce the tendency of sludge buildup. TBN is measure of the lubricant alkaline reserve, and mostly is applied to engine lubricants. Combustion acids attack TBN, e.g. sulphuric acid, decreasing as it consumes. Figure 4 shows the change of TBN for engine oils. A decrease of TBN is evident for both vehicles. Up to 5000 km TBN value does not exceed the allowed limit, except for A vehicle.

The flash point is the lowest temperature at which a vapor above a liquid will ignite when a flame is applied under standard conditions. In engine oil, decreases in flash point are usually due to distillate fuel dilution but may also in extreme conditions be a symptom of thermal cracking of the oil. Contamination by residual fuel may not appreciably depress the flash point but can, if the flash point of the fuel is naturally low.

Figure 5 presents the change of flash point for engine oils. A decrease in the flash point is noticeable, and by the end of testing exceeds the allowed limits (20%, Table 2) for B vehicle.

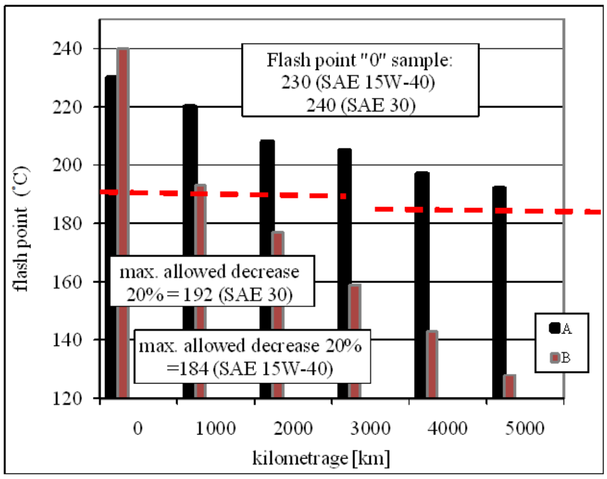

Figure 5. Change of the flash point [21]

An analysis of the metals content of the oil is very important. Metals particles are abrasive, and act as catalysts in the oxidation of oils. In engine oil, the origin of these metals may be from additives, wear, fuel, air and liquid for cooling. Metals from the additives can be Zn, Ca, Ba, or Mg and that indicates the change of additives. Metals originating from wear are: Fe, Pb, Cu, Cr, Al, Mn, Ag, Sn, and they point to the increased wear in these systems. Elements originating from the liquid for cooling are Na and B, and their increased content indicates the penetration of cooling liquid in the lubricant. The increased content of Si or Ca, which are from the air, points to the malfunction of the air filter. Metals such as iron (Fe) and copper

(Cu) were selected for identification because they are typical elements contained in the examined engines. On the basis of changes in their concentration in the oil charge it can be determined their origin from engine elements and the degree of wear.

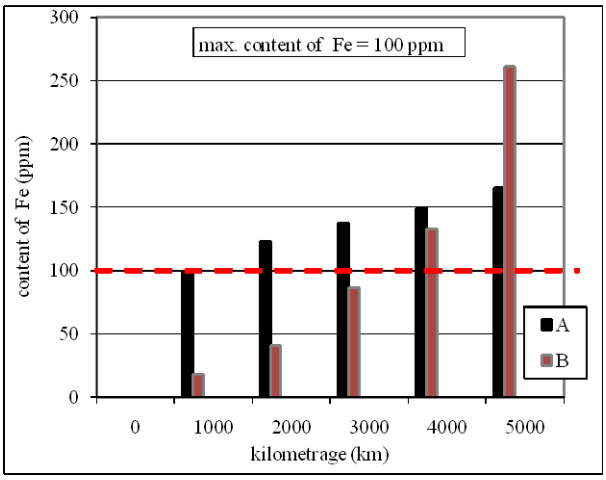

Figure 6. Change of Fe content [21]

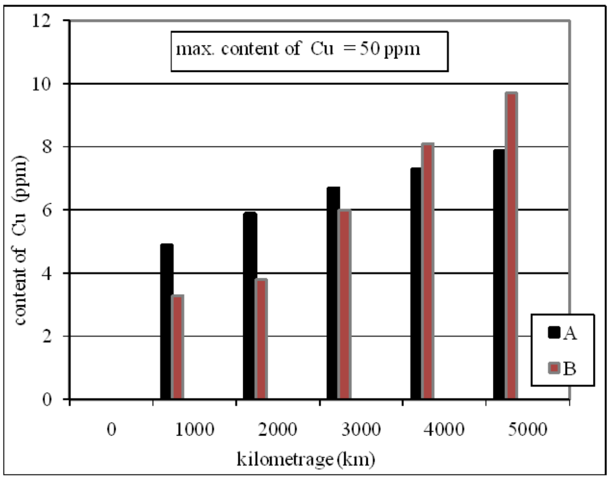

Figure 7. Change of Cu content [21]

The iron and copper content (Figs 6 and 7), because of wear in the oil contents increased progressively throughout. The content of iron is significantly above the allowable limits (100 ppm, Table 2) for A and B vehicles. However, the content of cooper is significantly below the allowable limits (50 ppm, Table 2) for A and B vehicles.

3. CONCLUSION

The engine lubricating oil ageing process is a very complex process during which degradation of the base oil and depletion of its additives take place simultaneously. Oxidative high temperature degradation and contamination by water, ethylene glycol, fuel, soot, and wear metals are the main factors.

By appropriate sampling and testing during exploitation, based on the model presented it is possible to identify the state of system elements and predict its future behaviour in exploitation. The conditions in which the engine elements are found as real tribomechanical system are complex and are determined to a large extent by oil properties. The complexity of the conditions is determined by temperature of elements in contact oil, temperature and properties, external load, that is the specific pressure in the contact zone, the dynamic character of contact.

Results obtained during the tests contain information about physical-chemical properties and products wear.

Based on the experimental investigation and presented results the following conclusions can be summarized:

1. During exploitation, the analysed oil has achieved its primary function and meets the intended replacement interval, which was determined by analysis of characteristic physical-chemical properties, concentration of wear products and tribological properties.
2. The changes in the physical-chemical and tribological properties of the lubricating oil from the vehicle engine are directly dependent on the functional characteristics of all the elements of the tribomechanical system.
3. Testing of physical-chemical and tribological properties of oil in the function of determining the state of engine as a complex tribomechanical system aims to identify mechanisms of change in the system elements.
4. Variation in the oil viscosity is often the first indicator of a global problem of the engine tribomechanical systems. When the oil loses its antioxygenic stability, the oil viscosity increases, and if measures are not taken in due time, this causes the

disturbance of the normal operation of the tribomechanical systems.

5. Metal particles, physical-chemical processes and contaminants, detected through laboratory analysis, is the appropriate base to identify possible disfunctionalities in tribomechanical systems, as well as to determine the life of usage of oil and its functionality in oil systems.
6. Metal particles in oil, regardless of their structure and origin, are a basic cause of tribological degradation process, and on the other side they present a clear indicator of the tribological process intensity and characteristics.
7. The appearance of water in the samples is not found. Water in oil is the main cause for appearance of corrosive processes on the contact surfaces.

REFERENCES

[1] R. Golloch, G. P. Merker, U. Kessen, S. Brinkmann: Functional Properties of Microstructured Cylinder Liner Surfaces for Internal Combustion Engines, Tribotest journal, Vol. 11, No. 4, pp. 307-324, 2005.

[2] N. G. Demas, R. A. Erck, G. R. Fenske: Tribological evaluation of piston skirt/cylinder liner contact interfaces under boundary lubrication conditions, Lubrication Science, Vol. 22, No. 3, pp. 73-87, 2010.

[3] T. Rabute, T. Tian: Challenges involved in piston top ring designs for modern SI engines, Journal of Engineering for Gas Turbines and Power, Vol. 123, No. 2, pp. 448-459, 2001.

[4] G. Ryk, Y. Kligerman, I. Etsion: Experimental investigation of laser surface texturing for reciprocating automotive components, Tribology Transactions, Vol. 45, No. 4, pp. 444-449, 2002.

[5] M. Priest, D. Dowson, M.C. Taylor: Predictive wear modeling of lubricated piston rings in a diesel engine, Wear, Vol. 231, No. 1, pp. 89-101, 1999.

[6] Y. Hu, H.S. Cheng, T. Arai, Y. Kobayashi, S. Aoyama: Numerical Simulation of Piston Ring in Mixed Lubrication – A Nonaxsymmetrical Analysis, Journal of Tribology, Vol. 116, pp. 470-478, 1994.

[7] T. Tian, I. B. Noordzij, V. W. Wong, J. B. Heywood: Modeling Piston-Ring Dynamics, Blowby, and Ring-Twist Effects, Journal of Engineering for Gas Turbines and Power, Vol. 120, No. 4, pp. 843-854, 1998.

[8] O. Akalin, G. M. Newaz: Piston ring-cylinder bore friction modeling in mixed lubrication regime: Part I – analytical results, Journal of Tribology, Vol. 123, pp. 211-218, 2001.

[9] Y. Wang, S. C. Tung: Scuffing and wear behavior of aluminum piston skirt coatings against aluminum cylinder bore, Wear, Vol. 225-229, part 2, pp. 1100-1108, 1999.

[10] Y. Wang, K. Brogan, S. C. Tung: Wear and scuffing characteristics of composite polymer and nickel/ceramic composite coated piston skirts against aluminum and cast iron cylinder bores, Wear, Vol. 250, pp. 706-717, 2001.

[11] J. J. Truhan, J. Gu, P. J. Blau: The effect of lubricating oil condition on the friction and wear of piston ring and cylinder liner materials in a reciprocating bench test, Wear, Vol. 259, No. 7-12, pp. 1048-1055, 2005.

[12] V. D. N. Rao, D. M. Kabat, D. Yeager, B. Lizotte: Engine studies of solid film lubricant coated pistons, SAE Transactions, Vol. 106, No. 3, pp. 20-33, 1997.

[13] R. Gahlin, M. Larsson, P. Hedenqvist: Me-C: H coatings in motor vehicles, Wear, Vol. 249, No. 3-4, pp. 302-309, 2001.

[14] C. Friedrich, G. Berg, E. Broszeit, E. Rick, J. Holland: PVD Cr_xN coatings for tribological application on piston rings, Surface & Coatings Technology, Vol. 123, pp. 211-218, 2001.

[15] M. Takiguchi, K. Machida, S. Furuhama: Piston friction force of a small high speed gasoline engine, Journal of Tribology, ASME, Vol. 110, No. 1, pp. 112-118, 1988.

[16] R. G. Kapadia, C. H. Bovington, I. lee-Prudhoe: A tribological investigation of lubricant effects on bearing friction and fuel economy for passenger car engines and heavy duty diesel engines, Lubrication Science, Vol. 19, No 1, pp. 11-23, 2007.

[17] A. Ruggiero, A. Senatore: On the role of the engine tribology in the reduction of noise and emissions, in: *Proceedings of the 8th Int. Conference on Urban Transport and the Environment in the 21st Century*, Seville, Spain, (2002).

[18] S. Cho, S. Choi, C. Bae: Frictional modes of barrel shaped piston rings under flooded lubrication, Tribology International, Vol. 33, No 8, pp. 545-551, 2000.

[19] V. D'agostino, D. Guida, A. Ruggiero, A. Senatore: A four stroke engine friction model, in: *Proceedings Aimeta Int. Tribology Conference*, AITC, L'Aquila, Italy, 2000.

[20] V. D'agostino, S. Della Valle, A. Ruggiero, A. Senatore: On the Effective Length of the Top Piston Ring Involved in Hydrodynamic lubrication, Lubrication Science, Vol. 17, No. 3, pp. 309-318, 2005.

[21] S. Peric: *The development of a method of diagnosis the condition from the aspect of physical-chemical and tribological characteristics of lubricating oils of vehicles*, PhD thesis, University of Defence in Belgrade, Belgrade, Serbia, 2009.

[22] A. Takeuchi: Investigation on lubrication condition of piston pin in real engine block with ultrasonic technique, Lubrication Science, Vol. 23, No. 7, pp. 331-346, 2011.

Serbian Tribology Society

SERBIATRIB '19

16th International Conference on Tribology

Faculty of Engineering
University of Kragujevac

Kragujevac, Serbia, 15 – 17 May 2019

TEMPERATURE EFFECT IN MINIMUM OIL FILM THICKNESS MEASUREMENTS IN A SIMPLIFIED SINGLE-RING TEST RIG USED TO SIMULATE THE PISTON-CYLINDER ASSEMBLY

Polychronis S. DELLIS[1]
[1]ASPETE, Department of Mechanical Engineering Educators, Athens, Greece, pasd@city.ac.uk
*Corresponding author: pasd@city.ac.uk

Abstract: *As part of the study of the complex lubrication phenomena between the piston-ring and the cylinder liner, it is important to characterize the oil film thickness in view of new designs that can be implemented for the piston-ring assembly. In previous studies parametric results of different lubricants, speed, load, temperature and piston-ring surface were presented to complement on the cavitation rheological phenomena (initiation and development) and to interpret the effect of physical-chemical properties of the lubricants in oil film thickness, friction and oil film pressure. Measurements were conducted in a simplified single-ring test rig, where a steady piston-ring section of overall width 5 mm is placed under a flat surface used as a reciprocating liner, taking advantage of significantly less uncertainties when compared to engine experiments. The advantage of this layout is that it can provide abundance of results that in turn, are being simultaneously interpreted in an easier and safer way prior to engine implementation and testing. In this manner, the effect of different operating conditions is assessed to achieve solid experimental results, useful in engine tribological applications in the piston-cylinder assembly, that comply with the emission regulations of today and the near future.*

This presentation is focused on the effect of temperature in minimum oil film thickness measurements (MOFT) for different lubricants. An electrical method is used in this set of experiments to measure the oil film thickness (capacitance). The testing is applied for different speeds and loads so that a complete picture of the lubricants behavior can be taken and, in parallel, friction measurements are presented to assess the MOFT results for specific parts of the stroke. The results show the effect of different lubricant properties in MOFT and give an insight of the conditions of cavitation occurrence at the early parts of the stroke as temperature rises. Further processing of these results provides very useful conclusions and the combination of the lubricants behavior under cavitating conditions, can lead to innovative additives design-formulation and new lubricant properties.

Keywords: *piston-ring, single-ring test rig, oil film, friction, capacitance, cavitation.*

1. INTRODUCTION

As part of the optimisation process of the lubrication in between and under the piston-rings of the piston-cylinder assembly, the development of the oil film thickness is studied to give an insight of the lubrication rheological phenomena. The above process is complemented with reduced friction losses, low oil consumption and minimised wear to meet the present and future tribological engine requirements.

Engine oil formulation should be specifically blended to provide optimum all-around performance according to the engineering specifications [1]. These include the enhancement of load carrying capacity, where the appearance of different forms of cavitation has the opposite effect [1, 2, 3].

According to Rastogi and Gupta [4] the primary purpose of the additives is to reduce the dependence of lubricant viscosity on temperature. Polymer addition enhances viscoelastic properties and the oil properties turn to slightly shear-thinning [1, 4]. It was speculated that shear-thinning results in a larger cavitation zone. Lubricant viscosity is subject to shear stress apart from the apparent temperature effect [1]. The addition of viscoelastic additives raises the load carrying capacity and reduces any wear that might occur [5].

The viscosity of different oils varies at different rates with temperature. The lubricant film thickness and load carrying capacity reduces significantly with temperature [6]. Viscosity has a damping effect on cavity growth and collapse, i.e. the reduced viscosity of shear thinning lubricants should lead to large sized cavities [4]. The significant loss of load capacity verifies the need to control the lubricant properties under these circumstances. Viscosity has a major impact on flow separation points, which in turn has an impact on oil film pressure distribution and cavitation [7].

A single ring test rig specially designed for lubrication experiments is the essential tool to provide abundance of parametric results as well as implementation of novel measuring techniques. The piston-liner interface is simulated by a steady parallelepiped piston-ring section with a curved top surface and a reciprocating flat liner, providing the necessary simplicity to avoid the complex lubrication and rheological phenomena of the engine experiments [3, 8, 9, 10]. Easy access to the ring-liner interface is its basic characteristic. Eventually a better understanding of the lubrication and the lubricant characteristics is achieved through a series of measurements from sensors mounted in this experimental set-up [2, 3, 8, 9].

In view of the above effects, a parametric study of different lubricants is presented, with results focused on minimum oil film thickness and friction, measured with a capacitance sensor and a force sensor respectively [10].

2. EXPERIMENTAL SET-UP

The test rig structure provides easy access to the ring-liner interface. In Figures 1 and 2 the photo and schematic of the simulation test rig is shown. Within the test rig, the speed, load and temperature can be adjusted.

The liner is driven by an electric motor coupled to the main drive train via rubber couplings. Reciprocation is achieved via a crank mechanism. Liner velocity is sinusoidal [1, 8, 9, 10].

For the minimum oil film thickness measurements, a capacitance sensor is used. This electrical method is a very popular technique for measuring oil film thickness [2, 8, 9]. The capacitance is directly proportional to the surface area and inversely proportional to their separation, which is around 30 microns. The sensor is mounted in such a way that the lubricant film can be measured throughout the 50 mm stroke regardless of the reciprocating velocity. The signal acquired from the custom made capacitance sensor is taken to a Capacitec signal conditioning unit, which converts the signal output to voltage and then is recorded via the data acquisition system. Films up to 10 microns thick can be measured with this popular technique [11]. Development of the lubricant film begins as the liner accelerates away from the top dead center. Close to the dead center of the stroke, asperity interaction between the surfaces remains significant but the squeeze film effect also takes place resulting in beneficial load support, as it is supported partly by the lubricant present in the contact. This region corresponds to the mixed lubrication regime and as velocity increases, the surfaces separate, asperity interaction decreases and the regime is full film-hydrodynamic. From near mid-stroke to bottom dead center, the opposite happens. As velocity lowers the regime from hydrodynamic turns to mixed and further on, the surfaces cannot separate and the lubrication returns to mixed lubrication. At this point the developed forms of cavities diminish into bubbles and the effect of the squeeze film takes place at the other end of the stroke [1, 8, 9, 12].

Friction is measured by a force measuring sensor (load cell), PCB 208B sensor, which is very sensitive to small displacements of the ring assembly due to axial friction during the reciprocating motion. Through the signal amplifier, the signal is being recorded from the data acquisition system.

In Figures 1 and 2 a schematic of the experimental set-up is shown accompanied by a photo.

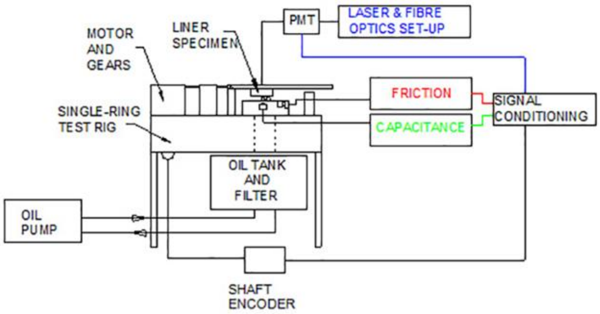

Figure 1. Schematic of the single-ring test rig [1, 3]

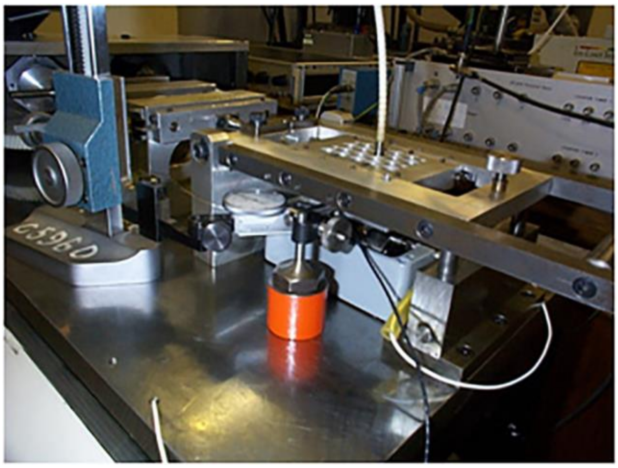

Figure 2. Photo of the single-ring test rig [1]

Figure 3(a) shows a close up of the test rig with the sensors when the liner surface is removed and in Figure 3(b) a 3-D schematic of the test rig which is focused on the mounting of the sensors.

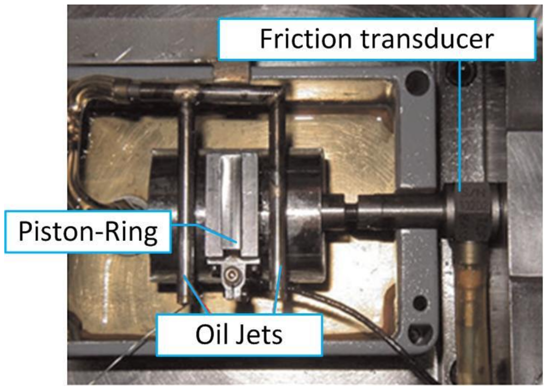

(a)

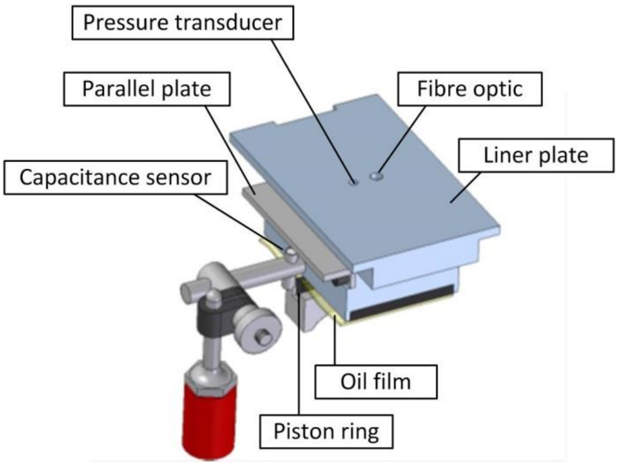

(b)

Figure 3. (a) Top view photo of the sensors layout and (b) 3D schematic of the capacitance measurement with the magnetic holder and the flat surface on top of the capacitor [2]

The load cell of the friction sensor, as shown in Figures 2 and 3, is mounted outside the oil bath [2, 10]. This movement results in tension or compression of the transducer and the tests, as validated by the capacitance minimum film thickness measurements show friction peaks close to the dead centers, where the lubrication is boundary and mixed (boundary and elastohydrodynamic). Increased surface separation decreases asperity contact in boundary lubrication conditions, which is evident as a lowering of the friction spike in the friction signal as it is acquired throughout the stroke [5].

Tested Lubricant Properties

For the parametric study the following set of six lubricants were used, as shown in Table 1.

Table 1. Oils tested for temperature investigations

Blend Code	003B	006E/02	005A/02	002A/02
Grade	0W-30	0W-40	0W-20	10W-40
HTHS (mPa s)	3.30	3.4	2.14	4.05
V_{100} (cSt)	12.16	12.8	6.04	14.97
V_{40} (cSt)	68.93	66.8	31	97.8
VI	182	196	146	160

The temperature effect was studied so that the oil behaviour under high temperature testing could be determined. The expected trend is that oil film decreases as oil temperature raises, i.e. similar behaviour as with the viscosity decrease. So, this study is going to be an investigation of viscosity and physical-chemical properties on minimum oil film thickness (MOFT) measurements [8].

3. RESULTS

3.1 Temperature Parametric Lubricant Testing

According to Walther's equation the kinematic viscosity of oil varies with temperature.

$$\log\log(v+0.7)=A+B\log T \qquad (1)$$

where v is the kinematic viscosity and T the temperature in Kelvin. A, B are constants different for each oil tested. Figure 4 shows the effect of temperature on the viscosity of oil 3B, that further explains the difference in oil film thickness measurements with the capacitance technique for the varying temperatures.

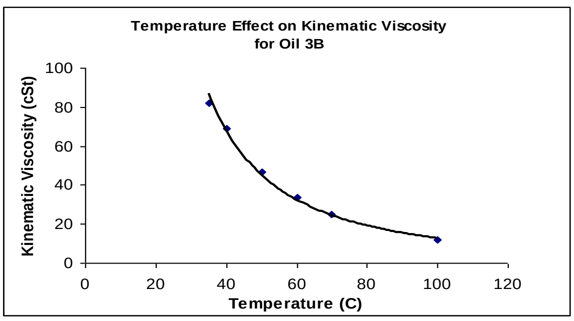

Figure 4. Temperature effect on kinematic viscosity, oil 3B

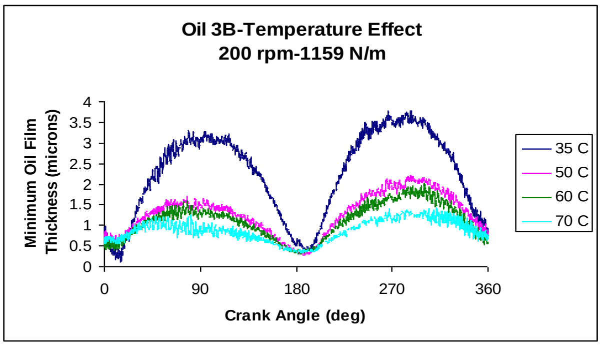

(a)

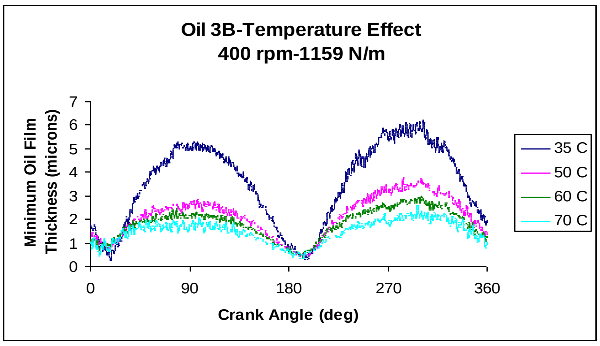

(b)

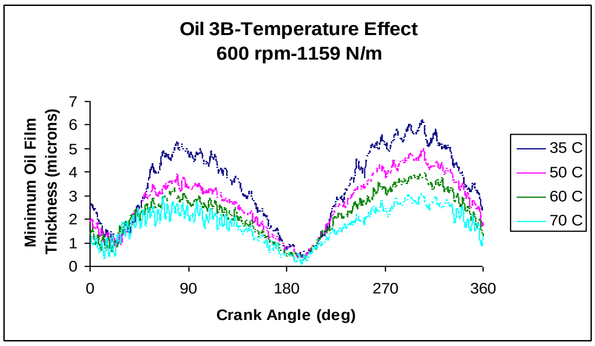

(c)

Figure 5. (a) Temperature effect at 200 rpm, 1159 N/m, (a) at 400 rpm, 1159 N/m and (c) at 600 rpm, 1159 N/m, oil 3B

The temperature results for oil 3B show the following trend: at higher temperatures the minimum film thickness decreases. There is a big gap between the ambient oil temperature (35^{o}C) and the higher ones and this is observed in every graph for oil 3B (Figures 5(a) - 5(c)). This "step" in all the speed cases can be interpreted by the viscosity variation with temperature seen in Figure 4. Viscosity changes dramatically from 35^{o}C to 50^{o}C. Afterwards it decreases again in a smoother curve. The oil film thickness decreases 46.58% (at 92.16 deg CA at 200 rpm) whereas the viscosity decreases 43.35% from 35^{o}C to 50^{o}C [8].

The results for oil 6E (Figures 6(a)-(c)) showed that the temperature effect on MOFT above 50°C is not comparable to the trend noticed for the previous oil 3B. Therefore for every speed test case in Figures 6(a) - (c), the minimum oil film thickness curves coincide. The viscosity variation with temperature according to Walther's equation (Figure 7) produced a similar curve for oil 6E as for oil 3B.

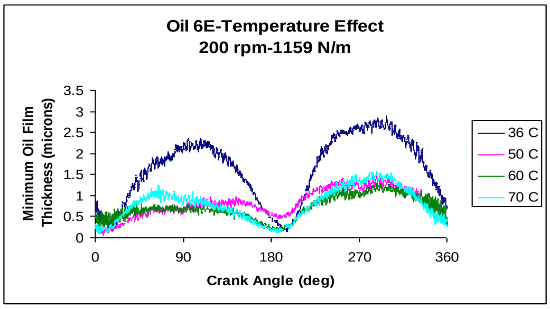

(a)

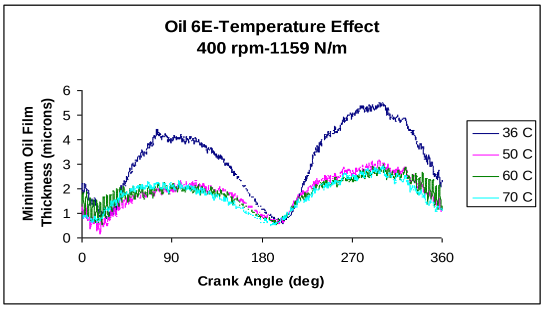

(b)

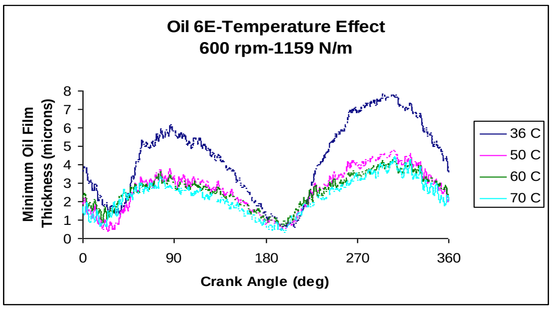

(c)

Figure 6. (a) Temperature effect at 200 rpm, 1159 N/m, (b) at 400 rpm, 1159 N/m and (c) at 600 rpm, 1159 N/m, oil 6E

Viscosity comparison between the two lubricants tested (3B and 6E) with rising temperature, showed that it has an increased value for oil 6E by 1% at 50°C, 2.6% at 60°C and 4.6% at 70°C. This slight increase by itself is not capable to justify the difference in the minimum oil film thickness temperature results between the two oils. It can be inferred by these results that the lubricant formulation-chemical properties can play an important role in changing the MOFT high temperature characteristics of a specific oil. The absolute oil film thickness measurement is greater in oil 3B than in 6E. The higher viscosity index of oil 6E does not justify by itself an increase in the minimum oil film thickness where it was shown that for higher viscosity index (VI), the minimum oil film thickness increases for the same grade of oil (0W-30) [2, 8].

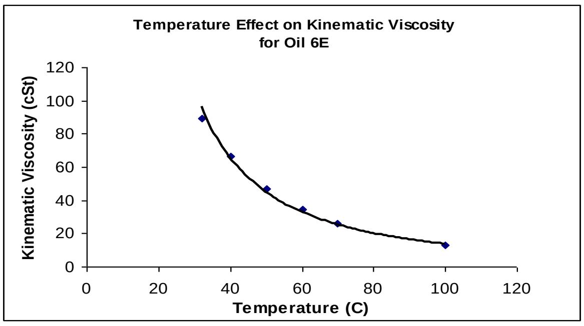

Figure 7. Temperature effect on kinematic viscosity, oil 6E

For oil 5A (Figures 8(a)-(d)) a similar trend to the previous oils (6E and 3B) is noticed. This time though, at very low speeds, MOFT has a low absolute value, maximum 2.7 μm at 200 rpm (Figure 8(a)), 33°C, compared to oils 6E and 3B. Temperature effect on viscosity provides an explanation regarding oil 5A behaviour, in Figure 9, where the viscosity values are almost 50% lower than oil 3B and 53% lower than oil 6E at 35°C. Similar trend is noticed for the high speed test (600 rpm – Figure 8 (d)). Higher viscosity results cannot be distinguished from the low viscosity ones at high temperature. At 600 rpm the reduction from ambient to 50°C is 16% compared to 200 rpm (Figure 8(a)) where the reduction in MOFT magnitude is 23%. Similar results were presented for oil 3B. At high speed (600 rpm – Figure 5(c)) the temperature effect does not have such a strong effect as at low speeds, the percentages this time at 600 rpm are 34% and 53% (reduction) respectively at 200 rpm (Figure 5 (a)). Oil 6E on the other hand shows greater stability in this aspect. MOFT reduces at 600 rpm by 47% (Figure 6(c)) which is comparable to 55% reduction at 200 rpm (Figure 6 (a)).

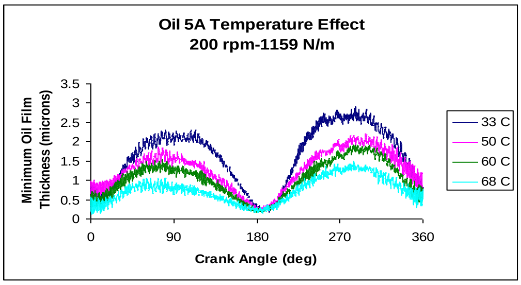

(a)

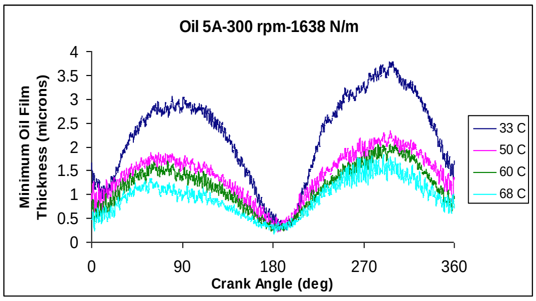

(b)

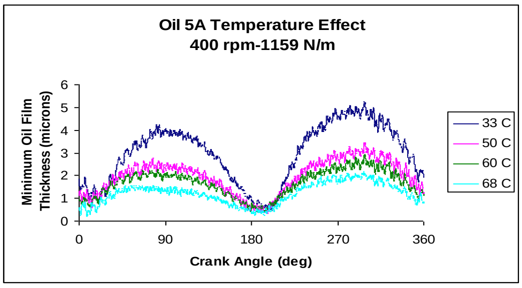

(c)

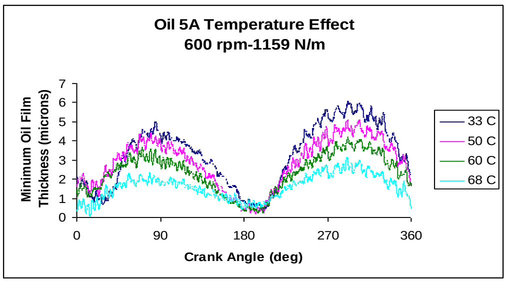

(d)

Figure 8. Load effect – high temperature testing, oil 5A: (a) at 200 rpm, 1159 N/m, (b) at 300 rpm, 1638 N/m, (c) at 400 rpm, 1159 N/m and (d) at 600 rpm, 1159 N/m

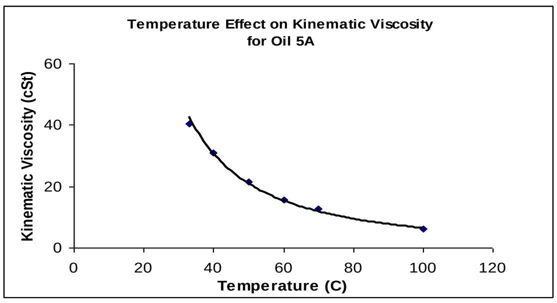

Figure 9. Temperature effect on kinematic viscosity, oil 5A

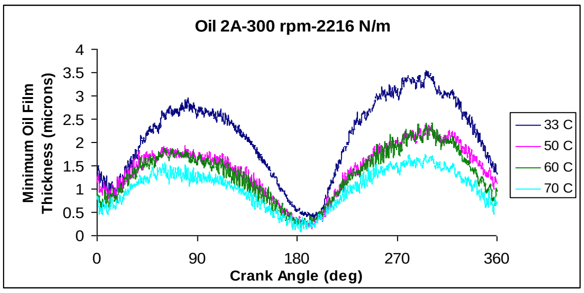

(a)

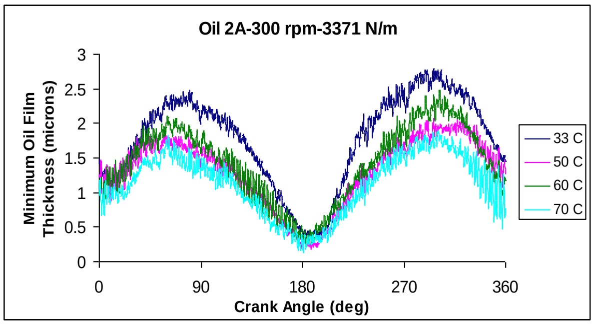

(b)

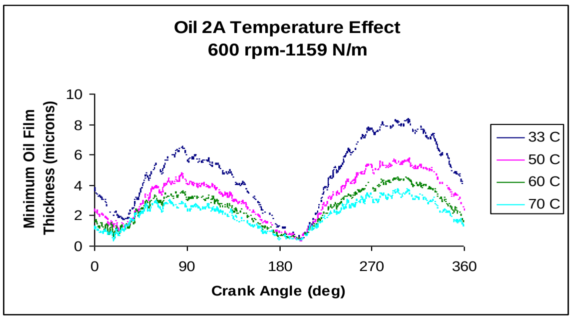

(c)

Figure 10. Load effect – high temperature testing, oil 2A: (a) at 200 rpm, 2216 N/m, (b) at 300 rpm, 3371 N/m and (c) at 600 rpm, 1159 N/m

Additionally, oil 5A does not have a similar behavior to 2A (compare Figure 8 (d) to Figure 10 (c)). Oil 2A follows the trends noticed for oils 3B and 6E that have considerably higher VI, V_{100}, V_{40} and HTHS values than oil 5A (see oil properties in Table 1). Figure 9 shows temperature effect on viscosity for oil 5A.

3.2 Load Effect in oil film Thickness at High Temperature

Oil 5A was tested for the effect of load on oil film thickness at high temperature. The results show the trend at 300 rpm (Figures 11 (a)-(c)) and 500 rpm (Figures 12 (a)-(c)). In all cases, there is a remarkably strong effect of load on the minimum oil film thickness, regardless the temperature. Eventually, as load gets higher (Figures 11 (b)-(c) and 12 (b)-c)) the temperature effect on minimum oil film thickness becomes less than in the low load test cases (they represent the temperature effect at 1159 N/m) [8]. The trend noticed is that the film thickness has a certain value (considerably low) which decreases by a slight margin for the highest temperature test case (68°C – Figures 11(a)–(c) and Figures 12(a)- (c)).

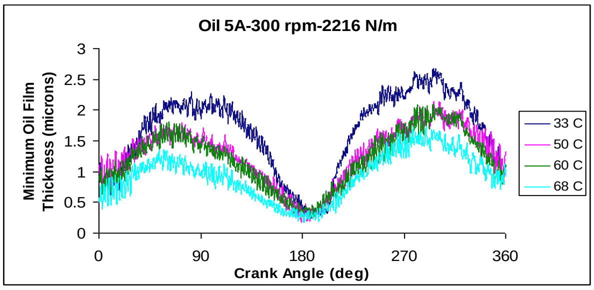

(a)

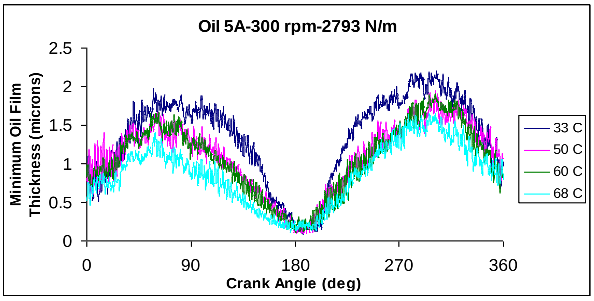

(b)

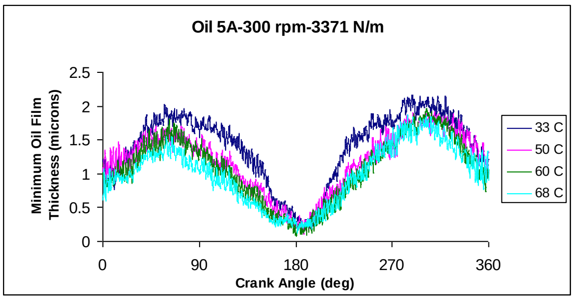

(c)

Figure 11. Load effect – high temperature testing, oil 5A: (a) at 300 rpm, 2216 N/m, (b) at 300 rpm 2793 N/m and (c) at 300 rpm 3371 N/m

According to Figures 11 (a)-(c) and 12 (a)-(c), MOFT is smaller close to BDC than at TDC which, in turn, has an effect on the squeeze film. The squeeze film itself, is not affected in terms of crank angle appearance in the high temperature cases. There is a slight shift towards the dead centers compared to the ambient temperature results (33°-35°C) and the load tests, in general, also showed that at high loads there is a marginal shift of the MOFT curves towards the dead centers [8].

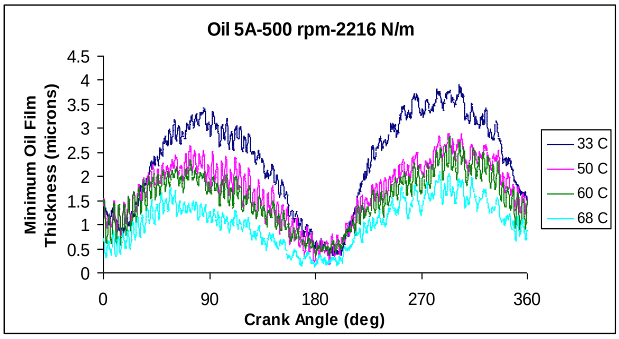

(a)

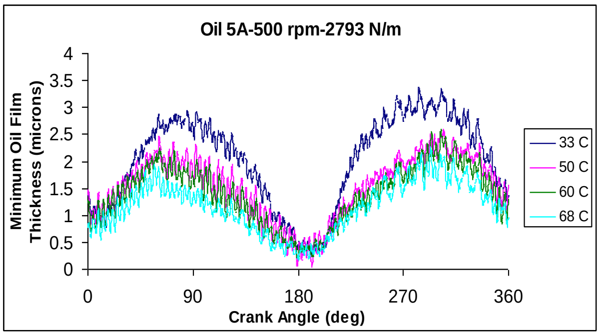

(b)

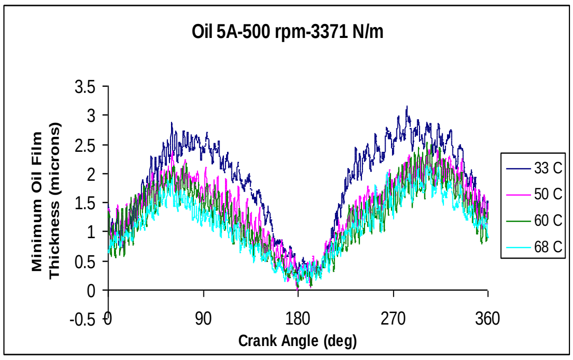

(c)

Figure 12. Load effect – high temperature testing, oil 5A: (a) at 500 rpm, 2216 N/m, (b) at 500 rpm, 2793 N/m and (c) at 500 rpm, 3371 N/m

The figures below show (Figures 13 (a)-(c)) how load is affecting the minimum oil film thickness, for oil 2A, with temperature variation. Oil 2A which has greater V_{40} and V_{100} (and VI) than oil 5A gave similar results, i.e. the temperature effect on MOFT is not evident at high loads.

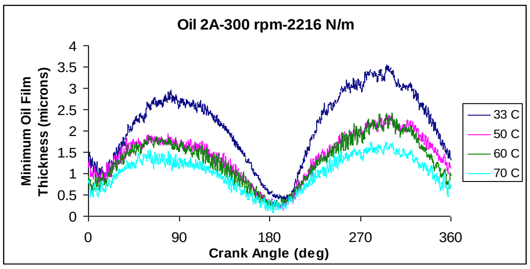

(a)

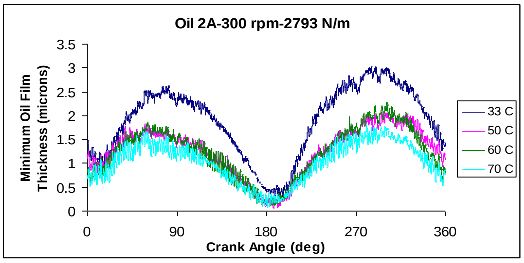

(b)

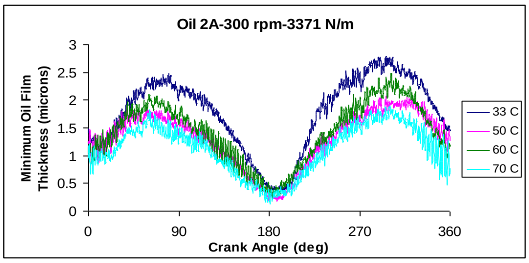

(c)

Figure 13. Load effect – high temperature testing, oil 2A: (a) at 300 rpm, 2216 N/m, (b) at 300 rpm, 2793 N/m and (c) at 300 rpm, 3371 N/m

3.3 Effect of High Temperature on MOFT for the Tested Oils at Different Speeds

The absolute value of the minimum oil film thickness can be directly compared to each one of the different oils used. The effect of high temperature is taken into account for these comparisons and graphs are presented for all the oils tested at high temperatures, at 50° C (Figs. 14(a)-(c)), at 60° C (Figs. 15(a)-(c)) and 68°-70°C (Figs. 16(a)-(c)).

(a) 50°C

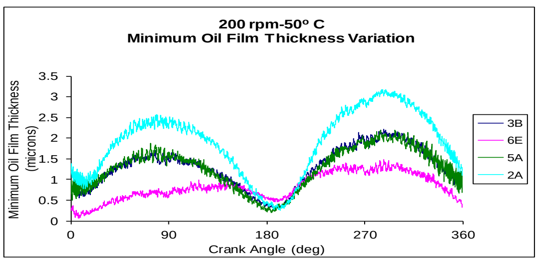

(a)

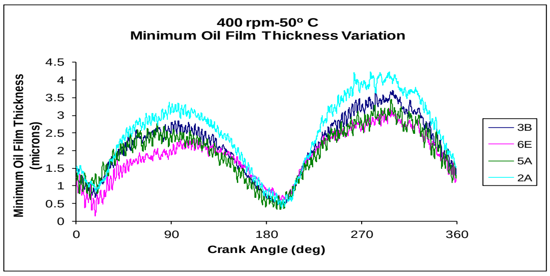

(b)

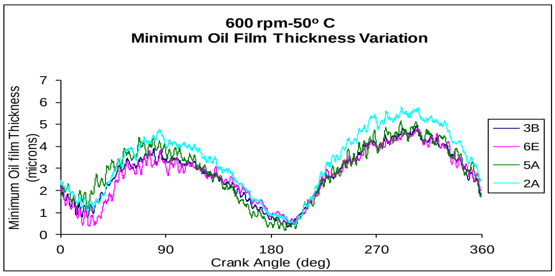

(c)

Figure 14. MOFT variation: (a) at 200 rpm, (b) at 400 rpm and (c) at 600 rpm – 50°C for all tested oils

(b) 60°C

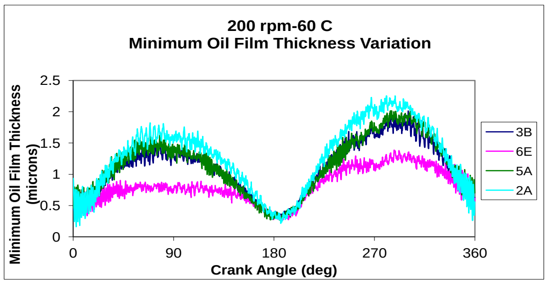

(a)

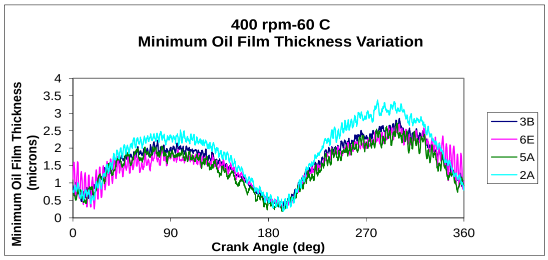

(b)

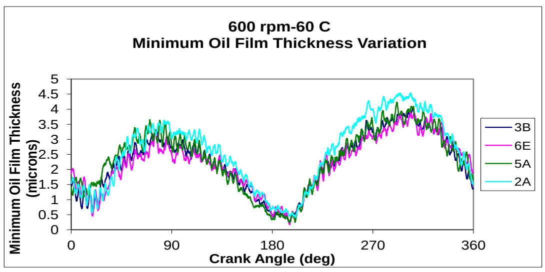

(c)

Figure 15. MOFT variation: (a) at 200 rpm, (b) at 400 rpm and (c) at 600 rpm – 60°C for all tested oils

(c) 68°-70°C

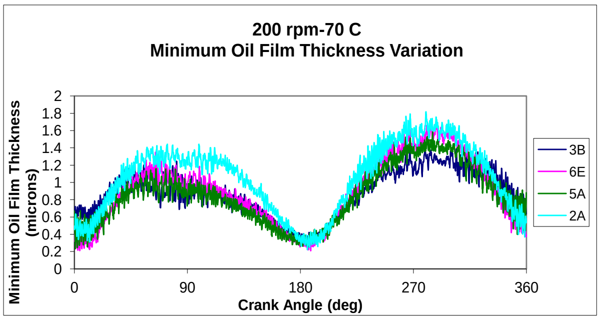

(a)

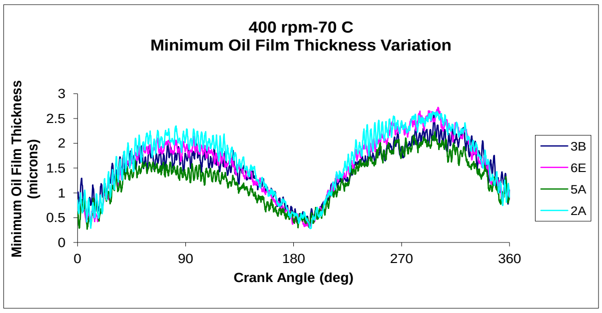

(b)

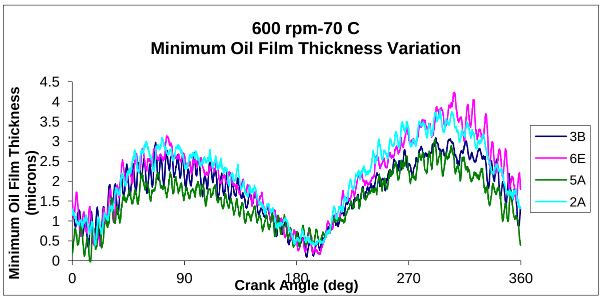

(c)

Figure 16. MOFT variation: (a) at 200 rpm, (b) at 400 rpm and (c) at 600 rpm – 68°-70°C for all tested oils

The majority of the testing showed that for the above series of experimental data (Figures 14 (a)-(c), Figures 15 (a)-(c) and Figures 16 (a)-(c)), oil 2A had the thickest film as the temperature varies in comparison to oils 6E, 5A and 2A. According to viscosity variation with temperature curves, oil 2A has the highest viscosity of all the tested lubricants at all temperatures. Oil 2A produces a thicker MOFT, which is more pronounced at 50°C (Figures 14 (a)-(c)) whereas at 60°C (Figures 15 (a)-(c)) and 68°-70°C (Figures 16 (a)-(c)) the MOFT curves of the tested oils become more even; oil 2A still producing marginally thicker films. Table 2 shows the viscosity variation for each oil tested at 50°, 60° and 70° C:

Table 2. Viscosity properties for the temperature-load effect experiments and VI properties

Blend Code		002A /02	005A /02	006E /02	003B
Viscosity (cSt)	50 °C	64.34	21.49	47.13	46.61
	60 °C	45.76	15.72	34.55	33.65
	70 °C	33.46	12.60	26.29	25.09
VI		160	146	196	182

3.4 Friction Experiments

The following test is considered to give evidence to the high friction peaks noticed when the oil viscosity changes. Oil 2A has been tested at maximum load (3371 N/m):

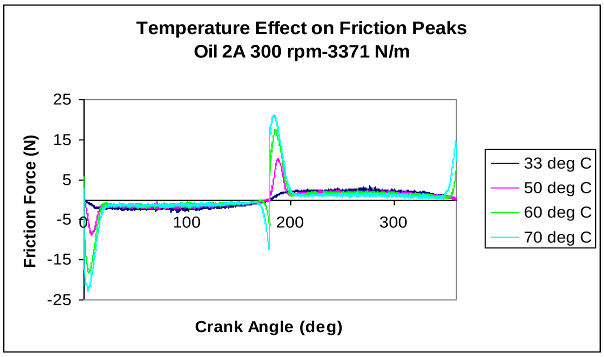

Figure 17. High temperature friction results for oil 2A

According to Figure 17, high friction results are taken at flow reversal points for the high temperature testing. The boundary and mixed lubrication region at high loads and high temperatures is more extensive. Friction force increases at high temperature when the interface between the liner surface and the piston ring is under these conditions (boundary and mixed). The formulation of the lubricant is an important factor because at higher temperatures the additives of the lubricant react in a different way with the surfaces in contact, thus increasing or reducing the effect of the resulting asperity contact. Additionally, friction force at the dead centres is reversing rapidly (steeper curve) compared to the ambient temperature results (33 °C).

4. CONCLUSIONS

This parametric study showed that there is a directly comparable amount of decrease in the minimum oil film thickness with increasing temperature. Results showed:

- MOFT is strongly viscosity dependent. Temperature affects capacitance offset [2].
- Lubricant chemistry plays an important role in MOFT measurements. At high rpm, however, it is not evident as at low rpm.
- The squeeze film seems to be partially affected for the different lubricants. There are differences between TDC and BDC, that are evident at high temperatures and high loads (shift towards dead centers) for each lubricant. The dynamic characteristics of the test rig and its geometry affect the lubrication but since this asymmetry in MOFT is more pronounced (Figs 11 and 12), it can be inferred that the squeeze film is altered, not in crank angle degrees (location) but in absolute thickness measurements.
- High temperature testing is combined with higher friction and extensive boundary and mixed lubrication areas compared to ambient temperature results. A rapid friction increase is also noticed for the boundary lubrication area.
- For higher VI, MOFT increases for the same grade of oil [2].
- Load and speed effect on cavitation initiation and number of (string) cavities [1] might accordingly apply to temperature effect results.

ACKNOWLEDGEMENT

This study was funded by a scholarship from the Greek State Scholarship Foundation (S.S.F). It is part of a project at CITY University, London, Research Center for Energy and the Environment, sponsored by CASTROL/BP. Many thanks are due to Professor C. Arcoumanis, (FREng, City University, London), supervisor of the project. The author gratefully acknowledges these contributions.

REFERENCES

[1] P. Dellis: LIF measurements in a single – ring test rig: Evidence of cavitation and the effect of different operating conditions and lubricants on cavitation patterns and initiation, Int. J. of Engine Research, 2019.

[2] P. S. Dellis: Piston-ring performance: limitations from cavitation and friction, International Journal of Structural Integrity, paper accepted for publication, IJSI-09-2018-0053.R1, 2019.

[3] P. Dellis: Aspects of Lubrication in a Reciprocating Single-ring Test Rig and Further Implementation to Engine Applications, Tribology in industry, Vol. 39, No. 2, pp. 260-269, 2017.

[4] A. Rastogi, R.K. Gupta: Effect of shear thinning on cavitation in lubricant films, SAE paper 922286, 1992.

[5] G. Stachowiak, A. W. Batchelor: *Engineering Tribology*, Butterworth-Heinemann, Elsevier, 2000.

[6] O. Akalin, G. M. Newaz: Piston ring-cylinder bore friction modelling in mixed lubrication regime. Part II: correlation with test bench data, Transactions of ASME, Journal of Tribology, 123, pp. 211–218, 2001.

[7] D. D. Joseph: Cavitation and the state of stress in a flowing liquid, J. Fluid Mech, Vol. 366: pp. 367–378, 1998.

[8] P. Dellis: *Aspects of lubrication in piston cylinder assemblies*, PhD thesis, Imperial College London, Department of Mechanical Engineering, London, 2005.

[9] P. Dellis, C. Arcoumanis: Cavitation development in the lubricant film of the piston-ring assembly, Proc. IMechE, Part J: J. Eng. Tribology, Vol. 218, pp. 157–171, 2004.

[10] P. Dellis: Effect of friction force between piston rings and liner: a parametric study of speed, load, temperature, piston-ring curvature, and high-temperature, high-shear viscosity. Proc IMechE, Part J: J Engineering Tribology, Vol. 224, No. 5, pp. 411–426, 2010.

[11] N. Grice, I. Sherrington: An Experimental Investigation Into the Lubrication of Piston Rings in an Internal Combustion Engine: Oil Film Thickness Trends, Film Stability and Cavitation, SAE 930688, 1993.

[12] N. W. Bolander, B. D. Steenwyk, F. Sadeghi, G. R. Gerber: Lubrication regime transitions at the piston ring–cylinder liner interface, Proc. IMechE, Part J: J. Engineering Tribology, Vol. 219, No. 1, pp. 19–31, 2005.

Serbian Tribology Society

SERBIATRIB '19

16th International Conference on Tribology

Faculty of Engineering University of Kragujevac

Kragujevac, Serbia, 15 – 17 May 2019

COEFFICIENT OF EXPLOSION OF GRAPE OIL REPAS IN RESPECT OF VARIETY, CONTENT OF HUMIDITY AND SURFACE

Ranko KOPRIVICA[1], Biljana VELJKOVIĆ[1,*], Jan TURAN[2], Dragoslav ĐOKIĆ[3], Dušan RADIVOJEVIĆ[4], Srećko ĆURČIĆ[5], Zoran MILEUSNIĆ[4], Igor BALALIĆ[6]

[1]Faculty of Agronomy Cacak, University of Kragujevac, Serbia

[2]Faculty of Agriculture University of Novi Sad, Serbia

[3]Institute for fodder crops, Krusevac, Serbia

[4]Faculty of Agriculture University of Belgrade, Serbia

[5]Faculty of Technical Sciences Cacak, University of Kragujevac, Serbia

[6]Institute of field and vegetable crops, Novi Sad, Serbia

* Corresponding author: biljavz@kg.ac.rs

Abstract: *Knowing the coefficient of friction of bio material is important in determining the angle of the grain elevator elevator when designing combines, as well as the angles of gravity tables and pipes in seed finishing. The basic characteristic of biological materials, or seeds of agricultural crops, is that they differ in their physical and morphological characteristics. Therefore, the friction depends on: the types of plants, variety, shape, dimensions and seed content, the humidity of the seed, the intensity of the normal force on the substrate and the roughness of the substrate. The paper presents the results of the study of the influence of individual factors (varieties, water content of the grain and the type of substrate) and their interactions on the grain friction coefficient. The domestic varieties that are grown in Serbia are selected for testing the fruiting grain fruity: Banaćanka, Jasna and Slavica. The experimental measurement of the static coefficient of grain slip friction was done using the level of the mechanical device Tribometr. Plastic, plywood, galvanized, steel, aluminum and stainless steel sheet are made for the experiment purposes. Research was carried out with different water content in grains: 6%, 11%, 16% and 24%. The variety Banaćanka had a lower friction coefficient compared to Jasna and Slavica varieties on all substrates and with all the water content of the grain. It was found that with the increase of water content in the grain, a significant increase in the friction coefficient of the grains of the tested varieties on all substrates was achieved. The highest friction coefficient for all water content of the grains of the tested varieties was on the base of the plywood board, and the smallest on the base of stainless steel sheet.*

Keywords: *oilseed rape, variety, static coefficient of friction, substrate, water content in grains.*

1. INTRODUCTION

Oilseed rape is among the four most important oil plants in the world next to soya, palm and sunflower. Oilseed rape is grown for grains containing 40-48% oil and 18-25% protein. Rape oil is used in people's eating, for the production of biodiesel, in the soap industry, for lubricating parts in machinery assemblies, etc. After grain pressing and oil extraction, oil rich cakes with proteins used in domestic animal feeding are obtained [1], [2], [3].

The development and design of agricultural mechanization and seed treatment equipment required the need to know the friction properties of bio-materials. Knowing the static coefficient of friction is important when determining the angle at which elevators and gravity tubes can be positioned for the smooth transport of grain, as well as the angles of gravity tables in seed finishing.

The basic characteristic of biological materials, or seeds of agricultural crops, is that they differ in their physical and morphological characteristics. During harvest, and even after harvest in the process of finishing, the seed moves on a surface, resulting in friction. The value of the friction coefficient depends on: the types of plants, variety, shape, dimensions and material of the individual seeds, the humidity of the seed, the intensity of the normal force on the substrate and the roughness of the substrate [4], [6], [7], [8] [9], [10], [11], [12], [13].

The static coefficient of friction of solid materials depends on the roughness of the friction surfaces and their microreef expressed by the number, shape, depth, width and surface of the holes, as well as the number and height of the ridge. Experiments have shown that the static friction coefficient decreases with decreasing roughness, ie the mean surface roughness (Ra) [14], [15]. Based on the studied friction parameters [15], they modeled the relief surface in order to reduce friction.

In addition to the roughness of the friction of solid materials, the nature of the surface of the body that touches is influenced, which depends on the composition of the material and the way of processing the base substrates. Surfaces with the same roughness values have different friction coefficients depending on the surface treatment of the substrate surface [14] [15], [16].

Research on the surface roughness of fruiting surfaces significantly influences the static friction coefficient of wheat grains of Jensen [11]. The smallest coefficient of wheat grain static friction was on the tar surface of roughness Ra = 0.93 µm, and the highest on Ra = 5.86 µm and ranged from 0.29 to 0.45.

Many researchers examined the static coefficient of friction of agricultural crops on various substrates, citing only the material from which the substrate was made, but not the values of the unevenness and the method of processing. Therefore, for some authors, the values of the coefficient of seed friction differ in the same types of plants and varieties on the same substrates. The authors also established a positive relationship between the friction coefficient and the content of water in the grains [4], [6], [7], [8], [12], [13], [17].

The only way to determine the precise static friction coefficient coefficient between the substrate of the two materials is in the labs using experiments using different methods [13], [14], [18], [19]. However, on the basis of the results of the previous measurement, the authors [13] developed mathematical models for determining the coefficient of friction in silos in the scaling and processing of wheat seeds. According to the above-mentioned authors, the developed models are sufficiently reliable to directly determine the coefficient of friction of wheat grain under conditions of storage and processing without the need for actual measurement.

The aim of the research is to determine the static coefficient of grain friction of three varieties of rapeseed on various substrates and water content of grains, and to determine their significance by means of statistical analysis of the trophactorial experiment. The obtained friction coefficient results can be used in the construction of transport and separation bodies on combines and equipment for storage and processing of seeds.

2. MATERIAL AND METHOD OF WORKŽ

To measure the coefficient of static friction, a pure grain of three varieties of rapeseed Banaćanka, Jasna and Slavica was used. All three varieties were created at the Institute of Field and Vegetable Crops in Novi Sad. The grain is cleaned on the Dakota selector from the presence of foreign matter (particles of soil, dust, stones, weed seeds, parts of plants, damaged grains). Determination of the static coefficient of friction of the rape seed was carried out with a humidity content of 6%, 11%, 16% and 21%.

The initial content of grain water was determined using a standard drying method in a drying oven at a temperature of 105°C. After drying, the samples with the grain were placed in a desiccator to cool for 15-20 minutes. The samples were after cooling, measured on a scale and calculated by the initial water content in the grain. By adding and mixing a certain amount of distilled water with grain, a higher content of water in grains of 11%, 16% and 21% was achieved. The amount of water added to the grain was calculated according to the following formula [4], [6], [7], [13].

$$w_2 \quad w_1 x \, \frac{M_2 \quad M_1}{100 \quad M_2} \tag{1}$$

Where: w_2 is the weight of the distilled water (kg), w_1 weight of the initial sample (kg), M_1 initial water content in the grain (%), and M_2 the desired water content in the grain (%).

Marked grain samples were placed in plastic bags and stored in a refrigerator for at least 7 days at a temperature of 5°C. During storage, the moisture was evenly distributed to all the grains in the sample, so that a uniform sample was obtained with the same moisture content. Before the start of the measurement, the samples were taken out of the fridge and left for two hours at room temperature. By re-measuring the grain mass after storage in the refrigerator, the true grain moisture for all varieties was determined (Table1). After that, the determination of the coefficient of static friction of the grain of rapeseed was started.

The values of the static friction coefficient coefficient were experimentally determined using a hair level on a mechanical device Tribometer T1 constructed at the Faculty of Mechanical Engineering in Kragujevac [14], [18], [19]. For the needs of the experiment, substrates made of different materials were made: galvanized sheet, steel sheet, stainless steel, aluminum sheet, plastic and plywood. Prior to each measurement of grain samples, the substrates were purified by distilled water and wiped with a dry cotton cloth to clean all impurities from them [11], [19]. To determine the friction coefficient coefficient of the same grain mass, the plastic hollow is placed in the hollow, which is placed on the flat Tribometer flat and slightly raised from the substrate.

Figure 1. Friction coefficient measuring device Tribometar 1

The analysis of the obtained data of the coefficient of the rapeseed rapeseed friction fracture was analyzed by the method of variance analysis (ANOVA) of the trophactorial experiment. Testing the significance of the difference between the mean values of the investigated properties (factors) was determined using the LSD test, for a level of significance of 5% and 1%.

3. RESULTS AND DISCUSSION

The content of grain water is a physical property on the basis of which the beginning of the harvest is determined, and after harvest the parameters in the process of drying and storing grains in order to preserve its quality. From the content of the grain moisture content and the operating mode of the combustion chamber of the combine depends on the quality of the performance of the grain, or the degree of grain damage during the harvest. Based on the known initial grain moisture content of the harvested grain in the field, the parameters and length of the grain drying process are determined. During storage of grain in warehouses, monitoring of the humidity and grain conditions, certain technological procedures are undertaken in order to preserve its quality.

During the study of the static coefficient of friction, the desired content of water in the genus Banaćanka, Jasna and Slavica varieties was approximate to the measured values. The indicated values of water content in the grain were achieved in the laboratory by the indicated method (Table 1.)

Table 1. Predicted and measured mean values of water content in rape seed

Predicted values of water content in grains *w* (%)		6	11	16	21
Realized mean value content of water in the grain *w* (%)	Banaćanka	6,04	11,44	16,03	21,17
	Jasna	5,82	11,15	15,91	20,90
	Slavica	5,98	10,73	15,97	20,46
The mean value of water content in the grain *w* (%)		5,74	11,11	15,97	20,84

The friction coefficient varied considerably under the influence of all three factors (Table 2), as well as the interaction of their interaction between the substrate / variety and the substrate / water content of the grains.

The smallest grain friction coefficient was measured in the Banaćanka variety (0,288), and it significantly differed from the Jasna variation (0,322), and Slavica (0,321), on all substrates and with all the water content of the grain.

The smallest grain friction coefficient was measured in the Banaćanka variety (0,288), and it significantly differed from the Jasna variation (0,322), and Slavica (0,321), on all substrates and with all the water content of the grain. The results of the survey [7] for the varieties Samurai, Jet Neuf and Capitol are also confirmed by the differences between the varieties of oilseed rape, irrespective of the types of water and the content of water in the grain, the coefficient of friction. The most significant coefficient of friction was the Capitol variety and the smallest variety of Samurai on all substrates at all grain moisture levels. Also, authors [6] found for the Orient least the smallest, and for the SLM variety, the greatest coefficient of static friction, regardless of the substrate and the content of the water in the grain.

Table 2. Friction coefficient depending on the type of substrate, variety and water content in the grain

Substrate type (A)	**n**	$\overline{X}$ $S\overline{x}$
Galvanized sheet	48	0,302±0,004^{c}
Steel sheet	48	0,308±0,006^{bc}
Prohrom sheet	48	0,271±0,005^{d}
Aluminum sheet	48	0,313±0,006^{b}
Plastics	48	0,331±0,007^{a}
Plywood	48	0,337±0,007^{a}
Sorta (B)		
Banaćanka	96	0,288±0,004^{b}
Jasna	96	0,322±0,004^{a}
Slavica	96	0,321±0,005^{a}
Vlažnost (C)		
6%	72	0,264±0,003^{d}
11%	72	0,298±0,003^{c}
16%	72	0,325±0,004^{b}
21%	72	0,354±0,005^{a}
Anova	***df***	
A	5	**
B	2	**
C	3	**
A ***x B***	10	**
A ***x C***	15	**
B ***x C***	6	Ns
A ***x B x C***	30	**

Mean values per columns marked with the same letters do not differ (P> 0.05) based on the LSD test.
* F-test significant at P <0.05; ** F-test significant at P <0.01; ns -F-test is not significant (P> 0.05).

Regardless of the variety and type of substrate, the static coefficient of friction increased significantly with the increase in water content in the grain.

In all substrates, irrespective of the variety, with the lowest content of grain water (6%), the smallest friction coefficient of 0.264 was significantly increased from 0.298 (11%) to 0.325 (16%), in order to achieve the highest value of 0.354 at the highest water content in a 21% grain (Table 2).

Therefore, the increase in the grain moisture content significantly influenced the increase in the coefficient of grain friction coefficients on all substrates. As the moisture content increases, the grains become sticky, and because of this, the cohesive forces between the grain and the contact surface increase, leading to an increase in the friction coefficient. Research on other authors [4], [6], [7], [20] confirms that the grain friction coefficient increases with the increase in the content of water in the beans. According to the results [6], the static coefficient of friction on different substrates increases non-linearly with increasing water content in the grain.

Table 3. Friction coefficient depending on the type of substrate and variety.

Substrate type	N	Friction coefficient $\overline{X}$ $S\overline{x}$		
		Sort		
		Banaćanka	Jasna	Slavica
Galvanized sheet	16	$0{,}293\pm 0{,}007^{hi}$	$0{,}312\pm 0{,}009^{efg}$	$0{,}301\pm 0{,}007^{gh}$
Steel sheet	16	$0{,}276\pm 0{,}009^{j}$	$0{,}329\pm 0{,}008^{cd}$	$0{,}319\pm 0{,}011^{def}$
Stainless steel sheet	16	$0{,}247\pm 0{,}009^{k}$	$0{,}285\pm 0{,}008^{ij}$	$0{,}283\pm 0{,}006^{ij}$
Aluminum sheet	16	$0{,}294\pm 0{,}009^{hi}$	$0{,}324\pm 0{,}008^{d}$	$0{,}322\pm 0{,}010^{de}$
Plastics	16	$0{,}308\pm 0{,}012^{fg}$	$0{,}337\pm 0{,}009^{bc}$	$0{,}347\pm 0{,}013^{ab}$
Plywood	16	$0{,}312\pm 0{,}010^{efg}$	$0{,}346\pm 0{,}011^{ab}$	$0{,}354\pm 0{,}014^{a}$

Note: The mean values per columns marked with the same letters do not differ (P> 0.05) based on the LSD test.

On average for all varieties and water content in the grain, the highest coefficient of friction was on the surface of plywood plate 0.337 and plastic 0.331. On rough and uneven surfaces, the substrate from the plywood plate and the plastic grain tend to slide, so the greatest friction coefficients are measured on them. There was no difference in the coefficient of friction between the substrate of aluminum 0.313 and the steel sheet 0.308 as well as the galvanized 0.302 and steel sheet (Table 2.) However, there is a deviation in the Banančanka variety between the coefficient of friction on the substrates of aluminum and steel sheet (interaction of the substrate / sort). In all varieties, there was also a difference in the coefficient of friction between galvanized and steel sheet (interaction of the substrate / variety) (Table 3). It was expected that the surface surfaces of the galvanized and steel sheet substrates, similar roughness, however, the results of the substrate/variety interactions did not confirm this. This can be explained by the fact that the surface of the steel sheet substrate is greater than the roughness of the galvanized sheet surface.

Table 4. Friction coefficient depending on the type of substrate and water content in the grain

Substrate type	n	Friction coefficient, $\overline{X}$ $S\overline{x}$			
		The content of water in the grain			
		2014 year			
		6%	11%	16%	21%
Galvanized sheet	12	$0{,}262\pm 0{,}004^{j}$	$0{,}295\pm 0{,}004^{gh}$	$0{,}315\pm 0{,}005^{f}$	$0{,}336\pm 0{,}005^{cde}$
Steel sheet	12	$0{,}264\pm 0{,}008^{j}$	$0{,}291\pm 0{,}010^{gh}$	$0{,}330\pm 0{,}009^{de}$	$0{,}347\pm 0{,}008^{bc}$
Stainless steel sheet	12	$0{,}232\pm 0{,}008^{k}$	$0{,}264\pm 0{,}007^{ij}$	0,288± 0,006h	$0{,}302\pm 0{,}005^{g}$
Aluminum sheet	12	$0{,}271\pm 0{,}007^{j}$	$0{,}302\pm 0{,}005^{g}$	$0{,}331\pm 0{,}006^{de}$	$0{,}350\pm 0{,}009^{b}$
Plastics	12	$0{,}274\pm 0{,}008^{ij}$	$0{,}312\pm 0{,}005^{f}$	$0{,}341\pm 0{,}006^{bcd}$	$0{,}392\pm 0{,}008^{a}$
Plywood	12	$0{,}284\pm 0{,}006^{hi}$	$0{,}321\pm 0{,}007^{ef}$	$0{,}347\pm 0{,}009^{bc}$	$0{,}397\pm 0{,}009^{a}$

Note: The mean values per columns marked with the same letters do not differ (P> 0.05) based on the LSD test.

The coefficient of friction on the plastic substrate did not differ from the coefficient of friction on the substrate of aluminum, steel sheet with the content of water in grains of 6% and 16%, as well as on the galvanized sheet with a water content of 6% grain content (substrate/water content) (Table 4). Most likely, when measuring the value of the friction coefficient, the water and oils content of the grain was transferred to the pores on the surface of the substrate on the plastic. Such a moist fret surface of the substrate has become smooth or rough roughness of the other substrates, except the substrate of stainless steel sheet. Up to the same conclusions came [13] in determining the friction coefficient of wheat grain.

The smallest friction coefficients of the grains of the tested varieties and all the water content of the grains were on the basis of stainless steel sheet (0,271). The smooth and flat-polished surface of stainless steel sheet allows the grain to slide smoothly over it without any resistance.

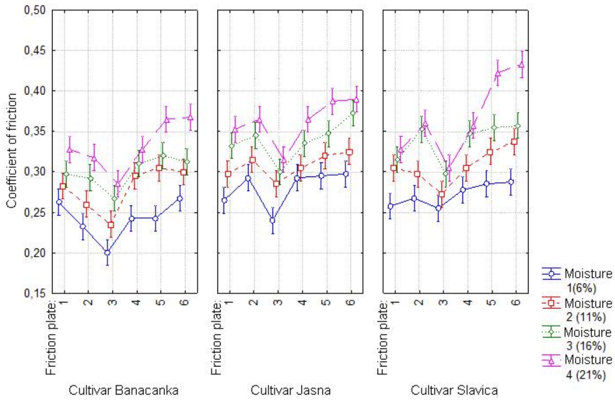

Types of substrate: 1. Galvanized sheet, 2. Steel sheet, 3. Stainless steel sheet, 4. Aluminum sheet, 5. Plastic, 6. Plywood plate

Figure 2. Friction coefficient depending on the type of substrate, variety and water content in the grain

Figure 2 shows the results of measuring the values of the static coefficient of slip friction depending on the variety, the type of substrate, the content of water in the grain and their interaction.

The order of the friction coefficient shown in this paper coincides with research [4] [7] for sheet metal, steel, aluminum and stainless steel sheets. The results of these investigations are also in agreement with the results [20] for friction coefficients on plastic, galvanized and stainless steel sheet. [21] have found that the smallest coefficient of friction of grain of rapeseed on the steel sheet (0.273) is approximately the value obtained in these studies. The research results [22] for coefficient of friction on galvanized substrates (0.318), aluminum (0.305) and stainless steel sheet (0.288) are similar to the values published in this paper.

The results of these studies for friction coefficients differ from the results [6], only in that the coefficient of friction on the surface of galvanized sheet is greater than the coefficient on the plastic substrate. This difference in friction coefficient values is most likely a consequence of the fact that the roughness of the surface of the plastic substrate in these researches was not the same as in the studies of the mentioned authors.

4. CONCLUSION

Friction coefficient is a physical feature that plays an important role in the construction of means of transport, seeds processing and storage design.

It was found that with the increase of water content in the grain, a significant increase in the friction coefficient of the grains of the tested varieties on all substrates was achieved.

The coefficient of friction of the Banaćanka variety is lower in relation to the varieties Jasna and Slavica on all substrates and with all the water content of the grain.

It was found that with the increase of water content in the grain, a significant increase in the friction coefficient of the grains of the tested varieties on all substrates was achieved.

The highest coefficient of friction for all water content of the grains of the tested varieties was on the base of plywood and plastic, and the smallest on the base of stainless steel sheet. However, the coefficient of friction on the plastic substrate did not differ from the coefficient of friction on the substrate of aluminum, steel and galvanized sheet metal in the content of water in a grain of 6% (substrate water/water content).

There is no difference in the coefficient of friction of the tested varieties for all grain moisture content on the base of aluminum and steel sheet, except for the Banaćanka variety. Also, there was no difference between the friction coefficient of grains of investigated varieties between the substrate of galvanized and steel sheet in all grain water content (substrate / variety interactions).

Based on the results of the research, mathematical models and computer simulations can be made for the direct prediction of the static friction coefficient, for the investigated substrates and the water content of the rapeseed grains, as they did [13] for grain wheat and [8] for soybean grain.

ACKNOWLEDGEMENT

The research presented in this paper is part of Project Ref. No. TR.31051 financially supported by the Ministry of Education, Science and Technological Development, Republic of Serbia.

REFERENCES

[1] A. Marjanović – Jeromela, A. Mikić, R. Marinković, V. Mihajlović, Dragana Miladinović: Prinosi semena i proteina uljane repice, Zbornik radova Instituta za ratarstvo i povrtarstvo, Vol. 44, No.1, pp. 237-241, 2007.

[2] M. Vujaković, A.Marjanović-Jeromela, D. Jovičić, N. Lečić, R. Marinković, N. Jakovljević, S. Mehandžić-Stanišić: Effect of plant density on seed quality and yield of oilseed rape (*Brassica napus* L.). Journal on Processing and Energy in Agriculture, Vol. 18, No. 2, pp. 73-76, 2014.

[3] I. Balalić, A. Marjanović-Jeromela, J. Crnobarac, S. Terzić, V. Radić, V. Miklič, D. Jovičić: Variabilty of oil and protein content in rapeseed cultivars affected by seeding date. Emir J Food Agric, Vol. 29, No. 6, pp. 404-410, 2017.

[4] S. Calisir, T. Marakoglu, H. Ogut, O. Ozturk: Physical properties of rapeseed (*Brassica napus oleifera* L), Journal of Food Engineering, Vol. 69, pp. 61–66, 2005.

[5] S. Razavi, S. Yeganehzad, A. Sadeghi, SH. Ebrahimzadeh, A. Niazmand: Some physical properties of Iranian varieties of canola seeds, Iranian Food Science and Technology Research, Vol. 2, No. 1, pp. 53-61, 2006.

[6] S. Razavi, S. Yeganehzad, A. Sadeghi: Moisture dependent physical properties of canola seeds, J Agric Sci Technol, Vol. 11, pp. 309-322, 2009.

[7] N. Izli, H. Unal, M. Sincik: Physical and mechanical properties of rapeseed at different moisture content, Int Agrophysics, Vol. 23, pp. 137-145, 2009.

[8] J. M. Boac, M. E. Casada, R. G. Maghirang, J. P. Harner: Material and interaction properties of selected grains and oilseeda for modeling discrete particles. American Society of Agricultural and Biological Engineers, Vol. 53, No. 4, pp. 1201-1216, 2010.

[9] V. Lončarević, M. Babić, S. Balešević Tubić, K. Đilvesi, M. Kostić, S. Štatkić: Dependet of moisture content soybean seed on physical properties, Journal on Processing and Energy in Agriculture, Vol. 14, No. 3, pp. 163-167, 2010.

[10] Lj. Babić, M. Radojčin, M. Babić, J. Turan, M. Zoranović, Sanja Stanišić: Physical properties and compression loading behavior of corn seed, International Agrophysics, Vol. 27, pp. 119-126, 2013.

[11] Z. Kaliniewicz, Z. Zuk: A relationship between friction plate roughness and the external friction angle of wheat kernels. International journal of food properties, Vol. 20. No S3, pp.2409-2417, 2017

[12] M. Bayram, E. Altuntas, M. Yilar: Geometriuc, volumetric, colour and frictional properties of selected *Salvia species* of Turkey, Afr J Tradit Complement Alter Med, Vol. 14, No. 3, pp.128-135, 2017.

[13] S.M. Shafaei, S. Kamgar: A comprehensive investigation on static and dynamic friction coefficients of wheat grain with the adoption of statistical analysis, Journal of Advanced Research, Vol. 8, pp.351–361, 2017.

[14] B. Ivkovic, M. Djukdjanovic, D. Stamenkovic: The Influenceof the Contact Surface Roughness on the Static Friction Coefficient. Tribology in industry,Vol. 22, No.3&4, pp. 41-4, 2000.

[15] M. Sedlaček, L.M.S. Vilhena, J. Vižintin: Surface topography modeling for reduced friction, Strojniški vestnik - Journal of Mechanical Engineering, Vol. 57, No. 9, pp. 674-680, 2011.

[16] H. Demir, A. Gullu, I. Ibrahim Ciftci, U. Seker: An investigation into the influences of grain size and grinding grinding forces when grinding, Strojniški vestnik - Journal of Mechanical Engineering, Vol. 56, 7-8, pp. 447-454, 2010.

[17] Z. Kaliniewicz, P. Markowski, A. Anders, K. Jadwisienczak: Frictional properties of selected seeds. Technical Sciences, Vol. 18, No. 2, pp. 85–101, 2015.

[18] S. Radonjić, J. Baralić, N Dučić: Određivanje statičkog koeficijenta trenja korišćenjem tribometra, *Tehnologija, informatika i obrazovanje za društvo učenja i znanja 6. Međunarodni Simpozijum*, Tehnički fakultet Čačak, 3-5. jun, 2011.

[19] M. Zuvić, N. Lazarević, M. Stojković: Eksperimentalno ispitivanje uticajnih faktora na statički koeficijent trenja klizanja, in: *13th International Conference on Tribology*, 15-17.05.2013, Kragujevac, Serbia, Fundamentals of friction and wear, Tribotesting and triposystem monitoring, 2013.

[20] S.J. Hong, J.W. Hon, H. Kim, Y.H. Kim, D.H. Keum, L.A. Duc: Physical properties of rapeseed (II), Agricultural Process and Food Engineering, Vol. 33, No. 3, pp. 173-178, 2008.
[21] I. Hazbavi, Saedin Minaei: Determination and investigation of some physical properties of seven variety rapeseed, Iranian Journal of Food Science and Technology, Vol. 5, No. 4, pp. 21-28, 2009.
[22] M.F. Baran, M.R. Durgut, T. Aktas, P. Ulger, B. Kayisoglu: Determination of some physical properties of rapeseed, International Journal of Enginering Technologies, Vol. 2, No. 2,pp. 49-55, 2016.

Serbian Tribology Society

SERBIATRIB '19

16th International Conference on Tribology

Faculty of Engineering University of Kragujevac

Kragujevac, Serbia, 15 – 17 May 2019

POSSIBILITY OF APPLICATION FOR ETHERS OF ACONITE ACID AS AW/EP ADDITIVE

I. MUKHORTOV[1], E. ZADOROZHNAYA[1,*], M. KANDEVA[1,2], I. LEVANOV[1]
[1]South Ural State University, Chelyabinsk, Russia, i.mukhortov@yandex.ru
[2]Tribology Center, Technical University – Sofia, Bulgaria, kandevam@gmail.com
*Corresponding author: Elena-nea@rambler.ru

Abstract: *The possibility of using substances containing only carbon, hydrogen and oxygen as antiwear additives for lubricating oils has been investigated. Studies have been conducted on the example of ethers of aconite acid and hexadecyl alcohol. This compound was chosen as a promising AW/EP additive for biodegradable greases based on vegetable oils. In addition, the anti-wear mechanism of substances that do not contain phosphorus, sulfur, chlorine, metals and other heteroatoms is very interesting. Aconite acid hexadecyl ester was added to rapeseed oil, to petroleum oil without additives, and to standard gear oil. Antiwear properties of the obtained compounds were identified and presented as results. Measurements were carried out both in laboratories of SUSU and at Sofia University at several stands under various friction conditions. It was established that the test additive exhibits anti-wear properties in all three lubricating oils. With the introduction of additives in rapeseed oil, wear is reduced by 25 ... 50% depending on the test conditions. The wear reduction is more significant in steel-bronze contacts than in steel-steel and steel-iron contacts. With the introduction of additives in hydrocarbon oil without additives, anti-wear effect is only slightly lower than with the introduction of ZDDP. Anti-wear effect increases with increasing load (contact pressure), as well as for ZDDP. The most pronounced effect for both vegetable and petroleum oil, obtained by testing the method of four balls according to the technique of ASTM D 4172. When hexadecyl aconite acid is added to gear oil (GL-5 standard) containing ZDDP and EP additives, wear is reduced to the same extent as when it is added to oil without additives. The welding load increases slightly. This suggests that the studied additive does not compete with ZDDP and can be used in mixed composition. The absence of heteroatoms in the studied additive indicates an adsorption mechanism of anti-wear action. The study results indicate the prospects for the use of esters of polyatomic acids as AW/EP additives for biodegradable lubricating oils and oils for food production equipment.*

Keywords: *antiwear additives, extreme pressure additives, aconite acid, biodegradable lubricating oil, friction machine.*

1. INTRODUCTION

In connection with the increase in the negative impact of industrial production, electricity production and transport on the nature and environment of humans, considerable attention has recently been paid to the environmental aspects of the functioning of technical devices. Major source of environmental danger and anthropogenic impact on natural systems are vehicles with internal combustion engines. Pollution is generated not only in the processes of extraction and processing of natural hydrocarbons and fuel combustion. Lubricants and hydraulic fluids that enter the soil and water are also significant sources of pollution. This especially applies to agricultural machinery and water transport. This circumstance is the cause of attention to the development and use of biodegradable lubricants. Synthetic esters and products of chemical modification of vegetable oils are considered promising. But special attention is paid to vegetable oils, as environmentally friendly and renewable materials.

Vegetable oils have fundamental limitations on the scope of use except advantages. The most significant disadvantage is low oxidation resistance. Reduced resistance to oxidation of vegetable oils due to their chemical composition [1]. As a rule, to improve this parameter, oils with a low content of unsaturated acids are used, for example, castor oil. However, castor oil is inferior to rapeseed and other oils for antiwear properties. For long-term operation at high temperatures, resistant synthetic esters are more suitable. However, the ability of synthetic esters to biodegradation in the natural environment decreases with increasing thermal stability. The same dependence is observed for anti-wear properties. For applications such as the ships engines used in inland waters (rivers and lakes), vegetable oils are the preferred lubricants.

The second disadvantage is the relatively low anti-wear properties. Despite the fact that the antiwear and antifriction properties of vegetable oils are higher than those of petroleum and synthetic base oils without additives [2 - 6], they are significantly lower than those of lubricants containing additive packages. It should be noted that hydrocarbon-based lubricants have come a long way of improvement, including cleaning technologies from components that are not resistant to oxidation, and the development of effective multifunctional additives, including anti-wear, extreme pressure and antifriction.

The anti-wear properties of vegetable oil-based lubricants can also be significantly enhanced by the addition of additives. However, the use of conventional anti-wear additives developed for hydrocarbon oils, such as ZDDP or triphenyl phosphorothionates, is either impossible or impractical. This is due to the fact that the effectiveness of additives varies significantly in base oils of different chemical composition. In addition, ZDDP can be destroyed by chemical interaction with the molecules of vegetable oils. And finally, the introduction of components containing sulfur, phosphorus and toxic metals, significantly reduces the environmental benefits of vegetable oils. The search for special additives for vegetable oils began only recently.

Three methods of enhancing anti-wear properties are used: introduction of solid lubricant components to lubricating oil, for example [7–11], chemical modification of vegetable oils, for example [12, 13], and introduction of oil-soluble antiwear components, for example [14–20]. The use of solid lubricant components is limited to greases. The use of nanosuspensions of metals and other inorganic components that are resistant to sedimentation affects the filterability of oils. This is an important parameter of oils for hydraulic systems and engines. In addition, operational impacts lead to a change in the composition of the oils. The oxidation of the oil and the presence of water can significantly affect the stability of the nanosuspensions. Chemical modification of vegetable oils, for example, the formation of thioesters, reduces the ability to biodegrade and can lead to the formation of corrosive products during operation.

From the standpoint of storing such advantages of vegetable oils as non-toxicity, no odor, ease of production, the authors consider the increase in the tribological parameters by adding fully soluble functional additives to be the most promising. This method gave excellent results for hydrocarbon-based lubricants. Some examples of such studies are given in papers [14–20]. Despite the successful use of some AW / EP components developed for hydrocarbon oils [16–18], a number of papers note that the effectiveness of additives is different in hydrocarbon and vegetable oils. Increased adsorption of vegetable oil molecules and esters on the metal surface prevents the adsorption of molecules of traditional AW / EP components. In this regard, the most effective are more polar substances than those used in hydrocarbon oils.

The main fields of application of biodegradable oils are water transport engines used in closed reservoirs, hydraulic systems and transmissions of agricultural machinery, equipment for food processing. The principles for the development of anti-wear additives for these applications are associated primarily with the adsorption mechanism of action of the additives. Efficiency should be expected from oil-soluble surfactants containing a massive polar group, prone to adsorption on the metal surface, and quite long hydrocarbon radicals, providing intermolecular interaction with the base oil.

This paper considers the possibility of using esters as an AW additive. These esters have chemical and environmental properties that are as close as possible to vegetable and animal fats. At the same time, they are characterized by an increased tendency to adsorb on metal surfaces. Vegetable oils are esters of monobasic organic acids and glycerin triatomic alcohol. In this work, as an additive, a tribasic organic acid and a monohydric alcohol was tested. The presence of tribasic acid, forming stable complexes with metals, suggests an increased ability to adsorb. The similarity of the chemical nature of additives and fats, as well as the choice of non-toxic components, suggest a good compatibility of additives with vegetable oil and the absence of a negative impact on biodegradability and toxicity.

A test determination of the antiwear efficacy of aconitic acid ester and hexadecanol-1 in hydrocarbon oil without additives, automobile transmission oil and rapeseed oil was carried out. Testing was performed to verify the compatibility of the developed additive with standard anti-wear and extreme pressure additives. The focus was on determining the effectiveness of the additive in rapeseed oil.

2. EXPERIMENTAL RESEARCH

2.1 Synthesis of the additive

Citric acid was used as tribasic acid. Hexadecanol-1 was used to ensure the solubility of ether and the products of its partial decomposition in oils. A mixture of acid and alcohol, taken in a molar ratio of 1: 3, was heated to 160...190 C. The reaction was carried out for 2...3 hours with occasional stirring. Under these conditions, the esterification takes place completely and does not require a catalyst. As a result of heating, citric acid separates water and turns into aconitic acid. The final product is a full ester of Hexadecanol and aconitic acid. The injected additive was called AAE-additive. The structural formula is presented in Figure 1. The resulting product has a wax consistency, the melting point is 60...65 C. It is soluble in hydrocarbons, but insoluble in water.

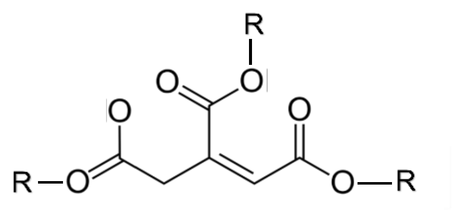

Figure 1. Formula aconitic acid trihexadecyl ester, where R is the residue of alcohol $C_{16}H_{33}$

2.2 Determination of the anti-wear properties of the AAE additive in petroleum lubricating oil without additives

Industrial oil without additives (viscosity grade ISO 32) was used as the base oil. The AAE-additive was administered in an amount of 3% by weight. For comparison, zinc dihexadecyl dithiophosphate (ZDDP) was used, which included the same hydrocarbon radicals as the additive under study. ZDDP was introduced into the base oil in an amount of 2% by weight.

The tests were carried out on the machine friction II-5018. The tests were carried out on the machine friction II-5018. Unlike the universal friction machine MTU-1 [21], the friction machine II-5018 allows to carry out tests under the conditions of contact "roller block". The diameter of the roller is 90 mm, the material is steel. The block is made of the liner of the tractor bearing, the material is bronze, the dimensions of the working surface are 24 × 2 mm. Test conditions: roller rotation speed 500 min^{-1}, load range 1000 N. Oil supply is drop, at the entrance to the friction contact, 0,2 ml/s.

The values of the friction coefficient μ were calculated based on the measured friction moment M at each load value F. The contact pressure P was calculated based on the load value and the contact area. Temperature T was measured by a thermoelectric transducer inserted into the side opening of the block. A general view of the friction machine II-5018, block image and contact assembly, is shown at Figure 2.

a)

b)

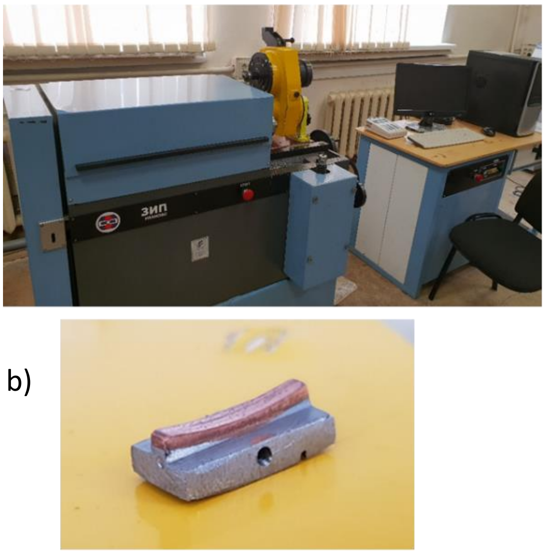

Figure 2. General view of the friction machine II 5018 (a), block (b)

The measurement results are presented in Table 1 and in Figure 3.

Table 1. Measurement results. The dependence of the coefficient of friction μ on the temperature when lubricated with oil without additives, the same oil with the addition of 3% aconitic acid trihexadecyl ester and 2% ZDDP

Friction unit temp., °C	Friction coefficient μ		
	Industrial Oil ISO 32	ZDDP	AAE
25	0,111	0,096	0,099
30	0,111	0,096	0,099
35	0,111	0,095	0,098
40	0,111	0,094	0,098
45	0,111	0,094	0,097
50	0,111	0,094	0,097
55	0,116	0,094	0,097
60	0,116	0,093	0,096
65	0,116	0,093	0,096
70	0,116	0,092	0,094
75	0,116	0,09	0,092
80	0,116	0,088	0,09
85	0,118	0,086	0,086
90	0,122	0,082	0,082
95	0,128	0,076	0,076
100	contact	0,074	0,075
105	-	0,072	0,074
110	-	0,07	0,074
115	-	0,070	0,072
120	-	0,068	0,072
125	-	0,068	0,074
130	-	0,068	0,074

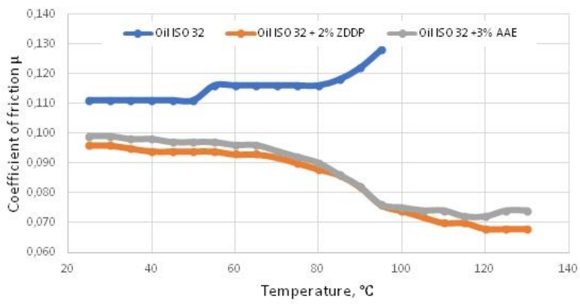

Figure 3. Effect of ZDDP and AAE on the dependence of the friction coefficient on temperature in a conformal slip contact

Due to the dependence of the friction coefficient on the temperature and the complexity of contact temperature control, the measurement of the dependence of the friction coefficient on the load was carried out at three load values. The load was constant during each measurement. The moment value was recorded when the temperature reached 80 C. Before performing each measurement, the surface of the roller was polished to achieve a roughness of Ra = 0,02. The lubricant used was the same oil and the same additive concentrations as in the measurements described above. The measurement results are shown in Table 2.

Table 2. Measurement results. The dependence of the friction coefficient μ on the load when lubricating with oil without additives, the same oil with additives of 3% aconitic acid trihexadecyl ester and 2% ZDDP

Load, N	Friction coefficient μ		
	Industrial Oil ISO 32	ZDDP	AAE
200	0,054	0,046	0,052
500	0,070	0,062	0,065
1000	contact	0,084	0,085

2.3 Determination of the anti-wear properties of the AAE additive in gear oil

Transmission oil LUKOIL API GL-5, SAE 75W-90 was used as the base oil. This oil contains antiwear and extreme pressure additives. The additive ZDDP was administered in an amount of 2% by weight, the additive AAE was introduced in an amount of 3% by weight.

Antiwear properties were determined by the four ball method on a standard ChMT-1 friction machine complying with the requirements of ASTM D 4172 [21] according to the ASTM D 4172 method at a rotation speed of 1200 rpm (0,46 m s). The normal load is 392 N, the temperature of the oil bath is 40 ± 5 C. The balls were made of steel, the hardness is HRC 64-66, the diameter is 12,7 mm. An optical microscope with an accuracy of 0,01 mm was used to measure wear spots. A general view of the friction machine is presented in Figure 4.

For the original gear oil made 6 measurements. For oil with additives ZDDP and AAE, 3 measurements were carried out. The measurement results were averaged. The measurement results are shown in tables 3 - 6. The type of wear marks is shown in Figure 5.

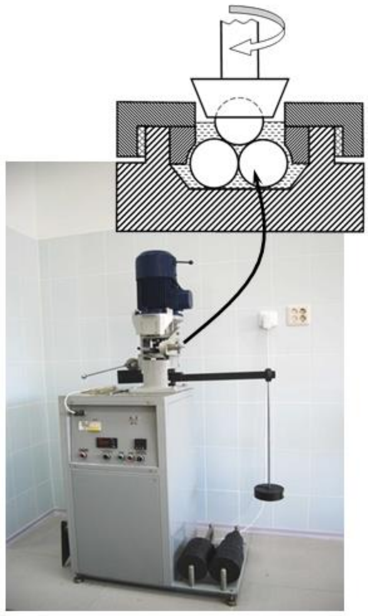

Figure 4. The view of the four-ball friction machine and the scheme of the friction unit

Table 3. The wear trace diameter for LUKOIL GL-5 SAE 75W-90 oil

№	1	2	3	4	5	6
The wear trace diameter, mm	0,44	0,46	0,46	0,45	0,46	0,43
	0,44	0,47	0,46	0,45	0,46	0,43
	0,45	0,46	0,46	0,45	0,46	0,44
	0,44	0,46	0,45	0,45	0,46	0,44
	0,43	0,42	0,45	0,45	0,44	0,41
	0,43	0,42	0,45	0,45	0,47	0,42
	0,44	0,43	0,45	0,45	0,44	0,43
	0,44	0,43	0,45	0,45	0,45	0,45
	0,43	0,44	0,45	0,45	0,45	0,43
Average value mm	0,452					

Table 4. The diameter of the wear trace for oil LUKOIL GL-5 SAE 75W-90, containing 2% ZDDP

№	1	2	3
The wear spot diameter, mm	0,335	0,346	0,335
	0,342	0,344	0,325
	0,348	0,345	0,329
	0,35	0,345	0,331
	0,345	0,34	0,339
	0,347	0,332	0,353
	0,348	0,332	0,357
	0,356	0,333	0,353
	0,347	0,339	0,338
Average value, mm	0,344		

Table 5. The diameter of the wear trace for oil LUKOIL GL-5 SAE 75W-90, containing 2% ZDDP

№	1	2	3
The diameter of the wear trace, mm	0,328	0,335	0,322
	0,332	0,334	0,328
	0,327	0,325	0,328
	0,326	0,328	0,332
	0,332	0,332	0,33
	0,333	0,332	0,323
	0,324	0,326	0,326
	0,328	0,334	0,328
	0,332	0,336	0,327
Average value, mm	0,328		

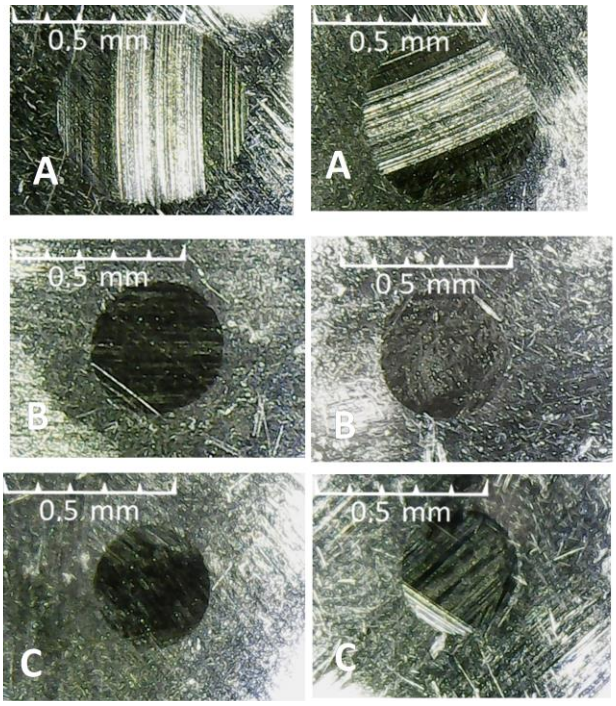

Figure 5. Type of wear spots when tested according to the four ball method: A - when lubricated with LUKOIL GL-5 SAE 75W-90 oil, B - the same oil with 3% AAE added, C - the same oil with 2% ZDDP added

2.4 Determination of the anti-wear properties of the AAE additive in gear oil

Tests were carried out at the Sofia Technical University (Bulgaria). To determine the presence of antifriction action of aconitic acid trihexadecyl ester (AAE) in a flat contact, technical rapeseed oil was used. The AAE addition was added in an amount of 4% by weight.

Table 6. The results of measurements of wear marks by the four-ball method (axial load is 392 N) for LUKOIL GL-5 SAE 75W-90 oil; and the same oil containing additional additives ZDDP and AAE

№	Lubricant	Average wear diametera, mm	Average contact patch area, mm^2	Minimum contact pressure reached during testing, MPa
1	LUKOIL GL-5	0,452	0,204	640
2	LUKOIL GL-5 + 3% AAE	0,344	0,118	1110
3	LUKOIL GL-5 + 2% ZDDP	0,328	0,108	1210

The measurements were performed on a laboratory device "Fixed Pin - Rotating Disk." The device is shown in Figure 6.

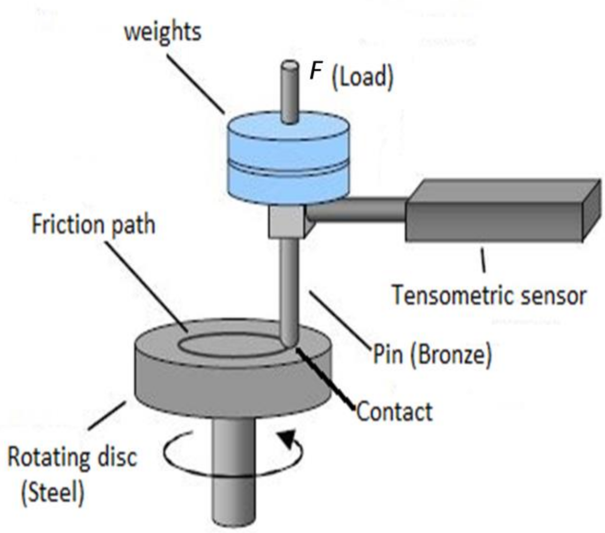

Figure 6. Scheme of the device for measuring the friction coefficient when lubricated with rapeseed oil with or without additive

A pin is a cylindrical specimen made of BrO10F1 tin bronze. The diameter is 19 mm. The rotating disk is made of alloy steel with a hardness of HRC56,9. The pin is fixed in the device, which can move freely in a plane parallel to the disk plane and along the normal to the surface. The pressing force F to the disk is created by placing weights on the device for the pin fastening. A tensometric sensor attached to the fastening of the pin.

Using the device shown in Figure 6, the friction force Ft acting on the pin from the disk was measured. The friction force was measured with an accuracy of 0,1 N. Each experiment at each load value was performed at the same values of time (friction path), disk rotation speed, and ambient temperature. The lubricant was applied to the contact by drip method (drip lubrication) at a rate of 30 drops/min. The experiment parameters are shown in Table 7.

Table 7. Parameters of the experiment

№	Parameters	Value
1	Load	F_1 = 60 N, F_2 = 100 N, F_3 = 140 N, F_4 = 220 N
2	Nominal contact area	A_a = 283,3 mm^2
3	Nominal contact pressure	P_{a1}= 21,2 N/cm^2, P_{a2}= 35,3 N/cm^2, P_{a3}= 49,5 N/cm^2, P_{a4}= 77,7 N/cm^2
4	Speed of rotation	n = 95 min^{-1}
5	Sliding speed of the center contact	V_C = 0,89 m/s
6	Initial rape oil temperature	T = 21°C
7	Ambient temperature	T = 21°C

The friction coefficient was calculated as the ratio of the friction force to the normal load (the force of pressing the pin to the disk). Rapeseed oil and rapeseed oil containing 4% aconitic acid trihexadecyl ester (AAE-additive) were used as a lubricant. The temperature of the lubricant supplied to the friction contact is equal to the ambient temperature 21   C.

Table 8 presents the results of measurements of friction coefficients at four load values. Figure 7 shows the dependence of friction coefficients on the load.

The diagram of the relative change of the friction coefficient ¯ under different normal loads is shown in Figure 8. The value ¯ is equal to the ratio of the friction coefficient for the oil with the additive to the friction coefficient for the original oil.

Table 8. The results of measurements of friction force Ft and friction coefficient μ

№	lubricating oil	Load, F			
		F_1 = 60 N		F_2 = 100 N	
		P_{a1}=21,2 N/cm^2		P_{a2}=35,3 N/cm^2	
		Ft_1, N	μ	Ft_2, N	μ
1	Rapeseed oil	4,5	0,075	6	0,06
2	Rapeseed oil+ AAE-Additive	2	0,03	4	0,04
№	lubricating oil	F_3 = 140 N		F_4 = 220 N	
		P_{a3}=49,5 N/cm^2		P_{a4}=77,7 N/cm^2	
		Ft_3, N	μ	Ft_4, N	μ
1	Rapeseed oil	9	0,064	15	0,068
2	Rapeseed oil+ AAE-Additive	6	0,042	10	0,045

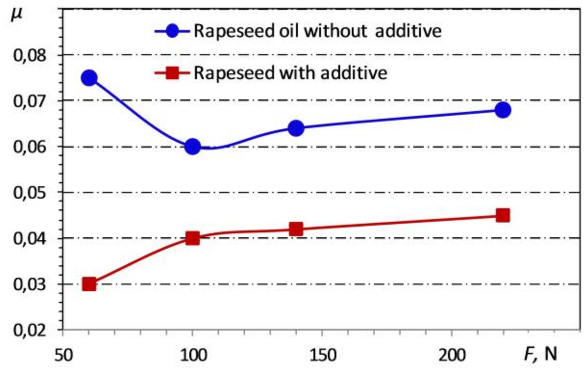

Figure 7. Dependence of friction coefficient on the normal load

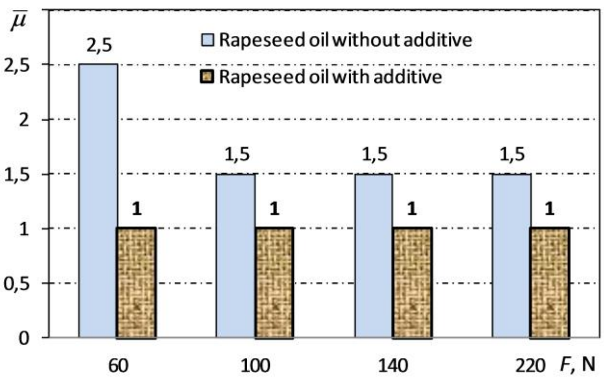

Figure 8. The diagram of the relative change of the friction coefficient ¯ under different normal loads

3. DISCUSSION

The results of the experiments showed that the introduction of aconitic acid trihexadecyl ester (AAE-additive) into the composition of vegetable oil significantly improves the antiwear properties (paragraph 2.2). In the conformal contact of sliding friction, imitating the bearing of the crankshaft of the tractor engine, the results of the introduction of the investigated additive are close to the results of the introduction of ZDDP with alkyl radicals of the same length and structure as in AAE-additive. This can be explained by the adsorption mechanism of action of the additives. The effect of the adsorbed surfactant layer extends to an extremely thin layer of liquid. Under conditions of simulating a radial friction bearing with low surface roughness, hydrodynamic pressures provide the separating layer of lubricant even at high contact pressures.

With the introduction of ZDDP and AAE in gear oil also obtained similar results. Both types of additives significantly increase the anti-wear properties of gear oil class API GL-5, which is quite unexpected. The results obtained in tests of paragraph 2.3 showed that AAE is compatible with ZDDP and can be used in conjunction with them, for example, to reduce the ash content of lubricating oils.

Tests (paragraph 2.4) indicate the presence of noticeable AW/EP action. However, the results suggest a slightly lower efficacy of AAE in rapeseed oil compared to the efficiency in hydrocarbon oils. Perhaps this is due to the higher anti-wear properties of vegetable oil compared to pure hydrocarbon oils. It should be noted that AAE is an ester and is chemically similar to vegetable oil. The main difference is the higher ability of AAE to adsorb onto metal surfaces. This confirms the assumption about the predominantly adsorption mechanism of action of this additive.

4. CONCLUSION

The results show that aconitic acid trihexadecyl ester exhibits anti-wear properties in both hydrocarbon and vegetable oils at high contact pressures. Aconitic acid ester can be used when it is necessary to enhance the AW/EP properties of lubricants based on hydrocarbon and vegetable oils in cases where low ash content, non-toxicity and biodegradability are particularly important. For example, in food processing equipment.

This additive can be used as a prototype for the synthesis of more effective additives with low toxicity.

ACKNOWLEDGEMENT

This work was supported by the Ministry of Education and Science of the Russian Federation (grant No 9.7881.2017/8.9).

REFERENCES

[1] N.J. Fox, G.W. Stachowiak: Vegetable oil-based lubricants - A review of oxidation, Tribology International, Vol. 40, No 7, pp. 1035-1046, 2007.

[2] Y.M. Shashidhara, S.R. Jayaram: Vegetable oils as a potential cutting fluid – An evolution, Tribology International, Vol. 43, No 5–6, pp. 1073-1081, 2010.

[3] A. Ruggiero, R. D'Amato, M. Merola, P. Valašek, M. Müller: Tribological characterization of vegetal lubricants: Comparative experimental investigation on Jatropha curcas L. oil, Rapeseed Methyl Ester oil, Hydrotreated Rapeseed oil, Tribology International, Vol. 109, No. 5, pp. 529-540, 2017.

[4] A. Rajendiran, A. Sumathi, K. Krishnasamy, S. Kabilan, D. Ganguli: Antiwear study on petroleum base oils with esters, Tribology International, Vol.99, No. 7, pp. 47-56, 2016.

[5] S.H. Hamdanab, W.W.F. Chongcde, J.-H. Ngadf, M.J. Ghazalig, R.J.K. Woode: Influence of fatty acid methyl ester composition on tribological properties of vegetable oils and duck fat derived biodiesel, Tribology International, Vol. 113, No. 9, pp. 76-82, 2017.

[6] C.J. Reeves, P.L. Menezes, T.-C. Jen, M.R. Lovell: The influence of fatty acids on tribological and thermal properties of natural oils as sustainable biolubricants, Tribology International, Vol. 90, No. 10 pp. 123-134, 2015.

[7] G. Zhang, Y. Xu, X. Xiang, G. Zheng, X. Zeng, Z. Li, T. Ren, Y. Zhang: Tribological performances

of highly dispersed graphene oxide derivatives in vegetable oil, Tribology International, Vol. 126, No. 10, pp. 39-48, 2018.
[8] R. Padmini, P.V. Krishna, G.K. Mohana Rao: Effectiveness of vegetable oil based nanofluids as potential cutting fluids in turning AISI 1040 steel, Tribology International, Vol. 94, No. 2, pp. 490-501, 2016.
[9] S. Alves, B. Barros, M. Trajano, K. Ribeiro, E. Moura: Tribological behavior of vegetable oil-based lubricants with nanoparticles of oxides in boundary lubrication conditions, Tribology International, Vol. 65, No. 9, pp. 28-36, 2013.
[10] M. Gulzar, H.H. Masjuki, M. Varman, M. Kalam, R. Mufti, N.M. Zulkifli, R. Yunus, R. Zahid: Improving the AW/EP ability of chemically modified palm oil by adding CuO and MoS_2 nanoparticles, Tribology International, Vol. 88, No. 8, pp. 271-279, 2015.
[11] F.L. Guzman Borda, S.J. Ribeiro de Oliveira, L.M. Seabra, M. Lazaro, A. Leiróz,: Experimental investigation of the tribological behavior of lubricants with additive containing copper nanoparticles, Tribology International, Vol. 117, No. 1, pp. 52-58, 2018.
[12] B.K. Sharma, A. Adhvaryu, S.Z. Erhan: Friction and wear behavior of thioether hydroxy vegetable oil, Tribology International, Vol.42, No. 2, pp. 353-358, 2009.
[13] O.N. Anand, V.P. Malik, K.D. Neemla: Studies on extreme pressure films – reactions of sulphurized vegetable oils and alkyl phenols with iron, Tribology International, Vol. 19, No. 3, pp. 128-132, 1986.
[14] G. Zheng, T. Ding, Y. Huang, L. Zheng, T. Ren: Fatty acid based phosphite ionic liquids as multifunctional lubricant additives in mineral oil and refined vegetable oil, Tribology International, Vol. 123, No. 6, pp. 316-324. 2018
[15] J. Martín-Alfonso, F. López-Beltrán, C. Valencia, J. Franco: Effect of an alkali treatment on the development of cellulose pulp-based gel-like dispersions in vegetable oil for use as lubricants, Tribology International, Vol. 123, No. 7, pp. 329-336, 2018.
[16] N.H. Jayadas, K.P. Nair, G.Ajithkumar: Tribological evaluation of coconut oil as an environment-friendly lubricant, Tribology International, Vol. 40, No. 2, pp. 350-354, 2007.
[17] B. Ozcelik, E. Kuram, M.H. Cetin, E. Demirbas: Experimental investigations of vegetable based cutting fluids with extreme pressure during turning of AISI 304L, Tribology International, Vol. 44, No. 12, pp. 1864-1871, 2011.
[18] U.S. Choi, B.G. Ahn, O.K. Kwon, Y.J. Chun: Tribological behavior of some antiwear additives in vegetable oils, Tribology International, Vol. 30, No. 9, pp. 677-683, 1997.
[19] X. Zeng, J. Li, X. Wu, T. Ren, W. Liu: The tribological behaviors of hydroxyl-containing dithiocarbamate-triazine derivatives as additives in rapeseed oil, Tribology International, Vol. 40, No. 3, pp. 560-566, 2007.
[20] L.A. Quinchia, M.A. Delgado, T. Reddyhoff, C. Gallegos, H.A. Spikes: Tribological studies of potential vegetable oil-based lubricants containing environmentally friendly viscosity modifiers, Tribology International, Vol. 69, No. 1, pp. 110-117, 2014.
[21] P. Kovalenko, S. Perepelkina, T. Korakhanov: Investigation of tribological properties of friction pairs duralumin – fluoropolymer used for design and manufacturing of biomechatronic devices, Tribology in Industry, vol. 39, No. 2, pp. 192-197, 2017.
[22] ASTM D4172–94 *Standard teste method for wear preventive characteristics of lubricating fluid (four ball method) ASTM International, West Conshohocken, PA, US,* 2010.

Serbian Tribology Society

SERBIATRIB '19

16th International Conference on Tribology

Faculty of Engineering University of Kragujevac

Kragujevac, Serbia, 15 – 17 May 2019

INVESTIGATIONS ON THE FRICTION IN ROLLING AND SLIDING BEARINGS DURING LUBRICATION BY RAPESEED OIL WITH NON TOXIC AND ASHLESS ADDITIVE

M. KANDEVA[1,2], E. ZADOROZHNAYA[2], I. MUKHORTOV[2], Zh. KALICHIN[3], I. LEVANOV[2]

[1]Tribology Center, Technical University – Sofia, Bulgaria, kandevam@gmail.com

[2] South Ural State University, Russia, i.mukhortov@yandex.ru

[3] SciBuCom 2 Ltd., P.O.Box 249, 1113 Sofia, Bulgaria, kalitchin@gmail.com

*Corresponding author: kandevam@gmail.com

Abstract: *Increasing of the environmental requirements to transport and industry poses to tribology a priority task related to the development of environmentally friendly lubricants and technologies. Vegetable oils and synthetic esters are most commonly used as biodegradable base oils. The fundamental constraints associated with their direct application are related to two parameters: stability towards oxidation and their contact characteristics, antifriction, wear and tear resistance. To increase oxidation stability, low unsaturated fatty acids contents are used, and the reduction of friction and wear is achieved by developing compatible composite additives towards the base vegetable oil.*

The present study presents results from a comparative investigation of friction characteristics and oil temperature in two tribosystems "Rolling Bearings" and „Sliding Bearing" when lubricated with pure rapeseed oil and rapeseed oil containing 4% non-toxic and ashless additive . The new additive is designed for biodegradable base oils.

The research was conducted in tribology laboratories in Southern Ural State University, Chelyabinsk, Russia, and at the Technical University of Sofia, Bulgaria

Keywords: *tribology, coefficient of friction, rapeseed oil, AW/EP additives, rolling bearings sliding bearings*

1. INTRODUCTION

The enhancement of the ecological requirements to the transport and the industry poses to tribology a priority task – to elaborate environmentally friendly lubricants and technologies. The development of the tribology in the near future decades will be connected with solving issues and problems in the machines, the mechanisms and the technological equipment of a new generation, which should be in correspondence with the ecological requirements [1÷6].

During the last 10-15 years an intensive developent of the world production is observed as well as of the respective investigations, associated with ecologically clean lubricating materials and liquids, obtainable from renewable resources on the basis of vegetable oils and synthetic esters, as well as composites consisting of vegetable and mineral lubricating oils having a high degree of bio-degradability. The vegetable oils and the synthetic esters are most often used as bio-degradable base oils. Both kinds of oils have fundamental limitations, connected with their immediate application.

The main problems are connected with two parameters: stability to oxidation and their tribological characteristics i.e. antifriction, wear resistance and anti-tear properties. The reduced oxidation stability of the vegetable oils is determined by their chemical composition and in order to improve the stability one often uses oils having low contet unsaturated acids.

The second problem originates from a specific feature of the tribosystems, which is the fact that their functional characteristics, being dependent on the combined complex influence of many factors, and moreover these are changing during the course of theirexploitation. Researchers try to find a solution by elaborating compatible composite additives to the basis bio-degradable vegetable and synthetic oil [7÷9]. Until the present moment the utilization of such materials is reduced mainly to ecologically sensitive areas such as forestry, agricultural technics and construction.

The great interest in vegetable oils originates from their main advantages, compared to petroleum oils – they are non-toxic, quickly degradable, renewable sources and easily accessible. It has been established that in regard to their physical-chemical and tribological characteristcs the vegetable oils satisfy the exploitational requirements only under certain conditions. The vegetale oils - rapeseed, linseed, sunflower, caster oil, cotton palmitic etc. oils contain considerable amount of organic surfactant compounds (SACs) in the form of unsaturated fatty acids – oleic, stearic, eruceic, linolenic and others. During friction they form on the surfaces polymolecular layers of spatially orientated dipoles, which possess aisotropic mechanical properties – large pressure resistance and low resistance in the tangential direction.

These layers exert dampering action in the contact during friction, they hamper the direct interaction between the asperities and the intercalation of abrasive particles as a result of the wearing off process of the surfaces. In this way the organic surfactants in the vegetable oils appear to be natural antiwear additives, especially in the cases of mixtures of vegetable and mineral oils composites. The vegetable oils have a higher viscosity index (VI) – about 200 in comparison with that of the mineral oils. This criterion is extremely important for the mechanisms and the intensity of the tribological processes. The lower VI leads to intensification of the processes of aging of the oil and respectively enhaces the wear. It becomes clear from the above said that the vegetable oils do not need any addition of viscous additives.

The main problems in the efficient application of pure vegetable oils in contacts and joints originate from their low oxidative and thermal stabilities (thermo-oxidative stability) and their low-temperature properties [4÷13].

The aim of the present research work was to obtain comparable results on the friction characteristics in two tribosystems- “rolling bearing” and sliding bearing “Shaft-bushing” during lubrication with pure rapeseed oil and rapeseed oil, containing 4% non-toxic ashless additive AW/EP. The additive contains an ester of aconitic acid and hexadecyl alcohol (aconitic acid ester (AAE)). Additive’s chemical properties are similar to ones of vegetable oils, but the former contains a three-carboxylic groups acid in its molecule. As a result, AAE is more effectively adsorbed on metal surfaces than vegetable oil molecules. The new additive AW/EP is taylor-made for bio-degradable base oils.

2. FRICTION IN ROLLING BEARINGS

The moment of friction is being studied as well as the reduced coefficient of friction in the bearing junction in case of lubrication with rapeseed oil without any additive and rapeseed oil with 4% non-toxic ash-free additive AW/EP under identical conditions of friction – constant number of revolutions per minute and several values of the loading.

2.1 Device and methodology

The studies on the moment and on the coefficient of friction, carried out by means of DM 28M device, are shown in Fig.1 and Fig.2.

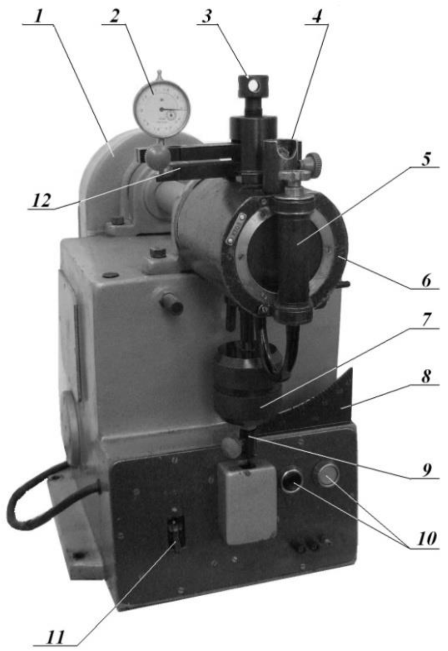

Figure 1. Outside appearance of device DM 28M

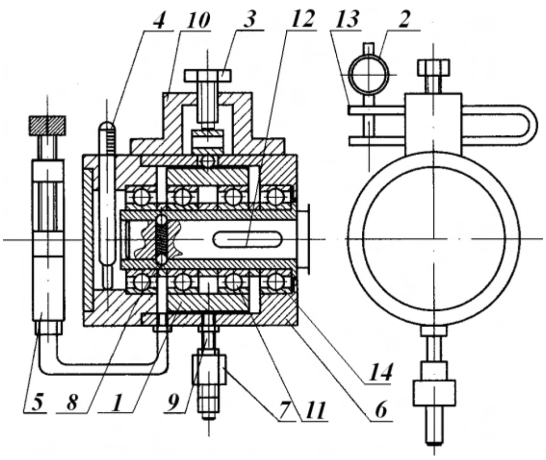

Figure 2. Bearing head of device DM 28M

The device consists of a body, in which a shaft is mounted (12), driven by means of belt transmission (1). At the end of the driving shaft the bearing head is attached (6), inside which there are four rolling bearings – two of them are in the middle (11) and the other two bearings are located at the two ends (14). The outer rings of the two middle bearings (11) are located in the common chamber. The outer rings of the two end bearings (14) are located in the body of the bearing head mounted tightly, whereupon they form close contact with the body of the head. The internal rings of the bearings (14) are attached by means of tightly screwed mount to the driving shaft (12). In this way the movement of the shaft (12) through the inner rings, ball pellets and the outer rings of the bearings is transferred to the body of the bearing head and this induces rotation in the direction of the rotating shaft. Thus during the rotation of the shaft the appearing friction moment drags the bearing head including the space location, where the middle bearings are attached. A pendulum (9) is attached stationary to the body of the bearing head. The magnitude of the friction moment is measured on the basis of the deviation of the pendulum (9) with respect to the vertical axis and the value is read on the scale (8), in units Nm. The adjustment of the pendulum in vertical position is done by means of the weight (7).

The normal loading is set on the middle bearings (11) by means of a screw for load adjustment (3) through dynamometric beam (13) and the value is read on the scale of the indicator (2) in units of Newton.

The lubricating oil is poured into the bearing node through an aperture, while its level is regulated by shifting the piston of the leveler (5). The temperature is measured using a thermometer (4), immersed in the oil.

The restriction of the abrupt rotation of the bearing head when the electric motor is switched on is achieved by restrictors.

The methodology for investigating the moment of friction and measuring the coefficient of friction consists of the following steps:

First the turnover number is set by adjusting the belt transmission (1). Lubricating oil is poured in (with or without additive) and then its level is adjusted by shifting the piston of the leveler (5). The pendulum is fixed in vertical position by means of the weight (7). The electric motor is switched on and the device is left to operate in this way for 5 minutes until a stable position of the pendulum is achieved and thereafter one reads the value on the scale (8), which corresponds to the magnitude of the moment of friction. By means of a distant turnover number metering device one can follow the number of revolutions of the shaft per unit of timeна aiming at measuring the magnitude of the friction moment upon reaching a constant number of revolutions. The friction moment is measured in regime without any loading, whereupon one reads the indications on the scale in 2 min intervals. The operator sets consecutively loadings of P_1, P_2, P_3,... by means of the screw (3) and measures the respective value of the moment of friction M_1, M_2, M_3,... The time interval for each loading value is 2 min. These operations are repeated in each next trial for the various lubricating oils. Upon changing the oil the bearing head is cleaned up by washing with gasoline or some other solvent and then it is dried up by warm air. All the trials are done at one and the same oil level – to the center of the bearing ball pellets, which guarantees identical conditions of lubrication in the bearing head.

The coefficient of friction μ is determined by the formula:

$$\mu = \frac{2M}{Pd} \tag{1}$$

where d=40 mm is the diameter of the internal ring of the bearing.

2.2 Results and analysis

Using the so described methodology and device results were obtained on the moment of friction, the coefficient of friction and the temperature of the lubricating oil in the bearing unit in the case of lubricating with rapeseed oil without additive and with rapeseed oil, containing 4% of the additive AAE anti-wear/extreme pressure (AW/EP).

The experimental runs were carried out under identical dynamic conditions: number of revolutions n = 970 min^{-1} and under loading P = 25 N, 250 N, 500 N, 1000 N и 1250 N.

The measurements were made during a period of 2 minutes and total duration of friction 10 minutes. The initial temperature of the oil was 21°C.

The experimental data are listed in Table 1 and Table 2.

Table 1. Moment of friction, coefficient of friction and temperature of the oil in case of lubrication with rapeseed oil without additive

Lubrication with rapeseed oil without additive					
Loading, N	25	250	500	1000	1250
Moment of friction, Nm	0.2	0.3	0.4	1.2	1.5
Coefficient of friction	0.4	0.06	0.04	0.06	0.06
Temperature of the oil, °C	21.3	21.7	22.2	30	40
Time, s	120	120	120	120	120

Table 2. Moment of friction, coefficient of friction and temperature of the oil in case of lubrication with rapeseed oil with additive

Lubrication with rapeseed oil with additive					
Loading, N	25	250	500	1000	1250
Moment of friction, Nm	0.3	0.3	0.4	0.8	1.1
Coefficient of friction	0.5	0.1	0.04	0.05	0.04
Temperature of the oil, °C	21	21	21.5	22	26
Time, s	120	120	120	120	120

The dependence of the moment of friction on normal loading in case of lubrication with rapeseed oil without additive and with the additive is represented in Fig. 3, while the values of the respective coefficients of friction are given in Fig. 4.

The dependence has non-linear character for both types of oil. Under low loading up to 250 N the moment of friction remains constant and it has the same values for the two oils.

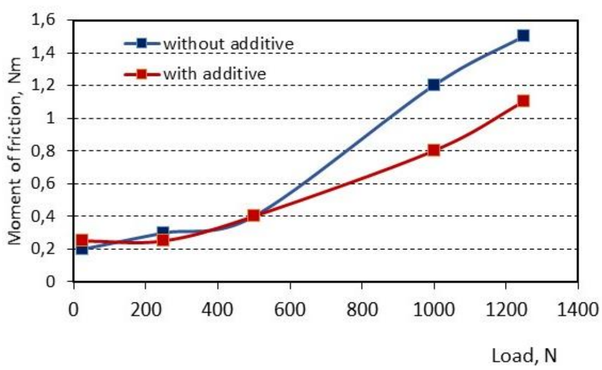

Figure 3. Dependence of the moment of friction on the loading in cases of lubrication with rapeseed oil without additive and with additive

When the loading is higher than 250N the moment of friction grows up non-linearly for both types of oil. One can see in Fig. 3 that for each value of the loading the moment of friction in case of rapeseed oil with additive AAE AW/EP is always smaller than the moment of friction for rapeseed oil without additive. The degree of decrease in the moment of friction when the loading is increase is only slightly different for the two oils. When the loading is 1000 N the presence of additive in the rapeseed oil leads to reduction of the moment of friction 1.5 times, while at higher loading 1500 N – 1.36 times.

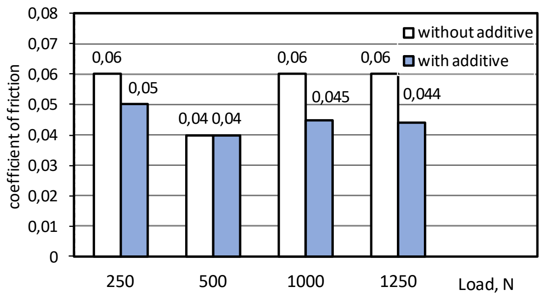

Figure 4. Diagram of the coefficient of friction in cases of lubrication with rapeseed oil without additive and with additive under different loadings

As one can see from the diagram in Fig. 4 the dependence of the coefficient of friction on the loading when lubricating with rapeseed oil without additive has non-linear character with well-expressed minimum under loading of 500 N. Under higher loading COF increases abruptly up to 1.5 times.

Upon lubrication with rapeseed oil with additive AAE AW/EP under higher loading of 500 N there is a little increase – 1.1 times and it remains constant. This could be explained by the fact that the presence of additive AAE AW/EP in the rapeseed oil leads to preservation of the lubricating film in the contact between the bearing rings and the ball pellets under higher loading. In case of lubrication with pure rapeseed oil the increase in COF upon increasing the loading is due to disruption of the lubricating film, increase in the local contact pressure as a result of the dominating mechanical component of the friction.

These results correspond to the nature of the dependence of the temperature of the two types of oils on the loading, represented in Figure 5.

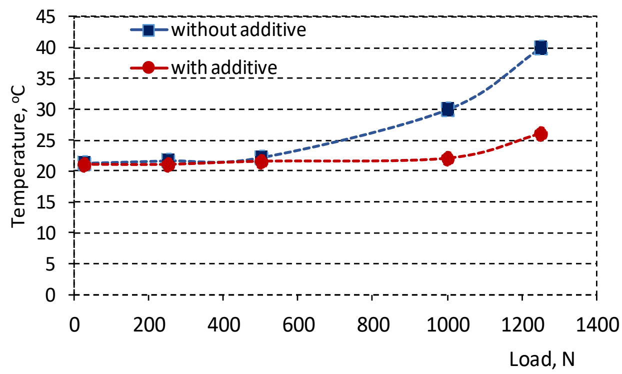

Figure 5. Dependence of the temperature of the oil on the loading during lubrication with rapeseed oil without additive and with additive

Up to loading of 500 N the temperatures of the two oils are the same and they are constant. Upon increasing the loading in case of rapeseed oil without additive the temperature starts to grow up. Upon increasing the loading 50 times, i.e. starting from 25N up to 1250N, the temperature of the rapeseed oil without additive increases almost 2 times - from 21,3 ^{o}C up to 40^{o}C (Table 1), while in the case of rapeseed oil with additive AAE AW/EP the temperature increases 1.2 times - from 21^{o}C up to 26^{o}C (Table 2).

3. FRICTION IN SLIDING BEARING „SHAFT-BUSHING"

A comparative study was carried out focused on the coefficient of friction and on the contact temperature in sliding bearing „Shaft-bushing" in case of drop-wise lubrication with rapeseed oil without additive and rapeseed oil with additive AAE AW/EP at several different values of the normal loading – 250 N, 500 N, 1000 N and 1500 N.

3.1 Device and methodology

The experimental determination of the coefficient of friction is accomplished using the device DM 29M, represented in Figure 6 and Figure 7.

The device consists of a body (1), inside which a sliding bearing „shaft-bushing" is mounted; driving mechanism; loading mechanism, measuring device and a system for feeding lubrican oil. The shaft (14) is positioned on supports of two rolling bearings and it is driven by electric motor (12) by means of three-step wedge-belt transmission (13).

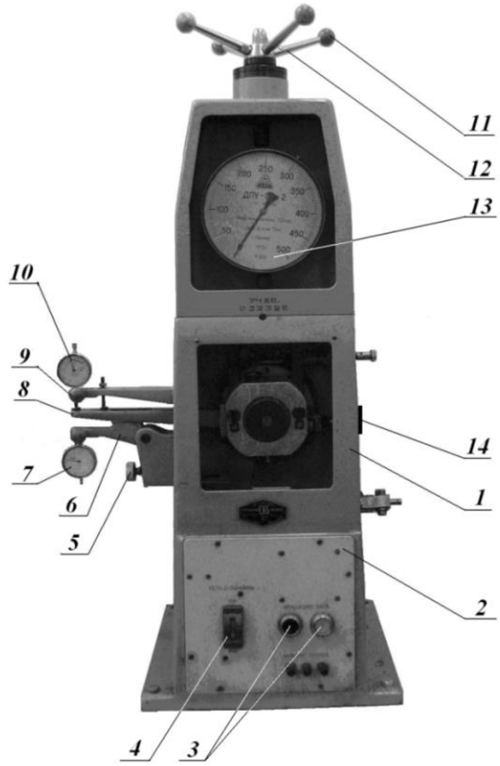

Figure 6. Photograph of device DM 29M

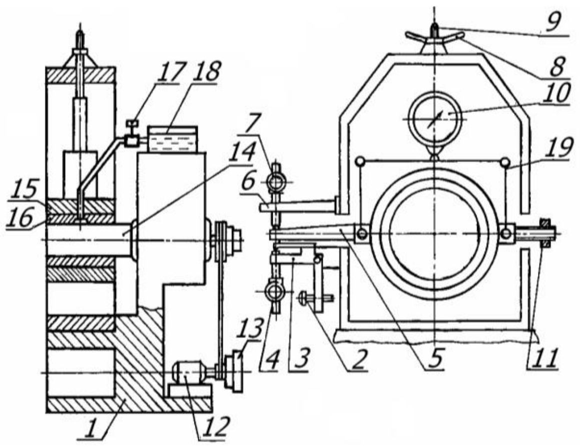

Figure 7. Scheme of device DM 29M

The tested bearing „shaft – bushing" is located in duraluminium body (15), whereupon the bronze bushing (16) is attached to a console at the end of the shaft (14).

The mechanism for loading of the bearing consists of loading screw (9) with a handle (8) and threaded bushing with sliding cotter, dynamometer (10), which is connected by a hinge with the threaded bushing, and loading framework (19). The framework (19) is connected by knuckle-joint to the body (15) and to the dynamometer (10). Upon rotating the handle (8) the screw (9) is shifted vertcally upwards and the loading framework (19) transfers the loading in the bearing from below upwards. The loading is measured on the scale of the dynamometer (10), graduated in Newtons - Fig.7. The Table 3 represents the technical characteristics of the tested sliding bearing.

Table 3. Characteristics of the tested sliding bearing.

Journal diameter	d = 60 mm
Bush length	l = 60 mm
Diametral clearance	C = 0.06 mm
Shaft (journal) material	Structural carbon steel 45 (GOST 8731-87); HRC = 35
Bush material	Lead bronze БрО5Ц5С5 (GOST 613-79); 60 HB
Lubricant	Rapeseed oil without and with 4% AW/EP additive

The measuring device consists of: measurement beam (5), attached to the body (15); fixed beam (6) with indicator (7); moveable beam (3) with measuring plate and indicator (4). The end-piece of the indicator (7) touches the measurement beam (5), while the end-piece of the lower indicator (4) touches the measuring plate, which is connected to the beam (5).

The system for feeding the lubricant oil to the bearing consists of oil bath (18), located in the upper part of the bodyand from there the oil flows down gravitationally at a rate of 30 - 40 drops per minute and along the pipeline with a valve (17) it enters the receiver channel of the bearing.

During the rotation of the shaft (14) in direction reverse to the clockwise direction under the effect of the moment of the forces of friction in the bearing the measurement beam (5) is bending and the arrow of the indicator (4) isdeviated to position δ.

The methodology for determination of the coefficient of friction is carried out in the following sequence: first the value of the revolutions per minute is set n = 1350 min^{-1} = const; the lubricating system is switched on by the valve (17) whereupon dropwise lubrication starts with rapeseed oil without/with additive; the normal loading value is set $P_1 = 250$ N by means of the loading screw (9); the settings on the two indicators are nullified (4) and (7); the electric motor is switched on and after a time period of operation 20 seconds at at nullified value setting on the indicator (7) on the fixed beam (6) the operator reads the indication δ of the indicator (4) on the moveable beam (3). Consecutively in time intervals of 40, 60......120 seconds one reads the indication δ.

The coefficient of friction f at any moment of operation is calculated by the formula:

$$f = k\frac{\delta}{P} \qquad (2)$$

where: k=0.23 is the constant of the device.

The experimental run is repeated upon consecutively setting the loading value - $P_2 = 500$ N; $P_3 = 1000$ N and $P_4 = 1500$ N. The device enables carrying out the experimental runs at turnover numbers n = 500 min^{-1} and n = 2400 min^{-1}.

3.2 Results and analysis

The experiments were carried out under identical dynamic conditions: revolutions per minute n = 760 min^{-1} and loading. The results are recorded at time intervals of 2 minutes having total duration of the friction process 8 minutes. The initial temperature of the oil was 23,1°C. The contact temperature was measured by means of laser infrared thermometer INFRARED.

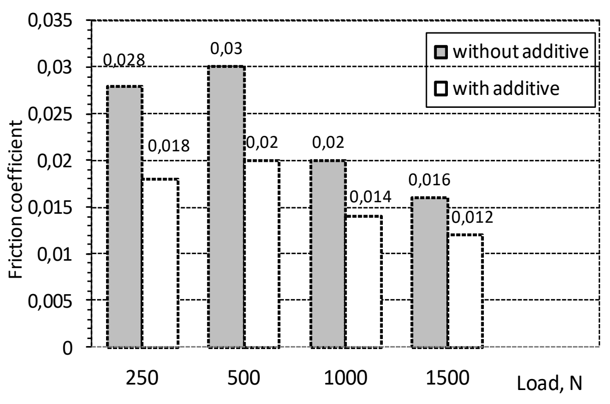

Figure 8. Coefficient of friction in cases of lubrication with rapeseed oil without and with additive under different normal loading

Figure 8 represents a diagram of the coefficient of friction, while Figure 9 illustrates the average contact temperature under different loadings in case of lubricating with pure rapeseed oil and with rapeseed oil having the additive AW/EP.

One can see from the diagram in Fig. 8 that under each loading value the coefficient of friction in case of lubrication with rapeseed oil having the AW/EP additive is lower than the coefficient of friction in case of lubrication with rapeseed oil without the additive.

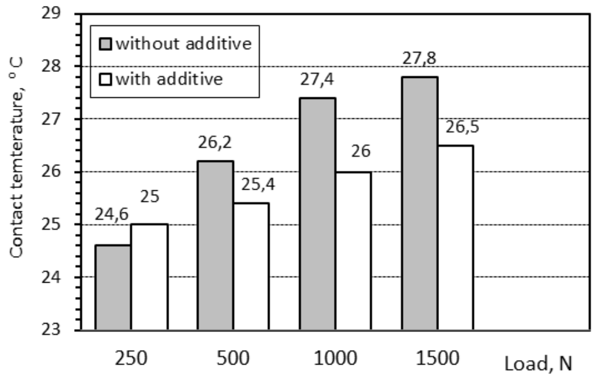

Figure 9. Average contact temperature (after 120 seconds) for rapeseed oil without and with additive under different normal loadings.

The dependence of the coefficient of friction on the loading has clearly expressed non-linear character. Upon increasing the loading the coefficient of friction grows up reaching the maximum value at P=500 N, and thereafter it is reduced. This character of the dependence is observed in the cases of both types of oils. The value of the maximum of the coefficient of friction for pure rapeseed oil is 0.03, while that for rapeseed oil with additive it is 0.02.

The influence of the additive AW/EP could be evaluated in first approximation based on the difference between the values of the coefficient of friction of the two oils. Under low loadings P_1=250N and P_2=500N this difference has the same value of 0.01. Upon increasing the loading the difference decreases: at P_3 = 1000 N it becomes 0.06, while at P_4 = 1500 N it is 0.04. This leads us to the conclusion, that under very high loadings one could expect that the influence of the additive will be reduced. This in its turn implies the necessity in the future to elaborate methodology and to study the influence of the additive upon the resource of rapeseed oil for various regimes of friction.

The obtained results are in harmony with the results on the changes of the contact temperature upon increasing the normal loading. One can see in Figure 9 that the presence of the additive AW/EP in the rapeseed oil leads to decrease in the contact temperature. During lubrication with rapeseed oil with additive under low loading P=250 N the temperature is with some 0.5^{o}C higher, but upon increasing the loading it remains lower under each loading with 1.3 ÷ 1.4 ^{o}C.

4. CONCLUSIONS

Comparative results have been obtained for the moment of friction, the coefficient of friction and the temperature of the lubricating oil under different loadings in rolling bearings and sliding bearing „shaft-bushing“ in the cases of lubrication with rapeseed oil without additive and rapeseed oil, containing 4% non-toxic ash-less additive AW/EP, which is designed for biodegradable base oils.

It has been found out that the presence of 4% non-toxic ash-free additive AW/EP in rapeseed oil leads to reduction of the moment of friction, the coefficient of friction and the contact temperature within the entire range of applied normal loading in both types of bearings. The difference between the coefficients of friction of the two types of lubricating oils upon increasing the loading is decreasing.

In the case of rolling bearings upon increasing the loading the coefficient of friction grows up for the pure rapeseed oil lubrication, while for the rapeseed oil with additive the coefficient of friction preserves a constant value. In the case of sliding bearing „shaft-bushing“under the conditions of boundary friction the coefficient of friction for both types of lubricating oils decreases with the increase in loading.

ACKNOWLEDGEMENT

The studies of the present research work have been carried out at the laboratory «Tribotechnika» in Southern Ural State University in Chelyabinsk, Russia and in the laboratory «Tribology» at the Technical University in Sofia, Bulgaria on the basis of Bilateral Cooperation Agreement between the two universities.

REFERENCES

[1] H.P. Jost: Tribology – from basics to productivity and employment, Opening Speech at the 5th World Tribology Congress, Torino, 2013.

[2] B. Bhushan (Ed.): *Modern Tribology Handbook*, CRC Press, Boca Raton, 2001.

[3] W.J. Bartz: Reducing the impairment of the environment, in: *Proceedings of the 2nd European Conference on Tribology ECOTRIB`2009*, Pisa, Italy, June, 2009.

[4] M. Nosonovski, B. Bhushan: Green tribology: principles, research areas and challenges. Phil.Trans.R.Soc.A, Vol. 368, pp. 4677-4694, 2010.

[5] A. Rac, A. Vencl: Ecological and technical aspects of the waste oils influence on environment, The Annals of University “Dunărea de Jos” of Galaţi, Fascicle VIII, Tribology, Vol. 18, No. 1, pp. 5-11, 2012.

[6] S. Sasakip: Environmentally friendly tribology (Eco-tribology), Journal of Mechanical Science and Technology, Vol. 24, pp. 67-71, 2010.

[7] R. Altõn, et al: The potential of using vegetable oil fuels as fuel for diesel engines, Energy Conversion and Management, Vol. 42, pp. 529-538, 2001.

[8] A. Abolle´, L. Kouakou, H. Planche: The viscosity of diesel oil and mixtures with straight vegetable oils: Palm, cabbage palm, cotton, groundnut, copra and sunflower, Biomassand bioenergy, Vol. 33, pp. 1116 – 1121, 2009.

[9] N.J. Fox, G.W. Stachowiak: Vegetable oil-based lubricants - a review of oxidation, Tribology International, Vol. 40, pp. 1035–1046, 2007.

[10] J.M. Perez, et al: Characterization of Tricresylphosphate Lubricating Films by Micro-Fourier Transform Infrared Spectroscopy, Tribology Transactions, pp. 131-139, 1990.

[11] A. M. Bugaev: Effect of the multifunctional additive "Valena" on the tribological properties of rapeseed oil, Agroengineering, M., FGOU VPO MSAU, 2008, No. 4, 99-101.

[12] E. Zadorozhnaya, I. Levanov, M. Kandeva: Tribological research of biodegradable lubricants for friction units of machines and mechanisms: Current state of research, Lecture Notes in Mechanical Engineering, Vol. 9783319956299, pp. 939-947, Springer Nature, 2019.

[13] M. Kandeva, Zh. Kalitchin, E. Zadorozhnaya: Tribological Investigations on Tribosystems Lubricated with Vegetable Oils and Mineral-Vegetable Composites with Metalplating Additive, Part II: Wear, Journal of Environmental Protection and Ecology, Vol. 19, No. 4, pp. 1678-1689, 2018.

SERBIATRIB '19

16th International Conference on Tribology

Serbian Tribology Society

Faculty of Engineering University of Kragujevac

Kragujevac, Serbia, 15 – 17 May 2019

TRIBOTECHNICAL PROPERTIES OF MOTOR AND INDUSTRIAL OILS WITH COPPER, TIN AND ZINC OLEATES

Igor LEVANOV[1,*], Elena ZADOROZHNAYA[1], Igor MUKHORTOV[1], Igor DOLGUSHIN[1]

[1] South Ural State University, Russia

*Corresponding author: levanovig@susu.ru

Abstract: *The purpose of this study is to determine the effect of metal ion on the tribological characteristics of metal oleates similar to copper (II) oleate which is the basis of well-known additives such as Valena, Servovit etc. The objects of study are copper (II), zinc (II) and tin (II) oleates. Salts of these metals are selected to clarify the role of such parameters of metal ion, as the active metal and the radius of the ion. Lubricant compositions were prepared with each additive sample. The mass concentration of the additive was 1% in synthetic motor oil of viscosity class SAE 5W-40 (API SN/CF) and in industrial oil I40A. The influence of metal oleates on the friction coefficient of the friction pair of steel 45-steel 10 was investigated. The friction coefficient was measured on the machine friction II5018 according to the scheme "roller-pad" at different temperatures. The investigated additives have the most significant effect on the coefficient of friction when introduced into the oil without additives and less significantly when introduced into the engine oil. The results show that copper oleate reduces the coefficient of friction in contact by 7% -15% when added to the engine oil. Zinc oleate leads to a similar effect and reduces the coefficient of friction by 5.5% -8.5%. Oleate of tin leads to a decrease in the friction coefficient of 23.5%-31%.*

Keywords: *motor oil, industrial oil, metal oleates.*

1. INTRODUCTION

Reducing energy losses and wear in friction units of machines and mechanisms is an important task. A significant reserve to reduce friction is hidden in lubricants and additives. Oleates of some metals are part of many lubricant compositions [1-12]. These lubricating compositions can significantly reduce the coefficient of friction and wear of machine parts. Copper oleate is most widely used as a component of so-called metal-plating additives for lubricants. The concentration of copper oleate is from 3 to 60% of metal-plating additives (MPA). Metal-plating additives are special additives to lubricants and provide the formation of secondary structures on the friction surfaces. These structures consist of a metal-clad film and boundary layers of various substances and surfing films [13]. Powders of metals and alloys (copper, tin, zinc, aluminum, bronze, etc.), oxides and salts of metals are used as MPA and improve tribotechnical characteristics of friction units [14]. Metal-plating additives in lubricants allow to realize the zero-wear effect in friction units. This effect is based on the phenomenon of selective transfer [13]. The phenomenon of selective transfer is widely described in the literature and many works are devoted to studies of the effect of metal-plating additives on the tribological characteristics of liquid and plastic lubricants in different friction units [15-20].

Prokopenko et al. [8] presented a metal-plating additive that contains 25 to 60% by weight of monovalent copper oleate. This additive (at a concentration of 0.075% by weight) reduces wear during run-in from 2 to 5 times. Dubinin and others [10] presented an additive with copper, magnesium, yttrium and lanthanide oleates. This additive reduces the friction coefficient by 50% in steel-steel contact.

Belolyubskij, Lozovskij and Afanas'ev [11] presented a lubricant containing copper powder, polytetrafluoroethylene, tributyl phosphate, a copper-containing additive and a soap plastic lubricant. The copper-containing additive contained 60% industrial oil, 20% copper oleate and 20% oleic acid. The authors determined the threshold of resistance to scoring and linear wear at the contact of a spherical steel samples with plasma samples. They found that the introduction of tributyl phosphate and copper-containing additives into the plastic lubricant provides an increase in its service life and at the same time significantly increases the anti-wear and extreme pressure properties.

Kozarov and Onischuk [19] presented a review study MPA and lubricants. The authors presented the classification of metal-plating lubricants depending on the type of MPA. Metal or alloy powders, metal oxides, metal salts, complex metal compounds, metalloorganic compounds and organic compounds are used as metal-plating additives to lubricants.

MPA [1, 12] provides antifriction and extreme pressure properties of the lubricant due to the effect of wearlessness in the friction pairs (steel-steel, steel-cast iron, steel-bronze, etc.) as a result of the formation of a protective (servovite) metal-coating film on the surfaces of parts in places of actual contact with a thickness of 1-3 microns and autocompensation of wear of friction pairs [20].

Oleate is the basis of well-known additives such as Valena [12], Servovit [1], etc. [2, 11]. The purpose of this study is to determine the effect of metal ion on the tribological characteristics of metal oleates similar to copper (II) oleate.

2. CHARACTERISTICS OF RESEARCH OBJECTS

The objects of study are copper (II), zinc (II) and tin (II) oleates. Salts of these metals are selected to clarify the role of such parameters of metal ion, as the active metal and the radius of the ion. With an equal degree of oxidation of the metal, these parameters are crucial for the adsorption of oleate from the lubricant, metal recovery on the surface of steel and other tribochemical processes due to the presence of additives. Tin is between iron and copper in a series of metal stresses. Zinc (as opposed to copper and tin) is a more active metal than iron. The radius of the zinc ion (II) is almost equal to the size of the copper ion (II). The radius of the tin ion (II) is almost 2 times larger. Table 1 presents the properties of copper (II), zinc (II) and tin (II) oleates.

Table 1. Properties of copper (II), zinc (II) and tin (II) oleates

Additive	Copper oleate	Zinc oleate	Tin oleate
Chemical formula	$Cu(C_{17}H_{33}COO)_2$	$Zn(C_{17}H_{33}COO)_2$	$Sn(C_{17}H_{33}COO)_2$
Molar mass	626.45 g/mol	628.29 g/mol	681.61 g/mol
Form	Amorphous, dark-green substance	White solid	Liquid, color depends on the original oleic acid
Melting point, ºC	20…35	70	- 5…+5
Solubility: - in water - in hexane	 Insoluble Soluble	 Insoluble Soluble	 Insoluble Soluble

Transition metal oleates are obtained by the interaction of aqueous solutions of alkali metal oleates with sulfates or transition metal chlorides [21]. This results in the formation of transition metal oleates insoluble in water and forming a separate phase. In the case of easily hydrolyzing metal salts, for example, Sn (II), the reaction of oleic acid with metal oxides in a non-aqueous medium is carried out [21, 22].

3. EXPERIMENT AND RESULTS

Lubricant compositions were prepared with each additive sample. The mass concentration of the additive was 1% in synthetic motor oil of viscosity class SAE 5W-40 (API SN/CF) and in industrial oil I40A [23]. Industrial oil I40A is a purified oil without additives for industrial equipment.

The influence of metal oleates on the friction coefficient of the friction pair of steel 45-steel 10 was investigated. The friction coefficient was measured on the machine friction II5018 according to the scheme "roller-pad" at different temperatures. The sliding speed in the friction contact was 2.3 m/s. The temperature on the friction contact was controlled by a thermocouple installed in a partial liner at a distance of 5 mm from the working surface. The lubricant with the additive was fed into the friction zone by gravity at an average speed of 1 drop per 2 seconds.

Each experience was repeated from 3 to 6 times. The averaged results of friction coefficient measurement are presented in figures 1-3.

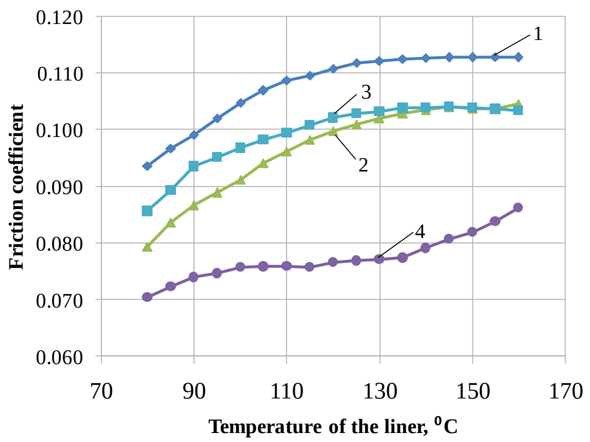

Figure 1. Temperature dependence of the friction coefficient (unit load of 8 MPa) for motor oil: 1- Motor oil SAE 5W-40; 2 - Motor oil SAE 5W-40 + 1% Copper oleate; 3 - Motor oil SAE 5W-40 + 1% Zinc oleate; 4 - Motor oil SAE 5W-40 + 1% Tin oleate

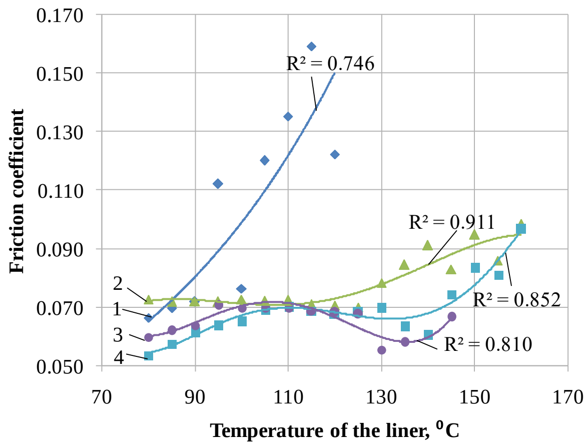

Figure 2. Temperature dependence of the friction coefficient (unit load of 8 MPa) for industrial oil: 1- Industrial oil I40A; 2 - Industrial oil I40A + 1% Copper oleate; 3 - Industrial oil I40A + 1% Zinc oleate; 4 - Industrial oil I40A + 1% Tin oleate

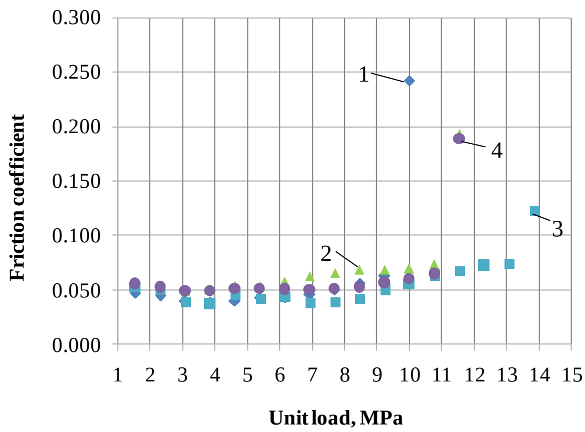

Figure 3. Dependence of friction coefficient on unit load for industrial oil

The results show that copper oleate reduces the coefficient of friction in contact by 7% -15% when added to the engine oil. Zinc oleate leads to a similar effect and reduces the coefficient of friction by 5.5% -8.5%. Oleate of tin leads to a decrease in the friction coefficient of 23.5%-31%.

The effect takes place in industrial oil. In this case, the temperature range of the industrial oil becomes significantly greater. Oil without additives leads to a sharp increase in the coefficient of friction in the contact of friction at a temperature above 95 degrees. In addition, copper, zinc and tin oleate increase the load at which the transition to the boundary mode of friction occurs.

Antiwear properties of lubricants were evaluated on the four-ball friction machine in accordance with GOST 9490-75. Figures 4, 5 show the measurement results of the mean wear scar diameter (MWSD). All lubricants were tested at a load of 392 N. Contact areas of samples after four-ball machine test are presented in figures 6 and 7.

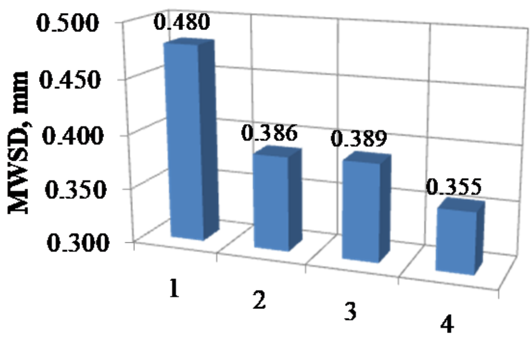

Figure 4. Mean wear scar diameter (Motor oil SAE 5W-40)

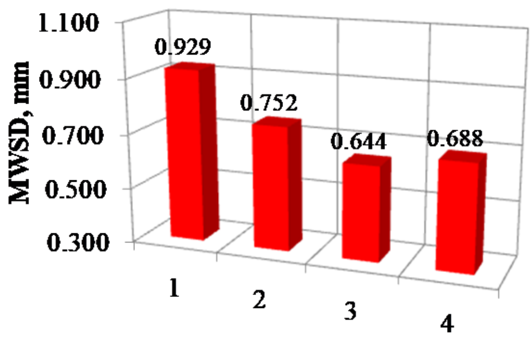

Figure 5. Mean wear scar diameter (Industrial oil I40A)

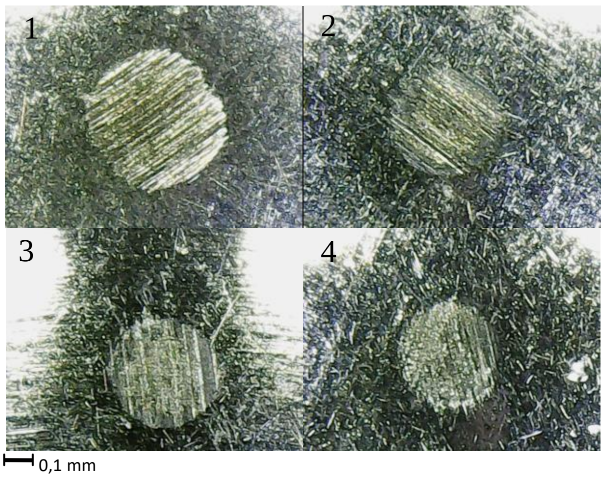

Figure 6. Contact area of samples after four-ball machine test (Motor oil SAE 5W-40)

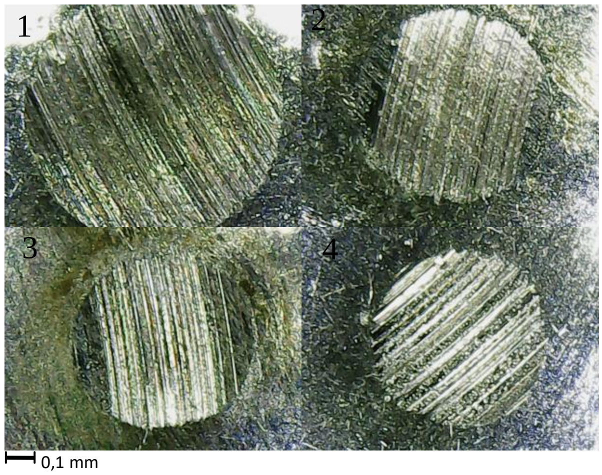

Figure 7. Contact area of samples after four-ball machine test (Industrial oil I40A)

4. CONCLUSION

The main conclusions drawn from this investigation are as follow:

1. The investigated additives have the most significant effect on the coefficient of friction when introduced into the oil without additives and less significantly when introduced into the engine oil. This is an obvious and expected result.
2. Tin oleate has the best anti-friction properties in both cases.
3. All investigated oleates slightly increase the coefficient of friction at temperatures below 80 ℃ for both additive-free oil and motor oil. In the temperature range of 80...150 ℃ effect of zinc and copper oleates in the engine oil varies slightly.
4. Zinc is a more active metal than iron, and copper is a less active metal than iron. Tin in the electrochemical series of metal stresses occupies an intermediate position between zinc and copper. The absence of significant differences in the tribological properties of zinc and copper oleate in steel-steel contact, as well as greater efficiency of tin oleate, indicate in favor of the adsorption mechanism of action of these additives. The contribution of tribochemical processes is insignificant. In addition, this is confirmed by the fact that the sizes of the ions of bivalent copper and zinc are almost equal, and the size of

the tin ion of bivalent is much larger. Consequently, the structure and dipole moment of tin oleate differs from the parameters of zinc and copper oleates.

5. Friction coefficients for all three additives converge with increasing temperature due to the processes of oleate dissociation. Thus, when the temperature increases, the effect of oleic acid on the friction process increases.
6. The dependence of the friction coefficients on the contact pressure confirms the assumption about the adsorption mechanism of oleate action. The highest contact pressure at which friction enters the boundary regime is observed for the most stable zinc oleate (see Fig. 3). Thus, anti-friction properties are manifested while maintaining the structure of oleates.
7. For further research are of interest oil-soluble salts of the same metals with other organic acids, including more complex structure. Since the tribological properties of the studied oleates are determined by adsorption processes, and at high temperatures are determined by the properties of oleic acid.
8. The results of anti-wear tests showed that all three oleates lead to almost the same decrease in wear. The wear spot diameter is reduced by 20...30 % by adding tin, zinc and copper oleates to motor and industrial oil.A comparison of the wear test results with the friction test results shows that the results of the four-ball machine tests were as close as those of the high-temperature tests. This may be due to the fact that the secondary adsorption structures due to the adsorption of oleates on the metal surface are destroyed at high contact pressures and shear stresses. These structures at moderate contact pressures and temperatures cause a difference in the antifriction properties of the additives.

Adsorption of degradation products of additives (oleic acid) plays a major role at high shear stresses, as well as at high temperatures. The influence of the metal ion parameters on the structure of the adsorbed layer is minimal.

ACKNOWLEDGEMENT

This work has been carried out within financial support of Russian Foundation for Basic Research (project № 16-08-01020\16). The work was supported by Act 211 Government of the Russian Federation, contract № 02.A03.21.0011.

REFERENCES

[1] V.G. Babel', D.N. Garkunov: Metal-coating multifunctional composition for motor, transmission and industrial oil, RU Patent 2,398,010, 6 Mar 2009. (on Russian)

[2] V.N. Bystrov, M.E. Stavrovskij, E.A. Lukashev: Metall-plaguing additive for lubricating compositions, RU Patent 2,293,758, 11 July 2005. (on Russian)

[3] S.V. Inshakov, V.I. Balabanov, S.A. Ishchenko, J.D. Kleptsova: Metal-coating additive for lubricant materials. RU Patent 2,503,713, 27 Nov 2012. (on Russian)

[4] V.I. Balabanov, V.J. Bolgov, S.A. Ishcenko, V.V. Lekhter: Metal plating restoration additive to plastic lubricating materials. RU Patent 2,432,386, 27 October 2011. (on Russian)

[5] V.N. Antonov, V.I. Balabanov, V.N. Bystrov: Metall-plaguing additive for lubricating compositions. RU Patent 2,044,761, 27 Sept 1995. (on Russian)

[6] V.I. Balabanov, S.A. Ishchenko, A.G. Gamidov: Metall-plaguing additive for lubricant materials. RU Patent 2,344,165, 20 Jan 2009. (on Russian)

[7] V.N. Bystrov, V.N. Antonov, Y.V. Lopatiyk: Metall-plaguing additive for lubricating compositions. RU Patent 2,186,834, 10 August 2002. (on Russian)

[8] A.K. Prokopenko, Y.S. Simakov, D.N. Garkunov, S.G. Krasikov: Metall-plaguing additive. SU Patent 859425, 30 August 1981. (on Russian)

[9] E.N. Sheveleva, Y.G. Savinyh, V.V. Harlamov, G.V. Bujskih, E.V. Kurdina: Metall-plaguing

additive for lubricating oils. SU Patent 1785263, 10 Jun 1999. (on Russian)
[10] E.L. Dubinin, V.V. Zaborskich, E.S. Koniychov: Metall-plaguing additive for lubricating oils. SU Patent 1721077, 23 Mar 1992. (on Russian)
[11] I.A. Belolyubskij, V.N. Lozovskij, V.A. Afanas'ev: Metall-plaguing lubricant. RU Patent 2000314, 7 Sept 1993. (on Russian)
[12] V. Babel, D. Garkunov, S. Mamikin, P. Kornik: Metal-containing oil-soluble composition for lubricant materials. RU Patent 2,277,579, 26 May 2005. (on Russian)
[13] D.N. Garkunov, I.V. Kragelskij, A.A. Polyakov: Izbiratel'nyj perenos v uzlah treniya (Selective transfer in friction units). Transport, Moscow, 1969. (on Russian)
[14] A.S. Kuzharov, N.Y. Onishchuk: Svojstva i primenenie metalloplakiruyushchih smazok (Properties and application of metal-plating lubricants). CNIITEHKHIM, Moscow, 1985. (on Russian)
[15] D.N. Garkunov: Tribotekhnika (iznos i bezyznosnost') (Tribotechnology (Wear and Non-wear)). Moscow, 2001. (on Russian)
[16] G.P. SHpen'kov: O yavlenii izbiratel'nogo perenosa. Dolgovechnost' trushchihsya detalej mashin. Vypusk 4 (On the phenomenon of selective transfer. The durability of friction parts of machines. Issue 4). Engineering, Moscow, p 3–11, 1990. (on Russian)
[17] A. Firkovskij, G. Pol'cer: Strukturirovanie tribologicheskoj sistemy v usloviyah izbiratel'nogo perenosa. Dolgovechnost' trushchihsya detalej mashin. Vypusk 4 (Structuring of tribological system under conditions of selective transfer. The durability of friction parts of machines. Issue 4). Engineering, Moscow, p 15–29, 1990. (on Russian)
[18] V.N. Bystrov: EHffekt bezyznosnosti i ego primenenie v tekhnike. Dolgovechnost' trushchihsya detalej mashin. Vypusk 5 (The effect of wearlessness and its use in technology. The durability of friction parts of machines. Issue 5). Engineering, Moscow, p 3–22, 1990. (on Russian)
[19] A.S. Kuzharov, N.Y. Onishchuk: Metalloplakiruyushchie smazochnye materialy. Dolgovechnost' trushchihsya detalej mashin. Vypusk 3 (Metal-plating lubricants. The durability of friction parts of machines. Issue 3). Engineering, Moscow, p 96–143, 1988. (on Russian)
[20] Kandeva M, Kalitchin ZH, Tribological investigations of tribosystems during lubrication using vegetable oils and mineral-vegetable oil composites containing metal-plating additive. Part I: Friction. Journal of Environmental Protection and Ecology 19: pp. 785–802, 2018.
[21] I.L. Knunyanc: Himicheskij ehnciklopedicheskij slovar' (Chemical encyclopaedic dictionary). Sovetskaya ehnciklopediya, Moscow, 1983. (on Russian)
[22] CRC Handbook of Chemistry and Physics. — 89th Edition. — Taylor and Francis Group, LLC, 2008-2009.
[23] GOST 20799-88 Industrial Oils. Technical conditions, 1988. (on Russian)

Serbian Tribology Society

SERBIATRIB '19

16th International Conference on Tribology

Faculty of Engineering University of Kragujevac

Kragujevac, Serbia, 15 – 17 May 2019

INVESTIGATION OF FILM THICKNESS OF GREASE-LUBRICATED THRUST BEARING: FROM BALL-ON-DISC TO BEARING

Josef FRYZA[1,*], Jiri KROUPA[1], Petr SPERKA[1], Ivan KRUPKA[1], Martin HARTL[1]

[1]Brno University of Technology, Brno, Czech Republic

*Corresponding author: Josef.Fryza@vut.cz

Abstract: *Rolling element bearings lubricated by greases represent the most used mechanical components in industry, thus the total volume of energy required to overcome their friction is enormous. Even small improvements can provide considerable savings. To reach these improvements, it is necessary to understand all the processes in the bearing, and especially those that take place in contacts of rolling elements. So far, most of the research was done on tribometers employing a ball-on-disc configuration. Tests on such devices are easy to perform but differ from conditions of actual bearings in some important aspects such as a contact geometry, presence of cage, number of contacts, spin motion of rolling elements, or action of centrifugal and capillary forces. The aim of this experimental study is to refer about film thickness during the initial running phase of simulated thrust rolling bearing and to reveal some patterns of lubricant behaviour for different conditions and greases. Measurements were carried out on unique apparatus of simulated thrust rolling bearing using optical methods with high speed camera. Results showed that the ball-on-disc configuration does not completely correspond to behaviour of actual bearings, mostly in terms of starvation and replenishment of grease. Multiple contacts in succession of simulated bearing do not tend to starve so rapidly and seriously during experiments as is presented in literature for ball-on disc configuration under similar conditions.*

Keywords: *grease lubrication, EHL, starvation, replenishment, film thickness, rolling element bearing*

1. INTRODUCTION

The main purpose of rolling element bearings is to reduce friction between two parts of different angular velocity. Holmberg et al. reported in 2017 [1] that 23% of total energy consumption is attributed to the operation of these tribological elements due to their wide application across the world. Majority of the rolling bearings operates in the EHL regime. This regime is described as a type of hydrodynamic lubrication where large contact pressure causes elastic deformations of contacting bodies and changes in viscosity of the lubricant [2]. Since the 1950s, a huge progress has been made in field of EHL regime. Satisfactory agreement between predictions and experimental results was reached. However, this achievement is limited to the cases including steady-state conditions, Newtonian fluids, and perfectly smooth surfaces [3].

Almost all rolling bearings (about 95%) are lubricated by greases. Even nowadays, it is still not possible to reliably predict grease behaviour in the bearing contacts as greases have complex (non-Newtonian, thixotropic) rheology. Experimental studies published on grease lubrication were performed mainly on ball-on-disc simulators [4-9] while there is only a few papers involving full-scale bearing simulators [10-13] which were focused principally on resulting bearing torque not on film thickness formed in bearing contacts.

Considering the limited scope of the article and the complexity of grease lubricated bearings, it is impossible to include a qualitative and quantitative description of all the effects occurring in the bearings in one study. The aim of this paper is to provide a fundamental insight into the film thickness trends during the initial running of grease lubricated thrust rolling bearing and to point out the differences with the ball-on-disc simulator, whose results are often misunderstood as the behaviour of grease in actual bearings.

2. MATERIAL AND METHODS

Experiments were performed on a unique apparatus involving 51220 thrust ball bearing, see Fig. 1. One steel washer of the bearing was replaced by a glass (BK7) disk to enable direct optical observation of grease film distribution.

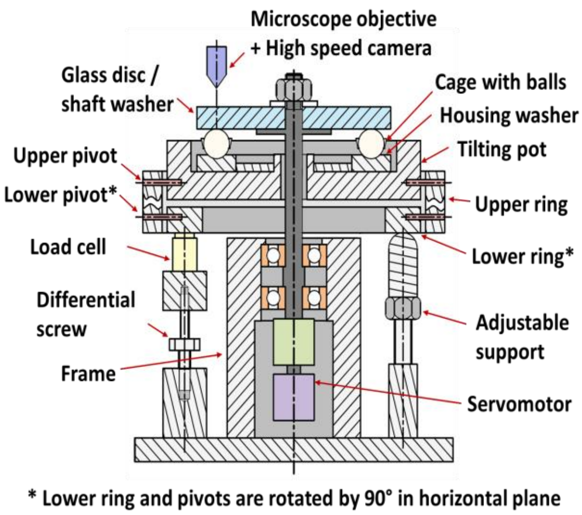

Figure 1. Full thrust ball bearing simulator

Film thickness was evaluated via the method of colorimetric interferometry [14,15]. Experiments were carried out under room temperature. Two industrial greases MOGUL LV 2-3 and LVS 3 were used as lubricants. Details of greases used in the experiments are summarized in Table 1.

Table 1. Details on used lubricants

Grease	LVS 3	LV 2-3
Base oil	mineral	
Base oil viscosity at 40 °C (mm^2/s)	110	50
Thickener	Li soap	
NLGI grade	3	2-3

Load of 20 N per ball contact was applied in the experiments performed on bearing simulator while 35 N was used on a ball-on-disc simulator (for more details on this simulator, see Ref. [15]) to ensure the same contact pressure. For comparison of starved and fully flooded (FF) film thicknesses, a film thickness of grease LVS 2-3 under FF conditions was estimated by means of Hamrock-Dowson film thickness formulas [16].

3. RESULTS AND DISCUSSION

Firstly, experiment with LV 2-3 grease was conducted on the ball-on-disc simulator for entrainment speed ranging from 0.05 to 0.8 m/s under FF conditions.

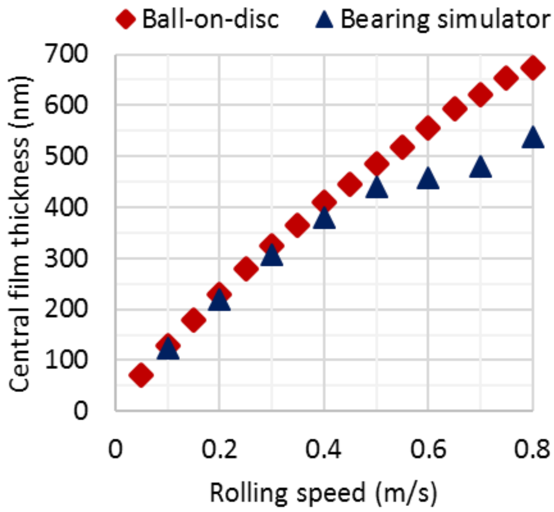

Figure 2. Central film thickness of LV 2-3 grease on ball-on-disc (fully flooded) and bearing simulator (2 g of grease)

Figure 2 compares the thickness curve from the ball-on-disc with the thicknesses obtained on bearing simulator. Before tests, 2 g of grease were applied on the disc. Film thickness was measured after 10 minutes of running at each speed. Film thickness in the bearing contacts was very close to the FF conditions at speeds up to 0.5 m/s where more pronounced starvation occurred. Beyond this point, bearing replenishment mechanisms ceased to be sufficient and were overcome by loss mechanisms causing reduction in film thickness by 20%.

For the same bearing conditions at fixed speed of 0.5 m/s, where a more pronounced deviation from FF thickness was found, a time test lasting 3 hours was curried out to study a development of film thickness during this period. Results for LV 2-3 and LVS 3 are shown in Fig. 3.

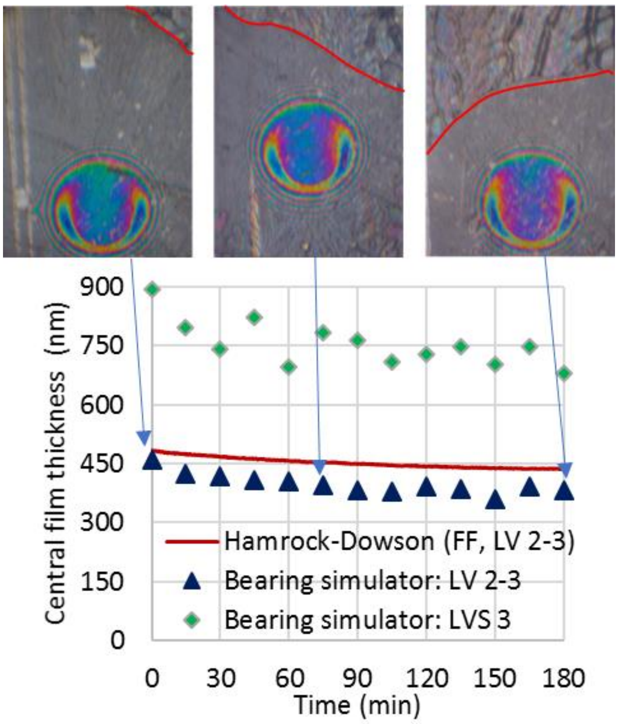

Figure 3. Film thickness development of LV 2-3 and LVS 3 at 0.5 m/s, 20 N/contact and corresponding interferograms with highlighted film meniscus

Measured film thicknesses of LV 2-3 are accompanied by corresponding interferograms of the circular contact and Hamrock-Dowson estimation of film thickness under FF conditions. The estimated thickness was calculated according to immediate conditions in the bearing thus it was reduced during the test as temperature increased in the bearing. The total temperature rise by 3 °C caused drop in the estimated film thickness by 10%. However, overall reduction in the measured film thickness of LV 2-3 was 17% with evident presence of film meniscus (air/lubricant interface) in front of the contact. The meniscus fluctuated (especially in the case of LVS 3 grease as seen in film thickness variations) and slightly approached to the contact during the time test. Nevertheless, it did not influence the film thickness significantly. The most distinctive decline in film thickness occurred during the first 30 minutes of bearing running for both the greases.

All these observations suggest that most of the film reduction in bearings is given due to temperature rise rather than by starvation itself during initial phase of its running. On the other hand, similar conditions was previously studied by Cann [4] on ball-on-disc simulator where a grease-lubricated circular contact without artificial replenishment began to starve very quickly and seriously despite precisely controlled temperature. For this reason, there seems to be a strong discrepancy in the results obtained on the ball-on-disc and full bearing simulators.

Further, more comparable experiments were performed to exclude influences of different lubricants, conditions, and experimental methodologies employed in this and Cann's study [4] on the discussed results. Film thickness behaviour of grease LV 2-3 was assessed at three rolling speeds of 0.1, 0.3, and 0.5 m/s on both simulators (ball-on-disc and full bearing) under starved conditions. In both the cases, 2 g of grease were applied on the disc before each test and no artificial mechanism of contact replenishment was involved.

It was observed that significant starvation occurred immediately after the start of the test on ball-on-disc simulator (see Figure 4) for all the speeds. Reduction of film thickness by about 80% from FF value to a certain stable level took only 30 seconds for speeds of 0.3 and 0.1 m/s where the film meniscus got at the contact boundary. It is worth noting that the film development differs for the high speed of 0.5 m/s where film thickness fluctuated dramatically and meniscus position was often out of the observable area. The average film thickness decline was around 65% compared to FF conditions. More pronounced, even if unstable, mechanism of replenishment was triggered by this speed.

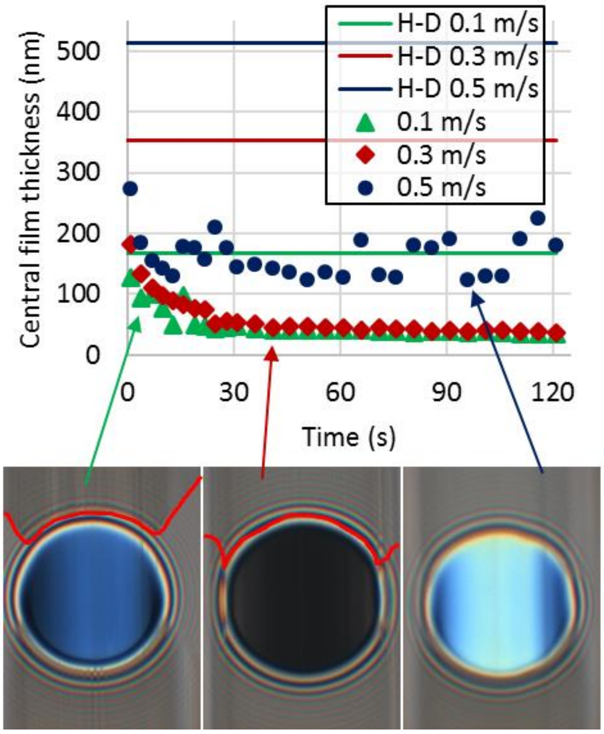

Figure 4. Film thicknesses of LV 2-3 measured on ball-on-disc simulator (symbols) with corresponding FF estimations (lines)

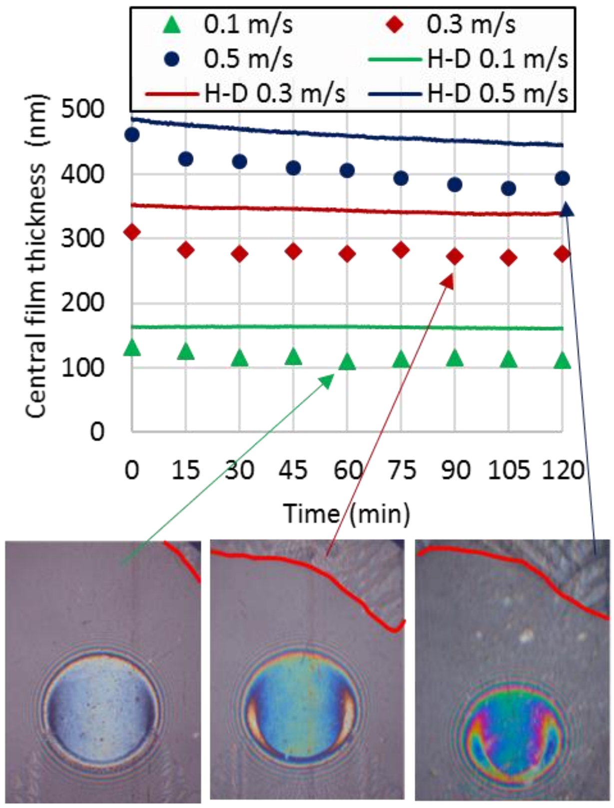

Figure 5. Film thicknesses of LV 2-3 measured on bearing simulator (symbols) with corresponding FF estimations (lines)

Notwithstanding, specific origin of this phenomena is unknown. No substantial changes were detected in lubricant temperature or test rig vibrations that could accelerate refilling of contact running track by the lubricant.

Compared to the ball-on-disc results, starvation was very mild on bearing simulator despite the much longer duration of the tests (2 hours), as illustrated in Figure 5. Starvation led to a decrease in film thickness by approximately 50 nm regardless of used speed. Relative decreases in thicknesses were 30, 18.5, and 11.5% of FF values for individual speeds sorted from the lowest to the highest. A temperature rise in the bearing was responsible for one-third of the decline.

4. CONCLUSIONS

The present work was focused on the comparison of film thicknesses formed in the contacts of grease-lubricated thrust rolling bearing and ball-on-disc simulator under various conditions.

It was shown that thrust bearings are capable to maintain a film thickness close to the fully flooded conditions (without severe starvation) according to bearing speed, even though they are lubricated by greases. Not negligible part of the film thickness reduction in bearings can origin from bearing heating rather than from starvation process, especially during the first hours of bearing running. On the contrary, if no artificial replenishment mechanism is involved in the ball-on-disc simulators during tests with greases, significant starvation usually takes place within a few seconds when film meniscus reaches the contact boundary.

From the above results it is evident that the consequences of grease starvation and replenishment mechanisms obtained on the ball-on-disc simulators cannot be directly transferred and applied to the actual bearings since these systems are very different from this point of view. Therefore, the use of full bearing simulators rather than ball-on-disc seems to be a more appropriate way to clarify the mechanisms of grease lubrication of actual bearings.

ACKNOWLEDGEMENT

This research was carried out under the project FSI-S-17-4415 with financial support from the Ministry of Education, Youth and Sports. Josef Fryza would like to thank Paramo for the provided lubricants.

REFERENCES

[1] K. Holmberg, A. Erdemir: Influence of tribology on global energy consumption, costs and emissions, Friction, Vol. 5, No. 3, pp. 263-284, 2017.

[2] G. Stachowiak, A. W. Batchelor: *Engineering tribology,* Butterworth-Heinemann, 2013.

[3] T. Lubrecht, D. Mazuyer, P. Cann: Starved elastohydrodynamic lubrication theory: application to emulsions and greases, Comptes Rendus De L Academie Des Sciences Serie Iv Physique Astrophysique, Vol. 2, No. 5, pp. 717-728, 2001.

[4] P.M. Cann: Starved grease lubrication of rolling contacts, Tribology Transactions, Vol. 42, No. 4, pp. 867-873, 1999.

[5] T. Cousseau, M. Bjorling, B. Graca, A. Campos, J. Seabra, R. Larsson: Film thickness in a ball-on-disc contact lubricated with greases, bleed oils and base oils, Tribology International, Vol. 53, pp. 53-60, 2012.

[6] S. Hurley, P.M. Cann, H.A. Spikes: Thermal degradation of greases and the effect on lubrication performance, Tribology for Energy Conservation, Vol. 34, pp. 75-83, 1998.

[7] P.M.E. Cann, A.A. Lubrecht: Bearing performance limits with grease lubrication: the interaction of bearing design, operating conditions and grease properties, Journal of Physics D-Applied Physics, Vol. 40, No. 18, pp. 5446-5451, 2007.

[8] B. Damiens, A.A. Lubrecht, P.M. Cann: Influence of cage clearance on bearing lubrication, Tribology Transactions, Vol. 47, No. 1, pp. 2-6, 2004.

[9] P.M. Cann, A.A. Lubrecht: The effect of transient loading on contact replenishment with lubricating greases, Transient Processes in Tribology, Vol. 43, pp. 745-750, 2004.

[10] P.M. Cann, M.N. Webster, J.P. Doner, V. Wikstrom, P. Lugt: Grease degradation in R0F bearing tests, Tribology Transactions, Vol. 50, No. 2, pp. 187-197, 2007.

[11] T. Cousseau, B. Graca, A. Campos, J. Seabra: Friction torque in grease lubricated thrust ball bearings, Tribology International, Vol. 44, No. 5, pp. 523-531, 2011.

[12] D. Goncalves, S. Pinho, B. Graca, A.V. Campos, J.H.O. Seabra: Friction torque in thrust ball bearings lubricated with polymer greases of different thickener content, Tribology International, Vol. 96, pp. 87-96, 2016.

[13] D.N. Olaru, M.R.D. Balan, A. Tufescu, V. Carlescu, G. Prisacaru: Influence of the cage on the friction torque in low loaded thrust ball bearings operating in lubricated conditions, Tribology International, Vol. 107, pp. 294-305, 2017.

[14] M. Hartl, I. Krupka, M. Liska: Elastohydrodynamic film thickness mapping by computer differential colorimetry, Tribology Transactions, Vol. 42, No. 2, pp. 361-368, 1999.

[15] M. Hartl, I. Krupka, R. Poliscuk, M. Liska, J. Molimard, M. Querry, *et al.*: Thin film colorimetric interferometry, Tribology Transactions, Vol. 44, No. 2, pp. 270-276, 2001.

[16] B.J. Hamrock, D. Dowson: Isothermal Elastohydrodynamic Lubrication of Point Contacts: Part III - Fully Flooded Results, Journal of Lubrication Technology-Transactions of the Asme, Vol. 99, No. 2, pp. 264-276, 1977.

Serbian Tribology Society

SERBIATRIB '19

16th International Conference on Tribology

Faculty of Engineering University of Kragujevac

Kragujevac, Serbia, 15 – 17 May 2019

EXCELLENT LUBRICATING PROPERTIES OF IONIC LIQUID – MYTH OR TRUTH

Darko LOVREC*, Vito TIČ

University of Maribor, Faculty of Mechanical Engineering, Maribor, Slovenia

*Corresponding author: darko.lovrec@um.si

Abstract: *Due to numerous good physical-chemical properties, Ionic Liquids should be ideal candidates for a new lubricant, suitable for use under harsh conditions, where conventional oils and greases fail* ***Error! Reference source not found.****. This is especially true for hydraulic fluid and gearbox oil. In the paper, the lubricating properties of selected Ionic Liquids have been tested and confirmed by using some of the classical tribological tests: e.g. the four-ball welding point test and wear test. Another approach to check the quality of lubrication is to do it with the Stribeck's curve, representing the friction coefficient, depending on the Stribeck's parameters, including viscosity, relative surface velocity, and loading. In most cases, the results achieved with Ionic Liquids have been considerably better than those achieved with classical mineral-based hydraulic oil.*

Keywords: *ionic liquids, lubricants, tribological tests, four-ball test, Stribeck's curve, results*

1. INTRODUCTION

Today, out of all the hydraulic fluids, mineral oils of different properties are used in 90 % of cases, whilst the remainder are fire-resistant and faster bio-degradable hydraulic fluids. As a minor share, the universal fluid lubricants are used for gearing, engine and hydraulic parts. Furthermore, in specific cases, e.g. in the foodstuff industry, those fluids compatible with foodstuffs are used, while elsewhere, sea water, as well as electro-rheological fluids are preferred. However, none of the fluids is so universal that it could meet the different requirements within their individual areas of use.

Engineers still exert substantial effort, time and resources into finding a lubricant that would be near the ideal fluid. It would have to be non-flammable, non-poisonous, and corrosion resistant, would have excellent lubricating properties, temperature-independent physical-chemical properties, be resistant, and guarantee a long service life for the components where it is used.

One of the principal duties of lubricant producers is searching for alternatives to existing lubricants, and accompanying the discoveries within related spheres. In that way, new market niches are opened, thus raising the market competitiveness. In the future, this might be essential for survival on the market, as, in the developed world, lubricant consumption is being reduced, and the number of lubricant producers diminishing, whilst the conditions on the lubricant market are being tightened up. Therefore, in spite of the great number of different conventional lubricants, an approximation to the ideal liquid is still being searched for.

2. IONIC LIQUIDS AS LUBRICANTS

Today, it is difficult to say which lubricant will have an important role in the future, in the pending “post-oil period”. That depends on the results of present and future research and tests on the development directions of fluid technology, fluctuations in the prices of raw materials on the world markets etc. However, in all probability, in the near future, a universal liquid of superior quality and near ideal will not be discovered to supersede all others.

Ionic Liquids (ILs) are one of the more promising candidates, because of their good properties with which they have already excelled within many spheres of industry.

The simplified definition of Ionic Liquids says that ILs are liquid or molten salts. The term IL was introduced in order to cover the systems of temperatures below 100 °C. One of the reasons for that was to avoid the words “molten salt” in terms such as the “molten salt ambient temperature”; another reason was to create the impression of coldness, and a possible third reason was the intention for patenting [1]. The IL “consists fully of ions (molten sodium chloride, while NaCl in water is only the water solution of ions). ‘It was formerly called molten salt, implying the idea of work at high temperatures with highly viscous and corrosive media” [2], [3].

Ionic Liquids with a melting point at ambient temperature consist of extensive and asymmetrical organic cations, such as 1-alkyl-3-methylimidazolium, 1-alkyl pyridine, 1-methyl-1-alkyl pyrrolydine or ammonium salts. The anions used range from simple halides, reducing the high temperatures of the melting point, to inorganic anions such as tetrafluoroborates and hexafluorophosphates, and to extensive organic anions such as bis(trifluorosulphony)amides, triflates or tosylates [4]. An example of a basic cation and anion structures is shown in Fig. 1.

The cations (usually organic) and anions (usually inorganic) present in IL are so formulated that the resulting salts hardly crystallize. Therefore. the IL is liquid within a wide temperature range [4]. An important feature of ILs is the possibility of adapting these physical-chemical properties through changing the natures of the anions and cations. The number of possible combinations is extremely high, that is why the best Ionic Liquid is supposed to be adapted for any case of use.

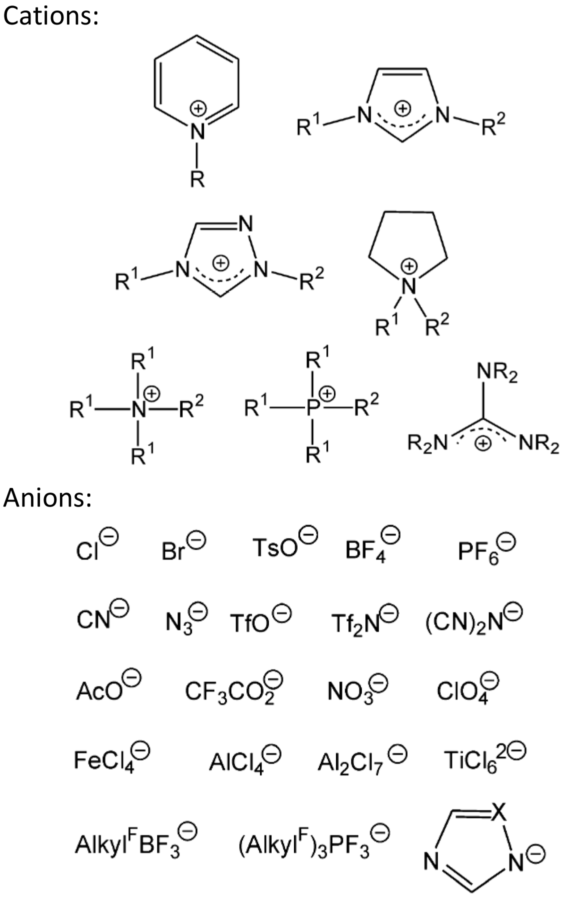

Figure 1. Basic structures of Ionic Liquids [4]

2.1 Impact of anions on lubrication

It must be emphasised that the anion and cation properties of Ionic Liquid cannot be differentiated between. However, such a division would be useful from the point of view of categorising those tribological properties affected dominantly by anions and cations.

In general, anions can be grouped into halogenated and non-halogenated. Most halogenated anions, particularly the fluorinated ones, are inappropriate as lubricants. Otherwise, the halogenated anions have good lubricating properties, because of their iron-halide layer formation, such as FeFx on the steel material's surface [5], [6].

However, in the presence of water during anion hydrolyses, aggressive hydrogen halide is formed, for example HF. The results are very high friction and wear, because of the corrosion and degradation of the steel material. This has been detected on the popular anions such as $NTf2^-$, $BF4^-$ or $PF6^-$. As far as $NTf2^-$ is concerned, a greater obstacle to its use as a lubricant is its high price and high toxicity [5], [6], [7], [8]. Here, a special place is occupied by the $PF6^-$ anion. It has been proved that it may have exceptional properties in comparison with other halogenated anions. It works as an anti-wear agent and corrosion inhibitor because of the phosphorus within its molecular structure. On the surface a phosphate film is formed, preventing the formation of Fe-halide and improving resistance to wear [7].

The adding of corrosion inhibitors, for example tricresyl phosphate, into the pure IL may allow good lubricating properties of those Ionic Liquids with halogenated anions, and the formation of a protective surface phosphate film [9]. However, the $PF6^-$ anion inclines towards hydrolysis, and decomposes within a short time when in contact with water.

In view of the negative effects of most halogenated anions in ILs (toxicity, non-resistance to water, corrosion, high wear), the use of IL with non-halogenated anions is highly recommendable. So far, the methyl sulphate anion ($MeSO4^-$) has already been used as an additive for the lubricant based on glycerol. The best results have been gained by the lowest tested concentration (0,625 weight per cent). In that case, the friction was reduced by 30 to 50 %, whereas the wear was 2,5 to 4,6 times smaller than with pure glycerol, depending on the cation used in the Ionic Liquid [10], [11].

This IL type seems to be suitable as an additive in poly-alcohol matrices, as it is already active in concentrations lower than 1 weight %. However, the methylsulphate anion is hydrolytically unstable, and causes corrosion over a longer time period according to the experiences of an IL-supplier. It has already been proved that, when using anions with phosphorus, the dimethylimidazolium dimethylphosphate is a worse lubricant than ILs with halogenated anions [9].

Various ILs with phosphorus groups in anions and/or cations are also already being used. In comparison with standard anti-wear additives, identical or better results with respect to friction and wear have been obtained with 1 % addition of IL. The best results were obtained when phosphorus was present in the anion and in the cation. Comparable results were gained by Zhang and colleagues, who did not find corrosion with the use of dialkylphosphate IL, and found intensive corrosion with the use of $BF4^-$ or $PF6^-$ as anions [12], [13]. Somers [14] used trihexyl(tetradekyl) phosphonium cations with various disubstituted phosphates, and also conventional (halogenated) anions as counter-ions for tests with steel balls.

In comparison with the engine oil SAE 15W-50 as a reference lubricant, better results were gained with respect to friction and wear with the use of the diphenylphosphate (DPP) anion. The IL with dibutylphosphate as the anion showed worse results, but better than the reference oil [14], [15]. It can be assumed that the aromatic phosphate anions in tribology are better than the aliphatic anions. It was also shown that the properties of IL as a lubricant do not only depend on the anion. A great impact is also exerted by the used load. At low loading the DPP had better properties than NTf2. That changed when higher loadings were used [16].

2.2 Impact of cations on lubrication

Also the cations within ILs for lubrication have so far been different. One of the more common IL-classes is IL based on imidazole cations. Qu [17] found out that the friction of those ILs was higher than that of the compared conventional oils. Fox and Priest [9] found that if lengths of imidazolium cation chains were used there was no friction and wear lowering or increasing trend. Only the "normal" 1, 3-dialkyl imidazolium cations have not been used as lubricants so far. Zhu [18] synthesised the imidazolium ILs, where, on one side of the ring they added the ester functionality. On the other side, there was the standard aliphatic chain.

For their ILs they used the halogenated anions. They used PFPE (perfluoropolyether) and BMIM-BF4 as references. The results of their new ILs were better than with PFPE, but worse than with BMIM-BF4. After the test, identical difficulties were noticed, as met with the majority of ILs with halogenated anions (e.g. corrosion).

Li [20] used another function, namely a hydroxyl group, on the cation. In the end, they obtained almost equal results as Zhu and colleagues. They obtained slightly higher friction coefficient and better anti-wear properties than with non-functionalised ILs. Li also tested other functionalised imidazole tetra fluoroborates $BF4^{-}$. They introduced the vinyl group on one side of the imidazolium ring, but they did not manage to produce an ionic liquid with better lubricating properties. Using the standard imidazolium tetra fluoroborates they could only perform tribological tests under 120-160 kg loading, whilst, with the new functionalised ILs, they could only carry out the tests with less than 50 kg loading. In some cases, the imidazolium cation functionalising could be a concept for ILs usable as a lubricant.

In regard to ILs based on ammonium cations, Qu [21] reached lower friction and wear, if compared with the usual oils. That was not only for pure liquids, but also in those cases when they were used as additives to the usual oil (10 weight %). Those $NTf2^{-}$ likely to cause the mentioned corrosion problems were used as anions in those liquids.

The ILs with phosphorus cations, if compared with ammonium cation Ionic Liquids, have proved to be of superior quality. Some researchers tested the holin (2-hydroxyethyl-trimethyl-ammonium)-based ILs and compared the two results with the standard engine oil SAE 5W-30.

The compared ILs had the same friction coefficient. However, the friction coefficient had already increased after a short time to the level as found during the dry sliding test without oil. Therefore, the ILs of such types are inappropriate as lubricants.

Jiang [8] introduced a new category of ILs, appropriate as lubricants, i.e. ILs with crown-shaped cations. They synthesised a few ILs with cations gained from crown-shaped ethers with (2-ethylhexyl) phosphate as the anion. The new ILs had better friction and anti-wear properties than ordinary lubricants, such as X1-P and PFPE. They may also be used at high temperatures.

Some authors have also researched ILs with phosphorus in the cations and anions. Somers has already been mentioned [14]. Yu [19] also synthesised some phosphonium alkylphosphates, and tested them as additives for ordinary lubricating oils. Comparison between the results of those compounds with pure base oil witnessed important friction and wear reduction. The ILs were thermally more stable than the standard lubricants, and were not corrosive for alloys.

3. USED TEST METHODS

Generally, the analyses were conducted by standard testing methods that are normally used for laboratory analysis of conventional hydraulic fluids. Lubricating properties can be determined and verified in different ways. As primary tests for the determination of lubricating ability they used the four ball welding point test and the wear test.

Another approach was to check the quality of lubrication based on Stribeck's curve, representing the friction coefficient depending on the Stribeck's parameter. Analyses were carried out in comparison with classical mineral based hydraulic oil HLP type and VG46 viscosity grade.

3.1 Welding-load and wear-diameter

Welding-load (or welding-point) and wear-diameter determination according to standardised procedure (e.g. IP 239-85), with the use of the four-ball apparatus (Hansa Press), is one of the common methods for testing the lubricating ability of a lubricant.

This method is based on load application to four standardised steel balls of 12,7 mm diameter. The top rotating ball slips onto the lower three fixed balls at constant loading, and at constant rotating velocity of 1440 min^{-1} (Figure 2). The welding-load measurement and the wear test of lubricating oils, can be performed on the same apparatus.

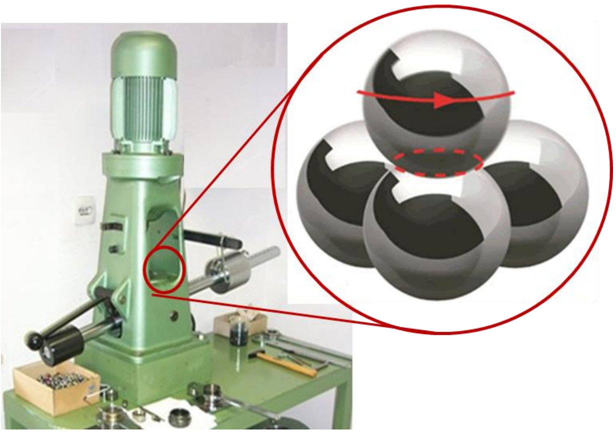

Figure 2. Principle of welding-load and wear-diameter measurement

The welding-load is measured at specific loading and/or to ball pressure for 10 seconds. The top ball rotates and presses with the test loading against the lower three immovable balls dipped into the tested liquid.

The measurement result is given in kg, and comprises two numbers (e.g. 140/160). The first number indicates the maximum loading at which ball welding did not occur during the test (10 s). The second number indicates the minimum loading at which complete steel ball welding and/or automatic deactivation of the device occurred during the test.

The wear test lasts much longer, namely for 60 min ±1 min at constant temperature and loading, depending on the tested hydraulic liquid. The ball wear depends on the loading, velocity, duration of the test, and the properties of the lubricant tested. As all parameters except the lubricating properties are constant, the result and/or the ball wear depends only on the lubricating properties of the liquid tested.

After completion of the test, the wear test result is obtained by measuring the wear of the lower three steel balls under a microscope, where the diameters of the wear cavities are measured on the three immovable balls. The wear extent is defined as the average diameter of ball wear under known conditions.

3.2 Stribeck's curve

The next approach to presenting the quality of lubrication is to do it with the so-called Stribeck's curve, representing the friction coefficient depending on the Stribeck's parameters, including viscosity, relative surface velocity, and loading.

Basically, the qualities of lubrications improve when moving on the horizontal axis of the Stribeck's curve to the right. The combination of low velocity, low viscosity and high loading will cause the boundary lubrication, characterised by a small quantity of lubricant in the space between the two surfaces and a great surface of direct contact. On the Stribeck's curve it can be seen that this is expressed by very high friction. In tribological systems, the boundary lubrication occurs at the start-ups and stoppages. In this range, the lubricant acts mainly chemically and has a very great influence. With the increase of velocity and viscosity or reduction of loading, both surfaces are gradually separated and the lubricating film is formed, which, though thin and imperfect, already improves the lubrication quality expressed by abrupt reduction of the friction coefficient. This range is called mixed lubrication. The surface separation continues with the increase of velocity and viscosity and decrease of loading, until a perfect lubricating film without direct surface contacts is created; as a result, the friction is minimised, and this implies passage into the hydrodynamic lubrication range, practically without wear. The lubricant within this range acts mainly physically.

The measurements of Stribeck's curve for the mineral hydraulic oil and Ionic Liquids were carried out using an MTM device for measuring friction and lubricating film thickness with ball-disc configurations. The appearance of the device is shown in Figure 3.

The ball, of 19,05 mm diameter with roughness Ra<0,02 µm and hardness 800 HV-

929 HV under loading, sits on a disc of 46 mm diameter with roughness Ra <0.01 µm and hardness 720 HV-780 HV. Both are made from identical material, DIN 100Cr6. The disc is dipped completely into the tested liquid, the quantity of which amounts to about 35 ml. The ball and disc are driven independently of each other, so that the test can be performed with different slide-to-roll ratios. The friction force between the ball and disc is measured by a force transducer.

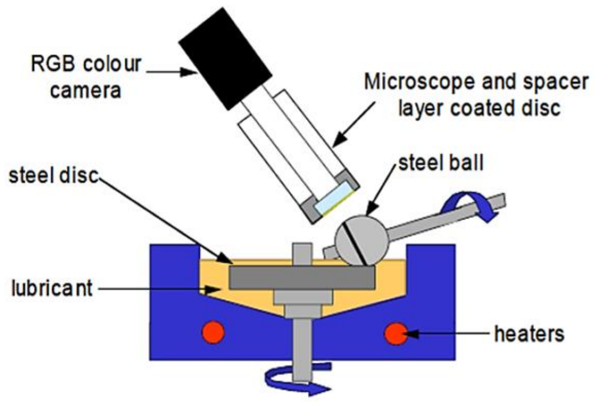

Figure 3. MTM device: pin on disc

During the Stribeck test the velocity wa changed with constant slide-to-roll ratio. In 2 logarithmic decrements the velocity wa reduced from 2 m/s to 0.01 m/s with a slide-to roll ratio of 50 %. In that way, differe lubrication modes were reached. The pressin force amounted to 35 N, giving the Hertzia contact pressure of 1 GPa with the given ball an disc geometry. The slide-to-roll ratio is define by equation (1). For a specific ratio, the devic during the measurement once rotates the dis faster, and the next time it rotates the ball faste

$$SRR = \frac{U_{slide}}{U_{av}} = \frac{|U_{ball} \quad U_{plate}|}{(U_{ball} \quad U_{plate})/2} \; 100 \; . \qquad (1)$$

where represent U_{slide} – sliding velocity of ball and disc, U_{av} – average sliding velocity of ball and disc, U_{ball} – ball velocity and U_{plate} – plate velocity.

Since, in devices, we do not only deal with rotational and rolling movements of sliding contacts, such as in bearings, camshafts or gears, we also tested the resistance to friction with the test, where the translational sliding movement is at the forefront. These movements of contact surfaces, in addition to the aforementioned rolling movements, occur in hydraulic energy conversion components, e.g. in all types of hydraulic pumps and hydromotors, and in almost all hydraulic valves, such as directional, pressure and flow valves, either by switching or continuous operation. In the latter case, these are hydraulic control valves, and the friction conditions are extremely important.

4. RESULTS

The pre-selection of tested ILs was carried out on the basis of a prior corrosion test in a humid chamber, compatibility with materials used predominantly within hydraulic components [22], and the selection of appropriate viscosity and density.

The comparison between the welding-loads and wear-diameters for different samples of ILs compared with mineral hydraulic oil (Hydrolubric) ISO VG46, are shown in Figure 4. The lubricating properties of some ILs samples are considerably better than those of the mineral oil.

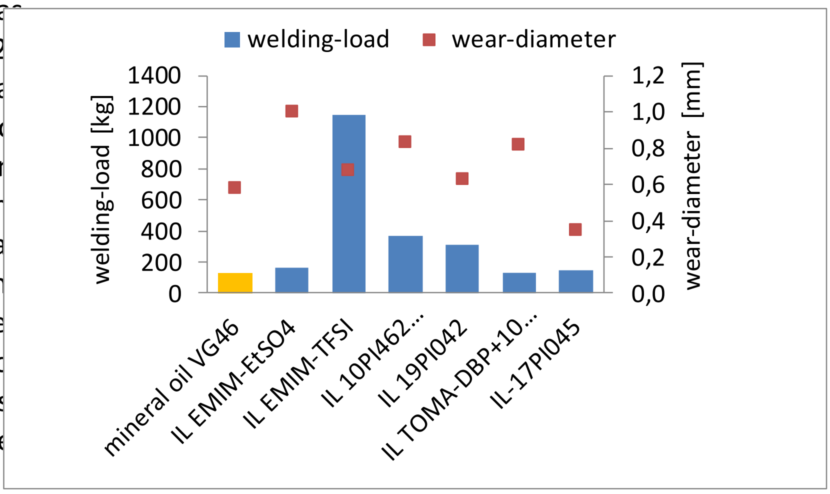

Figure 4. Welding-load and wear diameter of tested ILs vs. mineral oil

Some samples have an exceptionally high welding load, for example EMIM-TFSI had as much as 1150 kg, which pointed out exceptional properties at extreme pressures but, interestingly, the wear diameter was even greater than that of the mineral oil, implying that the anti-wear properties were worse. As in the case of hydraulic oils, the anti-wear properties are more important, so that liquid would be potentially more suitable for use in gearings, maybe even as metalworking fluid during metal machining. In regard to other liquids with high welding loads, the limitation was, in particular, bad corrosive protection in the presence of moisture, or in proper viscosity for use in hydraulic systems.

The measured Stribeck's curves for oil and two ILs at the ambient temperature T_o and 60 °C are shown in Figure 5.

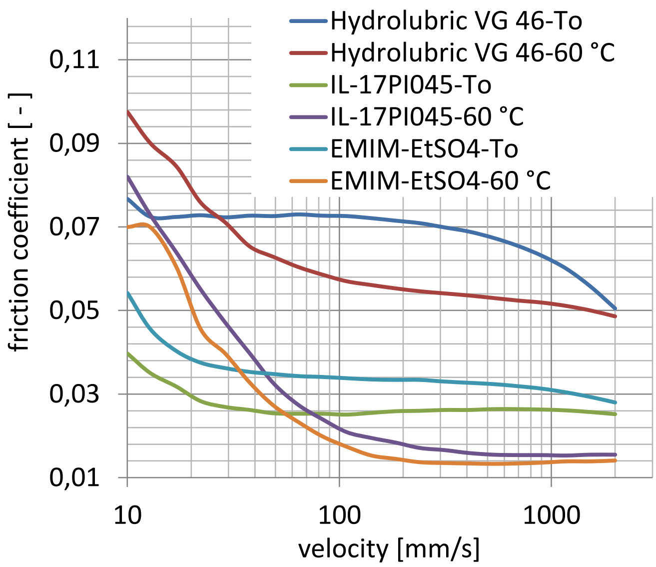

Figure 5. Stribeck's curves of two tested ILs vs. Hydraulic mineral oil

It can be seen that the friction coefficient of the mineral oil within the entire range is considerably higher than that of both Ionic Liquids. The two ILs have a very similar friction coefficient within the entire range, the IL-17PI045 having a slightly lower friction coefficient at room temperature, and the EMIM-EtSO4 at 60 °C. All three liquids showed much greater difference between the lowest and highest measured values at 60 °C than at room temperature. Furthermore, at higher temperature, the friction coefficient was higher in the range of boundary and mixed lubrication, and lower in the range of elastohydrodynamic lubrication. That is probably caused by a smaller lubricating film thickness at higher temperatures, resulting in more direct contacts of the ball and disc surfaces within the range of the boundary and mixed lubrication.

5. CONCLUSION

The performed lubrication tests based on standard test methods have proved that certain types of ILs have comparable, and in some cases much better, lubricating properties than conventional mineral oils.

That can be explained by the fact that ILs have unique bipolar structures, thus allowing them easy adsorption to the sliding surfaces of contacted mechanical parts. Consequently, an effective boundary film is formed, thus reducing friction and wear. That applies particularly, to lower contact pressures and large surface areas.

By measuring the welding-load and the wear-diameter on a four-ball apparatus, it was discovered that the tested ILs had better lubricating properties than the mineral hydraulic oil. This fact is also confirmed by the research results of other authors, who have used different types of ILs. But, it should be noted that these are more or less laboratory tests. The results of lubrication tests on real components, e.g. endurance pump-tests, carried out with the real, specified hydraulic pumps used under real, constant or changing operating conditions, can lead to different conclusions. Therefore, it is not always necessary, that the results of the durability pump-tests, correspond directly to the results of the laboratory tests.

For use within a hydraulic system additional pump tests regarding lubricating abilities need to be carried out to have complete information regarding the lubricating properties.

Apart from lubricating properties, it is necessary to check the applicative suitability of other physico-chemical properties of the ILs used as lubricants, e.g. suitable viscosity, viscosity index, density, thermal conductivity, compatibility with component materials, electrical conductivity and corrosion impact.

Before using ILs as a new type of lubricant, we need to obtain all the necessary information on important fluid properties. To this end, it is necessary to carry out a very extensive and relatively expensive selection process.

REFERENCES

[1] K. Johnson: *What's an Ionic Liquid? The electrochemical society interface*, Spring, pp. 38-41, 2007.

[2] M. Kambič: *Research regarding the usabilities of ionic liquids within hydraulic system*, Diss., University of Maribor, 2015.
[3] M. Freemantle: *An introduction to ionic liquids, Cambridge*, The Royal Society of Chemistry, Thomas Graham House, 2010.
[4] G. Laus, G. Bentivoglio, H. Schottenberger, V. Kahlenberg, H. Kopacka, T. Röder, H. Sixta: Ionic liquids: Current developments, potential and drawbacks for industrial applications, Lenzinger Berichte, Vol. 84, pp. 71-85, 2005.
[5] Y. Kondo, S. Yagi, T. Koyama, R. Tsuboi, S. Sasaki: Lubricity and corrosiveness of ionic liquids for steel-on-steel sliding contacts, Journal of Engineering Tribology, Vol. 226, No. 11, pp. 991-1006, 2012.
[6] B. Yu, D. Bansal, J. Qu: Oil miscible and non-corrosive phosphonium-based ionic liquids as candidate lubricant additives, Wear, Vol. 289, pp. 58-64, 2012.
[7] A.S. Pensado, M.J.P. Comunas, J. Fernandez: The pressure-viscosity coefficient of several ionic liquids, Tribology Letters, Vol. 31, No. 2, pp. 107-118, 2008.
[8] D. Jiang, L. Hu, D. Feng: Crown-type ionic liquids as lubricants for steel-on-steel system, Tribology Letters, Vol. 41, No. 2, pp. 417-424, 2011.
[9] M. Fox, M. Priest: Tribological properties of ionic liquids as lubricants and additives, Part 1: Synergistic tribofilm formation between ionic liquids and tricresyl phosphate, Journal of Engineering Tribology, Vol. 222, No. 3, pp. 291-303, 2008.
[10] V. Pejaković, M. Kronberger, M. Mahrova, M. Vilas, E. Tojo, M. Kalin: Pyrrollidinum sulfate and ammonium sulfate ionic liquids as lubricant additives for steel/steel contact lubrication, Journal of Engineering Tribology, Vol. 226, No. 11, pp. 923-932, 2012.
[11] V. Pejaković, M. Kalin, J. Vižintin. 1 butyl-1 methylpyrollidinium methyl sulfate ionic liquid as additive for glycerol in steel/steel contacts, Slotrib 2010, Proceedings, Ljubljana, pp. 109-117, 2010.
[12] M. Uerdingen, C. Treber, M. Balser, G. Schmitt, Ch. Werner: Corrosion behaviour of ionic liquids, Green Chemistry, Vol. 5, No. 7, pp. 321-325, 2005.
[13] L. Zhang, D. Feng, B. Xu: Tribological characteristics of alkylimidazolium diethyl phosphates ionic liquids as lubricants for steel-steel contact, Tribology Letters, Vol. 34, No. 2, pp. 95-101, 2009.
[14] A. Somers, P. Howlett, J. Sun, D. MacFarlane, M. Forsyth: Phosphonium ionic liquids as lubricants for aluminium-steel, Tribology and Design, Vol. 66, pp. 273-283, 2010.
[15] F. Shah, S. Glavatskikh, D. MacFarlane, A. Somers, M. Forsyth, O. Antzutkin: Novel halogen-free chelated orthoborate-phosphonium ionic liquids - synthesys and tribophysical properties, Physical Chemistry Chemical Physics, No. 13, pp. 12865-12873, 2011.
[16] A. Somers, P. Howlet, J. Sun, D. MacFarlane, M. Forsyth: Transition in wear performance for ionic liquid lubricants under increasing load, Tribology Letters, Vol. 40, No. 2, pp. 279-284, 2010.
[17] J. Qu, J. Truhan, S. Dai, H. Luo, P.J. Blau: Ionic liquids with ammonium cations as lubricants or additives, Tribology Letters, Vol. 22, No. 3, pp. 207-214, 2006.
[18] L. Zhu, L. Chen, S. Xiang, G. Chen, X. Yang: Tribological properties of functionalized ionic liquids containing ester-group as lubricants for steel-steel system, China Petroleum Processing and Petrochemical Technology, Vol. 14, No. 2, pp. 60-65, 2012.
[19] B. Yu, D. Bansal, J. Qu: Oil miscible and non-corrosive phosphonium-based ionic liquids as candidate lubricant additives, Wear, Vol. 289, pp. 58-64, 2012.
[20] X.F. Li, Z.G. Mu, X.X. Wang, S.X. Zhang, Y.M. Liang, F. Zhou: Tribological performance of ionic liquids bearing hydroxyl groups as lubricants in the aluminum-on-steel contacts, Conference on Advances in Materials and Manufacturing Processes (ICAMMP 2010), 6. Shenzhen, China, pp. 1147-1153, 2010.
[21] J. Qu, J. Truhan, S. Dai, H. Luo, P.J. Blau: Ionic liquids with ammonium cations as lubricants or additives, Tribology Letters, Vol. 22, No. 3, pp. 207-214, 2006.
[22] M. Kambič, R. Kalb, V. Tič, D. Lovrec: Compatibility of ionic liquids with hydraulic system components, Advances in production engineering & management, Vol. 13, No. 4, pp. 492-503, 2018.

Serbian Tribology Society

SERBIATRIB '19

16th International Conference on Tribology

Faculty of Engineering
University of Kragujevac

Kragujevac, Serbia, 15 – 17 May 2019

EXPERIMENTAL SPECIFICATION OF THE IMPACT OF MECHANICAL PARTS AND HYDRAULIC OIL CONDITION ON VEHICLE SHOCK ABSORBER PERFORMANCE IN ENERGY DISSIPATION

Antonios D. Tsolakis*, **Andreas A. Mallis**, **Chrysostomos D. Chatzis**
University of West Attica, Aigaleo, Greece
*Corresponding author: adtsolakis@uniwa.gr

Abstract: *The purpose of a damper, or so-called 'shock absorber', is to introduce controlled friction into the suspension system and dissipate the incoming-to-vehicle energy due to external excitations, in order to give dynamic stability to the vehicle. As damping of the incoming-to-vehicle energy is crucial for road handling and passengers comfort and safety, proper shock absorber operation plays α critical role in the proper and safe vehicle operation .In shock absorber operation, it is possible to identify three distinct types of friction: dry solid friction; fluid viscous friction; fluid dynamic friction. In this work, a common twin-tube shock absorber of a typical passenger car was investigated. The shock absorber had operated for about 150000 kilometres in normal every-day drive conditions. In order to investigate the impact of the worn mechanical parts separately from the quality of the hydraulic oil, numerous tests were run for all three conditions of the specific shock absorber: in the state it was delivered (used), after replacing all mechanical parts, and finally after replacing the hydraulic oil. The results were discussed assuming the manufacturer's standards and also comparatively between the three shock absorber refurnishing conditions.*

Keywords: *Shock absorber, vehicle, shock absorber test, shock absorber oil.*

1. INTRODUCTION

The design of vehicle suspension systems is one of the major problems of the automotive industry, because the road handling behaviour of vehicles and the comfort of passengers depend on it. Research in this area can be characterized as immense and intense but as suspensions are a critical part of one of the most widespread and profitable products, as a car is, brand manufacturers hermetically keep most of the scientific and experimental works.

The accessible works on passive suspension systems could be divided into two categories: those investigating the operation of all suspension systems as bodies of concentrated properties (elastic and damping properties) which significantly affect the dynamic behaviour of the vehicle [1,2,3] and those which investigate the parameters of the damper performance - being the element with the most complex operation – separately, as does the present work.

So, D. Bhuyan and K. Kumar simulated the hydraulic oil flow through the valves of a twin tube shock absorber. Their work contributed to deriving valuable results about fluid aeration, tube strength and temperature rise of the recommended by the manufacturer hydraulic fluid [4].For the same type of shock absorber, Y. Liu and J. Zhang studied the dynamic behaviours of absorbers by means of both computer simulation and real test. In this work, numerical predictions of dynamic responses were produced by the virtual prototype of the absorber and compared with experimental results [5]. Furthermore, J.C.Ramos, et al. developed a thermal mathematical model of automotive twin-tube shock absorbers [6]. In the same research field, A. Lion and S. Loose developed a thermomechanical model of the shock absorber in order to investigate the effects of hydraulic oil temperature rise on its damping behaviour. The dependence of the force on velocity under different temperature levels as well as the change in temperature dissipation during cyclic excitations were measured and compared with the recorded values of a vehicle test on a rugged test track [7]. Lastly, K. Lee developed a parametric computer model of an automotive single-tube damper in order to identify the required damper valve size for the desirable performance [8]. In the present work, a long- used twin-tube shock absorber of a typical passenger car was tested in three conditions: in the state it was delivered, after replacing all mechanical parts, and finally after replacing the hydraulic oil. The whole test was designed in order to investigate the impact of the worn mechanical parts and the quality of the hydraulic oil, separately, on its performance.

2. APPARATUS, SPECIMEN AND TEST METHOD

2.1 Specimen technical characteristics

A damper of the KW Company was used as the experimental specimen for the test, namely the Variant 2 model. The specific absorber is of a twin-tube type with a stainless steel body, fully repairable. The absorber is fully adjustable for height and compression-rebound performance. On Table 1 below, the main geometrical features are given and in Fig. 1 an exploited view of the mechanical elements of the damper is presented.

Table 1. Damper geometrical features

Geometrical Features	Values in mm
Piston diameter	33.2
Piston height	11
Inner tube inner diameter	34
Inner tube length	270
Rod length without threading	252
Total length	320
Outer diameter	51
Inner diameter	45.5

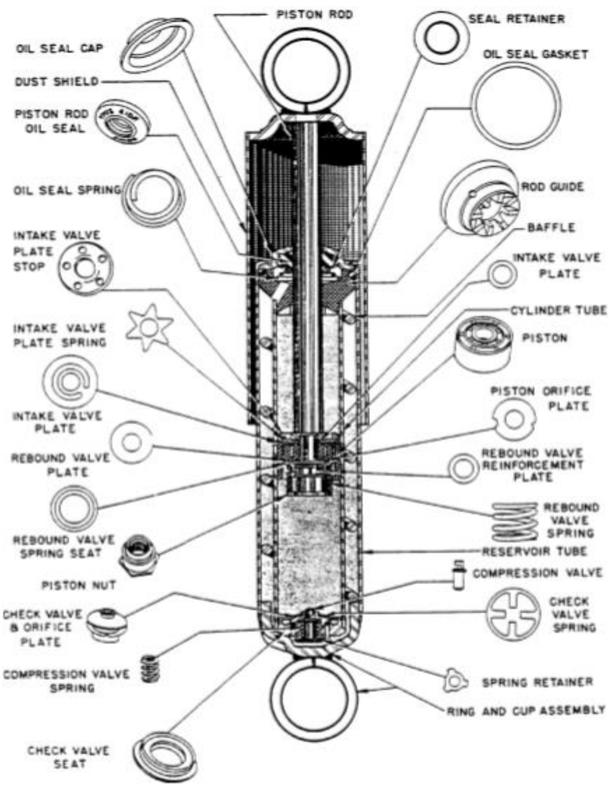

Figure 1. KW twin-tube exploited view

This shock absorber had already been used for 150,000 km and mounted on a conventional passenger car. The damper was subjected to a series of tests in the state it was received and then the same tests for two successive repair situations: after replacing all the mechanical parts and after replacing the hydraulic oil. The three discrete conditions of the damper that is tested will be referred to as ‘experimental conditions’ from now on.

2.2 Test Apparatus

In order to test the present work, a device for vehicle damper testing was used, which was developed and constructed by MTS in collaboration with Roehrig Engineering. Specifically, a MTS Roehrig SYD 2VS electro-mechanical crank dynos for performing single-specimen sinusoidal damper testing was used whose main features are given on Table 2 below.

Table 2. SYD Specification

Description	Units	Value
Peak Force	kN	5.5
Maximum Displecement	mm	50.0
Maximum Velocity	m/sec	0.5
Stated Performance	m/sec @ kN force	0.5 @ 3.0

Figure 2. Roehrig experimental apparatus

The mode of operation of the device as well as the arrangement of the damper to be tested are described in short:

Firstly, the inner cylinder of the damper is mounted on the upper end of the device while the outer cylinder is hinged to the bottom part which is connected to the central shaft of the device. In testing, the outer cylinder performs a reciprocating motion at a specified duration and speed, defined according to the manufacturer's standards of the individual damper. The device is connected to a computer that bears its program and all measurement and test results are displayed and stored on it. The program of the device is capable of displaying a multitude of combinational graphs, depending on what each person is searching in his tests. Subsequently, a temperature sensor was used according to the manufacturer’s recommendation, of the RACI3A type.

In Figure 2, the Roehrig experimental apparatus is shown with the shock absorber to be tested mounted on it. On the left vertical strut, the RACI3A temperature sensor is visible.

2.3 Test procedure

The whole experiment is divided into two parts:

In the first part ests were conducted in the first part so as to investigate whether the damper performance is within the limits set by the manufacturer. Three tests of 80sec were carried out, in a specific range of velocities specified by the manufacturer, in order to determine whether the shock absorber needs repair. Thus, the damper was excited within a certain range of velocities (0-0.524m/s), increasing the speed gradually to the maximum value and completing the cycle by reducing the speed until the iteration stopped at 80sec.

Next, in the second part, 30 iterations of 80sec were conducted each of which followed the same pattern and was identical to the one specified by the manufacturer, as described above. The time gap between each of these 30 iterations was 5sec.

During the test, temperature values were obtained, by means of a specific sensor that the device bears, in three parts of the shock absorber: in the sealing kit (top of tube), the centre of the shock absorber (in the middle of the tube) and the compression valve (at the bottom of the tube. These three temperature check points will be referred to as Temperature check points A, B and C.

Although the performance of the shock absorber was judged by the three initial tests, the ultimate goal of all continuous experimental tests, in each part of our experiment, was to investigate the rate of its temperature increase as well as its performance at higher temperatures.

The ambient temperature in each experiment was almost the same, diverging by one or two degrees since the experiments did not take place on the same day and in each part it was necessary for the shock absorber to be at its original temperature. The temperature values registered at the three points of the damper refer to the temperature of the outer cylinder since they were obtained by contact.

All tests mentioned above were conducted for all three different conditions of the damper.

3. OUTCOMES AND ANNOTATION

The test results are initially demonstrated in damping force-velocity graphs for each of the three tests separately and always considering the manufacturer's standards. Subsequently, graphs of the temperature development at checkpoints are presented for the long-lasting test. The three shock absorber conditions are referred to as 'experimental conditions' 1, 2 and 3 (abbreviated as EC1, EC2, and EC3) and correspond to the conditions described in the previous paragraph. The two separate tests are referred to as short tests and long test. All the numerical results are presented in F(V) graphs where the manufacturers limits are marked in red polylines. These graphs are retrieved from Roehrig software [9]. The manufacturer provides the force limits at certain excitation velocities and the values are shown on Table 2.

The values of the compression and rebound forces are sampled at the above velocity rates.

Finally, comparative graphs of the shock absorber performance in all three conditions are provided for the long-lasting test, both in the domain of damping forces and temperature.

Table 3. Manufacturers' limits for the specific shock-absorber type.

	force rebound (N)			force compression (N)		
speed (m/s)	mean	min.	max	mean	min.	max.
0	1	-29.1	31.1	-1	-29.1	31.1
0.026	105	64.5	145.5	-183	-134.7	-231.3
0.052	261	204.9	317.1	-287	-228.3	-345.7
0.078	445	370.5	519.5	-417	-345.3	-488.7
0.131	871	753,9	988.1	-627	-534.3	-719.7
0.183	1069	935.4	1202.6	-690	-591	-789
0.262	1243	1087.6	1398.4	-750	-645	-895

3.1 First experimental shock absorber condition

To start with, short test values for the first experimental shock absorber condition are presented in Figure 3 below, where the values are in a red colour curve while the limits set by the shock absorber manufacturer are given in blue.

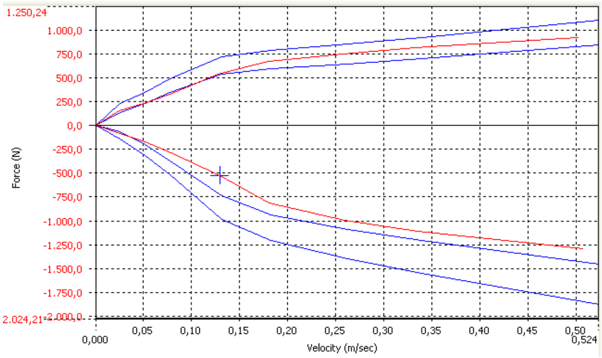

Figure 3. Short test results for EC1

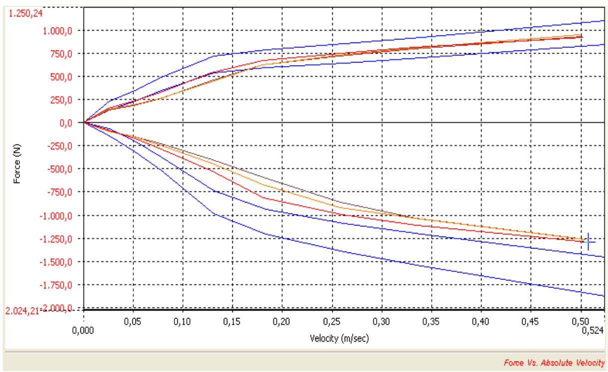

Figure 4. Long test results for EC1

Here, it is observed that the area of malfunction of the used shock absorber is located, mainly, in the rebound function

On the other hand, the long test, as already mentioned above, involves repeated iterations of short test (30) allowing a short rest interval (5sec). In the following diagram shown in Fig. 4, the values obtained during the 1st, 15th and 30th iterations are presented in yellow, red and black curves respectively and the limits set by the manufacturer are in blue colour curves.

Here, with respect to the positive values (compression forces), there is a significant deviation from the manufacturer's values at low excitation velocities as the temperature of the hydraulic medium increases, while the shock absorber performance at higher velocities is within the manufacturer's limits without being affected by any increase in temperature. In the rebound mode, where a high ambient temperature deviation was detected, the rise in temperature leads to a further diverting of the performance curve from that of proper operation, especially at low excitation rates.

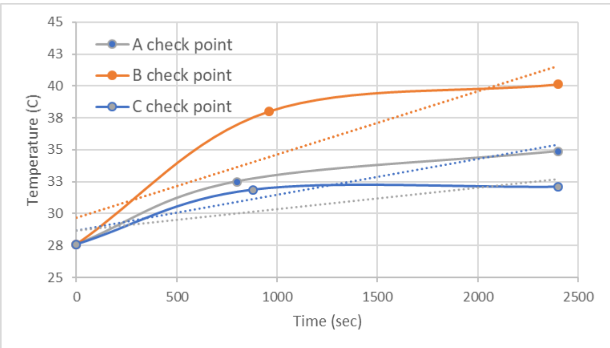

Figure 5. Temperatures measured for EC1

Additionally, the diagram above in Figure 5 shows the temperature development at three checkpoints during the long-lasting test.

3.2 Second experimental shock absorber condition

First, as shown in the following diagram in Figure 6, in the first implemented test, it was found that the damper performance has improved at higher rebound velocities: the curve is almost tangent to the manufacturer's upper limits. At low velocities, however, it retains divergent performance.

However, after performing 30 measurements and while the internal mechanical parts of the damper have been repaired, it is observed that, while it still does not meet the manufacturer's standards for rebound forces, the 15th and the 30th measurements have come closer, which shows an improvement of the damper qualities in relation to the previous state. The monitored values are shown in Figure 7 below.

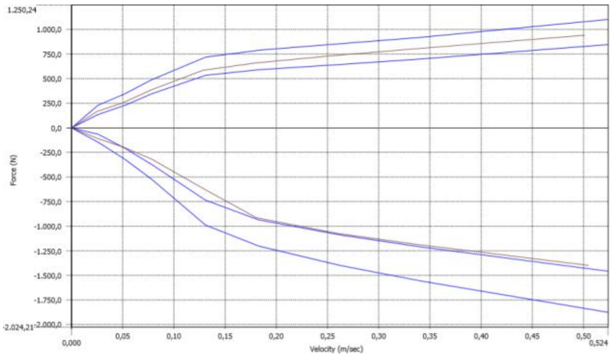

Figure 6. Short test results for EC2

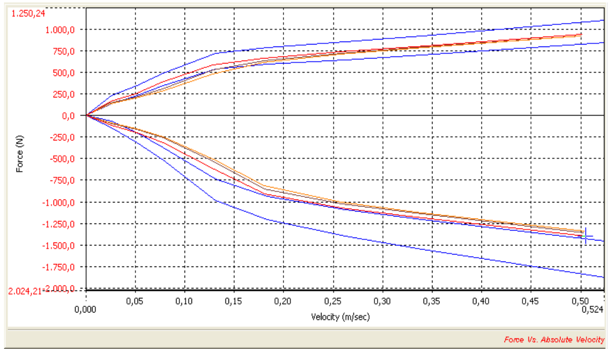

Figure 7. Short test results for EC2

In the following diagram, in Figure 8, the temperature development at three checkpoints during the long-lasting test for the EC2 is shown. The most interesting observation here is that the maximum temperatures at point A (sealing kit) as well as at mid point B (which best represents the temperature of the hydraulic medium) are, similarly, lower than those measured at EC1.

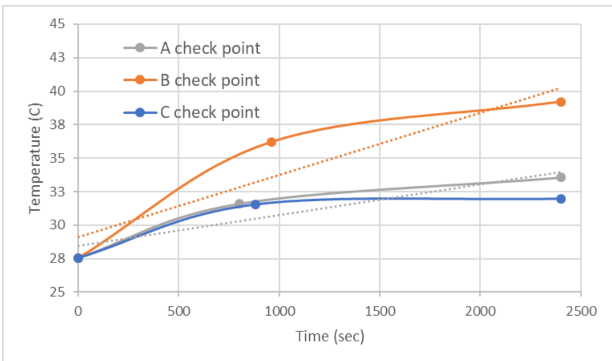

Figure 8. Temperatures measured for EC2

The explanation of course lies in the change of the elements on which the rod slides. These elements are responsible for dry friction on the rod. The observed lower max temperature has an almost linear dependence upon the lower dry friction forces. As the heat capacity of the body and the oil have not been changed compared to EC1, the max temperature decrease for EC2 in comparison to that for EC1 can approximately represent the dry to liquid friction ratio.

3.3 Third experimental shock absorber condition

At the final stage of repair of the damper and after it was found out in the two previous experimental conditions that the damper did not meet the manufacturer's specifications the same tests (long and short) were repeated.

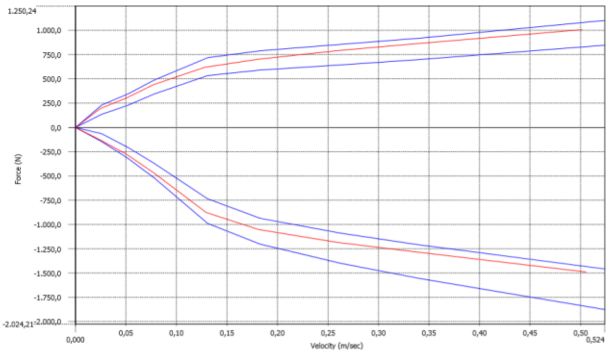

Figure 9. Short test results for EC3

At this stage, the used oil has been replaced with a new one. With a fully repaired damper, a short test was carried out initially, the results of which are shown in the following diagram in Figure 9. The conclusion that is drawn is that the damper meets all manufacturers' standards.

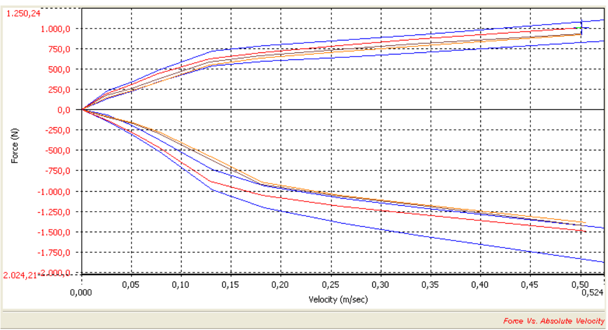

Figure 10. Long test results for EC3

Therefore, after the oil has been replaced with a new one and the damper has been fully repaired, it should be clear, as observed in the diagram above, that the first measurement is within the limits set by the manufacturer (which actually corresponds to the short test), while the 15th and 30th measurements, in the rebound mode, show a small deviation at higher velocities and a higher deviation at low velocities. Of course, the manufacturer's limits are for the short test, where there is no increase in temperature. However, it is used as a comparative element for comparisons between the different experimental conditions of the shock absorber, not for absolute conclusions.

As for the temperature values versus time for EC3 long- lasting test are given in the graph shown in Figure 11.

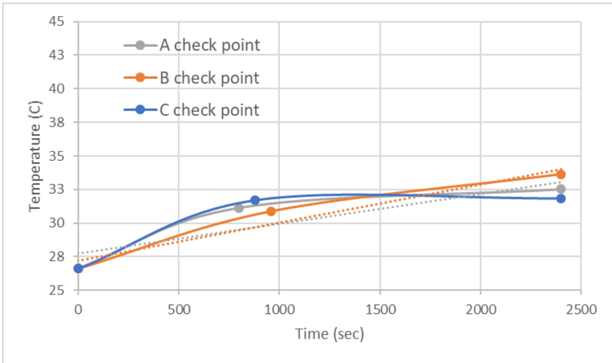

Figure 11. Temperatures measured for EC3.

Furthermore, it is observed that, at all three points of the damper, there is a lower temperature increase at the end of the 30 consecutive measurements, a quality that is clearly attributed to the change of the hydraulic medium.

3.4 Comparative results presentation

The final stage of the experimental study was the comparison of the compression - rebound forces in the individual experimental conditions. The values obtained and compared referred to predetermined points specified by the manufacturer. In each distinct iteration that lasted 80 seconds, there were nine specific points at which it was possible to take measurements related to (a) the compression force, (b) the rebound force, and (c) the temperature at each point throughout the testing procedure. These points are specified by the manufacturer and refer to 9 specific velocities run by the hydraulic medium during the experimental testing procedure.

In order to correctly compare the compression-rebound forces, in the following diagrams, the values of the force at control velocities in the 1st, 15th and 30th iterations are shown on the same graph for each iteration.

Starting from the first iteration of the long test, in the diagram shown in Fig. 12 below, it is observed that, on compression, the forces initially go beyond limits at low velocities for EC2 and EC3 but at the end of the iteration and while the velocity is increasing, the forces are within limits.

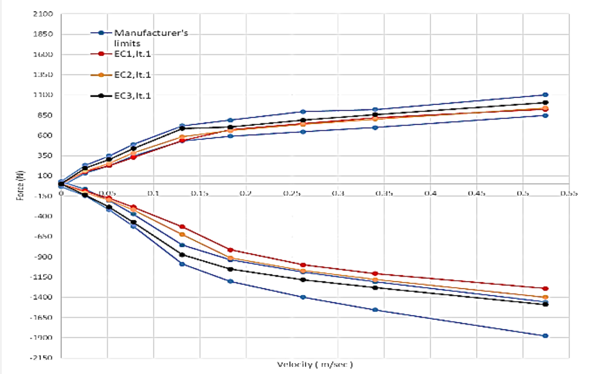

Figure 12. Comparative graphs of 1st Iteration

In particular, during the 1st iteration of the first experimental condition, it is observed that at low velocities of 0.052m/s and 0.078m/s the force values are beyond the manufacturer's limits while, at all the rest of velocities, the force values are within limits.

During the 1st iteration of the 2nd and 3rd experimental conditions, the forces are within the manufacturer's limits. Immediately after repairing the internal parts of the damper and then replacing the oil with a new one, the damper forces are within the desirable limits.

It should be noted that, during all iterations, the values on compression were almost always within limits. The problem in the damper occurred on rebound. After replacing the mechanical parts of the damper, it became clear that the problem was on the rebound valve spring.

As mentioned earlier, the problem in the damper occurred intensely on rebound when the forces are greater.

During the first iteration of the 1st experimental condition, it is observed that the rebound force is within limits only at the velocity of 0.026m/s, while, at all other velocities, the force is out of the manufacturer's limits, thus the damper being in need of repair.

During the first iteration of the 2nd experimental condition, and after having replaced the internal parts of the damper, it is observed that the rebound force is within limits only at the velocity of 0.026m/s again. At all other velocities, the force is out of limits, very close to the manufacturer's limits, though.

Finally, during the 1st iteration of the 3rd experimental condition, after having replaced the used oil with new one, it is observed that the rebound force of the damper is within limits throughout the iteration and at all velocities. This demonstrates the usefulness of the oil in the damper as well as that the damper meets the manufacturer's limits.

At the next stage, during the 15th iteration , comparative graph shown in Figure 13, of the first experimental condition, the compression force of the damper is beyond the limits at the velocities of 0.026m/s, 0.052m/s, 0.078m/s, 0.131m/s, and then the compression force returns within limits. At the same time, the rebound force throughout the iteration is out of limits the except for the velocity of 0.026 m/s. In the Figure 13 below the comparative graphs of all EC's for the 15th iteration of the long-lasting test are shown.

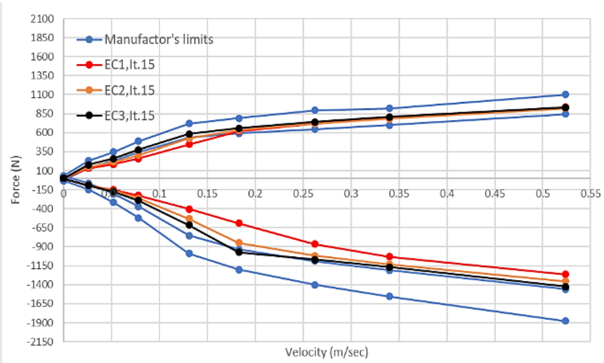

Figure 13. Comparative graphs of 15th Iteration

During the 15th iteration of the 2nd experimental condition, the compression force is off the limits at the velocities of 0.052m/s, 0.078m/s and 0.131m/s and then the force is within limits. The rebound force, as in the previous condition, goes beyond the manufacturer's limits, except for the velocity of 0.026m/s, while the compression forces are within the manufacturer's limits.

Finally, during the 15th iteration of the 3rd experimental condition, the compression force is within the manufacturer's limits throughout the iteration. As for the rebound force in the last iteration, it is observed that, at low velocities it is off the limits, at medium velocities it is within limits (0.183m/s), and at the end of the iteration, at high velocities, it goes beyond limits to a very short extent.

Eventually, during the 30th iteration of the first experimental condition the compression and rebound forces are out of the manufacturer's limits while the compression force is within limits from the medium velocities to the end of the iteration. The rebound force is off limits throughout the iteration.

During the 30th iteration of the 2nd experimental condition again, it is out of the manufacturer's limits, as is in the 1st condition. As for the compression force, it is observed, as in the previous condition, that it returns to the manufacturer's limits after the medium velocities while the rebound force is out of limits throughout the iteration.

Finally, during the 30th iteration of the 3rd experimental state, the compression force is within the manufacturer's limits until the end of the iteration while the rebound force is off limits but tends to be close to them despite the continuous strain the damper has suffered in the 30 iterations. For this reason, it cannot be claimed that the damper does not meet the manufacturer's specifications. In the Figure 14 below, the comparative graph of the 30th iteration is given.

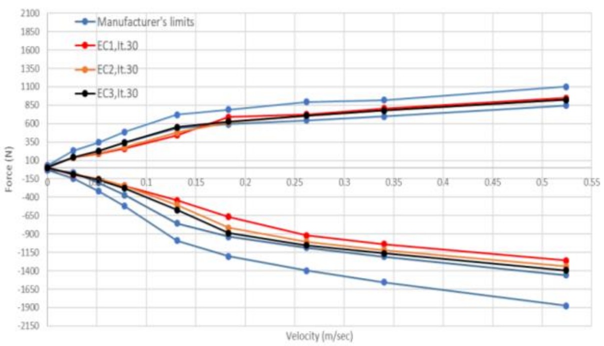

Figure 14. Comparative graphs of 30th Iteration

At the end, diagrams were formed in order to demonstrate the temperature difference among the 3 experimental conditions. Each of the following diagrams shows the difference in temperature at 3 selected points (sealing kit, compression valve, center) for the 3 conditions.

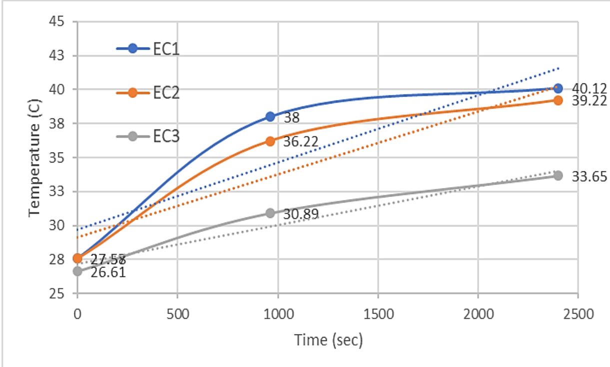

Figure 15. Temperature development in the middle of the absorber tube in the three experimental conditions

From the last two graphs a very important conclusion can be drawn: The temperature rise affects the performance in low velocities mainly and the highest impact is observed at the fully repaired absorber.

The temperature values monitored in the middle of the tube are most representative of the temperature of the hydraulic medium because the thickness of the damper metal at the centre is smaller than it is at the other two points and therefore the temperature difference is obvious. In Figure 15 the comparative graph of temperature development, at the middle point of the tube, versus test time is given for all three experimental conditions.

At this point, it is observed that there is no great temperature difference in the 1st and 2nd experimental conditions. This is due to the fact that, in both conditions, the operating oil is used, while in the third condition it has been replaced with a new one.

3.5 Chemical analysis of oils

The final part of the whole process was dedicated to the chemical analysis of both the new and used oils. On Table 4 below, the results of the analyses made on the two hydraulic means are presented in comparison with the referenced values of its grade. The used and the new oil were of RAVENOL brand and ISO 32 grade.

Table 4. Hydraulic oil physicochemical analysis

	Method			
		Used Oil	New Oil	Ref. Values
Appearance	Visual	Hazy	Red	Amber
Density at 20° C (Kgr/m^3)	ISO 12185	856	856.7	856
Viscosity at 100° C	ASTM D7042	5.765	5.283	5.8
Viscosity at 40° C	ASTM D7042	33.1	14.77	33.2
TAN (mg KOH/gr)	ASTM D664	0.29	1.59	-
Flash point °C	ASTM D93	155	90.5	220
Insolubles contents	ASTM D893	<0,05	<0.05	-
Water (% vol)	ASTM D6304	-	0.05	-
		Wear metals and contaminants (ppm)		
Tin (Sn)	ASTM D5185	1	3	-
Iron (Fe)	ASTM D5185	1	68	-
Copper (Cu)	ASTM D5185	0	68	-
Nickel (Ni)	ASTM D5185	0	2	-
Chromium (Cr)	ASTM D5185	0	7	-
Lead (Pb)	ASTM D5185	0	3	-
Magnesium (Mg)	ASTM D5185	0	32	-
Aluminim (Al)	ASTM D5185	1	40	-
Silicon (Si)	ASTM D5185	12	140	-
Vanadium (V)	ASTM D5185	0	0	-

The comments derived from the analysis are the following:

The water content was measured at alert level for unused hydraulic oil. In the chlorides test results, the water detected didn't appear to be of elevated salinity (fresh water), which means that the existing water in the oil was from the ambient moisture.

The viscosity at 40° C for the used oil was considerably lower than the minimum limit commonly accepted for the relevant oil grade thus the divergence of the forces.

The flash point had considerably dropped compared to fresh oil specifications.

The TAN (Total Acid Number) value determined, was measured at concern level and could indicate oil oxidation due the incoming moisture.

The silicon content was considerably elevated and could indicate contamination due to seals deterioration.

The iron, copper and aluminium contents were also elevated and indicate severe wear of the mechanical parts of the shock-absorber.

4. CONCLUSION

The purpose of this work was twofold: on the one hand, to investigate the operation of a long used damper and its reset to normal performance by partially replacing the mechanical parts first and then the hydraulic medium; on the other hand, the purpose was to study the performance of the damper, in all three conditions mentioned above, at elevated temperatures. It is considered that both goals have been successful. The force-velocity values obtained from the tests produce valuable conclusions on the whole issue. Thus, it has been observed that the performance of the damper is greatly improved by replacing the mechanical parts, especially those parts which control the fluid flow in the valves but do not reduce the energy remaining in the damper in the form of heat ultimately affecting its operation, altering the viscosity of the hydraulic medium. Replacing the hydraulic medium, apart from further improving damper performance, improves the temperature condition of the damper as well, since it has a lower heat capacity compared to the used oil that contains a multitude of foreign particles.

Another very important conclusion, which mentioned also in the previous paragraph, is that the temperature rise affects highly the performance in low velocities of the fully repaired absorber, and especially at the rebound operation.

Finally, the dry friction rate was compared to that of the fluid dynamic friction, estimating the temperature developed both in the used model and in that the mechanical parts of which had been replaced.

The temperature of a shock absorber may reach even 100 ° C; therefore, the study of damper performance at temperatures in this range would be of great interest and probably the subject of a future work.

ACKNOWLEDGEMENT

The authors would like to acknowledge, in advance, Mr A. Tsolis and Mr J. Mylonas of Trochos Ltd for providing the test apparatus and their technical support. Secondly, many thanks must be given to Mrs C. Drakakaki and Mrs E. Mante of Spectrum-Labs for the oil analysis and their useful comments on it.

REFERENCES

[1] M. Demic: A optimization of characteristics of elasto-dambing elements from the aspect of oscillatory comfort and vehicles handling, Int. J. of Vehicle Design, no 1, 1996.

[2] C.N. Spentzas and D.B. Koulocheris: *An optimal suspension system for ground vehicles*, in: Proceedings of the 4th International Conference on Comfort in the Automotive Industry – Recent Developments and Achievements, 06-07.07.97, Bologna, Italy, pp. 383-393,

[3] C.N.Spentzas and A.Tsolakis, An innovative suspension system for ground vehicle', *Mobility and Vehicle Mechanics-The International Journal for Vehicle Mechanics, Engines and Transportation*, Vol. 24, No.2 pp. 15-26, 1998.

[4] D. Bhuyan, K. Kumar: Computational Fluid Flow Analysis of Base Valve for Twin Tube Shock Absorbers, Materials Today: Proceedings, Vol. 4, No. 2, pp. 2308-2313, 2017.

[5] Y. Liu , J. Zhang: Nonlinear dynamic responses of twin-tube hydraulic shock absorber, Vol. 29, No. 5, pp. 359-365, 2002.

[6] J.C. Ramos, A. Rivas, J. Biera, G. Sacramento, J.A. Sala: Development of a thermal model for automotive twin-tube shock absorbers, Applied Thermal Engineering, Vol. 25, No. 11-12, pp. 1836-1853, 2005.

[7] A. Lion , S. Loose: A Thermomechanical Coupled Model for Automotive Shock Absorbers: Theory, Experiments and Vehicle Simulations on Test Tracks, International Journal of Vehicle Mechanics and Mobility, Vol. 37, No. 4, pp. 241-261, 2002.

[8] K. Lee: Numerical Modelling for the Hydraulic Performance Prediction of Automotive Monotube Dampers , Vehicle System Dynamics, Vol. 28, No. 1, pp. 25-39, 1997.

[9] MTS Systems Corporation: MTS Roehrig VS with Shocks Software, 2015.

Serbian Tribology Society

SERBIATRIB '19

16th International Conference on Tribology

Faculty of Engineering University of Kragujevac

Kragujevac, Serbia, 15 – 17 May 2019

INFLUENCE OF THE PRIMARY AND SECONDARY OXIDATION INHIBITORS ON THE OXIDATION STABILITY OF THE MINERAL BASE OILS

Branka DUGIĆ KOJIĆ[1]*, Pero DUGIĆ[2], Tatjana BOTIĆ[3], Goran DUGIĆ[4]

[1, 4]Oil Refinery Modriča, Modriča, Republic of Srpska, gdugic@modricaoil.com;

[2, 3]Faculty of Technology, University of Banja Luka, Republic of Srpska, pero.dugic@tf.unibl.or, tatjana.botic@tf.unibl.org

*Corresponding author: branka@modricaoil.com

Abstract: *Oxidation stability is one of the most important characteristics of both base oils and finished products. Based on this characteristic, it is possible to evaluate the ability of lubricants to provide a long usage time under different application conditions. In order to ensure the best possible resistance of the lubricant to oxidation, in the formulations of finished products it is necessary to add oxidation inhibitors that will protect lubricant against oxygen attacks. The rate of oxidation depends on the quality and type of the base oil, the used additive package, but also the type of oxidation inhibitor, as well as the conditions of use. The aim of this paper was to investigate the influence of primary and secondary oxidation inhibitors on the oxidation stability of mineral base oils. Two base oils of different viscosity gradations were used for the test, as well as two types of oxidation inhibitors, primary and secondary. Samples were inhibited with five different concentrations. A standard test method ASTM D 2272 was used to determine oxidation stability.*

Keywords: *oxidation stability, oxidation inhibitors, mineral base oils, primary and secondary oxidation inhibitors, standard method ASTM D 2272.*

1. INTRODUCTION

The characteristics of the base oils influence almost all the parameters of the finished product. Almost all the lubricant characteristics can be modified by adding suitable additives [1]. Oxidation stability is one of the key characteristics of lubricating oils. The oxidation process occurs during application, even during standstill. In addition to the components included in the finished product, oxidation stability is influenced by other parameters such as: the temperature that accelerates the oxidation process; presence of water - at elevated temperatures, hydrolysis and separation of additives and lubricants occurs; The presence of metal negatively affects oxidation stability as there is an exchange of the ions that catalyze the oxidation process [2,3]. The process of oxidation leads to the emergence of various products that lead to changes in the physical and chemical characteristics of the oil. It is very important to determine the limit of the oxidation inhibitor content, whereby further increase in concentration does not lead to product improvement in terms of prolonging the useage time. Oxidation is the main cause of the increase in viscosity, the formation of varnishes, the breakdown of the base oil film, the formation of rust and corrosion. Therefore, understanding and controlling oxidation is the main preoccupation of the lubricant manufacturers. Antioxidants are key additives that are an integral part of the lubricant formulation. They are designed to "sacrifice" themselves, that is, they oxidize before any other component in the lubricant [4]. They protect lubricants from oxidation degradation and thus enable the lubricant to fulfill the necessary requirements for application in engines and industrial conditions [5].

2. LUBRICANTS

Liquid lubricants, whether motor or industrial lubricants, constitute an indispensable part of each engine. Their basic role is lubrication ie. reducing friction between touching surfaces, in addition protecting against corrosion, draining heat and removing the residues [6].

Liquid lubricants consist of base oil which makes up over 90% of finished product and additives. Base oils also represent additives carrier and allow their application in a wide temperature range [7].

2.1 Additive

Additives are chemical compounds that are dissolved in base oil [8]. They are characterized by good thermal performance and low flushing [9]. Additives have three basic tasks:

- To improve the existing physical properties of lubricants (modifiers IV, antifoam, PPD)
- To improve the chemical propertiesa (antioxidants)
- By adding additive lubricant gets new features (corrosion inhibitors, EP additives, dispersants) [8].

2.2 Antioxidants

New technologies and industrial materials require the use of better performance lubricants [10]. One of the most important characteristics of the lubricant is oxidation stability because it is considered that it causes aging of lubricants, which results in oil tanning, formation of deposits, poor lubrication, etc [1]. Improvement of the oxidation characteristics is achieved by adding antioxidants to the lubricant formulation itself [11]. These are compounds that have the ability to control oxidation by preventing the interruption of the oil film and thickening, i.e. prevent the increase in viscosity, and ensure the performance of lubricants and longer service life [12]. Antioxidants are divided into two groups:

- Active components that remove radicals
- Active components that break down the peroxides

Active components that remove radicals are known as primary antioxidants. They donate a hydrogen atom that reacts with alkyl radicals or alkyl peroxy radicals, by stopping the chain reaction in the oxidation process. The primary antioxidant becomes a stable radical, the alkyl radical becomes hydrocarbon and the alkyl peroxy radical becomes alkyl hydroperoxide. The most well-known primary antioxidants are phenols and aromatic amines.

Secondary antioxidants include active ingredients that expose hydroperoxides. They react with oxygen or hydrogen peroxide, and in this way they promote their own oxidation. When the secondary antioxidant expires, accelerated oxidation of non-inhibited oils occurs. Secondary antioxidants include ZnDDP, phosphites and thioeters [5].

2.3. Oxidation mechanism

Oxidation is a multistage process involving the radicals process in three steps which, if left unconfirmed, will lead to the complete breakdown of the components in the lubricant [10]. The oxidation takes place through the reaction of the alkyl chain and the peroxide radical in three steps:

1. Initiation (initiation of chain reaction)
2. Propagation (duplication)
3. Temination (end of chain reaction) [5].

In the first step, the initiation step, external factors such as high pressure, heat or the presence of metals will activate the formation of free radicals obtained from organic components from lubricants. Either the bond within the organic sample between the two atoms is broken down to form a radical or the electron is taken from the molecule by an oxidized metal [10]. The ability of the homolithic breakdown of R-H to give free radicals is determined based on the strength of the C-H bond and results in stable radicals [5].

$$RH+O_2 \rightarrow R^{\bullet}+HOO^{\bullet} \qquad (1)$$

This reaction is relatively slow at room temperature, while the rise in temperature results in an acceleration of the reaction. Free radicals are highly reactive and can react with oxygen to form hydroperoxyl radicals [10]. As the initiation reactions continue, there is an increase in the peroxide content (ROOH and HOOOH), leading to secondary initiation (2), where peroxides are the sources of free radicals.

$$ROOH \rightarrow RO^{\bullet} + HO^{\bullet} \qquad (2)$$

In the propagation phase, there is an irreversible reaction between alkyl radicals and oxygen, whereby an alkyl peroxy radical is formed. These reactions take place quickly, and the speed depends on radical change [5].

$$R^{\bullet}+ O_2 \rightarrow ROO^{\bullet} \qquad (3)$$

In the second step of propagation, hydrogen is released from the hydrocarbons by the alkyl peroxy radical, whereupon hydroperoxide and the second alkyl radical are formed again. Alkyl peroxy radicals are present at a higher concentration than alkyl radicals. The reason is that the oxygen is present at a higher concentration and reacts more quickly with the alkyl radical relative to the slower reaction of the alkyl peroxy radicals with the hydrocarbon [5].

$$ROO^{\bullet}+RH \rightarrow ROOH+ R^{\bullet} \qquad (4)$$

2.4. Peroxide decomposition

Alkyl hydroperoxides are extremely reactive, and at high temperatures, their decomposition results in additional radicals. They can undergo further isolation and propagation reactions, thereby increasing total oxidation. Alkyl peroxides and alkyl peroxy radicals are further expanded to neutral oxidation products such as alcohols, aldehydes, ketones and carboxylic acids [5].

$$ROOH \rightarrow RO^{\bullet}+{}^{\bullet}OH \qquad (5)$$

$$2ROOH \rightarrow RO^{\bullet}+ROO^{\bullet}+H_2O \qquad (6)$$

$$RO^{\bullet}+ROOH \rightarrow \text{Različiti produkt} \qquad (7)$$

The last stage of the oxidation process is the termination that stops the oxidation process when the radical is combined. Two alkyl radicals can be combined and form a hydrocarbon molecule. In addition, the alkyl radical may react with an alkyl peroxy radical to form a peroxide, or a reaction may occur between the two alkyl peroxy radicals in which the peroxide is formed by separating the oxygen. The more efficient this step is, the lower the degree of oxidation [5].

$$R^{\bullet}+R^{\bullet} \rightarrow R\text{-}R \qquad (8)$$

$$R^{\bullet}+ROO^{\bullet} \rightarrow ROOR \qquad (9)$$

$$2ROO^{\bullet} \rightarrow ROOR+O_2 \qquad (10)$$

For this reason, the lubricant formulation also includes antioxidants, which stop the process of forming stable radicals. Antioxidants act either by decomposing peroxides or by reacting with free radicals.

2.5. Inhibition of oxidation

The mechanism of degradation of lubricants clarifies several possible counterproductive measures in order to control the degradation of lubricants. Blocking the power source is one way, but it is effective only for lubricants used in low shear and low temperature conditions. However, for most lubricants, it is more convenient filtering the catalytic impurities and decomposition of hydrocarbon radicals, alkyl peroxo radicals and hydroperoxides. This can be achieved by using active components that remove radicals, components that decompose peroxides and metal deactivators.

There are two types of metal deactivators: chelating agents and film formation agents. Helate agents will form a stable complex with metal ions, reducing the catalytic activity of metal ions. Accordingly, deactivators can exhibit an antioxidant effect. The film-forming agents behave in two ways. First, they cover the metal surface, thus preventing the metallic ions from reaching the oil. Second, they minimize corrosion attacks on the metal surface physically limiting the access of corrosive species to the metal surface [5].

3. EXPERIMENTAL PART

3.1. Materials and work methods

The experimental part consists of two parts. In the first part, the oxidation stability of the starting uninhibited mineral base oils was studied as:

- Mineral base oils BU1 and BU2

In the second part of the article, the oxidation stability of mineral base oils was studied, which were inhibited by two types of oxidation inhibitors, primary and secondary. Oxidation inhibitors are designated as:

- Primary oxidation inhibitor I1
- Secondary oxidation inhibitor I2

And the determination of the basic physical and chemical characteristics of mineral base oils was made using the standard methods of analysis shown in Table 1.

Table 1. Characteristics and test methods of the tested mineral base oils

Characteristics	Method	BU1	BU2
Viscosity at 40°C, mm²/s	BAS ISO 3104	21,681	32,58
Viscosity at 100°C, mm²/s	BAS ISO 3104	4,433	6,07
Viscosity index	BAS ISO 2909	122	136
Pour point, °C	BAS ISO 3016	-13	-9
Neutralisation number, mgKOH/g	ISO 6618	0,0052	0,0052

Table 2 shows the characteristics of the used oxidation inhibitors.

Table 2. Characteristics of oxidation inhibitors used in lubricant formulations

Characteristics	I1	I2
Viscosity at 40°C, mm²/s	-	100
Density at 20°C, mm²/s	1030	1120
Flash point, °C	≈127	>150
Neutralisation number, mgKOH/g	-	128

The inhibitor I1 belongs to the group of phenolic antioxidants, which are also commonly used in the formulations of liquid industrial lubricants. The most famous antioxidant from this group, with a single aromatic ring, is 2,6-ditert-butyl-4-methylphenol. It is used as an oxidation inhibitor for base oils, petrol and lubricants whose working temperature does not exceed 150° C [13].

The inhibitor I2 is based on zinc dialkildithiophosphate and belongs to a group of secondary antioxidants. ZnDDP is a multifunctional additive, i.e. In addition to being used as an antioxidant, it can also be used as an anti-wear additive and as a corrosion inhibitor [14].

There are several methods for determining the oxidation stability. The choice of the method itself depends on whether the base oil or finished product is tested, whether the control of the finished product or the development of a new product is carried out.

In this paper, the ASTM D 2272 method was used to determine the oxidation state, method B.

50 g of the oil sample is poured into a glass vessel, and then the water and the spiral coil of the copper catalyst are added. The glass vessel is placed in a bomb equipped with a pressure gauge and filled with oxygen until the pressure on the pressure gauge reaches a value of 620 kPa (90 psi). The glass bowl inside the bomb is rotated at a speed of 100 rpm at a constant temperature of 150 ° C. The bomb is set at an angle of 30 ° relative to the surface. The oxidation stability measure is the time

(min) required to reach a certain pressure drop on the pressure gauge. Upon completion of the analysis, in the diagram where the pressure drop in relation to time was recorded, the maximum pressure and time at the point of the falling part of the curve is read, where the pressure of 175 kPa (25.4 psi) is lower than the maximum pressure. That is, the time that elapsed from the start of testing to the drop of 175 kPa (25.4 psi) in relation to the maximum pressure represents the lifetime of the sample. The time to sharp drop in pressure is usually the induction period, and if the time before the start of a sharp drop in pressure is longer, tested oil has a better resistance to oxidation. After completion of the oxidation stability test, the sample is filtered through filter paper and then poured into the separation funnel to remove the remaining water [15].

In this paper, the oxidation stability of the initial uninhibited samples of mineral base oils BU1 and BU2, samples of mineral base oils inhibited with different concentrations of oxidation inhibitors I1 and I2 were determined. In order to investigate the synergistic effect of primary and secondary oxidation inhibitors on oxidation stability, two series of samples were prepared which were inhibited by the combination of the oxidation inhibitors I1 and I2.

4. RESULTS AND DISCUSSION

Two series of samples inhibited by inhibitors of oxidation I1 and I2 were added, which were added in concentrations from 0.1% m / m to 0.3% m / m, as well as a series of samples inhibited by the combination of inhibitors I1 and I2. Tables 3-5 give the results of tests of the characteristics of the mineral base oil BU1 and the formulated samples before and after the oxidation stability test.

Based on the results shown in FIG. 1, it can be seen that the BU1 inhibited inhibitor with oxidation inhibitor I1 reaches a maximum value at an inhibitor concentration of 0.25% m / m, while a mild decrease is observed at a concentration of 0.3% m / m. For the BU1 sample inhibited with the oxidation inhibitor I2, the maximum consistency is reached at a concentration of 0.15% m / m, while further increase in the concentration does not result in an increase in the oxidation stability value, but a decrease. The reason for this may be that, in addition, the oxidation inhibitor I2 performs the function of the secondary inhibitor, it also performs the function as a corrosion inhibitor or is used as an anti-wear additive. The maximum value of oxidation stability in the BU1 inhibited inhibitor combination I1 and I2 is achieved at a concentration of 0.3% m / m. It can be assumed that higher levels of oxidation stability would result in further concentration increase.

Table 3. Characteristics of BU1 inhibited with inhibitor I1

Characteristics	Oxidation inhibitor I1, %m/m					
	BU1	0,1	0,15	0,2	0,25	0,3
Before test						
Neutralisation number, mgKOH/g	0, 0052	0, 005	0, 0054	0, 010	0, 0054	0, 0055
After test						
Neutralisation number, mgKOH/g	1,40	2,43	1,52	1,32	1,31	1,30
Max. reached pressure, kPa	1292	1290	1288	1284	1253	1280
RBOT, min	100	155	163	231	295	293

Table 4. Characteristics of BU1 inhibited with inhibitor I2

Characteristics	Oxidation inhibitor I2, %m/m					
	BU1	0,1	0,15	0,2	0,25	0,3
Before test						
Neutralisation number, mgKOH/g	0, 0052	0,09	0,2	0,28	0,3	0,35
After test						
Neutralisation number, mgKOH/g	1,40	0,66	0,99	0,85	0,62	0,85
Max. reached pressure, kPa	1292	1273	1262	1255	1272	1262
RBOT, min	100	273	300	260	248	225

Table 5. Characteristics of BU1 inhibited with the combination inhibitors I1 and I2

Characteristics	Oxidation inhibitor I1+I2, %m/m					
	BU 1	0,1	0,15	0,2	0,25	0,3
Before test						
Neutralisation number, mgKOH/g	0, 0052	0, 051	0,02	0,07	0,07	0,11
After test						
Neutralisation number, mgKOH/g	1,40	0,88	1,43	1,03	0,86	1,06
Max. reached pressure, kPa	1292	1271	1278	1276	1264	1275
RBOT, min	100	168	160	230	241	273

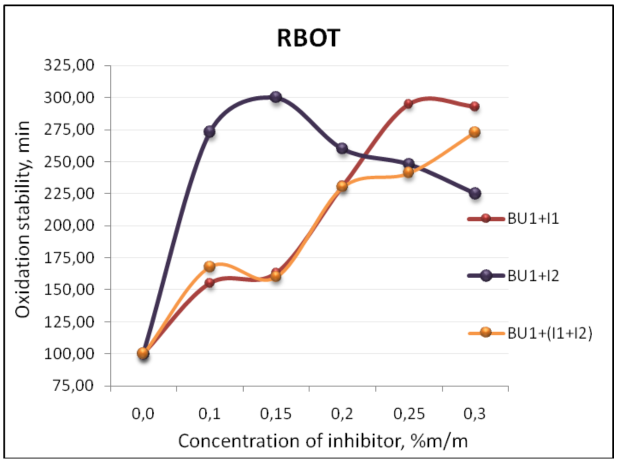

Figure 1. The dependence of oxidation stability of BU1 on the type and concentration of the oxidation inhibitor

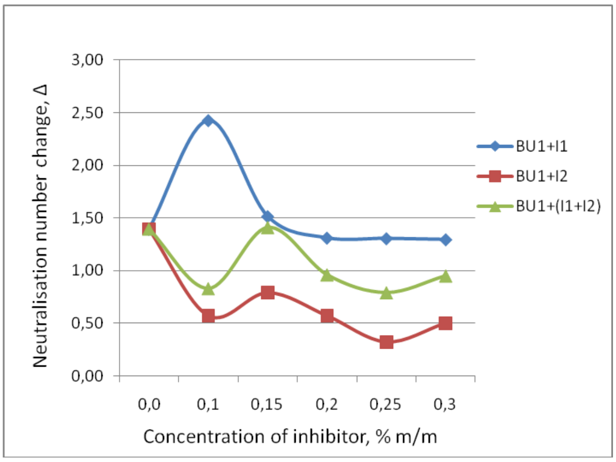

Figure 2. Change of the neutralization value (Δ) before and after the oxidation stability test

It can be noticed that the biggest changes in the neutralization number occur in the sample of HC base oil BU1 inhibited by the oxidation inhibitor I1, while for the sample of HC base oil BU1 inhibited with the oxidation inhibitor I2, the least of the neutralization number changes before and after the oxidation stability test. The values of the neutralization number change in the sample of the HC base oil BU1 inhibited with the combination of the oxidation inhibitor I1: I2 are between the values of the changes in the neutralization number of the HC base oil inhibited with oxidation inhibitor I1 and I2. A larger difference in the neutralizing number before and after the oxidation stability test, under the same conditions, means faster decay, i.e. poor oxidation stability.

Table 6-8 shows the results of the tests of the characteristics of the mineral base oil BU2 and the formulas samples, before and after the oxidation stability test.

From Figure 3 it can be noticed that for the sample of HC base oil BU2 inhibited with the oxidation inhibitor I1, the best oxidation stability value is achieved at a concentration of 0.3% m / m. Based on the diagram, it could be concluded that with further increase in inhibitor concentration, better oxidation stability times would be obtained, i. E. a trend of growth would continue. The maximum value of oxidation stability in a sample of HC base oil BU2 inhibited by oxidation inhibitor I2 is achieved at a concentration of I2 inhibitor of 0.15% m / m. With further increase in the concentration of inhibitors, poorer times for oxidation stability are obtained.

Table 6. Characteristics of BU2 inhibited with inhibitor I1.

Characteristics	Oxidation inhibitor I1, %m/m					
	BU2	0,1	0,15	0,2	0,25	0,3
Before test						
Neutralisation number, mgKOH/g	0, 0056	0, 0055	0, 0057	0, 056	0, 056	0, 0057
After test						
Neutralisation number, mgKOH/g	1,40	1,59	1,79	1,59	2,84	1,47
Max. reached pressure, kPa	1292	1221	1254	1236	1262	1239
RBOT, min	100	191	215	282	310	334

Table 7. Characteristics of BU2 inhibited with inhibitor I2

Characteristics	Oxidation inhibitor I2, %m/m					
	BU2	0,1	0,15	0,2	0,25	0,3
Before test						
Neutralisation number, mgKOH/g	0, 0056	0, 094	0,1	0,18	0,15	0,21
After test						
Neutralisation number, mgKOH/g	1,40	1,51	1,08	0,98	1,03	1,27
Max. reached pressure, kPa	1292	1242	1229	1283	1285	1278
RBOT, min	100	371	383	346	375	315

Table 8. Characteristics of BU2 inhibited with the combination of inhibitors I1 and I2

Characteristics	Oxidation inhibitor I1+I2, %m/m					
	BU2	0,1	0,15	0,2	0,25	0,3
Before test						
Neutralisation number, mgKOH/g	0, 0056	0, 027	0,03	0, 077	0, 095	0, 094
After test						
Neutralisation number, mgKOH/g	1,40	1,59	1,18	1,00	0,97	0,92
Max. reached pressure, kPa	1292	1278	1293	1283	1282	1280
RBOT, min	100	243	219	397	316	316

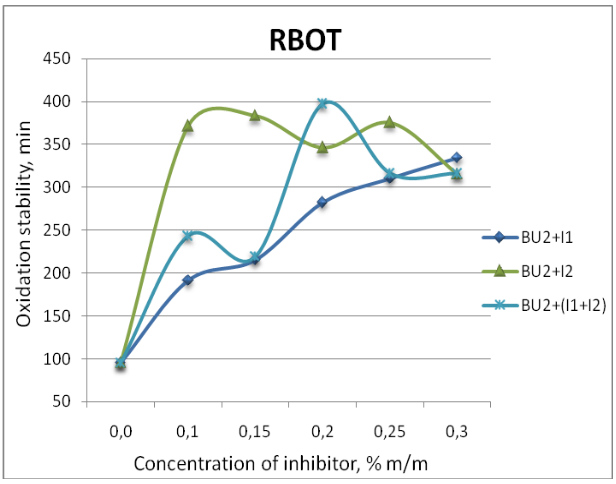

Figure 3. The dependence of oxidation stability of BU2 on the type and concentration of the oxidation inhibitor

By combining the oxidation inhibitor I1: I2 in a ratio of 1: 1, the maximum value of oxidation stability is reached at a concentration of 0.2% m / m. From the diagram, it can be noted that the values of the oxidation stability of the sample of HC base oil BU 2 inhibited by a combination of two inhibitors in a ratio of 1:1 are between the oxidation stability values of HC base oil samples that are inhibited by the oxidation inhibitors I1 and I2, individually.

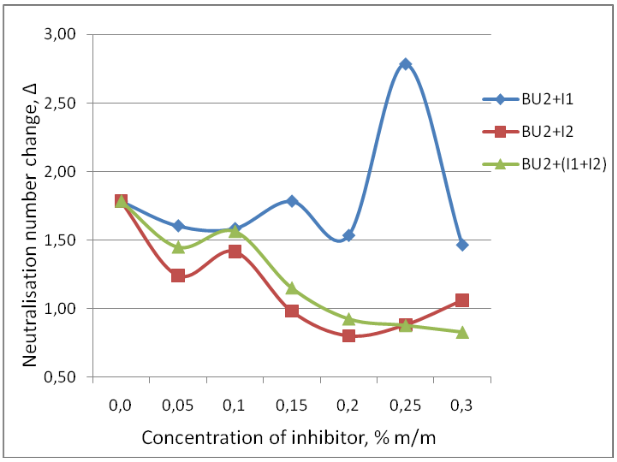

Figure 4. Change of the neutralization value (Δ) before and after the oxidation stability test

From Figure 4, it can be noticed that the largest changes in the neutralization number occur in the sample of the HC base oil BU2 inhibited by the oxidation inhibitor I1 at an inhibitor concentration of 0.25% m / m, while for the sample of HC base oil BU2 inhibited by the oxidation inhibitor I2 there was a slight change in the neutralization number before and after the oxidation stability test. The values of the neutralization number change in the sample of the HC base oil BU2 inhibited by the combination of the oxidation inhibitor I1: I2 are between the values of the changes in the neutralization number of HC base oil inhibited with oxidation inhibitor I1 and I2. A larger difference in the neutralization number before and after the oxidation stability test, under the same conditions, means faster decay, i.e. poor oxidation stability.

In Figures 5 and 6, the influence of oxidation inhibitors on the oxidation stability of various mineral base oils is shown for each type of inhibitor separately.

In the case of the inhibitor I1 (Fig. 5), similar behavior is observed, i.e. a similar change in oxidation stability with an increase in the concentration of inhibitors. Figure 6 shows the effect of oxidation inhibitors on the oxidation stability of different HC base oils. It can be noted that the inhibitor I2 gives the best results in HC base oil BU2.

By combining the oxidation inhibitors I1:I2, the best oxidation stability values are achieved with HC base oil BU2. The worst oxidation stability values are achieved with HC base oil BU1.

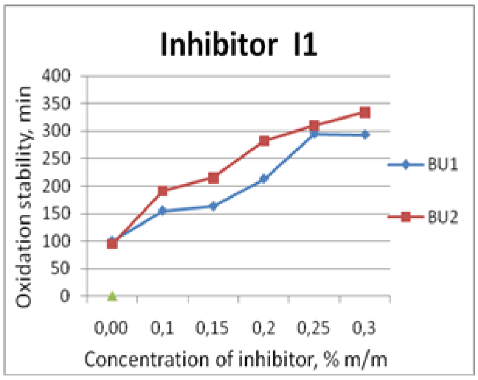

Figure 5. Effect of inhibitor I1 on the oxidation stability of mineral base oils

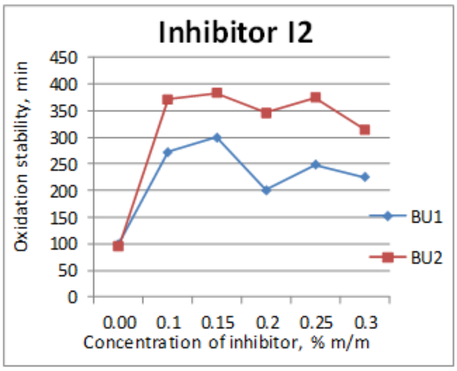

Figure 6. Effect of inhibitor I1 on the oxidation stability of mineral base oils

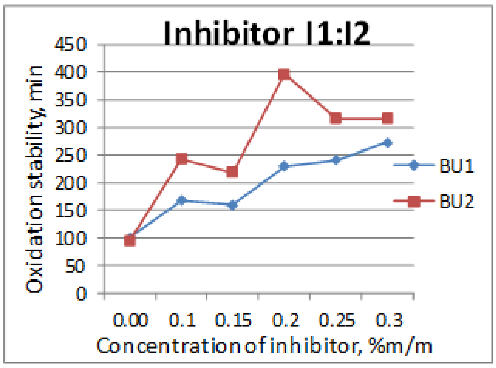

Figure 7. Effect of combinations of inhibitors I1 and I2 on the oxidation stability of mineral base oils

5. CONCLUSION

Based on the conducted testing and analysis of the obtained test results, and in accordance with the set goals, the results of the research can be summarized in the following conclusions:

- The oxidation stability study of the base base oils without additives has shown that the best oxidation stability time has a mineral base oil designated as BU1 with an induction period of 100 min;
- The primary oxidation inhibitor I1 was better with mineral base oil BU2. However, even in this case, the maximum value has not been reached, and it can be assumed that with further increase in the concentration of the inhibitor it can obtain better oxidation stability.
- The ZnDDP-based inhibitor was best in combination with mineral base oil BU2. The maximum value of oxidation stability is achieved with a concentration of 0.1% m/m.
- In most, but not in all cases, the combination of the primary inhibitor I1 and the secondary inhibitor I2, achieved oxidation stability was between the individual action of the oxidation inhibitor. The longest induction period of 397 min was achieved with base oil BU2 with 0.2% m/m of inhibitor combination I1 and I2 in a ratio of 1:1.
- The increase in oxidation inhibitor I1 content also increases the oxidation stability of lubricants. While increasing concentration of inhibitors I2, a maximum value in the concentration range of 0.10 - 0.15% m / m is reached, and then it does not change or slightly decreases.
- As the optimal formulation of the finished product in industrial proportions, a base oil BU2 inhibited with 0.2% m/m of the inhibitor combination I1 and I2.

REFERENCES

[1] S.J. Asadauskas: *Formation of Residues and Deposits in Lubricants during Oxidation*, Technische Akademie Esslingen, 2008.

[2] V. Bouillon: *Overview of oxidation laboratory tests on industrial lubricants*, Lubmat '16, 2016.
[3] P. Wiklund: *Studies on the Chemistry of Mineral Oil Oxidation*, Technische Akademie Esslingen, 2008.
[4] G. Livingstone, J. Ameye: *Antioxidants signal lubricant health*, Lubes'n'Greases Europe-Middle East-Africa, 2015.
[5] L.R. Rudnick: Lubricant Additives; Chemistry and Application, Marcel Dekker, Inc, pp. 1-29, 410-421, 2003.
[6] Maziva, available at: https://hr.wikipedia.org/wiki/Maziva
[7] P. Dugić et al: *Tehnologija prerade nafte, Univerzitet u Banjoj Luci*, Tehnološki fakultet, pp. 499-504, 2017.
[8] M. Stojilković: *Primena maziva*, NIS a.d. Novi Sad-Beograd, pp. 22-39, 2011.
[9] Lubricant Additives: Use and Benefits, August 2016, ATC Document 118, 2016.
[10] N. Canter: Antioxidants: Key additives enable lubricants to operate under more severe conditions, Tribology, Lubrication and Technology, 2016.
[11] Z.R. Petrović et al: Uticaj kiselinom aktiviranog bentonita na oksidacionu stabilnost hidrokrekovanih baznih ulja, Glasnik hemičara, tehnologa i ekologa Republike Srpske, Vol. 7, pp. 33-40, 2012.
[12] M. Soleimani et al: Antioxidants Classification and Applications in Lubricants, Lubrication – Tribology, Lubricants and Additives, 2018.
[13] Dokumentacija proizvođača aditiva
[14] Dokumentacija proizvođača aditiva J
[15] ASTM D 2272, *Standard Test Method for Oxidation Stability of Steam Turbine Oils by Rotating Pressure Vessel*

Serbian Tribology Society

SERBIATRIB '19

16th International Conference on Tribology

Faculty of Engineering
University of Kragujevac

Kragujevac, Serbia, 15 – 17 May 2019

BORON NITRIDE AS ADDITIVE IN RAPESEED OIL, TESTED ON FOUR BALL TESTER

Dionis GUGLEA[1], Traian Florian IONESCU[1], Constantin GEORGESCU[1], Dumitru DIMA[1], George Ghiocel OJOC[1, 2], Lorena DELEANU[1,*]
[1] "Dunărea de Jos" University of Galati, Faculty of Faculty of Engineering, Galati, Romania
[2] Maritime University Constanta, Romania
*Corresponding author: lorena.deleanu@ugal.ro

Abstract: *This paper presents the influence of BN as additive in refined rapeseed oil in a mass concentration of 1%wt on the tribological parameters. Tests are done on a four-ball machine. The test parameters were load: 100 N...300 N and the the sliding speeds of 0.38 m/s, 0.53 m/s and 0.69 m/s, respectively. Particles of hexagonal BN have 500 ± 100 nm. The rapeseed oil was supplied by Expur SA Bucharest. For the tested ranges of the parameters, the additivation of rapeseed oil with BN does not improve the friction coefficient, but the wear rate of WSD seems to be less sensitive for the more severe regimes when the vegetal oil is additivated. The additivation of rapeseed oil with BN is still efficient for the tested ranges of load and speed as compared to the neat rapeseed oil, but there is visible that friction coefficient and analysed wear parameter are less influenced by the regime for the concentration of 1% BN in rapeseed oil.*

Keywords: *rapeseed oil, additive, BN, four ball test, friction coefficient, wear rate*

1. INTRODUCTION

Rapeseed oil has a composition in fat acids that recommends it for lubricating systems that have to comply with more severe regulation concerning the environment protection, but designers have to make a compromise as its viscosity, life and acceptable regimes are lower than classical lubricants.

Anorganic additives are added in lubricants for improving their tribological parameters, for protecting initial texture of the bodies in contact. Most of them have lamellar or plaquette shapes and promote a fird-body friction instead on a direct contact between the triboelements.

In a recent review, Shahnazar et al. [1] dedicated a chapter for boron-based nanoparticles that could act like friction modifier (cerium borate, boric acid, hexagonal boron nitride), anti-wear additive (hexagonal boron nitride, titanium borate, ferous borate, magnesium borate), extreme pressure additive (potasium borate). One may notice that hexagonal boron nitride may reduce both friction and wear.

Wan et al. [2] found a an optimal BN nanoparticle concentration of 0.1 wt.% when comparing friction coefficient and aspect of wear surfaces of a commercial lubricating oil (SAE 15W-40, Sinopec Lubricants) and a new formulated lubricant based on this oil and hexagonal boron nitride nanoparticles with disk shape and an average diameter of ~120 nm and a single layer thickness of ~30 nm. Oleic acid was used as dispersant (25wt.% of

BN nanoparticle) for improving the stability of the suspension. Nano-BN oils containing 0.1wt.%, 0.5wt.% and 1.0wt.%, disk-on-disk tribo-tester, 500 N and The test time of 3 minutes is obviously too short to make the functioning stable or to compare to actual applications. The viscosities of all oils with/without BN nanoparticle additives decrease rapidly with the temperature increasing. Due to the polishing effect of the lubricating oil, all the worn surfaces become smooth after the friction test.

Hexagonal boron nitride (hBN) is attractive for replacing inorganic solid lubricants, such as graphite and molybdenum disulfide. Its lubricating performance is based on the easy shearing along the basal plane of its crystalline structure. Celik et al. [3] synthesized nano hexagonal boron nitride particles by reacting boron oxide with ammonia. Different amounts of nano hBN particles were added to an engine oil. The tribological properties of were investigated using a ball-on-disc tribometer. The addition of hBN particles did not change the viscosity of the lubricants, but changed the coefficient of friction. The presence of sufficient nano hBN additives in oil prevents direct contact and results in decreased friction and wear.

In a very recent review, Uflyand [4] mentioned the hexagonal boron nitride as additive in oils. Their mechanisms during lubrication are similar to those of metal and metal oxide nanoparticles.

The concentration of hBN in oil differs very much, also the basic oil could be mineral, synthetic and vegetal, the fast being in the research focus for formulating eco-friendly lubricants (Table 1).

Abdullah [5] reported results for seizure tests on four ball tribotester with ten increments of loading, from 196 N to 1,570 N, with 10 seconds for every test (at 1,760 rpm, 10 sec and initially 27°C). The test was repeated three times for each sample to ensure more precise and reliable results. The wear scar diameters lubricated with nano-additivated oil were smaller than those lubricated with SAE 15W-40 engine oil only. Severe adhesive wear was observed on the worn surface of a ball bearing lubricated with SAE 15W-40 diesel engine oil.

Table 1. Examples of lubricants with hBN as additive

Base oil	BN / size / concentration	Reference
SAE 15W-40 diesel engine oil	hBN / 70 nm / 0.5 vol%	[5]
castor oil	1, 2, 5 and 8 wt% hBN, silane coupling agent A-151 (1:20)	[6]
jatropha oils	hBN, ranging between 0.05 and 0.5 wt%	[7]
water	1%, 0.05%, 0.01wt% with and without organic functionalization, 200 nm flakes	[8]

Wang et al. [6] tested two regimes on ball-on-disk: high speed-low load (0.52 m/s, 9.8 N, 10 min) and low speed-high load (0.13 m/s, 120 N, 30 min), the sliding distance being 313,8 m and 235 m, respectively. Thus, a direct comparison of wear reducing capacity of the lubricants by the help of the wear scar diameters for the two regimes is not proper. For low load-high speed that the COF of pure castor oil was the lowest as compared to the same oil, additivated with hBN, this parameter increasing with additive concentration, but the COF of the 2 wt% nanofluid is almost the same as that of pure castor oil. At higher concentration (5 and 8%), COF is only 20...25% greater. Under high load and low speed, COF of neat oil is the highest, but all values still presume a full film lubrication. The depth of the wear track is smaller for the additivated oils.

Cho [8] concluded that the repeated exfoliation and deposit of h-BN occurred on the sliding surfaces, forming tribo- films which can reduce friction and wear. The h-BN nano-sheets, inexpensively dispersed in water, may be a promising ‘‘green’’ lubricant.

Talib [7] investigated the turning performances of modified jatropha oils, with and without hBN particles, were investigated in comparison to a synthetic ester. 0.05 wt% of hBN particles in jatropha oil reduced the cutting force (by 9%), cutting temperature and surface roughness (by 8%) and extended the tool life, in terms of cutting length, by 78%. However, the excessive amount of hBN particles (>0.05 wt%) caused particle agglomeration, leading to poor machining performances, in terms of cutting force, cutting temperature and surface roughness.

The aim of this study is to assess the influence of BN in coarse rapeseed oil on the tribological characteristics. The authors analyzed the friction coefficient and the wear rate of wear scar diameter, but also recorded the temperature in the oil cup, during the tests.

2. THE LUBRICANT AND THE TESTING METHODOLOGY

The hexagonal boron nitride was supplied by PlasmaChem [9] and has the following characteristics (Fig. 1): particle size full range: 100-1000 nm, Average particle size: 500 ± 100 nm, Specific surface: 23±3 m^2/g, purity: >98,5%; nitrogen content >55%, controlled admixtures, %: O<1; C<0,1;, B_2O_3 < 0,1. Boron nitride withstands high temperatures and high loads, it is also non-reactive, thermally conductive, electrically insulating [10], [11].

The formulated lubricant was obtained in small amounts of 200 g, each. The steps followed in this laboratory technology were similar to those presented by Cristea [12]:

- mechanical mixing of additive and an equal mass of dispersing agent (guaiacol, supplied by Fluka Chemica, with the chemical formula C6H4 (OH) OCH3, for 20 minutes;
- adding the rapeseed oil, mixing for 1 hour;
- ultrasonication + cooling of formulated lubricant in step of 10 minutes, for 6 times; The parameters of ultrasonic regime are power 100 W, frequency 20 kHz ± 500 Hz, continuous mode.

Table 2. Composition in fatty acids of the tested rapeseed oil (from Expur Bucharest)

Fat acid	Symbol	Composition, %wt
Myristic acid	C14:0	0.06
Palmitic acid	C16:0	4.60
Palmitoleic acid	C16:1	0.21
Heptadecanoic acid	C17:0	0.07
Heptadecenoic acid	C17:1	0.18
Stearic acid	C18:0	1.49
Oleic acid	C18:1	60.85
Linoleic acid	C18:2	19.90
Linolenic acid	C18:3	7.64
Arachidic acid	C20:0	0.49
Eicosenoic acid	C20:1	1.14
others		3.37

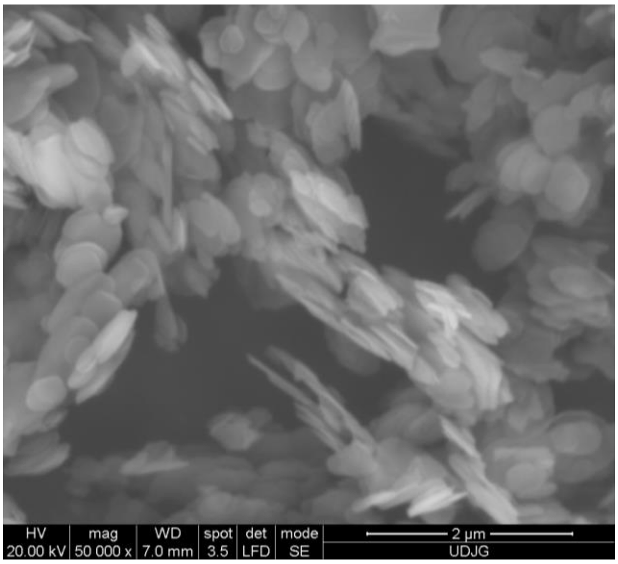

a)

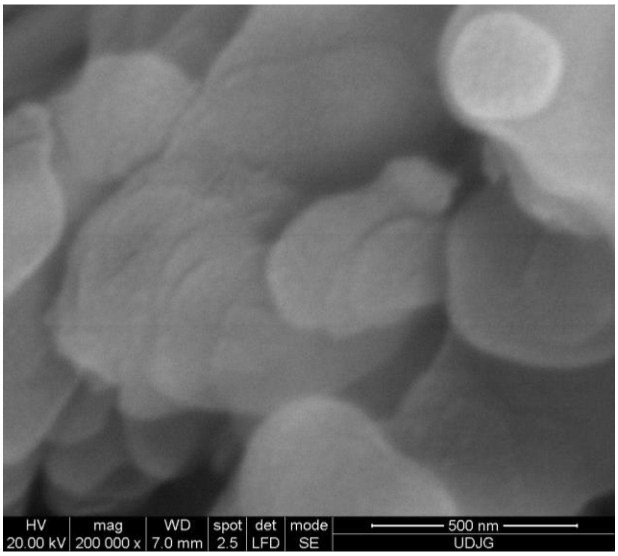

b)

Figure 1. SEM images of the nanoparticles of BN

The balls are lime polished, made of chrome alloyed steel balls, having 12.7±0.0005 mm in diameter, with 64-66 HRC hardness, as delivered by SKF. The sample oil volume required for each test was 8 ml ±1 ml. The test method for investigating the lubricating capacity was that from SR EN ISO 20623:2018 [13].

The test parameters for each test were:

- loading force on the machine spindle - 100 N, 200 N and 300 N (± 5%);
- sliding speeds of 0.38 m/s, 0.53 m/s and 0.69 m/s, corresponding to the spindle speeds of the four-ball machine 1000 rpm, 1400 rpm and 1800 rpm (± 6 rpm), respectively.

3. RESULTS

3.1. Friction coefficient

Figure 2 presents the evolution in time of the friction coefficient (COF) and one may notice the differences of the lines. Even if the addition of nano hBN particles does not reduce COF, the evolution in time of this tribological parameter is done in a narrow range and it seems to be less sensitive to load as compared to tests done with the same sliding speed, but with the neat vegetal oil as lubricant.

The more evident variation of COF was obtained for the tests done at v=0.38 m/s. Having as reference the average value of COF during 1h test, for F=100 N, for the rapeseed oil, COF increases with 88%. But for the additivated lubricant, there was a small reduction for COF, meaning 9%, when the load increased from 100 N to 300 N.

For the rapeseed oil, tested at F=300 N, COF decreases with the increase in sliding speed, meaning that a higher speed is favorable to generate a full fluid film. But for the additivated rapeseed oil, even if the average of COF for F=300 N and v=0.69 m/s (the most severe test) is lower as compared to that of the neat oil, there are oscillations produced by the behavior of nanoparticles, maybe agglomerated, in contact.

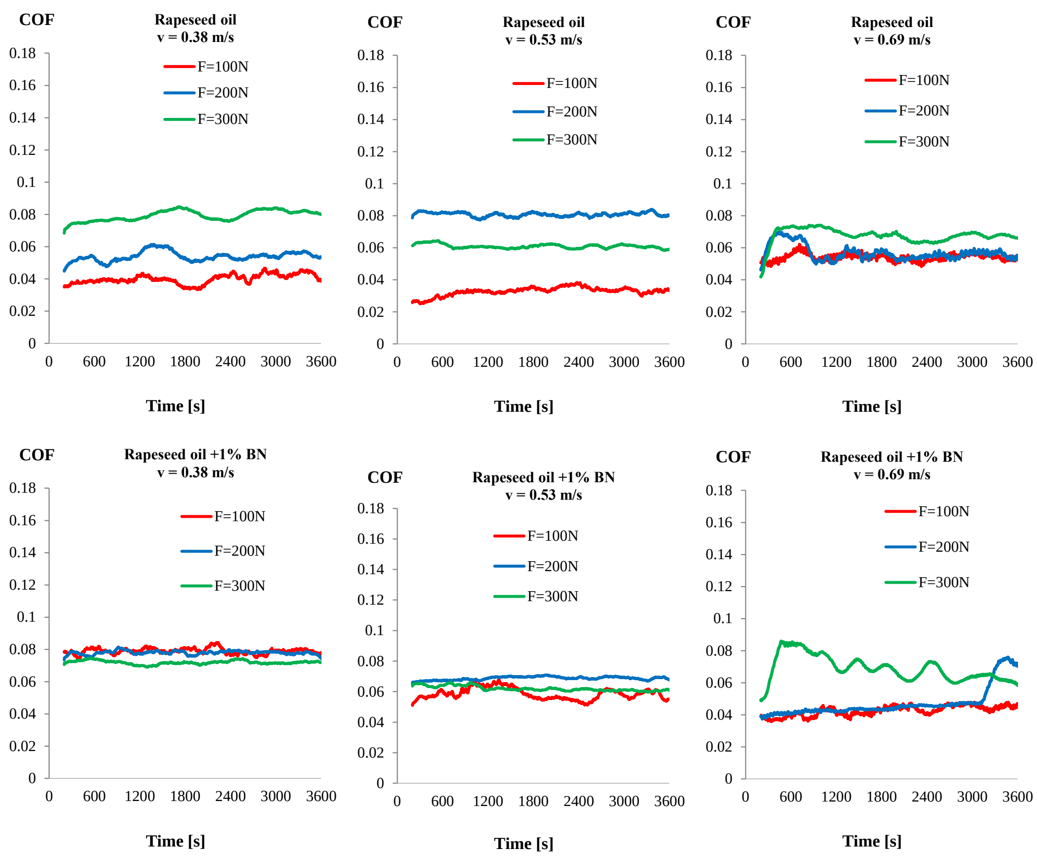

Figure 2. COF evolution in time

(2 sample per second and a moving average on 200 consecutive values)

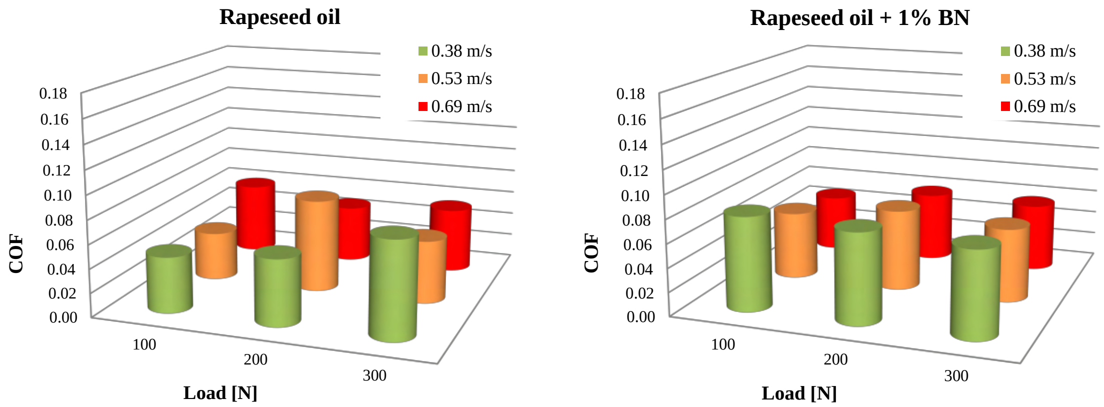

Figure 3. Average of COF for two values (two tests done under the same parameters)

Figure 3 presents the average value of COF as obtained from two tests, for both tested lubricants. It is obvious that the neat oil has lower values, especially for heavy regimes, but the additivated oil has this parameter less sensitive to sliding speed for F=300 N. This is recommended for machines that frequently change their working regime.

Lubrication may be theoretically done in three different regimes: boundary lubrication, mixed lubrication, and elastohydrodynamic lubrication. But the lines separating these regimes are very difficult to be drawn. Adding nanoparticles, generally increases the friction coefficient as average, but its evolution may have high or small oscillations.

3.2. Wear rate of the wear scar diameter

Measurement of wear trace diameters was performed with the optical microscope, in accordance with the procedure given in SR EN ISO 20623:2018 [13]. Three wear marks were obtained for each test, these being located on the three fixed balls. Two diameters, the first diameter measured along the sliding direction, the second diameter measured perpendicular to the first, were measured for each wear trace. With three traces of wear, six diameters were obtained and their mean value was calculated. This value represents the diameter of the wear scar, reported for each of the performed tests.

The lubricants with nano-BN are beneficial for tribosystem due to mending mechanism and the higher high thermal conductivity of the formulated fluid.

The graphs of the wear scar diameters (WSD) as a function of speed could not reflect in a relevant way the influence of testing regimes, because all tests has 1 h (with different sliding distances for each speed), and, thus, the authors studied the influence of additive concentration with the help of wear rate of the scar diameter, noted by w(WSD). The w(WSD) is calculated with the help of the following relationship:

$$\mathrm{w(WSD)} = \frac{WSD}{F \cdot L} \quad mm/(N \cdot mm) \ . \qquad (1)$$

where WSD is the average value of six measurements of the wear scar diameter, two on each fixed ball (one along the sliding direction and the other perpendicular to it), F is the load applied on the main shaft of the tribotester and L is the sliding distance. The product F×L is the mechanical work done by the tribotester. Thus, the wear rate of WSD reflects the modification of WSD for the unit of mechanical work.

Figure 4 shows images of the wear scars as obtained with the help of an optical microscope. One may notice that the contact surfaces as resulted after testing with the additivated oil is less damaged, this conclusion being more highlighted by comparing images for severe regime (v=0.69 m/s and F=300 N).

Figure 5 presents the wear rate of WSD, w(WSD). The values are lower for heavy regimes (F=200...300 N) for all sliding speeds, meaning the lubricant response is suitable for protecting the surfaces in contact. The additivated rapeseed oil have even lower values for the lower sliding speed (v=0.38 m/s).

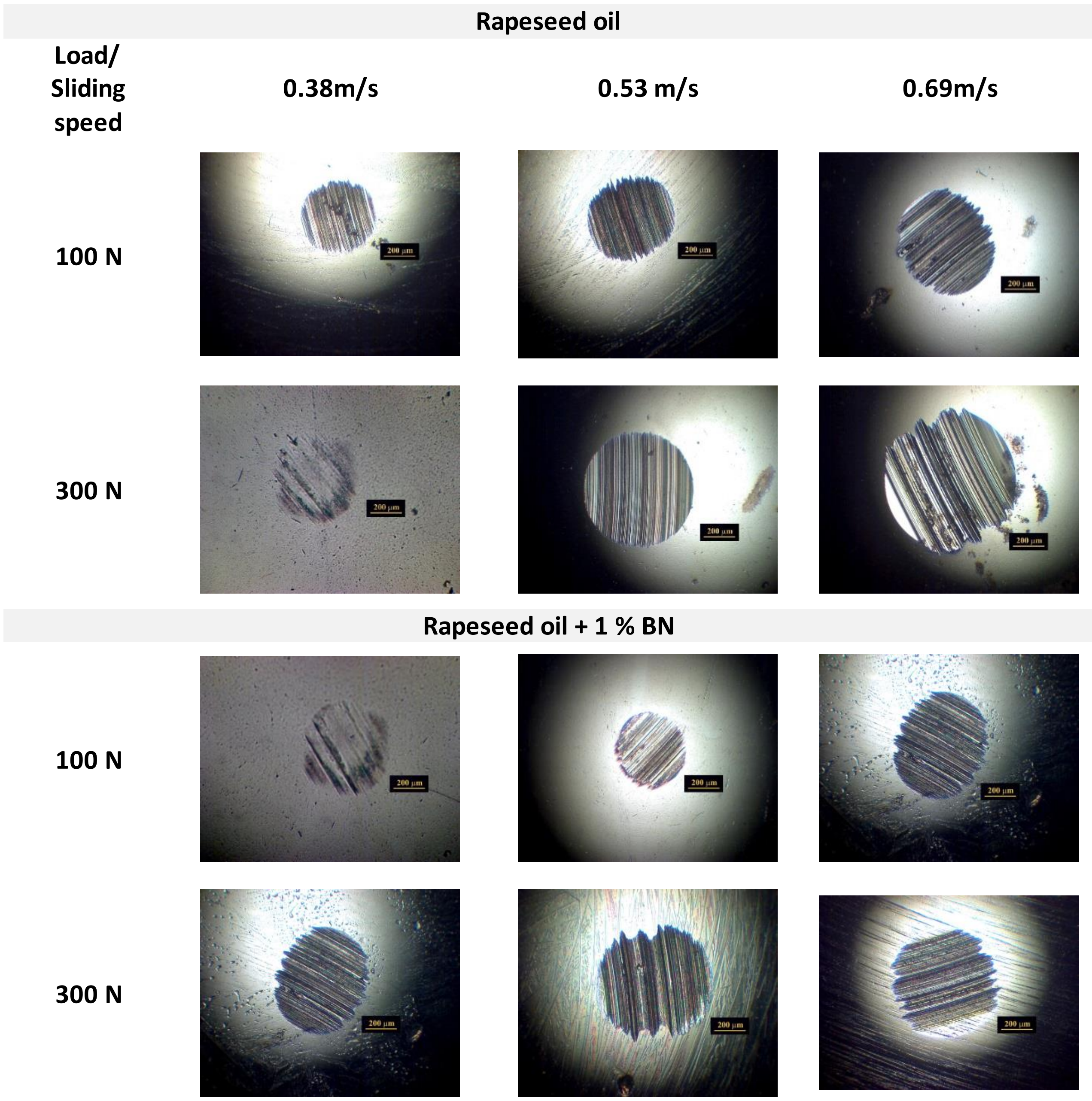

Figure 4. Typical wear scars for different regimes

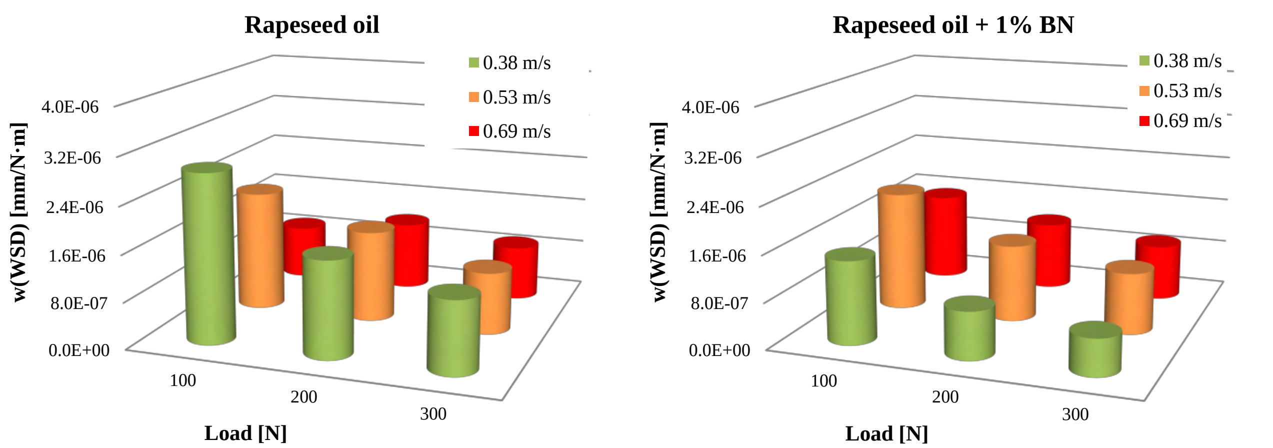

Figure 5. The wear rate of WSD for the base oil (rapeseed oil) and the new formulated lubricant with 1% BN in rapeseed oil

The reason of this better tribological behavior is that the nanoparticles act like rolling spacers between the solid macro bodies and prevent the wearing of them, even partially.

Table 3 presents the variation of w(WSD), in percentage, relative to the lowest load(100 N), for each sliding speed. Analysing the values in this table, one may notice that the new formulated lubricant has lower wear rate of WSD when the load increases, for each tested sliding speed. For the highest speed, the rapeseed oil has this wear parameter greater than that for mild regime (F=100 N).

Table 3. The variation of w(WSD), in %, relative to the lowest load (100 N)

Sliding speed	Variation of w(WSD), **%wt**			
	Rapeseed oil		rapeseed oil + 1% BN	
	200 N	300 N	200	300
0.38 m/s	-42%	-56%	-43%	-56%
0.53 m/s	-24%	-48%	-35%	-48%
0.69 m/s	28%	2%	-22%	-36%

3.3. Temperature in the oil bath

The evolution of oil bath temperature during a test of 1 h is given in Figure 6. The difference among final registration of temperature (at the end of the test) is small for low regimes (v=0.38...0.53 m/s) and its value is kept in the range 43...55°C, but for the highest speed (v=0.69 m/s), the temperature values are spread on a larger interval. For the most severe regime, the final recorded temperature for the rapeseed oil is about 70°C. The rapeseed oil additivated with BN has these temperatures a little bit higher, in the range of 50...60°C for v=0.38...0.53 m/s and for the highest speed the interval is larger (60...77 °C). The supplementary heat generation could be explained by the friction of intermediate particles of NB, rolling or being dragged in contact. But there is no significant modification in the temperature range when comparing the temperature evolution for both tested lubricant.

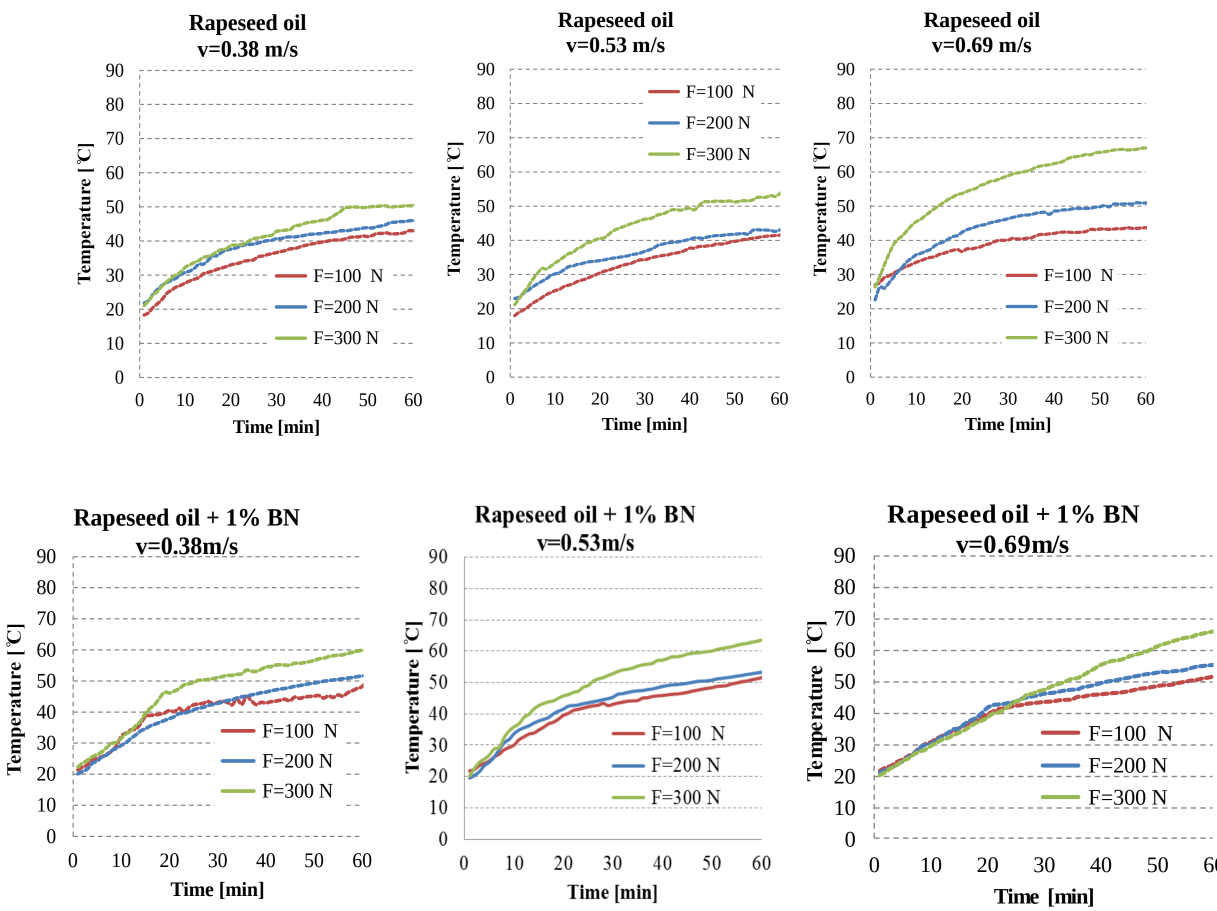

Figura 6. Temperature evolution in the oil bath

4. CONCLUSIONS

At least for the tested ranges of the parameters (v=0.38...0.69 m/s and F=100...300 N), the additivation of rapeseed oil with nanoparticles of BN improves the friction coefficient. But this additive was efficient for wear reduction, the authors pointed this out by comparing the values of the wear rate of wear scar diameter.

ACKNOWLEDGEMENT

This paper was supported by a grant of the Romanian Ministry of Research and Innovation, CCCDI-UEFISCDI, project no. PN-III-P1-1.2-PCCCDI-2017-0404/31PCCDI/2018, within PNCDI III and by Doctorale School for Mechanical and Industrial Engineering of "Dunarea de Jos" University of Galati.

REFERENCES

[1] S. Shahnazar, S. Bagheri, S. B. Abd Hamid: Enhancing lubricant properties by nanoparticle additives, International Journal of Hydrogen Energy, Vol. 41 pp. 3153-3170, 2016.

[2] Q. Wan, Y. Jin, P. Suna, Y. Ding: Tribological behaviour of a lubricant oil containing boron nitride nanoparticles, The 7th World Congress on Particle Technology (WCPT7), Procedia Engineering, Vol. 102, pp. 1038–1045, 2015.

[3] O.N. Celik, N. Ay, Y. Goncu: Effect of nano hexagonal boron nitride lubricant additives on the friction and wear properties of AISI 4140 steel, Particulate Science and Technology, Vol. 31, No. 5, pp.501-506, 2013.

[4] I.E. Uflyand, V.A. Zhinzhilo, V.E. Burlakova: Metal-containing nanomaterials as lubricant additives: State-of-the-art and future development, Friction, Vol. 7, No. 2, pp. 93–116, 2019.

[5] M.I.H.C., Abdullah, M.F.B. Abdollah, N. Tamaldin, H. Amiruddin, M.N.R. Nuri, C. Gachot, H. Kaleli: Effect of hexagonal boron nitride nanoparticles as an additive on the extreme pressure properties of engine oil. Industrial Lubrication and Tribology, Vol. 68, pp. 441–445, 2016.

[6] Y. Wang, Z. Wan, L. Lu, Z. Zhang, Y. Tang: Friction and wear mechanisms of castor oil with addition of hexagonal boron nitride nanoparticle, Tribology International, Vol. 124, pp. 10–22, 2018.

[7] N. Talib, E.A. Rahim: Performance of modified jatropha oil in combination with hexagonal boron nitride particles as a bio-based lubricant for green machining, Tribology International, Vol. 118, pp. 89–104, 2018.

[8] D.-H. Cho, J.-S. Kim, S.-H. Kwona, C. Lee, Y.-Z. Lee: Evaluation of hexagonal boron nitride nano-sheets as a lubricant additive in water, Wear, Vol. 302, pp. 981–986, 2013.

[9] Nanomaterials and related products, 2016, PlasmaChem, available at: http://www.plasmachem.com/download/PlasmaChem-General_Catalogue_Nanomaterials.pdf, accessed 20.02.2016

[10]S. Walker, M. Rahim: Boron nitride based lubricant additive, available at, https://patentimages.storage.googleapis.com/e7/46/65/637e7818688e92/US20070161518A1.pdf 2007, accessed: 23.04.2019

[11]R. Hutchinson, S. Reid: Lubriciant compositions, EP 1 808 478 B1, No. 07250119.0, available at: https://patentimages.storage.googleapis.com/f7/88/73/7df83f0d24447f/EP1808478B1.pdf, accessed: 23.04.2019, 2007.

[12]G.C. Cristea: *Tribological characterization of soybean oil additivated with nano materials based on carbon (black carbon, graphite and graphene*, PhD thesis, "Dunarea de Jos" University of Galati, Romania, 2017.

[13] SR EN ISO 20623 *Petroleum and related products. Determination of the extreme-pressure and anti-wear properties of lubricants. Four-ball method (European conditions)*, 2018.

Tribometry

Serbian Tribology Society

SERBIATRIB '19

16th International Conference on Tribology

Faculty of Engineering University of Kragujevac

Kragujevac, Serbia, 15 – 17 May 2019

WEAR TESTING MACHINE BY LASER BEAM ABLATION PATENT NO 24013 EGYPTIAN PATENT OFFICE

Hebata lrahman[1]

[1] Dr.eng Consultant in material science, Egypt

Hebatalrahman11@yahoo.com, Hebatalrahman11@gmail.com

Abstract: *Wear testing machine by laser ablation has been considered as a new method of wear testing which overcome the problems of old machines and systems. In this case, wear rate has occurred due to ablation by laser beam and test sample transformed from solid state to gas state directly (sublimation) and avoid relative movement and loss of material between sample and disk or plate. The different operation conditions such as temperature, chemicals, environmental conditions and different types of stresses has been considered. The new machine consists of two main parts optical and mechanical parts. The optical parts which include ultraviolet laser source, optical filter, lenses to concentrate the beam and manhole of laser beam to the sample tested in the control room. The mechanical parts includes The insulated chamber , dead weight , variable speed motor, sample holder, temperature and pressure sensor and ph meter. Mechanism of operation depend mainly on Ablation process which is removal of material from the surface of an tested object by vaporization .Ultraviolet laser beam is used as source of energy required for ablation process to avoid thermal effects. The new technique is suitable for all kinds of materials such as metals, alloys polymers, ceramics and composites in any shapes and sizes. The main factors affecting the new techniques are divided into factors related to the laser beam characteristics and factors related to material properties, the material properties include the surface roughness, thermal conductivity, specific heat ,density and mainly latent heat of sublimation.*

Keywords: *wear, ablation, sublimation, ultraviolet, laser.*

1. INTRODUCTION

The Pin on Disk Tribometer incorporates many features such as direct weighting. One important feature of all the Tribometers is that the wear automatically stops when a specified coefficient of friction reaches a threshold value, or when a desired number of rotations are completed [1]. All tribometers can be equipped with a depth measuring sensor for real-time display of depth information which is important in studying the time dependant wear properties[2],[3].

It is designed as a frictionless force transducer. The deflection of the highly stiff elastic arm, without parasitic friction, in the friction track. The wear and friction coefficient is determined during the test by measuring the deflection of the elastic arm and weight loss.

The Linear Tribometer Including calculation of a friction coefficient for both forward and backward movements of the stroke, generating data on Hertzian pressure via its software package, and static partner and sample wear rates. The reciprocating technique is also very useful for studying the variation over time of the static coefficient of friction - as opposed to the kinetic coefficient measured with the Pin-on-Disk geometry. Most contact geometries can be reproduced including Pin-on-Plate, Ball-on-Plate and Flat-on-Plate (others on request) [4].

A special heating module using a differential arm which compensates for changes in the temperature of the load arm can be attached to the standard tribometer allowing lubricated testing up to 150°C, The heating module uses a controlled temperature liquid, regulated to an accuracy of 0.1°C to heat the sample [5],[6].

Features of the Pin-on-Disk Tribometer

- Direct dead weight (weight directly over the pin) gives much higher stability [7].
- Precisely calibrated friction and wear measurements [8].
- Stable contact point with no parasitic friction.
- Pin, Ball and Plate on Plate testing.
- Automatic switch off at threshold coefficient of friction or total number of turns
- Plexiglas enclosure for testing in liquids, controlled humidity or inert gases[9].
- Testing compatible with ASTM G99 & DIN 50324 [10] :[16].
- Continuous wear depth recording (optional) [17].
- High Vacuum Testing (optional) [18].

Disadvantages of conventional wear techniques

1. The plate or disc must be changed every experiment, it is considered as expensive and relative technique [19].
2. Pin on disk and pin on plate are very complicated techniques [20].
3. The conventional method of wear detection such as pin-on-disk or pin on plate tribometry have only standards for specific applications [21].
4. The maximum load is 46N at frequencies up to 8Hz (25Hz optional) with a stroke range up to 60mm and a sliding radius of up to 35mm [22].

Liquid Heating Option up to 150°C can be installed on existing Pin-on-Disk and Linear Tribometers which is a very limited temperature range [23],[24].

2. EXPERIMENTAL WORK

An invention is developed to measure wear by laser ablation techniques instead of conventional machines (Pin on disc) or (pin on plate). The main component of the new machine is shown in fig.1. Wear coefficients for the tested material are calculated from the volume of material lost during the ablation process. This simple method facilitates the study of friction and wear behavior of almost every solid state material combination with or without lubricant. The technique can be used for liquid substances with special design of sample holder. Furthermore, the control of the environmental parameters, temperature, humidity and lubrication in the insulated test chamber allow a close reproduction to the real life conditions of practical wear situations. While the control test parameters such as laser power , fluence, number of pulses , repetition rate, speed of sample rotation, applied load and test time can introduce exact value of wear coefficient [22]. Fig.2 shows the steps and the main factors affecting the new wear measurement system by laser ablation.

The mathematical relation for The ablation rate (nm/pulse)

$$= \text{ablation rate} = \ ^{-1} lin(\ _{inc} / \ _{T}) \qquad (1)$$

$$_{T} = E / \ (1-R) \qquad (2)$$

Where

E - (Threshold) energy density,

- ablation rate (nm/pulse),

R - reflectivity,

- optical penetration depth,

$_{inc}$ - incident fluence,

$_{T}$ - threshold fluence.

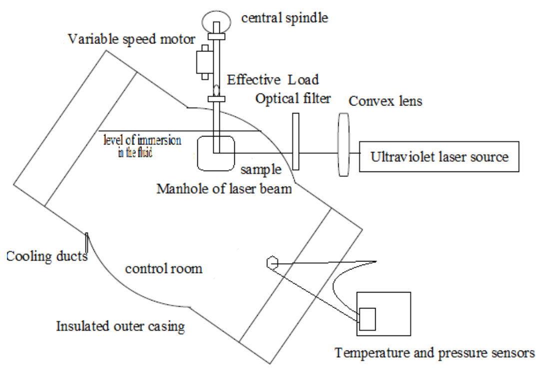

Figure 1. Wear testing machine by laser ablation

The paragraph indentation is to be 5 mm.

Leave one clear line before and after a main or secondary heading. Avoid leaving a heading at the bottom of a column, with the subsequent text starting at the top of the next page/column.

2.1 The main components of the wear testing machine by laser ablation

A) Optical parts

Laser source is the main utensil in the new technique, high power ultraviolet laser concentrated in a small area, using plan - polarized source incident on the surface at Brewster s angle to increase the amount of absorbed energy and achieve the ablation condition to change the state of the material from solid to vapor directly (sublimation), The main four parts in the optical system are:

1. Ultraviolet laser source,
2. Optical filter is used to eliminate defects and chromatic aberration,
3. Optical elements collected and focused laser beam, and
4. Convex lens (optical parts used in the focus of the laser beam).

B) Sample holding and movement

The new technique reproduces the reciprocating motion typical of many real world in situ mechanisms and also simulate the amount and type of applied pressure in static and dynamic load, sample holder and movement system consists of four parts:

1. The central spindle,
2. Variable speed motor to rotate the test sample,
3. Mask of the samples dipped in the control room, and
4. Effective Load.

The central spindle is loaded onto the test sample with a precisely known weight. The pin is mounted on a stiff lever, insures a nearly fixed contact point and thus a stable position in front of the laser beam. Variable speed motor is used to rotate the test sample with the same speed similar to the in situ operation conditions.

C) Control unit

The new wear measurement technique with laser ablation is supplied with a insulated chamber enclosure so that controlled atmospheres such as varying humidity or media with specific composition and PH can be used. Specialized control of the test chamber have been developed for high & low temperature operations, reciprocating motion and high and low vacuum testing are also available.

- Insulated outer casing of the control unit.
- The level of immersion in the fluid sample tested.
- Temperature and pressure sensors related to the control unit.
- Manhole of laser beam to the sample tested in the control room.

D) Environmental condition control

The new technique can be equipped with a heating and cooling utensils for testing under a wide variety of temperatures and environmental conditions so the system include:

1. Pipes to push acidic, basic or liquid to submerge the samples in operatin conditions,
2. Level of operating conditions,
3. Heaters to control the test conditions, and
4. Cooling ducts.

A convenient intermediate temperature solution for tribology work can be used in the new technique, The temperature range between the standard room temperature and the high temperature. With this option, the in-situ conditions for a range of deposition technologies, such as ion beam sputtering PVD and CVD, which use quartz lamp heating to attain similar temperatures, can be reproduced. This range of temperature is also ideal in the study of biomaterials where body fluid temperatures range +/-37° C. The new technique is suitable for high temperature services and carcinogenic applications, it is also ideal for space, aircraft and almost all engineering and building applications.

2.2 The factors affecting the process

When the laser strike the metal surface during wear test by laser ablation, the energy is absorbed and distributed along the tested sample. The variation of temperature with distance for different metals such as Iron, Tin , cupper , Aluminum, zinc and lead at the same laser source, clarify the rate of various properties including the specific heat , the latent heat of sublimation (evaporation) , and the variation of various parameters such as density, thermal conductivity, thermal diffusivity and reflectivity.

Fig.3 shows the temperature variation with depth at the beginning of ablation process at the surface for different metals with different thermal characteristics at the same laser irradiation conditions same laser power, fluence, repetition rate, number of pulse and duration time.

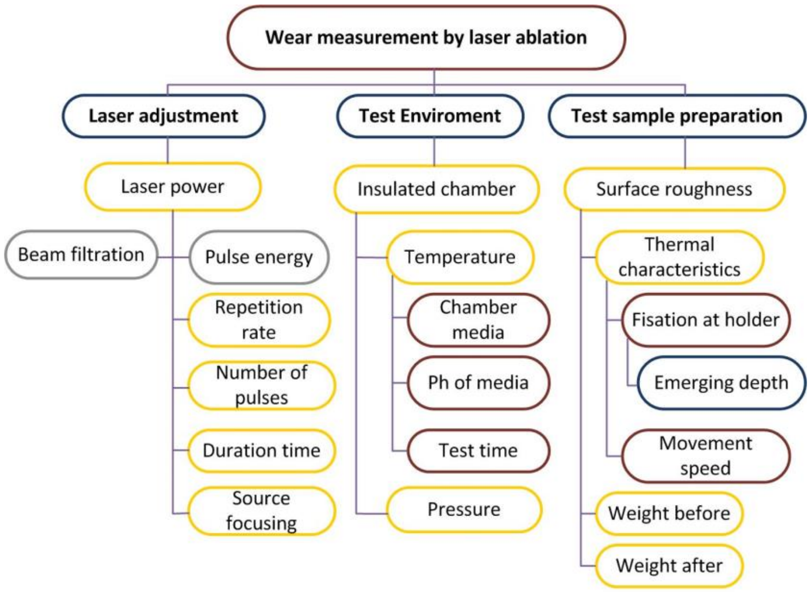

Figure 2. Steps of wear measurements by laser ablation technique

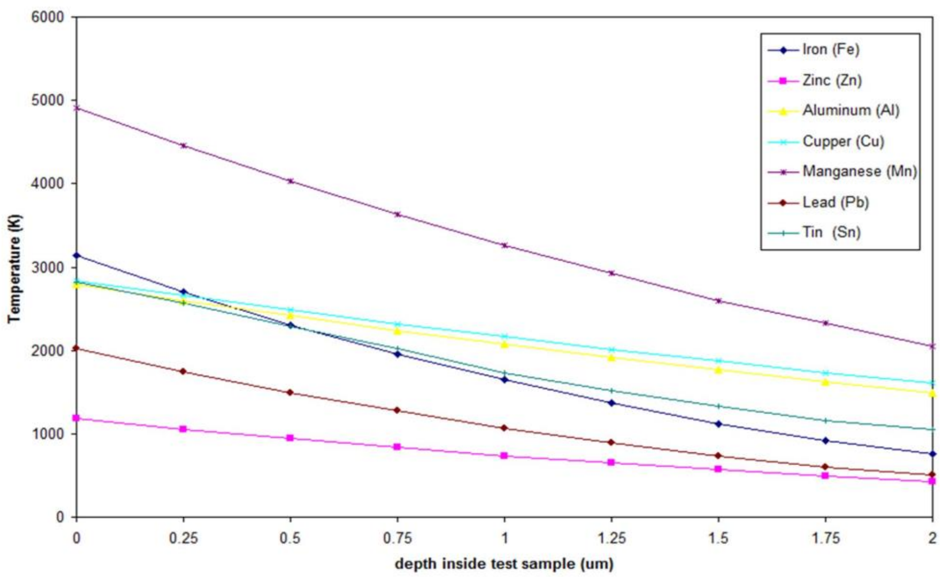

Figure 3. The temperature variation with depth at the begining of ablation process at the surface

The main parameters in the ablation process is the variation of velocity , ablation depth and time at the solid -vapor interface, which is also affected by the thermal characteristics of the tested materials at the same laser irradiation conditions. Table.1 shows the ablation characteristics during wear test for some pure metals, The variation in the ablation parameters is shown in both fig 4 and fig 5 respectively which show the variation in ablation depth and ablation velocity for different metals have different thermal characteristics.

Table 1. The ablation characteristics during wear test for some pure metals

Metal	Evaportion depth,μm	Time, Sec	Velocity, m/sec
Iron (Fe)	38.8	$9.42{\cdot}10^{-4}$	412.47
Zinc(Zn)	70.3	$41.6{\cdot}10^{-4}$	169.03
Aluminium (Al)	30.8	$4.2{\cdot}10^{-4}$	681.24
Cupper(Cu)	27.16	$2.5{\cdot}10^{-4}$	1068.79
Manganese(Mn)	25.5	$9.4{\cdot}10^{-4}$	270.9
Lead(Pb)	47.2	$17.1{\cdot}10^{-4}$	275.56
Tin (Sn)	10.2	$0.72{\cdot}10^{-4}$	1418.5

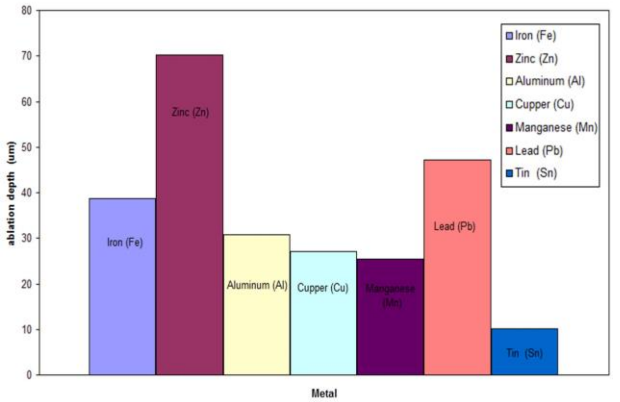

Figure 4. The abltaion depth of different metals exposed to the same laser source

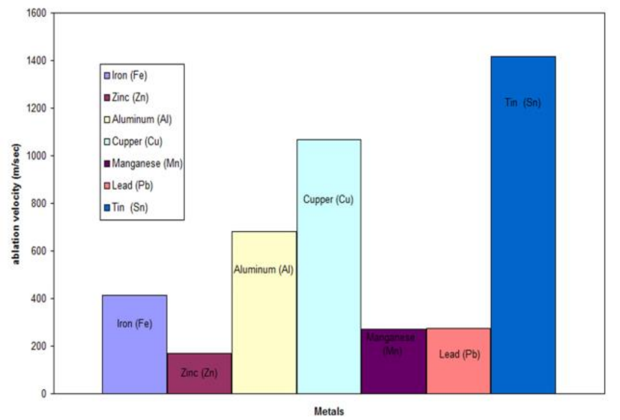

Figure 5. The abltaion velocity for different metals during wear measurement

The increase in ablation depth is related to the decrease in the ablation velocity at the solid -vapor interface and vice verse, so when comparing the wear rate of different materials the new technique is seem to be ideal for this type of comparison, which can not achieved in the conventional techniques.

2.3 Mechanism of operation

During wear test by the new method ablation is occurred from the surface of test sample. Ablation is removal of material from the surface of an object by vaporization , process begin when the amount of laser energy absorbed is more than the enthalpy of sublimation, or heat of sublimation, which is the heat required to change one mole of a substance from solid state to gaseous state at a given combination of temperature and pressure, usually standard temperature and pressure (STP). Fig.6 shows the mechanism of wear measurement by laser ablation. The insulated chamber which include the test sample may be considered as a closed system of fixed composition in solid state undergoing a temperature change from room temperature or preheat temperature to the sublimation (evaporation) temperature at constant pressure

$$H = H(T_{evap},p) - H(T_o,p)= dh= Cp\ dT= Qp \qquad (3)$$

Where Qp is The amount of heat required to raise the temperature of the system from room temperature T_o to the evaporation temperature T_{evap} , fig 7 shows the temperature distribution inside the tested sample just before the ablation process begin. after that the amount of laser energy equal to the latent heat of sublimation evaporation is also absorbed, then the ablation begin on the sample surface. The loss of energy due to scattering and reflection from the sample surfaces must be included in the total energy absorbed by the sample for ablation process. After removal of material from the surface the losses due th reflection is dropped down and scattering of energy in the ablated hole work as energy trap increase the amount of energy absorbed so the ablation rate increase. During the ablation volatile gaseous fragments are found and help to move larger molecular fragments away from the surface. The process begin with laser absorption up on the sample surface, surface reflectivity has pronounced effect up on the process rate, ablation takes place after the laser pulse is over so that shielding of pulse energy by the generated plume does, the absorbed energy per volume must exceed (Threshold) density E_T, re-deposition does not occur significantly.

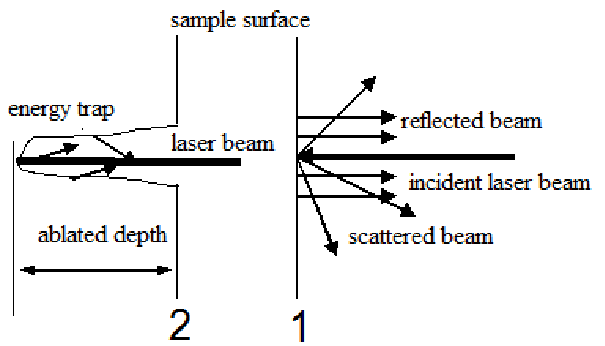

Figure 6. The mechanism of wear measurement by laser ablation

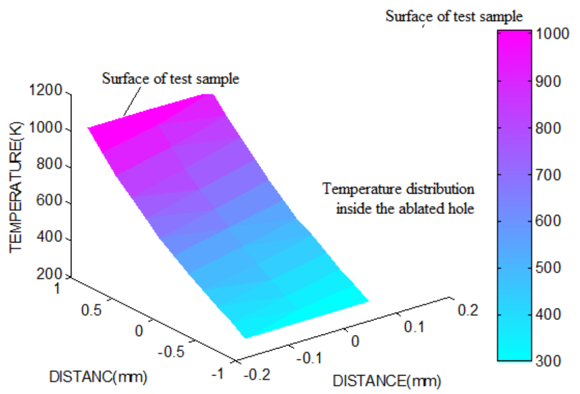

Figure 7. The temperature distribution in the ablated hole during wear test by laser

The method of exploitation

1. Can be used to measure the wear rate regardless of the thickness of the test sample and suitable for thin films.
2. Can be used to measure the absolute wear rate in metals and various materials while the old methods measure relative wear rate between test sample and disc or plate.
3. The laser beam's ability to pass through various liquids makes the machine measure wear rates of materials submerged in liquids or media in different conditions similar to operating conditions.
4. The machine can be used as an effective way to compare the resistance of materials varying in hardness and durability.
5. The machine can be used to measure the new materials with unknown hardness and composition.
6. Suitable for high temperature services materials and low temperature services materials which may be deformed in normal methods laser wear testing machine become the perfect.
7. The new method is suitable for treated materials regardless of the method of treatment (non-known hardness surfaces with high resistance).

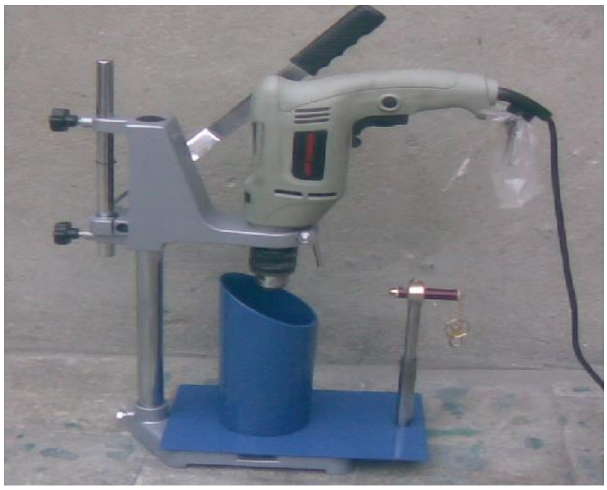

Figure 8. The prototype of the wear testing machine by laser ablation

8. The machine is used to test strong materials of great firmness and resistance, which cause high wear rates in the disk when tested with conventional methods. Fig.8 shows the prototype of the wear testing machine by laser ablation
9. Can be used in studying the time dependant wear properties.

Advantages of the invention

1. Replace the disk, or the plate at a regular machines with the laser beam.

2. New test machine is suitable for all types of materials and does not depend on the form or the shape of the sample
3. The laser beam has a uniform intensity and direction throughout the duration of the experiment, so the results are accurate and absolute values
4. Laser beam can be directed by the optical parts in the horizontal, vertical or diagonal directions, so any part of the test sample can be measured.
5. Thin film, electronic materials and other materials that are difficult to test by standard methods can be tested easily after the selection of the suitable laser wavelength and intensity.
6. The test condition can be adjusted at any temperature and there is no limitation related to test conditions.
7. Comparing the wear rate of different materials the new technique is seem to be ideal

3. CONCLUSION

1. The new wear testing machine depends on the interaction of lasers with matter.

2. The energy required for measuring wear rate by the new technique must be more than the latent heat of sublimation added to the dissipated energy due to reflection and scattering added to the energy required to heat the sample to evaporation temperature.

3. The rate of the process (time required for testing wear by new technique) is function of testing material characteristics such as diffusivity, specific heat , thermal conductivity and density.

4. The surface of the testing sample must be flat and relatively rough to avoid dispersion of energy due to reflectivity.

5. Cold laser beam in the range of ultraviolet lasers are recommended in the new technique to avoid thermal effects which has side effects on the quality of the process.

RECOMMENDATION

The new wear measurements technique must be included as the standard test method for measuring wear coefficient in the ASTM, DIN, BS, Egyptian standard and all international standards.

REFERENCES

[1] S.C. Lim: *Recent Development in Wear Mechanism Maps*, Technical report (University of Cambridge. Department of Engineering), 1986 reprinted in 2011.

[2] H.C. Meng, K.C. Ludema: Wear models and predictive equations: Their form and content, Wear, Vol. 181-183, pp. 443-457, 1995.

[3] R. Bosman, D.J. Schipper: Mild wear maps for boundary lubricated contacts, Wear, Vol 280, pp. 54-64, 2012.

[4] F.P. Bowden, D. Tabor: *Friction and Lubrication of Solids*, Clarendon Press, Oxford, 1950.

[5] I. Kleis, P. Kulu: *Solid Particle Erosion*, Springer-Verlag, London, 2008.

[6] K.-H. Zum Gahr: *Microstructure and wear of materials*, Elsevier, Amsterdam, 1987.

[7] J.R. Jones: *Lubrication, Friction, and Wear*, NASA-SP-8063, 1971.

[8] R.C. Hibbeler: *Mechanics of Materials*, Pearson prentice Hall, 2005.

[9] R. A. Higgins: *Materials for Engineering and Technician*, Elsevier Ltd, 2006.

[10] ASTM G99-17 *Standard Test Method for Wear Testing with a Pin-on-Disk Apparatus*, 2000.

[11] ASTM G76-13 *Standard Test Method for Conducting Erosion Tests by Solid Particle Impingement Using Gas Jets*, 2013.

[12] ASTM G77 - 17 *Standard Test Method for Ranking Resistance of Materials to Sliding Wear Using Block-on-Ring Wear Test*, 2017.

[13] *ASTM G176-03 Standard Test Method for Ranking Resistance of Plastics to Sliding Wear Using Block-on-Ring Wear Test - Cumulative Wear Method*, 2009.

[14] D. E. Ackerman: Some important variables encountered in wear tests on cast iron, ASTM international, 1937.

[15] DIN 50324 (1992-07*) Tribology; Testing of Friction and Wear Model Test for Sliding Friction of Solids (ball On Disc System)*, 2010.

[16] N. Axén, S. Hogmark, S. Jacobson: *Friction and Wear Measurement Techniques*, Modern Tribology Handbook, CRC Press LLC, 2001.

[17] https://en.wikipedia.org/wiki/Wear_and_tear

[18] R.N. Rao, S. Das: Effect of sliding distance on the wear and friction behavior of as cast and heat-treated Al–SiCp composites, Materials & Design, Vol. 32, No. 5, pp. 3051-3058, 2011.

[19] R.N. Rao, S.Das: Effect of SiC content and sliding speed on the wear behaviour of aluminium matrix composites, Materials & Design, Vol. 32, No. 2, pp. 1066-1071, 2011.

[20] N.Ch. Kaushik, R.N. Rao: The effect of wear parameters and heat treatment on two body abrasive wear of Al–SiC–Gr hybrid composites, Tribology International, Vol. 96, pp. 184-190, 2016.

[21] L.F. Tóth, J. Sukumaran, R. Nagarajan, G. Szebényi, W.J. Thanggiah, P. De Baets: Friction and Wear Properties of Jute/polyester Composite Systems, in 2nd International Conference on Polymer Tribology, 15-16.09.2016, Ljubljana, Slovenia, 2016.

[22] P. J. Blau: Sliding and adhesive wear, in: G.E. Totten (Ed) Friction, Lubrication, and Wear Technology, ASM International, pp. 313-322, 2017.

[23] BS ISO 18192-3 *Implants For Surgery - Wear Of Total Intervertebral Spinal Disc Prostheses - Part 3: Impingement-Wear Testing And Corresponding Environmental Conditions For Test Of Lumbar Prostheses Under Adverse Kinematic Conditions, British Standards Institution*, 2017.

[24] BS ISO 20808 *Fine Ceramics (Advanced Ceramics, Advanced Technical Ceramics) - Determination Of Friction And Wear Characteristics Of Monolithic Ceramics By Ball-On-Disc Method, British Standards Institution*, 2016.

Serbian Tribology Society

SERBIATRIB '19

16th International Conference on Tribology

Faculty of Engineering University of Kragujevac

Kragujevac, Serbia, 15 – 17 May 2019

INFLUENTIAL PARAMETERS OF FOOTWEAR SLIP RESISTANCE

Dušan STAMENKOVIĆ[1]*, Milan BANIĆ[2], Milan NIKOLIĆ[3], Aleksandar MILTENOVIĆ[4], Petar ĐEKIĆ[5]

[1]Faculty of Mechanical Engineering Niš, Serbia
[2]Faculty of Mechanical Engineering Niš, Serbia
[3]College of Applied Technical Sciences Niš, Serbia
[4]Faculty of Mechanical Engineering Niš, Serbia
[5]College of Applied Technical Sciences Niš, Serbia
*Corresponding author: stamendu@gmail.com

Abstract: *Slip resistance of footwear sole and floor coverings is the characteristic which seriously depend on safety of human movement. There are some adopted standards which prescribe methods of slip resistance testing, but they are often criticized and revised. Tribological parameters are very important in human walking, running, jumping, etc. Friction mechanism of viscoelastic materials on hard bases is described in this paper. Also, influence of some parameters, like rubber hardness, rubber hysteresis, contact condition (dry and wet) and sliding speed are analysed according the testing results obtained in performed experimental research.*

Keywords: *Slip resistance, friction, footwear, viscoelastic materials, hysteresis.*

1. INTRODUCTION

Friction between the footwear sole and floor coverings is necessary for human walking. Movement of the human foot on the floor is possible by the presence of the friction force. Skidding and injures are happening in the cases of a lack of frictional force. There are many researches dealing with the tribological aspects of human walking which mostly refer to the footwear and floor slip resistance.

Authors in the paper [1] point out that categorization of slip resistance for sliding of footwear on floor should base on knowledge of mechanics and mechanism of friction. The fundamental characteristic of slip resistance is relativity ie. accidental. There are cases where one flooring material could be more slip resistant than another under one set of conditions, but less slip resistant under another ones. Authors present the frictional model based on tribological system of the sliding interface between a shoe heel and floor surface.

Visco-elasticity and rubber state are described in [2]. Visco-elastic characteristics of polymers are very important in sliding of this type of material on rough hard surface why energy hysteresis exists.

Author in his extensive research [3] compares the mechanics in metallic friction and mechanics in rubber friction. A unified theory of rubber friction is presented in this work.

Author in his dissertation [4] makes a statement that four different mechanisms or physical principles at least exist in friction of elastic solids on hard and rough surfaces.

Author in his papers [5, 6] presents research of behaviour of the rubber sliding on the rough substrate. He describes how surface asperities of substrate exert oscillating forces on the rubber surface and according that energy dissipation which comes from internal friction in rubber.

Test methods for measuring and evaluating the slip resistance of footwear and flooring coverings, according the adopted standards are described and analysed in the paper [7]. One of the findings of this research is that the sole material of footwear is a main factor for safe walking in different cases like in leisure, travel or work.

Standards for foot protection are often reviewed according the current state of the art technology. The main changes are expected for the test methods and requirement of slip resistance [8]. In this article is indicated that slip should be given a high priority.

Investigation in area of the tribology in human walking that has been performed last five years at University of Niš [10, 11], treats tribology in human walking. Research of influential parameters of footwear slip resistance and analysis of friction mechanisms are presented in this paper. Experimental results refer that slip resistance of concrete footwear and floor is significantly accidental, but it is possible to affect on slip resistance using certain sole material for certain floor material and adjusting the movement according the currently environment conditions.

2. FRICTION MECHANISM OF VISCOELASTIC MATERIALS

Main goal of experimental researches in this area [2, 3, 4, 5, 6, 7, 10, 11] is determination of influential parameters of slip resistance and possibility of managing of frictional conditions in different circumstances. It is very important to introduce the friction mechanisms of viscoelastic materials.

The differences between the friction characteristics of metal and rubber are due to differences in the mechanism of frictional force creation. This mechanism is different because of differences in physical and chemical properties between their materials. In the friction of metal surfaces, most of the roughness peaks in the contact of the two surfaces are in the range of plastic stresses, and it can be said that asperities of contact surfaces are connected by "cold welding". Plastic deformation occurs in the regions of real contact and friction junctions are formed. Surrounding regions are deformed elastically. Tabor and Bowden determined: “Friction is the force required to shear intermetallic junctions plus the force required to plow the surface of the softer metal by asperities on the harder surface” [9].

Accordingly, the total friction force can be expressed as a sum of molecular (adhesion) and mechanical (deformation) components:

$$F_t \quad F_{tmol} \quad F_{tmeh} \quad F_a \quad F_d \tag{1}$$

Rubbers or elastomers consist of long linear molecules that are twisted and knit together forming an amorphous solid structure. Viscoelastic bodies, such as rubber, generate friction in three main ways: adhesion, deformation and wear.

According these three mechanisms of friction generating, total friction force can be expressed:

$$F_t = F_a + F_d + F_w \tag{2}$$

Where: F_t – total friction force, F_a – friction force from adhesion, F_d – friction force from deformation and F_w – friction force from wear.

Friction force from deformation is very different in case of solid bodies and in case of viscoelastic bodies.

The appearance of adhesion allows the body surface to „be glued” to other materials, i.e. to join. Adhesion is the result of molecular bonds between the two surfaces. The true area of the contact depends on the contact bodies shapes, the surface roughness, the material properties and the contact pressure. The larger real contact surface means greater adhesion between the surfaces and higher friction force. It is believed that this mechanism is important for sliding rubber on clean and relatively smooth surfaces, e.g. on glass.

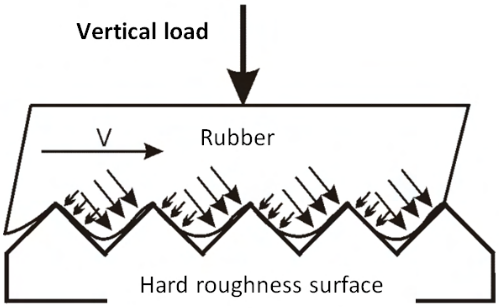

Figure 1. Contact between rubber and hard roughness surface

When rubber gets in contact with the rough surface of a rigid body (Fig. 1), the mechanism of the friction force generations due to deformation is dominant. The sliding of the rubber block on a rough hard surface causes rubber deformations due to the surface asperities. The load of the rubber causes the asperities to enter the rubber and rubber to wrap the asperities (Figure 1). The energy required for the asperities of the rubber is due to the difference in pressure between the asperities, due to the difference in pressure ahead and behind the asperities.

The friction force from the deformation represents the greatest part of the friction that occurs between the rubber and the wet surface, because the wet surface disables contact of the rubber and the surface, preventing the formation of adhesive force.

Viscoelasticity is the characteristic of rubber and some similar materials that when loaded and after unload, part of the energy is absorbed, i.e. hysteresis losses occur. Rubber with a small hysteresis (loss of energy) rapidly returns to its original position, while rubber with high hysteresis slowly returns to its initial state after deformation.

During the translational movement of the rubber on a hard rough surface, the surface asperities will cause pulsating rubber deformations, leading to viscoelastic dissipation of energy in the greater area of the rubber, which is a significant part of the friction. This energy dissipation mechanism is often called viscoelastic friction or a hysteresis share of friction.

Persson studied rubber friction for a rubber block that slides on a hard and rough surface with roughness on a number of different longitudinal wavelengths [4]. According to this study, the dissipation of energy from viscoelastic deformation of the rubber caused by surface roughness of the substrate requires that all the wavelengths scale of the roughness in the analysis be included because they can be equally importance. For example, the short wave wavelength component with wavelength λ_1 and amplitude h_1 can give the same contribution as a long wavelength component with λ_0 and h_0 if the ratio is $h_1 / \lambda_1 = h_0 / \lambda_0$.

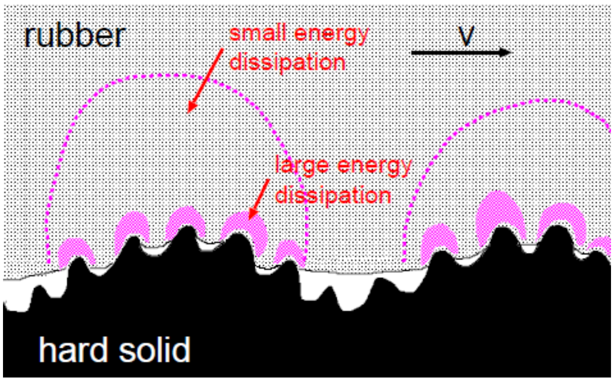

Figure 2. Viscoelastic deformation of the rubber due to surface roughness of the substrate on two different longitudinal wavelengths [4]

The dissipated (lost) energy per unit of rubber volume, as shown in Figure 2, is the highest in areas of contact with small asperities.

In addition to adhesion and deformation shares of friction, rubber produces cohesion-loss friction ie. wear friction. During the sliding, rubber can wear, and on that occasion small particles of the rubber are formed by the formation (spreading) of the cracks. As deformation forces and slip speed increase, local stress exceeds the tensile strength of the rubber, especially around the sharp aspirities. Large local stress can deform the inner structure of the rubber and overcome the elasticity limit. When the chains of polymer and transverse bonds are strained to the stress of breaking point, the rubber can no longer be recovered completely and this causes rupture. Breaking (rupturing) absorbs energy, causing additional friction force in contact.

3. SLIP RESISTANCE OF FOOTWEAR

Footwear producers have complex task to make comfortable and long lasting shoes. There are numerous types of footwear which are used in different conditions and different requirements. There are specific requirements for sports footwear, due to sports disciplines and the different ground and floor surfaces. Safety footwear (personal protective equipment) is special and their production is performed by specialized companies. Footwear outsole has a decisive influence on the slip resistance of footwear and is made of different types of viscoelastic materials like rubber, plastics, leather, etc. The surface of the soles is most often made with different relief structures, which have the function of preventing sliding (Fig. 3).

Figure 3. Different types of footwear outsole

Contact pressure depends on the person's weight and surface texture and shoe soles, and the relief (texture) of substrate. Velocity of sliding corresponding to human stroke has a great range, from slow walking to running.

Based on previous experience in friction research [10, 11], in experimental determination of friction coefficient it is significant to provide the following:

- Experimental samples should be made of real shoes sole/floor materials with determined mechanical properties,
- Surface structure (macro and micro structure, roughness, etc.),
- Contact pressure,
- Sliding velocity,
- Contact condition (temperature of contact bodies, lubricant, contaminants, etc.),
- Environment (temperature, humidity, etc.).

Determination of floor and footwear slip resistance is often conducted by measuring the coefficient of friction. Kinetic coefficient of friction is the most often determined, but static coefficient of friction is very important as well. Coefficient of friction can be determined by measuring of pulling force, friction angle (Ramp test) or energy loss (Pendulum test).

Different countries in Europe and the world have adopted different methods of testing and evaluation of slip resistance. Since these methods are based on different principles and are used in different conditions, there is no direct and precise correlation between them. No one of these methods is ideal and has certain advantages, but also certain disadvantages.

4. EXPERIMENTAL RESEARCH

Pulling force measurement, usually known as tribometric test method, is based on the measurement of the friction force (Figure 4 a). The body equipped with sliders is pulled at constant speed over the floor surface, at a certain length. Such a device was used in the research at the Faculty of Mechanical Engineering of the University of Niš (Figure 4b).

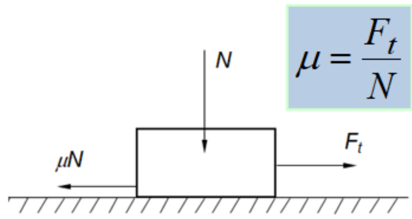

a)

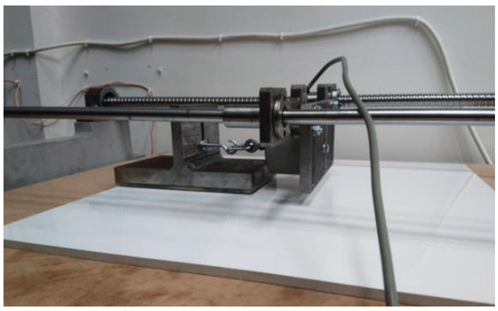

b)

Figure 4. Pulling force measurement method (a) and measuring equipment (b)

Applied measuring method is based on settings in standards EN 13893 and DIN 51131. The measurement was carried out on dry and wet surfaces. The test facility is equipped with sliders which are pulled parallel to the surface of the floor covering.

Three sliders with dimensions 10x40 mm are placed on the underside of the load (Fig. 5). Materials of sliders were rubber for shoe sole 80 Sh hardness, tensile strength 5.6 MPa and Yerzley hysteresis of 46.2 %. Yerzley hysteresis is determined on equipment in Laboratory at Faculty of mechanical engineering Nis according the standard ASTM D945, with compression test method (Fig. 6).

Figure 5. Sliders on the underside of the experimental load

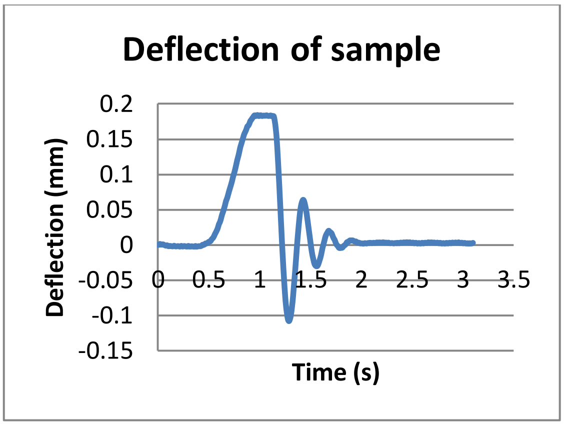

Figure 6. Deflection of sample in dynamic test according ASTM D945

Experimental samples of flooring covers were prepared from five different materials: ceramic tiles, granite tiles, laminate, vinyl and parquet. Values of surface roughness of experimental floor coverings samples are presented in Table 1. Contact pressures were 75 kPa and 140kPa. Sliding distance was about 500mm. Sliding velocities were: 5, 10 and 50 mm/s.

Table 1. Measured surface roughness parameters of experimental floor coverings samples

	Floor coverings	R_a (μm)	R_z (μm)	R_{max} (μm)
1.	Ceramic tiles	0.63	2.34	3.57
2.	Granite tiles	0.06	0.34	0.51
3.	Laminate	1.50	4.59	6.18
4.	Vinyl	0.83	3.54	5.51
5.	Parquet	0.42	1.90	2.77

A typical example of measured friction coefficient is presented in Figure 7.

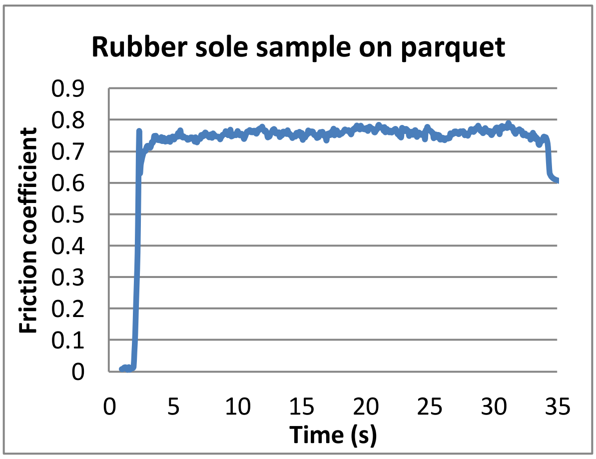

Figure 7. Friction coefficient measured in sliding rubber sole sample on parquet

There are numerous measuring data and friction coefficient values are very variable, ie, stochastic. Mean values of friction coefficient measured in experiment is presented in Table 2.

Table 2. Mean values of friction coefficient masured in experiment

Floor coverings	Contact pressures		Contact condition	
	75 kPa	140 kPa	Dry	Wet
Ceramic tiles	0.434	0.447	0.4167	0.4648
Granite tiles	0.692	0.835	0.8321	0.6956
Laminate	0.758	0.788	0.8232	0.7234
Vinyl	0.745	0.8545	0.7951	0.8046
Parquet	0.715	0.8230	0.7506	0.7881

In order to estimate the influence of individual parameter, comparing the friction coefficient values can be noticed in case of granite tiles, which have the smallest surface roughness, that friction coefficient values are bigger when contact pressure is bigger and also in the dry condition. That means that adhesive component of friction force is the most influential in that case. It is very similar (same trend) in case of laminate samples which have the biggest measured parameters of surface roughness, but laminate has smaller surface hardness.

In case of ceramic tiles friction coefficient is so similar in case of smaller and in case of bigger contact pressure, but in wet condition it is 11 % bigger than in dry condition.

In case of parquet samples coefficient of friction is 15 % bigger when contact pressure is bigger than in smaller pressure condition and 5 % bigger in wet than in dry condition.

The minimum values of friction coefficient are measured with floor sample from ceramic tiles in case of contact pressure 75 MPa and in sliding on 5 mm/s speed in dry condition, and their mean value is 0.37

The maximum values of friction coefficient are measured with floor sample from materials vinyl and laminate in case of contact pressure 140 MPa and in sliding on 50 mm/s speed in dry condition, and their mean value is 1.06.

5. CONCLUSION

In order to prevent the slip accident it is necessary to investigate and examine the friction influential parameters and according that it should be implemented certain measures. Knowledge of friction mechanism of viscoelastic materials is very useful for establishing the friction circumstances in human walking. According this knowledge can be estimated the most influential part of mechanism: adhesion, deformation and wear.

In performed experimental research, measuring data show that for the same shoe sole sample there are a wide range of friction coefficients values for different floor and conditions. Maximum value of friction coefficient is three time bigger than minimum value for same sole material sliding on different floor materials, like ceramic tiles and vinyl and laminate.

Some type of shoe sole material can't be the best on all different types of coverings and contaminants, and because of that it is necessary to investigate different combinations of materials and friction conditions.

REFERENCES

[1] I.J. Kim, H. Nagata: Research on Slip Resistance Measurement – A New Challenge, Industrial Health, No. 46, pp. 66-76, 2008.

[2] G.W. Stachowiak, A.W. Batchelor: *Engineering Tribology*, Butterworth Heinemann, Australia, 2005.

[3] R.H. Smith: *Analyzing friction in the design of rubber products and their paired surfaces*, Taylor & Francis Group, USA, 2008.

[4] B. Lorenz: *Contact mechanics and Friction of Elastic Solids on Hard and Rough Substrates*, Diss., RWTH Aachen University, 2012.

[5] B.N.J. Persson: Theory of rubber friction and contact mechanics, Journal of Chemical Physics, Vol. 115, No 8, pp. 3840-3860, 2001.

[6] B.N.J. Persson: Contact mechanics for randomly rough surface, Surface Science Reports, Vol. 61, pp. 201–227, 2006.

[7] C. Wetzel, U. Windhovel, D. Mewes, O. Ceylan: Slipping on pedestrian surfaces: methods for measuring and evaluating the slip resistance, International Journal of Occupational Safety and Ergomics, Vol. 21, No. 3, pp. 256-267, 2015.

[8] E. Wassmann: Panta Rhei, Foot and leg protection standards under revision, Health&Safety International, Vol. 76, pp. 15-23, 2018.

[9] F.P. Bowden, D. Tabor: *Friction An Introduction to Tribology*, Malabar Florida, Robert E. Kriger, Publishing Company, 1982.

[10] D. Stamenković, M. Banić, M. Nikolić, M. Mijajlović, M. Milošević: Methods and Principles of Determining the Footwear and Floor Tribological Characteristics, Tribology in Industry, Vol. 39, No. 3, pp.340-348, 2017.

[11] M. Nikolić, D. Stamenković, M. Banić, A. Miltenović: Biomechanic and Tribology in Human Walking, in: *Proceedings of 15th International Conference on Tribology SERIATRIB '17*, Kragujevac, pp. 631-636, 2017.

Serbian Tribology Society

SERBIATRIB '19

16th International Conference on Tribology

Faculty of Engineering
University of Kragujevac

Kragujevac, Serbia, 15 – 17 May 2019

DEVELOPMENT OF FULLY AUTOMATED TEST BED FOR MEASURING STATIC CHARACTERISTICS OF DIRECTIONAL HYDRAULIC VALVES

Vito TIČ[1,]*, Jörg EDLER[2]
[1]University of Maribor, Faculty of mechanical engineering, Maribor, Slovenia
[2]Graz University of Technology, Graz, Austria
*Corresponding author: vito.tic@um.si

Abstract: *Directional hydraulic valves are one of the basic and very important components of a hydraulic system as they control the direction and quantity of the flow of hydraulic fluid. In order to compare the performance of valves from different manufacturers, or in order to evaluate performance of the valve during its lifetime, a special test bed should be developed.*
The paper presents the development of fully automated test bed for measuring static characteristics of directional hydraulic vales according to ISO 10770-1. The test bed consists of hydraulic system equipped with modern sensors and is controlled by a soft PLC. The test procedure is fully automatic and the test results are displayed real-time.

Keywords: *hydraulic valves, directional valves, flow characteristics, pressure drop, test bed.*

1. INTRODUCTION

Directional hydraulic control valves are hydraulic components for regulating the flow direction of the fluid and the flow velocity in the hydraulic system. Their use in the hydraulic system allows the actuator to move (cylinder, hydraulic motor ...). The most common design of directional valves uses control spool that moves from the starting position (usually the middle) to the left or right operating position, depending on the desired direction of movement of the actuator. The movement of the spool is controlled by either lever, coil, hydraulic force or a spring. [1]

The properties and characteristics of directional hydraulic control valves have a strong influence on the behaviour of the entire hydraulic system. The performance of the valve is most influenced by its construction, but the characteristics also depend on the hydraulic fluid used, which changes the characteristics of the valve with different viscosity, compressibility and density.

With developed test bed for measuring static characteristics of directional hydraulic valves it is possible to obtain information on the properties of a particular valve of a particular manufacturer in combination with a particular hydraulic fluid based on standardized procedures. At a later repetition measurement of the same valve, we can conclude on its wear and degradation of the characteristics.

If we want to compare the characteristics of the hydraulic equipment between different manufacturers and evaluate the variation of the characteristic over the useful life of the valve, the characteristics must be comparable. Comparability is achieved by standardized tests and a standardized presentation of results.

2. ISO 10770 STATIC TESTS

ISO 10770 standard applies to electrically modulated hydraulic control valves and consists of three parts. The first part refers to the testing of four-port directional valves, the second part relates to the testing of three-port valves, and the third part to the pressure regulating valves [2].

The standard is divided into electrical tests, performance tests that are further divided into dynamic and static tests, and pressure impulse test. This paper focuses on the static performance tests of four-port directional valves. According to the standard these static tests exclude any dynamic effects. The standard also specifies the test conditions that are presented in Table 1.

Table 1. Required test conditions [2]

Ambient temperature	20 ±5 °C
Filtration	According to ISO 4406
Hydraulic fluid	Mineral hdraulic oil (ISO 6743-4) or other hydraulic fluids according to the valve
Hydraulic fluid temperature	40 ±6 °C at valve inlet
Fluid viscosity grade	VG 32 (ISO 3448)
Pressure	±2,5 % according to specific test
Pressure on the return line	According to manufacturer's recommendations

Further on, the paper will present development of fully automated test bed for measuring static characteristics of directional hydraulic valves and results of three most important and common test for four-port directional valves.

2.1 Internal leakage versus input signal

The internal leakage test measures the internal leakage flow between the individual valve ports. During the test both control ports are closed and the tank port is opened. The pressure port is loaded with 100 bar or with valve’s maximum pressure allowed.

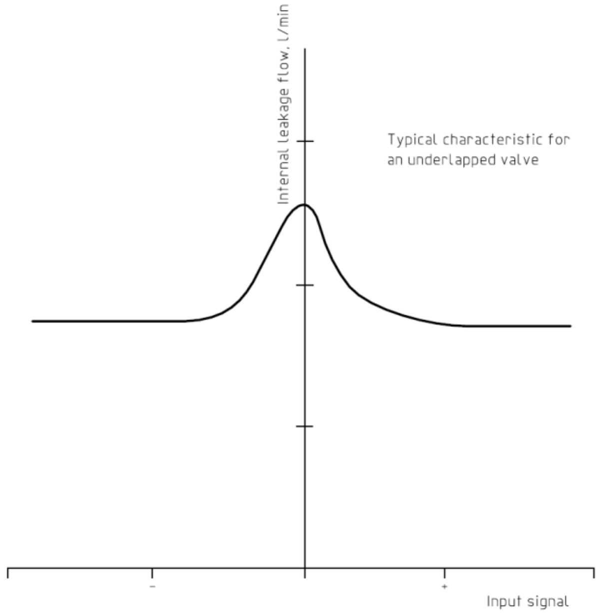

Figure 1. Internal leakage versus input signal [2]

Before performing the measurement, it is necessary to drive the valve several times over its entire control area. The flow of leakage on the tank port is then measured throughout the control area. The result is a graph of the leakage flow depending on the control signal as shown in Fig. 1 [2].

2.2 Output flow versus input signal at constant valve pressure drop

Figure 2 shows the static flow characteristics of the hydraulic fluid as a function of the control signal. This characteristic is defined at a constant pressure drop on the valve. Work ports are connected together via the flowmeter. The test is carried out at a pressure drop of 10 bar, of 70 bar or of one third of the maximum working pressure.

Before performing the measurement, it is necessary to drive the valve several times over its entire control area. During the test, the input control signal is adjusted from one limit (i.e. negative) to another limit (i.e. positive), while the flow value is recorded. The speed of the signal change must be slow enough so that the dynamic effects are not affected by the results. Between the test the pressure drop on the valve should be as constant as possible and should not deviate by more than 5 %.

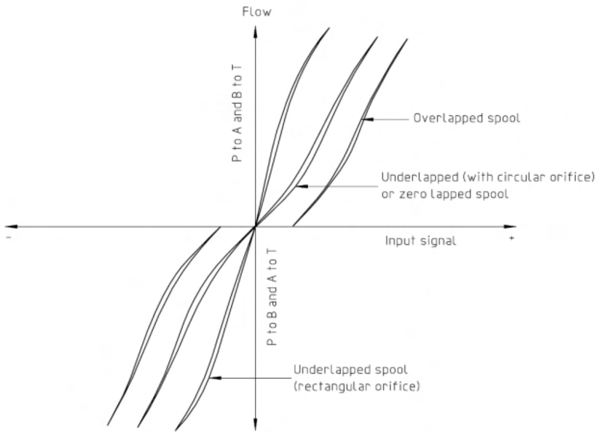

Figure 2. Output flow versus input signal at constant valve pressure drop [2]

In the obtained results, the following characteristics of the valve can be identified: output flow at rated signal, flow gain, linearity, hysteresis, null zone characteristics (i.e. spool lap condition, symmetry, polarity and limiting power [2].

2.3 Metering test

The purpose of this test is to determine the characteristics of each land of the main spool as shown in Fig. 3.

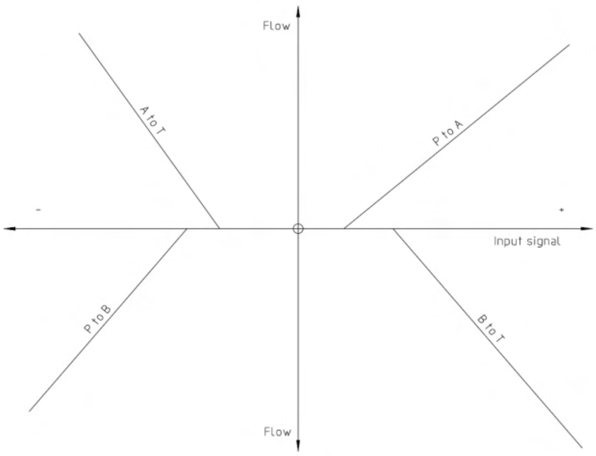

Figure 3. Metering test [2]

The test is made of four different measurements of the flow between two control ports at constant pressure drop: the flow from port P to A, P to B, A to T and flow from port B to T. [2]

3. DEVELOPMENT OF TEST BED

Based on the ISO 10770-1 test procedures (some described above) a test bed was designed and built (Fig. 4).

Figure 4. Test bed

The hydraulic system (Fig. 5) is mounted on the frame made of aluminum profiles. It consists of pipes, shut-off valves and several sensors for pressure, flow and temperature. Hydraulic power is provided by a hydraulic power unit with variable axial piston pump powered by a three-phase asynchronous motor, controlled via frequency converter.

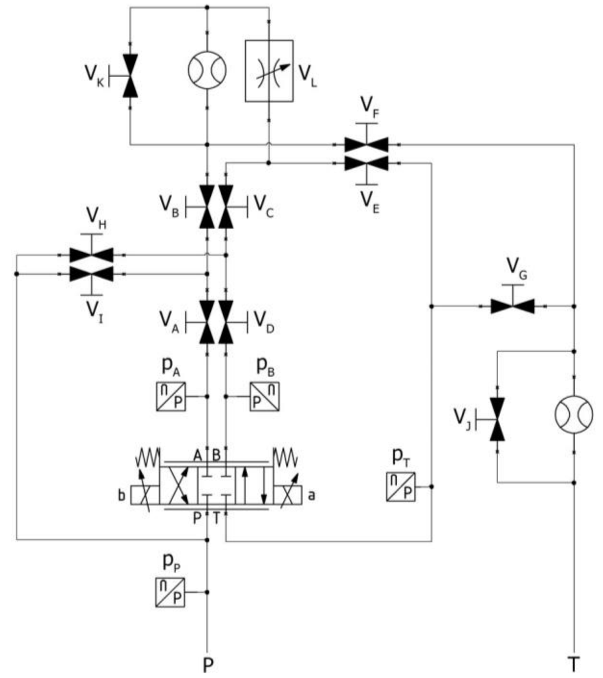

Figure 5. Hydraulic scheme of test bed

The use of variable axial piston pump powered by a three-phase asynchronous motor, controlled via frequency converter allows us to perform closed loop control (PID) of pump flow from 0 to 80 L/min to achieve desired constant pressure drop on the valve.

3.1 PLC control system

The PLC system is based on Beckhoff soft PLC with selected digital and analog input/output modules to control the system. Besides digital and analog modules, the system also incorporates counter modules to measure the flow by two gear type flow meters and a PWM current output module to control the coils of proportional directional valve. Using this special module (EL2535) allows us to have full control over pulse width modulation of closed loop current control together with PID parameters of PWM modulation and dither signal to the valve.

3.2 HMI and visualization

The user interface (shown in Figure 6) is made in C# Windows Forms where it is possible to include libraries for the graphical display of signals directly from the PLK.

The HMI graphical interface serves to select the test we want to perform, set the appropriate parameters, capture data and monitor the measurement. The results are displayed in the form of a graph and a table, and can be exported to Microsoft Excel XLS file.

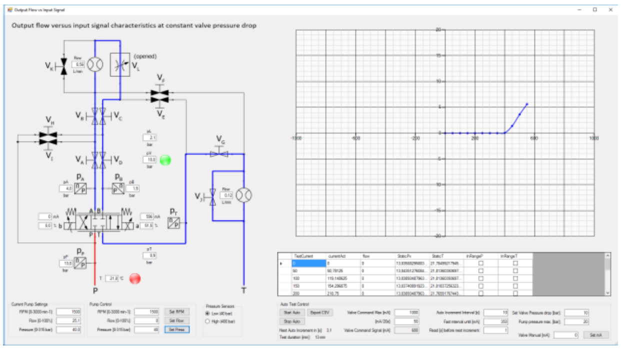

Figure 6. Windows application for HMI

HMI application window contains a hydraulic diagram that is equipped with digital displays of pressure and temperature values and a marked pathway of the current pipeline, thus making it easier to visualize the path of the hydraulic fluid. Under the hydraulic diagram we have indicators of current pump parameters: the rotational speed can be set from 0 to 3000 rpm, the flow can be set from 0 to 100 %, and the pressure can be set from 0 to 315 bar. The user can also define the desired pressure drop on the valve and time/step interval of performing individual measurements. On the right side of the window the results of the test are displayed in real time in in the form of a graph and a table.

4. RESULTS

Figure 7 shows the results of the internal leakage test.

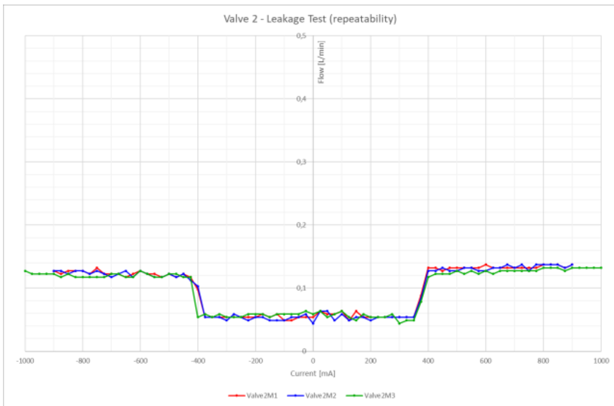

Figure 7. Results – Internal leakage test

During the test both control ports are closed (A and B) and the tank port (T) is opened. The pressure port was loaded with 300 bar and valve's internal leakage was recorded. The measurement was started with maximum negative signal and increased to maximum positive signal with 25 mA steps. To evaluate the accuracy and repeatability of the test bed, we have made three reiterations of each test (the results of each are shown as red, blue and green line).

The static flow characteristics of the hydraulic fluid as a function of the control signal is defined at a constant pressure difference on the valve. Since we were measuring a proportional directional control valve it was important to ensure a constant pressure drop of 10 bar. During the measurement, the signal changes from 0 to positive limit, then back to negative limit and back to 0. In this way also the hysteresis of the valve is recorded.

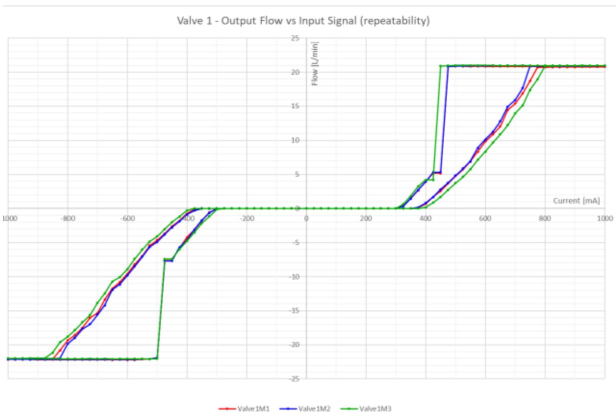

Figure 8. Results – Output flow vs Input signal

The obtained results can be seen in Figure 8 and show three reiterations of the test. A large hysteresis on the valve and poor linearity when decreasing control signal in both directions can be noticed.

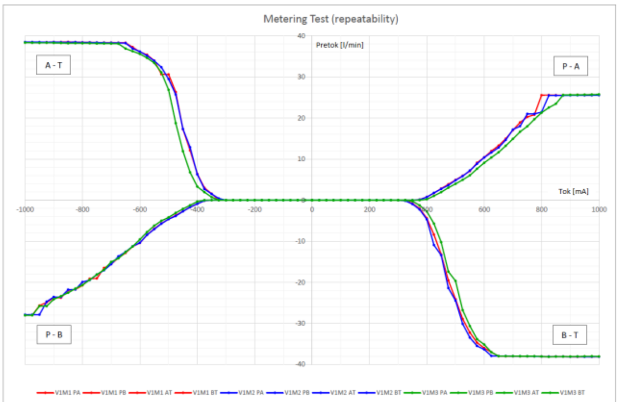

Figure 9. Results – Metering test

Additionally, the metering test is used to determine the flow characteristics of four individual connections: P-A, P-B, A-T and B-T. The measurement was also done with 25 mA step increase of current signal. The results of (three reiterations) of the test are presented in Figure 9. Better flow conditions can be recognized in A-T and B-T flow connections compared to P-A and P-B flow connections which have more flow restriction.

5. CONCLUSION

A fully automated test bed for measuring static characteristics of directional hydraulic valves was successfully developed and built. It allows us to perform all types of tests specified in ISO 10770-1 and determine the static characteristics of four-port directional hydraulic valves with desired accuracy and repeatability.

The test bed allows us to compare properties and characteristics of different new valves or to evaluate the performance of a single valve before and after being exposed to long-term endurance test, evaluating its performance after the endurance test.

REFERENCES

[1] D.Lovrec: *Uvod v hidravlično pogonsko-krmilno tehniko*. Maribor : Univerzitetna založba Univerze : Fakulteta za strojništvo, 2018. https://doi.org/10.18690/ 978-961-286-191-9.

[2] ISO 10770-1, *Hydraulic fluid power-Electrically modulated hydraulic control valves- Part 1: test methods for four-port directional flow-control valves*, 2009.

Serbian Tribology Society

SERBIATRIB '19

16th International Conference on Tribology

Faculty of Engineering University of Kragujevac

Kragujevac, Serbia, 15 – 17 May 2019

METHODOLOGY DEVELOPMENT OF AN IMPACT ABRASION TEST WITH VALIDATION BY COMPARISON WITH REAL INDUSTRIAL CASE

Haithem BEN HAMOUDA[1], Michiel CORRYN[1,*]

[1]ArcelorMittal Global R&D Gent - OCAS NV, Zwijnaarde, Belgium

*Corresponding author: michiel.corryn@arcelormittal.com

Abstract: *A testing methodology is proposed to simulate wear in dry conditions with a high-stress impact level. The studied impact abrasion test is known as the impeller-tumbler test. A methodology for this test was established based on a parametric study in order to investigate the corresponding influence on wear results. The rotation speed and the filling ratio of the abrasive particles were identified to have the highest influence on wear results, controlling the impact energy level on the material surface. Further parameters such as the particle size/type and contact duration were also inspected. Once stabilized, the methodology was applied on two industrial cases: stone crusher hammers from mineral processing and chute tour plates in mining application. Results for the first application showed wear mechanisms occurring on different positions of the HSI crusher hammers that are similar to the mechanisms observed on the impeller-tumbler abraded samples surface. For the mining application, a quantitative comparison of the wear rates was done showing a second validation case for the impact test. Finally, a predominant edge-concentrated wear was identified for all materials and was quantified using a 3D geometry reconstruction method.*

Keywords: *impact, abrasion, wear mechanism, 3D reconstruction, edge cutting, hammer mill, mining.*

1. INTRODUCTION

Abrasion is a major issue for component failure in applications such as mining, conveying and crushing of rocks. Selecting the most appropriate material for these applications is important to limit the high cost of repair and/or replacement and extending the component service life. For this purpose, accelerated abrasion tests are generally used to compare material performance. A reliable test methodology should give not only repeatable and reproducible results but also a representative ranking in the real application. In this work, the methodology developed to study materials abrasion performance under impact condition is detailed. A parametric study was done to investigate the test sensitivity. Finally, a comparison of this test to two test cases was done.

2. EXPERIMENTAL PROCEDURE

2.1 The impeller-tumbler test set-up

The impeller-tumbler was designed to simulate wear in dry conditions with a high-stress level and an impact abrasion mode. The test concept is not new and has been used in several references [1,2].

Figure 1 illustrates the working concept of the impeller tumbler test in dry condition. The test consists of two main components rotating independently: the tumbler and the impeller.

The impeller has a rotation speed of around 800 rpm while the tumbler is rotating at significantly lower rotation speed (about 50 rpm). The abrasive particles are placed in the tumbler and are continuously agitated by its rotation. The impeller is playing the role of sample holder holding simultaneously three samples and it rotates them to ensure impact contact with abrasive particles. The linear velocity of the samples can reach 38m/s.

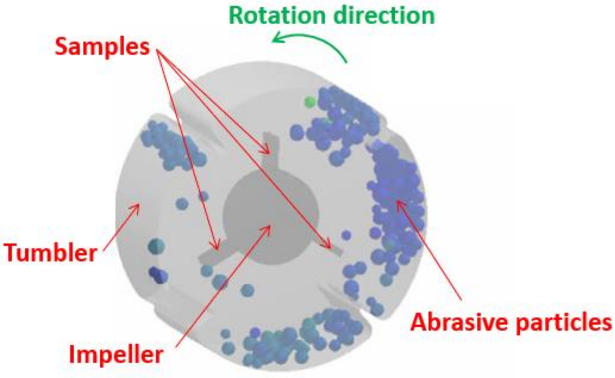

Figure 1. Schematic presentation of the impeller-tumbler

Table 1. Overview of influencing parameters

Parameter	Check
Abrasive particles	Size distribution of particles
	Fine versus coarse particles
	Renewal frequency
	Crushability of particles
Test duration	Transient and steady state regime
Samples	Position in holder
	Preparation
Rotational speed	Impeller speed
	Tumbler speed

Several test parameters were selected for test sensitivity analyses (Table 1). Preliminary parameter values were selected near the machine maximum capabilities in terms of speed and filling ratio. For the test duration, 3 hours was selected.

2.2 Material description

The reference material that was proposed in this study is a typical quenched fully martensitic steel with a Brinell hardness of 470, also referenced to as material A. In addition to this hard material, a soft pearlitic material was also studied (material B). An overview of the key mechanical properties of both materials is given in Table 2.

Table 2. Key properties of the reference materials

Material	Hardness [HBW]	Elongation [%]
Martensitic (A)	470	8
Pearlitic (B)	190	25

The samples were ground on all sides to prevent influences of sample geometry or roughness. The wear performance of both materials is analysed in the following sections.

2.3 Wear analyses methods

Wear losses were measured by mass loss obtained on a Mettler Toledo XSR603S precision balance with a repeatability of 0.5 mg. Mass losses were converted to volume losses by means of the density. Density values were obtained on the same balance using a corresponding density measuring kit.

A Field Emission Gun - Scanning Electron Microscope (FEG-SEM) was used for high-magnification observations of the worn surfaces. The model used in this work is a JEOL JSM-7001F SHL, with a magnification range of 10x to 10^6x.

A Taylor Hobson Talysurf CCI-HD, a non-contact surface roughness tool, was used to measure surface roughness parameters in accordance to ISO 22178-2. Topographical representation of a surface can be obtained with a vertical resolution of 0.1 nm over a full scan range plus a 0.4 µm lateral resolution.

To produce micro-hardness profiles, a Future Tech FM300 was used. Micro-Vickers values (HV 0.025) were accurate within 1% according to the latest calibration following ISO 6507-2.

A LK Evolution Coordinate Measuring Machine (CMM) was used to reconstruct the worn samples in 3D in accordance to ISO 10360-2. The CMM has a resolution up to 0.0023 mm.

3. RESULTS AND DISCUSSION

3.1 Effect of tribological parameters

The first test was performed on three reference material samples using the preliminary test parameters. Coarse, as-received granite particles (8-16mm) were used as abrasive. In this test, the goal is to observe the influence of the particle size distribution of the abrasive on the repeatability of the measurement. This could be observed by measuring the weight loss on the reference samples at every renewal of the abrasive. From the measurements on the three samples of the same material, the average volume loss was calculated at each time step (Fig. 2).

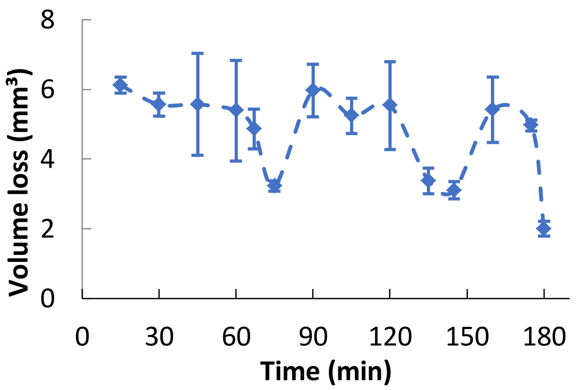

Figure 2. Volume losses at each time step for material A tested with abrasive as received

Figure 2 shows clear differences on the volume losses with high standard deviation especially in the time range of 40-120min. This shows a clear batch effect on the test results, which can be attributed to differences in the particle size distribution.

A close investigation of the abrasive particles shows the existence of several particles with significantly high aspect ratios. In fact, although the abrasive is sieved using standard sieves in the range of 8-16mm, some particles with a higher dimension can pass through the 8-16mm mesh due to their aspect ratio, leading to less homogeneous batches. Therefore, for every following test the abrasive batches were controlled by removing particles with high aspect ratio.

The second test repeated the conditions of the first test. However, now with the control of the abrasive particles' aspect ratio implemented. This test was repeated three times to obtain 9 measurements on the material A. The wear loss evolution showed a better fit to a linear tendency. The wear rate reduced slightly due to the removal of the heavier, high aspect ratio particles. However, for some points higher errors are observed in the beginning of the test (Fig. 3).

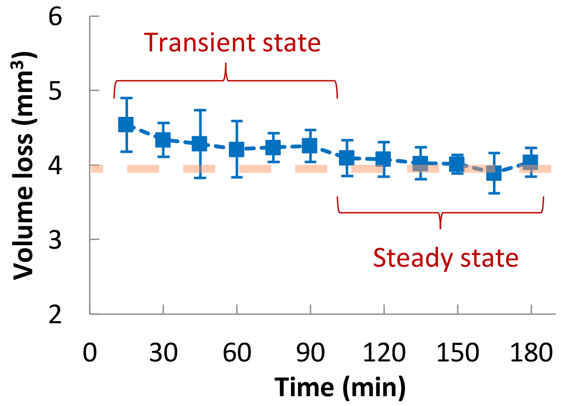

Figure 3. Volume losses at each time step for material A tested with controlled abrasive

A transient/running-in state was observed which was not clear from the preliminary test. During this initial state, a higher volume loss is combined with a higher error. Both reduce until around 100 minutes, where a steady state is reached. The final obtained error (averaged over the 9 tested samples) after 3 hours testing was around 3%. Such error value is lower than the acceptability criterion fixed in the ASTM-G65 standard test which is equivalent to 7% [3]. The initial higher wear can be attributed to the edge cutting effect, further elaborated in the next Section.

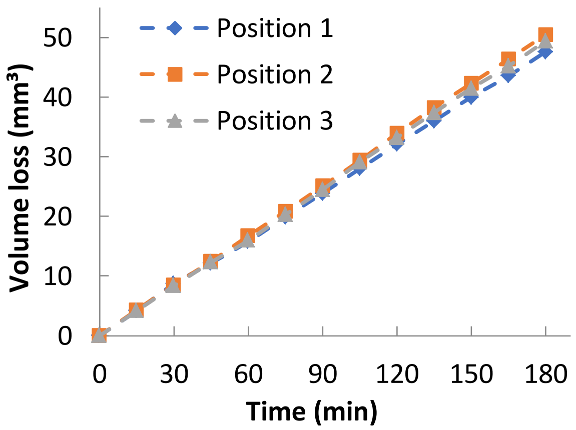

Figure 4. Cumulative volume losses for material A tested without sample rotation

Looking at the individual results from the same test, there is a difference in the volume loss between the three reference samples at different positions (Fig. 4). The difference between the curves increases with time, reaching a value of almost 4% after 3 hours. A possible explanation is the possible size deviations between the machine slots that hold the samples.

To assess this, the test was repeated, but with the additional step of changing the sample position every time the abrasive was renewed in a way to get the same testing time in each slot. This procedure is called sample rotation and the results are presented in Fig. 5. With this procedure, the difference between the samples was less than 1% averaged over 3 tests. Consequently, one can conclude that slot differences exist and can be supressed by rotating the samples. This enables better comparison of the different materials in the same test by deleting effects linked to slot geometry.

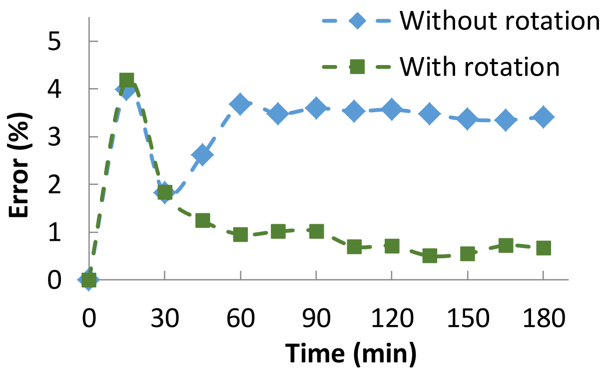

Figure 5. Volume losses at each time step for material A

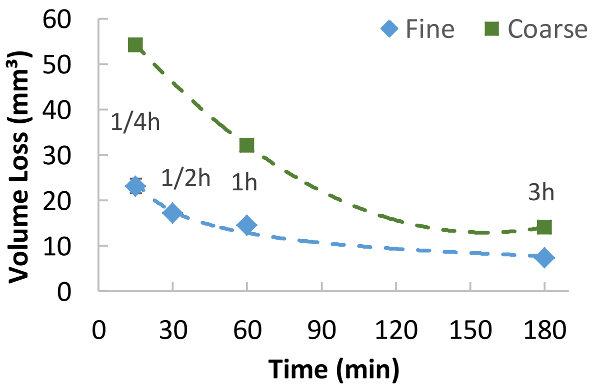

Figure 6. Cumulative volume losses for material A in function of abrasive renewal time step

The renewal of the abrasive batch every 15 minutes is an operator intensive task. Therefore, a study on the abrasive changing frequency was performed. The time step was varied from 15 minutes to 3 hours. The resulting cumulated volume loss after 3 hours, for both the fine and coarse granite, is plotted in function of the time step in Fig. 6.

The results show that increasing the time step to renew the abrasive batch, decreases the volume losses. This can be explained by the rounding of abrasive particles due to impact with the sample surface. This leads to a lower capability to remove material. This particle property is known as abrasiveness, which is linked to rock hardness, shape and sharpness [4]. For the coarse granite, this effect is more noticeable, with the volume loss for the ¼ hour time step being 69% higher than for a one hour time step and 284% higher than for a three hour time step.

The decrease in volume loss is non-linear. There is a steep decrease between the different time steps smaller than 1 hour. This can be explained by a fast degradation of the abrasive particles by breakage of the sharp edges. Once rounded, the particles have reduced size and limited abrasivity which can explain the obtained lower volume losses.

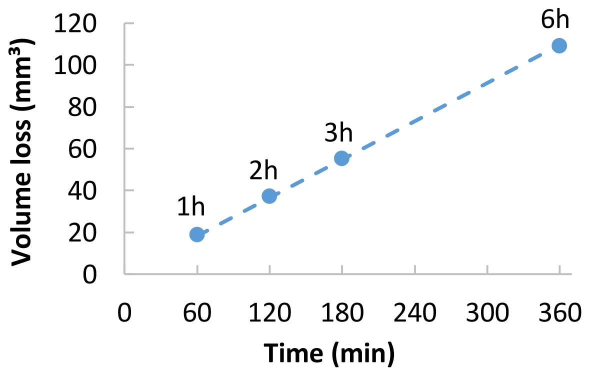

Figure 7. Cumulative volume loss for material A in function of experiment total duration

The aforementioned observations about the transient state, sample rotation, and abrasive renewal time step need to be considered before fixing the test duration. First, the test duration needs to be selected in the steady state regime to reach optimal accuracy. For reference material A, the steady state regime was established after almost two hours. Therefore, three hours might be an acceptable choice. Secondly, the time step of sample rotation (and abrasive renewal consequently) needs to be captured 3 or a multiple of 3 times to have even time in each sample slot. A test was performed with a duration of 6 hours, see Fig. 7. This shows that the linear tendency is respected in longer tests. Therefore, an optimized wear test does not need longer durations and can be extrapolated using the linear tendency.

The rotation speed of the impeller controls the impact energy at which the particles encounter the material surface. This is also the influenced by the particle weight. As such, fine granite particles (4-8 mm) have a lower impact energy than coarse granite particles. Both granite abrasives were tested under two different rotation speeds of the impeller. The results are plotted in Fig. 8. Indeed, by increasing the impeller speed from 50% to 90% of the maximum rpm resulted in an increase of the cumulated volume loss by a factor of 3 to 4. The size effect is demonstrated in the same figure as well. Both have a significant effect and can be used as a tuning parameter to control the impact energy induced on the material surface.

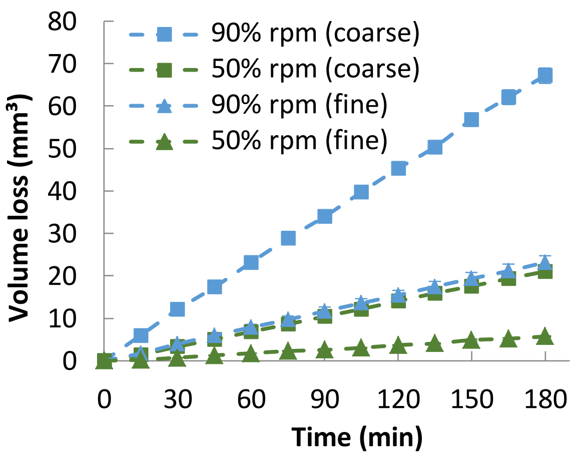

Figure 8. Cumulative volume losses for Material A in function of abrasive size and impeller rpm

The rotation speed of the tumbler can be controlled in a range to about 50 rpm. This rotation is necessary to agitate the particles. The effect of increasing the tumbler speed from a low value, to 3 times this value is represented in Figure 9. By increasing the rotation speed of the tumbler, the volume moss measured after 3 hours has increased by 87%. This increase in speed resulted in a higher agitation of the particles, leading to more impacts. However, a further increase will lead to less impacts due to centrifugal forces.

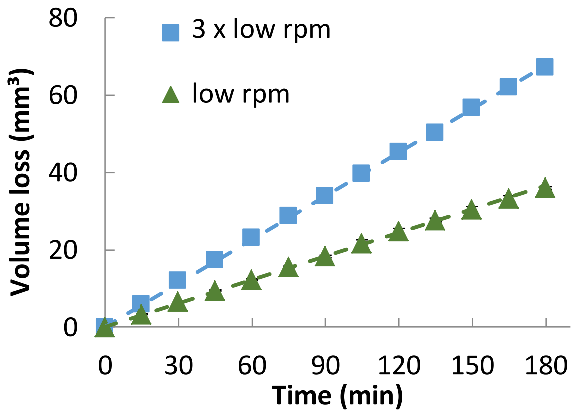

Figure 9. Cumulative volume losses for Material A in function of tumbler rpm

Another factor related to the abrasive particles is the crushability. Due to the high stress conditions, wear occurs in both the abrasive and the tested sample. For the abrasive, the wear test could play the role of a rock crusher, especially if the sample material has a high hardness. The abrasive renewal time step was reduced to prevent too much rounding of the particles. However, the sample hardness has an influence on the crushability of the particles and may make it not representative to compare results for materials with another hardness.

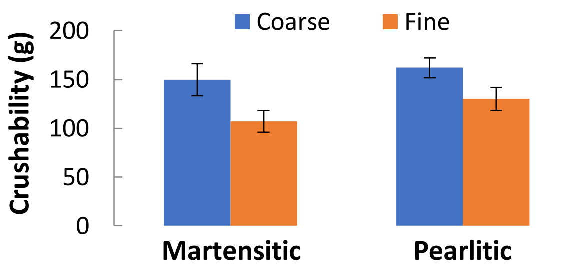

Figure 10. Crushability measured as mass loss of the abrasive particles during a time step tested on Material A and B

Measuring the weight loss of the abrasive particles after each time step gives an indication about the abrasive particles' crushability. For this study, two types of abrasives are studied: coarse and fine granite particles. The different stones were extracted from different quarries, so a risk of different hardness and crushability is possible. These were tested with two types of "crusher blades": reference material A (martensitic, 470 HBW) and material B (pearlitic, 190 HBW). Figure 10 shows the result of this comparison. For the same abrasive, there is no observed influence of the sample hardness on the particle crushability. However, the fine particles show a lower crushability than the coarse particles. This corresponds to the observations in Figure 6, where the renewal step time had less influence on the fine particles.

Table 3. Influencing parameters of the impeller-tumbler test

Parameter	**Influence**
Rotation speed impeller	From 50 to 90% of max rpm → Volume Loss times 3
Rotation speed tumbler	<10 rpm → Bad abrasive mixing (no impacts) >50 rpm → Less impacts
Abrasive changing time step	> 1h → Lower abrasiveness < ¼ h → Higher cost
Test duration	<2h → Steady state not reached >3h → gives no further information
Abrasive size	From fine to coarse particles → Volume Loss times 3
Abrasive particles distribution	Influences linear tendency
Sample position	Different results per position

The sensitivity of each influencing parameter was examined. Table 3 gives a summary of these with their influence on the test result.

3.2 Wear mechanisms

Samples subjected to the impeller tumbler were studied using various techniques with the aim to characterise the wear mechanisms at play. This was done for the hard reference material A and the softer material B to observe a probable change in mechanism.

From a visual inspection, one can remark that the contact surface is severely impacted at the edges, resulting in a rough surface. The edges are rounded as well. For the softer material, material was visibly ploughed to the edges, forming a burr. Also visible, is a decrease in impact density going from the edge to the impeller slot. Therefore, different locations were marked to see the difference in behaviour, see Fig. 11.

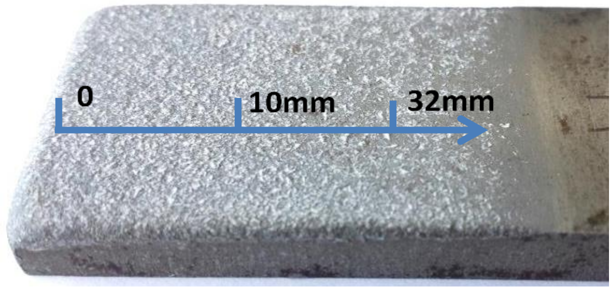

Figure 11. Sample with rounded edges and locations marked on sample

The FEG-SEM micrographs showed a severely deformed edge at position 0, characterized by a rough surface with a high density of craters/peaks on both materials. Close to the impeller slot, at 32 mm distance, localized deformation areas are visible. This could be attributed to single impacts of the abrasive particles.

At a higher magnification, embedded abrasive particles were visible on both materials. For the martensitic grade, small wear particles have been identified on the worn surface of the martensitic grade in Fig. 12. These particles, known as chips or chunks, are formed due to the cutting of material that was previously folded by plastic deformation to form the wedge of the crater/groove. This wear feature is characteristic of the micro-cutting mechanism.

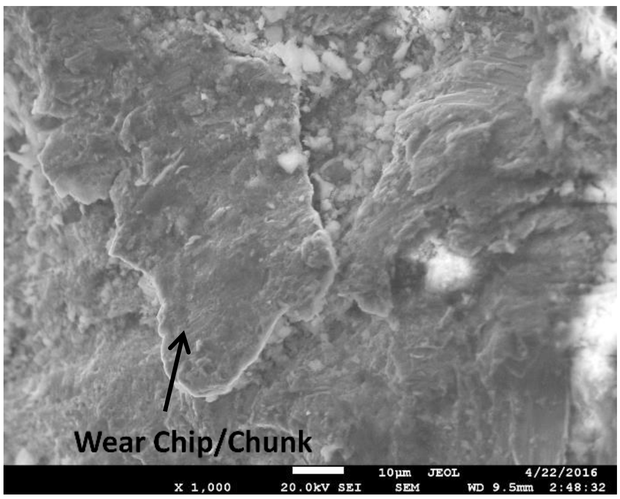

Figure 12. FEG-SEM of chunk particle in material A

Micrographs on the cross-section areas showed wavy patters with fibered substructures.

The observed waviness is more developed for the soft pearlitic material and could be defined as a superposition/folding of heavily deformed material chunks after subsequent impacts of the abrasive particles (Fig. 13). This mechanism is known as microstructure micro-forging by impact of abrasive particles. This observation was confirmed by EDX analysis which identified the presence of dust of abrasive grains.

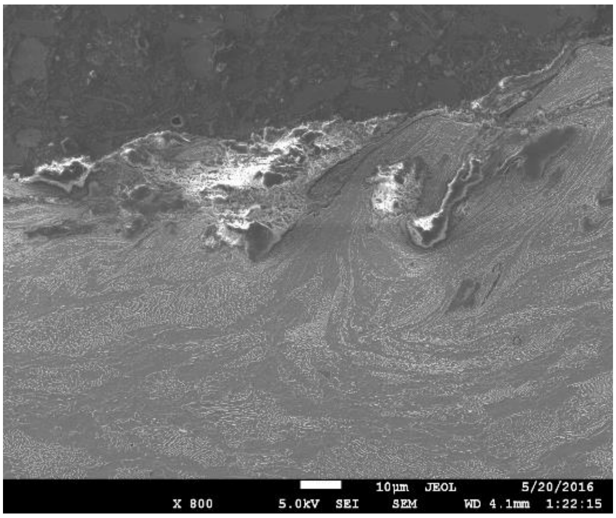

Figure 13. FEG-SEM of waviness in material B

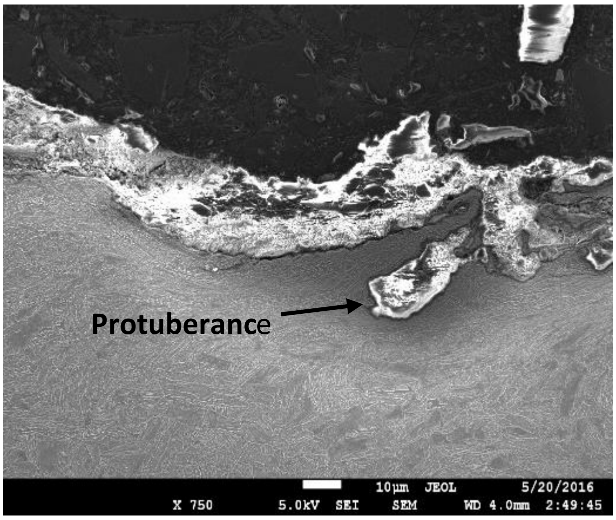

Figure 14. FEG-SEM of protuberance on material A surface

For the martensitic material, material folding/displacement was limited due to the lower strain hardening capability. This can explain the existence of maximum one layer/wave of folded material (protuberance) in the material surface because further deformation will lead to cutting of the protuberance to form a chunk/chip. This feature has been already identified for similar test conditions in previous research studies [1,2], see Fig. 14.

At a distance of 32mm far from the edge, no waviness is observed for any of the tested materials which can be explained by only single impacts present in this area. However, embedded particles are identified in the craters that were formed. This allows for a measurement of the penetration depth of a single particle: around 48 µm (Fig. 15).

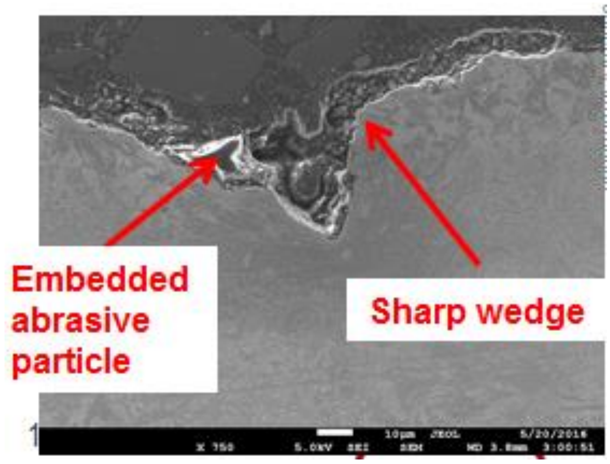

Figure 15. FEG-SEM of embedded particle in material A

To validate the micrographic analysis, surface profilometry was performed. The root mean square height parameter (S_q) is a stable indicator of the surface roughness. The evolution of this parameter for both samples is given in Fig. 16. For material B, there is a clear evolution from a rough surface at the end to a smoother surface near to the impeller slot. On the harder material A, the change is negligible.

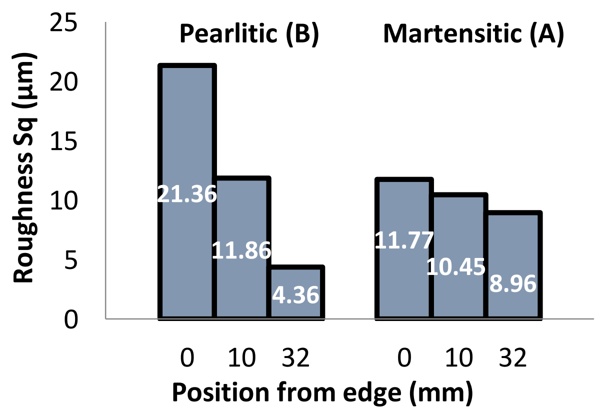

Figure 16. S_q at marked locations for both material A and B

Micro-hardness profiles were extracted as well. The aim was to observe the subsurface structures' hardness. During subsequent impacts by multiple abrasive particles a plastic strain gradient is formed progressively underneath. The maximum strain is found at the particle-sample interface; it decreases continuously with increasing depth and ultimately reaches zero at the elastic-plastic boundary. The thickness of this gradient in known as the subsurface hardened layer/lip generally characterized by deformed/elongated grains beneath the wear track (groove and crater).

For the pearlitic material, the micro-hardness cross-section profile is plotted in Fig. 17. The profiles representing the edge and the middle position show a hardening gradient beneath the contact surface. At the 0 mm position, a maximum hardness of around 350 HV was reached with a gradient of about 500 µm. At the 10 mm position this was 280 HV with a gradient of about 200 µm. Near the sample holding slot no hardening was observed, the measured values oscillate around the bulk hardness.

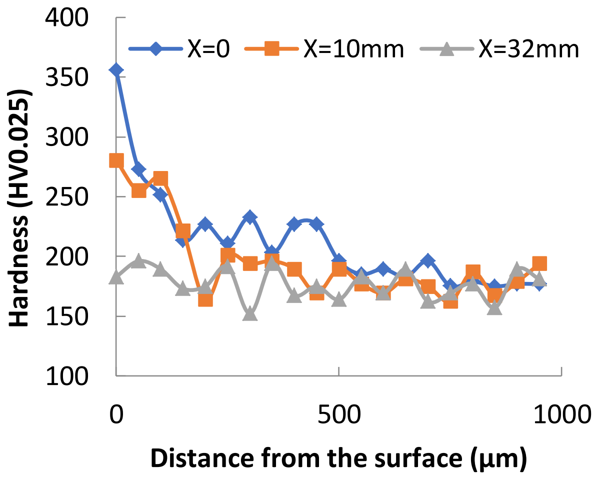

Figure 17. Cross-section micro-hardness profiles for the pearlitic grade

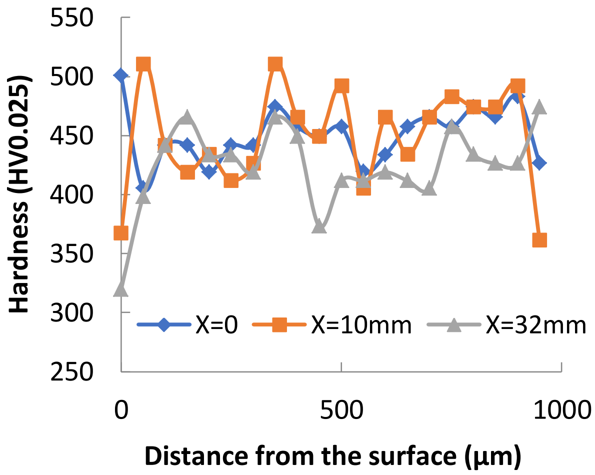

Figure 18. Cross-section micro-hardness profiles for the martensitic grade

The profiles measured on the martensitic grade do not show a clear hardness at any location (Fig. 18). As the step size of the measurement is 50 µm, it is possible that the layer was not measured. Observed from SEM images, the layer can be visually estimated to be around 5 µm thick.

The cross-thickness hardness profiles confirmed the wear mechanisms involved for both material A and B under high stress impact abrasion conditions. Micro-cutting is the main mechanism in the martensitic material, resulting in a thin hardened layer with a low fibering capacity. For the pearlitic material this is plastic deformation, therefore it develops a thick hardened layer/lip and shows a high fibering capacity.

Finally, a CMM was used to reconstruct the worn samples in 3D. The aim was to quantify how much the edge effect contributes to the total mass loss. Therefore, the reconstructed samples were divided into two parts defining the edge and inner part (Fig. 19). On the reference material A, about 85% of the total wear occurred at the sample edges. This was the case with both fine and coarse abrasive.

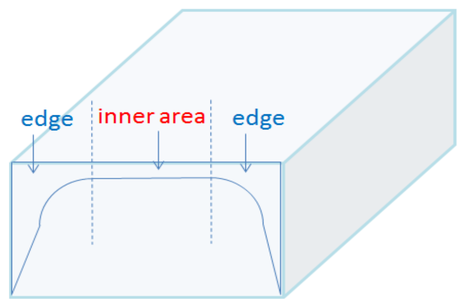

Figure 19. Separation of edge and inner area

With the wear mechanisms in mind for both materials, one could expect that the softer material would have a higher wear resistance due to the capability to absorb multiple impacts by plastic deformation. Therefore, both were subjected to an impeller-tumbler test using fine granite, see Fig. 20. The martensitic grade showed a linear behaviour due to the stable micro-cutting mechanism. However, the pearlitic material showed a wear behaviour in two stages. The first stage was very similar to the martensitic grade; the wear rate increased in the second stage. This change must be marked by a change in wear mechanism.

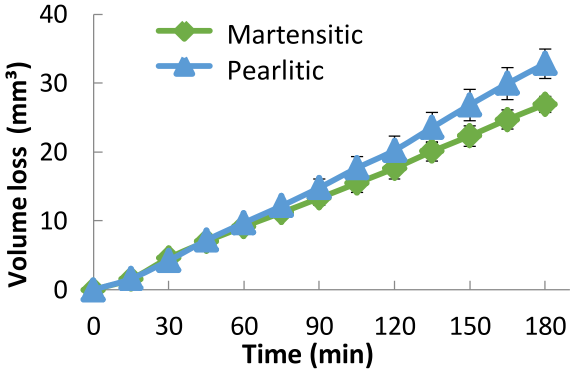

Figure 20. Cumulative volume losses for Material A and B

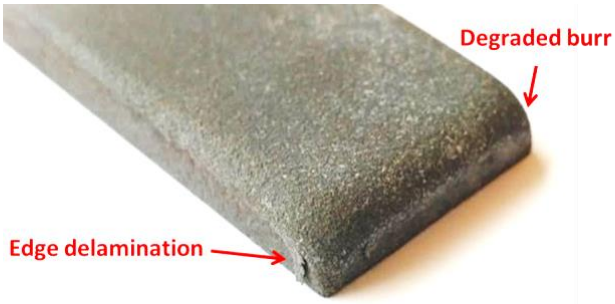

Figure 21. Edge delamination on the pearlitic material

After inspection of the soft material, the change in mechanism was observed. In the first phase, a burr is formed as a result of plastic deformation, as visible in Fig. 21. This burr keeps being developed as long as the material work hardening is not fully consumed at the edges. At a given time, the surface is fully hardened, and the formed burrs become large enough to be delaminated. This mechanism can explain the increase in wear rate in the second stage.

4. APPLICATION TO MINING CASES

The impeller-tumbler test is an edge concentrated wear test. Such edge effect is also existing in many other wear tests and applications exhibiting sharp contact surfaces. Therefore, it can be applied to various industrial cases with sharp contact surfaces. The test will be validated against two such cases.

4.1 HSI hammer crusher

An industrial case needed to be selected to validate the test procedure. A failed hammer from a limestone crusher was received. The part rotated at the edge of a spinning rotor wheel of almost 4 meters with the aim to crush limestone by impact. This part was mostly martensitic and will be subjected to a wear analysis.

By comparison of the occurring wear mechanism to the ones observed in our tests, a first validation of the developed method was made possible. When visually inspected, the received sample shows a worn edge and a rough surface. Again FEG-SEM, profilometry and hardness profiles will be used to further investigate the failure mechanism.

From the FEG-SEM images, it was shown that the worn middle section exhibited single craters. The craters were followed by grooves. This suggests that the impact occurred at low impingement angles. At the edge, the hammer showed a high number of craters. A cross-section showed the presence of protuberances piled up at the crater's wedge due to multiple impacts on the material surface at that position (Fig. 22). These features are similar to what was observed at the middle and edge of the martensitic sample worn by the impeller-tumbler test.

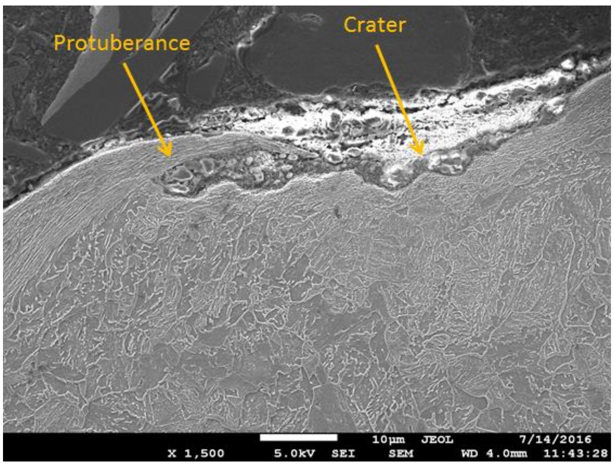

Figure 22. FEG-SEM of protuberance on hammer surface

The two other used techniques again showed results very similar to the observations on the test samples. The Hardness profiles did not show any hardening. However, the SEM images showed a gradient layer that was a few micrometres thick. Profilometry proved a higher roughness at the edge compared to the middle section.

4.2 Chute tour plates

A mining chute part was received in two materials, a martensitic material with a hardness of 400 HV and a similar material of 500 HV. Both had the same usage history. As such, their wear resistance could be compared. Impeller-tumbler samples were made from the same materials.

To compare the wear obtained in the application and the test, the life time was used. This unitless number compares the material wear resistance to a chosen reference material's resistance. The wear rate must be calculated first with the measured volume loss (VL), the area subjected to wear (WA), and the duration of the wear process (t). The calculation is laid out in formulas (1) and (2).

$$Wear\ rate\ \left[\frac{\mathrm{mm}}{\mathrm{s}}\right] = \frac{VL\ [\mathrm{mm}^3]}{WA\ [\mathrm{mm}^2] \times t\ [s]} \quad (1)$$

$$Life\ time = \frac{Wear\ Rate_{400\ HV}}{Wear\ Rate_{500\ HV}} \quad (2)$$

Table 4 shows the resulting values for both the field components and the lab samples. The good matching of the data indicates a successful choice of the test procedure to simulate the material life time in-service.

Table 4. Life time results

Test	Life time
Field	0.77 to 0.93
Lab	0.87

5. CONCLUSION

A wear testing methodology was detailed in this work showing different influence on the test results. Particle size and impeller rotation speeds were considered to be the most influencing parameters affecting directly the impact energy applied on the material. Moreover, characterization techniques showed the edge concentration wear in this test and the predominant impact abrasion mechanism.

The wear mechanism observed on the samples worn by the tumbler-impeller correspond to the mechanisms observed in the two selected mining applications. It was possible to obtain a material performance ranking representative of the application as well. As such, the test can be used to assess material performance and failure modes in application.

REFERENCES

[1] R. Wilson, J. *Hawk: Impeller wear impact-abrasive wear test*, Wear, Vol. 255-229, pp. 1248-1257, 1999.

[2] V. Ratia et al.: *High-Stress Abrasion and Impact-Abrasion Testing of Wear Resistant Steels*. s.l., s.n., 2011.

[3] ASTM G65-15 *Standard Test Method for Measuring Abrasion Using the Dry Sand/Rubber Wheel Apparatus,* 2015.

[4] G. Pintaude, M. Coseglio: *Severe metallic wear*, in: *Proceedings of 20th International Congress of Mechanical Engineering*, 15-20.11.2009, Gramado, Brazil.

Serbian Tribology Society

SERBIATRIB '19

16th International Conference on Tribology

Faculty of Engineering University of Kragujevac

Kragujevac, Serbia, 15 – 17 May 2019

ENERGY-ENTROPY TRIBOANALYSIS OF NATURAL MACHINE - TRIBOSUPERSYSTEM

Sergey V. FEDOROV
Kaliningrad State Technical University, Kaliningrad, Russia
fedorov@klgtu.ru

Abstract: *Machine is regarded as tribosupersystem which is composed of subsystems – tribosystems. From the position of energy-entropy analysis of adaptive-dissipative nature of states and properties of tribosystem a generalized machine rule is suggested. An idea is discussed about natural and real tribosystems and machines. A number of fundamental principles of tribosynthesis of natural and constructed machines are revealed.*

Keywords: *machine, tribosystem, energy, enthropy, balance, reliability, damageability, wear.*

1. INTRODUCTION

In theory of machines [1] their design starts to be analyzed by presenting machine in the form of structural kinematics scheme (machine skeleton). These kinematics schemes are composed of only two components – links performing relative movements and hinges – tribocouples (Fig.1). The basic problems in clever designed machines are the energy losses in tribocouples. Properly speaking it is this particular problem that makes tribology vital. By singling out a machine (mechanism) from environment by its material outer bounderies we attribute the meaning of system to it. The principle machine subsystem possessing basic functional sense of interconnection elements or movement (energy) transformation objects are friction couples – tribosystems. It is natural that in relation to tribosystems machines constitute tribosupersystems.

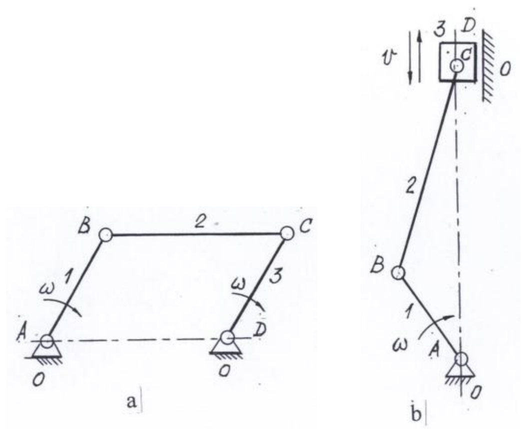

Figure 1. Elementary machines – the simplest lever mechanisms: a) hinge parallelogram; b) crank-type and connecting rod mechanism

2. GENERAL REGULARITIES OF TRIBOSYSTEM EVOLUTION (TRIBOCONTACT)

The study of tribosystem evolution regularities [2] demonstrate that the whole area of tribosystem evolution (Fig.2) can be divided into to characteristic stages – the stage of rinning-in, when preparation of size and structure of friction volume to forming critical equilibrium state takes place and a proper stage of compatible friction, embracing a wide spectrum of possible adapted (optimum) friction structures.

Tribosystem evolution, presented in the form of diagram (Fig.2) has adaptive-dissipative character (1)-(9) and reflects competitive (double) nature of friction.

Evolution curve has a set of principle points (1,2,3,4,5) of transition tribosystem states [2] which strictly obey balanced principle of friction; among these points there exist most characteristic areas of tribosystem behavior reflecting general properties of its non-linear dynamics.

Thus it is possible to see the following conditionly designated points and stages: 0-1 – the area of static friction and deformation strengthening; 1-2 – the area of pumping of excessive energy; 2 the point of seizure and transition of outer friction into the inner one (critical non-stability); 2-3 - the area of forming dissipative structures (formation of heat fluctuation in the friction volume); 3 – the point of minimum compatibility (maximum frictionness); 1-2-3 –the area of compatibility; 4 – the point of wearlessness (anomalous-low friction); 5 – the point of thermal seizure (grip).

An ideal tribosystem evolution is symmetrical. The process starts and finishes in areas of elastic behaviour. Between them there exists a plastic maximum of friction (a strongly-agitated state) as a condition of selforganization and adaptation.

Tribosystem's run in the area of the first stage is unstable and not expedient and associated with a high level of tribosystems damage up to catastrophic one (point 2) – grip and possible score. The area of normal tribosystem operation on the other hand, the area of compatible [3] (adapted [4]) friction which is characterized with the normal level of wear, corresponding to natural and optimum-minimum (as to the wear) reaction of friction volumes to the outer impact (load, enviroment).

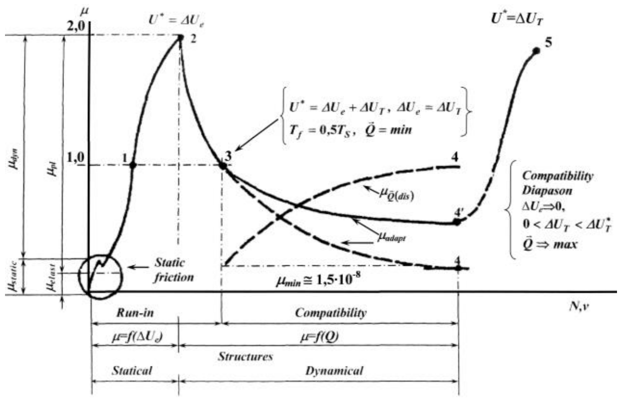

Figure 2. Structural-energy diagram of evolution for rubbing surfaces [2]. In the Figure U_T the change of heat component of internal energy of friction volume being deformed; v the speed of sliding in a friction couple. An asterisk designates critical (limit) friction parameters

3. ABOUT TWO COEFFICIENTS OF FRICTION OF COMPATIBLE FRICTION

The state of any tribosystem in conditions of compatible friction can be evaluated by friction coefficient, which within the frame of energy balance friction equation has the form:

$$adapt \quad dis_{\vec{Q}} \quad \frac{U_e}{N\ l_f} \quad \frac{\vec{Q}}{N\ l_f}$$

$$\frac{S_U}{S} \quad \frac{\vec{S}_Q}{S} \quad D_{TS} \quad O_{TS} \quad 1{,}0, \qquad (1)$$

where $U_e \quad V_f \quad u_e \quad V_{adapt} u_e$ - the change of latent energy within deformed friction volume; $\vec{Q} \quad V_f \vec{q} \quad V_{dis} \vec{q}$ - the heat friction effect in the form of dynamic dissipation energy; u_e, u_e - density change of latent energy and its critical magnitude in the contact volumes; V_f - critical volume of compatible (equilibrium) friction; $adapt$; $dis_{\vec{Q}}$ - adaptive (Leonardo da Vinci) friction coefficient and dynamic component of dissipative friction coefficient; S_U ; $\vec{S}_Q$; S - structural (configuration), inertia and critical enthropies of tribosystem; N ; l - normal load and friction way; D_{TS} ; O_{TS} - general parameters of disorder and order of elementary tribosystem (contact volume).

In this equation an integral parameter of state (resistance to movement and damageability) is an adaptive friction coefficient $_{adapt}$ of compatible friction. It is connected by enthropies relation $_{adapt} \quad S_U / S$ and so is a probability parameter non operationability state ("annigilation" of outer relative movement owing to accumulation of internal potential energy of different defects and damages of structure), damageability of tribosystem (contact):

$$_{adapt} \quad \frac{U_e}{N \;\; l_f} \quad \frac{S_U}{S} \quad Desorder. \qquad (2)$$

A dissipative coefficient of compatible friction on the other hand $_{dis_{\vec{Q}}}$ in this case also is an integral parameter of state (assistance to movement, i.e. capacity for work). It is connected by enthropies relation $_{dis_{\vec{Q}}} \quad \frac{\vec{S}_Q}{S}$ and so is a parameter of tribosystem normal operation probability (assistance to relative surfaces movement) or efficiency coefficient of tribosystem:

$$_{dis_{\vec{Q}}} \quad \frac{\vec{Q}}{N \;\; l_f} \quad \frac{\vec{S}_Q}{S} \quad Order. \qquad (3)$$

4. ABOUT DISSIPATIVE COEFFICIENT OF COMPATIBLE FRICTION AS AN EFFICIENCY COEFFICIENT OF TRIBOSYSTEM

Efficiency coefficient of mechanism (machine), possessing n tribosystems in succession can be determined by a well known formula for efficiency coefficient of mechanisms connected in sequence [1]:

$$_n \quad _1 \quad _2 \quad _3 \cdots \; _n \quad \frac{A_1}{A_{engine}} \; \frac{A_2}{A_1} \; \frac{A_3}{A_2} \quad \frac{A_n}{A_{n \;\; 1}} \quad \frac{A_n}{A_{engine}}.$$

Taking into account that each tribosystem (hinge) possesses a efficiency coefficient of its own by a relation of energy at the exit of tribosystem to energy at its entrance we obtain:

$$_n \quad _{dis_1} \quad _{dis_2} \quad _{dis_3} \cdots \; _{dis_n}$$

$$\frac{\vec{Q}_{dis_1}}{A_{engine}} \; \frac{\vec{Q}_{dis_2}}{\vec{Q}_{dis_1}} \; \frac{\vec{Q}_{dis_3}}{\vec{Q}_{dis_2}} \quad \frac{\vec{Q}_{dis_n}}{\vec{Q}_{dis_{n \;\; 1}}} \;, \qquad (4)$$

$$\frac{\vec{Q}_{dis_n}}{A_{engine}} \quad \frac{^{mach}}{_n}$$

where $\vec{Q}_{dis_n}$ - system energy at the exit, i.e. work which an operation system is capable to perform (power at the exit); A_{engine} - the work of outer forces (power at the entrance).

Thus, the general mechanic efficiency coefficient $_n$ of mechanism (machine), with n tribosystems arranged in sequence is equal to product of dissipative friction coefficients of separate tribosystems (tribosubsystems) $_{dis_i}$, making one general tribosupersystem – mechanism (machine). Here the whole machine may be characterized by some generalized dissipative friction coefficient of a machine - $^{mach}_{dis} \quad ^{mach}_{n}$ [2].

5. THE RULE OF NATURAL MACHINES AS A TRIBOSUPERSYSTEM

It is known that enthropy of any thermodynamic system equals the enthropies sum of its separate parts (subsystems), i.e. additive magnitude. Since relative critical (configurative) enthropy of tribosystem is equal to unit, then the number of tribosystems in a machine (complex system) determines in essence the machine number n_{mach} - the degree of its complexity or perfection. If we take into account that coefficients of compatible friction of separate tribosystems of machine in balance of each separate tribosystem is always less than a unit, and a machine number is always equal to a whole number then sums of both adaptive friction coefficients $_{adapt_i}$ and dissipative friction coefficients $_{dis_{\vec{Q}} \; i}$ of a machine (tribosupersystem) must be also equal to whole numbers.

Here we can deduce the first conclusion a machine possesses precisely attributes of machine when the sum of adaptive coefficients of compatible friction of its tribosystems comes to be equal to unit:

$$\overset{n}{\underset{1}{}} \; adapt_i \quad 1{,}0 . \qquad (5)$$

As a consequence, a mechanism (machine) is a device where a sum of adaptive coefficients of compatible friction (relative structural (configurative) enthropies of tribosystems) is equal to a unit:

$$\overset{n}{\underset{1}{}} \; adapt_i \quad \overset{n}{\underset{1}{}} \frac{S_{U_i}}{S} \quad {}^{mach}_{U} \quad 1{,}0 . \qquad (6)$$

It follows that a sum of dissipative coefficients of machine tribosystems or relative rotation-oscilation (inertia) enthropies of dissipative structures [2] is equal to the machine number n_{mach} minus a unit:

$$\overset{n}{\underset{1}{}} \; dis_{\vec{Q}\,i} \quad \overset{n}{\underset{1}{}} \frac{\vec{S}_{Q_i}}{S} \quad {}^{\to mach}_{Q} \quad n_{mach} \quad 1 \qquad (7)$$

6. INTERPRETATION OF MACHINE RULE IN THE ASPECT OF WEAR

Since dissipative coefficient of compatible friction $dis_{\vec{Q}}$ constitutes ability of dynamic dissipation to facilitate movement then it follows that the sum of dissipative machine friction coefficients $dis_{\vec{Q}\,i}$, equal to a whole number, is an index of capacity for work or some parameter of machine reliability P :

$$\overset{n}{\underset{1}{}} \; dis_{\vec{Q}\,i} \quad P \; . \qquad (8)$$

On the other hand, the sum of adaptive coefficients of compatible friction $adapt_i$ is a characteristic of resistance to movement within the whole machine (accumulated internal potential energy). As it follows from the above analysis, magnitude $adapt_i$ in a machine is always equal to a unit and it determines essence of every machine. Parameter of non-capacity for work (degradation of outer relative movement) in a machine (system) is not equal to zero. The sum of probabilities of tribosystems states (failures) in a machine is equal to a unit:

$$\overset{n}{\underset{1}{}} \; adapt_i \quad O \quad 1{,}0 . \qquad (9)$$

According to the model of moving critical friction volume [5] this result is to be interpreted in the following way: in a nominal (natural) machine at every particular moment there collapses being in a limiting state one elementary tribosystem – the value of wear is equal to the volume of one equilibrium contact [2]. It is precisely in this way we can enterpret condition (9). Friction coefficient $adapt$ equal to a unit [2] characterizes condition of limiting energy state of equilibrium friction contact (of elementary tribosystem).

Here this wear distributed along all tribosystems of a machine constitutes gradual failure which gradually moves tribosystems closer to a limiting wear. This wear concentrated in one tribosystem is to be interpreted as a sudden failure. For example, failure of the first tribosystem – fixed member of kinematic chain. Equality of friction coefficient to a unit for this tribosystem means its critical state. According to a diagram (Fig.2) tribosystem in point 1 got into the area of developing seizure, then score.

Thus, in absolute units the general index of machine functioning can be presented by machine member n_{mach}, which is the sum of indexes of capacity for work (Order) and non-capacity for work (Desorder) of tribosystems of
machine.

$$\overset{n}{\underset{1}{}} \; dis_{\vec{Q}\,i} \quad \overset{n}{\underset{1}{}} \; adapt_i \quad n_{mach} \quad 1 \quad 1 \; .$$

$$Order \quad Desorder \quad n_{mach} . \qquad (10)$$

In relative units the machine serviceability indexes may be presented in a familiar state reflecting principles of states relativity – Order and Disorder of tribosystems constituting machine

$$\frac{\overset{n}{\underset{1}{}} \; dis_{\vec{Q}\,i}}{n_{mach}} \quad \frac{\overset{n}{\underset{1}{}} \; adapt_i}{n_{mach}} \quad \frac{n_{mach} \; 1}{n_{mach}} \quad \frac{1}{n_{mach}} \quad 1 \qquad (11)$$

or principles of operation probability (reliability) and probability of failure (damageability) of system

$$P(t) \quad O(t) \quad 1. \qquad (12)$$

Where

$$\frac{\overset{n}{\underset{1}{}} \; dis_{\vec{Q}\ i}}{n_{mach}} \quad P(t), \qquad (13)$$

and

$$\frac{\overset{n}{\underset{1}{}} \; adapt_i}{n_{mach}} \quad O(t). \qquad (14)$$

It follows from these relations that probability of failure free operation of ideal machine grows with growing member of tribosystems (the degree of complexity or perfection), since absolute (instant) failure magnitude always equals collapse (limiting state) of one elementary tribosystem and, consequently, probability of failure diminishes.

7.TRIBOSUPERSYSTEM FRICTION COEFFICIENTS

In a most general case it is possible to write down the following relations for machine (complex system):

$$mach \quad \overset{n}{\underset{1}{}} \frac{S_i}{S} \quad \frac{S_1}{S} \quad \frac{S_2}{S} \quad \frac{S_3}{S} \quad \ldots \quad \frac{S_n}{S} \quad n_{mach};$$

$$\underset{U}{mach} \quad \overset{n}{\underset{1}{}} \frac{S_{U_i}}{S} \quad \frac{S_{U_1}}{S} \quad \frac{S_{U_2}}{S} \quad \frac{S_{U_3}}{S} \quad \ldots \quad \frac{S_{U_n}}{S} \quad 1{,}0$$

$$\underset{Q}{\rightarrow mach} \quad \overset{n}{\underset{1}{}} \frac{\vec{S}_{Q_i}}{S} \quad \frac{\vec{S}_{Q_1}}{S} \quad \frac{\vec{S}_{Q_2}}{S} \quad \frac{\vec{S}_{Q_3}}{S} \quad \ldots \quad \ldots \frac{\vec{S}_{Q_n}}{S} \quad n_{mach} \quad 1{,}0;$$

$$mach \quad \underset{U}{mach} \quad \underset{Q}{\rightarrow mach} \quad n_{mach}. \qquad (15)$$

Here S_i, S_n - enthropies of i and n machine and hinges numbers involved in it. In this connection tribosystems.

It is expedient to attribute to these relations the meaning of the most characteristic equations of machine. Here parameters $mach$, $\underset{U}{mach}$, $\underset{Q}{\rightarrow mach}$ - may be regarded as some generalized coefficients of machine friction.

8. TRIBOLOGICAL STRUCTURAL LEVELS OF NATURAL MACHINES

Information mentioned above about generalized properties of machines (tribosupersystems) allows to single out and regard some equally characteristic indexes of ideal (nominal) machines, i.e. machines, possessing optimum – natural properties. It follows from the rule $adapt_i \quad 1{,}0$ that not all digital values of adaptive coefficients of compatible (optimum) friction $adapt_i$ may in sum give unit, but only quite definite ones (Table 1).

Table 1. Possible set of natural tribosystems forming a machine (tribosupersystem)

$adapt_i$	$dis_{\vec{Q}\ i}$	$n_{mach_i} \quad \frac{1}{adapt_i}$
0,5	0,5	2
0,25	0,75	4
0,2	0,8	5
0,1	0,9	10
0,05	0,95	20
0,04	0,96	25
0,025	0,975	40
0,02	0,980	50
0,01	0,990	100
0,005	0,995	200
0,004	0,996	250
0,0025	0.9975	400
0,002…	0,998…	500…

And so on.

As it follows from Table 1, there exist a set of nominal (natural) tribosystems and correspondingly a set of natural machines (tribosupersystems). The whole diversity of tribosystems made by man should be regarded as real (constructed) tribosystems and machines.

9. THE RULE OF MACHINES TRIBOSYNTHESIS

In the theory of mechanisms and machines in the part concerning their making from the simplest constituents – links and elements, L. Assur rule [1] is well known Table 2, according to which the simplest level mechanisms obey the rule: relationship between the number of links n and link elements (hinges) p_5 in an attached to the leading link (the first class mechanism (Fig.3)) is equal to: $p_5 \quad 3/2 \; n$.

So any synthesized mechanism possesses discrete levels of links creating the rule of tribo-optimal machine $\quad adapt_i \quad 1{,}0$ with the rule of quantitative structural machine design has a considerable scientific and practical interest.

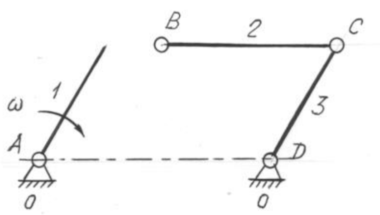

Figure 3. Scheme of kinematic chain of hinge parallelogram where link 1 and fixed member A – is the first class mechanism and the joined Assur group of the second class in the form of links 2 and 3 and hinges B, C, D

Table 2. Choice of friction coefficients in tribosystems for mechanisms (machines).

№	n	p_5	n_{mach}	$\overset{n}{\underset{1}{}} \; adapt\ i \quad 1{,}0$
1	2	3	4	0,25×4=**1,0**
2	4	6	7	0,05+0,25+(0,2×2)+(0,1×3) =**1,0**
3	6	9	10	0,1×10=**1,0**
4	8	12	13	(0,05×8)+0,2+(0,1×4)=**1,0**
5	10	15	16	0,05×12)+(0,1×4)=**1,0**
6 …	12 …	18 …	19 …	0,1+(0,05×18)=**1,0…**

Table 2 presents digital values of friction coefficients for friction couples of mechanisms, designed according to L. Assur rule. As it is seen, the calculated values of friction coefficients (Table 1) of optimal machines allow to forms tribo-optimal (nominal) machines. The rule of unit mentioned above accomplishes for any combination of links and hinges number within L. Assur model for flat mechanisms.

Possessing from digital regularities shown above, it is possible to construct and consider structural levels of natural (optimal) machines tabulated in Table 3.

10. ABOUT CAPACITY FOR WORK OF COMPLEX SYSTEM – TRIBOSUPERSYSTEMS

In real practice [6,7] capacity for work of complex systems is evaluated by probability of failure free operation as a product of subsystems probabilities:

$$P(t) \quad P_1(t)\ P_2(t)\ P_3(t)...P_n(t)\,. \qquad (16)$$

And it is believed that reliability of complex systems even with the same reliability of each subsystem $P(t) \quad P_i^n(t)$ drops abruptly. But this conclusion is not one – valued and needs analysis from physics and essential positions.

Really, if we just increase number of subsystems with equal probability of failure free operations of subsystems, then opinion [6,7] is supported. But if we increase the number of subsystems according to structural-hierarchical model (Table 3) with the corresponding lead of probability of dissipative friction coefficient and diminishing probability of non-capacity for work (adaptive friction coefficient) of each subsystem (Table 3) when we have the growth of probability for the whole system failure free operation (machine efficiency coefficient).

Let us take for example crank-rod mechanism with 4 hinges. According to Table 3 an adaptive coefficient of friction equals 0,25 and dissipative one – 0,75. Efficiency coefficient of such elementary machine equals $0{,}75^4 \quad 0{,}316$. Now it takes these friction coefficients, correspondingly 0,025 and 0,975. Here we get over to a new leading structural friction level. In this case efficiency coefficient of such tribosynthesized (constructed) machine will equal $0{,}975^4 \quad 0{,}9367$.

The calculation results presented in Table 3 convincingly demonstrates that probability value of failure free operation (reliability) of subsystems joined by common operation starts to increase with the increase of tribosystems (subsystems) member and sufficiently quickly reach some stable level equal to 0,367. On the other hand, probability of system capacity for work $P(t)$ constantly grows (wear aspect). The level of constancy $P(t)$ of complex systems as it follows from the value of reversed $P(t)$ possesses specific and deep physics meaning, since $\frac{1}{P(t)}$ constitutes global constant – limiting number $\mathbf{e}$. Since parameter $P(t)$ is nothing but product of dissipative friction coefficients of machine tribosystems or machine efficiency coefficient [2], then we should speak about constant character of efficiency coefficient of all natural machines. Really, all natural machines possess the same efficiency coefficient.

As it has been said above, if we form a system from subsystems of Table 1, then increase of subsystems number does not lead to diminishing reliability parameter, but on the contrary it takes place an increase of this parameter and its tendency to some constant value $\mathbf{e}$. Analysis of quantitative attributes of natural machines (Table 3) demonstrates [2] that equation of such natural or nominal machine may be an equation determining the principle of structuring limitation.

$$P(t) = \frac{1}{\mathbf{e}} = \mathbf{e}^{-1} \quad (17)$$

or

$$P(t) = \frac{1}{\left(1+\frac{1}{n}\right)^{n}} \approx \left(1-\frac{1}{n}\right)^{n}. \quad (18)$$

Substituting machine number n_{mach} for number n tending to infinite (non-limiting) increase, which characterize the number of its tribosystems (subsystems) we get an equation of ideal or nominal machine

$$P_{mach}(t) = \frac{1}{\left(1+\frac{1}{n_{mach}}\right)^{n_{mach}}} \approx$$

$$\approx \left(1-\frac{1}{n_{mach}}\right)^{n_{mach}} \approx \frac{1}{\mathbf{e}} = const. \quad (19)$$

Since value $P_{mach}(t)$ is nothing but value of machine efficiency or the efficiency coefficient η_{mach} (Table 3) [2], then equation of the machine gets naturally objective or physics meaning:

$$P_{mach}(t) = \eta_{mach} = \frac{1}{\left(1+\frac{1}{n_{mach}}\right)^{n_{mach}}} \approx$$

$$\approx \left(1-\frac{1}{n_{mach}}\right)^{n_{mach}} \approx \frac{1}{\mathbf{e}} = const. \quad (20)$$

Thus, when making complex systems from units composing this system, we should speak not about diminishing reliability of machine operation at increasing subsystems number, but about tending this value which is nothing but system efficiency to some characteristic number $\mathbf{e}$, which is in its turn a characteristics of system – of nominal machine or tribosupersystem as such. It follows from Table 3 that all nominal, i.e. natural machines possess equal efficiency and an increase of complexity degree (perfection) of natural systems is determined by their tendency to a state with universal constant.

11. SYNOVIA FRICTION COEFFICIENT OF NATURAL MACHINES

To check the calculated set of natural machines (Table 2,3) it is necessary to study real living machines, e.g. structural, kinematic schemes of man and horse. These structural kinematic schemes are skeletons of man and horse. The basis of these skeletons for kinematic couples: links – bones and tribopairs – joint hinges.

According to encyclopaedia information [8,9] human skeleton is composed of 270 bones in the early age and of 220 bones in mature age. The horse skeleton is composed of 252 bones. As it is seen this number of links (n_{mach}) in these living machines correspond to a calculated set of natural machines with the machine number $n_{mach} \approx 250$. This result allows to assess the value of friction coefficient of synovial liquid of joint hinges of living organisms (machines).

From Table 3 we have for n_{mach} 250 the value of adaptive friction coefficient equal to $_{adapt}$ $0{,}004$. This value should be taken for synovia friction coefficient. Modern tribology treats this level of friction coefficient as the level of superlubrication.

Naturally if we consider that friction in living machines has the most optimal, i.e. perfect level then quantitative level of the most perfect lubrication determined by modern tribology should be acknowledged as objective one.

Table 3. Natural machines structural levels

ad_i S_U	dis_i $\vec{S}_Q$	n_{mach}	$S_Q^{n_{mach}}$ $P(t)$	$\frac{1}{P(t)}$	$P(t)$ $\frac{n_{mach} \quad 1}{n_{mach}}$
0,5	0,5	2	$0{,}5^{2}$=0,25	4	0,5
0,25	0,75	4	$0{,}75^{4}$=0,316406	3,16049	0,75
0,2	0,8	5	$0{,}8^{5}$=0,32768	3,05175	0,8
0,1	0,9	10	$0{,}9^{10}$=0,348678	2,86797	0,9
0,05	0,95	20	$0{,}95^{20}$=0,358486	2,789509	0,95
0,04	0,96	25	$0{,}96^{25}$ =0,360396	2,774725	0,96
0,025	0,975	40	$0{,}975^{40}$=0,363232	2,753061	0,975
0,02	0,980	50	$0{,}980^{50}$=0,364169	2,745977	0,980
0,01	0,990	100	$0{,}990^{100}$=0,366032	2,732001	0,990
0,005	0,995	200	$0{,}995^{200}$=0,366957	2,7251088	0,995
0,004	0,996	250	$0{,}996^{250}$=0,367142	2,7237417	0,996
0,0025	0,9975	400	$0{,}9975^{400}$=0,367419	2,7216874	0,9975
0,002	0,998	500	$0{,}998^{500}$=0,367511	2,7210051	0,998
0,001	0,999	1000	$0{,}999^{1000}$=0,367695	2,719645	0,999
…					
0,0001	0,9999	10000	$0{,}9999^{10000}$=0,367861	2,718418	0,9999
…					
0,00001	0,99999	100000	$0{,}99999^{100000}$=0,367877	2,718295	0,99999

And so on.

12. THE RULE OF REAL MACHINES FORCING

As we see above (Table 3) the whole set of natural machines tends to some state where many living systems (machines) have a constant efficiency coefficient.

Real machines designed by man are made forced for larger operation, i.e. for larger efficiency coefficient.

The first way of making forced (heavily loaded) machine – is its tribological synthesis by transiting friction to a lower hierarchy level – diminishing adaptive friction coefficient (from $_{adapt}$ $0{,}25$ to $_{adapt}$ $0{,}025$), e.g. four-link crank-rod mechanism (one cylinder ICE). Here we may enlarge efficiency coefficient a great deal (see above - $^{4}_{diss}$ $0{,}975^{4}$ $0{,}9367$)). Here the machine rule is violated, i.e. we have $_{adapt\,i}$ $1{,}0$, but by means of forcing loading N and speed v (see diagram, Fig. 1) the machine rule $_{adapt\,i}$ $1{,}0$ is restored, and relative wear resistance increases.

The second way – is joining together the simplest mechanisms with the increased efficiency coefficient – transition from one cylinder ICE to multi-cylinder ones, e.g. to 10-

cylinder ICE (n_{mach} 40). Here efficiency coefficient diminishes to practically former level corresponding to 40-links mechanism ($^{4}_{diss})^{10}$ $(0{,}975^4)^{10}$ $0{,}363$. At the same time we see an increase of aggregated machine horse-power and relative wear resistance.

Further follows a new transition to a lower adaptive friction coefficient (Table 3), i.e. $_{adapt}$ $0{,}004$ correspondingly increases loading level N or speed v, increases relative wear resistance, efficiency coefficient:

$$^{40}_{diss} \quad 0{,}996^{40} \quad 0{,}8518.$$

If $_{adapt}$ $0{,}002$ $0{,}001$, machine efficiency coefficient equals $^{40}_{diss}$ $(0{,}998 \quad 0{,}999)^{40}$ $0{,}923$ $0{,}96$, etc.

13. CONCLUSION

The number of machines (degree of complexity) is determined by the number of kinematic pairs (tribosystems) of its kinematic chain.

The rule of machine (optimal) is determined by the sum of adaptive and dissipative friction coefficients of compatible tribosystems.

In a system-compatible, natural machine the sum of the adaptive friction coefficients of the kinematic chain joints must be equal to unit.

The rule $\overset{n}{\underset{1}{}} \; adapt_i$ $1{,}0$ shows that in any machine the operation of its tribosystems will strive for implement this rule. Exceeding this rule leads to increased damage to the machine.

All natural machines (living systems) have the same efficiency of 0.367.

To improve the performance of the machine and at the same time its reliability (probability of failure) should decrease the values of the coefficients of the adaptive friction of tribopairs taking into account the structural levels (tab.3) compatible friction parameters. It is to this that the essence of the tribological factor of reliability of machines is reduced.

Real, forced machines have a rule of the machine in the form of - $\overset{n}{\underset{1}{}} \; adapt_i$ $1{,}0$. This ensures the lowest wear of the machine tribosystems with an increased efficiency.

The coefficient of friction of synovia is about 0.004 and below. This coefficient of friction characterizes the super lubrication of the hinges of living systems (natural machines).

REFERENCES

[1] I.I. Artobolevsky: *Theory of Mechanisms and Machines* (in Russian), Nauka [Science], Moscow, 1975.

[2] S.V. Fedorov: Nano-structural standard of friction and wear, Tribology in Industry, Vol. 40, No. 2, pp. 225-238, 2018.

[3] N.A. Bushe, V.V. Kopyt'ko: *Compatibility of Friction Surfaces* (in Russian), Nauka [Science], Moscow, 1981.

[4] B. I. Kostetsky, I.G. Nosovsky, A. K. Karaulov and oth.: *Surface Strength of Materials at Friction* [in Russian], Technik, Kiev, 1976.

[5] S.V. Fedorov: The model of the moving critical friction volume, Friction & Lubrication in Machines and Mechanisms, [in Russian], No. 4, pp. 3-7, 2010.

[6] M. N. Ivanov: *Machines Parts* [in Russian], High School, Moscow, 1998.

[7] D. N. Reshetov: *Machines Parts* [in Russian], Mechanical Engineering, Moscow, 1989.

[8] Skeleton. Great Soviet Encyclopaedia [in Russian], Vol. 23, Soviet Encyclopaedia, Moscow, 1976.

[9] Horse skeleton, available at: http://www.horse-of-ream.vsau.ru/inter/bone.html

Serbian Tribology Society

SERBIATRIB '19

16th International Conference on Tribology

Faculty of Engineering
University of Kragujevac

Kragujevac, Serbia, 15 – 17 May 2019

APPROBATION OF TRIBOMETER WITH SEPARATED INPUT AND OUTPUT SIGNALS IN INVESTIGATION EXTERNAL FRICTION DYNAMICS STEEL AND BRASS MATERIALS

G. M. ISMAILOV[1], A. E. TYURIN[2], V. E. MINEEV[3]

[1, 3]Tomsk State Pedagogical University, Tomsk, Russian Federation
[2]Saint-Petersburg National Research University of Information Technologies, Mechanics and Optics, Saint-Petersburg, Russian Federation
Corresponding author: gmismailov@rambler.ru

Abstract: *This investigation suggests a method used to determine the evolution of metallic wear and friction by sliding. The problem of external dynamics friction is investigated through the definition of the dynamic characteristics such as damping factor and natural frequency. Some certain automatic control methods were applied for sliding friction contact, including parametric identification, ARX simulation and Newton's dynamic equation. The suggested approach allows using amplitude-frequency characteristics to assess the dynamic factors (coefficients) under friction interaction. The research findings indicate that the proposed method allows monitoring the evolution of metallic wear and friction. The friction of steel moving over brass was taken as example.*

Keywords: *dynamic characteristics, friction interaction, input-output model, damping coefficient, cyclic movement.*

1. INTRODUCTION

In most practical friction systems, metal, fiber, composite alloys in sliding contact with metal alloys were need to predict faticulare changes. This problem can be implement by other ways, only some of them: vibration and noise controle, oil fouling and near friction area temperature inspection [1, 2].

However, the creation an accurate forecast based on friction model in present time is not simple task, due to the complexity of the processes occurring during frictional interaction [3–7]. In this work aims to study internal dynamics processes of evolution and determination of adaptive model in sliding contact.

Research friction units based on input-output model has been widely discussed. An important aspect of this approach is to find the damping and vibration properties for tribology system. Model input-output is used for handling of applied problems in automatic control theory. Using the identification process, the applying of equations with different grades allows to simulate various motions of interactions and even intermediate layers for 4 orders and higher [8–11].

2. FUNDAMENTAL PRINCIPLES OF INPUT-OUTPUT MOTION

Introduce system is convenient to consider from the perspective of input-output. Where are input parameters of dynamic characteristics – sliding speed, rolling velocity, force and pressure. Output parameters tribological system vibration and heating power dissipation. When the system is influenced, it is possible to trace the response of the system to external influences. The main consequences of the process – friction resistance, wear, generation of temperature at the friction surface, grip.

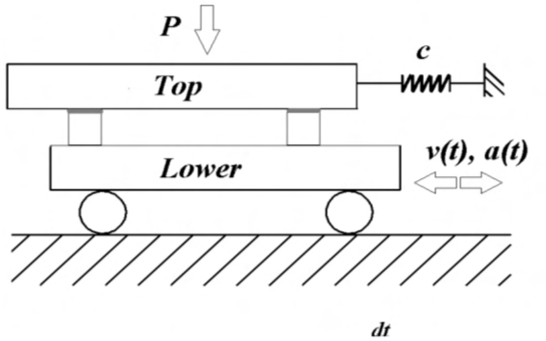

Figure. 1. Schematic diagram of the device operation and their components: P – loading, c – variable stiffness, $v(t)$, $a(t)$ – speed and acceleration of the given motion law

The result of the solution of the problem is the identification of the mathematical model presented in time or frequency domain. This model repeats adequate behaviour of the object.

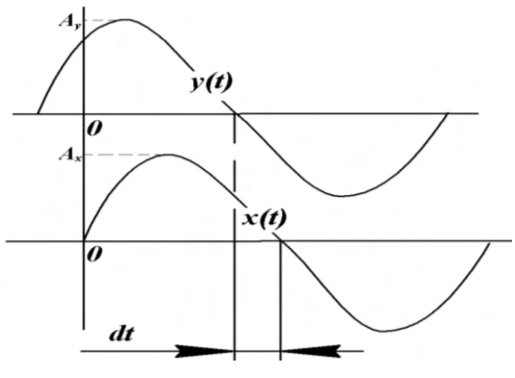

Figure. 2. The main mode of displacement curves, where dt is the phase shift, A_x, A_y are the oscillation amplitudes

Operating principle the "Tribal-T" device is shown in Fig. 1, realizing this concept, the device is intended for determining the friction coefficient, real-time process monitoring. The main difference from analogs of friction and wear consists from the free movement of the upper sample relative to lower.

On (Fig. 1, 2), the phase shift curve of the displacement curves is shown, the lower sample *x(t)* moves, the upper sample *y(t)* is delayed due to the spring elasticity and frictional forces affecting its movement. When the unit is operating in this mode, relative motion of the samples with characteristic sliding friction is observed [8].

2.1 Experimental apparatus

The experimental tribological complex "Tribal-T" (Fig. 3) for determining the tribological and mechanical properties of materials the idea of mutual measurement of displacements was realized. As an analogy was used device for rub testing, which was described in the inventor's certificate [12, 13].

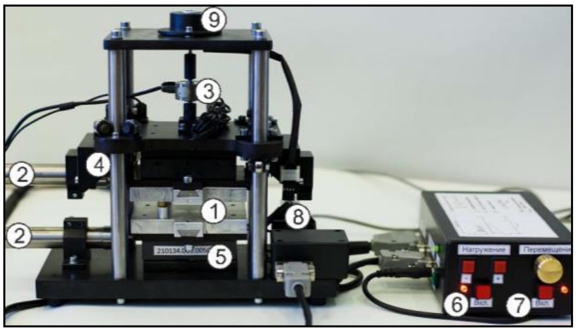

Figure 3. Appearance the "Tribal-T" tribometer and its main components

Lower specimens are in the cyclic reciprocating motion, driven by the external actuator. Upper specimens are in motion due to impact of frictional force. The tribometer is equipped by the displacement and pressure sensors, which allow tracking the absolute movement of specimens in the digital signals.

On Figure 3 shows main parts is *1* – specimens; *2* – displacement sensors; *3*, *4* – load sensors in normal and radial directions; *5* – precision roller slide tables; *6*, *7* – equipment control board of load and velocity; *8* – cyclic linear actuator; *9* – load actuator.

These measured signals are the inputs and outputs of the investigated system. The suggested approach provides by "Tribal-T" tribometer, which have a sliding contact and holders for investigated specimens (Fig. 4).

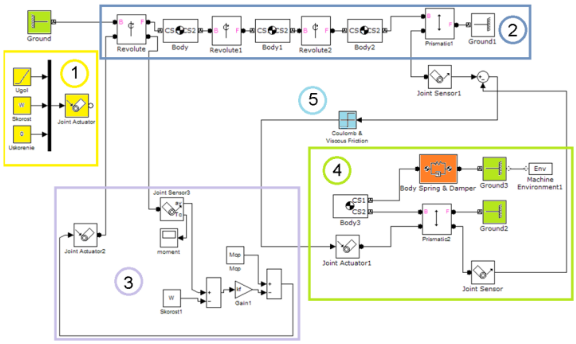

Figure 4. Simulink Dynamic model of Tribometer with block of variable viscous: *1* – angles, speeds and accelerate sensors; *2* – crank-slider mechanism used the upper linear slider; *3* – input force and speed impact for motion's law; *4* – crank-slider mechanism used of the lower linear slider; *5* – block of dry or viscous friction

2.2 Mathematical description of identification system

In the general case, the input and output signals of system "Tribal-T" can be described by differential equation [8, 14]. The n is equation order, parameters a_0, a_1 … a_n are selected based on the "input" (so-termed parametric identification), b_0, b_1 … b_n described "output", $x^{(n)} = d^n x/dt^n$ conditional upon $n > m$ are given:

$$a_0 x^{(n)} \quad a_1 x^{(n \quad 1)} \quad ...a_n x \qquad b_0 y^{(m)} \quad b_1 y^{(m \quad 1)} \quad ...b_m y \tag{1}$$

However, solution the equation starts with the account the order of differentiation, providing a physical interpretation. When n = 2 we get a differential equation of second order of motion:

$$\frac{d^2x}{dt^2} \quad 2n\frac{dx}{dt} \quad w_0^2 x \quad f(t) \tag{2}$$

Where: x – the input value, $f(t)$ – the output value, n – damping coefficient, which characterize a environmental resistance, w_0 – free-running frequency. Stress forces are located in the right side of the equation, a system behavior to the external stress on the side of the measuring system – on the left.

Numerical solution of system (1) find in the state space model for the second order dynamic characteristics will be obtained. The solution to this loss is based on the nonlinear autoregressive exogenous model (ARX). The basis of a mathematical model of a multi-dimensional system in the time domain is a vector-matrix form of a first-order system of differential equations, which is called the equation of state. The equation of state and structure completely describe the control object, the state vector contains object variables that uniquely describe its state.

The friction state-space model of the "Tribal-T" [4]:

$$x(t \quad Ts) \quad A \quad x(t) \quad B \quad u(t) \quad K \quad e(t), \qquad y(t) \quad C \quad x(t) \quad D \quad u(t) \quad e(t) \tag{3}$$

$$A \quad [2 \quad 2], B \quad [2 \quad 1], C \quad [1 \quad 2], \qquad K \quad [2 \quad 1], x(0) \quad [2 \quad 1] \tag{4}$$

Where: A – coefficient matrixs in state space; B – control coefficient matrix; C – coefficients matrix of the observer; K – noise matrix; $x(0)$ – initial condition; $Ke(t)$ and $e(t)$ – correlated stochastic processes. In the presence of stationarity, the matrix K selects an effective recursive Kalman filter [14].

3. EXPERIMENTAL APPROBATION AND DISCUSSION

This section presents the experimental approbation of mathematical primitive integral decision where input data it upper specimen's displacements and output lower specimen's displacements (Fig. 1). In sliding contact were studied specimen's from steel ShH15 (analogs: 1.3505, 100Cr6) and brass L90 (analogs: C22000, CuZn10). 10 samples with the same roughness (Ra 0.25) were prepared for the experiment.

Five tests were conducted at various time intervals: 30 min, 60 min, 90 min. Experiments were conducted in such a way that after each periodic interval of time, surface samples profiles were measured (Fig. 5). In each test series were recorded input $u(t)$ and output $y(t)$ data for the subsequent identification of the dynamical system [12].

In accordance with objectives of external dynamic, the following parameters have been found: *n* – damping factor, *w* – natural frequency. Figure 6 to display how changes in time periods damping factor and natural frequency. It may be noted, that under the experimental conditions of damping factors and frequencies of the natural vibrations are couple of competing parameters.

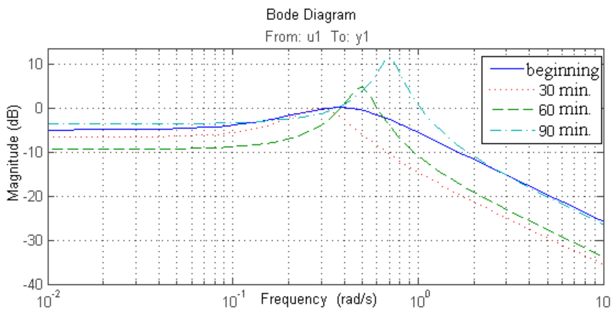

Figure 5. Bode diagram (amplitude characteristics) transfer functions at various time intervals as function of frequency: *1* – beginning, *2* – 30, *3* – 60, *4* – 90

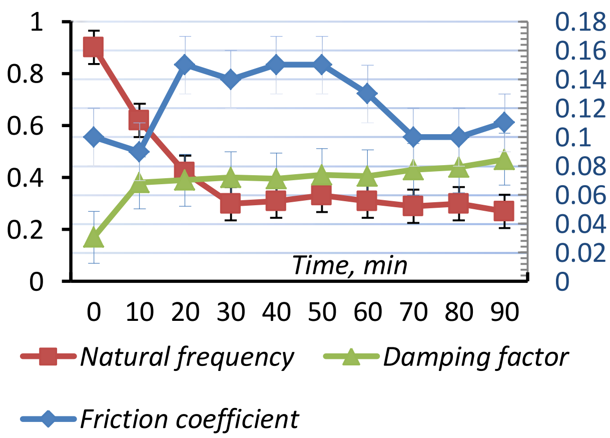

Figure 6. The diagrams show the variation in damping coefficient and natural vibration frequency (duration of the experiment 90 min)

This approach to the study of friction is useful in instrument making. In devices and mechanisms with moving parts made of brass and copper in contact with steel and metals. Reducing production costs for additional processing of rubbing surfaces can be eliminated knowing about the possibilities of self-working (self breaking-in) surfaces. The surface roughness at the level of Ra 0.25 corresponds to the finishing and semi-finishing milling or turning.

4. CONCLUSION

From the experiment, it is clear that the required breaking-in can occur in dry friction without additional effects. Over a period of time, the friction coefficient is aligned to a level of 0.12–0.1 and remains constant until the end of the experiment (Fig. 6).

The damping coefficient and the frequency of natural oscillations, respectively, tend to decrease in energy bursts in the contact. The system's damping increases and possible surges from surface geometry are reduced. The duration of the operation of such a friction pair in normal conditions can reach more than 5 000 Hours.

Further degradation of the contact will be associated with natural wear of the surfaces and a sharp violation of the geometry. The task of wear was not included in the scope of this work and will be considered further. Such a technique is not applicable for wear study, a variant of the experiment can be pin on disc of the installations in future experiment [10, 11].

REFERENCES

[1] A.V. Chichinadze et al.: *Fundamentals of tribology (friction, wear, lubrication)*, Mechanical Engineering, Moscow, 2001.

[2] A.E. Tyurin, G.M. Ismailov: Vibration-based diagnostics of self-sustained oscillations in tribo-couple PTFE-Alloys, in: *Composite materials constructions*, 2, pp. 58–64, 2013.

[3] F.P. Bowden, D. Tabor: *The Friction and Lubrication of Solids*, Clarendon Press, Oxford 2001.

[4] V.L. Popov: The Mechanics of Contact Interaction and Friction Physics. From Nanotribology to Earthquake, in: *Dynamics*: FIZMATLIT, Moscow, 2013.

[5] P. Kovalenko, S. Perepelkina, T. Korakhanov: Investigation of tribological properties of friction pairs duralumin – fluoropolymer used for design and manufacturing of biomechatronic devices, in: *Tribology in Industry*, IET 2017, Vol. 39, No. 2, pp. 192–197.

[6] S. Perepelkina, P. Kovalenko, R. Pechenko, K. Makhmudova: Investigation of the friction coefficient of various polymers used in rapid

prototyping technologies with different settings of 3D printing, in: *Tribology in Industry*, IET 2017, Vol. 39, No. 4, pp. 519–526, 2017.

[7] G.M. Ismailov: A Study of Flexible Cable Strength with Regard to Tribological Interaction of Its Elements, in: *Proceedings of the Institution of Mechanical Engineers, Part J: Journal of Engineering Tribology*, Vol. 233, No. 4, pp. 638–648, 2019.

[8] V.M. Musalimov, V.A. Valetov: *The dynamics of frictional interaction*, pp. 5–10, 2006.

[9] V. Musalimov, O. Dik, A. Tyurin: Energy parameter of discrete wavelet transform: an application to tribological and physiological signals, Scientific-technical Journal of Information Technologies, Mechanics and Optics, pp. 27–34, 2008.

[10] A.E. Tyurin, G.M. Ismailov, E.V. Beloenko, A.V. Baranov: Monitoring vibrations and microdisplacement for “pin on disc” tribology studies, Conf. Series: Journal of Physics, pp. 803, 2017.

[11] G.M. Ismailov, A.E. Tyurin: Experimental Study of Frictional Vibrations under Dry Friction Conditions, Tribology in Industry, IET 2018, Vol. 40, No. 3, pp. 392–400, 2018.

[12] G.M. Ismailov, A.E. Tyurin, Y.A. Vlasov: Device for the investigation of tribotechnical characteristics of materials, Pat. 2600080 Russian Federation. Priority as of September 9, 2015. Registered in the State Register. *Bul*. 2922.09.2016., Publ. October 20, 2016.

[13] G.M. Ismailov, A.E. Tyurin, V.M. Musalimov, Y.A. Vlasov, V.A. Metelitsa: Device for the investigation of tribotechnical characteristics of materials, Pat. 158916 Russian Federation, Cl. G01N 3/56. *Bul*. 2, publ. January 27, 2016.

[14] V. Dyakonov: *MATLAB. Analysis and modeling of systems. Special reference book*, Piter Publishing House, St. Petersburg, pp. 448, 2002.

Serbian Tribology Society

SERBIATRIB '19

16th International Conference on Tribology

Faculty of Engineering
University of Kragujevac

Kragujevac, Serbia, 15 – 17 May 2019

ON-LINE CONDITION MONITORING OF HYDRAULIC OILS – UNDERSTANDING THE RESULTS

Vito TIČ[1,*], Darko LOVREC[1]

[1]University of Maribor, Faculty of mechanical engineering, Maribor, Slovenia

*Corresponding author: vito.tic@um.si

Abstract: *On-line condition monitoring of hydraulic oils and other lubricants can not only protect the machine from sudden breakdowns, but can also be used as a tool for predictive maintenance of the machine. In order to monitor and track changes in hydraulic oil on-line the user should have good knowledge in complete hydraulic and monitoring system, such as sensors being used, operation of the hydraulic system, location and mounting of condition monitoring system, lubricant being used...*

In the first part the paper presents several sensors and quantities that are most commonly used to on-line measure the properties of hydraulic oils, such as temperature, viscosity, relative humidity, electrical conductivity, relative permeability and cleanliness class. Besides presenting the quantities paper also discusses potential miss-readings and inaccuracies of the sensors.

In the second part the paper presents and discusses several real case studies from on-line condition monitoring systems of hydraulic oils from industry. The study shows that some changes, such as increase of water content in hydraulic oil, can be detected on-line very reliable, whereas some other changes, such as increase or decrease of viscosity cannot be detected so easily and trustworthy.

Keywords: *lubricants, hydraulic oil, on-line condition monitoring, maintenance.*

1. INTRODUCTION

Latest trends in industrial applications are to increase machine's productivity and reliability and to minimize operating-costs and down-time of the machine. One of the ways to achieve these goals is the use of the predictive maintenance which is based on planned maintenance intervals and condition-based servicing. Due to a widespread availability of robust and cost-effective on-line sensors for measuring various fluid properties, latest developments deal with on-line oil condition monitoring to determine the condition of hydraulic system and fluid. This allows for maintenance work to be carried out based on the detected system condition.

However, measurement of the oil condition is much more complex then measurement of e.g. pressure or temperature. The oil condition cannot be determined with only one single parameter. Several parameters must be observed at the same time. For the best understanding and interpretation of the results we also have to track trends of these parameters.

2. ON-LINE MEASURED OIL PARAMETERS

Some of the most important physical and chemical changes in hydraulic oil, which can be detected using on-line sensors, are presented below.

2.1 Temperature

Temperature is certainly one of the basic and most important physical quantities, which requires continuous monitoring. Known fact is that the hydraulic fluids age much faster at high operating temperatures because of the accelerated rate of oxidation. It is believed that life expectancy of hydraulic mineral oil is halved for every 10 °C above 60 °C. Moreover, most of the other physical and chemical parameters of hydraulic fluid are highly dependent on the temperature. The temperature also influences viscosity, relative humidity, dielectric constant and electrical conductivity of the hydraulic fluid.

2.2 Viscosity

Also, the viscosity is very important physical property of mineral hydraulic oils because it affects the lubrication film and thus the friction and wear. The viscosity value is typically specified in a narrow band for a certain type of oil. However from oil to oil the viscosity might differ. From system and component view certain upper and lower threshold values for the operating viscosity are specified. Changes of the viscosity throughout the operation might result from oil deterioration and contamination with other oils respectively fluids. Thermal oxidation very often leads to an increase of the viscosity, whereas shearstress especially of long chain VI-improver-oils leads to a decrease of viscosity.

Viscosity measurement can be made by placing the quartz crystal wave resonator in contact with liquid. As the acoustic wave resonator supports a standing wave through its thickness the wave pattern interacts with electrodes on the lower surface (hermetically sealed from the liquid) and interacts with the fluid on the upper surface. Described measurement principle is very sensitive to surface contamination and formation of deposits, which is a common problem of most modern on-line sensors.

Hydraulic oil viscosity varies with pressure and temperature. Since the measurements take place at relatively low and constant pressure, the effect of pressure can be neglected. However, we should not ignore the impact of temperature. With increasing temperature the viscosity is sharply declining. In order to accurately determine the change of viscosity of hydraulic oil through its lifetime is therefore appropriate to take a baseline - the calibration curve, which shows the relationship between temperature and viscosity.

2.3 Relative humidity

Water is in practice one of the greatest threats to the hydraulic and lubricating oil. Lubricant film reduces the load and act as a catalyst in the processes of aging and degradation of oil. Water may be present in dissolved, emulsified or free form.

Capacitive sensors detect changes in relative humidity and show the percentage of saturation of the hydraulic oil. Oil is 100 % saturated if it contains the maximum amount of bound water at a certain temperature and pressure. In addition to a function of temperature and pressure, water solubility also depends on the chemical compatibility of the water and oil. Consequently, the level of saturation can significantly vary depending on the different base oils and various packages of additives [1].

For hydraulic systems is important to know the relative humidity, because it allows us to monitor the point of condensation from the moist when oil starts separating water droplets. This leads to the formation of mild emulsion, and, consequently, accelerated corrosion of components.

2.4 Electrical conductivity

The conductivity of a solution is a measure of its ability to conduct electricity. The electrical conductivity of a solution of an electrolyte is measured by determining the resistance of the solution between two flat or cylindrical electrodes separated by a fixed distance. An alternating voltage is used in order to avoid electrolysis. Typical frequencies used are in the range 1 to 3 kHz. The dependence on the frequency is usually small.

Specific fresh oil has its own characteristic conductivity, which is typically lower value. Because conductivity is oil specific it is a criterion for differentiating oils. Also the entry of foreign substances (solid/liquid) can be detected if such entry causes a change in conductivity. Thus oil changes, oil mixtures, and contamination can be detected.

In addition conductivity changes due to aging processes so that the course of aging can also be tracked based on conductivity.

2.5 Relative permittivity

The relative permittivity of the fluid is a measure of its polarity. Basic oils and additive packages with different chemistry and from different manufacturers can differ in polarity. Thus polarity of the fluid is a quality factor through which oil changes, oil mixtures and refreshing can be detected. Moreover, oils change their polarity during the aging process. It is also possible to monitor the trend of aging.

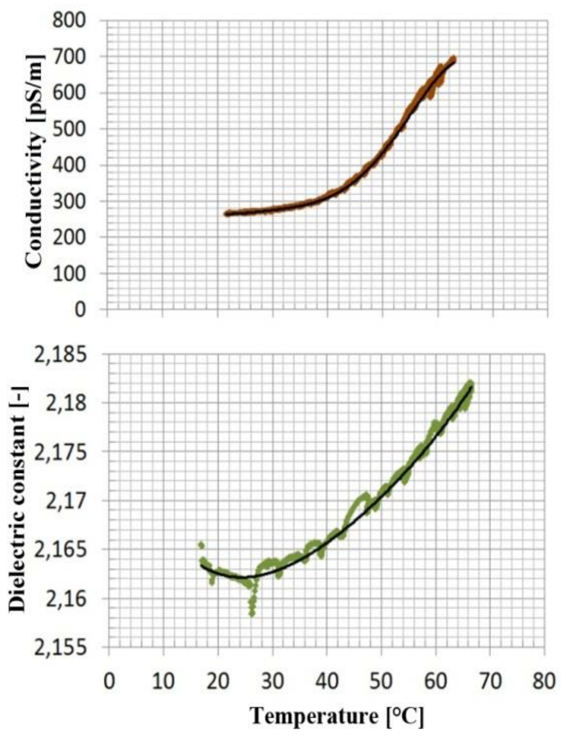

Figure 1. Temperature dependency of electrical conductivity and dielectric constant oil

Measurement of relative permittivity is based on a capacitive measurement transformer moistened with oil and is usually given as relative static permittivity or dielectric constant. Dielectric constant of the media is high, if its molecules are polar or highly polarized.

Figure 1 presents temperature dependency of electrical conductivity and dielectric constant for mineral hydraulic oil. Data shown on the figure were obtained experimentally and are further used to normalize temperature dependency of electrical conductivity and dielectric constant.

Like viscosity, the electrical conductivity and dielectric constant are also monitored at 40 °C to neglect the temperature effect on these two parameters. Since they cannot be always measured at 40 °C, they are normalized to 40 °C with post-calculation.

2.6 Cleanliness class

On-line measurement of particle contamination levels provides easy analysis of a machine's condition. Detecting failure mechanisms such as early detection of oil contaminants allows maintenance personnel to increase machine life and reliability.

The most widely deployed method today for determining fluid cleanliness is to use an automatic optical particle counter. There are a variety of instruments commercially available to optically count particles; from low-cost online optical particle counters, portable units for onsite use, to large, sophisticated lab-based instruments. However, all instruments, whether they be a hand-held unit or a full lab instrument use one of two methods, either a white light source, or more commonly today, a laser.

A sample of oil may contain a multitude of problems, which may interfere with the goal of accurately counting and sizing the solid particles. The most common problem is entrained air bubbles and water droplets, which scatter and block light, and are erroneously counted as particles by the optical automated particle counters. Without special sample preparation, an optical particle counter does not work well with fluid that is dark or fluids that are heavily contaminated with silt or soot. These conditions can produce so-called coincidence error, or in extreme cases may completely prevent the transmission of light.

3. REAL CASE STUDIES

A distinct advantage of on-line condition monitoring systems (Figure 2) is the continuous monitoring of individual fluids' parameters, thus knowing the oil condition at any time.

Figure 2. Industrial on-line oil condition monitoring system

In addition, any sudden changes are also detected (even an automatic SMS or E-mail alert can be triggered), whilst with off-line methods it cannot be. Figure 3 shows an example of on-line user interface of such on-line condition monitoring system.

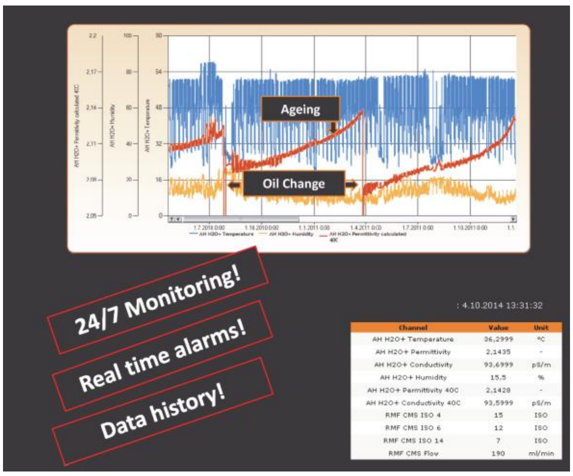

Figure 3. User interface of on-line condition monitoring system

Figure 4 presents detection of solid oil contamination. Our practical experiences show that there are many false alarms of oil contamination especially if the flow condition through the particle counter are unstable (i.e. bad installation of particle counter or at machine start-up phase). We have also noticed that larger water ingress can cause worse oil cleanliness class reading since water in free form (small droplets in oil) is detected as small particles. Thus, we should always monitor the relative humidity also.

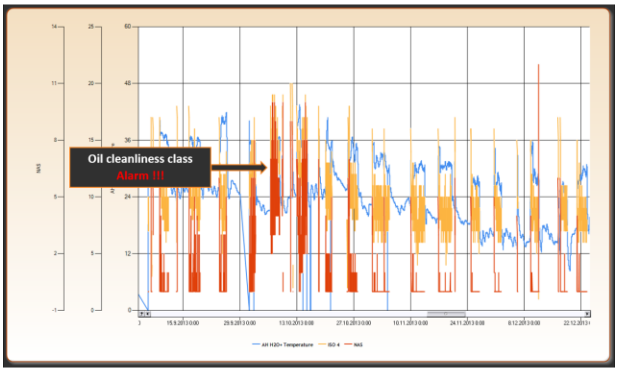

Figure 4. Detection of solid oil contamination (red)

Figure 5 presents detection of increased relative humidity (red) of oil because of water ingress due to damaged cylinder sealing. From our practical experiences the detection of increased relative humidity is often very reliable and even the smallest water ingress will increase relative humidity of oil. Humidity usually increases to 100 % very quickly, even at very small amounts of water. Since water ingress also increases electrical conductivity (yellow) and dielectric constant, we can use these two parameters to track water levels above 100 % relative humidity in oil.

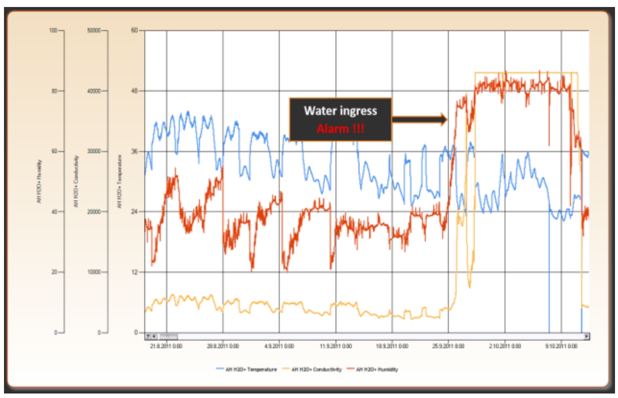

Figure 5. Detection of water ingress (red)

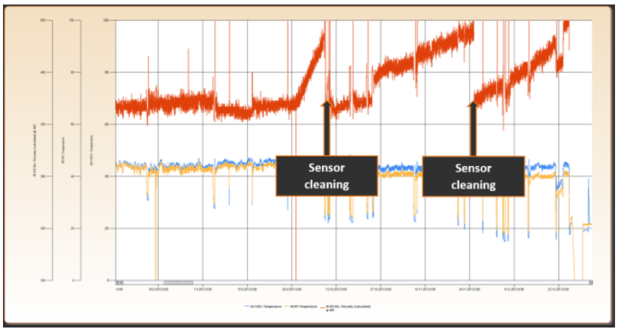

Figure 6. Miss-readings of viscosity (red)

Figure 6 presents miss-readings of viscosity measurements (red) of oil because of deposits of oil sediments on the sensor head. Since the vibrating piezo-electrical surface of the sensor head is contaminated with these sediments, the natural frequency of the measuring head is changed and thus, the viscosity is not measured correctly. The figure also presents two occurrences of sensor head cleaning which help maintain correct operation of the sensor. These miss-readings usually occur after 1 month or even earlier.

4. CONCLUSION

The use of on-line oil condition sensors together with appropriate knowledge of physicochemical changes in oil allows user to have constant overview of the oil quality and its properties. This information can sometimes be crucial to prevent damage and ensure reliable operation of the system.

Today's modern hydraulic systems often have a particle counter installed. However, since on-line particle counters cannot indicate all important fluid conditions (for example viscosity, water level, etc.), the proper on-line condition monitoring system should also include other sensors for evaluation of physical and chemical properties of hydraulic fluid and its condition. And it is also important to point out, that the most on-line sensors for condition monitoring of hydraulic fluids are basically only indicators for early detection of impending system damage. In order to obtain the most detailed, accurate and reliable information on hydraulic fluid state the on-line measurements should be updated with the periodical laboratory testing of the proper fluid sample.

REFERENCES

[1] G.W. STACHOWIAK, A.W. Batchelor, *Engineering Tribology*, 2nd edition, Butterworth-Heinemann, 2001.

Serbian Tribology Society

SERBIATRIB '19

16th International Conference on Tribology

Faculty of Engineering University of Kragujevac

Kragujevac, Serbia, 15 – 17 May 2019

DEVICE FOR DETERMINING THE COEFFICIENT OF SKIN FRICTION

Branislav Dimitrijević[1], Milan Banić[2], Dušan Stamenković[2]
[1]College of applied professional studies Vranje, Serbia,
[2]Faculty of mechanical engineering Niš, Serbia,
*Corresponding author: b.dimitrijevicvr@gmail.com

Abstract: *Skin tribology is very important scientific area because of its presence in everyday life in form of friction in contact of skin surface and various materials. The most often it appears between palm skin and fingers and object which are in someone hands (pencil, mobile phone, tools, etc), and friction between skin and clothing and footwear. It is very important to know the value of friction coefficient between human skin and different materials. This paper describes a device used to determine the coefficient of friction between the palm skin and fingers and various materials that are in daily contact with the skin. The friction coefficient is determined by the use of a special device (Tribometer) designed and constructed for this purpose. This paper describes the device, the measurement procedure performed on the skin of the fingers and the palm in vivo, and gives a summary of the results.*

Keywords*: Skin, tribology, coefficient of friction, measurement, tribometer*

1. INTRODUCTION

In order to get a clear picture of the value of the friction coefficient and how different materials affect the friction that occurs in contact with the skin, it has been necessary to develop a special device. The development process of the device is based on the dynamics caused by various factors: materials, sample size (hand), intensity of force... There are many authors who investigate contact between human skin and other materials.

Two different methodologies for assessing the friction between plantar skin and sock textiles are compared in paper [1]. The first approach uses a custom-built friction plate rig. The second approach uses a pneumatically-driven foot probe loading device. Both approaches allow friction coefficients to be calculated from load data collected during the sliding phase of movement. In the dry conditions tested, the cotton-rich sock was found to provide lower friction that the anti-blister sock material.

N. Veijgen, in his thesis [2] discuss about parameters in the interaction between human skin and other materials. First he gives some information about skin friction and current knowledge on skin friction, then presents the RevoltST, the tribometer that was specially developed for skin friction research and which meets the objectives described in the thesis and finally presents the results of the skin friction measurements obtained with the RevoltST.

Authors in paper [3] discuss the specific nature of tribological systems that include the human skin and argues that the living nature of skin limits the use of conventional methods.

Author in his papers [4] presents a research about various fundamental aspects of finger pad friction are reviewed, including the effects of applied force, skin moisture, material, surface texture etc., and the influence that they have on friction mechanisms such as adhesion, deformation, interlocking and hysteresis. The first is rugby balls and the effect the ball surface pimple pattern has on friction. The second study related to friction modifiers used in sports such as rock climbing and athletics Frisbee interactions were investigated.

Authors in paper [5] present an overview of different studies in area of every day tribology. Those are shoe-floor friction, vehicle movement of the road, friction between skis and snow, friction between ball and hands skin.

Paper [6] has developed an instrument that allows optical analysis and tribological measurements for contacts between solid bodies. An interferometric optical analysis can be used to measure and observe contact size, contact geometry, near contact topography, tribofilm formation, tribofilm motion, tribofilm thickness, wear debris formation, and wear debris morphology

Authors in paper [7] investigate friction of untreated human skin (finger) against a reference textile with 12 subjects, using a force plate. In touch experiments, in which the subjects assessed the surface roughness of the textile at normal loads of 1.5 ± 0.7 N, the average friction coefficients ranged from 0.27 to 0.71 and varied among individuals due to different states of skin hydration.

In paper [8] authors used IR sensors to measure the temperature of the ice track in front of and behind the contact region. In addition, thermocouples integrated into the polyethylene slider measured the temperature close to the interface.

Another device developed by authors is describe in paper [9]. Device have a property to provide an accurate measurement of skin friction between a reference material and the skin of the volar forearm.

This paper describes the device, the measurement procedure performed on the skin of the fingers and the palm in vivo, and gives a summary of the results.

2. SKIN FRICTION

The human skin is very interesting and important for tribology research. In daily life, the human skin is constantly in interaction with other materials, like wood, stone, silk, cotton, glass, skin, plastics, metals, etc. Interaction of human finger and mobile phone touch screen is everyday very illustrative example of skin friction. [6] There are many examples of skin friction like in sport, when the basketball or tennis player holds the ball, or when the athlete performs acrobatics.

Figure 1. Examples for skin friction

Skin friction involves the interaction of the skin and the contact material, and consequently it depends on the properties of the skin, the contact material and its properties, the parameters of the contact between the materials and the environment surrounding the materials [3].

Such a system includes not only the influence of the two materials, in this case the human skin and another material, but also the environment of the materials and the contact parameters, such as the force with which the two materials are pushed together (normal load), the type of movement and the velocity of the relative motion. The skin is a living material; therefore, it is not only the skin of the anatomical location of interest that is important for the frictional properties, but also the characteristics of the individual subject.

Other variables that influence the friction measured on the human skin include the environment and the contact parameters. These factors are usually described in terms of ambient temperature, relative air humidity, and normal load, relative velocity and type of movement respectively [3].

3. DEVICE DESCRIPTION

The device (Fig. 2) was developed for measuring a coefficient of friction between any two materials in laboratory conditions. The device consists of one force sensor that measure horizontal force F_H (force of friction), and the other force sensor that measure normal force F_N. The friction coefficient is determined by using the equation:

$$= \frac{F_H}{F_N} . \tag{1}$$

Using this device, one can determine coefficient of friction between hand palm and any material.

All parts of the device were made of aluminum alloy 1050. The device consists of several parts: basic housing of the device on which the bearings are placed in order to neutralize friction between device parts, force transducer (horizontal) is also hitched on basic housing with screw and measure the horizontal force (force of friction), the lower part of smaller housing carry another force transducer (vertical) and upper part of smaller housing, and all together slides over the bearings and hit the first sensor. The plate on which the test material was placed is connected with upper part of smaller housing with screws. All the elements of device were obtained by cutting the aluminum plate and welding the parts by the TIG procedure in workshop. After welding all elements were grinded.

Table 1. Characteristics of device

Device dimension	240 x 160 x 95 mm
Normal force value	Max 100 N
Horizontal force value	Max 500 N
Contact area dimension	140 x 190 mm

This device is made to determine coefficient of friction between palm of hand or fingers and other different materials, but can be used for determine coefficient of friction between any two materials.

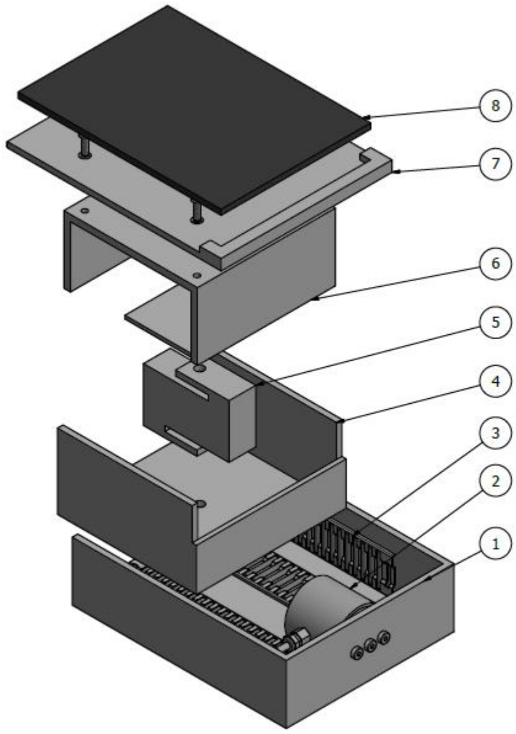

Figure 2. Exploded view of device

1) Basic housing, (2) Force transducer (horizontal), (3) Bearings, (4) Lower part of smaller housing, (5) Force transducer (vertical), (6) Upper part of smaller housing, (7) The plate, (8) Test material

The following force transducers were used – HBM S2M for the vertical (normal) force and HBM U1 for the horizontal (friction) force. The sensors are connected to the NI cDAQ universal data acquisition device connected to the computer with LabVIEW software via the USB interface.

4. MEASURING PROCEDURE

Skin interaction with various materials and some aspects of skin tribology have been studied by some researchers and they have found that the static friction coefficient for different areas of the body varies in a wide range from 0.05 to 3.86. Lately, experimental tests have been carried out and various procedures have been applied. Thus, measuring points for the contact of the human palm and certain objects that may have different contact conditions are designed.

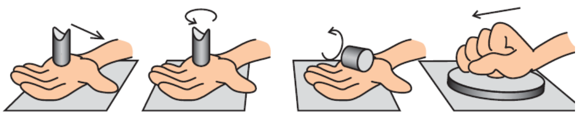

a b c d

Figure 3. Different types of hand and hard object contact

The following contact conditions can be identified: material moves linearly (a); the material rotates and the contact is conical (b); the material rotates, and the contact is by volume (v); skin, palm linear movement (g). Kinematics (d) was chosen because it is considered that this kinematics of motion corresponds most closely to real conditions.

Different tests were carried out using this device, but this paper show results only in one case. Procedure for determining coefficient of friction is very simple. In this case is necessary to determine coefficient of friction between palm of hand and rubber. Rubber sample are cut on predefined dimension and mounted on the device. Test was carried out between dry palm and rubber (hardness of rubber is about 90 shores). Determination of the friction coefficient was performed by three volunteers using the following procedure:

- Connect the sensors and the computer
- Place a sample of material on the surface of the device (rubber in this case)
- Place the palm on the surface of the material
- Gently move forward until the palm start sliding (Fig. 4)

Figure 4. Start position of testing

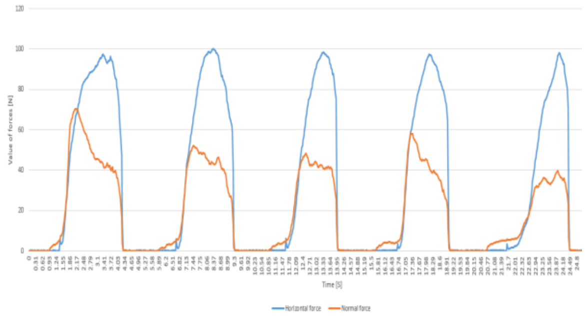

Figure 5. Diagram of normal and horizontal forces

When palm is placed on material surface (Fig. 4), the sensor inside the device registers a normal force (normal force is variable because one can't hold constant value) During the entire duration of the test, the sensor measures horizontal force, and in moment when hand slides, value of force corresponds to the kinetic friction force. Sensors are connected with acquisition device connected to the computer which captures in real time the values of normal and horizontal force. Fig. 5 shows the values of normal and horizontal force versus time in 5 subsequent measurements. The normal force oscillates due to inability of human operator to hold the steady value of normal force.

5. EXPERIMENTAL RESULTS

Average coefficient of friction between palm and rubber in this experiment ranged from 1.37 to 1.83. In table 2, in addition to all the measured friction coefficient values, one can see the average value. It can be concluded that the coefficient of friction for the same material varies depending on the palm of the volunteer.

Table 2. Values of friction coefficient

Coefficient of friction for value of normal force 50 N		
V1	V2	V3
1.79	1.31	2.03
2.03	1.18	1.65
1.93	1.36	1.89
1.77	1.62	1.54
1.59		2.00
Average value		
1.83	1.37	1.82

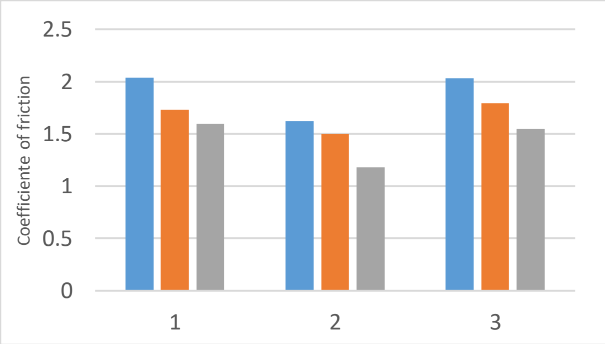

Figure 6. Diagrams of max, min and average friction coefficient for all three volunteers

The following diagram show the maximum (blue), average (orange) and minimum (gray) values of the friction coefficient when the value of normal force of 50N for all three volunteers.

6. CONCLUSION

The development of measuring devices is very important for skin tribology research because one can determine friction coefficient of the skin in contact with any materials. In this paper, the experimental research and determination of friction coefficient between palm skin and rubber is shown. One can conclude that coefficient of friction are obtained for different persons i.e. for different palms. It can be explained different palm surface (different topography, roughness, hardness, skin moisture, temperature, etc). The described procedure will be used in future research of skin friction with different materials and contact conditions, including lubricated (wet contact) conditions, different sliding speeds, temperature, etc.

REFERENCE

[1] M. Carréa, D. Tasrona, R. Lewisa, F. Hashmib: Investigating foot-sock friction: A comparison of two different methodologies, Procedia Engineering, Vol. 147, pp. 759-764, 2016.

[2] N. Veijgen: *Skin friction a novel approach to measuring in vivo human skin*, PhD Thesis, University of Twente, Enschede, NL, 2015.

[3] E. Van der Heide, X. Zeng, M. Masen: *Skin tribology: Science friction*, pp. 130-142, 2013.

[4] R. Lewisa, M.J. Carréa, S.E. Tomlinsona: Skin friction at the interface between hands and sports equipment, Procedia Engineering, Vol. 72, pp. 611 - 617, 2014.

[5] D. Stamenković, M. Nikolić, LJ. Vasin, M. Banić, A. Militenović: Research on tribology penomena in every day life, in: *14th International Conference on Tribology – SERBIATRIB '15*, Beograd, Serbia, pp. 535 - 542, 2015.

[6] B. Krick, J. Vail, B. Persson, G. Sawyer: *Optical* In Situ Micro Tribometer for Analysis of Real Contact Area for Contact Mechanics, Adhesion and Sliding Experiments, Tribology Letters, Vol. 45, No. 1, pp. 185 - 194, 2012.

[7] S. Derler, U. Schrade, L.-C. Gerhardt: Tribology of human skin and mechanical skin equivalents in contact with textiles, Wear, Vol. 263, pp. 1112 - 1116, 2007.

[8] L. Baurle, D. Szabo, M. Fauve, H. Rhyner, N.D. Spencer: Sliding friction of polyethylene on ice: tribometer measurements, Tribology letters, Vol. 24, No. 1, pp. 77 – 84, 2006.

[9] J. Asserin, H. Zahouani, Ph. Humbert, V. Couturaud, D. Mougin: Measurement of the friction coefficient of the human skin in vivo Quantification of the cutaneous smoothness, Colloids and Surfaces B: Bio interfaces, Vol. 19, pp 1 - 12, 2000.

Serbian Tribology Society

SERBIATRIB '19

16th International Conference on Tribology

Faculty of Engineering University of Kragujevac

Kragujevac, Serbia, 15 – 17 May 2019

SELECTION PROCEDURE OF HYDRAULIC VALVES FOR TRIBOLOGICAL RESEARCH

Darko LOVREC[1,*], Joerg EDLER[2]

[1]Institution University of Maribor, Faculty of Mechanical Engineering, Maribor, Slovenia

[2]Graz University of Technology, Graz, Austria

*Corresponding author: darko.lovrec@um.si

Abstract: *A number of methods are available to test the wear resistance of different hydraulic components, along with the known hydraulic fluid. Some of the methods have become standardised, while others are dedicated and of an internal nature, linked to a single manufacturer, either components or fluid. However, none of the represented methods allows a comprehensive insight into developments in all components of the hydraulic system. Tests concerned with lubricating properties and the service-lives of hydraulic components, usually use techniques and procedures similar to those occurring during the actual component usages, and are based mainly on testing the pumps – s. c. tribological standardised pump tests methods based on precisely defined pump types.*

Tribological tests of hydraulic valves, especially continuously acting control valves, also highly-loaded components of a hydraulic system, are mentioned very rarely, or not at all. For valve testing purposes it is necessary first, to establish the appropriate testing methodology and the corresponding test rig, to determine the correlations between operating conditions as input variables and valve performance criteria as output variables during a preliminary test series.

In order to provide a comparison of tribological testing results, it is necessary to select valves with exactly the same characteristics for these tests. In this paper, the selection process of valves with the same characteristics is presented in more detail. Only in this way, will the results of a long-lasting tribological testing be comparable, and the conclusions credible.

Keywords: *tribological tests, hydraulic control valves, characteristics, selection procedure, measurement*

1. INTRODUCTION

One of the more important tasks to be performed by any hydraulic fluid is to prevent direct contact of two metal parts. Producers of hydraulic components take this task very seriously and, thus, they pay significant attention to it. Inadequate lubricant's properties affect largely the component degradation and the machine operation reliability. Therefore, a large number of standardised tests have been developed and used in order to establish the relation between the fluid condition and the lubricating properties, and its effect on the component wear.

The tests concerned with lubricating properties and the service-lives of hydraulic components usually use techniques and procedures similar to those occurring during the actual component usages. Testing is performed in approximately identical environmental conditions as during actual use:

The temperature conditions, presence of contamination, water, metals, alternating pressure … and the operating conditions, in most cases, are tightened up (higher lubricant temperature, higher circulation number …).

Hydraulic fluid specifications themselves are not enough to assure that the hydraulic fluid used at normal operating conditions will provide adequate protection over the desired timeframe. Specifications provide a basis for performance, but the reality in today's environment is that equipment demands have increased, which has, in turn, increased the need for the fluid to perform properly in much harsher conditions.

So how does the lubrication industry measure or evaluate a hydraulic fluid's ability to perform under harsher conditions if the specifications haven't changed? There are a number of industry tests to answer this question. [1] Some of them are standardised, while others are used for targeted testing (tailored testing) or are adapted. They can be divided into two main groups of tests. The first group represents s. c. thermal oxidation tests for testing the oxidation stabilities of fresh and used hydraulic fluids (mainly oils), and determining the degradation behaviour of liquid lubricants, e. g. mineral based hydraulic oil (TOST, RPVOT, PDSC, UDS … and other more complex oxidation tests). [2], [3]

The second group of testing methods represent mechanical tests of hydraulic fluids using laboratory testing devices, such as four-ball, pin-on V-block, Timken anti wear test, Brugger test, Reichert test, Falex test, FZG test ... All of these mentioned tests, either oxidation or mechanical, are more or less laboratory tests related to the fluid. For example, the impact of a lubricant on a real hydraulic component, can only be observed or predicted indirectly.

The often used mechanical tests for determining the impact of tested fluid on the real hydraulic component, based on the standardised test procedure along with specific pump type, are s. c. pump tests. The Vickers test falls in this group of tests, for example, with an exactly prescribed type of vane pump, the Denison test with a defined vane or piston pump, as the most widely used, or the first such tests. This group includes a number of other tests: The Sundstrand test, Komatsu 500 hour test, Bosch-Rexroth test, Lapotko test ... to name only the most well-known. [4] Almost all of these test are very time consuming (they can last several days, weeks or months), they consume a lot of energy, they need a large amount of fluid, require the use of specified real components. So, they are more appropriate for the tribological investigation of used hydraulic pumps together with the used lubricant, and do not give an accurate, comprehensive and detailed answer regarding other components of a hydraulic system, e.g. hydraulic control valves.

2. VALVE TESTING METHODS

For all the methods mentioned above, the conclusions were related only to the pump. Other, also highly loaded components of the hydraulic system, e.g. valves, were not even mentioned at all.

A test method suitable for hydraulic valves should allow testing under variable conditions ranging from real to extreme. Therefore, an appropriate test procedure and test rig should be used, to determine the correlations between operating conditions as input variables and valve performance criteria as output variables during a preliminary test series.

2.1 Wear types inside hydraulic valves

Tribological systems in general are subject to different types of wear. Three of these types of wear are dominant in hydraulic valves (see Figure 1): Erosion, three-body abrasion, and impact wear. The characteristics of these wear types and the factors governing wear behaviour are discussed as follows.

In spite of any filtering measures, fluid power circuits are invariably subject to contamination with solid particles. When passing component walls and edges with high velocity, suspended particles effect *erosive* *wear* on the component material by washing it off subtly. This type of wear affects both spool and poppet valves, particularly at small valve openings with narrow flow channels, and all kinds of valve components – spool, sleeve, housing, poppet, and seat –, when they are paired tribologically with solid contaminants. Depending on the valve type, erosive wear phenomena are perceptible in the rounding of metering geometry, such as spool edges, spool notches, and sleeve orifices, or sealing geometry, such as poppet or seat edges.

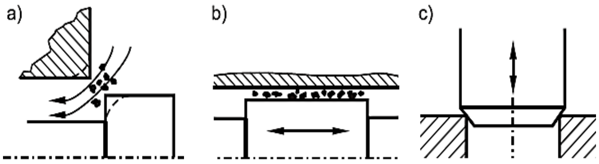

Figure 1. Valve wear mechanisms: a) Erosive wear, b) Abrasive wear, c) Impact wear)

When relative motion is imposed on the valve components in the presence of solid contaminants, *abrasive wear* occurs. This type of wear affects mainly spool valves during operation of the spool. The tribological pairing, in effect, consists of the spool, any solid particles, and the housing or sleeve. Component material is sheared off by the particles entering the valve gap when the components are moved. The results of three-body abrasion can be observed in gap widening and deformation of the housing.

In poppet valves, the poppet is frequently pressed into the seat with high velocity and energy when the valve is closed. Especially in pilot-operated valves, this implicates *wear due to the impact* of the components of the tribological pairing comprising poppet and valve seat. During continuous operation, material can be cracked out of the geometry under stress, resulting in fractures or pitting at the sealing edge or the seat. [5, 6, 7, 8, 9]

2.2 Wear tests of hydraulic valves

The tribological parameters governing the wear process inside hydraulic valves have been the subject of various investigations. Wear has been found to be aggravated mainly by the conditions (Table 1), of which only those marked in italics are examined at the wear test rig.

Compared to the tribological tests with pumps, there are very few tribological tests for valves, but they are not standardised. An example of the valve test is the so-called IFAS test.

Table 1. Wear influencing factors - IFAS test [8]

Category	Parameter
Fluid contaminants	*High particle concentration*
	Distribution of particle sizes around gap high
	Abrasive particle type (protrusive shape, high hardness)
Fluid conditions	*Low fluid viscosity/high temperatures*
	High flow velocities
	Large pressure drops
Duty cycle	*Large valve command amplitudes*
	Large valve command gradients/high spool velocities
	High impact energy when closing
Geometry	Small gap length/gap high ratio
	Small effective wear ratio
Material	Low component hardness

An IFAS test rig has been designed for examination of three-body abrasion, erosion, and impact wear in hydraulic directional spool and seat valves. Certain influence parameters from the fields of Fluid Contamination, Flow Conditions, and Duty Cycle, have been investigated experimentally. The focus is set on fluid contamination with ISO MTD (A3) test dust, as this is anticipated to accelerate the wear process significantly. More details about the IFAS test, the test rig, test procedure and conditions are available in the literature. [8]

The precondition for this test and all similar tests is the same: For comparison and conclusions, it is always necessary to use the same valves with identical baseline characteristics. These must be checked by standard measurement procedures.

3. VALVE CHARACTERISTICS` MEASUREMENT

If we want to compare the characteristics of the hydraulic equipment between different manufacturers, check the characteristics of the same valve types, of the same manufacturer, compare the characteristics and evaluate the variation of the characteristic over the useful life of the valve, or evaluate the wear impact … the characteristics must be comparable. Comparability is achieved by standardised tests and a standardised presentation of results. For continuously acting hydraulic control valves the Standard ISO 10770 is valid.

3.1 ISO 10770-1 static tests

The ISO 10770-1 Standard, applies to electrically modulated hydraulic control valves and consists of three parts. The first part refers to the testing of 4-port directional valves, the second part relates to the testing of 3-port valves, and the third part to the pressure control valves. [10]

The Standard is divided into electrical tests, performance tests that are further divided into dynamic and static tests, and pressure impulse tests. For the preselection of control valves, the static performance tests of 4-port directional valves are relevant. With this Standard different static tests resp. characteristics are defined: Proof pressure tests, internal leakage test, output flow versus input signal test, flows across lands versus input signal, output flow versus load pressure difference, output flow versus valve pressure drop, limiting output flow versus valve pressure drop, output flow versus fluid temperature, pressure difference versus fluid temperature etc.

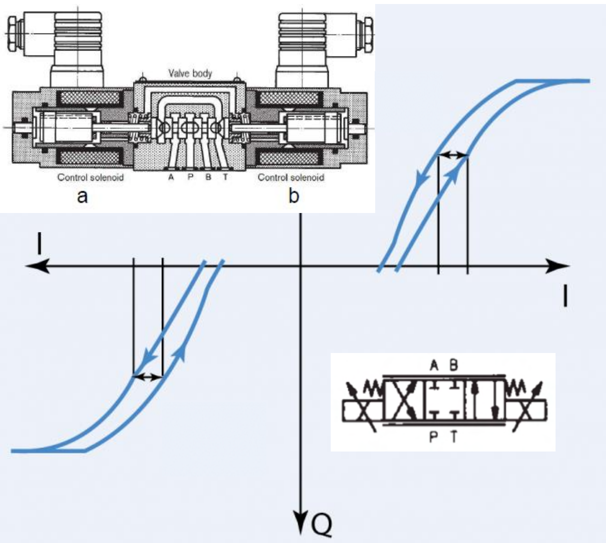

Figure 2. Typical flow-input signal characteristic of a 4-port directional proportional valve

Of the above tests, three are the most important for tribological research purposes: Output flow versus input signal at constant valve pressure drop, internal leakage versus input signal, and the metering test.

On the basis of these three tests, much information can be obtained about the valve properties linked to valve internal design and characteristic changes due to wear. Therefore, we can obtain information on, e.g., rated flow, flow gain, flow linearity, flow hysteresis, flow symmetry, flow polarity, spool lap condition, threshold etc. A typical characteristic flow vs. input signal for a directional proportional valve is shown in Figure 2.

3.2 Interpretation of valve flow characteristics

A much more detailed plan than given in the technical literature from valve manufacturers (=data sheet), if given, reveals several key valve operating characteristics, necessary to evaluate the valve condition of the valve. Characteristic detail is depicted in Fig. 3.

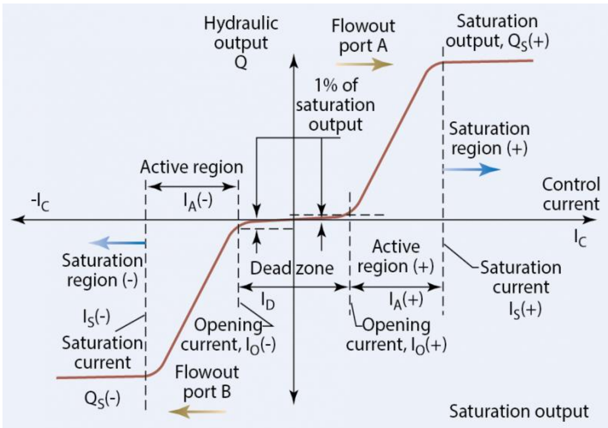

Figure 3. More detailed given valve flow characteristic [11]

A very important valve parameter is the *dead zone*. A valve with a substantial dead zone is rendered useless in applications that seek null as the ultimate operating conditions, such as in positioning systems and some pressure-control systems.

The valve *cracking point* is that instant where the valve just begins to open. That may seem a simple and clear statement, however, it is not. Because there is always leakage in spool valves, flow variations take place all through the overlap, or *dead zone* of the valve.

The next important parameter is the *valve linearity,* the degree to which the metering curve agrees with a best fit straight line.

For a proportional valve, *hysteresis* is the point of widest separation between the metering characteristic curve with increasing input relative to the characteristic with decreasing input, as measured along a horizontal line. This idea is presented in Figure 2 for a proportional valve with substantial overlap.

Threshold is an attempt to separate and measure the portion of valve hysteresis caused by friction from the portion caused by the magnetization properties of the torque motor's internal ferromagnetic parts. In that respect, the threshold represents the very minimum possible hysteresis when all the magnetic effects have been eliminated.

All very briefly mentioned parameters are important for the comparison of different valves, and for a later comparison of the condition of the degraded valve with its baseline condition.

4. RESULTS OF THE SELECTION PROCEDURE

Let's look at the importance of using a valve preselection procedure for further tribological research. For this research it is of extraordinary importance that we use valves with exactly the same respectively identical characteristics. The importance of the pre-selection process of valves is shown on an example of classical directional proportional valve type of usual market quality, without a control spool measuring system.

In the considered case, we used three identical valves of the same manufacturer, with the same label and code, and, thus, expected the same characteristics. The results of the preselection process are presented in the form of three different valve test-characteristics: A leakage test, metering test and output flow vs. input signal test. The results of the characteristics` measurements are shown in Figures 4, 5 and 6.

Based on a comparison of three different characteristics of the same type of valve, it is more than obvious that all valves are not identical, even though they are declared as the same type of valve.

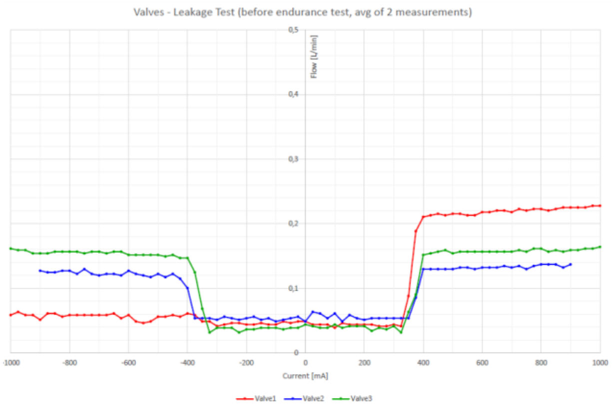

Figure 4. Comparison of an internal leakage test characteristic for three valves

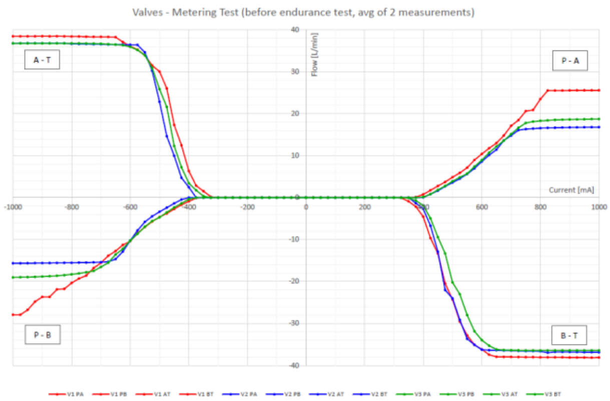

Figure 5. Comparison of a metering test characteristics for three valves

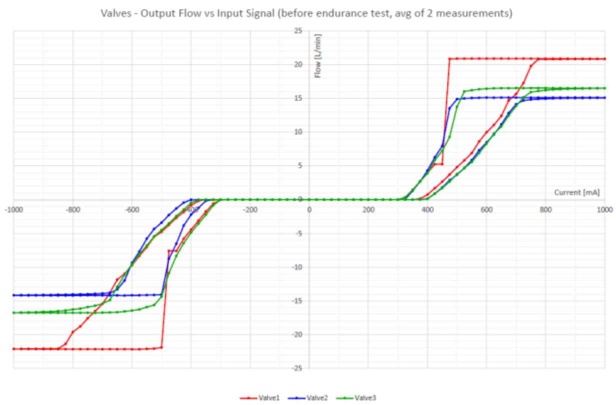

Figure 6. Comparison of output flow vs. input signal characteristics for three valves

The differences between the characteristics of valves occur due to a valve manufacturer's fault, whether an incorrect/different built-in valve spool, or the error is due to the incorrect code listed on the valve plate.

Whatever is the cause of the mistake in these differences, this is reflected consequently as different valves with different properties. When conducting the tribological research, in this case, false conclusions would arise. If we know exactly the baseline situation, we will be able to give an appropriate assessment of the condition of the valve leakage range, degree of wear, wear and change in the geometry of the control edges.

5. CONCLUSION

A number of methods are available to test the wear resistance of individual components, along with the known hydraulic fluid. Some have become standardised, others are dedicated and of an internal nature, linked to a single manufacturer, either components or fluids. However, none of the represented methods allows a comprehensive insight into developments in all components of the hydraulic system. This is especially true for hydraulic valves.

In the case of tribological tests with hydraulic pumps, the type of pump used is defined precisely. In the case of tribological tests with hydraulic valves, nothing is specified. In order to compare the behaviour of different lubricants with the same type of valve, it is necessary first of all to provide the same starting points. In this case, we can only rely on the valve characteristics, which are measured by standardised procedures.

Except for the use of identical valves in all subsequent tests, we have also come up with other important information, for example: To know the actual leakage rate of the new valve and the leakage rate of the already worn-out valve, to determine the actual valve characteristic compared to those available in data sheets, to know all the characteristics of the same valve according the Standard.

On the basis of later changes in the individual characteristics, we get the information about the impact of the lubricant on the individual valve component and, consequently, the impact of the valve on the hydraulic actuator behaviour and the entire controlled hydraulic system.

REFERENCES

[1] D. Wooton: Oxidation - The Lubricant's Nemesis. Practicing Oil Analysis, May 2007, http://www.machinerylubrication.com /Read/1028/ oxidation-lubricant, 2007.

[2] ASTM D943 Standard Test Method for Oxidation Characteristics of Inhibited Mineral Oils.

[3] D. Lovrec, V. Tič: Thermal tests for testing of degradation behaviour of mineral based hydraulic oils, in: *TMT 2016: proceedings, 20th International Research/Expert Conference "Trends in the Development of Machinery and Associated Technology"*, 2016.

[4] G.E Totten, G.H. Kling, D.J. Smolenski: Tribology of Hydraulic Pump Testing,Technology & Engineering, ASTM STP 1310, 1997.

[5] M. Lawrence: *Experimentelle und analytische Untersuchung der Verschmutzungs-empfindlichkeit hydraulischer Komponenten, Dissertation*, RWTH Aachen, Germany, 1989.

[6] S. Lehner: *Verschleißwechselwirkungen in hydraulischen Komponenten durch Feststoffverschmutzung des Druckmediums, Dissertation*, RWTH, Aachen, Germany, 1996.

[7] K. Zhang, J. Yao, T. Jiang, X. Yin, X. Yu: Degradation Behavior Analysis of Electro-Hydraulic Servo Valve under Erosion Wear, IEEE, 2013.

[8] O. Reinertz, K. Schlemmer, J. Schumacher, H. Murrenhoff: Development of an Accelerated Ageing Test for Hydraulic Spool and Poppet Valves, in: *7th International Fluid Power Conference*, Aachen 2010, pp. 1-13, 2010.

[9] P. Weber, J. Schumacher, H. Murrenhoff: Wear Characterization of Hydraulic Spool Valves by Means of Short Time Ageing Tests O+P Journal 1/2015, 2015.

[10] ISO 10770-1, Hydraulic fluid power-Electrically modulated hydraulic control valves - Part 1: test methods for 4-port directional flow-control valves, 2009.

[11] J. Johnson: More About How to interpret Valve Specifications, Hydraulics & Pneumatics, 2-2005, 2005.

Serbian Tribology Society

SERBIATRIB '19

16th International Conference on Tribology

Faculty of Engineering University of Kragujevac

Kragujevac, Serbia, 15 – 17 May 2019

A TRIBOLOGY FLIPPED CLASSROOM: AN INTRODUCTION OF TRIBOLOGY BASIC CONCEPTS IN THE CONTEXT OF A BLENDED LEARNING MACHINE DESIGN COURSE

Pavlos ZALIMIDIS[1], Kyparissia PAPANICOLAOU[2], Nikolaos VAXEVANIDIS[3]

[1]Machine Design Laboratory (MaDLaB), School of Pedagogical and Technological Education (ASPETE), Greece, *Corresponding author: e-mail pzalimidis@aspete.gr

[2]Laboratory of Distance Learning with Digital Technologies, Department of Education, School of Pedagogical and Technological Education, (ASPETE), Greece, kpapanikolaou@aspete.gr

[3] Laboratory of Manufacturing Processes and Machine Tools (LMProMaT), School of Pedagogical and Technological Education (ASPETE), Greece, vaxev@aspete.gr

Abstract: *This paper presents the application of the principles of Blended Learning to the teaching of the concepts of Tribology. Blended Learning is a fast developing approach towards the direction of transforming teaching of engineering courses by actively involving students into the learning process and thus reportedly resulting in higher levels of student achievement than purely face-to-face or purely online classes. Flipping the Classroom is a proposal in the context of Blended Learning which suggests that in-class students' activities, supported by learning material made available to them in advance, could replace the traditional scheme of teacher led lectures followed by homework. Trying to take advantage of the benefits of Blended Learning, we introduced a Tribology Flipped Classroom within a Machine Design course of the Mechanical Engineering Educators Curriculum. The lesson was planned following established design principles. The content was divided in (a): The preparation material which was mainly pre-existing resources including video, notes, slides, taking into account the difficulties that students face on the topic as well self-assessment tests; all these being available on-line. (b): In-class activities including a variety of problems such as, decision and design problems, logical exercises, and debates. In class students worked individually and in groups, participating also in a peer review activity. The evaluation of the project revealed a quite positive view of the participating students on the flipped classroom approach, in comparison to the traditional lectures which they have attended.*

Keywords: *Tribology; blended learning; flipped classroom; machine design; ICT in higher education.*

1. INTRODUCTION

Apart from being scientists and researchers, we are primarily teachers, responsible for the effective transmission of knowledge to our future colleagues. A plethora of diverse topics, contained in the curriculum of an engineering department, impose the use of increasingly efficient learning approaches and, of course, the widespread use of available technology. Modern educational methods should be implemented and their characteristics, in particular their effectiveness in the teaching of technological subjects, should be evaluated in the classroom. Problem-based learning, Project-based learning, Blended Learning are among many of the contemporary approaches that are proposed as alternatives to traditional teaching, and a number of advantages as well as some drawbacks have been associated to each one of them. The need to present the basic principles of Tribology in a short time frame was an ideal opportunity to apply the very promising Flipped Classroom method. After a review of the methodology, in section 2, containing also a brief presentation of the specific objectives of the project, a detailed presentation of the two phases of the method follows, i.e. the preparatory activities outside the classroom, in section 3, and the activities in the classroom, in section 4.

2. METHODOLOGY

Flipped Classroom is an instructional approach and a type of Blended Learning that reverses the traditional, lecture based, learning setting, by delivering instructional content, outside of the classroom and, thus, freeing teaching time for brain-stimulating and student-engaging activities, in the classroom.

Blended Learning had been identified, by the American Society for Training and Development, as one of the top ten emerging educational trends (cited in [1]). Blended Learning, being a way of combining instructional modalities [2, 3, 4, 5], instructional methods [6], or, simply, combining online and face-to-face instruction [7, 8, 9], has been proven more effective than purely face-to-face or purely online classes. Indeed, different implementation cases of Blended Learning resulted in meaningful increase in student engagement and academic achievement [10] In particular, experiments on the Flipped Classroom concept, showed that the replacement of live lectures with online lectures and other on-line material, followed by enriched, learner-engaging, in-class activities significantly enhanced the usefulness, convenience, and value of the course for the majority of students [11,12].

A drawback of Flipped Classroom and Blended Learning in general is that it takes a lot of time and effort to prepare the on-line material. The creation of audio-visual, educational material is a complex and demanding activity that requires the use of significant human time and often the provision of special technical means. The cost of all these may, also, be substantial. A solution to the problem could be to film lectures. Sadly, this often results in low-quality videos that are not attractive to students, and thus have little ability to induce and maintain their attention at an adequate level. Fortunately, due to the broad recognition of the important benefits of this method and also the digital progress in general, several tools, that can facilitate the creation and processing of high-quality educational material, are now available. Animation software, video editors, compilation and subtitling tools, voice production, etc., can significantly reduce the time, effort and cost of producing the material and give it high, almost professional quality.

In order to apply the Flipped Classroom principles and evaluate said advantages, we decided to implement a course referring to the basic principles of Tribology and in particular to Lubrication, an important issue, most relevant to the syllabus of Machine Design.

Tribology and Lubrication are not included in the curriculum of the Department of Educational Mechanical Engineering; neither as a separate lesson nor as part of a course. Specific concepts, such as surface roughness, Hertz pressure, friction loss, are fragmentarily presented, or simply referred to, in the context of lessons such as Chemistry, Manufacturing, and Machine Design. It is up to the student to combine this knowledge in order to obtain a comprehensive understanding of e.g. how friction is created in the machinery, how the adverse effects of this phenomenon are reduced by Lubrication and how the properties of Lubricants influence this process. Since all this requires a hands-on experience rather than a purely theoretical presentation, the above-mentioned desired result is usually achieved, by the student, later in practice.

The implementation of a Flipped Classroom seemed like a promising method to overcome the unavailability of time in the normal program and, at the same time, to maximize the learning outcomes associated with Friction and Lubrication. Another similar lesson [13, 14], which took place during a previous academic year, gave us a useful starting point for the design of the course: A key factor is the proper organization of the in-class activities in order to engage students with evidence-based practices that could significantly improve their learning outcomes. [15].

Out-of-class material should be designed in such a way as to cover the necessary theory as well as to provide the appropriate cognitive background for the implementation of classroom activities. It is imperative to control the extent of the on-line material and to assure that off-class working time of the students will be kept to a moderate level so as not to discourage them.

3. OFF-CLASS PREPARATION

The students were given a short introductory briefing four days before the in-class activity course, providing them with necessary guidance and practical information concerning the method of flipped classroom. They were also told to “keep an eye” for a relative announcement.

After that, they were invited via an automated e-class application, to attend a seminar on "Friction and Lubrication" which would be organized as a Flipped Classroom. The announcement, which was texted to them, contained a link to a hypertext called “Preparation Guide: Friction-Lubrication in Machinery in a Flipped Classroom”. Links on the hypertext led to on-line material, uploaded to Dropbox®.

The on-line material consists of a number of short videos with English narration. Most Greek students are fluent in English, however, Greek close captions were provided because the videos contained several technical terms, related to Tribology, which are not familiar to the students. Only freeware was used to prepare the on-line material. Videos were edited using YouTube Studio® (beta) and subtitled using Google’s Creator Studio Classic®. There are also a number of text readings in Greek.

The total duration of all the videos was 16:52 minutes. Considering that 40-50% of students would like to watch once again the videos and that they would spend about 10-15 minutes, reading the texts and responding to the quiz and evaluation, students were given an a total duration estimate of about 40 minutes.

The on-line material was divided in three sections. The first section was about basic concepts on friction, lubrication and lubricants. It aimed to provide a brief and comprehensive view of the various forms of friction and how they are dealt with by the different types of lubrication as well as what are the main categories of lubricants. The second section was about the properties of the lubricants, their effect to machine lubrication and the selection of lubricants based on the machine operation. The third and last section was about lubricants classification and standardization and also lubrication tooling and equipment.

After each of the first two sections, the students answered a small number of questions, in a quiz, related to the knowledge provided in the immediately preceding section. Quizzes were used because they can serve two purposes: On one hand, they can induce immediate "activation" of the recently acquired knowledge and, therefore promote its consolidation [16, 17]. On the other hand, quizzes can provide feedback to the teacher about the points of the on-line material that remained vague for the students, in order to clarify them in the classroom [18]. Quizzes were created using the Blank-Quiz template of Google Forms®, which simplifies questionnaire creation by choosing from a bunch of question options, from multiple-choice and dropdown menus to linear-scale rating, enriching them with pictures and video clips.

At the end of the off-class preparation, students were encouraged to evaluate the process and the on-line material, through a questionnaire. The questionnaire contained questions with a linear-scale response and students were also given the opportunity to express some views through a short paragraph. Eighty two percent (82%) of the participating students (19 people) filled the assessment form. According to their answers, the off-class preparation was a positive experience to the students. To the question: "How was the overall experience of the off-class preparation, with the on-line material", 79% of the participating students answered "Excellent" and 21% answered "Very Good".

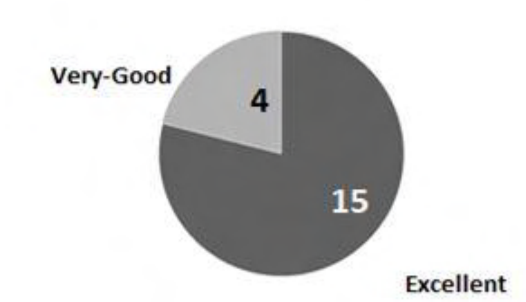

Figure 1. How was the overall experience of the off-class preparation, with the on-line material?

It, also, seems that the preparation was not time consuming. To the question: "How long it took you to get prepared, with the on-line material, in relation to the estimated duration?", 52% of the participating students answered "As Expected", 21% answered "Less Than Expected", 15% answered "Much Less Than Expected" and 10% answered "More Than Expected".

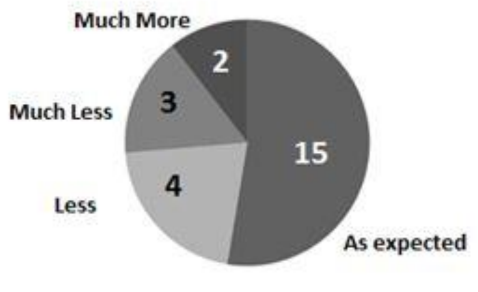

Figure 2. How long it took you to get prepared, with the on-line material in relation to the estimated duration?

4. IN-CLASS ACTIVITIES

Forty percent (40%) of the students, enrolled in the Machine Design Course, (25 people) participated in the in-class activities. Of those, 92% (23 people) participated in the preparation phase, watched and read the on-line material and replied to the quizzes and the evaluation questionnaire.

In-class activities began with a discussion, aimed at reviewing on-line material. Organized discussion activities and debates can be used to facilitate peer-to-peer knowledge exchange and a deeper engagement with the course content. Course concepts become more meaningful, diverse student assumptions are tested and perspectives explored. During the discussions or debates, students create teams with two or more members and, after each question, they are given the opportunity to discuss within their group and reach a joint answer announced by one of the members, as a representative of the group.

By a series of questions, posed by the instructor, students had the chance to retrieve and put forward the basic principles of friction, lubrication and lubricants.

Special attention was given to the points, which were characterized in the on-line quiz and questionnaire as more vague or obscure. Such structured and discretely steered discussions can help the instructor to evaluate student comprehension while facilitating the development of team spirit. Indeed students by assuming a, more active than usual, attitude, soon felt more confident and relaxed and started to enjoy the process.

It was a good time for the following class activities, which were based on the concept of Active Learning. The advantages of Active Learning are indicated in numerous papers [19, 20, 21, 22]. We consider the excitement created by this methodology [23], as its greatest advantage. Between various approaches of Active learning, we have chosen to use Experiential Learning.

In Experiential Learning activities, students learn through immersive, hands-on learning experiences. The pedagogical benefits of these learning experiences have been well-documented in the literature and demonstrate the efficacy of simulation environments and modeling in enhancing learning [24]. Experiential learning activities can take a number of forms, including role-playing, experimentation demonstrations, labs, computer simulations, competitions etc. The intensification of the learning process was pursued by the creation of a collaborative learning environment in which the students played active roles, using knowledge, gained outside the classroom. A group of students dealt with the organization and implementation of a friction study experiment, while a second group was involved in an experiment involving the study of viscosity. With the use of simple materials from the school's machine shop, two simple experimental arrangements were quickly assembled.

A small amount of two lubricants, was used: a “thin” SAE 10 basic machine lubricant and a “thick” SAE 90 gear lubricant.

Students of the first group used a handmade ramp (Fig.3), with an attached protractor and a maximum tilt indicator, to experimentally demonstrate to the class the development of dry and wet friction of metals. The friction angle was measured in the case of the aluminum on aluminum contact. Then, a thin layer SAE 10 lubricant was applied to the aluminum surfaces and the friction angle was measured again. The experiment was conducted at room temperature (20^{o}C). The whole process was repeated for the SAE 90 lubricant.

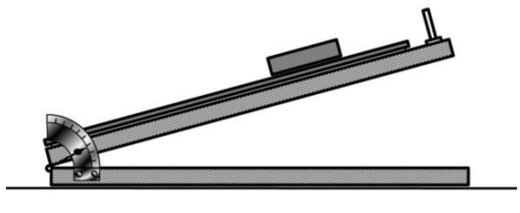

Figure 3. The friction angle measuring ramp

The second group of students used a handmade Engler viscometer (Fig.4), to present to the class the viscosity measurement of the two available lubricants (SAE 10 and SAE 90) at temperatures of 0 ° C, 20 ° C and 100 ° C. Glass bottles with containing the lubricants, were immersed in two baths, one with water and ice cubes and one with boiling water, in order to achieve temperatures of 0 ° C, and 100 °, whereas the temperature of 20 ° C degrees was the ambient temperature, at that time. The purpose of the activity was not to accurately measure viscosity, but to qualitatively understand the effect of temperature on a basic property of lubricants.

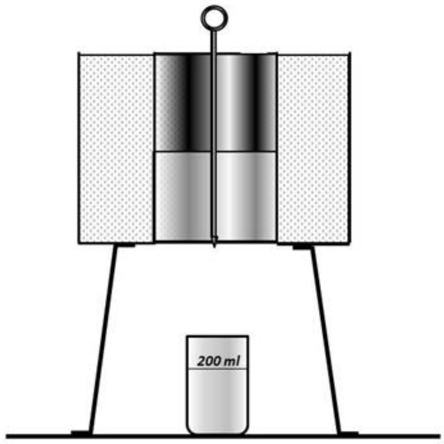

Figure 4. The Engler-type device

The results of the tests were used as a stepping stone for a consecutive discussion on the various applications of lubricants. Most students (more than 90%) were able to argue about the suitability of certain lubricants for use in specific applications, such as internal combustion engines, speed reducers, gas turbines, conveyors, building machines, cooling equipment etc.

During the last part of the course we dealt with the evaluation of in-class activities. During the discussion, students had the opportunity to express their views on Flipped Classroom, which in their vast majority were very positive. To the question: “How difficult did you find the in-class activities?” 72% of the participating students answered “Not at all”, 24% answered “Just a Bit” and 4% answered “A little”.

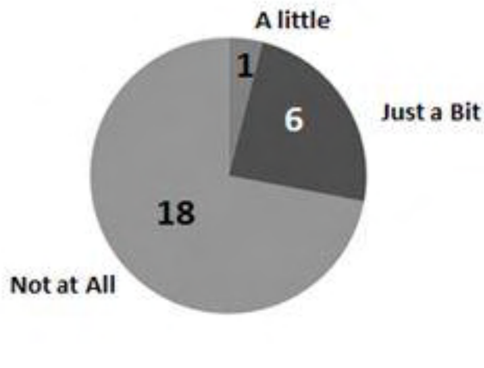

Figure 5. How difficult did you find the in-class activities?

To the question: “Do you think that in-class activities have helped you to improve the level of understanding of the lesson you achieved during off-class preparation?” 76% of the participating students answered “A lot” and 24% answered “Very much”.

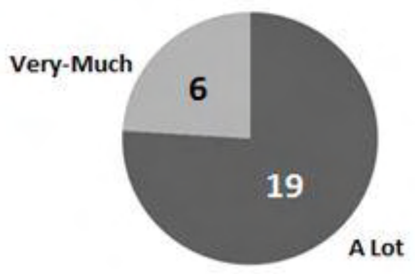

Figure 6. Do you think that in-class activities have helped you to improve the level of understanding of the lesson you achieved during off-class preparation?

5. CONCLUSION

During a two-hour class, a substantial part of the basic Tribology concepts, that are very important to the mechanical engineer, was dealt with. The achieved learning outcome turned out to be considerably large, in relation to the allocated teaching time. Although no control group was set up for a more direct quantitative comparison, an evaluation based on qualitative assessments on class characteristics, such as participation and interest shown in relation to the corresponding characteristics of a traditional teaching was possible and impressive improvement was observed. Learning, despite the intensification of the lesson, due to limited time, was accompanied by a significant level of satisfaction that has, in general, been found to contribute to the formation of long-term memory and the consolidation of knowledge. In conclusion, teaching “Tribology and Lubrication Basics” turned to be a great opportunity to implement and access Flipped Classroom and Blended Learning. They were confirmed as flexible and powerful knowledge transfer tools with many possibilities for broader implementation.

REFERENCES

[1] J.E. Rooney: Blending learning opportunities to enhance educational programming and meetings. Association Management, Vol. 55, No.5, pp. 26-32, 2003.

[2] Bersin & Associates. Blended learning: What works? An industry study of the strategy, implementation, and impact of blended learning, available at: http://www.learningcircuits.org/2003/jul200/bersin.htm, 2003.

[3] M. Orey: *Definition of Blended Learning*, University of Georgia, 2002.

[4] M. Orey: One year of online blended learning: Lessons learned, Paper presented at the Annual Meeting of the Eastern Educational Research Association, Sarasota, FL., 2003.

[5] H. Singh, C. Reed: A White Paper: Achieving Success with Blended Learning, Centra Software, 2001.

[6] M. Driscoll: Blended Learning: Let's get beyond the hype, E-learning, Vol. 54, 2002.

[7] J. Reay: Blended learning - a fusion for the future, Knowledge Management Review, Vol. 4, No. 3, pp. 6, 2001.

[8] P. Sands: Inside outside, upside downside: Strategies for connecting online and face-to-face instruction in hybrid courses, Teaching with Technology Today, Vol. 8, No. 6, 2002.

[9] J.R. Young: 'Hybrid' teaching seeks to end the divide between traditional and online instruction, Chronicle of Higher Education, pp. A33, 2015-07-04, 2002.

[10] Saritepeci et al: The effect of blended learning environments on student motivation and student engagement: A study on social studies course, Education and Science. (Eğitim ve Bilim), Vol. 40, No.177, 2015.

[11] M. Ronchetti: Using video lectures to make teaching more interactive, International Journal of Emerging Technologies in Learning , iJET, Vol. 5, No.2, pp.45-48, 2010.

[12] J.F. Strayer: How learning in an inverted classroom influences cooperation, innovation and task orientation, Learning Environments Research, Vol. 15, No. 2, pp. 171–193, 2012

[13] J. Kanelopoulos, K. Papanikolaou, P. Zalimidis: Flipping the Classroom to Increase Students’ Engagement and Interaction in a Mechanical Engineering Course on Machine Design, International Journal of Engineering Pedagogy (iJEP), Vol. 7, No. 4, 2017.

[14] J. Kanelopoulos, K. Papanikolaou, P. Zalimidis The experience of a flipped classroom in a mechanical engineering course on Machine Design: A pilot study, Global Engineering Education Conference (EDUCON-IEEE), 2017.
[15] L. Deslauriers, E. Schelew, C. Wieman: Improved Learning in a Large-Enrollment Physics Class, Science, Vol. 33, No. 6031, pp. 862-864, 2011.
[16] L.R. Squire: Mechanisms of memory, Science, Vol. 232, No. 4758, pp. 1612–1619, 1986.
[17] J. Karpicke, J. Blunt: Retrieval practice produces more learning than elaborative studying with concept mapping, Science, Vol. 331, No. 6018, pp. 772–775, 2011.
[18] G. Novak, E.T. Patterson, A.D. Gavrin, W. Christian: *Just-In-Time Teaching: Blending Active Learning with Web Technology*, Upper Saddle River, NJ: Prentice Hall, 1999.
[19] R.R. Hake: Interactive-engagement versus traditional methods: A six-thousand-student survey of mechanics test data for introductory physics courses, American Journal of Physics, Vol. 66, No. 64, 1998.
[20] S. Freeman, S.L. Eddy, M. McDonough, M.K. Smith, N. Okoroafor, H. Jordt, M.P. Wenderoth: Active learning increases student performance in science, engineering, and mathematics, in: *Proceedings of the National Academy of Scientists*, Vol. 111, No. 23, pp. 8410–8415, 2014.
[21] S.K. Saha: *Design for effective teaching and learning in technical education*, National Conference on Design for Product Life Cycle, BITS, Pilani, 2006.
[22] J. Wood, M. Campbell, K. Wood, D. Jensen: Enhancing the teaching of machine design by creating a basic hands-on environment with mechanical 'breadboards', International Journal of Mechanical Engineering Education, 2005.
[23] C. Bonwell, J. Eison: Active Learning: Creating Excitement in the Classroom, AEHE-ERIC Higher Education Report No. 1, Washington, D.C.: Jossey-Bass, 1991.
[24] D. Gordin, R.D. Pea: Prospects for scientific visualization as an educational technology, Journal of the Learning Sciences, Vol. 4, No. 3, pp. 249-279, 1995.

Serbian Tribology Society

SERBIATRIB '19

16th International Conference on Tribology

Faculty of Engineering University of Kragujevac

Kragujevac, Serbia, 15 – 17 May 2019

SUBSURCFACE MATERIAL CHARACTERISATION BY SIMULATION ON CARBURIZED ROLLING CYCLE FATIGUE TEST SPECIMENS

Szabolcs Szávai[1], Zoltan Bezi[2], Levente Béres[3], Sándor Kovács[4]

[1] Institute of Machine and Product Design, University of Miskolc, Miskolc, Hungary

[2]Bay Zoltán Nonprofit Ltd. for Applied Research, Miskolc, Hungary

[3]Bay Zoltán Nonprofit Ltd. for Applied Research, Miskolc, Hungary

[4]Institute of Physical Metallurgy, Metalforming and Nanotechnology, University of Miskolc, Miskolc, Hungary

*Corresponding author: szabolcs.szavai@bayzoltan.hu

Abstract: *The aim of the research is to determine the metallographical and mechanical properties (residual stresses, hardness, phases and texture) of carburized surfaces using finite element method and study the failure of surface during relative motion, and the possibilities of the test methods, which can give us information about the behaviour of these surfaces. This work focuses on contact fatigue tests and properties.*

Nowadays it can be established that application of finite element method is a reliable way to simulate carburization. It is possible to determine exact approximation for the hardness and carbon content values near the surface after carburization and quenching, but take into account that the simulation of tempering is still an issue, if the material contains retained austenit, the hardness values of the test will be higher near the surface, because of the retained austenit-bainit transformation, so the simulations had to be validated by carburized cylindrical (disc-like) specimens, made of low alloy case hardening steel (16MnCr5). These specimens were tested with glow discharge optical emission spectroscopy, to measure the chemical composition of the surface layer. It is important to know what kind of residual stresses can be observed in the surface after carburization, therefore it was extensively studied during the simulation. Furthermore the values of the hardness in the surface of the specimens have been determined. Having compared the simulation and experiments, good agreement has been found between the results, so the finite element method was validated successfully.

For high cycle rolling fatigue test rollers were manufactured. Two disc fatigue tests were carried out on five rollers. Four tests were stopped due to trigger sign by surface damage, while one of those was stopped due to break of the shaft after one millions of rotation. Microstructural investigations have been started on the rollers.

Keywords: *Fatigue, rolling contact, surface treatment, failure, FE analysis*

1. INTRODUCTION

The typical damage to the life of the contact surface pairs, such as bearings or gears, is fatigue. From the point of view of failure, the most critical zones appear at the edges of the contact area or are formed shortly below the surface. Surfaces are subject to high-cycle fatigue, however, the global damage accumulation methods are not applicable.

Although the answer to questions about the lifetime and condition of the parts is crucial, and while numerical and experimental methods are highly evolving, and modern testing methods are becoming more and more capable of characterizing such tribological events, there are still problems that require further multidisciplinary research.

Local strain energy density models based on kinematic or isotropic hardening material laws are the most promising for local determination of damage. In addition, mechanical properties of the surface should be known for its solution, however the determination or prediction of these properties are also challenging because of the surface treatments.

As a basis for the experimental work, due to the frequent application and previous experience, the 16MnCr5 case hardening steel was selected. On the disc samples made from model material, after the treatment, the tests were carried out to validate the numerical model suitable for determining the characteristics of the near-surface layer properties. By comparing the results, the model has been proved to be suitable for determining the layer characteristics of the rollers used for contact fatigue testing.

2. VALIDATION EXPERIMENTS

It is possible to determine exact approximation for the hardness and carbon content values near the surface after carburization and quenching, but take into account that the simulation of tempering is still an issue, so if the material contains retained austenit, the hardness values of the test will be higher near the surface, because of the retained austenit-bainit transformation, so the simulations had to be validated by carburized cylindrical (disc-like) specimens, made of low alloy case hardening steel (16MnCr5). The average chemical composition is shown in the Table 1.

Table 1. Chemical composition

C %	Si %	Mn %	P %	S %	Cr %
0.14 - 0.19	0.4	1.0 - 1.3	0.025	0.035	0.8 - 1.1

Carburization, quenching and tempering of 50 mm diameter, 10 mm wide disc-like 16MnCr5 grade specimens were performed. The carbonizing agent was $BaCO_3$ charcoal activator, 10%, after carbonizing, the specimens were quenched in oil and stress relief annealing was performed (Fig. 1).

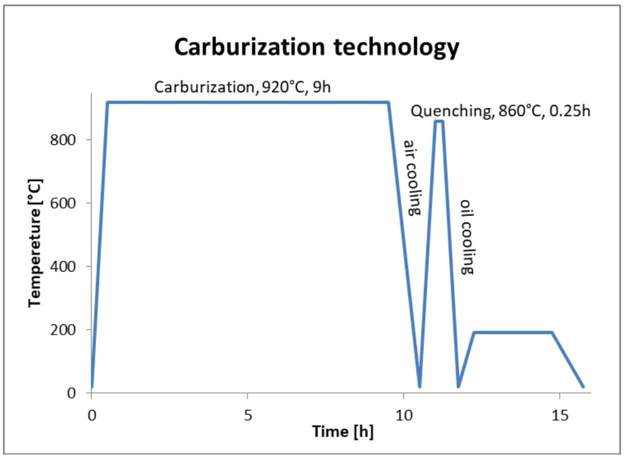

Figure 1. Heat treatment temperature-time diagram

The specimens were polished after cutting, and the surface of the specimen was etched with HNO_3 (nitric acid) 2% solution (nitrate etching agent) to show the carbonized layer. The cross section after preparation is shown in Fig. 2.

Figure 2. Specimen before hardness measurement

The hardness measurement of the specimen was carried out from outside to inside. The test was done by 0.05 and 0.1 mm increments. The thickness of the hard layer was also determined by measuring the hardness of the core before starting the measurement series, which in this case was 389 HV0.1. The boundary of the carbonized layer was marked with a hardness of 500 HV0.1 corresponding to the hardness of the hardened steel. Due to the determination of this layer thickness, 0.05 mm increments were taken near the boundary of the hardness. Based on the measurement results, a 1.65 mm carbonized layer was reached on the specimen using the applied technological parameters. Figure 3 illustrates a series of measurements with a microscope-mounted camera showing impressions and the average of the measurement results and distance from the surface at a given point. The distances are in millimeters and the hardness values are in HV0.1

0,02	0,07	0,12	0,17	0,22	0,27	0,32	0,37	0,47	0,57	0,67	0,77	0,87	0,97	1,07	1,17	1,27	1,37	1,47	1,57	1,67	1,72	1,77	1,82	1,87	1,92	1,97	2,02
747	713	723	730	689	676	724	694	707	717	727	692	693	671	663	630	612	576	549	526	483	485	479	444	454	422	443	431

Figure 3. Indentation on the surface

These specimens were tested with glow discharge optical emission spectroscopy, to measure the chemical composition of the surface layer. The result of the test shows that after the cementation a layer of carbon content of about 1.4% was formed on the surface. As a result of the test technique, the chemical composition of the surface was analyzed only up to 60 µm, the result of which confirms that when the carburisation is applied near the surface, the carbon content is significantly increased, then the measurement is continued in the direction of the core, the carbon content decreases as expected (Figure 6a).

In solid-cement carburisation, the maximum carbon content cannot be well controlled: the carbon content of charcoal is very high, so that the surface layer is also formed. The 1.4% carbon content determined by the measurement is too high because the amount of residual austenite is significant, which impairs the surface properties. This surface layer can be removed if necessary after finishing machining the parts (finishing, grinding).

3. NUMERICAL MODELL DEVELOPMENT

In order to validate the accuracy and dependability of FE simulation, experimental results of carburization of a cylindrical specimen are used to compare with the simulation results of FEM. During the process of the heat treatment cycle coupled thermo-metallurgical and mechanical calculations were carried out by considering the effect of carbon content and incorporating multi-phase transformation models. Numerical calculations were performed with commercial finite element software package Simufact.forming. The problem was solved numerically in a cylindrical coordinate system due to axial symmetry of the geometry. The geometry and finite element representation used in the modelling is shown in Fig. 4.

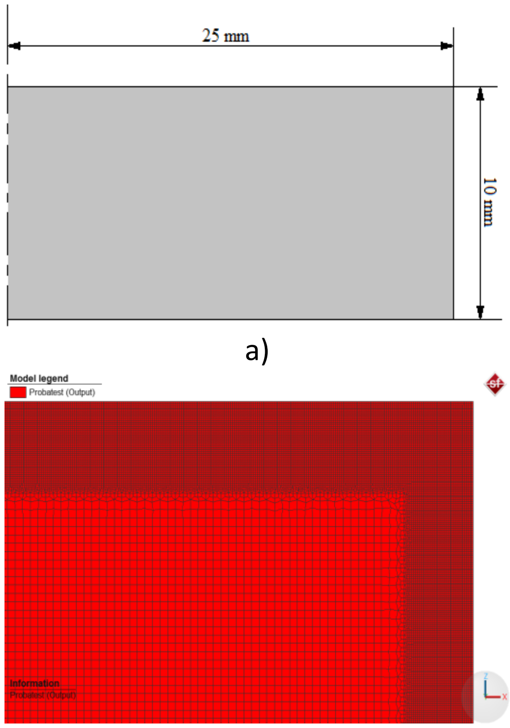

a)

b)

Figure 4. Geometry used in modeling

Four-node axisymmetric elements were used to model the specimens. Solid elements were employed to simulate the thermo-elastic-plastic behaviour of the specimen. The mesh is graded from fine to coarse according to the expected reduction in carbon content on moving away from the outer surface.

The mesh contained two-dimensional rectangular elements in the carburised layer 0.05 in the core layer 0.2 mm.

The temperature-dependent mechanical and thermal properties were taken into account in the calculations. The equilibrium transformation temperatures for the formation of austenite from an initial microstructure and the decomposition of austenite into ferrite and martensite are required in the heat treatment simulations. Material properties, based on their chemical composition, were determined using JMatPro software. The temperature-dependent, elastic-plastic isotropic hardening phase-dependent material model was used in the calculation. The thermo-metallurgy material properties of 16MnCr5 steel were generated with JMatPro software using the average chemical composition which can be seen in Table 1. Transformation data was calculated using Simufact.premap interface with 30 µm grain size starting at 920°C temperature.

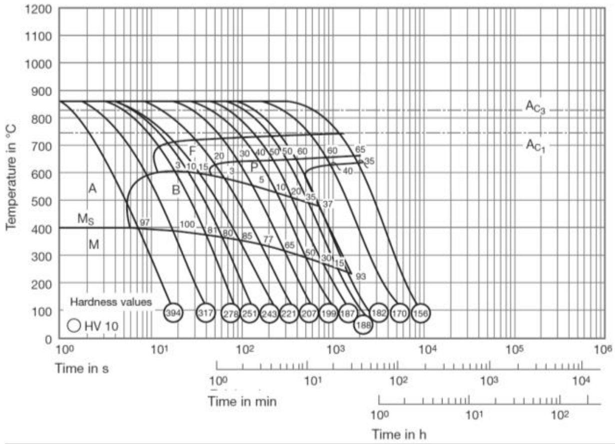

Figure 5. Continuous time-temperature-transformation diagram for 16MnCr5 [1]

The equilibrium transformation start temperatures for different carbon content were determined from the literature.

The numerical solution for the carburizing process can be expressed based on mass diffusion. Carbon atoms transfer from the atmosphere to the steel surface during carburizing and diffuse into the steel, which creates a carbon concentration gradient. The governing equations for diffusion-controlled carburizing are:

$$\frac{\partial C\%}{\partial t} = D\frac{\partial^2 C\%}{\partial x^2} \qquad (1)$$

where C is the carbon concentration, D is the diffusivity of carbon in austenite, t is time, and x is the average carbon atom diffusion distance. In the simulation, the carbon diffusivity was determined according to the Tibbetts [2] proposed relationship:

$$D(T, C\%) = 0.47e^{-1.6C\%}e^{-\frac{154893-27629C\%}{RT}}, \qquad (2)$$

where D is the diffusivity of carbon in cm^2/s, C% is the carbon content in mass percent, R is the gas constant in 8.314 J/mol/K, and T is the temperature in Kelvin.

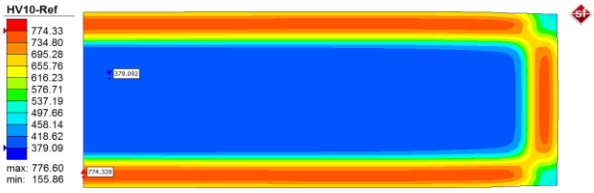

Figure 6. The calculated hardness distribution in the specimen

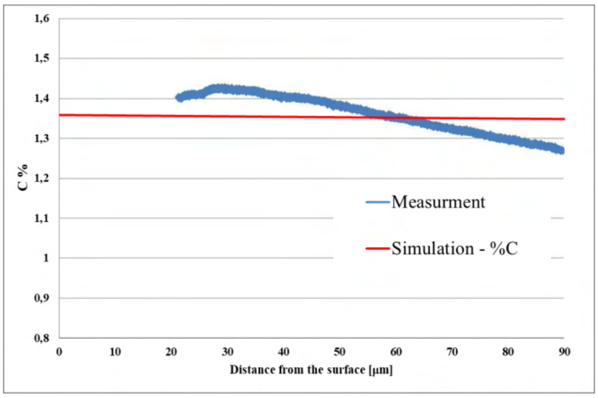

a) Measured and calculated carbon content

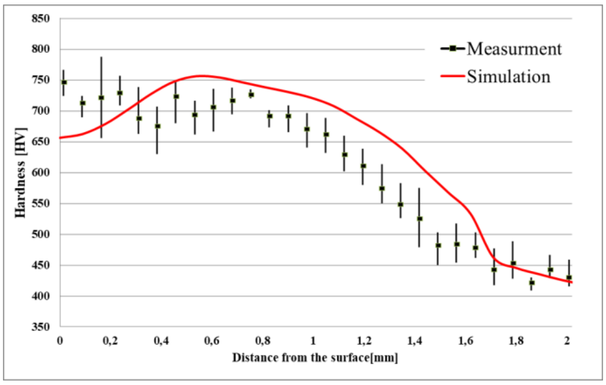

b) Measured and calculated hardness

Figure 7. Comparison of measured and calculated results

Maynier and coworkers [3] have developed a useful method to predict steel hardness. The total hardness of steel is calculated dependent on the volume fractions of the constituents of the microstructure:

$$HV = (FP\% * HV_{F-P} + B\% * HV_B + M\% * HV_M)/100, \qquad (3)$$

The hardness of the microstructures produced are given by:

$$HV_M = 127 + 949C\% + 27Si\% + 11Mn\% + 16Cr\% + 8Ni\% + 21logv_R, \qquad (4)$$

$$HV_B = -323 + 185C\% + 330Si\% + 153Mn\% + 144Cr\% + 191Mo\% + 65Ni\% + (logv_R)(89 + 53C\% - 55Si\% - 22Mn\% - 20Cr\% - 33Mo\% - 10Ni\%), \qquad (5)$$

$$\mathrm{HV}_{\mathrm{F-P}} = 42 + 223C\% + 53S\%i + 30Mn\% + 7Cr\% + 19Mo\% + 12.6N\%i + (\log v_R)(10 - 19Si\% + 8Cr\% + 4Ni\% + 130V\%) \quad (6)$$

where: v_R is the cooling rate in K/h.

The hardness values were calculated using the correlations published by Maynier [3] et all at 0.5 C%, while Leslie [4] suggested the relationship with higher carbon content:

$$HV = 1667C\% - 926C\%^2 + 150. \quad (7)$$

The results obtained are illustrated in Fig. 6.

4. FATIGUE TEST ROLLERS

As it was presented above the simulation were good agreement with the experiments, so the model has been proved to be suitable for determining the layer characteristics of the rollers used for contact fatigue testing.

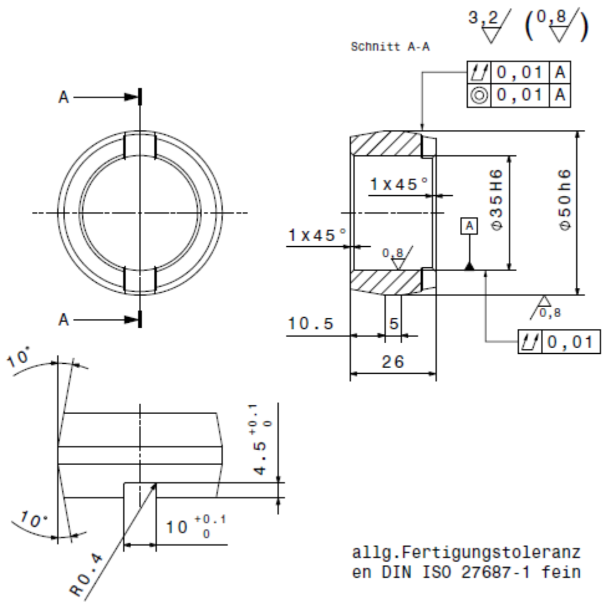

Figure 8. Test rollers' geometry

The geometry of the rollers (Figure 8) was defined by Montanuniversität Leoben, Lehrstuhl für Allgemeinen Maschinenbau (AMB) since as part of our bilateral cooperation the two disk high cycle contact fatigue tests were performed by AMB.

Rollers surface were treated with the described technology. In order to study the near surface properties, the sub-surface stersses, pahses and the hardness have been calculated with the verified methodology.

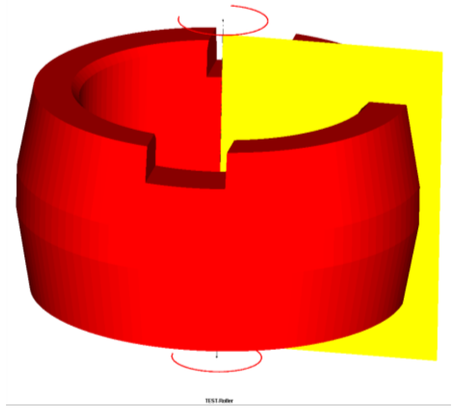

Figure 9. FEM model of the roller

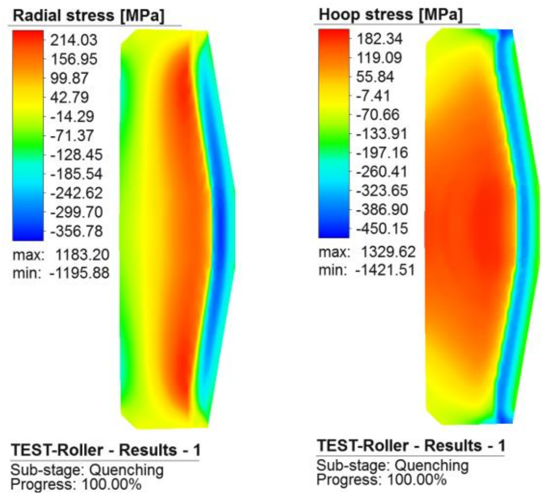

Figure 10. Subsurface stresses

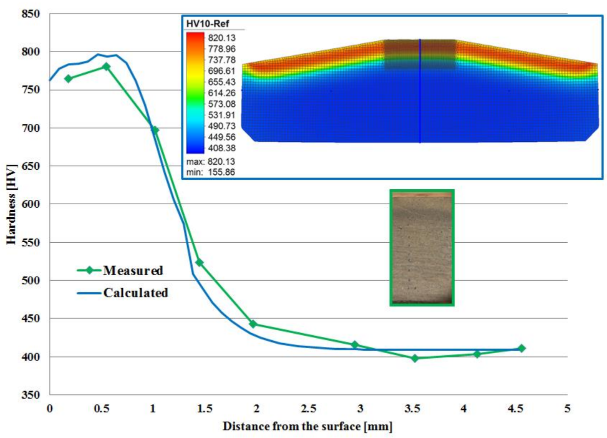

Figure 11. Hardness HV10

5. FATIGUE TESTS

Two disc fatigue tests were carried out on five rollers with different contact force. Four tests were stopped due to trigger sign by surface damage, while one of those was stopped due to break of the shaft after one millions of rotation.

Table 2. Cycles to failure

disk	p [GPa]	N [Cycles]	comment
TP1	2.25	4519100	TP2: shaft failure due to fretting
TP2	2.5	1024160	
TP3	2.75	1689382	
TP4	2.22	8028606	
TP5	2.5	7857350	

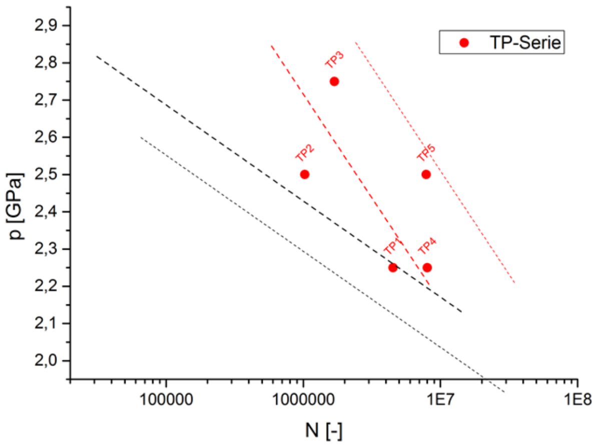

Figure 12. Test results

After the tests the rollers have been cut to pieces and microstructural investigations have been started on the rollers. Pieces of TP2 specimen can be seen on Fig. 13.

Figure 13. Pieces of TP2 specimen

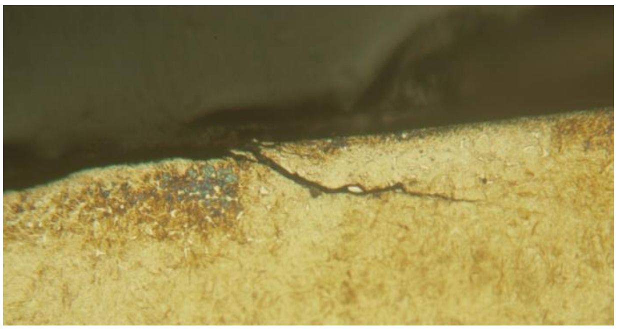

Figure 14. Pieces of TP2 specimen

In case of the TP2 specimen several developed cracks have been found, starting mainly from the edge of the contact zone as it is shown on the Fig. 14, however the test of the TP2 specimen was stopped before any trigger sign from surface damage. It shows that the incubation time was very short, the lifetime was almost 8 times longer, and crack propagation period cannot be neglected.

The other specimens show typical surface pitting damage as it shows the Fig. 16 due to the very brittle surface and high subsurface compression stress.

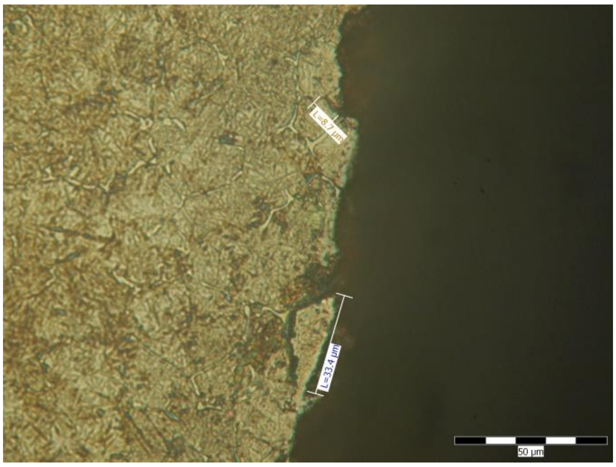

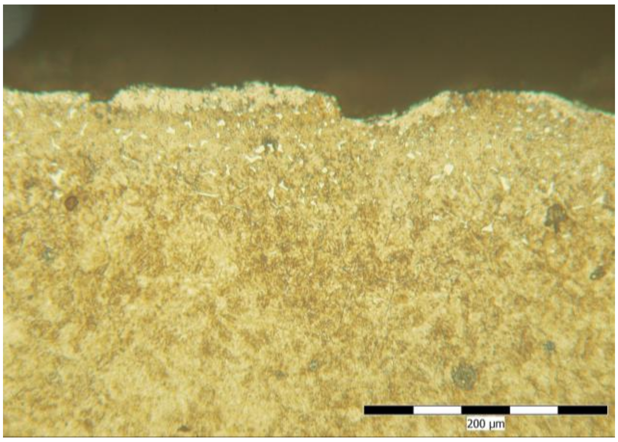

Figure 15. Surface pitting on TP5 specimen

In some case subsurface cracks have been observed as well as it is shown on Fig. 16.

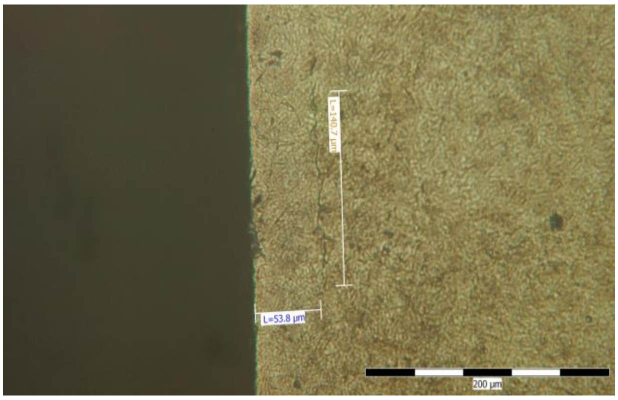

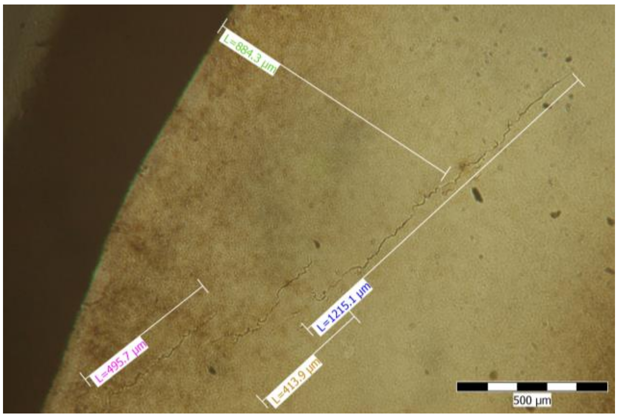

Figure 16. Subsurface crack on TP5 specimen

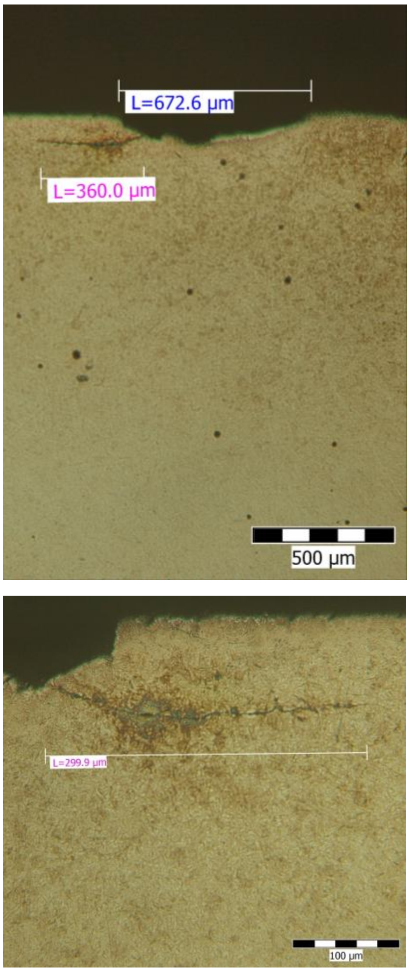

Figure 17. Spalling on TP3 specimen

In case of TP3 specimen when the load was the highest spalling damage also can be found.

6. CONCLUSION

As a basis for the experimental work, due to the frequent application and previous experience, the 16MnCr5 case hardening steel was selected. On the sample material made of the model material, the tests were carried out after the workout to validate the numerical model suitable for determining the characteristics of the near-surface layers. Based on a comparison of the results, the model proved to be suitable for determining the layer of the rollers used for contact fatigue testing. Two disc fatigue tests were carried out on five rollers. Microstructural investigations have been started on the rollers. Having proper material characteristics information local approach based modelling will be carried out to study the high cycle fatigue of surfaces under rolling-sliding condition.

ACKNOWLEDGEMENT

The research was supported by Bilateral Serbian-Hungarian project TÉT_16-1-2016-0164, the Bolyai Fellowship of the Hungarian Academy of Sciences and the by the únkp-18-4 new national excellence program of the ministry of human capacities. The authors would like to acknowledge the scientific and technical support of Montanuniversität Leoben, Lehrstuhl für Allgemeinen Maschinenbau.

REFERENCES

[1] Case-hardening steels, available at: https://www.schmolz-bickenbach.co.za/

[2] G.G. Tibbetts, Diffusivity of carbon in iron and steels at high temperatures, Journal of Applied Physics, pp. 4813-4816, 1980.

[3] P. Maynier et al, Creusot-Loire system for the prediction of the mechanical properties of low alloy steel products. In: Doane D.V. (ed.), Kirkaldy J.S. (ed.): Hardenability concepts with applications to steel, Metallurgical Society of AIME, pp. 518-545, 1978.

[4] W.C. Leslie, Physical Metallurgy of Steels, Mc Graw Hill, New York 1982.

Biotribology

16th International Conference on Tribology – SERBIATRIB ’19

15 – 17 May 2019, Kragujevac, Serbia

Serbian Tribology Society

SERBIATRIB '19

16th International Conference on Tribology

Faculty of Engineering University of Kragujevac

Kragujevac, Serbia, 15 – 17 May 2019

TRIBOLOGICAL IMPLICATIONS OF THP MODULARIZATION

Lucian CAPITANU[1], Liliana-Laura BADITA[2,*], Constantin TIGANESTEANU[1]

[1]Institute of Solid Mechanics of the Romanian Academy, Bucharest, Romania

[2]National Institute of Research and Development in Mechatronics and Measurement Technique, Bucharest, Romania

*Corresponding author: badita_l@yahoo.com

Abstract: *The aim of the paper is to highlight the advantages of the modularization of the femoral component of the Total Hip Prosthesis (THP), especially the tribological implications it presumes (fretting wear of the modular junctions, fatigue and corrosion by fretting, which can contribute to the increase of metal ions concentrations in the blood and the possibility of the femoral stem fracture at the femoral head junction). Experimental laboratory studies focused on the analysis of the tribological phenomena occurring at the conical junctions between the femoral head and neck, as well as the neck and femoral stem, highlighting the relevant qualitative tribological aspects. Femoral stems with two junctions allow even greater capacity for the independent fit of the proximal femoral, offset and limb length with the metaphysical dimension/ stem body. For this purpose, experimental junctions, tested on a universal MTS testing machine, were built. It emphasizes the importance of the materials used for the conical or trapezoidal joints components and the measures to reduce the micro-motion that lead to fretting phenomena and fretting corrosion. The influence of conicity on the tribological phenomena is analysed.*

Keywords: *THP, modular junctions, micro-motion, fretting wear, fretting corrosion, taper damage.*

1. INTRODUCTION

As H.J. Cooper et al. stated, [1], modularization of total hip prostheses (THP) started from the need to simplify the implants subsequent revision by changing only the femoral head. Also, the head modularity allows legs length adjustment, and also allows the use of other materials (ceramics) as bearing option. If the stem must be kept under revision, exposure can be improved by removing the head, which also offers the opportunity to apply a new head.

A. Srinivasan et al., [2], specified that this could be beneficial in terms of subsequent bearing wear. But, an increase in the use of modular interfaces can have negative effects. This because it can lead to an increase of the fretting corrosion and corrosion cracking at the conical junction. Corrosion products of taper junctions may contribute to the joint wear with the third body. Although the corrosion of taper is relatively rare in hips with metal on polyethylene (MoP) joints, corrosion products can lead to adverse local tissues reactions (ALTR). The authors defined the taper between the femoral head hole and the femoral stem trunnion as the "head-neck junction". This term will also be used by the authors of the present paper in their research.

A complete review of the femoral modularization, theoretical reason for modularity, and explored clinical results was published by H. Krishnan et al. [3]. Clinically relevant issues reported using modular neck femoral stems were also examined in this research. Beside this, the failure mechanism is important to be known to determine whether modular neck femoral stems will be used in the future and how patients who already have implants should be monitored.

S. Hussenbocus et al., [4], specified that "THP corrosion reduction seems to be related to geometric parameters, materials combinations and femoral head size". They described the pathogenesis, risk factors, clinical evaluation and corrosion management of taper from the head-neck junction. Under this aim, failed neck adapters were implanted during almost 2 years in a total of about 5000 devices. After this period, titanium neck adapters were replaced by cobalt-chromium adapters.

T.M. Grupp et al., [5], showed that the primary micro-motions initiated fretting within the modular connection of the femoral taper neck. A continuous abrasion and repassing process was carried out with a subsequent cold welding at the titanium alloy modular interface. Titanium oxide layers of 10-30 µm were observed on the surface. Surface cracks caused by fretting or fretting corrosion finally lead to fatigue fracture of titanium alloy modular neck adapters. Using a cobalt-chromium neck, micro-motions can be reduced three times, especially in the case of contaminated taper connection. The incidence of fretting corrosion was also substantially lower in the case of cobalt-chromium neck.

J.R. Goldberg et al., [6], investigated the effects of various factors (materials combination, metallurgical condition, bending stiffness, head and neck moment arm, neck length and implantation time) on corrosion and fretting of modular taper surfaces. The obtained results suggest that the in vivo corrosion of hip modular taper interfaces is attributed to a mechanically assisted corrosion process. The corrosion process that appears as a result of fretting can be reduced by using higher diameter necks that increase their rigidity. However, the increase of the neck diameter must be balanced, taking into account the decrease in the range of motion and the resulting stability of the joint.

S.Y. Jauch et al., [7], studied modular prosthesis neck adapter failures with the aim to investigate the influence of materials combinations and of assembly conditions on the micro-motions size at the stem-neck interface during cyclic loading. The largest observed micro-motions were located at the lateral edge of the taper neck connection, which is consistent with the cracks' location of the clinically failed prostheses. Higher micro-motions were observed in the case of titanium neck adapters and contaminated interfaces compared to cobalt-chromium neck adapters. Based on the fact that the excessive micro-motions from the stem-neck interface could be involved in the implant failure process, the main conclusion of their studies was that particular attention should be paid to the cleaning of the interface before assembling. The same attention should be paid, when adapters with titanium neck and titanium stems are used.

J.L. Gilbert et al., [8], tested hip femoral stems made of stainless steel (ASTM F-1568) combined with CoCr alloy heads (SS/CoCr), in an in vitro corrosion test, to evaluate the tendency to mechanically assisted corrosion. Three different aspects of the modular design were evaluated: (1) comparison of CoCr/CoCr materials combinations, (2) wet/ dry assembly for SS/CoCr couplings and (3) the 0, and 6 mm offset of the head for the SS/CoCr couplings. Fretting corrosion tests were performed by a range of cyclic loads up to 3300 N and continuous cyclic loading at 3300 N for 1 M cycles. The results of these studies showed that SS/CoCr couplings were more prone to the fretting corrosion than the CoCr/CoCr couplings. Dry assembly increased the debut loading, but did not prevent the fretting corrosion. 6 mm offset heads had greater visual evidences of fretting damage. Also, "micro-motion measurements indicated fretting motions in the range of 10 – 25 µm, where the 0 mm offset heads tended to piston on the stem trunnion, while the 6 mm offset heads tend to break".

S.I. Jauch et al., [9], had mechanically tested and investigated micro-motions at the stem-neck interface of two different prostheses models: Metha (Aesculap AG) and H-Max M (Limacorporate). Metha prostheses demonstrated a substantial number of in vivo fractures for Ti-Ti couplings, but there are no fractures documented for Ti-CoCr couplings. In contrast, for H-Max M prostheses with a Ti-Ti coupling, only a clinical failure was reported. The main results showed that "for Ti-Ti couplings, Metha prosthesis showed a tendency towards higher micro-motions compared to H-Max M (6.5 ± 1.6 µm vs. 3.6 ± 1.5 µm). Independent of design, the prostheses with Ti neck adapter have caused significantly higher micro-motions at the interface, than those with CoCr adapter (5.1 ± 2.1 µm vs. 0.8 ± 1.6 µm). No differences were observed in micro-motions between the Metha prosthesis with CoCr neck and H-Max M with Ti neck (2.6 ± 2.0 µm)".

Results of the experimental tests realized by P. Wodecki et al., [10], have shown that THP with modular femoral components (stem-neck interface) makes it possible to adapt to extramedullary femoral parameters (anteversion, offset and length). In this way, muscular function and stability are improved. However, "the addition of a new interface has some disadvantages, like: reduced mechanical strength, fretting corrosion and fatigue fracture of the material".

R.T. Mikkelsen et al., [11], conducted an analysis of modular neck femoral stems, compared to the non-modular femoral stems in total hip arthroplasty (THA), with regard to the clinical outcome of metallic ions levels and radiological findings. They showed that the modular neck femoral stem was introduced to optimize the outcome of THA, but this created concerns about pain, high levels of metallic ions in blood, and adverse reactions to metal debris, such as pseudotumor, linked to the corrosion between the femoral neck and stem.

A.M. Kop and E. Swarts, [12], analysed sixteen cases of double taper cones of recovered Margron hip prostheses. These exhibited a significant fretting and a corrosive cracking of the neck-stem taper with an average duration of 39 months after implantation. The remaining recoveries showed no corrosion after an average time of 2.7 months in situ. The final results demonstrated that the increased modularity can lead to fretting and corrosive cracking, generation of metallic ions and particles debris even in the case of a modern conical design and corrosion-resistant materials. All these, fretting and corrosive cracking, generation of metallic ions and particles debris, can contribute to periprosthetic osteolysis and loss of fixation.

M.B. Ellman et al., [13], have shown that a possible complication of modularity increase is the components fracture. This has been demonstrated in the case of fracture of the modular femoral neck. "The combined effects of cracking and fretting corrosion of the large diameter femoral head, long metal-to-metal modular neck, patient size and activity level, have all played integral roles in creating a susceptible environment for this classic fatigue fracture model".

H.H. Ding et al., [14], investigated the influences of diamond-like carbon (DLC) coatings and roughness on the fretting behaviour of Ti6Al4V. It has been shown that "without DLC coating, the friction coefficient was high, and under high motion conditions, the wear volume was high. Smoother surfaces have extended the sliding and rough regime to lower motion conditions under normal force conditions. For DLC coating tests, the coating response wear maps were divided into three areas: the coating working area (low motion conditions and low normal force), coating failure area (high conditions of motion and normal force) and the transition area. In the coating working area, DLC coatings could protect the substrate with low friction, low wear volume and slight damage of the coating. The state of operation has occurred under the gross sliding regime". The increase in normal force and motion accelerated the failure of the coating.

N.J. Hallab et al., [15], studied the fretting corrosion differences of the metal-metal and ceramic-metal modular junctions of total hip replacements (THR). Ceramics femoral head (zirconia, ZrO_2) and metal (Co alloy) on Co alloy stem components were investigated using an in vitro comparison of fretting. In vitro fretting corrosion testing consisted in the monitoring and potentiodynamic analysis of the metal loss in 28 mm zirconia and Co alloy femoral heads with similar surface roughness (R_a = 0.46 µm), on identical Co alloy stems, at 2.2 kN for 1 x 10^6 cycles, at 2 Hz. A metal release about 11 times larger at Co and a 3-times increase at Cr and the potentiodynamic fretting of metal-metal modular junctions, compared to ceramics-metal junctions was observed.

T. McTighe et. al., [16], published a review of the risk factors and benefits of modular taper junctions in THA. Fretting corrosion is one of the factors that produce the decline in clinical acceptance of hip modular implants. A main mechanism behind the fretting corrosion is the stress, whose increasing at the modular junction will increase proportionally the fretting corrosion. Stryker Ortopedics, Mahwah, NJ withdrawaled products (e.g. Rejuvanate™ and ABGII™) that had reduced tapered support (13 mm vs. 15 mm and 17 mm) with high bending and torsional moments. These produce much greater stresses at the modular junction and potentially lead to a faster corrosion speed, compared to the style of stems that keep the neck. Conical adapters for neck can have design limitations in that they have sockets that can interfere with the range of motion or can cause pressure, generating debris and/ or dislocations.

In another work [17], T. McTighe et al., reviewed the developments of the short femoral stems, which offer many advantages. First, with a few short stems' patterns, most of the femoral neck is kept. Surgically, this facilitates a minimally invasive surgical approach and attenuates soft and bone tissues damage. Femoral neck preservation, which provides a more natural barrier to the particles' debris migration, is associated with lower blood losses and less time and energy for hip rehabilitation, reducing the stress shielding of proximal femur (load's redistribution and subsequent loss of proximal femoral bone mass) and reducing the pain at the end of the coast. Considering all these advantages, the use of a short stem can make quicker and less painful the patient's rehabilitation. The new design feature inherent to short stem implants – namely, the preservation of bone and native proximal tissue – provides theoretically an easier revision if or when it becomes necessary. For these reasons, the short stem procedures also have wider indications as compared to recovery of hip surface. Finally, many models with short stems do not require many stem sizes.

R. Grunert et al., [18], have shown that modularity in THA allows the reconstruction of the hip biomechanical parameters. Starting from the observation that models of femoral stems structured using taper junctions contribute to the implant fracture, the authors assumed that a new modular neck-stem interface may result in lower implant breakage compared to conventional femoral stems. Realizing a new modular stem for THA, the authors developed three different variants of the interface mechanisms. These provide a simple connection between the stem and the modular neck, and allow an intraoperative adjustment. The authors have shown that with the new design of the three manufactured prototypes, it should be possible to detach intraoperative the modular stem and neck, to adapt to the anatomical situation. It has been also shown that modular implants have to be used with caution because of the high risk of breaking, fretting of taper, corrosion and disconnection.

In a previous work, L. Capitanu et al., [19], presented a study in which they analysed the loss of cemented stem stability of the THP under physiological stress conditions. The experimental study was conducted on a universal dynamic testing machine, MTS® Bionix. The authors reported the failure by the fretting fatigue of the cemented fixation of the stem at 2200000 variable loading cycles.

M.G. Bryant et al., [20], evaluated a bi-modular prosthesis (Rejuvenate™, Stryker, USA) with a Ti-Mo-Zn-Fe alloy femoral stem (TMZF™, Stryker, USA) and femoral modular neck made of CoCrMo (Vitallium™ Stryker, USA). Large amounts of material loss at the medial proximal edge of the CoCrMo neck trunnion were noticed. On the modular taper interface, a conserved stain was observed, surrounded by high wear areas. By CMM analyse, three areas of interest were highlighted, which were subjected to further examination. They indicated a reference area (i.e., unworn material outside the contact area), a fixed spot (i.e. the region located within the extremely worn area, where the original topography was maintained) and very worn areas (areas with the largest loss of material).

S.Y. Jauch et al., [21], investigated the magnitude of micro-motions at the stem-neck interface and behaviour during daily activities, the neck connection of a design made of different alloys. Modular hip prostheses (Metha®, Aesculap AG, Germany) with neck adapters ($CoCr_{29}Mo_6$ or Ti6Al4V) were incorporated into PMMA and subjected to cyclic loading with peak loads ranging from walking (F_{max} = 2.3 kN) to stumbling (F_{max} = 5.3 kN). The micro-translation and rotation motions from the taper interface and the layout characteristics during assembling and loading were determined using four eddy current sensors. Studies have shown that placement during loading after assembly of the implant was dependent on the size of the load, but not on the coupled material.

Characterization of fretting corrosion behaviour of the surface and debris from the head-taper interface, of two different hip models has been realized by C.T. dos Santos et. al., [22]. The first one was a SS/Ti cementless model with the stem made of ASTM F136 Ti6Al4V alloy and metallic head made of ASTM F138 austenitic stainless steel. The second one was a SS/SS cemented model with both components made of ASTMF 138 stainless steel. The results obtained after fretting corrosion tests according to ASTM F1875 standard criteria, showed that micro-motions caused mechanical wear and loss of material in the head-taper interface, resulting in fretting corrosion. After 10 million cycles, it has been demonstrated that the SS/Ti model was more resistant to fretting corrosion than the SS/SS model. But, in both cases there were various morphologies of residues. Small and crowded particles were observed in the SS/Ti model, and in the SS/SS model, irregular particles. All these released particles can cause local tissue reactions in the human body and the loss of THP stability.

Fretting of CoCrMo and Ti6Al4V alloys in modular prostheses was analysed by A.O. Oladokun et al., [23]. Fretting behaviour of CoCr-CoCr and CoCr-Ti couplings and their damage mechanisms were investigated. A tribometer with ball on plate contact with in situ electrochemistry was used to characterize the damage caused by tribocorrosion on the contact of the two couplings. The amplitudes of fretting motions of 10, 25 and 50 μm were evaluated at an initial contact pressure of 1 GPa. The results reveal a greater loss of metal volume in CoCr-CoCr alloys couplings compared to CoCr-Ti alloys, and the open-loop potential indicates a depassivation of the protective oxide layer at displacement amplitudes > 25 μm. The damage mechanisms of the CoCr-CoCr and CoCr-Ti contacts have been identified as the prevalent mechanisms of wear and fatigue.

2. EXPERIMENTAL STUDY

2.1 Theoretical approach

Currently, in the speciality literature, there is no theoretical approach of the fretting wear speed. The wear speeds are quantified applying the Archard's classic approach. It reports the wear volume as the product between the sliding distance and the normal load. A wear coefficient is then extrapolated and it is assumed that it determines the wear resistance of the studied material. This approach does not work when the friction coefficient is not constant. Consequently, it seems more relevant to consider the mechanical work of interfacial shearing as significant parameter of wear.

By identifying the wear energy coefficients, quantification of wear can be rationalized and the wear resistance of studied tribosystems can be quantified.

This seems to be a convenient approach to interpret different wear mechanisms. The energy balance confirms that a small part of the dissipated energy is consumed through plasticity, while most of it participates in the heat flow and debris through the interface. When introducing a load energy approach, an accumulated density of dissipated variable energy is considered to quantify the formation of the transformed tribological structure (TTS).

The described methodology allows the implementation of the "Archard" or "dissipated energy" law to predict the fretting wear. However, the wear energy approach is presented here as a unified prediction of a single wear energy coefficient in a wider range of strokes (from 50 mm to 1.3 mm) than Archard's law and as such has no a wide range of applications (S Fouvry et al., 2003 [24], R. Magaziner et al., 2008 [25], T. Liskiewicz and S. Fouvry, 2005 [26]).

Calculation of the volumetric wear is based on the wear energy law in Eq. (1), where the mechanical interfacial shearing work is the predominant parameter for determining the wear. Total volumetric wear W_v is obtained from product of the total accumulated local energy E that is dissipated and a worn energy coefficient α

$$W_v \qquad E \tag{1}$$

where

$$E \quad Q \ s \tag{2}$$

and Q is the shear traction, and s is the relative displacement of the contact surfaces, giving

$$W_v \qquad Q \ s \tag{3}$$

Dividing both members of Eq. (3) to the contact area, the depth of linear wear W_d can be calculated using Eq. (4), where τ is the shear stress of the contact surface

$$W_d = \alpha \cdot \tau \cdot s \tag{4}$$

For the numerical implementation of this wear law, the wear depth of in contact surfaces generated in a single loading cycle of the components (such as loading applied on hip in vivo, for a single walking step) is first determined. Subsequently, if the prostheses components will be as typically, the object of millions of loading cycles during their lifetime, this wear depth in a single cycle is multiplied by a wear coefficient, β, so that an analysis can be realized in an acceptable time period. The "wear scaling" factor represents a certain number of loading cycles, and its value depends on how accurate the wear evolution is calculated and the way it evolves over time. The in-contact surfaces geometry of the components changes after measuring the wear depth, to reflect the wear that would have occurred after a certain number of β cycles. Calculated wear can be applied to only one component or both, in equal or unequal quantities, depending on combinations of materials in contact. The process is then repeated using the updated geometry up to the number of loading cycles that have been applied, or until a predetermined wear depth has been reached.

Digitization of a loading cycle in several time intervals n is necessary to accurately model the effect on the wear of the variable load distribution over time, during the loading cycle (as it appears during walking). As such, the wear depth for a single loading cycle (the depth of cyclic wear W_c) can be calculated using Eq. (5),

$$W_c \qquad {}^{n}_{i\ 1} \qquad {}_{i}\ s_i \tag{5}$$

where τ_i and s_i are the shearing stress of the surface and the relative displacement, calculated at the end of a certain time interval, i.

The total wear depth W_d generated in a specified total number of loading cycles N can be determined from Eq. (6) where j is the specific "step of analysis" which reflects the evolution of wear.

$$W_c \qquad {}^{N/}_{j\ 1} \quad {}^{n}_{i\ 1} \qquad {}_{i}\ s_i \tag{6}$$

The accuracy and effectiveness of this approach depend on many factors and on the magnitude of the wear energy coefficient that has been used. The number of time intervals used for loading cycle discretization and the "wear coefficient" factor β requires a careful analysis of their influence on the accuracy and duration of the analysis.

2.2 Experimental approach

The fretting tests were performed on an Instron® device (Fig. 1) which simulates fatigue loading of a hip cemented stem during a walking cycle. It is installed on a MTS® Bionix multi-axial dynamic servo-hydraulic testing machine [19], equipped with a hip implants testing system.

Figure 1. Instron® fatigue testing device of total hip prosthesis

The device is mounted in a sealed chamber containing saline solution with a high concentration of sodium chloride (~ 0.2 M) at a temperature of 38 ^{0}C. The assembly has a temperature regulator and a circulation pump for in vivo testing. Flexible holder for the prosthetic stem allows testing of a large variety of hip prostheses stem geometries, offset angles, and materials. The device applies compressive, bending and torsional stresses to meet ISO 7206-4 requirements.

Tests were performed on THP made by assembling femoral stems with two junctions, with femoral head-neck junction combinations.

Femoral stems with two-junctions (Fig. 2) allow a greater independent fitting capacity of the proximal femoral version, of the offset, and limbs length with the metaphyseal dimension/ stem body.

(a) (b)

(c) (d)

Figure 2. Dual modular femoral stems. (a) Kinectiv and (b) ZMR - Zimmer, Warsaw, IN, USA (c) Rejuvenate and (d) Restoration - Stryker, Mahwah, NJ, USA

In order to study the fretting of the THP's modular junctions, taper and trapezoidal junctions of a femoral neck adapter, made of CoCr and Ti6Al4V (Fig. 3), were realized to match the stems with which current modular prostheses were equipped. They were subjected to dynamic fatigue tests, up to 2500000 cycles on the Instron® device.

The neck adapters were used in combination with femoral heads made of CoCr, Ti6Al4V and ceramics (Fig. 4).

To analyse how fretting corrosion is influenced by combinations of coupled materials, the authors have developed and analysed different couplings of the Kinectiv femoral stems with different neck junctions with the femoral heads. Combining the neck adapters with the three types of femoral heads, resulted six femoral head-femoral neck combinations: Ti6Al4V/Ti6Al4V, Ti6Al4V/CoCr, Ti6Al4V/ceramics, CoCr/Ti6Al4V, CoCr/CoCr, and CoCr/ceramics. Three of the six resulting combinations are shown in Fig. 5.

(a)

(b)

Figure 3. Taper and trapezoidal junctions of a femoral neck adapter made of CoCr (a) and Ti6Al4V (b)

(a)

(b)

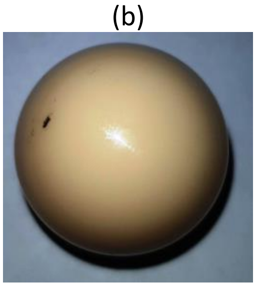

(c)

Figure 4. Femoral heads made of CoCr (a), Ti6Al4V (b) and ceramics (c), used

Figure 5. Femoral head – femoral neck combinations that have been tested

As shown in a previous work [19], the relatively large difference between the maximum and the minimum friction torque value, and the visual observation of the prosthesis's functioning through the transparent fastening holder, appeared to be a sign of the fretting wear manifestation. Testing was stopped when this difference occurred, at 2450000 cycles, and the prosthesis was removed from the Instron® device and qualitatively analysed. Tests were performed during this number of 2450000 cycles on the Instron® device with variable loading application of the normal load and of the flexion-extension (FE), abduction-adduction (AA) and external-internal rotation (IOR) motions.

3. RESULTS AND FINDINGS

After the tests, the resulting surfaces of the femoral head – femoral neck and femoral stem – femoral neck taper junctions were inspected visually and microscopically. All of these surfaces have shown, to a greater or lesser degree, evidences of fretting wear and fretting corrosion.

Fretting traces were revealed both on the taper and trapezoidal junctions of the femoral neck adapters, as well as inside the conical holes of the femoral heads.

Figs. 6 and 7 show the fretting and corrosion wear images on the surfaces of these junctions.

Figure 6. Taper and trapezoidal junctions of femoral neck adapters in CoCr (a) and Ti6Al4V (b) after 2450000 fretting cycles

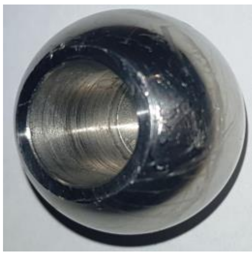

(a)

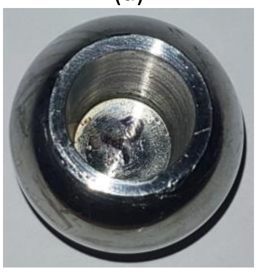

(b)

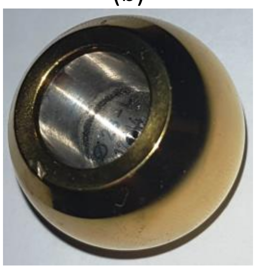

(c)

Figure 7. The fretting and corrosion wear of the inner taper of the femoral heads made of CoCr (a), Ti6Al4V (b) and ceramics (c) after 2450000 fretting cycles

4. DISCUSSION

Mechanistic model of tribocorrosion is one that takes into account all possible mechanical and chemical interactions, as follows:

$$W_T = W_m + \Delta W_{cw} + W_c + \Delta W_{wc} \qquad (7)$$

where W_T is total tribocorrosive wear, W_m and W_c are the material losses due to pure mechanical wear and pure corrosive wear. The terms ΔW_{cw} and $\Delta W_{wc,}$ respectively, represent the wear enhanced by corrosion and corrosion enhanced by wear, respectively.

4.1 Mechanical wear model

The current mechanical wear model uses a local form of Archard's equation to calculate the wear depth. In a ball on plane configuration, the local wear depth of each point on the surface is given by:

$$h\ x,y \quad W\frac{K}{R}\ P\ x,y \quad t\ \ v \qquad (8)$$

where H, K, P, v and Δt are material hardness, Archard's adimensional wear coefficient, local contact pressure, sliding speed and time step, respectively [19].

To use Archard's wear formula, the wear volume was divided to the wear track surface. Although not uniform, it provides a rough estimate of the wear depth.

Contact conditions vary from plate to ball. The balls are always in contact with the plate and move the contact's positions on the plate. Therefore, the numerical implementation of wear on the two surfaces must be different. Wear calculated from Eq. 5, taking into account the ball hardness is used directly to modify the geometry of the ball at each stage. However, the wear on the plate is calculated at each stage of the time, using a change factor.

Since the wear of the plate does not occur all the time, the wear calculated in Eq. 8 taking into account the plate hardness is divided by the ratio of the length of the wear track to the nominal contact surface, to find the balance. These wear values will then be deducted from the surface profiles, and the surfaces will be changed at each step of the time.

In simulation of the contact's mechanics, all parameters in Eq. 8 are calculated, except K. K is determined by calibration of the model. Depth of the mechanical wear calculated from

Eq. 5, is used to locally change the geometry of the surface, based on the asperity pressure's distribution. Total mechanical wear can be calculated by summing the mechanical wear from the loading cycles.

4.2 Corrosive wear model

Corrosive wear model is based on Faraday's law and the calculation of the volume of metal ions transferred to the surface and used to form the oxide. The formulation used for corrosive wear is as follows:

$$V_c = \frac{QM}{nF\rho} \tag{9}$$

where V_c is the volume of metal removed by the anodic reactions. Q is the total electrical charge passed and is calculated by integrating the current over time ($Q = \int_0^t idt$) when an excessive potential is being applied. M is the atomic mass of the metal, n is the charge for the oxidation reaction, ρ is the passive metal density, and F is Faraday's constant.

In an actual tribocorrosive wear environment, the anodic and cathodic currents are always equal to the free corrosion potential (E_{corr}), and the anodic current measured under this condition, will be true I_{corr} and should be used as a representation of the corrosion contribution. Applying the over-potentials on a sliding system will significantly alter the steady state so that the cathodic reaction becomes negligible, and the current measured will be only the anodic current from the working electrode. Working under such conditions is different from a real natural tribocorrosion state, which occurs around the E_{corr} of the metal alloy. Applying excessive potential can change the pH of the surface and may have an impact on corrosion. Therefore, strictly, I_{corr} used in any tribocorrosion study of metal alloys to measure the contribution of all mechanical and chemical components of tribocorrosion wear should be determined at E_{corr}. Despite this, most studies in the tribocorrosion area are applied over-potential and change surfaces from their natural free corrosion state.

An important parameter to be considered in the electrochemical wear model in Eq. 9, is the total electrical charge (Q). Calculation of Q will be possible when the current passage through the passive film is successfully captured. The electrochemical model is presented at the asperity scale, and the corresponding current density is calculated in a deterministic manner, considering the inhomogeneous nature of the surface asperities. The summation of the local current densities results in the calculation of the macro-current density, being comparable to the experimental results.

5. CONCLUSION

Failures of neck adapter at different models of modular prostheses extended research in this domain, and most scientists considered that the micro-motions at the stem-neck interface were responsible for these implant failures.

In the present paper the results of a study, in which the influence of materials combinations and assembly conditions on the micro-motions size at the stem-neck interface during cyclic loading were investigated, are presented.

The largest micro-motions were observed at the lateral edge of the taper neck connection. Larger micro-motions were shown in the case of titanium neck adapters, compared with CoCr ones and in the case of interfaces contaminated with fats or debris.

Fretting and fretting corrosion have occurred on all modular neck-stem recoveries, regardless of model. However, mixed metal couplings exhibited more corrosion than homogeneous couplings. This is due to the lower elasticity modulus of the titanium alloy used for the stem, which allows a greater metal transfer and surface damage when is loaded on a modular cobalt alloy neck.

The quantification of wear can be rationalized, and the wear resistance of the studied tribosystems can be quantified by identifying the wear energetical coefficients. In this way it is possible to interpret the various wear mechanisms.

The main results obtained after the studies realized in this project confirmed that different materials can be used to optimize the mechanical and tribological properties of hip modular prostheses. Even if this type of prostheses is flexible to fit to the anatomical variations, the micro-motions associated with the modular components can lead to fretting corrosion. Finally, the release of debris is produced and can cause negative local tissue reactions from the human body and the loss of THP.

ACKNOWLEDGEMENT

The authors thank the Romanian Academy and INCDMTM for the material and logistic support. The research was carried out within the project PN-II-P1-1.2-PCCDI-2017-0224, "Implementation of additive technologies for the manufacturing of complex and overloaded components”.

REFERENCES

[1] H.J. Cooper, C.J. Della Valle, R.A. Berger, M. Tetreault, W.G. Paprosky, S.M. Sporer, J.J. Jacobs: Corrosion at the head-neck taper as a cause for adverse local tissue reactions after total hip arthroplasty, Journal of Bone and Joint Surgery. American volume, Vol. 94, No. 18, pp. 1655-1661, 2012.

[2] A. Srinivasan, E. Jung, B.R. Levine: Modularity of the femoral component in total hip arthroplasty, Journal of the American Academy of Orthopaedic Surgeons, Vol. 20, No. 4, pp. 214-222, 2012.

[3] H. Krishnan, S.P. Krishnan, G. Blunn, J.A. Skinner, A.J. Hart: Instructional review: Hip. Modular neck femoral stems, The Bone & Joint Journal, Vol. 95-B, pp. 1011-1021, 2013.

[4] S. Hussenbocus, D. Kosuge, L.B. Solomon, D.W. Howie, R.H. Oskouei: Head-neck taper corrosion in hip arthroplasty, BioMed Research International, Vol. 2015, Article ID 758123, 9 pages, 2015.

[5] T.M. Grupp, T. Weik, W. Bloemer, H.P. Knaebel: Modular titanium alloy neck adapter failures in hip replacement - failure mode analysis and influence of implant material, BMC Musculoskeletal Disorders, Vol. 11, No. 3, 12 pages, 2010.

[6] J.R. Goldberg, J.L. Gilbert, J.J. Jacobs, T.W. Bauer, W. Paprosky, S. Leurgans: A multicenter retrieval study of the taper interfaces of modular hip prostheses, Clinical Orthopaedics and Related Research, Vol. 401, pp. 149–161, 2002.

[7] S.Y. Jauch, G. Huber, E. Hoenig, M. Baxmann, T.M. Grupp, M.M Morlock: Influence of material coupling and assembly condition on the magnitude of micromotion at the stem–neck interface of a modular hip endoprosthesis, Journal of Biomechanics, Vol. 44, No. 9, pp. 1747–1751, 2011.

[8] J.L. Gilbert, M. Metha, B. Pider: Fretting crevice corrosion of stainless-steel stem-CoCr femoral head connections: comparation of materials, initial moisture, and offset length, Journal of Biomedical Materials Research Part B Applied Biomaterials, Vol. 88, No. 1, pp. 162-173, 2009.

[9] S.Y. Jauch, G. Huber, H. Haschke, K. Sellenschloh, M.M. Morlock: Design parameters and the material coupling are decisive for the micromotion magnitude at the stem–neck interface of bi-modular hipimplants, Medical Engineering & Physics, Vol. 36, No. 3, pp. 300–307, 2014.

[10] P. Wodecki, D. Sabbah, G. Kermarrec, I. Semaan: New type of hip arthroplasty failure related to modular femoral components: Breakage at the neck-stem junction, Orthopaedics & Traumatology: Surgery & Research, Vol. 99, No. 6, pp. 741-744, 2013.

[11] R.T. Mikkelsen, M. Fløjstrup, C. Lund, P. Kjærsgaard-Andersen, T. Skjødt, C. Varnum: Primary arthroplasty. Modular neck vs nonmodular femoral stems in total hip arthroplasty - clinical outcome, metal ion levels, and radiologic findings, The Journal of Arthroplasty, Vol. 32, No. 9, pp. 2774-2778, 2017.

[12] A.M. Kop, E. Swarts: Corrosion of a hip stem with a modular neck taper junction. A retrieval study of 16 cases, The Journal of Arthroplasty, Vol. 24, No. 7, pp. 1019-1023, 2009.

[13] M.B. Ellman, B.R. Levine: Case report. Fracture of the modular femoral neck component in total hip arthroplasty, The Journal of Arthroplasty, Vol. 28, No. 1, pp. 196-e1, 2013.

[14] H.H. Ding, V. Fridrici, J. Geringer, J. Fontaine, Ph. Kapsa: Influence of diamond-like carbon coatings and roughness on fretting behaviors of Ti–6Al–4V for neck adapter–femoral stem contact, Wear, Vol. 406–407, pp. 53-67, 2018.

[15] N.J. Hallab, C. Messina, A. Skipor, J.J. Jacobs: Differences in the fretting corrosion of metal-metal and ceramic-metal modular junctions of total hip replacements, Journal of Orthopaedic Research, Vol. 22, No. 2, pp. 250-259, 2004.

[16] T. McTighe, D. Brazil, I. Clarke, L. Keppler, J. Keggi, T. Tkach, E. McPherson: Metallic modular taper junctions in total hip arthroplasty, Reconstructive Review, Vol. 5, No. 2, pp. 29-42, 2015.

[17] T. McTighe, D. Brazil, J.M. Keggi, L. Keppler, E.J. McPherson: Short-stem designs for total hip arthroplasty: neck stabilized femoral components, Chapter 64 in book: The Adult Hip "Hip Arthroplasty Surgery", Publisher: Wolters Kluwer, pp.823-849, 2016.

[18] R. Grunert, S. Schleifenbaum, R. Möbius, M. Kopper, C. Rotsch, W.G. Drossel, N. Hammer, T. Prietzel: Novel concept of a modular hip implant could contribute to less implant failure in THA: a hypothesis, Patient Safety in Surgery, Vol. 12, No.1, 2018.

[19] L. Capitanu, L.L. Badita, V. Florescu: Stability loss of the cemented stem of hip prosthesis due to fretting corrosion fatigue, Tribology in Industry, Vol. 39, No. 4, pp. 536-546, 2017.

[20] M.G. Bryant, D. Buente, A. Oladokun, M. Ward, G. Huber, M. Morlock, A. Neville: Surface and subsurface changes as a result of tribocorrosion at the stem-neck interface of bi-modular prosthesis, Biotribology, Vol. 10, pp. 1-16, 2017.

[21] S.Y. Jauch, G. Huber, K. Sellenschloh, H. Haschke, M. Baxmann, T.M. Grupp, M.M. Morlock: Micromotions at the taper interface between stem and neck adapter of a bimodular hip prosthesis during activities of daily living, Journal of Orthopaedic Research, Vol. 31, No. 8, pp. 1165-1171, 2013.

[22] C.T. dos Santos, C. Barbosa, M.J. Monteiro, I.C. Abud, I.M.V. Caminha, C.R.M. Roesler: Characterization of the fretting corrosion behavior, surface and debris from head-taper interface of two different modular hip prostheses, Journal of the Mechanical Behavior of Biomedical Materials, Vol. 62, pp. 71–82, 2016.

[23] A.O. Oladokun, M.P. Pettersson, M. Bryant, H. Engqvist, C. Persson, R. Hall, A. Neville: Fretting of CoCrMo and Ti6Al4V alloys in modular prostheses, Tribology - Materials, Surfaces & Interfaces, Vol. 9, No. 4, pp. 165-173, 2015.

[24] S. Fouvry, T. Liskiewicz, P. Kapsa, S. Hannel, E. Sauger: An energy description of wear mechanisms and its applications to oscillating sliding contacts, Wear, Vol. 255, No. 1-6, pp. 287–298, 2003.

[25] R. Magaziner, V. Jain, S. Mall: Wear characterization of Ti–6Al–4V under fretting – reciprocating sliding conditions, Wear, Vol. 264, No. 11-12, pp. 1002–1014, 2008.

[26] T. Liskiewicz, S. Fouvry: Development of a friction energy capacity approach to predict the surface coating endurance under complex oscillating sliding conditions, Tribology International, Vol. 38, No. 1, pp. 69–79, 2005.

Serbian Tribology Society

SERBIATRIB '19

16th International Conference on Tribology

Faculty of Engineering University of Kragujevac

Kragujevac, Serbia, 15 – 17 May 2019

DRY WEAR STUDIES ON REDUCED GRAPHENE OXIDE FILLED UHMWPE COMPOSITES

Ferda MINDIVAN[1,3*], Meryem GOKTAS[2,3], Alime COLAK[3]

[1]Bilecik Seyh Edebali University, Faculty of Engineering, Department of Biomedical Engineering, 11230, Bilecik, Turkey

[2]Bilecik Seyh Edebali University, Vocational College, Department of Metallurgy, 11230, Bilecik Turkey

[3]Bilecik Seyh Edebali University, Biotechnology Application and Research Centre, 11230, Bilecik, Turkey

*Corresponding author:ferda.mindivan@bilecik.edu.tr

Abstract: *Reduced graphene oxide filled ultra-high molecular weight polyethylene matrix composites were produced by a method of liquid phase ultrasonic mixing and then hot press molding. The wear and friction behavior of UHMWPE composites containing up to 3.0 wt. % RGO filler were investigated in sliding against an Al_2O_3 counterface by a constant loading (5 N) and sliding speed (1.7 cm s^{-1}) experiments carried out in a reciprocating friction testing machine under dry conditions at room temperature. The results showed that, when the content of RGO was up to 1.0 wt. %, wear resistances of the composites were improved significantly. To analyze wear mechanisms, wear surfaces were examined by field emission scanning electron microscopy (FE-SEM) and it was found that, as RGO was added into the UHMWPE matrix the tribological behavior of the UHMWPE composites transformed from fatigue wear to adhesive wear associated with the increase of interaction between RGO and UHMWPE matrix and lubricant and binder properties of RGO.*

Keywords: *Reduced graphene oxide, UHMWPE, Composite, Friction, Dry wear.*

1. INTRODUCTION

Ultrahigh molecular weight polyethylene (UHMWPE), with molar weights exceeding one million, has been extensively used as a bearing material for arthroplasty applications especially in knee and hip artificial implant due to its unique characteristics, such as high impact strength, good biocompatibility and low friction coefficient [1-3]. However, UHMWPE has several disadvantages such as the low surface hardness and Young's modulus, and anti-fatigue capacity [4-5]. Moreover, UHMWPE produces wear debris during application and these debris limits to the life time of UHMWPE joints [2]. Therefore, remedial approaches have been developed to enhance the mechanical and tribological properties of the UHMWPE. The use of graphene and graphene derivatives is one of the research efforts exploited to achieve this goal. The reduced graphene oxide (RGO) is chemical type of graphene, inexpensive and a new antibacterial filler material for bio based polymer composites [6-7]. There are several studies conducted to improve mechanical and wear properties of UHMWPE composites with graphene derivatives [1, 6, 8-9].

However, to the best of our knowledge, there are no previous studies reported in the literature about synthesis and wear properties of UHMWPE composites with RGO fillers that was synthesized by vitamin C. The objective of this work is to investigation of dry wear properties of UHMWPE composites with the use of RGO. A series of UHMWPE composites with RGO fillers were prepared to study the dry wear properties, such as the wear rate and friction coefficient, and compared with unfilled UHMWPE. Therefore, we concluded that RGO plays a pivotal role in enhancing the tribological properties because of the good interactions and excellent incorporation of RGO fillers into the UHMWPE matrix.

2. EXPERIMENTAL METHODS

GO was prepared according to a modified Hummers' method [10]. To prepare RGO, 1 g of GO was dispersed in 500 mL of DI water. pH of the GO suspension was adjusted to ~10 by using ammonia solution. Then 1 g of vitamin C was added to the mixture and heated at 95°C for 12 h. After that the mixture was filtered, washed with DI water several times and dried at 65°C for 12 h to obtain the RGO sample as a black powder.

A series of the composites were prepared with the mass ratios (RGO:UHMWPE) of 0.1, 0.3, 1.0, 2.0 and 3.0 wt%. The codes of unfilled UHMWPE and these five composites were UHMWPE, RGO-0.1/UHMWPE, RGO-0.3/UHMWPE, RGO-1.0/UHMWPE, RGO-2.0/UHMWPE, and RGO-3.0/UHMWPE. The prepared RGO powders were dispersed by ultrasonic treatment (30 min) in ethyl alcohol to form a well-dispersed suspension. After that, the suspensions were added into the UHMWPE powders and the mixture was stirred for 30 min and then ultrasonicated for 1h. Then the ethyl alcohol was removed at 60-70°C in an oil bath and the composite powders were completely dried in an oven at 60 °C. Finally, the unfilled UHMWPE and composite powders were molded by hot-pressing at 180°C under a 10 MPa pressure and holding at this pressure for 30 min. The synthesis process of UHMWPE composites was illustrated in Figure 1. Tribological properties of obtained composites were investigating using a reciprocating wear tester under dry sliding conditions. The ambient temperature was approximately 25 °C and the relative humidity was nearly 30 ± 5 %. The wear tests on all samples were performed under a constant load of 5 N using a 10 mm diameter Al_2O_3 ball at a sliding velocity of 1.7 cm s^{-1} , while sliding distance was 50 m. The wear was calculated by analysing width and depth of wear scars developing on composite surfaces with the help of a contact stylus profilometer (SJ400). Worn surface morphologies of composites were observed by using a Carl Zeiss AG, SUPRA 40 model field emission Scanning Electron Microscope (FE-SEM). Following the wear tests, the Al_2O_3 counterface surfaces were examined under an Optical Microscope (OM) in order to investigate the wear mechanisms.

3. RESULTS AND DISCUSSION

Wear rate and friction coefficient are the most two important representative values to characterize the tribological properties [11]. Fig. 2 showed the impact of loading content of RGO on the wear rate of the UHMWPE composites. As presented in Fig. 2, the wear rate of the UHMWPE composites was decreased by the high RGO content (up 1.0 wt. %).

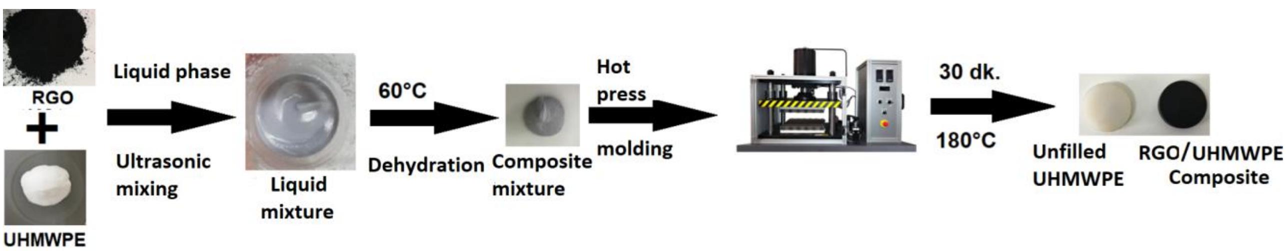

Figure 1. Illustration for the preparation of UHMWPE composites

The RGO filler improved the wear resistance of polymer matrix at a relatively high loading. The UHMWPE composite with 3.0 wt% RGO content showed the lowest wear rate under dry test conditions. The similar results have been found by Tai et al. [1]. RGO network transfered good load because ıt has ideal mechanical properties and high specific surface area [6]. Table 1 showed that the friction coefficient values of unfilled UHMWPE and UHMWPE composites. As can be seen in Table 1, the all composites with RGO fillers exhibited a continuously decreasing trend except for the composite with 1.0 wt% of RGO. For RGO-0.1/UHMWPE, RGO-0.3/UHMWPE, RGO-2.0/UHMWPE and RGO-3.0/UHMWPE composites, RGO displayed lubricant properties because of a decrease in the friction coefficient, when RGO was added into UHMWPE matrix. However friction coefficient increased, lubricating effect of graphene decreased in the composite with 1.0 wt% of RGO. This can be attributed to the encounter of lateral force with RGO-UHMWPE bond or RGO-RGO interlayer van der Waals bonds during wear process [8, 12].

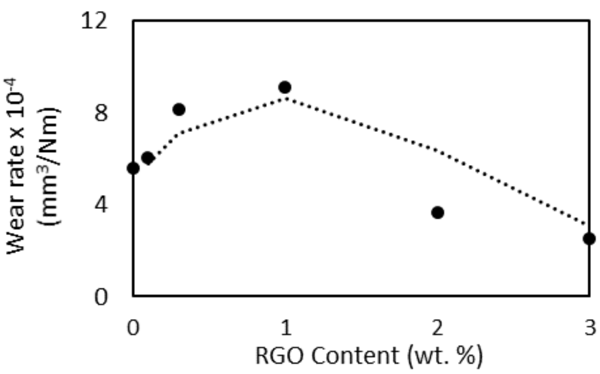

Figure 2. Wear rate of UHMWPE filled with various contents of RGO

In the present study, the worn surfaces of the UHMWPE composites were characterized using FE-SEM observation to understand the influence of the RGO loading content on its dry wear mechanism (Fig. 3a-f). Plastic deformation could be found on unfilled UHMWPE worn surface in the low magnified image (Fig.3a), which are the typical characteristics of adhesive wear [13]. The fatigue wear was found dominant where the surface layer of the unfilled UHMWPE were stripped large pieces of material in the high magnified image (Fig.3a) [6].

Table 1. Friction coefficient values of UHMWPE filled with various contents of RGO

Samples	*Friction coefficient*
UHMWPE	0,098
RGO-0.1/UHMWPE	0,068
RGO-0.3/UHMWPE	0,056
RGO-1.0/UHMWPE	0,062
RGO-2.0/UHMWPE	0,046
RGO-3.0/UHMWPE	0,036

The wear tracks of RGO-0.1/UHMWPE composites shown in Fig. 3b depicted smaller pieces of material as compared to the unfilled UHMWPE and adhesive wear tracks decreased on a large scale. From the image shown in Fig. 3(c), it can be seen that there were large flakes of wear debris, which indicated that delamination. Surface delamination in Fig. 3(c) is sign of fatigue wear [14]. For the RGO-1/UHMWPE composite, the debris obtained from the worn surface after the sliding wear test acted as a second body in between the contact surfaces which corresponded well with the previous analysis of the friction coefficient (Table 1). From the low magnified image shown in Fig. 3(d), it is clear that adhesive wear tracks increased on surface of composite. The obvious tear layers were observed on the surface of RGO-1/UHMWPE as shown in high magnified image (Fig. 3d), which indicated the shedding of composite material. The RGO-2/UHMWPE and the RGO-3/UHMWPE composites exhibited a smooth wearing surface after the test, although it had a small amount of debris. Thus, resulted in better tribological performance because of a lubrication mechanism by bonding the RGO and UHMWPE along the interlayer surface.

In order to explain the mechanisms involved in the wear process, the Al_2O_3 ball counterfaces were analyzed by OM. All wear tracks showed formation of a transfer layer on the Al_2O_3 ball surface. The worn surface morphology of Al_2O_3 ball against unfilled UHMWPE as shown in Fig. 4 are similar to that of RGO-0.1/UHMWPE and RGO-2/UHMWPE composites and they have a thin and uniform transfer film on the Al_2O_3 ball but the transferred debris increased on the surface of RGO-0.3/UHMWPE, RGO-1/UHMWPE and RGO-3/UHMWPE composites. At the same time, many particule-like wear debris was seen throughout over the Al_2O_3 ball surface of the rapidly wearing RGO-1/UHMWPE composite (Fig. 4). This image of counterface was consistent with the results obtained from wear rate and friction coefficient (Fig.2 and Table 1).

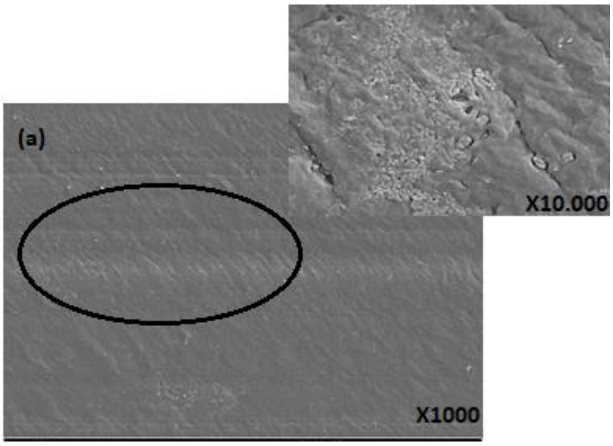

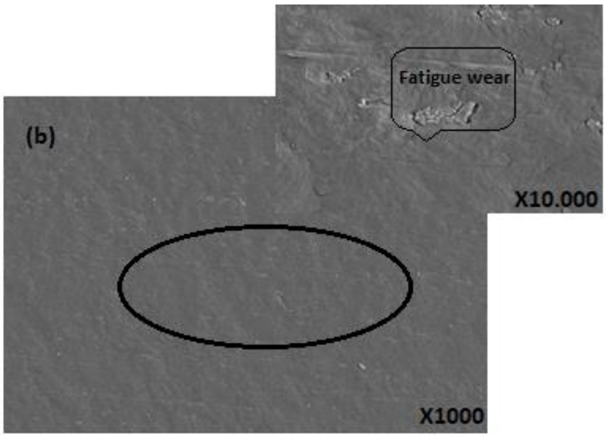

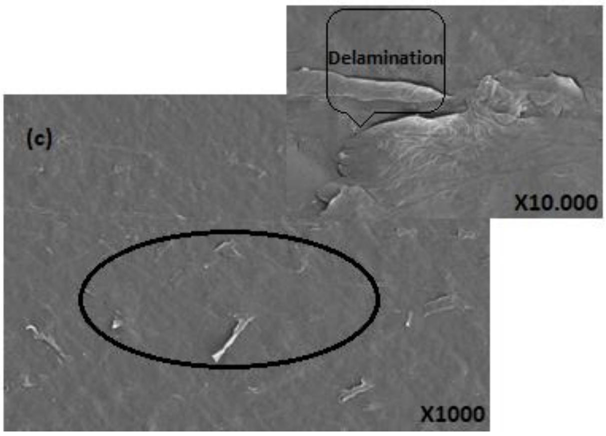

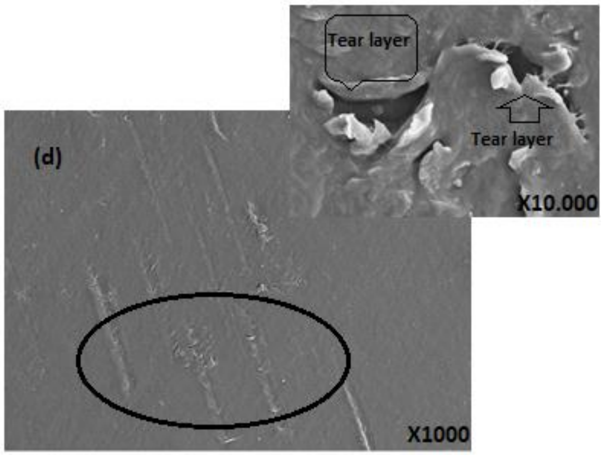

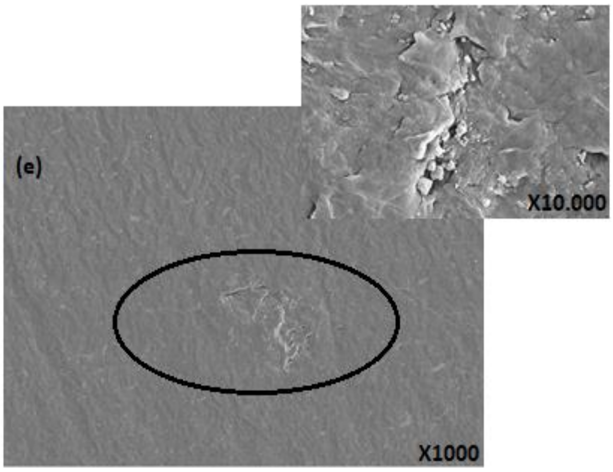

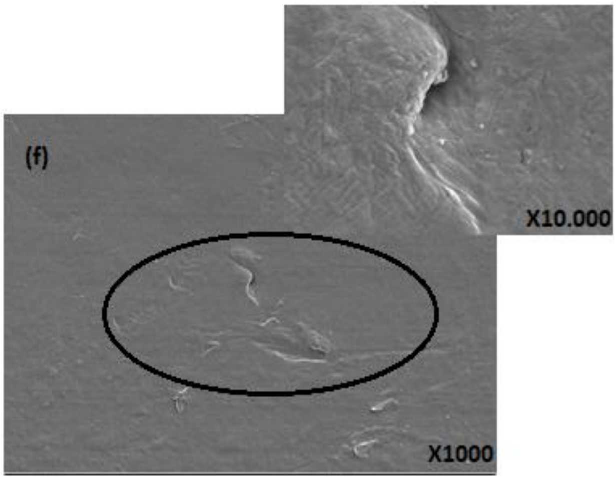

Figure 3. Low and high magnification SEM micrographs of wear tracks generated on the (a)UHMWPE, (b)RGO-0.1/UHMWPE, (c)RGO-0.3/UHMWPE, (d)RGO-1/UHMWPE, (e)RGO-2/UHMWPE and (f)RGO-3/UHMWPE composites

Samples	OM Images
Unfilled UHMWPE	
RGO-0.1/UHMWPE	
RGO-0.3/UHMWPE	
RGO-1/UHMWPE	
RGO-2/UHMWPE	
RGO-3/UHMWPE	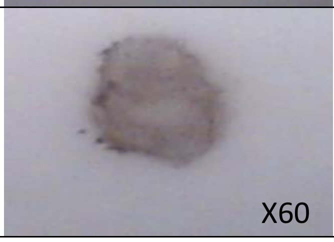

Figure 4. OM images of the Al_2O_3 balls sliding against the UHMWPE, RGO-0.1/UHMWPE, RGO-0.3/UHMWPE, RGO-1/UHMWPE, RGO-2/UHMWPE and RGO-3/UHMWPE composites.

4. CONCLUSIONS

The high aspect ratio and large surface area of RGO fillers provided a positive influence on the friction coefficient and in the wear rate. Also enhance the interaction between the polymer and the filler, resulting in an efficient load transfer from the matrix to the filler. At the high RGO percentages (2 and 3 wt%), the wear mechanism seems to be adhesive wear, while at the low RGO percentages (0.1, 0,3 and 1) fatigue wear predominates. The incorporation of RGO into UHMWPE in amounts around 2 and 3 wt. % can reduce the frictional coefficient and the wear rate. Under sliding contact, lubrication capability of graphene have a significantly effect.

ACKNOWLEDGEMENT

This study has been prepared as a part of the master thesis (Production and Characterization of Ultra High Molecular Weight Polyethylene (UHMWPE) Composites with Reduced Graphene Oxide (RGOC) using Vitamin C).

REFERENCES

[1] Z. Tai, Y. Chen, Y. An, X. Yan, Q. Xue: Tribological Behavior of UHMWPE Reinforced with Graphene Oxide Nanosheets, Tribology Letters, Vol.46, No. 1, pp. 55–63, 2012.

[2] J. C. Baena, J. Wu, Z. Peng: Wear Performance of UHMWPE and Reinforced UHMWPE Composites in Arthroplasty Applications: A Review, Lubricants, 3, pp. 413-436, 2015.

[3] F. Liu, Y. Wang, K. Li, L. Jiang, X. Wang, X. Shao, B. Zhang, F. Cui: Graphene Oxide/Ultrahigh Molecular Weight Polyethylene Composites: Ball-Milling Preparation Mechanical Performance and Biocompatibility Effects, American Journal of Biomedical Science and Engineering, Vol. 1, No. 5, pp. 51–57, 2015.

[4] W. Pang, Z. Ni, G. Chen, G. Huang, H. Huang, Y. Zhao: Mechanical and thermal properties of graphene oxide/ultrahigh molecular weight polyethylene nanocomposites, RSC Advances, Vol. 5, No. 77, pp. 63063-63072, 2015.

[5] X. Sánchez-Sánchez, A. Elias-Zuñiga, M. Hernández-Avila: Processing of ultra-high molecular weight polyethylene/graphite composites by ultrasonic injection moulding: Taguchi optimization, Ultrasonics Sonochemistry, Vol. 44, pp. 350- 353, 2018.

[6] W. Pang, Z. Ni, J. Wu, Y. Zhao: Investigation of tribological properties of graphene oxide reinforced ultrahigh molecular weight polyethylene under artificial seawater

lubricating condition, Applied Surface Science, Vol. 434, pp. 273–282, 2018.
[7] H. Hu, G. Zhang, L. Xiao, H. Wang, Q. Zhang, Z. Zhao: Preparation and electrical conductivity of graphene/ultrahigh molecular weight polyethylene composites with a segregated structure, Carbon, Vol. 50, pp. 4596–4599, 2012.
[8] I.K. Aliyu, A. Mohammed, A. Al-Qutub: Tribological Performance of Ultra High Molecular Weight Polyethylene Nanocomposites Reinforced with Graphene Nanoplatelets, Polymer Composites, 2018.
[9] A. Golchin, A. Wikner, N. Emami: An investigation into tribological behaviour of multi-walled carbon nanotube/graphene oxide reinforced UHMWPE in water lubricated contacts, Tribology International, Vol. 95, pp. 156–161, 2016.
[10] F. Mindivan: The synthesis and characterization of graphene oxide (GO) and reduced graphene oxide (RGO), Machines, Technologies, Materials, Vol. 6, pp. 32-35, 2016.
[11] J. Zhang, Z. Chen, H. Wu, J. Zhao, Z. Jiang: Effect of graphene on the tribolayer of aluminum matrix composite during dry sliding wear, Surface and Coatings Technology, Vol. 358, pp. 907-912, 2019.
[12] G. Huang, Z. Ni, G. Chen, and Y. Zhao: The Influence of Irradiation and Accelerated Aging on the Mechanical and Tribological Properties of the Graphene Oxide/Ultra-High-Molecular-Weight Polyethylene Nanocomposites, International Journal of Polymer Science, Vol. 2016, pp. 1-9, 2016.
[13] Q. Wang, H. Wang, Y. Wang, F. Yan: The influences of several carbon additions on the fretting wear behaviors of UHMWPE composites, Tribology International, Vol. 93, pp. 390–398, 2016.
[14] N. Shahemi, S. Liza, A.A. Abbas, AM Merican: Long-term wear failure analysis of uhmwpe acetabular cup in total hip replacement, Journal of the Mechanical Behavior of Biomedical Materials, Vol. 87, pp. 1–9, 2018.

Serbian Tribology Society

SERBIATRIB '19

16th International Conference on Tribology

Faculty of Engineering
University of Kragujevac

Kragujevac, Serbia, 15 – 17 May 2019

OBSERVATION OF LUBRICATION FILM IN SYNOVIAL JOINT

Pavel ČÍPEK[1,*], David REBENDA[1], Martin VRBKA[1], Martin HARTL[1]

[1] Brno University of Technology, Brno, Czech Republic
* Corresponding author: Pavel.Cipek@vut.cz

Abstract: *Painless movement is very important in active life; therefore, a proper function of our synovial joints is necessary. Synovial joints can be injured during human life in several ways. When a synovial joint is too damaged, it has to be replaced by an artificial joint. There is a common effort to postpone operations of total endoprosthesis as long as possible. The reason is limited lifetime of artificial joints. An operation can be postponed by alternative approaches, for example by viscosuplementation. The issue of lubrication in natural joints is not explored enough. The understanding of lubrication process can assist in the development and understanding of new suitable medical treatments. This study is focused on the observation of a lubrication film in a model of synovial joint. A contact is simulated between a cartilage pin and a glass desk in reciprocating tribometer and the contact area is observed. The goal of this study is to describe the contact area and correlation between friction trends and the formation of lubrication film.*

Keywords: *Biotribology, cartilage, reciprocating tribometer, friction, lubrication*

1. INTRODUCTION

The synovial joint is one of the main components of human motion system. It composes of two bones or more whose surfaces covered by cartilage are in mutual contact [1]. The synovial joints are lubricated by synovial fluid. The combination of special structure of cartilage and synovial fluid allow movement with very low friction coefficient. Cartilage is heterogeneous material with very low cell density and porous structure [2]. These attributes cause the specific tribological behaviour. The main component of the cartilage structure is an extracellular matrix (ECM). ECM is rich in type II collagen fibres and proteoglycan [3]. Hyaluronic acid (HA), proteins, decorins, chondrocytes, etc. are also included in the ECM [4]. The thickness of the cartilage is divided into the three zones, the superficial zone; the middle zone and the deep zone [1]. Each of them has the specific composition and orientation of the collagen fibres [5]. The water volume in cartilage tissue is also very important attribute with regard to lubrication properties [6, 7]. In terms of mechanical properties, the cartilage has very low elastic module (1 – 20 MPa) with respect to the position of the cartilage surface and type of joint [4]. All the mentioned specific properties are basis for lubrication processes in the synovial joint.

Apparently, there is very limited knowledge in terms of experimental investigation of lubrication in natural joints. Nevertheless, some studies focused on visualization of natural cartilage, or hydrogels, were published. All the published studies are focused on friction measurement or visualization of cartilage contact area separately. One of the first study dealt with visualization of hydrogel contact area by fluorescence microscopy [8]. The aim of the study was to determine the amount of the fluorescently marked particles in the contact area. The measurements were carried out with labelled proteins contained in the synovial fluid. Conclusions of this study were, that the γ-globulin protein has the main influence on the lubrication processes; however, the composition ratio of individual proteins and other components of the synovial fluid is very important. The fluorescence microscopy was used for the description of the gel-like layer formation on the cartilage surface. Forsey, et al. [9], showed that the HA is the main component for the formation of the gel-like layer; however, the process depends on the size of the HA molecules. The penetration of the cartilage structure was demonstrated. Particles of the HA bind with chondrocytes in the cartilage structure. Wu, et al., 2015 [10] studied the flow of the synovial fluid through the cartilage structure depending on the cartilage compression. The results showed that the large molecules of HA were caught on the cartilage surface, while the smaller particles penetrate the cartilage structure. The large molecules create the gel-like layer on the surface that protects the raw cartilage surface against a damage.

The fluorescent microscopy was also used for visualization of contact in joint replacement. Number of studies were carried out and published at our department. A lot of experience with the use of optical methods was obtained within the mentioned studies. Nečas, et. al. [11, 12] published the papers focused on soft contacts, or visualization of joint replacement contact, among others.

The previous studies have always dealt with the friction measurements or with visualization of contact area separately, it has never been measured simultaneously yet. This study combinates this two branches of biotribologic science and uses the optical methods at workplace and classical friction measurements together. The specially tailored tribometer was designed for this application which allows visualization of soft contact and friction measurements at the same time. Concept like the new designed tribometer have never been used yet. The goals of this study are to design the new tribometer, to develop the sampling process and experimental methodology and finally, to perform the pilot experiments.

2. MATERIALS AND METHODS

2.1 Experimental device

The tailored tribometer allows view into the contact area and it measures friction forces simultaneously in real time. For compliance of this requirements the pin-on-plate configuration of tribometer was used. The concept was adapted to be able to use fluorescent microscopy. This new design is close to concept of tribometer which was used in study [13]. The schema of newly designed experimental device is shown in Fig. 1. The cartilage sample is placed under the glass desk in order to visualize the contact area. The fluorescent microscopy is used for contact observation. The view is obtained by fluorescent microscope and it is record by high-speed camera. The mercury lamp was used as a light source. The contact area was flooded by a lubricant and heated to a human body temperature. The glass desk was designed as a moveable part which performs the reciprocating motion, while the specimen is stationary.

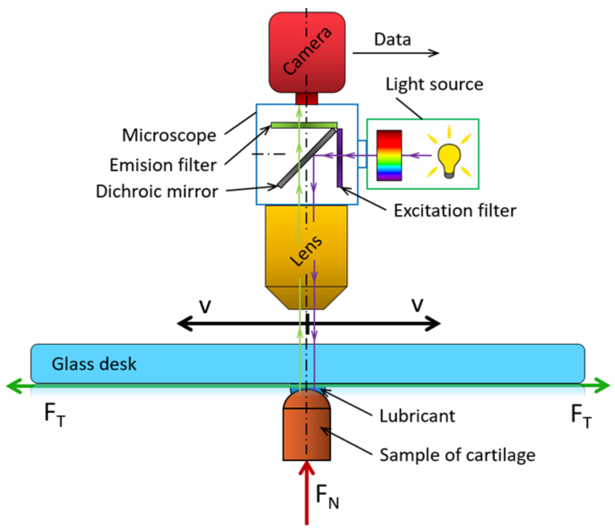

Figure 1. Schematic of the apparatus

According to the schema of function (Fig. 1) a concept of experimental device was designed. The device consists of several main unites, as is shown in Fig. 2.

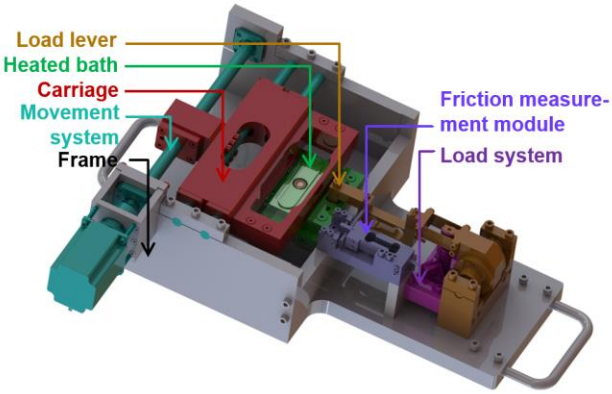

Figure 2. Real arrangement of apparatuses

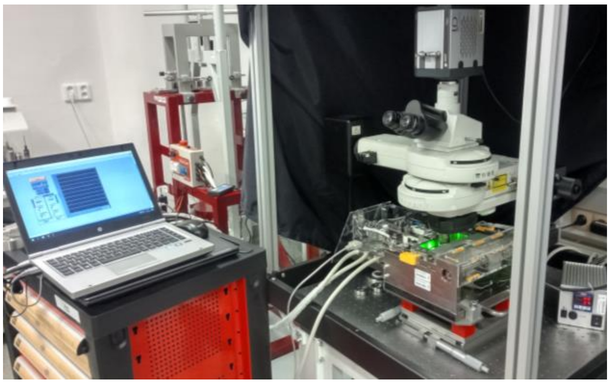

Figure 3. Real arrangement of apparatuses

The basis of the tribometer is a tough frame; all the other components are mounted on it. The moveable part, where the glass plate is mounted, performs the reciprocating motion. The accurate guide rods in combination with ball screw provide very accurate motion without clearances. The lubrication of the contact is provided by a bath. There is a sealing between the glass plate and the bath. Lever is mounted in two preloaded bearings. This arrangement allows the motion without clearance. Lever, on which specimen is attached, exerts the load on the contact. A strain gauge is connected in a serial to the lever and is used for measuring the load. The lever contains a deformable part which allows measuring of very low forces. The other strain gauge allowing friction measurement is connected to the lever in parallel. The whole tribometer is below the fluorescent microscope on an adjustable table. The tailored tribometer is shown in Fig. 3.

Measuring system is based on the National Instruments measuring card, whose data is processed, by LabVIEW script using PC. Control system is based on Arduino. The glass plate motion is ensured by the stepper motor and the load is provided by the linear stepper motor. The input parameters are defined via LCD display and encoder. The measuring system and control system work separately.

The verification and calibration of the device were performed on standard pairs of samples. The pin was made from PTFE-G400 and the plate was made from optical glass B270. The results were compared with commercial tribometer Bruker UMT TriboLAB. The mentioned material combination was used because the cartilage specimens show variance in results. The obtained compliance of the results using the two simulators was very good.

2.2 Specimens

Specimens from mature pigs were used in the present study. The samples were removed from canopy of the femoral head as soon as possible after the slaughter of animal. The hip joint is the most loaded joint in a human body, which leads to the best mechanical properties [4]. The sampling position was precisely defined through all sample bones, in order to the minimalize deviation of mechanical properties. The hollow drill bit with diameter of 6 mm was used and the specimens were deeply frozen (-20 ˚C) in PBS. This sampling process was used in some studies [14, 15] and it was verified in [16, 17] which proved that the tribological properties did not change. The samples were unfrozen just before testing due to fast degradation of samples. The sampling process is shown in Fig. 4.

Three variants of lubricant were used. The composition of all the used lubricants is shown in Table 1.

Tubule 1. Composition of the used lubricants

	Albumin (mg/ml)	γ-globulin (mg/ml)	HA (mg/ml)
Fluid 1	20	-	-
Fluid 2	-	3,6	-
Fluid 3	20	3,6	2,5

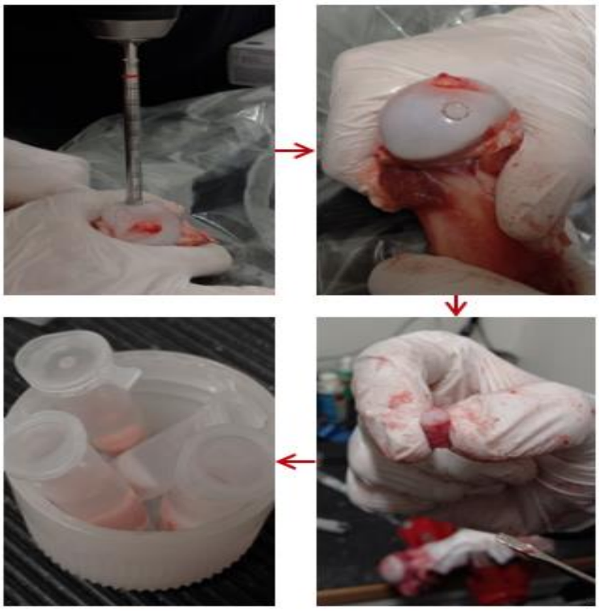

Figure 4. Specimen preparation process

For the experiments focused on visualization fluid 3 was used. The composition was constant for all the visualization experiments, only fluorescently stained component varied. In the first case, albumin was marked by Rhodamine-B-isothiocyanate (283924, Sigma-Aldrich) and in the second case, γ-globulin was marked by Fluorescein-isothiocyanate (F7250, Sigma-Aldrich).

2.3 Experimental methodology

In order to carry out the individual measurements comparable, all of the experiments in this study were measured with one sample. There are significant deviations between the measurements when they are performed with various samples. This deviation is caused by different mechanical and structural properties among individual animal bones. The comparability of measurements with one sample was validated in this study. The deviation of results was 5% in maximum.

All the experiments were performed according to strict procedure to minimize the results deviation. The sample was stored in PBS between experiments and the run-in procedure consisting of 20 reciprocating cycles at 10 N load was performed before each experiment. This procedure suppresses the effect of previous experiment.

In the first step, the experiments were focused on the friction measurement considering the lubricants 1 and 2. In the second step, the experiments focused on the combination of friction forces measurement and visualisation of the contact area. Lubricant 3 was used in two configurations; the first with stained albumin and the second with stained γ-globulin. The overall composition was always the same.

2.4 Experimental condition

The applied conditions were chosen based on the real conditions in human body in considered the hip joint. The load was 10 N, which provides the medium stress comparable with hip joint stress 1 MPa. Speed was 10 mm/s, which corresponds to slow walk. Stroke of reciprocating motion was taken from the previous studies and it was chosen to be 20 mm. Lubricant bath was heated to 37˚C.

3. RESULTS AND DISCUSION

The results of friction measurements are shown in Fig. 5.

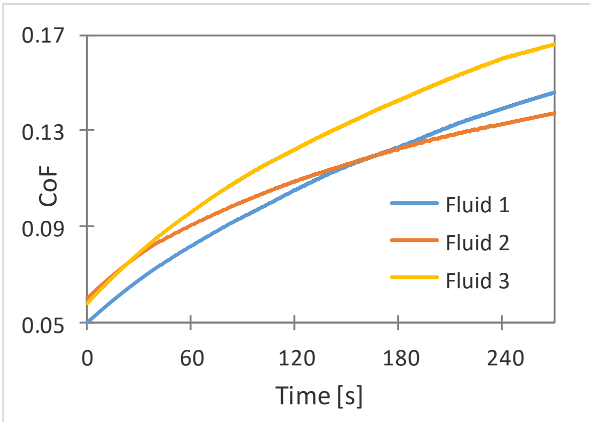

Figure 5. Friction trends, Fluid 1 – albumin, Fluid 2 - γ-globulin, Fluid 3 – model synovial fluid

Fluid 1 exhibits steeper increase of friction than fluid 2, which is the most probably caused by higher concentration of proteins and larger size of albumin molecules. These trends are confirmed by images from contact visualization, which show higher light image intensity in the case of measurement with marked albumin. Although two measurements were performed with fluid 3 composition, there is only one curve fluid 3, which represents both measurements. This one curve is representative for both measurements. In the first case, albumin protein was marked and in the other case ϒ-globulin protein was marked. Model synovial fluid (Fluid 3) shows higher friction than simple protein solutions; apparently, the grooving global volume of proteins in lubricant causes higher friction. Similar solutions were studied by Murakami, et. al., 2017 [18] who observed higher friction for γ-globulin proteins while complex synovial fluid showed lower friction. However, in the reference, the authors applied different concentration of proteins and different specimens, which explains the disagreement of the achieved results.

Fluid 3 was used for visualization of the contact area. The friction measurement was performed simultaneously with visualization of contact area with both the variations of fluid 3, which corresponds with friction curve fluid 3 in Fig. 5. The visualized contacts are shown in Fig. 6 and 7. White spots in these images are the proteins entrapped within the contact area.

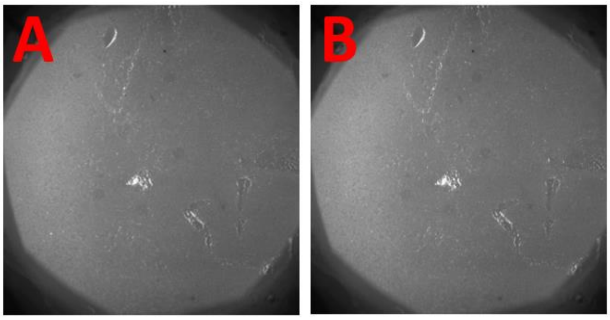

Figure 6. Contact area visualization, A, B – Fluid 3 with stained albumin at the beginning and end of the measurement.

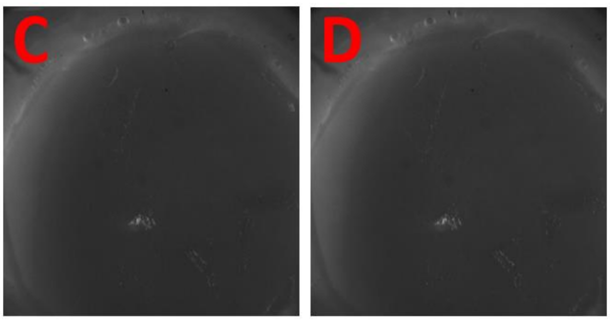

Figure 7. Contact area visualization, C, D – Fluid 3 with stained ϒ-globulin at the beginning and end of the measurement.

It is evident, that figure 6 shows higher global intensity of emitted light than figure 7, which means higher thickness of lubricant film formed by fluid 3 with labelled albumin. Figure 6 shows more and bigger aggregations of albumin particles. This fact means that the albumin protein is more represented constituent in the contact. Fig. 7 shows role of γ-globulin protein in lubrication forming process. Global intensity of emitted light is lower in comparison with Fig. 6 which is caused by lower concentration of γ-globulin proteins in fluid 3 and smaller size of γ-globulin molecules. The comparison of impacts of both marked proteins shows that the contribution of albumin is more important in terms of cartilage lubrication. There is a compliance considering the locations where the proteins are captured in both figures (Fig. 6, Fig. 7). Probably, there are small local damages of the cartilage in these places.

4. CONCLUSION

New specialized reciprocating tribometer in pin-on-plate configuration including measuring and controlling system was developed and designed. This concept connects opportunity of friction force measurement with contact area visualization. Fluorescence microscopy was chosen as a suitable optical method for visualization of cartilage contact area, because it was successfully used for soft contact visualization before. The methodology of specimen preparation and experimental setup were demonstrated in the present study. The new tribometer was validated and calibrated using commercial tribometer Bruker TriboLAB. The first pilot experiments, which were performed in order to demonstrate the possibilities of new the device, are introduced.

The pilot results revealed that the articular cartilage contact is unexplored; therefore, more extensive research is necessary. Future result could bring a significant contribution in the area of cartilage lubrication, which could eventually help in treatment of human joint diseases.

ACKNOWLEDGEMENT

This research was carried out under the project LTAUSA17150 with financial support from the Ministry of Education, Youth and Sports of the Czech Republic.

REFERENCES

[1] S.V. Eleswarapu, N.D. Leipzig, K.A. Athanasiou: Gene expression of single articular chondrocytes, Cell Tissue Res, Vol. 327, No. 1, pp. 43-54, 2007.

[2] V.C. Mow, A. Ratcliffe, A.R. Poole: Cartilage and diarthrodial joints as paradigms for hierarchical materials and structures, Biomaterials, Vol. 13, No. 2, pp. 67-97, 1992.

[3] J.B. Fitzgerald, M. Jin, A.J. Grodzinsky: Shear and compression differentially regulate clusters of functionally related temporal transcription patterns in cartilage tissue, Journal of Biological Chemistry, Vol. 281, No. 34, pp. 24095-24103, 2006.

[4] A.J. Almarza, K.A. Athanasiou, A. Kyriacos: Design characteristics for the tissue engineering of cartilaginous tissues. Annals of biomedical engineering, Vol. 32, No. 1, pp. 2-17, 2004.

[5] J. Becerra, J. A. Andrades, E. Guerado, P. Zamora-Navas, J. M. López-Puertas, A. H. Reddi: Articular cartilage: structure and regeneration. Tissue Engineering Part B: Reviews, Vol. 16, No. 6, pp. 617-627, 2010.

[6] T.M. Quinn, E.B. Hunziker, H.J. Häuselmann: Variation of cell and matrix morphologies in articular cartilage among locations in the adult human knee, Osteoarthritis and cartilage, Vol. 13, No. 8, pp. 672-678, 2005.

[7] E.M. Darling, K.A. Athanasiou: Rapid phenotypic changes in passaged articular chondrocyte subpopulations. Journal of Orthopaedic Research, Vol. 23, No. 2, pp. 425-43, 2005.

[8] S. Yarimitsu, K. Nakashima, Y. Sawae, T. Murakami: Influences of lubricant composition on forming boundary film composed of synovia constituents, Tribology International, Vol. 42, No. 11-12, pp. 1615-1623, 2009.

[9] R. W. Forsey, J. Fisher, J. Thompson, M. H. Stone, C. Bell, E. Ingham: The effect of hyaluronic acid and phospholipid based lubricants on friction within a human cartilage damage model, Biomaterials, Vol. 27, No. 26, pp. 4581-4590, 2006.

[10] T. T. Wu, X. Q. Gan, Z. B. Cai, M. H. Zhu, M. T. Qiao, H. Y. Yu: The lubrication effect of hyaluronic acid and chondroitin sulfate on the natural temporomandibular cartilage under torsional fretting wear, Lubrication Science, Vol. 27, No. 1, pp. 29-44, 2015.

[11] D. Nečas, M. Vrbka, F. Urban, I. Křupka, M. Hartl: The effect of lubricant constituents on lubrication mechanisms in hip joint replacements: Journal of the mechanical behavior of biomedical materials, Vol. 55, pp. 295-307, 2016.

[12] D. Nečas, M. Vrbka, P. Šperka, M. Druckmüller, P. Skládal, P. Štarha, I. Křupka, M. Hartl: Qualitative analysis of film thickness in rolling EHD contact by fluorescence technique, In Modern Methods of Construction Design, pp. 615-622, Springer, Cham, 2014.

[13] A. C. Moore, D. L. Burris: New Insights Into Joint Lubrication, Tribology & Lubrication Technology, Vol. 72, No. 2. pp. 26-30, 2016.

[14] J. Katta, Z. Jin, E. Ingham, J. Fisher: Effect of nominal stress on the long term friction, deformation and wear of native and glycosaminoglycan deficient articular cartilage, Osteoarthritis and cartilage, Vol. 17, No. 5, pp. 662-668, 2009.

[15] A. C. Cilingir: Effect of rotational and sliding motions on friction and degeneration of articular cartilage under dry and wet friction, Journal of Bionic Engineering, Vol. 12, No. 3, pp. 464-472, 2015.

[16] E. Northwood, J. Fisher: A multi-directional in vitro investigation into friction, damage and wear of innovative chondroplasty materials against articular cartilage. Clinical Biomechanics, Vol. 22, No. 7, pp. 834-842, 2007.

[17] J. E. Pickard, J. Fisher, E. Ingham, J. Egan: Investigation into the effects of proteins and lipids on the frictional properties of articular cartilage. Biomaterials, Vol. 19, No. 19, pp. 1807-1812, 1998.

[18] T. Murakami: Importance of adaptive multimode lubrication mechanism in natural and artificial joints, Proceedings of the Institution of Mechanical Engineers, Part J: Journal of Engineering Tribology, Vol. 226, No. 10, pp. 827-837, 2012.

Serbian Tribology Society

SERBIATRIB '19

16th International Conference on Tribology

Faculty of Engineering University of Kragujevac

Kragujevac, Serbia, 15 – 17 May 2019

EFFECT OF HYALURONIC ACID MOLECULAR WEIGHT ON FRICTION OF ARTICULAR CARTILAGE

David REBENDA[1,*], Pavel ČÍPEK[1], Martin VRBKA[1], Ivan KŘUPKA[1]
[1]Brno University of Technology, Brno, Czech Republic
*Corresponding author: David.Rebenda@vut.cz

Abstract: *Hyaluronic acid (HA) is among others one of the component of synovial fluid (SF) and is the main component which affects the rheology of SF. However, during various degenerative joint diseases like osteoarthritis, the concentration and molecular weight of HA in SF is decreasing. In recent times, injections with exogenous HA are gaining popularity as a one of the methods for non-invasive treatment of osteoarthritis. Exogenous HA should improve rheological properties of osteoarthritic SF and has also many physiological effects. One of the key parameters which affects the rheology of HA and the efficiency of viscosupplementation is the molecular weight of HA. In this study, the changes in coefficient of friction between intact porcine cartilage and glass plate during reciprocating sliding tests were analyzed to understand how the changes in molecular weight of HA affects the friction of articular cartilage model. The changes in friction between osteoarthritic SF and mixtures of SF and HA with different molecular weight were also analyzed to assess the significance of exogenous HA molecular weight on cartilage friction after viscosupplementation.*

Keywords: *hyaluronic acid, friction, biotribology, synovial fluid, viscosupplementation*

1. INTRODUCTION

Articular cartilage is a biological tissue which covers sliding surfaces in big synovial joints like hip or knee. Its porous structure is mainly composed of collagen fibers and proteoglycans [1]. Gaps between matrix are filled with SF which is mainly composed of water, proteins, etc. Interaction between these two phases stands behind its excellent tribological characteristics. Cartilage maintains great lubricating properties with extremely low friction and minimal wear under physiological conditions. It can also absorb impact loads quite well.

Osteoarthritis is one of the most common diseases of musculoskeletal system. These days, it afflicts about 70 % of 70 year olds [2]. It is characterized by excessive wear of cartilage structure which leads to higher friction and distraction of cartilage lubrication mechanism. Progression of osteoarthritis is also connected to changes in composition of SF [3]. Osteoarthritic SF is diluted by inflammatory effusion and the concentration and molecular weight of HA is lower [4].

The original theory about viscosupplementation, presented by Balazs et al. [5], assumed improvement of SF rheology by exogenous HA. Higher viscosity and better viscoelastic properties of synovial fluid should lead to lower friction and better shock absorption abilities. However, the positive effect of viscosupplementation on patients can be observed even after six months after viscosupplemenatiton [6], so exogenous HA has also some physiological effects such as reduction of inflammation or synthesis of endogenous HA in joint capsule.

One of the key parameters which affects the rheological properties of HA is its molecular weight. Other SF constituents do not have effect on SF rheology [7], so HA is also the main constituent which affects rheology of whole SF. HA with higher molecular weight has higher viscosity and exhibits better viscoelastic properties [8]. Even better results can be measured for cross-linked HA [9]. Addition of HA to osteoarthritic SF leads to better rheology of SF whilst results are strongly dependent on HA properties [10,11].

Reduction of friction by HA was already proved. HA solutions showed lower values of coefficient of friction compared to the simple solutions like phosphate buffer saline (PBS) [12] or Ringers solution [2]. Unlike the rheology, interaction between HA and other SF constituents plays an important role. Mixture of HA and phospholipids [13] leads to lower friction compared to simple phospholipids solution. Molecules of protein γ-globulin and HA have different electric charge so their molecules attract each other and form complex structures which contributes to the lower friction [14,15]. On the other hand, albumin and HA have the same electric charge and they repel each other. This interaction is unworthy for the reduction of friction [14,15]. Molecular weight of HA should also be one of the parameters which affects the friction of articular cartilage. However, no one focused on this problematic so far.

2. MATERIALS AND METHODS

2.1 Experimental methods

Frictional measurements were performed on a commercial tribometer Bruker UMT TriboLab in a pin-on-plate configuration (Fig. 1). Coefficient of friction was investigated as a function of time for the sliding pair of stationary glass plate from optical glass (B270) and moving porcine cartilage specimen. Cartilage specimen was loaded with constant load of 5 N which corresponds to contact pressure of 0.8 MPa. The sliding speed of 10 mm/s was selected and the reciprocating stroke was set to 20 mm. Contact was fully flooded with the tested lubricant. Both the lubricant and the contact pair were heated to 37 °C via heating cartridges mounted in the stainless steel chamber.

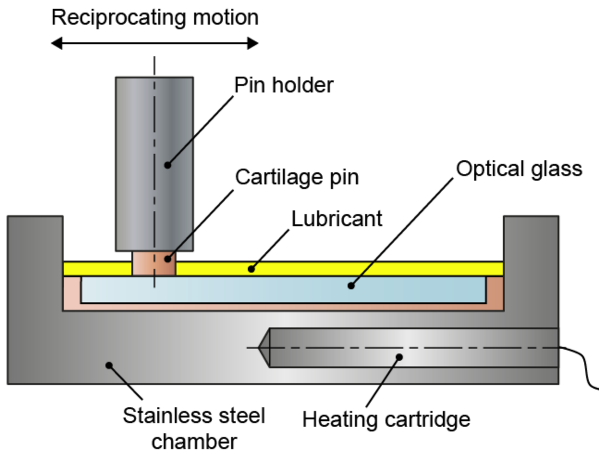

Figure 1. Scheme of experimental apparatus

Before each experiment, unloaded cartilage sample was immersed in the lubricant for 320 seconds. In the end of this preliminary phase, cartilage was loaded and the friction test started immediately. After 300 seconds (75 cycles, sliding distance of 2 780 mm), the sliding test was interrupted and the cartilage was unloaded for another 320 seconds. This unloaded phase is important for rehydration of cartilage specimen. Subsequently, the reciprocating test was restarted immediately after reloading and continued for another 300 seconds. The unloading phase was repeated two times so three tests under the same conditions were performed. Coefficient of friction was evaluated based on the values of normal and friction forces measured by biaxial force sensor mounted to the pin holder.

2.2 Materials

Cartilage specimen with underlying subchondral bone was taken from porcine femur. Cylindrical specimen of 5,6 mm diameter with intact cartilage layer was harvested from femoral head with a hollow drill. Specimen was prepared within few hours after slaughter.

Extracted cartilage was stored in PBS solution in freezer at -20 °C. This procedure should slow down the biological degradation of the cartilage tissue. Szarko et al. [16] also showed that this approach does not change the mechanical properties of the cartilage. Cartilage was stored in a freezer for no longer than one week. Half an hour before the experiments, cartilage was removed from the freezer to thaw naturally at room temperature.

In an effort to understand the effect of HA molecular weight on the friction of cartilage, the first series of experiments was performed using simple HA solutions with different molecular weight. In total, five HA solutions with HA concentration of 20 mg/ml and molecular weight of 77 kDa, 350 kDa, 640 kDa, 1 060 kDa and 2 010 kDa were tested. Solutions were prepared from HA powder by dissolution of required amount of powder in PBS. Solution was stirred by a magnetic stirrer and heated to 50 °C for at least 3 hours to ensure the proper dissolution of HA.

Table 1. Composition of model SF

	Albumin	γ-globulin	HA	Phospholipids
Concentration (mg/ml)	24.9	6.1	1.49	0.34

In the second series of the tests, HA solutions were mixed with model synovial fluid to analyze the effect of HA molecular weight on reaction between HA and SF components and to show how the changes in HA molecular weight affect the friction in cartilage-on-glass contact lubricated by HA and SF solution. Composition of synovial fluid was based on research performed by Galandáková el al. [3] where authors performed an extensive study focused on analysis of composition of SFs of different orthopedic patients. Composition of tested model SF should correspond to the SF of patients with osteoarthritis. Exact composition of SF and concentrations of individual components are stated in Table 1. SF was mixed with HA solution by magnetic stirrer in 1:1 ratio. This ratio is commonly used in medical practice during viscosupplementation.

3. RESULTS AND DISCUSSION

Higher molecular weight of pure HA solution leads to higher viscosity [8] but results of frictional measurements showed that higher viscosity of solution does not affect the friction in cartilage-on-glass contact. Figure 2 shows the results of coefficient of friction measurements for three HA solutions with different molecular weight – 350 kDa, 640 kDa and 2 010 kDa. Values of coefficient of friction varies for all the tested samples between 0,02 and 0,03 at the end of each measurement substep. Therefore, the effect of molecular weight of HA on friction in cartilage-on-glass contact seems to be negligible.

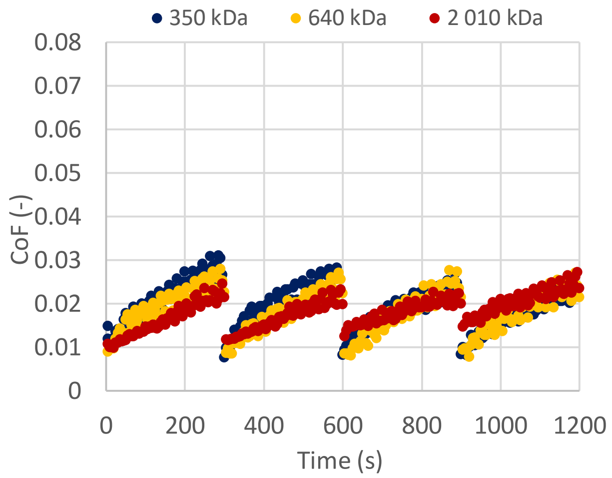

Figure 2. CoF as a function of a time for pure HA solutions with different molecular weight

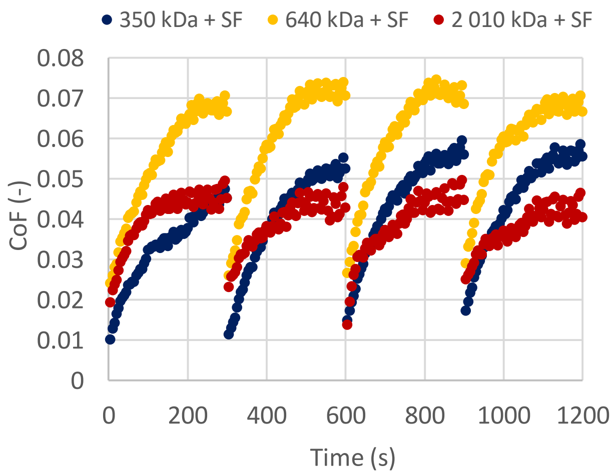

Figure 3. CoF as a function of a time for SF mixed with HA solutions with various molecular weight

Contrary to these results, Kwieciski et al. [17] observed linear dependence between HA molecular weight and friction. Higher molecular weight led to lower values of coefficient of friction in cartilage-on-cartilage contact.

Figure 3 shows results of experiments with mixtures of model SF and HA solutions. Results show higher values of coefficent of friction compared to the tests with simple HA solutions. Higher friction is probably caused by dilution of HA with water from SF and by reactions between HA and other SF components [13-15]. The effect of molecular weight is still minimal. The difference in coefficient of friction between solutions in Fig. 3 is only about 0,03 at the end of experimental substeps.

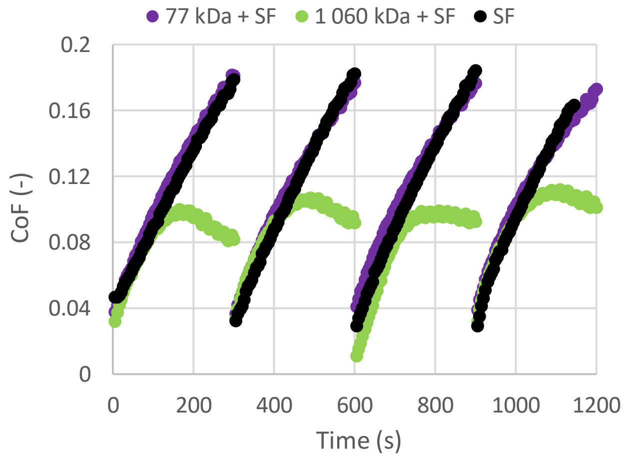

Figure 4. CoF as a function of a time for simple SF and mixtures with HA solutions with various molecular weight

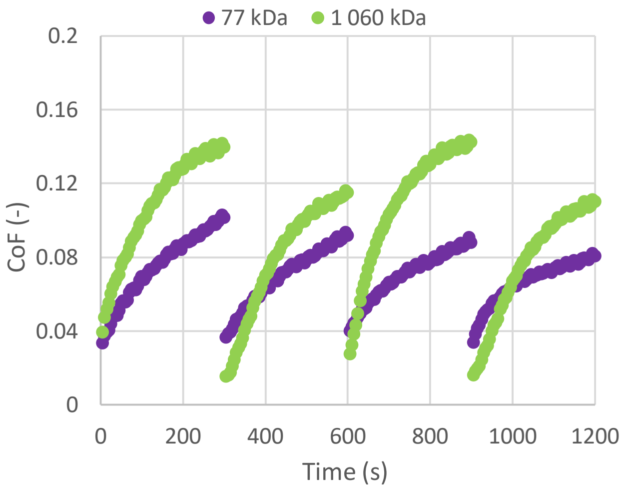

Figure 5. CoF as a function of a time for pure HA solutions with different molecular weight

Comparison of mixed solutions with simple osteoarthritic SF (Fig. 4) shows significant decrease of friction compared to the solutions in Fig. 3. These data support the theory about importance of HA in lowering of friction in osteoarthritic synovial joint. However, following tests with HA mixture solutions with molecular weight of 77 kDa and 1 060 kDa (Fig. 4) showed different results. Especially in the case of 77 kDa , the values of coefficient of friction are very similar to the results of simple SF. This is probably due to the adsorption of proteins on the surface of articular cartilage [14]. All the experiments were measured with one sample of articular cartilage. It is apparent that after the measurement with pure model SF, the structure of cartilage is saturated with proteins. These adsorbed proteins then influence the subsequent experiments. In the case of mixed solution with 1 060 kDa HA, the amount of adsorbed proteins is lower, so the results are more similar to other mixtures in Fig. 3.

This theory was subsequently tested by another experiments with HA solutions with molecular weight of 77 kDa and 1 060 kDa. Results in Fig. 5 show three and five times higher values of coefficient of friction compared to the results in Fig. 2. 77 kDa is lower molecular weight than samples which were tested before, so the friction could be different but molecular weight of 1 060 kDa lies in the range of molecular weight tested before. Measured results showed few times higher values of coefficient of friction at the end of each measurement substep which is attributed to the proteins adsorbed on the cartilage surfaces by the authors.

4. CONCLUSIONS

HA seems to be very effective in lowering of friction in cartilage-on-glass contact. However, the effect of HA molecular weight on friction seems to be insignificant for simple solutions and even for mixtures with osteoarthritic model SF. Results also showed that proteins from SF adsorb on the surface of articular cartilage and affect the results of the following tests. All the tests were performed using one sample of cartilage because repeatability across different cartilage samples is not satisfactory, in general. Therefore, some kind of cleansing process needs to be find for out further studies to remove the adsorbed proteins. Another way is to substitute cartilage with PVA hydrogel or silica – materials with similar properties but much easier to cleanse from proteins.

ACKNOWLEDGEMENT

This research was carried out under the project LTAUSA17150 with financial support from the Ministry of Education, Youth and Sports of the Czech Republic.

REFERENCES

[1] D. Lees, P. Partington: Articular cartilage, Orthopaedics and Trauma, Vol. 30, No. 3, pp. 265-272, 2016.

[2] R. Forsey, J. Fisher, J. Thompson, M. Stone, C. Bell, E. Ingham: The effect of hyaluronic acid and phospholipid based lubricants on friction within a human cartilage damage model, Biomaterials, Vol. 27, No. 26, pp. 4581-4590, 2006.

[3] A. Galandáková, J. Ulrichová, K. Langová, A. Hanáková, M. Vrbka, M. Hartl, J. Gallo: Characteristics of synovial fluid required for optimization of lubrication fluid for biotribological experiments, Journal of Biomedical Materials Research Part B: Applied Biomaterials, Vol. 105, No. 6, pp. 1422-1431, 2017.

[4] R.D. Altman: Status of hyaluronan supplementation therapy in osteoarthritis, Current Rheumatology Reports, Vol. 5, No. 1, pp. 7-14, 2003.

[5] E.A. Balazs, J.L. Denlinger: Viscosupplementation: A new concept in the treatment of osteoarthritis, Vol. 39, No. 39, pp. 3-9, 1993.

[6] P. Ghosh, D. Guidolin: Potential mechanism of intra-articular hyaluronan therapy in osteoarthritis: Are the effects molecular weight dependent?, Seminars in Arthritis and Rheumatism, Vol. 32, No. 1, pp. 10-37, 2002.

[7] Z. Zhang, S. Barman, G. F. Christopher: The role of protein content on the steady and oscillatory shear rheology of model synovial fluids, Soft Matter, Vol. 20, No. 32, pp. 5965-5973, 2014.

[8] D. Mazzucco, G. McKinley, R.D. Scott, M. Spector: Rheology of joint fluid in total knee arthroplasty patients, Journal of Orthopaedic Research, Vol. 20, No. 6, pp. 1157-1163, 2002.

[9] P. Mathieu, T. Conrozier, E. Vignon, Y. Rozand, M. Rinaudo: Rheologic behaviour of osteoarthritic synovial fluid after addition of hyaluronic acid: A pilot study, Clinical orthopadics and related research, Vol. 467, No. 11, pp. 3002-3009, 2009.

[10] P. Bhuanantanondh, D. Grecov, E. Kwok: Rheological study of viscosupplements and synovial fluid in patients with osteoarthritis, Journal of Medical and Biological Engineering, Vol. 32, No. 1, pp. 12-16, 2012.

[11] P. Bhuanantanondh, D. Grecov, E. Kwok, P. Guy: Rheology of osteoarthritic synovial fluid mixed with viscosupplements: A pilot study, Biomedical Engineering Letters, Vol. 1, No. 4, pp. 213-219, 2011.

[12] C.J. Bell, E. Ingham, J. Fisher: Influence of hyaluronic acid on the time-dependent friction response of articular cartilage under different conditions, Proceedings of the Institution of Mechanical Engineers, Part H: Journal of Engineering in Medicine, Vol. 220, No. 1, pp. 23-31, 2006.

[13] T. Murakami, S. Yarimitsu, K. Nakashima, Y. Sawae, N. Sakai: Influence of synovia constituents on tribological behaviors of articular cartilage, Friction, Vol. 1, No. 2, pp. 150-162, 2013.

[14] S. Yarimitsu, K. Nakashima, Y. Sawae, T. Murakami: Influences of lubricant composition on forming boundary film composed of synovia constituents, Tribology International, Vol. 42, No. 11-12, pp. 1615-1623, 2009.

[15] T. Murakami, K. Nakashima, S. Yarimitsu, Y. Sawae, N. Sakai: Effectiveness of adsorbed film and gel layer in hydration lubrication as adaptive multimode lubrication mechanism for articular cartilage, Proceedings of the Institution of Mechanical Engineers, Part J: Journal of Engineering Tribology, Vol. 225, No. 12, pp. 1174-1185, 2011.

[16] M. Szarko, K. Muldrew, J.E. Bertram: Freeze-thaw treatment effects on the dynamic mechanical properties of articular cartilage, BMC Musculoskeletal Disorders, Vol. 11, No. 1, pp. 231-239, 2010.

[17] J.J. Kwiecinski, S.G. Dorosz, T.E. Ludwig, S. Abubacker, M.K. Cowman, T.A. Schmidt: The effect of molecular weight on hyaluronan´s cartilage boundary lubricating ability – alone and in combination with proteoglycan 4, Osteoarthritis and Cartilage, Vol. 19, No. 11, pp. 1356-1362, 2011.

Serbian Tribology Society

SERBIATRIB '19

16th International Conference on Tribology

Faculty of Engineering University of Kragujevac

Kragujevac, Serbia, 15 – 17 May 2019

REVIEW OF EXISTING CLINICAL SOLUTIONS FOR ARTIFICIAL JOINTS

Zivana JOVANOVIC[1]*, Fatima ZIVIC[1], Nenad GRUJOVIC[1], Dragan ADAMOVIC[1], Slobodan MITROVIC[1]

[1]University of Kragujevac, Faculty of Engineering, Kragujevac, Serbia

zixi90@gmail.com, zivic@kg.ac.rs, gruja@kg.ac.rs, adam@kg.ac.rs, boban@kg.ac.rs

Abstract: *This paper presents short review of existing clinical solutions for artificial joints (knee joints, hip joints, shoulder joints, elbow joints, and spine segments). One of the main objectives in design of these implants is to minimise and eliminate friction and wear in moving elements and to provide full adhesion and cell proliferation for stable parts, such as for hip stem. Knee joint surgeries are important for young people, especially in sport, and they can be total or partial replacements. Hip joint surgeries are among the most performed procedures today, with increased number of young people undergoing it. Trabecular Metal technology, with porous structure, has emerged as the efficient approach to provide cell proliferation and adhesion of the hip stem. CoCr, Ti and stainless steel, together with polymers and ceramics are used for production of elements in hip replacement solutions. Shoulder joint replacements are very complex and require careful planning. Replacements of elbow joints are less present in comparison with other types of artificial joints. Solutions for vertebra, segments composing the spine, are the most important area of orthopedic trauma since it directly influences the quality of life in all the ways. This is important area of research that impact lives of millions humans. Beside standard production technologies and application of advanced CNC machines, 3D printing has emerged as efficient production technology offering custom design of personalised implants, very fast production with excellent quality, without significant post-processing as required in standard technologies, such as casting or forging.*

Keywords: *artificial joints, clinical solutions, trabecular metal, production technologies*

1. INTRODUCTION

Reducing friction and wear prolongs the work life of the tribomechanical system. According to [1] the laser sintered materials leads to improvement of elastic structure of the hip joint. Some authors [2] explain that spinal implants obtained by 3D printing of PEEK (Polyether ether ketone) have many advantages compared to metal, including friction and wear. Material of which implants are made has a significant impact on tribomechanical characteristics of hip joints. Hip joints have been made with three hard-on-hard prostheses: PCD (polycrystalline diamond)-on-PCD, ceramic-on-ceramic and metal-on-metal couples. They have been experimentally tested. The results confirmed that PCD on PCD have the best tribomechanical characteristics [3]. The proper selection of materials, the manufacturing technology and application of appropriate coating on implants reduce the possibility of pseudotumor formation, apoptosis, inflammation, and allergic reactions of the body [4]. Application of anti-frictional coatings on hip implants reduces the frictional heating in hip implants and therefore, there is no degradation of the material, which leads to better stability and longer work life of the implant [5]. Hip and knee joints produced by additive manufacturing are the new direction in their development, and resulting joints are lighter, and can be custom made per individual patient [6].

There are many orthopedic device companies nowadays offering numerous clinical solutions for artificial joints. Selection of the best solution is complex task, related to many factors, among which biomaterials of the implant and complexity of the surgical procedure are only some of them. Ten largest orthopedic device companies, according to sales reported for fiscal year 2017 are [21]:

1. Stryker, \$12.4B
2. DePuy Synthes, \$9.3B
3. Zimmer Biomet, \$7.8B
4. Smith & Nephew, \$4.8B
5. Medtronic (Spine Division), \$2.6B
6. DJO Global, \$1.2B
7. NuVasive, \$1.0B
8. Wright Medical, \$745M
9. Globus Medical, \$636M
10. Össur, \$569M

Comparison with that same report, 2 years ago, in 2016, shows that this market is rapidly growing and changing:

1. Stryker Corp, \$9.9 billion
2. DePuy Synthes, \$9.3 billion
3. Zimmer Biomet, \$6.0 billion
4. Smith & Nephew, \$4.7 billion
5. Medtronic Spinal, \$2.9 billion
6. DJO Global, \$1.1 billion
7. Integra Lifesciences, \$883 million
8. NuVasive Inc., \$811 million
9. Globus Medical, \$545 million
10. Wright Medical, \$415 million

It is clear that biomaterials market in orthopedics has extremely significant role in economy, beside its relation to health. Many new companies are emerging dealing with novel advanced biomaterials in this sector and improvements of existing solutions is ongoing process, aiming at ideal artificial joints.

2. BIOMATERIAL SOLUTIONS FOR KNEE JOINT

There are many commercially available solutions for knee joints that are already used in clinical practice:

- *Natural knee system* Zimmer - These tibial base plates have incorporated asymmetrical shape, thus resulting in optimal overlapping of the tibial plateau. They exhibit the best possible stability while at the same time minimizing the risk of impingement [7].
- *The NexGen Complete Knee Solution Legacy Posterior Stabilized (LPS) Flex Fixed Bearing Knee System* Zimmer – The system have been designed for patients with significant knee flexion [8].
- *NexGen CR Knee System* Zimmer and Triathlon Total Knee, Stryker - These systems provide secure flexion capability of up to 155° while maintaining the kinematic function for natural femoral rollback
- *NexGen LPS-Flex Mobile and LPS-Mobile Bearing Knee Systems* Zimmer – They have anteriorly positioned pivot point near the entry point of the anterior cruciate ligament.
- *NexGen CR Knee System* Zimmer – It provides secure flexion capability of up to 155° while maintaining the kinematic function for natural femoral rollback [9].
- *Innex System 2001* Zimmer – This system has mobile sliding surface platform and support the treatment of degenerative diseases of the knee joint [9].
- Scorpio Single Axis, Stryker has been implanted more than 500,000 worldwide, during the last 10 years.
- AOX Antioxidant Polyethylene, DePuy is made of advanced antioxidant polyethylene, thus promoting new biomaterials.
- Legion TKS, Smith & Nephew, comprising modular elements for total and partial

knee replacements. It can contain oxidized zirconium

The largest manufacturers of artificial joints today, are Zimmer (with approx 25% of all replacements today), Biomet (recently merged with Zimmer to Zimmer Biomet), DePuy, Stryker, Smith&Nephew and many smaller companies. There are also many solutions for partial knee joint replacement, such as Zimmer Gender Solutions Patello-Femoral Joint (for reduction of patellofemoral pain) and Persona Partial Knee with different gradual sizes available according to specific person [10, 11].

2.1 Revision knee system solution

Total knee replacement is one of the most successful procedures, especially important for sports injuries. However, over time, the replacement may fail for a variety of reasons and revision surgery is needed in such cases, usually total knee replacement.

Although both procedures have the same goal, to relieve pain and improve function, revision surgery is different than primary total knee replacement. It is a longer, more complex procedure that requires extensive planning, and specialized implants and tools to achieve a good result. There are currently several clinical options for revision knee systems.

The NexGen LCCK has been designed to provide stabilization related to medio-lateral, anteroposterior, or varus / valgus ligament function. This system is used when both basic ligaments have been removed and is used with shaft extensions [9].

The Zimmer Segmental System is a revision knee prosthesis to replace the distal femur, mid-femur, proximal femur, and / or entire knee in cases where extensive resection and recovery is required. This system enables complete replacement of the lower extremity, from mid-calf to hip. It is a modular system composed of leg extensions, segments, intercalar segments, sliding surfaces and distal femoral components [12].

The NexGen RH Knee has a modular joint mechanism that ensures that 95% of the load is on the femoral condyle. The femoral condyles remain centered on the tibia over the range of motion. Complex arthroplasty can involve more than one replacement solutions in one surgery, depending on the bone defects.

2.2 Manufacturing technology

Standard manufacturing technologies have been used, to produce implants with gradual changes in sizes, to fit specific patients. However, there is often a misfit of the implant in some degree. New 3D printing technologies have offered unique possibility to produce custom made implants with perfect fit to each patient, based on scan images of their own bone anatomy. Another important aspect of 3D printing is lower material loss, in comparison with standard production technologies, such as casting with subsequent processing technologies, such as cutting, polishing, drilling etc. 3D printing also enables small production batches with low cost of production and significantly less time needed for the final product.

A key element in this manufacturing process involves advanced digital imaging technology and 3D printing. The production process can start with computer tomography (CT) scan of the hip, affected knee, or ankle to ensure close resemblance of the patient anatomy. Engineers use specifi software solutions to convert CT scan images to 3D model of the implant, that is further processed by 3D printer and custom made implant produced. 3D printing can produce exact mold to cast the implant (e.g. femoral component of the knee). Post-processing usually requires polishing of the frictional surfaces to reduce wear [13]. Recently, 3D printing of metal and polymer parts has significantly advanced, enabling direct printing of the implant.

3. BIOMATERIAL SOLUTIONS FOR HIP JOINT

The hip is the second most agile joint in the human body. For that reason there are many injuries and natural defects. There are many existing clinical solutions for the complete or partial hip replacements, and some of the most used today are:

- *Fitmore stem,* Zimmer - The shape of this system is the result of close observation of individual anatomy in a large European and US patient sample. Three different medial shaft curvatures were designed. In the light of today's younger and more active patients, consideration has also been directed towards maintaining muscle tone and bone in the greater trochanter and compatibility with minimally invasive surgical procedures.
- *Alloclassic Zweymüller Shaft,* Zimmer - Since 1979, more than 500,000 hip joints have been replaced with this hip stem, making this cementless prosthesis one of the most widely used implants in the world [9].
- *CLS Spotorno hip stem* - Since 1984, this hip stem system, developed by Prof. Lorenzo Spotorno, has become one of the most successful implants in the Swedish national hip arthroplasty registry, with more than 560,000 replaced hip stems [14].
- *Zimmer M/L Taper hip prosthesis*, made of Ti-6Al-4V requires adequate bone tissue to be able to position it and provide secure mediolateral stability. This hip stem is available in 14 sizes from 4 *mm* to 22.5 *mm,* as well as standard and extended offsets.
- *CLS Brevius shaft with Kinectiv technology* enables adjustment of leg length, offset and antetorsion (Figure 1). The stem design is based on the original CLS Spotorno Hip Stem, which showed excellent survival rate of 95% in clinical use after 20 years [15]. The optimized shaft length also helps the surgeon maintain more bone and make the procedure less invasive.
- *Original M.E. Müller straight shaft* - Since its development in 1977, this system is essentially unchanged, with very good results over 20 years period. During first 26 years (1977-2003) this system was implanted more than one million times worldwide. The small proximal collar serves to compress the cement and prevent the stem from sinking into the cement. Together with the fine radiated surface of the straight shaft, a very stable anchoring of the implant was achieved.

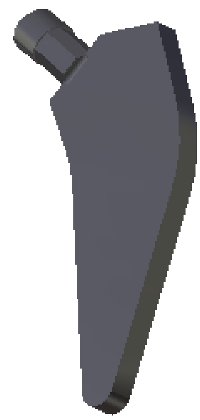

Figure 1. Hip joint in orthopedic surgery

3.1 Revision hip system solution

Revision surgeries are often needed, in case when hip replacement fails. The procedure may involve complete replacement of the previous implant, or some part of it. Clinical solutions for revision surgeries are often rather different than those used at the first surgery. Some existing solutions are described further.

The *Zimmer Trabecular Metal Acetabulum Revision System* combines Trabecular Metal technology with individualized solutions for different patients via modular design. This system is well adjusted for allogeneic bone graft without the risk of resorption or disease transmission. Important properties of the trabecular metal material include similarity to the bone in design and behaviour, close resemblance to natural bone structure, since it is three-dimensional porous material. It exhibits the highest biocompatibility among the endoprosthetic components and promotes the ingrowth of bones and soft tissue like no other material. Trabecular metal implants exhibits the following:

- 75-80% porosity: similar permeability as the bone,
- similar elasticity as bone with high strength and ductility,
- high levels of friction and stability,
- enables osteoconductivity and fixation,
- 10 years of clinical success [16, 17].

Revitan revision hip system has been designed with conical slope of 2 degrees to achieve rotational stability over 8 longitudinal ribs, which goes into the cortical bone. Its shape resembles anatomical shape for the natural antecurvation of the femur, in order to allow longer prosthesis stems without femur osteotomy to be implanted [9].

The *Wagner SL revision hip stem* has been designed to bridge the proximal bone defect for distal fixation and rotational stability. It has a proven blasted surface and a biocompatible titanium alloy. A tapered implant body and eight longitudinal ribs provide rotational stability. Different implant diameters and lengths are available to suit different patients.

3.2 Manufacturing technology

The process selection for fabricating a total hip prosthesis depends very much on the materials to use. Materials such as cobalt chrome, titanium and stainless steel are usually shaped by forging or investment casting, followed by rough machining, polishing and coating. For materials such as ultra-high molecular weight polyethylene, moulding and machining are essential. Ceramic biomaterials elements, such as alumina and zirconia femoral balls, are normally produced by sintering followed by grinding and polishing or lapping. The schematic is given in Figure 2. Polishing is one of the most efficient methods to achieve shape accuracy, surface roughness, and surface integrity of the prostheses. All of these characteristics are very important for longevity. Some elaborates that polishing has the key role in the good functioning of hip joint prostheses [18].

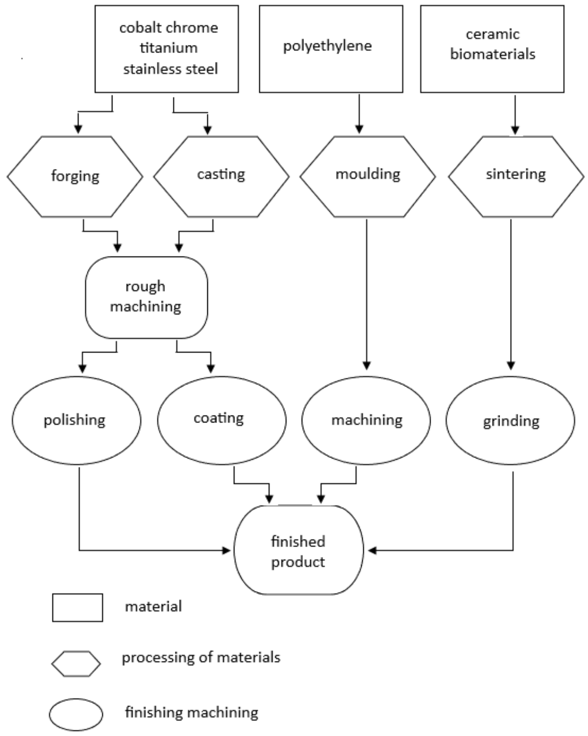

Figure 2. Manufacturing process of hip joint

4. BIOMATERIAL SOLUTIONS FOR SHOULDER JOINT

Shoulder is the most agile joint in human body. It has tremendous range of motion thus making the shoulder extremely unstable, far more prone to dislocation and injury than other joints. Surgical procedures for joint replacements are very complex and not so present as in case of other joints. There are clinical solutions for shoulder joint replacement, as the following:

- *Anatomical Shoulder Domelock System, Zimmer* - has modular design to provide accurate and reproducible reconstruction of the glenohumeral joint [9].
- *Anatomical Shoulder System, Zimmer*, has inverse / reverse system.
- The *Anatomical Shoulder Fracture, Zimmer* has been designed to treat complex fractures of the proximal humerus.

The coefficient of friction of the trabecular metal material, combined with its strength and flexibility, provides optimal initial stability. The osteoconductive properties of the trabecular structures promote vascularization and enable better bone formation and maintenance. Biomechanical tests have demonstrated higher initial, medium term and long term stability than polyethylene cemented glenoid.

4.1 Manufacturing technology

The process selection for fabricating the total shoulder prosthesis is similar to fabricating a hip joint. The mostly used materials are cobalt chrome, titanium and stainless steel and they are usually shaped by forging, followed by rough machining, polishing and coating. For materials such as ultra-high molecular weight polyethylene, moulding and machining are essential.

5. BIOMATERIAL SOLUTIONS FOR ELBOW JOINT

The elbow joint is located between the humerus in the upper arm and the radius and ulna in the forearm which allows the forearm and hand to be moved towards and away from the body. One of the existing clinical solutions is *Coonrad / Morrey elbow,* Zimmer and it has been used for a long time, also for treatment of rheumatoid and degenerative arthritis, beside fractures [19].

5.1 Manufacturing technology

The process selection for fabricating a total elbow prosthesis is consisted of ulnar, radial and humeral parts. The most used materials are titanium alloy Ti-6Al-4V for durable, lightweight construction shaped by forging, followed by rough machining, polishing and coating. Plasma spray coating provides enhanced cement fixation; implant intended to be used with bone cement for both immediate and long-term fixation. Special Poly Bushings constructed by Zimmer, with ultra-high molecular weight polyethylene, prevents metal-to metal contact, and for this materials moulding and machining are essential.

6. BIOMATERIAL SOLUTIONS FOR VERTEBRA - SEGMENTS COMPOSING THE SPINE

Each vertebra represents irregular bone. The size of the vertebrae varies according to placement in the vertebral column, spinal loading, posture and pathology. Along the length of the spine the vertebrae change to accommodate different needs related to stress and mobility. Vertebras are divided into: cervical, thoracic and lumbar. They have many functions. The main is the protection of the spine, along with mobility of the upper body, and carrying the weight of the body. They are often prone to injuries and during life vertebras goes through the pathologic changes. There are different clinical solutions related to main three areas: cervical, thoracic and lumbar vertebras. Some cervical vertebras are:

- *InViZia Anteriores Cervical Plate System* Zimmer, was developed for the anterior vertebral screw fixation of the cervical spine.
- *Trinica and Trinica Select Anterior Cervical Plate System* Zimmer are versatile implant systems that offer a wide range of plate and screw sizes to ensure better anatomical fit. These anterior cervical plate systems are designed for anterior vertebral screw fixation on the cervical spine. Secure-Twist anti-migration system secures up to three screws with a single turn of the wrist. It also provides common guidance for drilling, puncturing and screw placement.
- *TMS cervical fusion system* Zimmer is cervical spine implant made of trabecular metal. It provides a high coefficient of friction to prevent implant migration and expulsion, and has a low modulus of elasticity thus minimizing the stress shielding effect. With an average porosity of up to 80% and a uniform open-pored structure, the material closely replicates the architecture and mechanical properties of cancellous bone, and provide excellent environment for bone ingrowth and vascularization [9].

Some artificial thoraco lumbal implants are:

- *Ardis vertebral body system* Zimmer is self-distending posterior vertebral body fusion system.
- *Product Family Dynesys Dynamic Stabilizatio* Zimmer is non-fusion system for the spine, also used for degenerative diseases treatments.
- *TM-Ardis vertebral body system* Zimmer is made of trabecular metal, with an automatically-distracting implant tip, convex geometry and a wide range of sizes [9].
- *Universal Clamp spinal fusion system* Zimmer is a spinal implant system that provides segmental stability and provides compression, distraction, derotation, and transmission while maintaining pedicles and reducing contact stress on the implant and bone.

6.1 Manufacturing technology

3D printing manufacturing technology showed its benefits especially in this complex area of designing and fabricating spinal implants. The process starts from 3D scanning, as shown in Figure 3.

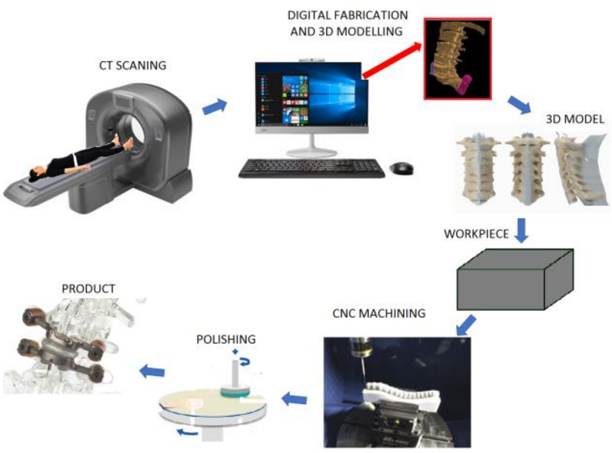

Figure 3. Vertebra manufacturing process based on CT scan images

Generated image slices are further imported into the 3D modelling software. Once all the images have been imported, appropriate image processing and meshing is done to eliminate errors due to different organic matter images, along with segmentation [20]. After all parameters have been set, the 3D model of the cervical spine can be generated and optimised prior to 3D printing or some other production route. Elements can be processed at CNC machines, with machining and polishing as final steps.

7. CONCLUSION

The main objective of this paper was to present different existing solutions of implants related to artificial joints that are clinically used: knee joints, hip joints, shoulder joints, elbow joints, and spine segments. There are many existing clinical solutions, depending on health issues that they address. Selection of specific solution depends on several factors, whereas health condition, type of trauma, implant material and complexity of surgical procedure are some of them.

The most beneficial materials for joints are novel titanium alloys and trabecular metals, together with new approaches in their processing and fabrication. New 3D printing technologies have emerged and enabled custom design and fabrication of joints' elements, according to specific patient needs. New technologies have shortened the production time and offered better fit of the implant to the human environment. However, even with many exisiting artificial joints solutions, and good results in clinical practice, they all have some drawbacks at certain percentage of patients, or developing over functional time. Research is still needed, related to the development of new materials and improvement of existing ones, as well as production technologies which governs the majority of functional properties of the implant.

ACKNOWLEDGEMENT

This work was supported by SELECTA (No. 642642) H2020-MSCA-ITN-2014 project; and Ministry of Science and Technological Development, Serbia, projects no. III41007, no. ON174028 and no. TR35021.

REFERENCES

[1] A. Sorin Mihai Croitoru; Adrian Pacioga; C. Stanca Comsa Personalized hip implants manufacturing and testing Applied Surface Science, Vol. 417, pp. 256-261, 2017.

[2] A.H.M Javaid: Polyether ether ketone (PEEK) and its 3D printed implants applications in medical field: An overview Clinical Epidemiology and Global Health Available online 4 January 2019

[3] M.S. Uddin, L.C. Zhang: Predicting the wear of hard-on-hard hip joint prostheses, Wear Vol. 301, No. 1–2, pp. 192-200, 2013.

[4] A.C. Marsh, N.P Chamorro, X. Chatzistavrou: Long-*term performance and failure of orthopedic devices*, Bone Repair Biomaterials (Second Edition) Regeneration and Clinical Applications Woodhead Publishing Series in Biomaterials, pp. 379-410, 2019.

[5] M.S. Uddin, P. Majewski: Frictional Heating in Hip Implants – A Review, Procedia Engineering Vol.56, pp. 725-730, 2013.

[6] S.P Narra, P.N. Mittwede, S. De Vincent Wolf, K. L. Urish: Additive Manufacturing in Total Joint Arthroplasty, Orthopedic Clinics of North America, Vol. 50, No. 1, pp 13-20, 2019.

[7] A.A. Hofmann, J.D. Evanich, R.P. Ferguson, M.P. Camargo: Ten to 14 year clinical follwup of the cementless Natural-Knee System, CORR No. 388, 2001.

[8] S. Naiwa: Hyperflexion in Japanese knee replacement design and clinical results, Paper presented at: The Wellinghton Knee Surgery Unit's Eighth International Teaching Meeting; March 5-6, 1998; London, England.

[9] Website: http://www.zimmersuisse.ch/ accessed: 29.03.2019.

[10] J.R. Foran et al: Long-term Survivorship and Failure Modes of Unicompartmental Knee Arthroplasty, Clin Orthop Relat Res, Vol. 471, No. 1, pp. 102–108, 2013.

[11] R.A. Berger et al: Results of unicompartmental knee arthroplasty at a minimum of ten years of follow-up, J Bone Joint Surg Am, Vol. 87, No. 5, pp. 999-1006, 2005.

[12] W.G. Ward, D. Haight, P. Ritchie, S. Gordon, J.J. Eckardt: Dislocation of rotating hinge total knee prosthesis. A biomechanical analysis, J Bone Joint Surg Am, Vol. 85-A, No.3, pp. 448-453, 2003.

[13] http://www.todaysmedicaldevelopments.com/article/tmd0614-knee-implants-innovations-manufacturing/ accessed: 28.03.2019

[14] www.jru.orthop.gu.se accessed: 29.03.2019.

[15] P.R. Aldinger et al: Uncemented Grit-Blasted Straight Tapered Titanium Stems in Patients Younger than Fifty-five Years of Age. Fifteen to Twenty-Year Results, J Bone Joint Surg Am, Vol. 91, pp. 1432–1439, 2009.

[16] J. Bobyn, G. Stackpool, S. Hacking, M. Tanzer, J. Krygier: Characteristics of bone in-growth and interface mechanics of a new porous tantalum biomaterial, J Bone Joint Surg, Vol. 81-B, No. 5, pp. 907-914, 1991.

[17] J. Bobyn, S. Hacking, J. Krygier, S. Chan, K. Toh, M. Tanzer: Characterization of a new porous tantalum biomaterial for reconstructive surgery, Scientific Exhibition: 66th Annual Meeting of the American Academy of Orthopaedic Surgeons, 04-08.02.1999, Anaheim, CA.

[18] L.C. Zhang, E.C.S. Kiat, A. Pramanik: A Briefing on the Manufacture of Hip Joint Prostheses, Advanced Materials Research, Vol. 76-78, pp. 212-216, 2009.

[19] B.F. Morrey, R.A. Adams, R.S. Bryan: Total replacement for post-traumatic arthritis of the elbow, J Bone Joint Surg, Vol. 73-B, No. 4, pp. 607-612, 1991.

[20] D.M. Dimitrov, *Development of a Framework for the Manufacture of Customized Titanium Cervical Cage Implants Using Additive Manufacturing*, University of Stellenbosch, South Africa, 2014.

[21] https://www.odtmag.com/issues/2018-08-01/view_features/2018-top-10-global-orthopedic-device-firms/accessed:17.04.2019.

Serbian Tribology Society

SERBIATRIB '19

16th International Conference on Tribology

Faculty of Engineering University of Kragujevac

Kragujevac, Serbia, 15 – 17 May 2019

NANOINDENTATION OF ZIRCONIUM DENTAL CERAMIC PREPARED WITH DIFFERENT FINISHING TECHNIQUES

Marko PANTIĆ[1,2], Dragan DŽUNIĆ[1*], Miroslav BABIĆ[1], Slobodan MITROVIĆ[1], Suzana PETROVIĆ SAVIĆ[1], Aleksandar ĐORĐEVIĆ[1], Aleksandra KOKIĆ ARSIĆ[2]

[1]University of Kragujevac, Faculty of Engineering, Kragujevac, Serbia

[2]Higher Technical Professional School in Zvečan, Zvečan, Serbia

*Corresponding author: dzuna@kg.ac.rs

Abstract: *This paper describes the nanomechanical characteristics of Zirconium (IPS e.max ZirCAD, Ivoclar Vivadent) treated with three different surface finishing techniques: polishing, glazing and grinding, using the Anton Paar nanoindentation. The hardness (HV) and Elastic modulus (E) of the surface structure were presented as results of nanoindentation measurements. Nanoindentation tests were done using Berkovich diamond pyramid and the experiment was organized in a 3x4 array. Indentation imprints were investigated using the optical and Atomic Force Microscopy. Also, AFM analysis was used in order to present the 3D surface topography and roughness parameter Ra. The obtained results show that the nanomechanical properties mostly depend of finishing technique.*

Keywords: *Zirconium, Nanoindentation, different finishing techniques: polishing, glazing, grinding.*

1. INTRODUCTION

The history of dental ceramics dates back to the period of ancient pharaohs, when dental crowns and prosthesis were made of glass or ivory and with the help of gold wire fixed at their places [1].

The increased demand for aesthetics led to the development of all ceramic restorations. The first use of zirconia in dentistry was present in the production of dental pins, fixed prosthesis and dental implants, and very often in the literature it was possible to find the term "white steel" [2,3]. However, the real breakthrough in aesthetic dentistry had come with the development of CAD/CAM technology [4]. Zirconium in combination with new CAD/CAM technology is increasingly being used and developed, due to its excellent characteristics of material, as well as due to the precision and rapid production. The production of dental restorations in this way allows perfect adherence of crowns and bridges to the gingiva, thus providing patients with excellent quality, comfort and longevity of compensation in all load zones [5,6].

The surface roughness and structural defects have big impact on mechanical properties of ceramic materials [1]. It is known that more favourable conditions are made with high roughness of 0.2 mm for higher appearance of tooth plaque and cavities [7]. On the other side, the smooth surface of the intraoral structure ensures the comfort of the patient and facilitates oral hygiene [8-10]. Moreover, inadequate polishing of the contact surface of the restoration can lead to residual surface roughness, which directly disturbs the mechanical and aesthetic characteristics of the contact surface of the material itself [11-13].

The aim of this study is to identify the nanomechanical properties of Zirconium (IPS e.max ZirCAD, Ivoclar Vivadent), under different finishing techniques (polishing, glazing and grinding), using the Anton Paar Nanoindentation. The obtained results of nanoindentation measurements were performed in order to define the Hardness (*HV*) and the Elastic modulus (*E*) of the surface structure as a function of the applied indentation load.

2. EXPERIMENTAL PROCEDURE

2.1 Material and samples preparation

IPS e.max ZirCAD is a presintered yttriumstabilized zirconium oxide block (Y - TZP) for the CAD/CAM technology (Fig. 1a). There are different sizes of *IPS e.max ZirCAD* blocks depending on the oral zone and the type of restoration that is being performed. The block is white, chalk structure and in poisoned state it is distinguished by porous morphology (50%). The hardness of the raw material is very small, which enables fast and easy processing of the block on the CAD/CAM system in the desired shape. After forming, the material is sintered in a high temperature furnace specially developed for oxide ceramics at a temperature of 1500 ° C. During the 8-hour sintering process, the crystals form the final tetragonal homogeneous structure and obtain their final bending strength of over 900 MPa. Chemical composition of *IPS e.max ZirCAD* is given in Table 1 [14].

Table 1. Chemical composition of *IPS e.max ZirCAD* [15]

Standard composition	(in % by weight)
ZrO2	87 – 95
Y2O3	4 – 6
HfO2	1 – 5
Al2O3	0.1 – 1

Experimental investigations were realised on 3 samples with dimensions 18x14x12 mm. After sintering, the contact surfaces of samples are prepared with 3 different finishing techniques (polishing, glazing and grinding), Figure 1b. Finishing techniques have been described thoroughly in a previous publication [16].

a)

b)

Figure 1. a) *IPS e.max ZirCAD* ceramic; b) samples prepared with 3 different finishing techniques

The surface of the samples was cleaned with 70 % alcohol using a soft cotton cloth, in order to remove any remaining surface contaminants. After that, samples were ultrasonically cleaned in distilled water for 30 min, and allowed to dry at room temperature.

2.1 Surface roughness

Nanomechanical tests were preceded by the AFM analysis in order to determine the roughness parameters Ra and 3D topography of each sample (Figure 2). Surface roughness was measured by AFM of NT-MDT manufacturers, which is located at the Tribology center on the Faculty of Engineering in Kragujevac. The measurement range on all samples is 100x100 µm and the surfaces roughness is measured along the same reference length. The obtained results of roughness parameter Ra is presented in Table 2.

Table 2. Comparative view of R_a under different finishing techniques of Zirconium

Measuring range, 100x100 µm	**Roughness parameter, R_a**
The polished surface	10.728 nm
The glazed surface	16.655 nm
The grinded surface	0.415 µm

Presented results, show that lowest values of Ra have polished finishing technique, as expected. It should be noted that aesthetic dentistry has always strived for material contact surface to be as smooth as possible [1].

2.2 Nanoindetation

Nanoindentation tests were done using *Anton Paar Nanoindenter*, which is located at the Tribology center on the Faculty of Engineering in Kragujevac.

Table 3 shows the defined conditions of nanoindentation test.

Table 3. Defined conditions of nanoindentation test

Test method
- Berkovich three-sided diamond pyramid - 3x4 array - Ambient temperature: 23±2 °C
Loads
- 50, 100, 200 and 400 mN
The loading and unloading rate
- 100 mN/min for load of 50 mN - 200 mN/min for load of 100 mN - 400 mN/min for load of 200 mN - 800 mN/min for load of 400 mN
Maximum load holding time
- 10 s

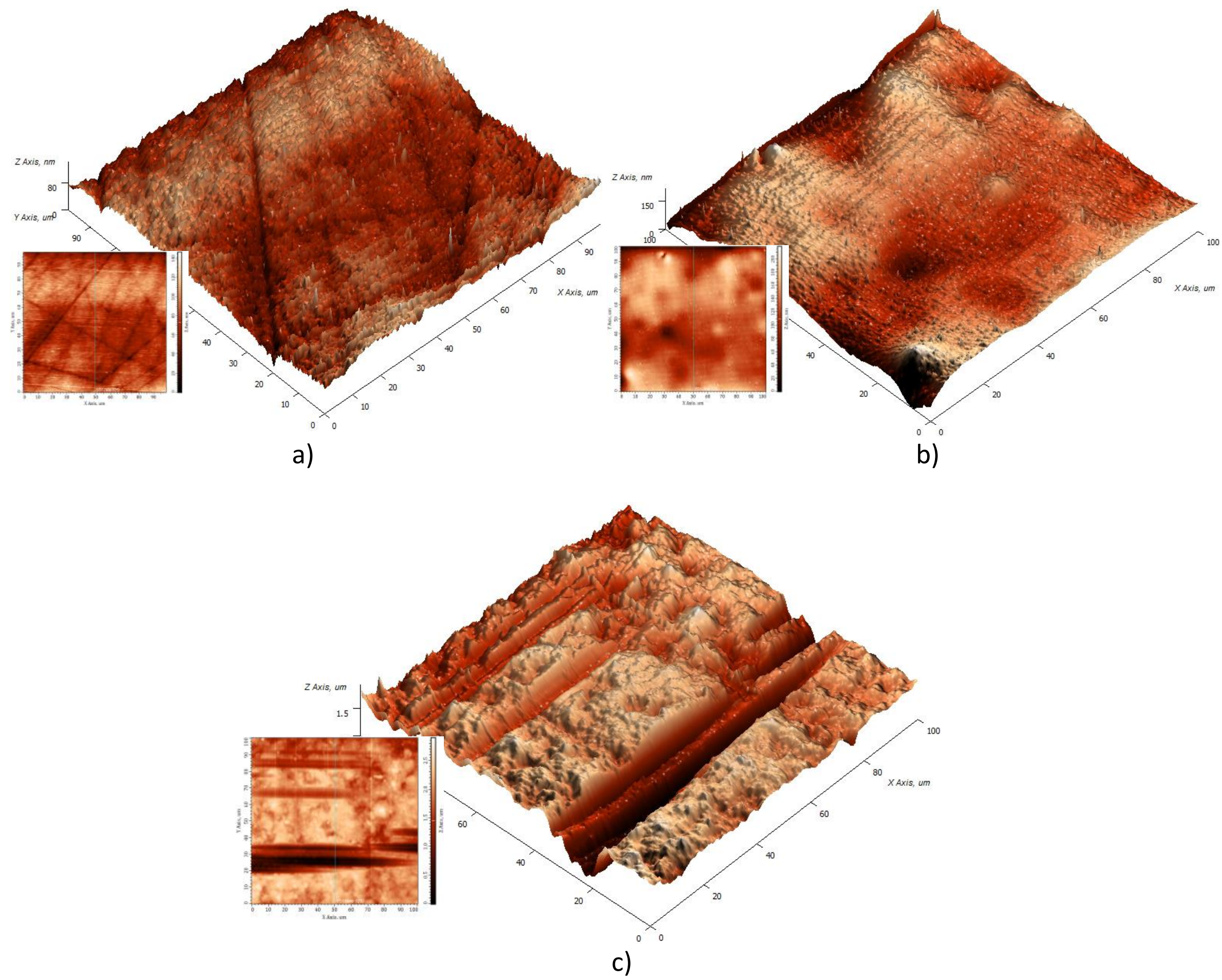

Figure 2. AFM analysis (3D topography) of samples: a) polished, b) glazed, and c) grinded surface

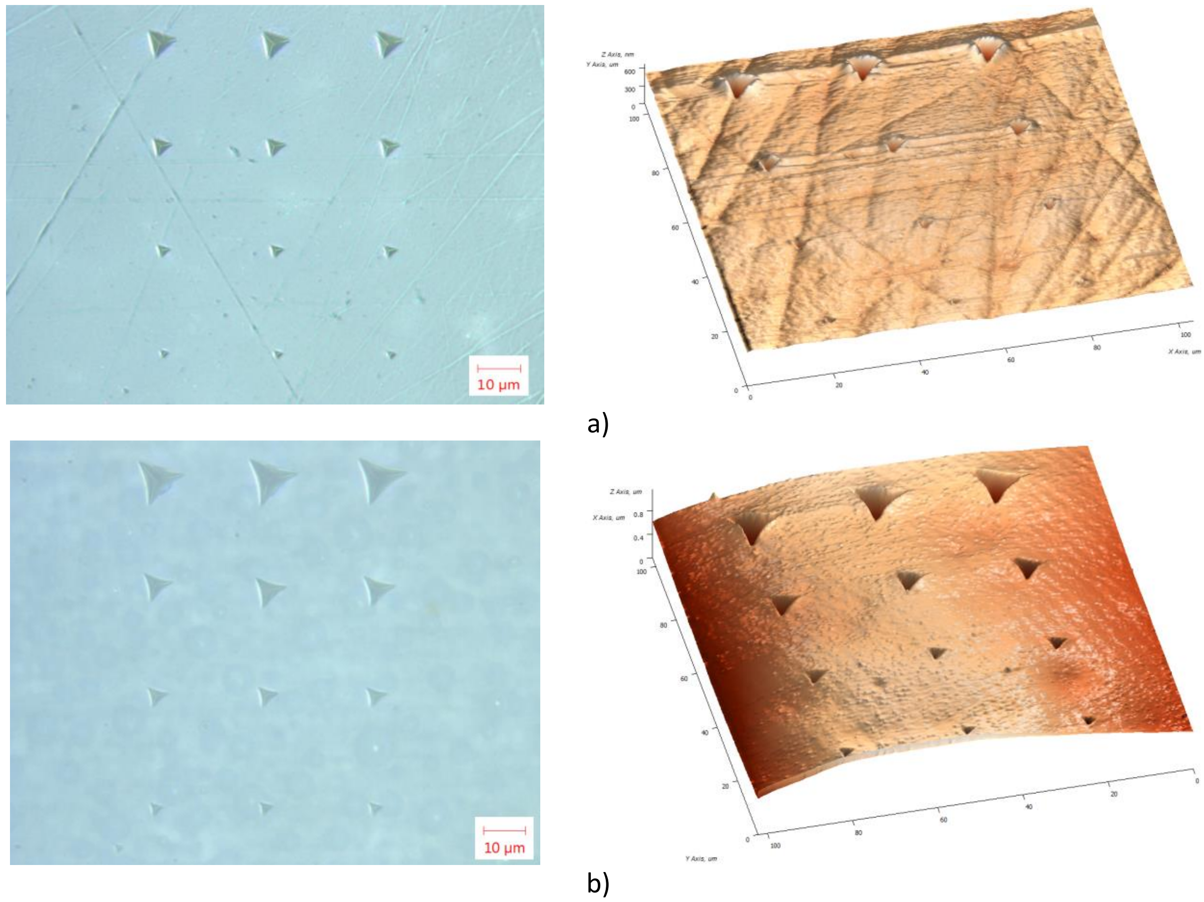

Figure 3. Indentation view of 3x4 array: a) polished and b) glazed surface

Each test was repeated three times, because the experiment was organized in a 3x4 array (Fig. 3). Distance between centres of imprints was 30 µm, it was taken into account that imprints were not too close to each other to avoid influence of work hardening on mechanical properties of tested material. The Poisson's ratio for LGC was 0.300 [1].

A Berkovich diamond indenter (three-sided pyramidal) was used for all indentations. Indentation imprints were investigated using the Optical and AFM microscopy.

3. RESULTS AND DISCUSION

The obtained results of nanoidentation values, hardness (*HV*) expressed in Vickers units and elastic modulus (*E*) are presented in Table 4.

In order to better understand the shown values in Table 4, the Figure 4 presents a histogram comparison of the obtained Hardness and Elastic modulus results of the tested material. From the Figure 4 it can be clearly seen that the highest value of hardness and Elastic modulus has a polished surface. Also, is visible trend for polished and grinded surfaces that hardness and elastic modulus decreases in a small range with increasing indentation load.

Table 4. Mean values of indentation process performed on Zirconium (*IPS e.max ZirCAD*) prepared with different finishing techniques

IPS e.max ZirCAD	Loads of indentation							
	50 mN	100 mN	200 mN	400 mN	50 mN	100 mN	200 mN	400 mN
	Hardness *(HV)*, Vikers				**Elastic modulus *(E)***, [GPa]			
The polished surface	1576.17	1558.33	1504.53	1494.10	288.17	278.85	269.03	257.72
The glazed surface	784.65	787.36	1120.46	1211.60	88.51	92.80	112.32	127.35
The grinded surface	1528.33	1427.40	1203.43	1103.84	282.51	271.64	260.16	249.12

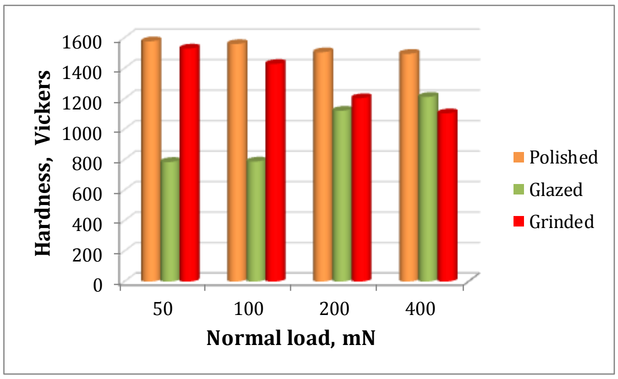

a)

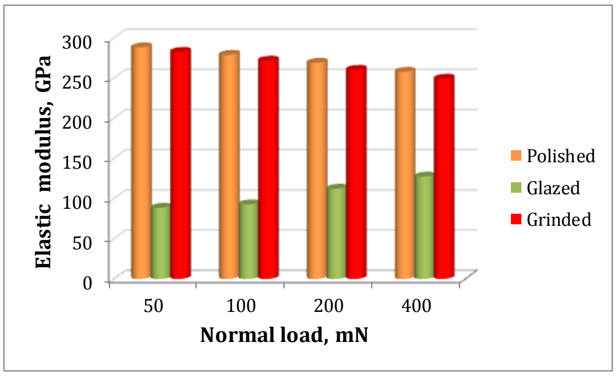

b)

Figure 4. Nanoindentation results: a) Hardness (*HV*); and (b) Elastic modulus (*E*)

The phenomenon of decreasing hardness by increasing the indentation load is known under the term "Indentation size effect (ISE)" [17,18].

Figures 4a and 4b clearly show that the glaze has a significant impact on the obtained results, i.e., provides poorer mechanical properties of the material itself. Glazed sample does not have a trend as polished and grinded surfaces, the trend of decreasing the hardness and elastic modulus with the increase of the indentation load is completely diametric compared to the results of the polished and grinded surfaces. In the case with smaller indentation loads (50 and 100 mN), the hardness value is well below the real hardness of the material itself (~785 Vickers). The thickness of the glaze has a large influence on the obtained results, because the penetration depth of the indenter into the glaze surface is much bigger than in the base material. The measured values of the indenter penetration depth, ranging from 670-950 nm with the indentation loads of 50 and 100 mN, are insufficiently large to properly characterize the real value of the hardness of the base material. The same conclusion can be attributed to the results of the Elastic modulus for the glazed surface, because the obtained results are characterized by the same trend as the results of the measured hardness values. Based on that it can be concluded that the obtained values of hardness and elastic modulus of glazed zirconium can be neglected when applying selected values of indentation loads.

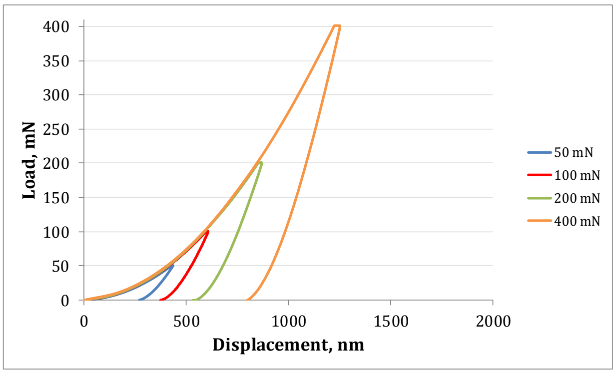

a)

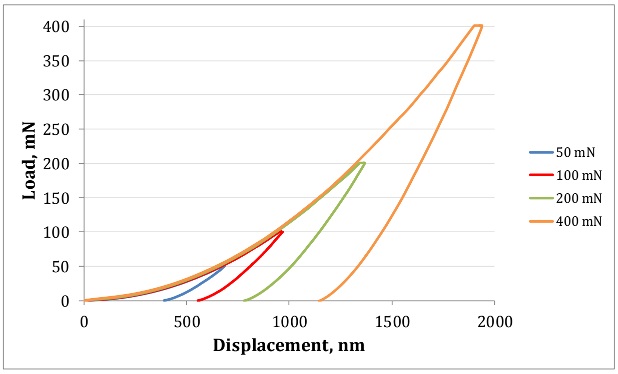

b)

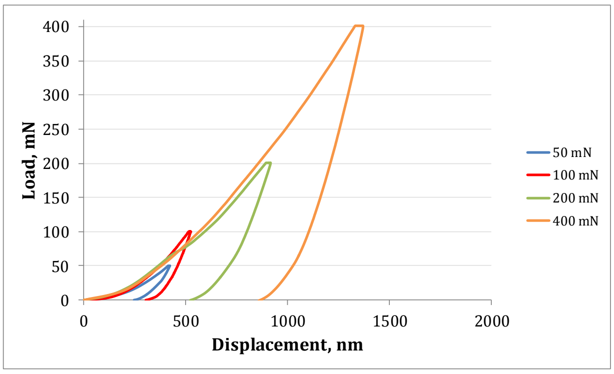

c)

Figure 5. Load-displacement curves under different finishing techniques: a) polished; b) glazed; and c) grinded

The Figure 5 shows the load-displacement curves for different prepared samples as mean values of three indentations for loads of 50, 100, 200 and 400 mN. The curves have proper form and clearly show that it is the maximum load holding time properly selected [19,20].

The diagrams (Figure 5) clearly show that the indentation depth proportionally increases with the increase of indentation load. There are no major differences in indentation curves for polished and grinded tested samples, while the glazed curve has a mild deviation from the previous two samples. The glazed finishing treatment has a significantly higher value of the load-displacement (maximum indentation depth) compared to other finishing techniques [1].

The Figure 6 shows representative indentation imprints (400 mN) of Zirconium under different finishing techniques, obtained on optical (x100) and AFM microscopy. Nanoindentation on grinding sample was presented just by optical microscopy because it was impossible to find indentation imprints on AFM due to their small size of imprints and big surface roughness of the material.

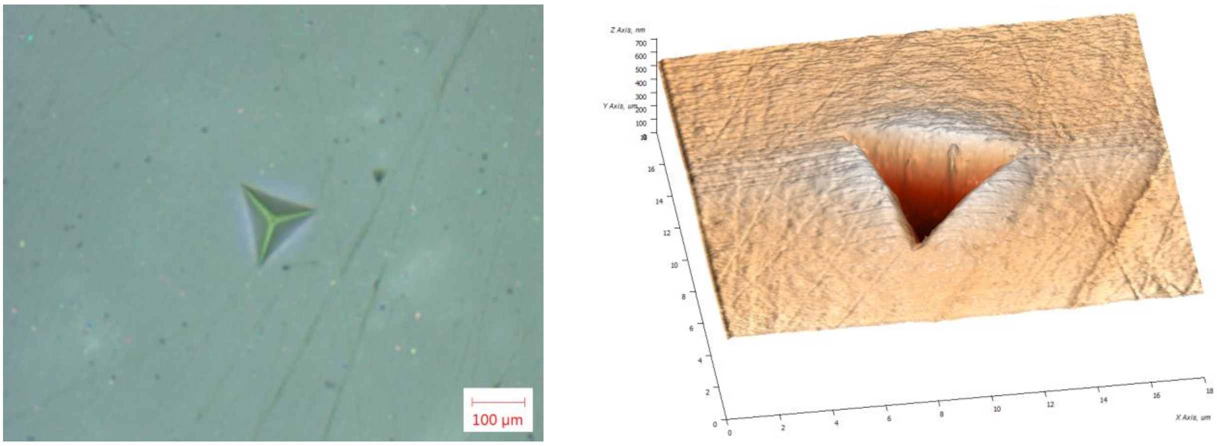

a)

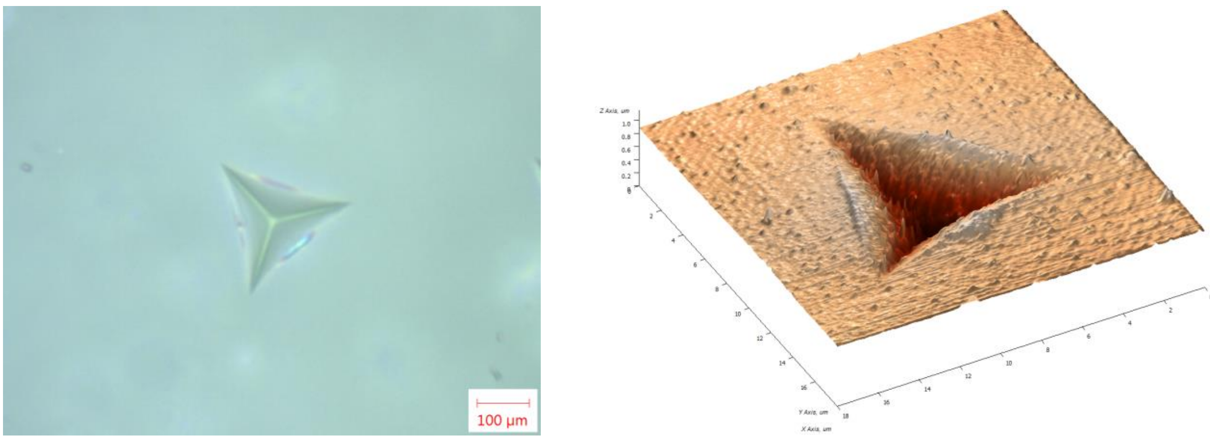

b)

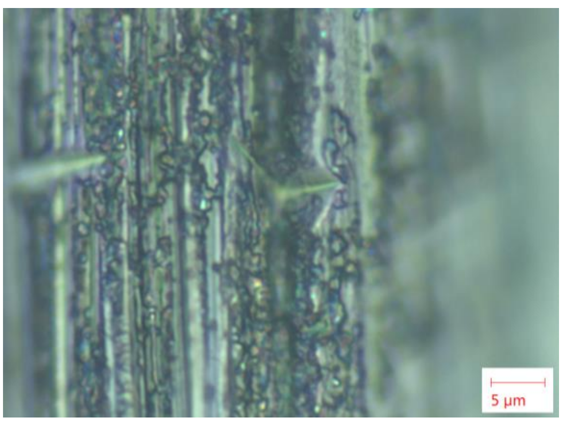

c)

Figure 6. Indentation imprints at load of 400 mN, analysed by optical (left, x100) and AFM microscopy (right): a) polished; b) glazed and c) grinded surface

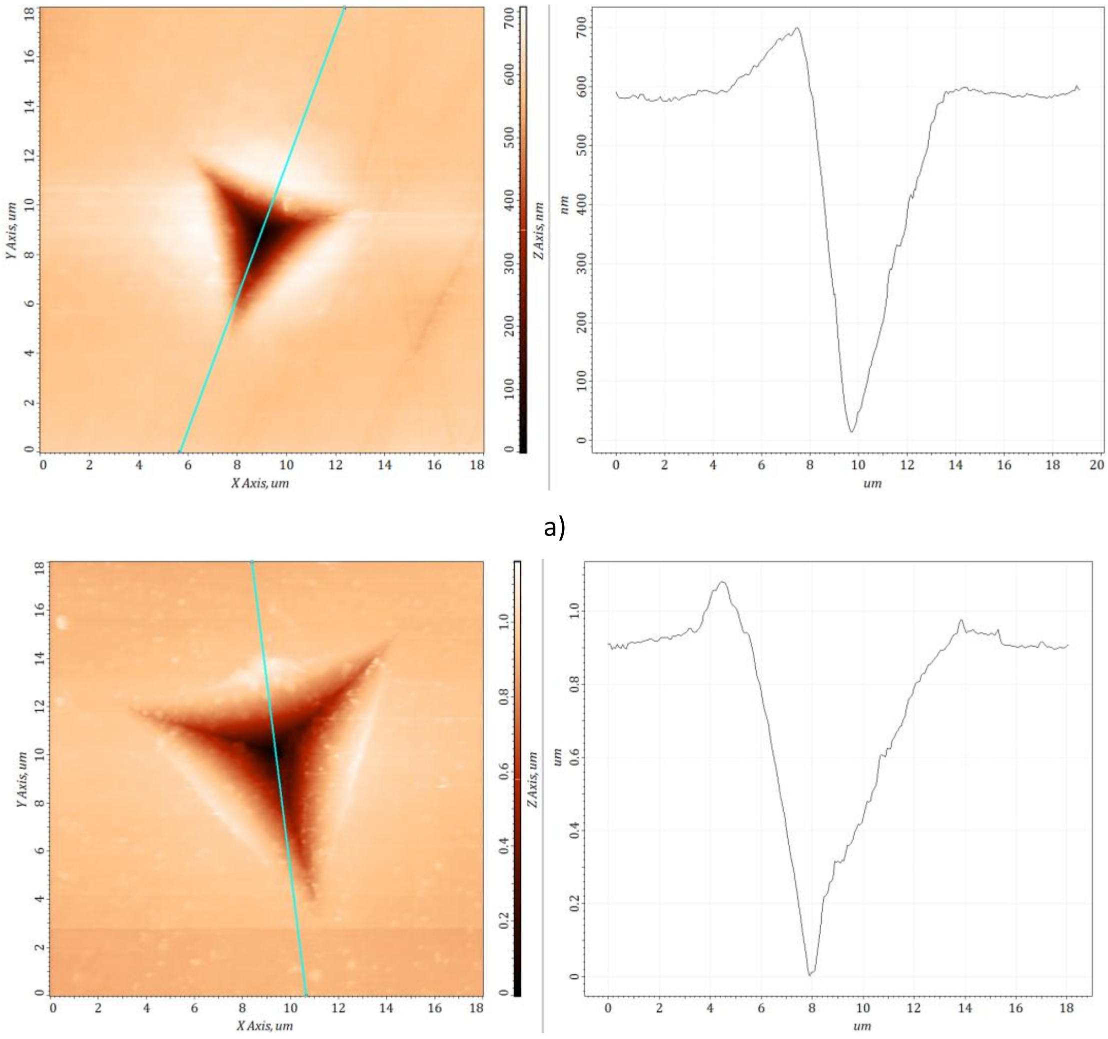

Figure 7. 2D view AFM analysis of nanoindentation and cross-section of the imprints depth profile, under indentation load of 400 mN, a) polished, and b) glazed surface

Indentation imprints are clearly formed with visible edges in the surface layer of material. A mild plastic deformation around imprints can be seen in Figures 7a and 7b (brighter zone), as a result of displacement of material (piling-ups) during the indenter penetration.

Material plastic creep along the side of the indentation marks can be considered as the basic physical process which softens the material due to the phenomenon of shear [21]. This is why the material plastic creep, by shearing, causes certain structural changes in the field of the material itself, which means that the deformation in that zone is much faster than in the other zone of the material [22]. Materials that move from the piling-up condition to the sinking-in condition become much more elastic [23]. This also shows the importance of the Elastic modulus, which present a measure of the material stiffness. Since the polished and glazed surfaces are most common in practice, therefore a mechanical property of materials has big importance on lifespan of dental restoration because they mostly depend on quality of the finishing techniques.

5. CONCLUSION

The mechanical properties of ceramic materials largely depend of the surface roughness and structural defects of the material itself. Based on the obtained results, it can be concluded that nanomechanical properties mostly depend on applied surface finishing techniques.

The polished sample has the highest value of Hardness and Elastic modulus. The obtained results of hardness and elastic modulus of glazed zirconium can be neglected when applying selected values of indentation loads (50, 100, 200 and 400 mN), because of the unrealistic obtained values. The thickness of the glaze has a large influence on the obtained results, because the penetration depth of the indenter into the glaze surface is much bigger than in the base material.

The presented results may be helpful in better comprehension of the nanomechanical behaviour of dental ceramic based on zirconium under different finishing techniques and thus facilitate the design, selection and CAD/CAM manufacture for dental restorations.

ACKNOWLEDGMENTS

Research presented in this paper was supported by Ministry of Education, Science and Technology Development of Republic of Serbia, Grant TR-35021.

REFERENCES

[1] M. Pantić, *Tribological Characterization of Advanced Dental Materials*, PhD thesis, University of Kragujevac, Faculty of Engineering, 2017.

[2] R.C. Garvi, R.H.J. Hannink, R.T. Pascoe, *Ceramic Steel?*, Nature Vol. 258, pp. 703–704, 1975.

[3] S. Sandhaus, H. Pasche*, Tenon radiculaire en zircone pour la realisation d'inlay-cores tout ceramiques*, Tribune dentaire, Vol. 2, pp. 2–17, 1994.

[4] C. Piconi, *Proprietà della zirconia*. In: Piconi C., Rimondini L., Cerroni L., editors. La Zirconia in Odontoiatria. Milano: Elsevier Masson, 2008.

[5] T. Sato, M. Shimada, *Transformation of Yttria-Doped Tetragonal ZrO2-Polycrystals by Annealing in Water*, J. Am. Ceram. Soc., Vol. 68, No. 6, pp. 356–359, 1985.

[6] F.F. Lange, G.L. Dunlop, B.I. Davis, *Degradation During Aging of Transformation-Toughened ZrO2-Y2O3 Materials at 250 °C*, J. Am. Ceram. Soc., Vol. 69, pp. 237–240, 1986.

[7] C.M.L. Bollen, P. Lambrechts, M. Quirynen, *Comparison of surface roughness of oral hard materials to the threshold surface roughness for bacterial plaque retention: a review of the literature*, Dent Mater, Vol. 13, pp. 258-269, 1997.

[8] M. Ono, T. Nikaido, M. Ikeda, *Surface properties of resin composite materials relative to biofilm formation*, Dent Mater J, Vol. 26, pp. 613-622, 2007.

[9] S.R. Jefferies, *Abrasive finishing and polishing in restorative dentistry: a state-of-the-art review*, Dent Clin North Am, Vol. 51, pp. 379-397, 2007.

[10] L.M. Cavalcante, K. Masouras, D.C. Watts, L.A. Pimenta, N. Silikas, *Effect of nanofillers' size on surface properties after toothbrush abrasion*, Am J Dent, Vol. 22, pp. 60-64, 2009.

[11] M. Morgan, *Finishing and polishing of direct posterior resin restorations*, Pract Proced Aesthet Dent, Vol. 16, pp. 211-217, 2004.

[12] H. Lu, L.B. Roeder, L. Lei, *Effect of surface roughness on stain resistance of dental resin composites*, J Esthet Restor Dent, Vol. 17, pp. 102-108, 2005.

[13] K.Z. Kantorski, R. Scotti, L.F. Valandro, *Surface roughness and bacterial adherence to resin composites and ceramics*, Oral Health Prev Dent, Vol. 7, pp. 29-32, 2009.

[14] T. Völkel, *Report No 17* - Research and Development Ivoclar Vivadent AG, FL-9494 Schaan / Liechtenstein, 2006.

[15] P. Bühler-Zemp, T. Völkel, *Scientific Documentation IPS e.max ZirCAD*, Ivoclar-Vivadent AG, Schaan, 2005.

[16] M. Pantić, S. Mitrović, M. Babić, D. Jevremović, T. Kanjevac, D. Džunić, D. Adamović, *AFM Surface Roughness and Topography Analysis of Lithium Disilicate Glass Ceramic*, Tribology in Industry, Vol. 37, No. 4, pp. 391-399, 2015.

[17] S.J. Bull, T.F. Page, E.H. Yoffe, *An explanation of the indentation size effect in ceramics*, Journal Philosophical Magazine Letters, Vol. 59, pp. 281-288, 1989.

[18] F. Pöhl, S. Huth, W. Theisen, *Detection of the indentation-size-effect (ISE) and surface hardening by analysis of the loading curvature C*, International Journal of Solids and Structures, Vol. 84, pp. 160-166, 2016.

[19] W.C. Oliver, G.M. Pharr, *An improved technique for determining hardness and elastic modul ususing load and displacement sensing indentation experiments*, J. Mater. Res., Vol. 7, pp. 1564–1583, 1992.

[20] D. Džunić, S. Mitrović, M. Babić, I. Bobić, M.

Pantić, D. Adamović, B. Nedeljković, *Nanoindentation of Za-27 Alloy Based Nanocomposites Reinforced with Al_2O_3 Particles*, Tribology in Industry, Vol. 37, No. 4, pp. 413-420, 2015.

[21] A.V. Sergueeva, N.A. Mara, J.D. Kuntz, E.J. Lavernia, A.K. Mukherjee, *Shear band formation and ductility inbulk metallic glass*, Philos. Mag., Vol. 85, pp. 2671–2687, 2005.

[22] A.-R. Alao, L. Yin, *Nano-mechanical behaviour of lithium metasilicate glass–ceramic*, Journal of the mechanical behavior of biomedical materials, Vol. 49, pp. 162–174, 2015.

[23] J. Alcala, A.C. Barone, M. Anglada, *The influence of plastic hardening on surface deformation modes around Vickers and spherical indents*, Acta Mater., Vol. 48, pp. 3451–3464, 2000.

[24] A.-R. Alao, L. Yin, *Loading rate effect on the mechanical behavior of zirconia in nanoindentation*, Materials Science & Engineering A, Vol. 619, pp. 247–255, 2014.

[25] A.-R. Alao, L. Yin, *Nano-scale mechanical properties and behaviour of pre-sintered zirconia*, Journal of the mechanical behaviour of biomedical materials, Vol. 36, pp. 21–31, 2014.

[26] C.M. Smith, D. Jiang, J. Gong, L. Yin, *Determination of the mechanical behavior of lithium disilicate glass ceramics by nanoindentation & scanning probe microscopy*, Materials Chemistry and Physics, Vol. 148, pp. 1036-1044, 2014.

[27] J.A. Arsecularatne, J.P. Dingeldein, M. Hoffman, *An in vitro study of the wear mechanism of a leucite glass dental ceramic*, Biosurf. Biotribol., Vol. 1, pp. 50–61, 2015.

[28] M. Pantić, S. Mitrović, M. Babić, D. Jevremović, D. Džunić, T. Kanjevac, D. Adamović, *Effects of Different Finishing tehniques onto Nanomechanical and Nanotribological Characteristics of Lithium Disilicate Glass Ceramics*, Tribological Journal BULTRIB, Vol. 6, pp. 137-146, 2016.

Authors Index

UTS
TRIBOLOG

A MULTI-FUNCTIONAL (MUDULAR) TRIBOMETER

- ✓ MODULAR TESTING PLATFORM
- ✓ FLEXIBLE DESIGN
- ✓ ACCURATE MEASUREMENT
- ✓ VERTICAL LOADING / DEAD WEIGHT OPTIONS
- ✓ USER-FRIENDLY SOFTWARE

MAIN MODULES

Pin-on-Disk (Rotary)

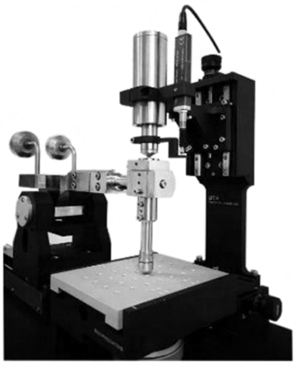

Linear (Reciprocating)

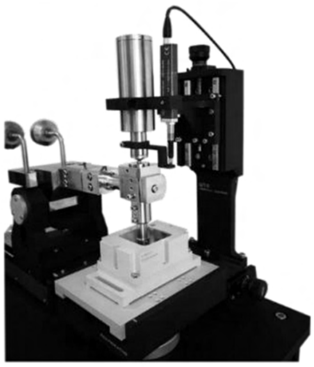

Lubrication- Lquid cup

High Temperature

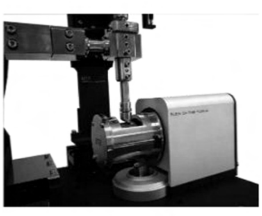

Block-on-Ring

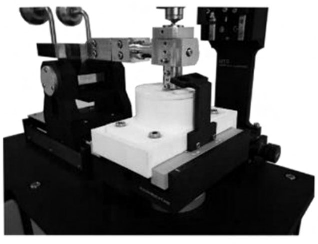

Tribo-corrosion

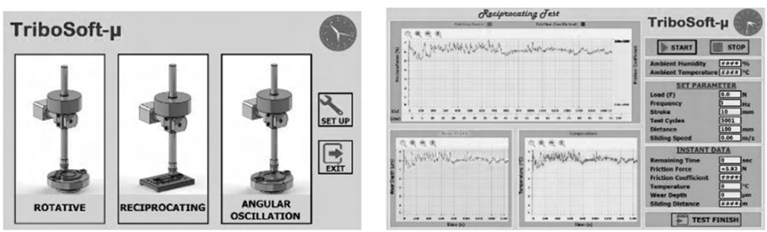

TriboSoft-μ
A tribological software

UTS Inc., Üniversite Mah., Hastane Cad. No:33A/102, 61080 Ortahisar/TRABZON
Tel: +90 533 335 3063 www.uts-design.com info@utsdesign.com

CIP - Каталогизација у публикацији
Народна библиотека Србије, Београд

62

PROCEEDINGS on Engineering Sciences / editors Slobodan Mitrović, Miladin Stefanović. – Vol. 1, no. 1 (2019)- . - Kragujevac : Faculty of Engineering University, 2019 - (Kragujevac : Inter Print). - 26 cm

Godišnje.
ISSN 2620-2832 = Proceedings on Engineering Sciences
COBISS.SR-ID 275951372

SERBIATRIB ‘19